I A V C E I

Field excursions to volcanic terranes in the western United States, Volume I: Southern Rocky Mountain region

Edited by Charles E. Chapin and Jiri Zidek

MEMOIR 46 New Mexico Bureau of Mines & Mineral Resources 1989

A DIVISION OF
NEW MEXICO INSTITUTE OF MINING & TECHNOLOGY

INTERNATIONAL ASSOCIATION OF VOLCANOLOGY AND CHEMISTRY OF THE EARTH'S INTERIOR (IAVCEI)
1989 GENERAL ASSEMBLY

Sponsors

U.S. Geological Survey
Institute for the Study of Earth and Man, Southern Methodist University
Los Alamos National Laboratory
New Mexico Bureau of Mines and Mineral Resources
University of New Mexico
Institute for Geophysics and Planetary Physics, University of California
National Science Foundation
American Geophysical Union
U.S. Department of Energy
Sandia National Laboratories

Organizing Committee

Chairman: MICHAEL DUNGAN, *Dallas*
Secretary: SCOTT BALDRIDGE, *Los Alamos*
Program: PETER LIPMAN, *Denver*
Field Trips: WOLFGANG ELSTON, *Albuquerque*
Publications: CHARLES CHAPIN, *Socorro*
Local Arrangements: GRANT HEIKEN, *Los Alamos*
KENNETH WOHLETZ, *Los Alamos*
IAVCEI Secretary General: HANS-ULRICH SCHMINCKE, *Bochum*

FRONT COVER—Shiprock, in northwestern New Mexico, is a 500 m high erosional remnant of an Oligocene diatreme. It consists mainly of minette (a potassic lamprophyre) tuff breccia cut by a few thin, irregularly shaped dikes. The tuff breccia contains abundant inclusions of the sedimentary rocks through which the vent penetrated as well as fragments of plutonic rocks from the Precambrian basement, approximately 2.7 km beneath the present summit. Mantle xenoliths are also present. Crude bedding formed by fallback of pyroclastic ejecta defines a shallow, saucer-shaped structure near the top and indicates that the original crater was not much higher. The tuff breccia is strongly cemented with calcite and is much more resistant to erosion than surrounding Cretaceous shales. Conspicuous vertical jointing, exploited by weathering and erosion, has produced a castellated appearance. Three dikes radiate from Shiprock; the south dike, shown here, extends 9 km from the vent. Photo H. L. James.

BACK COVER—Digitally enhanced multispectral Landsat image of north-central New Mexico centered on the Jemez Mountains and Valles caldera (Quaternary). The northern suburbs of Albuquerque are just visible along the Rio Grande at bottom edge of image. Santa Fe can be seen at lower right and Taos at upper right. The Sangre de Cristo Mountains form the right margin and the early Tertiary San Juan Basin occupies the left one-third of the image. The very straight Nacimiento oblique-slip fault is conspicuous at left center and trends N4°W along the west edge of the Nacimiento Range. The snow-covered mountains at top center are the Tusas Mountains. The Albuquerque, Española, and San Luis Basins form a right-stepping chain of en-echelon rift basins between the Sangre de Cristo Mountains on the right (east) and the Jemez and Tusas Mountains on the left (west). The Rio Grande Gorge and scattered stratovolcanoes of the Taos Plateau volcanic field (4.5–2 Ma) are prominent geomorphic features in the San Luis Basin at upper right. A southwest-trending prong of Servilleta Basalt from the Taos Plateau caps Black Mesa near the confluence of the Rio Grande and Chama River at right center. Black Mesa parallels the Embudo fault zone, an accommodation zone between the east-tilted San Luis Basin to the north and the west-tilted Española Basin to the south. The Embudo fault, the Valles caldera, and basalt-capped Mesa Prieta and Cebolleta Mesa at lower left lie on the Jemez lineament, a crustal flaw of Precambrian ancestry which has been one of the most active magmatic zones in the United States for the past 5 m.y. See Excursion 17B for details of the Valles caldera and Jemez volcanic field. Excursions 5A and 8A cover the southwestern projection of the Jemez lineament; Excursion 18B visits the Embudo fault zone, the Taos Plateau, and the northeastern extension of the Jemez lineament. Excursion 15B examines the Questa caldera (26 Ma) with its plutons and molybdenum mines (just visible at far upper right). The Dulce swarm of early-rift mafic dikes (23.5–27 Ma) is visible at upper left.

GEOPIC image provided by Earth Satellite Corporation, 7222 47th Street, Chevy Chase, Maryland 20815.

Memoir 46

New Mexico Bureau of Mines & Mineral Resources

A DIVISION OF
NEW MEXICO INSTITUTE OF MINING & TECHNOLOGY

Field excursions to volcanic terranes in the western United States, Volume I: Southern Rocky Mountain region

Edited by Charles E. Chapin and Jiri Zidek
New Mexico Bureau of Mines & Mineral Resources, Socorro, New Mexico 87801

Published for
IAVCEI GENERAL ASSEMBLY
Santa Fe, New Mexico, USA
June 25–July 1, 1989

SOCORRO 1989

Original Printing

Published by Authority of State of New Mexico, NMSA 1953 Sec. 63–1–4
Printed by University of New Mexico Printing Services, May 1989

Available from New Mexico Bureau of Mines & Mineral Resources, Socorro, NM 87801

Preface

This is Volume I of a two-volume set of field guides to volcanic terranes in the western United States published in conjunction with the General Assembly of the International Association of Volcanology and Chemistry of the Earth's Interior (IAVCEI), Santa Fe, New Mexico, June 1989. Volume I (Memoir 46) contains nine field guides to volcanic terranes in the Southern Rocky Mountain region. Volume II (Memoir 47) contains seven field guides to volcanic terranes in the Cascades and Intermountain West. Both volumes contain a combination of scientific papers and road logs designed to familiarize the reader with the geology of a particular volcanic field and then lead him through it. The technical papers contain much new data and should serve as useful references for many years.

The individual field guides were compiled from contributions of three to eleven authors each; a total of 105 authors contributed to the 16 field guides. Because of the large number of authors, their geographic separation, and the short time from submittal to publication, it was not possible to completely standardize the format. However, a detailed table of contents is available in the front of each volume. A list of references is provided at the end of each field guide. Abstracts of papers presented at the sessions in Santa Fe have been published as Bulletin 131 (340 pp.). The two volumes of field guides and the abstract volume can be obtained from Publications Office, New Mexico Bureau of Mines & Mineral Resources, Socorro, New Mexico 87801.

On behalf of IAVCEI and the Organizing Committee for the Santa Fe General Assembly, the editors take this opportunity to thank the authors for their contributions and the University of New Mexico Printing Services for a job well done.

Charles Chapin
Jiri Zidek


E A N

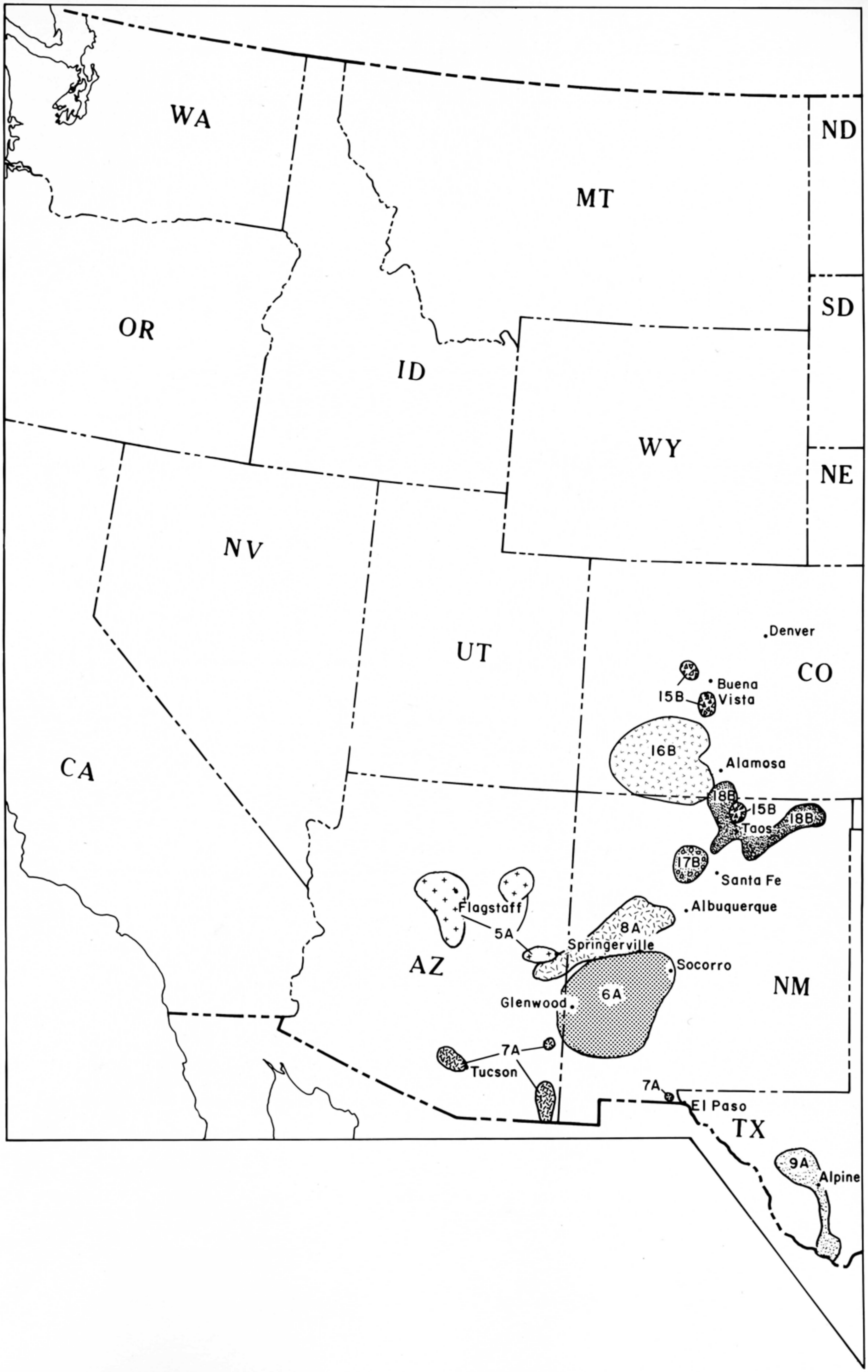

WA
MT
ND
SD
OR
ID
WY
NE
NV
UT
CO
Denver
Buena
Vista
15B
16B
Alamosa
CA
18B
15B
Taos
18B
17B
Santa Fe
Flagstaff
Albuquerque
5A
8A
Springerville
AZ
Socorro
NM
6A
Glenwood
7A
Tucson
7A
El Paso
TX
9A
Alpine

Contents

EXCURSION 5A: Miocene to Holocene volcanism and tectonism of the southern Colorado Plateau, Arizona

George E. Ulrich[1], Christopher D. Condit[2], Karen J. Wenrich[3], Edward W. Wolfe[4], Richard F. Holm[5], L. David Nealey[6], F. Michael Conway[7], Jayne C. Aubele[8], and Larry S. Crumpler[8]

[1]*U.S. Geological Survey, Reston, Virginia 22092;* [2]*University of Massachusetts, Amherst, Massachusetts 01003;* [3]*U.S. Geological Survey, Denver, Colorado 80225;* [4]*U.S. Geological Survey, Cascades Volcano Observatory, Vancouver, Washington 98661;* [5]*Northern Arizona University, Flagstaff, Arizona 86011;* [6]*U.S. Geological Survey, Flagstaff, Arizona 86001;* [7]*Michigan Technological University, Houghton, Michigan 49931;* [8]*Brown University, Providence, Rhode Island 02912*

Summary

A five-day field trip along the southern perimeter of the Colorado Plateau provides an overview comparison of the eruptive styles, lava compositions, and tectonic settings of five volcanic fields in Arizona (Fig. 1). An added stop in the Zuni–Bandera field of New Mexico will be made on the sixth day en-route to Santa Fe. The contrasts and similarities to be found illustrate the variety of volcanic processes that have operated over the past 17 m.y. Attention will be directed mainly to volcanic features that are less than 8 Ma, and the youngest volcano, Sunset Crater, which was active about 900 years ago.

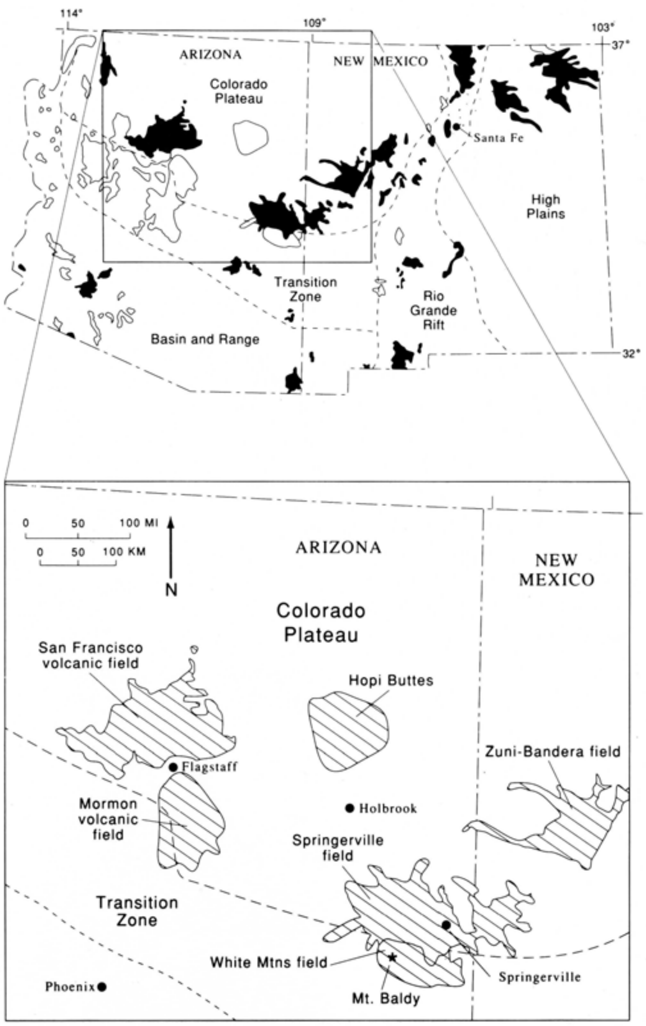

FIGURE 1—Distribution of late Cenozoic basaltic fields in Arizona and New Mexico (from Luedke and Smith, 1978). Dark areas, volcanic rocks of Pliocene to Holocene age (mostly younger than 5 Ma); unshaded outlined areas, volcanic rocks of Miocene or older age (6–16+ Ma). Enlarged area shows volcanic fields visited on Excursion 5A.

Field observations will begin for early arrivals in Flagstaff (our point of assembly) with a half-day visit to the rim of the partly glaciated Inner Basin of San Francisco Mountain to view its interior structure beneath Humphreys Peak, the highest point in Arizona. The first full day of Excursion 5A (part A) will begin south of Flagstaff in the Mormon volcanic field, where it straddles the boundary between the 2100 m high, relatively undeformed Colorado Plateau and the extensionally deformed Arizona Transition Zone. The structural control of basaltic cones and fissure vents by underlying fracture systems is pronounced in this field. A well-developed pattern of northwest-trending normal faults disrupts the Pliocene and older lava flows of the Mormon field, while the expression of faulting in other generally younger volcanic fields is much less prominent.

On the second day (part B), we will visit volcanic and structural features of the San Francisco field north of the Transition Zone. Structural elements there are more widely spaced than in the Mormon field and occur in three principal directions (northwest, northeast, and north–south). Five major eruptive centers of silicic to intermediate lavas occur on or near prominent fault zones and at projected intersections of fault zones. Aligned vents of basaltic composition are common and, as in the Mormon field, apparently reflect the ease of upward movement of low-viscosity magmas along simple fracture systems.

Day 3 of Excursion 5A (part C) will begin with a drive from Flagstaff through the eastern part of the San Francisco field and across the Little Colorado River valley to the older (8–4 Ma) Hopi Buttes volcanic field, whose dramatically eroded landscape has its origin in the explosive formation of diatremes and maars. Uranium is concentrated within some maar sediments. The structure of several maars is well exposed and various hypotheses for mode of formation can be debated at the outcrops.

The fourth day will begin with a drive from Holbrook to the Springerville area in eastern Arizona (part D), where the mafic volcanoes are similar in age and composition to those of the San Francisco field. The tectonic setting on the margin of the Colorado Plateau is also similar, but structurally aligned vents and intermediate lavas are notably rare and silicic lavas are absent. Intriguing structural elements in the Springerville field are expressed as west-northwest-striking flexures within some lava flows. These are broad folds that step down toward the northeast, away from the densely clustered vents of the central part of the field.

The older (mainly late Miocene) Mount Baldy complex in the White Mountains field is the subject of the fifth day of Excursion 5A. Overlying the Colorado Plateau margin, Mount Baldy was formed by a thick lava pile, reflecting little if any of the underlying structural patterns. A possible tectonic influence is indicated by the northeast elongation of its summit vent area, which may represent the Jemez lineament as commonly proposed in New Mexico. Evidence for this lineament has not been established elsewhere in the region. The field guide for the White Mountains trip is found in Excursion 8A, which joins this excursion in Springerville for days 4 and 5 (see Baldridge et al., this volume).

Comparison of the lava compositions of these five fields shows that many of the mafic volcanoes were largely monogenetic and represent a broad mineralogical and chemical range of small magma bodies. Three of the fields, the Mormon, San Francisco, and Springerville, are dominated by a variety of basalts, mostly alkali or transitional (olivine tholeiite) basalts as determined by chemical and CIPW normative compositions. Tholeiites in the Springerville volcanic field are distinguished chemically and locally petrographically. Hawaiites (plagioclase-phyric and aphyric basalts), basanitoids (clinopyroxene-rich, plagioclase-poor), basaltic andesites, and quartz basalts are additional lava types generally identifiable in the field. Monchiquite dikes and lavas of the Hopi Buttes are strongly silica-undersaturated and significantly higher in TiO_2 and P_2O_5, standing well apart from the mafic lavas observed elsewhere on this field trip. A pyroclastic variety of limburgite is common in many of the more than 300 maars.

The varied compositions of some mafic volcanoes indicate that the magma systems were locally complex, particularly in the San Francisco field where a number of small vents reveal clear evidence of evolving eruptive histories. Scattered large volcanic centers of silicic to intermediate compositions, notably in the Mormon and San Francisco fields and the Mount Baldy shield volcano, display greater compositional ranges; these centers represent larger magma systems and more complex tectonic control than the mafic volcanoes.

Ultramafic xenoliths are locally abundant in the basaltic vents of the Mormon and San Francisco volcanic fields. In contrast, several of the Hopi Buttes maars contain distinctive mica pyroxenite xenoliths. Such xenoliths are notably rare in the Springerville field. Several of the Hopi Buttes maars produced a variety of xenoliths similar to those of the younger western fields, although the host lavas are markedly different.

Finally, the growing number of reliable radiometric ages and magnetic-polarity investigations, combined with the well-determined stratigraphic relations, produced estimates on the direction and rates of volcanic migration and the frequency of eruptions for this region of the Colorado Plateau. By inference, these values also indicate the recent history of motion of this part of the North American plate. Tanaka et al. (1986) demonstrated that for the San Francisco field basaltic volcanism migrated northeastward at about 1.2 cm/yr from about 5 to 2.5 Ma, and for the past 2.5 m.y. it migrated eastward at about 2.9 cm/yr. The frequency of basaltic eruptions during this time period increased from about one per 17,000 yrs to one per 3000 yrs. Condit et al. (part D) calculate that for the Springerville field over the past 2.1 m.y. a similar eastward migration of about 2.5 cm/yr occurred.

The final, sixth day of Excursion 5A includes views of the Pliocene to Holocene Zuni–Bandera volcanic field as we cross the southeast part of the Colorado Plateau and the Rio Grande rift en-route to Santa Fe. At least one stop to discuss the basaltic vents and flows of the Zuni–Bandera field will be made en-route, enlisting the aid of A. W. Laughlin.

Acknowledgments

K–Ar age determinations by P. E. Damon and M. Shafiqullah (University of Arizona Isotope Geochemistry Laboratory) and E. H. McKee (USGS) have provided much of the basis for the geochronology reported here. They have been active collaborators on field expeditions and vital contributors to understanding the chronologic framework of volcanism in the Colorado Plateau and Arizona Transition Zone. E. M. Shoemaker and K. L. Tanaka have been valued relentless investigators in developing the polarity chronostratigraphy of the San Francisco volcanic field and in providing insights to the origin of magmas beneath the Colorado Plateau margin. Contributions by D. A. Gust in the Mormon field and J. E. White and E. M. Shoemaker in the Hopi Buttes field have been invaluable in providing background for the field guide. W. E. Elston was a sponsor, supporter, and advisor for part of the work in the Springerville, White Mountains, and San Francisco volcanic fields. The work reported in this field guide was supported by the Geothermal Research, Geologic Framework and Synthesis, and National Uranium Resource Evaluation programs of the U.S. Geological Survey. Early work (1979–1980) in the Springerville volcanic field was supported by Los Alamos National Laboratory and the Arizona Bureau of Geology and Mineral Technology. The authorship for each day's field guide is indicated at the start of the description for that trip.

A. First-day field trip: Mormon volcanic field

Richard F. Holm, L. David Nealey, F. Michael Conway, and George E. Ulrich

Introduction

The Mormon volcanic field is a predominantly basaltic field, mid-Miocene to late Pliocene in age, which straddles the boundary between the Colorado Plateau and the Transition Zone of central Arizona (Fig. 1 in Summary). The boundaries of the field are indistinct, but they extend from south of Flagstaff on the north to the confluence of the Verde and East Verde Rivers on the south. Basaltic vents form cinder cones, spatter cones, lava cones, and shield volcanoes. Two centers of intermediate to silicic volcanism within this field are the Hackberry Mountain complex of voluminous andesitic to rhyolitic flows and ash flows and the Mormon Mountain center of andesite and dacite domes and flows and one small rhyolite dome. The latter area, for which the field is informally named, will be the focus of this day's field trip (Fig. A1) and is shown on the geologic map of the Sedona quadrangle (Weir et al., 1989).

Structure

The structural imprint of underlying, steeply dipping faults and fracture patterns in the Mormon field is pronounced. Many of the tephra and lava cones are elongate or form aligned groups along northwest trends. Likewise, many shallow drainages and eroded basalt dikes follow inferred northwest fracture systems. Northwest-trending faults are most common, but the most prominent and youngest faults (3–6 Ma) are comprised of segments that strike north–south and northwest. Stop 1 provides an overview from the south margin of the Colorado Plateau of the tectonic setting of the Mormon field where it overlaps the Transition Zone.

Petrology

The lava flows and vent deposits of the Mormon field are a suite of primarily alkalic to transitional basalts with less voluminous andesites and dacites, and sparse rhyolites. Basalt types include alkali olivine basalt, hawaiite, olivine tholeiite, basanitoid, and one olivine nephelinite (Gust and Arculus, 1986; Nealey et al., 1986). These rocks represent magmas interpreted as being derived from a variety of processes and source materials. For basalts, partial melts of a metasomatized upper mantle and subsequent fractional crystallization and minor upper crustal contamination are proposed by Gust and Arculus (1986) and Unruh et al. (1988).

Intermediate rocks (andesites and some dacites) of the Mormon volcanic field may have more complex origins. Gust and Arculus call on partial melting of amphibolite within the crust and exclude, for the most part, fractional crystallization of a basaltic parent. On the other hand, Nealey et al. (1986) argue that some andesites may have formed completely by fractional crystallization of a basaltic parent or as fractionated magmas mixed with crustal melts, but they discount an amphibolite source because of the low K_2O content of the evolved Mormon lavas.

The silicic rocks (dacite and rhyolite) may have originated as partial melts of the lower crust (Nealey et al., 1986) or as fractional-crystallization products from andesitic parents (Gust and Arculus, 1986). Differences in rare-earth-element concentrations between the basalts/andesites and the dacites/rhyolites suggest that the latter are not related to the former by simple crystal fractionation. Neodymium- and strontium-isotopic ratios of the lavas are consistent with mixing of upper mantle and lower crustal magmas (Unruh et al., 1988).

Trace-element abundances and time-tectonic relationships separate the andesitic and silicic rocks in the northern part of the volcanic field into two petrochemical groups that appear unrelated in origin. Andesites that predate the high-angle Mormon Lake fault are relatively enriched in incompatible trace elements compared to andesite, dacite, and rhyolite that erupted after the faulting (Table A-1, Fig. A2). Although both groups of andesitic and silicic rocks have low Sr-isotope ratios (0.7035–0.7041), a crustal origin or a large crustal component in some of the lavas is not excluded because xenoliths of lower crustal granulites that could be source rocks for anatectic melts also have low ratios (0.7026–0.7037).

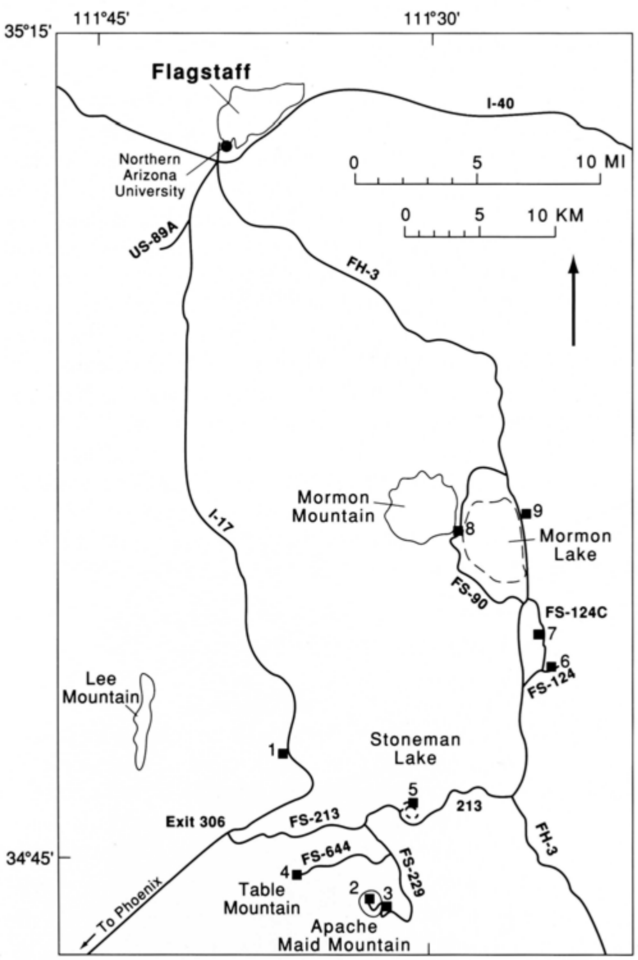

FIGURE A1—Map of field trip in the Mormon volcanic field. Stop locations shown by numbered solid squares.

Road log

Mileage

0.0 University Drive exit onto Milton Road. Drive south on I-17. Roadcuts for the first 6 mi south of the I-

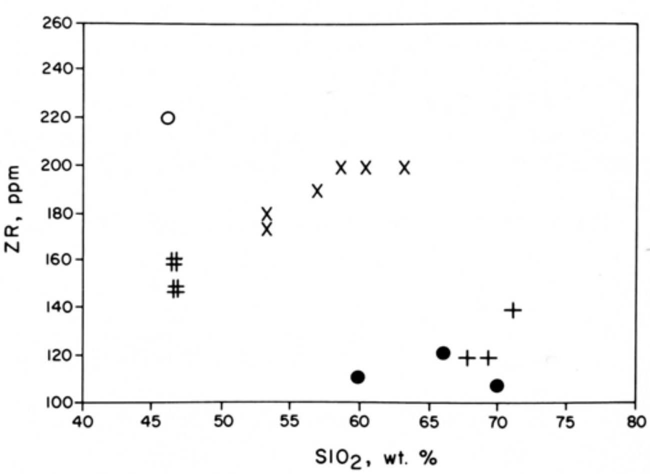

FIGURE A2—Variation of Zr (ppm) and SiO_2 (wt.%) for lavas in the Coyote Basin area (Stops 6 and 7) and Mormon Mountain (Stop 8). Symbols: prefault andesite (x) and basalt (o) of Coyote Basin cone; pre- and postfault basalt (#) of shield volcano; postfault dacite (+) of lookout tower dome and rhyolite dome (+) intruded into Mormon Lake fault; postfault andesite and dacite (●) of Mormon Mountain. Mormon Mountain data from Gust and Arculus (1986).

TABLE A-1—Chemical analyses and CIPW normative compositions, Mormon volcanic field, Arizona. Chemical analyses are original reported values. Iron reported is total iron expressed as Fe_2O_3 or FeO. CIPW normative minerals are calculated from analyses, adjusted volatile-free and for the ratio $FeO/Fe_2O_3 = 9.627 - 0.0921 \times SiO_2$ according to the least oxidized rocks of the San Francisco volcanic field. Analyses by x-ray spectroscopy except as otherwise noted. Rb, Th, and La by neutron activation except for MMT-13. Oxides in weight percent; trace elements in parts per million. nd = not determined; — = none present.

Sample No.	Apache Maid summit basalt flow UAMM-87	Apache Maid basanitoid dike NAM-8	Table Mtn. andesite flow NAM-26	Stoneman Lake basalt NSL-2	Prefault Coyote B. basalt HM42-1	Prefault Coyote B. andesite HM27-1	Postfault Coyote B. rhyolite HM37-1	Prefault shield basalt ML7-1	Postfault lookout tower hb-dacite ML19-1	Mormon Mountain px-dacite MMT-13	Prefault Mormon Lake basalt MM27-2
Stop	2	2–3	4	5	6	6	near 6	7	7	8	9
Map symbol					Tscl	Ta	Tr	Tscl	Td	Tmpd	Tsb
SiO_2	46.3	45.1	59.9	48.1	45.7	57.9	70.1	46.3	68.5	68.03	49.97
Al_2O_3	13.3	14.6	18.1	16.5	15.9	18.3	16.0	15.1	16.3	16.72	15.38
Fe_2O_3	10.9	11.1	5.4	13.2	11.8	6.63	2.43	11.2	2.7	nd	nd
FeO	nd	nd	nd	nd	nd	nd	nd	nd	nd	3.10	9.70
MgO	12.5	10.1	2.18	7.7	10.2	2.2	0.6	9.5	1.0	1.12	9.21
CaO	10.8	9.44	5.69	9.55	10.5	6.10	2.28	11.5	3.05	3.69	10.21
Na_2O	2.59	3.90	4.85	2.9	3.0	4.5	4.5	2.9	4.7	4.47	2.94
K_2O	0.70	1.88	1.60	0.58	0.85	2.02	2.38	1.13	2.30	2.17	0.73
TiO_2	1.46	2.23	0.78	1.30	1.50	0.85	0.29	1.62	0.36	0.53	1.33
P_2O_5	0.45	1.05	0.38	0.22	0.56	0.53	0.14	0.52	0.13	0.17	nd
MnO	0.17	0.17	0.09	0.19	0.18	0.14	0.03	0.18	0.04	nd	nd
H_2O/LOI	0.34	0.41	nd	nd	nd	nd	nd	nd	0.58	nd	nd
Total	99.51	99.57	98.97	100.24	100.19	99.17	98.75	99.95	99.08	100.58	99.47
Q	—	—	9.5	—	—	6.7	28.8	—	23.8	23.2	—
C	—	—	—	—	—	—	2.2	—	0.9	0.7	—
or	4.2	11.3	9.6	3.5	5.1	12.1	14.3	6.7	13.7	12.8	4.3
ab	17.1	12.2	41.7	24.8	16.2	38.6	38.6	14.2	40.2	37.8	25.0
an	23.0	17.0	23.2	30.6	27.6	24.1	10.5	25.1	14.4	17.2	26.7
di	23.0	19.0	2.4	13.0	17.2	2.6	—	23.6	—	—	19.5
hy	—	—	9.8	6.2	—	11.3	3.8	—	5.1	5.8	4.7
ol	23.7	20.0	—	16.2	22.2	—	—	18.0	—	—	14.8
ne	2.8	11.5	—	—	5.1	—	—	5.7	—	—	—
mt	2.3	2.3	1.4	2.9	2.5	1.7	0.8	2.4	0.9	1.1	2.4
il	2.8	4.3	1.5	2.5	2.9	1.6	0.6	3.1	0.7	1.0	2.5
ap	1.1	2.5	0.9	0.5	1.3	1.3	0.3	1.2	0.3	0.4	—
Sr		1400	1650	400	810	1250	800	670	960	1065	
Rb		26.5	14.3	9.5	13.2	28.2	24.4	16.0	23.1	23	
Th		8.61	5.30	1.32	6.50	13.4	3.80	6.19	3.52	nd	
La		62.8	46.7	14	37.7	70.6	21.5	40.7	24.8	29	
Nb		65	30	15	40	70	15	45	15	19	
Zr		280	170	<100	220	200	140	150	120	120	

Sample data

UAMM-87: Picritic basalt flow on summit of Apache Maid Mountain. Analysts: J. Taggart, A. Bartel.
NAM-8: Olivine basalt dike on west flank of Apache Maid Mountain. Analysts: J. Taggart, T. Frost, A. Bartel, K. Stewart, J. Budahn.
NAM-26: Fine-grained hornblende andesite from Table Mountain flow. Analysts: B. King, J. Budahn.
NSL-2: Olivine–plagioclase-phyric basalt flow on north side of Stoneman Lake. Analysts: T. Frost, D. McKown.
HM42-1: Olivine–clinopyroxene-phyric basalt flow on west side of Coyote Basin cone. Analysts: T. Frost, D. McKown.
HM27-1: Fine-grained hornblende andesite flow on footwall side of Mormon Lake fault. Analysts: T. Frost, D. McKown.
HM37-1: Intrusive rhyolite dome in Mormon Lake fault. Analysts: T. Frost, D. McKown.
ML7-1: Clinopyroxene–olivine basalt flow on a faulted shield near the summit. Analysts: T. Frost, D. McKown.
ML19-1: Hornblende dacite from small satellite dome near north-northwest-trending fault. Analysts: T. Frost, D. McKown.
MMT-13: Mormon Mountain pyroxene dacite flow. Major-element analysis by electron microprobe; trace elements by x-ray spectroscopy. From Gust and Arculus (1986).
MM27-2: Olivine basalt flow north of Mormon Lake. Analysis by electron microprobe. From Gust (1978).

17/I-40 interchange are in Lower Permian Kaibab Formation (mainly sandy dolomite). This is the sedimentary "basement" on which much of the San Francisco and Mormon volcanic fields were emplaced and serves to separate the San Francisco field to the north and west from the Mormon volcanic field to the south. At about 7 mi, the Kaibab disappears beneath lava flows and pyroclastic deposits, Pliocene and older in age, as the highway follows a valley bordered in part by eroded fault scarps and locally by ridges. These ridges, 40–50 m high and aligned in north–south to northwest–southeast directions, are formed by basalt flows and pyroclastic deposits that were fed by fissure systems paralleling the normal faults and joints that become increasingly prominent toward the Colorado Plateau margin. **28.4**

28.4 Exit I-17 on right to the overlook. **0.1**

28.5 **STOP 1. Verde Valley scenic overlook.** From this vantage point on the south edge of the Colorado Plateau, locally called the Mogollon (mo-gee-yon) Rim, several landmark features of the Verde basin can be seen (Fig. A3). The Valley is a tectonic depression extending 40 km northwest–southeast and approximately 25 km across. The broad piñon- and juniper-covered surface, sloping southwest toward the valley floor, is underlain by multiple basalt flows that are early Pliocene to late Miocene in age

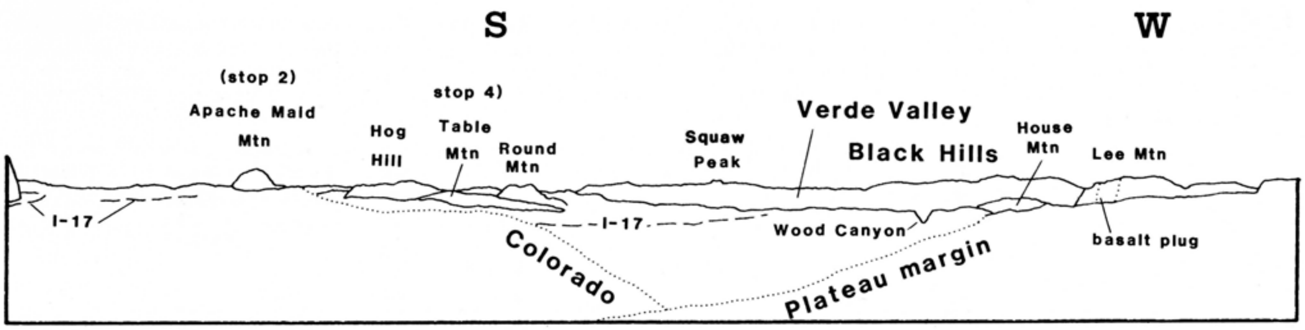

FIGURE A3—Panoramic drawing of the Verde Valley and part of the Mormon volcanic field from Stop 1. Dotted lines depict midfield horizons formed by multiple baslt flows that buried an ancestral Colorado Plateau margin in this area. Distance between Apache Maid Mountain and Round Mountain is 6.5 km. Vertical exaggeration is ×2.

(4.5–8.4 Ma; Peirce et al., 1979). The flows originated at vents on the Colorado Plateau and overflowed a deeply eroded, broken slope created by the subsidence of the Verde trough and active downcutting of the ancestral Mogollon Rim (Fig. A4). These flows were cut through by the larger drainages, exposing the underlying red, white, and gray sedimentary rocks of early Permian to Pennsylvanian age that form the well-known landscapes of the Sedona area.

Lee Mountain is a high ridge to the west and is on the upthrown (west) side of the Oak Creek Canyon fault that extends northward toward, and possibly beneath, the San Francisco peaks. The dark-gray mass near the left end of Lee Mountain is an intrusive basalt plug (Fig. A3) which fed the mesa-capping flow. To the left of Lee Mountain is the House Mountain shield volcano whose basaltic flows have yielded K–Ar ages of 13.2 and 16.8 Ma (Peirce et al., 1979). The far (southwest) side of the valley is a steep scarp formed by the Verde fault system, which separates the uplifted Precambrian basement from the downdropped basin-fill deposits that have a minimum (drilled) thickness of 900 m (Nations, 1974).

The area from Round Mountain to Apache Maid Mountain (south to southeast), prior to the earliest volcanism (>10 Ma, Peirce et al., 1979), was deeply eroded and generally faulted downward toward the Verde basin. In one 40 km long canyon, 30 to 53 faults are downthrown to the west or southwest for a net throw of 380 m; an additional structural downwarping of 300 m from east to west produces a combined lowering of 680 m toward the Verde basin from the east side (Ulrich, 1981). This gradual downwarping of the east side contrasts with the dramatic downward displacement of as much as 900 m on the opposite side of the basin along the narrow Verde fault zone (Wolfe, 1983). The area was subsequently filled in by gravels from the bordering Plateau margin and a thick series of basalts from vents like Apache Maid Mountain (Stop 2) and Hog Hill, and less abundant andesites from vents like Table Mountain (Stop 4) and Round Mountain.

Continue south on I-17. **5.5**

34.0 Take exit 306 off ramp on right. Drive east on FS-213 to end of pavement (6.5); continue on dirt road to intersection with FS-229 (0.2). **6.7**

40.7 Turn right (south) on FS-229. **4.6**

45.3 Turn right at sign "Apache Maid Lookout 5 mi"; stay on FS-229. **0.4**

45.7 Turn right at sign "Apache Maid L.O. 4" on FS-620. **4.2**

49.9 **STOP 2. Summit of Apache Main Mountain.** Apache Maid Mountain is the most prominent volcanic construct in the west-central part of the field. It is a large, asymmetrical scoria cone 300 m high, 1.6×2.1 km in diameter, and oblong in a northwest direction, as are many cones in the field.

The cone is a product mainly of pyroclastic eruptions and includes scoria, agglutinate, agglomerate, and small volumes of basaltic tuff. Numerous small-volume flows and dikes crop out on the cone summit and flanks. The cone is polygenetic, with a complex

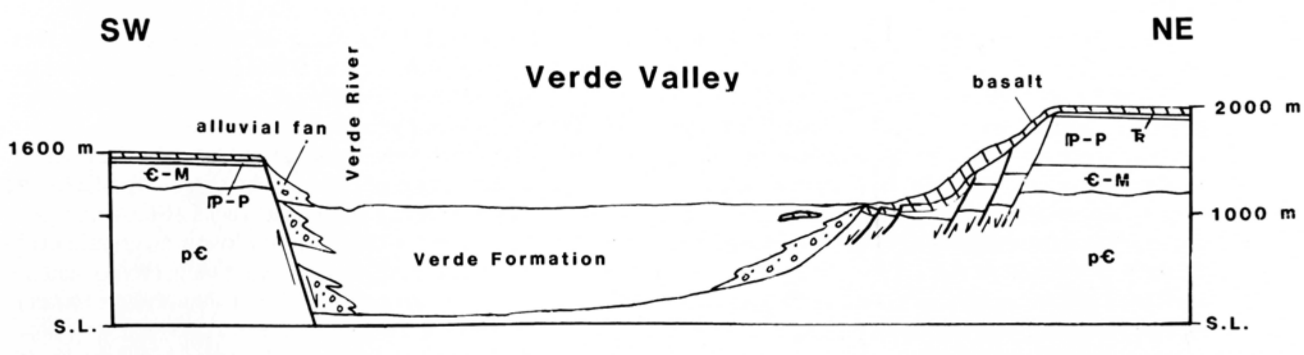

FIGURE A4—Schematic cross section of the Verde Basin approximately along I-17.

evolutionary sequence consisting of at least three stages (Conway, 1988). Construction of the initial cone marks the early stage. Weakly stratified scoria beds, agglutinate, agglomerate, and basaltic tuffs were deposited about a northwest–southeast elongate central vent or fissure. Patchy outcrops of palagonitized basaltic tuff at the base of the cone suggest initial eruptions were phreatomagmatic. As the eruption or series of eruptions progressed, the conduit became centralized, the style of eruption changed to Strombolian, and a voluminous spatter cone was built. The second stage in development resulted in emplacement of dike-fed basaltic flows. The majority of the flows issued from the summit area and cascaded down the flanks of the cone.

The third stage is characterized by emplacement of evolved lavas on the lower northwest flank of the cone. These are composite flows of mixed basalt and hornblende andesite exhibiting disequilibrium textures in plagioclase phenocrysts and quenched zones in basaltic xenoliths. Basalt types found at Apache Maid include picritic basalt (Table A-1, analysis UAMM-87), clinopyroxene–olivine basalt, aphyric basalt, and a single xenolith-rich basalt (located at Stop 3). Xenoliths of clinopyroxenite are locally present, and quartz xenocrysts with coronas of radiating clinopyroxene crystals are ubiquitous in these basalts.

Retrace route to base of Apache Maid Mountain. **2.3**

52.2 **STOP 3. Xenolithic basalt at base of Apache Maid Mountain.** A second-stage basalt dike parallels the Apache Maid lookout road at the base of the cone. Euhedral to anhedral clinopyroxene is the predominant mineral phase; olivine, sparse orthopyroxene and plagioclase, and accessory iron oxides and apatite are also present. Inclusions of spinel are common in clinopyroxene and olivine. Brown basaltic glass with inclusions of quenched olivine and plagioclase crystals is observed in areas surrounding partly melted plagioclase grains.

The dike contains a variety of ultramafic and sedimentary xenoliths. Ultramafic xenoliths are predominantly clinopyroxenites; phenocrysts are black clinopyroxene (as large as 1.5 cm) and olivine (as large as 0.5 cm). The xenoliths typically have allotriomorphic-seriate to granular textures similar to xenolith suites of the San Francisco and Mount Floyd volcanic fields (Stoeser, 1973, 1974; Nealey, 1980). Olivine is commonly poikilitic with grains of clinopyroxene. Pyroxene grains are often zoned, and exsolution lamellae of pyroxene in both clinopyroxene and orthopyroxene grains are common. Triple-grain boundaries occur in some xenoliths. The mineralogical and textural characteristics of these ultramafic xenoliths are consistent with a cumulate origin. Sedimentary xenoliths include fragments of the Kaibab Formation and Coconino Sandstone. Granitic xenoliths are rare in this unit.

Retrace route on FS-229 (north) to intersection with FS-644 at Watershed ranger camp. **5.2**

57.4 Turn left (west) on FS-644 to Table Mountain. **4.6**

62.0 **STOP 4. Table Mountain andesite flow.** Its construction did not extend to the dome-building stage that was reached by its neighbor, Round Mountain to the southwest, the largest andesite center in the western part of the field. Its composition, morphology, and structure are characteristic of an effusive Pelean-style of eruption. The flow is 2.7 km long, 1.75 km wide, and 45–60 m thick. Most of the flow is now covered by a carapace of andesitic crumble breccia. Table Mountain is similar in composition to other andesitic units in this part of the field (Conway, 1988; Table A-1, analysis NAM-26). The lavas are fine-grained, porphyritic rocks with phenocrysts of hornblende and sparse plagioclase. The groundmass is pilotaxitic and contains microlites of plagioclase and hornblende, and accessory apatite and Fe–Ti oxides. The flow is surrounded by older basalt derived partly from a small shield volcano about 1.5 km southeast of Table Mountain.

Based on the criteria of Peacock (1931) and Irvine and Baragar (1971), Table Mountain and other andesites in the western part of the field have calc-alkalic affinities. Rare-earth-element (REE) abundances of these andesites are also similar to each other; they are enriched in REE relative to chondrites and have moderate chondrite-normalized La/Yb ratios (25–40). They have lower REE content than a basanitoid from Apache Maid Mountain (Table A-1, analysis NAM-8). The low REE abundances of the andesites indicate that they were not derived from basanitoid liquid by removal of the observed phenocryst phases in the basanitoid. They could have been derived from basaltic melts by amphibole fractionation at high pressures (greater than 8 kb) and water contents of 3 wt.% (Eggler and Burnham, 1973). Amphibole fractionation is suggested by the occurrence of amphibole megacrysts in other basalts in the field. Alternatively, the andesites may have been derived by combined fractional crystallization of basalt and assimilation of lower crustal granulite (Unruh et al., 1988). A third model, that of partial melting of amphibolite within the crust to produce these andesites, was advanced by Gust and Arculus (1986).

Retrace route to FS-229. **4.6**

66.6 Turn left (north) on FS-229 to intersection with FS-213. **1.7**

68.3 Follow FS-213 straight ahead (2.1); take left fork (FS-213A) to Stoneman Lake (0.6). **2.7**
Park on right beside lake.

71.0 **STOP 5. Stoneman Lake.** The lake is in a circular basin about 90 m deep, surrounded by steep walls of basalt lava flows. The floor of the basin is underlain by at least 90 m of basin-fill sediments (Beus et al., 1966). Previous studies interpret the basin to have originated by collapse of the lavas; interpretations include collapse (1) into an evacuated magma chamber in the Paleozoic rocks (McCabe, 1971; Beus et al., 1966), (2) into fractures or caverns in the Paleozoic rocks (Beus et al., 1966), and (3) related to movement on regional northwest-trending faults (Scholtz, 1969).

We concur with Beus et al. that the basin formed by collapse above a breccia pipe in the Paleozoic rocks, one of many on the Colorado Plateau. This pipe is unusual because it surfaced in basaltic lavas. The flows in this area are mostly olivine and olivine–clinopyroxene-phyric rocks. An uncommon flow type is the olivine–plagioclase basalt on the north side of the lake, which is an olivine tholeiite having 6% normative hypersthene (Table A-1, analysis NSL-2). It is depleted in Sr (400 ppm), Nb (15), Ta (0.89), Th (1.3), U (0.3), and light REE (La = 44) and enriched in Cs (1.2 ppm) compared with other basalts. Because of its lower LREE contents, this unit cannot be related to other basalts by removal of the observed phenocryst phases.

Retrace route up hill, taking sharp left onto FS-213 (0.6); follow FS-213 east to FH-3 (6.3). **6.9**

77.9 Turn left (north) on pavement (milepost 310). Continue to intersection with unpaved FS-124. **5.0**

82.9 Turn right (east) on FS-124, driving past intersection with FS-124C (on left) and climbing up 45 m high scarp to top. **1.4**

84.3 **STOP 6. Mormon Lake fault and Coyote Basin cone.** The west-facing cliff at this stop is the eroded fault scarp of the Mormon Lake fault, about 21 km long (Fig. A5). At this point, the throw on the fault is about 45 m down on the west. Southward 6.5 km, the throw diminishes to where the fault dies. To the north, the throw increases to more than 75

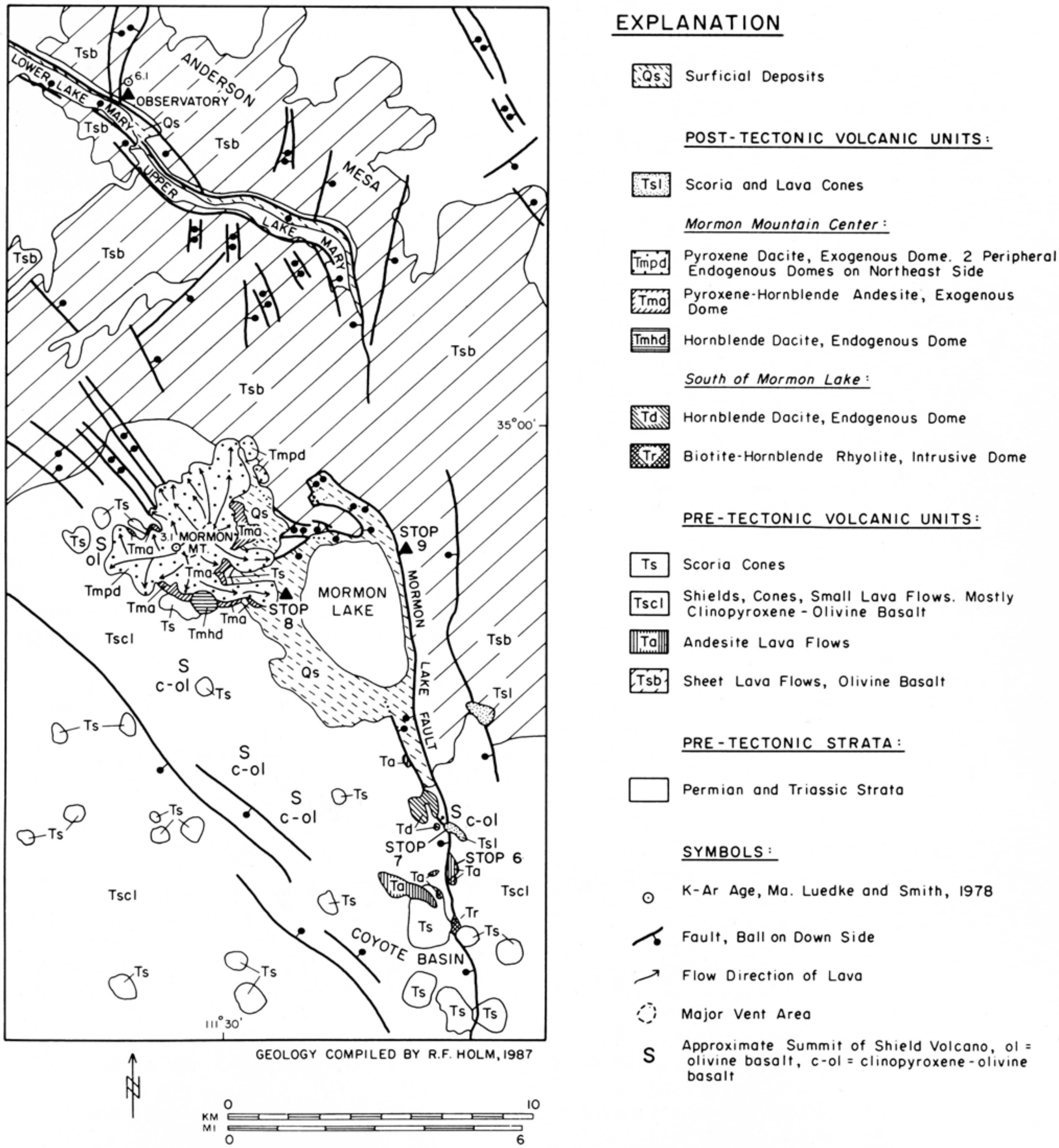

FIGURE A5—Generalized map of Mormon Mountain and the surrounding region, showing volcanic features and faults.

m on the south side of Mormon Lake. The fault ends abruptly about 14.5 km north of here. Movement on the Mormon Lake fault postdates most of the basaltic and andesitic volcanism in this part of the volcanic field, but small volumes of basaltic to silicic lavas were erupted locally after faulting.

Cropping out along the scarp is an andesite lava flow that was extruded from Coyote Basin cone seen about 1.0 km to the southwest. It is an elongate scoria cone that extruded several andesite lava flows from its north end; a variety of basalt lavas were extruded from vents in its middle and southern parts (Fig. A5). The andesites form an apparently differentiated series that ranges from low-silica to high-silica types (52.5–62.5 wt.% SiO_2). Trace-element contents suggest that the one analyzed basalt from Coyote Basin cone is not directly related to the andesites in this suite (Table A-1, analyses HM42-1 and HM27-1, respectively), and that they may be more closely related to the shield-forming basalts to be seen at the next stop (Figs. A2, A5).

Andesitic and basaltic vents on Coyote Basin cone are aligned in a northwest direction subparallel to prominent faulting on the southern Colorado Plateau. A postfault rhyolite dome (Table A-1, analysis HM37-1) was intruded along the Mormon Lake fault approximately where it intersects the structure that controlled Coyote Basin cone, and a basanitoid breccia pipe was intruded nearby. The rhyolite dome is not comagmatic with the andesites of Coyote Basin cone, and it may be an anatectic melt from the lower crust (Fig. A2). Immediately south of this stop is a basaltic lava cone that overlies the east flank of Coyote Basin cone and is deformed by the Mormon Lake fault. Thus the Coyote Basin cone is older than the Mormon Lake fault but younger than, or generally contemporaneous with, the northwest structure.

The andesite on the scarp is weakly porphyritic, carrying scattered phenocrysts of plagioclase (An_{64}) and hornblende, and microphenocrysts of clinopyroxene in a hypocrystalline matrix (Table A-1, analysis HM27-1). Across the road to the south is an overlying blocky lava flow from Coyote Basin cone of porphyritic andesite with phenocrysts of plagioclase (An_{56}) and hornblende and a similar chemical composition. Overlying the blocky andesite is a basalt flow from the lava cone to the south; it carries phenocrysts of olivine, plagioclase, and clinopyroxene in an intergranular matrix.

Retrace route to FS-124C and turn right (north). Road follows base of eroded fault scarp. Turn left at fork on FS-124B and park. **1.8**

86.1 **STOP 7. Lookout tower dome and shield volcano.** Highlights at this stop include: summit area of basaltic shield volcano; apex of wedge-shaped graben; postfault dacite dome; postfault basaltic scoria cones, lava flows, and dikes. The Mormon Lake fault crosses the summit of the basaltic shield volcano about 300 m east of the road intersection (Fig. A5). The lithology of the clinopyroxene–olivine basalt appears to be fairly uniform throughout the shield volcano (Table A-1, analysis ML7-1). The road crosses the north side of a small postfault scoria cone that was constructed on top of the fault scarp. Dikes that cut the cone crop out along the road. The summit of the scoria cone can be seen due south from the top of the scarp. Compositions of the postfault basalts on the shield are nearly identical to the prefault basalts (Fig. A2). Two possible relations of the faults and the lavas are: (1) faulting occurred by coincidence late during the active period of the shield, or (2) faulting resulted in, or allowed, renewed eruptions of small volumes of basalt on the shield.

The escarpment immediately north of this stop is the fault scarp of a south-southeast-trending fault, downthrown on the east, that intersects the Mormon Lake fault beneath the postfault scoria cone. A line of dikes and plugs follows the trend of this fault southeastward across the shield volcano, although no scarp is apparent (Fig. A5). Toward the northwest, the two faults diverge to form a wedge-shaped graben.

The low hill about 120 m west of the road intersection is a small postfault hornblende dacite dome (Table A-1, analysis ML19-1), the emplacement of which may have been controlled by the north-northwest-trending fault zone on the west side of the graben, even though the dome is about 150 m off of the projected structure.

An optional hike (about 40 minutes roundtrip) along the road reaches the summit of a large postfault hornblende dacite dome that was emplaced along the north-northwest-trending fault. Outcrops at the summit of the dome display inward-dipping flow banding and oriented hornblende phenocrysts. The route crosses small scoria deposits and thin lava flows of basalt that postdate the dacite dome; it also crosses an uplifted trapdoor of older lavas of the basaltic shield volcano.

The lookout tower domes and the Mormon Mountain silicic center (next stop) lie on a trend that is subparallel with northwest-striking faults of the southern Colorado Plateau (Fig. A5), and the positions of the domes ppear to have been controlled by regional crustal structures. Both silicic centers were emplaced on or near the summits of basaltic shield volcanoes, which belong to a group of overlapping shields that appear to have been controlled in location by northwest-trending structures (Fig. A5). Geochemistry of the lavas, however, indicates that the silicic rocks were not derived from basaltic parents that make up the shields (Fig. A2; Gust, 1978; Gust and Arculus, 1986; Nealey et al., 1986). The connection between the silicic and basaltic rocks may be simply one of position. Large volumes of mantle-derived basaltic magma may have introduced sufficient heat to the lower crust for partial melting to generate the silicic magmas. Major crustal structures appear to have controlled the subsequent emplacement of these magmas.

Continue north on FS-124C along the base of the fault scarp to paved FH-3. The cinder pit on the right is in a small cone that was buried by basalt sheet lavas that underlie the shield volcano. **2.1**

88.2 Turn left on highway. **0.8**

89.0 Turn right (west) on paved Mormon Lake Road (FS-

90) and continue through Mormon Lake village (2.0) around Mormon Lake to west side of lake (3.5). Parking area is on right side of road. **5.5**

94.5 **STOP 8. Mormon Mountain dacite flow.** The cliff is at the toe of a 55 m thick block lava flow of pyroxene dacite that was extruded from the south side of the summit of Mormon Mountain, about 4 km northwest of here. Mormon Mountain is an exogenous lava dome composed of radial flow lobes of pyroxene dacite (Table A-1, analysis MMT-13) that cover most of an older dome of pyroxene–hornblende andesite (Fig. A5). The oldest lava in the Mormon Mountain silicic center is a hornblende dacite dome on the south side (shown as rhyodacite by Weir et al., 1989) that is nearly identical to the lookout tower dome at Stop 7 in size, structure, petrography, and geochemistry. The Mormon Mountain suite of dacites and andesite has relatively low abundances of incompatible trace elements, like the other postfaulting silicic rocks in the volcanic field (Fig. A2); all of the rocks in this petrochemical group probably originated by the same processes of partial melting of generally similar crustal source materials. Mormon Mountain postdates the Mormon Lake fault system; faults on the east and north sides of the lake formed a low into which the lavas flowed from the east side of the dome. The purpose of this stop is to examine the lava-flow structures and petrography of the pyroxene dacite.

The bottom part of the flow is a highly fractured zone consisting of randomly oriented open fractures bounding blocks of small or no displacement, and autoclastic flow breccia of angular blocks. The middle part of the flow is a dense zone broken by moderately spaced (2–5 cm) ramping shear fractures that dip 60–70° west and northwest. Above the cliffs, the top of the flow is mantled by rounded (weathered) blocks of dacite, many of which appear to have little or no displacement. The dacite contains scattered phenocrysts of clinopyroxene (green), orthopyroxene (brown), and sparse hornblende in an aphanitic groundmass rich in plagioclase.

Continue on FS-90 around north end of Mormon Lake to FH-3. **4.3**

98.8 Turn right on FH-3 and drive south to Mormon Lake overlook on right side of road. **1.5**

100.3 **STOP 9. Mormon Lake overlook.** The purpose of this stop on the Mormon Lake fault is to review the volcanic history and structural geology of the northern part of the Mormon volcanic field. Olivine basalt sheet lavas that are exposed in the cliffs form the low-relief surface east of the lake and extend northward to cap Anderson Mesa, where a sample collected at the observatory (small white dot on the mesa 17.5 km to the northwest) yielded an age of 6.1 Ma (Damon et al., 1974). On Anderson Mesa, the sheet lavas cover the Lower Triassic Moenkopi Formation on a regional erosion surface that was graded northeastward to an ancestral Little Colorado River (Cooley, 1962; Damon et al., 1974). Apparently, the sheet lavas flowed northeast from sources primarily west and south of Mormon Mountain. Although some sheet lavas may have extruded from fissures (Gust, 1978; Ulrich et al., 1984), a shield volcano partly buried under the west side of Mormon Mountain was also a major source of the olivine basalts. The sheet lavas are primarily olivine tholeiite, but compositions range to more alkaline varieties (Table A-1, analysis MM27-2).

West and south of Mormon Mountain, the sheet lavas are covered by shield volcanoes, scoria cones, and small-volume lava flows composed primarily of clinopyroxene–olivine basalt, which ranges in composition from mildly to strongly alkaline varieties (Gust and Arculus, 1986). Several shields that coalesce on a northwest trend form the low broad hills seen beyond the southwest side of the lake. The shield examined at Stop 7 is due south of the lake along the fault scarp of the Mormon Lake fault; the narrow meadow at the south end of the lake is in the wedge-shaped graben that cuts the shield.

The Mormon Lake fault bends to the northwest about 1.6 km north of here, and ends abruptly in a box-end graben that forms the meadow north of the lake. Sheet lavas bounded on three sides by faults of the Mormon Lake fault system underlie the low mesa on the north side of the lake. Other faults, predominantly on north and northwest trends and presumably of the same general age as the Mormon Lake system, offset the sheet lavas and shields in the northern part of the volcanic field. Mormon Mountain has a K–Ar age of 3.1 Ma (Luedke and Smith, 1978) and postdates the faulting; a flow lobe of pyroxene dacite on the east side of the dome covers a fault of the Mormon Lake system, and flows on the west side poured down into two northwest-trending grabens on which the summit vents of Mormon Mountain appear to be located (Fig. A5). The time of major faulting in this part of the volcanic field, therefore, is bracketed between 6.1 Ma and 3.1 Ma. The roundtop hornblende dacite dome on the south side of Mormon Mountain is aligned with the postfault dome south of the lake (Stop 7) on the northwest trend of another graben west of Mormon Mountain (Fig. A5).

Prominent silicic centers seen to the north in the San Francisco volcanic field include Sitgreaves Mountain, Kendrick Peak, San Francisco Mountain, and O'Leary Peak.

Return north on FH-3 to Flagstaff. En route, the road skirts Upper and Lower Lake Mary, which are in northwest-trending grabens along the Anderson Mesa fault system. **23.3**

123.6 Northern Arizona University.

B. Second-day field trip: San Francisco volcanic field

George E. Ulrich, Richard F. Holm, and Edward W. Wolfe

Introduction

The San Francisco field covers approximately 5000 km^2 of the southern margin of the Colorado Plateau. It lies just north of the Arizona Transition Zone that separates the Basin and Range and Colorado Plateau provinces (Fig. 1 in Summary). More than 600 vents erupted through the Precambrian basement and approximately 1 km of overlying, nearly horizontal Paleozoic and Mesozoic sedimentary rocks. The field includes the composite volcano San Francisco Mountain and four other mountain centers of silicic and intermediate extrusive rocks surrounded by a "sea" of basaltic lava flows and cones (Fig. B1). Miocene to Holocene in age, the field forms the younger part of a chronological progression from the Transition Zone northeastward across the Plateau margin (Luedke and Smith, 1978) and eastward toward the Little Colorado River valley (Tanaka et al., 1986) where many Pleistocene volcanoes and a single known Holocene volcano now dominate the landscape.

Previous work

In the earliest comprehensive work on the San Francisco volcanic field, Robinson (1913) examined the compositional range of the lavas and assigned them to three general periods of eruption: an older basaltic period, a middle andesitic to rhyolitic period, and a younger basaltic period. Cooley (1962), using earlier work by Colton (1950, revised 1967), subdivided the volcanic features and their underlying surfaces into six eruptive stages, to which he assigned mid-Pliocene to Recent ages. Colton published a map inventory of 422 basaltic cones with their related lava flows in 1967; he cited the first few radiometric ages available from P. E. Damon's work in the region, adapting them to Cooley's six age groups. A more recent stratigraphic classification (Moore et al., 1976) was based on detailed mapping in the eastern and northern parts of the field. Subsequent discussion of the polarity chronostratigraphy of the complete field was provided by Tanaka et al. (1986). The structure beneath San Francisco Mountain, using a line of teleseismic P-wave measurements across the younger, central and eastern parts of the volcanic field, was interpreted by Stauber (1982) to include a low-velocity region representing compositional, fluid-bearing, or elevated thermal conditions at depths of 11–36 km below the surface.

Detailed geologic maps are published as a series covering the entire field (Wolfe et al., 1987a, b; Moore and Wolfe, 1987; Newhall et al., 1987; Ulrich and Bailey, 1987). A large-scale geologic map with cross sections of San Francisco Mountain, and Elden Mountain (Holm, 1988) is being published at this writing. A descriptive review by Wolfe (1984) provides a geologic introduction to the volcanic landscape of the field.

Basaltic rocks

Basaltic rocks of the San Francisco volcanic field are predominantly alkali basalt (ne = 0–5%), subalkaline basalt (or olivine tholeiite; ol + hy), and hawaiite. Basanitoid (ne>5%) occurs locally, and mugearite is rare. Phenocryst mineralogy correlates fairly well with compositional type. Generally, basalts with phenocrysts of olivine ± clinopyroxene are alkali or subalkaline basalts, generally indistinguishable in the field and termed olivine basalts; those that are aphyric or contain plagioclase phenocrysts are largely hawaiitic. However, the entire spectrum of basaltic rocks is a continuum, and there is a significant compositional overlap (Fig. B2) between the olivine basalts and the generally more evolved aphyric or plagioclase-phyric basalts.

Unusual basalts with clinopyroxene-rich groundmasses occur locally, especially among the older basalts in the southwestern part of the volcanic field, where they are associated locally with picritic basalt. Most of the strongly undersaturated basalts (basanitoids) are of this clinopyroxene-rich type; the group grades compositionally to alkali basalt and petrographically to olivine basalt.

Included among the basaltic rocks is basaltic andesite, which has the composition of SiO_2- and K_2O-enriched basalt. It commonly contains plagioclase displaying sieved texture, augite, and olivine, and may contain hypersthene, amphibole, or quartz. Quartz basalt is compositionally and petrographically transitional between basalt and basaltic andesite. Some basaltic andesite or quartz basalt was erupted from the same vents as, and apparently simultaneously with, olivine basalt and may best be interpreted as contaminated basalt.

Intermediate and silicic eruptive centers

Although andesite, dacite, and rhyolite occur locally as solitary domes and flows, such rocks are largely concentrated in five mountainous eruptive centers. Three of these centers, from southwest to northeast, Bill Williams Mountain, Sitgreaves Mountain, and Kendrick Peak, occur in the western part of the San Francisco field (Fig. B1). These centers consist primarily of closely spaced domes and some stubby flows. Dacite predominates at Bill Williams Mountain, and rhyolite predominates at Sitgreaves Mountain. The Kendrick Peak center contains a broader compositional range, andesite to rhyolite. The western centers are approximately aligned on or near the Mesa Butte fault system. Although there is some overlap in age from one western eruptive

FIGURE B1—Landsat image E-31041–17154D showing scheduled field stops, and map of volcanic and structural features in the San Francisco volcanic field. Major western eruptive centers: Bill Williams Mountain (BW), Sitgreaves Mountain (SIT), Kendrick Peak (KP) with the adjacent trachyte of Bull Basin Mesa (BBT). Major eastern eruptive centers: San Francisco Mountain (SF) and O'Leary Peak (OLP). Additional dacite domes or dome complexes: Davenport Hill (DAV), Dry Lake Hills (DLH), and Elden Mountain (EM). Additional rhyolite domes: RS Hill (RS), Government Mountain (GM), Slate Mountain (SLT), Hochderffer Hills (HH), White Horse Hills (WH), and Sugarloaf (SGLF). Sunset Crater (SC) cinder cone and related tephra blanket. Benmoreite vents in central part of volcanic field (heavy dots); benmoreite north of San Francisco Mountain is represented only by xenoliths in basaltic tuff. Area of lavas and ash deposits by vents of Brunhes age (stippled). Coconino Point (CPM) and Black Point (BPM) monoclines.

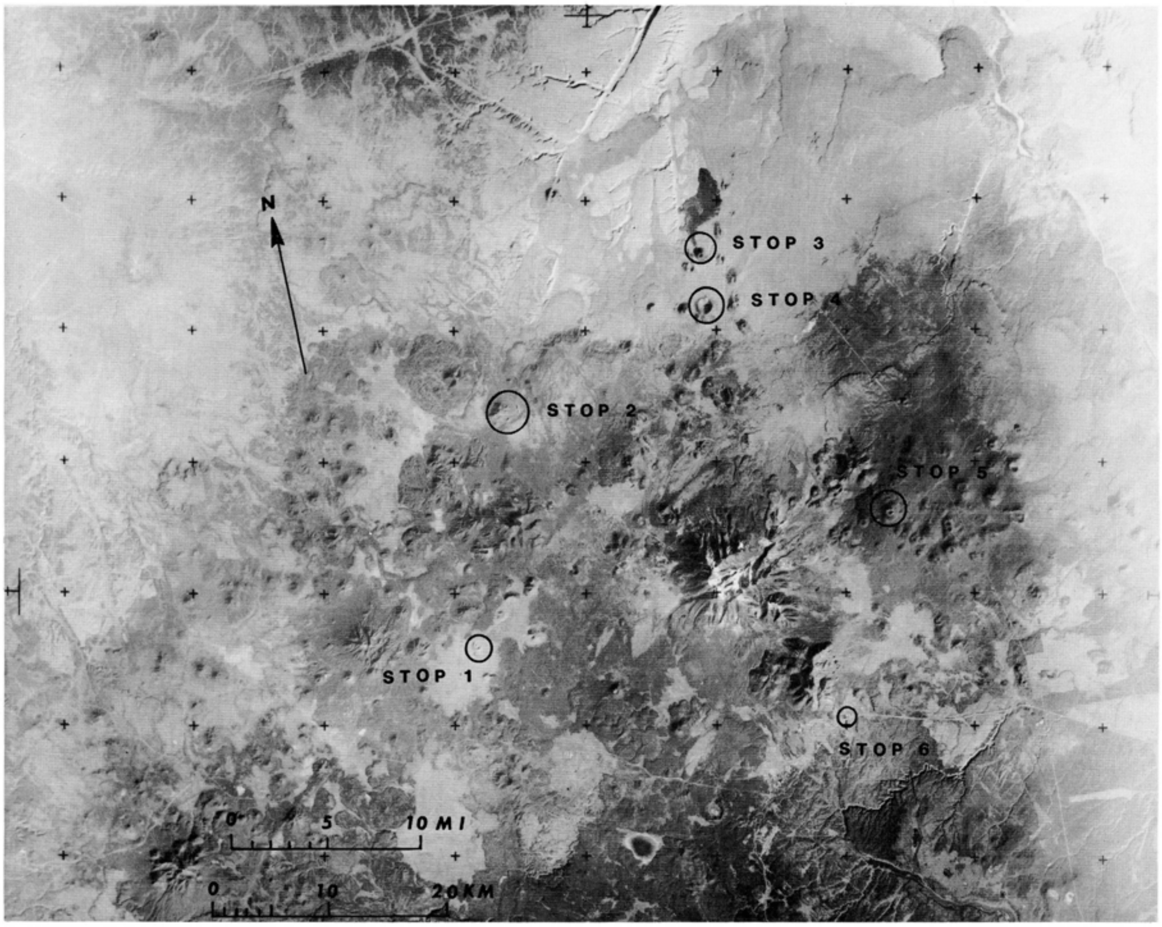
N
STOP 3
STOP 4
STOP 2
STOP 5
STOP 1
STOP 6
0 5 10 MI
0 10 20 KM

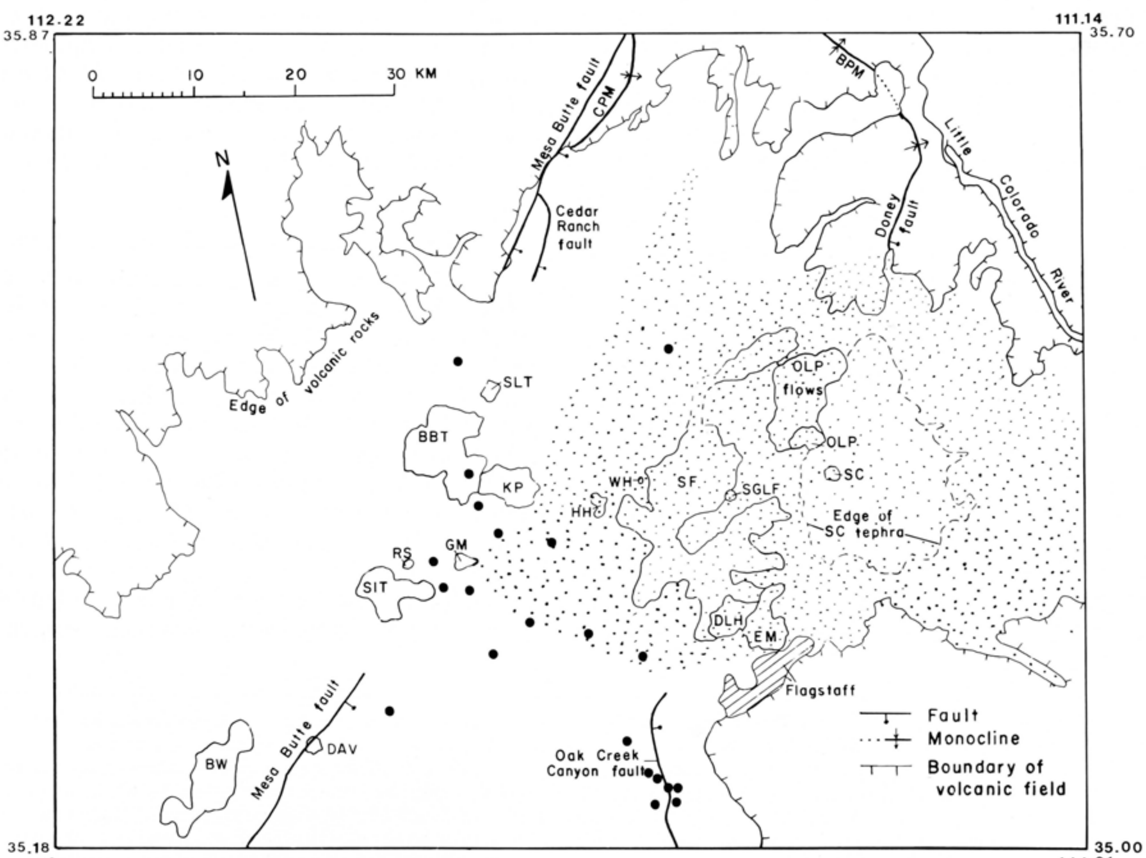
112.22
35.87
111.14
35.70
35.18
112.38
35.00
111.31
0 10 20 30 KM
N
Mesa Butte fault
CPM
BPM
Cedar Ranch fault
Little Colorado River
Doney fault
Edge of volcanic rocks
SLT
BBT
KP
OLP flows
OLP
SC
WH
HH
SF
SGLF
Edge of SC tephra
RS
GM
SIT
DLH
EM
Flagstaff
Fault
Monocline
Boundary of volcanic field
Oak Creek Canyon fault
BW
DAV

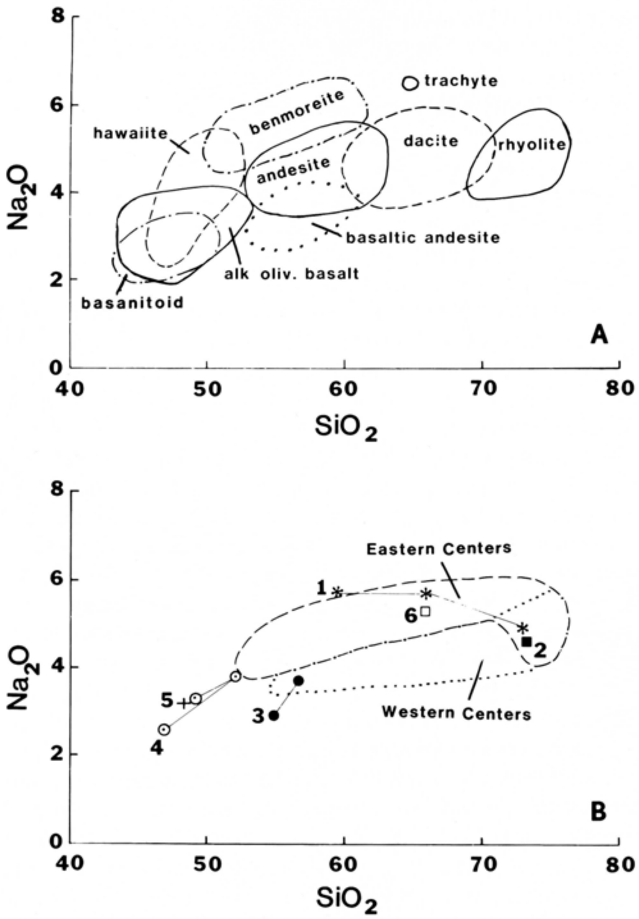

FIGURE B2—Diagram showing variation of soda and silica content in rocks of San Francisco volcanic field; values in weight percent. **A**, Compositional fields of rock types discussed in text. **B**, Compositional fields of the eastern and western intermediate-to-silicic centers. Numbered symbols indicate compositions of rock suites at Stops 1 through 6 from Table B-1.

center to the next, there is a general northeastward decrease in age from approximately 4.2 to 1.4 Ma, corresponding approximately with the migration of basaltic volcanism.

San Francisco Mountain, in the eastern half of the volcanic field, is a composite volcano whose upper stratified part is comprised mainly of porphyritic andesite and dacite flows with interlayered pyroclastic deposits erupted from about 1.0–0.4 Ma. Older dacite and rhyolite domes underlying the stratovolcano yield ages as old as 2.8 Ma. The formerly much higher cone was truncated by outward avalanching and erosion during the interval 0.4–0.2 Ma (Holm, 1988).

A rhyolite dome (Sugarloaf) erupted on the northeast flank of San Francisco Mountain at approximately 0.2 Ma. At about the same time, the O'Leary Peak eruptive center became active 9 km to the northeast. Flows and domes ranging from andesite to rhyolite were erupted from the O'Leary vents, which are roughly in alignment with the structural trend of San Francisco Mountain's Interior Valley and are located approximately over the buried extensions of the Oak Creek Canyon and Doney faults (Fig. B1).

The lavas of the eastern eruptive centers (San Francisco Mountain and O'Leary Peak) and western centers (Bill Williams Mountain, Sitgreaves Mountain, and Kendrick Peak) are broadly similar through their compositional ranges. However, the intermediate lavas (andesites and dacites) of the eastern centers are richer in Na_2O (Fig. B2) and, at comparable silica values, are depleted in MgO with respect to the lavas of the western eruptive centers. AFM diagrams (Fig. B3) reveal a trend in time and space from lower FeO: MgO in the lavas of the Arizona Transition Zone toward successively higher ratios in the western and eastern lavas of the San Francisco field. The coherent array of values for the two eastern centers may reflect a single magma system beneath them, in contrast to the broader compositional spreads of the western centers and the Transition Zone that reflect multiple magma systems.

Benmoreite and trachyte

Numerous benmoreite domes, cones, and flows and a voluminous trachyte flow were erupted north, west, and south of San Francisco Mountain (Fig. B1). Several of the benmoreites contain coeruptive dacite or rhyolite (Fig. B2) that deviate from the soda-enrichment trend from aphyric basalt through benmoreite to trachyte and resemble the composition of eastern-center lavas of similar SiO_2 content. At Stop 1, we examine a benmoreite cinder cone with a flank flow of dacite and a small central dome of rhyolite.

The benmoreites range in age from approximately 1.6–0.3 Ma. They are distinctly younger than, and presumably genetically unrelated to, nearby western eruptive centers such as Sitgreaves Mountain or Kendrick Peak. As a group, however, they are approximately contemporaneous with the San Francisco Mountain volcano.

Migration of volcanism and contemporaneity of basaltic and intermediate to silicic lavas

In addition to the broad pattern of migration of volcanism from central Arizona onto the Colorado Plateau in the San Francisco volcanic field over the past 15 Ma (Luedke and Smith, 1978), the average age of the surface lavas within the San Francisco field decreases northeastward and eastward. The very youngest lavas, including the late Holocene basalt of the Sunset Crater eruption, occur east or north of San Francisco Mountain. Lavas of Brunhes age (less than 0.7 Ma) occur only in the eastern half of the volcanic field (Fig. B1), and no lavas younger than Gauss age (2.5 Ma minimum) have been recognized in the southwesternmost part of the field near Bill Williams Mountain.

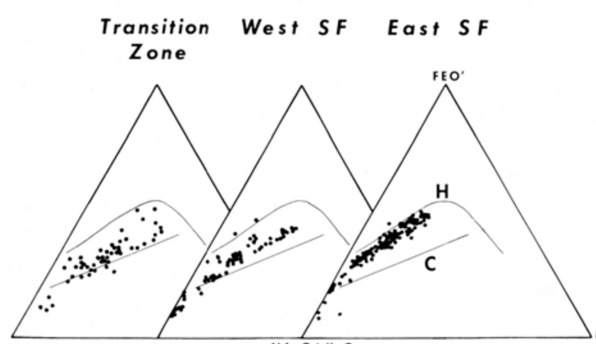

FIGURE B3—AFM diagrams for intermediate and silicic volcanic rocks of the Arizona Transition Zone and the San Francisco volcanic field. Transition Zone, includes middle to late Miocene and some Pliocene rocks of central Arizona. West SF, western centers, and East SF, eastern centers, of the San Francisco volcanic field are Pliocene and Pleistocene in age. H, Hawaiian alkalic trend (Macdonald, 1968); C, Cascades calc-alkalic trend (Carmichael, 1964).

The northeast-trending Mesa Butte fault system (Fig. B1) has served as a conduit for magmas throughout much of the history of the volcanic field. Vents on or near the fault zone erupted mafic to silicic lavas from the late Miocene near the Colorado Plateau margin (6+ Ma) to late Pleistocene (0.6 Ma) at its northeasternmost extension, 120 km distant. Slate Mountain, a rhyolite dome complex (1.9–1.5 Ma) at Stop 2, is one of these. The youngest known movement on the Mesa Butte fault system displaced a 1.04 Ma basalt flow located between Stops 2 and 3. Tanaka et al. (1986) concluded that basaltic volcanism migrated northeastward, centered along the Mesa Butte fault, at a rate of 1.2 cm/yr between 5.0 and 2.5 Ma; during the past 2.5 m.y., it has migrated generally eastward at 2.9 cm/yr. The average rate of progression northeastward on the fault zone for the past 6 Ma has been about 2 cm/yr.

Ages of the intermediate to silicic eruptive centers are approximately equivalent to the ages of the nearby basalts. Bill Williams Mountain (4.2–2.9 Ma) is entirely of pre-Matuyama age, Sitgreaves Mountain (2.8–1.9 Ma) is of Gauss and Matuyama age, and Kendrick Peak (2.7–1.4 Ma) is almost entirely of Matuyama age. Like the basalts that surround them, these western eruptive centers record northeastward volcanic migration along the Mesa Butte fault system.

Although the San Francisco Mountain volcano includes older rhyolite and dacite domes at depth, the bulk of the exposed stratified composite cone is of Brunhes age. Accordingly, San Francisco Mountain and the still younger O'Leary Peak center are largely surrounded by basalts of the Brunhes chronozone (Fig. B1).

Tectonism and origin of magmas

The San Francisco volcanic field is the recent locus of central-Arizona volcanism that migrated northeastward during the past 15 m.y. from the Transition Zone between the Basin and Range Province and the Colorado Plateau (Fig. 1 in Summary). Lavas of middle and late Miocene age across this zone are intricately faulted (for example, see Ulrich et al., 1984; Wolfe, 1983), primarily by northwest-trending normal faults that are approximately parallel in strike to the nearby edge of the Colorado Plateau. In contrast, lavas of Pliocene and Quaternary age, which comprise the bulk of the San Francisco field, are virtually unbroken by faults except along the Mesa Butte and Oak Creek Canyon faults in the southern part of the field and by small normal faults displacing a few flows near the northern edge of the field.

Keller et al. (1979) showed that the crust thickens across the transition zone from 30 km or less at its southwestern limit to 40 km or more near the northeastern edge of the San Francisco volcanic field. All of the Plio-Pleistocene basalt fields of the southern Colorado Plateau are within the zone of changing crustal thickness. Keller et al. suggested that the zones of crustal thinning and late Cenozoic volcanism and extensional faulting near the west, south, and east margins of the Colorado Plateau are enlarging at the Plateau's expense. This hypothesis is in accord with our geologic observations in the vicinity of the San Francisco field. We would add, however, that the extensional faulting of the brittle upper crustal rocks is apparently episodic and non-uniform in spatial distribution. Thus, the Verde fault (see first-day field trip), with 1 km or more of throw, is a tectonic boundary in this part of Arizona. Northeastward from the Verde fault, regional extension of the surface rocks dies out and has not been established thus far in the Pliocene and Quaternary lavas of the San Francisco field. If crustal thinning is a continuing process beneath the southern margin of the Colorado Plateau, it must be primarily ductile, resulting in only episodic and localized extensional faulting of the upper crust.

In order to explain the migration of volcanism within the San Francisco field, Tanaka et al. (1986) suggested that the basaltic volcanism is related to shear heating at the base of the lithosphere, and that the eastward drift of volcanic activity during Matuyama and Brunhes times (since 2.5 Ma) reflects absolute westward motion of the North American Plate. The broad contemporaneity of intermediate and silicic volcanism with the basaltic volcanism indicates a causal relation between the magmas. Except for the youthful O'Leary Peak center (0.2 Ma), the duration of activity at the major eruptive centers ranges from approximately 0.7 m.y. (Sitgreaves Mountain) to 2.6 m.y. (San Francisco Mountain). This implies the existence of long-lived andesitic to rhyolitic magma reservoirs beneath the eruptive centers. Teleseismic P-wave studies (Stauber, 1982) show a low-velocity body, possibly partly molten, beneath San Francisco Mountain at a depth of 9–34 km below sea level. A closed gravity low approximately coincident with Sitgreaves Mountain and Kendrick Peak may record the presence of a crustal pluton beneath those eruptive centers (J. D. Hendricks, written comm. 1981). Because the centers are surrounded by basalts of comparable age, we suppose that the source of heat, if not of some of the magma, was a flux of basaltic magma that became trapped beneath the eruptive-center reservoirs. Approximate coincidence of these centers with fault zones or with the buried projections of fault zones indicates that the faults imposed a tectonic control upon the localization of reservoirs of andesitic to rhyolitic magma.

Partial melting of deep crustal rocks, magma mixing, and crystal fractionation probably all contributed in varying degrees to producing the variety of intermediate to silicic San Francisco field lavas. The overwhelming predominance of rhyolite at Sitgreaves Mountain is most readily explained as a consequence of partial melting of deep crustal material. On the other hand, the occurrence of andesite and dacite as well as rhyolite at the other centers probably reflects mixing of rhyolitic and basaltic magma, crystal fractionation, or both. Wenrich-Verbeek (1979b) showed that some of the andesites and dacites of San Francisco Mountain can be related to each other by fractionation of their phenocrysts and that they could be derived from alkali basalt.

Lastly, a model is sought for the soda enrichment in the lavas of San Francisco Mountain and O'Leary Peak. One model may be found in the distribution of hawaiites, benmoreites, and trachyte, the most Na_2O-rich lavas of comparable SiO_2 content of the San Francisco field, around three sides of San Francisco Mountain. Association of hawaiite with the San Francisco Mountain volcano is shown directly by two observations: (1) A small hawaiite shield volcano was erupted on the lower west flank of San Francisco Mountain during part of the growth of the stratocone. (2) Although true basalt is unknown within the lavas of the stratovolcano, a small amount of mafic andesite, geochemically similar to hawaiite, is interlayered with andesitic lava exposed in the Interior Valley of the volcano. These occurrences suggest that soda-rich hawaiitic magma was involved as a mafic component in the San Francisco Mountain magma chamber and may be responsible for the soda imprint on the andesitic and dacitic lavas of San Francisco Mountain and O'Leary Peak. The depleted MgO content of the eastern centers compared with the western centers likewise may be related to the lower MgO content of hawaiitic parents.

Road log

This road log pertains to the younger central and eastern parts of the San Francisco volcanic field (Fig. B4). Its purpose is to examine the petrologic variety and tectonic relations in this field during the past 1–2 million years. Central to this area is San Francisco Mountain, Arizona's highest landmark (3850 m) and best known composite volcano, whose geology will be reviewed on a pre-excursion hike to its Inner Basin rim and is portrayed on a newly published geologic map (Holm, 1988; see also Holm, 1987a).

Leave Northern Arizona University by University Drive exit. Turn left (south) on Milton Road. Take I-40 West onramp. Start odometer.

Mileage

0.0 Drive west on I-40 past low roadcuts in mostly Pleistocene basalt and benmoreite flows. **7.0**

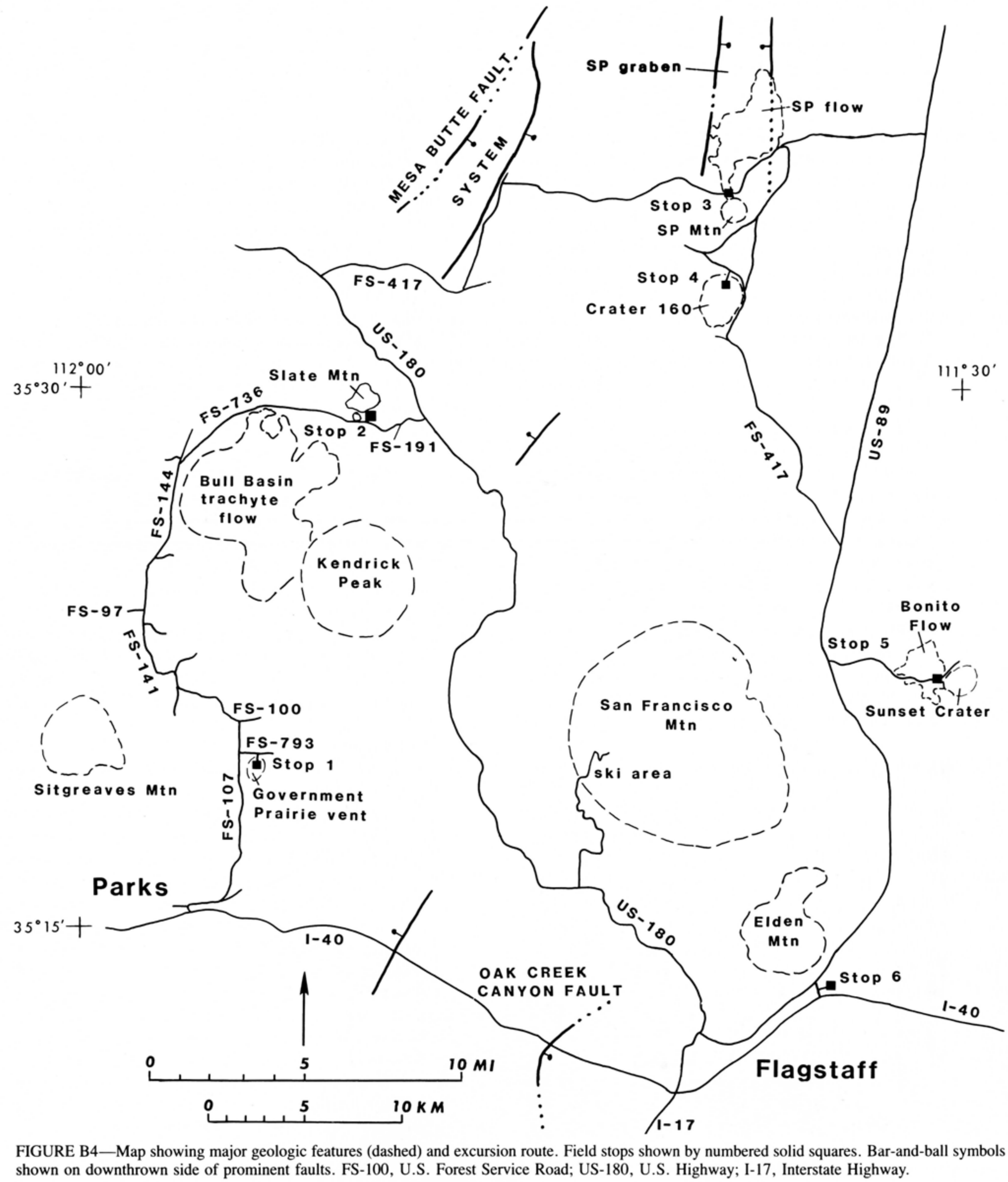

FIGURE B4—Map showing major geologic features (dashed) and excursion route. Field stops shown by numbered solid squares. Bar-and-ball symbols shown on downthrown side of prominent faults. FS-100, U.S. Forest Service Road; US-180, U.S. Highway; I-17, Interstate Highway.

7.0 Large roadcut in light-gray benmoreite flow on right. Source vent is 3 mi northeast of I-40; age of flow is 0.33±0.08 Ma. **7.3**

14.3 Roadcut in benmoreite flow from vent 1.2 mi north of I-40; age is 0.96±0.09 Ma. **1.8**

16.1 Exit right toward Parks. Take two short right turns to old paved road. **0.5**

16.6 Take left fork on FS-107; follow route north as shown in Fig. B4. **5.0**

21.6 Turn right (east) on FS-793 (0.6), then right (south) to water catchment (0.3). **0.9**

22.5 **STOP 1. Government Prairie vent (vent 2506).** This location is in the west-central part of the geologic map (MF-1959) of the central part of the San Francisco volcanic field (Wolfe et al., 1987a). At this stop we can see to the west the three western eruptive centers, aligned northeast–southwest near the buried Mesa Butte fault system, and to the east the younger stratovolcano, San Francisco Mountain. The tree-covered dome 3 km to the north is Government Mountain, a Pliocene rhyolite dome (2.1 Ma), separate from, but similar in composition and age to, the rhyolite dome complex of Sitgreaves Mountain (2.8–1.9 Ma) 10 km to the west. This location is near the center of a closed gravity low that includes both Sitgreaves Mountain and Kendrick Peak (11 km NE, 2.7–1.4 Ma), interpreted tentatively as the expression of a pluton underlying these silicic centers (J. D. Hendricks, written comm. 1981).

The Government Prairie vent produced a series of eruptions that began with the formation of a benmoreite cinder cone, followed successively by dacite and rhyolite lavas. K–Ar ages of the three lava types are approximately 1.4 Ma. The composition of the benmoreite cone is given in Table B-1 (analysis 2506). A hornblende dacite flow (analysis 2506B) erupted from the south flank of the cone (Fig. B5); it and the benmoreite occur in some bombs and xenoliths with interfingering fluidal texture, indicating their coexistence in a molten state. The final eruption at this vent produced a flow-banded rhyolite dome on the crater floor (analysis 3531A). The rhyolite contains inclusions of benmoreite, dacite, basalt, and Paleozoic sedimentary rocks.

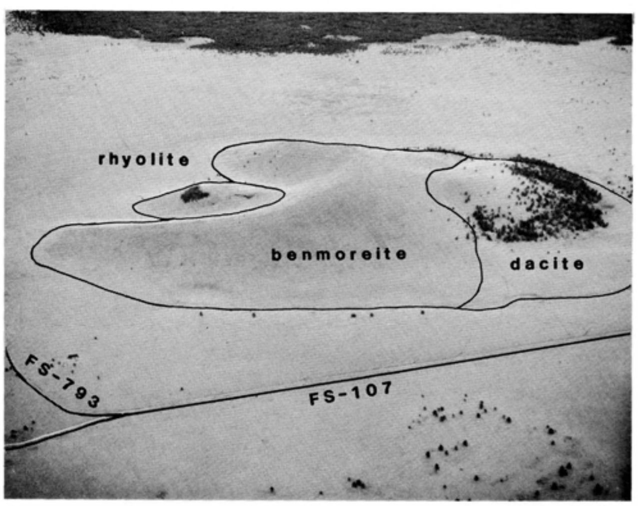

FIGURE B5—Aerial oblique view of the Government Prairie vent (vent 2506), showing distribution of erupted rock units. View is east.

The benmoreites and some of the hawaiites of the San Francisco field are strikingly similar in petrography and major-element composition to hawaiites and benmoreites of Mauna Kea Volcano, Hawaii. By analogy with their Mauna Kea counterparts (E. W. Wolfe, W. S. Wise, and G. B. Dalrymple, unpubl. data), these San Francisco field lavas, including the trachyte of Bull Basin Mesa, are the daughter products of extended fractionation of a clinopyroxene-rich assemblage from basaltic parent magmas.

While some of the benmoreites were forming by fractionation of basalt in deep crustal reservoirs beneath the central part of the volcanic field, heat transferred to the wall rocks apparently produced rhyolitic partial melts that ascended with the erupting benmoreite magmas and may have mixed with more mafic magma to produce dacite. Such dacites are commonly porphyritic; thus, minor crystal fractionation may explain deviation from the compositional linearity (Fig. B2) that should result from simple mixing of the rhyolite and benmoreite erupted at Stop 1. Crystal fractionation of benmoreite to produce these rhyolites seems untenable. For example, depletion of soda in the rhyolites would require fractionation of albitic plagioclase; however, there is no Eu-depletion to suggest that plagioclase fractionation has occurred.

Retrace route from Government Prairie vent to FS-107. **0.9**

23.4 Turn right (north) on FS-107. Government Mountain rhyolite obsidian dome at 12:00. **0.9**

24.3 Turn left (west) at T-intersection on FS-100. **2.0**

26.3 Turn right (north) on FS-141, which bends several times and becomes FS-144. **9.7**

36.0 Turn right on FS-736, following in part a buried pipeline. **2.4**

38.4 Lost Tank. Gully on right has distal outcrop of trachyte from Bull Basin flow seen to the south (Table B-1, analysis 4528). This flow has a volume of 5.7 km^3 and a K–Ar age of 1.1 Ma. Continue east. **0.6**

39.0 Take left fork. **2.5**

41.5 **STOP 2. Slate Mountain rhyolite dome complex.** This location is near the northwest margin of the geologic map (MF-1959) of the central part of the San Francisco volcanic field (Wolfe et al., 1987a). Slate Mountain is one of three silicic domes in the volcanic field that produced steeply upturned blocks of the overlying sedimentary cover. The purpose at this stop is to observe the rhyolite dome complex near its contact with the Paleozoic strata, now exposed as erosional hogbacks around its eastern perimeter (Fig. B6). The volcano was recognized as a trap-door structure formed by the forceful intrusion of magma and was termed a volcano-laccolith by Mintz (1942). Subsequent study by Lockrem (1983) examined the hypothesis that the magma was intruded into the northeast-trending Mesa Butte fault zone which projects beneath this part of the volcanic field. The trap door opened to the west, and rhyolite was extruded onto the surface, burying any expo-

TABLE B-1—Chemical analyses and CIPW normative compositions, San Francisco volcanic field, Arizona. Chemical analyses are original reported values. CIPW normative minerals are calculated from analyses, adjusted volatile-free and for the ratio $FeO/Fe_2O_3 = 9.627 - 0.0921 \times SiO_2$ according to the least oxidized rocks of the San Francisco volcanic field. nd = not determined. — = none present.

	Government Prairie Vent					SP Mountain		Crater 160				
				Bull Basin	Slate Mtn.	Basaltic andesite					Sunset Ctr.	Pyroclastic
	Benmoreite	Dacite	Rhyolite	trachyte	rhyolite			Lower wall	Basalt		Bonito	flow
	cone	flow	dome	flow	dome	Cone	Flow	agglutinate	flow	Red cone	flow	breccia
Sample No.	2506	2506B	3531A	4528	4502	5703	6723	5722A	5711	5715	3823A	1807
Stop	1	1	1	1–2	2	3	3	4	4	4	5	6
Map symbol	Qmbn	Qmdk	Qmrk	Qmt	Qslr2	Qam	Qam	Qby	Qby	Qby	Qbs	Qdbr
SiO_2	59.3	65.9	73.2	63.87	73.60	54.78	56.8	46.77	50.20	49.10	48.20	65.81
Al_2O_3	16.6	16.5	15.0	17.36	14.18	15.15	14.9	12.69	16.20	18.36	14.40	15.80
Fe_2O_3	6.50	3.20	1.40	3.49	1.61	2.32	2.5	9.39	5.00	10.08	3.70	4.9
FeO	0.56	0.04	0.04	0.08	0.07	4.91	4.1	1.17	4.30	0.43	7.38	nd
MgO	1.50	0.69	0.16	0.94	0.12	6.04	5.3	9.17	6.00	5.52	8.70	0.74
CaO	4.40	1.70	0.85	1.72	0.79	8.40	7.6	11.87	8.90	8.58	10.30	2.46
Na_2O	5.70	5.70	5.00	6.44	4.62	2.86	3.7	2.58	3.80	3.26	3.30	5.35
K_2O	2.30	3.50	4.30	4.10	4.42	1.81	2.4	1.35	1.30	1.00	0.80	3.11
TiO_2	1.20	0.40	0.12	0.53	0.08	1.17	0.95	2.17	2.00	1.58	1.91	0.50
P_2O_5	0.84	0.29	0.08	0.36	0.03	0.74	0.48	0.91	0.69	0.52	0.44	0.21
MnO	0.11	0.10	0.07	0.16	0.09	0.13	0.13	0.20	0.20	0.19	0.19	0.10
H_2O/LOI	0.75	0.75	0.41	0.49	0.36	0.80	1.04	1.73	0.81	1.46	0.26	nd
CO_2	nd	0.01	0.01	0.24	0.13	0.10	<0.05	nd	0.05	nd	0.06	nd
Total	99.76	98.76	100.63	99.78	100.10	99.21	99.90	100.00	99.45	100.08	99.64	98.98
Q	5.8	14.9	25.2	5.8	27.7	5.9	3.8	—	—	—	—	15.1
C	—	0.1	0.8	0.6	0.7	—	—	—	—	—	—	—
or	13.8	21.2	25.4	24.6	26.3	10.9	14.4	8.2	7.8	6.1	4.8	18.6
ab	49.0	50.2	42.3	55.4	39.4	24.7	31.7	18.2	32.8	28.2	25.4	45.9
an	13.1	7.4	3.6	4.7	2.9	23.6	17.2	19.6	23.8	33.3	22.3	10.1
di	2.8	—	—	—	—	10.8	14.5	28.1	13.3	5.6	21.1	0.8
hy	9.3	4.0	1.9	6.0	2.1	18.3	13.8	—	4.6	13.2	—	6.6
ol	—	—	—	—	—	—	—	15.0	10.1	7.1	17.6	—
ne	—	—	—	—	—	—	—	2.3	—	—	1.5	—
mt	1.9	0.9	0.5	1.0	0.6	1.9	1.8	2.3	2.2	2.3	2.6	1.4
il	2.3	0.7	0.2	1.0	0.2	2.3	1.8	4.2	3.9	3.1	3.7	1.0
ap	2.0	0.6	0.2	0.9	0.1	1.8	1.2	2.2	1.7	1.3	1.1	0.5

Sample data

2506: Benmoreite cinder cone. Analysis by rapid-rock method. Analyst: L. Artis.
2506B: Hornblende dacite. Analysis by rapid-rock method. Analyst: L. Artis.
3531A: Flow-banded, slightly porphyritic rhyolite. Analysis by rapid-rock method. Analyst: L. Artis.
4528: Slightly porphyritic biotite trachyte. Analysis by x-ray spectroscopy. Analysts: B. Fabbi, B. King, J. Tillman, and S. Neil.
4502: Aphanitic rhyolite. Analysis by x-ray spectroscopy. Analysts: J. Tillman, S. Neil, B. King, and B. Fabbi.
5703: Basaltic andesite cone of SP Mountain. Analysis by rapid-rock method and atomic absorption (AA). Analyst: R. Swenson.
6723: Basaltic andesite flow of SP Mountain. Average of 54 analyses from 56 m drill core through flow; rapid-rock method and AA. Analysts: P. Elmore et al.
5722A: Olivine basalt; average of 11 analyses of welded agglutinate from lower 75 m of Crater 160. From Cummings (1972).
5711: Slightly porphyritic basalt flow from Crater 160. Analysis by rapid-rock method and AA. Analysts: P. Elmore et al.
5715: Plagioclase-phyric basalt pyroclast from oxidized cone in Crater 160; latest eruptive product at that vent. From Cummings (1972).
3823A: Microporphyritic olivine basalt of Bonito flow from Sunset Crater. Analysis by rapid-rock method and AA. Analyst: D. Emmons.
1807: Dacite pyroclastic flow breccia from Elden Mountain. Analysis by x-ray spectroscopy. Total iron reported as Fe_2O_3. Analyst: L. Espos.

sures of the fault zone in the area. The eastward dip of the 1000 m thick section of sedimentary strata, presumed to extend downward to their normal position above the Precambrian basement, indicates that the magma was injected in the zone of unconformity between the Cambrian Tapeats Formation and the basement.

A gravity survey by Lockrem (1983) indicated that the base of the rhyolite body is no more than 1200–1500 m deep, placing it at a depth no greater than about 600 m below the top of the Precambrian. No Precambrian xenoliths have been observed in the Slate Mountain complex, but the gravity across the volcano (Fig. B7) requires that one or more large bodies, higher in density than the rhyolite, must reside near the surface. This model is consistent with the occurrence of discontinuous masses of sedimentary rocks on the flanks of the mountain (Figs. B6, B7C). The composition of the main rhyolite body is given on Table B-1 (analysis 4502).

Proceed east on FS-191 to U.S. Highway 180. **2.0**

43.5 Turn left (northwest) onto Highway (milepost 244). **3.3**

46.8 Turn right onto good ranch road with sign "Cedar Ranch 5 mi"; follow FS-417 east. **3.0**

49.8 View of landslides behind Cedar Ranch at 12:00. The mesa above is capped by late Miocene basalt (5.6 Ma), which overlies the lower part of the Triassic Chinle Formation that commonly forms unstable slopes. The clustered cinder cones of the SP Mountain area are visible at 11:00 about 15 km away. The Cedar Ranch eroded fault scarp extending to the northeast (9:00) is part of the Mesa Butte fault system. **0.6**

50.4 Stay left; right fork goes to Cedar Ranch. **0.3**

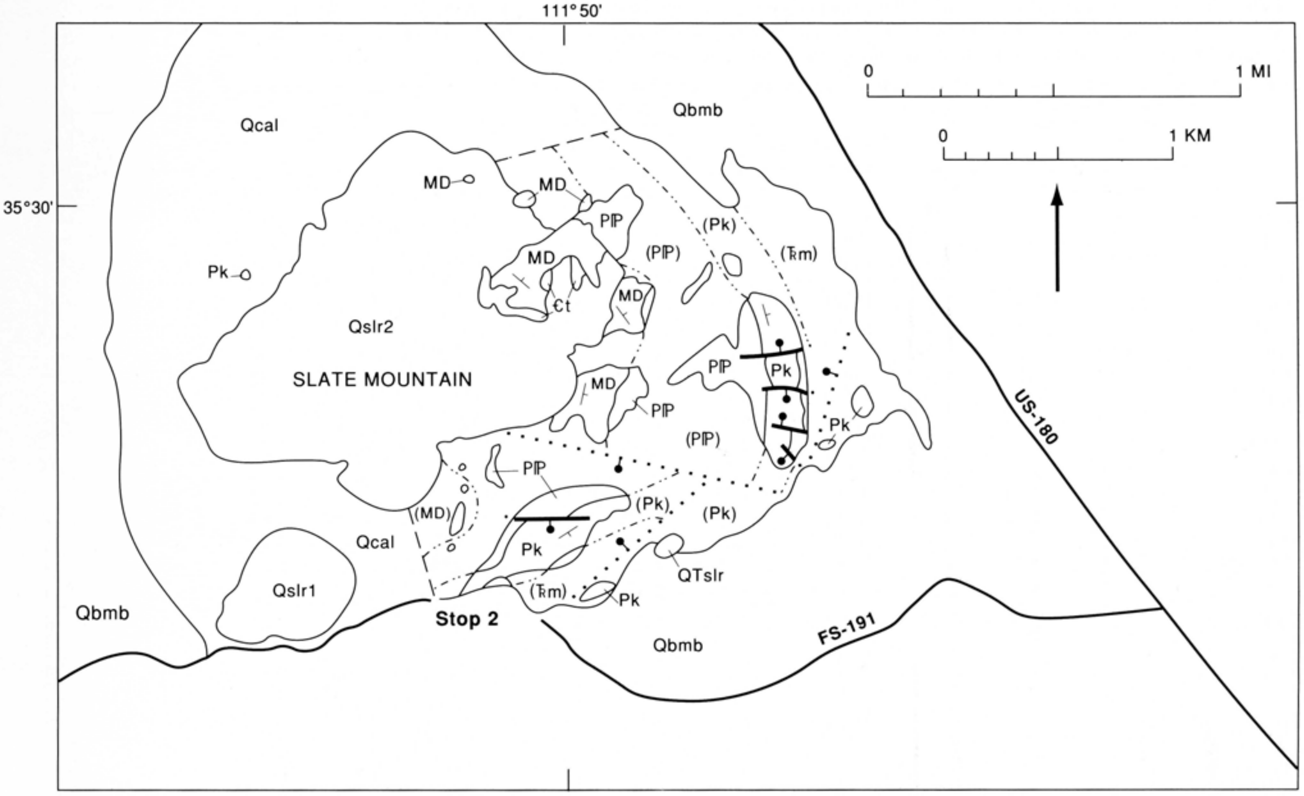

FIGURE B6—Geologic map of Slate Mountain rhyolite dome complex. From Wolfe et al. (1987a) and Lockrem (1983). Qcal = Colluvium and alluvium; Qbmb = Basalt flow of Brunhes or late Matuyama chronozone, mostly younger than 1 Ma; Qslr2 = Rhyolite dome complex of Slate Mountain, 1.54 ± 0.02 Ma; Qslr1 = Satellitic rhyolite dome, flow-banded, 1.90 ± 0.35 Ma; QTslr = Rhyolite obsidian flow; Ŧm = Triassic Moenkopi Fm., red sandstone and shale; Pk = Permian Kaibab Fm., dolomite; PIP = Permian–Pennsylvanian Toroweap Fm., Coconino Ss., and Supai Fm., undivided; MD = Mississippian–Devonian Redwall Ls. and Temple Butte Fm.; Ꞓt = Cambrian Tapeats Ss. Straight dashed line separates colluvium that completely buries dome margins from areas where scattered outcrops of sedimentary rocks occur. Dot-dashed lines are inferred buried contacts beneath Qcal. Heavy dotted lines are inferred buried faults. Symbols within parentheses are inferred buried units. Other symbols same as in Fig. B4.

50.7 Gate; take left fork beyond, paralleling Cedar Ranch fault scarp on left. **1.0**

51.7 Turn right (east) toward SP Mountain. **7.9**

59.6 **STOP 3. SP Mountain basaltic andesite (vent 5703).** This location is near the center of the geologic map (MF-1956) of the SP Mountain part of the San Francisco volcanic field (Ulrich and Bailey, 1987; also see Ulrich, 1987). The cone and lava flow of SP Mountain are good examples of basaltic andesite in the San Francisco volcanic field. The cone's sharp-rimmed profile, radial symmetry, and steep flanks mark it as the youngest volcano in the northern part of the field (Fig. B8); its age was determined as 71,000 ± 4000 yrs by Baksi (1974). The cone is 250 m high and 1200 m in diameter at its base; its slopes are covered with dense lapilli and bombs; fine cinders and ash are absent. Welded spatter forms a ruff around the crater's rim. The blocky lava flow, 15 m thick in this location, was extruded early in the vent's history and moved down a multiple graben for 7 km; it is 55 m thick near its terminus. It is characterized by coarse rubbly ridges following parallel- and cross-flow patterns and intervening areas of polygonal pavement where the flow surface fractured as it cooled but was not totally disrupted. Spatter from the cone contains phenocrysts of clinopyroxene, olivine, and embayed and sieved plagioclase in a hypocrystalline groundmass (Table B-1, analysis 5703). The flow is similar but contains, in addition, sparse orthopyroxene and embayed quartz (analysis 6723). The latest stage of cone formation is interpreted to be younger than the flow because the cone appears to overlie the flow and is not deformed by late-stage extrusion (Hodges, 1962). The lower flank of SP cone is partly overlain on its north side by protalus ramparts of coarse debris that slides down on winter snowbanks.

The two elongate cinder cones to the east are aligned on a fault that extends northward beneath the SP flow and forms the east margin of the SP graben. A prominent light-colored hill on the horizon (not shown in Fig. B8) to the north is the upthrown footwall side of the Mesa Butte fault system and is underlain by the Permian Kaibab Formation, which was seen between Cedar Ranch and this stop.

Continue on ranch road to intersection and sharp right turn (1.3); turn south toward San Francisco Mountain (1.1); take right fork (2.0); sharp left turn at intersection (0.8); turn right off road and drive through wire gate fence to base of large cinder cone (0.1). **5.3**

64.9 **STOP 4. Crater 160 (vent 5715).** This location is in the south-central part of the geologic map (MF-1956) of the SP Mountain area of the San Francisco volcanic field (Ulrich and Bailey, 1987). Crater 160 is a composite cinder, tuff, and spatter cone (Fig.

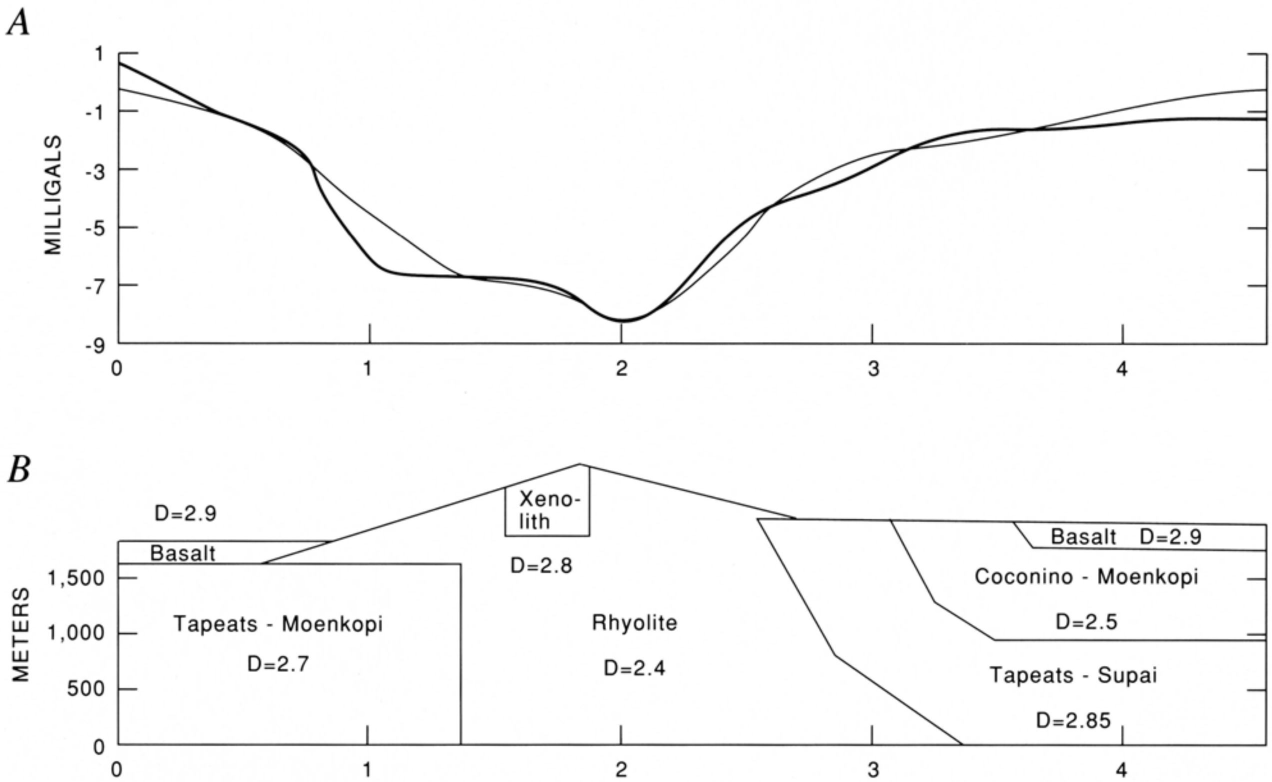

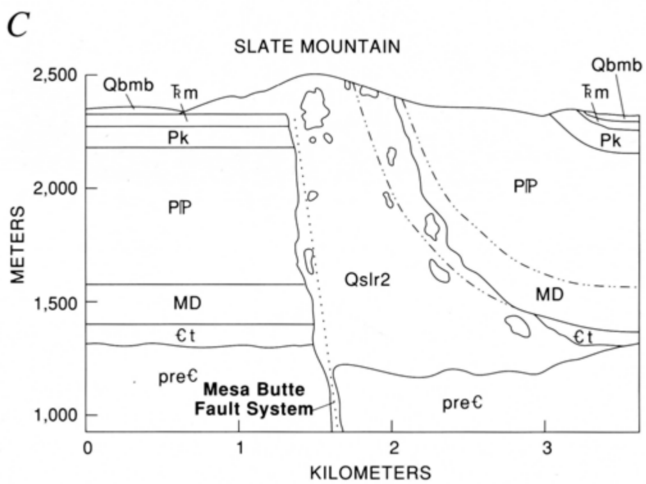

FIGURE B7—Gravity profile, gravity model, and schematic cross section drawn west–east across Slate Mountain. Gravity survey by Lockrem (1983) included 41 stations in 10 mi^2 area, half of which were on Slate Mountain. **A,** Gravity profiles. Heavy line is observed profile; light line is best-fit computer profile generated from B. **B,** Cross-sectional model showing measured densities (D) in gms/cc. **C,** Schematic geologic cross section of intrusive rhyolite forming Slate Mountain, tectonically controlled by Mesa Butte fault system and bearing inclusions of sedimentary strata partly assimilated from wall rocks above the Precambrian basement. Modified from Lockrem (1983).

B8), known mainly for its ultramafic xenoliths that weather out of a palagonitic tuff and to a lesser extent are found in the underlying welded spatter. The cone's growth began with the buildup of welded spatter and rootless flows of ne-normative basalt that forms the layers exposed in the lower crater walls (Table B-1, analysis 5722A). A dikelike body of spatter fragments in the northeast wall was the source of the hy-normative basalt flow to the north (analysis 5711). A later phreatic event deepened and widened the crater and deposited a mantle of the xenolith-bearing tuff. The most abundant xenoliths display cumulus textures and include clinopyroxenite, wehrlite, websterite, and gabbronorite. Classifications by Cummings (1972) and Stoeser (1974) are shown in Fig. B9. Other xenolith types present are anorthosite, granulite, older basalts, and Paleozoic sedimentary rocks.

The last event in the cone's history included one or more fire-fountain eruptions, producing a 35 m high oxidized cinder cone of plagioclase-phyric hawaiite (analysis 5715) on the floor. Scattered bomb fragments from this event can be collected on the upper east wall of the crater. The floor of the crater is about 80 m lower than the average surface outside.

Turn right (east) outside the fence. Leave gate open or closed, as found. **0.7**

65.6 Turn right at intersection and follow main dirt road southeast to U.S. Highway 89. **7.8**

73.4 Turn right (south) on Highway to entrance of Sunset Crater National Monument. **3.0**

FIGURE B8—Oblique photograph of SP Mountain (basaltic andesite cone at top center) and blocky lava flow beyond; Crater 160 composite cinder cone and tuff ring in foreground. View is north.

76.4 Drive east past visitor center to parking lot at base of Sunset cinder cone. **2.8**

79.2 **STOP 5. Bonito lava flow (vent 3823).** This location is near the west-central margin of the geologic map (MF-1960) of the east part of the San Francisco volcanic field (Moore and Wolfe, 1987; see also Holm, 1987b). The Bonito lava flow extruded from the northwest base of Sunset Crater (Hodges, 1962), a scoria cone built during an eruption that began in 1064–1065 A.D. (Smiley, 1958) and continued episodically for about 120 years (D. Champion, written comm. 1985). The basalt lava was extruded in at least three stages and ponded in an intercone basin (Colton, 1967; Holm and Moore, 1987). North of the Bonito flow is the O'Leary Peak center, which is composed of several dacitic to rhyolitic lava domes and flows (0.25–0.17 Ma) and an andesitic lava flow. The purposes of this stop are to: (1) examine the flow units and structures of the Bonito lava flow; (2) discuss the history of the Sunset Crater eruption; and (3) review the volcanic history of San Francisco Mountain.

Beginning at the parking lot (labeled P in Fig. B10) on the Bonito flow, proceed counterclockwise to observe: (1) stage 1 of the Bonito flow, covered with a thick mantle of tephra (Colton, 1967); (2) pahoehoe-type structures on stage 2B, lava that is at a level similar to stage 1 but has a thin and patchy mantle of tephra; (3) a squeeze-up that breaks through the crust of stage 2B; (4) stage-3 lava at a low topographic level; the flow is covered with aa clinkers and lacks a tephra blanket; (5) several hornitos above a lava tube; (6) large spheroidal bombs from the last summit eruption of Sunset cone on top of a small unit of stage 3 lava; (7) the stage-2A unit that was extruded onto the surface of the first stage; (8) a spatter rampart at the extrusion point of the stage-2A unit; (9) a pit crater that collapsed when stage-3 lava extruded; and (10) several large mounds of spatter, agglutinate, and rootless flows, some injected by shallow dikes, that were rafted by stage-1 lava when it breached an early cone of Sunset Crater. The composition of Bonito flow is given in Table B-1 (analysis 3823A).

The high part of the stage-2A unit provides a vantage point from which San Francisco Mountain can be seen. The Inner Basin originated between 0.43 and 0.22 Ma as a result of collapse that dis-

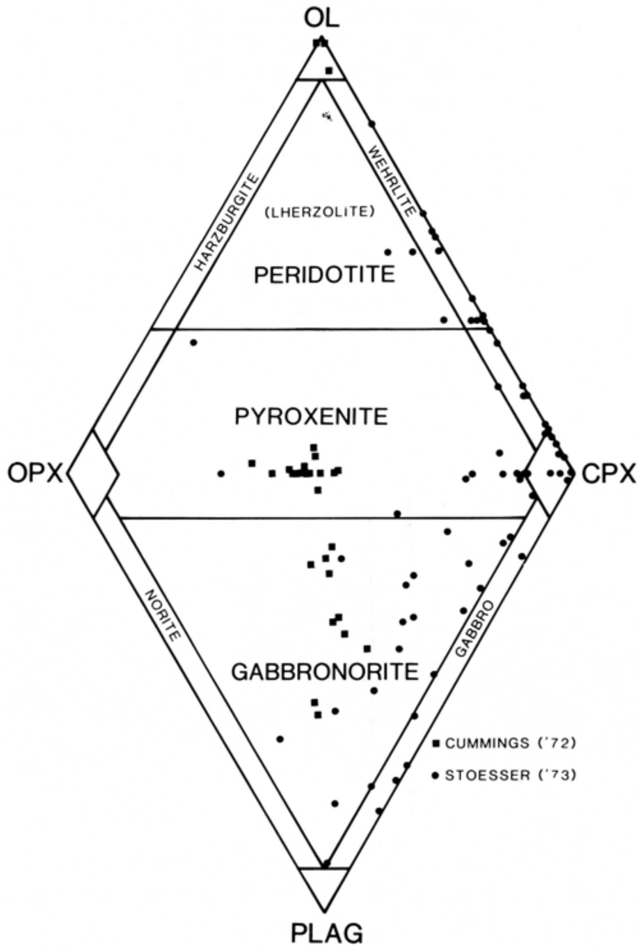

FIGURE B9—Classification of xenoliths from Crater 160 by Stoeser (1974) and Cummings (1972).

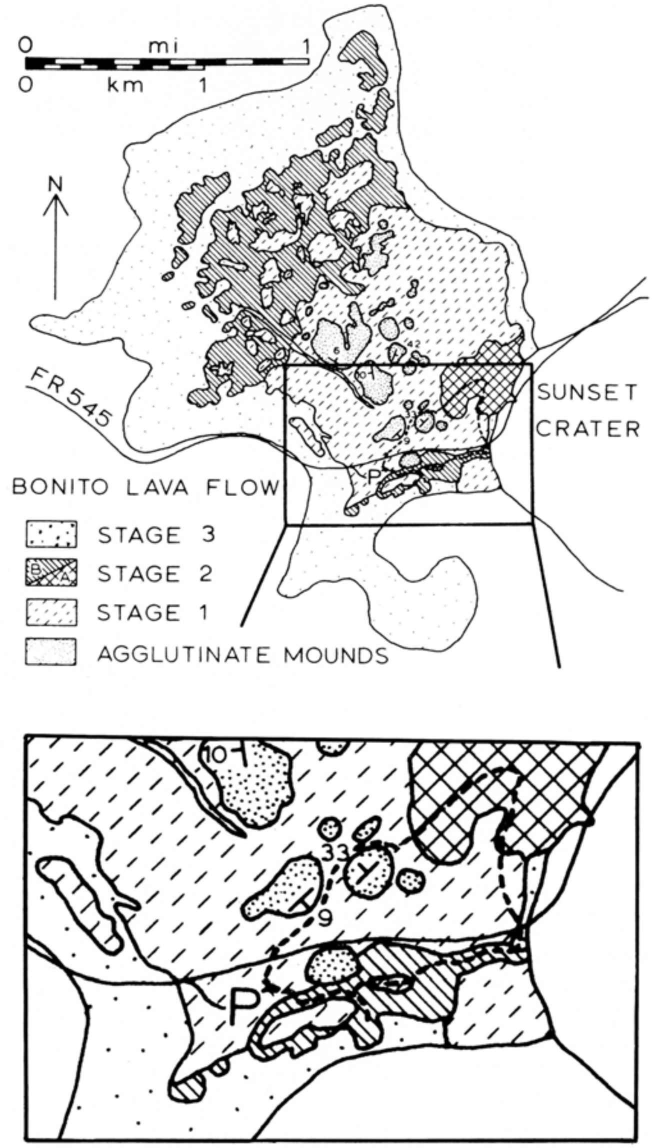

FIGURE B10—Geologic map of the Bonito lava flow. Dashed line shows traverse at stop. Strike and dip symbols indicate attitude of bedding in agglutinate mounds.

placed the top of San Francisco Mountain outward in debris avalanches and debris flows. Truncated lava and pyroclastic units and buried silicic domes form the walls of the caldera, and the central conduit system of the composite volcano is exposed on the northeast-trending Core Ridge; Sugarloaf Mountain (0.22 Ma) erupted through the largest debris fan.

Retrace route to Highway 89. **2.8**

82.0 Turn left (south) to Flagstaff. **8.9**

90.9 Take I-17/I-40 onramp; drive to intersection of Industrial Road on left. **0.5**

91.4 Turn left on dirt road to gate by trench with railroad spur near Ralston Purina plant. **0.2**

91.6 **STOP 6. Elden Mountain and pyroclastic flow.** This location is near the southeast corner of the geologic map (MF-1959) of the central part of the San Francisco volcanic field (Wolfe et al., 1987a). The southern part of Elden Mountain is a composite lava dome composed of bulbous, dacite lobes that flowed radially from at least two extrusion points onto the flat-lying Kaibab Formation (Fig. B11). K–Ar ages for the dome place its eruption at around 0.5–0.6 Ma. Prior to construction of the exogenous lava dome, Peléan-style eruptions 4–5 km north of this locality generated pyroclastic flows that deposited a block and ash fan south of the vent. The purpose of this stop is to examine the structure of

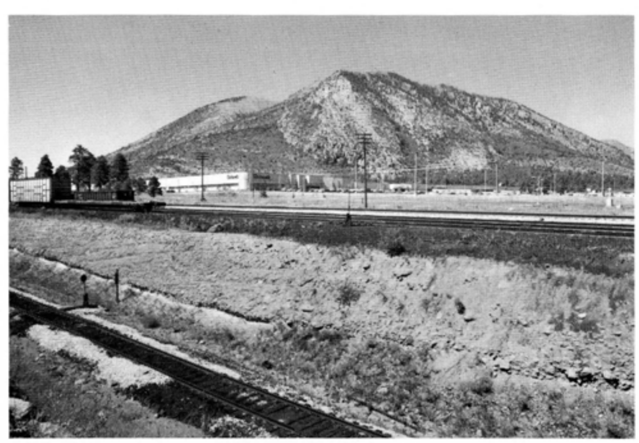

FIGURE B11—Elden Mountain dacite dome with flow lobes viewed across railroad cut near Ralston Purina Plant. Behind Elden lies source of the late Pleistocene pyroclastic flow breccia exposed in top 5 m of foreground exposure. Base of flow breccia forms sharp contact with soil-covered Permian Kaibab Formation into which a valley had been cut.

the lava dome and to study the block and ash deposit.

Six flow lobes, several of which overlap, are visible on the southeast dome of Elden Mountain. The lowest flow displays subhorizontal concentric benches that appear to be related to ramping shear fractures, whereas the highest flow is broken by longitudinal tension fractures (Kluth, 1974).

The preserved thickness of the block and ash deposit at this locality is about 5 m where it thickens in a paleovalley in the Kaibab Formation. The deposit consists of two parts: (1) a lower layer (0–25 cm thick) composed of poorly sorted, structureless to crudely stratified ash and fine lapilli, and (2) an upper layer composed of very poorly sorted ash, lapilli, and blocks up to 1 m in diameter (Fig. B11). The basal part of the upper layer (10–25 cm) ranges in character from fines-retained and matrix-supported to fines-depleted and clast-supported. The upper part of the upper layer, apparently structureless, contains matrix-supported essential blocks that range from dense dacite vitrophyre to poorly vesiculated pumice. Concordant paleomagnetic poles of the blocks indicate deposition above the Curie temperature (K. L. Tanaka, oral comm. 1981). Petrographic and chemical analyses (Table B-1, analysis 1807) of a dacite block from the breccia are very similar to those of feeder dikes believed to be the oldest rocks of Elden Mountain.

Return to I-40 ramp; turn left and take right on-ramp to I-40 west. **0.4**

92.0 Drive west to first exit on right (6.1); proceed north on Milton road. **1.0**

93.0 Northern Arizona University.

C. Third-day field trip: Hopi Buttes volcanic field

Karen J. Wenrich

Introduction

The dark-colored Hopi Buttes that dominate the surrounding red-, white-, and tan-colored landscape (Fig. C1) have captivated the interest of geologists for more than a half century. The diversity of geologic features offers a challenge to geologists of many disciplines. Perhaps the silica-undersaturated volcanic rocks and the maar sediments have attracted the most attention, but additional studies have been done on subjects varying from hydrogeology to uranium mineralization. This tour through the Hopi Buttes includes four stops that illustrate examples of all of these geologic features (Fig. C2). As one drives from the western part to the eastern part of the volcanic field, different levels of the diatremes can be observed; to the west the diatremes are eroded well below what was the original land surface, whereas to the east, maar-like sediments overlying the diatreme cores are preserved.

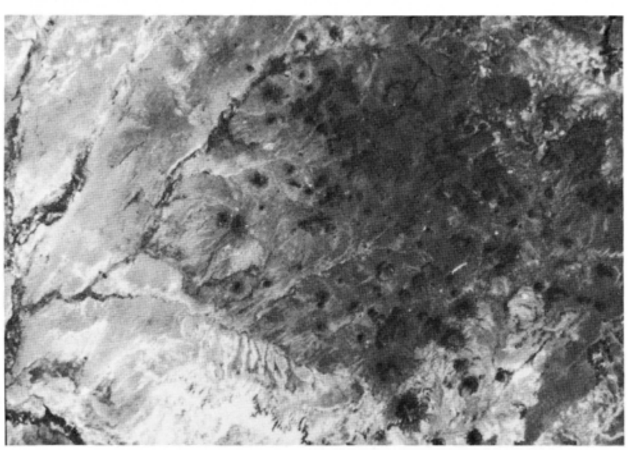

FIGURE C1—Landsat image of the Hopi Buttes volcanic field. The dark-colored buttes, each representing a diatreme or a complex of diatremes, dominate the surrounding pale-colored sedimentary rocks. Note the circularity of the area containing the buttes.

The buttes commonly rise to heights of 180 m above the surrounding countryside. Most are underlain by individual diatremes, some by a complex of diatremes. Several sediment-filled maars also crop out as inconspicuous low hills, while others may be buried beneath the alluvium. The diatremes and maars erupted into the late Miocene–early Pliocene Hopi Lake (Sutton, 1974). No region in the world is known to contain a greater density of such structures than the Hopi Buttes, where more than 300 diatremes occur within about 2500 km^2. The lacustrine sediments are the hosts for uranium mineralization that was probably syngenetic. In addition to the lacustrine sediments, the maar vents also contain limburgite tuff and tuff breccia; agglomerate; monchiquite dikes, necks, and flows; fine-grained clastic and carbonate rocks; and blocks of sedimentary rocks, especially the Wingate Sandstone, derived from the vent walls. Within many of the maars, these deposits dip inward at steep angles.

The volcanic rocks of the diatremes and maars are limburgite and monchiquite, which are distinguished from normal alkalic basalts of the Colorado Plateau by their extreme silica undersaturation and high water, TiO_2, and P_2O_5 contents. Many trace elements are unusually abundant, including Ag, Ba, Ce, La, Nb, Sr, U, Y, and Zr. Both the monchiquites and limburgites contain augite, olivine, and biotite phenocrysts, with augite the most abundant. In addition, the limburgites contain amygdaloidal opal and analcite, as well as glass and analcite in the groundmass.

Previous work

The first extensive work on the Hopi Buttes was published by Gregory (1917). Williams (1936) primarily studied the petrology of the volcanic rocks, while Hack (1942) studied the sedimentation and volcanism in the area and published detailed descriptions of many of the diatremes and maars. Shoemaker (1956) was the first to recognize anomalously high uranium concentrations in maars containing lacustrine sediments. His numerous publications on the diatremes and their mode of formation still stand as the most comprehensive and most cited work on the Hopi Buttes (1953, 1955a, b, 1956; Shoemaker et al., 1956, 1957a, b, c, 1962). More recent mapping of the area and an excellent summary of the geology of the Hopi Buttes was provided by Sutton (1974), who suggested that the explosive eruptions during diatreme formation were due to the interaction of magma with water-saturated rocks beneath Hopi lake; in contrast, Shoemaker et al. (1962) suggested that the violent nature of the eruption

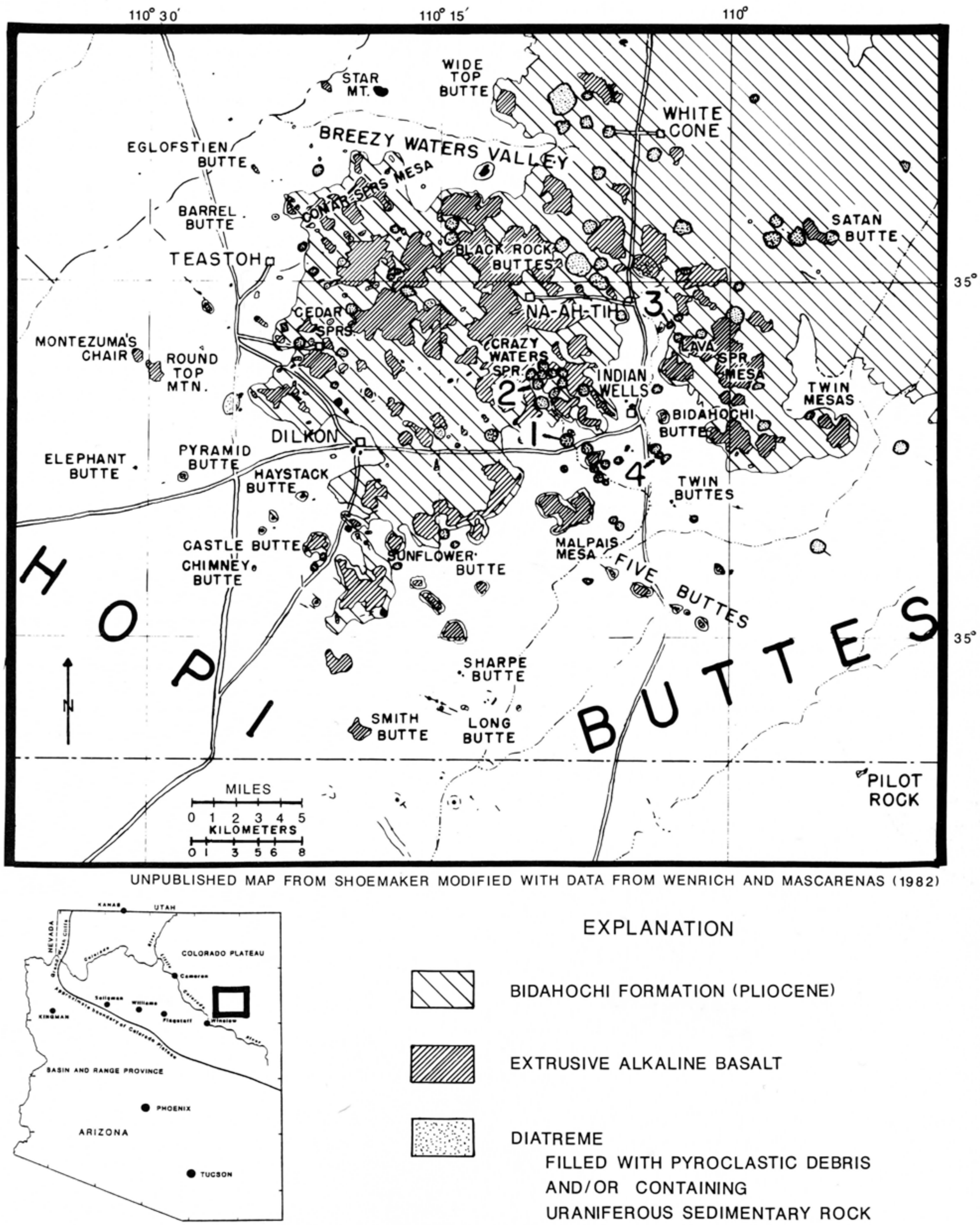

FIGURE C2—Location map showing the diatremes, maars, and monchiquite flows (extrusive alkaline basalts) and the four field-trip stops: (1) Coliseum, (2) Crazy Waters, (3) Morale, and (4) Hoskietso.

was due to exsolution of magmatic gas as magma ascended through the crust. A colored geologic map of the Flagstaff $1° \times 2°$ quadrangle (Ulrich et al., 1984) includes most of the volcanic field, but some diatremes and maars are not shown because of the small scale.

Numerous researchers have studied individual buttes: (1) Seth-La-Kai diatreme (Lowell, 1956), presently referred to as the Morale claim (Stop 3 of this field trip), (2) Shonto diatreme (Sutton et al., 1969), and (3) Tesihim Butte (Burmeier, 1977). Trace-element studies on the limburgite tuffs and monchiquites were completed by Laidley (1966) and Suda et al. (1982). Lewis (1973) studied the composition of ultramafic inclusions and concluded that the monchiquites and limburgites in the volcanic field are not related. Hydrologic investigations of the Hopi Buttes were published by Callahan et al. (1959), Cooley et al. (1969), Akers et al. (1971), and Scott (1975). Maar-lake sediments mineralized by uranium were mapped and their geochemistry was studied by Wenrich and Mascarenas (1982a, b), following earlier reports by Wenrich-Verbeek et al. (1982) and Wenrich-Verbeek and Shoemaker (1980). A complete bibliography of research published on diatremes and maars of the Hopi Buttes is available from the author.

Unanswered questions

Despite all of the past studies, many questions have not been answered. The following are queries to be pondered and discussed during the field trip:

1. Mechanism of emplacement: Were these ultrabasic rocks and their accompanying breccias violently emplaced by the rapid unmixing of gas from magma ascending through the crust along many separate fissures (Shoemaker et al., 1962), or was the explosive nature due to phreatic eruptions that occurred when the magma came in contact with water-saturated rock under Hopi Lake (Sutton, 1974)?

2. Dip of the beds: Within each maar how much of the dip of the interbedded lacustrine sediments and limburgite tuff is due to the original bedding angle and how much is due to collapse?

3. Genesis of the magma: Was this magma generated from a CO_2-rich part of the mantle, or did "normal" continental alkali basalt come in contact with water-saturated rock from a saline lake to acquire such a composition?

4. Relationship of limburgites and monchiquites: Are the limburgites an extrusive tuffaceous equivalent of the monchiquites, or were they generated from separate batches of magma as suggested by Lewis (1973)?

5. Origin of crossbedding and folding in the lacustrine sediments: Were these structures caused by slumping and wave action within the lakes, or were they a result of seeping of CO_2 from the underlying diatreme into the base of a stratified vent-lake and subsequent overturning and catastrophic CO_2 degassing as suggested by White and Fisher (1987), similar to the event in Cameroon, West Africa, in 1986?

6. Origin of the uranium mineralization: (1) Was the uranium mineralization a result of late-stage fluids of the monchiquitic magmas, or (2) was it from Colorado Plateau ground water similar to that which formed so many of the tabular orebodies in the northern Arizona/New Mexico area, or (3) was it from a mixing of the magmas with spring waters rich in CO_2 and uranium, such as hot springs present today at Ojo Caliente, New Mexico (Wenrich-Verbeek, 1977)—could these spring waters have been heated by deep circulation?

Structure and stratigraphy of the diatremes

Few faults or major structures occur within the area of the Hopi Buttes in sharp contrast to the area west of the Hopi Buttes (Coconino Plateau and the Grand Canyon). Basement structures, nevertheless, appear to have controlled the location of many of the diatremes. Some of the diatremes form distinct northwest alignments; none is so striking as the N55°W alignment of Five Buttes (Fig. C2). Structures oriented approximately N45°W and N50°E are prolific throughout northwest Arizona: (1) Many cinder cones in the San Francisco volcanic field are aligned in these directions, (2) uranium-mineralized solution-collapse breccia pipes form distinct northwest and northeast alignments in some areas, and (3) many of the major fault zones, such as the Bright Angel or Mesa Butte are oriented in these directions. Sutton (1974) pointed out that regional fractures strike predominantly N60°W and N40°E and that eruptions of the Hopi Buttes volcanics were largely localized along these fractures. Although some of the diatremes do appear to define northeast alignments, they are not as well developed as the northwest alignments.

The regional stratigraphy of the Hopi Buttes is best summarized by Sutton (1974): "The Bidahochi Formation lies with erosional unconformity on generally northward [shallowly] dipping Mesozoic strata. The lower member of the Bidahochi was deposited in Hopi Lake in the late Miocene or early Pliocene. The lake . . . approximately coincided in area with the volcanic field. A topographic barrier formed by resistant dipping beds of the Owl Rock Member of the Chinle Formation probably acted as a drainage divide separating the lake basin from the simultaneously developing valley of the Little Colorado River to the south. . . . The volcanic rocks, with associated crater deposits, comprise the middle member of the Bidahochi Formation. The upper member of the formation is largely fluviatile." The stops on the field trip will concentrate on rocks from the middle member of the Bidahochi Formation.

The igneous rocks of the middle member of the Bidahochi consist of monchiquite flows, dikes and sills, pyroclastic deposits of limburgite tuffs, and water-laid tuffs intercalated with lacustrine sediments. Structure and stratigraphy of maar-lake deposits are complex because tuffs apparently were deposited within lakes with active travertine-bearing springs and sufficient wave action to form crossbedding in the water-laid deposits as well as slumping from the maar rims. Many of the units are merely clastic deposits containing limburgite tuff fragments, with silt- and sand-sized detritus in a carbonate matrix (Fig. C3). These clastic units are commonly intercalated with travertines, and limburgite tuff beds. In many of the diatremes, particularly obvious at the Morale claim diatreme (Stop 3), some beds are highly convoluted, show soft-sediment deformation, and are discontinuous (Stop 2 at Crazy Waters also shows several good examples of this), as though they slumped from the maar rim inward toward the center of the diatreme. Another interpretation of these features by White and Fisher (1987) suggests that the "dunes" (crossbedding) and convoluted beds could have resulted from catastrophic CO_2 degassing similar to the 1986 event in Cameroon, West Africa. The basal unit in many of the maars is a very coarse breccia comprised mainly of fragments and blocks of Mesozoic sedimentary rocks; this is particularly obvious at the Hoskietso diatreme (Stop 4) where the highway cuts through the maar on its northwest corner. Here large blocks of the Rock Point Member of the

FIGURE C3—Core from a depth of 25.1–25.4 m, core hole #2, Morale claim diatreme. A limburgite tuff, composed primarily of brown glass and about 25% black iron oxides surrounding minor augite phenocrysts and about 40% calcite amygdules and open-space fillings, grades upward into a travertine containing limburgite lapilli of brown glass, iron oxide, calcite amygdules, and augite phenocrysts. Overlying this are finely laminated travertine beds, followed by more travertine with limburgite lapilli.

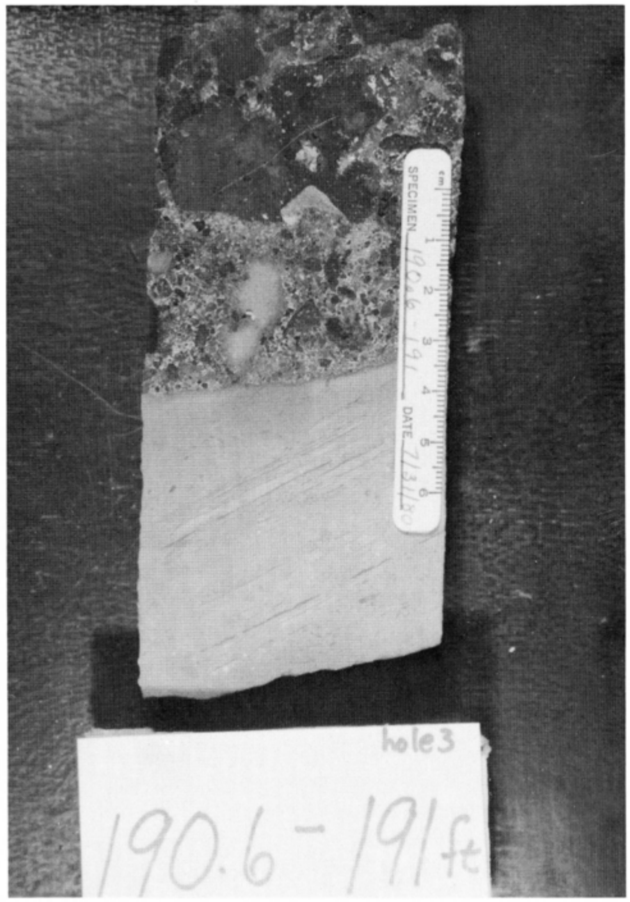

FIGURE C4—Core from near the bottom of the maar-lake sediments, core hole #3, Morale claim diatreme. The massive-looking rock at the bottom is a large block of red sandstone, probably the Rock Point Member of the Wingate Sandstone. This rock is a clast in the sedimentary breccia that probably formed as part of the first violent explosion forming the maar and scouring country rock from the vent wall as the gases streamed to the surface. Also note the clast of monchiquite (2.5 cm) near the left top.

Wingate Sandstone and some limburgite blocks lie in a tuff matrix. At the Morale claim (Stop 3) a similar breccia occurs near the base of the maar-lake bed sequence, as is shown in Fig. C4—a photograph of breccia from core taken from the drill hole on which the windmill presently sits in the Morale diatreme.

Age of the Hopi Buttes

The ages of the Hopi Buttes volcanic rocks appear to straddle the Miocene–Pliocene boundary. Fission-track ages determined by Naeser (1971) from annealed apatite and sphene obtained from Precambrian xenoliths from the Coliseum diatreme (Stop 1) are 2.1 ± 0.2 Ma, and from the Hoskietso diatreme (Stop 4) are 5.5 ± 1.1 Ma. Sutton (1974) considered the Coliseum date to be too young. Evernden et al. (1964) reported a K–Ar age of 4.1 Ma (considered minimum) from White Cone Peak (Fig. C2). Nineteen K–Ar age determinations on flows, dikes, and tuff beds by Shafiqullah and Damon (1985) established: "an episode of Mio-Pliocene volcanism in the Hopi Buttes volcanic field. . . . The bulk of volcanism and maar crater formation took place between 8.5 and 6 Ma. . . . Minor igneous activity extended until about 4.2 Ma."

A sample of organic material was collected from the lake beds of diatreme #7 during the study by Wenrich-Verbeek et al. (1982) and was sent to Bruce Cornet for a palynology study with the following results (personal comm. 1978): The sample was dominated by Compositae and Ambrosia pollen, placing the age of the lake bed as post Miocene, either Pliocene or possibly Pleistocene. The age is probably Pliocene, or at least a preglacial period of the Pleistocene, because sparse pine pollen and very delicate forms of all pollen were found, suggesting the climate was not wet. Interglacial periods of the Pleistocene are unlikely because of the absence of bisaccate pollen (the palynomorph assemblage was not diversified enough to give a representation of the regional palynoflora). Dinoflagellates and clumped tricolporate pollen were also found. The pollen clumping was either due to insect dispersal, or to the entire flower falling into the lake, perhaps as part of maar rim slumping due to subsidence in the diatreme.

Petrography and geochemistry

Volcanic rocks

The volcanic rocks of the Hopi Buttes diatremes were thoroughly described and classified by Gregory (1917) as analcite basalts or monchiquites (varieties of the silica-undersaturated rock, lamprophyre). The lavas and tuffs are distinguished from normal alkalic basalts of the southern Colorado Plateau by: (1) the absence or paucity of plagioclase, and the presence of zeolites and feldspathoids, and (2) their extreme silica undersaturation and high water, TiO_2, and P_2O_5 contents. Many trace elements, most notably the incompatible elements, are also unusally abundant; these include Ag, As, Ba, Be, Ce, Dy, Eu, F, Gd, Hg, La, Nd, Pb, Rb, Se, Sm, Sn, Sr, Ta, Tb, Th, U, V, Zn, and Zr (Table C-1).

The monchiquites occur as massive, relatively unaltered flows capping many of the mesas in the area. Those volcanic rocks that form tuffaceous deposits were referred to by Williams (1936) as limburgite tuffs in contrast to the monchiquites because of their glassy matrix. The limburgite tuffs are both air-fall and water-laid in origin. The major difference between the two rock types is textural, that is, they are similar mineralogically and chemically (Table C-1), but the monchiquites are coarser-grained, form flows, and have augite microlites in the groundmass in contrast to the glassy matrix of the limburgite tuffs. The limburgite tuffs are commonly composed primarily of brown glass with calcite amygdules and open-space fillings surrounded by black, opaque iron oxides (Fig. C3).

Both the monchiquites and limburgites are dominated by abundant augite and olivine phenocrysts and augite microlites. Petrographic studies of 13 monchiquite samples suggest that these volcanic rocks fall into two distinct types, or mixtures of the two:

1. An augite-dominated rock containing large phenocrysts and microlites of augite, with some vesicles in an extremely fine-grained felty matrix. Most augites are distinctly zoned with pleochroic brown outer rims, suggestive of titanaugite. Small cubic grains of magnetite with ilmenite lamellae, comprise about 10% of the monchiquites. Fig. C5 shows an example of this augite-rich monchiquite from a dike (sample 3A-D79) at Stop 3 (the chemistry is shown in Table C-1). The matrix of this dike is so fine-grained that it is difficult to identify analcite in the groundmass, except where it forms larger microlite-free blebs. For the most part, the matrix between the augite microlites appears to be a brown glass. These type-1 monchiquites are remarkably unaltered.

2. An olivine-dominated rock with minor augite phenocrysts. Few olivines are fresh; most have been altered to a greenish serpentine and some flows contain olivine with

TABLE C-1—Chemical analyses of Hopi Buttes samples. Values listed are given in parts per million unless indicated otherwise. — = not determined. H = analytical interference. T-Fe_2O_3 = total iron calculated as Fe_2O_3. Most major elements were done by x-ray fluorescence analysis (designated with an *x*). They are the most accurate, but were not available for half the samples; therefore, the less sensitive semi-quantitative emission-spectroscopy analyses are also shown. Sample 1B-D79 = Morale Claim; samples 2AR-D79 and 2E-D79 = Hoskietso; sample 3A-D79 = diatreme adjacent to Hoskietso; sample 20A-D79 = Coliseum. Analytical methods: aa = atomic absorption, s = emission spectroscopy, x = x-ray spectroscopy, na = neutron activation, dn = delayed neutron. The values for Bi, Au, Re, and W were below the analytical detection limits of 10, 10, 50, and 100 parts per million, respectively. Analysts: J. Baker, R. D. Bies, J. Budahn, M. Coughlin, J. Crock, S. Danahey, T. Fries, B. Hatfield, G. Kaczanowski, B. Keaten, R. Knight, S. W. Lasater, F. Luman, G. Mason, D. M. McKown, H. T. Millard, Jr., H. Neiman, J. Taggart, M. Schneider, V. Shaw, G. Shipley, M. Solt, W. R. Stang, J. Storey, J. Thomas, R. E. Vaughn, J. S. Wahlberg.

Element,	Monchiquites		Limburgite tuffs		Travertines	
-analyses	3A-D79	83A-D80	1B-D79	2AR-D79	2E-D79	20A-D79
Si_2O%-x	42.6	38.1	—	42.1	—	—
TiO_2%-x	4.5	3.5	—	4.3	—	—
Al_2O_3%-x	12.1	11.0	—	11.7	—	—
T-Fe_2O_3%-x	9.6	13.3	—	8.7	—	—
MnO%	0.13	0.21	—	0.12	—	—
FeO%	—	4.3	—	—	—	—
MgO%-x	6.1	6.7	—	4.7	—	—
CaO%-x	13.2	13.6	—	12.3	—	—
Na_2O%-x	2.4	3.1	—	3.1	—	—
K_2O%-x	2.1	1.2	—	1.0	—	—
P_2O_5%-x	1.6	2.0	—	3.1	—	—
H_2O%	—	2.9	—	—	—	—
H_2O^-%	—	1.3	—	—	—	—
CO_2%	—	2.3	—	—	—	—
Totals		99.51				
Ag-s	3.1	<1	2.1	3	<1	<1
As-aa	27	20	—	3	—	19
B-s	16	14	34	<10	<10	<10
Ba-s	960	780	410	3,000	89	130
Be-s	3.7	2.9	4.5	3	<1	<1
Ca%-s	9.1	6.4	2	8.7	>20	17
Cd-s	<2	<32	<2	<2	17	<2
Ce-s	240	170	280	480	H	<100
Co-s	27	40	210	36	25	6.8
Cr-s	210	110	21	—	16	15
Cs-na	2	0.76	—	20	—	<1
Cu-s	43	49	32	15	4.9	4
Dy-na	—	9.5	—	—	—	—
Eu-na	—	5.4	—	—	—	—
F%-aa	0.15	0.14	—	0.19	—	0.06
Fe%-s	5.8	6.6	8.7	5.6	3	1.6
Ga-s	25	19	27	21	<10	<10
Gd-na	—	13	—	—	—	—
Ge-s	—	<1.5	—	—	—	—
Hf-na	—	10	—	—	—	—
Hg-aa	<0.01	—	—	<0.01	—	<0.01
In-s	—	<6.8	—	—	—	—
K%-s	1.2	0.77	1	0.64	0.28	0.30
La-s	130	110	160	310	76	42
Li-aa	18	47	—	10	—	14
Lu-na	—	0.33	—	—	—	—
Mg%-s	3.5	3.3	2.9	2.6	0.56	11
Mn-s	740	2,100	660	740	2,200	750
Mo-s	34	6.3	18	48	H	<10
Na%-s	1.7	2.1	1.9	2	<0.15	0.20
Nb-s	95	89	98	130	<25	<25
Nd-na	—	112	—	—	—	—
Ni-s	53	76	410	48	44	20
P%-sa	>0.45	0.92	>0.45	>0.45	<0.02	0.03
Pb-s	<10	10	<10	<10	<10	<10
Pd-s	—	<1	—	—	—	—
Pr-s	—	<68	—	—	—	—
Rb-na	28	<10	—	10	—	<5
T-S%-aa	0.03	0.04	—	0.07	—	0.03
Sb-na	—	0.27	—	—	—	—
Sc-s	23	15	15	19	<10	<10
Se-x	<0.10	<0.10	—	<0.10	—	<0.10
Sm-na	—	20	—	—	—	—
Sn-s	<10	4.6	<10	<10	<10	<10
Sr-s	2,200	2,000	>5,000	>5,000	870	3,400
Ta-na	—	7.7	—	—	—	—
Tb-na	—	1.8	—	—	—	—
Te-s	<50	—	<50	<50	<50	<50
Th-dn	16	(na)14	<51	<52	<39	<51
Ti%-s	>1.5	0.65	>1.5	>1.5	0.04	0.09
Tl-s	<10	<4.6	<10	67	<20	<10
U-dn	3.6	4.8	196	206	163	222
V-s	190	170	120	110	26	98
Y-s	42	26	84	59	17	13
Yb-na	—	2.4	—	—	—	—
Zn-s	290	170	160	230	H	<50
Zr-s	710	360	840	>1,000	150	210

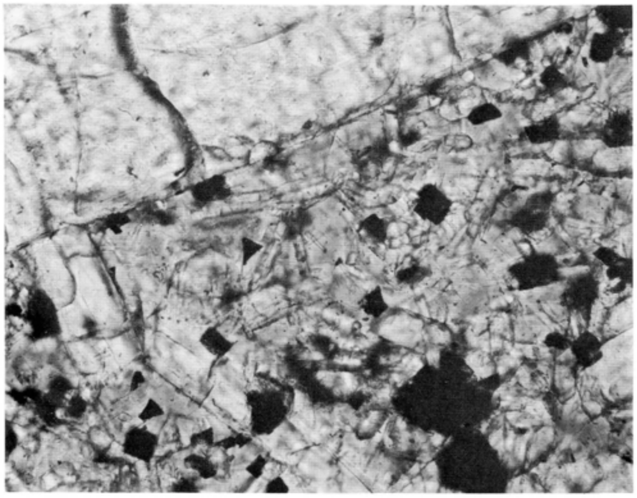

FIGURE C5—Augite-dominated monchiquite showing cubic magnetite grains and a large augite phenocryst in the upper left corner of the rock. The matrix contains augite microlites in a brown glassy groundmass (Type-1 monchiquite—Sample 3A-D79 from a dike dissecting a maar adjacent to the Hoskietso diatreme). Horizontal field of view is 0.34 mm.

bright-red iddingsite rims enclosing serpentine and/or calcite cores (Fig. C6—sample 83A-D80). In contrast to type-1 flows, these monchiquites all appear to contain microfractures that are commonly filled with calcite. The vesicles contain calcite or zeolites. The vesicles and fractures suggest that type-2 flows were more gas rich, specifically CO_2, which probably caused the iddingsite rims and serpentine alteration of the olivine. As in the type-1 flows, the matrix is extremely fine-grained with microlites of augite in a feldspathoidal groundmass.

Samples 3A-D79 and 83A-D80 were selected to illustrate the monchiquites of the Hopi Buttes because they appear to represent the two endmembers, both chemically and petrographically. Sample 117A-D80 (location shown by Wenrich and Mascarenas, 1982b) contains patches of each monchiquite type with the augites at the edge of type-1 pockets showing serpentine alteration where in contact with the type-2 rock. Such rocks appear to be a mixture of the two types.

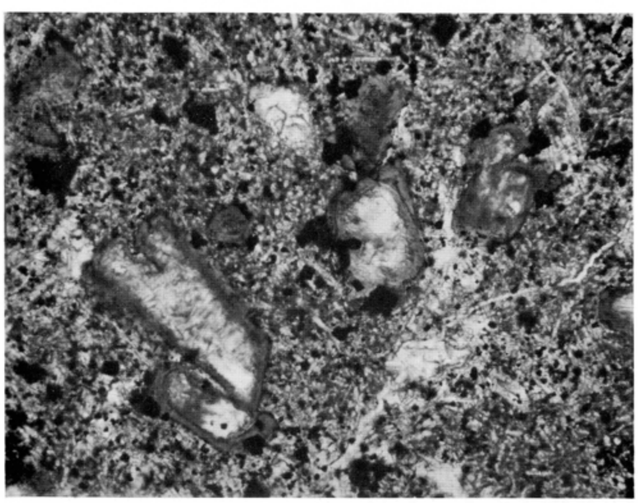

FIGURE C6—Type-2 monchiquite (sample 83A-D80) with olivines altered to serpentine and/or calcite with iddingsite rims. Augite comprises less than 1% of the phenocrysts; those present are unaltered. It does occur, though, as abundant microlites in an analcite-rich matrix. Horizontal field of view is 0.54 mm.

Table C-1 shows that both monchiquite types have similar chemistry, with the biggest contrast being the higher iron content (as would be expected) in the iddingsite-rimmed, serpentized, olivine-rich type-2 monchiquites. The type-1, augite-rich monchiquites have a higher SiO_2 content. It might be noted that the CaO content of the monchiquites is high (up to 13.6%) compared to most volcanic rocks.

Volcanic rocks with high CaO do not typically have high uranium, yet analyses of 14 monchiquite flows and dikes (Wenrich and Mascarenas, 1982a) have uranium concentrations that range from 3 to 9 ppm. Most of the limburgite tuffs have uranium contents that are an order of magnitude above that of the monchiquites (Table C-1). This is in sharp contrast to "normal" basalts and ultrabasic rocks that rarely have uranium concentrations exceeding 1 ppm. In fact, uranium concentrations in 52 basalts, andesites, and dacites (uranium is generally concentrated in more silicic rocks) from the San Francisco volcanic field (Wenrich-Verbeek, 1979a) are all below 3.8 ppm. With the exception of Ti and CO_2, all of the elements that are abnormally high in these monchiquites are elements that are typically concentrated within silicic igneous rocks rather than in ultrabasic igneous rocks. The rare-earth elements in 10 monchiquites have been normalized to chondrite values, and are plotted in Fig. C7. The data for all the samples form essentially identical trends: strong light rare-earth-element enrichment with no Eu anomaly. The absence of a Eu anomaly suggests that the magma did not reside for any appreciable length of time at depths less than 50 km, where plagioclase fractionation and Eu depletion would be expected to occur.

Numerous xenoliths of red granite, Tapeats Sandstone, Wingate Sandstone, amphibolites, and pyroxenites are present within many of the diatremes. Analyses of black, mica–amphibole–clinopyroxene inclusions and associated megacrysts and phenocrysts from one dike and several diatremes of the field reveal that the mica is titanium-rich phlogopite, and that the amphiboles are pargasites and kaersutites (Lewis, 1973). Large, euhedral, nonzoned titanaugite crystals from the limburgite tuff have a composition essentially equivalent to those of the megacrysts and the corresponding phase of the inclusions, implying that all are cognate precipitates (Lewis, 1973). Silver and Bass (1964) studied zircons from a "large boulder of red granophyric rhyolite porphyry" and found that the zircon crystallized 1730 ± 30 Ma. Their "red rhyolite porphyry" is believed to be the same type of xenolith that can be seen at both the Coliseum (Stop 1) and Crazy Water (Stop 2) diatremes.

Travertine and clastic rocks

The tops of many of the diatremes were once covered by maar-lake travertine, siltstone, claystone, and water-laid tuff deposits, which locally are interbedded with minor thin layers of gypsum and chert. The aggregate thickness of the lake beds preserved in some maars exceeds 300 m (Sutton, 1974: 661). The travertine is believed to have been deposited from rising thermal waters (Shoemaker et al., 1962), whereas the interbedded clastic rocks were derived from sediment washing into the lake from the maar rim, from eolian debris, and from ejecta from adjacent diatremes. Although the clastic rocks do contain a volcanic component, they are dominantly composed of quartz fragments with sparse feldspar and mafic minerals in a fine-grained clastic or calcite matrix (Fig. C8). The "travertines" vary from those with few clastic fragments to those containing limburgite lapilli composed

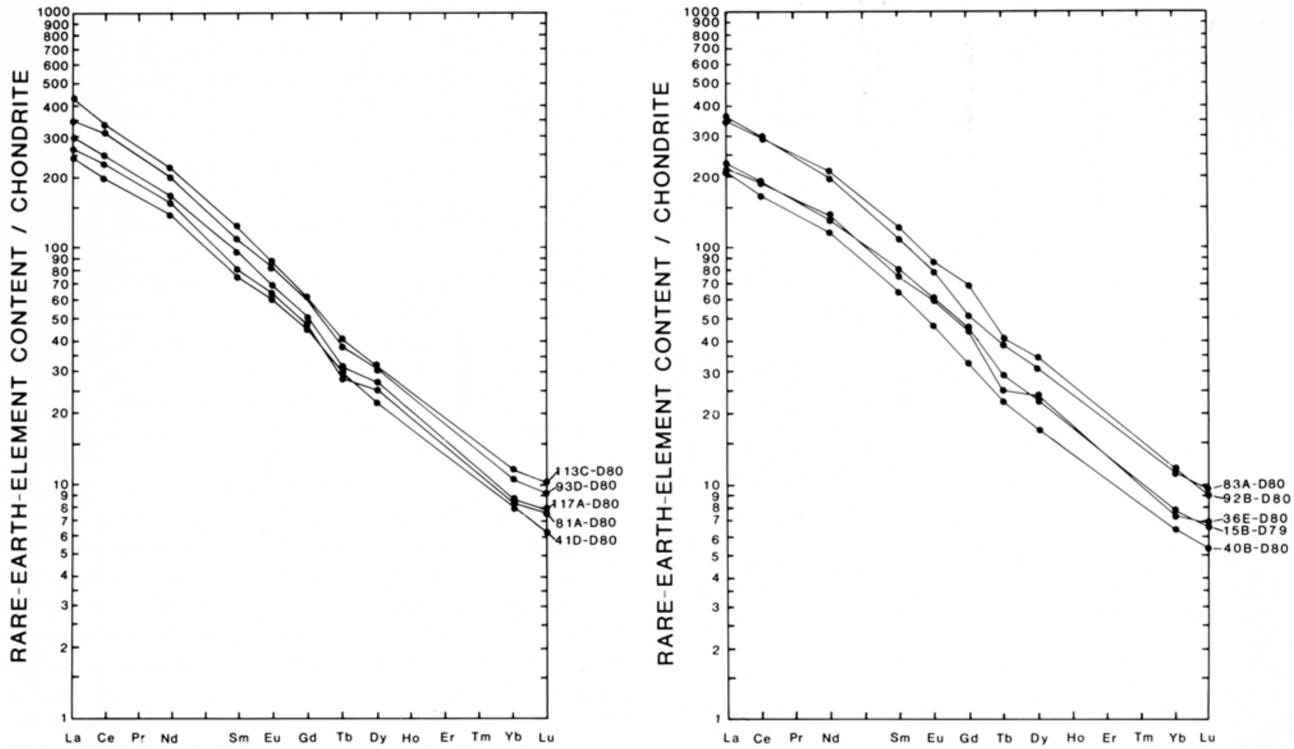

FIGURE C7—Rare-earth-element data for 10 monchiquites from the Hopi Buttes normalized to chondrite rare-earth-element concentrations.

of augite phenocrysts and amygdules of calcite in a brown glassy matrix (Fig. C3). The travertines are primarily calcite and dolomite with minor amounts of quartz and iron oxide. Essentially no clay was identified despite the argillaceous appearance of many specimens; even x-ray analyses of residues generated when samples were dissolved in hydrochloric acid to remove all calcite and dolomite showed no kaolinite, montmorillonite, or sercite—very small amounts of illite were observed in one sample.

The lacustrine sediments within most maars show evidence of abundant organic activity in the lake. Thin laminations in many travertines are indicative of depositional control by algal mats, which in some places have stromatolitic form. Thin sections reveal that oolites are common in the lake beds (Fig. C9). Fossils of fresh-water mollusks, fishes, and bird tracks occur within these lacustrine sediments (Sutton, 1974). A thin layer of organic-rich material was initially deposited at the bottom of a number of lakes as evidenced by its location immediately above limburgite tuff and below all other lacustrine sediments. Chalcedony and opal fill fractures within the travertine and appear to have replaced organic material.

Even the "pure" travertine beds are hardly pure calcium

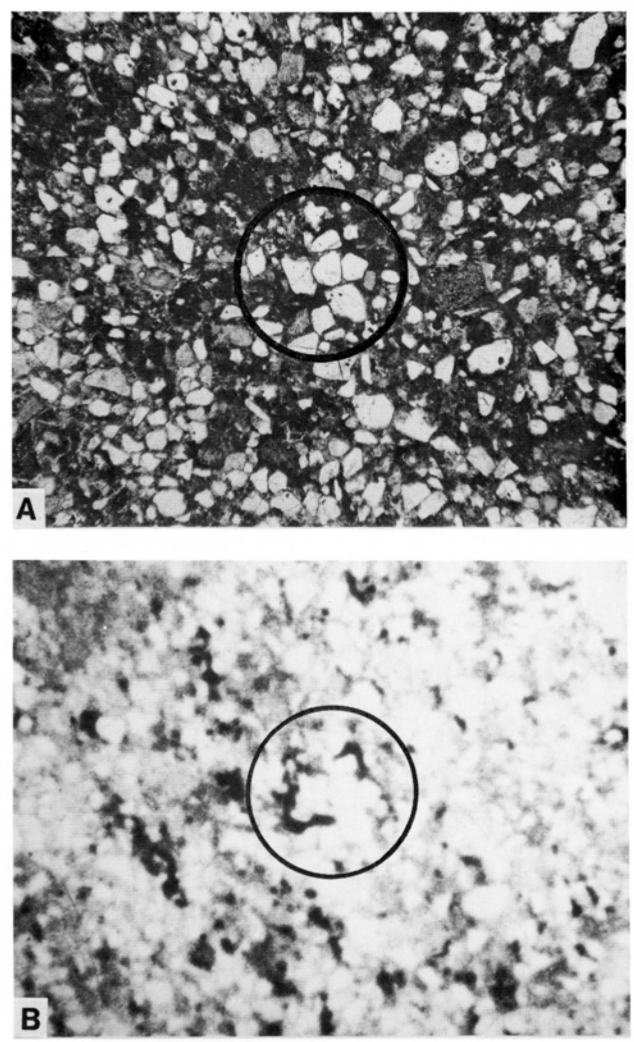

FIGURE C8—Photomicrograph and fission-track map of finely laminated siltstone unit. **A,** Photomicrograph with plane-polarized light (sample 27E-D79). These clastic rocks contain a volcanic component, but they are composed dominantly of detrital quartz with sparse feldspar and mafic minerals in a fine-grained clastic or calcite matrix. Circle encloses five detrital-quartz grains surrounded by opaque material—discussed in Fig. B. **B,** Fission-track map of the area shown in A. Dark areas are produced by abundant fission tracks and represent areas of high uranium. Note the five quartz grains in the center of the field surrounded by a uranium-rich area. This area of dense fission tracks precisely replicates the opaque material surrounding the quartz in A. The uranium was apparently adsorbed and concentrated by the iron–titanium oxides. Short dimension of field of view is approximately 3 cm.

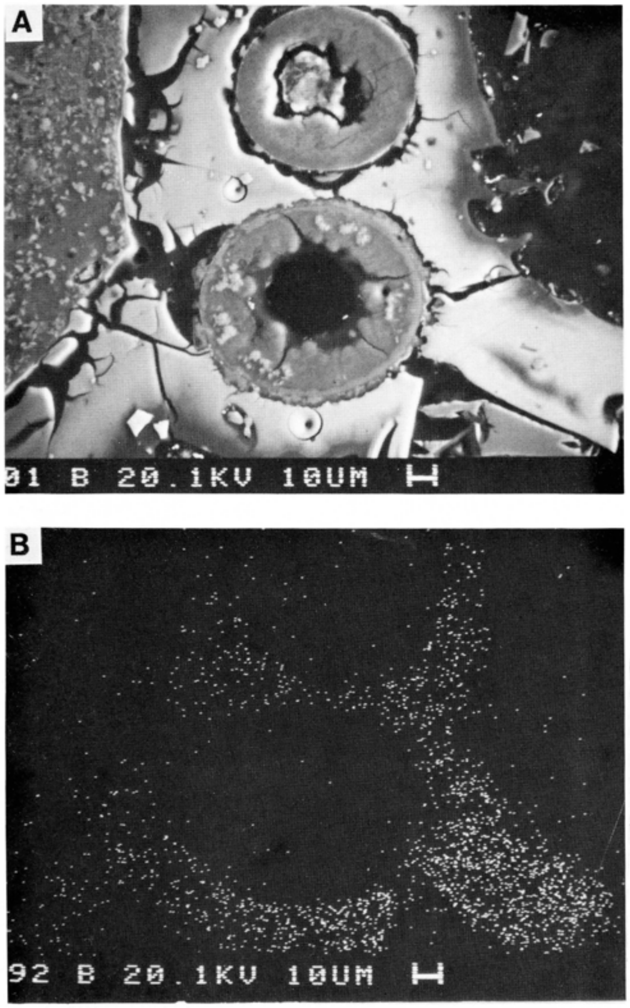

FIGURE C9—Backscattered electron image and x-ray map of siliceous oolites surrounded by an iron–titanium oxide (sample 1G-D79). In many samples, entire laminations are made up of oolites, but in this sample of clastic material, which includes lapilli of limburgite tuff within a calcareous siltstone host, the oolites are within a volcanic clast that apparently incorporated some sedimentary detritus. **A,** Electron image. **B,** Uranium x-ray map of the same area. Note how the uranium is concentrated in the iron–titanium oxides surrounding the oolites.

carbonate as can be seen from Table C-1. Many metals, particularly uranium, are enriched well above the average crustal abundance for carbonates. In fact, carbonates are rarely good hosts for uranium mineralization, and generally have uranium concentrations of less than 5 ppm, yet 90 of 127 (71%) travertine samples from 58 different diatremes contain more than 30 ppm uranium (Wenrich and Mascarenas, 1982a). Perhaps a modern analogue of the Hopi Buttes travertines are the modern travertine beds north of Ojo Caliente near La Madera, New Mexico. The Ojo Caliente travertines contain uranium concentrations of 25 ppm, and the warm springs (14–27°C) presently precipitating the travertine contain highly anomalous uranium concentrations of 23–150 ug/l (ppb) (Wenrich-Verbeek, 1977). Although the uranium concentration in the Ojo Caliente travertines is not as high as most of the Hopi Buttes travertines, nor is the environment a lacustrine one as in the Hopi Buttes, the uranium concentration in both travertines is anomalous for carbonates and the similar suite of anomalous metals suggests that a similar mechanism for metal enrichment might be invoked for both hot-spring sources.

Economic geology

The Hopi Buttes maar-lake sediments were the hosts for uranium mineralization. Although the diatremes themselves are not mineralized, almost all that still have maar-lake sediments exposed above them containing travertine deposits have anomalous uranium concentrations in most of their lacustrine sediments, including the clastic sediments, limburgite tuffs, and travertines. There are about 300 diatremes in the area, yet only about 25% presently have maar-lake sediments preserved overlying them; the bulk of these are located within the eastern part of the volcanic field where erosion has not been as intense. Uranium-rich travertines were probably present on the western side of the field too, but the volcanic structures are eroded to a level beneath the maar-lake sediments.

Of the 58 maars sampled, 23 have travertine beds with uranium concentrations exceeding 100 ppm, and the Morale claim diatreme (Stop 3) contained sufficient concentrations for uranium recovery during the 1950's. According to Shoemaker et al. (1962), "the production records of the U.S. Atomic Energy Commission, Grand Junction, Colorado, show that the tenor of the material mined ranges from 0.10% U_3O_8 to 0.18% U_3O_8 in truckload lots and averages 0.15% for 186 tons. Selected grab samples taken from the thinnest parts of the host beds contain as much as 0.40 to 0.50% U_3O_8." At the Morale claim, selenium is associated with the uranium to such an extent that *Astragalus patersoni* (Fig. C10) is abundant.

Within each maar, the highest uranium concentrations are in the travertines and clastic rocks, whereas lower uranium concentrations occur in limburgite tuffs and monchiquite flows. No uranium minerals, other than opaque oxides discussed below, were observed in any of the rock types of the Hopi Buttes. Those tuffaceous sandstones and other clastic rocks within diatremes not containing travertine deposits contain no gamma radioactivity above background. Within the travertine deposits, drilling has shown the highest concentrations of uranium to be near the base, just above the travertine contact with the limburgite tuffs. Fission-track maps show the uranium to be disseminated in all the la-

FIGURE C10—At the Morale claim diatreme, sufficient selenium is associated with the uranium to stimulate growth of *Astragalus patersoni*. This plant accumulates so much selenium that it is also known as "loco weed" because of its toxicity to cattle that graze on it. Its tap root extends for 10 m, which makes this plant a good geochemical prospecting tool for uranium deposits that are associated with selenium enrichments, as are most Colorado Plateau-type uranium deposits.

custrine sediments (Fig. C8), mimicking the sedimentary structures to the extent that it is difficult at a glance to distinguish the thin section from the fission-track map (Fig. C8). The uranium is concentrated in iron–titanium–oxide opaque rims surrounding: (1) detrital quartz grains within the clastic rocks, (2) lapilli within the limburgite tuffs, and (3) oolites (Fig. C9) or other detrital grains within the travertines. Electron-microprobe studies have not, as yet, been able to isolate discrete mineral phases which have concentrated the uranium, but areas in the clastic rocks with uranium concentrations as high as 8% U_3O_8 have approximate concentrations of $FeO = 26\%$, $TiO_2 = 19\%$, $SiO_2 = 7\%$, $Al_2O_8 = 7\%$, $P_2O_5 = 5\%$, and $MgO = 2\%$; Cao, MnO, K_2O, BaO, and SrO were each less than 1%.

Road log

Excursion 5A will depart from Flagstaff and drive 105 mi through the eastern part of the San Francisco volcanic field, across the Little Colorado River valley, and into the Black Mesa basin area. The geologic map of the Flagstaff 1° × 2° quadrangle (Ulrich et al., 1984) covers most of the area driven on this field trip. The map (MF-1960) of the eastern part of the San Francisco volcanic field (Moore and Wolfe, 1987) provides detail for the first 24 mi after leaving I-40.

Mileage

0.0 Depart Northern Arizona University from the west exit (University Drive). **1.0**

1.0 Take second onramp for I-40 (east) and drive to Cosnino exit. **11.0**

12.0 Take offramp, turn left, follow Cosnino road north. **2.0**

14.0 Turn right (southeast) on Leupp–Winona highway. **2.0**

16.0 Turn left (northeast) toward Leupp. **12.5**

28.5 The large fresh cinder cone on the left is Merriam Crater, a vent for several alkali olivine basalt flows, one of which dammed the Little Colorado River 12 km to the northeast and flowed an additional 24 km down the canyon. That flow has a K–Ar age of 0.15 ± 0.03 Ma. This area was used as an astronaut training site for the later Apollo missions because of its variety of volcanic landforms and stratigraphic relationships. **7.5**

36.0 Last outcrop of basalt. Road is on buff-colored Permian Kaibab Formation and red Triassic Moenkopi Formation from here to the river. **11.0**

47.0 Cross the Little Colorado River at Sunrise Trading Post. A hike in the White Mountains, down the headwaters of this major tributary of the Grand Canyon, is planned on Day 5. For the next 20 mi, the road climbs out of the river valley across, in succession, recent floodplain deposits, valley fill from the volcanic damming of the river, and eolian deposits derived from these materials. **25.0**

72.0 Paved road ends. **13.0**

85.0 Cross Highway 87. Continue east on pavement. **19.0**

104.0 **STOP 1. Coliseum maar.** The Coliseum maar is perhaps the most visited of the Hopi Buttes maars primarily because of its spectacular morphology, which is certainly reminiscent of a coliseum or Roman amphitheater (Fig. C11). An 800 m diameter basin is nearly surrounded by walls that reach almost 30 m in height and dip about 35° toward the center of the Coliseum. In places on the outside wall the beds are almost vertical. The walls are comprised dominantly of interbedded lacustrine sediments and limburgite tuff. The rock is cut by reverse faults that for the most part have small displacements and commonly die out as recumbent folds—Fig. C12 shows a reverse fault with an outward dip of about 20° and a displacement of about 30 cm terminating in a recumbent fold. Note that the lacustrine deposits of siltstone alternate with the limburgite tuff (Fig. C13). Could the dip to these beds all be original or has some downward displacement, perhaps due to magma withdrawal, created some of the steep dips? If this is original dip, did the limburgite tuff come from this maar, or did it perhaps come from an adjacent maar and settle into the lake that was present in this diatreme? Would that not explain the interbedded nature of the travertine sediments with the tuff? If they all came from

FIGURE C11—Aerial view of the Coliseum maar, 800 m in diameter. The inward dip of the beds and the circular nature of the maar distinctly resemble the Roman Coliseum. View is to the east.

FIGURE C12—The outer wall of Coliseum maar is cut by numerous reverse faults that generally have small displacements that die out in recumbent folds (such as that just above the rock hammer) as opposed to distinct fracturing of the rock. This fault can be observed just inside the diatreme on the west side where the road passes through the wall.

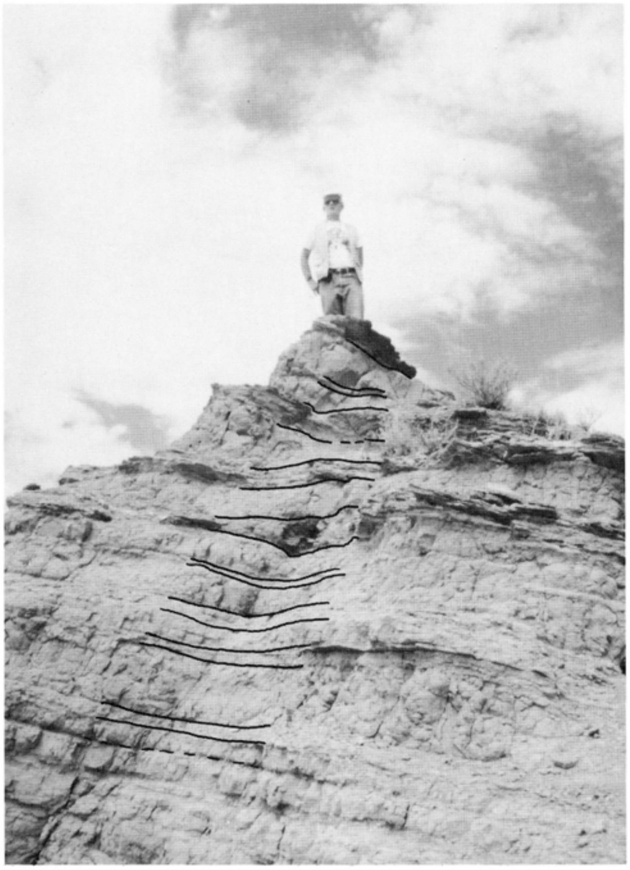

FIGURE C13—This sequence of alternating lacustrine deposits of siltstone/travertine and limburgite tuff beds lies at the outer edge of Coliseum maar, just north of the road where the maar units overlie the Rock Point Member of the Wingate Sandstone. Directly under the person's feet is the youngest siltstone/travertine bed in this photograph,one of 10 such beds that alternate with beds of quiescent periods from coarse-grained fractured tuffs of explosive origin.

this diatreme, would not subsequent eruptions have blown apart the lacustrine sediments and caused more slumping and folding?

Toward the outside of the maar in the basalmost limburgite tuff, casts of tree roots, or perhaps worm burrows, can be observed. Only a meter or so away, numerous granite and ultramafic xenoliths can be collected. Xenoliths of the underlying Paleozoic sandstones (such as the Cambrian Tapeats Sandstone, from deeper than 915 m beneath the present land surface) and limestones are also found.

Drive east to intersection of dirt road on left (1.0); turn left (northeast) and drive to Crazy Water springs diatreme (3.5). **4.5**

108.5 **STOP 2. Crazy Waters maar.** Although the geometry of this maar is not as obvious as those found elsewhere, this stop will provide the opportunity to observe and discuss some of the depositional processes that occurred during sedimentation within the maar lakes. In addition, numerous xenolith types can be collected from the top of the depositional sequence.

Crossbedded limburgite tuff is well exposed here (Fig. C14). Also present is an exposure of thinly laminated siltstone beds that exhibit soft-sediment deformation by an overlying bed of travertine-cemented limburgite tuff lapilli (Fig. C15). This outcrop raises several questions. Are these depositional features caused by wave action within the lake and slumping of sediment from the maar rim, or could it be from "Cameroon-style" catastrophic lake overturn above an alkaline diatreme as suggested by White and Fisher (1987). They suggest an exotic origin for the large dunes. In this interpretation, CO_2 from the underlying diatreme seeped into a stratified vent-lake and was stored in its lower levels until lake overturn triggered catastrophic CO_2 degassing, as recently occurred in Cameroon, West Africa. They inferred that the dunes at the Crazy Waters diatreme formed when large waves washed onto the inner walls of the maar and carried tephra back into the vent in powerful "'swash-like' currents" (James D. L. White, written comm. 1988). Were these lakes deep enough for such a process to have occurred?

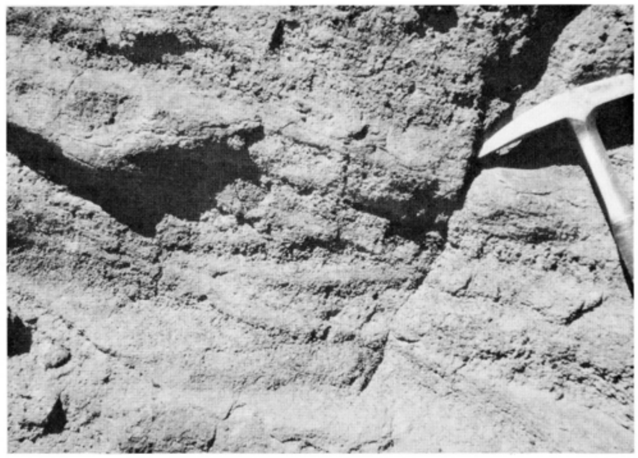

FIGURE C14—Crossbedded limburgite tuff in the Crazy Waters maar.

An excellent summary of the varieties of xenoliths present was provided by James D. L. White (written comm. 1988):

> The xenoliths tend to be partially segregated by type. Precambrian red granophyric granite is fairly common at the north end of the . . . ridge, whereas the Precambrian diorite clasts are more common to the south. Clinopyroxenite crystal masses and red Wingate sand-

FIGURE C15—Soft-sediment deformation of the finely laminated maar-lake siltstone by the overlying travertine-cemented limburgite lapilli. Crazy Waters maar.

stone clasts are the most abundant exotic components overall. Dense grey limestone, highly rounded chert pebbles, . . . coarsely calcite-cemented red granulestones . . . , and yellowish quartzose sandstone clasts have also been found. . . . The Precambrian diorite clasts are commonly jacketed with limburgite . . . , [in contrast] the red granite xenoliths are only rarely jacketed, but are commonly rounded. . . . A point of contention among Hopi Buttes workers centers on how deep-seated clasts arrive at the surface. [Some] workers have considered the Hopi Buttes eruptions to have been largely phreatomagmatic (Williams, 1936; Hack, 1942; Sutton, 1974 . . .). Phreatomagmatism is restricted to relatively shallow depths, and this interpretation requires that deep-seated Precambrian clasts be brought near the surface within the intruding magma, with subsequent shallow-level explosive hydrovolcanic fragmentation producing blocky pyroclasts and "freeing" whatever deep-seated xenoliths were being carried in the magma. Abundant jacketed clasts tend to support the "hydrovolcanic" interpretation. Shoemaker and others (1962) however suggest that the Hopi Buttes maar/diatreme eruptions were driven by magmatic volatiles, particularly CO_2. Opening of a fracture to the ground surface above advancing magma is believed to initiate a decompressional wave, which moves rapidly downward. Material behind (above) the descending wave travels upward as a fluidized gas/liquid magma mixture, and wall rocks are spalled into this mixture and carried up within it. In such a system jacketing should be less common, although some magma droplets could still adhere to the co-fluidized xenoliths.

Retrace route to highway (3.5); turn left (east, 4.0). **7.5**

116.0 Intersection with Highway 77 (Navajo 6); Bidahochi Trading Post across highway. Turn left (north, 4.0); turn right (east) on highway to Greasewood (2.0). **6.0**

122.0 Turn left (north) on dirt road to Morale mine workings. **1.5**

123.5 **STOP 3. Morale claim maar.** The Morale claim maar sits adjacent to the southwestern edge of monchiquite-lava-covered Red Clay Mesa. Its thick lacustrine-sediment sequence stands in sharp contrast to the neighboring black monchiquites (Fig. C16). Shoemaker et al. (1962) provided a detailed geologic map and description of the Morale claim maar: "The lower exposed part is filled with a chaotic assemblage of blocks and finer debris derived from prevolcanic members of the Bidahochi Formation and the volcanic 'White Cone' member, which range from detrital particles of the original sediments to large masses a few hundred feet long emplaced by inward slumping of the walls of the vent. . . . Resting unconformably on the chaotic slump debris is a sequence of laminated to massive siltstone, limy siltstone, and carbonate rock, which interfingers toward the walls of the vent with tuff and coarse volcanic breccia" (Shoemaker et al., 1962: 340). USGS drilling of 24 shallow holes into this maar in 1979 has shown that the presently preserved maximum thickness of travertine beds is 28 m. All holes were drilled through the entire thickness of the lacustrine sediments, limburgite tuffs and slump debris, and penetrated the underlying Wingate Sandstone at an average depth of approximately 60 m.

FIGURE C16—Morale claim maar located adjacent to the southwest side of Red Clay Mesa capped by a monchiquite flow. Note the sharp contrast of the whitish-yellow lacustrine sediments with the black monchiquite flow.

The adit from which 186 tons of uranium ore was removed is located just to the left of the road as it first climbs up onto the maar-lake sediments. The mine dump and scraps of wood are still visible below the adit opening. Note the abundance of *Astragalus patersoni* in the area and the garlic-like odor emitted from the plant due to its selenium enrichment. Also, note the anticlinal flexure in the clastic sediments at the mouth to the adit. Could this have had an influence on the uranium enrichment in this area?

The road continues up the hill to the center of the maar where a windmill sits on top of drill hole #3; artesian water was encountered near a depth of 60 m during the drilling of this hole. The drilling crew was forced to make a hasty retreat when the drill rig started to tip over backward due to ponding of water and saturation of the ground around the top of the hole. The Navajo Indians subsequently made a pumping waterwell out of this hole. The diatremes form an excellent vertical conduit for the movement of ground water in this part of the Navajo Reservation, and many of the producing waterwells are collared in the diatreme centers.

A short hike down the one gully dissecting the Morale maar (visible in Fig. C16) provides a good example of the crossbedding that occurs in the limburgite tuffs. Also, glassy limburgite tuff lapilli can be observed within travertine beds, suggesting that air-fall tuff may have been deposited from an adjacent diatreme into a quiescent hot-spring, travertine-producing lake.

Past the windmill, the road continues to the top of the maar where the contact between the maar and the monchiquites of Red Clay Mesa can be observed. Note the very steeply dipping beds of lacustrine sediments "plastered" up against the side of the mesa (Fig. C17). This appears to suggest that the Morale maar formed subsequent to the flows capping Red Clay Mesa. Is this original dip of the sediments or is some of it due to collapse into the center of the diatreme? This part of the maar contains the thickest preserved sequence of travertine beds.

Retrace route back to Bidahochi Trading Post. **7.5**

131.0 Continue south to Hoskietso maar–diatreme on left; turn off highway and park. **2.0**

133.0 **STOP 4. Hoskietso maar–diatreme.** This stop provides an opportunity to study three adjacent structures: two maars and one limburgite diatreme (Fig. C18) with a monchiquite dike cutting through

FIGURE C17—Steeply dipping beds of Morale claim maar-lake sediments are "plastered" against the edge of Red Clay Mesa. Similar beds in the center of the maar are flat lying.

FIGURE C19—This view to the southeast of the tuff/monchiquite butte shows another maar that forms a northwest-trending alignment with Hoskietso and the butte. Note the monchiquite dike (arrow) cutting through the northwest rim of the maar and extending across the north side of the butte.

its edge and into the maar to the southeast (Fig. C19). At the Hoskietso maar an excellent example can be observed of sedimentary breccia where the road dissects the western edge of the maar (Fig. C18). This sedimentary breccia is composed of large (up to 2 m across) red angular blocks of the Rock Point Member of the Wingate Sandstone and forms the basal unit of the tuff ring forming the maar. On the east rim of Hoskietso maar, thin platey siltstone beds and a massive agglutinate can be observed. This diatreme contained sufficient uranium within the northeast corner of the maar to cause one prospector to dig a pit into the sediments during the 1950's uranium boom. Surface samples collected from this area in 1978 contained up to 163 ppm uranium. The USGS drilled six holes into this maar in 1979, but the results were disappointing, showing only a thin sequence of lacustrine sediments with uranium concentrations less than 100 ppm.

The vent that adjoins the diatreme at the Hoskietso claim on the southeast (Fig. C18) is representative of a slightly different type. Shoemaker et al. (1962: 336) state: "It is only about 240 m in diameter, as contrasted with 760 m for the Hoskietso claim diatreme, and underlies a butte that rises about 150 m from the valley floor. It is filled mainly with rudely bedded coarse tuff and agglomerate intruded by irregular dikes and sills of monchiquite. The walls of the vent cut the Rock Point Member of the Wingate Sandstone and are exceptionally well exposed on the south side, where they are nearly vertical or dip 70–90° inward. Bedding in the tuff dips 20–35° from all sides toward the center of the vent."

Directly adjacent to this central butte on its southeast side is another maar slightly smaller than the Hoskietso maar. An augite-rich monchiquite dike cuts across its northwest rim (Fig. C19); sample 3A-D79 (Table C-1) was collected from this dike. What is the relationship between these three diatremes? Is the tuff/monchiquite diatreme older than the two maars? Note the relationship of the tuff ring to the Rock Point Member on the western side of this maar (Fig. C20). Here steeply dipping lacus-

FIGURE C18—The Hoskietso maar is located just to the left of the tuff/monchiquite diatreme forming the prominent butte. The road crosses the edge of the Hoskietso maar and exposes a spectacular basal sedimentary breccia containing large clasts of red Wingate Sandstone.

FIGURE C20—Steeply dipping lacustrine beds forming the maar rim of the diatreme located southeast of the monchiquite butte adjacent to Hoskietso. The lacustrine beds rest directly on flat-lying Rock Point Member of the Wingate Sandstone. Person is standing on the inside of the maar rim.

trine beds rest directly on flat-lying Rock Point sandstone beds. Is this evidence that the dip of the maar-lake sediments is original dip, or could these sediments still have collapsed back into the vent producing some soft-sediment deformation?

These three structures form a northwest-trending alignment, and the dike cutting through two of them also strikes northwest. These three structures provide examples of most rock types present in the Hopi Buttes area, and exhibit various levels within diatreme/maar systems.

Drive south on Highway 77 to Holbrook. **40.0**

173.0 Arrive in Holbrook, Arizona.

Acknowledgments

Dave Nealey, Gene Shoemaker, and James White provided advice on the selection of maars and diatremes to use in the field-trip stops. A special thanks goes to Gene Shoemaker for his advice and guidance over the years. The petrographic advice and help from Hoyt Sutphin and Ben Leonard was particularly helpful in sorting through the zeolites and feldspathoids in the monchiquites and limburgite tuffs. The oblique aerial photos were taken by G. E. Ulrich; aircraft was piloted by C. D. Condit. The manuscript was improved through reviews by G. E. Ulrich, Wendell Duffield, and James White. A special thanks goes to Bradley Van Gosen and Hoyt Sutphin for assistance in assembling the manuscript.

D. Fourth-day field trip: Springerville volcanic field

Christopher D. Condit, Larry S. Crumpler, and Jayne C. Aubele

Introduction

The Springerville volcanic field is the southernmost of seven dominantly alkalic fields located near the southern margin of the Colorado Plateau (Fig. 1 in Summary). Like the Mormon Mountain and San Francisco fields visited earlier, the Springerville field is late Tertiary to Quaternary in age, and consists dominantly of monogenetic cinder cones and their associated flows. In contrast to the San Francisco, Mormon, and White Mountains (Mount Baldy) volcanic fields, the Springerville field contains no silicic eruptive centers or large composite volcanoes. Most of the lavas are alkali olivine basalt; many are chemically transitional toward tholeiite, including a smaller proportion of more evolved alkalic rocks and tholeiite.

In earlier descriptions of the volcanoes of east-central Arizona, Merrill and Péwé (1977) combined the younger basaltic field north of Arizona Highway 260 with the older basalts and trachyte shield of Mount Baldy, generally south of Highway 260, into a single province called the White Mountains volcanic field. Due to the distinctive grouping of ages and volcano types in these areas, we have separated them, renaming the northern area of mainly monogenetic cinder cones, flows, and two basaltic shields, the Springerville volcanic field (late Pliocene to Pleistocene in age; less than 3.1 Ma) and restricting the White Mountains nomenclature to the older volcanic features, generally late Miocene to Pliocene(?) in age, south of the approximate boundary shown in Fig. D1. The area encompassed by volcanic rocks of the Springerville volcanic field is approximately 3000 km^2. Of this area, volcanic outcrops cover about 2600 km^2; the remainder consists of various surficial units and exposed windows of sedimentary bedrock.

The purpose of this day's 140 mi trip will be to review the volcanology, petrology, and tectonic setting of the Springerville volcanic field. The route has been designed to present an overview of the geochronology, chemistry, and areal distribution of the field's flows and vents. Map units have been distinguished on a flow-by-flow basis, using lithologic and morphologic criteria; we will inspect several of the lithologic (petrographic) types and their correlation to chemistry and flow characteristics. Vents will be examined from several interrelated aspects, including geomorphic type, chemistry, distribution, and migration patterns; the implications of these factors will be discussed with respect to petrogenesis and regional tectonic framework. Evidence and interpretations of the mostly post-volcanic structural deformation will also be presented. During this visit we will examine the field's general east–west symmetry in that the east and west sides of the field are flanked by early sheet-like flows (uniformly several meters in thickness and commonly several tens of km^2 in area) while a high concentration of cinder cones with more differentiated, but less voluminous, flows occurs in the south-central area. This combination gives the field a broad, low, shield-like appearance when viewed from a distance.

Areas, ages, and vents

The Springerville volcanic field is latest Pliocene and Pleistocene in age. Within the area mapped to date (2280 km^2 of volcanic outcrop, Fig. D1), 409 flow units have been recognized, and 408 assigned ages ranging from 0.3 to 2.1 Ma on the basis of stratigraphy, magnetic polarity and 30 K–Ar ages (Laughlin et al., 1979; Laughlin et al., 1980; Condit, 1984; Condit and Shafiqullah, 1985; Aubele and Crumpler, 1983; Aubele et al., 1986; Condit, in press; Condit et al., in press; Aubele, unpubl. data; Crumpler, unpubl. data). One unit found along the southern margin of this area has been dated at 3.06 ± 0.08 Ma by Laughlin et al. (1979). Two additional units located southeast of Lakeside along the southwestern edge of the area have their source within the Mount Baldy complex (Condit, 1984) and underlie lavas of the Springerville field. Laughlin et al. (1979) reported additional ages (2.9, 3.7, and 3.9 Ma) on basal lava flows east of Springerville, which are contiguous with the mapped area of this report. Because all other stratigraphically basal units have ages of less than 2.1 Ma, subsequent observations

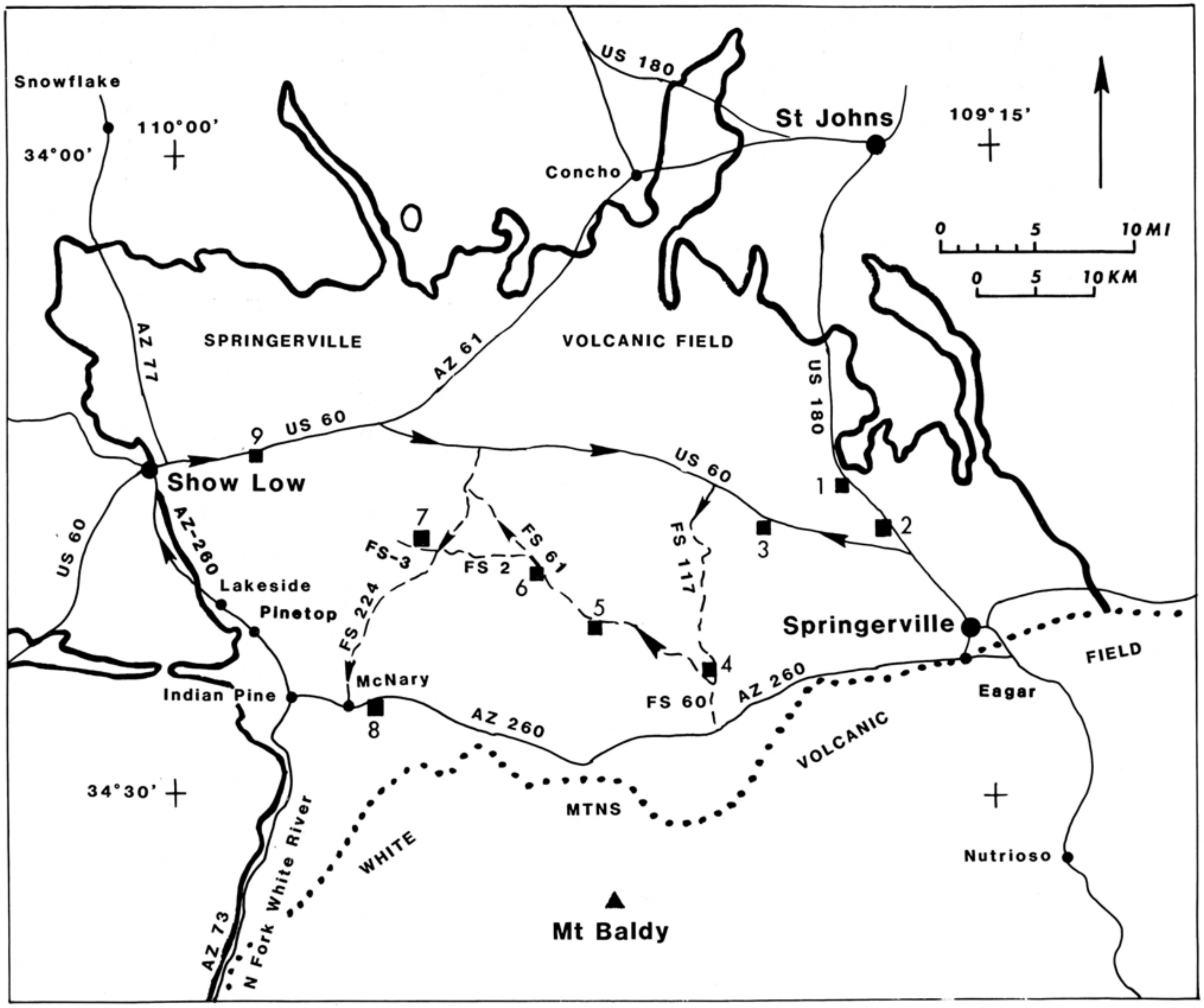

FIGURE D1—Map showing outline (heavy line) of Springerville volcanic field, field-trip route and stops. Heavy dotted line is the approximate boundary between the Springerville and the White Mountains volcanic fields. Arrows show direction of travel for field guide. Numbered solid squares are excursion stops.

pertain to units younger than 2.1 Ma. Of the total of 409 units, 257 covering about 1900 km^2 or 83% of the mapped area have been characterized chemically.

In contrast to the Mount Baldy center to the south (Fig. D1), which appears to have erupted from a single composite volcano, the Springerville lavas erupted from a large number of discrete locations over a broad geographic area. About 400 vents have been recognized; 375 appear to be simple monogenetic cinder cones, and five additional cones have multiple flows associated with them. Other less common vents include eight maar craters, two endogenous domes, two shield volcanoes and about 10 fissure vents associated with early flows of sheet-like habit. Unlike most other volcanic fields of the southern Colorado Plateau, large concentrations of centimeter-size ultramafic xenoliths are generally absent in vents of the Springerville field, although minor concentrations of small xenoliths occur in selected flows and cinder cones.

Compositions and volumes

The character and general petrologic history of the field can be summarized by a compilation of areal and temporal data from units characterized chemically. The separation of alkalic and tholeiitic compositions was accomplished by comparing 44 La/Yb ratios for rocks representative of the Springerville volcanic field with tholeiitic rocks of the Servilleta and Columbia River basalts. This comparison yielded the following averages, standard deviations and ranges, respectively: Springerville volcanic field—17.72 ± 6.5, 8.18–33.67; Servilleta basalts—5.35 ± 1.1, 3.79–9.32 (57 analyses, Dungan et al., 1986); and Columbia River basalts—6.36 ± 2.2, 2.9–10.7 (13 analyses, Carlson, 1984). Those rocks from the Springerville field that overlap with continental tholeiites serve as a reference to define tholeiitic basalts in the Springerville field (in addition to other trace-element parameters such as Y/Nb). Comparison of alkali–silica content and CIPW normative hypersthene from these reference samples indicates that most hypersthene-normative rocks (averaging about 5 wt.% hy) and falling below the Irvine and Baragar (1971) reference line are tholeiitic, providing a basis for classifying units without trace-element data. We use the terminology of Coombs and Wilkinson (1969) to describe the alkalic rocks, noting that several of the more evolved rocks, for which we retain the alkalic terminology, overlap slightly into the field of trachyandesites as defined by Cox et al. (1979).

Estimates of areal distributions of different rock types show the following proportions: 47% (890.7 km^2) alkali olivine basalt; 28.5% (539.7 km^2) hawaiite; 0.6% (10.5 km^2) mugearite; 0.2% (4.5 km^2) benmoreite; and 23.7% (449.8 km^2) tholeiite. The total volume of the field, estimated from well data and topography, is approximately 300 km^3. Effusion rates for each rock type can be estimated, given the assumption that the surface area of these 257 units is representative of volume. Because tholeiite dominates the outcrop pattern in the northern part of the field, where well data indicate a thinner accumulation of volcanic rock, this estimate may overemphasize its volume. This overestimation is offset by the observation that alkali olivine basalt and more evolved alkalic rocks overlie tholeiite in the interior parts of the field. Given these qualifications, we calculate the area of each rock type erupted within 250,000 yr intervals by summing the areal percent of units characterized chemically within that interval and using this value to infer effusion rates (volume/250,000 yrs). In this analysis, mugearite, benmoreite, and hawaiite are classified as evolved alkalic rocks.

The data (Fig. D2) show an early eruptive episode (2.0–1.75 Ma) dominated by large volumes of tholeiitic lavas, a middle period (1.75–1.0 Ma) of alkali olivine-basalt eruption, and a late pulse (1.5–0.5 Ma) of evolved alkalic rocks,

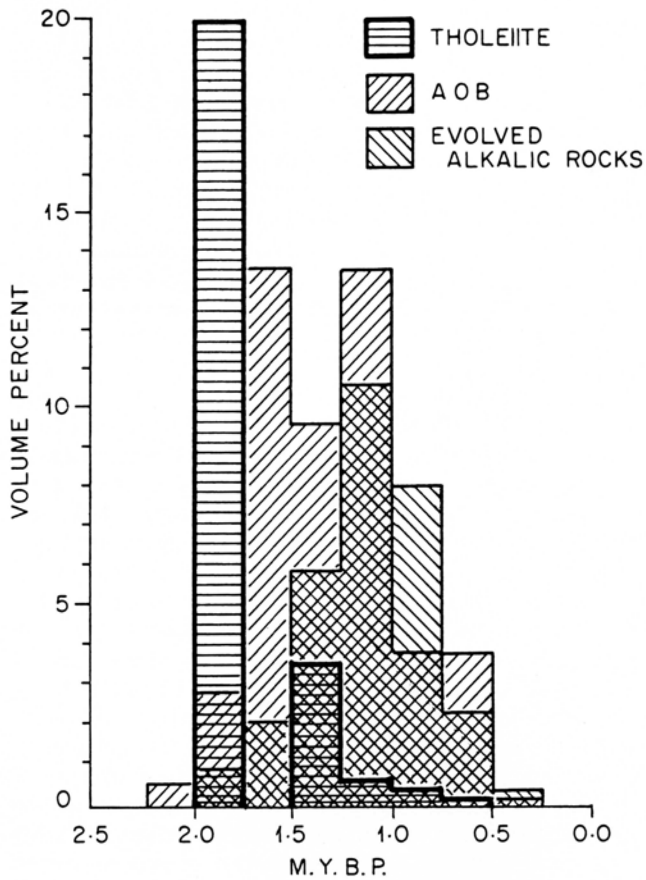

FIGURE D2—Estimated volume effusion rates for three rock types through time, viewed in 250,000 yr intervals. AOB = alkali olivine basalt (sensu stricto). Hawaiite, mugearite, and benmoreite are classified as evolved alkalic rocks. The peak in evolved alkalic rocks production, 0.5 Ma later than that for alkali olivine basalt, coupled with the eruptive recurrence interval of 4400 yrs, suggests these data represent the entire life cycle of the Springerville volcanic field.

with its peak of lava production lagging about 0.5 Ma after that of the alkali olivine basalt. The late peak in evolved alkalic rocks production, coupled with the eruptive recurrence interval of 4400 yrs between 2.1 and 0.3 m.y., suggests these data represent a complete life cycle of the Springerville volcanic field.

Two of many possible models may be invoked to explain the evolution of lava compositions described above: (1) Shear heating of a "bump" at the base of the lithosphere, as in Tanaka et al. (1986), provides early partial melting at depths around 40 km, high in volume and shallow enough to produce tholeiitic melts. Subsequent waning of the heat flux results in smaller degrees of melting that could produce alkali olivine basalts and eventually, as a result of probable fractional crystallization, evolved alkalic lavas. (2) A second model calls on a mantle diapir or plume that produces tholeiitic melts early on because it has to reach a region of lower pressure, higher in the mantle, to melt the first rocks. As the heat flux wanes with time, it becomes concentrated beneath the central area of the Springerville volcanic field and, by smaller increments of partial melting, produces alkali olivine basalt and evolved alkalic rock melts that are more geographically restricted than the tholeiites. The lag in peak production of evolved alkalic rocks behind that of alkali olivine basalt could be construed as a result of the increased residence time required for alkali-olivine basalt to evolve toward more alkalic rocks. In either of the above models, the depth of partial melting generating tholeiites or alkali olivine basalt is not well understood, given the possibility that lithospheric mantle may be enriched in incompatible elements relative to asthenospheric mantle, complicating any interpretation (Perry et al., 1987).

Temporal variations in composition and vent loci

Major-element analyses of 312 representative samples from the above 257 units show a progression away from tholeiitic affinities through time (Fig. D3). Of the rocks erupted before 1.6 Ma, 22.5% fall below the silica–alkali line of Irvine and Baragar (1971). The percentage decreased to 15.9% in the interval between 1.6 and 1.2 Ma and diminished to about 9% for the remaining eruptive history of the field.

Cinder-cone migration patterns in the Springerville volcanic field are consistent with those found in the San Francisco volcanic field to the west (Tanaka et al., 1986). Migration rates have been inferred by calculating the average location for vents erupted before and after the median age of all vents estimated at 1.2 Ma. The distance between centroid locations for the two periods was then divided by the difference in the average of the estimated ages of the vents within each period. Migration rates calculated for 230 cinder cones show an eastward progression (106° ± 13 azimuth) at 2.5 ± 0.8 cm/yr. Vent migration for 101 alkali olivine basalt units was also eastward (93° ± 22 azimuth) at 2.9 ± 1.1 cm/yr; that for more evolved alkalic rocks proceeded at a slower rate (1.8 ± 1.6 cm/yr) southeastward (azimuth 134° ± 45). Although the statistics for migration of alkali olivine basalts and evolved alkalic rocks overlap, the lower migration rate for evolved rocks may reflect the longer residence time needed for magmatic differentiation. If so, the low $^{87}Sr/^{86}Sr$ ratios for three evolved alkali rocks, between 0.70319 and 0.70366, suggest a depleted source and argue against any residence time in areas where contamination plays a part either from a crustal component (unless characterized by unradiogenic Sr), or

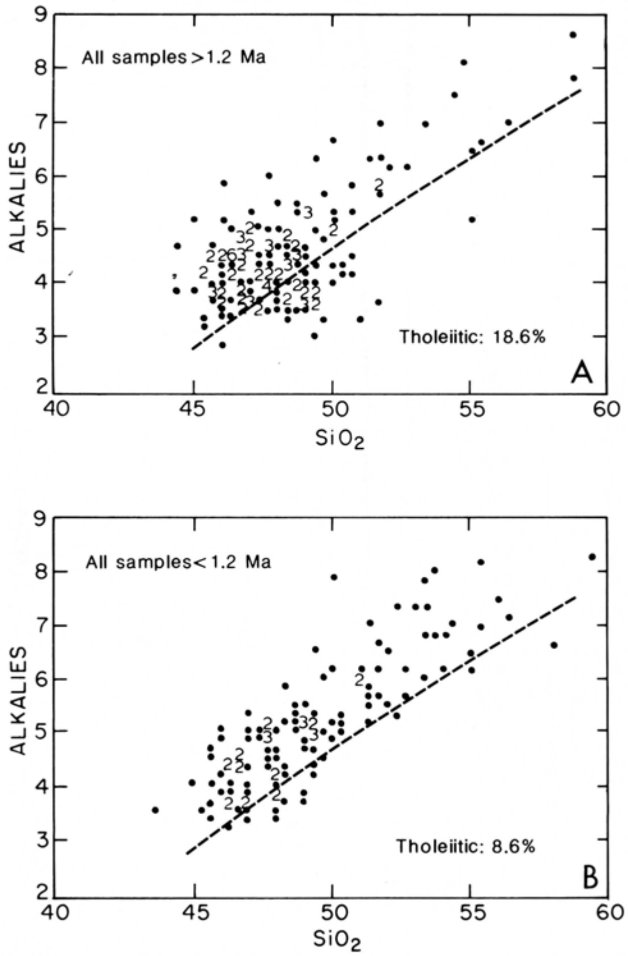

FIGURE D3—Alkalies versus silica variation diagrams for the Springerville volcanic field. Amounts are in weight percent. Dots represent single data points; numbers represent superimposed data points. **A,** Rocks older than 1.2 Ma. Approximately 19% plot in the tholeiitic field, as defined by Irvine and Baragar (1971). **B,** Rocks younger than 1.2 Ma. Approximately 9% plot in the tholeiitic field. Comparison of A and B shows a clear trend toward alkalic compositions in younger rocks, also reflected in Fig. D2.

from an enriched upper mantle, such as proposed by Perry et al. (1987) in the Mount Taylor region. Alternatively, it may reflect derivation at depth by decreasing degrees of partial melting, or simply the narrower geographic location of more evolved rocks, which tend to cluster in the central part of the field. In the San Francisco volcanic field, Tanaka et al. (1986) calculated a migration rate of 2.9 ± 0.3 cm/yr along an azimuth of $93° \pm 5$ for 463 alkali basalt (sensu lato) vents from Matuyama through Brunhes (2.48 Ma–1000 yrs) chronozones, in close agreement with that calculated for alkali olivine basalt in the Springerville volcanic field. This agreement supports a model of absolute westward motion of the North American plate over the past 2.5 Ma; no evidence for magmatic migration northward from the Colorado Plateau margin during this time-frame is recognized.

Tectonism

Detailed mapping of individual flow units has shown that some of the flows have undergone complex tilting and/or faulting in the past million years. Tectonic features occur most commonly along strike of several prominent down-to-the-northeast topographic steps that result in more than one kilometer of relief across the field. The steps are continuous, parallel, linear to arcuate, and change strike from west-northwest in the southern part of the field to northwest in the northern part. They appear not to be the result of simple normal faulting because the type of deformation along strike of a given topographic step can change from synthetic and antithetic faults to anticlinal folds, graben, and/or possible oblique-slip faults.

Road log

Excursion 5A will follow US-180 south and east from Holbrook through Saint Johns for 76 mi to Stop 1. At a point 10 mi from Holbrook, the view to the south (right) presents a panorama of the Springerville volcanic field. Stop 1 is 4.3 mi south of the first roadcut in basalt. An alternative start, coming from Springerville, is at Junction US-180 and US-60 (3.3 mi northwest of Springerville; Fig. D1). From this point, proceed north 6.2 mi on US-180, turn left (west) on Hall Ranch Road; park at edge of young basalt flow.

Mileage

0.0 **STOP 1. Hall Ranch Road flow.** This flow (K–Ar age of 0.75 ± 0.13 Ma, Laughlin et al., 1980), is one of several flows erupted from a vent complex 1 mi to the west. Another flow from that vent is the youngest dated flow in the Springerville field, with a K–Ar age of 0.308 ± 0.07 Ma (Aubele et al., 1986). The flow contains 2–6% olivine phenocrysts and is the most common lithologic type in the field. Chemically, the unit is an alkali olivine basalt (Table D-1, sample LLS99, unit Qkc4). The K–Ar age of the flow on the skyline to the north along US-180 is 1.98 ± 0.6 Ma. This is the basalt flow of the northeast edge of the field, and it lies on sedimentary rocks of Cretaceous to Triassic age. To the north, many of the swales and slopes in the basalt surface are the result of gentle structural flexures (Aubele et al., 1987). These subtle but pervasive west-northwest-trending down-to-the-northeast features are concentrated in the northern and eastern parts of the field.

Drive south on US-180. Stop on right (west) side of road at shallow roadcut. **2.9**

2.9 **STOP 2. Basal sheet lava flow.** This is a diktytaxitic composite unit (Table D-1, sample S94, unit Qag2), sheet-like in habit, and is typical of basal flows commonly found along the east and west margins of the field. The K–Ar age for this flow (1.67 ± 0.09 Ma, Laughlin et al., 1980), and its negative magnetic polarity are typical of these early sheet lava flows. To the south about 0.5 mi, one can see a small topographic rise, which is a remnant of one of the vents. These flows are typically about 5% hy-normative, and range from 6% ne-normative to 13% hy-normative. Coyote Hills to the east is one of two shield volcanoes in the field; the other (Blue Ridge Mountain) is located just north of Pinetop near the field's southwest edge. The tree-covered basalt-capped 600 m high mesa to the south marks the north margin of the White Mountain field. The basal flow of this mesa yielded a K–Ar age of 6.03 ± 0.43 Ma (Laughlin et al., 1980) from a sample collected 12 mi west of Eagar.

Proceed south to junction US-60 (3.2) then west

TABLE D-1—Selected chemical analyses and CIPW normative compositions, Springerville volcanic field, east-central Arizona. Chemical analyses are original data in weight percent. Major-element analyses by x-ray fluorescence spectroscopy, with total iron ($FeTO_3$) analyzed as Fe_2O_3. LOI = lost on ignition 900°C. CIPW normative minerals are calculated from analyses adjusted volatile-free and for the ratio $FeO/Fe_2O_3 = 9.627 - 0.0921 \times SiO_2$ according to the least oxidized rocks of the San Francisco volcanic field. La and Yb determined by INAA. Y and Nb determined by x-ray fluorescence spectroscopy. nd = not determined. — = none present.
Major-element analyst(s): Sample 19SLS not available. Sample SN24 J. S. Wahlberg, J. Baker, J. Taggart. Sample R34 S. Ramage. Samples 229L, BB123, BB113 J. S. Wahlberg, J. Taggart, J. Baker. Samples S94 and LLS97, A. J. Bartel.
INAA analyst(s): Samples LLS99, BB123, R34 J. S. Mee. Samples SN24, 19SLS L. J. Schwarz. Samples BB193, BB194 G. A. Wandless.
Trace-element XRF analyst(s): Samples 19SLS, SN24, BB193, BB194 R. Johnson, H. J. Rose, B. McCall, G. Sellers, J. Lindsay. Samples R34, BB123 J. Leister, G. A. Wandless, P. Hearn. Sample LLS99 R. Johnson, K. Dennen. Sample BB123 J. Sparks.

	Olivine basalt flow	Dikty-taxitic flow	Aphyric flow	Aphyric flow	Olivine–pyroxene flow	Aphyric flow	Wolf Mountain		Dikty-taxitic flow	Picritic flow
							hbl-phyric dome	pl-phyric flow		
Sample No.	LLS99	S94	SN24	R34	BB113	BB123	BB194	BB193	19SLS	229L
Stop	1	2	3	4	5	6	7	7	8–9	9
Unit	Qkc4	Qag2	Quh4	Qgh7	Qja2	Qjh4	Qek	Qel	QTsf	Qmb4
SiO_2	46.60	47.50	54.80	50.23	47.00	55.40	55.00	57.80	48.27	45.40
Al_2O_3	15.60	16.10	18.00	18.17	16.10	18.80	18.10	18.00	16.18	13.70
$FeTO_3$	12.00	12.41	9.46	10.31	13.01	8.79	8.66	7.96	12.43	13.10
MgO	8.85	7.59	1.80	4.23	7.79	2.60	2.20	1.31	7.39	12.30
CaO	9.51	10.90	4.86	7.46	10.10	6.47	5.99	3.73	9.72	9.74
Na_2O	2.97	2.61	4.80	4.08	3.40	4.90	4.40	5.46	3.27	2.35
K_2O	1.20	0.65	2.50	1.80	1.03	2.16	2.41	3.06	0.82	0.84
TiO_2	2.22	1.91	1.21	1.92	2.50	1.23	1.26	0.79	1.74	2.23
P_2O_5	0.45	0.31	0.89	0.74	0.40	0.88	0.67	0.68	0.25	0.36
MnO	0.17	0.18	0.19	0.15	0.18	0.17	0.19	0.22	0.18	0.17
LOI	0.02	<0.01	<0.01	nd	<0.01	nd	0.4	0.10	nd	0.32
Total	99.57	100.16	98.51	99.09	101.51	101.40	98.87	98.99	100.25	100.20
Q	—	—	2.20	—	—	—	2.55	2.41	—	—
C	—	—	0.68	—	—	—	—	—	—	—
or	7.20	3.88	15.13	10.84	6.07	12.69	14.54	18.38	4.89	4.96
ab	21.61	22.26	41.52	35.11	20.72	41.14	37.90	46.95	26.89	15.59
an	26.03	30.53	18.75	26.38	25.49	22.73	22.93	14.32	27.26	24.30
di	15.32	17.99	—	5.30	17.82	2.91	2.47	—	16.18	17.43
hy	—	3.89	14.96	3.58	—	14.02	13.57	12.31	—	—
ol	19.86	14.41	—	11.02	17.24	0.08	—	—	17.76	27.83
ne	2.09	—	—	—	4.28	—	—	—	0.54	2.30
mt	2.55	2.66	2.30	2.32	2.73	2.10	2.10	2.03	2.69	2.69
il	4.28	3.66	2.35	3.71	4.73	2.32	2.43	1.52	3.33	4.23
ap	1.00	0.74	1.00	1.78	0.94	1.00	1.00	1.00	1.00	0.83
La/Yb	13.1	nd	23.4	22.3	nd	25.0	33.7	27.9	8.4	nd
Y/Nb	0.7	nd	0.3	0.5	0.5	0.5	0.3	0.6	1.2	nd

on US-60 (7.9) through roadcut, pull off road beyond roadcut on right side of highway. **11.1**

14.0 **STOP 3. Sag flowout.** The broad flat valley to the east, surrounded by ridges similar to the one through which this road is cut, appears to be a large sag in the center of a flow lobe. One of the few east-trending fissures of the field erupted through the southeast margin of the sag and fed olivine–pyroxene–plagioclase lavas and olivine-phyric lavas from separate vents. The flow at this roadcut is aphyric, a common type found toward the center of the Springerville field (Table D-1, sample SN24, unit Quh4). It has a K–Ar age of 1.04 ± 0.05 Ma, has about 55% SiO_2, 3% MgO, and 7% alkalies, and, although 13.5% hy-normative, has an alkalic signature (La/Yb = 23.4), demonstrating the transitional character of these basalts between alkalic and tholeiitic compositions.

Continue west on US-60; turn left (south) on Greens Peak road. **4.0**

18.0 Stay on main road (FS-117) to junction with FS-61. **13.2**

31.2 Turn right (west) on FS-61 (0.4); then right (north) up Greens Peak (1.4) to lookout tower. **1.8**

33.0 **STOP 4. Greens Peak lookout.** At an elevation of 3090 m, this overlook on the 200 m high cone of Greens Peak is the topographic highpoint of the Springerville field. Greens Peak is also near the center of the highest concentration of vents and the most evolved rocks within the field. To the south, the 9–2 Ma Mount Baldy trachyte–basalt shield volcano, the subject for the fifth day's field trip, is visible above the Sunrise ski area. Closer in, the approximate boundary between the Springerville and the White Mountains volcanic fields occurs at the southern extent of a flat grass-covered park. The best preserved younger flows and cinder cones can be seen to the northeast of Greens Peak. Surrounding (and probably underlying) the central concentration of vents, older sheet flows extend as much as 20 mi west, north, and east. Greens Peak is an aphyric hawaiite (Table D-1, sample R34, unit Qgh7) and contains xenoliths of sedimentary rocks. Nearby cinder cones are the source for aphyric and olivine–clinopyroxene-phyric flow units that extend radially from the topographic summit of the field.

Retrace route to base of Greens Peak. **1.4**

34.4 Turn right (west) on FS-61 toward Vernon; stay on

FS-61 heading northward until Harris Lake. Park on right side of road. **5.8**

40.2 **STOP 5. Flow at Harris Lake.** On left side of road, this basalt flow (Table D-1, sample BB113, map unit Qja2) is an example of the more mafic compositions (olivine–pyroxene-phyric) of the field. This alkali olivine basalt contains centimeter-size gabbroic xenoliths. The source vent, northeast of the road, is a maar whose rim consists in places of palagonitic ash and accidental debris.

Continue north on FS-61. At junction with FS-2 from the west, park on right. **2.6**

42.8 **STOP 6. Juan Garcia Mountain flow.** The aphyric flow (Table D-1, sample BB123, unit Qjh4) on northwest side of junction of FS-61 and FS-2 is one of four lavas that appear to emanate from Juan Garcia Mountain, one of only five vents that produced multiple flows. The Juan Garcia sequence of flows is characterized by successively more mafic lavas, in which aphyric hawaiite and mugearite flows formed the basal units. The last spatter to erupt was an olivine–pyroxene–plagioclase-phyric hawaiite.

Continue on FS-61, to junction with FS-224. **6.7**

49.5 Turn left on FS-224. Wolf Mountain, the object of our next stop, is seen to the southwest (3:00) across a park. **4.6**

54.1 Turn right (west) on FS-3 (Dripping Vat Road). **1.2**

55.3 Park on right side of road.

STOP 7. Wolf Mountain dome. This mugearite (Table D-1, sample BB194, unit Qek) is one of six hornblende-bearing units of the field, and one of two endogenous domes. The 200 m high dome is nestled on the south side of a benmoreite cinder cone. The cone has a small plagioclase-phyric flow (Table D-1, sample BB193, unit Qel) on its north flank, and is one of two benmoreites, the most evolved rock in the field. The K–Ar age of Wolf Mountain (1.56 ± 0.05 Ma) and the even older benmoreite that erupted from the cinder cone demonstrate that, although evolved rocks tend to be erupted late (Fig. D2), they also occur early in the field's history. This, and the wide range in incompatible trace-element ratios for all rocks of the field may reflect the derivation of these rocks from a large number of discrete magma batches (Condit, 1984), some of which may be the product of open system fractionation (Cooper and Hart, 1986).

Return to the junction with FS-224 (1.2); turn right (south) to McNary (10.9). **12.1**

67.4 In McNary, turn left (east) on AZ-260 to intersection with unpaved Apache Tribe 76B. **3.2.** NOTE: PERMISSION IS NECESSARY TO ENTER WHITE MOUNTAIN APACHE TRIBAL LAND.

70.6 Turn right (south) on Apache Tribe 76B. **1.1.** Park and walk south 100 m to top of escarpment.

71.7 **STOP 8. Mogollon Rim overlook.** This viewpoint is at the south edge of the Colorado Plateau, capped here by a sequence of four basalt flows overlying sandy early Tertiary Rim Gravels (see Price, 1950). The large toreva block field at the base of the escarpment was formed by the removal of these gravels by the North Fork of the White River, presently 160 m below and 2.4 km south of this point. The basal basalt flow (unit QTsf) at this point has been constrained by stratigraphic relations, six K–Ar ages, and 16 paleomagnetic-polarity determinations to be between 1.6 and 1.9 Ma (Condit, 1984; Condit and Shafiqullah, 1985; Peirce et al., 1979; Castro et al., 1983). The escarpment has retreated between 1 and 2.4 km, suggesting a horizontal rate of retreat of the Mogollon Rim at this location of 1–1.5 km/Ma over the past 1.6–1.9 m.y.

Retrace route on Apache Tribe 76B to AZ-260 (1.1); turn left (west) on AZ-260 and drive through McNary to Hon Dah (Indian Pine) and junction of AZ-73 (6.2). **7.3**

79.0 Stay right on AZ-260, continue northwest. **4.1**

83.1 In Pinetop, an 8.97 Ma flow that has been correlated with the Mount Baldy shield volcano 25 mi east-southeast of here (Condit, 1984), crops out about 0.5 mi south of the highway. The mesa-capping flow overlies Rim Gravel and partially underlies the basal flows of the Springerville field.

Continue northwest toward Show Low. **10.7**

93.8 One mile south of Show Low two basalt flows can be seen across an alluvial valley on the right. These form the basal flow unit (Table D-1, sample 19SLS, unit QTsf) on the western side of the field, overlying Cretaceous sandstone in this area. Similar flows form the basalt unit on top of Rim Gravel at Stop 8. These sheets are similar in composition, diktytaxitic texture, and stratigraphic position to the flow seen at Stop 2 on the eastern side of the field. As discussed at Stop 8, K–Ar ages for this tholeiitic composite flow unit range between 1.6 and 1.9 Ma; the unit is the largest of the field, extending 16 km to the north and covering more than 346 km^2. Tongues of this unit also flowed 85 km south of the main body of the field, down drainages that cross the edge of the Colorado Plateau to the Salt River.

Continue to Show Low (1.0) and turn east on Deuce of Clubs Highway (US-60). Park on right side, opposite Bourdon Ranch Road. **5.5**

99.3 **STOP 9. Picritic basalt flow.** Flow on right side of road is the largest olivine-rich (picritic) basalt flow in the field (Table D-1, sample 229L, unit Qmb4), covering 14.4 km^2, and overlying the basal diktytaxitic flow unit (QTsf) seen south of Show Low. Its chemistry is typical of olivine-rich flows, with 45.4% SiO_2, 12.3% MgO, 3.2% alkalis, and $Mg \times 100/Mg + Fe^{++} = 70.1$. The flow contains 14–23 modal % olivine (Fo_{81}) phenocrysts, which are unzoned except for thin rims. The rock probably represents a cumulate residuum. The flow continues north from here 13 km and an underlying diktytaxitic unit continues 6.5 km beyond that point to the edge of the field, with a few scattered vents poking through it.

Continue east past the junction of AZ-61 and US-60 (6.0); stay right on US-60. Drive beyond junction (0.5). **6.5**

105.8 The basal flow in this area, seen to the south, appears to be structurally warped on both sides of a valley.

Continue east to junction with US-180. **31.2**

137.0 Stay on US-60; continue into Springerville. **3.3**

140.3 End of field trip.

References

Akers, J. P., Shorty, J. C., and Stevens, P. R., 1971, Hydrogeology of the Cenozoic igneous rocks, Navajo and Hopi Indian reservations, Arizona, New Mexico, and Utah: U.S. Geological Survey, Professional Paper 521-D: 18 pp.

Aubele, J. C., and Crumpler, L. S., 1983, Geology of the central and eastern parts of the Springerville volcanic field, Arizona (abs.): Geological Society of America, Abstracts with Programs, 15(5): 303.

Aubele, J. C., Crumpler, L. S., and Condit, C. D., 1987, Tectonic deformation of the late Cenozoic Springerville volcanic field, southern margin of the Colorado Plateau, Arizona (abs.): Geological Society of America, Abstracts with Programs, 19(7): 576.

Aubele, J. C., Crumpler, L. S., and Shafiqullah, M., 1986, K–Ar ages of Late Cenozoic rocks of the central and eastern parts of the Springerville volcanic field, east-central Arizona: Isochron/West, no. 46: 3–5.

Baksi, A. K., 1974, K–Ar study of the SP flow: Canadian Journal of Earth Sciences, 11: 1350–1356.

Beus, S. S., Rush, R. W., and Smouse, DeF., 1966, Geologic investigations of experimental drainage basins no. 7–14, Beaver Creek drainage basin, Coconino County, Arizona: Northern Arizona University, Flagstaff, 47 pp.

Burmeier, T. L., 1977, Geology of north Tesihim Butte, Hopi Buttes volcanic field, Arizona: Unpublished M.A. thesis, State University of New York (Buffalo), 61 pp.

Callahan, J. T., Williams, K., and Akers, J. P., 1959, The occurrence of ground water in diatremes of the Hopi Buttes area, Arizona: Plateau, 32(1): 1–12.

Carlson, R. W., 1984, Isotopic constraints on Columbia River basalt genesis and the nature of the subcontinental mantle: Geochimica et Cosmochimica Acta, 48: 2357–2372.

Carmichael, I. S. E., 1964, The petrology of Thingmuli, a Tertiary volcano in eastern Iceland: Journal of Petrology, 5: 435–460.

Castro, J., Brown, L., and Condit, C. D., 1983, Paleomagnetic results from the Springerville–Show Low volcanic field, east-central Arizona (abs.): American Geophysical Union (EOS), Transactions, 64: 689.

Colton, H. S., 1967, The basaltic cinder cones and lava flows of the San Francisco Mountain volcanic field: Museum of Northern Arizona, Bulletin 10: 58 pp. (revised edition).

Condit, C. D., 1984, The geology of the western part of the Springerville volcanic field, east-central Arizona: Unpublished Ph.D. dissertation, University of New Mexico, Albuquerque, 453 pp.

Condit, C. D. (in press), Lithologic map of the western part of the Springerville volcanic field, east-central Arizona: U.S. Geological Survey, Miscellaneous Investigations Series Map I-1993, scale 1:50,000.

Condit, C. D., and Shafiqullah, M., 1985, K–Ar ages of Late Cenozoic rocks of the western part of the Springerville volcanic field, east-central Arizona: Isochron/West, no. 44: 3–5.

Condit, C. D., Crumpler, L. C. Aubele, J. C., and Elston, W. E. (in press), Patterns of volcanism along the southern margin of the Colorado Plateau: the Springerville field: Journal of Geophysical Research.

Conway, F. M., 1988, Volcanology and petrology of the west-central part of the Mormon Mountain volcanic field, northern Arizona: Unpublished M.S. thesis, Northern Arizona University, Flagstaff, 141 pp.

Cooley, M. E., 1962, Geomorphology and the age of volcanic rocks in northeastern Arizona: Arizona Geological Society Digest, 5: 97–115.

Cooley, M. E., Harshbarger, J. W., Akers, J. P., and Hardt, W. F., 1969, Regional hydrogeology of the Navajo and Hopi Indian Reservations, Arizona, New Mexico, and Utah: U.S. Geological Survey, Professional Paper 521-A: 61 pp.

Coombs, D. S., and Wilkinson, J. F. G., 1969, Lineages and fractionation trends in undersaturated volcanic rocks from the East Otago volcanic province rocks: Journal of Petrology, 10: 440–501.

Cooper, J. L., and Hart, W. K., 1986, Geochemical variations across the Colorado Plateau–Basin and Range transition zone, east-central Arizona (abs.): Geological Society of America, Abstracts with Programs, 18: 348.

Cox, K. G., Bell, J. D., and Pankhurst, R. J., 1979, The interpretation of igneous rocks: Allen & Unwin, Boston, 450 pp.

Cummings, D., 1972, Mafic and ultramafic inclusions, crater 160, San Francisco volcanic field, Arizona; *in* Geological Survey Research 1972: U.S. Geological Survey, Professional Paper 800-B: 95–104.

Damon, P. E., Shafiqullah, M., and Leventhal, J. S., 1974, K–Ar chronology for the San Francisco volcanic field and rate of erosion of the Little Colorado River; *in* Karlstrom, T. N. V., Swann, G. A., and Eastwood, R. L. (eds.), Geology of northern Arizona, with notes on archaeology and paleoclimate; part I, regional studies: Geological Society of America, Rocky Mountain Section Meeting, Flagstaff, Arizona, pp. 221–235.

Dungan, M. A., Lindstrom, M. M., McMillian, N. J., Moorbath, S., Hoefs, J., and Haskin, L. A., 1986, Open magmatic evolution of the Taos Plateau volcanic field, northern New Mexico 1. The Petrology of the Servilleta Basalt: Journal of Geophysical Research, 91: 5999–6028.

Eggler, D. H., and Burnham, C. W., 1973, Crystallization and fractionation trends in the system andesite–H_2O–CO_2–O_2 at pressures to 10 kb: Geological Society of America, Bulletin, 84: 2517–2532.

Everndon, J. F., Savage, D. E., Curtis, G. H., and James, G. T., 1964, Potassium–argon dates and the Cenozoic mammalian chronology of North America: American Journal of Science, 262: 145–198.

Gregory, H. E., 1917, Geology of the Navajo country; a reconnaissance of parts of Arizona, New Mexico, and Utah: U.S. Geological Survey, Professional Paper 93: 92–103.

Gust, D. A., 1978, Petrology and geochemistry of the Mormon Mountain volcanic field, Arizona: Unpublished M.S. thesis, Rice University, Houston, 84 pp.

Gust, D. A., and Arculus, R. J., 1986, Petrogenesis of alkalic and calc-alkalic volcanic rocks of Mormon Mountain volcanic field, Arizona: Contributions to Mineralogy and Petrology, 94: 416–426.

Hack, J. T., 1942, Sedimentation and volcanism in the Hopi Buttes, Arizona: Geological Society of America, Bulletin, 53(2): 335–372.

Hodges, C. A., 1962, Comparative study of S.P. and Sunset Craters and associated lava flows: Plateau, 35(1): 15–35.

Holm, R. F., 1987a, San Francisco Mountain: A late Cenozoic composite volcano in northern Arizona; *in* Beus, S. S. (ed.), Centennial Field Guide, Rocky Mountain Section of the Geological Society of America, 2: 389–392.

Holm, R. F., 1987b, Significance of agglutinate mounds on lava flows associated with monogenetic cones: An example at Sunset Crater, northern Arizona: Geological Society of America, Bulletin, 99: 319–324.

Holm, R. F., 1988, Geologic map of San Francisco, Elden Mountain, and Dry Lake Hills, Coconino County, Arizona: U.S. Geological Survey, Miscellaneous Investigations Map I-1663, scale 1:24,000.

Holm, R. F., and Moore, R. B., 1987, Holocene scoria cone and lava flows at Sunset Crater, northern Arizona; *in* Beus, S. S. (ed.), Centennial Field Guide, Rocky Mountain Section of the Geological Society of America, 2: 393–397.

Irvine, T. N., and Baragar, W. R. A., 1971, A guide to the chemical classification of the common volcanic rocks: Canadian Journal of Earth Sciences, 8: 523–548.

Keller, G. R., Braile, L. W., and Morgan, P., 1979, Crustal structure, geophysical models and contemporary tectonism of the Colorado Plateau: Tectonophysics, 61: 131–147.

Kluth, C. F., 1974, Geology of the Elden Mountain area, Coconino County, Arizona: Unpublished M.S. thesis, Northern Arizona University, Flagstaff, 89 pp.

Laidley, R. A., 1966, An X-ray fluorescent analysis study of the distribution of selected elements within the Hopi Buttes volcanics, Navajo County, Arizona: Unpublished Ph.D. dissertation, University of Arizona, Tucson, 99 pp.

Laughlin, A. W., Brookins, D. G., Damon, P. E., and Shafiqullah, M., 1979, Late Cenozoic volcanism of the central Jemez Zone, Arizona–New Mexico: Isochron/West, no. 25: 5–8.

Laughlin, A. W., Damon, P. E., and Shafiqullah, M., 1980, New K–Ar dates from the Springerville volcanic field, central Jemez Zone, Apache County, Arizona: Isochron/West, no. 29: 3–4.

Lewis, P. H., 1973, Mica pyroxenite inclusions in limburgite, Hopi Buttes volcanic field, Arizona: Brigham Young University Geological Studies, 20(4): 191–225.

Lockrem, T. M., 1983, Geology and emplacement of the Slate Mountain volcano–laccolith, Coconino County, Arizona: Unpublished M.S. thesis, Northern Arizona University, Flagstaff, 103 pp.

Lowell, J. D., 1956, Occurrence of uranium in Seth-la-kai diatreme, Hopi Buttes, Arizona: American Journal of Science, 254(7): 404–412.

Luedke, R. G., and Smith, R. L., 1978, Map showing distribution, composition, and age of late Cenozoic volcanic centers in Arizona and New Mexico: U.S. Geological Survey, Miscellaneous Investigations Series Map I-1091-A, scale 1:1,000,000 and 1:500,000, 2 sheets.

Macdonald, G. A., 1968, Composition and origin of Hawaiian lavas: Geological Society of America, Memoir 116: 477–552.

McCabe, K., 1971, Geology and botany of Stoneman Lake area, Coconino

County, Arizona: Unpublished M.S. thesis, Northern Arizona University, Flagstaff, 104 pp.
Merrill, R. K., and Péwé, T. L., 1977, Late Cenozoic geology of the White Mountains, Arizona: Arizona Bureau of Geology and Mineral Technology, Special Paper no. 1: 65 pp.
Mintz, Y., 1942, Slate Mountain volcano laccolith: Plateau, 14(3): 42–47.
Moore, R. B., and Wolfe, E. W., 1987, Geologic map of the east part of the San Francisco volcanic field, Arizona: U.S. Geological Survey, Miscellaneous Field Studies Map MF-1960, scale 1:50,000.
Moore, R. B., Wolfe, E. W., and Ulrich, G. E., 1976, Volcanic rocks of the eastern and northern parts of the San Francisco volcanic field, Arizona: U.S. Geological Survey, Journal of Research, 4(5): 549–560.
Naeser, C. W., 1971, Geochronology of the Navajo–Hopi diatremes, Four Corners area: Journal of Geophysical Research, 76: 4978–4985.
Nations, J. D., 1974, Paleontology, biostratigraphy, and paleoecology of the Verde Formation of Late Cenozoic age, north-central Arizona; *in* Karlstrom, T. N. V., Swann, G. A., and Eastwood, R. L. (eds.), Geology of northern Arizona, Pt. II, Area studies and field guides: Geological Society of America, Rocky Mountain Section Meeting, Flagstaff, Arizona, pp. 580–591.
Nealey, L. D., 1980, Geology of Mount Floyd and vicinity, Coconino and Yavapai Counties, Arizona: Unpublished M.S. thesis, Northern Arizona University, Flagstaff, 144 pp.
Nealey, L. D., Holm, R. F., and Conway, M. F., 1986, Petrology of the Mormon Mountain volcanic field, Coconino and Yavapai Counties, Arizona (abs.): Abstracts of the Symposium on Southwestern Geology and Paleontology, Museum of Northern Arizona, p. 12.
Newhall, C. G., Ulrich, G. E., and Wolfe, E. W., 1987, Geologic map of the southwest part of the San Francisco volcanic field, north-central Arizona: U.S. Geological Survey, Miscellaneous Field Studies Map MF-1958, scale 1:50,000.
Peacock, M. A., 1931, Classification of igneous rocks: Journal of Geology, 39: 54–67.
Peirce, H. W., Damon, P. E., and Shafiqullah, M., 1979, An Oligocene(?) Colorado Plateau edge in Arizona: Tectonophysics, 61: 1–24.
Perry, F. V., Baldridge, W. S., and DePaolo, D. J., 1987, Role of asthenosphere and lithosphere in the genesis of Late Cenozoic basaltic rocks from the Rio Grande rift and adjacent regions of the southwestern United States: Journal of Geophysical Research, 92: 9193–9213.
Price, W. E., 1950, Cenozoic gravels on the rim of Sycamore Canyon, Arizona: Geological Society of America, Bulletin, 61: 501–507.
Scholtz, J. F., 1969, Structural control of the Stoneman Lake basin: Arizona Academy of Science, Journal (Proceedings Supplement), 5: 36.
Scott, K. C., 1975, Hydrogeologic and geophysical analysis of selected diatremes in the Hopi Buttes area, Arizona: Unpublished M.S. thesis, Northern Arizona University, Flagstaff, 129 pp.
Shafiqullah, M., and Damon, P. E., 1985, Geochronology of the Hopi Buttes volcanic field, northeastern Arizona (abs.); *in* Abstracts of the Symposium on Southwestern Geology and Paleontology: Museum of Northern Arizona, Flagstaff, Arizona, p. 9.
Shoemaker, E. M., 1953, Collapse origin of the diatremes of the Navajo–Hopi Reservation (abs.): Geological Society of America, Bulletin, 64 (12, pt. 2): 1514.
Shoemaker, E. M., 1955a, Diatremes on the Navajo and Hopi Reservations: U.S. Geological Survey, Report TEI-590: 61–71.
Shoemaker, E. M., 1955b, Occurrence of uranium in diatremes on the Navajo and Hopi Reservations, Arizona, New Mexico, and Utah; *in* Page, L. R., Stocking, H. E., and Smith, H. B., Contributions to the geology of uranium and thorium by the United States Geological Survey and Atomic Energy Commission for the United Nations International Conference on Peaceful Uses of Atomic Energy, Geneva, Switzerland, 1955: U.S. Geological Survey, Professional Paper 300: 179–185.
Shoemaker, E. M., 1956, Diatremes on the Navajo and Hopi Reservations, Arizona: U.S. Geological Survey, Report TEI-620: 75–85.
Shoemaker, E. M., and Moore, H. J., II, 1956, Diatremes on the Navajo and Hopi Reservations: U.S. Geological Survey, Report TEI-640: 197–202.
Shoemaker, E. M., Byers, F. M., Jr., and Roach, C. H., 1957c, Diatremes on the Navajo and Hopi Reservations, Arizona: U.S. Geological Survey, Report TEI-740: 158–168.
Shoemaker, E. M., Hensley, F. S., Jr., and Hallagan, R. W., 1957a, Diatremes on the Navajo and Hopi Reservations, Arizona: U.S. Geological Survey, Report TEI-690: 389–398.
Shoemaker, E. M., Roach, C. H., Byers, F. M., and Milton, F., Jr., 1957b, Diatremes on the Navajo and Hopi Reservations, Arizona: U.S. Geological Survey, Report TEI-700: 141–151.
Shoemaker, E. M., Roach, C. H., and Byers, F. M., Jr., 1962, Diatremes and uranium deposits in the Hopi Buttes, Arizona; *in* Petrologic studies—A volume in honor of A. F. Buddington: Geological Society of America, New York, pp. 327–355.
Silver, L. T., and Bass, M., 1964, Age of a basement fragment in the Bidahochi Formation, Hopi Buttes region, Arizona (abs.): Geological Society of America, Special Paper 76: 293–294.
Smiley, T. L., 1958, The geology and dating of Sunset Crater, Flagstaff, Arizona: New Mexico Geological Society, Guidebook 9: 186–190.
Stauber, D. A., 1982, Two-dimensional compressional wave velocity structure under San Francisco volcanic field, Arizona, from teleseismic P residual measurements: Journal of Geophysical Research, 87: 5451–5459.
Stoeser, D. B., 1973, Mafic and ultramafic xenoliths of cumulus origin, San Francisco volcanic field: Unpublished Ph.D. dissertation, University of Oregon, Eugene, 260 pp.
Stoeser, D. B., 1974, Xenoliths of the San Francisco volcanic field, northern Arizona; *in* Karlstrom, T. N. V., Swann, G. A., and Eastwood, R. L. (eds.), Geology of northern Arizona, Pt. II, Area studies and field guides: Geological Society of America, Rocky Mountain Section Meeting, Flagstaff, Arizona, pp. 530–545.
Suda, C. E., Brookins, D. G., and Della Valle, R. S., 1982, Uranium and other trace element geochemistry of the Hopi Buttes volcanic province, northeastern Arizona: Economic Geology, 77(5): 1210–1220.
Sutton, R. L., 1974, The geology of Hopi Buttes, Arizona; *in* Geology of northern Arizona with notes on archaeology and paleoclimate; Part II, Area studies and field guides; Hopi Buttes–Navajo Buttes area: Geological Society of America, Rocky Mountain Section, Guidebook 27: 647–671.
Sutton, R. L., Hendricks, J. D., Ackermann, H. D., 1969, Geology and geophysics of Shonto diatreme Hopi Buttes volcanic field, Navajo County, Arizona (abs.): Geological Society of America, Abstracts with Programs, pt. 5: 80–81.
Tanaka, K. L., Shoemaker, E. M., Ulrich, G. E., and Wolfe, E. W., 1986, Migration of volcanism in the San Francisco volcanic field, Arizona: Geological Society of America, Bulletin, 97: 129–141.
Ulrich, G. E., 1981, Colorado Plateau margin in the West Clear Creek region of central Arizona; *in* Howard, K. A. et al. (eds.), Tectonic framework of the Mojave and Sonoran Deserts, California and Arizona: U.S. Geological Survey, Open-File Report 81-503: 116–118.
Ulrich, G. E., 1987, SP Mountain cinder cone and lava flow, northern Arizona; *in* Beus, S. S. (ed.), Centennial Field Guide, Rocky Mountain Section of the Geological Society of America, 2: 385–388.
Ulrich, G. E., and Bailey, N. G., 1987, Geologic map of the SP Mountain part of the San Francisco volcanic field, Arizona: U.S. Geological Survey, Miscellaneous Field Studies Map MF-1956, scale 1:50,000.
Ulrich, G. E., Billingsley, G. H., Hereford, R., Wolfe, E. W., Nealey, L. D., and Sutton, R. L., 1984, Map showing geology, structure, and uranium deposits of the Flagstaff $1° \times 2°$ quadrangle, Arizona: U.S. Geological Survey, Miscellaneous Investigation Series Map I-1446, scale 1:250,000, 2 sheets.
Unruh, D. J., Nealey, L. D., and Holm, R. F., 1988, Trace element and isotopic constraints on the origin of the Mormon Mountain volcanic field, central Arizona (abs.): Geological Society of America, Cordilleran Section, Program with Abstracts, 20: 238–239.
Weir, G. W., Ulrich, G. E., and Nealey, L. D., 1989, Geologic map of the Sedona $30' \times 60'$ quadrangle, Yavapai and Counties, Arizona: U.S. Geological Survey, Miscellaneous Investigations Series Map I-1896, scale 1:100,000.
Wenrich-Verbeek, K. J., 1977, Anomalous uranium in the waters of the Rio Ojo Caliente, New Mexico; *in* short papers in the U.S. Geological Survey Uranium and Thorium Research and Resources Conferences, 1977: U.S. Geological Survey, Circular 753: 73–78.
Wenrich-Verbeek, K. J., 1979a, Chemical compositions and partition coefficients for bulk rock and constituent phases of a sequence of lavas from San Francisco Mountain, Arizona: U.S. Geological Survey, Open-File Report 79-0998: 278 pp.
Wenrich-Verbeek, K. J., 1979b, The petrogenesis and trace-element geochemistry of intermediate lavas from Humphreys Peak, San Francisco volcanic field, Arizona: Tectonophysics, 61: 103–129.
Wenrich-Verbeek, K. J., and Mascarenas, J. F., 1982a, Diatremes of the Hopi Buttes, Arizona; chemical and statistical analyses: U.S. Geological Survey, Open-File Report 82-0740: 131 pp.
Wenrich-Verbeek, K. J., and Mascarenas, J. F., 1982b, Maps showing uranium-bearing diatremes of the Hopi Buttes, Arizona: U.S. Geological Survey, Miscellaneous Field Studies Map MF-1310, scale 1:50,000, 2 sheets.
Wenrich-Verbeek, K. J., and Shoemaker, E. M., 1980, Uranium mineralization in Hopi Buttes, Arizona: American Association of Petroleum Geologists, Bulletin, 64(5): 802.

Wenrich-Verbeek, K. J., Spirakis, C. S., Billingsley, G. H., Hereford, R., Nealey, L. D., Ulrich, G. E., Verbeek, E. R., and Wolfe, E. W., 1982, National Uranium Resources Evaluation, Flagstaff quadrangle, Arizona: U.S. Department of Energy, Open-File Report PGJ/F-014 (82): 59 pp., maps' scale 1:250,000.

White, J. D. L., and Fisher, R. V., 1987, Possible "Cameroon-style" catastrophic lake overturn above an alkaline diatreme, Hopi Buttes, Arizona (abs.): Geological Society of America, Abstracts with Programs, 19(7): 889.

Williams, H., 1936, Pliocene volcanoes of the Navajo–Hopi country: Geological Society of America, Bulletin, 47: 111–172.

Wolfe, E. W., 1983, Geologic map of the Arnold Mesa Roadless Area, Yavapai County, Arizona: U.S. Geological Survey, Miscellaneous Field Studies Map MF-1577-B, scale 1:24,000.

Wolfe, E. W., 1984, The volcanic landscape of the San Francisco volcanic field; *in* Smiley, T. L., Nations, J. D., Péwé, T. L., and Schafer, J. P. (eds.), Landscapes of Arizona, the geological story: University Press of America, pp. 111–136.

Wolfe, E. W., Ulrich, G. E., Holm, R. F., Moore, R. B., and Newhall, C. G., 1987a, Geologic map of the central part of the San Francisco volcanic field, Arizona: U.S. Geological Survey, Miscellaneous Field Studies Map MF-1959, scale 1:50,000.

Wolfe, E. W., Ulrich, G. E., and Newhall, C. G., 1987b, Geologic map of the northwest part of the San Francisco volcanic field, north-central Arizona: U.S. Geological Survey, Miscellaneous Field Studies Map MF-1957, scale 1:50,000.

EXCURSION 6A: Eocene–Miocene Mogollon–Datil volcanic field, New Mexico

James C. Ratté[1], Steven M. Cather[2], Charles E. Chapin[2], Wendell A. Duffield[3], Wolfgang E. Elston[4], and William C. McIntosh[2]

[1]*U.S. Geological Survey, Box 25046, MS 905, Denver, Colorado 80225;* [2]*New Mexico Bureau of Mines & Mineral Resources, Socorro, New Mexico 87801;* [3]*U.S. Geological Survey, 2255 North Gemini Drive, Flagstaff, Arizona 86001;* [4]*Department of Geology, University of New Mexico, Albuquerque, New Mexico 87131*

Summary

This trip begins at Socorro, New Mexico, where Day 1 will be spent examining Oligocene to modern magmatism and structure along the Socorro accommodation zone, a leaky transverse structure in the Rio Grande rift. During Day 2 we travel westward from Socorro along the northern edge of the Mogollon–Datil volcanic field to view late Eocene and early Oligocene volcaniclastic rocks of the alluvial apron constructed around the nucleus of the volcanic pile. Included in Day 2 are visits to debris-flow complexes, some of which contain kilometer-scale exotic blocks of Paleozoic limestones, and down-to-the-basin detachment faults with associated soft-sediment deformation.

Days 3 to 7 will comprise a circumnavigation of the Mogollon Plateau, the central core of the Mogollon–Datil volcanic field. On Day 3 we follow the northern and western margins of the plateau from Socorro to Glenwood, near the western edge of the Mogollon Mountains caldera cluster. Along the way we will examine an early Oligocene pyroclastic deposit near Old Horse Springs. The afternoon of Day 3 will be spent observing landslide breccias and other moat deposits along the topographic wall at the western margin of the Bursum caldera, in the Mogollon (Mo-go-yohn') mining district.

Most of Day 4 will follow up with examination of the structural wall, caldera-fill breccia, and moat intrusions, also along the western margin of the Bursum caldera in the Mogollon mining district. A final, brief stop at Leopold Vista, south of Glenwood, will afford a panoramic view of the western and southern trace of the Bursum caldera as outlined by ring-fracture silicic volcanism.

After spending the night in Silver City, we will travel through the Emory caldera (35 Ma) at the southern end of the Black Range, ending Day 5 in Truth or Consequences. Day 6 will focus on the physical volcanology of the Taylor Creek Rhyolite (28 Ma) and its associated tin mineralization. We will stop overnight at the Trail End Ranch on the western flank of the Black Range. Day 7 will consist of a final Taylor Creek Rhyolite stop, followed by examination of direction-of-transport features in the Bloodgood Canyon Tuff and the tuff of Triangle C Ranch at Coyote Well. After the final stop, participants will return to Socorro and continue to Santa Fe.

This field guide consists of seven papers authored by geologists who have studied particular portions of the Mogollon–Datil field. A road log is not provided for the first day because detailed road logs are included in New Mexico Geological Society Guidebook 34 (1983) available at the Publications Office of the New Mexico Bureau of Mines & Mineral Resources in Socorro. Copies of these logs will be available for the IAVCEI field excursion. Future users of this volume should check with the New Mexico Bureau of Mines & Mineral Resources for the latest publications on the Socorro area, which is one of the most intensely studied areas, both geologically and geophysically, in the United States. The presence of magma bodies, modern uplift, and high seismicity in the Socorro area, together with its accessibility and large number of resident geoscientists, ensures that it will continue to be the site of numerous investigations. For this volume, C. E. Chapin has written a summary paper on the Socorro accommodation zone which includes references to many of the studies completed since the 1983 guidebook.

Overview of the Mogollon–Datil volcanic field

Wolfgang E. Elston

Introduction

The Mogollon–Datil volcanic field of southwestern New Mexico covers about 40,000 km^2, a small part of a $\sim$1 million km^2 volcanic zone that extends over the Basin and Range province and adjoining plateaus (Fig. 1). During the mid-Tertiary (late Eocene to early Miocene, about 40 to 20 Ma), before the present fault-block physiography was fully developed, most of this region was buried beneath hundreds to thousands of meters of calc-alkalic volcanic rocks. The climax of activity was during the "ignimbrite flareup," between about 36 and 24 Ma. The Sierra Madre Occidental (Fig. 1) of western Mexico is the largest plateau within this huge volcanic province; the Mogollon–Datil volcanic field can be regarded as an outlier, separated from the main mass by a prong of the Mexican Highlands section of the Basin and Range province (Fenneman, 1933). It can also be re-

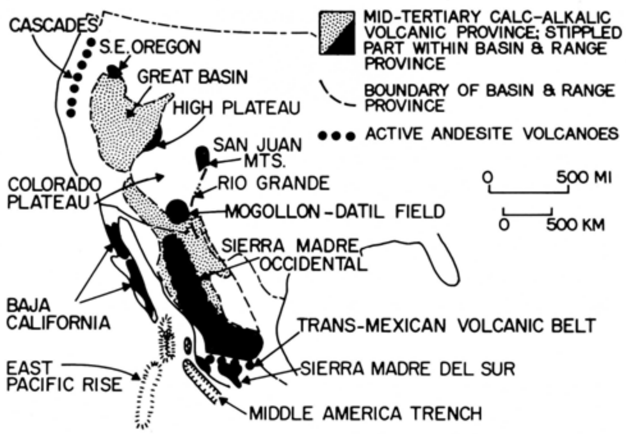

FIGURE 1—Location of the Mogollon–Datil volcanic field in the transition from Basin and Range province to Colorado Plateau. From Elston and Bornhorst (1979).

garded as one of several mid-Tertiary volcanic fields that overlap the relatively stable Colorado Plateau; the others are the Marysvale (High Plateau) field of Utah, the White Mountains field of Arizona, and the San Juan field of Colorado. Within these volcanic fields, and in the Sierra Madre Occidental, faulting is relatively minor and volcanic stratigraphic units can be traced for long distances from their eruptive centers. In neighboring Basin and Range country, however, similar units and volcanic centers tend to be more difficult to study, because ranges with excellent exposures and up to 10 km of structural relief are separated by broad basins with no exposures at all. The relative lack of disruption of the Mogollon–Datil field will allow us to examine the varied facies of volcanic rocks and their distribution around eruptive centers.

Stratigraphy and petrography

About 150 named Tertiary units occur in the vicinity of the Mogollon–Datil volcanic field. They have been broadly dated or bracketed by K–Ar or fission-track methods; the ages of key ignimbrite sheets are known with greater precision from $^{40}Ar/^{39}Ar$ dates (McIntosh et al., 1986; McIntosh, this volume). The groupings of units used here are those adopted by the New Mexico Geological Society (1982):

T1: Eocene continental clastic sedimentary rocks, such as the Baca Formation seen on Days 2 and 3.

T2: Late Eocene to early Oligocene andesite, such as the Rubio Peak Formation seen on Day 5, characterized over most of the field by phenocrysts of andesine and oxyhornblende (lamprobolite) ± augite ± minor enstatite and rare traces of olivine altered to "iddingsite." Potassium content is higher in the northern part of the field, and T2a rocks seen on Days 2 and 3 (lower part of the Datil Group) contain biotite as a conspicuous ferromagnesian phase. Although the mode of T2a rocks is about 58% SiO_2 (andesite), they range from rare basalt (about 50% SiO_2) to rhyolite (about 68% SiO_2); the distribution is skewed toward the siliceous end.

T3r: Early Oligocene high-Ca rhyolite (quartz latite) pyroclastic rocks and lavas, including products of major ash-flow tuff (ignimbrite) resurgent calderas. Examples include Kneeling Nun Tuff and Mimbres Peak Rhyolite lavas and pyroclastic rocks of the Emory caldera seen on Day 5. The lower part of this group interfingers with the upper part of T2a. The two groups also show chemical gradations. The ignimbrites that characterize T3r have phenocrysts of oligoclase–andesine, sanidine, and biotite; quartz ranges from absent to abundant. Oxyhornblende and augite are rare, orthopyroxene has not been reported. SiO_2 ranges from 63 to 78%, with gaussian distribution about a mode of 71%.

T3a: Mid-Oligocene andesite and associated rocks, with nearly the same SiO_2 range and mode as T2a, but skewed toward lower SiO_2 (basaltic andesite). Bear Springs Basaltic Andesite and andesite of Poverty Creek are examples seen on Days 5 and 6, respectively. Some of the rocks resemble T2a types, but typical T3a rocks are higher in incompatible elements (including REE) and have anhydrous ferromagnesian phenocrysts (augite ± enstatite ± olivine altered to "iddingsite").

T4r: Late Oligocene high-SiO_2, low-Ca rhyolite pyroclastic rocks and lavas, including products of major resurgent calderas, such as the Bursum caldera seen on Day 4. Ignimbrites typically have about 76% SiO_2 and phenocrysts of quartz, sanidine, and biotite. Plagioclase (generally albite–oligoclase) is either less abundant than sanidine or entirely absent as phenocrysts, although commonly present as submicroscopic lamellae in sanidine cryptoperthite ("moonstone"). Hornblende and/or augite are rare. Bloodgood Canyon Tuff (Day 3) is a typical "moonstone tuff."

T4a: Late Oligocene to early Miocene andesite, from stratovolcanoes and shield volcanoes that include some of the highest mountains of the Mogollon–Datil volcanic field (Bearwallow Mountain Formation). These rocks have the same range of compositions as T2a and T3a but continue the trend toward anhydrous basaltic andesite, higher in Fe and incompatible elements.

T5a: Minor early to middle Miocene siliceous rocks occur as local domes and flows. Examples include high-K rhyolites of the Magdalena area; dacites and high-K rhyolites of Socorro Peak; and dacitic plug domes in some T4a volcanoes.

T6b: Middle to late Miocene and Pliocene basalt flows cap high mesas on the fringe of the Mogollon–Datil volcanic field and intertongue with fill of fault-bounded basins. They are true olivine alkali basalt, chemically and isotopically unlike basaltic andesites of groups T2a, T3a, and T4a, which have calc-alkalic affinities. In many parts of New Mexico, eruptions of alkali basalt and tholeiite have continued through the Quaternary; these flows (Qb) cap low mesas and terraces and occupy the floors of present-day valleys.

Geologic structures

It is no coincidence that the mid-Tertiary volcanic province includes most of the Basin and Range extensional tectonic province. During mid-Tertiary volcanism, heat flow was so high that the ductile–brittle transition in the lithosphere must have been shallower than at present, giving rise to ductile deformation in the early stages of extension. As the lithosphere cooled, increasingly brittle extension gave rise to the modern fault-block physiography (Eaton, 1982). The beginning of extension is uncertain, but along the Rio Grande valley ductile extension was well under way during volcanic stage T4r. Domino-style faulting in the Lemitar Mountains north of Socorro (Day 1) failed to provide topographic obstacles to T4r ash flows (Chamberlin, 1983). Sedimentary basins developed, but not necessarily with the same trends as modern basins (Morgan et al., 1986). A magma lull between T4a calc-alkalic basaltic andesite and T6a basalt corresponds to the transition from predominantly ductile to predominantly brittle extension. In detail, stress directions varied greatly with time and place (Aldrich et al., 1986).

Ignimbrite calderas

In addition to structures related to regional stress fields, local structures are related to the collapse of T3r and T4r calderas and their subsequent resurgence. On Day 5 we will see evidence that at least some caldera margins were controlled by earlier faults and that faults related to caldera collapse and resurgence were reactivated during subsequent basin and range block faulting. Fig. 2 shows only the major

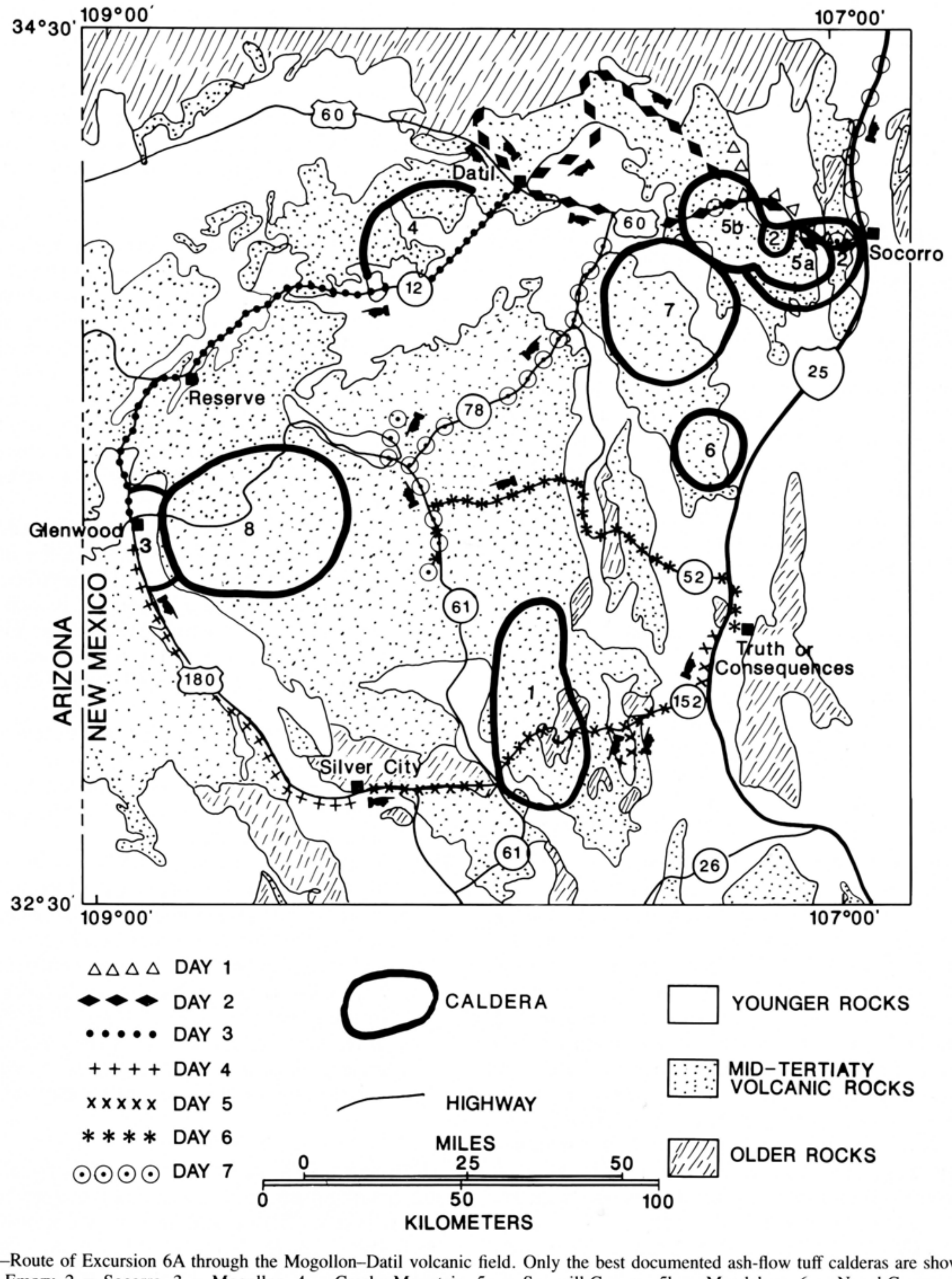

FIGURE 2—Route of Excursion 6A through the Mogollon–Datil volcanic field. Only the best documented ash-flow tuff calderas are shown, in order of age: 1 = Emory, 2 = Socorro, 3 = Mogollon, 4 = Crosby Mountain, 5a = Sawmill Canyon, 5b = Magdalena, 6 = Nogal Canyon, 7 = Mount Withington, 8 = Bursum. For details, see Osburn and Chapin (1983), Ratté et al. (1984), and Elston (1984). Map simplified from New Mexico Geological Society (1982).

caldera complexes about which there is some measure of agreement; judged by the number of ash-flow-tuff sheets that have no known sources, there must be many more. During stages T3r and T4r, rising siliceous magmas apparently coalesced to form granitic plutons. As they neared the surface, roofs of their cupolas foundered during explosive vesiculation of volatile-rich magmas and rapid evacuation of magma chambers (Ratté et al., 1984; Elston, 1984). As long as bodies of low-density, high-viscosity siliceous magmas remained active, basaltic andesite magmas could not reach the surface in recognizable form. Only after siliceous magmas had solidified, could more mafic magmas penetrate to the surface and erupt in stages T3a and T4a.

Volcanism along the Socorro accommodation zone, Rio Grande rift, New Mexico

Charles E. Chapin

Introduction

The town of Socorro, New Mexico, is located on a boundary between two domains of imbricate fault blocks (dominoes) that are tilted in opposite directions (Figs. 1, 2). The boundary is at least 70 km long and trends east-northeast across the Rio Grande rift, from the San Mateo Range on the southwest to beyond Socorro on the northeast (Figs. 2, 3, 4). The domains of domino-style fault blocks to either side cover approximately 1100 km^2 to the north and 1500 km^2 to the south. The tilt domains extend over much larger areas, but with wider blocks and gentler tilts (Fig. 3). Several other domain boundaries (Fig. 2) have been recognized in the Rio Grande rift (Chapin, 1988), but the one at Socorro is the best exposed and transects an area mapped in detail. Such domain boundaries are now known to occur in all areas of regional extension and are generally referred to as transfer faults (Gibbs, 1984) or accommodation zones (Bosworth, 1985). Few detailed studies are available, however, and many fundamental questions have yet to be resolved before the kinematics and significance of these structures are understood. The purpose of this paper is to describe the Socorro accommodation zone (SAZ) and its influence on synrift volcanism, and, hopefully, to shed some light on the role of accommodation zones in regional extension.

Accommodation zones

Important petroleum discoveries on passive continental margins and in rifts during the past two decades, together with marked expansion of seismic-reflection profiling and the recognition of detachment terranes (metamorphic core complexes) in the Basin and Range province, have led to greatly increased interest in styles of regional extension. Bally (1982: 329–330) pointed out that "half-grabens and systems of multiple half-grabens are the rule, and reflection seismic evidence for symmetrical grabens is virtually absent." He described how the asymmetry (polarity) may change within a graben, such that two segments of opposing master-fault systems appear to be separated by a transform fault.

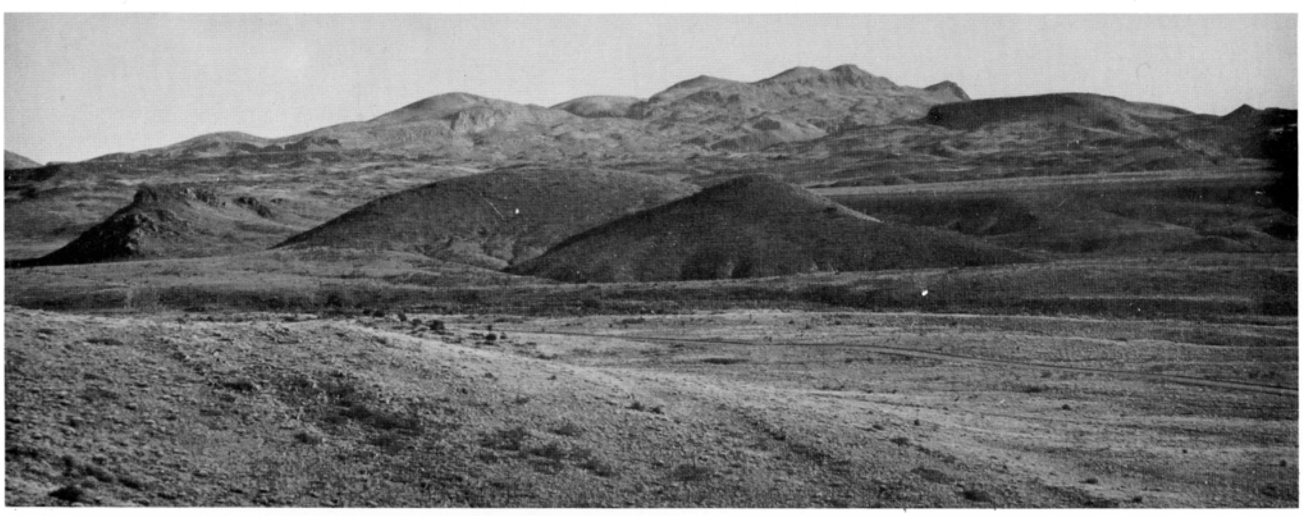

FIGURE 1—View northward across the Socorro accommodation zone (SAZ) from the north end of the Chupadera Mountains. Socorro Peak on the skyline is capped by 7–12 Ma silicic flows and domes which dip 10–15° to the west. Cauldron-facies Hells Mesa Tuff (32 Ma) in the foregound dips about 65° to the east. The nearly horizontal basalt of Socorro Canyon (4.1 Ma) at left middle distance and the beveled top of the rhyolite dome of 6001 Mesa (9 Ma) at right middle distance mark the SAZ which acts like a null plane between two domains of fault blocks tilted in opposite directions. In the Lemitar Mountains, to the north behind Socorro Peak, the Hells Mesa Tuff is tilted as steeply as in the foreground, but to the west (see Fig. 7).

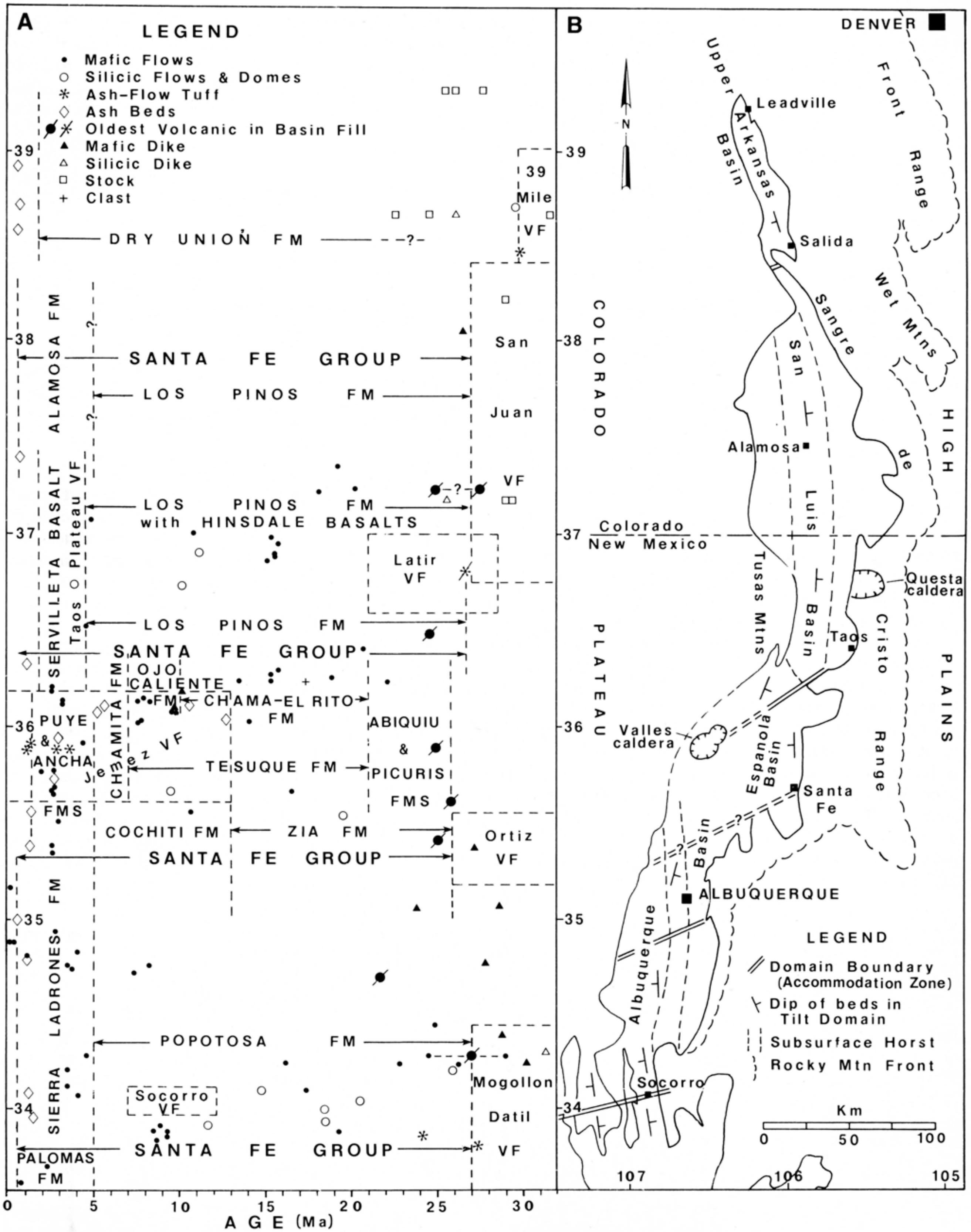

FIGURE 2—**A,** Latitude vs. age plot of radiometric ages of igneous rocks and stratigraphic nomenclature for axial basins of the northern and central Rio Grande rift. Major volcanic fields are shown as time–space boxes without plotting individual ages except for rocks that constrain boundaries of synrift sedimentary units. References and details of the radiometric ages are available in a databank at the New Mexico Bureau of Mines & Mineral Resources. Older K–Ar ages have been adjusted for the current IUGS constants using the table of Dalrymple (1979). Mafic flows include some andesites. From Chapin (1988) with addition of several new radiometric ages in the Socorro area. See Chapin (1988) for discussion of stratigraphic nomenclature. **B,** Sketch map showing axial basins of the northern and central Rio Grande rift (same scale as A). All basins are half-grabens with asymmetry changing across accommodation zones that separate domains of west-tilted vs. east-tilted strata. Most accommodation zones developed where the rift broke across pre-existing lineaments. Major prerift subsurface horsts are shown to underlie the Albuquerque (Baars, 1982) and San Luis (Tweto, 1979; Gries, 1985) Basins. Base modified from Tweto (1978) and Woodward et al. (1978).

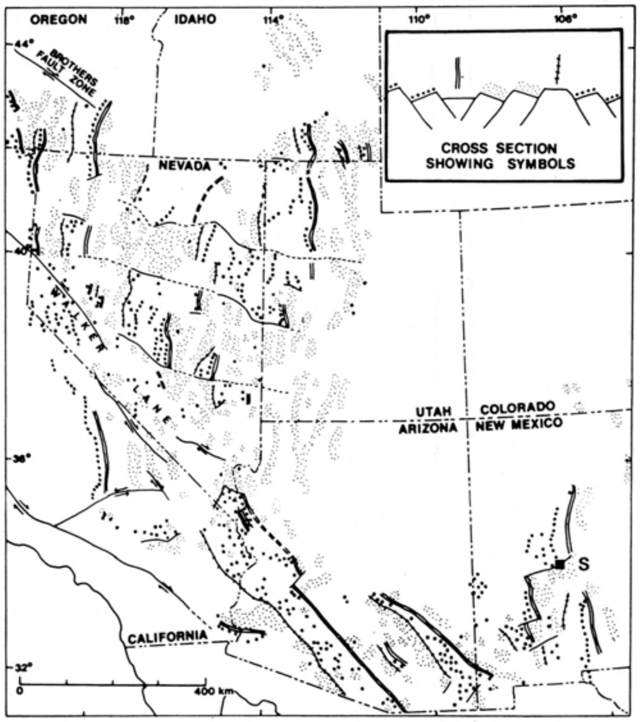

FIGURE 3—Tilt patterns of late Cenozoic Basin and Range fault blocks in the western United States. S = Socorro; light stipple = east or northeast tilt; heavy stipple = west or southwest tilt; double line = antiformal boundary; cross-hatched line = synformal boundary; single line = transverse zone or boundary. From Stewart (1980) with permission of the Geological Society of America.

Gibbs (1984: 616) discussed structural evolution of extensional basins and proposed the term "transfer fault" for the cross-faults that "are indeed characteristic of all extensional terranes and allow 'leakage' between extension faults with differing slip rates."

Bosworth (1985) proposed the term "accommodation zone" as a more general substitute for transfer fault. In a subsequent paper on the Gregory rift, Bosworth et al. (1986) suggested that when rifting is initiated, two opposing detachment systems form, separated by 30–50 km, producing the classic full-graben form. If they cross at depth, one is likely to lock up and the result is half-graben asymmetry. That the detachment faults are listric in cross section has been documented by many studies, but Bosworth (1985) and later Rosendahl (1987) pointed out that they are also concave toward the hanging wall in plan view. Concavity toward the footwall is apparently not kinematically viable. Bosworth et al. (1986: 577) visualize rift propagation as follows:

> As the rift and its opposing detachments propagate laterally the bounding faults tend to curve inward, producing a "neck" in the rift. This is a well-documented but poorly understood process, which leads to the eventual inability of a single detachment system to continue its lateral propagation. At or beyond this neck, two new detachments appear, and the rift grows in length in the form of a new sub-basin. The area of interaction between the detachments converging at the neck will be referred to as an "accommodation zone" . . . and represents a major crustal structural feature. Across the accommodation zone, one detachment will again dominate, producing another half graben, with the sense of asymmetry usually reversed.

Lister et al. (1986a, b) emphasize that transfer faults are a general feature of extended terranes. They postulate that transfer faults result because normal faults nucleate at different places along strike, and mismatches between different fault blocks must be accommodated.

Rosendahl (1987) published a comprehensive treatment of the architecture of continental rifts as an outgrowth of project PROBE, a seismic-reflection study of the East African rifts supported by petroleum companies and the World Bank. In it he develops a systematic nomenclature for structural elements of different size that make up rift systems and proposes a classification scheme for types of accommodation zones. His "low-relief accommodation zones" occur between overlapping, opposing half-graben and are generally expressed as gentle arches ("hinged highs") separating sub-basins. They are parallel or at a low angle to the trend of the rift and thus nearly perpendicular to the extension direction. His "high-relief accommodation zones" separate non-overlapping, opposing half-graben and are generally expressed as steep-sided faulted horsts oblique to both the trend of the rift and the extension direction. Faults paralleling high-relief accommodation zones have oblique-slip displacements caused by subsidence of the bordering half-graben in opposite directions. Where the high-relief accommodation zones are narrow with vertical boundaries dominated by strike–slip faulting, Rosendahl calls them "strike–slip accommodation zones."

None of the accommodation zones illustrated by Rosendahl parallel the extension direction, or are readily applicable to nested half-graben, and thus do not fit the Socorro accommodation zone. The SAZ developed along a major prerift lineament (the Morenci lineament; Chapin et al., 1978) which was parallel to the early-rift extension direction and controlled the location and orientation of the accommodation zone. In contrast, cross-structures of the western branch of the East African rift system, studied by Project PROBE, are at a low angle to the rift trend.

The SAZ was first described by Chapin et al. (1978); they called it a transverse shear zone and suggested that it acted as a transform fault connecting en-echelon axes of extension. Shortly thereafter, Stewart and Johannesen (1979) and Stewart (1980) analyzed tilt patterns of fault blocks throughout the Basin and Range province and around the southern margin of the Colorado Plateau to the Socorro area (Fig. 3). They divided the extended terranes into areas of dominantly east or west tilt and described three types of domain boundaries: (1) transverse boundaries parallel to the extension direction (as at Socorro); (2) antiformal boundaries perpendicular to the extension direction and with tilts away from the boundary to either side; and (3) synformal boundaries, also perpendicular to the extension direction but with tilts toward the boundary from either side. Stewart (1980) postulated that the antiformal boundaries may have been the initial sites of rupture with faulting and block rotation progressing outward on both sides. Synformal boundaries would be formed by the meeting of tilt domains progressing in opposite directions from two antiformal boundaries.

An accommodation zone in the highly extended terrane of the Colorado River extensional corridor in northwestern Arizona and southern Nevada has recently been mapped in detail by J. E. Faulds and described by Faulds et al. (1988a, b, in press). This accommodation zone has many characteristics in common with the SAZ. As summarized by Faulds et al. (1988a), the zone is about 5 km wide and 40 km long; trends east–west parallel to the extension direction; fault-block tilting on either side generally exceeds 60° in rocks

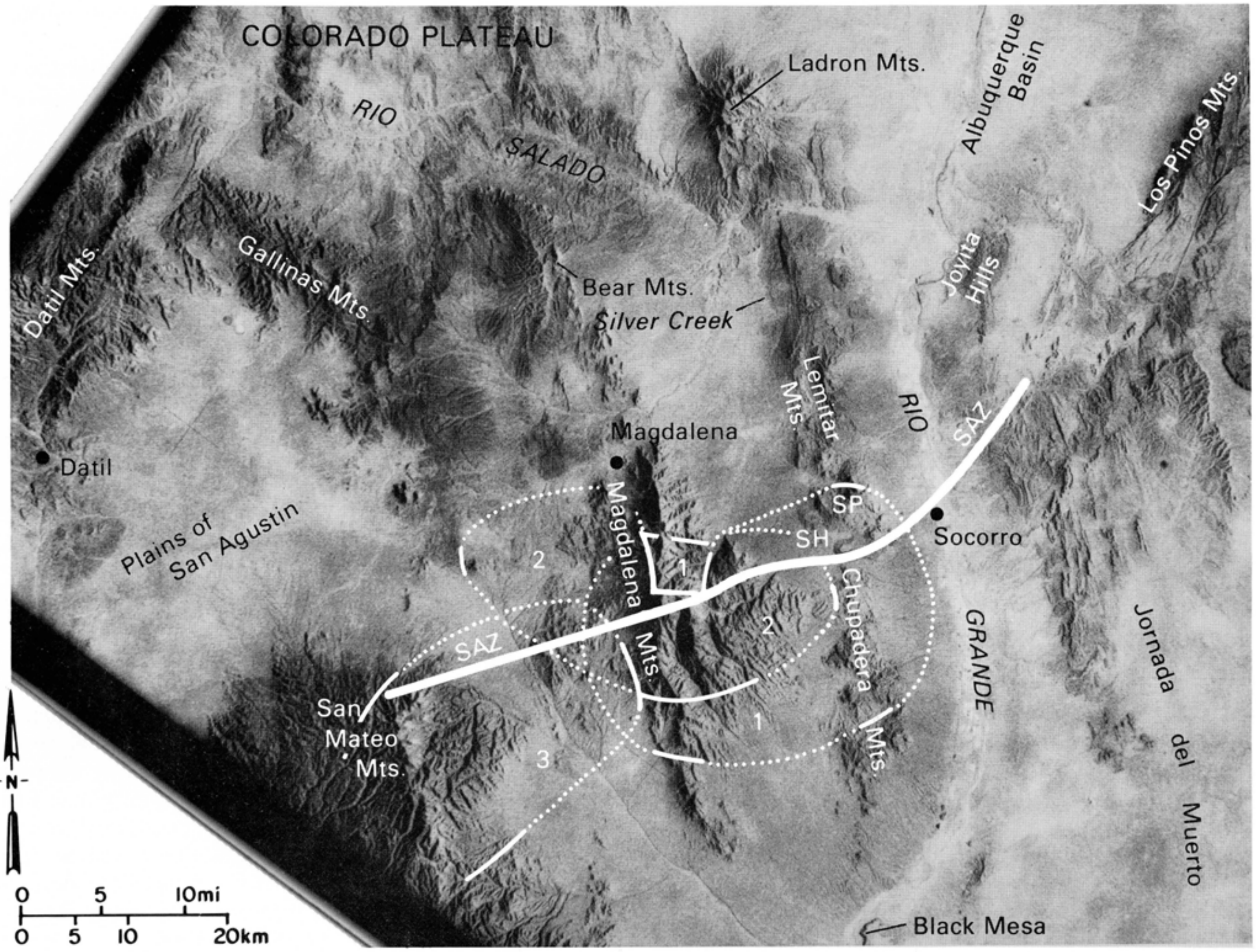

FIGURE 4—Skylab photograph of west-central New Mexico showing location of the Socorro accommodation zone (SAZ), domains of domino-style normal faulting, and early-rift calderas. Calderas and their respective ash-flow tuffs are: (1) Socorro caldera—Hells Mesa Tuff (32 Ma), (2) Sawmill Canyon–Magdalena caldera—La Jencia Tuff (28.8 Ma), and (3) Mt. Withington caldera—South Canyon Tuff (27.3 Ma). Caldera boundaries modified according to recent mapping by Ferguson (1988) and Osburn et al. (1985, 1989). SP = Socorro Peak, SH = Sedillo Hill. Note that the SAZ is approximately perpendicular to the structural grain of synrift normal faults evident in the topography. Base is NASA Skylab infrared photograph (G30A026195000). Modified from Osburn and Chapin (1983a).

that are mid-Miocene or older; tilting progressively decreases toward the axis of the accommodation zone; fault spacing decreases concomitant with decreasing tilt; east- and west-dipping faults are equally common within the accommodation zone, whereas one or the other dominates in tilt domains to either side; along the axis of the accommodation zone, minor scissor-like faults separate gently (20–35°) tilted fault blocks of opposing tilt; and evidence of strike–slip faulting is lacking.

Faulds et al. (in press) present several possible scenarios that could account for lack of strike–slip displacement along the accommodation zone. The most intriguing model is as follows:

> The opposing tilt-block domains are depicted as two sets of dominoes rotating about horizontal axes (i.e. tilting). The rotational axis of one block in each domain is fixed in an arbitrary reference frame. The blocks containing the "fixed" axis of rotation undergo pure rotation, whereas the other blocks experience both translation and rotation. If the "fixed" axis of rotation and magnitude of extension do not change across the accommodation zone, only torsional strain should occur along the entire zone. Relative to the "fixed" rotational axis, blocks to the east, which would include the Colorado Plateau in this case, are translated eastward and blocks to the west move westward.

Most authors assume that low-angle detachments underlying tilt-domains switch dip directions across an accommodation zone. However, if tilt-domains simply develop by progressive imbricate normal faulting away from en-echelon sites of initial rupture, as suggested by Stewart (1980), and the magnitude of extension is the same in both domains, little or no strike–slip displacement is required. This could occur if the area were undergoing extension by pure shear above a thermal anomaly or if the low-angle detachment were of regional dimensions and uniform dip. The SAZ may provide a test because it crosses several calderas whose boundaries do not seem to be offset by strike–slip faulting (Fig. 4).

Besides the presence or absence of strike–slip faulting, several other questions about accommodation zones remain to be resolved: (1) Do accommodation zones cut both the upper and lower plates of detachment faults or are they restricted to the upper plate? (2) Do detachment faults reverse dip on opposite sides of accommodation zones? (3) Precisely how is the reversal of tilt direction of fault blocks accomplished across an accommodation zone? (4) Must accommodation zones in highly extended terranes parallel the extension direction? (5) Do pre-existing structures control the location and orientation of accommodation zones? (6) Why do accommodation zones tend to be structural highs, both within basins and between basins? (7) Why do accommodation zones tend to leak magmas?

Volcanic history

The composite stratigraphic column in Fig. 5 provides a convenient summary of volcanism in the Socorro area. The Hells Mesa Tuff (32.0 Ma) separates the prerift volcanic record, covered during Day 2, from the synrift volcanic history discussed during Day 1. Eruption of the Hells Mesa Tuff and consequent foundering of the Socorro caldera (Fig. 4) is the earliest volcanic event that has been linked to the Socorro accommodation zone. The Hells Mesa eruption occurred in a weak tensional stress field (Cather et al., 1987) before rapid extension began along the Rio Grande rift at about 29 Ma. Several intrusive bodies were emplaced following formation of the Socorro caldera; these include the Water Canyon quartz monzonite stock (31 Ma) on the caldera's north margin, a large north-northeast-trending rhyolite dike in the Joyita Hills (31 Ma), and several intermediate-composition dikes (30 Ma) on Chupadera Mesa northeast of Socorro. It can be argued, inconclusively, that the Socorro caldera and subsequent intrusions reflect the existence of the Morenci lineament, a major northeast-trending lineament which determined the location of the SAZ, before the SAZ came into being as a domain boundary in the embryonic Rio Grande rift.

Extrusion of the Hells Mesa Tuff was followed by a 2.4 to 3.2 m.y. lull in pyroclastic volcanism (Fig. 6), during which a regional unconformity developed over most of the Mogollon–Datil volcanic pile (McIntosh et al., 1986; McIntosh, this volume) and perhaps much of the Southern Rocky Mountain region. This lull in volcanism was followed by eruption of immense volumes of silicic ash-flow tuffs and mafic lava flows during the interval 28.9–27.3 Ma (Fig. 6; McIntosh, this volume). The magnitude of this volcanism, its bimodal character, and evidence for the beginning of domino-style faulting mark this period as clearly rift-related. In the Lemitar Mountains (Fig. 7) north of the SAZ, Chamberlin (1983) has used changes in thickness of volcanic units and angular unconformities to document existence of strike valleys prior to, during, and following eruption of the 27.9 Ma Lemitar Tuff. Westward-thickening wedges of mafic lavas in these strike valleys indicate that the domain of west-tilted fault blocks north of the SAZ began to form prior to 27.9 Ma. Fault scarps apparently reached 10–60 m in height (Chamberlin, 1983) during emplacement of the Lemitar Tuff. Chamberlin (1983) reports that progressive domino-style rotation of fault blocks is indicated by systematic decreases in present-day westerly dips of proressively younger strata: Vicks Peak Tuff (28.5 Ma) 55–70°, Lemitar Tuff (27.9 Ma) 40–50°, South Canyon Tuff (27.3 Ma) 35–40°, lower Popotosa Formation (27–20 Ma) 30–35°, upper Popotosa Formation (20–12 Ma) 20–25°, Socorro Peak Rhyolite (12–7 Ma) 10–15°, and Sierra Ladrones Formation (4.5–0.5 Ma) 0–10°. Stratal tilts compiled by the author from seven areas on a geologic map of the Lemitar Mountains (Chamberlin, 1982) reveal approximately concordant dips between Hells Mesa (32.0 Ma), La Jencia (28.8 Ma), and Vicks Peak (28.5 Ma) tuffs, but an average discordance of 12° between the Vicks Peak and Lemitar (27.9 Ma) tuffs. This is rather impressive considering the Lemitar Tuff is only 0.6 m.y. younger than the Vicks Peak. Angular discordances of approximately 5° between the Lemitar (27.9 Ma) and South Canyon (27.3 Ma) Tuffs and 14° between the South Canyon Tuff and the basal synrift sediments of the Popotosa Formation were also noted.

During the early-rift burst of pyroclastic volcanism, a series of overlapping calderas formed along the SAZ (Fig. 4). Three are well documented; at least three others probably exist. Calderas and their respective ash-flow tuffs are: Socorro caldera—Hells Mesa Tuff (32.0 Ma), Sawmill Canyon–Magdalena composite caldera—La Jencia Tuff (28.8 Ma), and Mount Withington caldera—South Canyon Tuff (27.3 Ma). Caldera sources have not yet been delineated for the tuff of Caronita Canyon (27.9 Ma), Lemitar Tuff (27.9 Ma), and tuff of Turkey Springs (24.3 Ma). The Vicks Peak Tuff (28.5 Ma) is a major unit in the Socorro area but was erupted from a caldera at the south end of the San Mateo Range.

Significant volumes of mafic lavas were erupted between major pyroclastic events. They are quite variable in composition but monotonous in field appearance and are generally termed basaltic andesites. Eruption of this type of lava began at about 36 Ma, when regional compression changed to weak tension (Cather et al., 1987; Cather and Chapin, this volume) but increased markedly after eruption of the Hells Mesa Tuff. In the Lemitar Mountains and Joyita Hills, multiple thin flows of mafic lavas accumulated to thicknesses of 30–200 m between emplacement of each ash-flow-tuff sheet. A large, shield-like accumulation of these lavas in the Bear Mountains apparently prevented emplacement of the Lemitar and South Canyon Tuffs. A swarm of north-trending mafic dikes extends for tens of kilometers onto the Colorado Plateau from the north end of the Bear Mountains; the swarm consists of hundreds of dikes in a zone at least 30 km wide. Other centers of mafic volcanism are known in the Lemitar Mountains and Joyita Hills. The mafic lavas are very widespread north of the SAZ, but are less abundant to the south. Major silicic plutons beneath the caldera complexes probably prevented ascent of mafic mag-

FIGURE 5—Composite stratigraphic column for the northeast Mogollon–Datil volcanic field. The base of the volcanic pile rests on rocks of Precambrian (p€), Paleozoic (Pz), Mesozoic (Mz), or Eocene age (Baca Fm.) depending on geographic location relative to Laramide uplifts and basins. The late Eocene to Pleistocene section can be divided into three main parts: (1) Datil Group: lower Datil (40–36 Ma), volcaniclastic rocks of intermediate composition; upper Datil (36–32 Ma), a bimodal suite of silicic ash-flow tuffs and basaltic andesite lava flows with derivative volcaniclastic rocks. (2) A bimodal suite of rhyolitic ash-flow tuffs and basaltic andesite lava flows (32–27 Ma). (3) Santa Fe Group: bolson sedimentary deposits and interbedded bimodal basaltic and rhyolitic rocks of Rio Grande rift (27–0.5 Ma), with axial river deposits of ancestral Rio Grande in upper part (4.6–0.5 Ma). The youngest major ash-flow sheet of the Mogollon–Datil field, the tuff of Turkey Springs (24.3 Ma, McIntosh, this volume) is locally interbedded with sedimentary deposits of the basal Santa Fe Group. It was previously thought to be part of the South Canyon Tuff (Osburn and Chapin, 1983a, b). Standard patterns denote sedimentary and Precambrian rock types. Mafic lava flows shown with black rectangles if plagioclase-phyric, and with gray cloth-like pattern if aphyric (La Jara Peak type). Crystal-rich ash-flow tuffs shown with squiggly lines plus black triangles; crystal-poor ash-flow tuffs shown with squiggly lines only. Basalt flows in Santa Fe Group shown in solid black; rhyolites shown in white with flow lines. Modified from Osburn and Chapin (1983a, b).

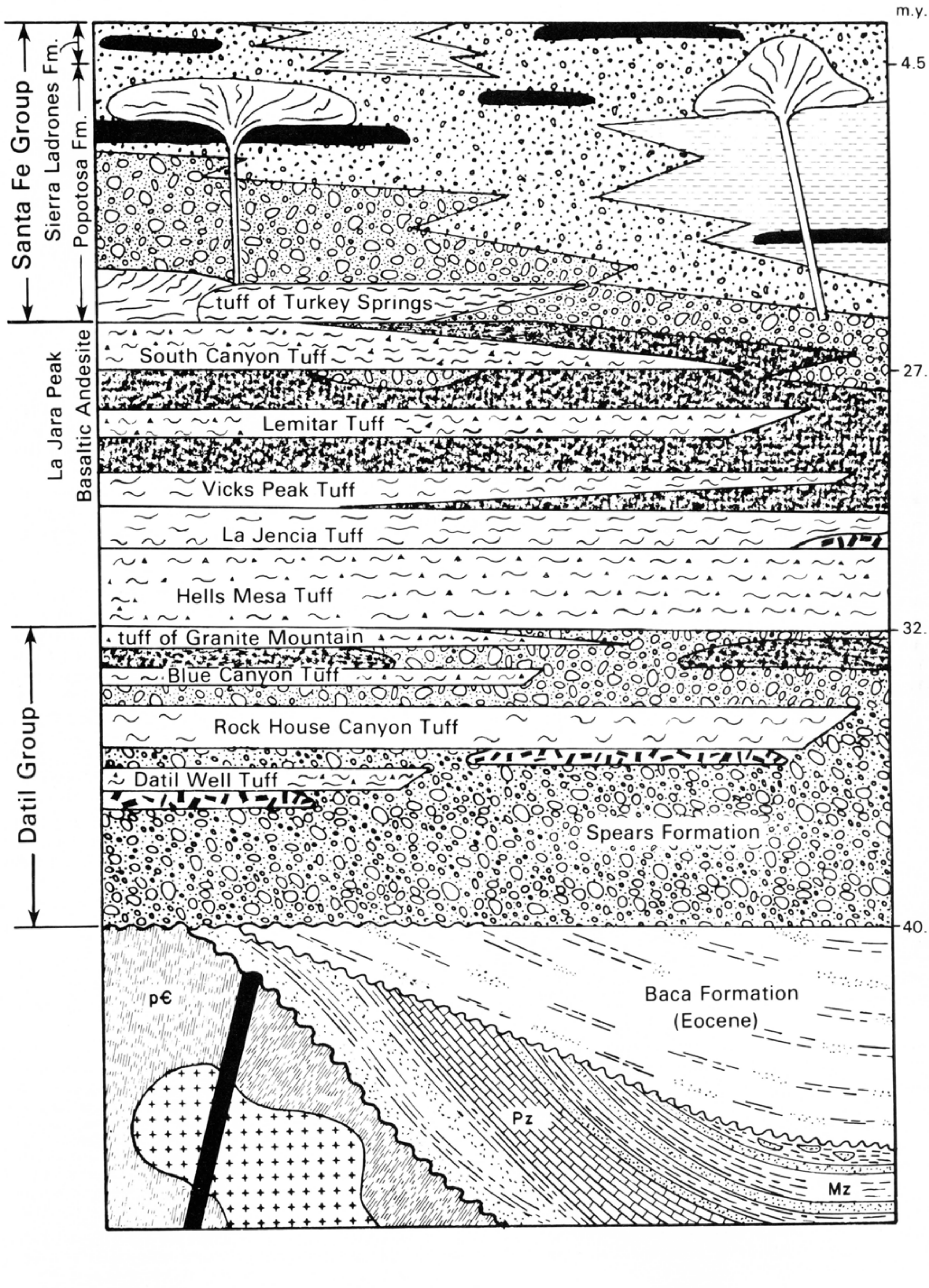
m.y.
4.5
27.
32.
40.
Santa Fe Group
Sierra Ladrones Fm.
Popotosa Fm.
La Jara Peak Basaltic Andesite
Datil Group
tuff of Turkey Springs
South Canyon Tuff
Lemitar Tuff
Vicks Peak Tuff
La Jencia Tuff
Hells Mesa Tuff
tuff of Granite Mountain
Blue Canyon Tuff
Rock House Canyon Tuff
Datil Well Tuff
Spears Formation
Baca Formation
(Eocene)
p€
Pz
Mz

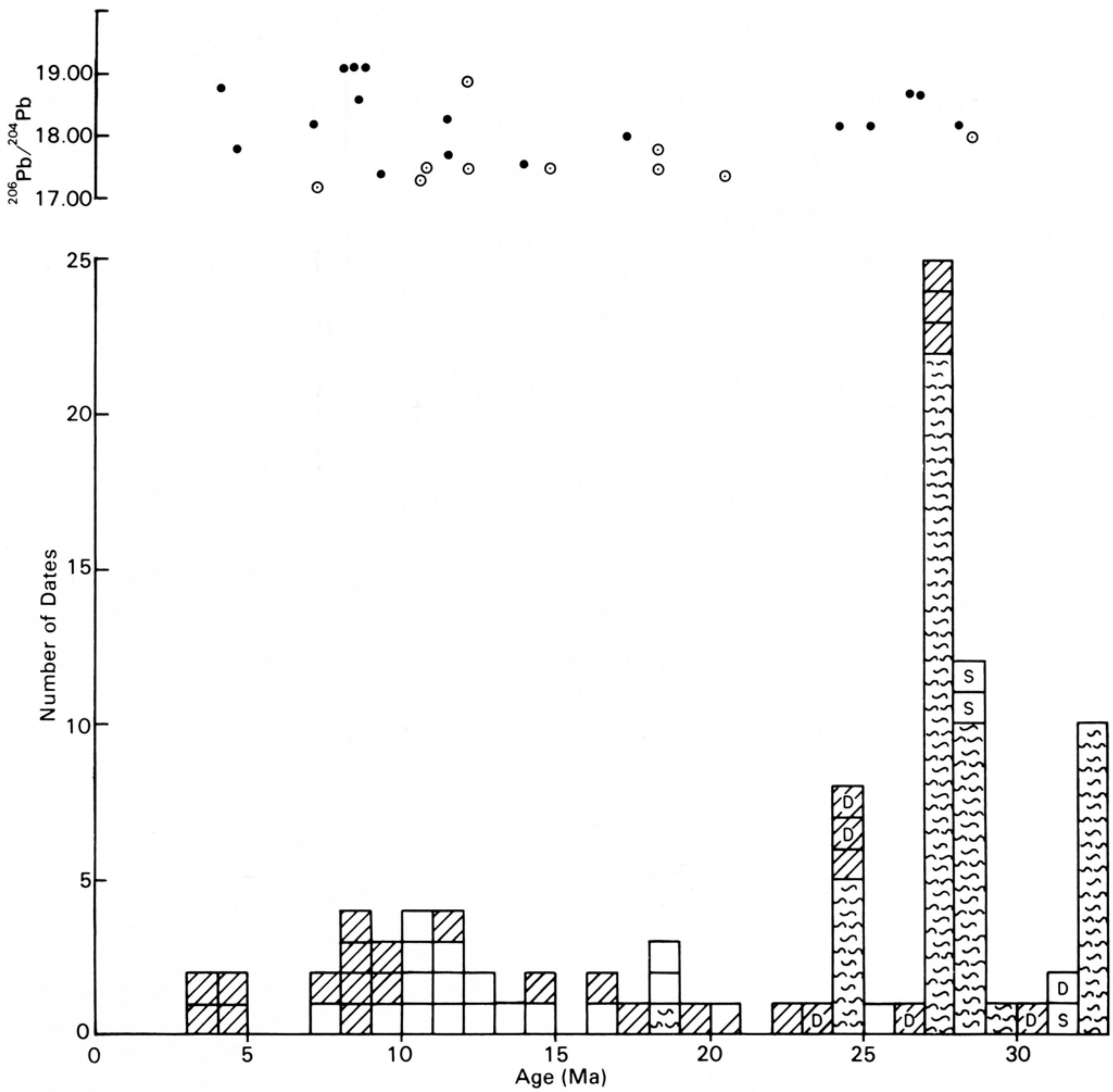

FIGURE 6—**Lower part:** Histogram of radiometric ages of igneous rocks emplaced during development of the Socorro accommodation zone (SAZ). Because of uncertainties concerning routes of ascent of magmas and distances traveled by lava flows, rocks of known age within 30 km of the SAZ are included in the histogram. Volumes were not calculated because of fragmentary outcrops and large areas of sedimentary cover. Major ash-flow tuffs were arbitrarily assigned 10 units and moderate-volume tuffs five units to more clearly portray the importance of early-rift ignimbrite eruptions. Diagonally ruled boxes = mafic lavas, open boxes = silicic lavas and domes, squiggly lines = ash-flow tuffs, S = stock intrusion, D = dikes. **Upper part:** $^{206}Pb/^{204}Pb$ vs. age for mafic lavas (solid dots) and silicic flows and domes (open circles) in the vicinity of the SAZ. Isotopic analyses by Heatherington (1988).

mas to the surface. Basaltic andesite lavas form thick, wedge-shaped accumulations within the northern Sawmill Canyon caldera but thin rapidly to the south.

As can be seen in Fig. 6, bimodal volcanism has continued episodically along the SAZ from eruption of the last major ash-flow tuff at 24.3 Ma (the tuff of Turkey Springs) to eruption of four small-volume basalt flows between 4.6 and 3.6 Ma. The volume of rhyolite erupted exceeds basalt because of the relatively large volumes of silicic lavas and domes in the Magdalena Peak (13.5–18.4 Ma), Socorro Peak (7.2–12.1 Ma), and Pound Ranch (10.8–12.1 Ma) volcanic centers (Fig. 8). Except for the basaltic andesite of Silver Creek (16 Ma; Weber, 1971), mafic lavas erupted during this interval are relatively small-volume flows that were easily dissected by erosion and their original volumes are difficult to estimate. Mafic lavas range from high-K andesite through basaltic andesite to alkali olivine basalt (Fig. 9); silicic rocks range from high-K dacite to high-K, high-silica rhyolite (Bobrow et al., 1983). Silicic lavas from all four volcanic centers are similar geochemically, isotopically, and petrographically (Bobrow et al., 1983).

Also plotted in Fig. 6 are $^{206}Pb/^{204}Pb$ ratios determined by Heatherington (1988) for dated volcanic rocks along the SAZ. Heatherington and Bowring (1988) report that: "Ba-

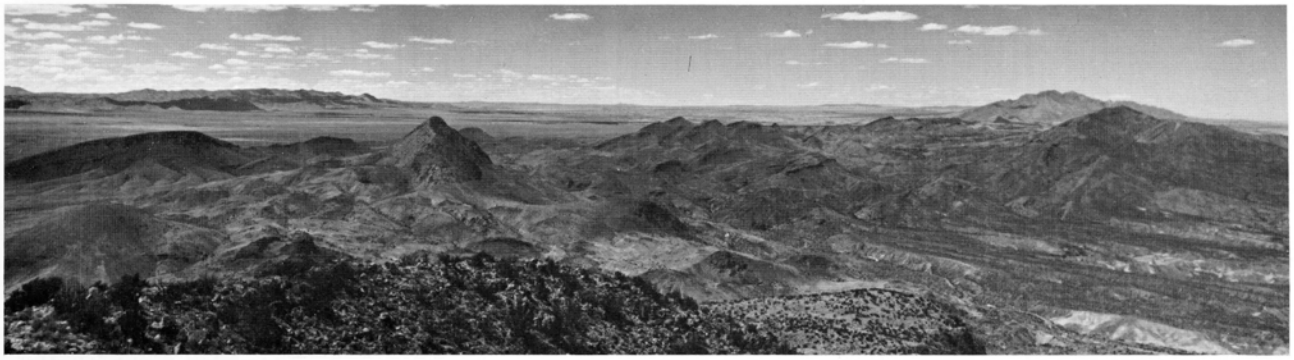

FIGURE 7—View northwestward from Socorro Peak across the domain of west-tilted fault blocks north of the SAZ. Bear Mountains on left skyline, Ladron Peak on right skyline, Lemitar Mountains in middle distance, Strawberry Peak at left center. The Lemitar Mountains are a highly extended terrane characterized by domino-style normal faulting, westward tilting of strata, and repetition of the stratigraphic section (Chamberlin, 1983). Early-rift strata commonly dip westward 50–70° and locally approach vertical. Chamberlin and Osburn (1984) estimate 100–200% extension across a north-trending 25 km wide belt that includes the Lemitar Mountains.

salts less than 9 Ma old from Socorro south to T or C (Truth or Consequences) are geochemically distinct from older samples, with more radiogenic Pb ($^{206}Pb/^{204}Pb > 18.8$), less radiogenic Sr ($^{87}Sr/^{86}Sr < 0.7055$), lower concentrations of incompatible elements, and lower $^{87}Sr/^{86}Sr$ for a given $^{206}Pb/^{204}Pb$." Everson and Silver (1978) had previously reported unusually radiogenic $^{206}Pb/^{204}Pb$ (19.2 to 19.6) for Pliocene and Quaternary basalts between Socorro and Las Cruces as compared to $^{206}Pb/^{204}Pb$ for basalts of similar age north of Socorro (17.3 to 18.5). They suggested that the source regions for basalts south of Socorro resemble those of ocean-island basalts and that this implies "penetration of the continental lithosphere by deeper mantle materials." The five highest $^{206}Pb/^{204}Pb$ ratios in Fig. 6 for basalts younger than 9 Ma are from samples collected on the SAZ (basalt of Socorro Canyon, 4.1 Ma) or south of the SAZ in the Chupadera Mountains. Three basalts erupted south of the SAZ during the interval 11.5 to 9.3 Ma have $^{206}Pb/^{204}Pb$ ratios (17.4 to 18.3) similar to older mafic lavas of the Mogollon–Datil volcanic field. Thus the SAZ seems to be the northern boundary of asthenospheric upwelling that began to dominate basalt production at about 9 Ma. The SAZ is also the southern boundary of the mid-crustal magma body delineated by microearthquake studies (Fig. 10).

Heatherington and Bowring (1988) also report that samples 40–9 Ma define a linear array above the oceanic trend

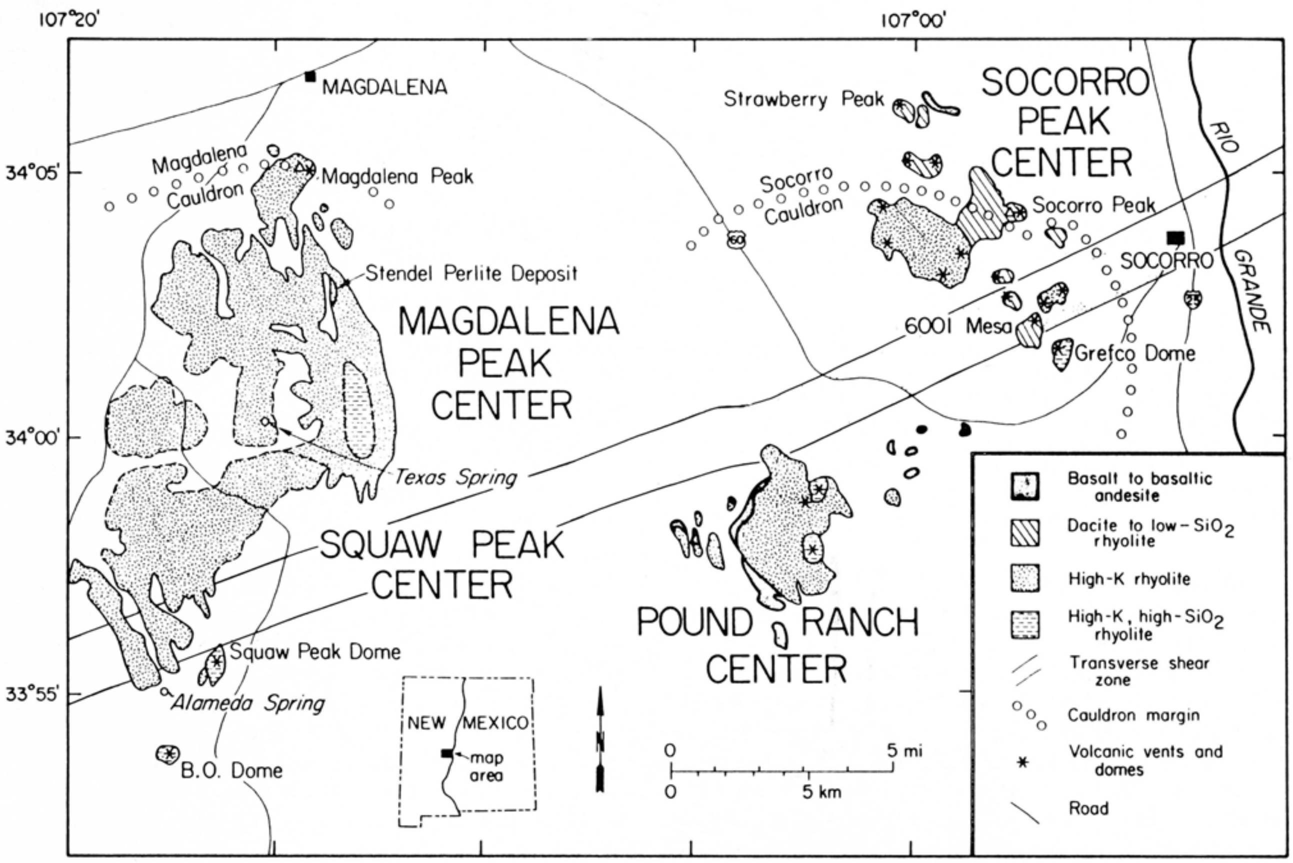

FIGURE 8—Four principal centers of middle to late Miocene silicic volcanism along the Socorro accommodation zone. Igneous rocks older than 19 Ma and several basalt flows in the 9–4 Ma range not shown. From Bobrow et al. (1983) with permission of the New Mexico Geological Society.

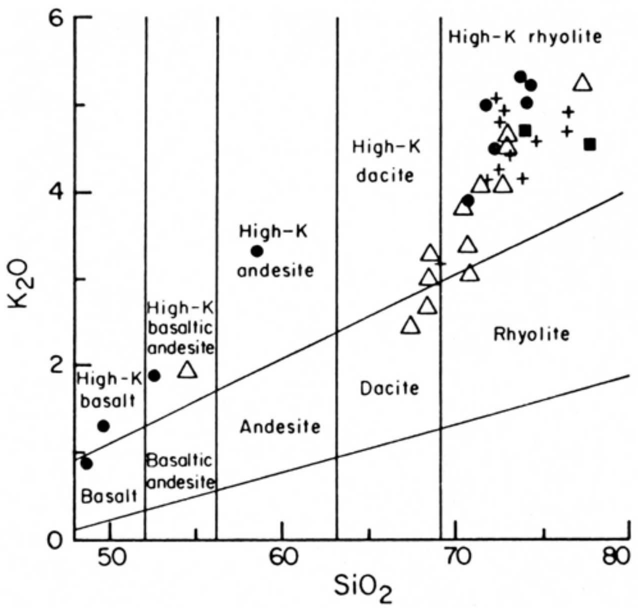

FIGURE 9—K_2O vs. SiO_2 plot for middle to late Miocene volcanic rocks shown in Fig. 8. Plot modified from Ewart (1979). Open triangles = Socorro Peak center, solid circles = Pound Ranch center, crosses = Magdalena Peak center, solid squares = Squaw Peak center. From Bobrow et al. (1983) with permission of the New Mexico Geological Society.

on a common lead plot, with the array yielding a secondary isochron age of 1.7 Ga, the age of the Proterozoic basement. Basalts younger than 9 Ma deviate from this trend with lower $^{207}Pb/^{204}Pb$ for a given $^{206}Pb/^{204}Pb$. They interpret the data to indicate that magmas were derived from lithospheric sources during the 40 to 9 Ma period and from an asthenospheric source (south of Socorro) after 9 Ma. Bowring and Heatherington (1987) reported that a plot of age versus $^{206}Pb/^{204}Pb$ shows two peaks centered at 30 Ma and 7 Ma, which correlate with times of rapid extension. The database for Fig. 6 is too limited to clearly show the earlier peak, but there is a suggestion of a peak at about 28 Ma. They interpret the two peaks as indicating that partial melting of depleted lower crust dominated during periods of slow extension, whereas magma generation occurred mainly in relatively enriched lithospheric mantle (or asthenosphere <9 Ma south of Socorro) during periods of rapid extension. Their database consisted of 74 samples collected from an area extending south to Truth or Consequences, west to Datil, and north to Belen.

It is also apparent from Fig. 6 that the Socorro area is overdue for the next pulse of volcanism. The gap in volcanism from 3.6 Ma to present is the longest hiatus in volcanism during the 32 m.y. span of the histogram. Alternatively, one could argue that volcanism is waning and there may be no further eruptions. However, a considerable

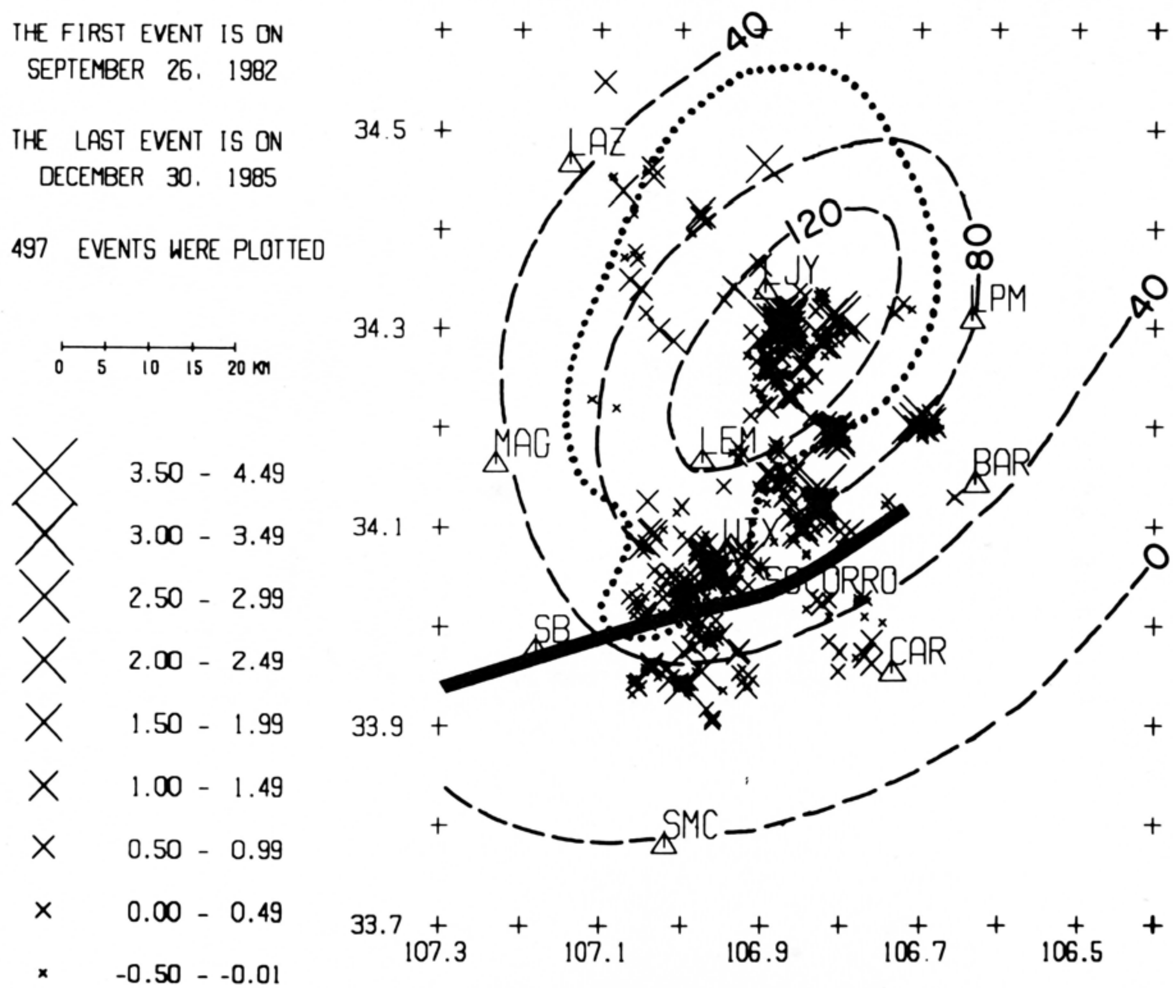

FIGURE 10—Earthquake activity in the Socorro area from September 1982 through December 1985. Superimposed on the seismicity map are dashed contours of uplift in millimeters for the period 1911 through 1980 (Larsen et al., 1986), the dotted outline of the mid-crustal magma body (Rinehart and Sanford, 1981), and the Socorro accommodation zone. Seismograph stations are shown by triangular symbols with letter designations. From Sanford et al. (in press) with addition of SAZ.

body of geophysical data indicates that the next batch of magma is already in the plumbing system. An extensive layer of magma at a depth of approximately 19 km was first detected by microearthquake studies (Sanford et al., 1973; Sanford et al., 1977; Rinehart et al., 1979) and later confirmed by seismic-reflection profiling by the Consortium for Continental Reflection Profiling (COCORP) (Brown et al., 1979, 1980). The magma body has a minimum areal extent of 1700 km^2 (Fig. 10) and its thickness is approximately 130 to 190 m (Brocher, 1981; Ake and Sanford, 1988).

The presence of the magma body is substantiated by other lines of evidence. Releveling of elevation benchmarks indicates that the ground surface over the magma body has been uplifted more than 120 mm (Fig. 10) between 1911 and 1980 (Reilinger and Oliver, 1976; Reilinger et al., 1980; Larsen et al., 1986). The uplifted area is centered over the magma body; geomorphic evidence indicates an average rate of uplift for the central area of 1.8 mm/yr over the past 20,000 yrs (Ouchi, 1983). A convex-upward hump in the longitudinal profile of the Rio Grande between Belen and Socorro coincides with the area underlain by the magma body (Ouchi, 1983). Bachman and Mehnert (1978) had previously noted that late Pliocene sand deposits of the ancestral Rio Grande rise 85 m in elevation over a distance of about 11 km along the east side of the Rio Grande north of Socorro. Sanford et al. (in press) calculate a tectonic change in elevation of 74 m, assuming the ancestral Rio Grande had the existing river gradient of 1 m/km; from this, and assuming an uplift rate of 1.8 mm/yr, they estimate that uplift began about 40,000 yrs ago. The thickness of the magma body indicates an age of 70,000 to 105,000 years, assuming the same rate of uplift (Sanford et al., in press). Modeling studies indicate that the observed surface uplift can be explained by inflation of the mid-crustal magma body (Larsen et al., 1986). Current seismicity is centered over the magma body (Fig. 10) and shows little correlation with known faults (Sanford et al., in press). The intensity of seismicity in the Socorro area and its separation from other seismogenic zones by regions of very low seismicity also suggests a relationship to magmatic activity.

Shallow magma bodies may also exist in the Socorro area. Earthquake swarms are generally considered evidence for injection of magma into the crust (Stuart and Johnston, 1975; Sanford and Einarsson, 1982). Swarms have been noted in the Socorro area since 1849 and a swarm in 1906–1907 reached moderately severe levels (Sanford and Einarsson, 1982). This swarm began in July 1906 and lasted well into 1907 with shocks felt nearly every day and at times reached a frequency of one perceptible tremor an hour. Sanford and Einarsson (1982) report that three of these shocks attained a Rossi-Forel intensity of VIIII at Socorro and were felt over areas of about 275,000 km^2.

Jarpe et al. (1984) monitored a swarm of approximately 300 recorded shocks that occurred between February 25 and March 16, 1983, near the center of the region of surface uplift. A magnitude 4.0 earthquake, the largest in the Socorro area since 1961, was included in the swarm. The hypocenters of the main shock and the aftershocks defined a tabular crustal volume striking N25°E, dipping 50° east, and extending over a depth interval of 4.8 to 7.8 km (Jarpe et al., 1984). Upward migration of magma from the mid-crustal magma body into the seismogenic zone was suggested by unusual P-wave first motions for some of the aftershocks which could not be explained by the standard double-couple-without-moment (DCWM) model of faulting. These focal mechanisms were almost totally compressional in all quadrants; Japanese seismologists have reported similar mechanisms in earthquake swarms underlying volcanoes (Shimizu et al., 1987). Jarpe et al. (1984) concluded that magmatic intrusion along the fault plane of the main shock could explain the first-motion distributions by simultaneous shear and dilation along an existing normal fault.

Another area of suspected injection of magma into the upper crust is located about 16 km southwest of Socorro near where US-60 tops Sedillo Hill and turns northwest to cross the La Jencia Basin. Microearthquake swarms in this area are directly on the SAZ and have been studied by A. R. Sanford and several of his students. Anomalously high Poisson's ratio (the ratio of the lateral unit strain to the longitudinal unit strain in a body that has been stressed longitudinally within its elastic limit) and low seismic velocities were reported in this area by Caravella (1976) and Ward et al. (1981). Carpenter and Sanford (1985) report three regions of anomalously low Q values (a measure of seismic-wave attentuation due to intrinsic absorption, scattering, and inhomogeneity in a rock body) in the upper crust within 20 km southwest of Socorro. One of these regions corresponds with the area of high microearthquake activity near Sedillo Hill. Very high heat flows (up to 490 mW/m^2; 11.7 HFU) have been measured in the Socorro Mountain block northeast of Sedillo Hill (Reiter and Smith, 1977), and the Socorro thermal springs discharge waters at about 32°C where the SAZ crosses the frontal fault of the Socorro Mountain block, approximately 10 km northeast of Sedillo Hill. Barroll and Reiter (1989) suggest that the west-tilted Socorro Mountain block acts as a "hydrologic window" between thick, relatively impermeable playa claystone deposits in the Socorro and La Jencia Basins, allowing heated ground waters to flow upward and elevate near-surface heat flows. Whether the source of the heat is magma injected into the upper crust or merely upflow of deeply circulating waters is not known. However, the proximity of high heat flows to an anomalous volume of crust with microearthquake swarms at depths between 7.2 and 10.3 km (Carpenter and Sanford, 1985), low Q values, high Poisson's ratio, abnormally high P/S amplitude ratios (Roach, 1982), and anomalously low P-wave velocities (Ward et al., 1981) suggest a region of intense fracturing possibly induced (or utilized) by intrusion of magma. Carpenter and Sanford (1985) calculate that the anomalous seismic parameters for this area could be explained by a small volume of magma; if in the form of a sill or dike, a maximum width of 50 m would be sufficient.

It is interesting to note that the SAZ passes through the array of epicenters shown in Fig. 10 along a path which intersects relatively few epicenters. The low level of seismicity directly on the SAZ, except for the anomalous area discussed above, may be a function of weakness in the crust due to shearing (Sanford et al., in press). High fracture intensity is also indicated by location on the SAZ of thermal springs which supply much of Socorro's water, and the unusually large Baldy Spring, near Langmuir Laboratory, which feeds a perennial stream in Sawmill Canyon. The most intense K-metasomatism of volcanic rocks (caused by migration of alkaline saline brines; Chapin and Lindley, 1986) in the Socorro area is also found along the SAZ, again indicating a zone of ground-water movement.

The risk of future volcanic activity in the Socorro area is also indicated by the temporal distribution of volcanism along the axis of the Rio Grande rift. Volcanism has not occurred for more than 3 m.y. within a 127 km long segment of the rift extending from Los Lunas volcano on the north to Black Mesa near San Marcial on the south (Fig. 2). To the north of this volcanic gap, several basaltic centers have been active within the last 1.1 Ma, some as young as 0.14 Ma (Kudo et al., 1977). To the south of the volcanic gap, the large-volume Jornada flows were emplaced at about 0.76 Ma (Bachman and Mehnert, 1978). Much of the gap is now underlain by an extensive magma body at about 20 km depth—i.e. the gap is pregnant. It seems likely that this deep magma body is basaltic in composition because of its low aspect ratio and the prevalence of basaltic eruptions along the rift axis. The shallow magma bodies near the SAZ may be either mafic or silicic, but the odds favor silicic. As evident in Fig. 6, rhyolitic magmas outnumber basaltic magmas both in frequency and volume during the 32 m.y. history of the SAZ.

Discussion

What do existing data allow us to say about the Socorro accommodation zone that is relevant to understanding the role these structures play in regional extension? First, let us consider the observations discussed in the previous sections. The SAZ:

1) follows a pre-existing structural lineament oriented parallel to the early-rift extension direction;
2) is a relatively linear feature oriented at a high angle to the trend of the Rio Grande rift;
3) is a boundary between two domains in which domino-style fault blocks are tilted in opposite directions with stratal dips as high as 60–70°;
4) is a zone about 2 km wide, within which stratal tilts are subhorizontal to gently tilted;
5) is approximately perpendicular to the structural grain of synrift faults; very few faults parallel the SAZ;
6) crosses the boundaries of three early-rift calderas without noticeable strike–slip offset;
7) is not marked by a conspicuous shear zone at the surface;
8) is relatively aseismic in a highly seismogenic region;
9) is a zone of ground-water movement as indicated by location of the largest springs in the area and the most intense K-metasomatism;
10) was initited at the beginning of rifting, as indicated by the alignment of early-rift calderas along it and by stratigraphic evidence in the north domain that stratal tilts have increased progressively since before 27.9 Ma;
11) has leaked magmas episodically since at least 32 Ma;
12) is the boundary between late Miocene (<9 Ma) to Quaternary basalts to the south with highly radiogenic $^{206}Pb/^{204}Pb$ (18.8–19.6), and basalts of similar age to the north with less radiogenic $^{206}Pb/^{204}Pb$ (17.3–18.5) similar to values for the northern two-thirds of the rift and the Colorado Plateau;
13) is the southern boundary of the mid-crustal magma body.

The above observations point to the following conclusions: The SAZ is a near-vertical structural discontinuity that inherited its location and trend from a pre-existing lineament which was oriented nearly perpendicular to the developing rift and parallel to the early-rift extension direction. The SAZ has not undergone much strike–slip movement because: (1) it is not marked by a shear zone at the surface, (2) very few faults parallel the SAZ, (3) it crosses early-rift calderas without appreciable offset of their boundaries, and (4) it is relatively aseismic in a highly seismogenic region. Because the SAZ has leaked magmas episodically for at least 32 m.y. and appears to bound both asthenospheric penetration of the lithosphere and a laterally extensive mid-crustal magma body, it must not be confined to the upper plate of the Socorro detachment terrane.

Several fundamental questions remain, however. Most perplexing is the mechanics of changing tilt directions of fault blocks across the accommodation zone without noticeable strike–slip faulting and without even developing a visible fault system parallel to the accommodation zone. The SAZ is virtually invisible on detailed (1:24,000) geologic maps and a 1:200,000 geologic map of Socorro County (Osburn, 1984). It is only noticeable in systematic differences in tilt directions of strata to either side, in the distribution of synrift volcanic rocks, and as a structural high crossing rift basins.

It is not known whether detachment faults reverse dip on opposite sides of the SAZ. While the structural style and magnitude of extension in the Socorro area seem to require detachment faulting beneath the tilt domains, specific evidence for detachment faults is thus far only available from seismic-reflection profiling by COCORP in the southern Albuquerque Basin, 40 km north of the SAZ. Possible outcrops of detachment faults have been found near these lines on the east flank of the Ladron Mountains (the Jeter fault; Gillespie-Nimick, 1986) and in the Joyita Hills, but their interpretation is controversial. COCORP lines 3 and 4, which cross the SAZ, failed to show reflections from detachment faults, but the quality of the seismic data was very poor.

It seems likely that the SAZ represents a special class of accommodation zone that is controlled by a prerift lineament which happened to parallel the extension direction. Thus the observations and conclusions reached in this paper may not be applicable to other types of accommodation zones, such as those described by Rosendahl (1987) and Morley (1988) in the Western rift of East Africa. The Comment by Bosworth (1986) and the Reply by Lister et al. (1986b) present an informative discussion of problems in extrapolating accommodation-zone characteristics to different regions. Bosworth (1986: 890) stated that transfer faults ". . . are seldom oriented in an orthogonal position relative to rift-trend faults, nor are they parallel to the regional extension direction." Lister et al. (1986b: 891) argued that ". . . there is the geometric requirement that the movement direction on the normal fault must lie in the plane of the transfer fault, at least at moderate to large extensions . . ." and ". . . where the normal (and detachment) faults are essentially dip–slip, steeply dipping transfer faults must be perpendicular to them and will therefore contain the extension direction." Lister et al. (1986b) ascribed these differences in opinion to variations in amount of extensional strain between the East African rift system (generally <10%) studied by Bosworth and highly extended terranes studied by them in the Basin and Range province (locally exceeding 100%) and in passive continental margins (successful rifts). Lister et al. (1986b: 892) reasoned that: "At extensions of a few percent, distributive faulting throughout the rock mass can accommodate the along-strike variations in normal fault geometry, and the geometric requirements for compatibility between fault motions need not be strictly obeyed."

This discussion of behavior of accommodation zones with respect to degree of extension may be pertinent to problems in locating the two ends of the SAZ. In Fig. 4, I projected the SAZ northeastward from its exposure at Socorro Peak across the Socorro Basin (no data) and along a conspicuous change in structural grain on the east side of the basin. To the north of this boundary, rocks are obviously in the west-tilted domain, but to the south the situation is complicated by lack of sufficient outcrops of Cenozoic rocks and complex Laramide and Paleozoic structures. Sparse outcrop data in Pliocene and younger strata within the Socorro Basin suggest that the SAZ may make a 90° dogleg and commence its northeastward course about 16 km to the south, near the village of San Antonio (S. M. Cather, oral comm. 1989). Faulds et al. (in press) describe a similar 90° dogleg in the accommodation zone mapped in southern Nevada. The structural boundary along which I projected the SAZ may be the pre-Pliocene location of the SAZ or merely a continuation of the Morenci lineament. The amount of extension east of the Socorro Basin is much less than to the west, so behavior of the SAZ may be less constrained. A similar problem exists at the southwest end of the SAZ, where the boundary between west-tilted and east-tilted strata appears to undergo a similar 90° offset southward along the crest of the San Mateo Range (C. A. Ferguson, written comm. 1989). More work is required to resolve these problems.

I estimate extensional strain in the Socorro area to average about 50% based on thinning of the crust beneath the rift (Moho at ~33 km vs. 50 km beneath High Plains) and elongation of the Socorro caldera (~33 km parallel to extension direction vs. 22 km at right angles and assuming equidimensional initial shape). Chamberlin and Osburn (1986) also estimate an average of about 50% extension across the rift at Socorro from restored cross sections and the shape of the Socorro caldera. Calculations based on tilting of strata have yielded estimates as high as 100 to 200% extension (dips of 50–70°) for a relatively narrow belt along the present rift axis (Chamberlin and Osburn, 1984). The SAZ resembles accommodation zones in highly extended areas such as those described by Lister et al. (1986a) and by Faulds et al. (in press) more than those described by Bosworth et al. (1986) and Rosendahl (1987). However, all accommodation zones probably have some features in common because of their role in accommodating along-strike variations in magnitude of extension and normal fault geometry. Much additional work is needed before these interesting but enigmatic structures are adequately understood.

Acknowledgments

The impetus for writing this paper came from a field trip and stimulating discussions with James E. Faulds concerning an accommodation zone in the Colorado River extensional corridor. The manuscript was improved during discussions and reviews by S. A. Bowring, S. M. Cather, R. M. Chamberlin, J. E. Faulds, W. C. McIntosh, and A. R. Sanford. Radiometric ages are based on $^{40}Ar/^{39}Ar$ dating of ash-flow tuffs by W. C. McIntosh (this volume) and K–Ar dating of other rocks by Muhammad Shafiqullah at the Isotope Geochemistry Laboratory of the University of Arizona. Details of the K–Ar ages will be reported in a subsequent paper. Isotopic analyses were done at Washington University, St. Louis, Missouri, by A. L. Heatherington and S. A. Bowring. Permission to use their unpublished data is gratefully acknowledged. Geophysical data concerning the Socorro magma bodies were kindly provided by A. R. Sanford, who patiently helped me understand their significance. I also wish to thank the many graduate students of New Mexico Tech and other universities who over a period of 20 years have built the extensive database which made this paper possible. Lynne McNeil typed the manuscript and Michael Wooldridge drafted several figures.

Timing and distribution of ignimbrite volcanism in the Eocene–Miocene Mogollon–Datil volcanic field

William C. McIntosh

Ongoing $^{40}Ar/^{39}Ar$ dating work and paleomagnetic analysis are providing tight constraints on the history of ignimbrite volcanism in the Mogollon–Datil volcanic field. High-precision (± 0.15 Ma) sanidine plateau ages have been obtained from most of the 25+ voluminous (100–1200 km^3) regional ignimbrites. The age determinations range from 36.1 to 24.3 Ma and agree closely with established stratigraphic order (Fig. 1). Age and paleomagnetic data allow reliable correlation of ignimbrites among isolated ranges, providing an integrated time-stratigraphic framework for the entire volcanic field (Fig. 2).

Mogollon–Datil ignimbrite activity was strongly episodic, being confined to four brief (<2.6 m.y.) eruptive episodes separated by 1–3 m.y. gaps during which no caldera-forming eruptions occurred (Fig. 1). Ignimbrite activity generally tended to migrate from the southeast toward the north and west.

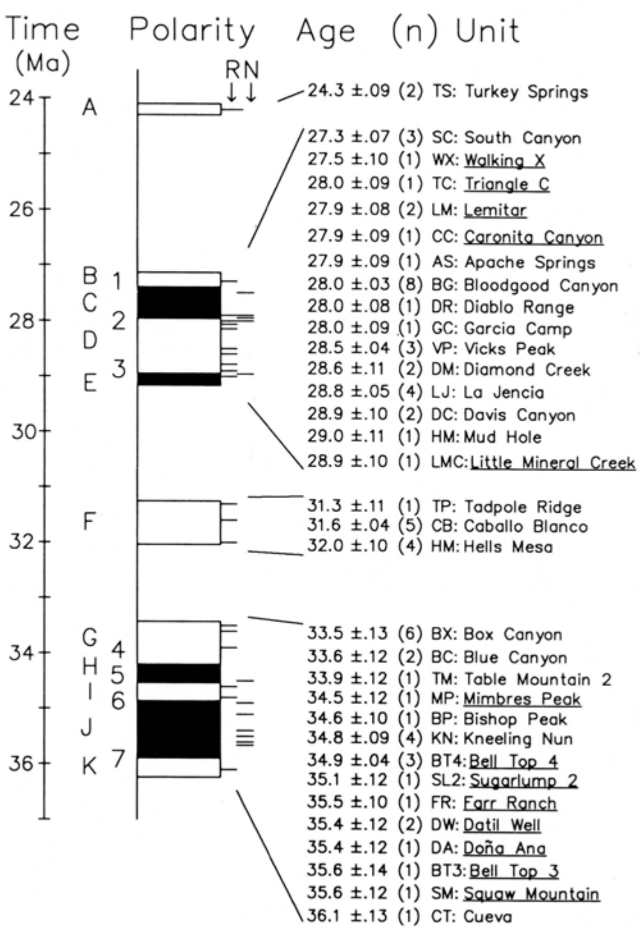

FIGURE 1—Ages and magnetic-polarity record of well-constrained Mogollon–Datil ignimbrites. Right column gives mean $^{40}Ar/^{39}Ar$ plateau ages, unit names and their abbreviations (used in Fig. 2), and the number of age determinations (in parentheses). Units are in stratigraphic order and normal units are underlined. Left column shows interpreted polarity record, with lettered polarity intervals and numbered reversals. The tic marks to the right of the polarity column each depict a dated ignimbrite; tics denoting normal polarity units are offset to the right. Ages are calculated relative to a Fish Canyon Tuff sanidine monitor (FCT-3; 27.78 Ma). Errors represent the standard deviation of plateau ages for units with n>2, and the analytical error for units with $n \leq 2$.

Episode 1 (36.1–33.5 Ma): Rhyolitic ignimbrite activity, dominantly low-silica, commenced at the southeast edge of the field with eruption of the Organ Mountains caldera and associated outflow sheets at 36.1 and 35.6 Ma, closely followed by eruption of the nearby Doña Ana caldera at 35.4 Ma. Two thin 35.5–35.4 outflow sheets are also present in the northeastern portion of the field (Fig. 2), but their source is unknown. Major caldera-forming activity shifted 100 km northwest of the Organ Mountains with eruption of the Kneeling Nun Tuff (>900 km^3) at 34.8 Ma. Several less voluminous ignimbrite eruptions followed in the interval from 34.8 to 33.5 Ma. Sources for most of these units were near the eastern edge of the field, although Box Canyon Tuff (33.5 Ma; Fig. 2) was almost certainly erupted from a caldera south of the Mogollon–Datil volcanic field.

Episode 2 (32.0–31.3 Ma): After a 1.5 m.y. hiatus, low-silica rhyolitic ignimbrite activity shifted north and west, producing the Hells Mesa (32.0 Ma, 1200 km^3), Caballo Blanco (31.6 Ma, a.k.a. Fall Canyon), and Tadpole Ridge (31.3 Ma) Tuffs.

Episode 3 (28.9–27.3 Ma): Following a 2.4 m.y. hiatus, the "ignimbrite flare-up" occurred, producing within a span of 1.6 m.y. more than 12 regional units, primarily high-silica rhyolites, totaling >6000 km^3. Well-dated units within this interval include Davis Canyon (28.9 Ma), La Jencia (28.8 Ma), Vicks Peak (28.5 Ma), Bloodgood Canyon (28.0 Ma), Lemitar (28.0), and South Canyon (27.3 Ma) Tuffs. Calderas for these units were located near the western and northern margins of the volcanic field. At least one caldera to the south of the Mogollon–Datil field was also active during this interval, as evidenced by a 27.5 Ma distal-facies outflow sheet in the Big Burro Mountains (Fig. 2).

Episode 4 (24.3 Ma): After a 3.0 m.y. hiatus, Mogollon–Datil ignimbrite activity ended with eruption of the high-silica rhyolite tuff of Turkey Springs at 24.3 Ma, from a caldera near the northern edge of the field.

Mogollon–Datil ignimbrite episodes 1, 3, and 4 closely parallel the timing of ignimbrite activity in the San Juan volcanic field of Colorado, indicating regional tectonic control of caldera-forming rhyolitic eruptions.

Paleomagnetic data and $^{40}Ar/^{39}Ar$ plateau ages precisely constrain seven geomagnetic-polarity reversals that occurred during Mogollon–Datil activity (Fig. 1). This polarity record can be confidently correlated with the polarity record of well-dated San Juan units and has potential to aid in radiometric calibration of the worldwide Magnetic Polarity Time Scale (MPTS) determined from marine magnetic anomalies. At present, the Mogollon–Datil polarity record best fits the MPTS if normal intervals C and J are respectively correlated with marine normal anomalies 10 and 16. This fit suggests that Mogollon–Datil ignimbrite episode 1 is Eocene, and implies an Eocene/Oligocene boundary age near 34.0 Ma.

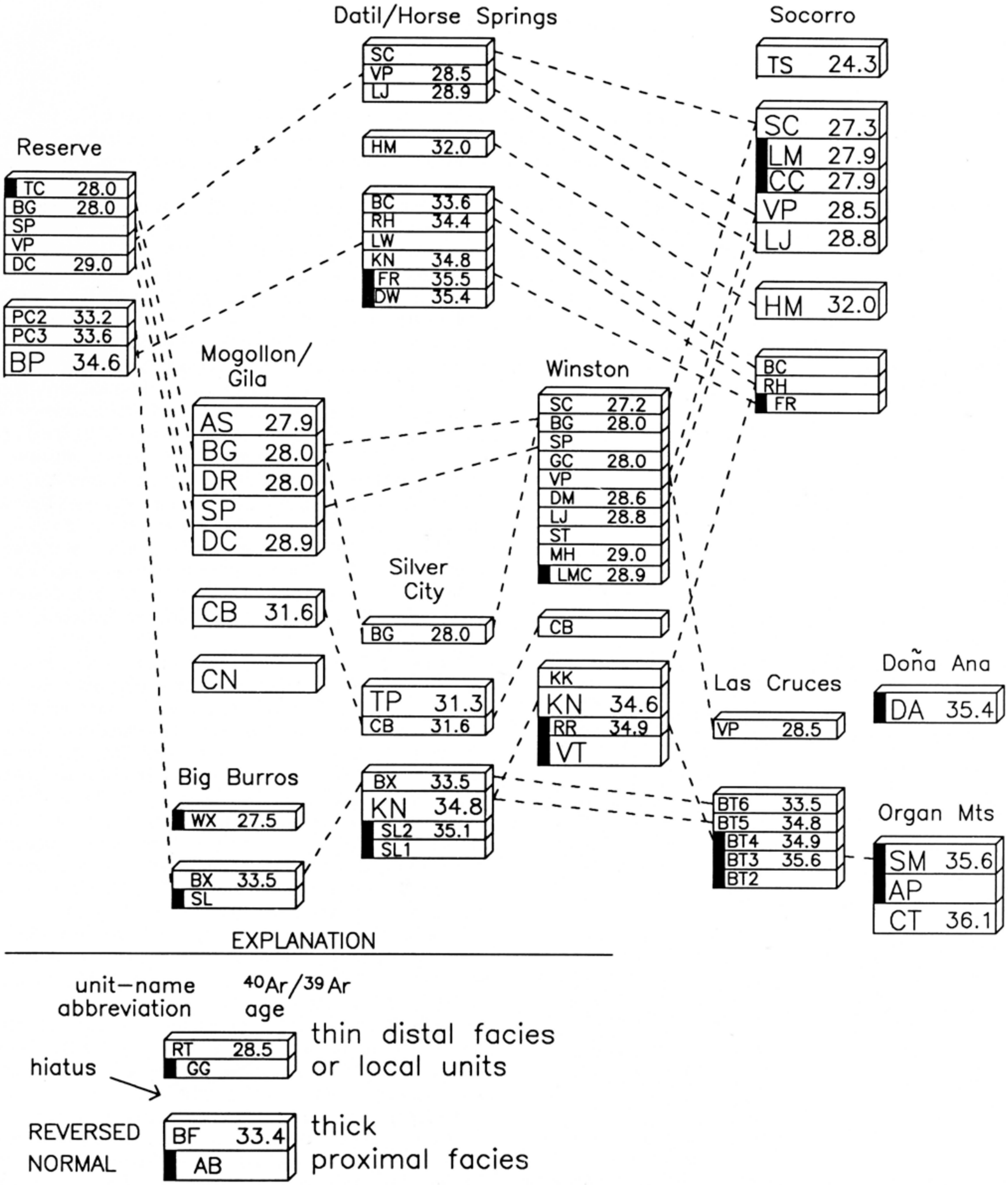

FIGURE 2—Stratigraphic framework for the Mogollon–Datil ignimbrites. Generalized stratigraphic columns are placed in their approximate geographic positions and dashed lines show proposed correlations. The $^{40}Ar/^{39}Ar$ ages refer to local data; some of these ages differ slightly from the regional means presented in Fig. 1. Most of the unit-name abbreviations are given in Fig. 1. Additional abbreviations are: SP = Shelly Peak, ST = Stiver Canyon, CN = Cooney, LW = Lebya Well, RH = Rockhouse Canyon, KK = Koko Well, PC2 = Pueblo Creek 2, PC3 = Pueblo Creek 3, BT6 = Bell Top 6, BT5 = Bell Top 5, BT2 = Bell Top 2, RR = Rocque Ramos, SL = Sugarlump, SL1 = Sugarlump 1, VT = Victoria Tank, AP = Achenback Park.

Day 2: Field guide to upper Eocene and lower Oligocene volcaniclastic rocks of the northern Mogollon–Datil volcanic field

Steven M. Cather and Charles E. Chapin

Summary

Lipman et al. (1972) and Christiansen and Lipman (1972) broadly divide Tertiary volcanism in western North America into an early intermediate-composition phase and a later, fundamentally basaltic or bimodal phase. In the northern Mogollon–Datil field, the transition between these volcanic phases occurred about 36 Ma during deposition of the Datil Group (Fig. 1). We employ the informal terms *lower Datil Group* and *upper Datil Group* to denote the lower, intermediate-composition part and upper, dominantly bimodal part of the Datil Group, respectively. The contact between the lower and upper Datil Group is defined as a first up-section occurrence of more than 50% basaltic andesite detritus in volcaniclastic-dominated parts of the outcrop belt, and by initial occurrence of mafic lavas in near-vent areas.

Today's field trip will focus on Datil Group exposures in the Gallinas, Datil, and Sawtooth Mountains (Fig. 2). The following is a brief synopsis of the Datil Group based on a regional study of the unit by Cather (1986).

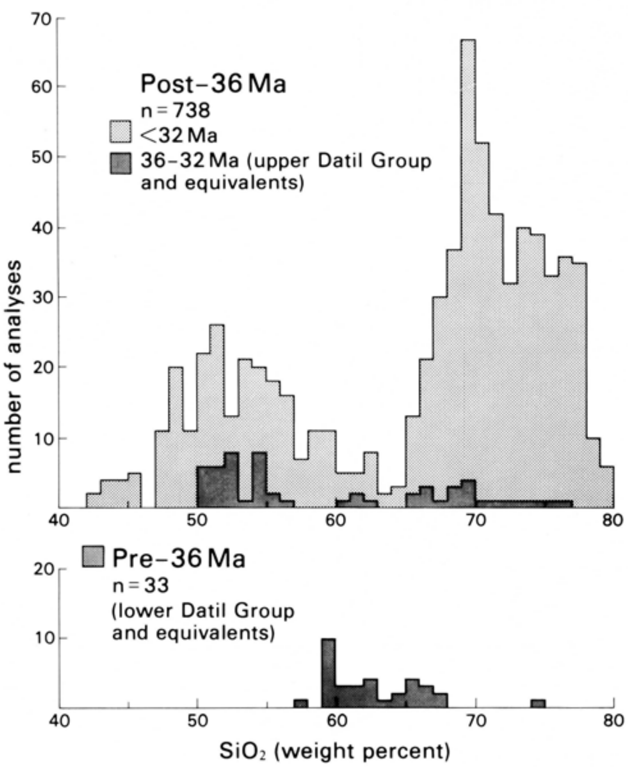

FIGURE 1—Histogram compilation of SiO_2 contents of volcanic rocks from all available analyses in the northern Mogollon–Datil field (north of 33°30′). Analyses are divided into pre- and post-36 Ma groups, on the basis of inferred timing of the post-Laramide tectonic transition in west-central New Mexico (Cather, 1986). Note the predominance of intermediate-composition rocks in the older suite of analyses (pre-36 Ma rocks are volumetrically under-represented; see Fig. 4) and the bimodal character of the post-Laramide rocks. Data sources are Atwood (1982), Bornhorst (1976, 1980), Baldridge et al. (this volume), Broulliard (1984), Cather (1986), D'Andrea (1981), Deal (1973), Fodor (1975, 1976), Jones (1980), Jicha (1954), Kedzie (1984), Lindley (1979), Lopez (1975), New Mexico Bureau of Mines & Mineral Resources (unpubl. data), Ratté (1980, 1986), Ratté et al. (1969), Ratté and Grotbo (1979), Rhodes and Smith (1976), Smith (1976), Spradlin (1976), Stinnett (1980), and Tonking (1957).

The Datil Group (sensu Osburn and Chapin, 1983) comprises a sequence of volcaniclastic conglomerate, sandstone, and mudstone with interbedded ash-flow tuffs and lavas that crops out along a broad, west-trending swath of exposures in west-central New Mexico. The Datil Group is the oldest volcanic unit (40–32 Ma; Fig. 3) in the northern Mogollon–Datil field and ranges from about 300 m to more than 1 km in thickness.

Exposures of the lower Datil Group are dominated by a compositionally monotonous series of intermediate-composition volcaniclastic rocks and minor lavas that are characterized by phenocrystic plagioclase (An_{20}–An_{60}), amphibole, and titanomagnetite (±biotite, clinopyroxene) and groundmass alkali feldspar, silica, and plagioclase. Silica content ranges from about 58 to 64 wt%; K_2O averages about 2.9 wt%. According to the classification method of Ewart (1979, 1982), these rocks are dominantly high-K andesite and high-K dacite. Herein, we refer to these rocks simply as andesite. Minor amounts (less than about 5%) of rhyolite are also present as conglomerate clasts in the lower Datil Group; mafic lithologies are virtually absent.

The lower Datil Group ranges from about 200 m to 700 m in thickness in the study area. Although relatively few chemical analyses are available for these rocks (Fig. 1), the volumetric abundance of andesite represented by the lower Datil Group and equivalent units in the northern Mogollon–Datil volcanic field is large. Estimated volume for these rocks, based on stratigraphic abundances extrapolated from the northeastern part of the field, is about 11,500 km^3, or about 47% of the total volume of eruptive products in the northern Mogollon–Datil field (Fig. 4).

Throughout most of the northern Mogollon–Datil field, the lower Datil Group transitionally overlies late Laramide, synorogenic deposits of the Eocene Baca Formation (Cather and Johnson, 1984, 1986). Where deposited on Laramide uplifts, the Datil Group typically overlies strata of Pennsylvanian or Permian age with angular disconformity. Such disconformable contact relations are exposed at Horse Mountain, in the Black Range, and in the Lemitar, Chupadera, southern San Mateo, and Magdalena Mountains (Fig. 2).

In nearly all exposures that were examined, non-volcanic detritus identical to that of the Baca Formation is present through most or all of the lower Datil Group (Fig. 5). This detritus consists dominantly of fragments of upper Paleozoic limestone, sandstone, and siltstone with subordinate amounts of Precambrian lithologies, and is important because it documents the persistence of late Laramide positive areas following the onset of intermediate-composition volcanism in west-central New Mexico. Abundance of non-volcanic detritus in the lower Datil ranges from individual beds of nearly pure Paleozoic and Precambrian detritus to trace amounts

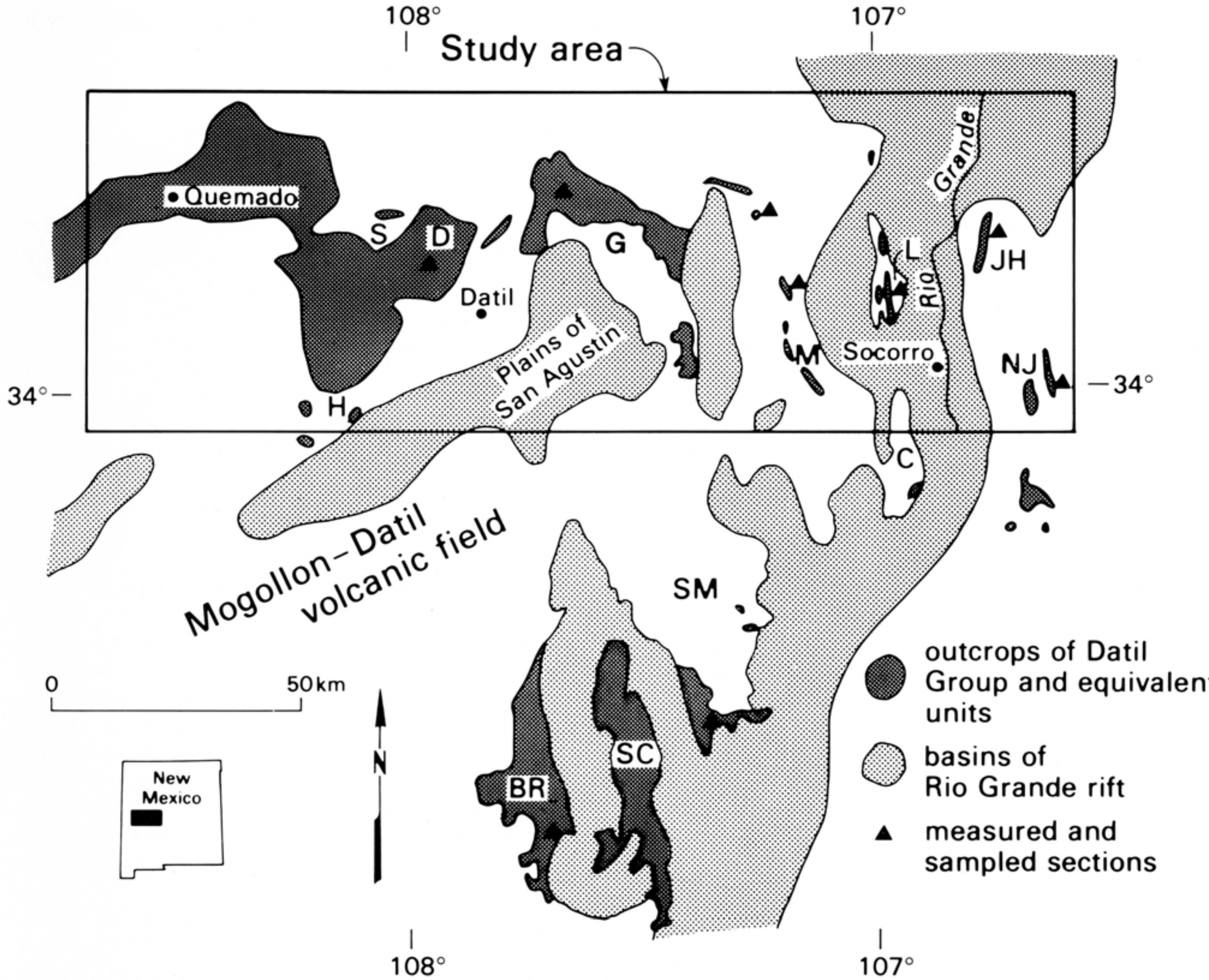

FIGURE 2—Map of west-central New Mexico depicting study area, outcrops of Datil Group, basins of Rio Grande rift, and location of measured and sampled sections (Cather, 1986). Selected geomorphic features: JH, Joyita Hills; NJ, northern Jornada del Muerto; L, Lemitar Mountains; C, Chupadera Mountains; M, Magdalena Mountains; G, Gallinas Mountains; D, Datil Mountains; S, Sawtooth Mountains; H, Horse Mountain; SM, San Mateo Mountains; SC, Sierra Cuchillo; BR, Black Range. Base map from New Mexico Geological Society (1982).

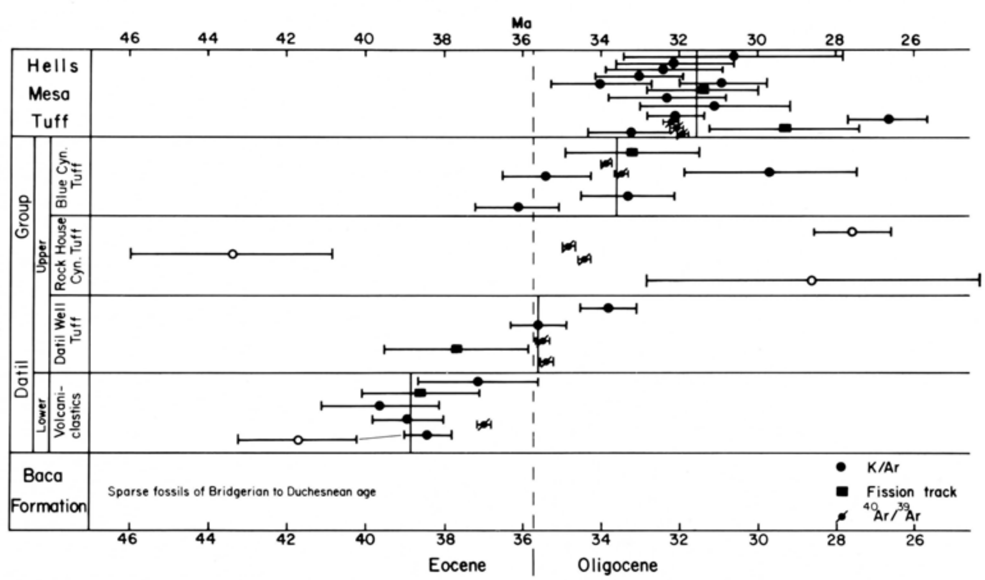

FIGURE 3—Summary of radiometric ages for Datil Group and overlying Hells Mesa Tuff, and vertebrate-fossil data for Baca Formation. Brackets indicate one standard deviation about the mean; vertical lines indicate averages for individual units, dashed vertical line is approximate Eocene–Oligocene boundary according to Montanari et al. (1985). Fine line connects analyses from same sample; open symbols represent geologically improbable dates. Modified from Cather et al. (1987) and McIntosh (this volume).

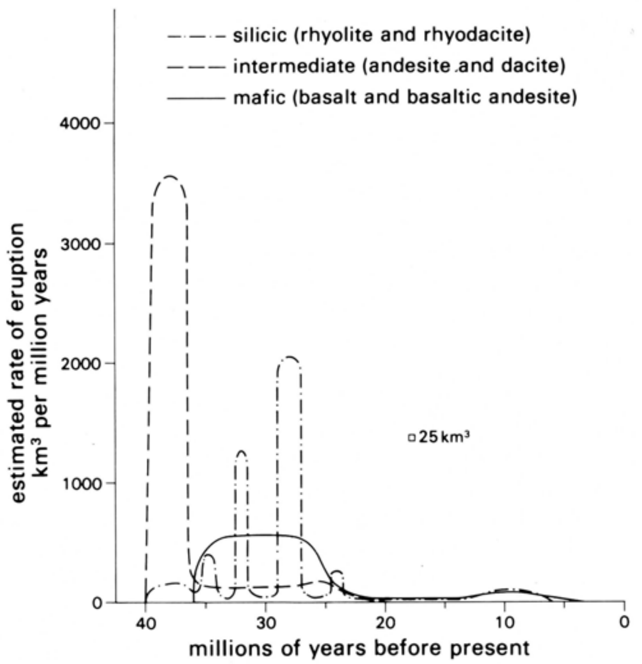

FIGURE 4—Graph of estimated volumetric abundances of mafic, intermediate, and silicic volcanic rocks in northern Mogollon–Datil field (north of 33°30′), based on extrapolated stratigraphic abundances in northeastern part of field from Osburn and Chapin (1983) and Cather (1986). The following calculations and assumptions were utilized: (1) *area* of northern Mogollon-Datil field = *19,101 km²;* (2) *average total thickness* of Tertiary volcanic and volcaniclastic rocks = *1295 m;* (3) *average thickness* of pre-36 Ma volcanic and volcaniclastic rocks = *602 m* (46.5% of total thickness), post-36 Ma tuffs = *317 m* (24.5%), post-36 Ma mafic and intermediate rocks = *375 m* (29%); (4) *total volume* of Tertiary volcanic and volcaniclastic rocks in northern Mogollon–Datil field = *24,736 km³;* (5) *volume* of pre-36 Ma rocks = *11,502 km³*, of which ~95% are andesite and dacite and ~5% are rhyodacite and rhyolite (Cather, 1986); this ratio is depicted in graph; (6) *volume* of post-36 Ma rocks = *13,234 km³*, of which *6060 km³* are silicic and *7173 km³* are mafic (<57 wt% SiO_2) and intermediate (based on Fig. 1, the ratio of mafic to intermediate post-36 Ma rocks is about 4:1; this ratio is depicted in graph); (7) onset of Tertiary volcanism at 40 Ma and beginning of mafic volcanism at 36 Ma from Cather (1986) and Cather et al. (1987); (8) slight peak in abundance of intermediate rocks at ~25 Ma corresponds to Bearwallow Mountain Formation; (9) peaks in silicic volcanism correspond to pulses in ash-flow-tuff volcanism as documented by McIntosh et al. (1986) and McIntosh (this volume); (10) slight peak in abundance of mafic and silicic rocks at ~10 Ma represents late Miocene volcanism (cf. Chapin and Seager, 1975; Bobrow et al., 1983).

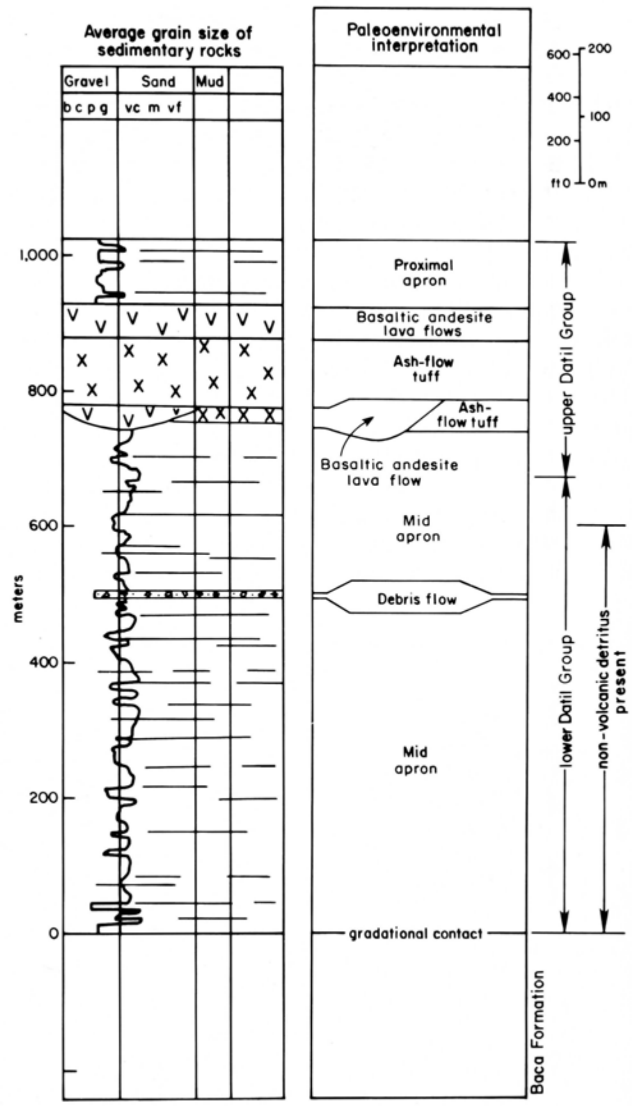

FIGURE 5—Representative stratigraphic section of Datil Group showing informal units and distribution of lithologies. Section measured in northern Jornada del Muerto by S. M. Cather.

of such lithologies as scattered clasts in volcaniclastic conglomerates.

The upper Datil Group consists of a fundamentally bimodal suite of mafic lavas, silicic ash-flow tuffs, and volcaniclastic rocks derived from these lithologies. Subordinate amounts of intermediate-composition lithologies are also present, as they are in the superjacent, bimodal to basaltic sequences that dominate post-Eocene volcanism in the northern Mogollon–Datil volcanic field (Fig. 1). However, intermediate-composition volcanic products are not abundant, and are a relatively minor constituent in the estimated regional abundance of upper Datil and younger lithologies (Fig. 4). Unlike lower Datil, the upper Datil does not contain non-volcanic detritus.

Mafic volcanic rocks, herein termed basaltic andesites, are the most abundant lithology in the upper Datil Group [they are dominantly high-K basaltic andesites and shoshonites according to Ewart's (1979, 1982) classification]. Basaltic andesites range in silica content from about 50 to 56 wt% and are characterized by phenocrysts of plagioclase (An_{30}–An_{65}), clinopyroxene, and titanomagnetite (±olivine, amphibole) and groundmass plagioclase and alkali feldspar. Basaltic andesite lavas are widespread in the upper Datil; composite thickness for such lava flows locally exceeds 150 m (Laroche, 1981).

Five ash-flow tuffs of regional extent dominate the silicic mode of upper Datil volcanism. Using the terminology of Osburn and Chapin (1983) and Ratté and McIntosh (in press), these are the Datil Well Tuff, tuff of Farr Ranch, Rock House Canyon Tuff, Blue Canyon Tuff, and tuff of Granite Mountain. Silicic detritus derived from domes or lavas is also a locally important component of upper Datil volcaniclastic rocks. Herein, we use the term rhyolite to denote the silicic mode of late Datil volcanism, although rhyodacites are also present. The upper contact of the Datil Group is marked by the base of the Hells Mesa Tuff ($^{40}Ar/^{39}Ar$ age 32.0±0.15 Ma; Kedzie et al., 1985; McIntosh, this volume), a thick, regionally extensive ash-flow tuff in the northern Mogollon–Datil volcanic field.

Sedimentary rocks of the lower Datil Group are mineralogically similar to their volcanic progenitors, with the following major exceptions: (1) nonwelded tuffs are not represented in conglomerates; (2) phenocryst phases are preferentially concentrated in sandstones; (3) groundmass constituents and devitrification products are over-represented in mudstones, claystones, and detrital matrix in sandstones. Upper Datil sedimentary rocks are mineralogically highly variable due to the increased diversity of source lithologies during late Datil time.

Cements in Datil Group sedimentary rocks include clays, silica (quartz and opal-CT), heulandite-group zeolites, and calcite. Propylitic alteration (epidote–chlorite–sericite–calcite) is locally well developed near igneous intrusions. The diverse coloration of Datil deposits (gray, buff, red, green, purple) results dominantly from the effects of diagenesis and alteration on iron chemistry and mineralogy.

Paleocurrents and distribution of sedimentary facies indicate that the physiographic framework established during late Laramide time persisted throughout deposition of the Datil Group. Datil sediments accumulated in two foreland basins (Figs. 6, 7) of Laramide ancestry (the Baca and Carthage–La Joya Basins); eruptive centers were located on, or near, Laramide positive areas. A coalesced series of laterally extensive, low-gradient alluvial fans dominated Datil sedimentation in the study area. A large, closed lake existed near the eastern end of the Baca Basin and represented the culmination of lacustrine conditions that began prior to the onset of volcanism. Major volcaniclastic debris flows were emplaced during early Datil time in an actively subsiding portion of the Baca Basin, between the Puertecito and Hickman fault zones (Fig. 6). Datil Group debris flows commonly transported large blocks of Paleozoic limestone and were associated with profound soft-sediment deformation near the basin center. These debris-flow deposits will be the main topic of today's field trip.

The transition from waning Laramide crustal shortening to incipient mid-Tertiary extension occurred at about 36 Ma in west-central New Mexico, as shown by sedimentologic and structural relations in the Datil Group. This tectonic transition was approximately synchronous with the switch

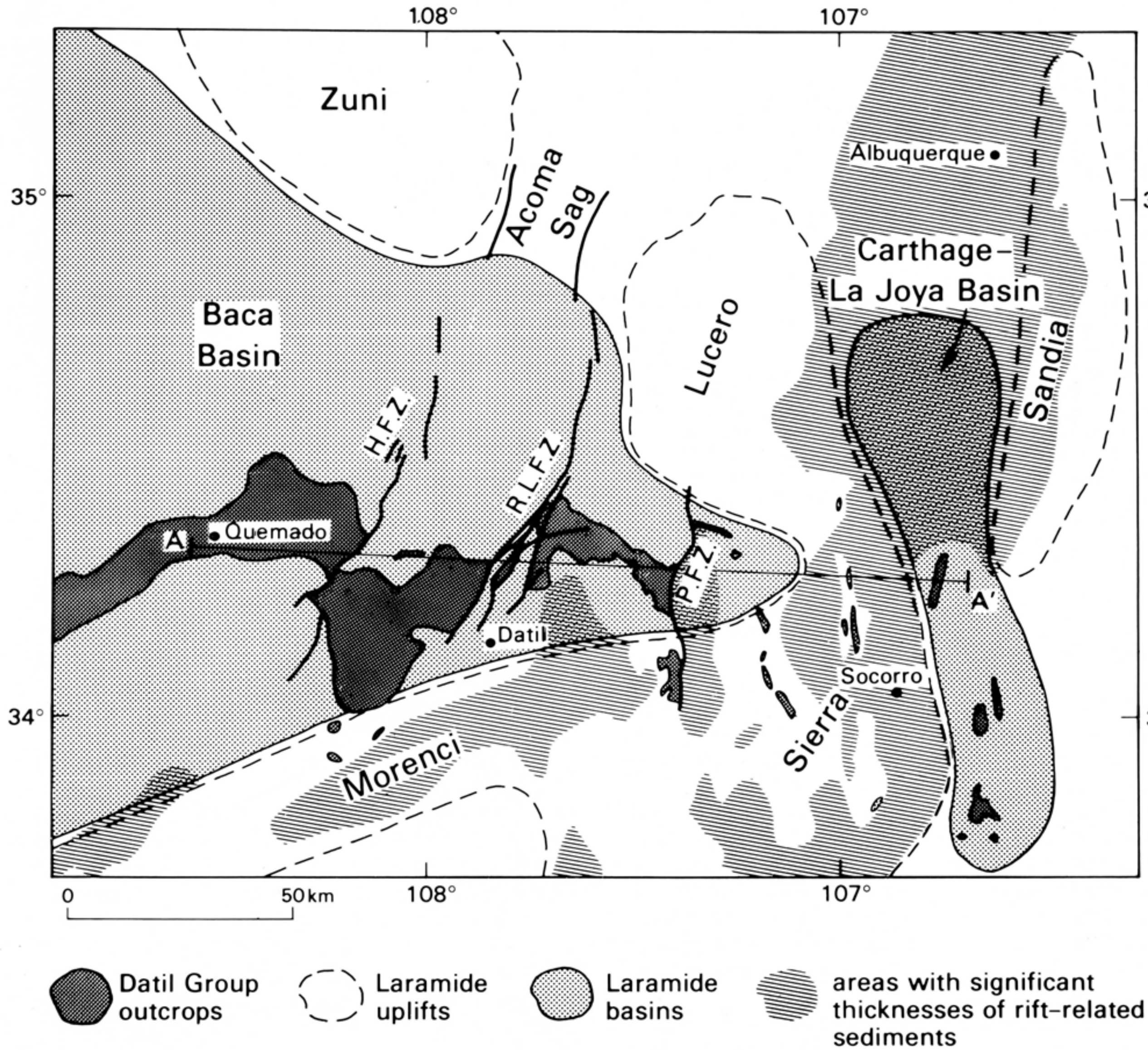

FIGURE 6—Late Laramide (Eocene) paleogeographic map showing basins, uplifts, intrabasin fault zones, and modern outcrops of Datil Group. Lined pattern indicates distribution of younger rift basins, which have formed largely by collapse of Laramide uplifts. P.F.Z., Puertecito fault zone; R.L.F.Z., Red Lake fault zone; H.F.Z., Hickman fault zone. A–A' is line of section in Fig. 13. Base maps from Cather and Johnson (1984, 1986) and New Mexico Geological Society (1982).

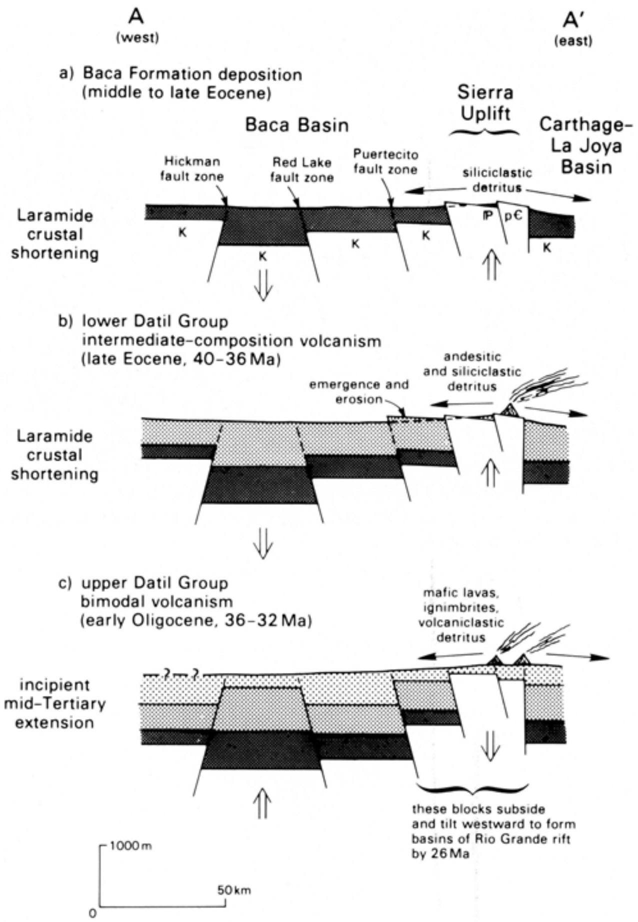

FIGURE 7—Schematic cross sections depicting middle Eocene to early Oligocene uplift and subsidence patterns, sedimentation, and volcanism in west-central New Mexico. Note continuation of Laramide-style tectonism **(a)** during early Datil andesitic volcanism **(b).** Laramide reverse faults begin to be reactivated as normal faults and the Sierra uplift began to subside about 36 Ma **(c),** coincident with the onset of late Datil Group bimodal volcanism. Baca Formation subcrop indicated by symbols in upper cross section. Stratigraphic-thickness data from Cather and Johnson (1984, 1986) and Cather (1986).

from andesitic to bimodal volcanism, represented by the lower Datil–upper Datil contact. Stress regimes may have provided a common link between changes in tectonism and volcanism during Datil time, and lithospheric stress appears to have exerted important controls on modes of magma ascent (Cather, 1986).

Road log

Mileage

0.0 Begin road log at New Mexico National Guard Armory, approximately 1 mi southwest of Socorro on US-60. **13.5**

13.5 Junction with Forest Road 235 to Water Canyon and Langmuir Laboratory on left. La Jencia Basin on right. **9.4**

22.9 Magdalena Peak rhyolite dome (~13.5 Ma; Bobrow et al., 1983) at 10:00. **1.0**

23.9 Entering Magdalena, New Mexico, elevation 2006 m. **1.1**

25.0 Turn right on NM-52 (Alamo Road) at west end of Magdalena. **5.1**

30.1 Cross La Jencia Creek. **3.7**

33.8 Gallinas Mountains 9:00 to 11:00; Bear Mountains 1:00 to 3:00. **5.6**

39.4 Top of Corkscrew Canyon. **2.8**

42.2 Synorogenic Laramide red beds of Baca Formation (Eocene) in roadcuts. **0.9**

43.1 Mt. Taylor on skyline at 12:00. **0.3**

43.4 Entering Alamo Band Navajo Reservation. **5.9**

48.9 Turn left (west) onto dirt road. **0.4**

49.3 **STOP 1. View of northeast-facing escarpment of Gallinas Mountains.** This stop affords a good overview of the middle Eocene to lower Oligocene stratigraphy of west-central New Mexico (Fig. 8). High peaks on skyline to south are lower Oligocene ash-flow tuffs, lavas, and volcaniclastic strata that dip gently (average 5–10°) to south-southwest. At base of escarpment are fluvio-lacustrine red beds of Baca Formation (middle to upper Eocene), which also dip gently to south-southwest. Stratigraphically between these units is a chaotic interval dominated by breccias (here interpreted as large-volume volcaniclastic debris-flow and related deposits, although pyroclastic-flow and debris-avalanche deposits may also be present) of the lower Datil Group (upper Eocene). This interval was termed the Dog Springs Member of the Spears Formation by Osburn and Chapin (1983); it commonly weathers to form irregular knobs and pinnacles (Fig. 9).

Soft-sediment deformation (Figs. 10, 11, 12) related to debris-flow deposition has produced bedding orientations that differ drastically from the gentle tectonic tilts of the region (Fig. 13). At least two distinct mechanisms are responsible for the pronounced soft-sediment deformation in the lower Datil Group: (1) basinward slumping and detachment faulting of kilometer-scale masses of sediment, presumably in response to rapid loading and overpressurization of unconsolidated deposits during rapid debris-flow sedimentation, and (2) basal shear by overriding debris flows.

Volcaniclastic sediments of the Datil Group were deposited in two basins of Laramide ancestry, the Baca and Carthage–La Joya Basins (Fig. 6; Chapin and Cather, 1981, 1983; Cather and Johnson, 1984,

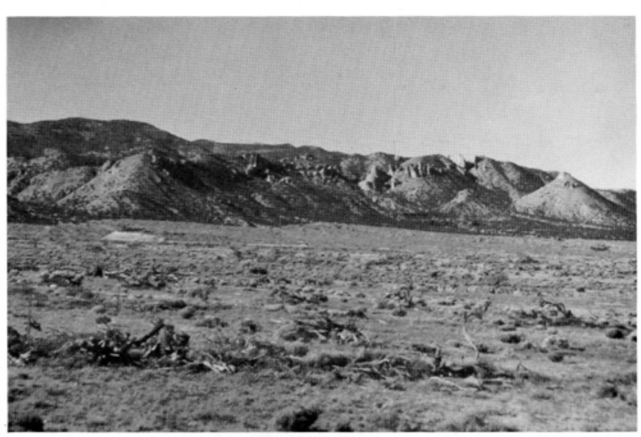

FIGURE 8—View of northeast-facing escarpment of Gallinas Mountains. Knobs and pinnacles are chaotic debris-flow deposits in Dog Springs Member of Spears Formation, lower Datil Group. Strata above and below this interval dip gently and uniformly to south-southwest.

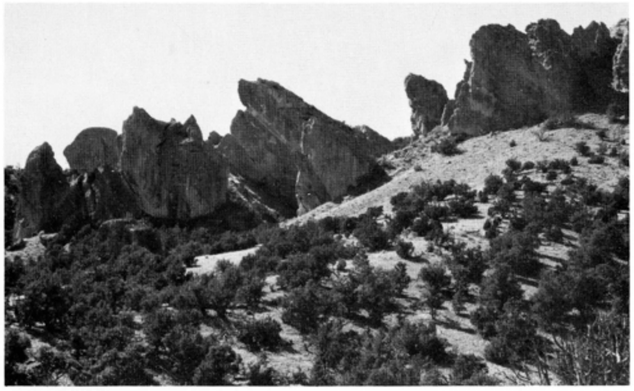

FIGURE 9—Pinnacles formed by erosion of massive debris-flow deposits in the Dog Springs Member of the Spears Formation (lower Datil Group). Location 1.7 mi south of Pinto Tank, Indian Mesa quadrangle (T1N, R7W, unsurveyed).

FIGURE 12—Steeply upturned volcaniclastic sediments beneath large gravity-slide mass 1.2 mi southwest of Bugger Well (T2N, R8W, unsurveyed, Table Mountain quadrangle).

FIGURE 10—Thrust fault in gravity-slide mass of volcaniclastic rocks near Cottonwood Well, 1.7 mi southwest of Burns–Lindsey Headquarters (SE1/4 sec. 33, T2N, R7W, Indian Mesa quadrangle). Spectacular folds with amplitudes to 60 m are present beneath the thrust. Sediments along the thrust deformed plastically (Fig. 11).

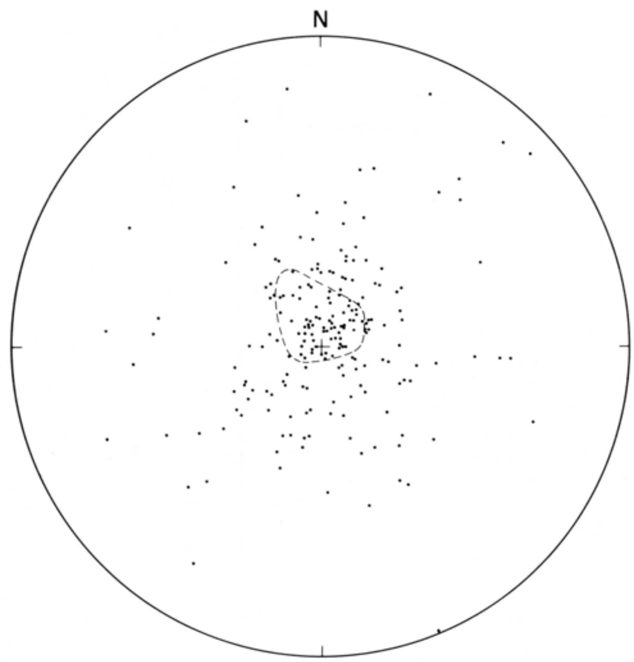

FIGURE 13—Lower-hemisphere stereographic projection of poles to bedding in Dog Springs Member. Dashed line encloses field for poles to bedding (not depicted) of underlying and overlying strata; the regional dip of these strata is approximately 8° to the south-southwest. The shotgun pattern of poles to bedding of Dog Springs strata reflects pervasive down-to-the-basin slumping and soft-sediment deformation. Bedding orientation data from Harrison (1980), Coffin (1981), Robinson (1981), and Brouillard (1984).

FIGURE 11—Plastically deformed volcaniclastic sediments along the thrust shown in Fig. 10.

1986). Debris-flow and associated deposits are widespread in the lower Datil Group, but occurrence of thick, laterally extensive sequences of such deposits is restricted to the area between the Hickman and Puertecito fault zones (Fig. 6). These fault zones represent systems of late Laramide reverse faults that bounded an area of Laramide intrabasin subsidence within the eastern Baca Basin. Beginning about 36 Ma, reverse faults within these zones began to be reactivated as normal faults in a regime of weak extensional strain and Laramide uplifts began to subside (Fig. 7). At about the same time, andesitic volcanism was supplanted by bimodal volcanism in the northern Mogollon–Datil volcanic field (Cather, 1986).

We are presently near the eastern limit of major debris-flow deposits in the lower Datil Group. In the remaining three stops today, we will examine debris-flow deposits and associated soft-sediment deformation to the west. **1.0**

50.3 Entering Burns–Lindsay Ranch, leaving Alamo Band Navajo Reservation. **2.6**

52.9 Junction with road to Burns–Lindsey Headquarters on left. Keep right. (Note to subsequent field trips: stop at the Burns–Lindsey Headquarters for permission to make Stop 2.) **4.2**

57.1 Junction with road to Table Mountain on right. Keep left. **3.3**

60.4 Junction with road to Dog Springs Canyon. Keep left. Drive past old Martin Ranch Headquarters on right and continue straight ahead through corrals (close gates). **0.5**

60.9 Cross dry bed of Dog Springs Canyon. **0.2**

61.1 **STOP 2. Marginal lacustrine deposits, debris-flow deposits, and exotic blocks in Dog Springs Member of Spears Formation of Datil Group (upper Eocene).** Walk to knoll at 9:00, about 50 m to southeast. Knoll is composed of prevolcanic (middle to upper Eocene) sandstone and mudstone of Baca Formation. Composition of scattered pebbles and sandstone petrology indicate dominance of Paleozoic and Precambrian lithologies in Laramide source regions (Cather, 1980).

Walk south-southwest (upsection) from knoll, across saddle and up hill. Color change from red to gray in lacustrine mudstone about half-way up hill marks base of volcaniclastic Spears Formation of Datil Group. Note locally abundant horizontal burrows along bedding splits at top of hill. Similar fluvio-lacustrine sandstone and mudstone units underlie debris-flow sequences throughout the northern Gallinas Mountains.

Proceed south-southwest along spur to next peak. Note increasing soft-sediment deformation of fluvio-deltaic beds and first occurrence of debris-flow deposits as we move upsection toward debris-flow-dominated part of section. Top of peak marks approximate stratigraphic base of debris-flow-dominated part of Spears Formation. Total thickness of debris flows and related deposits in this area exceeds 600 m (Cather, 1986).

Ledge-like outcrops to south and southeast are beds in a very large (0.5 km long and 50 m thick), rootless block of Paleozoic limestone within the Dog Springs Member. Exotic blocks of limestone or volcanic breccia ranging in size from a few meters to nearly 1 km are common in the Gallinas Mountains (Harrison, 1980; Coffin, 1981; Brouillard, 1984; Cather, 1986). They are restricted in occurrence to the debris-flow-dominated part of the Spears Formation between the Puertecito and Red Lake fault zones (Fig. 6). Blocks of limestone were presumably derived from the Morenci uplift (Fig. 6), a Laramide uplift to the south that persisted throughout early Datil time (Cather, 1986; Cather and Johnson, 1984, 1986). Blocks appear to have been transported by large-volume debris flows, but the details of this process are in need of further study.

Return to vehicles and continue south. **0.3**

61.4 Car-sized blocks of Paleozoic limestone at 3:00. **0.2**

61.6 **STOP 3. Debris-flow deposits, soft-sediment deformation, and clastic dikes.** Examine outcrops on west side of canyon. Features to note include debris-flow fabrics, monotonous lithology of andesite–dacite clasts, soft-sediment deformation related to slumping, and clastic dikes produced by dewatering of debris flows and deformed sediments.

Several lines of evidence argue for a debris-flow origin for these deposits: (1) nearly complete lack of vitric components (pumice, shards; see for example, Tonking, 1957; Coffin, 1981; Cather, 1986); (2) common presence of rounded, stream-worn cobbles and boulders; (3) lack of juvenile clasts with chilled and cracked rinds; (4) the well-mixed nature of clast and matrix lithologies (G. A. Smith, oral comm. 1989); (5) limited paleomagnetic data involving progressive thermal demagnetization of clasts indicate that deposition occurred below maximum blocking temperatures of about 580°C (W. C. McIntosh, oral comm. 1987); (6) widespread development of clastic dikes suggests flows were mobilized by interstitial water, which argues against deposition by gas-mobilized or inertially mobilized media (pyroclastic flows, debris avalanches). Additionally, the unbrecciated nature of exotic blocks (some with high aspect ratio) is suggestive of transportation by non-turbulent flow.

Return to vehicles and retrace route past old Martin Ranch Headquarters to junction with dirt road. **1.2**

62.8 Junction with dirt road. Turn left. **0.1**

62.9 Continue straight through red gate. **0.4**

63.3 Continue straight through gate. **0.5**

63.8 Junction with road to Red Lake Ranch. Turn left up hill. **0.8**

64.6 Gate. Continue straight. **2.3**

66.9 Leaving Burns–Lindsay Ranch. **4.8**

71.7 Junction with road up Thompson Canyon on right (west). Continue straight. **0.1**

71.8 Junction with road on left. Continue straight. **5.3**

77.1 Cattleguard. Entering Plains of San Agustin. **3.4**

80.5 Cattleguard. North Lake Basin on left (east). Alfalfa is grown on dry lake bed using water from wells. **0.1**

80.6 Junction with road to North Lake. Turn right (west). **1.5**

82.1 Water tank at Antelope Well on right. **2.0**

84.1 Sharp turn to left (west) at West Chavez Well. **6.7**

90.8 Junction with US-60. Turn right (west) toward Datil. **2.6**

93.4 Catron County line. **2.9**

96.3 Concrete culvert. Twin Peaks at 11:00 consists of ash-flow tuffs in Oligocene South Crosby Peak Formation capped by La Jencia Tuff and basaltic andesite of Twin Peaks (Lopez and Bornhorst, 1979). Datil Mountains at 12:30 to 3:00. **4.4**

100.7 Junction with NM-12 in village of Datil. Continue straight. **0.9**

101.6 Road to Datil Well Campground on left. Type section of Datil Well Tuff (35.41 Ma; McIntosh, this volume) on right. **1.1**

102.7 Main Canyon and junction with Forest Road 100 on right. Volcaniclastic sediments of upper Spears Formation (lower Oligocene) in roadcut on left. **1.9**

104.6 Forest Road 66 on left. Numerous northeast-trending faults in this area (Lopez and Bornhorst, 1979) are part of Red Lake fault zone (Wengerd, 1959; Chamberlin, 1981; Cather and Johnson, 1984, 1986). Cliffs ahead are ash-flow tuffs in upper Datil Group. **0.6**

105.2 Roadcuts in volcaniclastic rocks of Spears Formation of upper Datil Group. **1.0**

106.2 Crossing westernmost strand of Red Lake fault zone, a major down-to-the-east structural zone in west-central New Mexico. This zone was down to the west during late Laramide (Eocene) time. **0.4**

106.6 Highway Department picnic table on right. Debris-flow deposits in Spears Formation of lower Datil Group form cliffs across valley. **0.6**

107.2 Milepost 71. Dike-like outcrop at 11:00 is erosional fin of debris-flow breccias in lower Datil Group. **2.5**

109.7 Junction with Forest Road 6 on right. Stop 4 can also be reached via a 23.7 mi loop which follows FR-6 up Davenport Canyon, across the Datil Mountains at Monument Saddle, and then westward along the edge of the Colorado Plateau physiographic province. Good views of the Upper Cretaceous Mesaverde Group, the Eocene Baca Formation and debris-flow and fluvial deposits in the lower Datil Group are available on this drive. **3.3**

113.0 Junction with Forest Road 6 on right. Turn right toward Sawtooth Mountains. **3.8**

116.8 Sawtooth Mountains sign. **0.3**

117.1 Turn right on faint woodcutters' road leading east toward Monument Rock. **0.1**

117.2 Junction of two tracks. Keep left. **0.6**

117.8 **STOP 4. Spectacular soft-sediment deformation in lower Datil Group.** Park vehicles in meadow on left. Two peaks to northeast are volcaniclastic deposits of lowermost Datil Group. Red-bed fluvial deposits of Baca Formation are visible near base of peak on left and also in lower part of pyramid-shaped peak to northwest. Peaks to northeast are capped by steeply dipping debris-flow deposits and fluvial sandstones that overlie a strongly deformed sequence of sandstones and conglomeratic sandstones of dominantly fluvial origin (Fig. 14). Note ptygmatic folds, thrust faults, and angular truncation of bedding beneath soft-sediment detachment fault (Fig. 15). In contrast to the extensional slumping seen previously at Stop 3, deformation in beds beneath the detachment fault is dominated by layer-parallel shortening. Granular reorganization and fluidization of sediments presumably occurred during detachment faulting. Fluidization of sediments may be responsible for the general lack of internal stratification within the deformed beds.

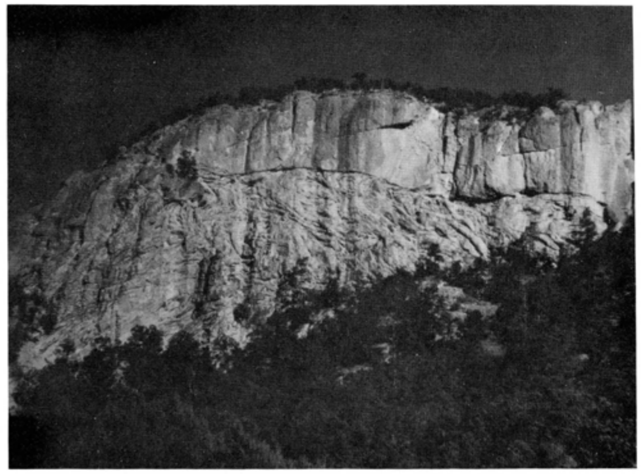

FIGURE 14—Deformed sediments beneath detachment fault in lower Datil Group at Stop 4. Vertical height of tilted beds above detachment fault is about 30 m.

Hike to notch in peak on right to view detachment fault and overlying tilted beds. Then proceed northwest along base of cliff to examine underlying deformed sediments.

To summarize, the following observations and interpretations pertain to the large-volume debris-flow deposits of the lower Datil Group:

1. Major debris-flow deposits are stratigraphically related to the early andesitic phase of volcanism (40–36 Ma) in the northern Mogollon-Datil field. They were geographically restricted to an actively subsiding area between the Puertecito and Hickman fault zones; present exposures are near the hydrographic center of the Baca Basin.

2. Large, exotic blocks of Paleozoic limestone are stratigraphically restricted to debris-flow-dominated parts of the section, but occur only in the area between the Puertecito and Red Lake fault zones.

3. There is a one-to-one relation between strongly deformed sediments and the presence of major debris-flows deposits in the Datil Group.

4. Anomalously thick debris-flow deposits and

FIGURE 15—Detailed view of deformed sediments and detachment fault at Stop 4. Note truncation of bedding by subhorizontal fault.

intense soft-sediment deformation in the Gallinas, Datil, and Sawtooth Mountains may result from deposition in basin-center environments, which caused ponding of debris flows and enabled fluidization of sediments due to presence of shallow ground water. In contrast, debris-flow deposits in more proximal environments are generally less than a few meters thick and are not associated with deformed sediments (Cather, 1986).

The lower Datil Group has been studied in detail only in a few areas (cf. Spradlin, 1976; Coffin, 1981; Harrison, 1980; Brouillard, 1984; Lopez, 1975; Cather, 1986). Much is not yet known about the volcano-sedimentary evolution of this fascinating unit, particularly with respect to the processes of transportation and deposition of the sequences we have examined today.

Return to vehicles and retrace route to US-60. **4.7**

122.5 Junction with US-60. Turn left (east) toward Datil. **3.3**

125.8 Junction with Davenport Canyon segment of Forest Road 6 on right. Continue straight. **9.0**

134.8 Junction of US-60 and NM-12 in Datil. Continue straight. **3.3**

138.1 Entering Plains of San Agustin. Datil Mountains at 7:00–10:00, Gallinas Mountains at 10:00–11:45, Tres Montosas at 11:45, Magdalena Mountains at 11:45–1:00, San Mateo Mountains at 1:30–2:30, Pelona Mountain at 2:30. **4.1**

142.2 Socorro County line. Headquarters of Very Large Array (VLA) radio telescope at 1:00. **5.5**

147.7 Highway Department rest stop and information about VLA on right. **2.3**

150.0 Junction with NM-52 on right. Turn right (south). **2.5**

152.5 Junction with NM-166. Turn right (west) toward VLA then into Visitor Parking area at VLA Visitor Center. **1.7**

154.2 **STOP 5 (optional). Very Large Array Radio Telescope, the world's largest radio-telescope array.** After stop retrace route to US-60. **4.1**

158.3 Junction with US-60. Turn right (east) toward Magdalena. **3.2**

161.5 Road to rock quarry on left. Upper Oligocene basaltic andesite flow quarried for railroad ballast used at VLA. Tres Montosas at 10:00, Grey Hill at 1:30. **4.3**

165.8 Junction with NM-78 on right. **2.7**

168.5 Roadcuts in highly sheared and hydrothermally altered volcaniclastic rocks of Spears Formation and light-colored 34.8 Ma Rock House Canyon Tuff (McIntosh, this volume). A small oxide copper deposit is present in the Rock House Canyon Tuff about 0.5 km south of the highway. **0.2**

168.7 Entering Mulligan Gulch graben, a north-trending shallow graben between the Gallinas and San Mateo Mountains on the west and the Bear and Magdalena Mountains on the east. **1.6**

170.3 Small knob on right is capped by 17 Ma Council Rock Basalt overlying poorly indurated gravels of the Mulligan Gulch graben. **3.9**

174.2 Leaving Mulligan Gulch graben. Roadcuts are in highly altered La Jencia Tuff (28.8 Ma; McIntosh, this volume). A monzonite stock is exposed in the arroyo about 0.4 km north of highway. **3.3**

177.5 Junction with NM-169 on left at west end of Magdalena. Continue straight and retrace route to Socorro. **29.8**

207.3 National Guard Armory on right at southwest edge of Socorro.

Acknowledgments

We benefitted from discussions and reviews by J. Boryta, R. M. Chamberlin, P. R. Kyle, W. C. McIntosh, and G. A. Smith. The figures were drafted by Becky Titus; the manuscript was typed by Lynne McNeil. We also acknowledge the many contributions made by graduate students whose theses are cited herein.

Days 3 and 4: Selected volcanic features of the western Mogollon–Datil volcanic field

James C. Ratté

with contributions on the mineralogy of the inclusions in the pumice breccia of Old Horse Springs by Peter J. Modreski

Day 3 a.m.: Socorro to Old Horse Springs via Datil

Introduction

The San Agustin Plains region, where we will spend the morning, is within the transition zone between the relatively undeformed Colorado Plateau to the west and north and the Rio Grande rift section of the Basin and Range province to the east (Fig. 1). The plains are the geomorphic expression of a middle to late Cenozoic graben that may have formed as a split of the Rio Grande rift (Chapin, 1971). The plains today are a closed drainage basin near the northern edge of the Mogollon–Datil volcanic field, and are the site of Pleistocene Lake San Agustin and two smaller lakes that occupied the basin until about 5000 years ago (Markgraf et al., 1983).

Major structural features of this largely volcanic region between the Colorado Plateau and the Rio Grande rift include the Mogollon–Datil volcanic field and its related caldera complexes (Fig. 2), the N30E Morenci–Reserve fault

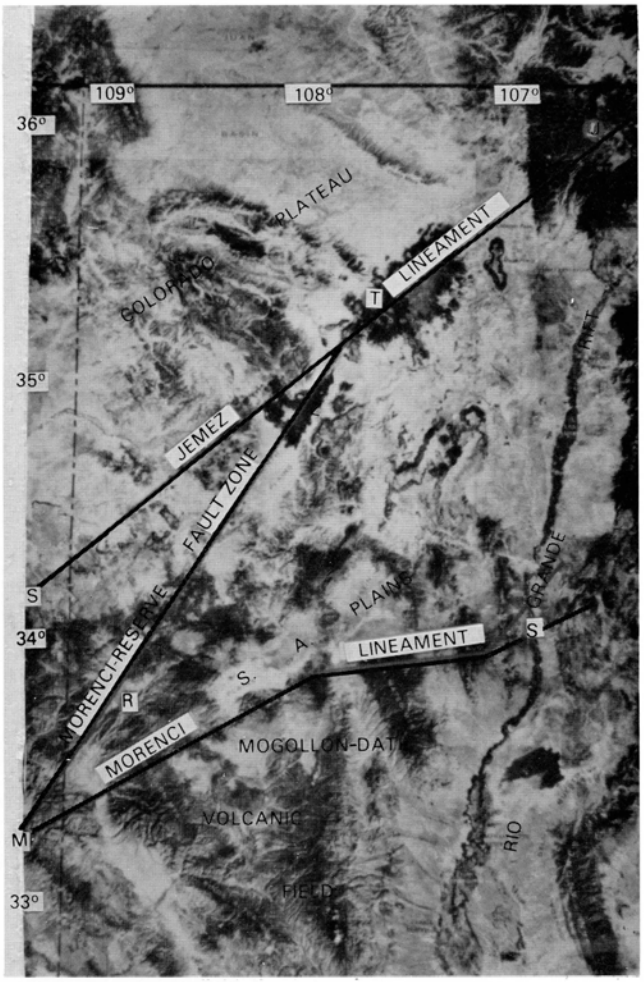

FIGURE 1—Northwestern part of photo map of New Mexico showing the San Agustin Plains (S.A. Plains), the Morenci–Reserve fault zone, the Jemez lineament, and the Morenci lineament. J = Jemez Mountains, M = Morenci, R = Reserve, S = Socorro (right) and Springerville (left), T = Mount Taylor, Z = Zuni–Bandera basalt field.

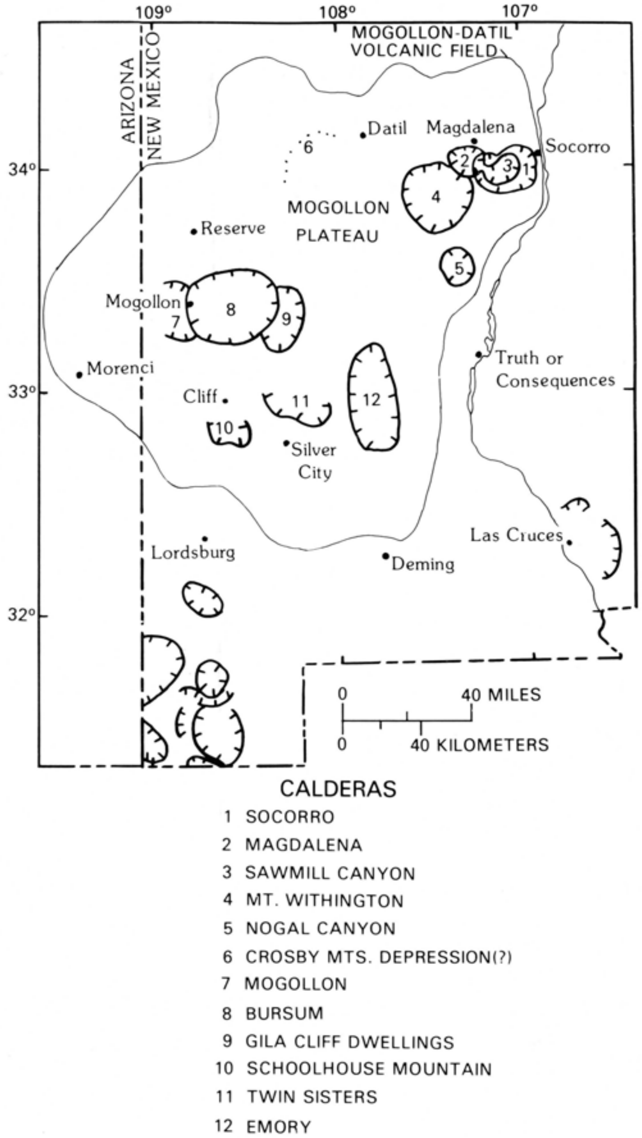

FIGURE 2—Sketch map of the Mogollon–Datil volcanic field showing the major caldera clusters of the Mogollon Plateau and outlying calderas of the Basin and Range part of the volcanic field.

zone (Fig. 1; Ratté, 1989), and the essentially parallel, N55E, Morenci and Jemez lineaments (Chapin et al., 1978; Aldrich et al., 1981). The San Agustin Plains segment of the Morenci lineament is expressed by the San Agustin graben, by high-angle normal faults that trend parallel to the axis of the plains, and by the alignment of several andesitic shield volcanoes (25–27 Ma) along the southeast side of the plains.

When we leave the San Agustin Plains area after Stop 3-1, on our way to Glenwood and Stop 3-2 at the Bursum caldera, we will move off the Morenci lineament and into the Reserve graben part of the N30E Morenci–Reserve fault zone. This fault zone traces from southwest of Morenci, Arizona, through the Reserve graben, and projects northeast through the Zuni–Bandera basalt field (Fig. 1) to an acute intersection with the Jemez lineament at Mount Taylor (4.4–0.001 Ma; Lipman and Mehnert, 1979). The Jemez lineament is defined by the N55E alignment of several late Cenozoic volcanic fields.

Road log

Leave Socorro at 7:30 a.m. Drive to Datil on US-60, where this road log begins.

Mileage

0.0 Junction of US-60 and NM-12 in Datil (Fig. 3). Turn left. **0.4**

0.4 Mileage marker 74. Crosby Mountains to west (right) are capped by andesite flows (~24 Ma) which overlie the volcaniclastic South Crosby Peak Formation (~32 Ma) (Lopez and Bornhorst, 1979), eruption of which has been proposed as the cause of subsidence of the Crosby Mountains depression (Elston, 1984). Roadcuts for next 6 mi are in Hells Mesa Tuff (32 Ma distal outflow from the Socorro caldera and generally less than 30 m thick in this area) and poorly welded pyroclastic flows of the overlying South Crosby Peak Formation. **8.7**

9.1 Approaching mileage marker 65. Low, rounded outcrops along highway on left are Cerrito Viejo quartz diorite intrusion (~21 Ma?). Horse Mountain at 1:00 is a composite dacite–rhyolite dome with flanking flows (~10 Ma). **2.3**

11.4 Mileage marker 63. Luera Peak (9:00), Pelona

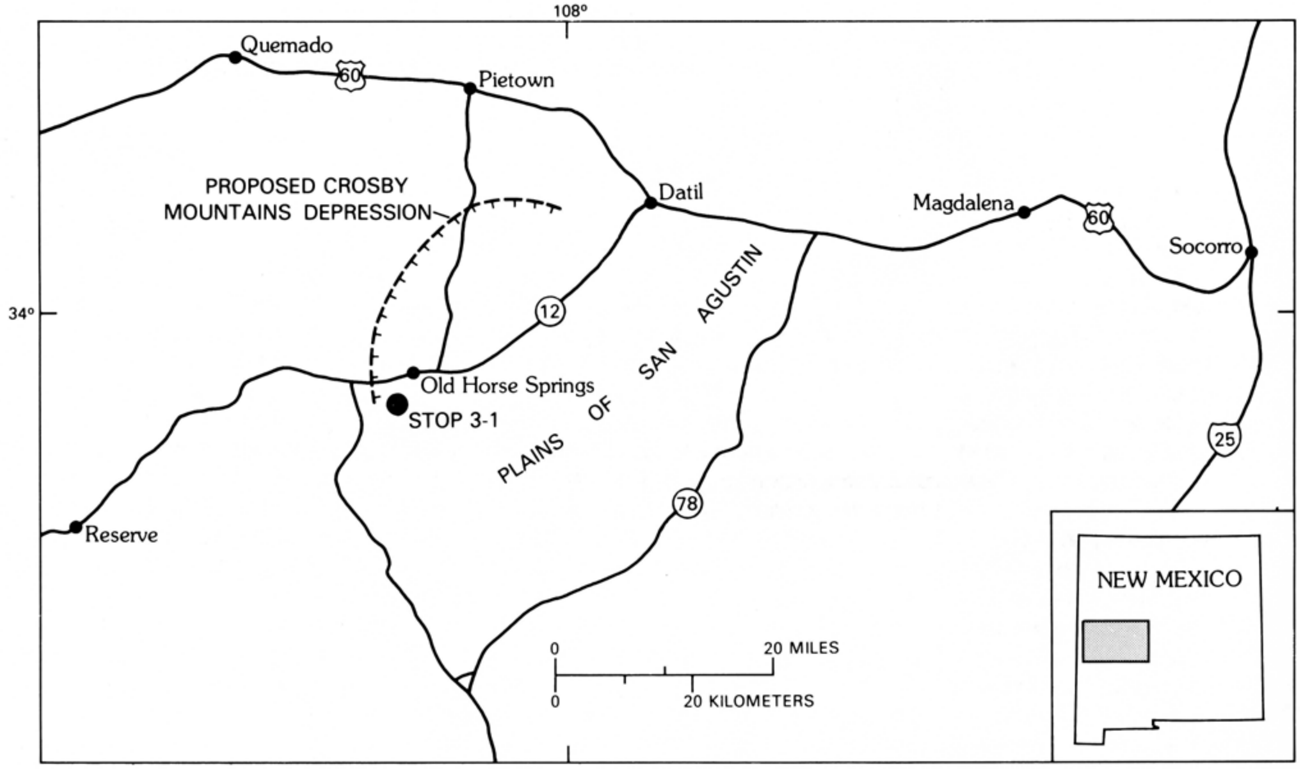

FIGURE 3—Index map, Socorro to Old Horse Springs, via US-60 and NM-12, showing location of Stop 3-1 near south end of Plains of San Agustin and the proposed Crosby Mountains depression.

Mountain (10:00), and O Bar O Mountain (11:00) are Bearwallow Mountain Andesite shield volcanoes along south side of San Agustin Plains. **9.8**

21.2 Approaching mileage marker 53. Highway crosses old shoreline onto Pleistocene Lake San Agustin alluvium. Low hogback ridge, about 1.6 km north of highway, is a fault block of Permian sedimentary rocks. **4.2**

25.4 Mileage marker 49. Approaching New Horse Springs. Pinkish-brown bluffs at 11:00 are pumice breccia of Old Horse Springs at Stop 3-1. **3.0**

28.4 Mileage marker 46. Having just passed through Old Horse Springs, turn left 0.25 mi ahead at ranch road with cattleguard and locked cable. Follow lead car to parking area at Stop 3-1 about 2 mi from locked cable. **2.0**

30.4 **STOP 3-1. Pumice breccia of Old Horse Springs.** The pumice breccia of Old Horse Springs is an early Oligocene (~33 Ma) pyroclastic deposit and related vent south of Highway 12 (NM-12) at Old Horse Springs. We will discuss the geologic setting of this deposit relative to possible cauldron collapse, but the main focus of Stop 3-1 is on the eruptive characteristics of the pyroclastic flows and the origin of mineralized jasperoid inclusions in this pumiceous dacite breccia.

Elston (1984, 1978) and Bornhorst (1976) proposed that the Crosby Mountains, west of NM-12 southwest of Datil, are within a large (~50 × 25 km), shallow, asymmetrical, trapdoor volcano-tectonic depression, which is hinged on its east side beneath the Plains of San Agustin (Fig. 3). They compared this volcano-tectonic depression to the Goodsite–Cedar Hills depression in the southern Rio Grande rift near Las Cruces; both structures are cited as examples of a specific cauldron type, characterized as forming early, at or near the periphery of a volcanic field, by multiple small ash-flow eruptions. Such cauldrons are described as typically asymmetric and having a partial ring fracture on one side of the subsided block, which is hinged on the other side to form the trap door (Elston, 1984, table 1, p. 8746). The pumice breccia vent at Old Horse Springs was presented as the main evidence of the proposed ring fracture of the Crosby Mountains depression. Subsidence of the depression was related either to eruption of the volcaniclastic rocks of the South Crosby Peak Formation (Elston, 1978, table 1) or, alternatively, to eruption of the pumice breccia of Old Horse Springs (Elston, 1984, table 1), both of which are stratigraphically above Hells Mesa Tuff (Table 1). The pumice breccia of Old Horse Springs was originally named tuff breccia of Horse Springs Canyon (Bornhorst, 1976: 50); it has been changed here because of the absence of Horse Springs Canyon on modern topographic maps of this area.

At this time there seems to be inadequate geologic evidence to support a Crosby Mountains depression as previously described. The pumice breccia of Old Horse Springs and the volcaniclastic rocks of the South Crosby Peak Formation probably are the products of small-volume, local, pyroclastic cones rather than regional ash-flow tuffs that might have caused the magnitude of subsidence proposed for the Crosby Mountains depression.

The pumice breccia of Old Horse Springs crops out only in close proximity to Old Horse Springs, where it occurs in a roughly north–south belt about 5 km wide and 20 km long (Fig. 4). The maximum

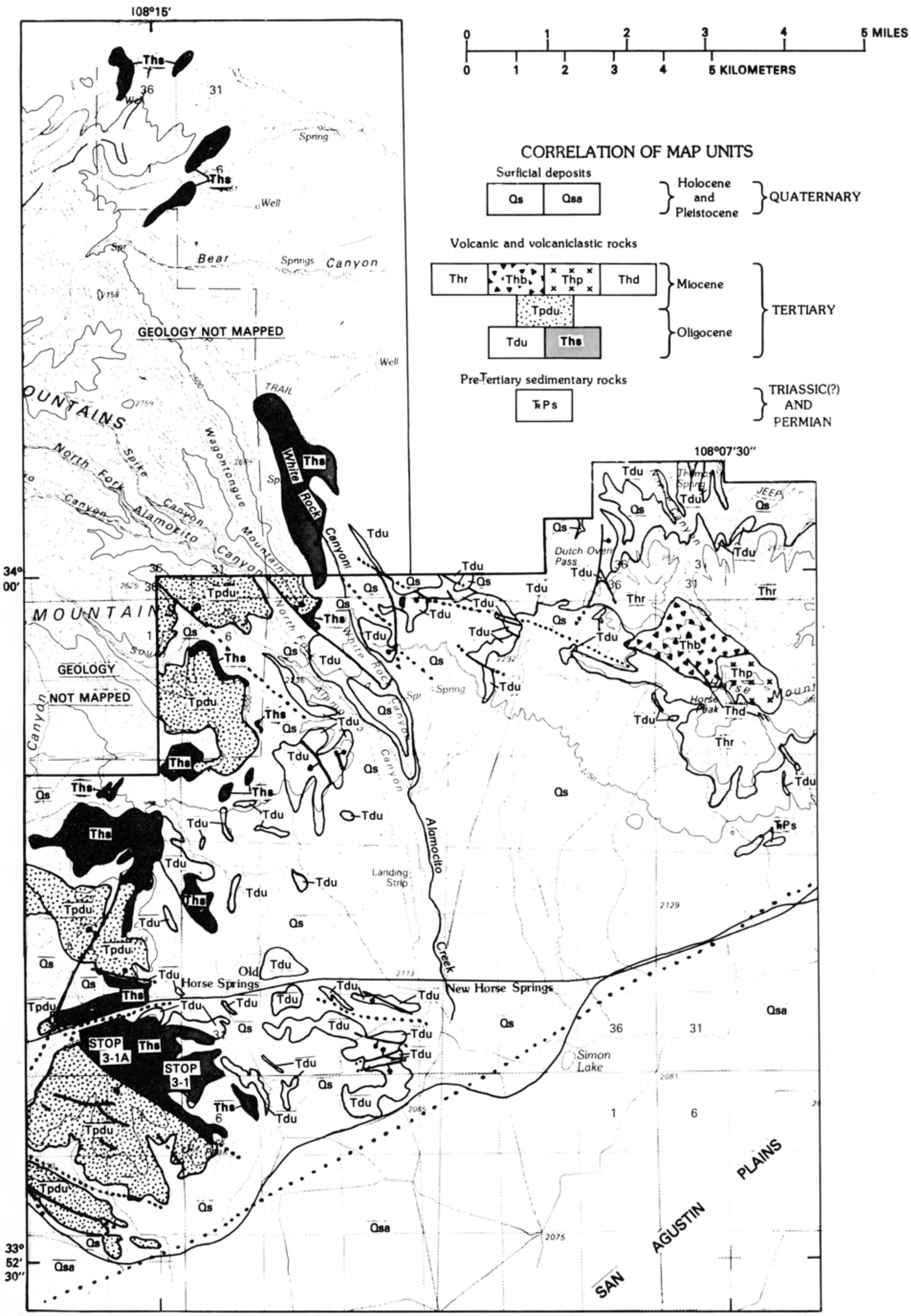

FIGURE 4—Geologic map showing known distribution of pumice breccia of Old Horse Springs. Modified from Ratté et al. (1988, plate 1). Qa = Surficial deposits, undivided (Holocene and Pleistocene); Qsa = fluviolacustrine deposits of Lake San Agustin (Holocene and Pleistocene); Thr = dacite and rhyolite lava flows of Horse Mountain volcano (Miocene) (about 13 Ma); Thb = dacite and rhyolite domal vent breccias of Horse Mountain volcano (Miocene); Thp = rhyolitic plug rock of Horse Mountain volcano (Miocene); Thd = rhyolitic dikes of Horse Mountain volcano (Miocene); Tpdu = post-Datil Group volcanic and volcaniclastic rocks, undivided (Miocene? and Oligocene); Tdu = volcanic and volcaniclastic rocks of Datil Group (Oligocene); Ths = pumice breccia of Old Horse Springs (Oligocene) (~33 Ma); ŦPs = Triassic(?) and Permian sedimentary rocks.

TABLE 1—Partial list of ash-flow-tuff sheets in the Mogollon–Datil volcanic field. Ages listed are $^{40}Ar/^{39}Ar$ ages from McIntosh (this volume). Italicized tuffs are included in the Datil Group (Osburn and Chapin, 1983). Units in parentheses are probable or possible correlatives of unit on same line. Datil Group tuffs are interlayered with volcaniclastic rocks and subordinate mafic to intermediate-composition lava flows, which are called Spears Formation east of the Continental Divide and Pueblo Creek Formation (Ratté, 1989) west of the Divide, and overlie the Eocene basin-fill Baca Formation. $^{40}Ar/^{39}Ar$ ages have analytical error of about ±0.15 m.y. Dash (—) indicates $^{40}Ar/^{39}Ar$ ages not available; *indicates age established by tight stratigraphic bracket of dated units.

Age (m.y.)	Ash-flow sheet	Caldera or source area
24.3	Tuff of Turkey Springs	(?)
27.3	South Canyon Tuff	Withington
27.9	Caronita Canyon Tuff	Sawmill–Magdalena
27.9	Lemitar Tuff	Northern San Mateo Mts.
28.0	Tuff of Triangle C Ranch	Bursum(?)
28.0	Bloodgood Canyon and Apache Spring Tuffs	Bursum
28.0*	Shelley Peak Tuff	Gila Cliff Dwellings(?)
28.5	Vicks Peak Tuff	Nogal Canyon
28.8	La Jencia Tuff	Sawmill–Magdalena
28.9	Davis Canyon Tuff	Gila Cliff Dwellings(?)
31.3	Tadpole Ridge Tuff	Twin Sisters(?).
31.6	Caballo Blanco Tuff (Fall Canyon Tuff)	Black Range(?)
32.0	Hells Mesa Tuff (Fall Canyon Tuff)	Socorro
33.6	*Blue Canyon Tuff*	(?)
34.6	*Rock House Canyon Tuff*	(?)
—	Cooney Tuff (Tuff of Bishop Peak and Tuff of Lebya Well)	Mogollon
34.8	Kneeling Nun Tuff	Emory
35.5	Tuff of Farr Ranch	(?)
35.4	*Datil Well Tuff*	(?)

observed thickness of the pumice breccia, about 250 m, is just southwest of Old Horse Springs, south of NM-12. The source vent is probably located in the area of maximum known thickness, as indicated also by the coarse size (2–3 m) of pumiceous dacite blocks in the upper one-third of the pyroclastic breccia, and the concentration of cognate quartz monzonite inclusions, also as blocks up to 2–3 m in diameter. The breccia thins northward and is less than 30 m thick where last observed (Jones, 1980, plate 1).

The pumice breccia of Old Horse Springs overlies 33.6 Ma Blue Canyon Tuff (Table 1), dated by the $^{40}Ar/^{39}Ar$ method (McIntosh et al., 1986). Biotite and plagioclase from the pumice breccia also have been dated by the conventional K–Ar method, yielding ages between 31.3 and 35.5 Ma (Marvin et al., 1987; Bornhorst et al., 1982). Zircon fission-track ages for the pumice breccia and cognate quartz monzonite inclusions are 32.4 and 32.7 Ma, respectively (Bornhorst et al., 1982). The dacite pumice breccia and its quartz monzonite inclusions thus are about 33 Ma.

On the east side of the main pumice breccia outcrops, southwest of Old Horse Springs (Fig. 5), the deposit consists of two or more thick pumice flows (labeled 1 and 2 in Fig. 5), which are composed of reversely graded pumice blocks as much as 30 cm in diameter (Fig. 6). The pumice flows are overlain by about 100 m of very coarse pyroclastic breccia. The upper breccia (labeled 5 in Fig. 5) is separated from the underlying pumice flows by a discontinuous layer of bedded, pyroclastic-surge deposits 0–2 m thick (labeled 3 in Fig. 5). Above the surge beds, the lower part of the coarse, upper pumice breccia is commonly a 10–20 m cliff that marks a zone of conspicuous fossil fumaroles (labeled 4 in Fig. 5). Another ca. 100 m of pumice breccia underlies these outcrops at lower elevations.

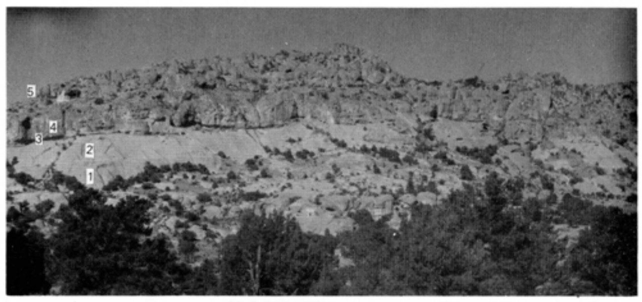

FIGURE 5—Pumice breccia of Old Horse Springs in east-facing bluffs southwest of Old Horse Springs. Numbers 1–5 indicate the following: 1 and 2 = non-welded pumice flows, each on the order of 50 m thick; 3 = discontinuous, crossbedded, ash-cloud surge deposits at top of pumice flow number 2; 4 = fossil fumaroles in cliffs at base of coarse pumiceous breccia (block and ash deposit); 5 = parting ledge within concentration of 2–3 m pumiceous blocks and cognate quartz monzonite clasts. Mineralized jasperoid inclusions are concentrated above this parting.

FIGURE 6—Pumice flow no. 2 (Fig. 5) beneath fluted cliffs with fossil fumaroles. Tape stretched across outcrop was used to measure size of pumice blocks, which show reverse grading.

Where its base is exposed, the pumice breccia commonly consists of a few meters to a few tens of meters of volcaniclastic sediments and meso- to megabreccia consisting of blocks of older rocks, such as Blue Canyon and Rock House Canyon Tuffs and Datil Group conglomerate, in a matrix of pumice breccia of Old Horse Springs. This coarse breccia occurs in scattered outcrops along the basal contact for at least 6–7 km, from south of NM-12 to Alamocito Canyon north of the highway (Fig. 4). We may look at this coarse, mixed breccia briefly near Stop 3-1 if time permits.

The pumice breccia of Old Horse Springs is a pinkish-brown, pumiceous, fine-grained granular rock that contains 1–4 mm phenocrysts, mainly of sodic plagioclase (oligoclase–andesine), about equal amounts of biotite and clinopyroxene, and traces of opaque oxides, zircon, and apatite. The breccia is a dacite (Table 2).

Inclusions in pumice breccia

Inclusions are of three kinds: (1) pre-Tertiary sedimentary rocks, (2) cognate porphyritic quartz monzonite, and (3) older volcanic rocks of the Datil Group of Oligocene age.

Jasperoidized inclusions (Fig. 7) of pre-Tertiary sedimentary rocks probably correspond to the Lower Permian sequence of the Yeso Formation (calcareous to argillaceous sandstone), Glorieta Sandstone, and San Andres Limestone, overlain by Triassic(?), sandstone, all exposed nearby in outcrops at the foot of Horse Mountain, north of the

TABLE 2—Chemical and modal analyses of pumice breccia of Old Horse Springs and quartz monzonite inclusions. Analysts: Sample numbers 1, 2, 3, 4 by USGS. Major oxides by J. Baker, A. Bartel, D. Siems, K. Stewart, J. Taggart, J. Wahlberg; trace elements by D. Fey, R. Yeoman, and D. Bove. Sample number 5 by Bornhorst (1980: 593). Dash (—) indicates not analyzed or not found.

Sample No.	1	2	3	4	5
Field No.	P-5-78	BP-1-88	BP-2-88	BP-6A-85	T-377
MAJOR OXIDES (weight percent, recalculated water-free)					
SiO_2	66.6	67.5	66.4	67.6	67.8
Al_2O_3	15.6	15.7	15.7	15.6	15.7
Fe_2O_3	3.86*	4.56*	4.64*	2.86*	3.02
MgO	1.32	1.03	1.07	1.34	1.42
CaO	3.53	2.31	3.12	3.54	3.17
Na_2O	3.51	3.16	3.60	4.19	3.34
K_2O	4.55	4.70	4.37	3.94	4.25
TiO_2	0.62	0.68	0.67	0.58	0.53
P_2O_5	0.33	0.23	0.30	0.21	0.18
MnO	0.11	0.07	0.11	0.04	0.04
FeO	—	—	—	—	0.19
Total	100.03	99.94	99.98	99.90	99.64
*Total iron as Fe_2O_3					
TRACE ELEMENTS (parts per million; L, indicates detected at limit shown)					
Ba	—	898	1002	860	969
Cr	—	—	—	9	25
Cu	—	78L	78L	11	18
Ga	—	16L	20	17	<25
Ni	—	—	—	8	19
Rb	—	145	119	—	114
Sr	—	384	514	520	481
Th	—	18L	18L	17	19.4
V	—	—	—	45	41
Y	—	32	28	22	30
Zn	—	79	71	35	134
Zr	—	247	215	—	245
MODES (volume percent)					
Groundmass	72	72	71	61	61.9
Quartz	—	Trace	Trace	—	0.3
Sodic plagioclase	21	24.3	22.6	30	28.9
Biotite	3.5	1.4	2.0	3.5	5.1
Clinopyroxene	3	1.1	2.7	3	2.2
Hornblende	—	—	—	1	—
Opaque oxide	0.5	0.5	1.5	1.5	1.5
Zircon	—	—	Trace	Trace	—
Apatite	Trace	—	Trace	Trace	—
Total	100	99.3	99.8	100	99.9

Sample descriptions

1. Pumice blocks from roadcuts on north side of NM-12, west of Old Horse Springs near Stop 3-1A.
2. Pumice block from outcrops (elevation about 7260 ft) south of NM-12 near Stop 3-1A.
3. Pumice block from outcrops (elevation about 7420 ft) south of NM-12 near Stop 3-1A.
4. Quartz monzonite block from outcrops (elevation about 7500 ft) in slope west of Stop 3-1.
5. Quartz monzonite block from outcrops south of NM-12 near Stop 3-1A. Collected and analyzed by T. J. Bornhorst (1980: 593).

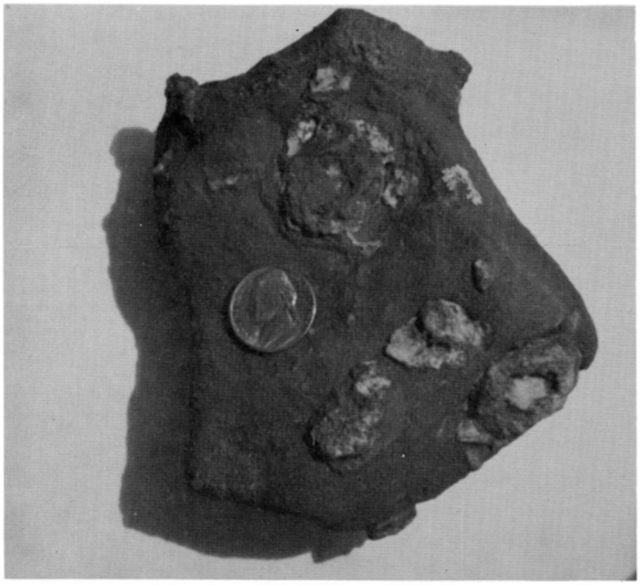

FIGURE 7—Fine-grained, brick-red jasperoid inclusion containing relict chert nodules. Iron mineralization is most conspicuous in the relict chert nodules.

San Agustin Plains (Fig. 4). The jasperoid inclusions that are altered limestone are not only mineralized but, where found in outcrop, also generally have a bordering reaction zone a few centimeters thick (Fig. 8), which consists mainly of diopside, with or without andradite garnet, phlogopite, and clay minerals. Similar reaction zones border inclusions believed to be calcareous and argillaceous sandstone, but are not present around inclusions thought to consist originally of sandstone or quartzite.

The coarsely porphyritic quartz monzonite inclusions are very similar chemically to the enclosing dacite pumice breccia (Table 2) and both have essentially the same mineralogy, suggesting that they were derived from the same magma. The quartz monzonite may have formed as a crystalline border phase, at the roof of the magma chamber, that was ripped-up and entrained in the culminating eruptions of the dacite pumice breccia. Miarolitic cavities in the quartz monzonite contain tiny pseudobrookite and diopside crystals; the pseudobrookite indicates a shallow, oxidizing environment at the time the quartz monzonite crystallized.

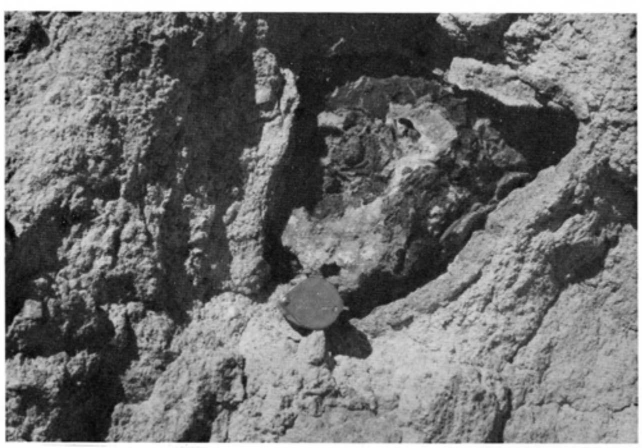

FIGURE 8—Jasperoid inclusion in place in pumice breccia of Old Horse Springs, showing calc-silicate skarn reaction rim consisting mainly of granular diopside and minor andradite garnet.

Mineralogic observations relating to the genesis of jasperoid, zinc mineralization, and calc-silicate skarn rims

The jasperoid inclusions vary in mineral composition from nearly pure quartz, to quartz plus abundant calcite and iron oxides, to dominantly iron oxides. Many inclusions have a concentrically banded core of layers rich in quartz and iron oxides surrounded by brick-red, massive, spherulitic jasperoid (Fig. 9A). Most of the analyzed nodules were collected from float and probably represent the cores of larger jasperoid blocks (Fig. 9B, C, D); others, which show relict bedding, may have been originally sandstone or quartzite rather than limestone. Most of the quartz in the xenoliths exhibits fibrous or radiating (spherulitic) crystallization indicating an origin by replacement or recrystallization, but some shows relict clastic texture of the original sandstone or siltstone.

Iron in the xenoliths forms an unusual suite of ferric-iron minerals, including coarsely crystalline, black, lustrous plates of hematite and red, very fine-grained crystals of magnesioferrite ($MgFe^{3+}{}_2O_4$), which are disseminated in the silica and concentrated along quartz-grain boundaries. The jasperoid nodules typically have brick-red, fine-grained outer zones (colored by a fine magnesioferrite dust) and cores of coarsely crystalline quartz, hematite, and calcite. Forsteritic olivine occurs as inclusions in hematite crystals; it contains approximately 1.8% total iron (Table 3), which the bright-red cathodoluminescence of the forsterite suggests to be all ferric iron. This assemblage of ferric-iron minerals indicates a high oxygen fugacity during formation, which may have involved recrystallization of pre-existing iron oxides. Although no magnetite has been observed in the nodules, which contain only ferric-iron phases and Mn^{3+} (Table 4), textural evidence, mainly fine-grained aggregates of iron oxide that have pseudomorphic outlines, indicates probable replacement of pre-existing iron-oxide crystals.

Zinc in the jasperoid inclusions seems to be dominantly in the magnesioferrite (0.33–2.93 wt% ZnO; Table 5). Zinc is also present in aluminum spinels (1–27 wt%; Table 5), but the spinels are a very minor phase volumetrically. The zinc-bearing phases may have been produced by recrystallization and oxidation during thermal metamorphism of earlier formed oxides, such as magnetite and franklinite, or by desulfidization of sphalerite. Zinc and other trace metals in the mineralized jasperoid inclusions are shown in Table 6, where zinc is seen to be as much as 1% (10,000 parts per million) of some inclusions.

Reaction zones between the jasperoid inclusions and the enclosing dacite pumice breccia have a largely different mineral assemblage than the inclusions themselves. Calc-silicate skarn consists of greenish-yellow, diopside-rich border zones a few centime-

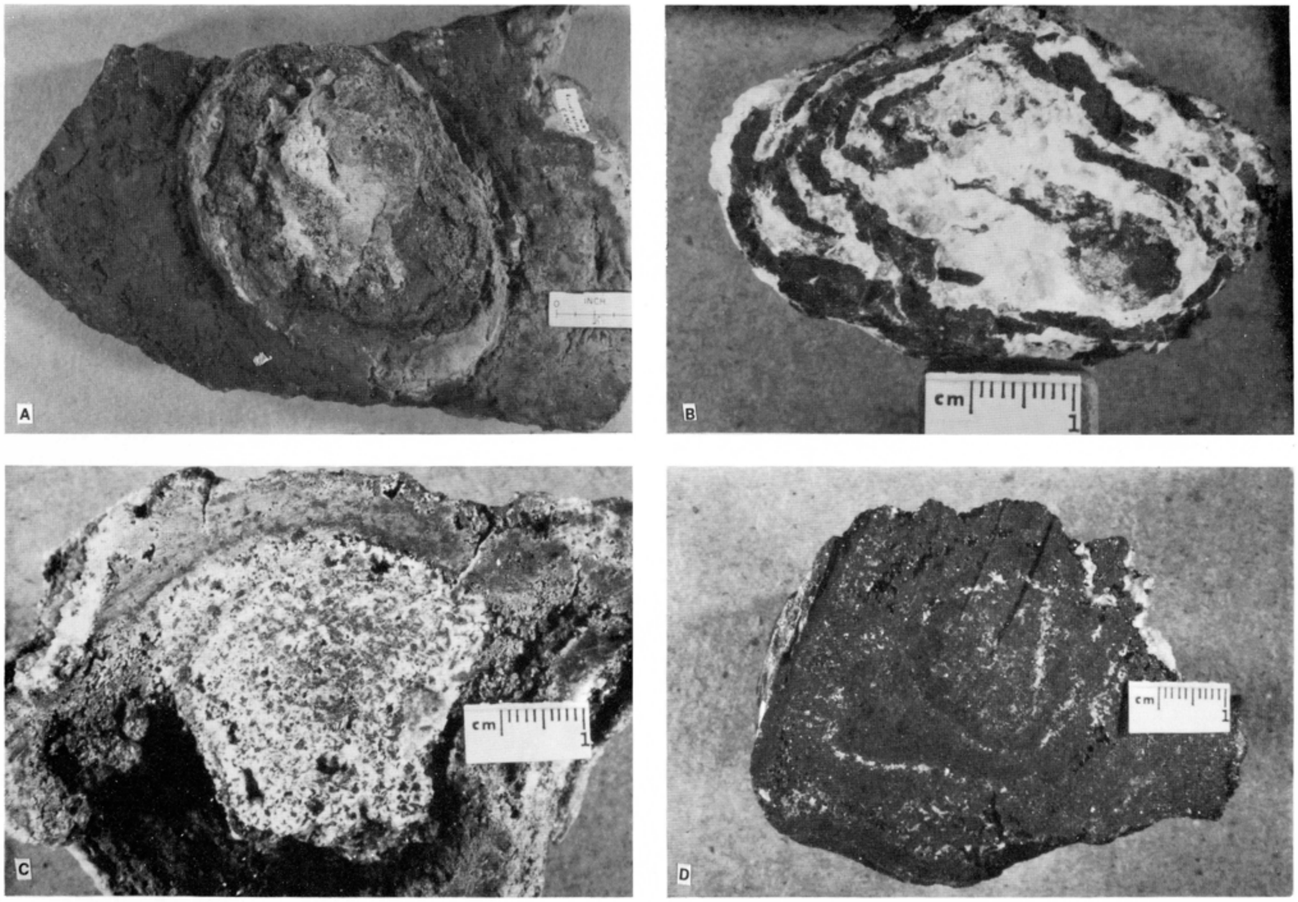

FIGURE 9—Mineralized jasperoid inclusions showing different form and composition. A, Jasperoid inclusion with core of quartz, hematite, and calcite surrounded by jasperoid containing fine-grained magnesioferrite. **B,** Jasperoid nodule with concentric bands of quartz–calcite and iron oxides. **C,** Jasperoid nodule with core of calcite, quartz, hematite, and magnesioferrite surrounded by red outer zone of quartz, hematite, and magnesioferrite. **D,** Iron-oxide-rich jasperoid nodule of hematite, magnesioferrite, and quartz.

ters thick around many of the in-situ jasperoid nodules. Euhedral diopside crystals are commonly zoned, and FeO ranges between about 4 and 15% (Table 7). Diopside in the skarn reaction zones may be accompanied by green to brown, euhedral andradite garnet that ranges in composition from about andradite$_{90}$–grossular$_{8}$ to andradite$_{63}$–grossular$_{34}$ (Table 7). Other minerals found in the reaction zone include light-pink montmorillonite clay and phlogopite mica (Table 3). Within the tuff adjacent to the reaction zone, plagioclase phenocrysts are altered to a fine-grained mixture of clays, micas, and other unidentified K and Mg silicates.

Diopside also occurs as free-growing, transparent, yellowish-green prisms a few tenths of a millimeter long, in vugs and fractures in the jasperoid inclusions, and in miarolitic cavities in the cognate quartz monzonite blocks, where it commonly is accompanied by hematite and prismatic to bladed pseudobrookite ($Fe^{+3}_2TiO_5$; Table 4). Titanite is observed to coat some pseudobrookite crystals.

Origin and significance of mineralized inclusions

Two main problems of the formation of the mineralized inclusions are:

1. Place of origin and physical–chemical environment of jasperoid development and associated mineralization.
2. Place of origin and physical–chemical environment of calc-silicate border zones on jasperoid inclusions.

Two alternative explanations are:

1. Both mineralized jasperoid and calc-silicate reaction zones formed in the same place as parts of a single alteration process.
2. The mineralized jasperoid and the reaction zones formed in separate places as a result of different processes.

Some of the considerations in choosing between these alternatives are:

1. The delicate, granular, calc-silicate reaction zones around jasperoid inclusions are essentially unbroken where they are found in place, but are almost never found attached to the inclusions in float, attesting to their vulnerability during transport.
2. The mineral assemblage in the calc-silicate zones consists of variable proportions of diopside, garnet, phlogopite, and clay minerals. Except for the clays, this assemblage is consistent with the pyroxene–hornfels facies of contact metamorphism, indicating a formation temperature between about 550 and 700°C. The intensity of

TABLE 3—Microprobe analyses of mineral phases in jasperoid, calc-silicate skarn reaction rims, and altered pumice breccia. Dash (—) indicates not analyzed.

	Phl-1	For-1	Cc-1	Pla-1	Alt-1	Alt-2
			(weight percent)			
Na_2O	0.57	—	—	7.54	—	0.29
K_2O	9.80	—	—	1.04	8.14	0.15
MgO	28.15	59.08	0.03	0.02	0.21	9.48
CaO	0.14	0.02	53.82	5.25	6.32	1.24
SrO	—	—	0.02	—	0.00	—
MnO	0.00	0.08	0.00	0.02	0.00	0.00
FeO	0.59	1.82	0.00	0.24	0.21	0.81
ZnO	0.07	0.03	—	0.01	—	0.02
Al_2O_3	10.03	0.01	0.08	22.07	25.12	16.87
Cr_2O_3	0.00	—	—	0.00	—	—
SiO_2	44.26	39.11	0.00	61.80	59.37	56.65
TiO_2	0.14	0.04	—	0.00	—	0.01
CO_2	—	—	42.28*	—	—	—
Total	93.75	100.19	96.23	98.01	99.37	85.52
			(cation proportions)			
Na	0.078	—	—	0.663	—	0.039
K	0.882	—	—	0.060	0.650	0.013
Mg	2.961	2.087	0.001	0.001	0.020	0.974
Ca	0.011	0.001	0.997	0.255	0.424	0.092
Sr	—	—	0.000	—	0.000	—
Mn^{+2}	0.000	0.002	0.000	0.001	0.000	—
Fe^{+2}	0.035	0.036	0.000	0.009	0.011	0.047
Zn	0.004	0.001	—	—	—	—
Al	0.834	—	0.002	1.179	1.855	1.370
Si	3.122	0.927	0.000	2.802	3.719	3.904
Ti	0.007	0.001	—	0.000	—	—
Σox.	11.000	4.000	1.001	8.000	11.000	11.000

Sample descriptions

Phl-1 = phlogopite mica at contact of jasperoid nodule BP-46-86 with skarn rim.
For-1 = olivine inclusion in hematite, within jasperoid nodule BP-6B-85.
Cc-1 = calcite intergrown with quartz in jasperoid nodule BP-6G-85.
Pla-1 = unaltered core (sodic andesine) of plagioclase phenocryst in tuff, within outer part of calc-silicate reaction rind around nodule BP-46-86.
Alt-1 = altered rim of plagioclase phenocryst (mineral composition unknown).
Alt-2 = Mg–Al-silicate (mineral identity unknown) surrounding an altered plagioclase phenocryst.
*calculated amount of CO_2 in calcite.

alteration around the jasperoid decreases outward into the pumice breccia.

3. The jasperoid mineral assemblage of mainly quartz, calcite, and hematite is typical of low-temperature metasomatism. However, magnesioferrite and tiny forsterite inclusions in the hematite indicate a higher temperature of formation.
4. The pumice breccia deposit is not welded.
5. Unaltered carbonate xenoliths have not been observed.
6. The fossil fumaroles lack evidence of iron or other sublimates deposited during degassing of the pumice breccia.

TABLE 4—List of minerals in the jasperoid inclusions, calc-silicate skarn reaction rims, and altered pumice breccia.

Hematite
Magnesioferrite
Spinel (zincian)
Franklinite/gahnite
Pseudobrookite
Sphene
Forsterite
Diopside
Andradite
Phlogopite
Montmorillonite
Quartz
Calcite

7. The anomalous abundance of several metals, notably iron, zinc, and manganese, and in lesser amounts copper, vanadium, nickel, and lead, is evidence of some type of active mineralizing process.
8. Quartz replacement textures observed are typically low-temperature jasperoidization.
9. Iron-oxide replacement textures in the jasperoid nodules suggest replacement by magnesioferrite of pre-existing, probably lower-temperature, iron oxides.

Conclusions: The observed field relationships, mineral phases, and textures suggest the following sequence of events:

(1) Jasperoidization and iron and zinc mineralization of pre-Tertiary wall rocks and formation of iron oxides by hydrothermal solutions at the top of a dacitic magma chamber preceded eruption of the dacite pumice breccia. Crystallization of the coarse-grained quartz monzonite may have occurred in the roof zone of the magma chamber at this time.

(2) Volatile pressure in the magma chamber eventually exceeded the confining pressure and initiated eruption of pyroclastic pumice flows, which contain small accidental inclusions of quartz monzonite but no pre-Tertiary jasperoid inclusions.

(3) After the premonitory eruptions, continued accumulation of volatiles renewed the pressure in

TABLE 5—Microprobe analyses of oxide minerals in jasperoid inclusions.

	Hem-1	Hem-2	Hem-3	Mgf-1	Mgf-2	Mgf-3	Spn-1	Spn-2	Spn-3
				(weight percent)					
MgO	0.22	0.35	0.16	21.71	21.62	20.72	27.11	10.39	5.59
CaO	0.01	0.00	0.00	0.01	0.92	0.18	0.06	0.03	1.25
MnO	0.04	0.74	0.17	1.22	3.32	3.85	0.25	10.61	10.91
ZnO	0.01	0.00	0.00	0.33	0.47	2.93	1.05	11.10	27.46
Fe_2O_3	98.29	99.10	100.39	79.22	68.14	72.52	16.61	30.28	34.49
Al_2O_3	0.23	0.08	1.03	0.29	5.37	0.98	53.97	11.87	8.95
SiO_2	0.01	0.01	0.07	0.02	0.01	0.22	0.22	0.13	0.16
TiO_2	0.14	0.04	0.02	0.00	0.00	0.04	0.00	0.04	0.06
Total	98.95	100.32	101.84	102.80	99.85	101.44	99.27	96.79	88.87
				(cation proportions)					
Mg	0.009	0.014	0.006	1.037	1.029	1.002	1.029	0.537	0.329
Ca	—	—	—	—	0.032	0.001	0.002	0.001	0.053
Mn^{+3}	0.001	0.015	0.003	0.033	0.090	0.106	0.005	0.312	0.365
Zn	—	—	—	0.008	0.011	0.070	0.020	0.284	0.802
Fe^{+3}	1.981	1.973	1.958	1.910	1.637	1.770	0.318	1.374	1.026
Al	0.007	0.003	0.032	0.011	0.202	0.038	1.620	0.485	0.417
Si	—	—	0.002	0.001	—	0.007	0.006	0.004	0.006
Ti	0.003	—	—	—	—	0.001	—	0.001	0.002
Oxygen atoms	2.999	3.000	3.000	3.978	3.966	3.960	3.978	4.088	3.912

Sample descriptions

Hem-1 = coarse hematite in jasperoid nodule BP-6G-85.
Hem-2 = coarse hematite in jasperoid nodule BP-6C-85.
Hem-3 = coarse hematite, host for olivine inclusions in jasperoid BP-6B-85.
Mgf-1 = magnesioferrite, intergrown with hematite in jasperoid BP-6A-85.
Mgf-2 = magnesioferrite crystal (about 20 microns) in jasperoid BP-6G-85.
Mgf-3 = fine-grained magnesioferrite in jasperoid BP-6A-85.
Spn-1 = yellowish-brown spinel crystal in jasperoid BP-6B-85.
Spn-2 = fine-grained spinel (complex solid solution) in jasperoid BP-6E-85.
Spn-3 = very fine-grained spinel (franklinite/gahnite) in jasperoid BP-6G-85.

the magma chamber to the point where a massive failure of the chamber roof led to eruption of the pumice breccia and the entrainment of abundant shattered quartz monzonite roof rocks, and lesser amounts of jasperoidized and mineralized pre-Tertiary wallrock. Similarities in composition between pumiceous dacite blocks and more massive, but vesicular to miarolitic, quartz monzonite inclusions suggest gradation in the roof of the magma chamber between pumiceous dacite and porphyritic quartz monzonite.

(4) During cooling of the dacite pumice breccia, reaction between the mineralized jasperoid xenoliths and the hot pumice breccia produced the diopside-rich skarn zones. Original magnetite and (or) other iron oxides in the jasperoid xenoliths may have been recrystallized to the ferric phases hematite, magnesioferrite, and ferric-iron-rich forsterite at this time. Diopside and pseudobrookite, found in miarolitic cavities in the quartz monzonite, may also have formed then (according to Lindsley, 1965, pseudobrookite is unstable below 585°C). Montmorillonite clay, phlogopite, and other minerals were formed by alteration of the pumice breccia at lower temperatures, as cooling of the pumice breccia proceeded.

A low to moderate potential for resources of base and ferrous metals, particularly zinc and iron, and possible associated silver and gold, is indicated by the anomalous metals (Table 6) in the mineralized jasperoid inclusions. The most likely type of deposit would be a contact-metasomatic deposit accompanied by replacement and vein deposits related to intrusion of a silicic pluton into pre-Tertiary sedimentary rocks at shallow depths. Pre-Tertiary rocks may be within a few hundred meters of the surface in the vicinity of the probable source vent of the pumice breccia of Old Horse Springs, as indicated by outcrops of pre-Tertiary sedimentary rocks about 10 km northeast of the proposed vent. The zinc-rich middle Tertiary ore deposits in pre-Tertiary limestones in the Magdalena district, less than 100

TABLE 6—Atomic absorption (AA) and semiquantitative spectrographic analyses (6 step D-C arc method) of mineralized jasperoid inclusions. G, greater than value shown; N ( ), not detected at value shown; L ( ), detected but less than value shown. Analysts: D. E. Detra, R. T. Fairfield, L. S. Landon, and C. D. Taylor.

	AA		Percent				Parts per million										
Field No.	Au	Ag	Fe	Mg	Ca	Ti	Mn	B	Ba	Be	Co	Cu	Ni	Pb	Sn	V	Zn
BP-2-85	N(0.05)	N(0.05)	G20	1	L(0.05)	0.15	300	30	200	N(1)	70	100	100	N(10)	N(10)	300	2000
BP-3-85	N	N	2	3	5	0.15	200	30	N(20)	2	10	15	15	N	N	15	N(200)
BP-6A-85	N	N	3	1	1.5	0.3	500	10	700	1.5	15	10	7	15	N	70	N
BP-6B-85	N	N	20	1	0.2	0.03	2000	15	20	L(1)	70	100	100	10	20	150	7000
BP-6D-85	N	N	15	2	2	0.02	3000	20	50	N	50	300	30	70	15	70	10000
BP-6E-85	N	N	G20	1	0.7	0.03	2000	10	20	N	70	50	100	N	15	300	1000
BP-6F-85	N	N	20	1	2	0.015	1500	10	20	N	50	100	70	50	N	100	5000

TABLE 7—Microprobe analyses of diopside and garnet in calc-silicate skarn reaction rims. Dash (—) indicates not analyzed.

	Di-1	Di-2	Di-3	Di-4	Di-5	And-1	And-2	And-3	And-4
				(weight percent)					
Na_2O	—	—	—	—	0.35	0.00	0.01	0.01	0.02
K_2O	0.02	0.03	0.02	0.00	0.00	0.00	0.00	0.01	0.01
MgO	17.52	13.29	15.03	13.71	9.40	0.19	0.20	0.17	0.18
CaO	25.19	24.96	23.18	24.37	22.78	32.52	32.84	33.24	33.11
SrO	0.00	0.06	0.02	0.01	—	—	—	—	—
MnO	0.05	0.14	0.76	0.04	0.13	0.09	0.11	0.10	0.12
FeO	4.06	6.34	9.00	10.58	14.75	28.44*	27.09*	24.78*	20.38*
ZnO	—	—	—	—	0.03	0.00	0.00	0.00	0.03
Al_2O_3	2.95	5.43	0.64	3.58	2.17	1.73	2.58	4.41	7.20
Cr_2O_3	—	—	—	—	0.00	0.01	0.00	0.00	0.02
SiO_2	53.57	51.16	53.85	50.48	48.90	35.78	35.58	36.27	37.14
TiO_2	—	—	—	—	0.12	0.24	0.42	0.07	0.13
Total	103.36	101.41	102.50	102.77	98.63	99.00	98.83	99.06	98.34
				(cation proportions)					
Na	—	—	—	—	0.027	0.000	0.001	0.002	0.003
K	0.001	0.001	0.001	0.000	0.000	0.000	0.000	0.001	0.001
Mg	0.928	0.725	0.818	0.754	0.549	0.024	0.025	0.021	0.022
Ca	0.959	0.979	0.907	0.963	0.957	2.938	2.975	2.960	2.913
Sr	0.000	0.001	0.000	0.000	—	—	—	—	—
Mn	0.002	0.004	0.024	0.001	0.004	0.007	0.008	0.007	0.008
Fe	0.121	0.194	0.275	0.326	0.484	1.805	1.724	1.550	1.259
Zn	—	—	—	—	0.001	0.000	0.000	0.000	0.002
Al	0.123	0.234	0.028	0.156	0.100	0.172	0.257	0.432	0.697
Cr	—	—	—	—	0.000	0.001	0.000	0.000	0.002
Si	1.903	1.872	1.967	1.861	1.917	3.017	2.983	3.015	3.050
Ti	—	—	—	—	0.004	0.015	0.027	0.004	0.008
Σox.	6.001	5.999	6.000	6.000	6.000	12	12	12	12

Sample descriptions

Di-1 = unzoned diopside crystal in calc-silicate rind on nodule BP-46-86.
Di-2 = diopside crystal in calc-silicate rind on nodule BP-6F-85.
Di-3 = colorless core of diopside crystal in rind on BP-46-86.
Di-4 = yellowish-green rim of diopside crystal in rind on BP-46-86.
Di-5 = brown zone in a diopside crystal in rind on BP-46-86.
And-1 = core of andradite garnet crystal in calc-silicate rind, BP-6-86.
And-2 = rim of same garnet crystal.
And-3 = garnet crystal in calc-silicate rind, BP-6-86.
And-4 = garnet crystal in calc-silicate rind, BP-6-86.
*iron in garnet analysis is expressed as Fe_2O_3.

km east of the Horse Springs area, provide a possible model for the type of deposit that could be present beneath the surface here.

From Stop 3-1 we can survey much of the San Agustin Plains to the northeast (Fig. 10), and on a clear day we can expect to see the radio dishes of the VLA (Very Large Array) in front of the rounded peaks of Tres Montosas to the northeast. Closer at hand, we can see the 10–12 Ma Horse Mountain dacite dome on the north side of the plains and the fault block of Permian rocks low on its south side, just north of NM-12. On the south side of the plains are the low shields of Bearwallow Mountain Andesite volcanoes (24–27 Ma) that mark the Morenci lineament at Luera Peak, Pelona Mountain, and O Bar O Mountain (just behind the ridge and Jack Peak to the south of us). The low hills east of us and those north of NM-12 consist mainly of Spears Formation conglomerate and thin, interlayered outflow tuffs of the Datil Group (>32 Ma).

The pumice breccia of Old Horse Springs is faulted down just across the canyon south of us, between here and Jack Peak. There, as well as north of the highway, the pumice breccia is overlain by porphyritic rhyolite flows of local origin and younger

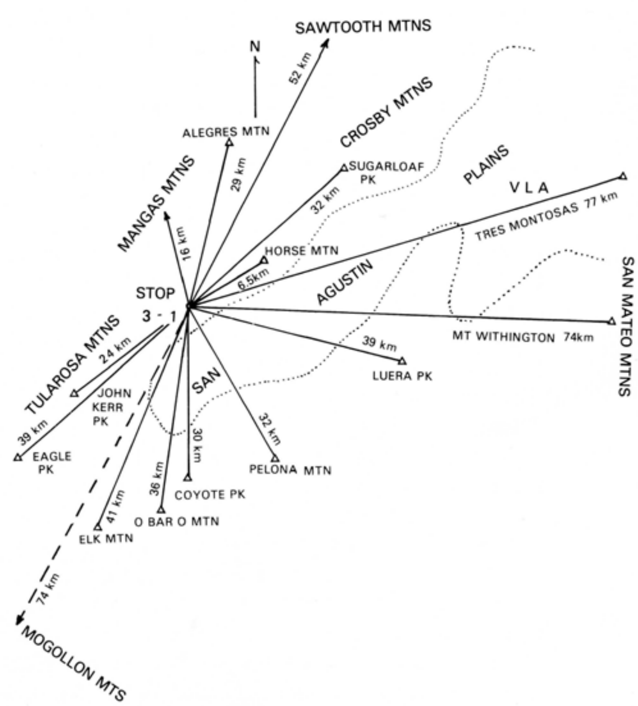

FIGURE 10—Panoramic location of Old Horse Springs–San Agustin Plains area from top of ridge at Stop 3-1.

volcanic rocks that are mostly andesite flows, but which include distal outflow of regional ash-flow tuffs (Vicks Peak, Shelley Peak, Bloodgood Canyon Tuffs) (Table 1).

Cross the shallow gulch to the northwest and climb through about 100 m of pumice flow to the base of the coarse, pyroclastic breccia in the cliffs above the discontinuous pyroclastic surge beds of probable ash-cloud origin. The lower pumice flows (1 and 2 of Fig. 5) contain pumice blocks up to 30–50 cm in diameter and seem to show reverse grading. Note the partings such as between pumice flows 1 and 2 (best seen from a distance), and decide if these are boundaries between discrete pyroclastic flows or if you think they represent gradational boundaries within a continuous deposit, as from a pulsating eruption column. These partings appear to be accentuated locally as animal trails. While traversing the lower flows, note also the presence of small block- and lapilli-size fragments that can be recognized as inclusions of quartz monzonite by their less pumiceous texture, though they are petrographically similar to the pumice. Pumice flows 1 and 2 may qualify as near-vent co-ignimbrite, lag-fall deposits (Wright and Walker, 1977; Fisher and Schmincke, 1984: 222), but if so, any associated ignimbrite sheets have been eroded from the surrounding terrain.

An attempt was made to quantify reverse grading in pumice flow no. 2 (Fig. 5) by measuring the dimensions of pumice blocks and lapilli along a tape stretched perpendicular to its base (Fig. 6). The average dimension of pumice, measured perpendicular to the tape, was plotted against the midpoint of 3 m intervals above the base of the pumice flow. This crude approximation of pumice size distribution suggests upward coarsening in two intervals within the pumice flow (Fig. 11), with a discontinuity at about 27 m above its base. The measurements are probably biased by a tendency to preferentially measure the larger, more discrete pumices rather than the smaller ones, because the latter are more difficult to distinguish from the matrix. However, these measurements are believed to support the visual indications of reverse grading.

In the cliffs above the crossbedded, ash-cloud, surge deposits (Fisher and Schmincke, 1984) at the top of this slope, the upper pyroclastic flow breccia coarsens dramatically; both the primary pumiceous dacite blocks and the associated quartz monzonite inclusions attain dimensions of 2–3 m. The quartz monzonite blocks are not merely non-pumiceous dacite but, as shown by the much larger phenocrysts, a separate intrusive phase of the dacitic magma. The cliffs here also show a highly fluted structure interpreted to be fossil fumarole tubes or degassing pipes. They are depleted in fines and show no evidence of fumarolic mineralization during degassing. Their occurrence at the base of a cooling unit rather than near the top is somewhat unusual (Ross and Smith, 1961), but lends some credence to the idea that the distribution of fumaroles and the most cavernous, as well as thickest and coarsest, pumice breccia of Old Horse Springs may indicate the vent or vent areas for this deposit.

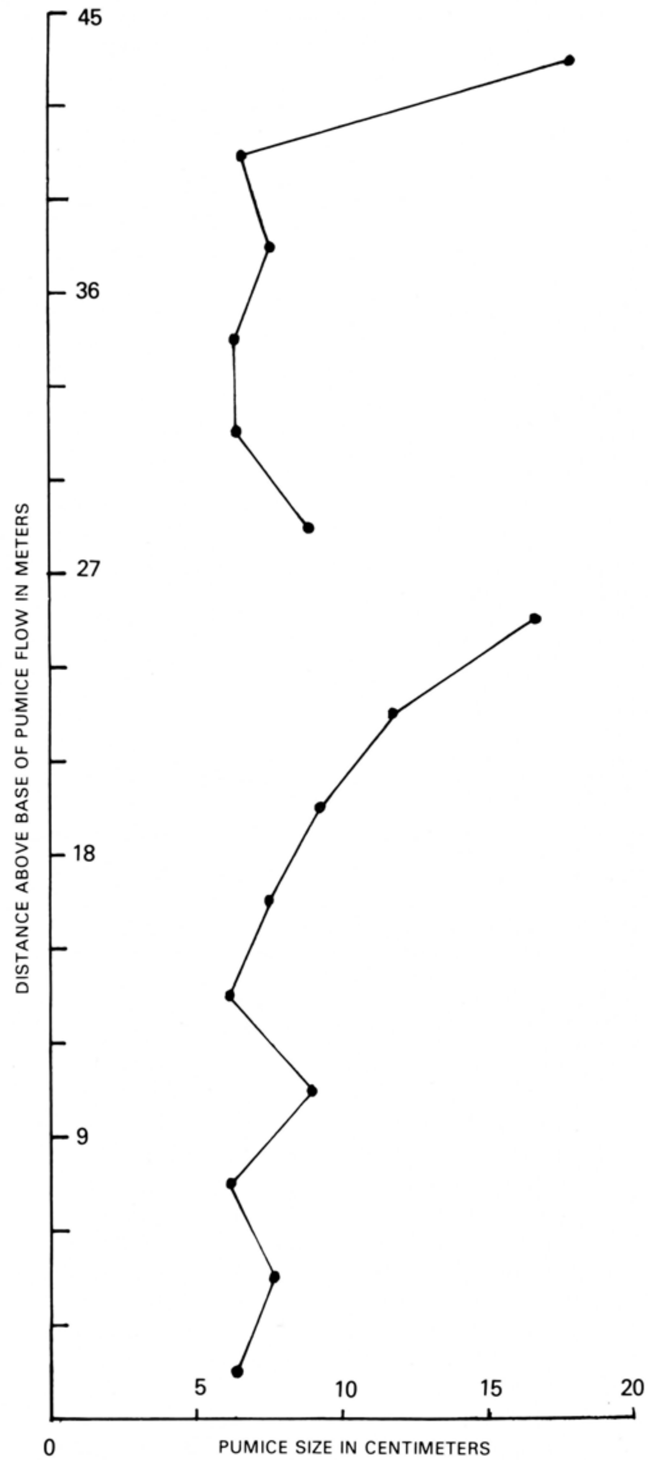

FIGURE 11—Average dimensions of pumice blocks and lapilli in 3 m intervals plotted against position above base of pumice flow no. 2 (Fig. 5). Pumice measured in plane of foliation perpendicular to a tape stretched across the outcrop (Fig. 6).

Now traverse left about 200 m along the base of the cliffs until a suitable route gives access to the next higher bench 30–50 m above. Most of the mineralized jasperoid inclusions that we have seen in outcrop occur in close proximity above this irregular bench which can be traced several hundred meters along this east-facing bluff at about 7500 ft elevation. Jasperoid inclusions have been seen only rarely in outcrops of the pumice breccia north of NM-12, but are abundant in float in most outcrop areas, at least to White Rock Canyon (Fig. 4) in the northern part of the Horse Springs area.

Please refrain from collecting specimens from the inclusions in outcrop. There is abundant float material in this area, and at our lunch stop there will be an opportunity to collect mineralized jasperoid specimens from an area of ample float within about 100 m north of the highway.

Xenoliths seem to be most abundant to the north along this bench. Notice the different types of pre-Tertiary inclusions to be seen: (1) red jasperoid with skarn reaction zones; (2) tan sandstone lacking reaction zones; (3) tan, calcareous argillite with reaction zones; and (4) dark, iron-rich inclusions with relict bedding.

After examining the various pre-Tertiary inclusions and the other features of the dacite pumice breccia, you may choose to return to the vehicles and ride around to the other side of the ridge for our lunch stop (Stop 3-1A; Fig. 4), or you may wish to climb through the pumice breccia to the top of the ridge and traverse down the other side to the lunch spot. To the top is less than 100 m elevation gain, and a little more than that down the other side. You will probably not find any mineralized inclusions in place on this traverse above the bench, but you should find evidence of them in float right to the top. At the ridge crest you may get a little better perspective of the distribution of the pumice breccia. There is a preferred route across the ridge to keep from getting cliffed on the other side, so those who choose to go across may want to stay more or less together, or at least get some directions from the leader; access down on the other side gets progressively easier south along the ridge.

Gather at Stop 3-1A on the north side of the ridge for lunch, discussion, and collection of mineralized jasperoid from float across the highway. Those who choose to drive to Stop 3-1A will return to NM-12 and drive about 2 mi west to a pullout on the left side of the highway just short of mileage marker 44.

Day 3 p.m.: The Bursum caldera

Geologic setting

The Mogollon Mountains (Fig. 12) are the probable source of at least five regionally distributed ash-flow-tuff (ignimbrite) sequences. The ash-flow sheets and their probable source calderas are: Cooney Tuff (Mogollon caldera); Davis Canyon and Shelley Peak Tuffs (Gila Cliff Dwellings caldera?); Bloodgood Canyon and Apache Spring Tuffs (Bursum caldera). The stratigraphic position of the tuffs and the location of the calderas relative to other calderas on the Mogollon plateau are shown in Table 1 and Fig. 3, respectively.

The approximately 25 × 40 km Bursum caldera is the best documented caldera in the Mogollon Mountains. It is flanked on the west by the older Mogollon caldera, and on the east by the slightly older Gila Cliff Dwellings caldera. The Mogollon caldera (Ratté and Finnell, 1978) is represented only by fragments of an intracaldera-tuff sequence in the Mogollon mining district and outflow remnants to the southeast along the Mogollon Range front, and to the southwest near Morenci (Ratté et al., 1984, fig. 4). Cooney Tuff within the Mogollon caldera is well exposed along the Catwalk Trail in the canyon of Whitewater Creek in the southern part of the Mogollon quadrangle and in Cooney Canyon near Stop 3-2 (Ratté, 1981; Fig. 12). The Gila Cliff Dwellings caldera has been tentatively interpreted as the result of subsidence related to eruption of the Davis Canyon and (or) Shelley Peak Tuffs (Ratté et al., 1984). The Bursum caldera is believed to have subsided initially in response to eruption of about 1000 km^3 of Bloodgood Canyon Tuff, followed by a similar volume of Apache Spring Tuff, which apparently is confined to the caldera. The high-silica rhyolite Bloodgood Canyon and rhyolitic to quartz latitic Apache Spring Tuffs form a normally zoned compositional sequence. The Bloodgood Canyon Tuff outflow apparently ponded in the older Gila Cliff Dwellings caldera, where it is at least 350 m thick, and forms the east wall of the Bursum caldera where the two calderas intersect.

The Mogollon mining district in the Mogollon quadrangle provides a cross section of the western margin of the Bursum caldera from the topographic wall, across the moat (5–8 km wide), to the edge of the resurgent dome (Fig. 15; Ratté, 1981, cross sections A-A′, B-B′, C-C′). The structural wall of the Bursum caldera is largely buried by moat deposits and its actual position through the mining district is an open question at this time. The caldera geology is complicated by late Cenozoic basin-and-range faulting and associated silver, gold, and copper mineralization and alteration.

Road log: Old Horse Springs to Deep Creek Ranch road and margin of Bursum caldera

Mileage

0.0 After lunch, reset mileage at mileage marker 44 and head west on NM-12. It is 37 mi to Reserve, 44 mi to junction with US-180, and 67 mi to Deep Creek Ranch road. **1.0**

1.0 Ahead and to the left from mileage marker 43, the Tularosa Mountains (Fig. 12) include the dacitic–rhyolitic composite domes of John Kerr Peak (~15 Ma) and the dacitic volcano at Eagle Peak (~9 Ma) at about 10:30 and 11:00, respectively.

Between Horse Springs and Reserve we skirt the southwest edge of the San Agustin Plains, cross the Continental Divide (elevation 2240 m) about 0.5 mi west of mileage marker 35, and descend into the Tularosa River drainage on the Pacific side of the divide. In this area, the distinction between the N55E Morenci lineament and the N30E Morenci–Reserve fault zone is obscured by largely younger northwest- and west-northwest-trending faults. Roadcuts ahead expose Bloodgood Canyon Tuff from the Bursum caldera, about 70 km south of here. The Bloodgood Canyon Tuff is overlain by Bearwallow Mountain Andesite and Gila Group conglomerate along the road to the west. Basin-fill sedimentary rocks post-dating Bearwallow Mountain Andesite (~24 Ma) have interlayered basalt flows in this area, and the formal rank used here thus is the Gila Group. Bearwallow Mountain flows

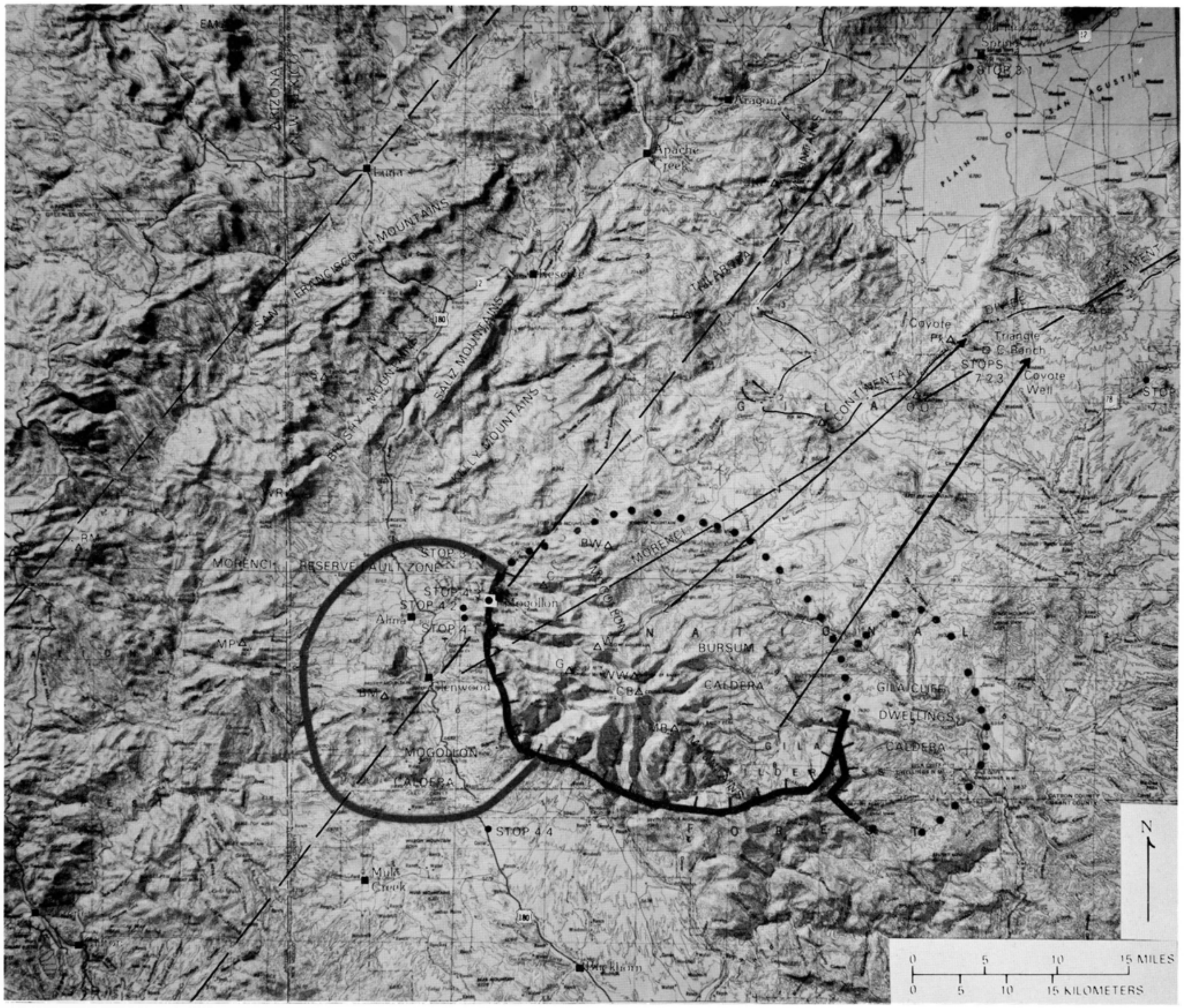

FIGURE 12—Index map of San Agustin Plains and Mogollon Mountains region showing field-trip stops for Days 3, 4, and part of Day 7. Stops 3-2 and 4-1, 2, 3 are all at Mogollon at northwest end of Mogollon Mountains. BM = Brushy Mountain, BW = Bearwallow Mountain, C = Cooney Peak, CB = Center Baldy, E = Eagle Peak, EM = Escudilla Mountain, H = Horse Mountain, JP = Jack Peak, JKP = John Kerr Peak, MB = Mogollon Baldy, MP = Maple Peak, O-O = O Bar O Mountain, P = Pelona Mountain, RM = Red Mountain, RP = Rose Peak, S = Saddle Mountain, W = Willow Mountain, WR = Whiterocks Mountain, WW = Whitewater Baldy. Arrows labeled 1 and 2 show direction of transport indicated by tuff outcrops at Coyote Well and Coyote Peak, respectively. Heavy dashed lines show approximate boundaries of Morenci–Reserve fault zone.

are well exposed in Canyon del Buey, as seen to the right from the bridge just east of mileage marker 30 and the Sand Flat road junction. **16.0**

17.0 At about mileage marker 27, we cross east–west faults into downfaulted conglomerate of the Gila Group in the Reserve graben segment of the Morenci–Reserve fault zone (T. Finnell, USGS, unpubl. mapping 1988), which we will be traversing for the most part from here to the Deep Creek Ranch road and Glenwood. **1.0**

18.0 Continue through the village of Aragon (Fig. 12) and on to Apache Creek at junction of NM-32 to Quemado. At mileage marker 21, Eagle Peak is visible at 11:30. Basalt flows at creek level, east of Apache Creek, where the colorful pickup-truck beds serve as cattle feeders, have a whole-rock age of 13 Ma, and are interlayered with conglomerates of the Gila Group. However, olivine basalt flows that cap the mesas on both sides of the highway at Apache Creek are 0.9 Ma, and are confined within the Reserve graben. **10.0**

28.0 Continue southwest in Reserve graben. Terrane east of highway (to left) shows faulted, pink to gray basin-fill sediments of the Gila Group locally tilted at low to moderate angles beneath untilted basalt flows (T. Finnell, USGS, unpubl. mapping 1987). **5.0**

33.0 Bloodgood Canyon Tuff in outcrops on left side of highway. **3.0**

36.0 Approaching bridge across San Francisco River at northern edge of Reserve. Turn sharply to right just beyond Phillips 66 gas station, continuing about 7 mi to US-180 junction. At bridge in Starkweather Canyon, 1.5 mi west of Reserve, we cross a fault, leave the Gila Group in the deepest part of the Reserve graben, and enter a westward-tilted block of older rocks. Rocks exposed in Starkweather Canyon are mainly Bloodgood Canyon Tuff with a white, cavernous, poorly welded zone at the top, overlain by typically thin flows of Bearwallow Mountain Andesite and Gila Group conglomerates. Shelley Peak Tuff, also with white, poorly welded tuff at its top and with crossbedded, pink, volcaniclastic sandstone both above and beneath, underlies Bloodgood Canyon Tuff just west of the bridge. **3.0**

39.0 At the head of Starkweather Canyon the road curves westward and continues through roadcuts in the Gila Group for 5 mi to the junction of NM-12 and US-180. Scarps along the front of the San Francisco Mountains (Fig. 12), north of highway, mark trace of the San Francisco Mountains fault zone (Ratté, 1989), which repeats the sequence we came through in Starkweather Canyon, plus older rocks, including conglomerates transitional to the Eocene Baca Formation (Cather and Johnson, 1984) beneath the Datil Group (Table 1). The Baca-type conglomerate is best exposed in roadcuts about 1 mi west of the NM-12 and US-180 junction, where the conglomerate contains clasts of Paleozoic limestone and Precambrian crystalline rocks, as well as abundant early Tertiary volcanic clasts. **5.0**

44.0 Junction of NM-12 and US-180. Turn left and continue south on US-180. Trace of San Francisco Mountains fault zone continues along scarp to west. Low peaks include small dacitic–rhyolitic intrusions (~15–16 Ma) along the fault zone. The intrusions show weak pyritic and argillic alteration, but no other indications of mineralization (Ratté, 1988). They are examples of the magmatism associated with the Morenci–Reserve fault zone. **4.6**

48.6 Junction with Pueblo Park road on right. Cinder deposits exposed at edge of road on south side of junction, and bombs and dikes in cinders under bank on left side of road, are related to basalt flows (15–19 Ma) interlayered in Gila Group sediments (Marvin et al., 1987, entry nos. 150, 200). **5.1**

53.7 Saliz Pass. From Pueblo Park road, highway descends along Saliz Canyon to bridge at Cottonwood Creek, then climbs to Saliz Pass along the complex Brushy Mountains fault zone. Route provides excellent exposures of proximal andesitic mudflows of the Pueblo Creek Formation, which is equivalent to the Spears Formation of the Datil Group farther north. Here the Pueblo Creek Formation is unconformably overlain by an ash-flow-tuff sequence that includes outflow of Davis Canyon, Shelley Peak, and Bloodgood Canyon Tuffs. The best exposures of unfaulted sequences are on the left, just south of Cottonwood Canyon bridge, and high on ridge to right, as seen intermittently on the way up to Saliz Pass. The basalt (~12 Ma) at the pass is interlayered in the Gila Group. **3.3**

57.0 Highway crosses east–west fault into Gila Group sedimentary fill of Alma Basin (Houser, 1987). Last outcrops on right, before descending into Alma Basin, show Bloodgood Canyon Tuff above Shelley Peak Tuff, separated by a few meters of red, volcaniclastic sandstone. Views ahead and to left as highway descends into Alma Basin are of Mogollon Mountains and the resurgent dome of the Bursum caldera. **6.6**

63.6 US-180 bridge across San Francisco River. **3.0**

66.6 Junction of Deep Creek Ranch road and US-180. Turn left onto Deep Creek Ranch road (14 mi to Stop 3-2). **Open range—watch for cattle on road. 4.1**

70.7 At confluence of Copper Creek and Deep Creek turn left, across Copper Creek. **0.9**

71.6 Deep Creek Ranch. Bear right to top of mesa; road in conglomerate of Gila Group. **1.5**

73.1 Now on Mogollon quadrangle (Ratté, 1981). View ahead, to east, is across range-front (basin and range) fault into northwest part of Mogollon mining district. Silver Peak is at 4:00; we are headed for Stop 3-2 on east side of peak. **1.0**

74.1 Cross saddle and range-front fault. Fault cuts beds of Gila Group that are younger than the 5.6 Ma basalt of Harve Gulch (Houser, 1987; Ratté and Finnell, 1978). Across fault, road continues on Bearwallow Mountain Andesite, which buried the caldera wall and moat deposits in this area, as well as most of the northern margin of the caldera. The Bearwallow Mountain Andesite here is probably from the type locality at Bearwallow Mountain (Fig. 12), one of the andesitic shield volcanoes along the N55E Morenci lineament. Cross cattleguard at sharp bend. **2.9**

77.0 About 0.5 mi ahead road crosses northern extension of the north–south Queen fault, a major vein structure in the Mogollon district to the south, which probably is the reactivated structural wall of the Bursum caldera. Here the fault is marked mainly by float of vein quartz. **0.8**

77.8 Cross Copper Creek at site of old mining settlement of Claremont. This is a good place to **engage four-wheel drive** for rough terrane ahead. Good exposures of Queen fault and vein zone are about 100 m down creek. Veins here show some copper mineralization but consist mainly of quartz and calcite. **0.2**

78.0 Leave Copper Creek road and follow jeep trail up slope to right about 0.45 mi to top of ridge, then west along ridge crest to wire gate. At trail junction just west of gate, take right fork **after closing gate.** Trail crosses splits of Queen fault on both sides of saddle at trail junction. **2.6**

80.6 **STOP 3-2. Moat deposits and topographic margin of Bursum caldera.** Park at end of trail at cliff overlooking Cooney Canyon of Mineral Creek, the discovery site of the Mogollon mining district in 1875. Here in cliffs overlooking Mineral Creek we are on the moat-filling Last Chance Andesite (23–25 Ma), which is a correlative of the Bearwallow Mountain Andesite and overlies 10–20 m of rhyolite tuff (Deadwood Gulch Member of Fanney Rhyolite), which in turn overlies more moat-fill andesite (Mineral Creek Andesite, which also is a correlative of the Bearwallow Mountain Andesite) and associated moat-fill sedimentary rocks (Fig. 13; Ratté, 1981).

Silver Peak, toward which we are headed, is on the topographic (erosional) wall of the Bursum cal-

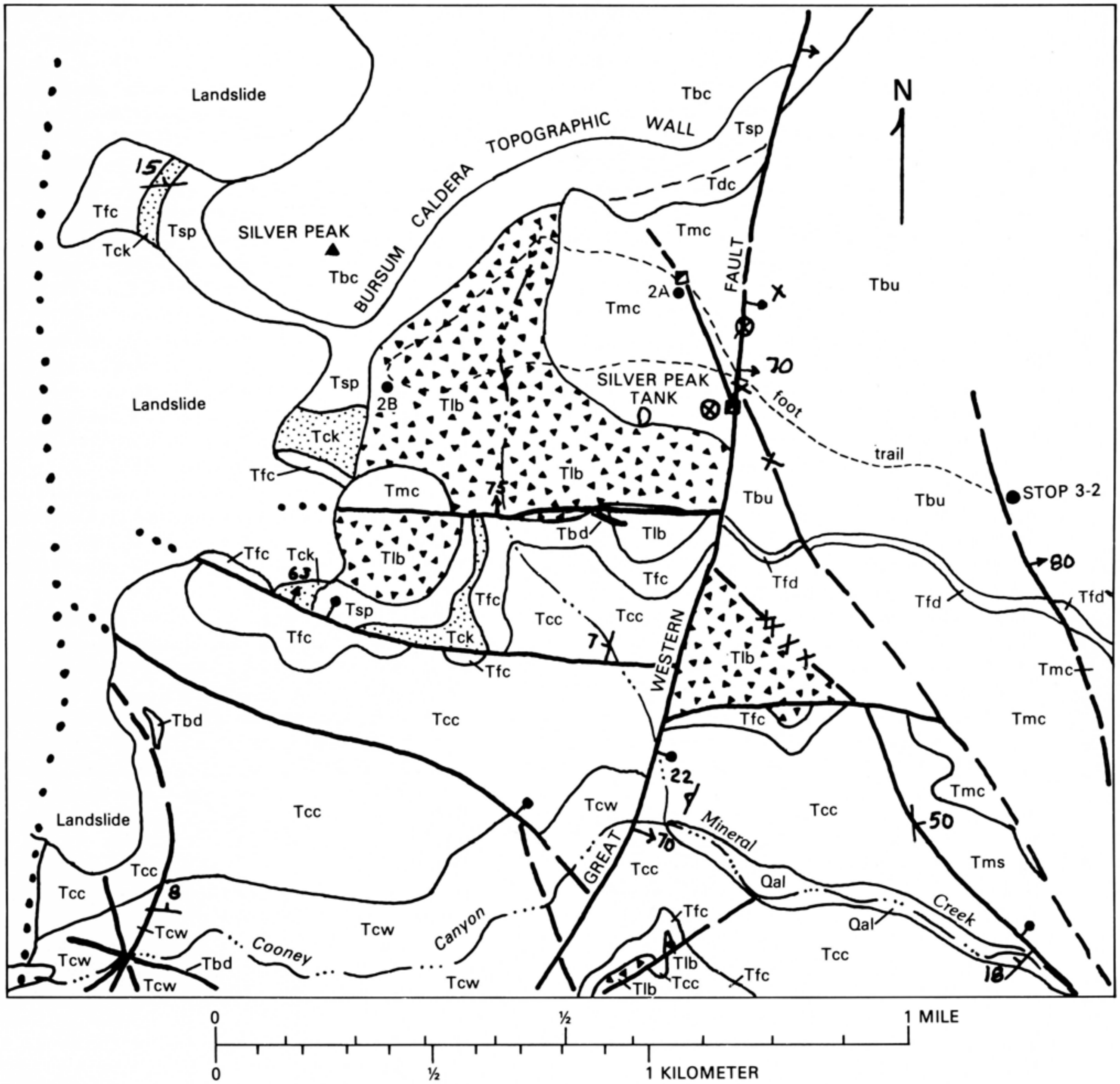

FIGURE 13—Geologic map of the topographic wall and moat of the Bursum caldera near Silver Peak, showing approximate route (foot trail) from Stop 3-2 to Silver Peak. Modified from Ratté (1981). X = prospect, circled X = several prospects, half-shaded square = shaft. Qal = Quaternary alluvium. **Moat-fill rocks:** Tbd = Andesite dikes; Tbu = post-Bursum caldera, Bearwallow Mountain Andesite, undivided; Tfd = Deadwood Gulch Member, Fanney Rhyolite; Tmc = Mineral Creek Andesite; Tms = volcaniclastic sandstone; Tlb = slide breccia from topographic caldera wall. **Pre-Bursum caldera rocks:** Tbc = Bloodgood Canyon Tuff; Tsp = Shelley Peak Tuff; Tdc = Davis Canyon Tuff; Tck = Cranktown Sandstone; Tfc = Fall Canyon Tuff, Cooney Tuff; Tcc = Cooney Canyon Member; Tcw = Whitewater Creek Member.

dera (Fig. 14). The moat andesites and associated sedimentary rocks extend from the topographic wall at Silver Peak to the resurgent dome about 10 km to the east on Mineral Creek, where the Apache Spring Tuff which fills the caldera is exposed (Fig. 15).

Between us and the topographic wall at Silver Peak, the Great Western fault (Fig. 13) cuts the moat deposits here, but on the south side of Cooney Canyon of Mineral Creek it appears to coincide with the topographic caldera wall. The Great Western fault dips 65–70° eastward toward the center of the Bursum caldera; it has a hanging wall of moat fill and a footwall of Cooney Tuff (~34 Ma). The Cooney Tuff is interpreted to be the fill within the older Mogollon caldera (Fig. 12), which is largely buried by younger deposits and exposed only along the range front of the Mogollon Mountains. In Cooney Canyon of Mineral Creek, on the western side of the Great Western fault, the Cooney Tuff consists of a lower thick, simple cooling unit of phenocryst-poor rhyolitic ash-flow tuff, the Whitewater Creek Member, which makes the slickrock cliffs that form the box in the lower part of the canyon. The Whitewater Creek Member is 200–300 m thick and its base is not exposed; its eruption is believed to have

FIGURE 14—Silver Peak segment of topographic wall of Bursum caldera. Aerial view from southeast above Mineral Creek.

caused the initial subsidence of the Mogollon caldera. Overlying the Whitewater Creek Member are multiple thin, varicolored ash-flow-tuff cooling units of more dacitic composition. These are interlayered with thin sedimentary beds that are interpreted as caldera fill deposited during episodic subsidence related to eruption of the Cooney Canyon Member of the Cooney Tuff.

On the north side of Mineral Creek and on the south slopes of Silver Peak, Cooney Tuff is overlain sequentially by Fall Canyon Tuff, Cranktown Sandstone, Shelley Peak Tuff, and Bloodgood Canyon Tuff, representing the complete sequence of pre-Bursum caldera rocks exposed in the caldera wall in this area (Fig. 13).

Within the moat, at the caldera wall on the east side of Silver Peak, slide breccias from the wall (map unit Tlb, Fig. 13) and moat-fill andesite (map unit Tmc, Fig. 13) overlie Fall Canyon Tuff and Cooney Tuff. Insofar as the precaldera ignimbrites and the moat-fill deposits are offset equally by the Great Western fault, it cannot be the structural caldera wall, which must be farther east, beyond the easternmost Cooney Tuff outcrops in Mineral Creek and closer to the Queen fault (Fig. 15).

From the parking place at Stop 3-2, take the trail west along the ridge crest to the prospect shaft in andesite west of the main Great Western fault (point 2A, Fig. 13). The trail is somewhat elusive, particularly on the east slopes of Silver Peak. Continue west across the contact between andesite and slide (moat) breccia, cross the shallow draw, and contour around on rubbly slopes of moat breccia to the caldera wall at about the 6800 ft level (point 2B, Fig. 13), where megabreccia blocks of Bloodgood Canyon Tuff are best exposed. Observe the attitudes of compaction foliation in the large, disoriented blocks of Bloodgood Canyon Tuff adjacent to the topographic wall (Fig. 16). Was the Bloodgood Canyon hot at the time it slid from the wall? Uniform paleomagnetic orientation of breccia clasts of Bloodgood Canyon Tuff at the eastern wall of the Bursum caldera at Hells Hole (Ratté and Gaskill, 1975; Ratté

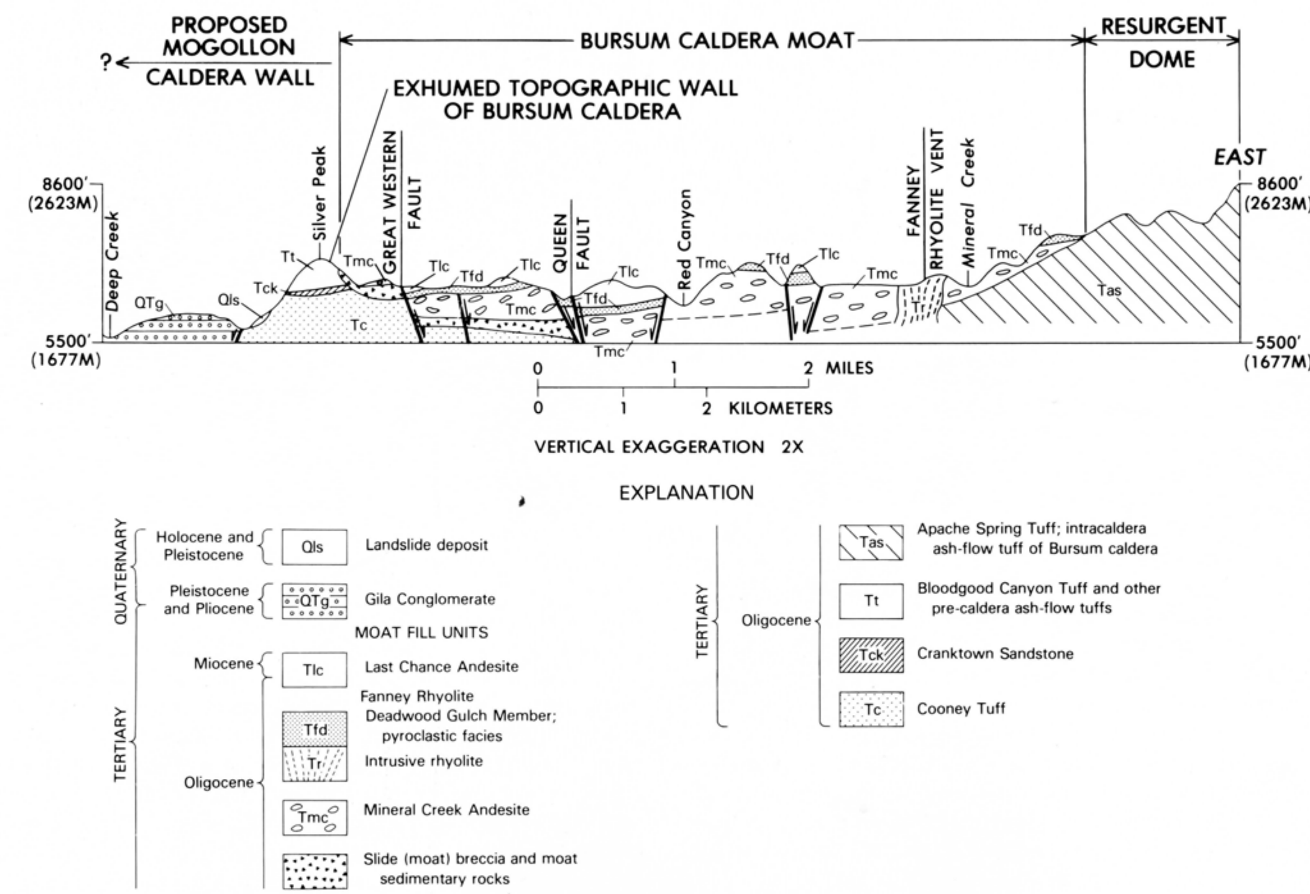

FIGURE 15—Cross section through Bursum caldera moat from Silver Peak to resurgent dome on Mineral Creek (modified from Ratté and Finnell, 1978, fig. 83.2c).

FIGURE 16—Slide-breccia blocks of Bloodgood Canyon Tuff on the topographic wall of the Bursum caldera at Silver Peak. Hammer head parallels healed contact between blocks with different orientation of compaction foliation (pencils) in densely welded tuff. There is a remarkable paucity of finely brecciated material along such contacts. Photo Earl Brooks.

et al., 1984) indicates that the Bloodgood Canyon Tuff in that part of the Bursum caldera wall was still above the Curie temperature when it slid into the caldera (W. C. McIntosh, oral comm. 1988). A similar study might be appropriate here.

Looking east from the upper slopes at the south end of Silver Peak, symmetrical, cone-shaped Cooney Peak can be seen at the inner edge of the moat on the north side of Mineral Creek, about 7 km east of Silver Peak. Cooney Peak is capped by a young basalt flow (whole-rock K–Ar age of 15 Ma, Marvin et al., 1987) and underlain by moat andesite and rhyolite. About 200 m of pyroclastic rocks (Deadwood Gulch Member of Fanney Rhyolite) are intruded by Fanney Rhyolite in a vent at the level of Mineral Creek (Fig. 15) beneath Cooney Peak.

If time permits, you may want to return to the cars by dropping directly down to the gulch east of point 2B and up the opposite slope toward Silver Peak Tank (Fig. 13), picking your own path between point 2B and the foot trail east of the Great Western fault. The moat breccia is more varied in composition south and west of Silver Peak Tank, where it contains blocks of Shelley Peak Tuff and Cranktown Sandstone as well as Bloodgood Canyon Tuff. Note particularly the absence of an ash-flow-tuff matrix to the moat breccia at this stop, which is in contrast to the caldera-fill breccia that we will see tomorrow.

Return to cars by 5 p.m. in order to assure arrival at Los Olmos Lodge in Glenwood by 6 p.m.

Backtrack the 14 mi to US-180. **14.0**

94.6 Turn left toward Glenwood. **3.3**

97.9 Alma is one of the earliest settlements in the region and the site of an Indian massacre in 1883, at which time Sgt. Cooney, who discovered the Mogollon mining district, was killed in the defense of the settlement. Only after the Apache chief Geronimo and his followers were driven from the area in 1885 was the mining industry able to develop.

Alma is also the site of the W.S. Ranch (see sign on west (right) side of highway north of Alma), which was the locale of a western history classic *Recollections of a Western Ranchman* by an adventurous English gentleman Captain William French. His two-volume account of the early days in southwestern New Mexico is enhanced by his British style and viewpoint (French, 1965a, b).

Along the San Francisco River, behind Alma to the west, low ledges of 5.6 Ma tholeiitic basalt of Harve Gulch are visible interlayered in the Gila Group. Looming ahead on the right, as we go through Alma, is "Glenwood" Brushy Mountain (at about 1:00), as distinguished from several other Brushy Mountains in the area. It is another Bearwallow Mountain Andesite volcano along the N50–60E Morenci lineament. **1.1**

99.0 Junction with NM-78 on left, to Mogollon and the Mogollon mining district. Other segments of the Bursum caldera topographic wall, like that at Silver Peak, are silhouetted on the skyline to the east, particularly at the gunsight notch across Silver Creek Canyon (Fig. 17). **0.8**

99.8 US-180 crosses Harve Gulch, type locality for 5.6 Ma basalt of Harve Gulch, which crops out along gulch below the highway to the west. **2.6**

102.4 Los Olmos Lodge on left, at north end of Glenwood. Excellent exposures of fanglomerates of Gila Group in roadcuts along winding descent into Glenwood.

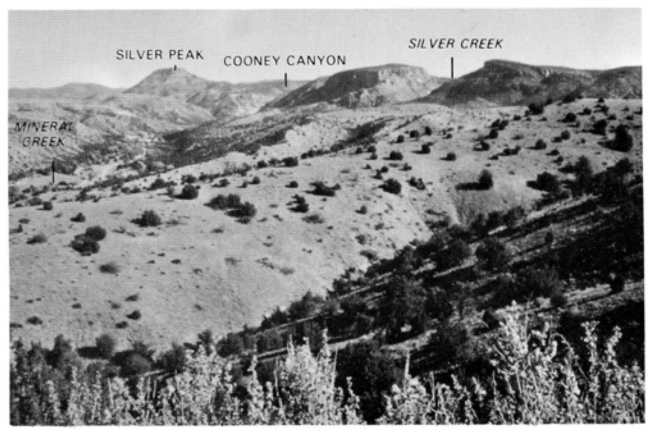

FIGURE 17—North end of Mogollon Mountains and Mogollon mining district viewed northeast from Whitewater Mesa. East-facing scarps between Silver Peak and south side of Silver Creek mark exhumed segments of the Bursum caldera topographic wall.

Time permitting and bodies willing, there may be transportation available after dinner for those who would enjoy a stroll between spectacular cliffs of Cooney Tuff at the Catwalk, a major tourist attraction in this area, about 5 mi from Los Olmos Lodge. The Catwalk trail follows an old flume along the walls of Whitewater Creek Canyon. The flume was constructed to carry water from the forks of Whitewater Creek, about 2 mi above the canyon mouth, to the original mill site for the Mogollon district at Graham, near the canyon mouth. The narrow gorge with its tumbling cataracts and deep, quiet pools and cheery calls of the canyon wren, offers a cool respite after a hot day. It is not uncommon to see Rocky Mountain sheep coming to drink in the evening, and, if inclined, one can sneak a closeup look at the intracaldera Cooney Tuff and interlayered sediments.

Day 4: Bursum caldera: Caldera-fill megabreccia and post-caldera magmatism at the western caldera margin in the Mogollon mining district

Mileage

0.0 Leave Los Olmos Lodge and turn right on US-180, retracing our route of last night. **3.4**

3.4 Turn right onto Bursum Road (NM-78) toward Mogollon. Road climbs up to Whitewater Mesa, past roadcuts in conglomerates of Gila Group, and provides views of the Mogollon mining district section of the Mogollon Mountains. Silver Peak, on the topographic caldera wall (Stop 3-2), can be seen at the north end of the range front. Farther south along the front, the prominent notch at the canyon of Silver Creek marks another segment of the east-facing scarp that is the topographic wall of the Bursum caldera. **3.0**

6.4 Topping out on Whitewater Mesa, view at about 12:00 is looking up the canyon of Whitewater Creek. Canyon walls are Cooney Tuff, within the proposed Mogollon caldera. Cliffs high on the north side of the canyon, on left, are intrusive Fanney Rhyolite, a partly unroofed laccolith, along the Bursum caldera ring-fracture zone. The continuation of the Bursum caldera topographic wall is along the east face of the low ridge at the head of the mesa, on the north side of Whitewater Canyon.

At head of mesa, road turns north, parallel to the range front. **Dangerous narrow road with sharp curves ahead.** The roadcuts along the range front are in wallrocks of the Bursum caldera. The road crosses through these older rocks into the highly faulted caldera moat, which is filled mainly with Mineral Creek Andesite (Fig. 18). **2.6**

9.0 **STOP 4-1. Intraeruption caldera-fill breccias**

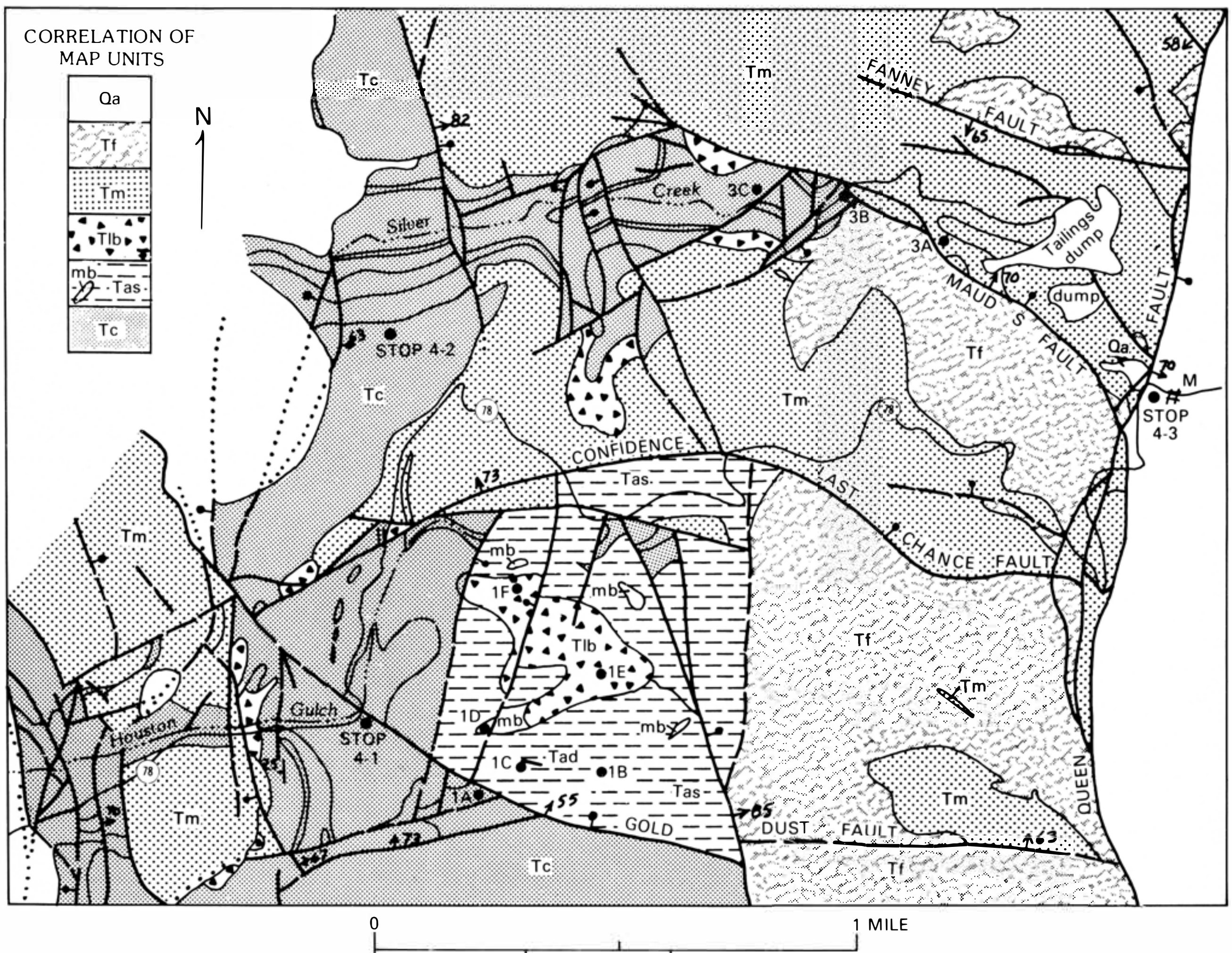

FIGURE 18—Generalized geologic map of the Bursum caldera moat in the southwestern part of the Mogollon (M) mining district, showing the location of Stops 4-1, 2 and 3; also shows points 1A to 1F (Stop 4-1) and points 3A, B, and C (Stop 4-3) discussed in text. Patterned map units are superimposed on the more detailed geologic contacts and unlabeled map units as modified slightly from Ratté (1981). Qa = Quaternary alluvium and landslide. **Miocene and (or) Oligocene rocks:** Tf = Fanney Rhyolite; Tm = moat deposits, mainly Mineral Creek Andesite and associated volcaniclastic sedimentary rocks; Tlb = moat and (or) caldera-fill breccia; Tas = Apache Spring Tuff caldera fill with megabreccia blocks, *mb;* Tc = caldera wall sequence of pre-Bursum caldera ash-flow tuffs and volcaniclastic sedimentary rocks; includes Cooney Tuff, Cranktown Sandstone, and Fall Canyon, Davis Canyon, Shelley Peak, and Bloodgood Canyon Tuffs.

versus posteruption moat breccias. Pull off to the right before the bridge across Houston Gulch and park for STOP 4-1. The problem here is to distinguish intraeruption caldera-fill breccia from post-collapse moat breccias formed by gravity slides off the topographic wall, in order to establish the position of the caldera structural wall. At Silver Peak, we saw moat breccias where breccia clasts and matrix both consist of material derived from the caldera wall. Here we will see breccias in which the clasts are of older rocks from the caldera wall, but the matrix consists of quartz-bearing Apache Spring Tuff, thus defining what is mapped as caldera-fill breccia. Caldera-fill breccia contains clasts that range from lapilli size to slabs of mappable proportions, i.e. megabreccia (Fig. 18). Because of the mineralogical and textural similarity of Bloodgood Canyon Tuff in the caldera wall and intracaldera Apache Spring Tuff, distinguishing megabreccia or disaggregated blocks of Bloodgood Canyon Tuff from matix can also be a problem.

The main structural wall of the Bursum caldera, as mentioned at Stop 3-2, is believed to be at the Queen fault, 1–2 km east of here (Fig. 18). This is based on the distribution of Cooney Tuff at the surface and at shallow depths of a few hundred meters, as indicated by mining exploration along the Queen fault. Thus, the presence of caldera-fill breccia west of the main structural wall, as at Stop 4-1, indicates either that the structural wall is not a single fault but a stepped-down-to-the-east structural zone at least 1–2 km wide, or the caldera-fill megabreccia west of the structural wall was produced by calving of the structural wall while eruption and subsidence were in progress (Fig. 19). In effect this produced an early, intraeruption, preresurgence topographic wall, as distinguished from the postresurgence topographic wall.

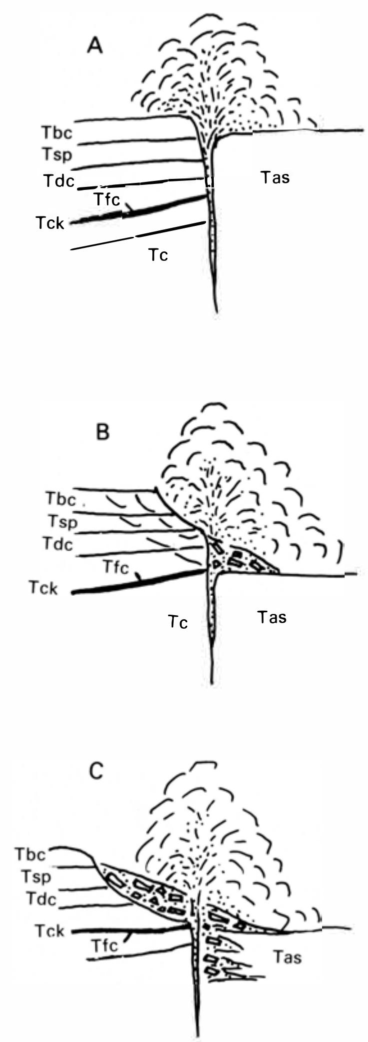

FIGURE 19—Diagrammatic sketch showing development of caldera-fill breccia in Houston Gulch area. **A,** Early stage of Apache Spring Tuff eruptions and concurrent caldera collapse. **B,** Initial calving of caldera structural wall. **C,** Caldera-fill breccia overlaps caldera structural wall onto *pre-resurgent* topographic wall. Tas = Apache Spring Tuff, Tfc = Fall Canyon Tuff, Tck = Cranktown Sandstone, Tdc = David Canyon Tuff, Tsp = Shelley Peak Tuff, Tbc = Bloodgood Canyon Tuff.

Time does not permit a thorough examination of the relationships here, which are complicated by the superimposed faulting and alteration associated with mineralization in the Mogollon district. However, the traverse from Stop 4-1 is offered as a sample of some of the complexities at a caldera margin.

Climb about 150 m east of the parking area to the low saddle in dark porphyritic andesite, thought to be a sill of moat andesite (Mineral Creek Andesite) within Cranktown Sandstone on the caldera wall. Contour around the slope to east, about 300 m to point 1A (Fig. 18), where a northwest-trending fault separates pre-Bursum caldera Cooney Tuff on the south side of the fault from Apache Spring Tuff within the Bursum caldera on the north side. Cooney Tuff on the south side of the fault at point 1A looks superficially like the Apache Spring Tuff on the north side; both have biotite and feldspar phenocrysts, but Apache Spring Tuff contains round quartz phenocrysts, which are absent in the more quartz latitic Cooney Tuff.

Continue contouring around the slope toward a low waterfall on Gold Dust Gulch, about 300 m farther east at point 1B (Fig. 18), where Apache Spring Tuff contains megabreccia blocks of pre-Bursum Davis Canyon Tuff as much as 10 m long. Davis Canyon Tuff is a phenocryst-poor, high-silica rhyolite that characteristically contains highly flattened pumice lapilli in a fine-grained vitroclastic matrix. The pumice here is white as a result of argillic alteration associated with mineralization in the Mogollon mining district.

From point 1B, traverse gradually back upslope and westward to point 1C along a pink ledge of shaly weathering Apache Spring Tuff, which contains abundant lithic inclusions, mainly of Davis Canyon Tuff, and is cut by an andesite dike at point 1C. Then climb up to the base of a large Davis Canyon Tuff megabreccia slab showing contact with underlying, but younger, Apache Spring Tuff. There appears to be a bit of reworked material at the contact here and also to west about 10 m above the end of the fence that is tied to a dead juniper tree. Red Cooney Tuff is also present as inclusions in Apache Spring Tuff beneath the Davis Canyon Tuff megabreccia.

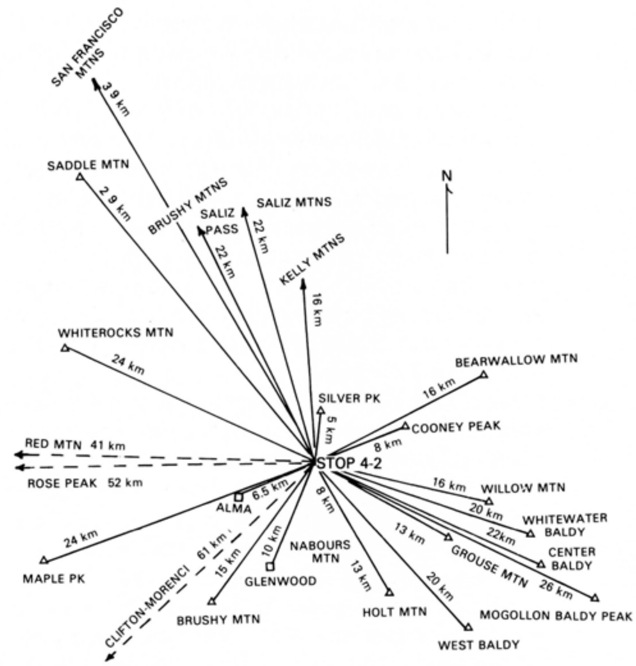

FIGURE 20—Panoramic location diagram for Mogollon area from Stop 4-2.

Now cross a north–south fault into the highly shattered quartz-rich tuff at point 1D. Traverse around the base of this outcrop and climb up through it, noting its resemblance to the topographic-wall breccia of Bloodgood Canyon Tuff seen at Stop 3-2 yesterday at Silver Peak. There is some uncertainty whether this is Bloodgood Canyon Tuff slide breccia from the topographic wall, or Apache Spring Tuff. Where the rocks are as highly altered as they are here, distinguishing Bloodgood Canyon from Apache Spring Tuff can be difficult, but the lack of appreciable biotite in this rock and absence of abundant lithic inclusions favor Bloodgood Canyon Tuff.

From point 1D at the top of this quartz-phyric breccia, traverse up the nose to the northeast to point 1E. The breccia above Davis Canyon Tuff, to top of ridge, was mapped as slide breccia from the topographic wall (map unit T1b, Fig. 18), but this call is open to question because the breccia seems to have a quartz-bearing matrix locally, which is diagnostic of the intracaldera breccia. However, toward the top of the ridge, the breccia seems to lack the tuff matrix, and thus both types of breccia may be present here. Shelley Peak Tuff, also common as breccia blocks here, is a reddish-white, phenocryst-rich welded tuff similar in color and mineralogy to Cooney Tuff. Shelley Peak phenocrysts are generally 3–4 mm long, whereas those in Cooney Tuff generally have dimensions of only 1–2 mm.

From point 1E, traverse northwest along the ridge crest about 300 m, then downslope to the north, to the cliffs overlooking Houston Gulch at point 1F. From point 1F, we have a view of the Bursum caldera topographic wall south of Silver Creek, as viewed to the northwest across the Confidence–Last Chance fault, one of the major mineralized structures in the Mogollon district (Fig. 18). On the skyline ridge, west of the road in Houston Gulch, Bloodgood Canyon Tuff in the topographic caldera wall is overlapped by moat deposits of Mineral Creek Andesite and moat sediments and breccias. At point 1F, we must be just inside the structural caldera wall, as modified by slumping during eruption and subsidence.

From point 1F move to east into Apache Spring Tuff, climb down to the dam with the silted-up pond on Houston Gulch and observe the large megabreccia blocks of Davis Canyon Tuff on both sides of the canyon below the dam. **Watch for rattlesnakes.** Return to cars, about 0.75 mi down Houston Gulch. Then continue on road toward Mogollon. **1.0**

10.0 Jeep trail on left. We will proceed on the jeep trail from this road junction to a parking area about 0.25 mi north and then, taking lunches with us, climb to the top of the topographic caldera wall for an overlook into Silver Creek and along the topographic wall to the north.

STOP 4-2. Lunch on topographic wall overlooking Silver Creek (Fig. 18). From the ridge top at Stop 4-2, the following features can be observed on a reasonably clear day (Fig. 20). Starting to the north at Silver Peak (Stop 3-2) and moving westward (counterclockwise) the Kelley, Saliz, Brushy, and San Francisco Mountains (Fig. 12) are the tilted, block-faulted ranges in the Reserve graben which we drove through yesterday. Saddle Mountain, at about 11:00, is a hornblende–pyroxene andesite composite volcano (~33 Ma), one of the source volcanoes of the precaldera, calc-alkaline suite in this part of the Mogollon–Datil field. Whiterocks Mountain at 10:00, on the New Mexico–Arizona state line, consists of Davis Canyon, Shelley Peak, and Bloodgood Canyon Tuffs overlain by Bearwallow Mountain Andesite. At about 9:00 on a *really* clear day one can see Red Mountain and Rose Peak on the western horizon, about 41 km and 52 km away, respectively. Rose Peak is another andesitic to basaltic volcano of Bearwallow Mountain age; Red Mountain is a rhyolite center (~21 Ma; Ratté et al., 1969). Maple Peak at about 8:00 and "Glenwood" Brushy Mountain at 6:30 are also Bearwallow Mountain Andesite volcanoes; "Glenwood" Brushy is underlain by a rhyolite dome with flows and associated pyroclastic deposits, and is much like the ring-fracture Fanney Rhyolite in both age and composition. Between Maple Peak and "Glenwood" Brushy, at about 7:00, one used to be able to see the smelter plume at Clifton–Morenci (about 61 km), a world-class porphyry copper deposit of Laramide age at the southwest end of the Morenci–Reserve fault zone. However, the smelter operations were recently moved south, near the Mexican border. Southeast of us are the high peaks of the Mogollon Range along the ring-fracture zone and on the resurgent dome of the Bursum caldera, largely blocked from our view by intervening topography. Cooney Peak, at about 2:15, at the inner edge of the Bursum caldera moat, is mainly rhyolite pyroclastics above a Fanney Rhyolite vent, capped by Last Chance Andesite, volcaniclastic sediments, and a ~15 Ma basalt flow. Bearwallow Mountain, at

2:00, is the type locality of the Bearwallow Mountain Andesite and is close to the projected northern, buried margin of the Bursum caldera.

Return to the Mogollon road (NM-78). **0.1**

10.1 Cross the Confidence–Last Chance fault and pass from Mineral Creek Andesite into caldera-fill breccia. For the next 0.5 mi, large red blocks of Cooney Tuff can be seen surrounded by a white matrix of quartz-bearing Apache Spring Tuff. **0.2**

10.3 Forest Service road 722 to right; large trash burner to left. Starting here, excellent views of eastward-facing segments of the Bursum caldera topographic wall. **0.3**

10.6 Shaft on the left is at the intersection of the east–west Confidence–Last Chance fault and the north–south Pacific fault. Cross the Confidence–Last Chance fault again at the sharp curve to the right. **0.8**

11.4 Another sharp bend to the right brings the tailings dump at the Little Fanney mine across Silver Creek into view (Fig. 18). Production from the Mogollon district is on the order of 300,000–400,000 oz. gold, 15 million oz. silver, 500 tons copper, and 10 tons lead. The mines were closed by the government during World War II and have never really recovered. However, exploration has intensified in the last few years, with drilling concentrated in the largely unexplored hanging wall of the Queen fault.

Mineralization is dated as about 16–18 Ma, based on vein adularia. A rectilinear "ladder and box" fault pattern (Steven, 1989) is unique to the district, in this area, and probably indicates an intrusion beneath the district that is likely to be related to mineralization. The 10 m.y. gap between caldera-related volcanism (28 Ma) and mineralization (~16–18 Ma) suggests that mineralization accompanied early basin and range extension and related magmatism and that its association with the Bursum caldera is one of structural accommodation with no dependence on caldera-related magmatism.

For the next 0.5 mi the road is close to the upper contact of the Fanney Rhyolite and its roof of Mineral Creek Andesite. **0.5**

11.9 Sharp switchback to left; road follows Deadwood Gulch along branching trace of Queen fault. **0.3**

12.2 Dirt road on right, up South Fork of Silver Creek; outcrops of layered, pyroclastic Deadwood Gulch Member of Fanney Rhyolite. Eberle mine, on left, is site of recent small-scale mining along Queen fault. **0.2**

12.4 Road turns sharply right, up Silver Creek, into town of Mogollon. Quartz-filled Queen vein is exposed in bank across creek. Park immediately before first buildings on right.

STOP 4-3. Intrusive relationships of ring-fracture Fanney Rhyolite in caldera moat. From the parking area, we will walk down Silver Creek about 1.5 km to the outer structural(?) wall of the Bursum caldera. However, the main purpose of this stop is to examine the intrusive character of the ring-fracture rhyolite (Fanney Rhyolite) in the caldera moat as exposed in this canyon.

The Fanney Rhyolite in the Mogollon district, as seen in surface exposures and encountered in underground workings and exploratory drill holes, forms an extensive tabular body that is rather uniformly 100–200 m thick in most places (Ferguson, 1927; Ratté, 1981). Originally considered to be domal extrusive flows (Ferguson, 1927: 14–16), much of the Fanney is now recognized as having been intruded beneath a cover of Mineral Creek Andesite (Ratté and Finnell, 1978; Ratté, 1981). Locally, the rhyolite does thicken substantially to as much as 350 m south of the Gold Dust fault (Fig. 18) and ~300 m north of Fanney Hill, where these local domal or laccolithic bulges in the roof of the intrusion are interpreted to be above feeder vents, as shown in cross section C-C′ of Ratté (1981). Elsewhere, as east of the Queen fault, Fanney Rhyolite is known to have vented to the surface and produced the voluminous tuff breccia and partially welded ash flows of the Deadwood Gulch Member of Fanney Rhyolite.

About 150 m down Silver Creek, the Maud S fault, on the south side of the Silver Creek graben, drops Mineral Creek Andesite on the north side of the fault down about 150 m against Fanney Rhyolite. Fanney Rhyolite is typically high-silica, nearly aphyric, spherulitic rhyolite. Continue down canyon in altered (silicified and argillized) Fanney Rhyolite in the footwall of the Maud S fault, then cross into the Mineral Creek Andesite hanging wall at the toe of the Fanney tailings dump. Intrusive features (Fig. 21) at the contact between Fanney Rhyolite and Mineral Creek Andesite and associated moat sedimentary rocks are well displayed on both sides of the canyon near point 3A (Fig. 18), but are probably best seen on the north side of the canyon, west of the tailings dump, where the contact is more extensively exposed.

After examining the intrusive relationships, continue down canyon to point 3B, about 500 m beyond the tailings dump, where the canyon boxes up at a low waterfall and turns sharply southwest (left) back into the footwall of the Maud S fault. For about the next 300 m, the rocks are a somewhat enigmatic mixture of silicified ash-flow-tuff units, which have been interpreted previously as a megabreccia of rocks from the Bursum caldera wall in a matrix of Apache

FIGURE 21—Intrusive contacts between Fanney Rhyolite and volcaniclastic sandstone at base of Mineral Creek Andesite near Deep Down mine on north side of Silver Creek below Mogollon. Tf = Fanney Rhyolite, Tms = volcaniclastic sandstone.

Spring Tuff within the caldera (Ratté, 1981). Note what appear to be quartz phenocryst-free blocks (Shelley Peak Tuff?) in a silicified quartz-bearing matrix (Apache Spring Tuff?). This is what led to the interpretation of a structural wall here. However, an alternative explanation, that these rocks are pervasively faulted and tectonically mixed units of the caldera wall, is favored now. Although positive identification of the altered rocks at point 3B is difficult, particularly the distinction of Bloodgood Canyon Tuff of the caldera wall from intracaldera Apache Spring Tuff, sufficient stratigraphic relationships can be pieced together to suggest that this is not the structural wall.

This alternative hypothesis is supported by several lines of evidence. Most convincing, perhaps, is the distribution of precaldera Cooney Tuff. North of Silver Creek, in Cooney Canyon (Fig. 13), rocks of the Bursum caldera wall, particularly Cooney Tuff, are exposed beneath moat deposits to within less than 1 km from the Queen fault, and Cooney Tuff has been identified in drillcore and in underground workings at relatively shallow levels of a few hundred meters in the footwall near and *at* the Queen fault, north of Mogollon.

Continuing down canyon from point 3B, we cross into a series of fault blocks in which the tuff sequence, from Davis Canyon Tuff in the canyon bottom through 10–15 m of Shelley Peak Tuff and about 30 m of Bloodgood Canyon Tuff, seems to be more straightforward. Finally, the fault at point 3C brings up a block of Cranktown Sandstone with a thin, white, interbedded layer of Fall Canyon Tuff, and there is no doubt that we are in the Bursum caldera wall.

Return up canyon to cars and retrace route to US-180. **9.0**

21.4 Turn left on US-180 and return to Glenwood. **3.7**

25.1 Bridge across Whitewater Creek in Glenwood. "Glenwood" Brushy Mountain is at 2:00. The light-colored pyroclastics on lower slopes, seen from south edge of town, are part of a rhyolite dome that underlies northeast flank of the andesite volcano.

Continue south through Pleasanton. Roadcuts and exposures close to highway are mainly fanglomerates of Gila Group. Mogollon Mountains east of highway constitute the resurgent dome of Bursum caldera; ring-fracture rhyolites dominate the range front, and precaldera rocks are present only in the lower slopes, where they are overlapped along northwest-trending range-front faults by Gila Group. **12.0**

37.1 Mileage marker 60. Cross Big Dry Creek. **1.0**

38.1 **STOP 4-4. Leopold Vista.** Pull off highway into parking area on left. A plaque on the stone monument here honors Aldo Leopold, a U.S. Forest Service official and dedicated conservationist, who was largely responsible for establishment of the Gila Wilderness, in 1924, as the first area administered as wilderness in the United States. Most of the 25 × 40 km Bursum caldera is within the Gila Wilderness.

Using the panoramic photograph displayed at Leopold Vista as a location guide, the following geologic features can be seen. The wall of the Bursum caldera, from left to right, traces across the lower third of the slopes on Nabours and Holt Mountains and through Sheridan Mountain, which all are manifestations of intrusive and extrusive ring-fracture-related postcaldera rhyolite volcanism. The caldera wall continues eastward across Big Dry Creek in front of Crown Mountain and beneath Haystack Mountain, which is a ring-fracture rhyolite dike, and up Mogollon Creek, which is the low area to left of 74 Mountain and Shelley Peak. Shelley Peak is the type locality for Shelley Peak Tuff; 74 Mountain is a rhyolite dome. Sacaton Mountain and Mogollon Baldy Peak mark the top of the resurgent dome of the caldera (Ratté and Gaskill, 1975), although Mogollon Baldy is capped by post-resurgence Bearwallow Mountain Andesite.

Upon leaving Leopold Vista, our attention is directed to the northwest–southeast Mangas trench (Trauger, 1972), which we will follow most of the way to Silver City. This graben defines the southwestern edge of the Mogollon Plateau (Elston, 1965), much as the Reserve graben and the San Agustin Plains define its northwestern edge. The graben is bounded on the northeast by the Mogollon fault zone (Leopoldt, 1981), along the front of the Mogollon Mountains, where the cumulative throw is about 2000 m. Recurrent movement along this zone dates from Laramide time to latest Pliocene or Pleistocene; the faults are basically extensional, dip–slip faults, but oblique lateral movement has occurred at various times according to Leopoldt (1981). **4.0**

42.1 Junction of US-180 with NM-78 on right. Low hills west of highway consist of Bloodgood Canyon Tuff and rhyolite of Mule Creek (~17 Ma) (Ratté and Brooks, 1983). We are now within Pliocene and Pleistocene Buckhorn lake in the Mangas graben. **7.0**

49.1 Bloodgood Canyon Tuff crops out on right, west side of highway, at mileage marker 72. White layers in roadcuts and other exposures ahead are lake beds that include diatomite layers and vitric-ash beds, which are zeolitized locally and have been mined on a small scale where nearly pure clinoptilolite forms beds as much as 90 cm thick (Sheppard and Gude, 1987). The zeolitized tuffs also contain pellets and ooids of sedimentary fluorite to as much as 20–30% of the tuff (Sheppard and Mumpton, 1984); in addition, the lake beds contain Magadi-type chert (Sheppard and Gude, 1987) and anomalous lithium (Tourtelot and Meier, 1976). **5.0**

54.1 Mileage marker 77; approaching side road on right to zeolite pit. Continue on US-180 through Cliff to Silver City. Our route continues to follow the Mangas graben southeast from Cliff for about 16 mi. The roadcuts are mostly mid-Tertiary volcanic rocks from the Schoolhouse Mountain caldera complex to the south (Wahl, 1980), and from the volcanic complex of the Tadpole Ridge–Reading Mountain area (Drewes et al., 1985; Finnell, 1976a, b, 1982, 1987). **22.0**

76.1 Mileage marker 99. Approaching junction, about 0.5 mi ahead on right, to Tyrone. US-180 leaves valley of Mangas Creek here and turns east through roadcuts in fanglomerates of the Gila Group. At the Silver City fault zone, about 1 mi west of Silver City, we cross out of Gila Group into Paleozoic rocks, which are host to manganese and silver deposits in Silver City district (Cunningham, 1974). Continue through Silver City to Holiday Motel at east edge of town, on right side of US-180 and NM-90 on the way to Central.

Day 5: Field guide to the Emory caldera along NM-152 and in Tierra Blanca Canyon

Wolfgang E. Elston

Summary

Day 5 covers the geology of the Emory caldera, one of the largest and best exposed Valles-type resurgent ash-flow-tuff (ignimbrite) calderas discovered to date (Fig. 1). We will examine: (1) various facies of the principal eruptive product, Kneeling Nun Tuff, including outflow sheet, caldera-fill deposits, and intracaldera megabreccias; (2) rhyolite lava domes, flows, and associated pyroclastic flows of the Mimbres Peak Formation, interpreted as ring-fracture and moat deposits; (3) deformed and metamorphosed Paleozoic sedimentary rocks below the caldera's floor, above and adjacent to the subcaldera pluton; and (4) the relationship of volcanic rocks and their cognate inclusions to underlying intrusions. Block faulting and erosion provide unusual opportunities for examining the interior of the Emory caldera in three dimensions, down to its plutonic roots.

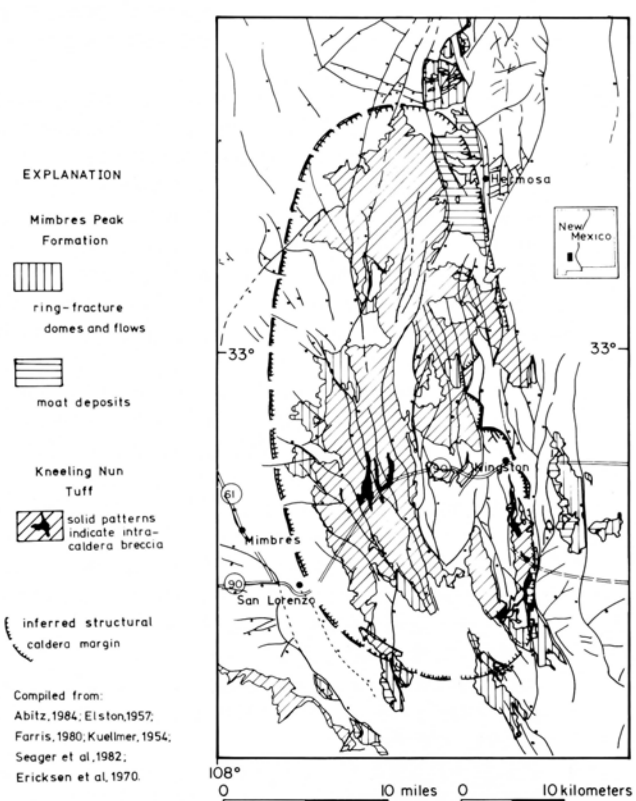

FIGURE 1—Geologic sketch map of the Emory caldera.

The stratigraphic column of the Emory caldera region is shown in Fig. 2. Mid-Tertiary volcanism began about 38 Ma, with eruption of andesite and latite lavas of the Rubio Peak Formation (T2a) followed by deposition of tuffaceous volcaniclastic sediments and pyroclastic flows of the Sugarlump Formation. The rocks of the Emory caldera suite are high-Ca rhyolite (quartz latite) of stage T3r. The steps in the formation of the Emory caldera are shown in Fig. 3. Eruption of Kneeling Nun Tuff, about 35.3 Ma ($^{40}Ar/^{39}Ar$ age, McIntosh et al., 1986), led to collapse of an elliptical 55 × 25 km caldera, elongated north–south, parallel to the Rio Grande rift (Fig. 1). It seems likely that the northern and southern segments of the Emory caldera collapsed separately, to form a double caldera, dumbbell-shaped in plan (Abitz, 1986). The exact structural and temporal relationships of the northern and southern segments have not yet been worked out, but the gross petrography of the rocks is similar. The present excursion deals entirely with the southern end.

Resurgence lifted the caldera into a dome with north–south elongation. This dome makes up the entire southern half of the Black Range and is transected by a horst instead of the more usual graben. Following resurgence, the caldera was enlarged by erosion. Lava domes of the Mimbres Peak Formation erupted in many places along concentric ring-fracture faults within the caldera and on the flanks of the volcano. Most lavas were preceded by pyroclastic flows, which partly filled the moat between the resurgent dome and the topographic caldera wall. The volcano was then progressively buried by ignimbrite and andesite from other sources.

During Miocene time, many of the faults associated with caldera collapse were reactivated in the course of normal faulting that resulted in the present topography of the Basin and Range province and Rio Grande rift. Movement, in the same sense as during caldera collapse, resulted in about 75% of present fault displacement. Today, dips of Kneeling Nun Tuff within the resurgent dome average about 40°, away from the dome axis. As post-resurgence rocks dip around 30°, the dips immediately after resurgence must have been about 10°. A negative Bouguer anomaly of about −30 mgals indicates the extent of the underlying pluton (Fig. 4). Late Cenozoic erosion has locally uncovered the caldera floor within the central horst.

The original volume of Kneeling Nun Tuff is unknown. The present outflow sheet extends about 100 km east–west

Age	Rock Unit	Lithology & Absolute Dates	Thickness (ft)	Description
Miocene-Pleistocene	Gila-Santa Fe strata	6.5my, <0.5my	0-2000	Brown fanglomerate with few interbedded basalt flows.
				unconformity
Oligocene	Swartz Rhyolite	27.3 my	75	Gray flow-banded rhyolite
Oligocene	Bear Springs Basalt		0-650	Basaltic andesite, gray to black, vesicular flows, red-brown iddingsite grains; contains interbedded brown sandstone and conglomerate.
Oligocene	Razorback Fm.		300-800	Lower black to dark-gray fine-grained andesite and upper dark-gray to black rhyolite; rhyolite is often glassy, contains spherulites; air-fall and epiclastic tuff and breccia is interbedded.
Oligocene	Piloncillo sediments		0-500	Tan to brown sandstone, fanglomerate; may include lake beds near Hillsboro.
				unconformity
Oligocene	Caballo Blanco Rhyolite	31.6my	0-300	Pumiceous crystal tuff; doubly terminated quartz crystals.
Oligocene	Rustler Basalt		50	
Oligocene	Box Canyon Rhyolite 33.5*		75	Massive porphyritic ignimbrite
				unconformity
Oligocene	Mimbres Peak Fm. 34.5*; flow-banded rhyolite; Pollack quartz latite		0-1000	"Moat" deposits and domes associated with Emory cauldron. Rhyolitic to latitic air-fall tuff and breccia, talus breccia, and associated epiclastic rocks; lesser amounts of interbedded ash-flow tuff and vitrophyre unit includes numerous intrusive-extrusive flow-banded rhyolite complexes near the margin of Emory cauldron and locally contains dark-colored, fine-grained andesite flows. Pollack Quartz Latite is a porphyritic, dark to medium-colored siliceous rock occurring as domes and flows within and adjacent to Emory cauldron.
Oligocene	Kneeling Nun Tuff; rhyolite porphyry	34.8*my	0-3000	Crystal-vitric ash-flow tuff, pale tan to pale red; abundant sanidine and quartz and large pumice lumps; multiple-flow, compound cooling unit; very thick in Emory cauldron (cauldron facies, generally > 1000 ft thick); generally less than 500 ft thick in outflow facies.
				unconformity (?)
Late Eocene-early Oligocene	Sugarlump Tuff; Rubio Peak Fm.; quartz monzonite porphyry	35.1my	0-5000	Mostly andesitic to latitic laharic breccia, sandstone and siltstone, generally pale purple, grayish-purple, greenish-gray, or various shades of maroon; tuffaceous; some air-fall tuff beds, and andesitic to latitic flows. Flows and breccia clasts are mostly porphyritic types with hornblende and plagioclase phenocrysts. Abundant zeolitic alteration of tuffaceous beds.
				unconformity
Late Cretaceous	Andesite of Copper Flat; quartz monzonite of Copper Flat	75.1my	1000+	Andesite and andesite porphyry flows, generally dark gray to purplish-gray; probably contains laharic and other strata of epiclastic origin that are poorly exposed.
				unconformity
Permian	Abo Fm.		700	Sandstone, siltstone and shale, red to red-brown.
Pennsylvanian	Magdalena Group		650	Limestone, gray, fine-grained, sparse to abundant chert in different beds; fossiliferous; and green to black shale and shaly limestone; minor limestone pebble conglomerate; cyclic repetition of lithologies.
Mississippian	Lake Valley Fm.		140	Limestone, gray to black, cherty, locally very fossiliferous.
Devonian	Percha Shale		148	Shale, green to black, fissile, and yellow calcareous siltstone.
Silurian	Fusselman Fm.		85	Dolomite, fine-grained, massive, minor chert.
Ordovician	Montoya Fm.		161	Limestone and dolomite, gray to black with middle cherty member, basal sandstone.
Ordovician	El Paso Ls.		280	Limestone, gray, fine-grained, slably to massive, yellow-brown siliceous streaks and laminae.
Cambro-Ordovician	Bliss Fm.		100	Sandstone, hematitic, glauconitic; shale, green, glauconitic; minor gray to black limestone.
				unconformity
Precambrian				Graywacke, granite, metadiabase.

NOTE: Section compiled from: Kuellmer 1954, Geologic section of the Black Range at Kingston, N.M.: N.M. Bur. Mines Bull. 33, and Elston, 1957, Geology of Dwyer Quad: N.M. Bur. Mines Bull. 38.

FIGURE 2—Composite stratigraphic column of the Emory caldera region, compiled by W. R. Seager (*in* Elston et al., 1975). K–Ar ages adjusted for new IUGS constants and partly replaced by $^{40}Ar/^{39}Ar$ ages* (McIntosh, this volume).

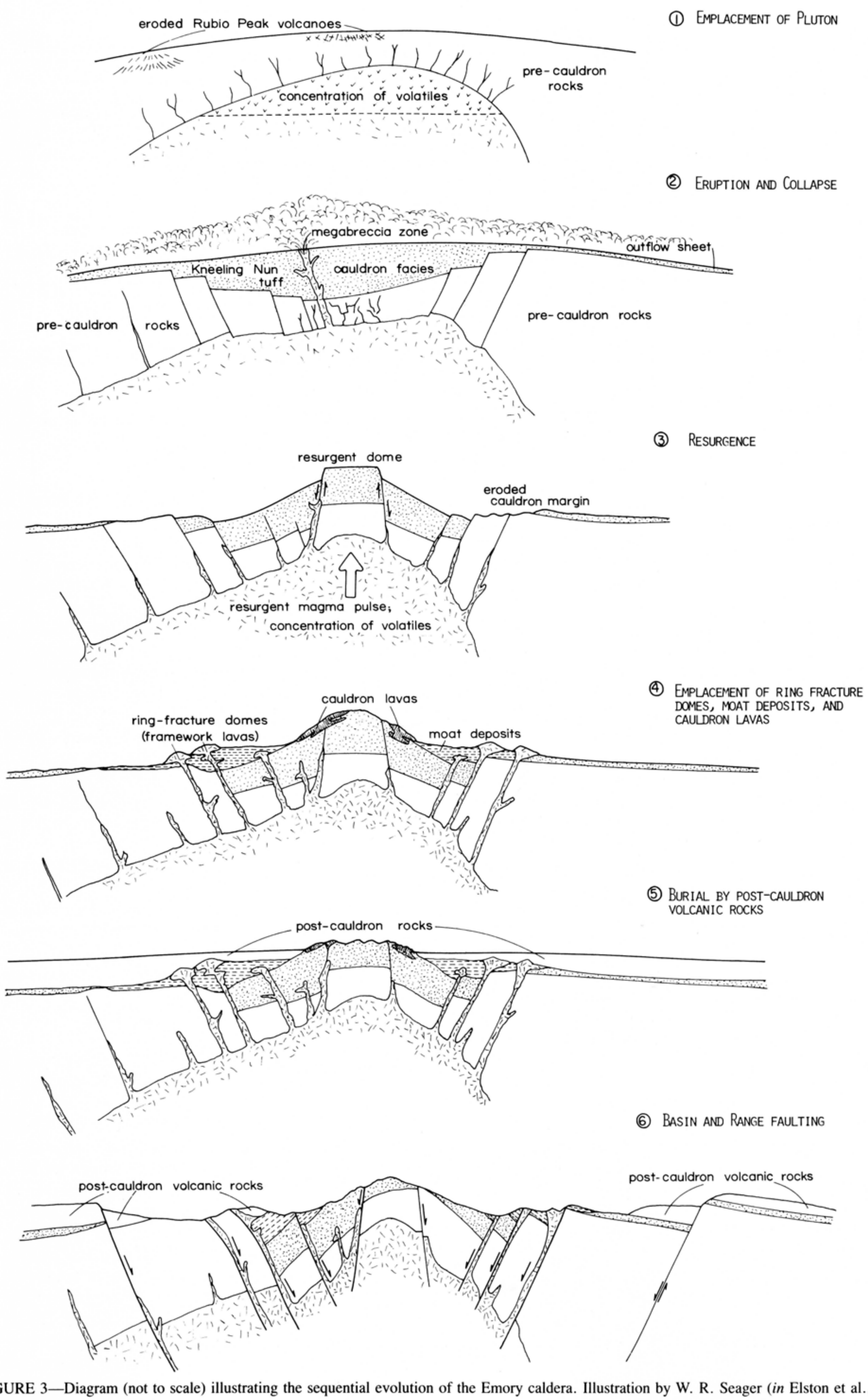

FIGURE 3—Diagram (not to scale) illustrating the sequential evolution of the Emory caldera. Illustration by W. R. Seager (*in* Elston et al., 1975).

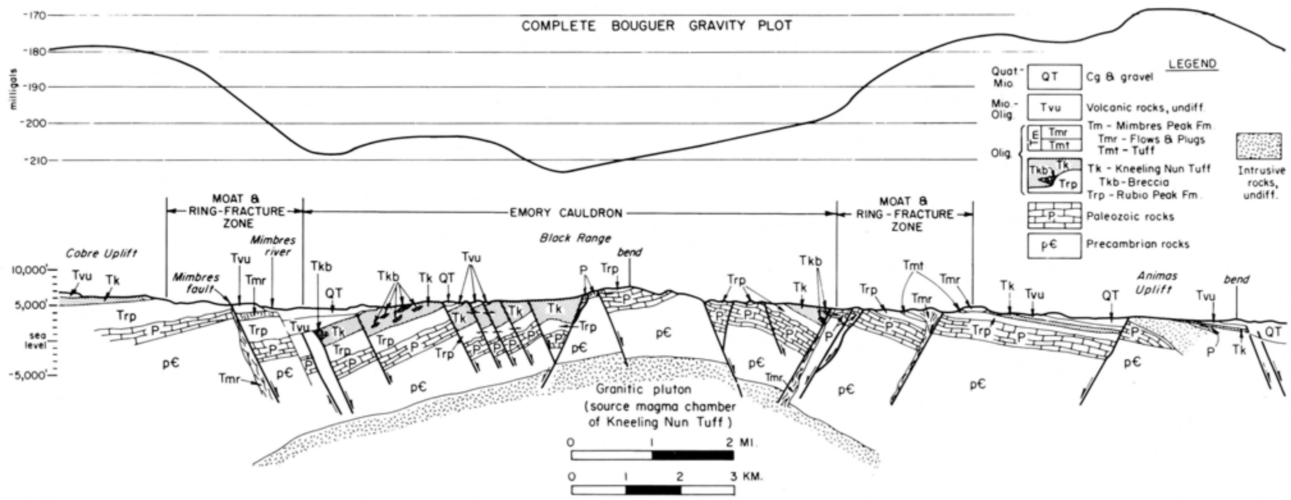

FIGURE 4—Geologic section and gravity profile through the Emory caldera, at the approximate latitude of NM-152. No vertical exaggeration. Compiled by W. R. Seager (*in* Elston et al., 1987).

and north–south but is still as much as 75 m thick where last seen in outcrops. The thickness of caldera fill is also unknown. Base and top are not exposed in the same sections and the displacements of faults are impossible to measure in the absence of stratigraphic markers. The minimum thickness is about 800 m; actual thickness could be much greater. A reasonable estimate of volume is about 1500 km^3; if ring-fracture lavas, moat deposits, and fines carried away by the winds are added, the total would exceed 2000 km^3.

Documentation of what is now interpreted as the Emory caldera began with Kuellmer (1954), who mapped a section across the Black Range, noted its anticlinorial structure, the great thickness of Kneeling Nun Tuff, the megabreccia zones, and the relationship of Kneeling Nun Tuff to intrusive rocks. He concluded that Kneeling Nun Tuff had erupted from fissures marked by megabreccia zones; the concept of resurgent calderas was unknown in 1954. Jicha (1954) mapped the outflow sheet and ring-fracture zone of the southern end; Elston (1957) mapped a small segment of the structural caldera wall on the southwest side of the caldera and more of the ring-fracture zone and outflow sheet. Further mapping of the southern caldera segment was done by Hedlund (1970), Lambert (1973), Farris (1981), and Seager et al. (1982); Elston (1981) published a partial compilation of their maps. Caldera structure and bilateral symmetry of the Black Range were only recognized in the early 1970's, during regional reconnaisance mapping by W. R. Seager and R. E. Clemons, and documented by Elston et al. (1975, 1987) and Seager et al., (1978). Mineralogical and major-element zoning of Kneeling Nun Tuff in the southern segment of the Emory caldera was studied by Giles (1967); O'Brient (1979, 1986) studied cognetic granitic and rhyolitic intrusions. The northern segment was covered by the reconnaissance map of Ericksen et al. (1970) and most of it was mapped in detail by Abitz (1989). The work of R. J. Abitz also includes a petrogenetic model based on mineralogy, major- and trace-element geochemistry, and Sr-isotope systematics; a preliminary account was published in 1986.

Road log

Mileage

0.0 Silver City, traffic light at junction of US-180 (14th Street) and NM-152 (formerly NM-90; Silver Heights Boulevard). **4.0**

4–6 Distant glimpses of the Kneeling Nun of Santa Rita can be seen ahead. It is an isolated column of Kneeling Nun Tuff in front of the cliff formed by the outflow sheet. In the distance to the left, the principal ignimbrite of the Pinos Altos Range is the Tadpole Ridge Tuff (about 31 Ma); Kneeling Nun Tuff is only preserved in small patches at its base. Roadcuts are in sandstone and shale of the Late Cretaceous Colorado Formation, intruded by a dense swarm of Late Cretaceous and Tertiary dikes. **1.5**

7.5 Intersection. Turn **left** on NM-152. **2.2**

9.7 Kneeling Nun lookout. **2.3**

12.0 Hanover, turn **right** on NM-356. Ahead, dumps from the Blackhawk mine are on the right, Chino mine on the left. **2.5**

14.5 Vanadium. Turn **left** on Santa Rita Mine Road. **0.4**

14.9 Cross bridge, turn **right** on Groundhog Mine Road. **0.5**

15.4 Pass foundations of former ASARCO Groundhog mine office building, continue ahead on descending dirt road. **0.25**

15.65 Turn **left** on primitive road up Lucky Bill Canyon. **0.05**

15.7 Pass through gate. **STOP 1. Kneeling Nunn Tuff.** In Lucky Bill Canyon, northeast-trending fault blocks expose an Oligocene volcanic section, beginning with tuffaceous sandstone and air-fall pyroclastic deposits of the Sugarlump Formation and continuing upward through outflow facies of Kneeling Nun Tuff (130 m), a thin vitrophyre correlated with the Mimbres Peak Formation, Box Canyon Tuff (rhyolite ignimbrite), local lenses of Rustler Canyon Basaltic Andesite, Caballo Blanco Tuff (rhyolite ignimbrite), and Bear Springs Basaltic Andesite (Fig. 2). The sources for the Box Canyon and Caballo Blanco ignimbrite sheets are unknown. The section of Kneeling Nun outflow sheet is about 20 km from the southwestern segment of the caldera margin. Giles (1968) described the Lucky Bill Canyon section as follows (metric units inserted into the original):

The dominant exposures in the canyon are of the compound cooling unit of the Kneeling Nun, which in this area is around 125 m (420 ft) thick. Five distinct and genetically related flow units have been recognized in the sheet; the upper four comprise the top 45 m (150 ft). The basal flow unit, 80 m (270 ft) thick, is a simply zoned cooling unit. It has a partially welded top and base (the grayish-pink slope formers) and a thick middle zone of dense welding (the bold red cliffs). Partings have been recognized in this flow unit, but they are scattered and discontinous. The variations in welding are gradational and this part of the sheet has been interpreted as the results of a continuous eruptive episode.

Phenocrysts in the unit range from 25 to 60%, and consist of quartz, sanidine, sodic plagioclase, biotite, opaque oxides, and trace amounts of sphene, zircon, hornblende, and clinopyroxene. The groundmass has been completely crystallized (devitrified), and there is a well-developed vapor-phase zone. The unit shows strong vertical compositional zoning that ranges from a basal quartz latite crystal-vitric tuff to an overlying latite crystal tuff. Variations may be abrupt but they are systematic, and consist of an upward increase in the number and size of phenocrysts, and in the proportion of ferromagnesian and plagioclase phenocrysts, with an accompanying decrease in the amount of quartz and the alkali feldspar/plagioclase ratio. Examples of such variation in the Lucky Bill Canyon section are the upward decrease in quartz from 36 to 5% (of phenocrysts) and of the alkali feldspar/plagioclase ratio from 2.0 to 0.25. Detailed studies have been carried out on major and trace elements in biotites and their matrix. The chemical data substantiates and complements the modal indications of a systematic vertical compositional zonation. Examples for biotite are the upward increases in Cu, Sr, Ba, and Ca, and a decrease in Rb and Mn.

All of the data are consistent with the explanation of an upward gradation and differentiation of progressively silicic and less crystal-rich melt within the pre-eruptive Kneeling Nun magma chamber . . . effectively resulting in an inverted replica of the compositionally zoned magma.

In the writer's interpretation, the initial compositional zoning in the Kneeling Nun magma resulted from protracted crystal settling concurrent with upward volatile (and alkali?) migration or transfer. . . . The Caballo Blanco Rhyolite, which is compositionally zoned similarly to the Kneeling Nun, has also been studied in detail. The general petrogenesis is identical to that of the Kneeling Nun.

Details of vertical zoning in the lower unit of Kneeling Nun Tuff are shown in Table 1.

Typically, major ignimbrite sheets of the Mogollon–Datil volcanic province are most densely welded directly above the base; basal vitrophyre zones are common. This suggests that the erupting mass was not cooled in an adiabatically expanding plinian column. More likely, it spilled out of a caldera ring fracture as a dense, ground-hugging flow, which has been likened to milk boiling over a covered pot. Kneeling Nun Tuff is unusual in that, at least locally, the basal ignimbrite is poorly welded and is underlain by surge and ash-fall deposits. Perhaps a plinian column developed locally above a constricted vent in the ring-fracture zone, before more widespread caldera collapse led to a general "boiling over." Welding zones are independent of zones based on chemical composition and mineralogy. The illustration of the base of the Kneeling Nun section in Lucky Bill Canyon (Fig. 5b) was described as follows by Michael F. Sheridan (letter to W. E. Elston, June 24, 1976):

Here is my interpretation of the base of the Kneeling Nun sheet.
A—The lowermost 30 cm is a typical air-fall unit representing the explosive initial stage of the eruption.
B—The next unit is a 12-cm series of planar beds representing the deflated portion of a base surge cloud.
C—The next unit is composed of 20 cm of sand-wave beds representing the inflated portions of the surge cloud.
D—Then come the thick massive beds of the ash flow. It seems like the crossbedding in the sand waves should give the direction of flowage.

After examining the basal part of the Kneeling Nun outflow sheet, return to Hanover junction (mile 12.0). **3.6**

19.3 Hanover junction, turn **right** on NM-152. Mine workings on left are from the Empire and Republic mines, developed on contact-metasomatic zinc deposits at south end of the Laramide Hanover–Fierro stock. **1.1**

20.4 **STOP 2 (optional). Chino mine lookout** at former

TABLE 1—Major-element analyses (in water-free weight percent) and modes (in volume percent) of outflow sheet of lower unit, Kneeling Nun Tuff, Lucky Bill Canyon (32°46′19″ N, 108°6′24″), Grant County, New Mexico. From D. L. Giles (unpubl.), cited by Bornhorst (1980).

Distance above base, m	0.3	4.5	5.7	12	18	28	42	57	72	96
SiO_2	67.60	70.70	72.40	72.60	69.90	67.80	66.90	65.70	65.20	65.30
Al_2O_3	15.20	13.90	13.60	13.70	14.10	14.30	15.10	15.40	15.40	16.10
FeO*	2.60	2.00	2.40	2.10	2.90	3.60	3.00	3.90	3.50	3.10
MgO	1.60	0.70	1.00	0.60	1.40	1.40	1.80	1.20	1.20	1.50
CaO	2.20	1.80	0.90	0.80	1.30	2.00	2.10	2.60	3.10	2.60
Na_2O	4.80	4.80	2.20	2.20	3.90	4.80	5.80	5.10	6.00	6.10
K^2O	5.40	6.10	6.50	7.20	5.70	5.40	5.20	5.60	5.10	5.00
Total	99.40	100.0	99.00	99.20	99.20	99.30	99.90	99.50	99.50	99.70
Welding	Partial	Partial	Partial	Partial	Partial	Dense	Dense	Dense	Partial	Partial
Mode, vol.%										
Groundmass	73.7	72.7	67.2	74.6	55.1	55.3	48.0	44.7	59.9	62.3
Quartz	8.9	7.5	9.8	6.9	9.9	4.2	3.8	3.5	2.2	3.0
Plagioclase	6.0	7.2	8.2	5.3	17.5	25.7	26.5	28.4	24.1	21.9
K-feldspar	8.4	10.3	10.2	10.2	12.6	9.3	11.4	11.3	7.1	5.7
Biotite	Pr	Pr	Pr	Pr	Pr	Pr	Pr	Pr	Pr	Pr
Oxyhornblende	—	Tr	—	—	Tr	Tr	Pr	Tr	Pr	Tr
Augite	—	—	—	—	—	Tr	—	Tr	Tr	Tr
Opaques	Pr	Pr	Pr	Pr	Pr	Pr	Pr	Pr	Pr	Pr
Sphene	Tr	Tr	Tr	Tr	—	Tr	Tr	Tr	Tr	—
Zircon	Tr	Tr	Tr	Tr	Tr	Tr	—	Tr	Tr	Tr
Apatite	Tr	Tr	Tr	Tr	Tr	Tr	Tr	Tr	Tr	Tr
Total mafic	2.9	2.8	4.6	3.0	4.9	5.5	10.3	12.1	6.7	7.2
Total	99.9	100.0	100.0	100.0	100.9	100.0	100.0	100.0	100.0	100.1

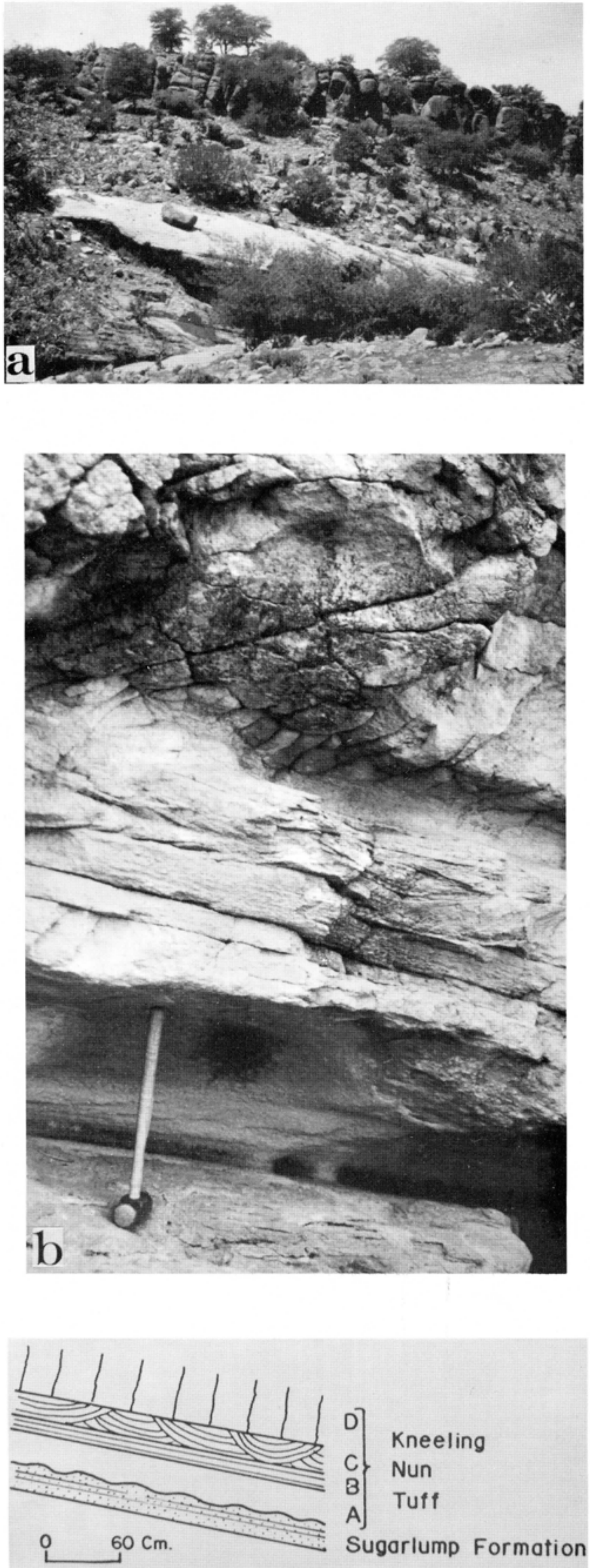

FIGURE 5—Base of Kneeling Nun Tuff outflow sheet, Lucky Bill Canyon (Stop 1). **a,** The poorly welded base forms the prominent white band in the lower half of the photograph. **b,** Closeup of lower contact, showing transition from basal ash-fall deposit (A), to planar (B) and sand-wave (C) surge deposits, to ash-flow deposit (D). Interpretive sketch by M. J. Sheridan (*in* Seager et al., 1978) (see text).

site of Santa Rita, New Mexico (Fig. 6). The Chino porphyry copper deposit is one of the largest of its type in the world. The present (1989) ownership is Phelps Dodge Corp. (two-thirds) and Mitsubishi (one-third); about 45,000 tpd are milled at Hurley, New Mexico (Paul Novotny, Phelps Dodge, pers. comm. 1989). McDowell (1971) obtained four K–Ar dates between 57.3 ± 1.7 and 60.4 ± 1.8 Ma (corrected for 1976 IUGS decay constants) for the Chino granodiorite–quartz monzonite porphyry, which places it within the Laramide magmatic–metallogenic episode and about 20 m.y. older than the earliest mid-Tertiary volcanic rocks that overlie it unconformably. Mid-Tertiary volcanic rocks played an important role in the preservation of the Chino ore body. During the hiatus between Laramide and mid-Tertiary events, the Chino porphyry was unroofed by erosion, deeply weathered, and leached. Paleobotanical evidence suggests that elevations were lower than at present and that the climate was humid subtropical (Axelrod and Bailey, 1976). The present dry climate does not favor supergene processes, but in early Tertiary time a supergene chalcocite blanket formed below the water table and was protected from further erosion by a blanket of early Oligocene volcanic rocks. The widespread post-Laramide volcanic cover raises a tantalizing question: How many more $\$10^9$ ore bodies are hidden beneath the Tertiary volcanic blanket? At least one such subsurface porphyry deposit was discovered by aeromagnetic surveys and drilling by Bear Creek Mining Co. (affiliated with Kennecott Copper Corp.) at Whitehorse Mountain (Caballo Blanco), about 15 km southeast of the Chino mine. **2.7**

23.1 Black Range in distance (12:00) is the resurgent dome of the Emory caldera. Cooke's Peak (the Matterhorn-like peak at 2:30) is a 38.8 ± 1.4 Ma granodiorite intrusion (Loring and Loring, 1980), more or less coeval with the andesitic Rubio Peak Formation. The mountain with tilted cap in front of, and to the right of, Cooke's Peak is Whitehorse Mountain (or Caballo Blanco). Andesite and latite flows of the Rubio Peak Formation (absent at the

FIGURE 6—Outflow sheet of Kneeling Nun Tuff (cliff) and bedded volcaniclastic and pyroclastic deposits of the Sugarlump Formation (wooded slope) lie unconformably on the Laramide Santa Rita porphyry copper deposit (Stop 2). The column in front of the cliff, near its left end, is the Kneeling Nun Tuff of Santa Rita.

Chino Pit but here about 800 m thick) and Sugarlump Formation make up the lower slopes of Whitehorse Mountain. The middle ledge is Kneeling Nun outflow; above the ledge, a white spot marks Caballo Blanco Tuff. The upper slopes and cap are intermediate to mafic lavas of the Razorback and Bear Springs Formation (Fig. 2).

For the next 4.7 mi the road passes through several fault blocks of Cambrian through Mississippian sedimentary rocks. Black, fissile Upper Devonian Percha Shale makes an excellent marker between Silurian Fusselman Dolomite below and Mississippian Lake Valley Limestone above. The incompetent Percha Shale also hosts numerous sills. **4.4**

27.5 Across canyon on left, Upper Cambrian Bliss Sandstone is separated from Proterozoic greenstone by a thin zone of diamictite(?). **0.8**

28.3 Entering the Mimbres fault zone, a major northeast-trending structure with several thousand meters of displacement and a long and complex history. Locally, it is part of the ring-fracture zone of the Oligocene Emory caldera but most of its displacement occurred later, during the main stage of Miocene Basin and Range faulting. To the right, the Mimbres fault brings Miocene sedimentary fill of the Mimbres Valley against the Ordovician El Paso Limestone. On the opposite side of a cross fault that follows the valley on our left, it brings Proterozoic greenstone against Miocene valley fill; the entire Paleozoic, Cretaceous, and mid-Tertiary section has been faulted out. The valley-fill sediments of the Mimbres Valley (and its westward continuation, the Sapillo Valley) straddle the Continental Divide. They are the connecting link between the older parts of the Gila Group to the west and the Santa Fe Group to the east.

The overall trend of the Mimbres fault, and its continuation on the east side of the Cookes Range, is to the northwest, but its trace is curved, convex to the northeast. However, south of our present location, a 20 km segment of the fault is concave to the northeast, concentric with the general outline of the Emory caldera. This segment of the Mimbres fault becomes very complex because it was invaded by rhyolite ring-fracture domes of the Emory caldera, part of the Mimbres Peak Formation (Elston, 1957). At our present location, the structural wall of the Emory caldera is buried by Miocene fill of the Mimbres Valley, but it is locally exposed at Mimbres Hot Springs, about 11 km to the southeast. There the Mimbres Hot Springs fault, probably a splay of the Mimbres fault, coincides with the structural caldera wall and also controls the modern hot springs. The escarpment on the west side of the Mimbres Valley, on either side of us, can be interpreted as the topographic wall of the Emory caldera.

Post-Oliogocene movement of the Mimbres fault occurred concurrently with, and/or later than, deposition of valley-fill sediments. In a 10 km stretch that begins at Gatton's Park (about 30 km northwest from here) the fill of the Mimbres–Sapillo Valley can be bracketed between steeply tilted T4a basaltic andesite flows (whole-rock K–Ar age of 21.1 ± 0.5 Ma) that form the foundation of Roberts Dam and a nearly flat-lying mesa-top T6b basalt flow (6.5 ± 0.4 Ma). Sediments between the dated lavas are mainly fanglomerate derived from rising basin and range fault blocks; the dates therefore bracket the main stage of basin–range faulting in this area. An age of 21.2 ± 1.5 Ma was also obtained from a basaltic andesite flow near the base of fill in the Gila Valley, about 100 km to the west (Elston et al., 1973). **1.35**

29.65 Junction with NM-61. Continue ahead on NM-152. For supplemental road logs to country north and south, respectively, see Elston and Kuellmer (1968) and Elston and Netelbeek (1965). **0.35**

30.0 Cross Mimbres River at San Lorenzo. Roadcuts beyond San Lorenzo are in unconsolidated Quaternary terrace gravels that flank the Mimbres Valley and in semiconsolidated Miocene valley-fill sediments. **3.7**

33.7 Fault zone. To the left, a sliver of Caballo Blanco Tuff (T3r) is exposed unconformably beneath valley-fill sediments and is faulted against Bear Springs Basaltic Andesite (T3a), which in turn lies on reddish sandstone of the Piloncillo Formation. Caballo Blanco Tuff is exposed again 0.3 mi ahead. Note a large flow fold in Bear Springs Basaltic Andesite. This unit is typical of the high-K "iddingsite"-bearing basaltic andesites of the Mogollon–Datil volcanic field. **0.4**

34.1 Caldera-fill facies of Kneeling Nun Tuff. For the next 10.6 mi, a great thickness of this unit will be the only rock in sight, as we penetrate the interior of the resurgent dome. Contrast the appearance between caldera-fill facies here (lack of columnar joints, presence of alteration and brecciation) with outflow facies at Stop 1. The dip is about 40° west, away from the axis of the resurgent dome, compared with about 30° west for Caballo Blanco Tuff. **1.0**

35.1 Megabreccia block of Rubio Peak andesite in Kneeling Nun Tuff. **1.1**

36.2 Cattleguard, enter Gila National Forest. Dirt road on left leads to a trail which leads to the Rabb Park complex (Kelly and Branson, 1947; Kuellmer, 1954; O'Brient, 1979, 1986), about 5 km to the north-northwest. The rhyolitic–granitic intrusive complex is cogenetic with Kneeling Nun Tuff and gives important clues on the connection between plutons and resurgent calderas. We will see granitic rocks similar to those in the complex as cognate inclusions in Kneeling Nun Tuff (Stop 3; mile 37.8).

O'Brient (1979) summarized the Rabb Park complex as follows:

> The rocks of the complex, which constitute a middle Tertiary cogenetic suite, range from fine-grained porphyritic tuff to very coarse-grained, nearly holocrystalline pegmatite. Five major textural facies have been distinguished: pre-complex welded tuff and rhyolite porphyry, sanidine granite, sanidine aplite, and sanidine pegmatite of the complex. Each rock contains a high-temperature phase assemblage that includes cryptoperthitic sanidine, dipyramidal quartz, and vesicular groundmass; these are regarded as indicative of crystallization and rapid cooling of granitic magma in a near-surface environment.
>
> The major mappable unit within the complex is a mass of rhyolite porphyry that is cornucopia-like in plan. Steeply inward-dipping flow structures delineate a main funnel-shaped part of this mass that is elongate in a NE-SW direction; it is approximately one kilometer in maximum exposed dimension. This funnel cuts a slightly

older, arcuate arm of complexly folded rhyolite porphyry that is present along the eastern edge of the complex. The rhyolite porphyry grades inward from a strongly sheared, pyroclastic vesicular, non-fragmental core.

Fragments of nearly holocrystalline granite, aplite, and pegmatite that range in size from a few centimeters to more than 120 meters are enclosed within the rhyolite porphyry. They are interpreted as cognate xenoliths rafted into place by the rising froth-like porphyry mass.

Modal and chemical compositions of the Rabb Park rock types suggest that they constitute a consanguineous series. The granite–aplite–pegmatite assemblage and the welded tuff-rhyolite porphyry assemblage represent two possible textural derivatives of the same parent magma. A near-surface plug of granite evidently crystallized almost to completion with subsequent evolution of pegmatite and aplite from vapor saturated residual melt. The porphyry represents a less advanced stage of crystallization whose evolution was interrupted before reaching a pegmatitic stage, probably by catastrophic pressure relief owing to volcanic venting of the complex.

Experimental study of three natural starting materials from the Rabb Park Complex indicates that at 1 kb, the rhyolite porphyry, sanidine granite, and sanidine pegmatite have essentially identical phase assemblage (T-X_{H_2O}) diagrams. The experimental data are consistent with high-temperature, low-pressure crystallization of the Rabb Park rocks, perhaps above 900° and below 1 kb. Isothermal or adiabatic crystallization in response to falling pressure and "osmotic" escape of the evolving vapor phase must be considered as real possibilities for the Rabb Park rocks.

A gravity profile of Emory caldera (Fig. 4) provides further evidence that a pluton underlies the entire Emory caldera. Elsewhere in the Mogollon–Datil volcanic field, outcrop areas of pre-Tertiary rocks are marked by positive Bouguer gravity anomalies, because crystalline basement is relatively close to the surface. Pre-Tertiary rocks crop out across much of the resurgent dome of the Emory caldera, but a negative gravity anomaly suggests that they are rootless, i.e. separated from crystalline basement by igneous intrusions. It is unknown to what extent the intrusions are granitic, as suggested by the Rabb Park complex and cognate xenoliths seen at mile 37.8, or more mafic, as suggested by the monzonite seen between miles 49.45 and 52.2. **0.7**

36.9 **STOP 3 (optional). Kneeling Nun Vista Point.** This stop allows a westward view across massive caldera-fill facies of Kneeling Nun Tuff in the foreground, the Mimbres Valley ring-fracture zone and topographic caldera wall (mile 28.3) in the middle ground, to the outflow sheet on the skyline. A cut on the south side of the road shows typical, densely welded, crystal-rich caldera-fill facies of Kneeling Nun Tuff, dipping about 40° west, with prominent fiamme and centimeter-size accidental lithic inclusions. A prominent larger inclusion (Fig. 7a) consists of aplitic granite and is probably cognate, similar to aplite in the Rabb Park complex. **Please do not sample this inclusion.** If you wish to collect cognate granitic inclusions in Kneeling Nun Tuff, please do so at mile 37.8. **0.9**

37.8 Abundant accidental centimeter- to meter-size lithic clasts in altered or vitrophyric Kneeling Nun Tuff consist of andesite from the Rubio Peak Formation. In addition, there are abundant centimeter- to decimeter-size, light-colored granitic clasts. They have not been studied in detail, but the rock types correspond to granitic phases of the Rabb Park complex described by O'Brient (1979; see mile 36.2). They are therefore interpreted as cognate inclusions. Both equigranular and porphyritic types are present (Fig. 7b). **0.7**

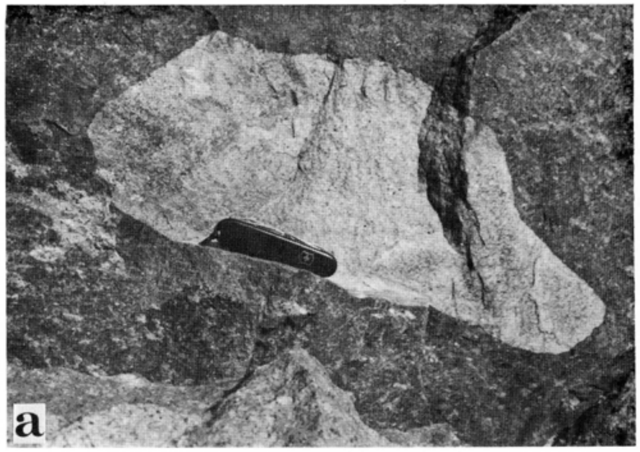

FIGURE 7—Granite inclusions, interpreted as cognate, in caldera-fill facies of Kneeling Nun Tuff. **a,** Aplitic granite, Stop 3. **b,** Coarse equigranular granite, mile 37.8. Wolf Elston's Swiss Army Knife (seen here and elsewhere) is 9 cm long.

38.5 Cattleguard, **STOP 4. Megabreccia in Kneeling Nun Tuff.** Kuellmer (1954) mapped four branching megabreccia zones in this part of the Emory caldera; each zone is up to 5 km long, elongated north–south, and 800 m wide. As xenoliths are scattered throughout Kneeling Nun Tuff, the boundaries of the zones are somewhat arbitrary. Similar megabreccia zones have been found elsewhere in the Emory caldera. In this vicinity, xenoliths are up to 25 m long and consist mainly (about 90%) of andesite from the Rubio Peak Formation. The remainder are, in decreasing order of abundance: (1) red sandstone and shale of the Permian Abo Formation, (2) limestone from the Pennsylvanian Magdalena Group, and (3) limestone and black fissile shale from the Mississippian Lake Valley Limestone and Devonian Percha Shale, respectively. Abundances are in reverse stratigraphic order, i.e. the most abundant clasts were derived from units highest in the section. In addition, there are cognate granitic clasts, as seen at miles 36.9 and 37.8. At the present locality, tuffaceous matrix is less abundant than xenoliths. The matrix is highly fluidized and able to penetrate millimeter-wide cracks (Fig. 8a). In places, the matrix of the megabreccia clasts

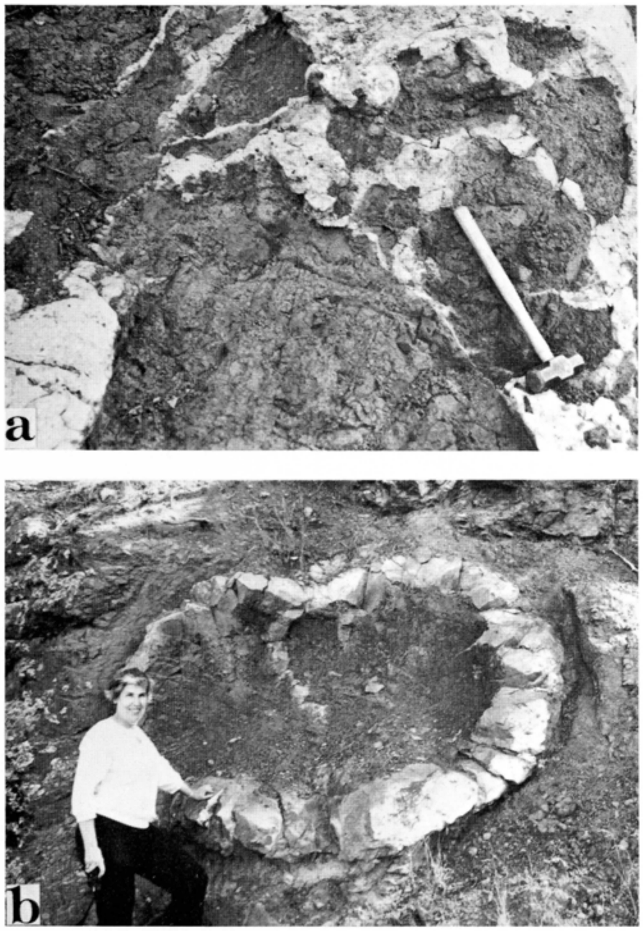

FIGURE 8—Megabreccia zone in caldera-fill facies of Kneeling Nun Tuff. Stop 4. **a,** Tuffaceous matrix (light color) penetrates minute fractures in clasts of Rubio Peak andesite. **b,** Rounded clast of Rubio Peak andesite, enveloped in an accreted rind of Kneeling Nun Tuff. The clast and its rind are surrounded by black vitrophyric Kneeling Nun Tuff.

is glassy, probably because it was quenched in contact with cold clasts. One 2×3 m rounded andesite clast is enveloped in a rind of ash-flow tuff; the orientation of fiamme follows the outline of the clast. The rind seems to have accreted on a rolling clast, in a snowball fashion (Fig. 8b). Details were described by Kuellmer (1954).

In keeping with the concepts of that day, Kuellmer (1954) interpreted megabreccia as vent agglomerate, parallel to the structural grain of the Black Range and Rio Grande valley. As the concept of resurgent calderas developed, alternative interpretations were suggested. The megabreccia could be a caldera-collapse breccia, as described by Lipman (1976). The present locality is far from the inferred structural caldera margin, but collapse could have been stepwise. The problem has not been solved, because there has been no detailed study since Kuellmer (1954). However, a few new pieces of evidence have come to light. Daniel S. Barker (University of Texas) found evidence in support of the vent-breccia interpretation. In a letter to William R. Seager (New Mexico State University), dated April 12, 1978, he wrote:

I've checked my notes and the thin sections again, and here is a summary of my observations (based on samples from only a few localities, as you know) concerning variations in the Kneeling Nun. All three facies (vent, cauldron, and outflow) contain about 5% amphibole phenocrysts and 5% biotite phenocrysts. In the vent facies, both minerals are fresh and pleochroic in olive-green to brown, not red; however, in the outflow, both minerals are fresh but strongly pleochroic in red-browns, suggesting oxidation. In the cauldron facies, the amphibole is thoroughly altered to opaque oxides plus chlorite, and the biotite is partly chloritized, with the surviving biotite having a red-brown tint.

All three facies contain about 20% glass lumps. In the vent facies, these are nonvesiculated, having a strange polygonal fracture pattern, and fine granular to axiolitic devitrification. In the cauldron facies, the glass is *also* nonvesicular, without the polygonal fractures but with coarser spherulitic devitrification. The outflow facies contains highly vesiculated pumice fragments (flattened in the welded part). Either the vesicles had not formed, or were completely kneaded out during compaction, in the vent and cauldron facies. The textural evidence of vertical flow lines in the vent facies suggests that the bubbles were never formed, not that they collapsed entirely.

The only other differences in the vent samples are the presence of fine granitic fragments that appear to be more highly oxidized in the cauldron facies and are lacking in my thin section of the outflow, and the presence in the vent facies of sparse megacrysts of clinopyroxene, which appear to be xenocrysts from dissagregation of inclusions of Rubio Peak Formation; this clinopyroxene was not noticed in the other facies, and appears identical in thin section to that in the Rubio Peak.

In turn, Seager found evidence that seems to support the interpretation as caldera-collapse breccia. In an undated letter (probably written in July 1980) he wrote to Wolf Elston:

[It is] beginning to look to me like the xenoliths are in layers conformable to foliation in Tkn [Kneeling Nun Tuff] suggesting they are landslide blocks rather than vent breccias . . . some blocks are truly gigantic.

If the megabreccia is part of a vent, the preponderance of xenoliths from the highest part of the stratigraphic column suggests that it was funnel-shaped. If it is a caldera-collapse breccia, collapse mainly affected the higher parts of the caldera wall; rocks older than Percha Shale apparently did not crop out on the caldera wall. Actually, the two interpretations need not be in conflict. Vents are likely to have been controlled by ring fractures near the collapsing caldera wall and caldera-wall collapse may have occurred simultaneously with eruption from a widening vent. **1.4**

39.9 Exposures in this area, Devil's Backbone, are in the lower part of the caldera-fill facies of Kneeling Nun Tuff. The rock is densely welded and closely jointed (Fig. 9). Evidently, it cooled so slowly that albite exsolved from sanidine on an angstrom-unit scale, to form cryptoperthite (moonstone) with silky luster. Note the religious shrine high up on the cliff ahead. **1.8**

41.7 Base of Kneeling Nun Tuff, which here lies on andesite flows of the Rubio Peak Formation. Caldera-fill facies of Kneeling Nun Tuff will not be seen again along this road, but crops out on the ridges above the road. **1.0**

42.7 **REST STOP,** if needed. Iron Creek Campground with picnic tables and toilets. **0.7**

43.4 **STOP 5. Thermal metamorphism of cherty limestone.** Park and walk back about 150 m to examine the effects of thermal metamorphism on cherty limestone of the Alamogordo Member of the Lake Valley Limestone (Mississippian). These exposures were studied in detail by Maggiore (1981), who described

FIGURE 9—Densely welded caldera-fill facies of Kneeling Nun Tuff with closely spaced parallel vertical joints, in contrast to the widely spaced columnar joints of the outflow facies (Fig. 5a). Devil's Backbone, mile 39.9.

their unmetamorphosed equivalents in the Santa Rita quadrangle as follows:

> The Alamogordo Member overlies the Andrecito and is a distinctive cliff-forming, fine-grained (0.125–0.25 mm) dark gray, massive cherty limestone. Black, brown, or white chert nodules, usually 2 to 5 cm thick and 10 to 15 cm long are distinctive. Many nodules are banded and have a sedimentary pinch-and-swell structure that resembles boudinage. Crinoids, corals and bryozoans dominate the fauna in this member, but Jones and others (1967) noted that the Alamogordo Member is the least fossiliferous member of the Lake Valley Limestone. Calcite makes up about 90 percent of the rock (excluding chert nodules); quartz, clay and opaques make up the remaining 10 percent.

The present exposures are in the septum between the caldera floor and the underlying pluton. The rocks are not notably deformed, in contrast to their appearance on the eastern flank of the resurgent dome, but they have been recrystallized to a coarse calc-silicate marble. Wollastonite and minor tremolite–actinolite form conspicuous reaction rims around chert nodules; garnet (zoned andradite–grossularite), clinopyroxene (diopside–salite) epidote, and vesuvianite occur principally in veinlets (Fig. 10). From observed phase relations, Maggiore (1981) attempted to constrain temperature and X_{CO_2} (Fig. 11). Depth of burial was assumed to be between 1.5 and 3.0 km, equivalent to hydrostatic pressure

FIGURE 10—Lake Valley Limestone, Alamogordo Member, below the caldera floor, recrystallized to marble (Stop 5). A chert nodule is surrounded by a reaction rim of wollastonite and minor tremolite; veinlets in marble contain andradite–grossularite and other silicates.

between 0.5 and 1.0 kb. Maggiore (1981) summarized his conclusions as follows:

> Mineral assemblages from metacarbonates located on the west side of the Emory cauldron include garnet + epidote + tremolite–actinolite + calcite + clinozoisite as well as garnet + diopside + wollastonite + calcite. Analysis of phase stability and estimated overburden thickness yields T = 420 − 620°C, P = 0.5 − 1.0 Kb, with X_{H_2O} above 0.55. A lack of invarient assemblages suggests that P_{H_2O} may have been buffered externally, perhaps by meteoric waters or by fluids associated with a crystallizing pluton. petrologic and gravity data suggest the presence of a pluton buried below the cauldron.

0.6

44.0 Disturbed and partly hornfelsized red beds of the Abo Formation (Permian). **1.0**

45.0 Andesite of the Rubio Peak Formation. **1.1**

46.1 Emory Pass, on the Continental Divide. Turn left, to Vista Point. Emory Pass was named in honor of Lt. W. H. Emory, who commanded a force that crossed the Black Range at this point during the Mexican War, in 1846. The caldera is named after the pass. Elevation of the pass is 2691 m (8828 ft). **0.15**

46.25 **STOP 6. Emory Pass Vista Point.** We are standing on Rubio Peak Andesite below the caldera floor; caldera-fill facies of Kneeling Nun Tuff forms the

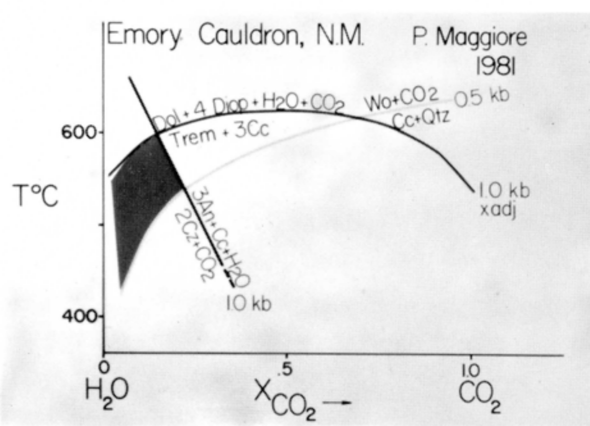

FIGURE 11—Constraints on probable temperature, pressure, and X_{CO_2} from phase relations in metamorphosed Alamogordo Member of the Lake Valley Limestone (Mississippian) in the septum between caldera floor and the inferred underlying pluton (from Maggiore, 1981).

ridges above us and to the north. In the foreground, looking east, the light-colored rocks of a sharp peak are of intrusive rhyolite porphyry, probably cogenetic with Kneeling Nun Tuff. In the middleground, the settlements of Kingston and Hillsboro lie below us, in the valley of Percha Creek. The principal ring fracture of the Emory caldera (or structural caldera wall), which terminates the resurgent dome and thick section of caldera-fill tuff on the east side, begins directly east of Kingston (mile 54.1). The topographic caldera wall is about 10 km farther east, about 5 km west of Hillsboro (mile 60.0). The moat between the structural and topographic caldera walls is marked by ridges of the Mimbres Peak Formation consisting of light-colored, bedded pumiceous moat deposits, capped and intruded by rhyolite lava. The lava domes are controlled by outer ring-fracture faults. Pumiceous moat deposits and lavas are cogenetic phases of the Mimbres Peak Formation.

On a clear day, Sierra Blanca Peak, the highest mountain of southern New Mexico (3658 m, 12,002 ft) can be seen in the far distance. The basins and ranges between the foot of the Black Range and Sierra Blanca Peak have been designated as part of the Mexican Highlands section of the Basin and Range province (Fenneman, 1931) or, more recently, as branches of the Rio Grande rift (Chapin, 1971). East of Hillsboro, the ranges and basins are, respectively, the Animas Hills, the Palomas Basin segment of the Rio Grande valley, Caballo Mountains, Jornada del Muerto Basin ("Journey of Death," presciently named by Spanish conquistadores; the first atomic bomb was exploded there in 1945), San Andres Mountains, Tularosa Basin, and Sacramento Mountains (which include Sierra Blanca Peak).

Sierra Blanca Peak is part of an andesite–trachyte volcanic complex, with intrusions of hornblende–biotite monzonite (Rialto stock), biotite syenite (Bonito Lake stock), and alkalic to peralkalic syenite (Three Rivers stock) (Thompson, 1973). At this latitude, it is the easternmost of the Oligocene volcanic fields, located in the transition zone between the High Plains and the Basin and Range–Rio Grande rift province. The rocks are distinctly more alkalic than those of the Mogollon–Datil volcanic field.

Several Oligocene ash-flow-tuff calderas can be seen in the distance to the southeast. On the east side of the Rio Grande, the Organ batholith forms the core of the rugged Organ Mountains on the skyline; it is part of the Organ caldera complex. According to Seager (1981), the batholith formed part of the magma chamber into which the caldera subsided. Caldera-fill ignimbrite (Cueva and Soledad Tuffs, 36.1–35.7 Ma, McIntosh, this volume) is more than 3 km thick. In front of the Organ Mountains, the low Doña Ana Mountains are the eroded stumps of the nested Doña Ana and Dagger Flat calderas (Seager et al., 1976). Farther to the right, west of the Rio Grande, the low dome of the Sierra de las Uvas marks the site of the Goodsight–Cedar Hills depression, a broad (80 × 38 km) but shallow (about 550 m) trapdoor structure hinged to the west and intruded by rhyolite domes on the east side. The depression is filled with sediments, a basalt unit and seven ash-flow-tuff sheets (Bell Top Formation), erupted between 36 and 33.5 Ma (McIntosh, this volume); some are indigenous, others from external sources. Doming occurred after eruption of Uvas Basalt (~26 Ma), several million years after siliceous volcanism had ceased. Seager (1973) described the Goodsight–Cedar Hills depression as "a long-lived structure" transitional in character between a fault basin and a partly developed cauldron."

Return to NM-152. **1.45**

47.7 Deformed Beartooth Sandstone (Cretaceous, approximately equivalent to Dakota Sandstone of the Rocky Mountains–Great Plains region) above red beds of the Abo Formation (Permian). For the next 2.75 mi, these and other rocks between the caldera floor and the inferred underlying pluton are intensely faulted and brecciated, and also folded on a scale of meters. The units are still in stratigraphic order, though sheared and faulted. The style of deformation contrasts with metamorphism and lack of disruption seen at Stop 5 (mile 43.4); recrystallization and metamorphism are much less in evidence. **1.3**

49.0 **STOP 7 (optional). Deformed precaldera rocks.** Intensely folded and sheared Pennsylvanian sedimentary rocks (Magdalena Group) below deformed red beds of Abo Formation (Permian). Fig. 12 illustrates the intensity of deformation. **0.45**

49.45 **STOP 8 (optional). Quartz monzonite or quartz latite porphyry, intrusive into Percha Shale (Devonian).** From right to left, the roadcut shows altered quartz monzonite porphyry, a xenolith, contact between quartz monzonite porphyry and hornfelsized Percha Shale, and fault contact between Percha Shale and Lake Valley Limestone (Mississippian). The intrusion is one of many in the area; Kuellmer (1954) interpreted most of them as thick sills controlled by incompetent sedimentary units, such as Percha Shale or a shale at the base of the Pennsylvanian Magdalena Group. Alteration of primary plagioclase, K-feldspar, biotite, and epidote has made the rock green. Weathered surfaces are stained brown by limonite, formed by weathering of abundant pyrite. Alteration makes the rock difficult to date, but Maggiore (1981) obtained a zircon fission-track age of 34.0 ± 2.8 Ma. It is known to intrude the Rubio Peak Formation (~38 Ma) but not Kneeling Nun Tuff (34.8 Ma, McIntosh, this volume). Because of pervasive alteration, its chemistry has not been studied, hence it is not known if it is linked genetically to the pluton inferred to be beneath the Emory caldera. For the next 4 km (2.5 mi), roadcuts are in deformed Lake Valley Limestone and Percha Shale, intruded by monzonite porphyry. **3.65**

53.1 Rubio Peak andesite. **0.5**

53.6 Leaving Gila National Forest. **0.5**

54.1 Kingston, one of several mining camps within the Emory caldera or on its periphery. Between 1880 and 1904, the district produced silver and lead, then valued at about $6.6 million. There seems to be a crude zonal arrangement of ore-deposit types, concentric with the outline of the Emory caldera: Pb–

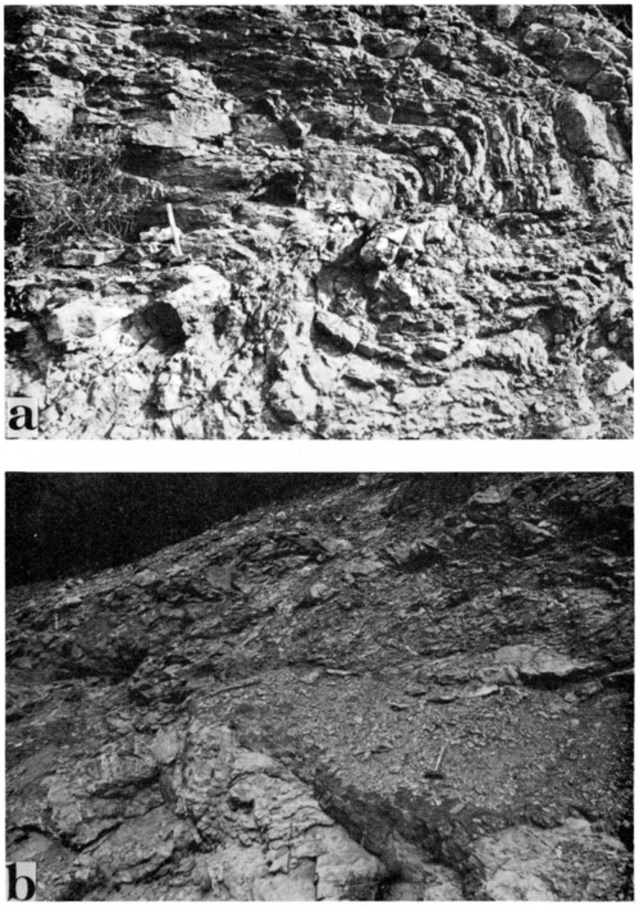

FIGURE 12—Deformed limestone and siltstone of the Magdalena Group (Pennsylvanian) in the septum between the collapsed caldera floor and the inferred underlying pluton, Stop 7. **a,** Meter-scale recumbent folds. **b,** Low-angle faults in brecciated sedimentary rocks.

Zn skarn deposits in the inner zone (Carpenter district on the west side of the resurgent horst block), carbonate-hosted Pb–Ag deposits (Hermosa, Kingston, Tierra Blanca within the ring-fracture zone), oxidized carbonate-hosted Ag or Ag–Mn deposits (Georgetown, Lake Valley, 10–12 km from the structural caldera wall) and fluorspar (northern Cooke's Range, about 15 km from the structural caldera wall). However, none of these deposits have been dated and the evidence linking them to the Emory caldera is purely circumstantial. Elsewhere, some resurgent calderas have been shown to be linked genetically with spatially associated ore deposits (e.g., Questa, New Mexico; Lake City, Colorado); in others (e.g., Mogollon, New Mexico; Silverton, Colorado), fractures related to the development of a cauldron have merely acted as conduits for mineralizing fluids at a much later date.

We are now entering the moat of the Emory caldera, i.e. the zone between the resurgent dome (terminated by the structural caldera wall) and the topographic caldera wall. Beginning on the east side of Kingston and continuing for about 3 km (1.9 mi), the road crosses three major north–south faults that constitute segments of the structural caldera wall (Seager et al., 1978). Collectively, they bring volcaniclastic andesite of the Rubio Peak Formation to the west against Paleozoic sedimentary rocks. Near Kingston, exposures of the faults are poor; farther south, the three strands join into one major fault which we will see later this day in Tierra Blanca Canyon. Behind us, to the west, Paleozoic sedimentary rocks are part of the septum between caldera floor and inferred pluton and were intensely disturbed and/or metamorphosed during caldera collapse; ahead of us they were disturbed only near major faults and igneous intrusions. **2.6**

56.7 Entering a 2 mi zone of pumiceous moat deposits and ring-fracture rhyolite domes and flows, all belonging to the Mimbres Peak Formation. Bedded pumiceous moat deposits to the left. **0.4**

57.1 **STOP 9 (optional).** Bedded pyroclastic moat deposits from 10 to 11:00; rhyolite ring-fracture domes in distance from 11 to 12:00. **0.6**

57.7 Bedded pyroclastic moat deposits on right, in contact with flow-banded rhyolite lavas. **0.4**

58.1 Andesite flows interlayered with rhyolitic moat deposits. **1.2**

59.3 For the next several hundred meters, roadcuts on the right are in steeply tilted lignite-bearing lake beds. They seem to occupy part of the moat of the Emory caldera but lie on Caballo Blanco Tuff (^{40}Ar/^{39}Ar age 31.6 Ma, McIntosh, this volume) which makes them at least 3.7 m.y. younger than Kneeling Nun Tuff. According to Axelrod and Bailey (1976), the flora "is dominated by numerous cones and fascicles of a pine similar to bristle-cone pine (*Pinus aristata*) . . . its sole associates are a spruce (*Picea,* 1 specimen) and an evergreen barberry (*Mahonia,* 5 specimens)." They interpreted the flora as subalpine, living at elevations about 900 m higher than the present 1600 m. If their rather complicated assumptions and calculations are correct, the east flank of the Emory caldera was appreciably higher than at present at the end of the resurgence but subsided later, perhaps as a result of extension of the Rio Grande rift. **0.7**

60.0 The entrance to the Percha Box corresponds more or less to the topographic wall of the Emory caldera. The walls of the box are of basaltic andesite, approximately equivalent to the Bear Springs Basaltic Andesite at mile 33.7. **0.6**

60.6 The valley in which Hillsboro is located, between the Black Range and Animas Hills, is a prong of the Rio Grande rift, filled with coarse clastic sedimentary rocks of the Santa Fe Group (see discussion of valley-fill sediments at mile 28.3). **2.0**

62.6 Downtown Hillsboro, former seat of Sierra County. Turn **right** on NM-127. **1.2**

63.8 Plio-Pleistocene basalt caps Santa Fe Group on mesas from 12:00 to 3:00. **6.2**

70.0 Turn **right** onto graded Forest Service Road 522, up Tierra Blanca Canyon. In Sibley Mountain, to the east, Kneeling Nun outflow sheet is sandwiched between the Rubio Peak Formation below and Bear Spring (or Uvas) Basaltic Andesite above. **3.5**

73.5 Outflow sheet of Kneeling Nun Tuff beneath Bear Spring (Uvas) Basaltic Andesite. Kneeling Nun Tuff rests on ash-fall deposits of the Sugarlump Formation (see Stop 1); together, the two units are about 120 m thick. **0.7**

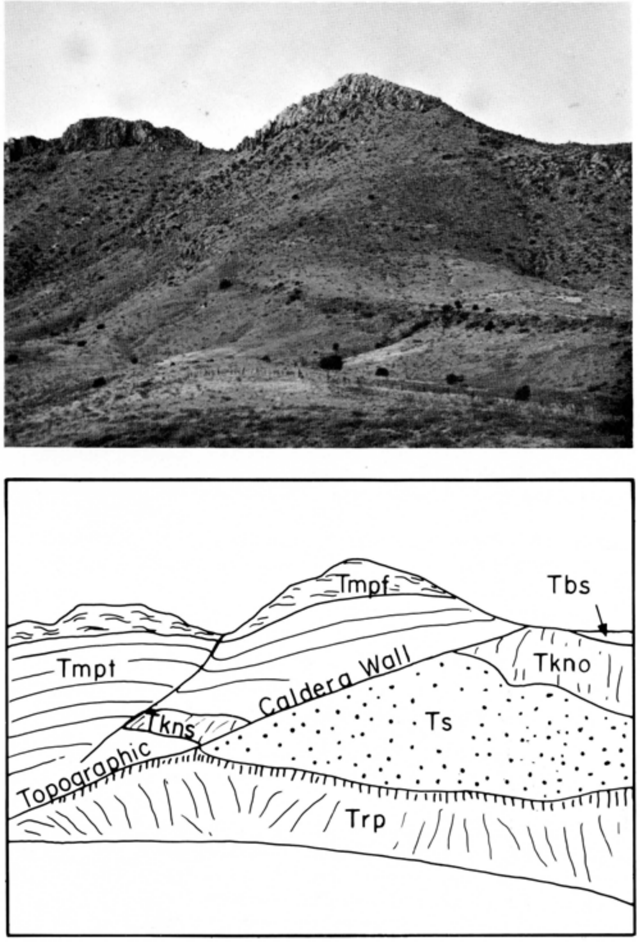

FIGURE 13—Topographic caldera wall of the Emory caldera, buried by moat deposits of the Mimbres Peak Formation, Tierra Blanca Canyon (Stop 10). Tbs = Bear Springs Basaltic Andesite; Tkno = outflow sheets of Kneeling Nun Tuff; Tkns = slump block of Kneeling Nun Tuff; Tmpf = rhyolite lava flow, Mimbres Peak Formation; Tmpt = bedded pumiceous moat-fill deposits, Mimbres Peak Formation; Trp = Rubio Peak andesite; Ts = Sugarlump Formation.

74.2 **STOP 10. Overview of topographic caldera wall and ring-fracture zone in moat of the Emory caldera.** Climb low hill of andesite of the Rubio Peak Formation to left (south) of road. Fig. 13 illustrates the scene before us. A northerly view toward McClede Mountain (Fig. 13 and right end of Fig. 14) shows Kneeling Nun outflow sheet and underlying Sugarlump Formation truncated by the topographic caldera wall, which in turn was buried by rhyolite pyroclastic moat deposits of the Mimbres Peak Formation. A rhyolite flow of the Mimbres Peak Formation caps McClede Mountain. The 10° difference in dip between Kneeling Nun Tuff and Mimbres Peak Formation indicates outward tilting on the flanks of the volcano, presumably during rise of the resurgent dome. To the west (Fig. 15 and left side of Fig. 14), rhyolite domes of the Mimbres Peak Formation (middleground) mark the location of a major ring fracture. The wooded mountain range on the skyline is the resurgent dome, with massive exposures of caldera-fill facies of Kneeling Nun Tuff and basement rocks (mainly Precambrian crystalline rocks). Across the moat, between the topographic caldera wall and the resurgent dome, Kneeling Nun Tuff is missing over a distance of about 8 km; moat deposits of the Mimbres Peak Formation lie on pre-caldera rocks. The principal ash-flow tuff is absent or spotty in moats of many resurgent calderas and may be the reason why the connection between resurgent caldera and ore deposits has not been recognized more widely. Structural and hydrologic conditions of moats favor mineralization, but it is possible to map an entire mining district without seeing any indication that its principal geologic event was the eruption of 10^2 to 10^3 km^3 of siliceous pyroclastic rocks. **0.7**

74.9 To the left, Rubio Peak volcaniclastic mudflow deposits are capped by an andesite lava flow; to the right, a low red hill is an exhumed Rubio Peak

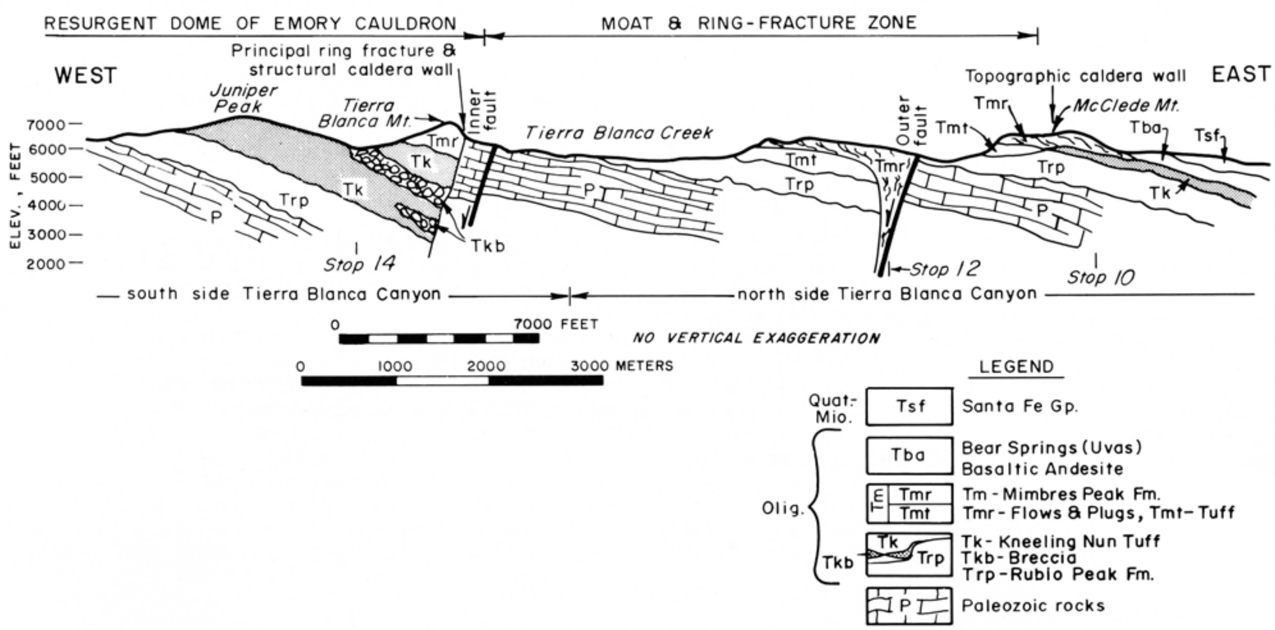

FIGURE 14—Geologic section through the eastern margin of the Emory caldera, Tierra Blanca Canyon. No vertical exaggeration. Section by W. R. Seager (*in* Elston et al., 1987).

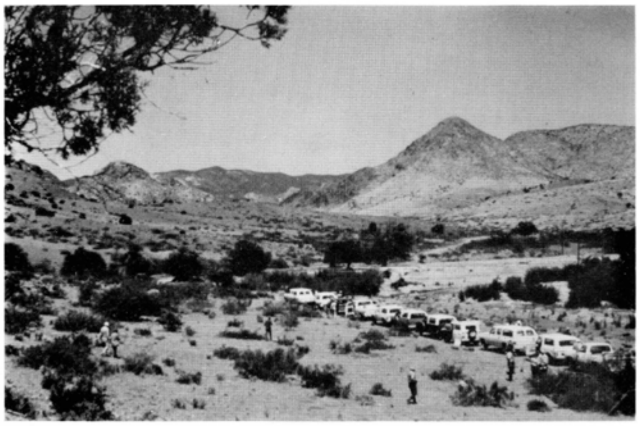

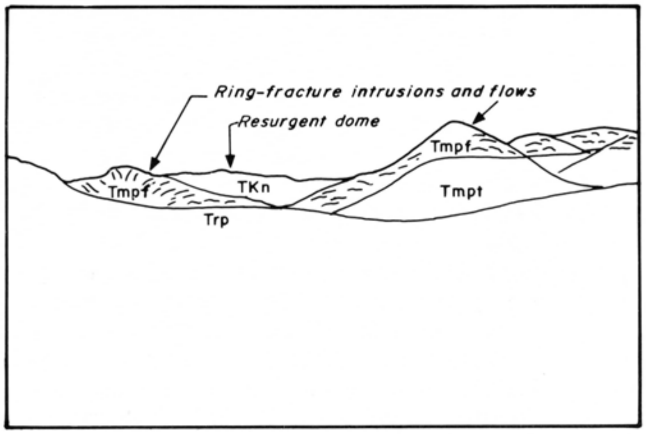

FIGURE 15—View from Stop 10 westward. Peaks in the middle ground are rhyolite ring-fracture domes of the Mimbres Peak Formation, wooded range on the skyline is part of the resurgent dome. Tkn = Kneeling Nun Tuff; Tmpf = rhyolite lava flows and domes, Mimbres Peak Formation; Tmpt = bedded pumiceous moat deposits, Mimbres Peak Formation; Trp = Rubio Peak Formation.

cinder cone. Even though it is quite insignificant, it is one of the few known centers for T2a andesitic rocks. Is it possible that the major ignimbrite calderas are superimposed on andesitic stratovolcanoes that foundered during caldera collapse and are therefore hidden from view? This was proposed by Lipman (1984) for the San Juan volcanic field of Colorado. It may well apply to New Mexico also, but it has not been demonstrated. **1.1**

76.0 **STOP 11. Pyroclastic moat deposits and ring-fracture domes of the Mimbres Peak Formation.** Ahead of us, on the north side of Tierra Blanca Creek, a funnel-shaped mass of flow-banded rhyolite penetrated 100+ m of bedded pyroclastic flows and spread out above them as a lava flow (Fig. 14). The succession from pyroclastic flows to lava has been recognized in many other moat and ring-fracture deposits; the two rock types are clearly cogenetic. Elsewhere, pyroclastic flows of the Mimbres Peak Formation contain sparse clasts of the lava that intrudes them. Evidently, partly solidified rhyolite magma penetrated close to the surface, vesiculated, and repeatedly erupted explosively as successive pyroclastic flows. During the eruption, solid pieces from the chilled part of the intrusion were incorporated in pyroclastic flows. Later, the partly molten part of the intrusion penetrated to the surface.

The pyroclastic rocks appear to have been deposited from small, low-temperature, high-density ash flows. At this locality they have not been studied in detail, but elsewhere they have given no preferred paleomagnetic orientation. Either they were still mobile after they passed through the Curie temperature, or magnetic minerals were obliterated by pervasive hydrothermal alteration. Flows are from <1 m to about 10 m thick. Subangular to angular clasts, mostly <10 cm in diameter, are scattered throughout the flows but are commonly more concentrated in crude zones, not necessarily at the base. At this locality, they are predominately of Rubio Peak andesite, but also include granite and metamorphic rocks (especially amphibolite) from the crystalline basement, as well as samples from the Paleozoic section. At one contact between two tuff beds there are meter-size rounded boulders of Kneeling Nun Tuff, evidently swept to this locality from the topographic caldera wall or the resurgent dome (Fig. 16).

In the pyroclastic flows, pumice clasts are somewhat compressed and poorly welded or unwelded, but are indurated with secondary minerals. On the

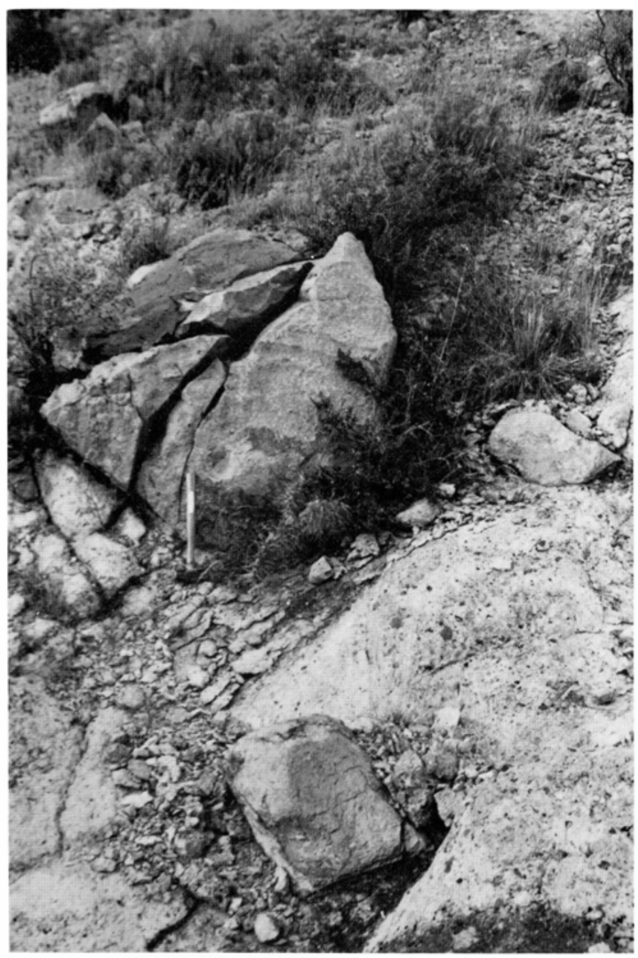

FIGURE 16—Boulders of Kneeling Nun Tuff in bedded pumiceous moat deposits of the Mimbres Peak Formation, Stop 11. Aside from these boulders, Kneeling Nun Tuff is absent in this locality and in the entire moat zone, between the structural and topographic caldera walls.

FIGURE 17—Inclusions of pumiceous moat deposits (with dark lithic clasts of Rubio Peak andesite), kneaded into flow-banded rhyolite of a ring-fracture dome, Mimbres Peak Formation. (Stop 12).

west side of the Emory caldera, I have identified zeolites (probably clinoptilolite) and smectite clays. In addition, there locally are millimeter to centimeter thick quartz veinlets in envelopes of hematitic alteration (Elston, 1957). Evidently, water played a major role in the posteruptive history of these rocks.

On the flanks of the intrusion and below the capping flow, pyroclastic rocks were fused to black perlitic vitrophyre. In partly fused rocks, only pumice fiamme are glassy; the matrix is strongly altered and has a greenish hue. **0.6**

76.6 **STOP 12 (optional). Ring-fracture rhyolite lavas of the Mimbres Peak Formation.** The lavas are on the south side of the funnel-shaped vent we saw from Stop 11. The flow-banded and flow-folded lava incorporates xenolithic boudins of an older and more porphyritic rhyolite from the Deer Peak dome, on the south side of Tierra Blanca Canyon. It also contains xenoliths of the tuff we saw at Stop 11 (Fig. 17); they appear to have been soft and were kneaded into the lava. **0.8**

77.4 Road forks, keep to the right on a steep and rutted road, **not suitable for passenger cars!** If you continue, please visit the Wittenberry Ranch on the left fork and inform the rancher of your presence. You can walk to Stop 13. **0.1**

77.5 **STOP 13 (optional).** Gate. Photo stop for view of pyroclastic moat deposits of the Mimbres Peak Formation invaded by the funnel-shaped ring-fracture intrusion mentioned in Stop 11, and capped by rhyolite lava that issued from the funnel. Pyroclastic rocks are fused to black vitrophyre at their contact with rhyolite lava (Fig. 18). **0.3**

77.8 Road junction. Continue on right fork, through gate. **1.1**

78.9 Road forks; continue on left fork. The structural wall of the Emory caldera is expressed as a fault on the north side of Tierra Blanca Mountain (9:00 to 10:00 o'clock). The fault brings the Mimbres Peak Formation against Paleozoic limestone. Dumps on hillsides are from small lead–silver mines and prospects of the Tierra Blanca mining district; their

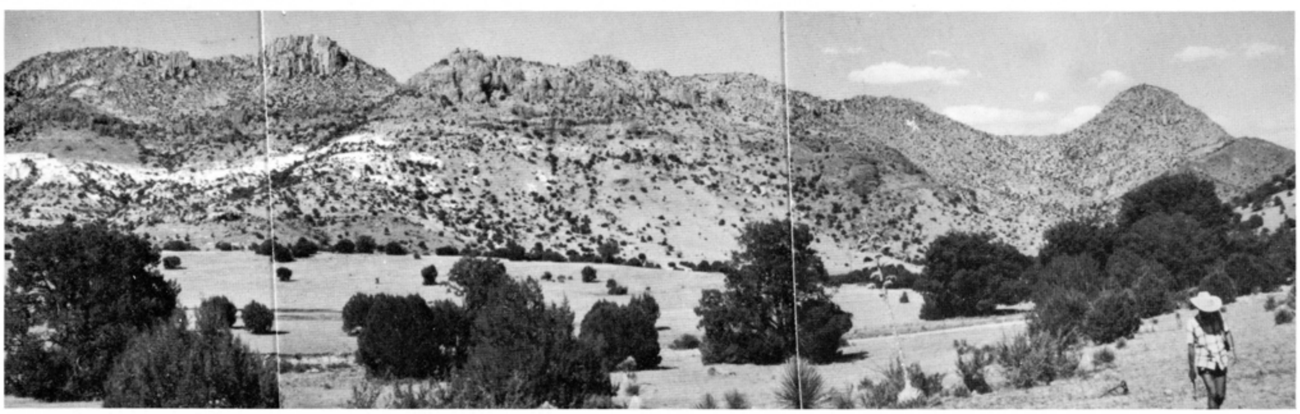

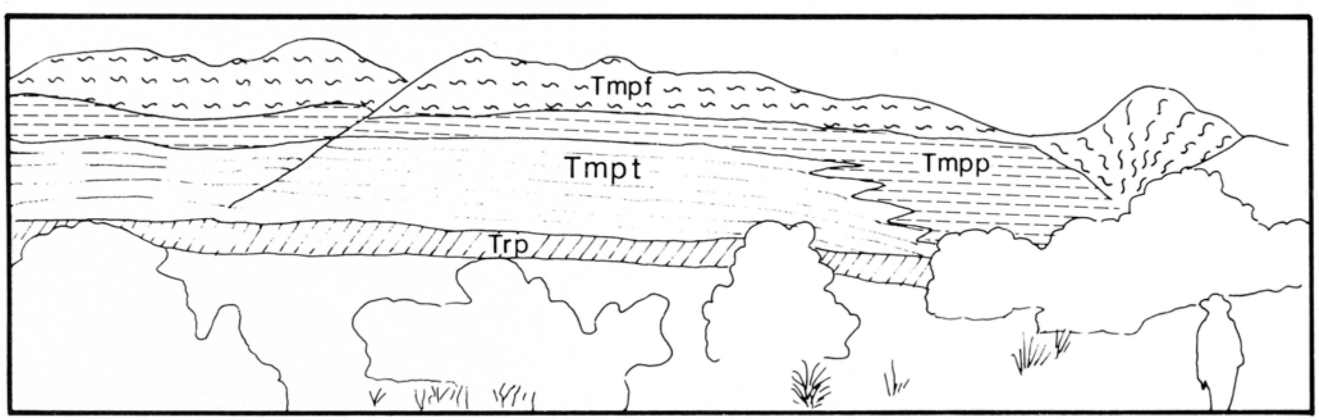

FIGURE 18—View from Stop 13, eastward toward moat deposits and a funnel-shaped ring-fracture intrusion grading into a lava flow. Pumiceous moat deposits adjacent to lava have fused to black perlitic glass. Tmpf = Mimbres Peak Formation, funnel-shaped, ring-fracture intrusion and rhyolite flow; Tmpp = bedded pumiceous moat deposits of Mimbres Peak Formation, fused to black perlitic glass; Tmpt = bedded pumiceous moat deposits, Mimbres Peak Formation; Trp = precaldera andesite lava flows of the Rubio Peak Formation.

FIGURE 19—Caldera-fill facies of Kneeling Nun Tuff, Tierra Blanca Canyon, Stop 14. Apparent dip to the west (right) is an illusion, the layering is caused by joints. Foliation of flattened pumice lenses actually dips about 40°E (to the left). Photo W. R. Seager (from Seager et al., 1978).

total production between 1885 and 1931 was $270,000 at prevailing prices (Northrop, 1959). The ore, now oxidized, partly replaced uppermost Fusselman Limestone (Silurian) below an impermeable cap of Percha Shale (Devonian). **0.2**

79.1 Cross structural caldera wall. Road forks, continue straight ahead. **0.3**

79.4 **STOP 14. Caldera facies of Kneeling Nun Tuff.** Olive-green volcaniclastic sandstone and minor andesite lava of the Rubio Peak Formation are poorly exposed on the grassy slope west of us. Chaotic dips suggest that this rock is allochthonous, probably part of a large megabreccia wedge that slid off the topographic wall during caldera collapse and was engulfed by Kneeling Nun Tuff. Kneeling Nun Tuff crops out on the ledges (west) of us and across Tierra Blanca Canyon. The tuff appears to dip west, but this is an illusion; the prominent partings are joints, not bedding (Fig. 19). The foliation of flattened pumice lenses dips 30–40°E, off the resurgent dome. About 800–900 m is exposed in Tierra Blanca Canyon; the base is cut off by a fault. Return to Hillsboro the way you came. **16.8**

96.2 Hillsboro. Turn right (east) on NM-152. **1.6**

97.8 For the next 1.4 mi, roadcuts are in hornfelsized Paleozoic sedimentary rocks, in contact with diorite and monzonite intrusions. **1.4**

99.2 Propylitized Late Cretaceous andesite in fault contact with altered Pennsylvanian sedimentary rocks. **1.6**

100.8 Outflow facies of Kneeling Nun Tuff on left. This is the last place we will see Kneeling Nun Tuff today. However, this is not the full extent of the outflow sheet. It is still about 30 m thick some 30 km east of here, in the Caballo Mountains, east of the Rio Grande (W. R. Seager, pers. comm. 1989). Its distribution was evidently unaffected by the present basin and range topography. **0.3**

101.1 Road left leads to Copper Flat, a mineralized Late Cretaceous quartz monzonite plug (73.4 ± 2.5 Ma; Hedlund, 1977). It was emplaced in the middle of a nearly circular area of propylitized andesite, about 7 km in diameter, dropped by faults (see mile 99.2) against Paleozoic sedimentary rocks. Latite dikes, some bordered by quartz veins, radiate from the quartz monzonite body and cut both andesite and quartz monzonite. The veins have yielded copper and gold and are a source of placer gold. A breccia pipe within the quartz monzonite stock was developed as an open-pit copper–gold–silver–molybdenum mine by Quintana Minerals Corp. in the late 1970's and early 1980's, and then abandoned when the price of copper collapsed. Total production of the district was about $8 million, mainly in gold before 1935 (Dunn, 1982). Dunn (1982) interpreted the quartz monzonite as the core of an andesite caldera. Lipman and Sawyer (1985) identified the matrix of andesite breccia as quartz-bearing tuff and interpreted the andesite as collapse breccia in an ash-flow tuff. If so, caldera fill and outflow from the caldera have been completely eroded. Drill holes, 900 m (3000 ft) deep, did not reach the base of the andesite (Dunn, 1982). **12.6**

113.7 Intersection of NM-152 and I-25. Turn left (north) on I-25 and drive about 12 mi to Truth or Consequences.

Days 6 and 7: Field guide to the Taylor Creek Rhyolite, Black Range, New Mexico

Wendell A. Duffield

Introduction

The main objectives of this part of the field trip are to examine structural and textural features of a group of Tertiary high-silica rhyolite lavas, the Taylor Creek Rhyolite, that locally contain cassiterite-bearing veins, and to evaluate evidence suggestive of a genetic link between the lavas and the tin in these veins. The Taylor Creek Rhyolite includes 20 lava domes and flows (Fig. 1; Duffield et al., 1987). Each of the lavas is devitrified, flow-foliated, and moderately porphyritic. Because of these shared characteristics, the lavas generally are indistinguishable from one another in outcrop and hand sample. Whole-rock and feldspar-phenocryst chemical compositions also are approximately constant throughout the lava field (Table 1). To facilitate subdivision into eruptive units during field mapping, outcrops have been interpreted with reference to a three-dimensional structural model derived from studies of young silicic lavas (Fig. 2). Interflow contacts are marked locally by erosional remnants of flow-generated breccia that enveloped each lava during emplacement and by sequences of pyroclastic deposits sandwiched between flows.

Each lava is interpreted to have been fed from its own

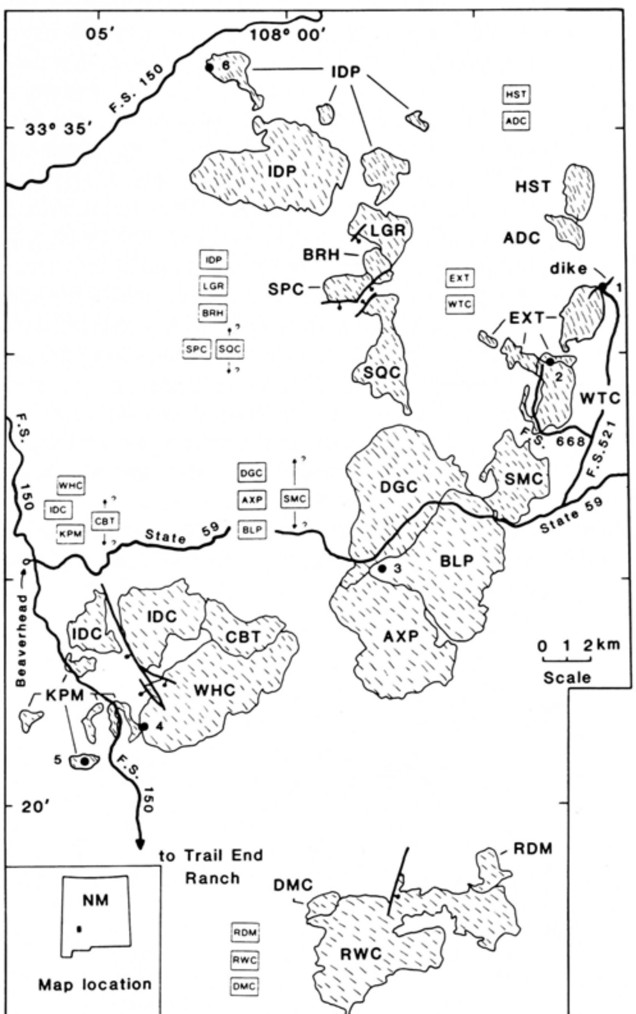

FIGURE 1—Map showing distribution of domes and flows of the Taylor Creek Rhyolite, generalized after Duffield et al (1987). Three-letter symbols for the map units are abbreviations for local geographic features. Each map unit is interpreted to represent a single lava dome or flow emplaced from its own vent. Stratigraphic relations based on field evidence are shown next to groups of overlapping lavas. Age relations among non-overlapping lavas are unknown. Field-trip stops are numbered.

TABLE 1—**(A)** Mean whole-rock composition with standard deviation and CIPW norm of the Taylor Creek Rhyolite. The mean is of 17 analyses recalculated to 100% on a volatile-free basis. Original analyses included between 1.1 and 0.2 weight percent volatiles lost on ignition at 900°C. Map units WHC, CBT, IDC, KPM, BLP, DGC, SMC, AXP, SQC, SPC, BRH, LGR, WTC, and EXT are represented. Analyses by x-ray fluorescence in USGS laboratories at Menlo Park, California, and Denver, Colorado. Analysts: J. Ardith, K. Bartel, T. Frost, J. Stewart, and J. Taggart. All 17 complete analyses are reported in Duffield et al. (1987).
(B) Mean compositions with standard deviations for sanidine and plagioclase phenocrysts of the Taylor Creek Rhyolite. Three grains of each feldspar species were analyzed at core, intermediate, and rim positions for each of 27 studied samples; these samples represent all 20 map units, the dike of Taylor Creek Rhyolite that crosscuts map unit EXT, and two deposits of vitrophyric tephra of Taylor Creek Rhyolite. Analyses by electron microprobe. Analyst: Edward A. du Bray, USGS, Denver, Colorado.

(A)	Mean	SD
SiO_2	77.82	0.10
TiO_2	0.14	0.00
Al_2O_3	12.12	0.07
Fe_2O_3	1.12	0.03
MnO	0.05	0.00
MgO	0.14	0.01
CaO	0.29	0.03
Na_2O	3.40	0.06
K_2O	4.89	0.03
P_2O_5	0.03	0.00
Total	100.00	

Q	38.61
C	0.78
Or	28.88
Ab	28.76
An	1.24
Hy	0.35
Il	0.11
Hm	1.12
Ru	0.08
Ap	0.07
Total	100.00

	Sanidine		Oligoclase	
(B)	Mean	SD	Mean	SD
SiO_2	66.53	0.10	65.26	0.13
Al_2O_3	19.06	0.09	21.10	0.11
FeO	0.12	0.01	0.17	0.01
CaO	0.36	0.01	2.28	0.06
Na_2O	5.96	0.11	8.94	0.07
K_2O	7.90	0.11	2.04	0.10
Total	99.93		99.79	

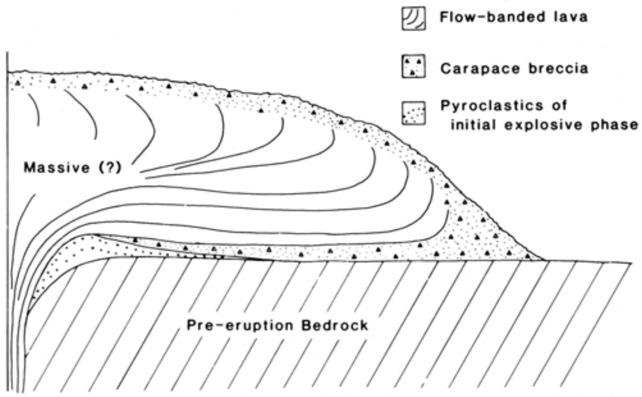

FIGURE 2—Structural model of an idealized rhyolitic lava flow in cross section. The relative volumes of the three principal elements may vary greatly from flow to flow. Most outcrops of Taylor Creek Rhyolite correspond to the flow-banded part of the model. Most carapace breccia has been removed by erosion, and pyroclastic deposits are partly eroded and inferred to be partly buried.

vent. Though specific locations are generally unknown, vents are interpreted to lie within lava outcrop areas and thus are distributed within the several hundred square kilometers covered by these rocks. High-precision $^{40}Ar/^{39}Ar$ age determinations on sanidine phenocrysts indicate that the growth of the lava field probably lasted no more than 100,000 years at about 28.2 Ma (Dalrymple and Duffield, 1988). A typical eruptive sequence began with a pyroclastic phase, which was followed by the apparently quiet effusion of lava that fed a dome or flow. Beds of agglutinate represent welded fallback from lava fountains, and gradation of agglutinate into lava suggests that some flows were fountain-fed (Duffield, in press); rocks formed by this eruptive process will be examined at Stop 2. Individual domes and flows range from about 0.2 to 10.5 km^3 in volume and cumulatively amount to about 55 km^3; an uncertain but potentially equal or greater volume of pyroclastic products also was emplaced during the growth of the rhyolite field.

The cassiterite-bearing veins that crosscut lavas typically are no larger than 1 cm × 10 m × 10 m, and areas of veining are few and far between. The veins represent partial filling of open joints. Recent mapping (Duffield et al., 1987) demonstrates that the veins are in the outermost rind of newly emplaced, cooling lava, an environment characterized by steep gradients in temperature, vapor pressure, and vapor composition. Cassiterite at one locality (Stop 3) occurs as euhedral crystals on the walls of miarolitic cavities, again in the outermost part of a lava where the steep gradients mentioned above favored mineral deposition from vapor escaping lava as it cooled and devitrified. Comparison with experimentally determined phase relations indicates that bixbyite and pseudobrookite in the miaroles grew at a temperature of at least 500°C (Lukfin, 1976). Temperatures of homogenization of primary fluid inclusions in cassiterite and other vein minerals range from about 700 to 150°C (Eggleston and Norman, 1986), again consistent with initial formation in a cooling-lava environment. Studies of vein-mineral paragenesis indicate that temperature of deposition decreased monotonically with time (Foord and Maxwell, 1987). Some early-deposited, high-temperature vein materials may have been partly redistributed during a hot-water hydrothermal regime that followed the initial vapor-dominated regime, as the boiling-point isotherm migrated into cooling lava (Duffield, in press).

Maxwell et al. (1986) estimated that 70,000 pounds of tin have been mined from veins in the Taylor Creek Rhyolite (mostly as derivative placer deposits) and that about 10,000,000 pounds of tin remains in unmined mineralized rocks. Mobilization and subsequent concentrated deposition of 1 part per million (ppm) tin from an estimated 55 km^3 of rhyolite lava could provide at least an order of magnitude more tin than this estimated 10^7 pounds. Devitrified Taylor Creek Rhyolite contains from 1 to 7 ppm less tin than its vitrophyre (Fig. 3), which is an indication that at least 1 ppm tin was released during devitrification; nearly all of the estimated 55 km^3 of lava is devitrified. This mass-balance consideration suggests that much tin has been lost from the lava system. Some "missing" tin almost certainly was removed during erosion of the outermost rind of each lava, the inferred favored site of cassiterite deposition. Some tin also may have been lost to the atmosphere around fumaroles rooted in cooling Taylor Creek lavas; tin is known to be highly mobile in a vapor phase, probably as halogen complexes, in a cooling-lava environment (Krauskopf, 1979). In addition, tin may have been lost to the atmosphere from Taylor Creek Rhyolite magma during lava fountaining. A quantitative assessment of the relative roles of these processes in affecting the disposition of tin contained in Taylor Creek magma is not possible, but the presence of welded fallout deposits, indicative of emplacement by lava fountaining, suggests that not all of the original magmatic tin was mobilized and lost simply by erosion and by outgassing at fumaroles.

Road log: Day 6

Leave Truth or Consequences to the north on Date Street. Turn north onto Interstate 25 at entrance 79 and go north 4.8 mi to exit 83. Take New Mexico 181 to the northwest 3.8 mi. Turn left onto NM-52 and follow this highway 35.8 mi to the intersection with NM-59 (Beaverhead Road). Follow this road 13.6 mi to the intersection with Forest Service Road 521 (Adobe Ranch Road). Geological features along the route from Truth or Consequences to this point have been described by Osburn et al. (1986). Basically, the route ascends a broad field of Cenozoic alluvium that dips gently to the east; crosses the Sierra Cuchillo, a north-trending,

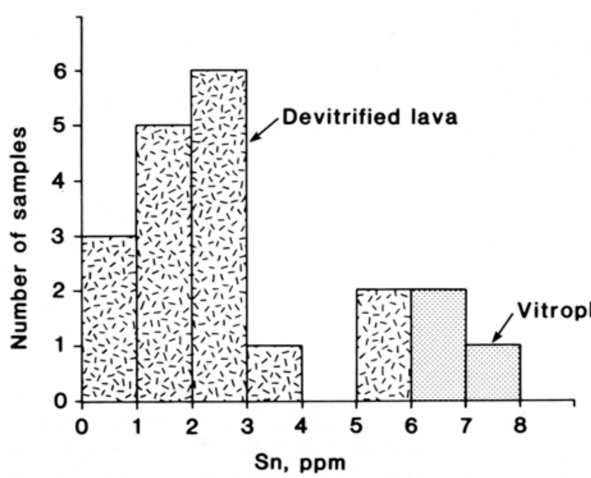

FIGURE 3—Histogram showing tin content of whole-rock samples of the Taylor Creek Rhyolite keyed to the character of the groundmass. Analyses by inductively coupled plasma spectrometry. Analyst, Jean Kane, USGS, Reston, Virginia.

fault-bounded range underlain by Paleozoic sedimentary rocks and Tertiary intrusives and volcanics; follows northward along the axis of Cenozoic alluvial deposits in the Winston graben; and climbs westward onto the Black Range, where the Taylor Creek Rhyolite crops out as part of the Mogollon–Datil volcanic field.

Follow FS-521 to the north 5.9 mi (Fig. 1).

STOP 1. The purpose of this stop is to examine a dike of rhyolite that is interpreted to be part of the vent system for adjacent lava of Taylor Creek Rhyolite (Fig. 1, map unit EXT). The dike extends about 400 m to the north and slightly less to the south of the road, but does not crop out at the road itself. Dike contacts are vertical or nearly so. The trace of the dike forms an open **S** shape whose average trend is northeast. This trend is roughly parallel to that of normal faults that offset Taylor Creek Rhyolite a few kilometers to the south and west and may reflect structural control of dikes that fed Taylor Creek eruptions in this part of the lava field.

North of the road, the dike intrudes a rhyolitic ash-flow tuff, and south of the road it intrudes a gently dipping sequence of variably welded rhyolite agglutinate, which is stratigraphically above this tuff. The south end of the dike appears to merge with rhyolite lava that overlies the agglutinate, but outcrops are too poor to unequivocally define this relation. The dike is chemically and modally indistinguishable from the intruded agglutinate and overlying lava. Moreover, the compositions of feldspar phenocrysts are the same in all of these rocks. These features are consistent with the interpretation that the dike represents part of the feeder system for the vent that produced the agglutinate and lava. Although the dike clearly crosscuts the agglutinate at the present level of exposure, it may have grown upward through these deposits as an eruption progressed.

South of the road, the dike is about 30 m thick, and to the north it thins to a tapered termination. Whereas nearly all of the exposed parts of the dike are characterized by a devitrified groundmass, a several centimeters thick selvage of vitrophyre is preserved along the contact with country rocks at the tapered end, presumably because the margin of this thin part of the dike cooled quickly enough to preclude devitrification. Please do **not** sample the vitrophyre, because glass is not abundant here and is **rare** throughout the Taylor Creek Rhyolite lava field.

Note that much of the dike outcrop exhibits a gently south-plunging lineation. My interpretation is that this lineation is an expression of axes of a tightly folded flow foliation and intersections of this foliation with joint surfaces. Presumably such structures formed as magma flowed upward, toward the site of eruption. In view of the fact that the present level of exposure may have been at shallow depth (100–200 m?) during dike emplacement, the structures also could have formed during drainback into the eruptive fissure at the end of eruption.

Return to vehicles. Backtrack 4.2 mi to intersection with FS-668. Follow this road 1 mi west and 1.5 mi north to the Nugget Gulch cassiterite-placer area.

STOP 2. Nugget Gulch is eroded along the contact between a lava dome (Fig. 1, map unit WTC) and a sequence of pyroclastic deposits at the base of another lava that overlies this dome. Part of the carapace breccia of the dome is preserved along the streambed, evidence that the stream is at or very near the pre-erosion outermost rind of the dome. Cassiterite-bearing veins are concentrated in this area. The dome is locally silicified and contains quartz veins, products that mark the shallow roots of a hot-spring system. Nuggets of wood tin, presumably eroded from veins in the dome, are present in modern stream sediments. The overlying pyroclastic deposits are not mineralized, which is consistent with mineralization of the dome immediately following emplacement and prior to deposition of the overlying rocks.

Mapping demonstrates that most of the pyroclastic beds are the products of fallout from lava fountaining. These beds drape a pre-eruption landscape whose configuration is mimicked by the pattern of dips exhibited by the drapery. The beds range from one to several meters thick and show various degrees of welding, which generally increases upward through the sequence (Fig. 4). About 30 m stratigraphically above the base of the sequence near Nugget Gulch, one encounters a dense, massive rhyolite that simulates a lava flow. In thin section, this rock is seen to be of thoroughly welded particulate origin. Immediately above this type of rock, in outcrops about 2 km north of Nugget Gulch, dense, massive rhyolite shows no evidence of a welded particle origin in thin section. However, because they are part of a continuous succession that includes considerable agglutinate, a succession that appears to represent the products of a single eruption, such rocks may also be the products of lava fountaining whose fallback homogenized enough to obliterate evidence of a particulate eruptive history. Knowledge of the character of eruption, quietly effusive versus fountaining, is critical to an accurate reconstruction of the volatile constituents of a magma, and is thus an important factor in evaluating the tin budget of Taylor Creek Rhyolite magma.

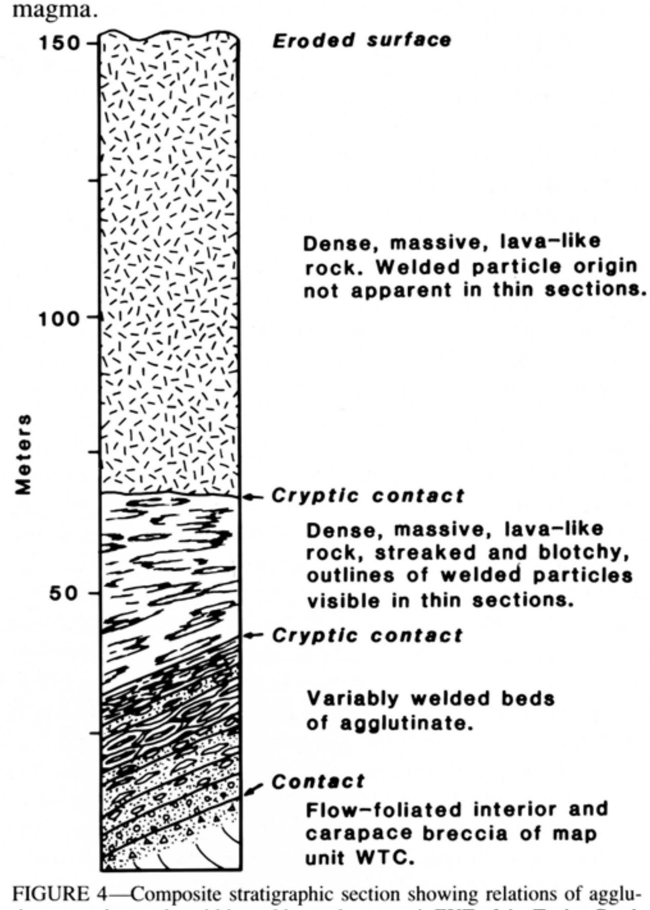

FIGURE 4—Composite stratigraphic section showing relations of agglutinate to other rocks within and beneath map unit EXT of the Taylor Creek Rhyolite, at and near field-trip Stop 2.

Backtrack to intersection with NM-59. Drive 5.9 mi west. All but the first 2 mi of this drive is over lavas of Taylor Creek Rhyolite. Park on the south side of the highway, opposite a water pond just north of the road, and walk about 100 m south to the rim of Paramount Canyon.

STOP 3. The frothy, vesicular rhyolite at the canyon rim represents rock near the pre-erosion margin of a lava flow (Fig. 1, map unit BLP); erosional remnants of the carapace breccia of this lava crop out about 100 m to the northeast and to the southwest of this locality. Tin mineralization here occurs as thin veins, mostly of hematite and cassiterite, and as rare cassiterite crystals attached to the walls of vesicles. Other minerals in vesicles include quartz, hematite, topaz, bixbyite, pseudobrookite, and beryl. These minerals were deposited from a vapor phase at a temperature of at least 500°C (Lufkin, 1976). Much of the cliff below this locality consists of white, bleached rhyolite that has experienced considerable vapor-phase crystallization, directly analogous to the zone of vapor-phase crystallization described by Smith (1960) for ash-flow tuffs. Apparently, this locality was the site of intense degassing of the lava flow as it cooled to ambient temperature, and many volatile constituents were deposited in the outermost rind of the flow during this process. The locality is within 100–200 m of contacts with two younger lavas (Fig. 1, map units AXP and DGC), neither of which is mineralized here. Thus, similar to the situation at Stop 2, mineralization apparently was completed in rocks of the host flow before overlapping younger flows were emplaced.

A sequence of pyroclastic deposits of Taylor Creek Rhyolite crops out about 100 m northeast of the mineralized locality. These beds overlie the lava flow that is host to mineralization and are in turn overlain by another flow (DGC). They extend at least 3 km to the northeast, dip as much as 45° off the conformable, steeply dipping flank of the underlying lava, and are densely welded in part. These features suggest a local origin, perhaps as products of an initial pyroclastic phase of the eruption that fed the DGC lava dome. Fragments of Taylor Creek Rhyolite vitrophyre are present in some of the pyroclastic beds, providing some of the few samples of non-devitrified rock.

Return to the vehicles and continue 11.2 mi west on NM-59 to the intersection with NM-61 (FS-150), at Beaverhead Ranger Station. Most of the exposures along this part of the road are in alluvium that is derived in large part from the Taylor Creek Rhyolite. Turn south on NM-61 and drive 6.9 mi, to where the road reaches the floor of the valley of Taylor Creek. Exposures along this part of the road include more alluvium, Tertiary mafic lavas younger than Taylor Creek Rhyolite, and a few outcrops of the Taylor Creek Rhyolite.

STOP 4. If gate is locked, walk 0.5 mi upstream along Taylor Creek; otherwise drive this distance. Walk another 0.5 mi upstream to where the valley narrows into a nearly vertical-walled canyon eroded across the terminus of a 7.3 km long flow of Taylor Creek Rhyolite (Fig. 1, map unit WHC). Excellent views of carapace breccia are available in the canyon walls. The breccia is a poorly sorted mass of foliated lava-flow fragments that are tumbled into diverse orientations. Fragments range from ash to blocks as wide as several meters. The breccia is crudely layered, a structure that probably formed during recurring episodes of gravity-driven debris avalanches caused by repeated oversteepening at the snout of the advancing lava flow. Continuing upstream, one sees that the contact between breccia and coherent, flow-foliated lava is irregular but broadly parallel to layering in the breccia. Cassiterite-bearing veins are present in the coherent rhyolite and within the base of the breccia.

Return to vehicles and continue 0.7 mi southwest on FS-150 to Wall Lake Campground.

STOP 5. Walk about 600 m west-southwest to the top of a hill that overlooks, to the west, 60 m high, nearly vertical cliffs eroded in Taylor Creek Rhyolite. Note the first-order pattern of flow foliation, which steepens and locally overturns northward across the outcrop. This sort of foliation steepening, sometimes called ramping, is relatively common near upper and distal parts of Taylor Creek lavas and tends to steepen upstream, thus providing an indication of the local horizontal component of lava flow during emplacement. Elsewhere, within the core of a lava flow or dome, foliation tends to be horizontal or nearly so, perhaps due simply to the relatively large load of overlying material. Steep foliation that fans upward in Taylor Creek lavas was initially interpreted to mark fissure vents immediately beneath the fan structure (Fries, 1940; Ericksen and Wedow, 1976). However, such structure probably is a common feature in the outer parts of a dome or flow, where upward lava movement is expected along the unconfined free surface, and is thus not necessarily related to the location of a vent.

Return to the vehicles and continue southward on FS-150, 5.1 mi to intersection with FS-225. Turn right on FS-225 and drive 6.3 mi to Trail End Ranch, the lodging facilities for the night.

Road log: Day 7

Backtrack to intersection of FS-150 and NM-59. Drive north 7.0 mi and then northeast 9.5 mi on FS-150 (NM-61 and NM-78, respectively). Follow dirt track about 0.3 mi southeast to base of cliff capped by Taylor Creek Rhyolite (Fig. 1, map unit IDP).

STOP 6. This stop is optional and may be cancelled for lack of time. This is one of the few lava flows of Taylor Creek Rhyolite with an exposed base. The flow overlies an ash-flow sheet, the tuff of Garcia Camp as described by Lawrence (1985), which represents the product of an initial pyroclastic phase in an eruption that then produced the overlying lava. The tuff is almost completely unwelded and consists of multiple superposed ash flows. Discoidal pumice lumps are locally imbricate, thus giving evidence of local horizontal flow direction; at this locality flow appears to have come from the south-southeast.

The basal breccia of the rhyolite lava flow is fairly consolidated, probably due to compaction and minor welding caused by the load of the overlying hot lava flow. Lateral facies of carapace breccia, as seen at Stop 4 yesterday, tend to be less consolidated and are often crudely layered with steep dips. These differences, though often subtle, help one to interpret isolated outcrops of carapace breccia in terms of the overall textural and structural zones of a lava as illustrated in Fig. 2.

Return to vehicles and backtrack to junction of FS-150 (NM-78) and NM-61 to pick up road log for next segment of field trip. **9.5**

Day 7: Direction-to-source indicators in Bloodgood Canyon Tuff and tuff of Triangle C Ranch at Coyote Well

James C. Ratté

Summary

Furrows having a wavelength of 1–2 m, and associated grooves and striations in the Bloodgood Canyon Tuff, and imbricated clasts in the overlying tuff of Triangle C Ranch (Triangle C tuff for brevity) are directional features that can be used to point toward their eruptive sources. The source of the Bloodgood Canyon Tuff has been identified previously as the Bursum caldera (Ratté et al., 1984), the nearest margin of which is about 35 km southwest of Coyote Well (Stop 7-2 in Fig. 12 of Day 3, p.m.). The source of the Triangle C tuff is not known, nor is it known for sure how, or if, the Triangle C correlates with other regional ash-flow tuffs in this area. The Bloodgood Canyon and Triangle C are both high-silica rhyolite tuffs nearly identical in composition and texture, and their $^{40}Ar/^{39}Ar$ ages are indistinguishable at 28.0 Ma (McIntosh, this volume). Thus, it seems likely that the Triangle C tuff is a late eruptive unit of Bloodgood Canyon *magma,* due to erosion preserved only locally in some sectors of the outflow sheet. The Triangle C tuff has normal magnetic polarity, whereas the Bloodgood Canyon Tuff is reversed, indicating that at least a few thousand years separated their eruption.

Until recently, the Triangle C tuff had been recognized only in the Triangle C Ranch area (Ratté et al., 1989), but it is now known to be present east of Reserve, at about the same distance from the Bursum caldera as here. These additional Triangle C tuff localities, in a different sector relative to the Bursum caldera, are believed to lend credence to the idea that the Bursum caldera is its source.

Only the upper part of the Bloodgood Canyon Tuff is exposed at Coyote Well, but the tuff is 60–70 m thick near Coyote Peak about 8 km to the northwest (Fig. 12 of Day 3, p.m.). At Coyote Well, Bloodgood Canyon Tuff crops out in the creek bottom above the well, where it is overlain by about 2 m of brownish-gray, crystal-rich, crudely bedded pyroclastic surge(?) deposits, which in turn are overlain by pinkish-white, poorly welded, pumice-rich Triangle C tuff (Fig. 1).

At the contact between the Bloodgood Canyon Tuff and the overlying crudely bedded pyroclastic deposit, the Bloodgood has a silicified rind 0 to about 4 cm thick (Fig. 2). The silicified rind mimics the meter-scale furrows on the top of the Bloodgood Canyon Tuff (Fig. 3A), and the furrows are filled in by the overlying pyroclastic deposit. Where the silicified rind is exposed in plan view, it is seen to be marked by centimeter-scale grooves or striations (Fig. 3B) which generally parallel the axes of the furrows, but in at least one exposure diverge across the crest of a furrow. The grooves originated as gouges where lithic fragments were plucked (Fig. 3B) from the Bloodgood Canyon Tuff; these gouges have the appearance of glacial chattermarks and are believed to be useful in the same way as their glacial counterparts in interpreting the direction of movement of the agent that caused them. At Coyote Well, the grooves trend S35W parallel to the axes of the longer wavelength furrows, and both features are radial to the Bursum caldera as shown in Fig. 4. Near Coyote Peak, about 8 km northwest of Coyote Well, less well exposed but identical markings at the top of the Bloodgood Canyon Tuff are aligned S25-50W, pointing more toward the center of the Bursum caldera.

The Triangle C tuff in the Coyote Well and Coyote Peak areas ranges from 0 to about 50–60 m thick, and generally thins to the north, east, and west, which suggests a source to the south. It is a nonwelded to poorly welded ignimbrite in most places, commonly pink in its lower part and light-gray to nearly white above. It contains pink to white, glassy pumice lapilli and lumps (blocks) as much as 10–15 cm long, and consists of high-silica, alkali rhyolite with about 10% small (1–3 mm) phenocrysts of moonstone (sanidine), quartz, and sparse biotite.

In the Coyote Peak area, the tuff consists of several thin pyroclastic flows and interlayered bedded ash-fall tuffs totaling about 40 m and overlain by another 15–20 m of light-gray, pumiceous, poorly welded ignimbrite. Accidental lithics of both rhyolite and andesite are common in the lower part.

Imbricated, silicified, rhyolitic clasts occur mainly within about 10 m of the base of the Triangle C tuff near Coyote Peak and near Coyote Well. These clasts are unique because of their platy discoidal form and more or less uniform 2–3 cm thickness (Fig. 5). Their form and petrography would seem to leave little doubt that the clasts were derived from a silicified rind, such as that observed at the top of the Bloodgood Canyon Tuff near Coyote Well, and presumably elsewhere.

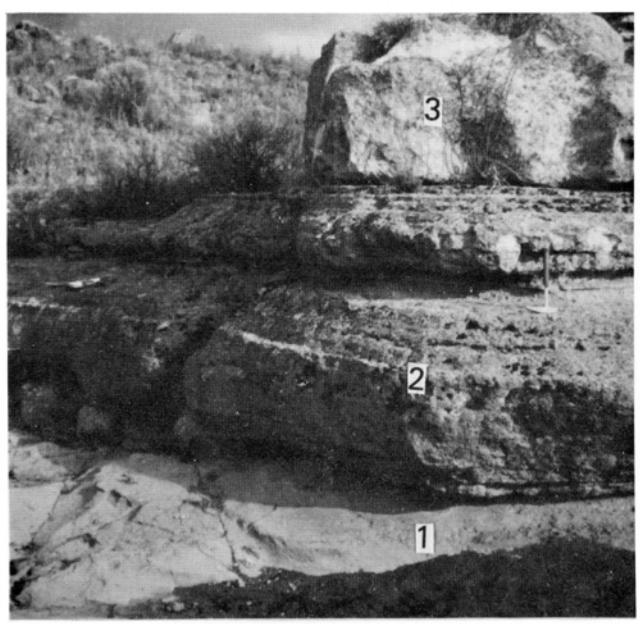

FIGURE 1—Volcanic sequence along Coyote Canyon above Coyote Well. 1 = Bloodgood Canyon Tuff; 2 = crystal-rich pyroclastic surge deposit; 3 = tuff of Triangle C Ranch.

FIGURE 2—Silicified rind at top of Bloodgood Canyon Tuff along Coyote Canyon above Coyote Well. **A,** Silicified rind (2) marks top of Bloodgood Canyon Tuff (1), overlain by crystal-rich pyroclastic surge deposit (3). **B,** Closeup view of silicified rind at top of Bloodgood Canyon Tuff. Pen for scale.

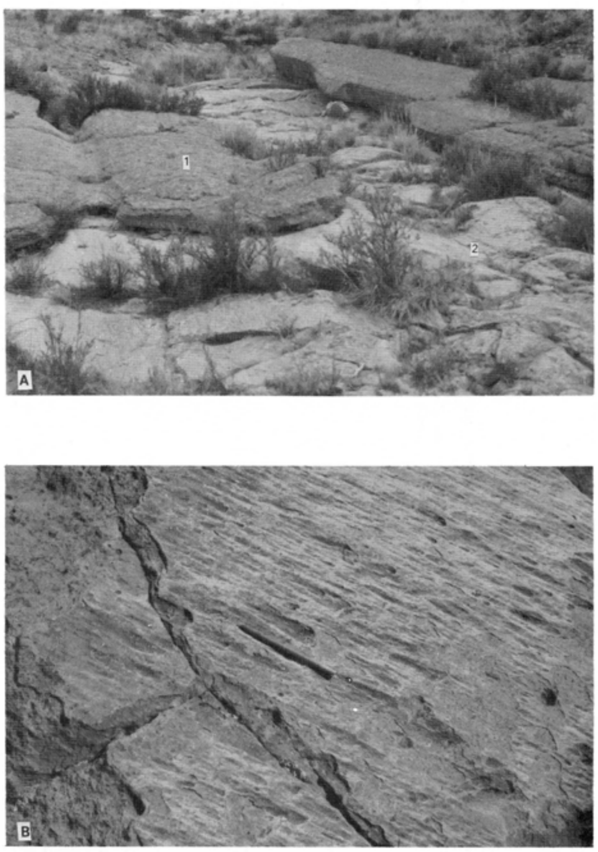

FIGURE 3—Transport-direction indicators at top of Bloodgood Canyon Tuff in Coyote Canyon above Coyote Well on Triangle C Ranch. **A,** crystal-rich pyroclastic surge deposit (1) fills meter-wavelength furrows on top of striated surface of Bloodgood Canyon Tuff (2). **B,** Small-scale grooves in top of Bloodgood Canyon Tuff show chattermarks where lapilli-size lithic inclusions were plucked from the tuff, scouring its top.

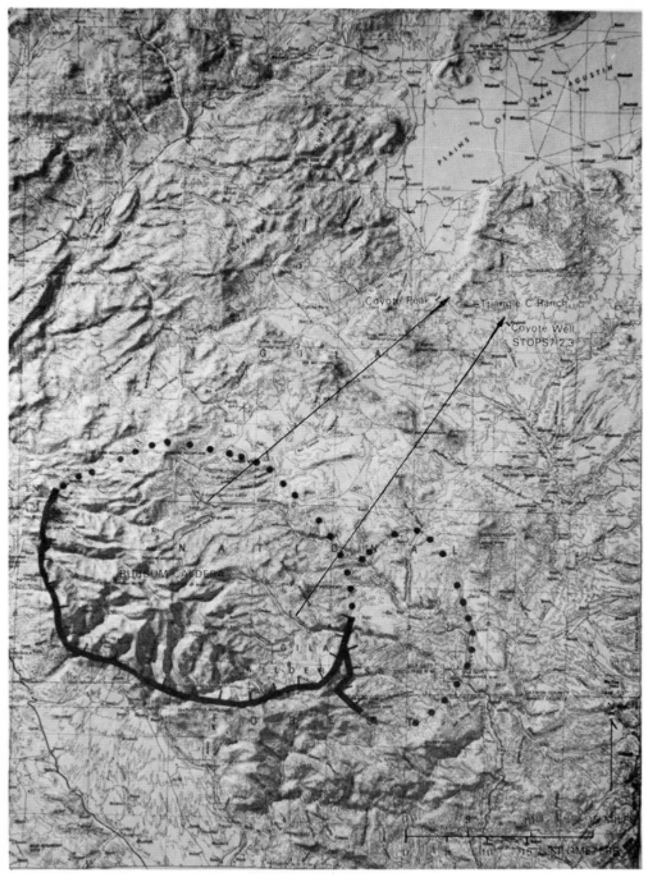

FIGURE 4—Raised-relief map of western Mogollon Plateau showing outlines of Bursum and Gila Cliff Dwellings calderas. Arrows (1, 2) indicate transport directions for pyroclastic surge deposits overlying Bloodgood Canyon Tuff as indicated by furrows and grooves in upper Bloodgood Canyon Tuff near Coyote Well (1) and Coyote Peak (2).

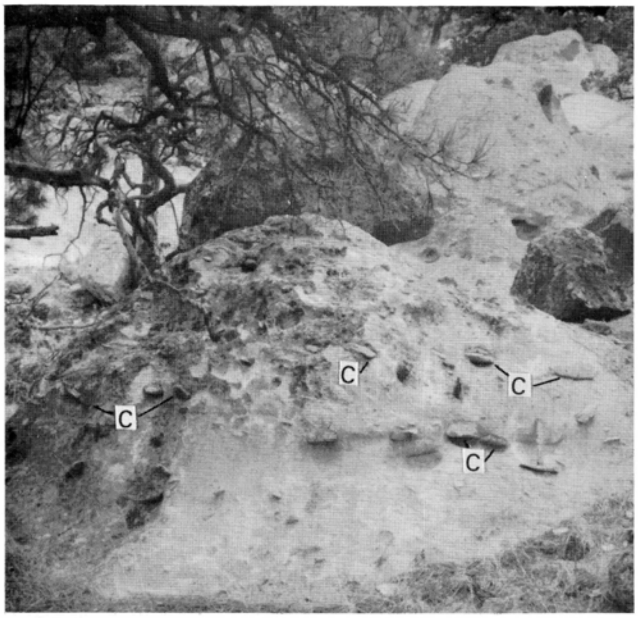

FIGURE 5—Imbricate clasts (c) of silicified Bloodgood Canyon Tuff in lower part of tuff of Triangle C Ranch near Coyote Peak. Similar imbricate clasts are present at Stop 7-2 near Coyote Well.

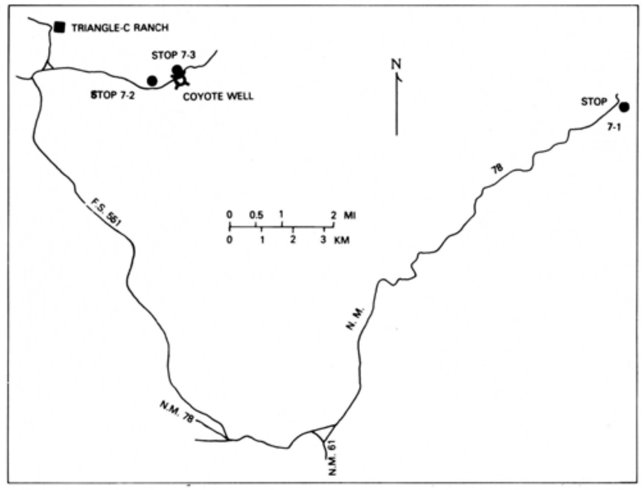

FIGURE 6—Index map showing location of Coyote Well area and Stops 7-2 and 7-3. Map ties into map for Day 6 and Stop 7-1.

Whereas measurements of transport direction for imbricate clasts near Coyote Peak (most of which are exposed mainly in profile) seem to indicate a source to the southeast, clasts in Triangle C outcrops near Coyote Well are exposed in plan as well as profile and show transport directions from the southwest as commonly as from the southeast. A transport direction from the southwest is consistent with a source within the Bursum caldera, the same as for the underlying Bloodgood Canyon Tuff. This suggests that the tuff of Triangle C Ranch really is a last gasp of Bloodgood Canyon Tuff eruptions, as was considered on the basis of stratigraphic position and petrographic similarity when first observed. The radiometric ages of the two tuffs are consistent with this interpretation and would seem to closely bracket a magnetic polarity reversal. However, measurements of clast transport directions from additional sites are needed to better define the source of the tuff of Triangle C Ranch.

Road log

Return to junction of FS-150 (NM-78) and NM-61 (Fig. 6).

Mileage

0.0 Reset mileage and turn right on NM-78. **2.0**

2.0 Intersection of three roads (locally called the turkey track). Take the road on extreme right (FS-551) and continue about 8 mi to next signed junction. **8.0**

10.0 Turn right toward Triangle C (Boyd) Ranch. **0.7**

10.7 Turn right and continue 0.5 mi east to gate through fence. Much of the land in this area is private, and the rest is largely leased by ranchers from the State, U.S. Bureau of Land Management, or U.S. Forest Service. **Users of this guide who are not participating in prearranged field trips should seek permission to enter from local ranchers.** Secure gate behind last vehicle. **1.5**

12.2 **STOP 7-2. Imbricated clasts in tuff of Triangle C Ranch.** Park along side of road near foot of draw at junction with right-hand fork of Coyote Canyon. Walk 100–200 m north of road to small outcrops of Triangle C tuff containing imbricated clasts of Bloodgood Canyon Tuff. Climb onto upper surface of outcrops to see discoidal clasts exposed in plan view. Transport directions here are from the southwest and southeast. Note silicified character, phenocryst composition and abundance, and thickness of clasts for comparison with silicified rinds at Stop 7-3.

Drive about 0.5 mi farther, cross cattleguard, and park near pine trees on right between road and creek. **0.5**

12.7 **STOP 7-3. Furrows, striations, and silicified rind at top of Bloodgood Canyon Tuff.** Starting at point 1 (Fig. 7) in creek bottom, 150 m up from cattle-

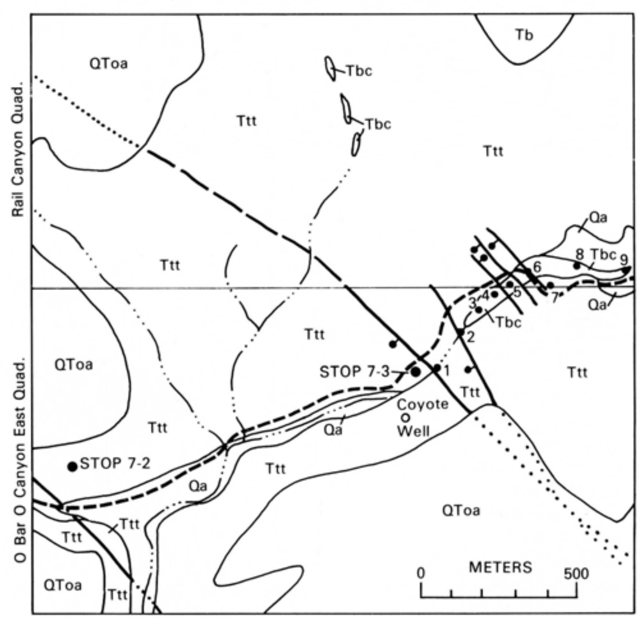

FIGURE 7—Geologic sketch map of Coyote Well area showing Stops 7-2 and 7-3, and points 1–9 discussed in text at Stop 7-3. Qa = Quaternary alluvium; QToa = Quaternary–Tertiary older alluvium; Tb = Bearwallow Mountain Andesite; Ttt = tuff of Triangle C Ranch; Tbc = Bloodgood Canyon Tuff. Modified from Richter (1987) and unpublished 1987 USGS mapping by J. C. Ratté and V. A. Lawrence.

guard, white Triangle C tuff with gray, glassy pumice is exposed for another 150 m to point 2, where a northwesterly fault brings pink Triangle C tuff up to creek level. Continue upstream about 50 m to first exposures of Bloodgood Canyon Tuff, overlain by bedded pyroclastic deposits, at point 3. About 75 m beyond point 3 are first good exposures of furrows and striations. Point 4 is the locality where McIntosh and Osburn drilled Bloodgood Canyon Tuff for paleomagnetic samples and recognized the paleovalley aspects of the overlying Triangle C tuff (W. C. McIntosh and G. R. Osburn, oral comm. 1985). Here we see the silicified rind mimicking the wavy upper surfaces of Bloodgood Canyon Tuff and overlain by about 2 m of pumiceous and crystal-rich pyroclastic beds, in turn overlain by white tuff of Triangle C Ranch.

At point 5, 65 m up creek from point 4, across a narrow graben of pink Triangle C tuff, are excellent exposures of the silicified rind, in cross section showing an irregular base and deeper penetration along some joints in the Bloodgood Canyon Tuff (Tbc). Point 5 is on the boundary between the O Bar O Canyon East and Rail Canyon $7^1/_2$ min. quadrangles. Point 6 (Fig. 7) is in road at creek crossing, about 40 m above point 5. Polished Bloodgood Canyon Tuff is exposed about 5 m downcreek from road, but weathered Triangle C tuff in road indicates another narrow fault block. Point 7 is in Bloodgood Canyon Tuff, but the top of the Bloodgood Canyon is about 20 m north of center of creek here, where grooves trending N37E are visible. At point 8 in bend of creek, a grooved surface is exposed in the north bank. At point 9, about 15 m downstream from fence, is the last observed polished surface with grooves trending about N43E. About 65 m downstream from point 9, Triangle C tuff overlies Bloodgood Canyon with no crystal-rich bedded pyroclastic material between them.

The following interpretation is proposed: Following deposition of the main Bloodgood Canyon Tuff, a late, high-velocity surge of fluidized, crystal-rich pyroclastic flow scoured the top of the Bloodgood Canyon, creating both the meter-wavelength furrows and the finer-scale grooves and striations, and deposited the crystal-rich pyroclastic beds. The silicified rind was then formed by ground-water action at the top of the main Bloodgood Canyon Tuff, at the interface between the permeable, crystal-rich pyroclastic beds above and the relatively impermeable top of the Bloodgood Canyon. During the eruptions of the tuff of Triangle C Ranch, the crystal-rich pyroclastic surge beds on top of the Bloodgood Canyon Tuff were eroded by passage of the Triangle C ash flows, and locally they ripped through the silicified top of the Bloodgood and incorporated fragments of it in the basal Triangle C tuff. This scenario and the transport directions indicated by both the furrows and striae in the Bloodgood Canyon Tuff and the imbricated clasts in the tuff of Triangle C Ranch suggest that both tuffs were erupted from a common source, the Bursum caldera, but a more thorough analysis, particularly of the imbricated clasts, would be helpful. The furrows may be analogous to similar features described beneath the lateral blast deposits at Mount St. Helens (Kieffer and Sturtevant, 1989).

Estimated time 12:00–12:30 p.m. Remain here for lunch or return to NM-78 at the Turkey Track junction and drive to Santa Fe via NM-78 to US-60 at the VLA. Turn right (east) on US-60 to Socorro via Magdalena; turn north on I-25 at Socorro and continue on to Santa Fe via Albuquerque.

References

Abitz, R. J., 1986, Geology of mid-Tertiary volcanic rocks of the east-central Black Range, Sierra County, New Mexico: Implications for a double-cauldron complex in the Emory cauldron; *in* Clemons, R. E., King, W. E., Mack, G. H., and Zidek, J. (eds.), Truth or Consequences Region: New Mexico Geological Society, Guidebook 37: 161–166.

Abitz, R. J., 1989, Geology and petrogenesis of the northern Emory caldera, Sierra County, New Mexico: Unpublished Ph.D. dissertation, University of New Mexico, Albuquerque, 174 pp.

Ake, J. P., and Sanford, A. R., 1988, New evidence for the existence and internal structure of a thin layer of magma at mid-crustal depths near Socorro, New Mexico: Seismological Society of America, Bulletin, 78: 1335–1359.

Aldrich, M. J., Jr., Ander, M. E., and Laughlin, A. W., 1981, Geological and geophysical signatures of the Jemez lineament: A reactivated Precambrian structure; *in* Proceedings of the Fourth International Conference on Basement Tectonics: International Basement Tectonics Association, Publication 4: 77–85.

Aldrich, M. J., Jr., Chapin, C. E., and Laughlin, A. W., 1986, Stress history and tectonic development of the Rio Grande rift, New Mexico: Journal of Geophysical Research, 91: 6199–6212.

Atwood, G. W., 1982, Geology and geochemistry of the San Juan Peak area, San Mateo Mountains, Socorro County, New Mexico: with special reference to the geochemistry, mineralogy, and petrogenesis of an occurrence of riebeckite-bearing rhyolite: Unpublished M.S. thesis, University of New Mexico, Albuquerque, 156 pp.

Axelrod, D. I., and Bailey, H. P., 1976, Tertiary vegetation, climate, and altitude of the Rio Grande depression, New Mexico–Colorado: Paleobiology, 2: 235–254.

Baars, D. L., 1982, Paleozoic history of the Albuquerque trough; Implications of basement control on Rio Grande rift; *in* Grambling, J. A., Wells, S. G., and Callender, J. F. (eds.), Albuquerque Country II: New Mexico Geological Society, Guidebook 33: 153–157.

Bachman, G. O., and Mehnert, H. H., 1978, New K–Ar dates and late Pliocene to Holocene geomorphic history of the central Rio Grande region: Geological Society of America, Bulletin, 89: 283–293.

Bally, A. W., 1982, Musings over sedimentary basin evolution: Royal Society of London, Philosophical Transactions (A), 305: 325–338.

Barroll, M. W., and Reiter, M., 1989, Hydrogeothermal phenomena in the Socorro Known Geothermal Resource Area (abs.): New Mexico Geological Society, Proceedings Volume, 1989 Spring Meeting, April 7, 1989, Socorro, New Mexico, p. 44.

Bobrow, D. J., Kyle, P. R., and Osburn, G. R., 1983, Miocene rhyolitic volcanism in the Socorro area of New Mexico; *in* Chapin, C. E., and Callender, J. F. (eds.), Socorro Region II: New Mexico Geological Society, Guidebook 34: 211–217.

Bornhorst, T. J., 1976, Volcanic geology of the Crosby Mountains and vicinity, Catron County, New Mexico: Unpublished M.S. thesis, University of New Mexico, Albuquerque, 113 pp.

Bornhorst, T. J., 1980, Major- and trace-element geochemistry and mineralogy of Upper Eocene to Quaternary volcanic rocks of the Mogollon–Datil volcanic field, southwestern New Mexico: Unpublished Ph.D. dissertation, University of New Mexico, Albuquerque, 1108 pp.

Bornhorst, T. J., Jones, D. P., Elston, W. E., Damon, P. E., and Shafiqullah, M., 1982, New radiometric ages on volcanic rocks from the Mogollon–Datil volcanic field, southwestern New Mexico: Isochron/West, no. 35: 13–14.

Bosworth, W., 1985, Geometry of propagating continental rifts: Nature, 316: 625–627.

Bosworth, W., 1986, Comment on "Detachment faulting and the evolution of passive continental margins": Geology, 14: 890–891.

Bosworth, W., Lambiase, J., and Keisler, R., 1986, A new look at Gregory's rift: The structural style of continental rifting: EOS (American Geophysical Union, Transactions), 67: 577, 582–583.

Bowring, S. A., and Heatherington, A. L., 1987, Isotopic constraints on the magmatic evolution of the south-central Rio Grande rift (abs): Geological Society of America, Abstracts with Programs, 19: 597.

Brocher, T. M., 1981, Shallow velocity structure of the Rio Grande rift north of Socorro, New Mexico: A reinterpretation: Journal of Geophysical Research, 86: 4960–4970.

Brouillard, L. A., 1984, Geology of the northeastern Gallinas Mountains, Socorro County, New Mexico: Unpublished M.S. thesis, New Mexico Institute of Mining & Technology, Socorro, 161 pp.

Brown, L. D., Chapin, C. E., Sanford, A. R., Kaufman, S., and Oliver, J., 1980, Deep structure of the Rio Grande rift from seismic reflection profiling: Journal of Geophysical Research, 85: 4773–4800.

Brown, L. D., Krumhansl, P. A., Chapin, C. E., Sanford, A. R., Cook, F. A., Kaufman, S., Oliver, J. E., and Schilt, F. S., 1979, COCORP seismic reflection studies of the Rio Grande rift; *in* Riecker, R. E. (ed.), Rio Grande rift: Tectonics and magmatism: American Geophysical Union, pp. 169–184.

Caravella, F. J., 1976, A study of Poisson's ratio in the upper crust of the Socorro, New Mexico area: Unpublished M.S. independent study, Geophysics Open-file Report 11, Geoscience Department, New Mexico Institute of Mining & Technology, Socorro.

Carpenter, P. J., and Sanford, A. R., 1985, Apparent Q for upper crustal rocks of the central Rio Grande rift: Journal of Geophysical Research, 90: 8661–8674.

Cather, S. M., 1980, Petrology, diagenesis, and genetic stratigraphy of the Eocene Baca Formation, Alamo Navajo Reservation, Socorro County, New Mexico: Unpublished M.S. thesis, University of Texas at Austin, 243 pp.

Cather, S. M., 1986, Volcano-sedimentary evolution and tectonic implications of the Datil Group (latest Eocene–early Oligocene), west-central New Mexico: Unpublished Ph.D. dissertation, University of Texas at Austin, 484 pp.

Cather, S. M., and Johnson, B. D., 1984, Eocene tectonics and depositional setting of west-central New Mexico and eastern Arizona: New Mexico Bureau of Mines & Mineral Resources, Circular 192: 33 pp.

Cather, S. M., and Johnson, B. D., 1986, Eocene depositional systems and tectonics in west-central New Mexico and eastern Arizona: American Association of Petroleum Geologists, Memoir 41: 623–652.

Cather, S. M., McIntosh, W. C., and Chapin, C. E., 1987, Stratigraphy, age, and rates of deposition of the Datil Group (upper Eocene–lower Oligocene), west-central New Mexico: New Mexico Geology, 9: 50–54.

Chamberlin, R. M., 1981, Uranium potential of the Datil Mountains–Pie Town area, Catron County, New Mexico: New Mexico Bureau of Mines & Mineral Resources, Open-file Report 138: 51 pp.

Chamberlin, R. M., 1982, Geologic map, cross sections, and map units of the Lemitar Mountains, Socorro County, New Mexico: New Mexico Bureau of Mines & Mineral Resources, Open-file Report 169, 3 plates, scale 1:12,000.

Chamberlin, R. M., 1983, Cenozoic domino-style crustal extension in the Lemitar Mountains, New Mexico: A summary; *in* Chapin, C. E., and Callender, J. F. (eds.), Socorro Region II: New Mexico Geological Society, Guidebook 34: 111–118.

Chamberlin, R. M., and Osburn, G. R., 1984, Character and evolution of extensional domains in the Socorro area of the Rio Grande rift, central New Mexico (abs.): Geological Society of America, Abstracts with Programs, 16: 467.

Chamberlin, R. M., and Osburn, G. R., 1986, Tectonic framework character, and evolution of upper crustal extensional domains in the Socorro area of the Rio Grande rift, New Mexico; *in* Beatty, B., and Wilkinson, P. A. K. (eds.), Frontiers in geology and ore deposits of Arizona and the southwest: Arizona Geological Society Digest, 16: 464.

Chapin, C. E., 1971, The Rio Grande rift, Part I: Modifications and additions; *in* James, H. L. (ed.), San Luis Basin: New Mexico Geological Society, Guidebook 22: 191–201.

Chapin, C. E., 1988, Axial basins of the northern and central Rio Grande rift; *in* Sloss, L. L. (ed.), Sedimentary cover—North American craton: U.S.: Geological Society of America, The Geology of North America, vol. D-2: 165–170.

Chapin, C. E., and Cather, S. M., 1981, Eocene tectonics and sedimentation in the Colorado Plateau–Rocky Mountain area;; *in* Dickinson, W. R., and Payne, W. D. (eds.), Relations of tectonics to ore deposits in the southern Cordillera: Arizona Geological Society Digest, 14: 173–198.

Chapin, C. E., and Cather, S. M., 1983, Eocene tectonics and sedimentation in the Colorado Plateau–Rocky Mountain area; *in* Lowell, J. E. (ed.), Rocky Mountain foreland basins and uplifts: Rocky Mountain Association of Geologists, Denver, Colorado, pp. 33–56.

Chapin, C. E., and Lindley, J. I., 1986, Potassium metasomatism of igneous and sedimentary rocks in detachment terranes and other sedimentary basins: Economic implications; *in* Beatty, B., and Wilkinson, P. A. K. (eds.), Frontiers in geology and ore deposits of Arizona and the southwest: Arizona Geological Society Digest, 16: 118–126.

Chapin, C. E., and Seager, W. R., 1975, Evolution of the Rio Grande rift in the Socorro and Las Cruces areas; *in* Seager, W. R., Clemons, R. E., and Callender, J. F. (eds.), Las Cruces Country: New Mexico Geological Society, Guidebook 26: 297–321.

Chapin, C. E., Chamberlin, R. M., Osburn, G. R., Sanford, A. R., and White, D. L., 1978, Exploration framework of the Socorro geothermal area, New Mexico; *in* Chapin, C. E., and Elston, W. E. (eds.), Field guide to selected cauldrons and mining districts of the Datil–Mogollon volcanic field, New Mexico: New Mexico Geological Society, Special Publication 7: 115–129, plate in pocket.

Christiansen, R. L., and Lipman, P. W., 1972, Cenozoic volcanism and plate tectonic evolution of the western United States. Part 2, late Cenozoic: Royal Society of London, Philosophical Transactions (A), 271: 249–284.

Coffin, G. C., 1981, Geology of the northwestern Gallinas Mountains, Socorro County, New Mexico: Unpublished M.S. thesis, New Mexico Institute of Mining & Technology, Socorro, 202 pp.

Cunningham, J. E., 1974, Geologic map and sections of Silver City quadrangle, New Mexico: New Mexico Bureau of Mines & Mineral Resources, Geologic Map 30, scale 1:24,000.

Dalrymple, G. R., 1979, Critical tables for conversion of K–Ar ages from old to new constants: Geology, 7: 558–560.

Dalrymple, G. R., and Duffield, W. A., 1988, High precision $^{40}Ar/^{39}Ar$ dating of Oligocene rhyolites of Mogollon Datil volcanic field using a continuous laser system: Geophysical Research Letters, 15: 463–466.

D'Andrea, J. F., 1981, Chemical changes associated with potassium metasomatism of ash-flow tuffs near Socorro, New Mexico: Unpublished M.S. thesis, Florida State University, Tallahassee, 243 pp.

Deal, E. G., 1973, Geology of the northern part of the San Mateo Mountains, Socorro County, New Mexico: A study of a rhyolite ash-flow tuff cauldron and the role of laminar flow in ash-flow tuffs: Unpublished Ph.D. dissertation, University of New Mexico, Albuquerque, 136 pp.

Drewes, H., Houser, B. B., Hedlund, D. C., Richter, D. H., Thorman, C. H., and Finnell, T. L., 1985, Geologic map of the Silver City 1° × 2° quadrangle, New Mexico and Arizona: U.S. Geological Survey, Miscellaneous Investigations Series Map I-1310-C, scale 1:250,000.

Duffield, W. A. (in press), Eruptive fountains of silicic magma and their possible effects on the tin content of fountain-fed lavas; *in* Stein, H. J., and Hannah, J. L. (eds.), Ore-bearing granite systems: Petrogenesis and mineralizing processes: Geological Society of America Special Paper.

Duffield, W. A., Richter, D. H., and Priest, S. S., 1987, Preliminary geologic map of the Taylor Creek Rhyolite, Catron and Sierra Counties, New Mexico: U.S. Geological Survey, Open-file Report 87-515, 1:50,000.

Dunn, P. G., 1982, Geology of the Copper Flat porphyry copper deposit, Hillsboro, Sierra County, New Mexico; *in* Titley, S. R. (ed.), Advances in Geology of the Copper porphyry deposits: University of Arizona Press, Tucson, pp. 313–326.

Eaton, G. P., 1982, The Basin and Range province: Origin and tectonic significance: Annual Review of Earth and Planetary Sciences, 10: 409–440.

Eggleston, T. L., and Norman, D. I., 1986, A summary of the geology, geochemistry, and tin occurrences in the Black Range, New Mexico; *in*

Clemons, R. E., King, W. E., Mack, G. H., and Zidek, J. (eds.), Truth or Consequences Region: New Mexico Geological Society, Guidebook 37: 173–177.

Elston, W. E., 1957, Geology and mineral resources of Dwyer quadrangle, Grant, Luna, and Sierra Counties, New Mexico: New Mexico Bureau of Mines & Mineral Resources, Bulletin 33: 88 pp.

Elston, W. E., 1965, Rhyolite ash-flow plateaus, ring-dike complexes, calderas, lopoliths, and moon craters: New York Academy of Science, Annals, 123: 817–842.

Elston, W. E., 1978, Mid-Tertiary cauldrons and their relationship to mineral resources, southwestern New Mexico: A brief review; *in* Chapin, C. E., and Elston, W. E. (eds.), Field guide to selected cauldrons and mining districts of the Datil–Mogollon volcanic field, New Mexico: New Mexico Geological Society, Special Publication 7; 107–113.

Elston, W. E., 1981, Assessment of the geothermal potential of southwestern New Mexico: New Mexico Energy Research & Development Program, Report EMD 2-62-2123: 39 pp.

Elston, W. E., 1984, Mid-Tertiary ash-flow tuff cauldrons, southwestern New Mexico: Journal of Geophysical Research, 89: 8733–8750.

Elston, W. E., and Bornhorst, T. J., 1979, The Rio Grande rift in context of regional post-40 m.y. volcanic and tectonic events; *in* Riecker, R. E. (ed.), Rio Grande rift: Tectonics and magmatism: American Geophysical Union, pp. 416–438.

Elston, W. E., and Kuellmer, F. J., 1968, Road log, second day; *in* Titley, S. R. (ed.), Southern Arizona Guidebook III: Arizona Geological Society, Tucson, pp. 266–294.

Elston, W. E. and Netelbeek, T. A., 1965, Road log from Mimbres Valley to Silver City; *in* Fitzsimmons, J. P., and Lochman-Balk, C. (eds.), Southwestern New Mexico II: New Mexico Geological Society, Guidebook 16: 36–42.

Elston, W. E., Seager, W. R., and Clemons, R. E., 1975, Emory cauldron, Black Range, New Mexico; *in* Seager, W. R., Clemons, R. E., and Callender, J. F. (eds.), Las Cruces Country: New Mexico Geological Society, Guidebook 26: 283–292.

Elston, W. E., Seager, W. R., and Abitz, R. J., 1987, The Emory resurgent ash-flow tuff (ignimbrite) cauldron of Oligocene age, southwestern New Mexico: Geological Society of America, Centennial Field Guide—Rocky Mountain Section, pp. 441–445.

Ericksen, G. E., and Wedow, H., Jr., 1976, Tertiary extrusives and related intrusions in the Black Range, New Mexico; *in* Elston, W. E., and Northrop, S. A. (eds.), Cenozoic volcanism in southwestern New Mexico: New Mexico Geological Society, Special Publication 5: 63–67.

Ericksen, G. E., Wedow, H., Jr., Eaton, G. P., and Leland, G. R., 1970, Mineral resources of the Black Range Primitive Area, Grant, Sierra, and Catron Counties, New Mexico: U.S. Geological Survey, Bulletin 1319-E, 162 pp.

Everson, J. E., and Silver, L. T., 1978, Lead systematics of late Cenozoic basalts from the Rio Grande rift (abs.); *in* Program and Abstracts of the 1978 International Symposium on the Rio Grande rift, Santa Fe, October, 1978: Los Alamos National Laboratory, Conference Proceedings LA-7487-C: 36–37.

Ewart, A., 1979, A review of the mineralogy and chemistry of Tertiary–Recent dacitic, latitic, rhyolitic, and related salic volcanics; *in* Barker, F. (ed.), Trondhjemites, dacites and related rocks: Elsevier Publ. Co., Amsterdam, pp. 13–121.

Ewart, A., 1982, The mineralogy and petrology of Tertiary–Recent orogenic volcanic rocks: With special reference to the andesitic–basaltic compositional range; *in* Thorpe, R. S. (ed.), Andesites–orogenic andesites and related rocks: John Wiley & Sons, New York, pp. 25–95.

Farris, S.R., 1981, Geology and mid-Tertiary volcanism of the McKnight Canyon area, Black Range, Grant County, New Mexico: Unpublished M.S. thesis. University of New Mexico., Albuquerque, 87 pp.

Faulds, J. E., Mawer, C. K., and Geissman, J. W., 1988a, Geometry and kinematics of a major accommodation zone in the highly extended upper-plate rocks of the northern Colorado River trough, northwestern Arizona and southern Nevada (abs.): Geological Society of America, Abstracts with Programs, 20: 159.

Faulds, J. E., Hillemeyer, F. L., and Smith, E. I., 1988b, Geometry and kinematics of a Miocene "accommodation zone" in the central Black and southern Eldorado Mountains, Arizona and Nevada; *in* Weide, D. L., and Faber, M. L. (eds.), This extended land, geological journeys in the Southern Basin and Range: Geological Society of America, Cordilleran Section, Field Trip Guidebook, pp. 293–310.

Faulds, J. E., Geissman, J. W., and Mawer, C. K. (in press), Structural development of a major extensional accommodation zone in the Basin and Range province, northwestern Arizona and southern Nevada: Implications for kinematic models of continental extension; *in* Wernicke, B. (ed.), Basin and Range extensional tectonics near the latitude of Las Vegas, Nevada: Geological Society of America, Memoir.

Fenneman, N. M., 1931, Physiography of the Western United States: McGraw–Hill Book Co., Inc., New York & London, 534 pp.

Ferguson, C. A., 1988, Geology of the Tenmile Hill 7.5′ quadrangle, Socorro County, New Mexico: New Mexico Bureau of Mines & Mineral Resources, Open-file Report 283: 21 pp., map, scale 1:24,000.

Ferguson, H. G., 1927, Geology and ore deposits of the Mogollon mining district, New Mexico: U.S. Geological Survey, Bulletin 787: 100 pp.

Finnell, T. L., 1976a, Geologic map of the Twin Sisters quadrangle, Grant County, New Mexico: U.S. Geological Survey, Miscellaneous Field Studies Map MF-779, scale 1:24,000.

Finnell, T. L., 1976b, Geologic map of the Reading Mountain quadrangle: U.S. Geological Survey, Miscellaneous Field Studies Map MF-800, scale 1:24,000.

Finnell, T. L., 1982, Geologic map of the Dorsey Ranch quadrangle, Grant County, New Mexico: U.S. Geological Survey, Miscellaneous Field Studies Map MF-1431, scale 1:24,000.

Finnell, T. L., 1987, Geologic map of the Cliff quadrangle, Grant County, New Mexico: U.S. Geological Survey, Miscellaneous Investigations Series Map I-1768, scale 1:50,000.

Fisher, R. V., and Schmincke, H.-U., 1984, Pyroclastic rocks: Springer-Verlag, New York, 472 pp.

Fodor, R. V., 1975, Petrology of basalt and andesite of the Black Range, New Mexico: Geological Society of America, Bulletin, 86: 295–304.

Fodor, R. V., 1976, Volcanic geology of the northern Black Range, New Mexico; *in* Elston, W. E., and Northrop, S. A. (eds.), Cenozoic volcanism in southwestern New Mexico: New Mexico Geological Society, Special Publication 5: 68–70.

Foord, E. E., and Maxwell, C. H., 1987, Mineralogy of the Black Range tin district, Sierra and Catron Counties, New Mexico: New Mexico Geology, 9(1): 20–21.

French, W., 1965a, Some recollections of a western ranchman, New Mexico, 1883–1889: Argosy-Antiquarian, New York, vol. 1: 263 pp.

French, W., 1965b, Further recollections of a western ranchman, New Mexico, 1883–1889: Argosy-Antiquarian, New York, vol. 2: 264 pp.

Fries, C., Jr., 1940, Tin deposits of the Black Range, Catron and Sierra Counties, New Mexico, a preliminary report: U.S. Geological Survey, Bulletin 922: 355–370.

Gibbs, A. D., 1984, Structural evolution of extensional basin margins: Geological Society of London, Journal, 141: 609–620.

Giles, D. L., 1967, A petrochemical study of compositionally zoned ash-flow tuffs: Unpublished Ph.D. dissertation, University of New Mexico, Albuquerque, 176 pp.

Giles, D. L., 1968, Ash-flow tuffs of the Cobre Mountains; *in* Titley, S. R. (ed.), Southern Arizona Guidebook III: Arizona Geological Society, Tucson, pp. 289–291.

Gillespie-Nimick, K., 1986, Geology and structural evolution of the east flank of the Ladron Mountains, Socorro County, New Mexico: Unpublished M.S. thesis, University of New Mexico, Albuquerque, 98 pp.

Gries, R. R., 1985, Seismic lines in the San Luis Valley, south-central Colorado; *in* Gries, R. R., and Dyer, R. C. (eds.), Seismic exploration of the Rocky Mountain region: Rocky Mountain Association of Geologists, Denver, Colorado, pp. 267–274.

Harrison, R. W., 1980, Geology of the northeastern Datil Mountains, Socorro and Catron Counties, New Mexico: Unpublished M.S. thesis, New Mexico Institute of Mining & Technology, Socorro, 137 pp.

Heatherington, A. L., 1988, Isotope systematics of volcanics from the south-central Rio Grande rift and the western Mexican volcanic belt: Implications for magmatic and tectonic evolution of Cenozoic extensional regimes in western North America: Unpublished Ph.D. dissertation, Washington University, St. Louis, Missouri, 207 pp.

Heatherington, A. L., and Bowring, S. A., 1988, Isotopic characterization of Cenozoic magma sources in the south-central Rio Grande rift (abs.): EOS (American Geophysical Union, Transactions), 69: 519.

Hedlund, D. L., 1977, Geologic map of the Hillsboro and San Lorenzo quadrangles, Sierra and Grant Counties, New Mexico: U.S. Geological Survey, Map MF-900A, scale 1:48,000.

Houser, B. B., 1987, Geologic map of the Alma quadrangle, Catron County, New Mexico: U.S. Geological Survey, Geologic Quadrangle Map GQ-1610, scale 1:24,000.

Jarpe, S. P., Sanford, A. R., and Jacksha, L. H., 1984, Evidence for magmatic intrusion during an earthquake swarm in the central Rio Grande rift (abs.): EOS (American Geophysical Union, Transactions), 65: 1001.

Jicha, H. L., Jr., 1954, Geology and mineral deposits of Lake Valley quadrangle, Catron, Luna, and Sierra Counties, New Mexico: New Mexico Bureau of Mines & Mineral Resources, Bulletin 37: 93 pp.

Jones, D. P., 1980, Volcanic geology of the Alegros Mountain area, Catron County, New Mexico: Unpublished M.S. thesis, University of New Mexico, Albuquerque, 76 pp.

Jones, W. R., Hernon, R. M., and Moore, S. L., 1967, General geology of the Santa Rita quadrangle, Grant County, New Mexico: U.S. Geological Survey, Professional Paper 555: 144 pp.

Kedzie, L. L., 1984, High-precision $^{40}Ar/^{39}Ar$ dating of major ash-flow tuff sheets near Socorro, New Mexico: Unpublished M.S. thesis, New Mexico Institute of Mining & Technology, Socorro, 197 pp.

Kedzie, L. L., Sutter, J. F., and Chapin, C. E., 1985, High-precision $^{40}Ar/^{39}Ar$ ages of widespread Oligocene ash-flow tuff sheets near Socorro, New Mexico (abs.): EOS (American Geophysical Union, Transactions), 17: 625.

Kelley, V. C., and Branson, O. T., 1947, Shallow high-temperature pegmatites, Grant County, New Mexico: Economic Geology, 42: 699–712.

Kieffer, S. W., and Sturtevant, B., 1989, Erosional furrows formed during the lateral blast at Mount St. Helens, May 18, 1980: Journal of Geophysical Research (in press).

Krauskopf, K. B., 1979, Introduction to geochemistry, 2nd edition: McGraw-Hill, New York, 617 pp.

Kudo, A. M., Kelley, V. C., Damon, P. E., and Shafiqullah, M., 1977, K–Ar ages of basalt flows at Canjilon Hill, Isleta Volcano, and the Cat Hills volcanic field, Albuquerque–Belen Basin, central New Mexico: Isochron/West, no. 18: 15–16.

Kuellmer, F. J., 1954, Geologic section of the Black Range at Kingston, New Mexico: New Mexico Bureau of Mines & Mineral Resources, Bulletin 33: 100 pp.

Lambert, R. L., 1973, Geology of the country east of the Santa Rita mining district, Grant County, New Mexico: The San Lorenzo area: Unpublished M.S. thesis, University of New Mexico, Albuquerque, 81 pp.

Laroche, T. M., 1981, Geology of the Gallinas Peak area, Socorro County, New Mexico: Unpublished M.S. thesis, New Mexico Institute of Mining & Technology, Socorro, 145 pp.

Larsen, S. C., Reilinger, R. E., and Brown, L. D., 1986, Evidence of ongoing crustal deformation related to magmatic activity near Socorro, New Mexico: Journal of Geophysical Research, 91: 6283–6292.

Lawrence, V. A., 1985, A study of the Indian Peaks tin-bearing rhyolite dome–flow complex, northern Black Range, New Mexico: Unpublished M.S. thesis, University of Colorado, Boulder, 112 pp.

Leopoldt, W., 1981, Neogene geology of the central Mangas graben, Cliff–Gila area, Grant County, New Mexico: Unpublished M.S. thesis, University of New Mexico, Albuquerque, 160 pp.

Lindley, J. I., 1979, Chemical changes associated with propylitic alteration of two ash-flow tuffs, Datil–Mogollon volcanic field, New Mexico: Unpublished M.S. thesis, University of North Carolina, Chapel Hill, 197 pp.

Lindsley, D. H., 1965, Iron–titanium oxides: Carnegie Institute of Washington, 1964 Yearbook, pp. 144–148.

Lipman, P. W., 1976, Caldera-collapse breccias in the western San Juan Mountains, Colorado: Geological Society of America, Bulletin, 87: 1397–1410.

Lipman, P. W., and Mehnert, H. H., 1979, Potassium–argon ages from the Mount Taylor volcanic field, New Mexico: U.S. Geological Survey, Professional Paper 1124A-F: B1–8.

Lipman, P. W., and Sawyer, D. A., 1985, Mesozoic ash-flow caldera fragments in southeastern Arizona and their relation to porphyry copper deposits: Geology, 13: 652–656.

Lipman, P. W., Prostka, H. J., and Christiansen, R. L., 1972, Cenozoic volcanism and plate tectonic evolution of the western United States. Part I, early and middle Cenozoic: Royal Society of London, Philosophical Transactions (A), 271: 217–248.

Lister, G. S., Etheridge, M. A., and Symonds, P. A., 1986a, Detachment faulting and the evolution of passive continental margins: Geology, 14: 246–250.

Lister, G. S., Etheridge, M. A., and Symonds, P. A., 1986b, Reply to comment on "Detachment faulting and the evolution of passive continental margins": Geology, 14: 891–892.

Lopez, D. A., 1975, Geology of the Datil area, Catron County, New Mexico: Unpublished M.S. thesis, University of New Mexico, Albuquerque, 72 pp.

Lopez, D. A., and Bornhorst, T. J., 1979, Geologic map of the Datil area, Catron County, New Mexico: U.S. Geological Survey, Miscellaneous Geologic Investigations Map I-1098, scale 1:50,000, 1 sheet.

Loring, A. K., and Loring, R. B., 1980, K/Ar ages of middle Tertiary rocks from southern New Mexico: Isochron/West, no. 28: 17–20.

Lufkin, J. L., 1976, Oxide minerals in miarolitic rhyolite, Black Range, New Mexico: American Mineralogist, 61: 425–430.

Maggiore, P., 1981, Deformation and metamorphism in the floor of a major ash-flow tuff cauldron, the Emory cauldron, Grant and Sierra Counties, New Mexico: Unpublished M.S. thesis, University of New Mexico, Albuquerque, 133 pp.

Markgraf, V., Bradbury, J. P., Forster, R. M., McCoy, W., Singh, G., and Sternberg, R., 1983, Paleoenvironmental reassessment of the 1.6 million-year-old record from San Agustin basin, New Mexico; *in* Chapin, C. E., and Callender, J. F. (eds.), Socorro Region II: New Mexico Geological Society, Guidebook 34: 291–297.

Marvin, R. F., Naeser, C. W., Bikerman, M., Mehnert, H. H., and Ratté, J. C., 1987, Isotopic ages of post-Paleocene igneous rocks within and bordering the Clifton $1° \times 2°$ quadrangle, Arizona–New Mexico: New Mexico Bureau of Mines & Mineral Resources, Bulletin 118: 50 pp.

Maxwell, C. H., Foord, E. E., Oakman, M. R., and Harvey, D. B., 1986, Tin deposits in the Black Range tin district; *in* Clemons, R. E., King, W. E., Mack, G. H., and Zidek, J. (eds.), Truth or Consequences region: New Mexico Geological Society, Guidebook 37: 273–281.

McIntosh, W. C., Sutter, J. F., Chapin, C. E., Osburn, G. R., and Ratté, J. C., 1986, A stratigraphic framework for the eastern Mogollon–Datil volcanic field based on paleomagnetism and high-precision $^{40}Ar/^{39}Ar$ dating of ignimbrites—a progress report; *in* Clemons, R. E., King, W. E., Mack, G. H., and Zidek, J. (eds.), Truth or Consequences Region: New Mexico Geological Society, Guidebook 37: 183–195.

Montanari, A., Drake, R., Bice, D. M., Alvarez, W., Curtis, G. H., Turrin, B. D., and DePaolo, D. J., 1985, Radiometric time scale for the upper Eocene and Oligocene based on K/Ar and Rb/Sr dating of volcanic biotites from the pelagic sequence of Gubbio, Italy: Geology, 13: 596–599.

Morgan, P., Seager, W. R., and Golombek, M. P., 1986, Cenozoic thermal, mechanical, and tectonic evolution of the Rio Grande rift: Journal of Geophysical Research, 91: 6263–6276.

Morley, C. K., 1988, Variable extension in Lake Tanganyika: Tectonics, 7: 785–801.

New Mexico Bureau of Mines & Mineral Resources, 1981, Satellite photomap of New Mexico: Resource Map 12, scale 1:1,000,000.

New Mexico Geological Society, 1982, New Mexico Highway Geologic Map: scale 1:1,000,000.

Northrop, S. A., 1959, Minerals of New Mexico, revised edition: University of New Mexico Press, Albuquerque, 665 pp.

O'Brient, J. D., 1979, Hypabyssal crystallization and emplacement of the rhyolitic Rabb Park complex, Grant Conty, New Mexico: Unpublished Ph.D. dissertation, Stanford University, Palo Alto, California, 198 pp.

O'Brient, J. D., 1986, Preservation of primary magmatic features in subvolcanic pegmatites, aplites, and granite from Rabb Park, New Mexico: American Mineralogist, 71: 608–624.

Osburn, G. R., 1984, Geologic map of Socorro County, New Mexico: New Mexico Bureau of Mines & Mineral Resources, Open-file Report 238: 13 pp., map, scale 1:200,000.

Osburn, G. R., and Chapin, C. E., 1983a, Nomenclature for Cenozoic rocks of northeast Mogollon–Datil volcanic field, New Mexico: New Mexico Bureau of Mines & Mineral Resources, Stratigraphic Chart 1.

Osburn, G. R., and Chapin, C. E., 1983b, Ash-flow tuffs and cauldrons in the northeast Mogollon–Datil volcanic field: A summary; *in* Chapin, C. E., and Callender, J. F. (eds.), Socorro Region II: New Mexico Geological Society, Guidebook 34: 197–204.

Osburn, G. R., Bowring, S. A., Nelson, L., Roth, S. J., and others, 1985, Geologic map of the Puertecito Gap 7.5′ quadrangle, Socorro County, New Mexico: New Mexico Bureau of Mines & Mineral Resources, Open-file Report 235: 7 pp., map scale 1:24,000.

Osburn, G. R., Bowring, S. A., Roth, S. J., Petty, D. M., Chapin, C. E., and Nelson, L., 1989, Geologic map of the South Baldy quadrangle, Socorro County, New Mexico: New Mexico Bureau of Mines & Mineral Resources, Open-file Report 352, scale 1:24,000.

Osburn, G. R., Harrison, R. H., Eggleston, T. L., Lozinsky, R. P., and Maxwell, C. H., 1986, First-day road log, from Truth or Consequences to Sierra Cuchillo, Winston graben, Winston, South Fork Cuchillo Negro Creek, Fluorine, and central Black Range; *in* Clemons, R. E., King, W. E., Mack, G. H., and Zidek, J. (eds.), Truth or Consequences region: New Mexico Geological Society, Guidebook 37: 1–19.

Ouchi, S., 1983, Effects of uplift on the Rio Grande over the Socorro magma body, New Mexico; *in* Chapin, C. E., and Callender, J. F. (eds.), Socorro Region II: New Mexico Geological Society, Guidebook 34: 54–56.

Ratté, J. C., 1980, Geologic map of the Saliz Pass quadrangle, New Mexico: U.S. Geological Survey, Miscellaneous Field Studies Map MF-1203, scale 1:24,000.

Ratté, J. C., 1981, Geologic map of the Mogollon quadrangle, Catron

County, New Mexico: U.S. Geological Survey, Geologic Quadrangle Map GQ-1557, scale 1:24,000.

Ratté, J. C., 1986, Preliminary geologic map and section of the Bull Basin quadrangle, Catron County, New Mexico: U.S. Geological Survey, Open-file Report 86-0194, scale 1:24,000.

Ratté, J. C., 1989, Geologic map of the Bull Basin quadrangle, Catron County, New Mexico: U.S. Geological Survey, Geologic Quadrangle Map GQ-1651, scale 1:24,000 (in press).

Ratté, J. C., and Brooks, W. E., 1983, Geologic map of the Mule Creek quadrangle, Grant County, New Mexico: U.S. Geological Survey, Miscellaneous Field Studies Map MF-1666, scale 1:24,000.

Ratté, J. C., and Finnell, T. L., 1978, Road log from Silver City to Reserve via Glenwood and the Mogollon mining district; *in* Chapin, C. E., and Elston, W. E. (eds.), Field guide to selected cauldrons and mining districts of the Datil–Mogollon volcanic field, New Mexico: New Mexico Geological Society, Special Publication 7: 49–63.

Ratté, J. C., and Gaskill, D. L., 1975, Reconnaissance geologic map of the Gila Wilderness study area, southwestern New Mexico: U.S. Geological Survey, Miscellaneous Investigations Map I-886, scale 1:62,500.

Ratté, J. C., and Grotbo, T., 1979, Chemical analyses and norms of 81 volcanic rocks from part of the Mogollon–Datil volcanic field, southwestern New Mexico: U.S. Geological Survey, Open-file Report 79-1435.

Ratté, J. C., and McIntosh, W. C. (in press), Geology of the Horse Mountain West quadrangle: U.S. Geological Survey, Open-file map, scale 1:24,000.

Ratté, J. C., Landis, E. R., Gaskill, D. L., and Raabe, R. G., 1969, Mineral resources of the Blue Range Primitive Area, Greenlee County, Arizona, and Catron County, New Mexico, with a section on aeromagnetic interpretation by G. P. Eaton: U.S. Geological Survey, Bulletin 1261-E: 91 pp., map scale 1:62,500.

Ratté, J. C., Marvin, R. F., Naeser, C. W., and Bikerman, M., 1984, Calderas and ash-flow tuffs of the Mogollon Mountains, southwestern New Mexico: Journal of Geophysical Research, 89: 8713–8732.

Ratté, J. C., Saltus, R. W., and Turner, R. L., 1988, Mineral resources of the Horse Mountain and Continental Divide Wilderness Study Areas, Catron County, New Mexico: U.S. Geological Survey, Bulletin 1734-C: 8 pp., map scale 1:100,000.

Reilinger, R. E., and Oliver, J. E., 1976, Modern uplift associated with a proposed magma body in the vicinity of Socorro, New Mexico: Geology, 4: 583–586.

Reilinger, R. E., Oliver, J. E., Brown, L. D., Sanford, A. R., and Balazs, E., 1980, New measurements of crustal doming over the Socorro magma body, New Mexico: Geology, 8: 291–295.

Reiter, M., and Smith, R., 1977, Subsurface temperature data in the Socorro Peak KGRA, New Mexico: Geothermal Energy Magazine, 5 (10): 37–41.

Rhodes, R. C., and Smith, E. I., 1976, Geology and tectonic setting of the Mule Creek caldera, New Mexico, U.S.A.: Bulletin Volcanologique, 36: 401–411.

Richter, D. H., 1987, Geologic map of the O Bar O Canyon East quadrangle, Catron County, New Mexico: U.S. Geological Survey, Miscellaneous Field Studies Map MF-1976, scale 1:24,000.

Rinehart, E. J., Sanford, A. R., and Ward, R. M., 1979, Geographic extent and shape of an extensive magma body at midcrustal depths in the Rio Grande rift near Socorro, New Mexico; *in* Riecker, R. E. (ed.), Rio Grande rift: Tectonics and magmatism: American Geophysical Union, pp. 237–251.

Roach, J. M., 1982, The mapping of shallow magma bodies near Socorro, New Mexico, by the use of seismic attenuation: Unpublished M.S. independent study, Geophysics Open-file Report 42, Geoscience Department, New Mexico Institute of Mining & Technology, Socorro.

Robinson, B. R., 1981, Geology of the D Cross Mountain quadrangle, Socorro and Catron Counties, New Mexico: Unpublished M.S. thesis, University of Texas at El Paso, 213 pp.

Rosendahl, B. R., 1987, Architecture of continental rifts with special reference to East Africa: Annual Reviews of Earth and Planetary Sciences, 15: 445–503.

Ross, C. S., and Smith, R. L., 1961, Ash-flow tuffs: Their origin, geologic relations and identification: U.S. Geological Survey, Professional Paper 366: 81 pp.

Sanford, A. R., and Einarsson, P., 1982, Magma chambers in rifts; *in* Palmason, G. (eds.), Continental and oceanic rifts: American Geophysical Union, Geodynamics Series, 8: 147–168.

Sanford, A. R., Alptekin, O. S., and Toppozada, T. R., 1973, Use of reflection phases on microearthquake seismograms to map an unusual discontinuity beneath the Rio Grande rift: Seismological Society of America, Bulletin, 63: 2021–2034.

Sanford, A. R., Jaksha, L. H., and Cash, D. J. (in press), Seismicity of the Rio Grande rift in New Mexico; *in* Slemmons, D. B., Engdahl, E. R., Blackwell, D., and Schwartz, D. (eds.), Neotectonics of North America: Geological Society of America, Decade of North American Geology, CSMV-1.

Sanford, A. R., Mott, R. P., Jr., Shuleski, P. J., Rinehart, E. J., Caravella, F. J., Ward, R. M., and Wallace, T. C., 1977, Geophysical evidence for a magma body in the crust in the vicinity of Socorro, New Mexico; *in* Heacock, J. G. (ed.), The Earth's Crust: American Geophysical Union, Geophysical Monograph 20: 385–403.

Seager, W. R., 1973, Resurgent volcano-tectonic depression of Oligocene age, south-central New Mexico: Geological Society of America, Bulletin, 84: 3611–3626.

Seager, W. R., 1981, Geology of Organ Mountains and southern San Andres Mountains, New Mexico: New Mexico Bureau of Mines & Mineral Resources, Memoir 36: 97 pp.

Seager, W. R., Clemons, R. E., and Elston, W. E., 1978, Road log from Truth or Consequences to Silver City via Hillsboro and Tierra Blanca Canyon; *in* Chapin, C. E., and Elston, W. E. (eds.), Field guide to selected cauldrons and mining districts of the Datil–Mogollon volcanic field, New Mexico: New Mexico Geological Society, Special Publication 7: 33–49.

Seager, W. R., Kottlowski, F. E., and Hawley, J. W., 1976, Geology of the Doña Ana Mountains, New Mexico: New Mexico Bureau of Mines & Mineral Resources, Circular 147: 36 pp.

Seager, W. R., Clemons, R. E., Hawley, J. W., and Kelley, R. E., 1982, Geology of northwest part of Las Cruces $1° \times 2°$ sheet, New Mexico: New Mexico Bureau of Mines & Mineral Resources, Geologic Map 53, scale 1:125,000.

Sheppard, R. A., and Gude, A. J., III, 1987, Mineralogy and genesis of the Buckhorn zeolite deposit, Grant County, New Mexico; *in* Mumpton, F. A. (ed.), Zeo-Trip '87, An excursion to selected zeolite and clay deposits in southwestern New Mexico and eastern Arizona, October 22–25, 1987, pp. 13–26.

Sheppard, R. A., and Mumpton, F. A., 1984, Sedimentary fluorite in a lacustrine zeolitic tuff of the Gila Conglomerate near Buckhorn, Grant County, New Mexico: Journal of Sedimentary Petrology, 54: 853–860.

Shimizu, H., Sadato, U., and Junji, K., 1987, A tensile-shear crack model for the mechanism of volcanic earthquakes: Tectonophysics, 144: 287–300.

Smith, E. I., 1976, Structure and petrology of the John Kerr Peak dome complex, southwestern New Mexico; *in* Elston, W. E., and Northrop, S. A. (eds.), Cenozoic volcanism in southwestern New Mexico: New Mexico Geological Society, Special Publication 5: 71–78.

Smith, R. L., 1960, Zones and zonal variations in welded ash flows: U.S. Geological Survey, Professional Paper 354-F: 149–159.

Spradlin, E. J., 1976, Stratigraphy of Tertiary volcanic rocks, Joyita Hills area, Socorro County, New Mexico: Unpublished M.S. thesis, University of New Mexico, Albuquerque, 73 pp.

Steven, T. A., 1989, Mosaic faulting as a guide to mineral exploration in the Richfield $1° \times 2°$ quadrangle: U.S. Geological Survey, Circular 1035: 71.

Stewart, J. H., 1980, Regional tilt patterns of later Cenozoic basin–range fault blocks, western United States: Geological Society of America, Bulletin, 91: 460–464.

Stewart, J. H., and Johannesen, D. C., 1979, Map showing regional tilt patterns of late Cenozoic basin–range fault blocks in western United States: U.S. Geological Survey, Open-file Report 79-1134, scale 1:2,500,000.

Stinnett, J. W., 1980, A geochemical study of calc-alkaline andesites and associated volcanic rocks from the Mogollon–Datil field, southwestern New Mexico: Unpublished Ph.D. dissertation, Miami University, Ohio, 271 pp.

Stuart, W. D., and Johnston, M. J. S., 1975, Intrusive origin of the Matsushiro earthquake swarm: Geology, 3: 63–67.

Thompson, T. B., 1973, Mineral deposits of the Nogal and Bonito mining districts, New Mexico: New Mexico Bureau of Mines & Mineral Resources, Circular 123: 30 pp.

Tonking, W. H., 1957, Geology of the Puertecito quadrangle, Socorro County, New Mexico: New Mexico Bureau of Mines & Mineral Resources, Bulletin 41, 67 pp.

Tourtelot, E. B., and Meier, A. L., 1976, Lithium in the Gila Conglomerate, southwestern New Mexico; *in* Vine, J. D. (ed.), Lithium resources and requirements by the year 2000: U.S. Geological Survey, Professional Paper 1005: 125–127.

Trauger, F. D., 1972, Water resources and general geology of Grant County, New Mexico: New Mexico Bureau of Mines & Mineral Resources, Hydrologic Report 2: 211 pp.

Tweto, O., 1978, Tectonic map of the Rio Grande rift system in Colorado: New Mexico Bureau of Mines & Mineral Resources, Circular 163, plate 1, scale 1:1,000,000.

Tweto, O., 1979, The Rio Grande rift system in Colorado; *in* Riecker, R. E. (ed.), Rio Grande rift: Tectonics and magmatism: American Geophysical Union, pp. 33–56.

Wahl, D. E., Jr., 1980, Mid-Tertiary volcanic geology in parts of Greenlee County, Arizona, Grant and Hidalgo Counties, New Mexico: Unpublished Ph.D. dissertation, Arizona State University, Tempe, 148 pp.

Ward, R. M., Schlue, J. W., and Sanford, A. R., 1981, Three-dimensional velocity anomalies in the upper crust near Socorro, New Mexico: Geophysical Research Letters, 8: 553–556.

Weber, R. H., 1971, K–Ar ages of Tertiary igneous rocks in central and western New Mexico: Isochron/West, no. 71-1: 33–45.

Wengerd, S. A., 1959, Regional geology of the Lucero region, west-central New Mexico; *in* Weir, J. E., Jr., and Baltz, E. H. (eds.), West-central New Mexico: New Mexico Geological Society, Guidebook 10: 121–134.

Woodward, L. A. et al., 1978, Tectonic map of Rio Grande rift region in New Mexico, Chihuahua, and Texas: New Mexico Bureau of Mines & Mineral Resources, Circular 163, plate 2, scale 1:1,000,000.

Wright, J. V., and Walker, G. P. L., 1977, The ignimbrite source problem: Significance of a co-ignimbrite lag-fall deposit: Geology, 5: 729–732.

EXCURSION 7A: From silicic calderas to mantle nodules: Cretaceous to Quaternary volcanism, southern Basin and Range province, Arizona and New Mexico

Compiled by John S. Pallister

U.S. Geological Survey, Denver, Colorado 80225

Geologic framework of the southern Basin and Range

David A. Sawyer and John S. Pallister

U.S. Geological Survey, Denver, Colorado 80225

Introduction

Mesozoic to Quaternary volcanism in southern Arizona and New Mexico is closely related to the structural and tectonic evolution of the Basin and Range province. Although the volcanic centers described in this guidebook are compositionally and temporally diverse, they share a common basement framework. This overview attempts to establish a broad tectonic perspective from which to consider volcanism in the southern Basin and Range, and to point out similarities in eruptive processes at several volcanic centers.

Arizona and western New Mexico are divided into two main physiographic and crustal-structure provinces, the Colorado Plateau and the Basin and Range (Fig. 1). The eastern boundary of these provinces is the Rio Grande rift, beyond which lies the North American craton, undeformed by late Cenozoic tectonism and largely unaffected since late Paleozoic/early Mesozoic orogeny. The Rio Grande rift merges

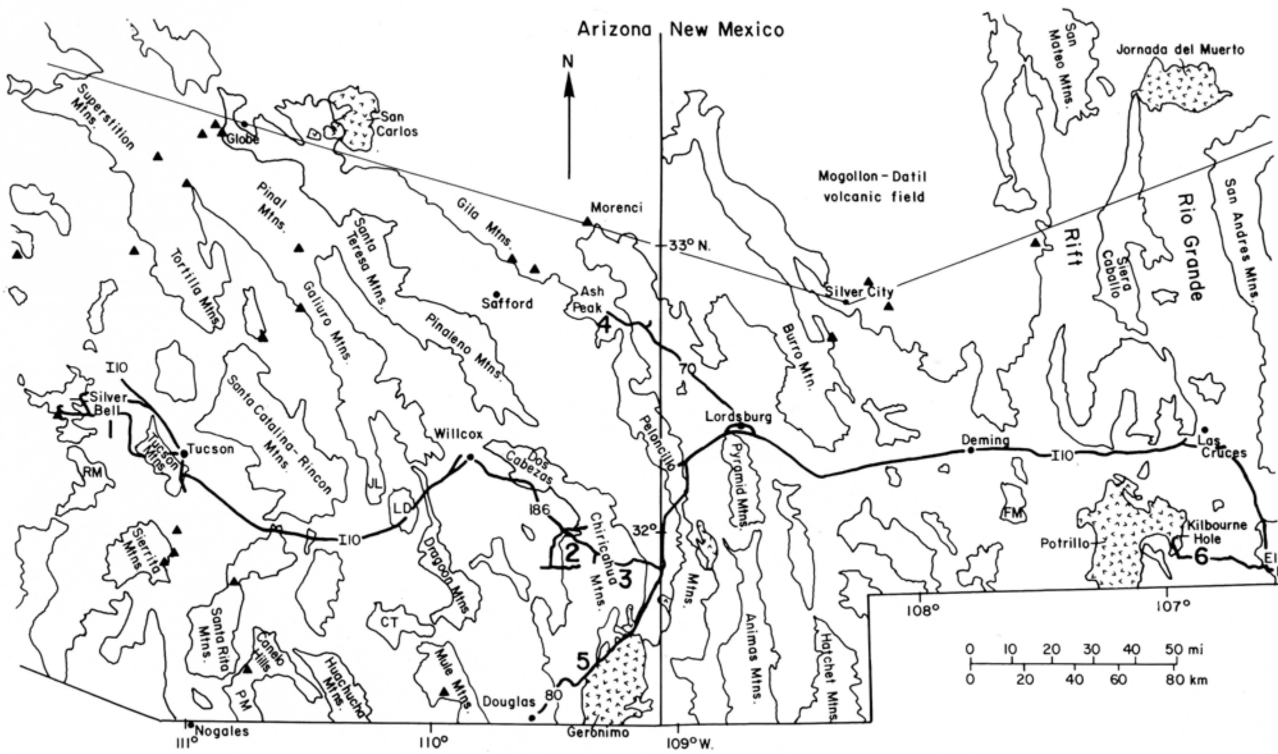

FIGURE 1—Sketch map showing field-trip localities and prominent geographic features in southern Arizona and New Mexico. Major Pliocene–Quaternary volcanic fields are shaded; triangles show the locations of major porphyry copper deposits in the southern Basin and Range. Approximate trace of crustal cross section of Fig. 2 is shown by line from Globe through Morenci to Silver City, then bending northeast through the San Andres Mountains. Actual line of cross section in Fig. 2 extends much farther west across Arizona to the Colorado River. Mountain-range abbreviations: RM = Roskruge Mountains, PM = Patagonia Mountains, JL = Johnny Lyons Hills, LD = Little Dragoon Mountains, CT = Charleston–Tombstone caldera area, FM = Florida Mountains.

with the Basin and Range in southern New Mexico and extends southeast into west Texas and Chihuahua, Mexico (Seager and Morgan, 1979; Olsen et al., 1987). The southern Basin and Range is characterized by rugged mountain ranges that rise abruptly from broad alluvial valleys. This topography is mainly the result of late Tertiary and Quaternary tectonics, and is simply the last layer of geologic complexity in a region that has experienced numerous episodes of magmatism and orogeny since the Proterozoic.

This field guide takes one through magmatic systems of progressively younger ages, which represent magmatic processes that took place at varying depths in the crust and mantle. The Silver Bell and Tucson Mountains expose eroded caldera-fill sequences and ring-dike intrusions of Late Cretaceous age. Mid-Tertiary calderas and rhyolite vent complexes of the Chiricahua and Peloncillo Mountains are exposed at levels that range from the juvenile volcanic surface to eroded surfaces within comagmatic shallow crustal magma reservoirs. Finally, the late Tertiary to Quaternary Geronimo and Potrillo basalt fields provide insight into both surficial volcanology and lower crustal and mantle magmatic and metamorphic events.

Plate-tectonic framework

The southern Basin and Range is composed primarily of rocks produced during multiple episodes of tectonism and magmatism related to plate-boundary interactions to the south and west (Dickinson, 1981; Engebretson et al., 1984, 1985). Middle Proterozoic rocks southwest of the Archean Wyoming craton are thought to represent intraoceanic island arcs and marginal basins accreted to the North American continental margin between about 1.8 and 1.6 Ga (Condie, 1982). A northeast-trending boundary, between compositionally distinct 1.8–1.7 Ga rocks to the northwest and 1.7–1.6 Ga rocks to the southeast, passes through central Arizona, roughly between Phoenix and Prescott. This boundary is a diffuse zone with significant overlap in age of post- and syn-orogenic plutonism (Karlstrom et al., 1987). A marked contrast between strongly deformed island-arc volcanic rocks and batholiths to the northwest (Anderson and Silver, 1976) and less deformed supracrustal silicic volcanics, sedimentary rocks, and coeval batholiths to the southeast (Conway and Wrucke, 1986) may require juxtaposition of these terranes by accretion after 1.69 Ga (Karlstrom et al., 1987). The oldest exposed crust in southeast Arizona is composed principally of quartz–muscovite schist, the Pinal Schist, that appears to have formed in deep-water turbidite basins (Silver, 1978). Recent work has suggested deposition of the Pinal protoliths either near a north-dipping subduction zone (Swift, 1987), or in an extensional (rift) setting (Condie et al., 1985).

These 1.8–1.6 Ga metamorphic and associated syn- and post-deformation plutonic rocks were regionally intruded by anorogenic granite plutons between 1.44 and 1.42 Ga (Anderson, 1983). These coarse, K-feldspar megacrystic biotite granites are the dominant Precambrian rocks in many ranges in the southern Basin and Range. Depositionally overlying these plutons are undeformed, weakly metamorphosed, sedimentary rocks of the Apache Group (Shride, 1967). These sedimentary rocks are cut by diabase intrusive sheets and dikes dated at 1.11–1.12 Ga (Silver, 1978); deposition of sediments and intrusion of diabase probably occurred during a rifting event (Davis et al., 1981). Proterozoic supracrustal rocks in the Franklin and Carrizo Mountains of west Texas were deposited(?) and intruded by alkalic granite at about the same time (Condie, 1981). Cambro-Ordovician alkalic magmatism has recently been documented by U–Pb ages on an alkali-granite pluton in the Florida Mountains, southwest New Mexico (Evans and Clemons, 1988); other undated alkali-granite plutons assumed to be 1.4 Ga may also be of this age.

Latest Precambrian–Paleozoic tectonics were initially typical of a stable craton, but middle Paleozoic tectonism along the transcontinental arch generated minor variation in sedimentary facies, and late Paleozoic basins were activated by the collisional effects of the Ouachita orogeny to the southeast (Kluth, 1986; Stewart, 1988; Armin, 1987). The Paleozoic history of southern Arizona is dominated by the accumulation of a 1–2 km thick section of platform sedimentary rocks (mostly carbonates). The southern passive margin of the Paleozoic North American continent was just south of the U.S.–Mexico border; off-shelf deep-water eugeoclinal sediments were deposited during early and middle Paleozoic time approximately 200 km to the southwest in Sonora (Stewart, 1988). No igneous activity is recorded in this fairly complete Paleozoic depositional record.

Phanerozoic continental-arc magmatism in the southern Basin and Range is first recorded by Jurassic volcanic rocks and caldera fragments. These, and subsequent periods of arc magmatism, can be related to subduction/accretion events in the Cordillera to the west. The earliest episode ranged from 210 to 185 Ma in western and southern Arizona. The latest Jurassic magmatic rocks (165–145 Ma) overlap in age with the Nevadan orogeny (150–160 Ma; Schweickert et al., 1984), a period when metamorphosed middle Paleozoic to Jurassic oceanic and island-arc assemblages were accreted to the continental margin in the western foothills belt of the Sierra Nevada.

Cordilleran thrust faulting affected much of the southern Basin and Range in Arizona and New Mexico from about 90 to 75 Ma, coincident with the Sevier orogeny in Utah, Wyoming, and Idaho. Calc-alkaline arc magmatism migrated eastward from the continental margin in California, in both the Sierra Nevada (Chen and Moore, 1982) and the Peninsular Ranges (Silver, unpubl. data; summarized in Keith and Wilt, 1986), and into Arizona by 75 Ma. From 75 Ma to approximately 60 Ma (actual crystallization ages are poorly known due to resetting of K–Ar ages), widespread calc-alkaline magmatism in southern Arizona and New Mexico constituted a major continental interior arc province (Lipman and Sawyer, 1985). Plutonism related to this volcanic episode is responsible for the majority of the porphyry copper deposits in southwestern North America (Titley, 1982), one of the two largest porphyry copper-producing provinces in the world. This outbreak of magmatism has been related primarily to a sharp increase in plate-convergence rates between 75 to 50 Ma (Engebretson et al., 1984). The eastward migration of magmatism has been linked to flattening of the subducted plate (Coney and Reynolds, 1977), although the origin of continental-interior magmas in the late Cretaceous and Tertiary remains controversial (Lipman, 1980; Wernicke et al., 1987; Larson et al., 1987).

Middle Tertiary volcanism in the Basin and Range took place during a period of transition from convergent margin continental-interior arc magmatism to extensional continental tectonics, the tectonic setting that dominated the remainder of the Tertiary. This change in tectonic regime is generally considered to have resulted from the collision of the East Pacific Rise with the North American plate at about 28 Ma (Atwater, 1970). The collision resulted in a subsequent change from calc-alkaline andesite–rhyolite magmatism to bimodal basalt–rhyolite magmatism (Christiansen and Lipman, 1972). Subduction of the Mendocino fracture zone may have affected the migration of mid-Tertiary and younger magmatism (Glazner and Supplee, 1982). Extreme extension in the Basin and Range accompanied the early development of a transform boundary (the San Andreas fault) along the west margin of North America in the early Miocene. Peak mid-Tertiary magmatism may have accompanied this distension, as in eastern Nevada (Gans et al., 1987), but detailed temporal relations between extension and volcanism in the southern Basin and Range remain poorly known. Since the middle Miocene, high-angle faulting has accommodated a more limited extension of the crust, and has resulted in the present Basin and Range physiography. First transitional (calc-alkaline to alkaline) basalts and then alkali basalts and basanites were erupted in the Basin and Range during the prolonged late Tertiary–Quaternary period of extension.

Mesozoic history

Mesozoic history of the southern Basin and Range consisted of several episodes of magmatic activity, punctuated by deposition of continental sediments. The history has been reviewed by several authors (Hayes and Drewes, 1978; Dickinson, 1981), but details are obscured by limited exposures, large uncertainties in geochronology, and lack of focused study. At least two Jurassic magmatic episodes at 210–185 Ma and 165–145 Ma are indicated by U–Pb zircon dating (Haxel et al., 1984; Wright et al., 1981; Riggs, 1987; Reynolds et al., 1987; Asmerom et al., 1988) and paleomagnetic studies (Kluth et al., 1982; May and Butler, 1987).

This magmatism is probably related to the sweep of a Jurassic arc through southwestern North America (Anderson and Silver, 1978; Dickinson, 1981), and many of the volcanic rocks probably accumulated in calderas (Lipman and Sawyer, 1985). Recent work on the Jurassic and Lower Cretaceous parts of the Mesozoic in southern Arizona is summarized in Dickinson and Klute (1987). Lower Cretaceous Bisbee Group sedimentary rocks were deposited in a northwestern extension of the Chihuahua trough (Bilodeau, 1982). The lowest unit of the Bisbee, the Glance Conglomerate, is a syntectonic fan conglomerate (Bilodeau et al., 1987) derived from high-angle, fault-bounded block uplifts bordering graben or half-graben basins. The interfingering of Jurassic volcanic rocks with coarse clastic rocks suggests that Glance deposition extends back into the Jurassic (Vedder, 1984); alternatively, these clastic rocks could represent debris shed into local volcanic-subsidence basins and not be correlative with the type Glance. In southeast Arizona and New Mexico, the Glance was succeeded by shallow marine carbonate and clastic deposits. To the west, the thick Bisbee Group marine sedimentary rocks are correlated with continental sedimentary deposits, such as the Amole Arkose in the Tucson Mountains (Risley, 1987).

Late Cretaceous compressive deformation

After deposition of Bisbee Group sediments and before Late Cretaceous magmatic activity, a period of erosion and major compressive deformation affected southern Arizona. The style and extent of this compressional deformation remain controversial (Davis, 1979; Drewes, 1980, 1981). Drewes (1981) regards thrust faulting as being continuous in style with the thin-skinned thrust belt of the northern and central Cordillera and the Sierra Madre Oriental of Mexico. Rocks in southeast Arizona are interpreted as a belt of stacked, thin, thrust sheets with as much as hundreds of kilometers of horizontal translation. The inferred peak of this orogenic activity was about 75–80 Ma in the area around Tucson; welded tuff of the Salero Formation in the Santa Rita Mountains, dated at 72–73 Ma, postdates deformation. Compressive deformation in the Sierrita Mountains may involve some Late Cretaceous volcanic units (Fridrich, 1987).

In contrast, a basement-cored uplift model has been advocated by Davis (1979). Response to regional compression was interpreted as markedly inhomogeneous, causing homoclinal tilting, cylindrical folding, and high-angle reverse faulting in discrete structural domains during Late Cretaceous–early Tertiary deformation. Absence of regional thrust faulting was attributed by Davis (1979) and Haxel et al. (1984) to a rigid Precambrian basement covered by a thin, massive Paleozoic shelf sequence which resisted overthrusting. Dickinson (1984) has interpreted a major strand of the Hidalgo thrust of Drewes (1981) as a low-angle normal fault of mid-Tertiary age.

Late Cretaceous–early Tertiary magmatism

Late Cretaceous and early Tertiary volcanism and related plutonic activity in southern Arizona have been summarized by Lipman and Sawyer (1985). They identified 10 or more Late Cretaceous calderas in southeastern Arizona and southwestern New Mexico and recognized that Cenozoic faulting had disrupted these volcanic centers, resulting in preservation of caldera fragments in isolated ranges. Most exposed Late Cretaceous volcanic rocks appear to have accumulated in calderas, with the exception of mafic volcanic rocks in the Williamson Canyon volcanics (Koski and Cook, 1982) near Christmas, and the early Tertiary(?) andesitic volcanic rocks north of Safford, Arizona; both of these sequences probably formed as parts of andesitic stratovolcanoes. Similar mafic/intermediate-composition volcanic rocks are associated with the porphyry copper deposits in the vicinity of Santa Rita, New Mexico, and may also occur in the Pedregosa Mountains of southeast Arizona. Ash-flow tuff overlying andesitic volcanic rocks in the northern Santa Rita and Roskruge Mountains of Arizona may be the only remnants of the outflow facies of this extensive caldera field.

Porphyry copper mineralization related to Late Cretaceous–early Tertiary calc-alkaline plutons is extremely widespread in the southern Basin and Range province of Arizona and New Mexico (Fig. 1). At a number of localities, including Silver Bell (Sawyer, this volume), Sierrita, Copper Flat, Red Mountain, and possibly Ajo, porphyry copper ore deposits are associated with silicic caldera volcanism (Lipman and Sawyer, 1985). Strong porphyry copper alteration and mineralization at Charleston/Tombstone and Courtland/Gleason may also be related to Late Cretaceous calderas. Restoring extension across the San Pedro basin shows that the large porphyry copper deposit at San Manuel adjoins, and is the same age as, a caldera associated with the Copper Creek porphyry copper deposit east of the San Pedro. Intrusions below the level of any volcanic cover are associated with porphyry copper deposits in the Globe–Miami, Ray, Morenci, Lakeshore, and Sacaton–Casa Grande areas (Titley, 1982). The porphyry copper deposits of this province have accounted for more than half of U.S. production in the last century.

Northwest-trending faults and their relation to Late Cretaceous porphyry copper mineralization have been discussed widely (Schmitt, 1966; Titley, 1976; Drewes, 1981; Keith and Wilt, 1986); west-northwest trends dominate in the Silver Bell Mountains, the southern Pinaleno Mountains, and the Dos Cabezas Mountains. Studies in southwest New Mexico (Seager, 1983) identified right-lateral strike–slip motion of latest Cretaceous–early Tertiary age along west-northwest and northwest-trending faults that are related to basement-cored uplift. Stratigraphic offsets at Silver Bell indicate that oblique strike–slip faults were active concurrent with the final Late Cretaceous volcanism and intrusion; this style of faulting may have continued into middle Tertiary, but was complete by 25 Ma.

Cenozoic rocks and structure

The southern Basin and Range has experienced several episodes of deformation and magmatism in the Tertiary. There is little depositional record of the early Tertiary; it was probably a time of uplift and erosion. During the Oligocene and Miocene (36–15 Ma), there was widespread intermediate and silicic magmatism in southern Arizona (Shafiqullah et al., 1978; Drewes et al., 1986), perhaps beginning as early as late Eocene in New Mexico. In the Mogollon–Datil volcanic field (Excursion 6A), and the Chiricahua, Galiuro, Superstition, Peloncillo, Pyramid, and Animas Mountains, large silicic calderas erupted widespread ash-flow sheets and proximal lava flows; regional correlations between these centers have not yet been worked out. Middle Tertiary granite plutons occur in the Santa Teresa Mountains adjoining the Galiuro volcanics, in the Dos Cabezas Mountains and Peloncillo Mountains, and subvolcanic plutonic rocks are exposed in the Chiricahuas. The middle Tertiary granite plutons at Cochise Stronghold and in the Dos Cabezas Mountains may be analogues for deeper plutonic levels than hypabyssal rocks exposed in the mid-Tertiary Turkey Creek caldera of the Chiricahua Mountains. Pallister and du Bray (this volume) call on eruption of ash-flow tuff from ring and central vents, which were then intruded and clogged by less fractionated monzonitic magma from lower levels of a stratified chamber.

In addition, much of the middle Tertiary volcanic activity, especially in the Peloncillo, Whitlock, and Gila Mountains, resulted in development of extensive fields of basaltic andesite to andesite lava flows and numerous non-caldera silicic eruptive centers (Richter et al., 1981, 1983). These silicic eruptive centers range from relatively small dacite and rhyolite plugs and domes to large rhyolitic dome-flow complexes and associated pyroclastic deposits, such as the Rhyolite Peak–Ash Peak complex in the central Peloncillo Mountains (Walker and Richter, this volume). Many of the larger silicic eruptive centers are compositionally zoned; some have extremely evolved high-silica rhyolites.

Relation of the middle Tertiary calderas and other eruptive centers to regional tectonics is currently a matter of conjecture. Drewes (1981) projects regional thrust faults through basement rocks below the Turkey Creek caldera; his Apache Pass fault projects into a thick sequence of middle Tertiary rhyolite lavas, ash flows, and "intrusive" tuffs near Cochise Head, in the northern Chiricahua Mountains. It is intriguing to speculate about possible relationships between silicic magmatism and regional structures; were shallow magma chambers being tectonically unroofed by low-angle normal faults, or were magmas accumulating and venting along regional faults? Basin and Range extension clearly overlapped middle Tertiary silicic magmatism in the Mogollon–Datil volcanic field, and possibly in the Chiricahua, Superstition, and Galiuro Mountains; the degree to which range uplift and tectonic denudation are direct results of intrusion of silicic magma to shallow crustal levels remains an unanswered question.

Regional middle to late Tertiary extensional deformation dominates the structure and physiography of the southern Basin and Range. Two different generations and styles of extensional tectonism have been identified: an early period of extreme extension along low-angle normal or detachment faults (Anderson, 1971; Proffett, 1977; Davis and Hardy, 1981), and a later Miocene–Pliocene period of high-angle faulting that formed the current deep alluvial basins separated by bedrock horsts (Scarborough and Pierce, 1978; Eberly and Stanley, 1978). Some mountain-front contacts may follow the older extensional structures (Dickinson et al., 1987). The age of the older extensional faulting is probably between 25 and 13 Ma in southern Arizona (Coney, 1980). It is characterized by the development of low-angle detachment faults which separate ductilely deformed lower-plate mylonitic gneisses from brittlely deformed upper-plate middle Tertiary volcanic and sedimentary rocks; the latter are commonly rotated along listric normal faults that sole into the detachment (Davis, 1980, 1983). Middle Tertiary plutonism accompanied extensional deformation, and mylonitic fabrics were developed in some rocks as young as 21 Ma (Reynolds et al., 1986). Middle Tertiary mineralization is almost exclusively epithermal in character, in strong contrast to the dominant Late Cretaceous porphyry style of ore deposition.

South-central Arizona has little active seismicity; as a result, many of the basin boundary faults have been buried by late Tertiary and Quaternary sediments. Further east, in southeast Arizona and near the Rio Grande rift, late Quaternary faulting is more significant (Machette et al., 1986). Large volumes of late Pliocene and Quaternary basaltic rocks have been extruded concomitant with faulting in the Geronimo volcanic field, the Animas Valley, the Potrillo volcanic field, and the Rio Grande rift.

Geophysics

A crustal cross section for southern Arizona and New Mexico, based on seismic and gravity data (Sinno et al., 1981; Gish et al., 1981; Sinno et al., 1986) is shown in Fig. 2. Crust beneath the southern Basin and Range is about 25 km thick, and thickens east of the Rio Grande rift to about 50 km. The attenuation of crustal thickness in the southern Basin and Range may have occurred concurrent with Miocene and younger extension (Sinno et al., 1981; Perry et al., 1987). In these areas, the lithosphere has been greatly thinned, and asthenosphere is interpreted to be in contact with the base of the crust (Sinno et al., 1986; Olsen et al., 1987). The apparent thickening of crust from eastern Arizona into southwestern New Mexico (Fig. 2) may be only an artifact of the seismic transect, which cuts obliquely across the Basin and Range–southern Colorado Plateau boundary. Depth-to-basement, derived from gravity data (Oppenheimer and Sumner, 1980), reveals that elongate ranges of the southern Basin and Range are more continuous (as shallowly buried bedrock horsts) than is evident from

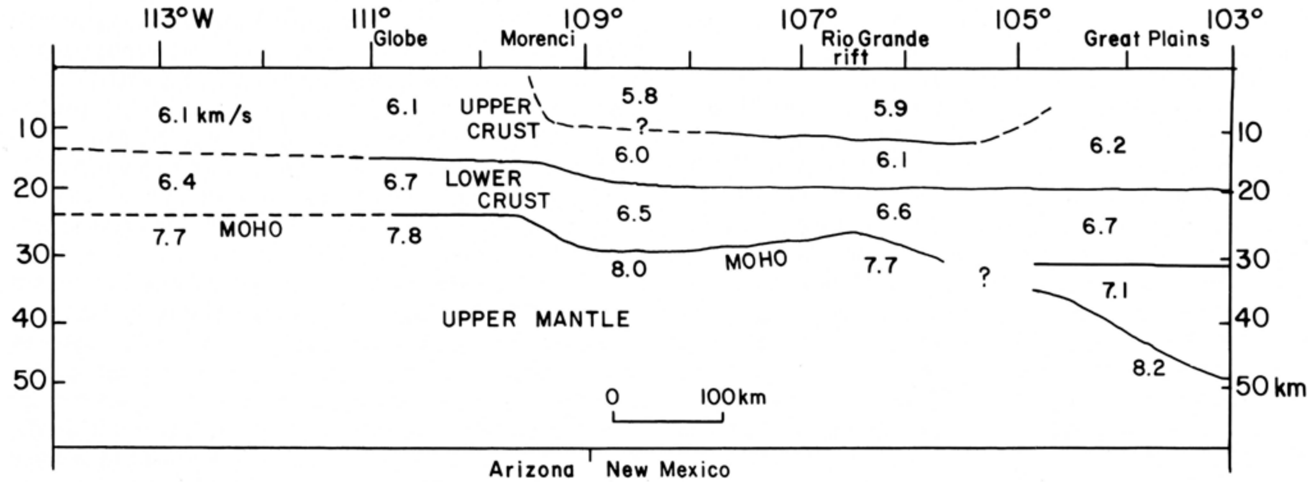

FIGURE 2—East–west cross section of southern Arizona and New Mexico showing crustal structure as inferred from seismic data (Sinno et al., 1981; Gish et al., 1981; Sinno et al., 1986). Approximate location of the cross-section line is shown in Fig. 1.

the distribution of mountainous areas at the surface. The basins are steep-sided and are filled with as much as 3–6 km of unconsolidated to partly consolidated sediments. Basin development is mainly post-Oligocene; more than 6 km of sediment has accumulated in the Tucson basin in the past 25 Ma (Anderson, 1987).

Xenolith studies

Mantle

The composition and geochemical characteristics of the mantle beneath southern Arizona are constrained by xenolith studies and by seismology. Upper mantle P_n seismic velocities range from 7.6 to 7.8 km/s (Sinno et al., 1981; Gish et al., 1981), corresponding to seismic velocities of pyroxene-rich, olivine-poor peridotites. Two major xenolith localities have been well studied within the Basin and Range of southern Arizona. These are the San Carlos locality at Peridot Mesa, north of Globe, and the Geronimo (San Bernadino) volcanic field in the southeasternmost corner of the state. Frey and Prinz (1978) described spinel lherzolites and spinel harzburgites (Cr-diopside group or Type I—Wilshire and Shervais, 1975; Frey and Prinz, 1978) as the dominant rock types in the San Carlos suite, along with pyroxene-rich xenoliths of alkaline igneous affinity (Al–Ti augite group or Type II). Type I spinel lherzolites and harzburgites are considered to be the residue from various degrees of partial melting and basaltic melt extraction and represent fragments of the upper mantle. Some harzburgitic lherzolites and harzburgites appear to have been metasomatically enriched in LIL-elements (K, U, LREE). The upper mantle harzburgites and lherzolites were invaded by veins of pyroxene-rich peridotite ($\pm$ amphibole, phlogopite) and reflect the complexity and heterogeneity of mantle processes.

A generally similar distribution of ultramafic xenoliths has been described from the Geronimo volcanic field (Kempton et al., 1984; Kempton and Dungan, this volume). Clinopyroxene-depleted spinel lherzolites and harzburgites are the dominant rock types and attest to significant partial melting of the upper mantle on a regional scale. Clinopyroxenes in these rocks are Cr-diopsides that can be subdivided into two groups, one exhibiting LREE depletion (Type Ia), and the other having enriched LREE (Type Ib), attributed to metasomatic infiltration, possibly involving CO_2- and H_2O-rich fluids (Kempton et al., 1984).

The isotopic characteristics of these two suites show a broad range of variation. Initial Sr-isotope compositions of minerals and rocks range from 0.7017–0.7058 in the San Carlos olivine-rich rocks (Frey and Prinz, 1978) to 0.70197–0.70488 for the Geronimo xenoliths (Menzies et al., 1985) and 0.70177–0.70453 for Kilbourne Hole (Roden et al., 1988). Nd-isotope data for clinopyroxenes from the Geronimo Type I rocks have elevated values (0.513350–0.512584) typical of LREE-depleted sources that resemble oceanic mantle (Menzies et al., 1985); Kilbourne Hole Type I and II nodules range from 0.513326 to 0.512797. Alkali basalts also have depleted to moderately enriched mantle Nd- and Sr-isotopic signatures, similar to the ranges defined by mid-ocean-ridge basalt (MORB) and ocean-island basalt (OIB). Pb-isotopic data (Zartman and Tera, 1973) for xenoliths from San Carlos and Potrillo plot below the crustal-evolution curve of Stacey and Kramers (1975), but above MORB (Tatsumoto, 1978). The combined petrologic and geochemical data suggest a heterogeneous upper mantle dominated by long-term depletion of lithophile elements and subsequent metasomatic enrichment beneath the Basin and Range province of southern Arizona (Kempton et al., 1984).

Lower crust

Lower crustal rocks are not exposed in the Southwest, but characteristics of the lower crust can be inferred from xenoliths and geophysical measurements. However, caution should be exercised in such interpretations, as Padovani and Reid (this volume) note that seismic velocities and densities of metasedimentary xenoliths from Kilbourne Hole overlap with those of potentially underplated basaltic materials.

Lower crustal xenoliths from the western-interior craton of North America are dominantly granulitic rocks (Kay and Kay, 1981). Granulites from Kilbourne Hole in the Rio Grande rift (Padovani and Carter, 1977a) are both meta-igneous (two-pyroxene granulites) and metasedimentary (sillimanite–garnet granulites) in origin. Charnockites (orthopyroxene-bearing granite) and minor anorthosite also occur. Metasedimentary garnet granulites are probably residues of pelitic sediments from which water-rich granitic melts were extracted. Nd- and Sr-isotopic studies of the Kilbourne xenoliths by Richardson et al. (1980) showed that metamorphic recrystallization occurred within the last 10 Ma, but Pb systematics and a Rb/Sr isochron on one sample (Reid et al., 1982) indicate an original Proterozoic age. In contrast to inferences about the composition of the lower crust from other sources, Kilbourne Hole peletic granulites do not show evidence of long-term Rb, Th, and LREE depletion, nor do they show evidence of oxygen exchange (Padovani and Reid, this volume). La Olivina in Chihuahua (Cameron et al., 1983) has a similar assemblage of garnet granulitic metapelites to those from Kilbourne Hole. The many Colorado Plateau xenolith localities (McGetchin and Silver, 1972, and others summarized in Kay and Kay, 1981) also have similar lower crustal xenolith populations plus garnet–clinopyroxene and/or amphibole-bearing rocks such as Franciscan-type eclogite (Helmstaedt and Doig, 1975) and amphibolite.

Crustal xenoliths from the southern Basin and Range province may differ from those of the Colorado Plateau and Rio Grande rift. Recent work by Kempton (cited above) on mantle xenoliths from the Geronimo volcanic field in southeastern Arizona has been extended to crustal xenoliths (Kempton and Dungan, this volume). Lower crustal xenoliths are dominantly one- and two-pyroxene granulites that equilibrated at 840–960°C (Kempton and Dungan, this volume). These granulites are mafic to intermediate in composition and are divided into two groups based on their mineralogy and geochemistry: metagabbro with positive europium anomalies (cumulates), and metadiorites of calc-alkaline affinity. No mineral assemblages indicate a metasedimentary parentage. Absence of garnet indicates either that these granulites equilibrated at lower pressure than those from the Rio Grande rift or Colorado Plateau, or that appropriate aluminous protoliths were not present. Kempton (this volume) reports a 1.4 ± 0.4 Ga $^{207}Pb/^{206}Pb$ secondary isochron on the combined Geronimo granulite xenolith suite. She interprets the metacumulates as crystallization products of Cenozoic alkalic magmas that were contaminated with lower to middle crustal rocks similar to the Geronimo metadiorites. Padovani and Reid (this volume) obtained a 1.6 Ga Rb–Sr isochron by sampling individual layers in paragneiss xenoliths from Kilbourne Hole; however, they note that mineral isochrons (Rb–Sr and Sm–Nd) have been reset by heating related to Rio Grande rift formation.

Lower crustal nodules from San Carlos include garnet granulites and amphibolites, as well as two-pyroxene granulites (W. I. Ridley, oral comm. 1988). The crustal xenoliths provide lower crustal analogues that can be used in modeling crustal components in Mesozoic and Cenozoic silicic magmas in the southern Basin and Range. This approach has been applied at the Late Cretaceous Silver Bell caldera (Sawyer, 1987). It would clearly be appropriate to use the Geronimo suite for modeling a potential lower crustal component in the adjacent Chiricahua magmatic rocks. The distinctiveness of crustal xenoliths from the adjoining Potrillo and Kilbourne Hole localities (Padovani and Carter, 1977a) suggests caution in extrapolating lower crustal rock types from one area to another. However, it is probably reasonable to assume a dominantly granulitic (rather than eclogitic) lower crust beneath the Conrad discontinuity, based on seismic-refraction studies (Sinno et al., 1981).

Physical volcanology

The Ash Peak–Rhyolite Peak eruptive complex (Walker and Richter, this volume) provides a conceptual link between caldera-forming eruptive processes in the Chiricahua Mountains and basaltic volcanism in the Geronimo and Potrillo basalt fields. Pallister and du Bray (this volume) observed transitions between high-energy Plinian eruptions that produced ash-flow tuff deposits, and effusive eruptions that produced rhyolite lavas in eroded vents within the Turkey Creek caldera. At Ash Peak, transitions from Pelèean to Strombolian eruptions are inferred from rhyolite deposits that include pyroclastic flows, bedded-ash and base-surge deposits (some with bombs and impact structures), and rhyolite lava that appears to represent agglutinated rhyolitic spatter. Ash Peak is a pyroclastic breccia cone that is morphologically similar to the basaltic cinder and spatter cones of the Geronimo volcanic field.

Strombolian-style eruption of rhyolitic magma implies relatively low volatile contents or efficient pre-eruptive degassing (Eichelberger et al., 1986), a feature that characterized other mid-Tertiary rhyolite magma systems in the southern Basin and Range. Strombolian eruption, analogous to Hawaiian fire-fountaining, and low volatile contents are inferred for rhyolite lavas of the Black Range in southwestern New Mexico on the basis of field evidence and mineral chemistry (Duffield, this volume). Caldera formation in the Chiricahua Mountains was preceded by development of a high-silica rhyolite lava field; it would appear that volatile contents only episodically built up to the point necessary to drive large-scale Plinian eruptions and caldera collapse.

Although the Ash Peak rhyolite was probably relatively "dry," the ash and lapilli are largely converted to zeolites. The timing of zeolitization is unknown. It is possible that some Ash Peak eruptions may have been phreatomagmatic, offering an alternative driving mechanism for the ballistic and surge deposits. Phreatomagmatic explosions are commonly cited as an important mechanism for maar formation. Kilbourne Hole maar has a tuff ring composed mainly of comminuted sedimentary rocks, and was formed primarily by phreatomagmatic explosions that took place when alkali basalt, containing abundant lower crustal nodules, came into contact with ground-water-saturated sediments of the Santa Fe Group within the Rio Grande rift. In contrast, maars of the Geronimo volcanic field are dominated by juvenile basaltic cinder and spatter, favoring a magmatic volatile-driven eruptive (diatreme) mechanism.

Field guide to the Late Cretaceous Silver Bell caldera and porphyry copper deposits in the Silver Bell Mountains

David A. Sawyer

U.S. Geological Survey, Denver, Colorado 80225

Introduction

The field trip will examine evidence for a Late Cretaceous caldera at Silver Bell that is closely associated in time and space with the porphyry copper deposits of the district. The main emphasis will be on the volcanic sequence on the east side of the Silverbell Mountains and caldera-collapse megabreccia composed of Paleozoic sedimentary blocks on the southwest side of the mountains. These sedimentary rocks are host to major skarn deposits along strike with a caldera-collapse megabreccia horizon. There will be one hike of about 2 km and less than 300 m elevation gain. A more detailed road log (containing additional stops and intermediate mileage) is available in Sawyer (1986), and detailed petrology, geochemistry, and stratigraphic descriptions can be found in Sawyer (1987).

Starting from downtown Tucson, the mileage begins at the intersection of I-10 West and Speedway Boulevard. This is the same starting point as for the Tucson Mountains caldera field guide (Lipman, this volume), although, if both trips are planned for the same day, it is possible to go directly from Silver Bell to Gates Pass in the Tucson Mountains (instructions at the end of this log).

Road log

Mileage

0.0 **Head northwest** on I-10 West from Speedway Blvd. **3.0**

3.0 Overpass over Prince Road. To the west are the Tucson Mountains, site of this afternoon's field trip. The Tucson Mountains are also a Late Cretaceous caldera with related intrusive rocks (Lipman, this volume). **8.0**

11.0 Cortaro Road exit. To the west is Safford Peak, a mid-Tertiary dacitic intrusive plug (Brown, 1939). The northern Tucson Mountains are entirely mid-Tertiary volcanic rocks. View to the northeast at about 1:30–2:00 of the Tortolita Mountains, a metamorphic-core-complex range discussed by Davis (1980). **9.0**

20.0 **Turn right** off I-10 at the Marana exit. **Turn left** at the stop sign and continue underneath the freeway overpass; pass frontage road; **turn right** at the next intersection (a Chevron station is on the southeast corner of the intersection, and a Circle K convenience mart on the southwest). Proceed west on Trico–Marana Road. **1.5**

21.5 Heading west on Trico–Marana Road after passing the Post Office, a regional view of the mountain ranges around the Silver Bell Mountains (see Fig. 1 of Introduction for reference) is as follows: Tucson Mountains to the south (at 8:30); farther south (9:00) are the Sierrita Mountains. The largest Laramide batholith in southern Arizona, the Ruby Star Granodiorite, outcrops in this range. Upper Cretaceous volcanic rocks accumulated in a caldera associated with the large Pima district porphyry copper deposits in the Sierrita Mountains (Lipman and Sawyer, 1985; Fridrich, 1987).

Low mountains in the foreground (10:00) are the Roskruge Mountains, composed of Upper Cretaceous volcanic rocks, minor Upper Cretaceous intrusive rocks, and mid-Tertiary volcanic rocks. The Upper Cretaceous volcanic rocks are mainly rhyolite welded tuffs, the only remnant of a larger ash-flow plateau. In the foreground, north of the Roskruge Mountains (11:00), are the Waterman Mountains which are composed of complexly faulted Paleozoic sedimentary rocks and only a few Upper Cretaceous or middle Tertiary igneous rocks.

The central Silver Bell Mountains (11:00 to 12:00) are composed of Upper Cretaceous volcanic rocks and comprise most of the view to the west. The highest peak at the south end of the central Silver Bell Mountains is Silver Bell Peak. The very jagged high peak at the north end of the Silver Bell Mountains is Ragged Top, an Oligocene rhyolite dome that was emplaced along the Ragged Top fault. The geology of the east side of the Silver Bell Mountains will be described in more detail at Stop 1.

Low hills to the northeast (12:00 to 1:00) of the Silver Bell Mountains are the Samaniego Hills. Middle Tertiary volcanic rocks, mostly basalt to basaltic andesite in composition (R. Ashley, unpubl. mapping), unconformably overlie a basement of Precambrian granite north of the Ragged Top fault. Picacho Peak, at 3:00 to the north, is also middle Tertiary volcanic rocks, mostly andesitic lavas and breccias. The Picacho Mountains to the north of Picacho Peak are composed of core-complex mylonitic gneiss (Davis, 1980). **4.6**

26.1 Stop sign at junction of Trico–Marana Road with Trico Road; **continue straight** ahead. For approximately the next 15 mi the trip will be on unpaved roads. **0.5**

26.6 Second stop sign on Trico–Marana road; junction with Silver Bell Road. **Turn right** on Silver Bell Road and head north. **1.7**

28.3 Intersection with Cherokee Road; road forks. **Bear left** and continue west on Silver Bell Road toward the Silver Bell Mountains. **4.8**

33.1 To the left at 9:30 is Red Hill, a small knoll made up of Precambrian biotite granite containing K-feldspar megacrysts. It is lithologically similar to other members of the 1.40–1.45 Ga transcontinental anorogenic granite suite (Anderson, 1983). Leached K-feldspar from this locality gives a 1.4 Ga common-Pb model age using the Stacey/Kramers curve (1975). **1.6**

34.7 Fork in the road. **Bear left,** as Silver Bell Road bends sharply away to the north. Head west toward the Silver Bell Mountains. **1.0**

35.7 Junction with the El Paso Natural Gas pipeline road. **Turn left** (south). First stop is 1 mi south on gas pipeline road. **1.0**

36.7 **STOP 1. Overview of the east side of the Silver Bell Mountains.** All directions are given facing in the direction of the central Silver Bell Mountains (west) as 12:00. The peak at the south end of the range is Silver Bell Peak, the highest elevation in the range at 1299 m (4261 ft). Ragged Top, elevation 1191 m (3907 ft) is the prominent sharp peak at 2:00, northeast of the main range. The geology of the east side of the Silver Bell Mountains is illustrated on the geologic map of the Silver Bell Mountains (Fig. 1), which shows the general route of the field trip.

The Upper Cretaceous stratigraphic section is capped by the Cat Mountain Tuff, erupted from the Tucson Mountains caldera (P. W. Lipman, D. A. Sawyer, and J. Hagstrum, unpubl. data). This unit was previously called the tuff of the Mount Lord Volcanics (Sawyer, 1987). It is a eutaxitic rhyolite welded tuff about 200 m thick that makes up all the high peaks of the central Silver Bell Mountains. Because the Silver Bell Mountains have been tilted 30–35° east-northeast by post-Cretaceous faulting (probably during middle Tertiary extension), most of the east flank of the range is a dip-slope developed on this resistant rock. The southeast spur of Silver Bell Peak has been lifted up to the south by a northeast-trending normal fault. The stratigraphic succession below the lower contact of the Cat Mountain Tuff can be seen on this ridge.

Underlying the Cat Mountain Tuff are the Silver Bell Volcanics, a sequence of andesitic to dacitic extrusive rocks and related volcaniclastic rocks. On the ridge, these rocks are represented by a thin (less than 30 m) layer of debris-flow deposits containing dacitic clasts. The Silver Bell Volcanics are best exposed in the pedimented area on the east side of the Silver Bell Mountains in the immediate foreground. The Cat Mountain Tuff wedges out against a paleo-Silver Bell volcano at about the range front.

Beneath the Silver Bell Volcanics, on the southeast spur of Silver Bell Peak, is a thin sequence of Claflin Ranch Formation bedded pyroclastic deposits. Underlying these volcaniclastic rocks, the middle and lower reaches of the slope are made up of the tuff of Confidence Peak, which is the intracaldera tuff of the Silver Bell caldera. It is a low-silica rhyolite welded tuff that will be seen at Stops 2 and 3. It is also exposed in the pedimented area southeast of Ragged Top, over an area of several square kilometers, where it was uplifted as a fault block. Through the saddle south of Silver Bell Peak, a major swarm of quartz monzodiorite porphyry dikes extends east-northeast from the Oxide pit mineralized center. Most of the low hills east-southeast

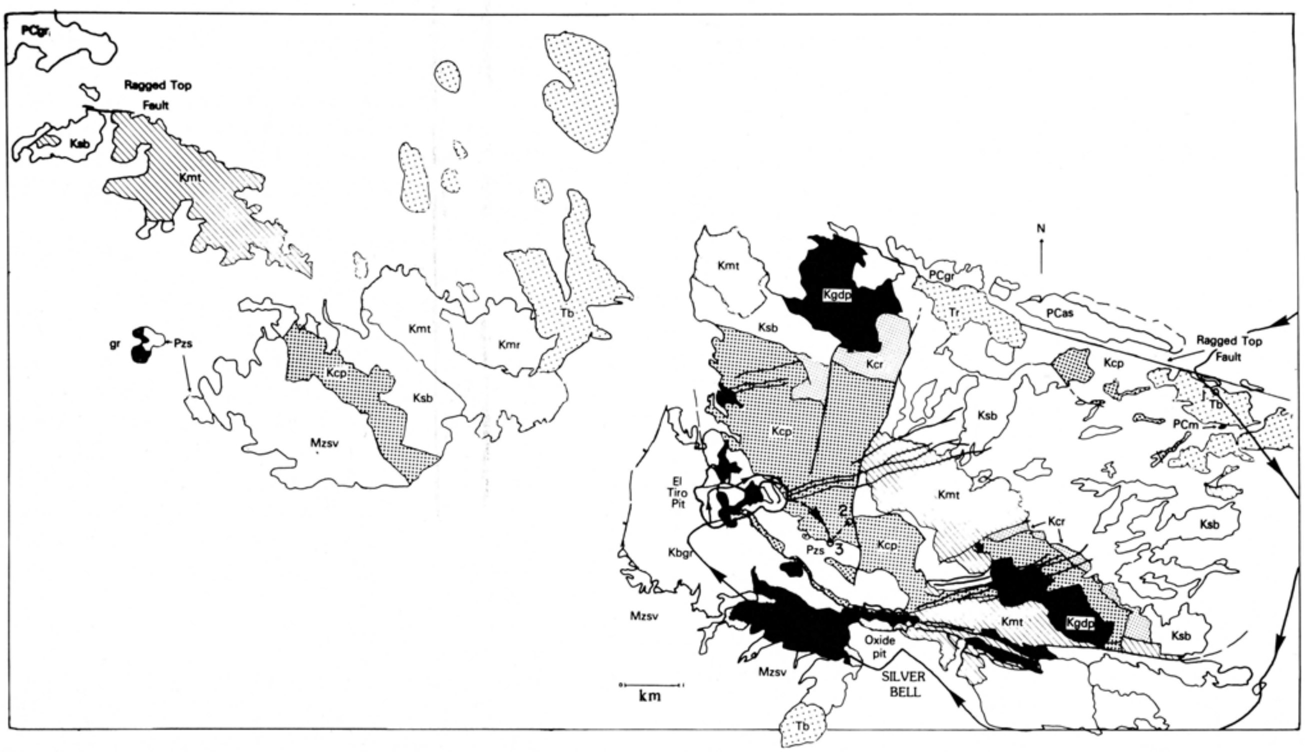

FIGURE 1—Geologic map of the Silver Bell and West Silver Bell Mountains, showing road route and stops on field trip. Field-trip route enters map area by road on the northeast side of map, north of the Ragged Top fault. Map symbols: PCgr = Precambrian 1.4 Ga granite; PCm = Precambrian metamorphic rocks; PCas = Precambrian Apache Group sedimentary rocks; Pzs = Paleozoic sedimentary rocks (entirely caldera-collapse megablocks in the central Silver Bell Mountains); Mzsv = Mesozoic sedimentary and volcanic rocks; Kbgr = El Tiro biotite granite; Kcp = Cretaceous tuff of Confidence Peak; Kcr = Cretaceous Claflin Ranch Formation; Ksb = Cretaceous Silver Bell Volcanics; Kgdp = Cretaceous granodiorite porphyry; Kmt = Cat Mountain Tuff; Kmr = Cretaceous Mount Lord Volcanics, flow-banded rhyolite member; black pattern-Kqmp = quartz monzodiorite porphyry suite and monzodiorite porphyry; Tb = Tertiary basaltic or mafic volcanic rocks; Tr = Ragged Top rhyolite; gr = granite, unknown age.

of Silver Bell Peak are composed of the tuff of Confidence Peak overlain by Claflin Ranch Formation sediments and Silver Bell Volcanics. These units are cut (in this area) by a granodiorite porphyry pluton that predates the Cat Mountain Tuff. The Upper Cretaceous volcanic stratigraphy and related plutons are shown in a schematic geologic column (Fig. 2). Detailed descriptions of the lithologic characteristics and petrology of the units are given by Sawyer (1987).

At Stop 1, subcrop exposures and float are of middle Tertiary volcanic rocks that unconformably overlie the Late Cretaceous sequence. These flows, domes, and low shields form a belt extending from the Samaniego Hills, to the north at 4:00, across the pedimented east slope of the central Silver Bell Mountains, down to the Pan Quemado Hills east of the Waterman Mountains at about 9:30. They range in composition from basalts to dacites; basaltic andesites and andesites occur most abundantly. The low hills due south of Stop 1 are erosional remnants of an andesite flow that has been dated at 28.6 Ma (Mauger et al., 1965, recalculated to new constants).

Beyond the low hills southeast of Silver Bell Peak are the sharp peaks of the Waterman Mountains.

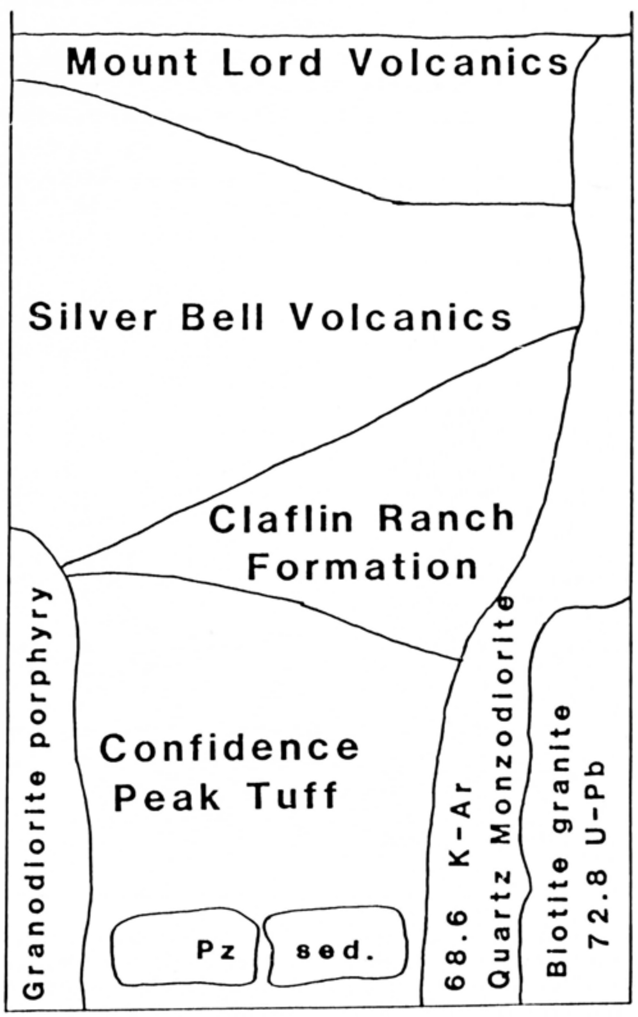

FIGURE 2—Schematic geologic column, central Silver Bell Mountains, showing the principal Upper Cretaceous igneous units and their stratigraphic relationships.

The Paleozoic section of the Waterman Mountains is complexly faulted and the rocks are lithologically and structurally distinct from Paleozoic rocks exposed in the Silver Bell Mountains. Mesozoic sediments that predate Late Cretaceous igneous activity occur in the low area between the Silver Bell and Waterman Mountains. A major west-northwest-trending fault zone separates the thick Upper Cretaceous section in the Silver Bell Mountains from Mesozoic and Paleozoic sedimentary rocks to the south.

A similar west-northwest-trending fault that had strike–slip movement bounds the Silver Bell block to the north. The Ragged Top fault is a N75–80W structure, where tightly constrained from south of Red Hill to Ragged Top, and extends for at least 5 km and probably 20 km farther west. Ragged Top is an Oligocene (25.7 Ma; Mauger et al., 1965) rhyolite dome erupted along the trace of the Ragged Top fault. It was extruded after fault movement. An Upper Cretaceous granodiorite porphyry pluton is truncated by the fault, constraining the age of the movement on the Ragged Top fault to between latest Cretaceous and Oligocene time.

North of the Ragged Top fault are rocks that have had a fundamentally different history than those in the Silver Bell block. Precambrian granite and Middle Proterozoic Apache Group sedimentary rocks (in low hills just east of Ragged Top) are unconformably overlain by middle Tertiary volcanic rocks in the Samaniego Hills. The Silver Bell block can thus be viewed as a relative down-dropped graben containing 2–3 km of Upper Cretaceous volcanic, plutonic, and sedimentary rocks. It is separated from areas with differing geologic histories by west-northwest-trending faults that had probable strike–slip movement. Precambrian rocks in the Silver Bell block are quartz–muscovite schist, different in age and lithology from those north of the Ragged Top fault.

Return to vhicles; **head south** on gas pipeline road. **1.2**

37.9 White gate: **open, bear left** through fence line and continue on main road after **closing gate. 0.5**

38.4 **Turn right** on dirt road heading southwest, just ahead of white gas-line sign on right side of road. Continue southwest on principal dirt track, ignoring small roads splitting off to either side. **2.1**

40.5 Cocio Wash; **continue south across wash** on main route. On far side of wash **turn right** (west-southwest) at road junction. Continue on main track, avoiding fork to left and two forks to right along powerlines. **1.4**

41.9 Intersection with Avra Valley Road; **turn right** on paved road. **3.2**

45.1 American Smelting and Refining Company (ASARCO) office at Silver Bell. Gate at entrance to mine is locked most of the time. **Permission to enter must be obtained from ASARCO** Southwest Regional Office in Tucson and waivers signed before entering mine property. If mine is open, **check in at office. Proceed** onto ASARCO property for continuation of field trip.

Head north from the entrance of the mine. **Take**

left fork at the first junction, pass the pit office and maintenance buildings to the left and veer right up to the main haulage road. **Turn left** (west) on the main haulage road. Be sure to **drive on the left side** of the road. **0.9**

46.0 Precipitation plant to east. Striking east beneath the precipitation plant is the fault that separates Mesozoic sedimentary rocks south of Silver Bell from the Upper Cretaceous quartz monzodiorite porphyry and volcanic rocks to the north. The Oxide pit porphyry copper deposit of the Silver Bell mining district occurs behind the waste dumps to the east and north. **1.8**

47.8 Pass waste dumps of the El Tiro pit porphyry copper deposits as we enter it from the south. **0.5**

48.3 Enter the main El Tiro pit. **0.8**

49.1 Daisy pit on the left, main El Tiro pit on the right. Both pits are principally mined for supergene chalcocite mineralization. These secondary copper blankets are underlain by quartz monzodiorite porphyries having potassic alteration and stockwork chalcopyrite mineralization. **0.4**

49.5 Quartzite Hill on the left, probably Cambrian Bolsa Quartzite. It is a Paleozoic block in caldera-collapse megabreccia within the intracaldera tuff of Confidence Peak. **0.2**

49.7 Drop into the East Extension of El Tiro pit; Confidence Peak is straight ahead, with the microwave tower atop the peak. **0.2**

49.9 **Turn left** on the road going along the east side of the East Extension of El Tiro pit. Without 4WD vehicle this stretch of road will have to be hiked. Views to the west are of skarn mineralization in the East Extension. The relatively unmineralized Imperial pluton can be seen on the northwest shoulder of the pit. Road is closed after ~1 km at berm. **1.0**

50.9 **STOP 2. Confidence Peak Viewpoint.** Park and hike to the viewpoint. The easiest route is up the road that heads southwest along the edge of the waste dumps, and then south up a ridge composed of tuff of Confidence Peak containing caldera-collapse megabreccia of Paleozoic sedimentary rocks. Upon reaching the ridge crest, head east and intersect a road that runs along the crest of the ridge to the microwave tower.

Stop just east of the microwave tower at the top of the mountain. Confidence Peak is a central viewpoint that provides a panorama of the entire western side of the Silver Bell Range, and all the mountain ranges to the west and north. At this observation point we will discuss the geology of the west side of the Silver Bell Range.

Walk to the east end of the parking area at the top of Confidence Peak. Facing east, directly ahead in the central Silver Bell Mountains is Angel Peak. This will be our 12:00 reference point.

Starting to the south at 3:00 (right), is the Oxide pit of the Silver Bell mining district. Just beyond it are the Waterman Mountains which have been described previously. At 1:00, Silver Bell Peak can be seen. At 11:00 is an unnamed peak to the north of Angel Peak, and just beyond it Ragged Top, the Tertiary rhyolite dome. Looking back at about 7:00 to 8:00 is the El Tiro mineralized center of the Silver Bell mining district. Beyond the El Tiro mineralized center are mountain ranges rising to 2500–3000 ft that make up the West Silver Bell Mountains.

The geology of the central Silver Bell Mountains that can be seen from this point will be described starting with the youngest stratigraphic unit. Silver Bell Peak, Angel Peak, and all of the main ridge crest of the central Silver Bell Mountains are capped by Cat Mountain Tuff. The lower contact of the Cat Mountain Tuff can clearly be seen on the northwest side of Silver Bell Peak at 1:30. It dips to the east-northeast at 25–30°. Following the skyline ridge downslope from Silver Bell Peak, some yellowish-tan knobs can be seen. These are outcrops of the northwest-trending middle Tertiary rhyolite dikes that cut through the Silver Bell district. Stratigraphically beneath the Cat Mountain Tuff are the Silver Bell Volcanics which are between 100 and 350 m thick on the west side of the Silver Bell Range. Rocks in the Silver Bell Volcanics in this vicinity are mostly volcaniclastic, either clast-supported, texturally variable andesite breccias or andesitic mudflow material. Beneath the Silver Bell Volcanics occurs a very thin (less than 2 m) layer of Claflin Ranch Formation sediments, mostly pyroclastic material in this area. The Mount Mammoth fault drops the main Silver Bell Range down to the east against the tuff of Confidence Peak on Confidence Peak.

The tuff of Confidence Peak is at least 1.5 km thick west of Silver Bell Peak and Angel Peak in the Silver Bell caldera. This is a minimum thickness, because holes have been drilled through the tuff into Paleozoic sediments and back into tuff, where they bottomed. Looking to the south from Confidence Peak to the Oxide pit, bluffs of white Paleozoic limestones can be seen. These are made of Devonian Martin Formation and the Mississippian Escabrosa Limestone. They are caldera-collapse megabreccia contained within the Silver Bell caldera, and will be visited at Stop 3, which will be a hike on the west side of Confidence Peak. This zone of caldera-collapse megabreccia occurs low within the tuff of Confidence Peak, about 1 km beneath its top.

The Paleozoic sedimentary caldera-collapse megabreccia grossly comprises a horizon that extends from the Oxide pit through the El Tiro pit. The western contact of the Paleozoic sediments, out of view from this point, is the ring fault of the Silver Bell caldera. The ring fault of the Silver Bell caldera extends east-southeast of the Oxide pit on the south side of the Silver Bell Mountains (Richard and Courtright, 1966). From the Oxide pit to the El Tiro pit, it trends N45–50W. West of the ring fault is precaldera biotite granite that is cut by the fault. The tuff of Confidence Peak and caldera-collapse megabreccia included within it are dropped down to the east against the steeply dipping ring fault. North of El Tiro, the trend of the ring fault changes to N10W so that it makes an arcuate trend from west-northwest to north-northwest along the southwest side of the range. The ring fracture is mainly intruded by plutons of the quartz monzodiorite porphyry. Large intrusions occur at the main mineralized centers at Oxide, El Tiro, and North Silver Bell. Smaller dike-like intrusions occur between the El Tiro and the Oxide pits.

From the north side of the parking area we will examine the geology to the north. The El Tiro mineralized center and its three pits can be seen to the northwest. In the East Extension of El Tiro pit, Paleozoic sediments are mineralized to form significant skarn-ore reserves. Approximately 30 million tons of skarn ore was mined from the East Extension of El Tiro. In the main El Tiro pit, a chalcocite blanket overlies hypogene potassic alteration and porphyry copper ore in the quartz monzondiorite porphyry. The Daisy pit to the north of the main El Tiro pit is also chalcocite-blanket mineralization, and has hypogene potassic alteration and mineralization beneath it. Beyond the El Tiro pit, megabreccia of Paleozoic sedimentary rocks extends north to the BS & K mine.

The West Silver Bell Mountains can be seen extending to the west beyond the El Tiro pit. Paleozoic sedimentary rocks occur in the very southwest corner of the West Silver Bell Mountains and are overlain by Lower Cretaceous sedimentary rocks partly equivalent to the Amole Arkose (Banks and Dockter, 1976). These rocks were tilted by Late Cretaceous deformation and are unconformably overlain by the Upper Cretaceous volcanic rocks erupted from the Silver Bell caldera. The central northwest-trending ridge in the West Silver Bell Mountains is made up of a series of five small-volume pyroclastic flows that represent outflow of the tuff of Confidence Peak outside the Silver Bell caldera. The swale between the middle ridge and the northern northwest-trending ridge is made up of Silver Bell Volcanics overlying the tuff of Confidence Peak. The highest peaks on this northwest-trending ridge are made up of Cat Mountain Tuff. In the West Silver Bell Mountains, the Cat Mountain Tuff (equivalent to that seen in the central Silver Bell Mountains) is overlain by sediments and flow-banded rhyolites of the Mount Lord Volcanics (Banks and Dockter, 1976). Overlying the Upper Cretaceous volcanic rocks are middle Tertiary volcanic rocks extending to Malpais Hill, which is made up of basalt. The peak at the very northwest end of the West Silver Bells is composed of Precambrian granite north of the Ragged Top fault.

The area north and west of Silver Bell shows why southern Arizona is the leading copper producing state, with its many porphyry copper deposits. To the north-northwest is the Sacaton porphyry copper deposit and the Case Grande West mineralization hidden beneath the alluvium adjoining it. West of the West Silver Bells are the Slate Mountains and the Lakeshore porphyry copper deposit on the west side of the range. Beyond it is Vekol Mountain (the nipple-shaped peak) with another significant porphyry copper deposit not yet exploited.

STOP 3. Caldera-collapse megabreccia. Hike 150 m west of the microwave tower parking lot, to the switchback where the road curves back down the hill. Note the strong epidote-facies propylitic alteration of the tuff of Confidence Peak here, as well as the common lithic fragments. Large, relatively mafic pumice can be seen in some blocks of tuff. Drop approximately 100 m and walk 0.75 km west from here. The purpose of this stop is to examine relationships between the intracaldera tuff of Confidence Peak and the caldera-collapse megablocks of Paleozoic sedimentary rocks. Our route will include stops at five areas to look at particular exposures (3A–3E; Fig. 3). Textures of remobilized limestone and tuff at the contact between these two units are seen at Stop 3A. Different Paleozoic rock types will be identified through varying degrees of thermal alteration (Stop 3B–3D). Criteria for distinguishing caldera-collapse megabreccia from caldera floor will be discussed. At the contacts of many discrete megabreccia blocks, tuff can be observed to penetrate the contacts and blocks. At the southern limit of the hike (Stop 3E), a quartz monzonite dike that contains large orthoclase phenocrysts and has an intrusive breccia sleeve will be seen. The intrusive breccia sleeve has a variety of clast types, including Paleozoic limestones and biotite granite clasts.

From Confidence Peak return to the parking area at the waste dump east of El Tiro, and then back to the road where it enters the East Extension of El Tiro pit. **1.0**

51.9 **Optional STOP 4. Skarn mineralization in East El Tiro.** When the haulage road is intersected at the East Extension of El Tiro, **park and hike** southwest down into pit. Geology and mineralization are described in Graybeal (1982) and Einaudi (1982). A geologic cross section showing relationships between tuff of Confidence Peak, biotite granite, and quartz monzodiorite porphyry intrusions, and the different styles of mineralization in the El Tiro mineralized center, is shown as Fig. 4, modified from Graybeal (1982).

After visiting the East Extension of El Tiro, **double back** to main El Tiro pit. **Turn left** into main pit of El Tiro. **2.3**

54.2 **Optional STOP 5. Bottom of El Tiro pit** (2550 level). Examine hypogene potassic alteration and mineralization in the quartz monzodiorite porphyry suite. Features of the mineralization and alteration in the main El Tiro pit are described by Richard and Courtright (1966) and Graybeal (1982).

From here **return to ASARCO Silver Bell Mine Office** and then to Tucson (41.1 mi) via Avra Valley Road. To join with the Tucson Mountains half-day trip (Lipman, this guide) without returning to Tucson: (1) Turn south at Sandario Road; the turn-off is 17.9 mi east of the Silver Bell Mine Office on Avra Valley Road (across from the Avra Valley Airport); (2) Head south on Sandario Road, turn left onto Mile-Wide Road and follow signs first to Sonora Desert Museum and then to Gates Pass; (3) Pull off at parking area south of the major bend in the road immediately before climbing final stretch to Gates Pass—this is the second parking area (Point B) of Lipman (this guide), where his Stop 1 hike begins.

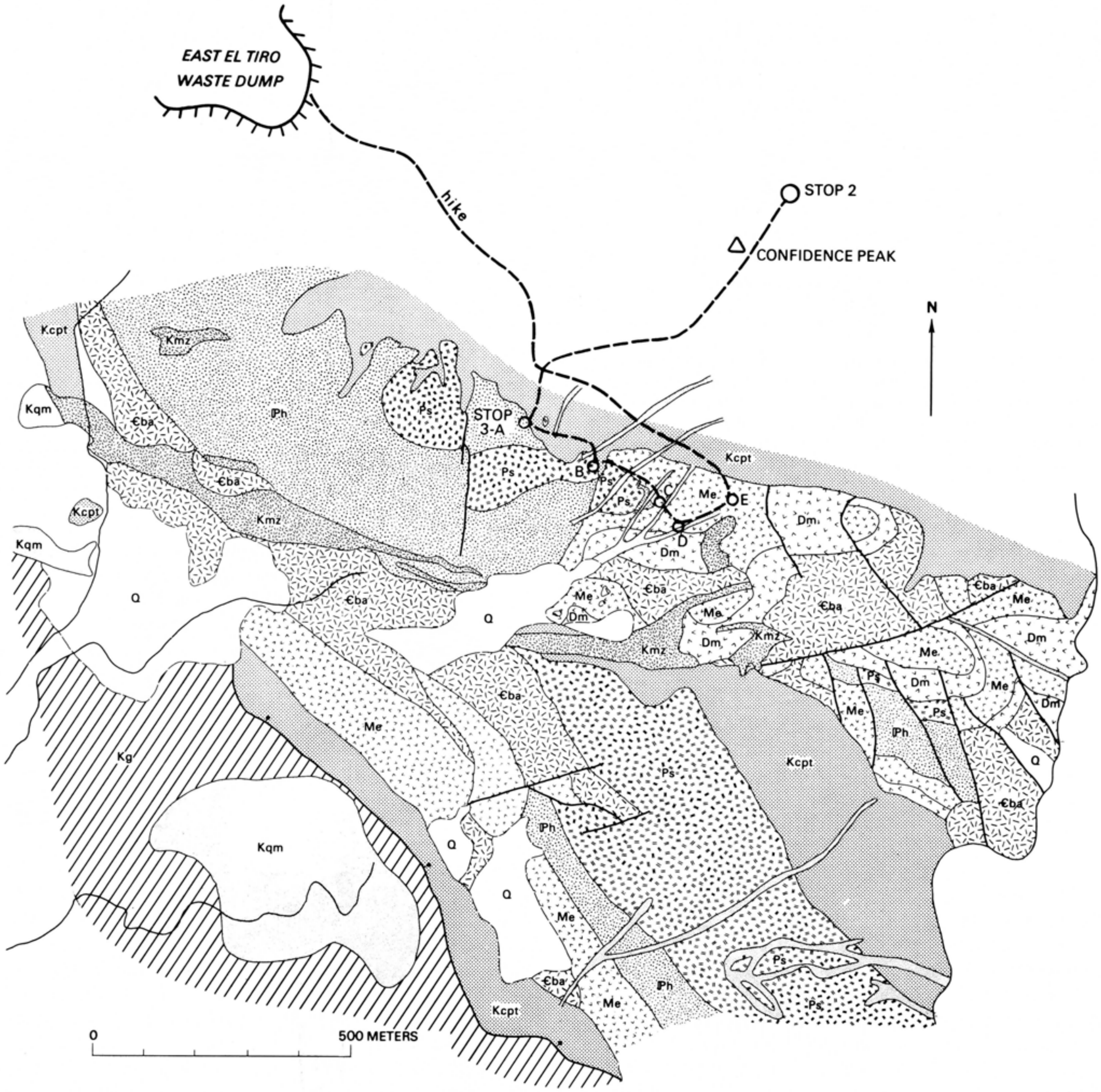

FIGURE 3—Geologic map of caldera-collapse megabreccia in the area between El Tiro and Oxide pits. Hiking route depicted from East El Tiro waste-dump parking area to Confidence Peak. Stop 2 is an observation point on the east side of Confidence Peak. Stop 3, and its five substops, A–E, show relationships between the intracaldera Confidence Peak Tuff and caldera-collapse megabreccia composed of Paleozoic sedimentary blocks. Map symbols: Kg = Cretaceous El Tiro biotite granite; Kcpt = tuff of Confidence Peak; Kqm = Cretaceous orthoclase quartz monzonite porphyry; and Kmz = Cretaceous monzodiorite porphyry. Different slabs of caldera-collapse megabreccia are represented by their protolith Paleozoic sedimentary composition: Cba = Cambrian Bolsa Quartzite and Abrigo Formation; Dm = Devonian Martin Formation; Me = Mississippian Escabrosa Limestone; Ꝑh = Pennsylvanian Horquilla Limestone; Ps = Pennsylvanian–Permian sedimentary rocks, especially Earp Formation. Elongate gray bands and irregular bodies are Cretaceous quartz monzodiorite porphyry or orthoclase–quartz monzonite dikes.

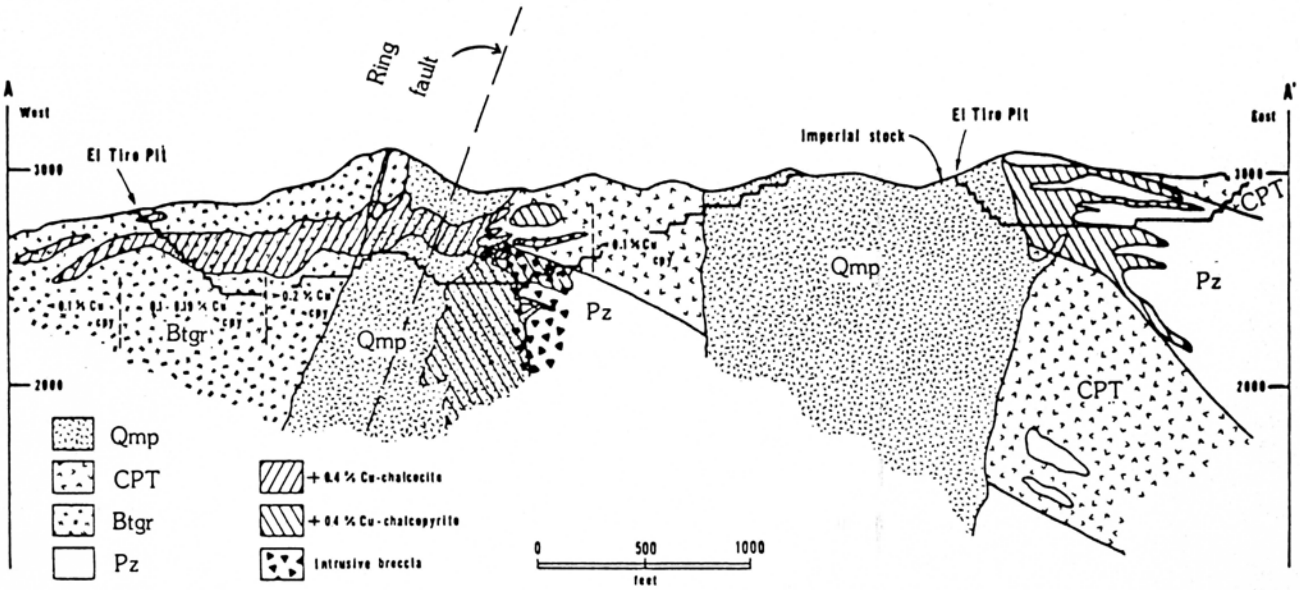

FIGURE 4—Cross section of El Tiro pit area, slightly modified from Graybeal (1982: 490, fig. 24.3) to reflect present stratigraphic nomenclature. QMP = quartz monzodiorite porphyry suite intrusions including quartz monzodiorite, and biotite–quartz-monzonite porphyries, intruded along the ring-fracture zone; CPT = the intracaldera tuff of Confidence Peak, within the Silver Bell caldera; Btgr = precaldera biotite-granite intrusion that is cut by the ring fault; Pz = Paleozoic sedimentary rocks included as caldera-collapse megabreccia within the intracaldera tuff of Confidence Peak. Vertical scale along side axes is in feet above sea level.

Field guide to the Tucson Mountains caldera

Peter W. Lipman

U.S. Geological Survey, Denver, Colorado 80225

Introduction

The Tucson Mountains, a low desert range just west of Tucson (Fig. 1), are underlain largely by Upper Cretaceous volcanic rocks interpreted as parts of the fill of a large ash-flow caldera (Lipman and Sawyer, 1985).

The origin of these rocks has been much discussed. The range was mapped in its entirety by Brown (1939), and several small areas were restudied by University of Arizona graduate students in the 1960's, working largely under the direction of Evans Mayo (Mayo, 1963, 1971a, 1971b; Assadi, 1964; Bikerman, 1963; Kinnison, 1958; Knight, 1967). Brown (1939) mapped an upper unit, the Cat Mountain Rhyolite (Tuff, of general present usage), overlying a breccia unit which he called the Tucson Mountain Chaos and interpreted it as related to regional thrusting. Mayo (1963, 1971a) interpreted the breccia as volcanically erupted intrusive breccia related to a regional "volcanic orogeny." Bikerman (1963) recognized the ash-flow origin of the Cat Mountain Tuff, but inferred that the chaos breccia represented stoped fragments, rafted from deeper levels by the rising pyroclastic magma that later erupted the Cat Mountain Tuff. A similar interpretation was developed in more detail by Mayo (1971b). Brown, Mayo, and Bikerman all considered the chaos to be a basal layer beneath the Cat Mountain Tuff. Drewes (1981, pl. 9) remapped the central Tucson Mountains, also showing the breccia blocks to underlie the Cat Mountain Tuff in a matrix that he assigned to the Silver Bell Formation—mapped by him as a regional Upper Cretaceous andesitic unit extending at least from the Silver Bell Mountains on the north to the Santa Rita and Sierrita Mountains on the south.

Lipman (1976) inferred, largely from published descriptions, that the Tucson Mountain Chaos was landslide breccia associated with collapse of an Upper Cretaceous ash-flow caldera within which the Cat Mountain Tuff had ponded. In-progress fieldwork confirms such an interpretation and also shows that the slide breccias, rather than underlying the Cat Mountain Tuff, have a matrix of nonwelded tuff and interfinger with welded tuff at multiple horizons (Figs. 2, 3). A major implication of this interfingering is that the exposed thickness of the caldera-filling Cat Mountain Tuff is at least 3–4 km, many times that previously reported. Megablocks are up to 0.5 km across and include Paleozoic sediments, Jurassic silicic volcanic rocks, Cretaceous andesitic lavas, and tuff of Confidence Peak erupted from the Silver Bell caldera. Dominant breccia types vary greatly

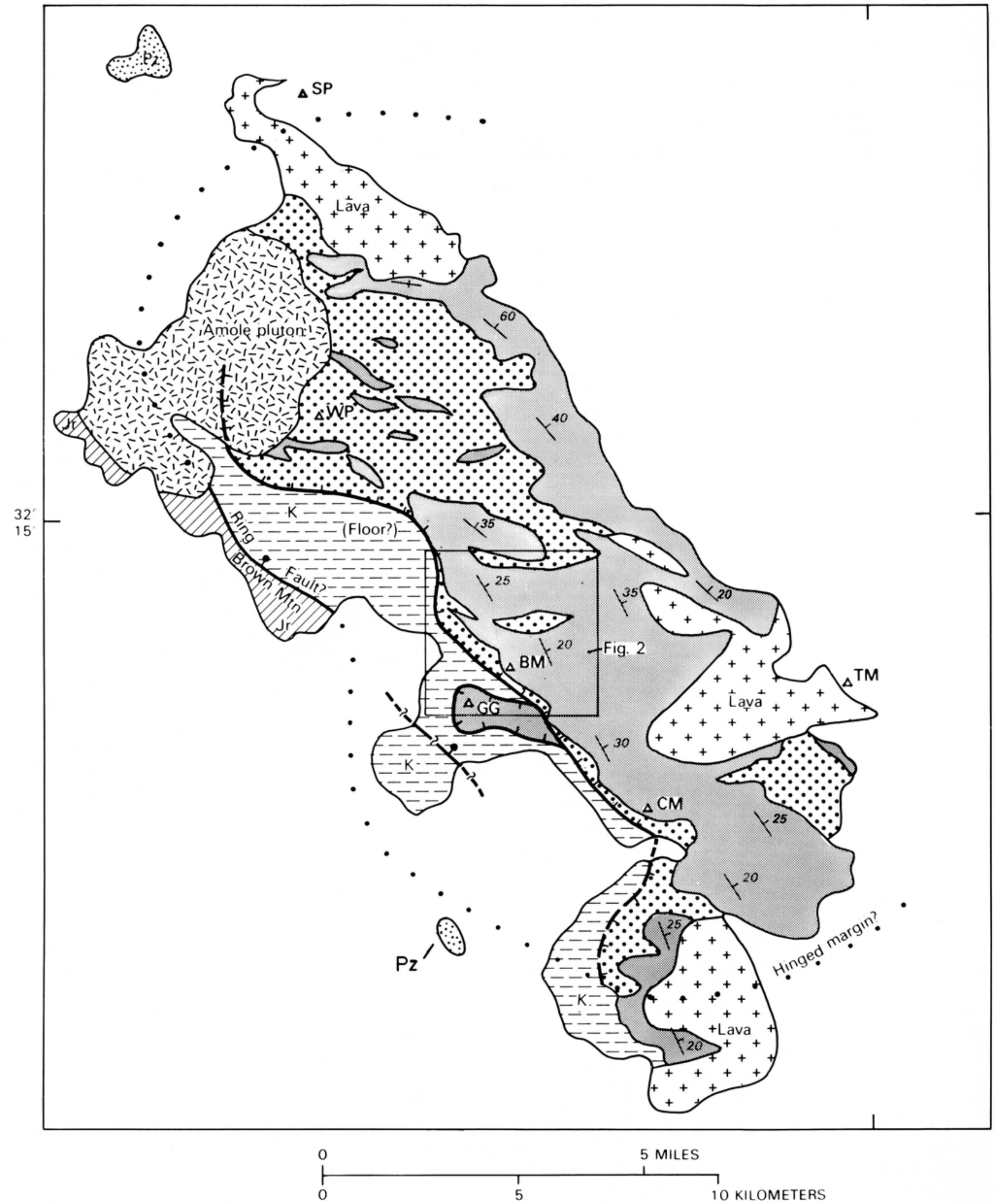

FIGURE 1—Generalized geologic map of early Tertiary and older rocks, showing structural interpretation of the Tucson Mountains caldera (based on mapping by Lipman, 1986–87; in part modified from Brown, 1939). Many small Tertiary normal faults omitted. Extracaldera units: Pz, Paleozoic sedimentary rocks; Jr, Jurassic(?) sedimentary and volcanic rocks. Caldera-floor rocks: K, Cretaceous Amole Arkose of the Bisbee Group. Caldera-related igneous rocks of Laramide age: shaded unit, intracaldera Cat Mountain Tuff; dotted unit, intracaldera landslide-breccia deposits ("Tucson Mountain Chaos"), containing megablocks up to 0.5 km across; crosses, caldera-filling lava flows ranging in composition from andesite to rhyolite. Amole pluton is interpreted as ring intrusion. Hachured contact indicates base of caldera-filling tuffs and breccias. Geographic localities: BM, Bren Mountain; CM, Cat Mountain; GG, Golden Gate Mountain; SP, Safford Peak; TM, Tumamoc Hill; WP, Wasson Peak.

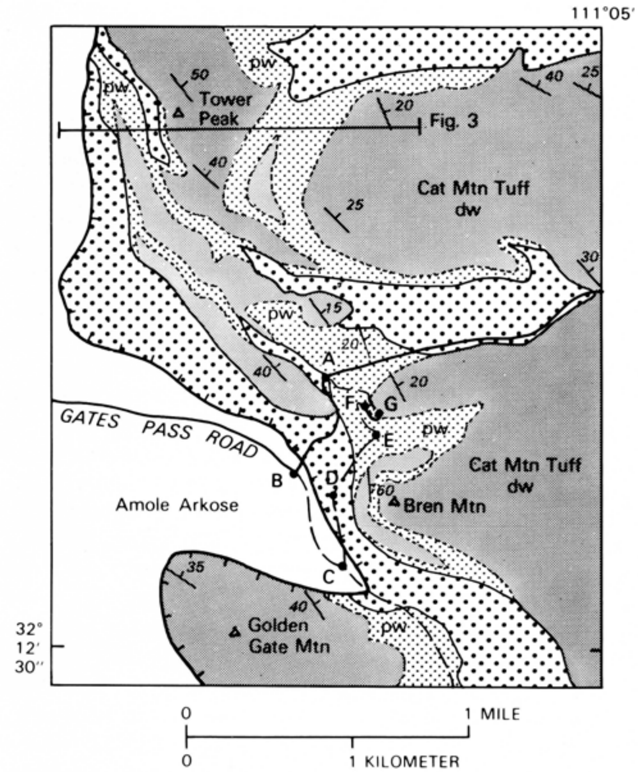

FIGURE 2—Preliminary geologic map of Tucson Mountains caldera fill in the Gates Pass area (mapping by Lipman, 1987–88). Units: Cat Mountain Tuff, nonwelded to partly welded (pw, light stipple) and densely welded (dw, shaded unit); intracaldera slide breccias (dotted). Hachured line indicates base of caldera-fill deposits, against autochthonous Cretaceous sedimentary rocks (Amole Arkose). Dashed line, trail followed by field-trip route; reference points indicated by letters (A to G).

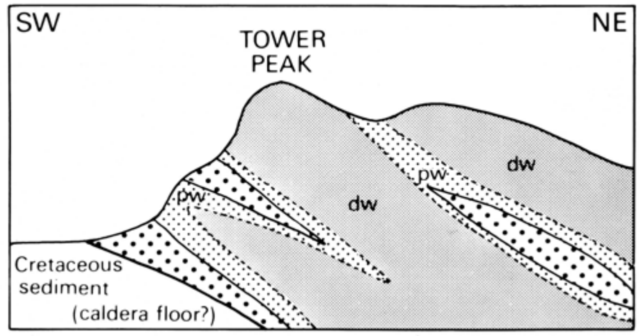

FIGURE 3—Diagrammatic cross section through the west margin of the Tucson Mountains caldera north of Gates Pass, illustrating interfingering relations between Cat Mountain Tuff (pw, nonwelded to partly welded; dw, densely welded) and intracaldera slide breccias (dotted pattern).

between various caldera sectors. Small bodies of rhyolitic rock in the northern Tucson Mountains, previously mapped as irregular intrusions by Brown and Drewes (Amole Latite, Latite Porphyry), are reinterpreted as discontinuous lenses of Cat Mountain Tuff that fill interstices between large disrupted masses of Mesozoic sedimentary rock. The result of this interpretation is to include a sizeable additional area as caldera-fill breccia.

A small segment of the structural boundary of the caldera may be represented by an arcuate fault along the northwest flank of the range that drops Cretaceous sedimentary rocks against Jurassic rocks on Brown Mountain (Fig. 1). Cretaceous sedimentary rocks, exposed low along the west flank of the mountain range, may represent part of the caldera floor, or they may be low on the western caldera wall between the exposed outer ring fault and concealed inner structures to the east. An unresolved problem, if the sediments are part of the caldera floor, is the apparent absence of in-place precaldera andesitic lavas above the sediments, even though such lavas occur widely as slide blocks within the caldera fill.

Along the northeast and southeast flanks of the Tucson Mountains, the Cat Mountain Tuff is conformably overlain by andesitic to rhyolitic lavas that are interpreted as erosional remnants of a thick caldera-fill sequence emplaced soon after collapse and involved in caldera resurgence. These lavas obscure the northern and southern caldera margins. The large, zoned, granodioritic to granitic Amole pluton exposed along the northwest flank of the Tucson Mountains appears to be a resurgent ring intrusion that arches the caldera fill, including postcaldera lavas, upward to the east and north. In addition, the entire range, including flanking middle Tertiary lavas, is variably tilted eastward, probably due to rotation along largely concealed listric normal faults associated with middle Tertiary uplift of the Catalina–Rincon core complex east of Tucson. The ages of the caldera-related volcanic rocks are well constrained as Late Cretaceous by published conventional K–Ar ages (Bikerman and Damon, 1966), but further work would be desirable to evaluate more precisely the time span between eruption of the Cat Mountain Tuff and emplacement of the apparently resurgent Amole pluton.

Within northern parts of the caldera fill, slide breccias dominate over ash-flow tuff (Fig. 1), documenting catastrophic subsidence in this sector. In contrast, along the inferred southern caldera margin, the thickness of tuff decreases to only about 100 m, and megabreccia is virtually absent; these relations suggest a hinged southern caldera margin and overall trap-door geometry. Thus, virtually the entire mountain range is interpreted as an oblique section through the structurally disrupted interior of a caldera; the caldera margins are largely concealed by Tertiary basin fill. Although poorly constrained, especially to the east, the overall dimensions of the Tucson Mountains caldera are about 20 × 25 km, slightly smaller than the Pleistocene Long Valley caldera, and well within the spectrum of late Cenozoic calderas in the western United States (Fig. 4).

The single field-trip stop, at Gates Pass, permits a 2–3 hour loop hike that provides a partial section from caldera floor up through lower parts of the caldera fill, leading to a panoramic view of the northern Tucson Mountains from a scenic highpoint.

Field mapping and petrologic studies of the igneous rocks of the Tucson Mountains are currently in progress (1988), and interpretations presented here are preliminary.

Road log

Mileage

0.0 Central Tucson: intersection of I-10 and Speedway Blvd.; **proceed west on Speedway.** Ragged ridge crest of Tucson Mountains to west is capped entirely by Upper Cretaceous Cat Mountain Tuff. The general structure is a homoclinal sequence dipping 15–35° eastward. **3.1**

3.1 Passing Painted Hills Road. Hills to south are Upper Cretaceous(?) dacite lava dome of Twin Hills, con-

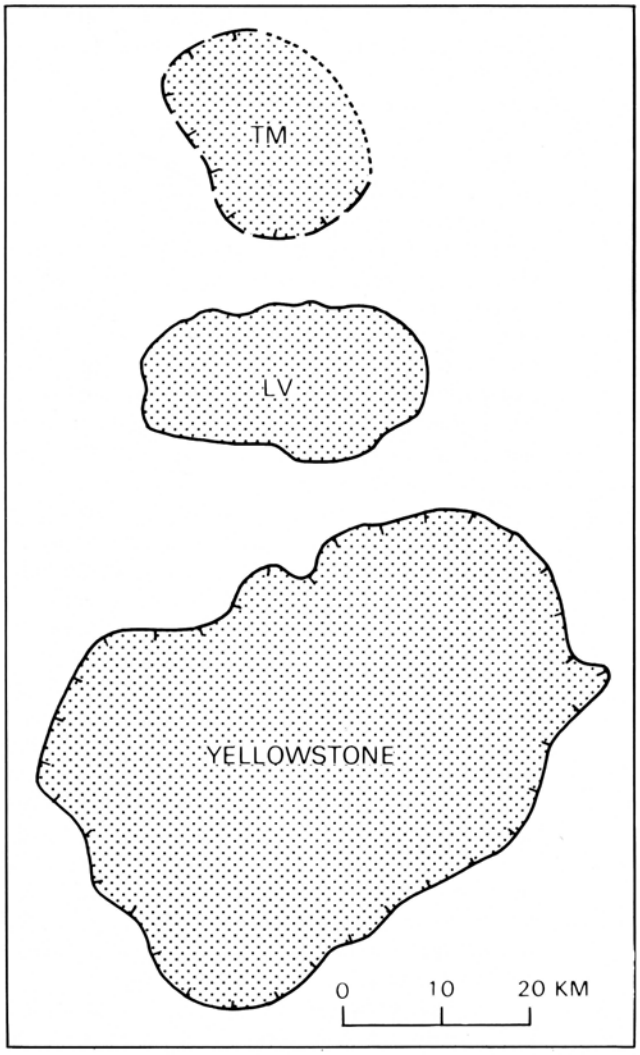

FIGURE 4—Inferred map outline of the Tucson Mountains caldera (TM), in comparison with large young calderas of the western United States (LV, 0.7 Ma Long Valley; 0.6 Ma Yellowstone).

formably overlying the ash-flow fill of the Tucson Mountains caldera. **0.9**

4.0 Contact in a small gully between dacite lava and underlying east-dipping Cat Mountain Tuff to west, dropped along small northwest-trending fault against more Cat Mountain Tuff to east. **0.6**

4.6 **Bear left,** following Gates Pass Road (to Old Tucson). **1.6**

6.2 Entering Tucson Mountains Park. As we proceed up toward pass, variably colored rocks in gully to right are megablocks of diverse lithologies along welding break within Cat Mountain Tuff. The largest and most conspicuous blocks in this area consist of flow-layered and locally spherulitic rhyolitic lava of probable Jurassic age. These were considered to be intrusions by Brown (1939), Bikerman and Damon (1966), and other earlier workers. **1.0**

7.2 **STOP 1. Gates Pass loop** (Fig. 2). Pull off into parking lot on right, about 25 m before crest of pass. **Proceed on foot** from Point A 0.45 mi (750 m) across pass (3172 ft elevation) and down-section along paved road to second parking area (Point B) at major bend in road **(ROAD TRAFFIC IS HEAVY AND VISIBILITY IS POOR; EXTREME CAUTION NEEDED).**

At this point we will be in Cretaceous sedimentary rocks, seemingly part of the caldera floor. The trip route will **follow a foot trail** to a saddle between Bren Mountain (3988 ft) and Golden Gate Mountain (4288 ft), remaining within the Cretaceous sedimentary rocks. Then, we will angle back toward Gates Pass on a higher foot trail to the east, which provides excellent exposures of diverse block lithologies within the Cat Mountain Tuff. Eventually, we will climb to top of the 3530 ft point, providing a panoramic view of the northern Tucson Mountains and adjacent ranges. Finally, continuing along the foot trail, we will return to Gates Pass.

Leaving the Gates Pass parking area, we cross the pass, carved in a large steeply dipping megablock of Cretaceous sandstone. These sedimentary rocks are locally called the Amole Arkose (Brown, 1939), though they include interbedded sandstone, siltstone, and finely bedded local limestone; they are part of the Bisbee Group. Most contacts between the block and adjacent tuff are poorly exposed, but along the road about 50 m west of the pass, the block of Amole Arkose is in contact with lithic-rich, weakly welded Cat Mountain Tuff. The Cat Mountain Tuff is a compositionally uniform, low-silica rhyolite (70–72% SiO_2) that contains phenocrysts of quartz, feldspar, and sparse biotite (where not obscured by alteration).

The Cat Mountain Tuff here also contains blocks of andesitic lava at least several meters across. Note that as the tuff becomes less lithic-rich upward from road level, it also becomes more welded as indicated by collapsed-pumice foliation. Such features are typical of caldera-filling tuff, in which large lithic fragments act as heat sinks and inhibit welding (Fig. 3).

About 0.15 mi (250 m) west of pass along road, prominent rugged outcrops at road level are a densely welded zone of Cat Mountain Tuff containing relatively sparse lithic fragments. This welded zone is both overlain and underlain by less welded tuff containing abundant large blocks of andesite and other rock types. Note the irregular foliation and decrease in welding adjacent to blocks beneath the most densely welded tuff, in contrast to sparsity of blocks within the most welded tuff. The disaggregated mass of reddish sandstone here was probably derived from the Jurassic Recreation Redbeds, which are exposed in place on Brown Mountain near the Tucson Desert Museum about 5 km to the northwest.

Looking back across road to the north, note similar densely welded tuff dipping southeastward beneath the megablock zone just examined in the roadcuts. Some faulting may be present in this area, but no major faults can thus far be mapped for any distance.

At 0.35 mi (550 m) west of pass, where road bends to the left, is exposed a block of Paleozoic limestone several meters across, along with other brecciated sedimentary lithologies in obscure contact with weakly welded quartz-bearing tuff.

Just before road curve to the northwest, with large parking area on south side (Point B), are exposures of gently dipping Amole Arkose that are apparently in place on the caldera floor, or possibly low on the wall.

From this parking area, **walk south up the trail to the saddle** that separates Bren Mountain (on the northeast) from Golden Gate Mountain (on the southwest). The trail is entirely within Amole sedimentary rocks of the caldera floor that are discontinuously exposed beneath the colluvial debris.

At trail crossing the main gully, the many boulders of densely welded Cat Mountain Tuff are typical of the cliffs above and similar to the late welded tuffs (Mount Lord Volcanics) that cap the crest of the Silver Bell Mountains 50 km to the northwest. The good exposures ahead along the east side of the gully are Amole Arkose. Detailed mapping of these sedimentary rocks by Assadi (1964) for a M.S. thesis at the University of Arizona, and also by Harald Drewes of the U.S. Geological Survey (1981, pl. 9), show that they are broadly folded around north-northwest-trending axes.

About 100 m up-valley along the trail, exposed in a side gully to the east between exposures of Amole Arkose, is a large dark-gray block of limestone (Permian?). The block is enclosed within the nonwelded lower part of the Cat Mountain Tuff, beneath large massive cliffs of lithic-poor welded tuff. Linear yellowish-brown outcrops, trending along the slope just above the limestone megablock, are exposures of a dike of Cretaceous dacite, part of a regional swarm (Silver Lily Quartz Latite) in this sector of the Tucson Mountains. This area was mapped in great detail by Mayo (1971a, 1971b, fig. 2).

At the saddle (Point C), **bear left** (east) on a more obscure trail that leads toward the limestone megablock and back towards Gates Pass. Note the eastward and southeastward dips indicated by slabby jointing of the tuff on Golden Gate Mountain to the west. The section to the east is probably raised by a small fault through the saddle. The high point visible through the pass to the south, just east of the large trailer-park development, is geographic Cat Mountain; it consists entirely of densely welded Cat Mountain Tuff overlying megablocks and in-place Amole sedimentary rocks at the base of the slope adjacent to the trailer park. In the far distance are the Santa Rita Mountains, site of another Cretaceous caldera fragment (Lipman and Sawyer, 1985); a high point in the range (Mount Hopkins, elevation 8550 ft), barely visible to the right, consists mostly of granitic rocks along the east margin of this caldera.

Heading back along the upper trail toward the conspicuous block of Paleozoic limestone, the trail crosses Cretaceous sandstone near the contact between in-place Amole Arkose (caldera floor?) and overlying megablock debris in a tuffaceous matrix at the base of the Cat Mountain Tuff. Large dark-brown outcrops, just to the right (south) of the Paleozoic limestone, are blocks of Cretaceous andesitic lava, again as megablocks enclosed in a tuff matrix.

About 75 m along the trial, in a small gully just before the limestone block, are reddish sediments of Jurassic Recreation Redbed type, juxtaposed with fragments of laminated limestone of a type locally characteristic of the Amole Arkose.

Beyond the Paleozoic block is voluminous float of porphyritic andesite, derived from blocks of such Cretaceous volcanic rocks upslope. **Be alert for a fork in the trail (Point D); stay high.** At this point the trail is obliquely traversing the contact zone between in-place Cretaceous sedimentary rocks and overlying megablock-rich Cat Mountain Tuff. Below the trail, the sedimentary rocks are stratigraphically and structurally coherent; at trail level and above, blocks of Amole Arkose are incorporated as fragments, along with the other rock types just noted, in a tuff matrix.

The trail then crosses below and around a large mass of brecciated and mostly structureless (but locally flow-laminated) rhyolitic lava of probable Jurassic age. This block is at least 15 m across.

The trail continues northward, mainly through talus of welded Cat Mountain Tuff from cliffs above, to a spur ridge that descends directly toward the parking area below. Above the trail on this spur is another large mass of light-colored rhyolitic lava. The trail then climbs obliquely upward, around and through the margins of this rhyolite mass, where contacts are locally exposed between the rhyolite and partly welded Cat Mountain Tuff containing small angular fragments of andesite. Here, the Cat Mountain has compaction foliations that dip anomalously steeply to the north, reflecting draping around the rhyolite block.

The trail continues ahead toward a prominent spur, where it crosses about 25 m above the upper contact of another large mass of light-colored brecciated rhyolite. On the way, the trail crosses several smaller masses of Cretaceous andesitic lava and Amole sandstone enclosed by somewhat altered, partly welded Cat Mountain Tuff.

From the rhyolite block, the **trail continues obliquely upward** through partly welded, light-colored tuff, toward more welded, brown, cliff-forming outcrops, **then descends below the cliffs.** Dips in these welded tuffs are variable, from 30° to 50° east; some variation may be due to slumping on the steep slopes, but much is interpreted as due to variable draping arund and over the large megablocks below trail level.

Looking north across the main road, we can see several prominent cliff-forming welded horizons in the Cat Mountain Tuff, separated by benches or gentler slopes, along which large megablocks are also present (Fig. 2). Thus, the megablocks occur at multiple horizons within the Cat Mountain Tuff, not just beneath it as previously thought. This relation becomes increasingly pronounced northward along the range front and to the northeast. Also, looking northward, try to distinguish where we saw densely welded tuff and megablocks at road level.

Continue eastward to the conspicuous saddle (Point E), then descend northward following an obscure and rather eroded trail. Descending and contouring northward, we pass another large block of Cretaceous sandstone that is mostly above the trail. Consider how irregular the contact is between the densely welded tuff above us and the zone of megablocks below. How much is due to depositional irregularities, versus possible faults in the saddle?

The **trail then switchbacks up** through variably welded and altered Cat Mountain Tuff, to a prominent shoulder southeast of Gates Pass parking area (Point F).

Across Gates Pass to the northeast, the ridge crest is capped by densely welded Cat Mountain Tuff. The dip is steeper than it appears, 20–30° or greater, because this ridge is nearly parallel to the strike of the tuff. Below the cliffs of welded tuff, several large light-colored knobs and more obscure darker ones are masses of volcanic rock enclosed in tuff; the light knobs are Jurassic rhyolite like that just crossed along the trail, and the dark exposures are Cretaceous andesite. This zone of decreased welding containing megablocks is stratigraphically above the level at which we are standing.

Continue up to the viewpoint southeast from the shoulder (10 min.), following the eroded **trail** that **first switchbacks upward** and **then contours counterclockwise** around south side of the hill. This trail provides access to excellent exposures of densely welded Cat Mountain Tuff, previously seen only in talus, and also some welcome afternoon shade if the day is hot.

All slopes in sight to the south and east are Cat Mountain Tuff. The subtle variations in jointing and color, though not well understood, probably reflect mainly initial variations in welding and crystallization of the thick caldera-filling tuff.

From the top of this knob (Point G) we can see for the first time the Silver Bell Mountains, 50 km to the northwest, and some of the ASARCO tailing ponds from the porphyry copper open-pit operations. This is an excellent place to discuss relations between the Silver Bell and Tucson Mountains calderas. In a nutshell, tuff erupted from the Silver Bell caldera (tuff of Confidence Peak) is present as megablocks within the younger Tucson Mountains caldera, and the welded tuff member of the Mount Lord Volcanics that caps the Silver Bell Mountains is interpreted as outflow Cat Mountain Tuff from the Tucson Mountains caldera. These correlations are confirmed by distinctions in petrography and minor-element compositions, as well as paleomagnetic-pole positions (unpubl. data, J. Hagstrum, USGS).

Also visible from here are: Brown Mountain, the Tucson Desert Museum, and the approximate location of the possible caldera boundary fault that drops the Cretaceous against Jurassic sediments in that area (Fig. 1). The hills to the northeast expose the south margin of the Amole pluton that appears to have resurgently uplifted the northwest side of the caldera, perhaps localized along this ring fault.

Major remaining field problems involve determining the total thickness of the caldera fill, including postcollapse lava flows of Late Cretaceous or early Tertiary age, the structural position of the Amole Arkose (true caldera floor, or low on the wall), and the amount of rotation and transport of the Cretaceous rocks along middle Tertiary detachment faults.

Retrace route downslope to shoulder; then **follow trail northwest to Gates Pass parking area** (Point A).

Field guide to volcanic and plutonic features of the Turkey Creek caldera, Chiricahua Mountains, southeast Arizona

John S. Pallister and Edward A. du Bray

U.S. Geological Survey, Denver, Colorado 80225

Summary—Erosion and Basin–Range faulting in the Chiricahua Mountains expose multiple levels through the ~25 Ma Turkey Creek caldera. The caldera is 20 km in diameter and its structural boundary is occupied by an annular ring of quartz monzonite and monzonite porphyry; this porphyry appears to represent the margin of a saucer-shaped (upper surface) intrusion that is also exposed centrally within the caldera. Stratigraphic and structural data indicate that emplacement of the porphyry closely followed eruption of ash-flow tuff of the Rhyolite Canyon Formation; gradational textures and compositions suggest that the tuff and the porphyry were derived from the same magma reservoir.

The Turkey Creek caldera is unusual in preserving relicts of feeder zones for ash flows. Field, petrographic, and geochemical data document a gradation between high-silica rhyolite welded tuff and monzonite porphyry. The annular ring of porphyry is interpreted as the feeder zone for basal dacite lava flows within the caldera moat; textures in the ring grade from porphyritic granophyre to glass-matrix lava. Compositions cluster at ~66% SiO_2 and 77% SiO_2, but a few samples have intermediate silica abundances. The high-silica porphyry overlaps compositionally with the Rhyolite Canyon Formation tuff. Rocks that are mineralogically and texturally transitional between monzonite porphyry and ash-flow tuff occur within the ring body, as well as along fault-controlled feeder zones within the caldera. The latter suggest local brittle failure of the caldera-floor rocks (mainly preaccumulated intracaldera tuff) during the waning stages of ash-flow eruption, resulting in central, as well as ring-fracture, eruption of ash-flow tuff and rhyolite to dacite lava. These features indicate that ash-flow tuff was erupted from vents which were intruded and then clogged by less fractionated magma (the monzonite porphyry).

An unusual roof breccia occurs at the contact between the central monzonite intrusion and overlying intracaldera tuff. Regionally, the roof breccia is a complex zone that contains fragmental rocks with both tectonic and pyroclastic or magmatic/hydrothermal origins. Monolithologic granophyre roof breccias are considered tectonic, but lack clear evidence of megascopic shear. Instead, they show characteristics of low-pressure shock metamorphism. Working models to explain the brecciation of these rocks include: (1) the combined effects of intrusion, cooling, and inflation of a laccolithic body of monzonite within the caldera, (2) magmatic explosions with foci within an underlying magma reservoir and focusing of compression or rarefaction waves at the porphyry—welded tuff contact, (3) hydrothermal brecciation produced during fluid migration and degassing of the underlying monzonite intrusion.

Thick sedimentary breccias and volcaniclastic sandstones in the southern part of the caldera unconformably overlie, and contain clasts of, Rhyolite Canyon Formation tuff and monzonite porphyry. The sedimentary rocks are overlain in turn by aphyric high-silica rhyolite moat lavas. The temporal progression from high-silica rhyolite ash-flow tuff to dacite moat lava and monzonite porphyry to aphyric rhyolite moat lavas and dikes defines a chemical trend from >75% SiO_2 to <65% SiO_2, and then (after an erosional interval) back to >75% SiO_2.

The features described above are consistent with a magma chamber and eruptive model in which the less-evolved lower parts of a stratified magmatic reservoir were drawn up into, and locally erupted effusively from, the same conduits and vents that initially fed large-volume ash-flow eruptions of high-silica rhyolite. The near-absence of precaldera rocks within the Turkey Creek caldera (caldera-floor rocks) is difficult to reconcile with the classical caldera paradigm. If the central monzonite intrusion represents the in-situ lower part of the source magma chamber for the ash-flow tuff, a very shallow magma chamber (with a thin and ephemeral roof) is required. However, the central intrusion may also represent a thick (>1 km) sill or laccolith that was intruded into the intracaldera tuff during the waning stages of caldera collapse. Interpretation of the roof breccia is pivotal to distinguishing between in-situ magma chamber and syn- or post-collapse laccolith-intrusion models.

Introduction

In the Chiricahua Mountains, faulting and erosion have combined to expose a three-dimensional view of an ash-flow caldera, its host rocks, and its comagmatic intrusive rocks. Here, we can directly observe both the volcanic and hypabyssal to plutonic levels of a single mid-Tertiary magmatic system.

Darwin Marjaniemi (1969) first recognized the Turkey Creek caldera and produced an excellent reconnaissance-scale (1:125,000) geologic map of the Chiricahua Mountains (Fig. 1). The caldera is a collapse structure 20 km in diameter that developed in basement composed mainly of Lower Cretaceous Bisbee Group sedimentary rocks and mid-Tertiary rhyolites, but regionally also containing a thick and tectonically complex sequence of Paleozoic carbonates and Precambrian crystalline rocks. Caldera collapse (at 25–26 Ma) and eruption of ash-flow tuffs of the Rhyolite Canyon Formation was preceded by development of a field of high-silica rhyolite lavas and domes (~28–26 Ma) and by collapse of the adjacent Portal caldera in the eastern Chiricahua Mountains (Bryan, this volume). Intrusive rocks related to the Turkey Creek caldera crop out in a broad ring dike and central intrusion composed of monzonite to quartz monzonite porphyry. These rocks are feldspar porphyries with granophyre (quartz–alkali feldspar) groundmasses; they overlap the monzonite–quartz monzonite model boundary (IUGS nomenclature). For the sake of brevity, we refer to these intrusive rocks as "monzonite," although we acknowledge both the hypabyssal porphyritic texture and the range in modal composition from monzonite to quartz monzonite (and locally to more quartz-rich compositions).

Early workers (Raydon, 1952; Epis, 1956; Sabens, 1957; Cooper, 1959; Fernandez and Enlows, 1966) recognized and mapped Tertiary rhyolite lavas and ash flows in the region. Enlows (1955) defined the Rhyolite Canyon Formation on the basis of stratigraphic sections in the outflow sequence at Chiricahua National Monument, but Marjaniemi (1969) alone defined the volcanic framework for this and other "process-oriented" studies. Marjaniemi estimated the volume of ash flows within the Rhyolite Canyon Formation to be about 500 km^3. His K–Ar mineral ages (recalculated using IUGS constants—Steiger and Jager, 1977) show that the Rhyolite Canyon Formation tuff (25.5 ± 0.6 Ma) is distinctly younger than underlying rhyolites of the Faraway Ranch Formation (28.6 ± 2.0 Ma; 28.3 ± 0.8 Ma) but overlaps with ages (25.1 ± 1.2 Ma; 26.3 ± 0.8 Ma) of stratigraphically older ash-flow tuffs in the eastern Chiricahua Mountains. Ash-flow tuff eruption, caldera formation, and porphyry intrusion at Turkey Creek are constrained to a period of less than 1 million years by a biotite K–Ar age of 25.4 ± 0.7 Ma on a rhyolite dike that intrudes the porphyry.

Drewes and Williams (1973) produced a 1:62,500 scale map of the east-central part of the caldera as part of their study of the Chiricahua Wilderness, and the outflow stratigraphy of the Rhyolite Canyon Formation has been revised and mapped at 1:24,000 scale by Drewes (1982) and Latta (1983). In addition, Latta (1983) mapped a transect from the outflow sequence in the National Monument through the moat of the caldera and into the central intrusion. He noted an up-section decrease in the dips of moat rhyolites and suggested that resurgent doming began before and continued after eruption of these rocks. Latta also defined informal members of the Rhyolite Canyon Formation, correlated the uppermost ash-flow member of the formation outside the caldera with the intracaldera tuff, and argued that 60–70% of the main eruptive sequence was ponded in the caldera. Latta noted that the thickest outflow-tuff sections derived from the Turkey Creek caldera (Fig. 3, Monument member) are about 430 m, but the intracaldera tuff is 1.2 to 1.5 km thick in the northern part of the caldera, prima fascia evidence for collapse. On the basis of reconnaissance geochemistry, he described compositional zoning similar to that in the Bishop Tuff and interpreted the main eruptive sequence as the product of a single compositionally zoned magma chamber.

This guide is a preliminary account of the geology of the Turkey Creek caldera. It is based on our first two seasons of geologic mapping and on our initial interpretations of petrographic and geochemical data. Because this is an ongoing project, we expect our interpretations to evolve as we continue mapping and as we apply new analytical, geochronologic, and geophysical techniques to the Turkey Creek rocks. Accordingly, we advise the reader that we intend to explore working models during the field trip in addition to reviewing models proposed by earlier workers; we anticipate that some of our ideas will be controversial and that alternative interpretations will develop during the trip.

Day 1,
Part 1. Willcox to Chiricahua National Monument: Outflow tuff and "basement" rocks

The largest erosional remnant of the outflow tuff from Turkey Creek caldera is exposed north of the caldera in Chiricahua National Monument. This area probably represents a paleobasin where outflow tuff ponded adjacent to highlands to the north and east (Marjaniemi, 1969). Three different stratigraphic divisions have been proposed for the ash-flow tuffs and associated rocks of the Rhyolite Canyon Formation exposed outside the caldera in the National Monument (Enlows, 1955; Drewes, 1982; Latta, 1983). The type

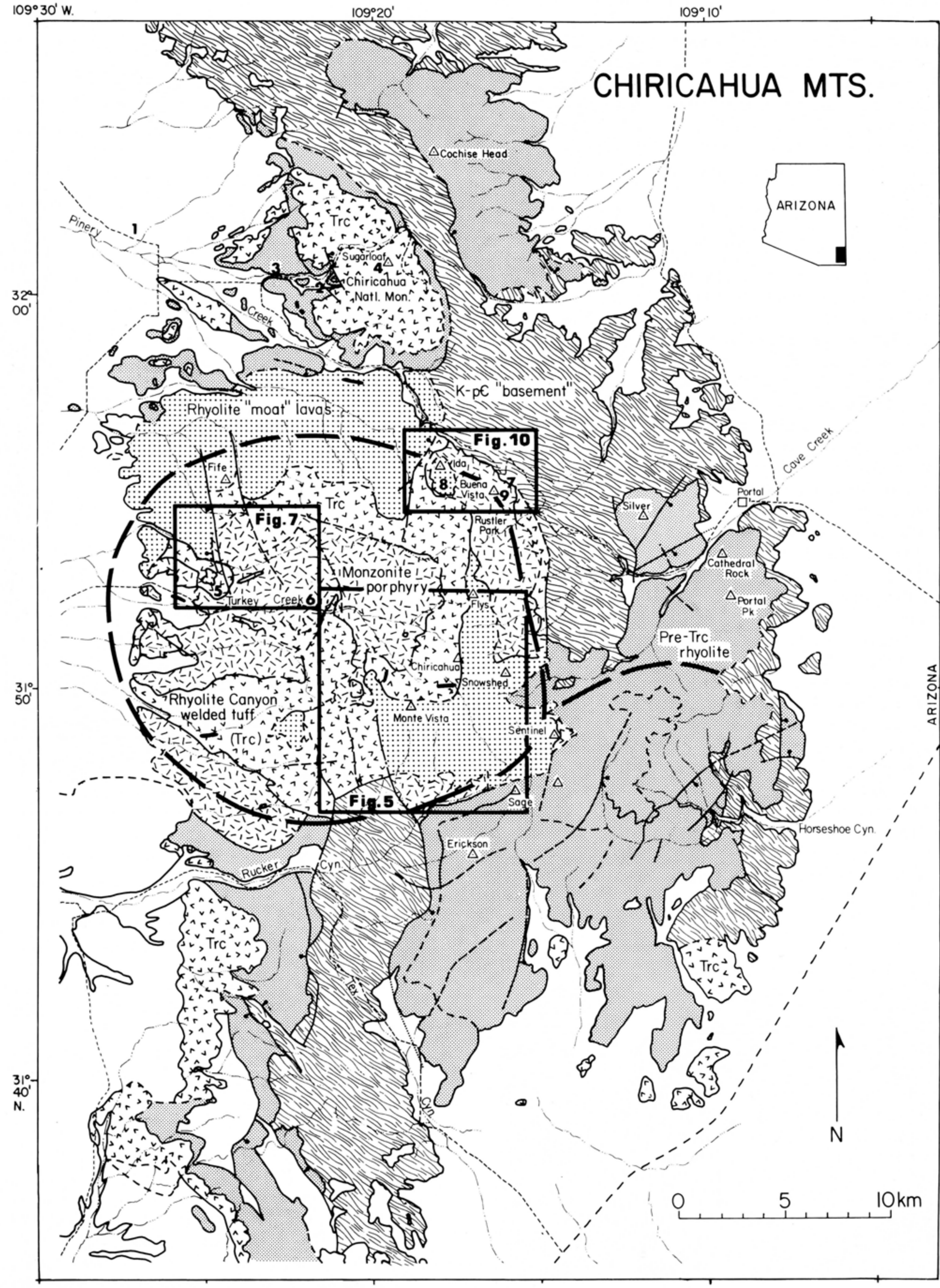

FIGURE 1—Geologic index map of the Chiricahua Mountains (after Marjaniemi, 1969), showing field-trip localities (by number) and areas of more detailed map figures. Trc = welded tuff of Rhyolite Canyon Formation; K–p€ = Cretaceous to Precambrian rocks. Approximate structural boundary of the Turkey Creek caldera and northwest boundary of the Portal caldera indicated by heavy lines.

section of Enlows (1955) is between Rhyolite and Bonita Canyons (east-northeast of the visitor center) where the greatest thickness (≥400 m) of the formation is exposed (see Fig. 2 and map by Drewes, 1982). Here, Enlows defined eight informal rhyolitic tuff members, capped by a dacite lava member (an erosional remnant recognized only atop Sugarloaf Mountain). Drewes (1982) mapped seven pyroclastic map units below the capping lava; he discriminated these units mainly on the basis of variation in welding and crystal content.

In contrast, Latta (1983) considered the Rhyolite Canyon Formation outflow to contain a lower Jesse James Canyon ash-flow member that is petrographically and chemically distinct from the overlying informal Monument member. He defined the Monument member as the outflow sequence of the Turkey Creek caldera, a composite ash-flow sheet with only three principal cooling units; the source caldera for the Jesse James Canyon member is uncertain. A comparison of the stratigraphic nomenclature is shown in Fig. 3. For the purposes of this guide, we prefer the genetic divisions of Latta, and we use his "units I, II, and III" for the lower, middle, and upper cooling units of the Monument member. The three units correspond approximately to Drewes' units Trls, Trus, and Trat + Truw, respectively (Fig. 3 and Drewes, 1982).

Latta recognized a cooling break within the intracaldera tuff, and, on the basis of major-element chemistry, he correlated the *lower* cooling unit of the intracaldera sequence with his *upper* cooling unit of the outflow tuff (Monument member, unit III) (Figs. 3, 4), leaving correlation of the upper unit of the intracaldera tuff and the two lower cooling units of the outflow tuff in question. He suggested that the later part of the main eruptive sequence (upper cooling unit of intracaldera tuff) ponded in the caldera and that the outflow sequence includes units erupted before and after caldera collapse. The lower cooling units of the outflow tuff may have erupted during the initial stages of caldera formation, prior to significant collapse, and accordingly are not preserved inside the caldera; alternatively, they may exist in the subsurface, below a central monzonite porphyry intrusion (see discussion).

We also note the chemical similarity of the upper cooling unit of the outflow sequence with the intracaldera tuff. Although there is considerable variation in the alkalis and rubidium, the more immobile elements show good agreement between the two units (Table 1).

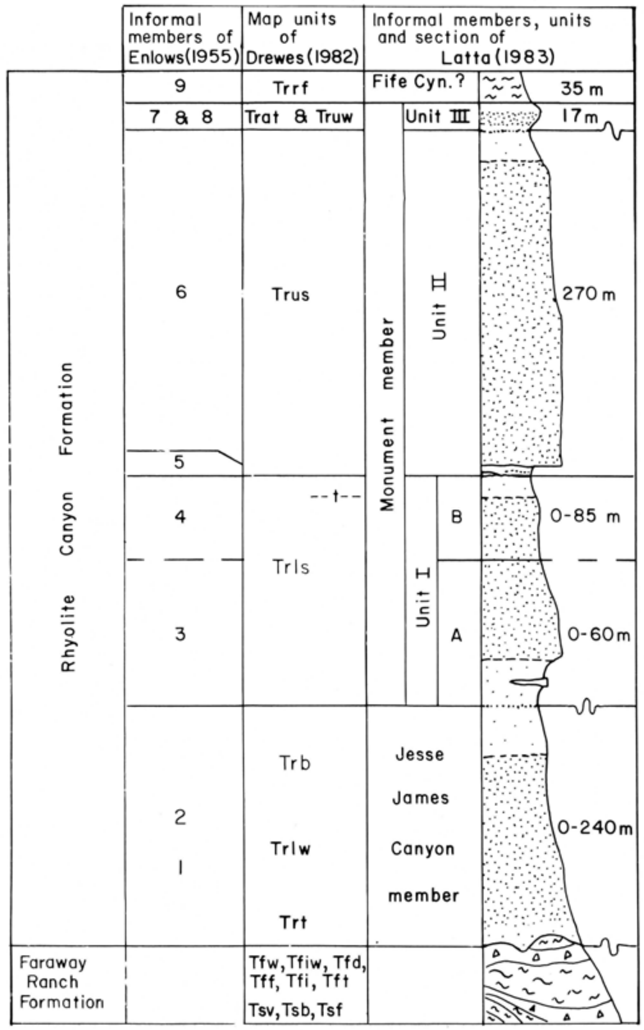

FIGURE 3—Correlation chart for stratigraphic units of the Rhyolite Canyon Formation. Colored map by Drewes (1982), provided with field-trip material, is also available at National Monument Visitor Center.

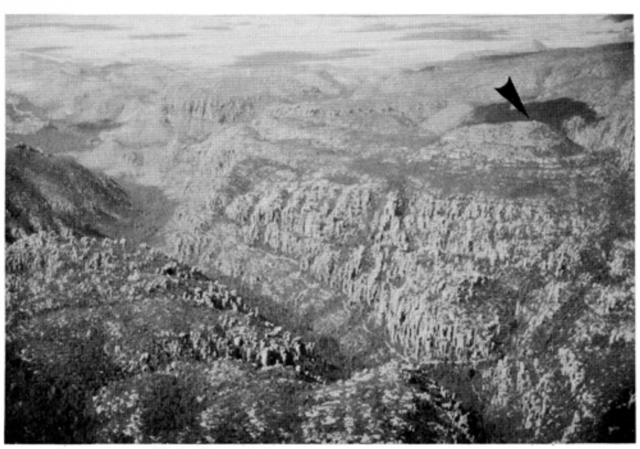

FIGURE 2—Oblique aerial photograph of Rhyolite Canyon Formation in Chiricahua National Monument. View is to northwest down Rhyolite Canyon drainage. Sugarloaf Mountain (at arrowhead) is dacite lava that caps outflow welded tuff from Turkey Creek caldera.

Dacite lava overlying the ash-flow sequence in the National Monument (dacite of Sugarloaf Mountain) is chemically and petrographically similar to porphyry of the ring intrusion and to the earliest lavas erupted from the ring intrusion of the caldera at Barfoot Peak (Table 1; locality is near Ida Peak in Fig. 1). Because of the lack of vent structures closer to Sugarloaf Mountain and the similarity in chemistry and petrography, a ring-dike source, about 8 km south, is suggested.

Mileage

0.0 **Begin road log: Downtown Willcox,** Arizona, corner of Haskell (Business I-10) and Maley (AZ-186) streets. **Drive east on Maley** (AZ-186) for 31.5 mi to AZ-181, then **east** on AZ-181 for an additional 3.1 mi to Chiricahua National Monument. **29.8**

29.8 **STOP 1. Overview of outflow tuff of the Rhyolite Canyon Formation and northern margin of Turkey Creek caldera.** Brief "arm-waving" stop (best with late-afternoon light). Cone-shaped hilltop (Sugarloaf Mountain) on horizon at 11:00 is dacite lava

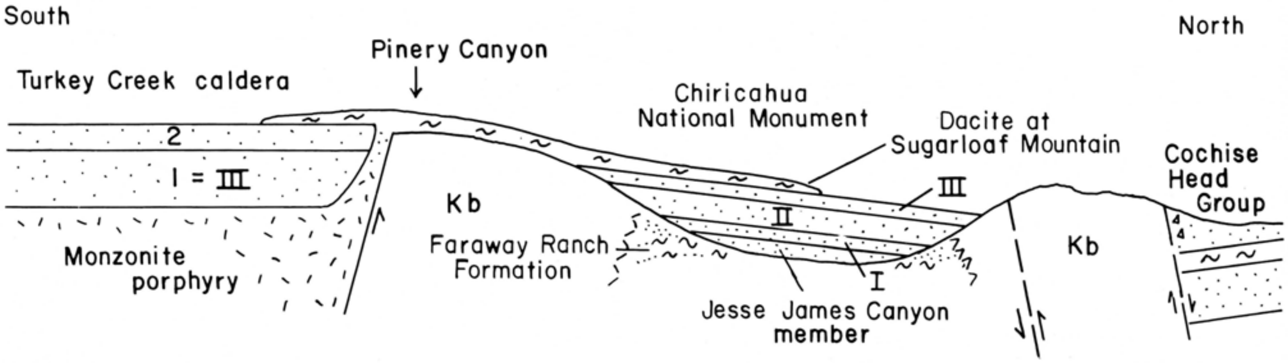

FIGURE 4—Cartoon showing correlation of lower part of the intracaldera tuff of Rhyolite Canyon Formation (I) with upper cooling unit of outflow sequence (III) (as suggested by Latta, 1983). Topography now partly inverted; uplifted Bisbee Group (Kb) now underlies valleys (e.g., Pinery Canyon). The Jesse James Canyon member and units I, II, and III are informal divisions of the Rhyolite Canyon Formation (see Fig. 3). The informal Cochise Head Group of Latta (1983) includes welded tuffs mapped as part of the rhyolite of Rough Mountain by Drewes (1982).

capping outflow Rhyolite Canyon Formation tuff. Low-angle outflow tuff sheet dips to south away from high ground to north, flattens below Sugarloaf Mountain, and climbs to south toward the caldera margin. Outflow tuff overlies rhyolite lavas and pyroclastic flows of Faraway Ranch Formation (low hills in foreground). Topographic margin of the caldera follows Pinery Canyon at 1:00; high terrain on horizon to southeast follows eastern ring intrusion of the caldera. **1.7**

31.5 Intersect AZ-181. **Turn left** (east) on AZ-181. **3.0**

34.5 Junction with Pinery Canyon Road. **Curve left** (stay on **pavement and enter Chiricahua National Monument**). Note flow-banded rhyolite flow-dome of Faraway Ranch Formation in hill immediately ahead. **1.7**

TABLE 1—Major-element analyses (normalized to 100% by weight, volatile-free), CIPW norms and trace-element abundances (in ppm) for igneous rocks of the Chiricahua Mountains, southeast Arizona. Averages and standard deviations given for "n" analyses of each map unit. LOI = loss on ignition. Molar FeO/FeO + Fe_2O_3 set to 0.8 prior to calculation of norms. Trc = Rhyolite Canyon Formation; Tmp = monzonite porphyry. [1]An informal unit.

				Trc (outflow)				
Unit:	Faraway Ranch Fm. lavas	Jesse James Cyn. tuff[1]	Trc intracaldera	I	II	III	Transitional Tmp-Trc	Transitional Tmp-lava
n	2	5	15	6	12	3	10	4
SiO_2	73.39±0.05	77.60±0.22	76.45±1.08	77.38±0.23	77.58±0.21	75.99±0.26	75.60±2.49	65.95±0.84
Al_2O_3	14.95±0.10	12.36±0.19	12.38±0.60	12.06±0.08	12.09±0.11	12.47±0.03	12.66±0.85	15.55±0.16
Fe_2O_3	0.25±0.01	0.20±0.02	0.40±0.04	0.32±0.01	0.30±0.02	0.41±0.01	0.40±0.15	0.93±0.06
FeO	0.89±0.01	0.73±0.08	1.44±0.16	1.16±0.03	1.09±0.08	1.47±0.02	1.44±0.54	3.36±0.20
MgO	0.26±0.01	0.32±0.08	0.19±0.09	0.08±0.09	0.06±0.09	0.30±0.25	0.31±0.20	1.64±0.31
CaO	1.22±0.05	0.39±0.12	0.24±0.12	0.24±0.19	0.25±0.07	0.30±0.01	0.40±0.40	3.48±0.34
Na_2O	3.92±0.09	3.31±0.18	2.84±0.97	3.67±0.15	3.47±0.14	3.48±0.42	2.65±1.30	3.83±0.53
K_2O	4.89±0.14	4.88±0.08	5.79±1.05	4.91±0.04	4.96±0.08	5.30±0.15	6.19±1.55	4.10±0.70
TiO_2	0.18±0.01	0.14±0.01	0.23±0.03	0.11±0.00	0.12±0.02	0.21±0.01	0.27±0.17	0.78±0.07
P_2O_5	<0.05	<0.05	<0.05	<0.05	<0.05	0.05±0.0	0.05±0.08	0.30±0.02
MnO	0.05±0.0	0.05±0.01	0.03±0.02	0.07±0.01	0.06±0.02	0.07±0.01	0.04±0.03	0.09±0.01
LOI	3.41±0.30	1.56±0.38	1.20±0.6	0.59±0.30	0.69±0.28	0.98±0.92	1.40±1.35	1.89±1.14
Q	28.31	37.86	36.07	35.77	37.01	33.40	34.44	17.43
C	0.98	0.92	1.01	0.26	0.56	0.45	0.99	0.0
or	28.87	28.84	34.23	29.02	29.32	31.29	36.55	24.23
ab	33.18	28.04	24.05	31.08	29.38	29.47	22.44	32.43
an	6.07	1.94	1.14	1.21	1.24	1.50	1.66	13.10
di	0.00	0.00	0.00	0.00	0.00	0.00	0.00	1.84
hy	1.88	1.84	2.47	1.99	1.83	2.88	2.71	7.45
mt	0.36	0.30	0.58	0.47	0.44	0.59	0.58	1.35
il	0.35	0.27	0.44	0.21	0.23	0.41	0.51	1.48
ap	0.00	0.00	0.00	0.00	0.00	0.00	0.12	0.70
n	4	5	22	14	15	4	10	8
Rb	175±11	304±10	336±115	425±14	381±34	294±3	406±116	221±91
Sr	250±22	28±6	34±11	20±5	23±7	36±6	62±44	306±64
Y	25±3	43±4	60±8	72±21	74±20	66±1	61±12	46±5
Zr	162±4	166±4	407±72	291±11	279±9	381±43	324±78	442±88
Nb	15±3	35±4	43±5	63±3	57±5	46±1	48±13	25±3
Ba	841±29	21±9	70±25	17±9	28±18	68±9	192±195	806±64
La	51±3	40±6	110±26	58±16	61±20	106±10	68±17	75±13
Ce	91±6	79±10	204±43	131±20	136±17	206±25	133±20	139±23
Nd	40±7	29±4	83±16	50±12	56±18	77±8	60±11	68±9

(Table 1, continued)

Unit	Monzonite porphyry East ring	Monzonite porphyry Core	Moat rhyolite Upper	Moat rhyolite Lower	Moat rhyolite Other	Moat tuffs	201533 Sugarloaf dacite	86P-31 Barfoot dacite	86P-71 Ida Pk. aphy. rhy.	86P-73 Ida Pk. qz. rhy.
n	9	5	8	7	4	3				
SiO_2	64.86±0.92	65.78±3.42	77.44±0.62	76.79±1.18	74.70±2.15	77.70±0.42	65.21	66.29	76.06	76.41
Al_2O_3	15.68±0.26	15.29±0.57	12.66±0.35	12.76±0.52	13.59±1.12	12.24±0.31	15.72	15.45	13.37	12.98
Fe_2O_3	0.96±0.05	0.97±0.27	0.21±0.01	0.27±0.01	0.38±0.02	0.22±0.01	0.98	0.93	0.22	0.28
FeO	3.47±0.17	3.48±0.98	0.77±0.04	0.96±0.05	1.36±0.07	0.79±0.04	3.53	3.35	0.81	0.99
MgO	1.53±0.17	1.48±0.58	0.08±0.06	0.15±0.07	0.48±0.11	0.15±0.02	1.90	1.57	0.0	0.16
CaO	3.12±0.49	2.81±1.08	0.23±0.22	0.64±0.19	1.42±0.33	0.25±0.06	3.76	3.52	0.11	0.64
Na_2O	3.87±0.28	3.68±0.22	3.75±0.48	3.73±0.54	2.92±0.83	3.44±0.02	3.37	4.54	3.76	3.83
K_2O	5.14±0.45	5.14±0.71	4.67±0.89	4.47±0.62	4.79±0.77	5.01±0.09	4.40	3.06	5.46	4.48
TiO_2	0.93±0.05	0.96±0.28	0.15±0.03	0.18±0.01	0.27±0.02	0.15±0.01	0.77	0.88	0.16	0.18
P_2O_5	0.35±0.03	0.32±0.12	<0.05	<0.05	0.06±0.04	<0.05	0.30	0.31	<0.05	<0.05
MnO	0.10±0.02	0.10±0.03	0.06±0.02	0.05±0.01	0.03±0.02	0.04±0.02	0.08	0.10	0.04	0.05
LOI	2.17±0.62	1.67±0.11	1.74±2.28	4.07±1.39	2.80±1.40	0.51±0.10	1.74	3.34	0.50	5.02
Q	13.43	15.89	36.68	35.74	34.98	37.23	17.09	17.88	32.56	34.74
C	0.00	0.00	1.03	0.61	1.16	0.70	0.00	0.00	1.08	0.67
or	30.36	30.37	27.59	26.43	28.33	29.63	25.99	18.07	32.27	26.47
ab	32.73	31.10	31.70	31.59	24.67	29.12	28.49	38.42	31.79	32.42
an	10.26	10.05	1.12	3.20	6.65	1.24	14.77	12.74	0.56	3.17
di	2.46	1.47	0.00	0.00	0.00	0.00	1.59	2.21	0.00	0.00
hy	6.81	7.16	1.30	1.71	3.01	1.47	8.51	6.93	1.11	1.79
mt	1.40	1.40	0.31	0.39	0.55	0.32	1.42	1.35	0.33	0.40
il	1.76	1.81	0.28	0.34	0.51	0.29	1.45	1.67	0.31	0.34
ap	0.82	0.76	0.00	0.00	0.15	0.00	0.70	0.74	0.00	0.00
n	22	9	12	11	5	8	1	1	1	1
Rb	203±49	211±58	455±114	404±98	248±30	352±47	174	189	403	422
Sr	227±28	222±56	25± 23	39±19	174±51	25± 7	381	382	15	91
Y	48± 5	48± 5	49± 15	56±14	38± 6	52±10	39	45	43	68
Zr	526±57	481±20	193± 8	211±22	171±14	206±22	335	514	201	228
Nb	26± 2	26± 2	53± 10	41±10	13± 4	48± 7	21	25	49	40
Ba	709±66	712±90	10± 4	77±10	691±83	52±31	856	727	6	82
La	83± 7	89±13	33± 9	72±11	52± 5	50±13	60	86	38	79
Ce	150±11	164±18	84± 15	136±30	105±14	107±24	114	168	78	160
Nd	73± 5	73± 7	30± 9	60±15	53± 7	43± 9	57	77	29	68

36.2 Pass pullout on left. We will return here for Stop 3. **1.3**

37.5 **STOP 2. National Monument Visitor Center** (restrooms). Backtrack 0.55 mi down canyon to west for Stop 3. **0.5**

38.0 **STOP 3. Faraway Ranch Formation**—"Basement rhyolites." Pull off on right (north) just before boulders. This is a **blind curve,** so **watch out for traffic! Climb to top of hill north of road.** This stop is in the eroded upper carapace breccia of a rhyolite (72% SiO_2, Table 1) lava within the Faraway Ranch Formation (shown as Tff on the geologic map by Drewes, 1982). Much of the outcrop is devitrified, but glassy zones are preserved near the cliff at the north edge of the outcrop. Note the presence of biotite and sphene; these minerals (and hornblende) are common in the rhyolites and dacites that predate the Turkey Creek caldera, but they are rare in the ash-flow tuffs that were derived from the caldera (the Monument member of the Rhyolite Canyon Formation). Biotite from similar rhyolite on Erickson Ridge (S30W, ~1/2 mi) was dated at 28.2±0.8 Ma by Marjaniemi (1969).

An unfaulted section through the overlying Rhyolite Canyon Formation is visible at Riggs Mountain (N40E, ~1/2 mi). The base of the prominent nose extending south from Riggs Mountain is underlain by Faraway Ranch Formation rhyolite carapace breccia similar to that exposed here (shown as Tsv by Drewes, 1982). The carapace breccia is overlain by a pyroclastic flow and airfall tuff (Trt), then by a salmon-colored, biotite-bearing, welded tuff (Trb). These tuffs (Trt and Trb) are mapped as the informal Jesse James Canyon member of the Rhyolite Canyon Formation by Latta (1983), who considers it to be a single cooling unit, distinct from overlying ash flows derived from the Turkey Creek caldera (Latta's informal Monument member). The Jesse James Canyon member is overlain by unit I of the Monument member (Trls), then by the prominent cliff-forming unit II of the Monument member (Trus).

We found that each of the map units below unit I of the Monument member (Trt, Trlw, Trb) is characterized by relatively low Rb and Zr (~300 and ~170 ppm, respectively) compared to higher Rb and Zr (~400 and ~290 ppm) in units I and II of the Monument member (Table 1). We believe that this geochemical and cooling break may be the most genetically significant contact in the section, possibly separating ash flows derived from two separate calderas; however, additional work is needed before suggesting stratigraphic revision.

Continue west (down canyon) 0.5 mi to Faraway Ranch entrance. **Turn around** here and **proceed back up canyon to east. 1.7**

39.7 **Curve left** (north) at Visitor Center and **drive up Bonita Canyon.** Road climbs from Faraway Ranch Formation through unit I of the Monument member (within 1 mi) and remains in unit II for most of way to Stop 4. Hoodoos are in unit II. **0.6**

40.3 Pass campground entrance on left. **1.8**

42.1 35 cm thick welded tuff (on right). This thin ash flow occurs at the base of unit II and preserves a complete welding profile through a thickness of only 35 cm. If time permits, we will stop for a closer inspection after lunch. **1.3**

43.4 "Ancient lake beds." Oligocene(?) shales and sandstones underlying Rhyolite Canyon Formation along the east side of the paleobasin in which the outflow sequence accumulated. **1.7**

45.1 Sugarloaf/Echo Canyon Road intersection. **Turn right** (west). **0.1**

45.2 **Pass Echo Canyon parking lot. 0.5**

45.7 **STOP 4. Rhyolite Canyon Formation**—Outflow sequence. **Hike up Sugarloaf trail to lookout** (~2 hours, round trip). **Bring lunch** and camera. Localities given relative to parking lot elevation of 6820 ft, see map by Drewes (1982). Trail begins in uppermost part of unit II of the Monument member (Fig. 3).

6830 ft. Map contact between Drewes' Trus (densely welded tuff) and Trat (air-fall tuff) map units. Latta includes both in his unit II. Outcrops above and below the mapped contact contain abundant large pumices, a characteristic of unit II in this area, and have similar trace-element chemistry (Table 1). We locate the contact between units II and III at the welding break farther up-section (near 6960 ft elevation on trail—see below), on the basis of an abrupt decrease in abundance of pumice and lithic fragments, a decrease in welding, and a change to less evolved chemistry.

6960–7000 ft. Weakly indurated, moderately to weakly welded tuff with surge beds. Undercut exposure at base of densely welded zone of unit III of the Monument member (Fig. 3). Exposure at far (west) end of undercut reveals 0–20 cm thick cross-laminated (dune-form) surge bed. Laminated bed is apparent source region for Liesegang bands that crosscut laminations and extend upward into the overlying tuff. Directly above is a fines-depleted pipe that may represent a fossil fumarole. Similar fines-depleted pipes and irregular veins are exposed throughout this area in both the poorly indurated basal zone of unit III and extending into the overlying densely welded zone.

7120 ft. Contact between unit III of the Monument member tuff and overlying dacite lava flow, Sugarloaf dacite (Trrf), exposed from here to top. As noted previously, the chemical composition of the lava is similar to dacite and monzonite porphyry from the caldera ring intrusion near Barfoot Peak (Table 1). Note that the dacite contains large (to 0.5 cm) feldspar phenocrysts and fine-grained mafic xenoliths. Remember these features for comparison with the ring intrusion and related lavas (to be seen tomorrow).

7310 ft. **Lunch!** Lookout post at top of Sugarloaf Mountain. Building is constructed from glassy dacite prophyry lava. The lookout provides an excellent view of Cochise Head (to the northeast), part of a thick accumulation of rhyolitic welded tuff and tuff breccia east of the Apache Pass fault that apparently overlaps in age with the Faraway Ranch Formation.

The high terrain forming the skyline to the southeast is supported by the eastern ring intrusion that defines the structural margin of the Turkey Creek caldera. Ida and Barfoot Peaks (Figs. 1, 10a) are visible in the middle ground. Ida Peak is capped by rhyolite moat lavas that overlie the most northwesterly exposures of the ring intrusion. Barfoot Peak is capped by dacite lava very similar to that underfoot and preserves rocks that are transitional into the ring-intrusion porphyry.

Pinery Canyon, the principal east–west-trending drainage to the south, follows the former northern topographic margin of the caldera. The morphology of the caldera is partly inverted due to erosion of the less resistant Bisbee Group sedimentary rocks outside the structural margin. We will drive up Pinery Canyon and across the pass at its head tomorrow morning, en-route to exposures of the ring intrusion on the south side of Barfoot and Ida Peaks.

Return to cars and **backtrack out of National Monument** to intersection of AZ-186 and AZ-181 (12 mi). **ROAD-LOG MILEAGE STARTS OVER AT THIS INTERSECTION.** If time permits, we will **stop briefly** at the 35 cm thick welded tuff **on our way out of the Monument** (at **mileage 49.3,** 3.6 mi from here). For future users of this guide who wish to spend additional time in the National Monument, Massai Point (1.5 km southeast of Sugarloaf Mountain) provides spectacular views of eroded columns in welded tuff of the Rhyolite Canyon Formation.

Part 2. AZ-181/AZ-186 intersection to Turkey Creek: Central intrusion, intracaldera tuff, and moat rhyolites

From the AZ-181/AZ-186 intersection we drive south on AZ-181 for 10.5 mi, then east on a gravel road into the core of the Turkey Creek caldera (Fig. 1). The core of the caldera is deeply eroded ($\geq$2 km), exposing hypabyssal levels of a monzonite to quartz monzonite porphyry intrusion over an area of about 40 km^2. Outcrop pattern, as well as similarity in petrography and chemistry, suggest that the intrusion is continuous in the subsurface with a monzonite to dacite ring intrusion that is discontinuously exposed around more than 180° of the caldera circumference. Note that ring and central phases of the monzonite are separated by a segment of intracaldera tuff only about 1 km wide in the southwest (Fig. 1).

Marjaniemi (1969) referred to the central phase of the monzonite porphyry as the "dome monzonite." Both Marjaniemi and Latta (1983) related resurgence of the caldera to intrusion of the porphyry, and Marjaniemi pointed out that intrusion is bracketed closely in time by eruption of the overlying Rhyolite Canyon Formation tuff (25.5 ± 0.6 Ma) and by a K–Ar biotite age of 25.4 ± 0.7 Ma on a rhyolite dike that intrudes the porphyry. Latta noted angular discordance between radial dips away from the center of the caldera of about 25° for the intracaldera Rhyolite Canyon Formation tuff and about 15° for lower moat rhyolites, as well as a further decrease in dip of units higher in the moat sequence. On this basis, he proposed that resurgence began shortly after caldera collapse, but continued during moat lava eruption. However, sedimentary rocks in the caldera record a significant erosional/depositional hiatus prior to eruption of the high-silica rhyolite moat lavas.

Thick sections of volcaniclastic breccias (mainly lahars) and tuffaceous sandstones in the southeastern part of the caldera (Fig. 5) contain clasts of Rhyolite Canyon Formation tuff and monzonite porphyry. These sedimentary rocks were deposited on an erosional surface that cuts through the tuff and into the porphyry, and they are overlain by rhyolite moat lavas. We believe that porphyry in the core of the caldera was uplifted; but, we are not convinced that resurgent *intrusion* of the porphyry magma was the cause of uplift; later intrusion of moat rhyolite magma may also have caused uplift (see discussion and Fig. 12a). Because of the presence of monzonite clasts in moat sediments, the por-

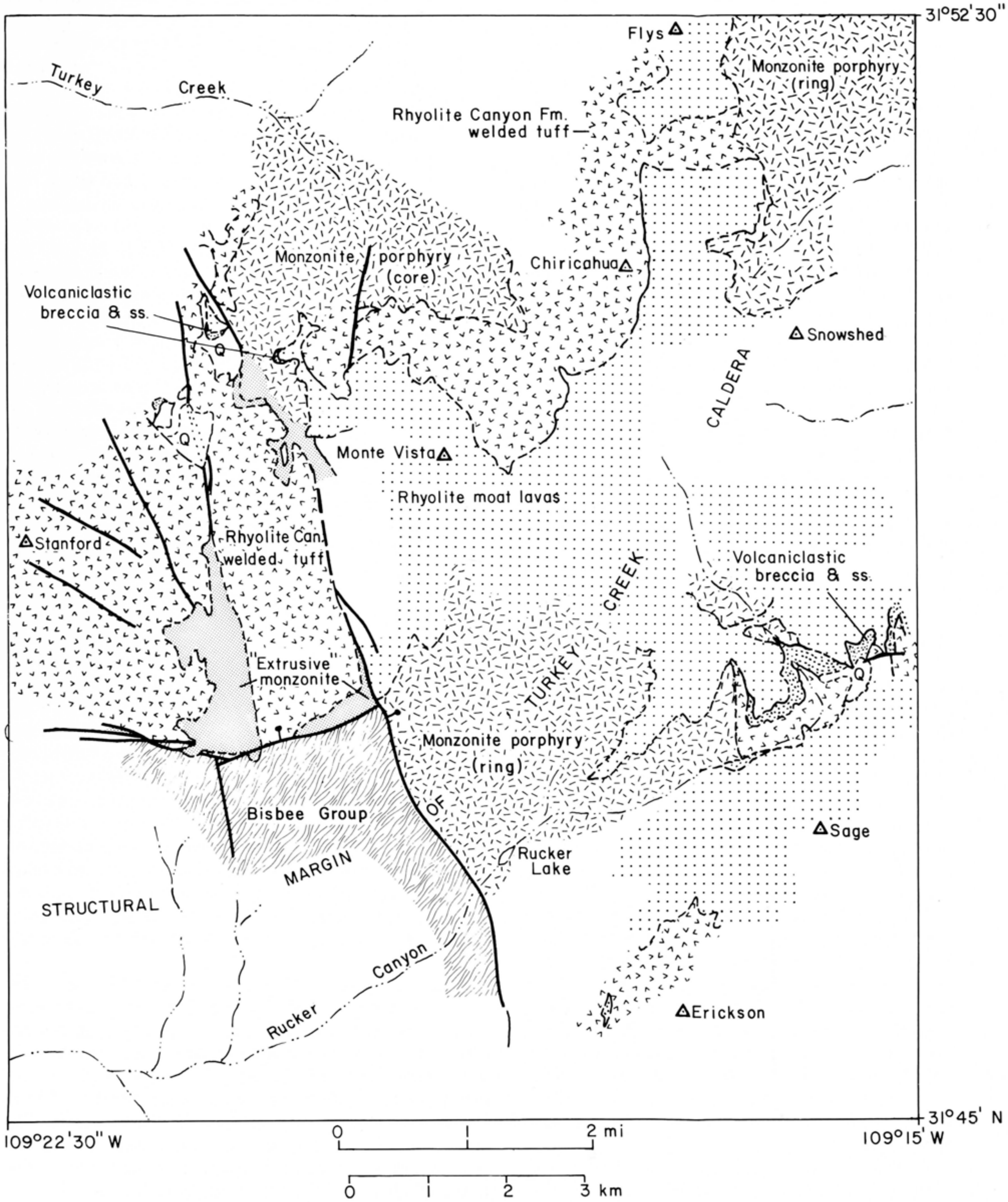

FIGURE 5—Preliminary geologic map of the southeastern part of the Turkey Creek caldera showing thick sequence of volcaniclastic and sedimentary rocks deposited unconformably on Rhyolite Canyon Formation tuff and on both the central and ring phases of the monzonite porphyry. Extrusive equivalents of the monzonite occur within the caldera along fault zones (see text). Q = Quaternary deposits.

phyry was probably already emplaced at its present stratigraphic level during at least the latest stages of uplift. As explained below, it is locally gradational with the Rhyolite Canyon Formation tuff and probably represents either the in-situ or reintruded residue of the source magma chamber for the tuff.

The monzonite intrusion (central and ring phases) is exposed at a hypabyssal level; it is porphyritic, with large (0.5 to several cm) andesine phenocrysts in a granophyric groundmass. Fresh samples from relatively deep exposures are magnetite–clinopyroxene–hornblende–biotite-bearing monzonite to quartz monzonite. Small (1–2 cm) mafic hornfels inclusions are a sparse but characteristic feature of both the central and the ring intrusions.

Although most of the monzonite is non-foliated porphyritic granophyre, abrupt transitions in texture, petrography, and chemistry occur within both the central and ring intrusions. We will visit a locality tomorrow atop the ring intrusion where quartz monzonite porphyry grades into and feeds porphyritic dacite lava flows. Similar relations are also observed along faults in the southern part of the central intrusion, where transitions from homogeneous quartz monzonite porphyry, through miarolitic porphyry, to vesicular, quartz-bearing, porphyritic lava occur over a few meters. The lavas are flow-folded but appear gradational with densely welded intracaldera tuff of the Rhyolite Canyon formation. These zones of extrusive porphyry (Fig. 5) bound fault blocks in the intracaldera tuff, indicating eruption from vents that formed as the floor of the caldera (roof of the magma chamber) was broken up during late stages of caldera collapse.

Chemical data for the Rhyolite Canyon Formation tuff and for the hypabyssal quartz monzonite porphyry (Table 1, Fig. 6) document the change to a less siliceous (monzonitic) magma. Central and ring vents for the ash-flow tuff were intruded and then clogged by this viscous magma. The abrupt transition from high-silica ash-flow tuff to quartz-bearing dacite lava and then to quartz monzonite and monzonite porphyry suggests that high-silica rhyolite was evacuated from a source chamber in which a distinct compositional interface existed between high-silica rhyolite and underlying low-silica monzonitic magma.

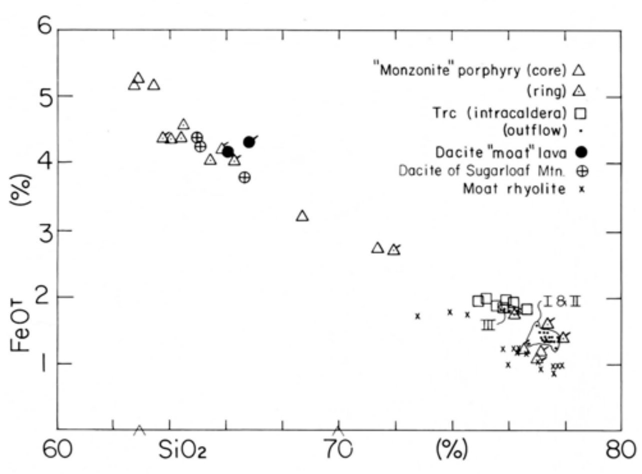

FIGURE 6—SiO_2–FeO^T variation diagram comparing monzonite porphyry and transitional intrusive–extrusive rocks of core and ring intrusions to dacite and rhyolite moat lavas and Rhyolite Canyon Formation tuff (Trc). Symbols with tick-marks are texturally transitional between intrusion and lava flow.

In lower Turkey Creek canyon (Fig. 7; Stop 5) we will investigate the contact between the central intrusion and the overlying intracaldera Rhyolite Canyon Formation tuff. In this area, the upper contact of the central intrusion is a monolithologic roof breccia composed of disaggregated monzonite porphyry and quartz-phyric granophyre. Brecciation could have been produced by magmatic inflation and/or caldera collapse, perhaps coupled with intrusion of the central phase of the porphyry as a laccolith within, or at the base of, the intracaldera tuff. But, the lack of megascopic shear fabric is difficult to reconcile with a purely tectonic interpretation.

The breccia is strongly altered and hematized or sericitized. Brecciation may have been hydrothermal, produced by hydrofracturing during devolatilization of the porphyry intrusion. Another possibility is that the roof breccia is analogous to the crush zone in nuclear blast craters (e.g., Derlich, 1970), or to breccias which occur at the borders of bolide impact craters (e.g., Pohl et al., 1977; Stöffler et al., 1979). Our preliminary investigations suggest low-pressure shock metamorphism. A possible interpretation is that magmatic explosion(s) with foci in the underlying core intrusion created shock waves that brecciated the chilled border of the intrusion. Eruption of Rhyolite Canyon Formation tuff may have evacuated the upper siliceous part of the magma chamber during caldera collapse, such that monzonite from low in the chamber was drawn up into contact with the quartz-bearing (siliceous) breccia. Alternatively, brecciation may be related to magmatic inflation and/or caldera collapse; perhaps coupled with intrusion of the central monzonite as a laccolith within the intracaldera tuff.

Merits of the various explanations will be discussed at the outcrop. Recent mapping of the Rhyolite Canyon/porphyry contact to the northeast has revealed complex field relations. Dikes and sills of rhyolite and granite occur near the contact and intrude both the overlying tuff and the underlying monzonite. Monzonite porphyry dikes also locally intrude the overlying tuff. The concentration of rhyolite and granite dikes and sills near the contact suggests a possible origin by melting of intracaldera tuff by the porphyry. Some breccia outcrops contain pyroclastic-matrix breccias with clasts of precaldera(?) dacite; other breccias contain plastically deformed clasts. However, brecciated joint-blocks of porphyry are observed near Turkey Creek. These relations indicate that although some of the porphyry (deeper levels?) was probably still at super-solidus temperatures during formation of the roof breccia, other regions were cooled and jointed prior to fragmentation. Our recent field work favors an intrusive contact between the porphyry and the tuff, but the process(es) that led to brecciation have yet to be established.

Mileage

0.0 Intersection of AZ-181 and AZ-186, west of Chiricahua National Monument. **Turn left** and drive south on AZ-181. **10.5**

10.5 Right-angle curve in road at **intersection with Turkey Creek Road. Turn left** (east) onto gravel Turkey Creek Road. **2.7**

13.2 Contact between intracaldera tuff and central monzonite intrusion trends up valley between two low hills at 3:00. **2.5**

15.7 **STOP 5. Roof breccia of core intrusion, intracaldera Rhyolite Canyon Formation tuff, moat**

rhyolites. Park on left where road widens. Assemble on exfoliation surface on right (south) side of road. This is a typical porphyritic monzonite of the core intrusion. We will climb fence on north side of road, hike across field, and climb ridge to north. Duration: ~2 hrs.

FUTURE GUIDEBOOK USERS: DO NOT CLIMB FENCE WITHOUT PERMISSION OF RANCHER (THIS LAND IS POSTED—NO TRESPASSING). ,

A simplified geologic map and cross section of the traverse we will make is given in Fig. 7. We climb through a section, within a graben block, that takes us from monzonite porphyry of the central intrusion through roof breccia and into intracaldera Rhyolite Canyon Formation tuff. The tuff is overlain by bedded volcaniclastic breccia and sandstone, then by moat rhyolite. It is possible to see all these units in a relatively short distance because the intracaldera tuff is anomalously thin (400–500 m), at least in part due to erosion. Magmatic excavation of the basal intracaldera tuff provides an alternative means to thin the section; however, we have not observed inclusions of the tuff in the porphyry, and a similar roof breccia is exposed below a much greater thickness (~1 km) of intracaldera tuff to the northeast (Fig. 7).

The porphyry is locally fractured and a few quartz veins can be found in outcrops along Turkey Creek (we cross the creek en-route to the base of the section). A zone of monzonite to quartz-phyric granophyre breccia is exposed at the base of the section. This is a monolithologic, cataclastic, autobreccia that is composed of decimeter-to-millimeter-scale clasts of monzonite and granite granophyre porphyry in a granulated matrix (mainly clast-supported). Veins of hematitic, matrix-supported breccia are locally exposed and indicate limited fluidization. Thin sections reveal that clasts are cut by thin (<1 mm) mylonite bands and microfaults and that quartz phenocrysts are shattered (Fig. 8).

The lower "crush" zone of the breccia contains clasts of granophyric monzonite porphyry; clasts in the upper "fracture" zone are quartz-phyric gran-

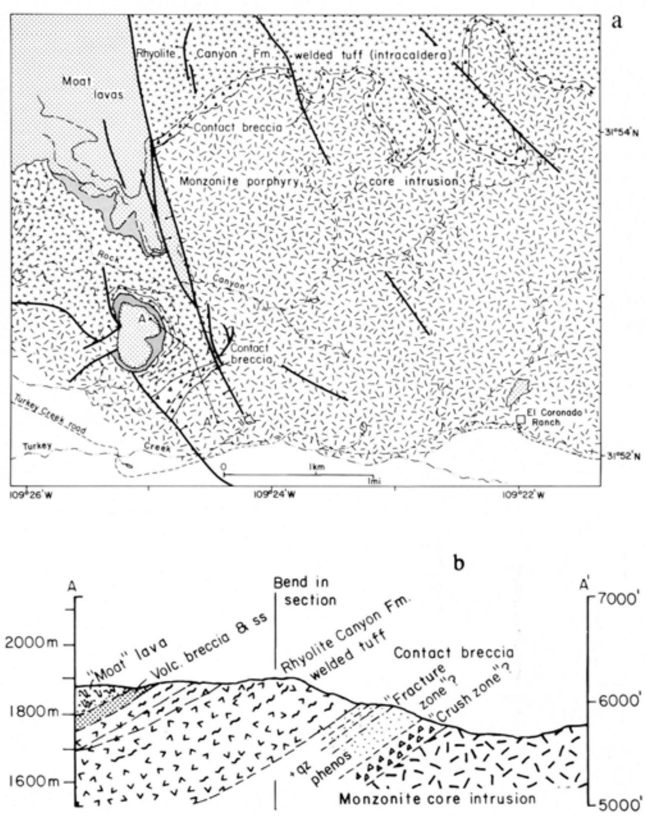

FIGURE 7—Simplified geologic map **(a)** and cross section **(b)** of area north of lower Turkey Creek. Scale bar and latitude–longitude grid approximate; base from aerial photograph. Horizontal = vertical scale in section.

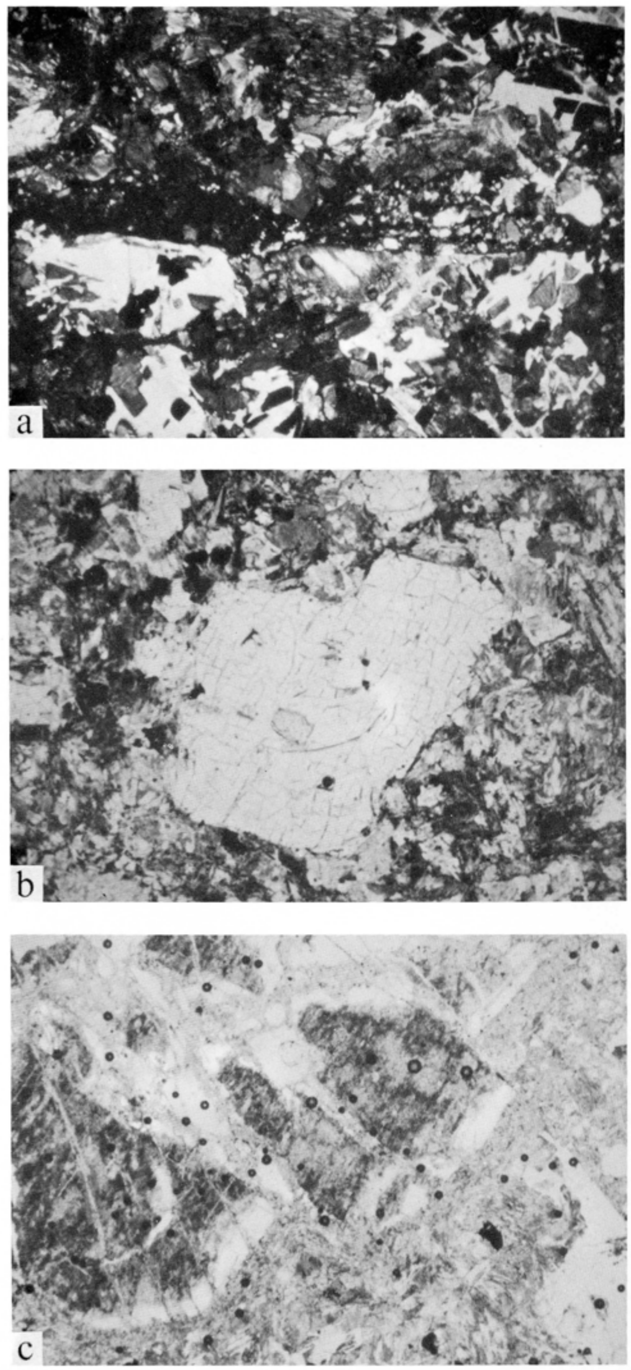

FIGURE 8—Photomicrographs of granophyre clasts in monzonite roof breccia, showing: **a,** mylonite band; **b,** micro-fractured quartz phenocryst; **c,** micro-faulted feldspar phenocryst. Image widths = 3.6 mm.

ophyre. We interpreted the upper zone rocks as highly fractured and altered, and/or melted, Rhyolite Canyon Formation tuff because of the presence of rounded quartz phenocrysts and low-angle foliation. Marjaniemi (1969) also recognized an increase in degree of alteration and fracturing of the tuff over a distance of up to several hundred meters from the monzonite contact. He regarded granophric textures in the tuff close to the contact as indistinguishable from those in the monzonite, and relied on the presence of quartz phenocrysts to identify the tuff. Marjaniemi attributed these effects to contact metamorphism of the tuff by the monzonite. This is the simplest and likely correct explanation, but, having seen quartz-phyric magmatic phases of the monzonite elsewhere (some with surficial lava features, such as flow folds), we believe that the presence of relict quartz phenocrysts does not uniquely identify the tuff. Therefore, we have also entertained an alternative working hypothesis: that the quartz-phyric granophyre might represent a quenched upper border zone of the intrusion. However, this explanation would require unconventional ideas about roof rocks to the intrusion (or lack thereof), as explained in the discussion.

The welded tuff exposed above the cataclastic breccia interval contains several cooling breaks and may be divided into two or three ash-flow deposits. Compaction foliation attitudes are variable in the lower part of the exposed welded tuff, suggesting large-scale rheomorphic folding.

The welded tuff is locally overlain by several tens of meters of brown-to-tan-weathering, bedded, tuffaceous clastic breccia and ash-rich sandstone. This sedimentary unit contains clasts of Rhyolite Canyon Formation welded tuff and rhyolite lava. Similar clastic breccias occur in equivalent stratigraphic positions in several areas of the caldera (e.g., upper Rucker Canyon, Fig. 9). Clast populations elsewhere are dominated by Rhyolite Canyon Formation tuff and monzonite porphyry; exposures here in Turkey Creek are unusual by virtue of also containing rhyolite lava clasts; the source of these clasts is unknown.

FIGURE 9—Photograph showing thick section of crossbedded clastic breccias and sandstones (br) that unconformably overlie Rhyolite Canyon Formation tuff and are conformably overlain by rhyolite moat lavas (Tmr). The breccias contain abundant Rhyolite Canyon Formation welded-tuff clasts. In the floor of upper Rucker Canyon (off-frame to left), the breccias unconformably overlie monzonite porphyry and contain porphyry clasts.

The dominance of Rhyolite Canyon clasts and the stratigraphic position of the sedimentary unit below the moat lavas indicate that an erosion–deposition cycle took place after caldera collapse and Rhyolite Canyon eruption, but prior to eruption of most (if not all) moat rhyolite. The presence of monzonite porphyry clasts in breccias of upper Rucker Canyon indicates that sufficient time passed for local erosional unroofing of the porphyry prior to eruption of dacite and high-silica rhyolite moat lavas.

The section north of Turkey Creek is capped by an erosional remnant of biotite–sanidine rhyolite of the moat-lava sequence. The lava has a basal carapace breccia that is in depositional contact with the underlying sedimentary unit. From the crest of this knob, a thick section of moat lavas overlying Rhyolite Canyon Formation tuff is visible to the north. To the northeast, the smooth-weathering outcrops of the central porphyry intrusion are easily distinguished.

Backtrack to cars and continue east 2.6 mi to Coronado Ranch (University of Arizona Field Camp).

18.3 **STOP 6. Coronado Ranch** (overnight). If time and light permit, outcrops of monzonite porphyry of the core intrusion may be examined in the bed of Turkey Creek near the gate to Coronado Ranch.

Day 2,
Part 3. Intrusive–extrusive transitions in the ring intrusion

From Coronado Ranch we return to AZ-181 and drive to the intersection with Pinery Canyon road (0.1 mi west of entrance to Chiricahua National Monument). Road-log mileage begins at this intersection. We drive east, up Pinery Canyon and parallel to the northern topographic margin of Turkey Creek caldera. Near the head of Pinery canyon, we climb through Bisbee Group sedimentary rocks to Onion Saddle, just outside the structural margin of the caldera. Turning south, we cross into the ring intrusion of the caldera (Fig. 10a) and investigate field relations atop the ring intrusion at Barfoot and Ida Peaks.

The structural margin of the Turkey Creek caldera is intruded by a wide (2–4 km) ring dike of monzonite porphyry (Fig. 1). Where the ring dike is not present at the surface, the structural margin of the caldera is buried by rhyolites and dacites of the moat-lava sequence. We have identified only one feeder for the moat rhyolites, a subvertical dike exposed in the south wall of Pinery Canyon northeast of Ida peak (Fig. 10). This dike cuts the outer margin of the ring intrusion, as well as Bisbee Group sedimentary rocks immediately outside the caldera.

We believe that Rhyolite Canyon tuff eruption and caldera collapse were followed immediately by intrusion of monzonite porphyry into the Rhyolite Canyon feeder zones (both ring dike and faults in the caldera floor). These shallow intrusions erupted dacite lavas to form the stratigraphically lowest lavas now exposed atop the ring dike, as well as local accumulations that overlie Rhyolite Canyon tuff along linear zones within the caldera (Fig. 5). The latter may represent porphyry that was extruded from fault-controlled

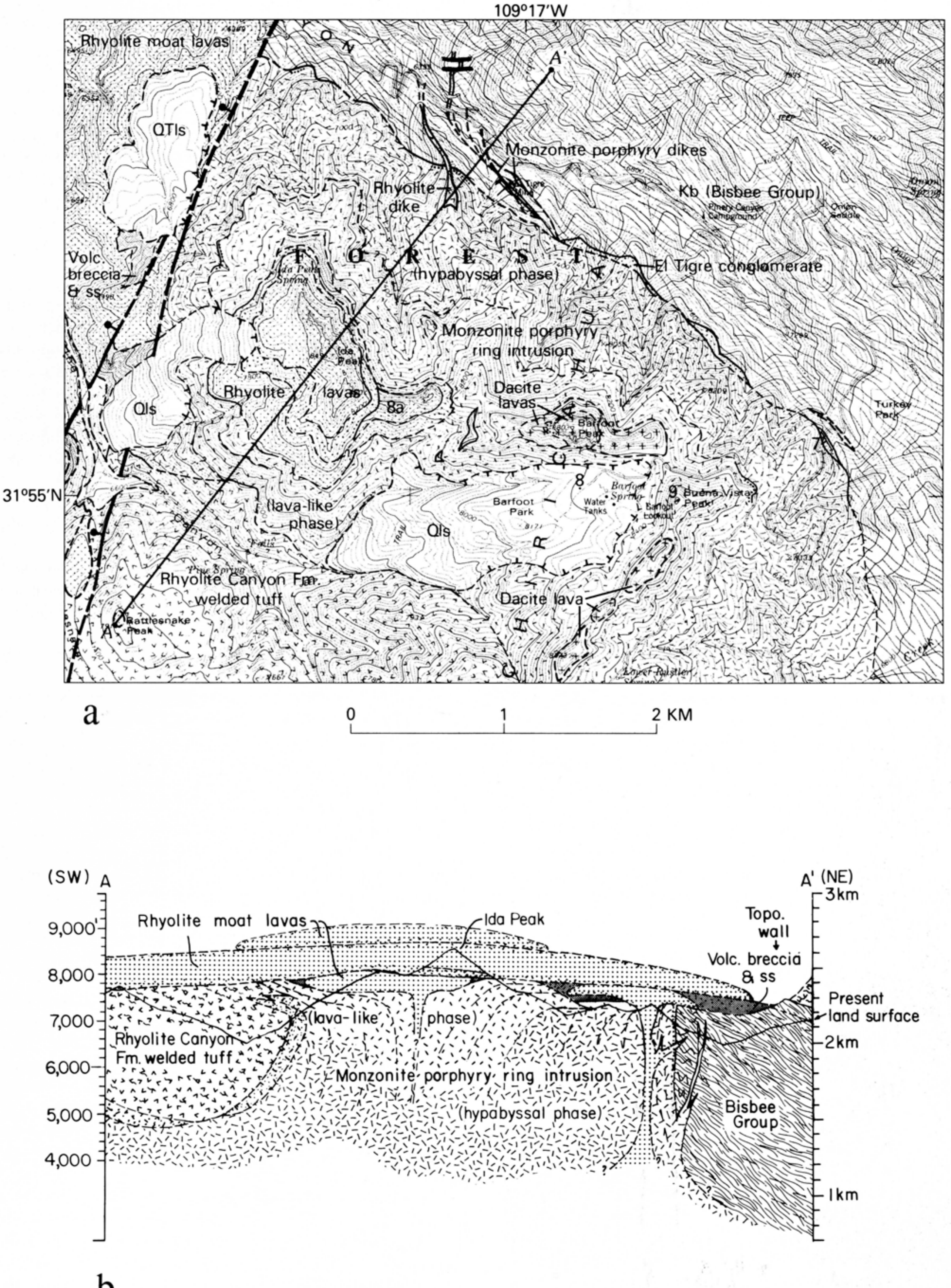

FIGURE 10—Geologic map **(a)** and interpretative cross section **(b)** of the northeastern segment of the ring intrusion, Turkey Creek caldera. Field-trip localities are indicated by stop number. Profile line shows present topography. Stippled areas represent carapace breccia. Qls = Quaternary landslide deposits, QTls = Quaternary or Tertiary landslide deposit.

dikes formed as the roof of the magma chamber broke up during caldera collapse. Transitional intrusive–extrusive textures and morphologic features (described below) are seen atop the ring intrusion and in the central outcrops of extrusive porphyry.

Results of drilling into rhyolite feeder dikes at the Inyo domes, California, has led to the suggestion that significant degasing of rhyolite magma may take place at shallow levels within the intrusive environment; that rhyolite magma may vesiculate, degas, and weld itself back together in the conduit (Eichelberger et al., 1986). Scandone and Malone (1985) argue for an interplay between magma supply rate and disruption level within the Mount St. Helens conduit to explain transitions between sustained and pulse eruptions during the 1980 plinian eruptions. Although there are questions regarding the primary volatile contents of rhyolites and mechanisms of degasing in a vent (Friedman, 1988), it is apparent that given a zoned or layered magma reservoir, pyroclastic eruption would be succeeded by effusive eruption as more volatile-poor parts of the reservoir are vented. We believe that transitions between pyroclastic and effusive rocks observed in the near-surface vent environment of the Turkey Creek caldera record such a process.

Mileage

0.0 Intersection of AZ-181 and Pinery Canyon Road. **Turn right** (south) on Pinery Canyon Road. **1.0**

1.0 View to north of local pyroclastic flows in Faraway Ranch Formation. **6.4**

7.4 Methodist Camp Road junction. **Continue straight** on Pinery Canyon/Onion Saddle Road. **FUTURE USERS:** If time permits, good exposures of moat rhyolite lavas and pyroclastic flows are available in the roadcuts of Methodist Camp Road near Downing Pass (~1 mi). **1.8**

9.2 El Tigre mine road junction, continue straight to Onion Saddle. The El Tigre is a small silver and silica-flux mine located on quartz veins developed subparallel to the outer contact of the ring intrusion. **3.0**

12.2 Onion Saddle and junction with Rustler Park Road (FS-42D). **Veer right (south) on Rustler Park Road. 1.2**

13.4 **STOP 7. Structural margin of Turkey Creek caldera.** Pull off on right. This is the contact between the ring intrusion and precaldera sedimentary and volcanic rocks (Fig. 10). A southwesterly dipping section of sandstone, siltstone, conglomerate, and minor limestone beds make up the precaldera rocks near the contact here. These rocks are part of a dominantly clastic Tertiary(?) unit that overlies Lower Cretaceous Bisbee Group sandstone and limestone. The clastic unit is mapped as the informal El Tigre conglomerate by Tsugii (1984) and may correlate with the Cretaceous or Tertiary Nipper Formation of Sabins (1957), as noted by Drewes and Williams (1973). Breccia clasts of limestone from the underlying Cretaceous or Paleozoic rocks, as well as dacitic and rhyolitic volcanic rocks are common in exposures of the unit between here and the El Tigre mine.

Examine the roadcuts between the quartz-vein zone (exposed behind the cars) and the monzonite porphyry ahead (~100 m southwest). The quartz veins are a continuation of the El Tigre vein system that trends northwesterly, subparallel to, but locally branching away from, the margin of the ring intrusion where they intrude Bisbee and Nipper rocks.

An important question to consider here is the nature of the contact. Although the porphyry regionally intrudes Bisbee and Nipper rocks, sediments that overlie the Nipper here appear to have ponded against the eroded porphyry (and are therefore correlative with moat sediments exposed elsewhere in the caldera). Examine the altered breccia beds immediately adjacent to the porphyry, which contain highly altered porphyry clasts (some quartz-phyric).

Note that the porphyry has a fine-grained (but not glassy) groundmass near the contact. Miarolitic cavities containing terminated quartz crystals are well exposed in outcrops about 30 m from the contact. A thin air-fall tuff bed(?) *within* the porphyry (exposed in a roadcut 0.4 mi to the southwest) indicates that the porphyry was partly extrusive. Thicker pyroclastic intervals form benches within the porphyry cliffs to the south and east. These occurrences suggest that we are within an eroded ring-vent complex, where exposures of porphyry proximal to (and deeper within) the locus of ring intrusion show intrusive features; more distal exposures have characteristics of thick lava flows.

Continue southwest on the Rustler Park Road. **0.9**

14.3 Junction with Barfoot Park (Scout Camp) Road (FS 357). **Turn right** (toward Barfoot Park). **0.8**

15.1 **STOP 8. Barfoot Park. Hike to Barfoot–Ida Peak saddle** (~3 hrs. round trip). Extrusive phase of monzonite porphyry and moat rhyolite flows. **Walk down the valley to the west; intercept and hike northwest (right turn) on the Ida Peak Forest Service trail.** The Ida Peak trail contours along the southwest flank of Barfoot Peak to a saddle between Barfoot and Ida Peaks. We walk through a large landslide deposit for the first 0.4 mi, then climb up to the saddle. Look for outcrops of glassy-matrix porphyry and erosional remnants of moat breccia (with Rhyolite Canyon Formation welded-tuff clasts) as the trail rounds the western spur of Barfoot Peak and climbs to the saddle (Fig. 10).

This is an area that we mapped in moderate detail, building on the thesis work of Karl Tsugii (1984). Tsugii recognized several andesitic to rhyolitic lava flows overlying the ring intrusion here. We agree with this interpretation, but we regard the lower (mainly dacitic) lavas as intrusive–extrusive features. We believe that the dacitic lavas, which form prominent benches on the low flanks of Ida Peak and cap Barfoot Peak, represent the extrusive equivalents of the monzonite porphyry. Transitional textures and compositions of the lavas and underlying porphyry intrusion (Figs. 6, 11, Table 1) indicate that we are seeing various levels through a caldera ring-intrusion and vent complex, as shown by the cross section in Fig. 10b. These relations suggest that the transitional intrusive–extrusive rocks of the Turkey Creek caldera preserve an abrupt compositional gradient that may have formerly been a layer

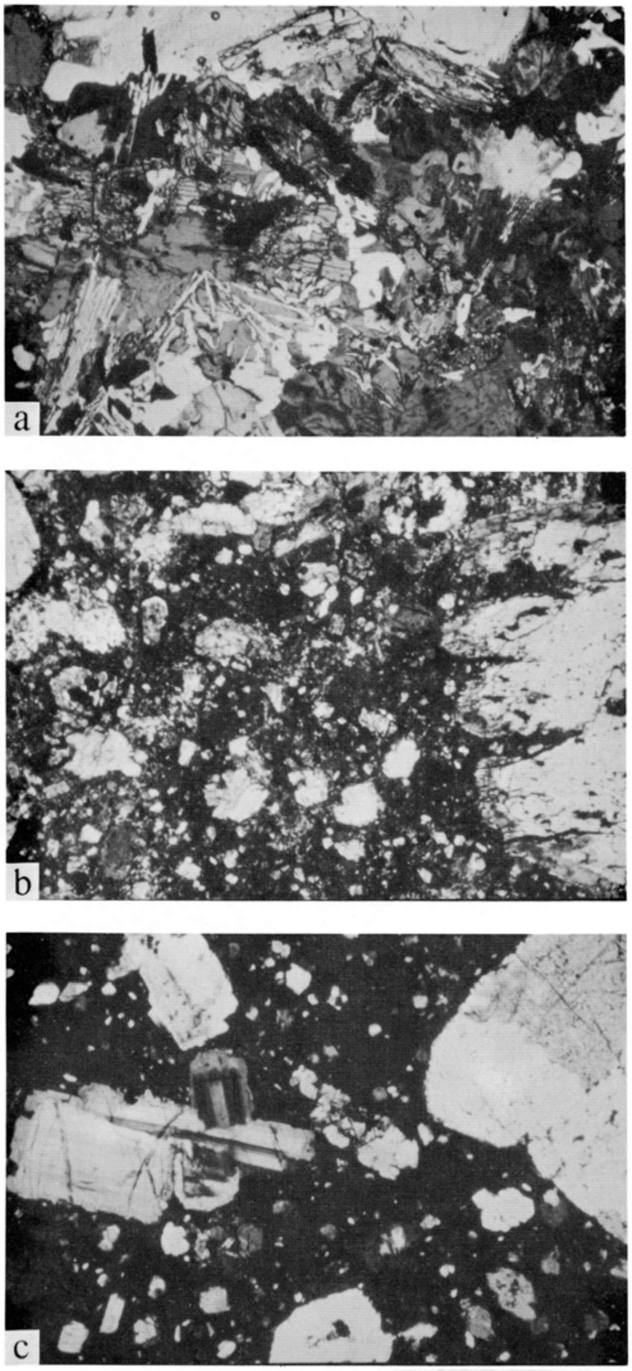

FIGURE 11—Photomicrographs (frame width 3.6 mm) showing a transition from granophyre-matrix **(a)** biotite–clinopyroxene–hornblende–two-feldspar monzonite porphyry to microcrystalline **(b)** and glass-matrix **(c)** porphyry lava. Note the presence of quartz phenocrysts in the glass-matrix lava. Samples from the flanks of Barfoot Peak.

interface within the source magma chamber. This hypothesis is further developed in the discussion.

STOP 8a. Barfoot–Ida Peak saddle (elevation 8140 ft). The saddle is within the lower of two rhyolite lava flows of the moat sequence that caps Ida Peak. **Hike up the ridge to the east** (toward Barfoot Peak). This traverse takes us down-section through flow-folded rhyolite lava and lower carapace breccia of the lower moat rhyolite, then into platy-jointed dacite/monzonite porphyry with local remnants of moat breccia on its erosional(?) surface, and finally into glass-matrix dacite lavas that cap Barfoot Peak. **Please keep together;** we will not climb to the top of Barfoot Peak; instead congregate on the western spur-ridge, then "peel off" to the south to intercept the Ida Peak trail back to the cars. We then drive back toward Onion Saddle. **0.7**

15.8 **STOP 9. Barfoot Lookout** (Buena Vista Peak). **Pull off on left near cattleguard. Take lunch** and climb trail to Barfoot Lookout (30 min. up). The Barfoot Lookout provides good views of the ring intrusion and overlying lavas (Stop 8) as well as an overview of the northern edge of the Portal caldera and underlying rhyolites at Silver Peak to the southeast and east.

Discussion: "Working models" for the Turkey Creek caldera

Mid-Tertiary magmatism in the Chiricahua Mountains began at about 30 Ma, with eruption of voluminous rhyolite lavas and pyroclastic flows to form the Faraway Ranch Formation and coeval deposits that predate both the Portal and Turkey Creek calderas. Older mafic magmatism is recorded by basaltic to andesitic lavas interbedded with clastic rocks (Nipper Formation?) that overlie the Bisbee Group, and by gabbro intrusions in the upper part of the Bisbee Group; both of these rock types are seen in sections east of Onion Saddle. A 31.8 ± 0.7 Ma whole-rock K–Ar age on an andesite lava interbedded with the Nipper Formation(?) along the road east of Onion Saddle is reported by Shafiqullah et al. (1978).

Hypothetical structural models for the Turkey Creek caldera are outlined in Fig. 12a, b. Model 12a begins (stage 1) with the formation of a high-silica rhyolitic cupola atop a monzonitic magma chamber. We have shown a free-air surface and granophyre chilled margin on the cupola in Fig. 12a. We realize this is a departure from traditional caldera models, but, given the lack of precaldera floor (magma-chamber roof) rocks in the eroded core of the caldera, we have adopted this simple geometric solution as one of two working models. Intrusion of monzonite magma as a sill or laccolith during late stages of caldera formation provides a more traditional explanation for the apparent lack of caldera floor rocks (Fig. 12b). We present both models here in the hope that they will foster lively discussion during the field trip. The character of the quartz-phyric granophyre border zone of the monzonite (Stop 5) may provide the answer. If the zone represents quenched Rhyolite Canyon magma, the free-air surface model would be preferred; if the border is a contact metamorphic zone, the laccolith model gains credence.

Circumstantial support for the free-air surface model is provided by the character of rhyolitic magmatism preceding the Turkey Creek caldera. A large volume of rhyolite was erupted effusively in the Chiricahua Mountains prior to development of the Portal and Turkey Creek calderas. It is apparent that large reservoirs of high-silica magma were developing at shallow crustal levels, and that these magmas were relatively volatile-poor; only at Portal, Turkey Creek, and Cochise Head (the latter in the northeast Chiricahua Mountains) did large-scale Plinian eruptions and caldera collapse occur. If ash-flow tuff eruption is viewed as magmatic "boiling" rather than explosive ballistic ejection, the need for a confinement vessel (and magma-chamber roof) is obviated. In this context, the development of a cupola of

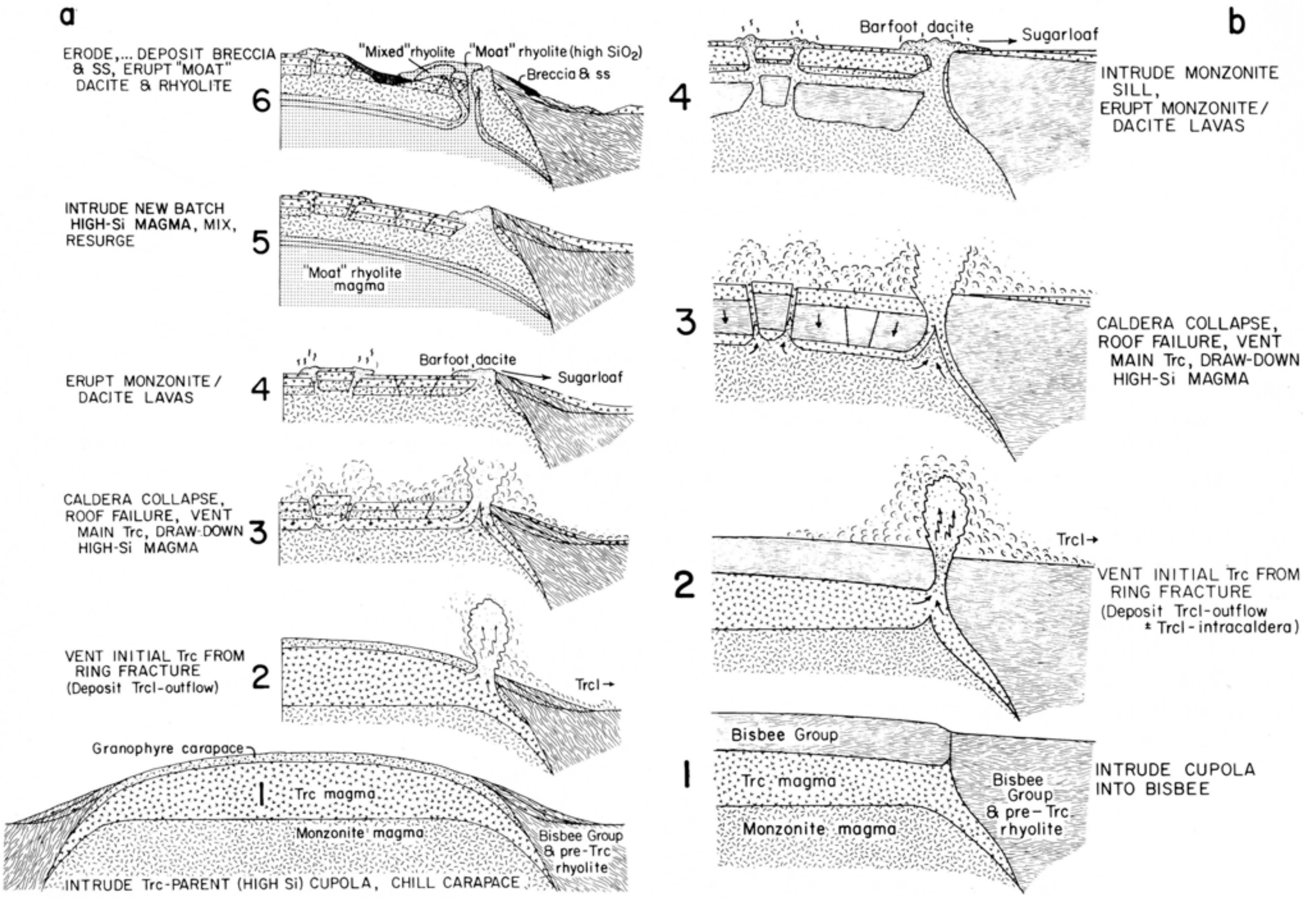

FIGURE 12—Working models for structural stages in the evolution of the Turkey Creek caldera. **a,** free-air surface model; **b,** laccolith model. Trc = tuff of Rhyolite Canyon Formation; Trcl = lower members (units I and II of Latta, 1983) of outflow tuff of Rhyolite Canyon Formation.

relatively volatile-poor, high-silica magma, that was progressively unroofed prior to eruption, is easier to envision. This concept is not new, batholiths with free air were proposed 20 years ago (Hamilton and Myers, 1967).

During stage 2 (Fig. 12a, b), initial eruption of Rhyolite Canyon Formation tuff took place and resulted in deposition of units I and II of the Monument member in the National Monument. The apparent lack of intracaldera equivalents of these lower units may be explained by the lack of a topographic depression at this early stage of caldera formation. Alternatively, intracaldera equivalents of the lower units could have accumulated, only to have become sole rocks to a monzonite laccolith intruded into the caldera fill at a later stage (Fig. 12b, stage 4). Intrusion, metamorphism, and melting of the intracaldera tuff by the underlying porphyry is observed at some localities along the roof-breccia contact, relations that favor the laccolith model. In the Portal caldera, a dacite porphyry sill intruded and mingled with intracaldera tuff (Bryan, this volume), providing a nearby analogue for sill or laccolith intrusion into intracaldera tuff. In the general context, withdrawal of magma from deep reservoirs may favor foundering of intracaldera tuff and redistribution of magma as sills and laccoliths within a thick intracaldera sequence. Only where extensive sections and very deep levels of intracaldera rocks are exposed can such hypabyssal intrusive relations be observed. Even at Turkey Creek, where erosion penetrates several kilometers into the caldera, the distinction between source pluton and laccolith is not readily made.

Stage 3 shows Plinian activity, with caldera collapse accompanying eruption of unit III of the Rhyolite Canyon Formation tuff, and accumulation of most of the unit III ash-flow deposits within the caldera. The interface with underlying monzonitic magma was drawn up into both ring and central vents as high-silica rhyolite was evacuated from the chamber by eruption.

Stage 4 models the eruption of monzonitic magma to form transitional intrusive–extrusive rocks, now preserved within the upper levels and margins of the ring intrusion and along fault zones within the caldera; the latter record the disruption of the caldera floor (magma-chamber roof) during collapse. Monzonitic magma erupted at this stage may have fed a dacite lava flow that reached the National Monument (dacite of Sugarloaf Mountain, Stop 4). This is the stage of the laccolith model at which monzonite magma must have been intruded into the intracaldera tuff, or at the Bisbee–Rhyolite Canyon tuff contact (Fig. 12b).

Stage 5 records resurgence, brought about by the arrival of a new batch of high-silica magma into the shallow magmatic system. A period of erosion and deposition ensued between the close of stage 4 and the onset of stage 6. Breccias containing clasts of Rhyolite Canyon tuff and monzonite porphyry were deposited in the developing caldera moat during this hiatus in magmatism.

Finally, during stage 6, high-silica rhyolite lavas were erupted and filled the caldera moat (locally to overflowing). The lower rhyolite moat lavas are less evolved, and may represent mixed magma derived from the interface between monzonite magma remaining from the Turkey Creek cycle and new high-silica magma.

Mid-Tertiary volcanism in the eastern Chiricahuas: The Portal caldera

Charles R. Bryan

Department of Geology, University of New Mexico, Albuquerque, New Mexico 87131

Introduction

The central Chiricahua Mountains are dominated by a thick section of mid-Tertiary silicic volcanic rocks, which are associated with at least two well-exposed ash-flow tuff calderas: the Portal caldera, source of the tuff of Horseshoe Canyon, and the Turkey Creek caldera, source of the Rhyolite Canyon Formation tuff (Marjaniemi, 1969). These two calderas are closely linked both chemically and temporally; collapse of the Turkey Creek caldera occurred shortly after formation of the Portal caldera, and resurgence of both occurred simultaneously.

The Portal caldera is exposed in the eastern half of the Chiricahua Mountains (Fig. 1). It is a relatively shallow trap-door caldera hinged at the north in the vicinity of Portal Peak and deepening to the south. Its fill, the tuff of Horseshoe Canyon, reaches a maximum thickness of at least 500 m near the mouth of Horseshoe Canyon. The resurgent dome is cut by a north-northeast-trending graben, in which the outflow sheet from the adjacent Turkey Creek caldera (Rhyolite Canyon tuff) is preserved. The western boundary is obscured by the younger Turkey Creek caldera, and the eastern half is buried beneath the San Simon Valley.

Geologic overview

The oldest rocks exposed in the eastern Chiricahuas are folded and thrust-faulted units of Paleozoic and Mesozoic age. They are unconformably overlain by Late Cretaceous–early Tertiary(?) andesitic and dacitic lava flows, ash flows,

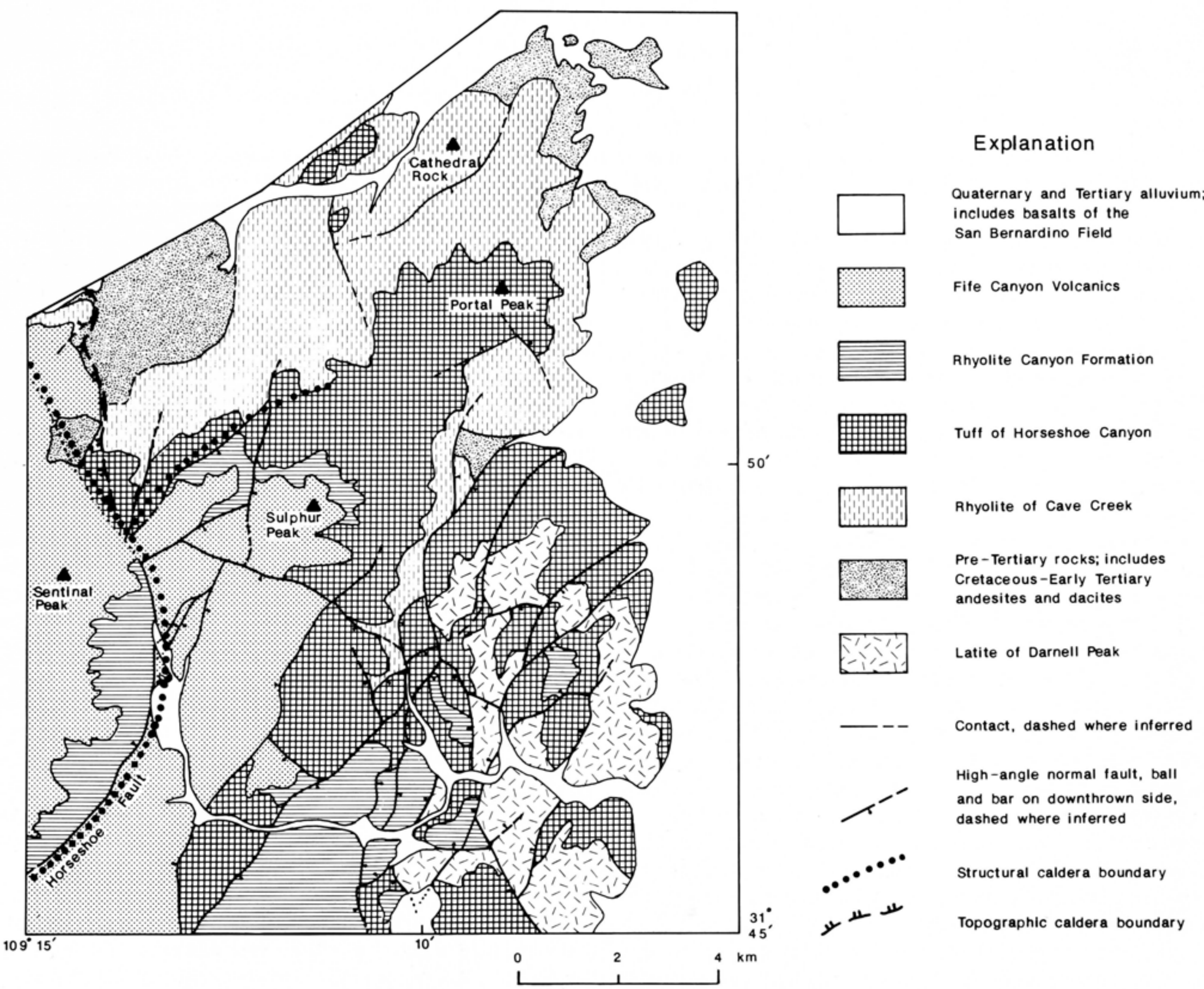

FIGURE 1—Simplified geologic map of the eastern Chiricahua Mountains, showing rock units and major structural features associated with the Portal and Turkey Creek calderas.

and volcanic sediments, which in turn are unconformably overlain by the mid-Tertiary silicic volcanic rocks shown in Fig. 1. The lowermost of the late Oligocene volcanic rocks is the rhyolite of Cave Creek. This unit is composed of crystal-poor, commonly highly altered and brightly colored high-silica rhyolite lava flows and related tuffs, breccias, and volcaniclastic sediments. North of Portal Peak, three large lava flows, each up to 250 m thick, dominate the unit. The rhyolite of Cave Creek is overlain by the tuff of Horseshoe Canyon: the ash-flow tuff that was derived from, and fills, the Portal caldera.

The tuff of Horseshoe Canyon consists of two members; the lower member is a densely welded single cooling unit, zoned from quartz, sanidine, high-silica rhyolite at the base to two-feldspar latite at the top (Fig. 2). South of Horseshoe Canyon, the central and upper parts of the lower member contain abundant mafic and felsic fiamme, each up to 30 cm long. Cognate(?) angular inclusions are also present. The uppermost part of the member has been rheomorphically mobilized; fiamme have been extremely flattened and even isoclinally folded. Rheomorphism may have been caused by intrusion of the latite of Darnell Peak, which occurs as a 300 m thick sill between the lower and upper members of the tuff in this area. The upper member is rhyolitic, much subordinate in volume, and occurs only in the southern part of the area. The tuff of Horseshoe Canyon is 350–500 m thick in most areas, and is interpreted as caldera fill; two 100–150 m thick fault-bounded blocks in Cave Creek Canyon have been tentatively identified as outflow facies.

The tuff of Horseshoe Canyon has been radiometrically dated several times. Marjaniemi (1969) obtained ages of 26.4 ± 0.7 Ma (K–Ar, biotite) and 25.1 ± 1.2 Ma (K–Ar, sanidine, upper member). Bryan (1988) obtained a K–Ar biotite age of 27.6 ± 0.7 Ma, and a Rb–Sr isochron age, on a suite of 10 samples from the lower member, of 25.3 ± 0.5 Ma (2 sigma). The Rb–Sr age is preferred; field relations are consistent with the tuff of Horseshoe Canyon having been erupted immediately prior to the Rhyolite Canyon Formation (average age 25.2 Ma; Latta, 1983).

The lower member of the tuff of Horseshoe Canyon is strongly zoned from 77 to 65% SiO_2; chemical variation in the tuff is given in Table 1. Major- and trace-element trends

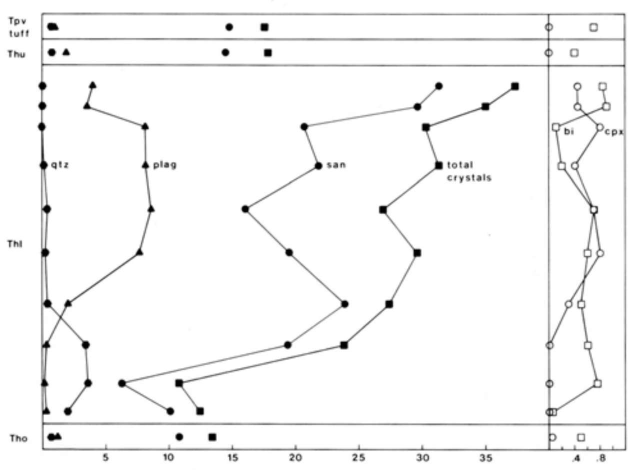

FIGURE 2—Distribution of phenocrysts in the tuff of Horseshoe Canyon. Tho = outflow sheet; Thl = lower member; Thu = upper member; Tpv = thin tuff in unit of Pothole Canyon.

are broadly linear with respect to silica. Compatible vs. incompatible trace-element trends are hyperbolic, suggesting that the variation represents fractional crystallization; however, the abundance of mafic and felsic fiamme in the tuff shows that mixing of several different layers or levels in the magma chamber occurred during eruption. Strontium 87/86 initial ratios for the tuff are slightly scattered (Table 1); there is no consistent change with silica content. The scatter may be due to wall-rock contamination during eruption; possible contaminants are Precambrian granite and Tertiary(?) granite; xenoliths of both are present in the tuff of Horseshoe Canyon.

A thin, heterogeneous section of rocks occurs locally between the tuff of Horseshoe Canyon and the Rhyolite Canyon Formation tuff in the area of the Portal caldera. These rocks are referred to as the unit of Pothole Canyon, but extent is not sufficient to show in Fig. 1. The unit includes volcaniclastic sediments, a thin rhyolite ash-flow tuff, a porphyritic latite lava flow, and a basaltic andesite lava flow—the most mafic mid-Tertiary unit in the area.

The Rhyolite Canyon high-silica welded tuff occurs in the mapped area as both thick (650 m) caldera fill, within its source Turkey Creek caldera west of the Horseshoe fault, and as outflow east of the fault. As in Chiricahua National Monument, the outflow sheet has two major cooling units, although the lower one is only locally present. Unlike in the Monument, however, Rhyolite Canyon outflow sheet in the Portal caldera is pervasively altered, with a chalky-gray matrix and characteristic white, clayey sanidines.

Moat deposits of the Turkey Creek caldera, the Fife Canyon volcanics (Latta, 1983), are present along the structural boundary of the Turkey Creek caldera and extend into the Portal caldera (Fig. 1). The lowermost member of the Fife Canyon volcanics is a thick (several hundred meters) sequence of porphyritic latite lava flows, which are the extrusive equivalent of the monzonitic stock that intrudes the resurgent dome of the Turkey Creek caldera. Several local members, including epiclastic breccias, rhyolite lava flows, air-fall tuffs, and quartz latite ash-flow tuff and lava flows, occur on top of this unit, and the entire section is capped by a group of voluminous, aphyric, flow-banded, high-silica rhyolite lava flows.

The latite of Darnell Peak occurs primarily as a large sill, up to 300 m thick, which intrudes the tuff of Horseshoe Canyon, typically between the lower and upper members, in the vicinity of Horseshoe Canyon. It contains about 40% phenocrysts, mostly sanidine and plagioclase as euhedral phenocrysts to 1.2 cm, and minor clinopyroxene, biotite, and opaque minerals. Its contact with the lower member is locally diffuse over a distance of a few meters, suggesting that the sill intruded while the tuff of Horseshoe Canyon was still hot.

Structure and caldera evolution

Stages in the development of the Portal and Turkey Creek calderas are summarized in the east–west schematic cross sections of Fig. 3. The Portal caldera is a trap-door collapse feature in north–south profile and has a hinge zone in the north, near Portal Peak. The structural margin is exposed in South Fork Canyon; tuff and wall rocks are intensely altered, lithic fragments are abundant near the base of the caldera-fill tuff, and a ring-fracture fault and ring-fracture intrusions are present.

Only a small part of the Portal caldera is exposed; esti-

TABLE 1—Analyses of mid-Tertiary volcanic units in the central Chiricahua Mountains. *Below detection limits. 1 = rhyolite of Cave Creek; 2–5 = tuff of Horseshoe Canyon, lower member, bottom to top; 6 = tuff of Horseshoe Canyon, upper member; 7 = basaltic andesite flow, unit of Pothole Canyon; 8 = Rhyolite Canyon Tuff, vitrophyric base of outflow sheet; 9 = Rhyolite Canyon Tuff, caldera fill; 10 = Fife Canyon Volcanics, porphyritic latite member; 11 = Fife Canyon Volcanics, upper rhyolite member.

Sample #	1	2	3	4	5	6	7	8	9	10	11
SiO_2	75.20	77.06	73.81	70.52	63.82	71.25	53.20	73.71	76.77	64.08	77.15
TiO_2	0.10	0.16	0.26	0.45	0.82	0.39	1.59	0.14	0.16	0.81	0.10
Al_2O_3	13.18	11.90	13.29	15.17	16.88	14.43	17.15	11.47	11.24	15.05	12.67
Fe_2O_3	0.58	0.76	1.18	1.69	2.33	1.51	6.61	0.96	0.84	2.64	1.10
FeO	0.40	0.12	0.07	0.19	0.67	0.02	1.41	0.58	0.11	1.50	0.07
MnO	0.07	0.06	0.08	0.07	0.09	0.08	0.11	0.09	0.04	0.10	0.09
MgO	0.02	0.07	0.15	0.28	0.66	0.10	4.52	0.10	0.03	1.06	0.03
CaO	0.48	0.17	0.27	0.62	1.76	0.26	7.25	0.78	0.11	3.28	0.56
Na_2O	3.41	3.07	3.31	4.21	4.00	1.57	3.56	4.27	0.84	3.45	3.82
K_2O	5.15	5.66	6.33	6.22	6.32	9.08	2.27	2.92	8.60	5.18	4.58
P_2O_5	*	*	*	0.04	0.15	*	0.36	*	*	0.24	*
H_2O^+	0.55	0.28	0.35	0.43	.0.58	0.62	2.11	4.29	0.29	2.63	0.37
H_2O^-	0.06	0.00	0.00	0.00	0.02	0.00	0.68	0.18	0.04	0.06	0.04
Total	99.20	99.31	99.10	99.89	98.10	99.31	100.82	99.49	99.07	100.09	100.58
Sc	1.39	2.21	3.08	4.93	6.69	3.96	23.40	2.13	2.27	9.00	1.50
Zn	49	61	66	62	69	54	103	96	54	81	54
Rb	681	404	371	249	162	539	67	624	670	208	636
Sr	11.10	9.76	23.0	65.9	284	22.8	550	85.5	11.2	184	4.07
Y	170	88	90	76	55	154	46	191	127	71	181
Zr	142	152	230	393	847	353	345	271	159	497	146
Nb	67	32	30	26	19	30	17	55	29	27	66
Cs	7.40	5.08	5.40	7.30	2.68	9.50	0.61	56.70	12.20	6.60	7.60
Ba	*	*	182	648	4300	310	835	*	55	859	*
La	32.7	36.3	51.1	88.0	62.3	90.9	52.6	114	36.1	96.0	45.6
Ce	92	83	104	179	135	206	123	167	89	209	114
Nd	43	64	50	66	51	88	74	97	36	96	42
Sm	6.2	4.09	7.1	12.2	8.7	19.7	9.8	20.6	5.13	13.4	9.7
Eu	0.106	0.19	0.72	2.10	3.32	1.15	2.35	0.28	0.21	1.86	<0.07
Tb	1.69	0.72	1.30	1.35	1.04	3.19	1.34	3.47	0.52	0.93	2.43
Dy	9.5	5.5	6.5	8.3	6.1	16.9	6.9	19.0	5.7	7.0	14.4
Yb	12.70	4.97	5.60	4.90	3.49	8.30	3.76	11.40	5.22	5.60	14.10
Lu	1.98	0.75	0.80	0.86	0.576	1.09	0.597	1.69	0.74	0.76	2.12
Hf	9.3	7.46	10.50	15.4	21.2	13.6	8.93	13.7	8.20	14.5	9.2
Ta	9.9	4.58	2.75	2.99	2.65	4.07	1.38	7.24	4.36	2.89	10.5
Th	66.9	31.8	28.9	26.2	13.0	25.1	9.8	56.9	33.7	27.2	59.6
U	12.00	6.27	4.27	4.44	2.25	4.06	1.137	13.90	7.12	5.21	8.89
$Sr(87/86)_o$	0.7140	0.7140	0.7134	0.7137	0.7135	0.7151	0.7085	0.7103	0.7129	0.7097	0.7134

mating the size of the caldera is difficult. A minimum diameter is 12–15 km; a minimum volume for the tuff of Horseshoe Canyon is about 70 km^3. The abundance of large mafic and felsic fiamme and Precambrian and Tertiary(?) granitic inclusions in the tuff of Horseshoe Canyon, just south of the mouth of Horseshoe Canyon, indicates that a source vent for the tuff may have been in this area.

Eruption of the Rhyolite Canyon Formation at about 25.2 Ma caused collapse of the Turkey Creek caldera (Marjamiemi, 1969; Fig. 3c). About 500 km^3 of ash was erupted, forming a caldera about 21 km in diameter. The eastern edge of the caldera is well exposed in the western part of the mapped area (Fig. 1); it truncates the older Portal caldera. Within the zone of overlap, the structural and topographic margins of the Turkey Creek caldera coincide, and the outflow sheet of Rhyolite Canyon Formation tuff extends right up to the ring fracture, the Horseshoe fault of Marjaniemi (1969); apparently, the thick, densely welded tuff of Horseshoe Canyon supported the caldera wall and prevented slumping during formation of the wall of the Turkey Creek caldera. The structural and topographic rims diverge northeast of Sentinal Peak, where the less resistant rhyolite of Cave Creek forms the caldera wall.

Resurgence of the Turkey Creek caldera began before eruption of the porphyritic latite lava flows at the base of the Fife Canyon volcanics (Latta, 1983). The ring fracture of the Portal caldera was an important structure within the younger caldera; the latite lavas are several hundred meters thick north of Sentinal Peak, but are absent within the zone of overlap of the two cauldrons. The latite apparently formed a sill in this area, lifting the intracaldera facies of the Rhyolite Canyon Formation tuff, west of the Horseshoe fault, above the outflow sheet to the east (Fig. 3d).

Continued resurgence of the Turkey Creek caldera triggered resurgence of the Portal caldera, causing doming of the tuff of Horseshoe Canyon and the formation of a northeast-trending graben in which the outflow sheet of Rhyolite Canyon tuff has been preserved. The intracaldera facies of the Rhyolite Canyon tuff in the zone of overlap was also tilted; it dips ~10° away from the dome of the Portal caldera toward the center of the Turkey Creek caldera (Fig. 3e). The high-silica rhyolite lava flows which are the uppermost unit of the Fife Canyon volcanics were then emplaced, forming an angular unconformity on the flanks of the somewhat eroded resurgent dome of the Portal caldera.

Road log

This log is a continuation of the Turkey Creek field trip; the first stop is equivalent to Stop 9 of Pallister and du Bray (this volume).

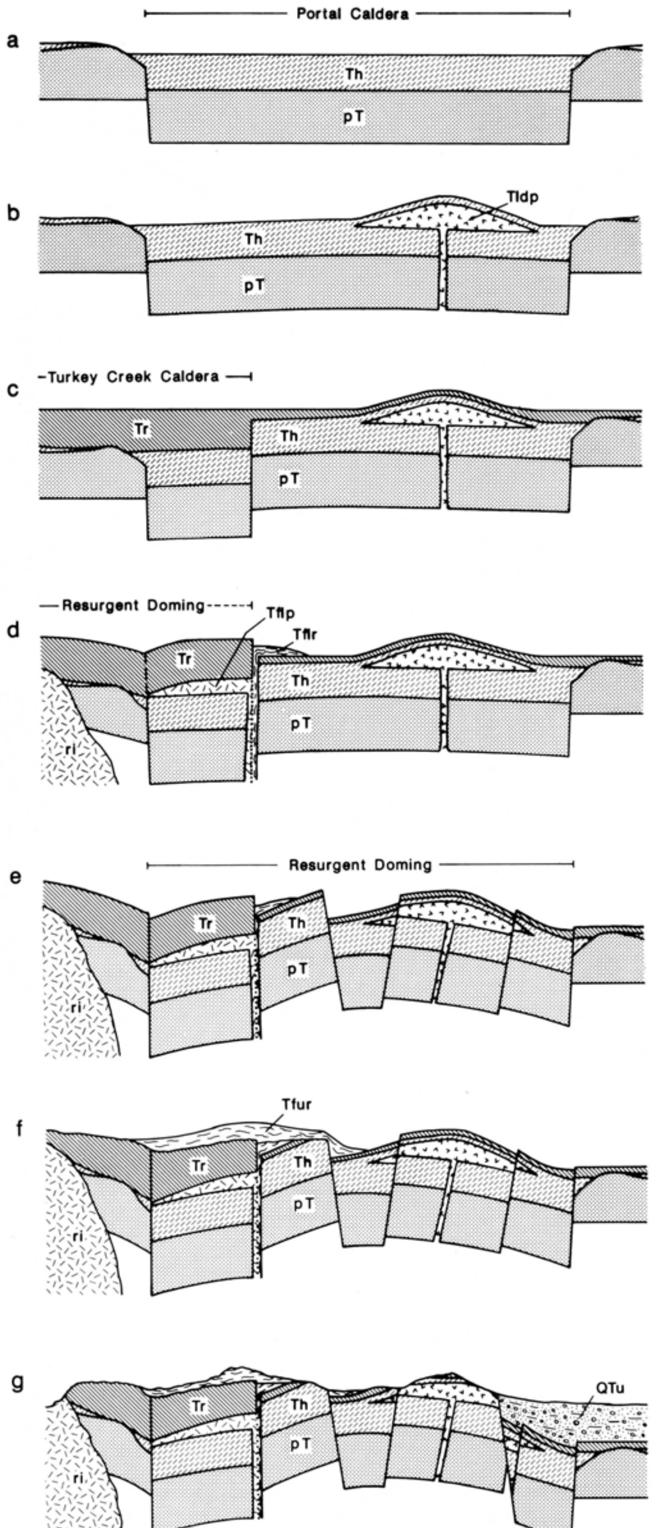

FIGURE 3—Schematic cross sections, showing structural development of the eastern Chiricahuas: **a,** formation of the Portal caldera; **b,** intrusion of the latite of Darnell Peak; **c,** formation of the Turkey Creek caldera; **d,** beginning of resurgence of the Turkey Creek caldera and intrusion of latite porphyry in the zone of overlap that lifts caldera-fill above outflow sheet of Rhyolite Canyon Formation; **e,** resurgent doming of the Portal caldera; **f,** eruption of the upper rhyolite member of the Fife Canyon volcanics; **g,** Basin and Range faulting and erosion produces present-day topography. pT = pre-Tertiary rocks; Th = tuff of Horseshoe Canyon; Tldp = latite of Darnell Peak; Tr = Rhyolite Canyon Formation; Tflp = porphyritic latite member, Fife Canyon volcanics; Tflr = lower rhyolite member, Fife Canyon volcanics; ri = resurgent intrusion; Tfur = upper rhyolite member, Fife Canyon volcanics; QTu = Quaternary deposits, undifferentiated.

Day 1

Mileage

0.0 **STOP 1. Barfoot Lookout** (Buena Vista Peak). Overview of the northern sector of the Portal caldera and precaldera rhyolites of Cave Creek. Backtrack to Onion Saddle. **0.1**

0.1 **Turn left** onto FS-42D. **2.0**

2.1 Onion Saddle. **Turn right** (east) and descend into the Cave Creek drainage. **3.3**

5.4 Paradise Road fork. **Veer right** (uphill) toward Portal, Arizona. **4.1**

9.5 Southwestern Research Station (SWRS) and Herb Martyr road intersection. **Continue straight** (on pavement). **1.2**

10.7 **STOP 2. Outflow sheet of tuff of Horseshoe Canyon.** Pull off on right. Cross meadow on left side of road and examine cliffs on north side of Cave Creek. This is outflow tuff of Horseshoe Canyon, preserved in a downfaulted block along Cave Creek. Equivalent Horseshoe Canyon tuff is exposed high on Portal Peak, and a possible erosional remnant occurs atop Silver Peak to the north (Pallister, written comm. 1988). The Horseshoe Canyon is characterized by sparse quartz (1 mm rounded grains), chalky sanidine (1–2 mm laths), and very sparse biotite. Here, the tuff is densely welded (eutaxitic) and relatively lithic-poor; except for the few biotite grains, it is very similar in outcrop appearance to Rhyolite Canyon tuff. However, the tuff of Horseshoe Canyon is generally more alkaline than the Rhyolite Canyon (compare analyses in Table 1 with those in table 1 of Pallister and du Bray, this volume).

Return to cars and continue down-canyon to east. **0.7**

11.4 Pass Sunny Flat campground (on left). Cliffs above Sunny Flat are rhyolite lava flows of Cave Creek, stratigraphically below the tuff of Horseshoe Canyon. **0.1**

11.5 Pass South Fork Road (FS-42E); **bear left** toward Portal. **4.1**

15.6 Paradise Road junction (FS-42B); **bear right** (continue on pavement). **0.6**

16.2 Portal, Arizona; store and gas station; **continue straight** on main road. **0.7**

16.9 Junction with dirt road to San Simon (just beyond cattleguard); **continue straight** on main road. **5.7**

22.6 Junction with State Line Road (dirt road at cattleguard, also known as Portal Road; sign indicates direction to Douglas and Apache). **Bear right** (south toward Apache) on State Line Road (if very wet, proceed on pavement to US-80; then resume mileage at intersection of US-80 and State Line Road). **4.1**

26.7 Junction with US-80 at Arizona–New Mexico state line. **Continue south** on US-80. **2.35**

29.05 **Turn right** (west) on dirt access road to Horseshoe Canyon. Road is identified by second yellow real-estate sign on right and by mailbox labeled "Zent." Cross cattleguard and old railroad grade, then **veer left at Y** (toward corral and windmill). **2.75**

31.8 Cross old track parallel to mountain front. **0.5**

32.3 **STOP 3. Tuff of Horseshoe Canyon and latite of Darnel Peak.** Corral and gate at mouth of Horseshoe Canyon. Park here. The outcrop on the north side of the canyon exposes a fault sliver of the tuff of Horseshoe Canyon in contact with the latite of Darnel Peak. The tuff is exposed at creek level and in the lower part of the outcrop. Eutaxitic texture is poorly developed and the tuff contains large (to 30 cm) mafic and small (3–5 cm) felsic inclusions or fiamme. Outcrops high on the ridge south of the canyon mouth show spectacular mingling between the tuff and the latite sill, suggesting that both were fluid when brought into contact. This area may be close to a feeder zone for the ash-flow tuff. Consider possible origins of the inclusions here. Are the felsic inclusions recrystallized pumices (fiamme) . . . or melt inclusions?

Walk down wash to view exposures of latite sill (latite of Darnel Peak). Latite is also exposed in upper part of outcrop, but watch for loose rocks and rattlesnakes.

Walk through gate and across canyon to south. Exposures here show mingled Horseshoe Canyon tuff with angular felsic inclusions and irregular to angular mafic inclusions in mixed(?) gray matrix.

Return to cars and backtrack to Southwest Research Station.

Day 2

We complete the Portal caldera segment of the field trip in the early morning hours, en-route to the Ash Peak–Rhyolite Peak eruptive complex (Walker and Richter, this volume). Mileage begins at Southwest Research Station. **Follow previous route** from Southwest Research Station, 13.1 mi east (through Portal), **to intersection of Portal Road with State Line Road.**

13.1 **STOP 4. Overview stop** (with low-angle morning light). Good view (to west) of maroon to tan, massive, cliff-forming tuff of Horseshoe Canyon within the Portal caldera. The tuff dips to the south above a very thick section of rhyolite lavas and pyroclastic-flow deposits (rhyolite of Cave Creek) that underlie Portal Peak. The latite of Darnel Peak forms a thick sill within the tuff of Horseshoe Canyon; it is visible along the skyline south of Sulfur Draw.

Continue east on Portal Road, **turn north** on US-80 through Rodeo, New Mexico, and continue to junction with New Mexico Route 9, where the Ash Peak–Rhyolite Peak field-trip road log begins (Walker and Richter, this volume).

Ash Peak–Rhyolite Peak eruptive complex

Robert J. Walker[1] and Don H. Richter[2]

[1]*Radiation Center, Oregon State University, Corvallis, Oregon 97331;* [2]*Box 79, Winston, New Mexico 87943*

Introduction

The early Miocene (23.1 Ma, Richter et al., 1981, 1983) Ash Peak–Rhyolite Peak eruptive complex in southeastern Arizona (Fig. 1) affords an excellent opportunity to observe volcanic features resulting from different modes of rhyolitic and andesitic eruption. The geologic setting is well suited to investigate genetic relations between andesitic and rhyolitic magmas and to speculate on the association of magmatism and mineralization.

Rhyolite magmatism at the Ash Peak eruptive center began with the eruption of moderately crystal-rich, low-silica (73.5% SiO_2) then high-silica (76.2% SiO_2) rhyolite flows and pyroclastics, was followed by nearly aphyric high-silica (76.7% SiO_2) rhyolite flows and domes, and terminated (at the Rhyolite Peak eruptive center) with low-silica (72.6% SiO_2) porphyritic rhyolite flows and domes. Following the close of rhyolitic volcanism at these two centers, extrusion of andesite and basaltic andesite blanketed the area. The basement of the eruptive complex is comprised of basaltic andesite and andesite (51.4–61.7% SiO_2), probably of late Oligocene age (Richter et al., 1983). These andesitic flows are altered, generally oxidized, and amygdaloidal. They characteristically contain anomalously high potassium (to 9% K_2O), apparently concentrated in finely crystalline groundmass K-feldspar, which suggests post-eruption alkali metasomatism. Andesites erupted after the cessation of rhyolitic volcanism are distinctly different from the basement andesitic units. They are unaltered, vesicular, and show no evidence of potassium metasomatism.

Volcanology

Perhaps the most extraordinary volcanic feature at Ash Peak is the exposed interior of a pyroclastic breccia cone and vent plug that marks one of the principal eruptive sites. The interior of the breccia cone provides classic examples of impact structures, base-surge deposits, and epiclastic beds formed by reworking of the deposits between eruptions. Construction of the breccia cone took place relatively early in the rhyolitic cycle, but followed the extrusion of biotite rhyolite and the last of the basement andesite flows. Eruptions that built the pyroclastic breccia cone are interpreted to have been principally Vulcanian (characterized by "moderate to violent ejection of solid or very viscous hot fragments of new lava," Macdonald, 1972).

The base of the cone is composed of pale-yellow, lithic-poor, moderately crystal-rich biotite tuff. The main mass of the cone consists of pale-yellow to orange, pumice-lithic-crystal pyroclastic breccias that are now mostly altered to

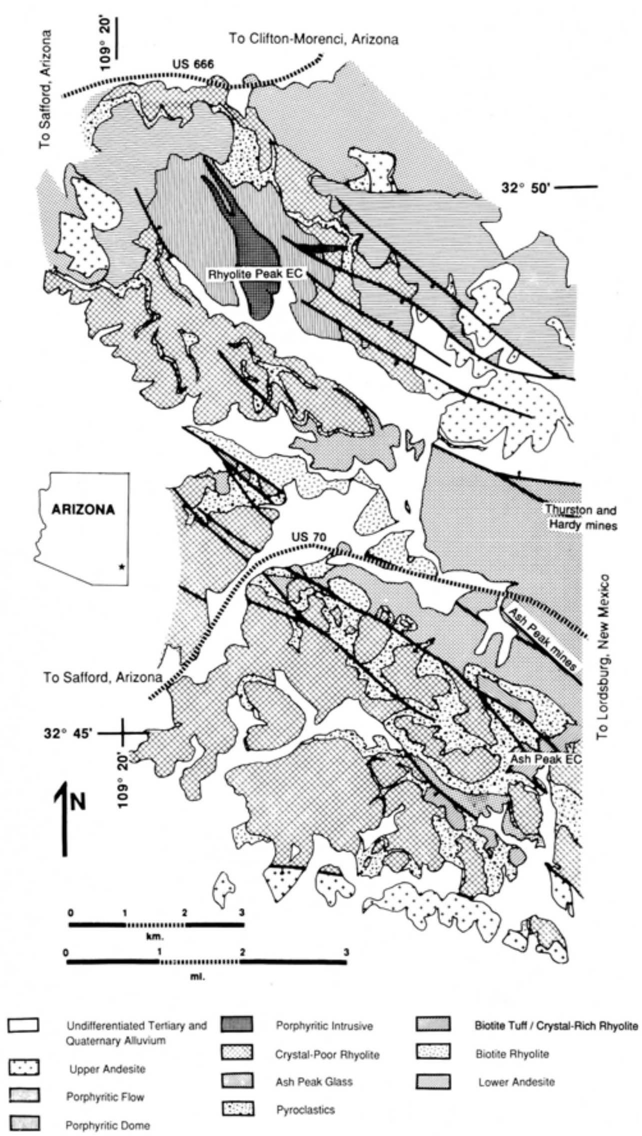

FIGURE 1—Location map and general geology of the Ash Peak–Rhyolite Peak eruptive complex (EC), southeastern Arizona (modified from Richter et al., 1981, 1983).

zeolite (chiefly clinoptilolite, Richter et al., 1981). Thin- to thick-bedded (0.5–3 m) pumice-lithic-crystal pyroclastic-breccia layers become finer-grained and pinch out over a distance of 3 km from the central vent. Intercalated with the early pyroclastic breccias and forming the vent plug are crystal-rich rhyolite flows and peripheral domes. Slope angles and the inferred basal diameter indicate that the pyroclastic-breccia cone was at least 200 m high. The upper portion of the cone preserves a pronounced angular discordance with overlying pyroclastic layers dipping inward toward the vent. This discordance has been interpreted to indicate that the principal vent varied in location during the construction of the cone (Richter et al., 1981). With the change in vent location, new eruptions blasted out preexisting material forming a summit crater. Subsequent eruptions filled the crater with material and deposited tephra on the inward-dipping surface.

Sparse, thin, poorly welded ash-flow horizons are interlayered with the thin- to thick-bedded breccias. Ash layers, accretionary lapilli, agglutinate, and epiclastic beds are minor components of the pyroclastic-breccia cone; all are generally altered to clinoptilolite (Richter et al., 1981).

The enigmatic Ash Peak Glass covers the west side of the pyroclastic cone. It is approximately 30 m thick, with a pumiceous basal breccia and a vitric upper zone containing a central zone of large spherulites. From near the summit of Ash Peak, the unit extends 1.2 km to the west and 1.8 km to the southwest, where it is entirely vitric and 4–5 m thick. The thickness and aspect ratio of the Ash Peak Glass, its glassy character, and presence of sparse lithic clasts suggests that it was not the product of a typical flow-dome building eruption. Available evidence suggests that the Ash Peak Glass is in fact an agglutinate formed by a Strombolian-type eruption of silicic magma following the construction of the major part of the pyroclastic cone.

Petrology and geochemistry

The Ash Peak–Rhyolite Peak eruptive complex provides an ideal example of trace-element immobility, despite extensive zeolitic alteration. Rhyolitic rocks associated with the Ash Peak eruptive center have been classified into five litho-chemical groups based on distinctive petrologic and/or geochemical characteristics. The five litho-chemical groups, from earliest to latest, are: biotite rhyolite, biotite tuff/crystal-rich rhyolite (BioT/Xtal-R), pyroclastics, Ash Peak Glass, and crystal-poor rhyolite.

The biotite rhyolite is moderately crystal-rich, biotite-bearing, usually vitric rhyolite. This unit represents the earliest rhyolitic flows in the area and locally is intercalated with the basement andesite. Samples of biotite rhyolite exhibit the most primitive geochemical signatures of the rhyolites analyzed in the Ash Peak area (Fig. 2).

Biotite tuff and crystal-rich rhyolites (up to 10% phenocrysts, dominantly sanidine) are petrologically dissimilar, but geochemically identical, rock types that stratigraphically and geochemically follow biotite rhyolite (Fig. 2). Chemical evidence for their consanguinity provides the basis for classification as a single litho-chemical group.

Chemical analyses have not been obtained on the pumice of the pumice-lithic-crystal pyroclastic breccias that make up the breccia cone. However, their stratigraphic position suggests that they post-date eruption of BioT/Xtal-R and mostly pre-date eruption of the Ash Peak Glass.

The litho-chemical group classified as the Ash Peak Glass has a complicated chemistry, exemplified by data from the

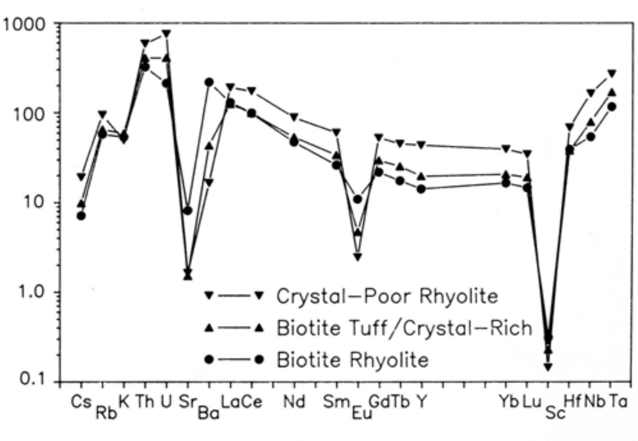

FIGURE 2—Cl chondrite-normalized geochemical patterns of principal rhyolite types associated with the Ash Peak eruptive center (Gd interpolated between Sm and Tb).

thick vitric mass forming the western shoulder of Ash Peak. Trace-element patterns are intermediate between BioT/Xtal-R rhyolite and crystal-poor rhyolite, although they are strongly depleted in light rare-earth elements (LREE) as shown in Fig. 3. Abundances of La, Ce, and Nd in the Ash Peak Glass are less than those of biotite rhyolite.

The latest and most voluminous rhyolites associated with the Ash Peak eruptive center are crystal-poor to aphyric, high-silica rhyolite flows and domes. These rocks are the most evolved geochemically; they exhibit the highest concentrations of incompatible elements (REE, U, Th, Rb, Nb, and Ta) and the lowest abundances of compatible elements (Ba, Sr, Eu, and Sc) (Fig. 2).

Despite differences in their macro- and microscopic appearance, the lower and upper andesites exhibit virtually identical trace-element patterns (Walker, 1988). With regard to trace-element abundances, the andesites are significantly higher in total REE than the early formed rhyolites (Fig. 4). Using available partition coefficients and appropriate liquidus mineralogies, it is not possible to form the Ash Peak rhyolites either by crystal fractionation or by partial melting of the last erupted basement andesites.

Assuming a parent magma of approximately biotite rhyolite composition, the other groups of rhyolite can be generated by simple incremental crystal-fractionation models. The fractionation trend from biotite rhyolite to crystal-poor rhyolite shows compatible-element depletion coupled with incompatible-element enrichment. Observed phenocryst mineralogies and modes were used to model the proportions of the liquidus constituents. Partition coefficients were taken from the available literature (Mahood and Hildreth, 1983; Nash and Crecraft, 1985). Modeled liquids, using 18 elements, match the analytical data for the various litho-chemical groups within experimental error (Walker, 1988).

Mineralization

In addition to lending its name to the eruptive complex, Ash Peak also refers to the mining district encompassing the mines, prospects, and claims to the north and east. The most important producers of the district are the shafts and declines located along the Ash Peak vein, approximately 0.8 km northeast of Ash Peak. The vein consists of silica and lesser carbonate replacement and fracture fillings in a northwest-trending fault zone that crosscuts basement andesite. Since the beginning of the century, mining has been intermittent, with silver (approximately 97,000 kg) as the most important commodity. In addition, minor amounts of gold, copper, and lead have been recovered (Lines, 1940). Today, silica is extracted for use as a flux by the various smelters servicing the large porphyry copper deposits of Arizona and New Mexico. The expense of transporting the silica is offset by recovery of the precious metals during smelting. North and east of Ash Peak, epithermal calcite–manganese-oxide veins were exploited, especially during wartime. Development is restricted to a number of shallow trenches and shafts (maximum depth 26 m) with beneficiation of the ore by hand-cobbing methods. Total production of nearly 1700 metric tons of 40% Mn ore has been reported (Wilson and Butler, 1930; Richter and Lawrence, 1983).

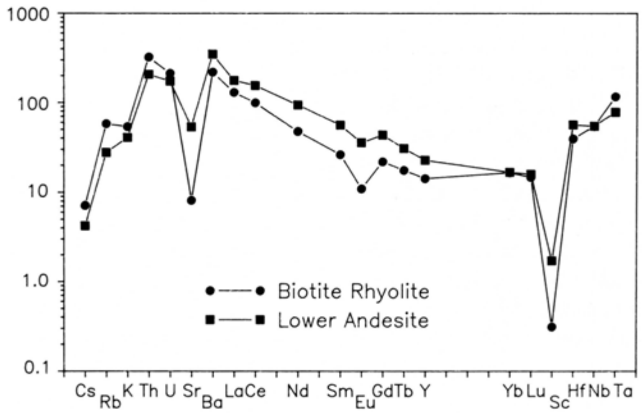

FIGURE 4—Cl chondrite-normalized geochemical patterns of the last-erupted andesite and first-erupted rhyolite (Gd interpolated between Sm and Tb).

Work in progress suggests that the manganese ore-forming solutions may have been derived in part from residual fluids concentrated during the last stages of crystallization of the rhyolite magma. Late-stage magmatic fluids, possibly in conjunction with meteoric waters, may have interacted with the nearly solidified magma before mixing with meteoric waters and migrating to the fracture zones. Elevated LREE patterns similar to those of the crystal-poor rhyolites, negative Ce anomalies, slight positive Eu anomalies, and very high concentrations of Ba, As, and Sb support this hypothesis. Although definitive chemical evidence is lacking, a similar genesis is postulated for the formation of the precious metal–silica veins at Ash Peak. The Ash Peak veins may represent a deeper level of exposure of the nearer-surface calcite–manganese-oxide system.

In addition, very thin and discontinuous veinlets of cassiterite and hematite occur in rhyolites of the Rhyolite Peak eruptive center. These occurrences of tin do not appear to be economically significant. However, their presence suggests the possibility of tin, tungsten, and/or molybdenum stockwork or porphyry-type deposits at depth.

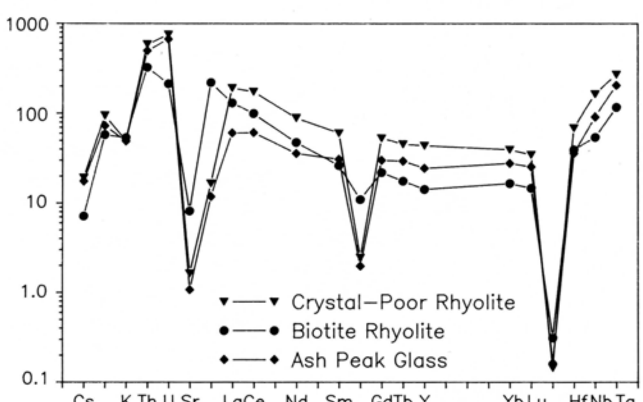

FIGURE 3—Cl chondrite-normalized geochemical pattern of the Ash Peak Glass and its relationship to other rhyolites associated with the Ash Peak eruptive center (Gd interpolated between Sm and Tb).

Discussion

Local intercalations of the last erupted andesites and first-erupted rhyolites, elevated trace-element abundances in andesite relative to rhyolite, and xenoliths with anatectic textures from rhyolite associated with the Rhyolite Peak eruptive center suggest that two different magmatic systems produced the andesites and the rhyolites. These data indicate that the rhyolites formed from partial melting of preexisting (Cretaceous–early Tertiary?) basaltic andesites rather than from modification of the middle Tertiary basement andesites (Walker and Richter, 1987).

The changes from andesitic to rhyolitic and back to andesitic volcanism may be in part due to major changes in the local tectonic regime (Gans, 1987; Gans et al., 1987). Deep crustal extension associated with the formation of the Pinaleno Mountains metamorphic core complex may have permitted basaltic magma to rise rapidly through the crust and act as a heat source for partial melting, rather than fractionating to andesite during a slower ascent (Walker and Richter, 1987). By changing the tectonic regime, parental basalts may either fractionate to intermediate compositions or act as heat sources for partial melting. This theory allows the lower and upper andesite to have the same geochemical signature despite their separation by large volumes of rhyolite and considerable time. Alternatively, a shallow crustal reservoir of silicic magma may have provided a "shadow zone" free of more mafic volcanism during the main rhyolitic episode, as suggested for several Pleistocene volcanic centers (Bacon, 1985).

Road log

This trip focuses primarily on the Ash Peak silicic eruptive complex in the northern Peloncillo Mountains approximately 60 mi north of the Southwest Research Station (SWRS) in Portal, Arizona. During the course of the trip we will cross and then roughly parallel the east side of the Peloncillo Mountains. With the exception of a relatively small area in the central Peloncillo Mountains, the entire range is underlain by middle Tertiary (35 to 25 Ma) volcanic rocks that range in composition from basalt to high-silica rhyolite (Drewes et al., 1985). Minor late Tertiary (6–2 Ma) activity has produced a few small-volume alkali basalt flows. Most of the volcanic rocks are products of rift eruptions, composite volcanoes, and dome-flow complexes; one shallow volcanic caldera, the 34–35 Ma Steins caldera, contains a thick section of densely welded intracaldera tuff and is outlined by a series of rhyolite domes (Richter et al., 1988).

The area of the Peloncillo Mountains not underlain by middle Tertiary volcanic rocks, between Granite Gap and Stein's Pass, exposes a sequence of Precambrian granitic rocks, Paleozoic sedimentary rocks, and Mesozoic sedimentary and volcanic rocks intruded by an Oligocene granitic pluton.

Mileage

0.0 Intersection of US-80 and NM-9, 5 mi north of Rodeo, New Mexico. **Drive north on US-80. 13.4**

13.4 Granite Gap. An 8 km^2 Oligocene ($\sim$32 Ma) quartz monzonite pluton is exposed in the roadcut. Small base-metal vein and replacement deposits (Cu–Pb–Zn–Ag ores) and scheelite-bearing skarns replace Paleozoic limestones proximal to the Granite Gap pluton. Mineralization is spacially associated with quartz monzonite or dacite porphyry dikes, which are chemically similar to, and probably comagmatic with, the Granite Gap pluton (Williams, 1978). **11.2**

24.6 At the small community and truck stop of Road Forks we **turn east** on I-10 and begin to cross the broad Animas Valley. Like many of the basins in the southern Basin and Range province with interior drainage systems, the Animas Valley contains a number of alkali playa lakes. **17.5**

42.1 **Leave I-10 at exit 22 and turn north on US-70** through the city of Lordsburg, New Mexico. Lordsburg, county seat of Hidalgo County, was the main residential and support community for the mines in the Lordsburg mining district to the southwest, which has produced more than 60 million dollars, chiefly in gold, silver, and copper. The mines have been inactive since 1975. The deposits are fissure-fillings along prominent northeast- and east-trending faults that transect the contact zone of a porphyritic granodionite pluton (56–59 Ma) which intrudes a sequence of Late Cretaceous andesite flows and breccias (Richter and Lawrence, 1983). **2.8**

44.9 **Veer left a Y-intersection** and continue driving northwest on US-70. Continue on US-70, off the Lordsburg Mesa, and into Duncan, Arizona, on the modern flood plain of the Gila River. Cliffs along the highway expose the Gila Conglomerate, a 2–20 Ma sequence of moderately indurated alluvial silt, sand, gravel, and conglomerate that is locally tuffaceous. **Continue through Duncan on US-70** and climb out of Gila River valley, through excellent exposures of Gila Conglomerate, and into the foothills of the northern Peloncillo Mountains. Roadcuts 10 mi west of Duncan expose massive andesite flows that pre-date the rhyolite eruptives at Ash Peak–Rhyolite Peak. **45.4**

90.3 **STOP 1. Ash Peak Mines. Turn left (south) off US-70** onto the dirt Ash Peak mines road; **continue about 0.5 mi to mine workings** for a brief discussion of the deposit. Future guidebook users: this area is posted and blasting is possible; **obtain permission before entering. Continue about 0.5 mi** on barely visible dirt road to broad saddle on east flank of Ash Peak. From here, a 1–3 mi hike (take lunch) will take us onto the pyroclastic cone of Ash Peak where we will examine the pyroclastic deposits of the breccia cone, and contemplate eruptive mechanisms for the Ash Peak Glass.

The walk begins on amygdaloidal basement andesite that underlies the cone. We cross a wide rhyolite dike, showing vertical flow-banding, then traverse the lower pyroclastic beds of the cone. From here to the eroded crater of the cone (on the east shoulder of Ash Peak), surge beds, bomb sags, and accretionary lapilli can be seen in a variety of pyroclastic-flow and air-fall deposits. At the crater, a prominent angular unconformity between outward-dipping cone deposits and inward-dipping vent deposits is well exposed. An irregular rhyolite plug is exposed in the eroded base of the crater.

The more adventuresome may hike up through more cone deposits to the Ash Peak Glass, about 100 m above the crater.

Geology and petrology of basalts and included mafic, ultramafic, and granulitic xenoliths of the Geronimo volcanic field, southeastern Arizona

Pamela D. Kempton[1] and Mike A. Dungan[2]

[1]*Department of Earth Sciences, The Open University, Milton Keynes, England MK7 6AA;*
[2]*Department of Geological Sciences, Southern Methodist University, Dallas, Texas 75275*

Introduction

In this paper, we review the geology and petrology of a type example of alkaline (as opposed to calc-alkaline; see Sawyer and Pallister, this volume) Basin and Range volcanism, the basaltic Geronimo volcanic field (GVF). Aspects that will be discussed are: (1) a general geologic overview of the volcanic field, (2) magmatic evolution of the Geronimo basalts, (3) petrogenesis of Type II ultramafic xenoliths and relationships to their host basalts, (4) magma/mantle interactions or mantle-enrichment processes in the sub-Geronimo mantle, and (5) petrology of GVF lower crustal granulites and evolution of the lower crust. More detailed discussion of each of these topics can be found in Kempton (1984, 1987), Kempton et al. (1984, 1987), and Menzies et al. (1985).

Geologic overview of the Geronimo volcanic field

The GVF is located in a Basin and Range graben at the intersection of the San Bernardino Valley with the San Simon Valley (Fig. 1). Although the San Bernardino Valley is several hundred kilometers in length, Pleistocene and Pliocene volcanic activity is localized for the most part at the intersection of the north–south-trending Basin and Range faults with the older northwest–southwest-trending structures (Fig. 2). It has been suggested that a preferred alignment of cinder cones parallel to the north–south-oriented, graben-bounding faults indicates the presence of concealed faults having similar orientations throughout the valley (Drewes, 1981; Lynch, 1978).

Most of the southern Arizona Basin and Range is tectonically quiescent, but the San Bernardino Valley has been historically active (Herd and McMasters, 1982; Drewes, 1981). Initiation of block faulting was probably coincident with the voluminous rhyolite extrusions which form a large part of the graben-bounding mountains, but the most recent reported activity was in 1887 when an earthquake resulted in the formation of a 76 km long, high-angle fault scarp along the southern extension of the valley (Aguillera, 1888; Herd and McMasters, 1982). As a result of concurrent faulting and volcanism, GVF basalts exposed on the flanks of the valley are older (3.5–9 Ma) and less voluminous than those on the valley floor (0.26–3.6 Ma; see Fig. 2) (Kempton et al., 1987).

Two lava groups are recognized on the basis of chemical and petrographic characteristics, as well as by physiographic and age distribution. *Flank lavas* are alkali olivine basalts, hawaiites, and mugearites; they are generally more evolved (Mg values range from 0.31 to 0.63), are relatively low in alkalis, and have low normative Ne contents (0–7 wt%) (Table 1). They also contain relatively few ultramafic xen-

TABLE 1—Major-element compositions of representative GVF basalts.

	Valley basalts				Flank basalts				
	Basanites			Nepheline Hawaiite	Alkali olivine basalt	Hawaiite	Mugearite		
Sample	D2[1,8]	pk-G-22[2,9]	Cochise maar[3,9]	pk-G-66[4,8]	D3[5,8]	pk-G-63[6,8]	pk-G-58[7]	Avg. valley	Avg. flank
SiO_2	45.75	45.12	44.93	47.29	46.67	48.74	52.48	46.29	47.93
TiO_2	2.16	2.05	2.32	1.89	2.20	2.57	1.48	2.23	2.11
Al_2O_3	16.18	16.32	16.29	16.67	15.64	16.79	17.35	15.89	16.08
Fe_2O_3	11.10	10.60	10.83	10.90	11.71	12.19	10.07	11.35	11.58
MnO	0.19	0.22	0.19	0.20	0.18	0.22	0.21	0.18	0.18
MgO	7.83	8.88	7.59	6.16	8.73	3.42	1.99	8.07	7.18
CaO	8.86	8.56	9.11	7.55	9.11	6.98	4.88	8.97	8.43
Na_2O	4.30	4.46	4.54	4.74	3.99	4.31	4.76	3.76	3.47
K_2O	2.13	2.55	2.20	2.66	0.85	2.15	3.11	1.90	1.52
P_2O_5	0.71	0.42	0.55	0.69	0.52	1.06	0.60	0.59	0.53
H_2O	0.85	0.74	0.91	—	1.10	1.43	1.73	—	—
Total	100.06	99.92	98.75	98.74	100.70	99.86	98.66	99.22	99.04
$Mg/(Mg+0.9\ Fe^{+2})$	0.61	0.65	0.61	0.55	0.62	0.38	0.30	0.61	0.58
Normative Ne	12.3	16.8	15.7	11.8	5.6	0.98	(Hy = 2.89)	7.9	1.0

[1]Dated basanite flow from Stop 1B, this road log; NW of Krentz Ranch, 31°40′N 109°18′W.
[2]Basaltic bomb from xenolith-bearing cone 1.5 mi SE of US Hwy 80, Stop 2A, this road log, 31°31′N 109°17′W.
[3]Maar ~4.5 mi SE of US Hwy 80, 31°27′N 109°16′W.
[4]Flow ~2 mi NW of Geronimo Trail, 31°23′N 109°17′W.
[5]Flow south of Mulberry Canyon, Pedregosa Mountains, 31°37′N 109°19′W.
[6]Mesa-capping flow, east side of Skeleton Canyon, Peloncillo Mountains, 31°35′N 109°04′W.
[7]Flow ~2 mi NE of Fairchild Ranch, Peloncillo Mountains, 31°32′N 109°06′W; average of analyses by 8 and 9.
[8]Analysts J. G. Fitton and D. James, University of Edinburgh; H_2O analyses by P. Kempton, NASA-JSC.
[9]Analyst P. Kempton, NASA-JSC (XRF).
Concentrations reported in wt%.

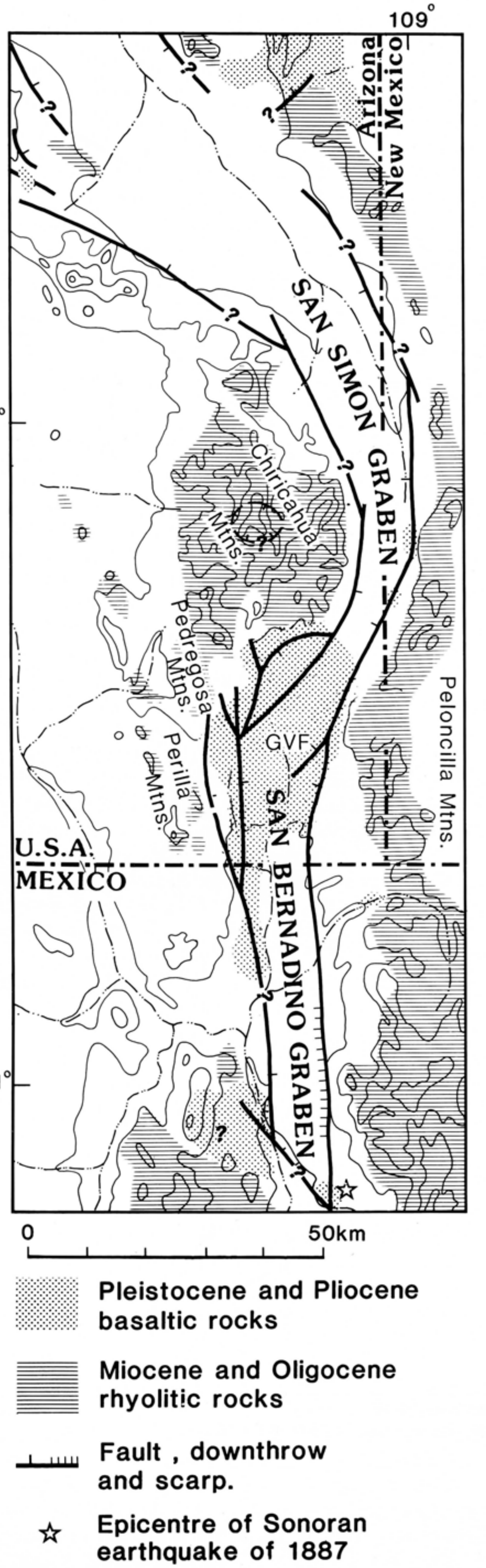

FIGURE 1—Basin and Range faults and general location of the Geronimo volcanic field. After Drewes (1981).

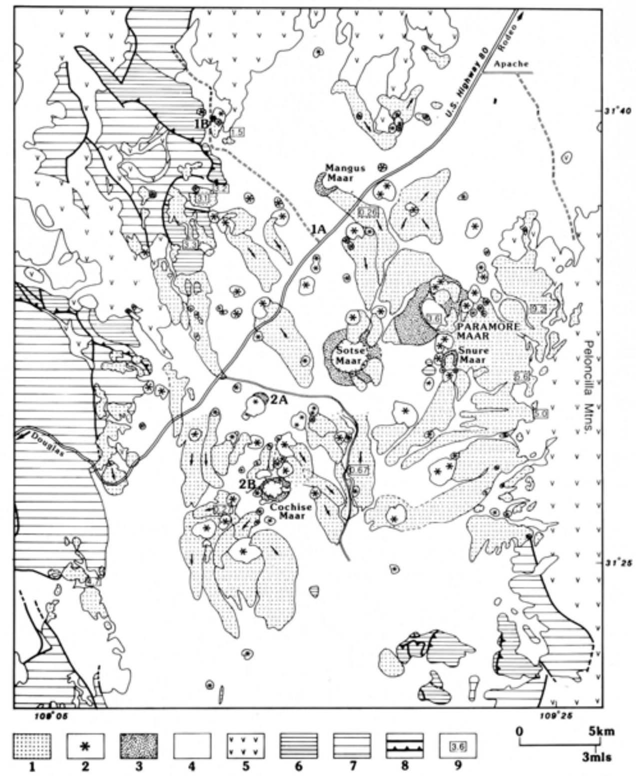

FIGURE 2—Geologic map of the Geronimo volcanic field. (1) GVF lava flows, (2) GVF cinder cones, (3) GVF pyroclastic units surrounding maars, (4) Quaternary alluvium, (5) Tertiary rhyolite and associated volcanic rocks, (6) Paleozoic sedimentary rocks, undifferentiated, (7) Mesozoic sedimentary and volcanic rocks, undifferentiated, (8) fault, (9) locations of dated GVF samples and age. Stratigraphy and distribution of rocks older than GVF volcanics generalized from Cooper (1959).

oliths, although megacrysts of plagioclase and anorthoclase and small felspathic xenoliths are common. Megacrysts of aluminous augite, spinel, olivine, orthopyroxene, and apatite occur less commonly. In contrast, the younger *valley lavas* are more strongly silica-undersaturated basanites and nepheline hawaiites; normative nepheline contents range from 5 to 18 wt% (Table 1). They exhibit a more limited range and include generally higher average Mg values (0.53–0.68), many of which are within the range for liquids calculated to be in equilibrium with mantle olivine compositions. Mafic, ultramafic and granulitic xenoliths, up to 45 cm in diameter, are common and locally abundant. Megacrysts of aluminous augite, olivine, spinel, plagioclase, and anorthoclase occur in most flows. In contrast to flank lavas where feldspar megacrysts predominate, augite and spinel are most common in valley basalts. Locally, amphibole and apatite are abundant.

In general, GVF alkali olivine basalts of the flank-lava group are fine-grained, porphyritic or microporphyritic rocks with groundmass textures ranging from intergranular to intersertal (Fig. 3a). Phenocrysts of plagioclase and olivine up to 2 mm in size are common, while clinopyroxene is generally confined to the groundmass. In contrast, the younger valley lavas are finer-grained and textures range from glassy to intersertal; less commonly, they have intergranular textures (Fig. 3b). Phenocrysts or microphenocrysts of plagioclase and olivine occur in the valley lavas, but clinopyroxene is far more abundant modally, both in the groundmass and as a phenocryst phase, than in flank lavas.

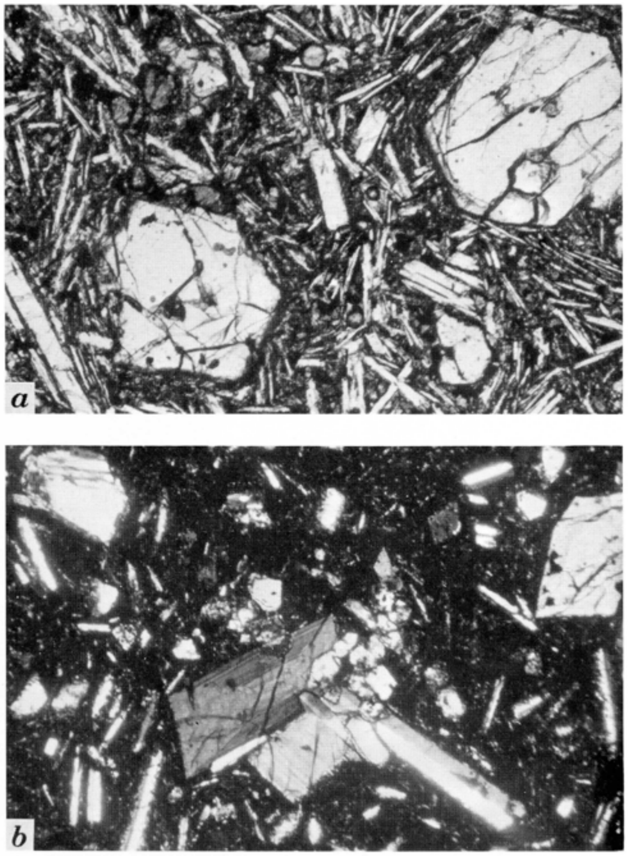

FIGURE 3—Photomicrographs of GVF flank and valley basalts. **a**, Sample pk-G-50, flank basanite; fine-grained, olivine + plagioclase microporphyry. **b**, sample 90-7, valley basanite; fine-grained, plagioclase + olivine + clinopyroxene microporphyry. Note sector zoning in clinopyroxene. Field of view 2.6 mm.

Magmatic evolution of the Geronimo volcanic field

Major-element mass-balance calculations and trace-element modeling (Kempton et al., 1987) indicate that flank basalts and some valley basalts record the effects of significant polybaric fractional crystallization that occurred as these magmas established conduits to the surface. These calculations demonstrate that low-pressure fractional crystallization alone cannot account for the compositional variations in relatively evolved lavas. Instead, fractionation of aluminous clinopyroxene + spinel ± olivine at moderate pressures, coupled with additional fractionation of kaersutite or plagioclase and Na- and Fe-rich pyroxene at lower pressure could have generated the compositional spectrum (see Table 1 and Kempton et al., 1987, for a summary of GVF basalt chemistry).

Conventional magma reservoirs did not exist within the crust beneath GVF. Instead, fractional crystallization took place by crystal plating against the walls of conduits as magmas ascended to the surface. Such interactions between alkalic basalts and conduit walls are recorded by crosscutting intrusive relations in composite xenoliths from GVF. The mineral assemblages and the relative proportions of phases subtracted in GVF mass-balance calculations are generally the same for evolved lavas from both flank and valley groups, regardless of the initial normative nepheline content (Kempton et al., 1987). These modal proportions are also similar to the relative abundance of these phases in Type II (aluminous augite group, see below) xenoliths. This suggests that these modal assemblages reflect cotectic proportions.

Although it has been generally maintained that basaltic rocks with greater than 5% normative nepheline fractionate to more silica-undersaturated compositions, away from the critical plane of silica undersaturation (Coombs and Wilkinson, 1969; Macdonald and Katsura, 1964), the cumulative effect of fractionating the described assemblages is to decrease the degree of undersaturation in the melt. This is primarily due to crystallization of spinel. At lower pressures where plagioclase crystallizes with olivine and clinopyroxene from alkalic basalt melts instead of spinel, fractionation could produce increasing silica undersaturation of the melt. However, fractionation of clinopyroxene + spinel + olivine from GVF alkali olivine basalts and basanites at moderate pressures results in decreasing silica undersaturation.

Petrogenesis of aluminous clinopyroxenites and amphibole peridotites

The majority of mantle-derived xenoliths included in alkalic basalts can be divided into two groups, the Cr-diopside series, or Type I, and the Al-augite series, or Type II (Wilshire and Shervais, 1975; Frey and Prinz, 1978). Type I xenoliths are generally regarded as the mantle source rocks to alkali basalts and their parent magmas. Type II xenoliths are thought to represent the mantle-level crystallization products of alkali basalts. The "type" terminology is adopted here, but the two groups are further subdivided to include the subgroups Type Ia, with light rare-earth elements/heavy rare-earth elements (LREE/HREE) in clinopyroxene <1, and Type Ib, with LREE/HREE in clinopyroxene >1) as defined by Kempton et al. (1984), and subgroups Type IIa and Type IIb as defined below.

In general, Type II xenoliths are more enriched in Fe, Al, Ti, and incompatible trace elements than Type I spinel lherzolites, and they exhibit a much greater spectrum of petrographic and chemical characteristics. Primary mineral phases in Type II xenoliths are aluminous augite + Al-spinel ± olivine, kaersutite, phlogopite, apatite, plagioclase, orthopyroxene, magnetite, and Fe-sulfides. Secondary glass, produced by the breakdown of clinopyroxene or amphibole, and rhönite, produced during the breakdown of amphibole or phlogopite, may also be present. Type II xenoliths present at GVF include clinopyroxenite, wehrlite, kaersutite peridotite, and rare websterite.

The spectrum of textural and chemical varieties of Type II xenoliths at GVF can be subdivided into two major groups. *Type IIa* inclusions have igneous textures in which clinopyroxene varies from irregularly shaped grains occurring with more equant olivine, to large poikilitic crystals which totally enclose olivine and spinel. Amphibole rarely occurs, except as minute patches replacing clinopyroxene, and only one spinel phase (pleonaste) is present. Exsolution of aluminous spinel from Type IIa clinopyroxene is characteristic (Fig. 4a); exsolution of orthopyroxene occurs, but is far less common. Relative to other Type II xenoliths, Type IIa peridotites have lower LREE/HREE and total Al_2O_3, but higher CaO, MgO, Sc, Cr and tetrahedral aluminum (Table 2).

Textures of anhydrous *Type IIb* mineral assemblages are essentially granoblastic (Fig. 4b). Crystals are equant in shape and grain boundaries are subplanar. Poikilitic relationships are uncommon. Clinopyroxene is characteristically free of both spinel and orthopyroxene exsolution. In addition, these xenoliths contain two spinel minerals, mag-

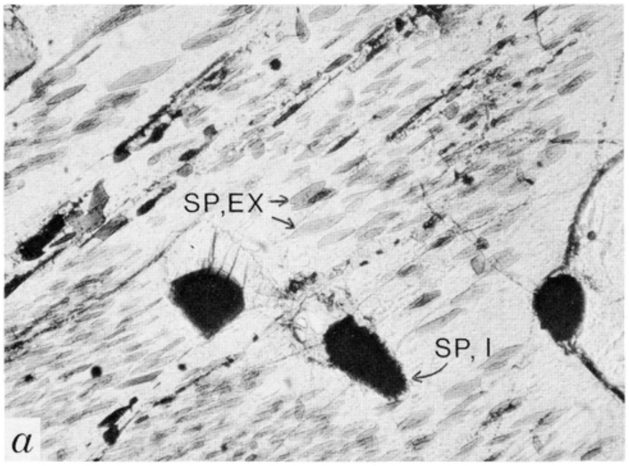

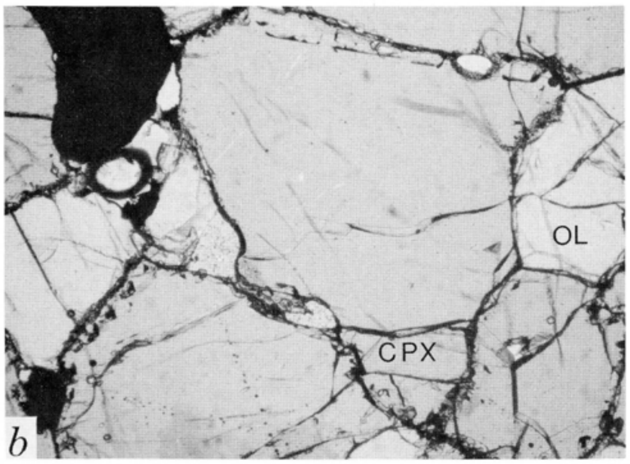

FIGURE 4—**a,** Photomicrograph of sample 20-5 from locality pk-G-20. Type IIa clinopyroxenite with abundant exsolution of spinel platelets (SP, EX) and spinel inclusions (SP, I). Uncrossed polars. Width of field 1.3 mm. **b,** Photomicrograph of sample 23B-7 from locality pk-G-23b. Type IIb olivine clinopyroxenite. Photomicrograph shows lack of exsolution in clinopyroxene phase. Uncrossed polars. CPX = clinopyroxene, OL = olivine. Width of field 2.6 mm.

TABLE 2—Major- and trace-element compositions of representative type II clinopyroxenes and amphiboles, GVF.

Sample	20-5[1]	20-8[2]	22-11[3]	23-M3[4]	22-11[5]	22-16[6]
SiO_2	49.17	47.80	47.56	47.02	40.10	42.52
TiO_2	1.38	1.98	1.88	2.02	6.11	3.44
Al_2O_3	6.38	8.93	9.04	9.46	14.54	14.78
FeO	5.68	7.86	7.21	7.46	9.29	5.79
MnO	0.16	0.17	0.16	0.20	0.15	0.10
MgO	14.23	12.84	12.88	12.88	13.28	16.44
CaO	22.54	19.26	19.43	19.75	10.97	10.33
Na_2O	0.53	1.33	1.31	1.34	2.58	3.35
K_2O	—	—	—	—	1.60	1.05
F	—	—	—	—	0.30	n.d.
H_2O	—	—	—	—	1.29	n.d.
Total	100.07	100.17	99.47	100.13	100.21	97.80
$Mg/(Mg+Fe^{+2})$	0.87	0.79	0.81	0.84	0.72	0.84
Al^{IV}/Al^{VI}	2.21	1.46	1.43	1.67	6.58	3.39
La	2.7	3.8	5.9	4.9	5.5	6.3
Ce	12	15	17	17	15	31
Nd	13	16	16	16	21	21
Sm	3.79	4.97	4.56	4.99	4.68	5.91
Eu	1.5	1.4	1.7	1.5	1.4	1.0
Tb	0.80	0.78	0.75	0.81	0.79	1.15
Yb	2.1	2.2	1.6	1.9	1.5	3.1
Lu	0.26	0.17	0.14	0.29	0.14	0.14
Cr	1800	60	100	47	90	1200
Ni	135	35	49	58	61	680
Sc	72	55	58	63	54	43
La/Yb	1.29	1.73	3.69	2.58	2.03	3.67

[1]Clinopyroxene from Type IIa anhydrous clinopyroxenite, from small spatter cone, pk-G-20, south of Cochise maar. 31°27′N 109°16′W.
[2]Clinopyroxene from Type IIb anhydrous clinopyroxenite. Same location as 1 above.
[3]Clinopyroxene from Type IIb amphibole-bearing clinopyroxenite. Sample location pk-G-22, ~1.5 mi SE of US Hwy 80. 31°31′N 109°17′W.
[4]Clinopyroxene megacryst from locality pk-G-23. Cinder cone ~1.5 mi SW of Cochise maar. 31°27′N 109°18′W.
[5]Vein amphibole attached to spinel lherzolite xenolith. Sample location pk-G-22.
[6]Amphibole from Type IIb hydrous clinopyroxenite. Same sample as 3 above.

Major elements reported in wt%. Analyst P. D. Kempton, Southern Methodist University (microprobe). Trace elements reported in ppm. Analyst P. D. Kempton, NASA-JSC (INAA).

netite, and pleonaste. Fe-sulfide globules are usually present as inclusions in all other mineral phases. Compositionally, they have higher LREE/HREE and total Al_2O_3, but lower CaO, MgO, Sc, Cr, and tetrahedral aluminum (Table 3).

Amphiboles can be found in both Type IIa and Type IIb xenoliths, but it is in xenoliths with textural and compositional characteristics of Type IIb that large poikilitic kaersutite amphibole crystals occur. These single, optically continuous crystals are commonly several centimeters in size and are observed in thin section enclosing or replacing clinopyroxenes of varying crystallographic orientations (Fig. 5a). Contacts between clinopyroxene and kaersutite may occur as distinct grain boundaries or as lobate replacement interfaces (Fig. 5b). Compositional zonation of clinopyroxene (depletion in Al_2O_3 and TiO_2 and enrichment in FeO) is observed adjacent to these contacts. Magnetite and Fe-sulfide globules are always present in Type IIb amphibole peridotites from GVF. The Fe-sulfides occur predominantly as spherical inclusions in amphibole, but may be found in clinopyroxene, olivine or spinel as well. Rhönite is present in trace amounts in most amphibole-bearing peridotites from GVF. It occurs as small prisms, in association with Ti-augite, olivine, Fe–Ti oxides, and glass, generally less than 150 μm in size, but crystals as large as 500 μm have been observed.

Amphibole and mica also occur as selvages or as discrete interstitial crystals in Type I xenoliths. Major-element compositions of amphiboles vary as a function of occurrence, such that amphibole megacrysts and Type II peridotite amphiboles are highest in FeO (9–10 wt%), while amphiboles associated with Type I xenoliths have FeO contents as low as 3.5 wt% (Table 2). Cr and Ni concentrations are generally low (less than 400 ppm Cr, 190 ppm Ni) except in amphibole associated with Type I lherzolites, where Cr_2O_3 concentrations may be as high as 1.4 wt% and Ni ranges from 650 to 700 ppm.

Some Type II xenoliths recrystallized subsequent to formation. In sample pk-G-21-4, a partially recrystallized Type IIa clinopyroxenite, the primary igneous clinopyroxene exhibits typical exsolution of spinel platelets (Fig. 6a). In recrystallized clinopyroxene, the spinel habit is more rod-like but maintains essentially the same orientation developed during exsolution of the primary clinopyroxene. Patches of amphibole replacing primary and recrystallized clinopyrox-

TABLE 3—Major- and trace-element compositions of representative GVF granulite xenoliths.

	GN21-6[1]	GN21-4[2]	GN42-2[3]	GN22-1[4]	GN22-5[5]
SiO_2	51.91	53.99	45.68	57.50	73.15
TiO_2	0.26	0.96	2.75	0.84	0.46
Al_2O_3	22.30	20.13	14.99	17.26	12.77
Fe_2O_3	4.29	7.63	11.82	6.91	2.92
MnO	0.07	0.14	0.17	0.10	0.06
MgO	5.28	3.93	8.75	4.01	0.76
CaO	11.32	7.40	11.08	6.40	1.95
Na_2O	3.69	4.68	3.02	4.15	2.77
K_2O	0.28	0.83	0.79	2.07	3.38
P_2O_5	0.03	0.30	0.17	0.22	0.10
Total	99.43	99.99	99.22	99.46	98.32
$Mg/(Mg+0.9\ Fe^{+2})$	0.74	0.55	0.63	0.58	0.38
Rb		1	7	38	196
Sr	1072	815	966	542	144
Zr	20	10	93	148	172
Nb	2	6	20	7	16
Y	7	13	24	23	29
Ba	226	635	273	663	502
La	4.5	17.6	12.0	22.5	46.8
Ce	8.2	35.8	28.0	49.9	93.4
Nd	4	23	18	30	40
Sm	1.12	3.60	5.15	5.15	9.04
Eu	0.74	1.94	1.98	1.40	1.11
Tb	0.16	0.56	0.92	0.63	1.20
Yb	0.56	1.01	2.01	2.22	2.58
Lu	0.05	0.16	0.31	0.35	0.41
Hf	0.53	0.51	2.5	4.0	5.6
Th	0.13	0.064	1.8	0.19	27
U	0.066	0.051	1.8	0.20	8

[1]One-pyroxene granulite, metacumulate, from sample locality pk-G-21 (Little Cochise crater). 31°27′N 109°16′W.
[2]Two-pyroxene granulite, metacumulate, sample locality pk-G-21.
[3]Amphibole-bearing, one-pyroxene metacumulate granulite. Sample locality large cinder cone, pk-G-42, 3 mi SW of Fairchild Ranch. 31°30′N 109°11′W.
[4]Two-pyroxene, two-feldspar metadiorite granulite from sample locality pk-G-22. 31°31′N 109°17′W.
[5]Anorthoclasite from sample locality pk-G-22.

Major elements and trace elements Rb, Sr, Zr, Nb, Y, and Ba analyzed by J. G. Fitton and D. James, University of Edinburgh (XRF). Rare-earth elements for all samples and U, Th, and Hf for samples GN22-1, GN42-2 and GN22-5 analyzed by P. Kempton, Open University (INAA). U, Th, and Hf for samples GN21-6 and GN21-4 analyzed by J. R. Budahn, U.S. Geological Survey, Denver.

ene are present along cleavage or exsolution lamellae, associated with spinel inclusions or exsolution (Fig. 6b). Thus, petrographic evidence shows that amphibole replacement was subsequent to spinel exsolution. This relationship establishes that amphibole in a given mantle xenolith need not have formed during crystallization of a single liquid. In this case, sufficient time elapsed for spinel exsolution to occur. The timing of amphibole crystallization in Type IIb amphibole peridotites is less well constrained, but the replacement textures, as well as the disequilibrium demonstrated by the compositional gradients in clinopyroxene observed adjacent to replacement interfaces (above and Kempton et al., 1982), indicate that amphibole and clinopyroxene did not crystallize together.

As a group, LREE enrichment in Type II xenoliths from GVF increases with decreasing Mg number, and with decreasing Cr and Ni contents from Type IIa to Type IIb, suggesting that Type IIb xenoliths were crystallized from slightly more evolved liquids. These and other differences in trace-element and major-element compositions of Type

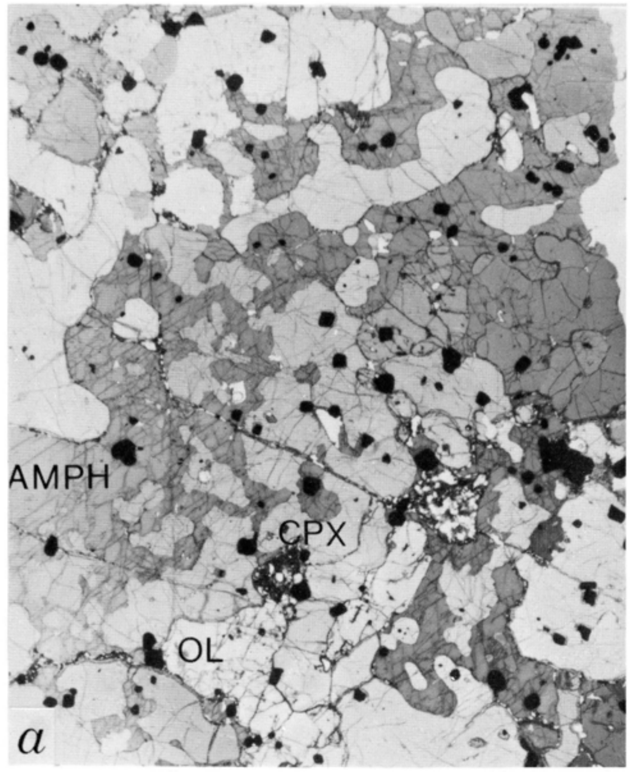

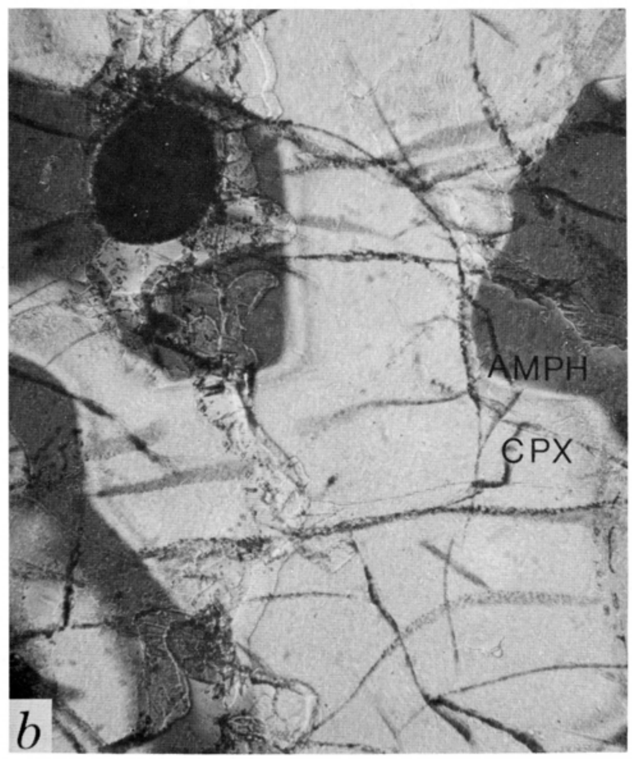

FIGURE 5—**a,** Photomicrograph of sample 90-37-2 from locality pk-G-22. Type IIb amphibole peridotite. Figure shows poikilitic amphibole that replaces clinopyroxenes of varying crystallographic orientations throughout the field of view. Uncrossed polars. Width of field 1.9 cm. **b,** Photomicrograph of sample 22-11 from locality pk-G-22. Type IIb kaersutite peridotite. Poikilitic amphibole in replacement association with clinopyroxene and amphibole. Width of field 1.9 mm. AMPH = amphibole, OL = olivine, CPX = Al-augite clinopyroxene.

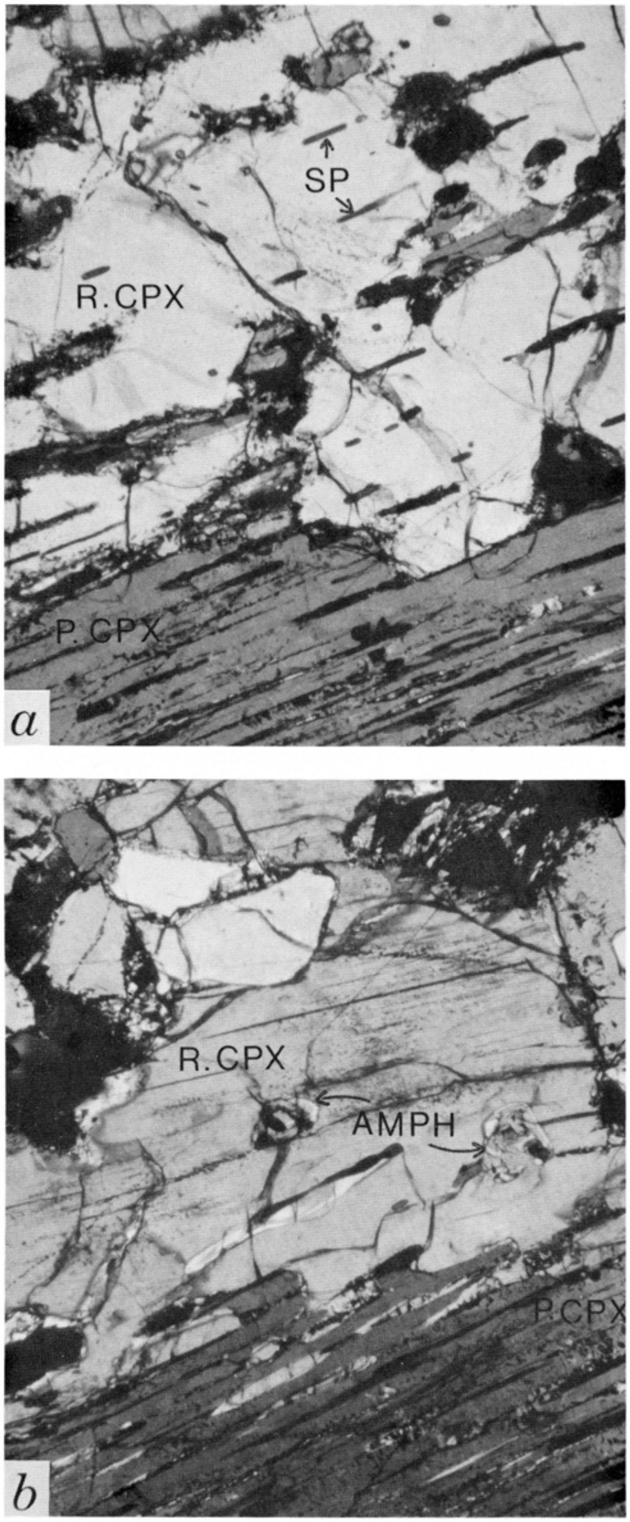

FIGURE 6—Photomicrographs of partially recrystallized Type IIa olivine clinopyroxenite 21-4 from locality pk-G-21. The primary clinopyroxene (P.CPX) contains exsolution lamellae of orthopyroxene and platelets of spinel. The recrystallized clinopyroxene (R.CPX) contains spinel inclusions which are elongate parallel to the original exsolution direction; orthopyroxene exsolution is absent. Amphibole replacement occurs in both recrystallized and unrecrystallized clinopyroxene and is frequently associated with spinel inclusions or exsolution (**b**). Crossed polars. Width of field 1.9 mm.

II pyroxenes can be attributed to relatively small degrees of crystal fractionation from a range of initial magma compositions like that seen in the GVF primitive lava suite (Kempton, 1984).

All Type II amphiboles, micas, and clinopyroxenes from GVF have radiogenic Nd-isotopic ratios and non-radiogenic Sr-isotopic ratios ($^{87}Sr/^{86}Sr$ = 0.70277–0.70331; $^{143}Nd/^{144}Nd$ = 0.51284–0.51311) which overlap the isotopic values for GVF basalts ($^{87}Sr/^{86}Sr$ = 0.70285–0.70379; $^{143}Nd/^{144}Nd$ = 0.51299–0.513037; Menzies et al., 1984, and Kempton, unpubl. data). The identical isotopic ratios measured in these minerals and the host magmas at Geronimo argue for a close genetic link. Just as major- and trace-element modeling of GVF basalts suggests that fractionation of Type II mineral assemblages can account for much of the compositional variation in these basalts, similar modeling for Type II assemblages suggests that, although not cognate, these xenoliths are probably cumulates from crystallization of basaltic magmas that were similar in composition to their host lavas.

Magma–mantle interactions and mantle-enrichment processes

It is currently accepted that Type I peridotites represent mantle that was variously depleted by extraction of crust, but that many Type I xenoliths have undergone varying degrees of secondary enrichment by reaction with Fe–Ti silicate melts or K-rich hydrous fluids that migrated through the upper mantle (Hawkesworth et al., 1984). Type examples of the former (i.e., mantle–silicate-melt interactions) are found at GVF in the form of composite and modally metasomatized xenoliths.

Structural relationships between Type I and Type II xenoliths at GVF can be summarized using the following four categories.

1. Type I/Type I composite xenoliths have either Cr-diopside, websterite, or clinopyroxenite veins crosscutting spinel lherzolite or harzburgite hosts. Contacts between lherzolite wall rock and pyroxene-rich vein assemblages are usually sharp and planar, and the veins are thin (1–2 cm). Grain size is generally uniform throughout the rock, but some vein pyroxenes may be significantly larger than the host phases; these often exhibit broad exsolution lamellae. In contrast, the host pyroxenes are typically free of exsolution. Type I veins are generally oriented parallel or subparallel to foliation in the host.

2. Type II/Type I composites consist of olivine-rich lherzolite hosts crosscut by more Fe-, Al-, and Ti-rich vein assemblages, usually clinopyroxenite. Contacts are sharp and the orientation of the vein is typically not parallel to foliation in the host. Pyroxene-rich layers which branch, intersect, and locally appear to have been folded or faulted are found at Kilbourne Hole and San Carlos (Irving, 1980). Veins up to 5 cm in width have been observed at GVF, but larger veins (10–15 cm) are reported from other localities (Wilshire and Shervais, 1975; Irving, 1980). Vein minerals average 1 to 2 mm larger than those in the host. Compositional gradients adjacent to the host–vein boundary are inferred from thin sections in which pale-green Cr-diopside and golden-brown Cr-spinel in the lherzolite wall rock become progressively more gray and grayish green toward the vein contact. Such changes indicate progressive substitution of Fe and Al for Cr in the two minerals.

3. Type II/Type I *hydrous* composite xenoliths at GVF consist of the assemblage kaersutite ± phlogopite ± pla-

gioclase ± spinel ± apatite ± sulfides. Amphibole veins and selvages typically transect the plane of mineral layering or foliation at a high angle, indicating that the amphibole veins postdate the anhydrous mineral layering of the peridotite. Amphibole in the host lherzolite part of some GVF Type II/Type I hydrous composites preferentially occurs as single crystals poikilitically enclosing Cr-spinel. Clinopyroxene is completely replaced by amphibole within a 1–2 mm wide zone adjacent to the amphibole selvages. The degree of cpx replacement decreases with distance from the selvage.

4. The composite relationship in which Type II lithologies crosscut a host with transitional Type I–II characteristics (Type II/Type II) consists typically of dark Al-augite clinopyroxene and spinel ± olivine veins which crosscut wehrlite hosts. Olivine is far more abundant in the host than in the vein; it is typically enclosed in sub-poikilitic to poikilitic fashion by aluminous augite in the host. Veins range from anastomosing, millimeter-size veinlets to centimeter-size dikes. Compositionally, the wall-rock phases of this composite type are intermediate between Mg-rich Type I inclusions and Fe-rich Type II xenoliths and, thus, have been interpreted as representing extensively modified Type I lherzolite wall rock (Kempton, 1984; Wilshire, 1984).

Compositional variations in mineral chemistry adjacent to veins in composite xenoliths at GVF are described in detail by Kempton (1987); similar variations for several other localities in the western U.S. are given by Wilshire et al. (1985). The major conclusion drawn from these studies is that silicate- or H_2O-rich fluids which interact with the mantle may alter the major- and trace-element composition of the original mantle and result in modal metasomatism, e.g., in xenoliths bearing secondary hydrous phases or exhibiting composite relationships. Modal metasomatism may be superimposed upon the range of mantle compositions produced by differing degrees of partial melting (Type Ia) and upon the enigmatic LREE-enriched Type Ib inclusions.

Most anhydrous veins in composite samples are attributed to crystallization of basanite magma within conduits as the magmas ascend through the mantle. These interactions may involve re-equilibration of incompatible trace elements, REE and isotopes, or more complete major-element readjustment as in Type II/Type II composite rocks. This process enriches the upper mantle in Al, Ti, Ca, Fe, and incompatible elements by modifying the compositions of primary mineral phases adjacent to veins.

Whole-rock enrichment of incompatible trace elements plus Na and K is greatest where secondary hydrous phases have crystallized in the wall rock. However, compositional variations in primary lherzolite mineral phases adjacent to amphibole selvages and veins are distinct from those adjacent to anhydrous vein types. As a result of reaction with the hydrous fluid represented by the vein minerals, clinopyroxene in the wall rock immediately adjacent to an amphibole selvage is often totally replaced by amphibole. The overall effect of crystallizing amphibole within the peridotite wall rock is to increase the concentrations of Al, Ti, and Fe; but, where present, primary clinopyroxene, orthopyroxene, and spinel show *decreasing* concentrations of Al and Ti toward the selvage. With respect to the vein minerals, concentrations of the compatible elements Mg and Cr are highest in amphibole which has crystallized within the wall rock farthest from the selvage; concentrations of incompatible elements such as Ti and K are constant in the selvage, but *decrease* away from the contact. The latter is significant because it implies that enrichment in incompatible elements may not necessarily increase farther from veins by transport of CO_2–H_2O fluids, as has been suggested by Menzies et al. (1985).

Whole-rock trace-element analyses of host and vein fractions of composite xenoliths indicate that veins typically have significantly higher concentrations of incompatible trace elements than the adjacent host (Irving, 1980; Kempton, unpubl. data). This is essentially a function of the higher modal proportion of incompatible element-rich phases such as clinopyroxene or amphibole in the veins; REE concentrations in clinopyroxene are essentially identical in both host and vein regardless of composite xenolith type (Kempton et al., 1984; Frey and Prinz, 1978). This observation contrasts markedly with the compositional gradients observed for major elements in host–vein composite pairs (Kempton, 1987; Wilshire et al., 1985).

It has been suggested that the enrichment in incompatible trace elements in Type Ib lherzolites is due to infiltration of trace-element-enriched CO_2 fluids exsolved from magmas adjacent to veins like those in composite xenoliths (Menzies et al., 1985). Yet, in addition to their elevated LREE/HREE ratios, Type Ib pyroxenes are known to have substantially lower Al_2O_3 contents and higher MgO and Cr/Al ratios than Type Ia (Kempton, 1987). Aside from the problem of exsolving a CO_2-rich fluid from a silicate melt at mantle pressures and temperatures (Pasteris, 1987), such fluids dissolve only minor quantities of major elements (Eggler, 1987) and would, therefore, be unable to produce a significant change in the Cr/Al or Mg/Fe ratio of the mantle through which they pass. In addition, variations in mineral chemistry across host–vein contacts (Fig. 7) do not result in Type Ib characteristics, clearly demonstrating that veining and modal metasomatism are not responsible for this enigmatic peridotite type. Downes (1987) has suggested a correlation of trace-element enrichment with petrographic characteristics for spinel lherzolites from the Massif Central, but this correlation is as yet undocumented in xenolith suites from the southwestern U.S.

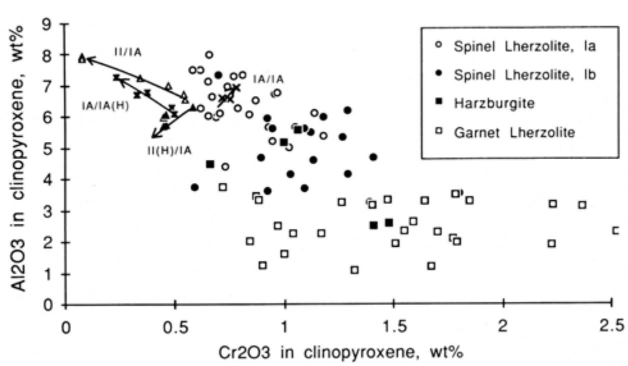

FIGURE 7—Al_2O_3 versus Cr_2O_3 concentrations in clinopyroxenes from Type Ia and Type Ib spinel lherzolites, garnet lherzolites, and harzburgites. Variations in pyroxene composition associated with vein formation are shown by arrows; arrows point from the host toward the vein. Composite samples include Type I/Type I (20-9), Type II (anhydrous)/Type I (20-10), pargasite-bearing Type I/Type I (23b-3) and Type II (hydrous)/Type I (22-16). Spinel lherzolite and harzburgite data from Frey and Green (1974), Frey and Prinz (1978), Jagoutz et al. (1979), Kempton (unpubl. data), Kurat et al. (1980), Press et al. (1986); garnet lherzolite data from MacGregor (1979) and Ehrenberg (1982).

Nature of the lower crust beneath GVF

GVF granulite xenoliths are fine- to medium-grained, foliated or banded, feldspathic, metaigneous gneisses. Mineralogically and compositionally, the xenoliths fall into four groups. The first group contains two-pyroxene granulites that are composed of plagioclase (andesine to labradorite) + clinopyroxene (Mg-augite) + orthopyroxene (hypersthene) + apatite + K-feldspar + ilmenite ± quartz. These typically contain abundant, large primary mineral/melt inclusions in which apatite, K-feldspar, and quartz are the major crystalline phases. The second group is more diverse compositionally and modally, but lacks K-feldspar. As in the first group, some xenoliths in the second group also contain two pyroxenes (Mg-augite and hypersthene), plagioclase (andesine to labradorite), magnetite, and traces of apatite. Others, however, contain only one pyroxene, an aluminous Mg-augite, plus a more calcic plagioclase (labradorite to bytownite) + an aluminous spinel ± olivine ± apatite ± magnetite. Clinopyroxene and spinel compositions in this group are remarkably similar to the Type II ultramafic peridotite minerals described previously. The third group contains members from both of the groups described above, but, in addition, secondary amphibole and rare scapolite are present. Samples in the fourth group are effectively devoid of mafic silicate phases; they consist of K-feldspar (anorthoclase or microcline) ± plagioclase ± quartz ± apatite ± magnetite.

Because none of the GVF granulites contain garnet, pressures of equilibration cannot be directly estimated, but temperature calculations based on two-pyroxene pairs yield values of 890–960°C for the Wells geothermometer and 840–940°C for the Wood–Banno geothermometer. Assuming a geothermal gradient of approximately 30°C/km (Padovani and Carter, 1977a), the Geronimo granulites would have equilibrated between 28 and 32 km depth, roughly the position of the MOHO beneath the Basin and Range.

Compositionally, the granulites are mafic to intermediate rocks (44–73 wt% SiO_2; Mg numbers, 38–79), and as a group demonstrate poor correlation of major- and trace-element concentrations with Mg number. The K-feldspar-bearing inclusions exhibit limited variation in major-element composition and differ from all other GVF granulites in being quartz normative ("Meta-Diorites" Fig. 8A), having higher SiO_2 and alkalis, and lower CaO (Table 3). In contrast, the one- and two-pyroxene, K-feldspar-free granulites range from Ne to Hy normative (Fig. 8A). The one-pyroxene granulites are further distinguished by their higher Mg numbers, similar to the Type II ultramafic cumulate xenoliths occurring at GVF (Table 3). GVF granulites are compositionally unlike their host basalts, but the K-feldspar-bearing inclusions have major- and trace-element compositions which are similar to high-K andesite or diorite. In fact, these granulites have trace-element characteristics not unlike the calc-alkaline volcanic rocks from the Sierra Madre Occidental in eastern Mexico (Gunderson et al., 1986). In trace-element discrimination diagrams (Pearce and Cann, 1973), the K-feldspar-bearing metadiorites have calc-alkaline affinities.

All GVF granulites are LREE enriched relative to HREE, but the K-feldspar-bearing metadiorites are more enriched in total REE (La = 67–74 x chondrites), and have smooth (Eu/Eu* = 0.8–0.9), moderately steep (La/Yb = 5–6) patterns (see Fig. 9a, b). One-pyroxene granulites and K-feldspar-free, two-pyroxene granulites have lower total REE (La = 8–53 x chondrites) with distinct, positive Eu anomalies (Eu/Eu* = 1–2) and more variable LREE enrichment (La/Yb = 3–11), typical of rocks in which plagioclase is a cumulus phase. These rocks are termed "metacumulates" in the figures.

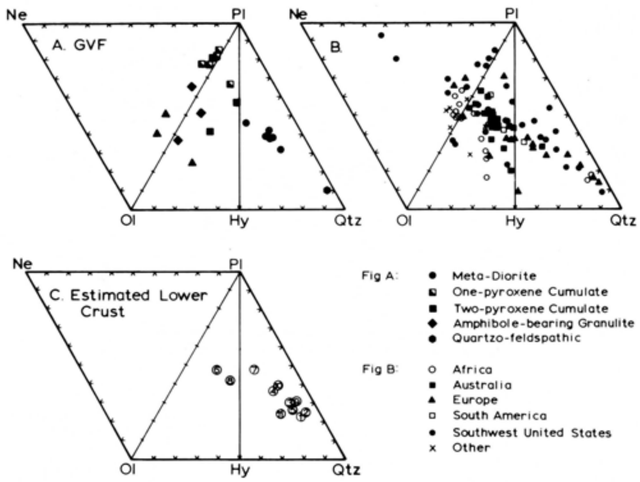

FIGURE 8—**A,** Normative compositions of GVF granulites. See text for discussion. **B,** Normative compositions of representative granulite xenoliths worldwide. Note the predominance of hypersthene-normative compositions. Data are from Padovani and Carter (1977), Selverstone and Stern (1983), Kay and Kay (1981, 1983), Stosch et al. (1986), Leyreloup et al. (1977), Rogers (1977), and Ehrenberg and Griffin (1979). **C,** Estimated crustal compositions recalculated to normative mineralogy: (1) Archean upper crust, (2) Archean middle crust, (3) Archean lower crust, (4) post-Archean mid/lower crust (Weaver and Tarney, 1984), (5) average crust (Weaver and Tarney, 1984), (6) lower crust (Poldervaart, 1955), (7) lower crust, island-arc model (Taylor, 1977), (8) whole crust, average based on crustal xenoliths in kimberlite from the Colorado Plateau (McGetchin and Silver, 1972), (9) lower crust based on Scourian gneisses, Scotland (Sheraton et al., 1973), (10) lower crust, based on mixtures of acidic and basic metamorphic rocks constrained by seismic velocities (Smithson, 1973), (11) lower crust based on metamorphic rocks in the lower 10 km of 40 km section from the Ivrea–Verbano zone (Mehnert, 1975).

All GVF granulites are, not unexpectedly, depleted in the radiogenic-heat-producing elements, Th and U, but only the metacumulate granulites have relatively low K as well (Fig. 9b, Table 3). Metacumulate granulites are enriched in relatively compatible elements such as Sr, while the metadiorites are more enriched in the highly incompatible elements Rb, Ba, REE, Zr, Nb, Hf, and alkalis (Fig. 9a, b). Trace-element concentrations in GVF metadiorites are remarkably similar to average Lewisian tonalite (Weaver and Tarney, 1984) with the notable exception that GVF metadiorites have higher K_2O and heavy REE's and essentially no depletion in Rb. All GVF granulites are distinct from the metasedimentary granulites found at Kilbourne Hole (Fig. 9b).

As a group, Sr-isotopic values for GVF granulites vary from 0.70301 to 0.81853 and $^{143}Nd/^{144}Nd$ varies from 0.513074 to 0.511987 (Kempton, unpubl. data). The two-pyroxene metadiorites, however, exhibit a much smaller overall range of values with lower $^{143}Nd/^{144}Nd$ (0.51219–0.51227) and higher $^{87}Sr/^{86}Sr$ (0.70795–0.71322) while one-pyroxene metacumulates overlap the isotopic values for GVF ultramafic Type II xenoliths and GVF basalts ($^{143}Nd/^{144}Nd$ = 0.51250–0.51282; $^{87}Sr/^{86}Sr$ = 0.70433–0.70961); two-pyroxene cumulates have an intermediate range of values ($^{143}Nd/^{144}Nd$ = 0.51222–0.51257; $^{87}Sr/^{86}Sr$ = 0.70779–0.71243). Most GVF granulites have Rb/Sr ratios which are too low to support the observed $^{87}Sr/^{86}Sr$, suggesting loss of Rb relative to Sr during the metamorphism, with the result

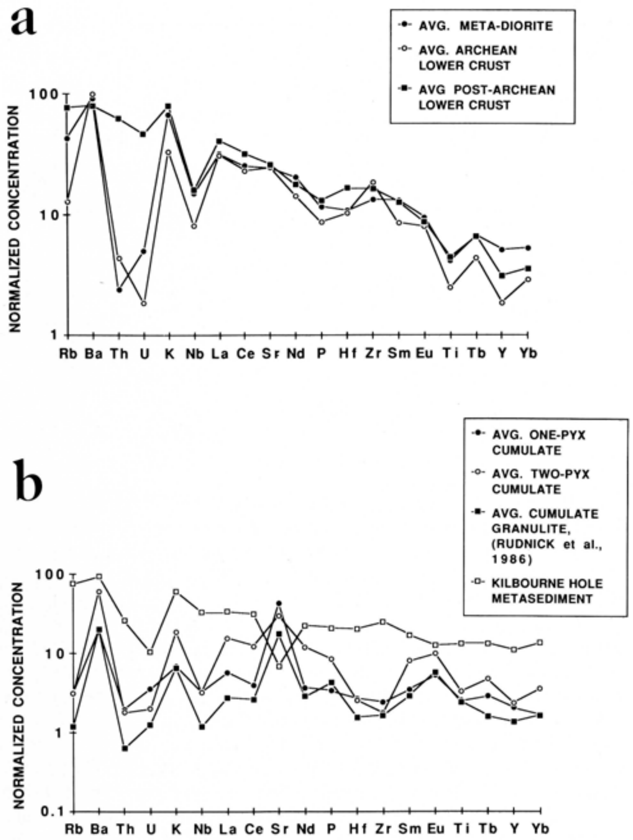

FIGURE 9—**a,** Incompatible trace-element concentrations in average GVF metadiorite compared with average Archean and post-Archean lower crust based on studies of Lewisian tonalite (Weaver and Tarney, 1984). **b,** Incompatible trace-element concentrations in average one- and two-pyroxene GVF metacumulate granulites compared with average metacumulate granulite from Queensland, Australia (Rudnick et al., 1986) and a metasedimentary granulite from Kilbourne Hole (Kempton, unpubl. data). All concentrations normalized to primordial-mantle values of Wood et al. (1981).

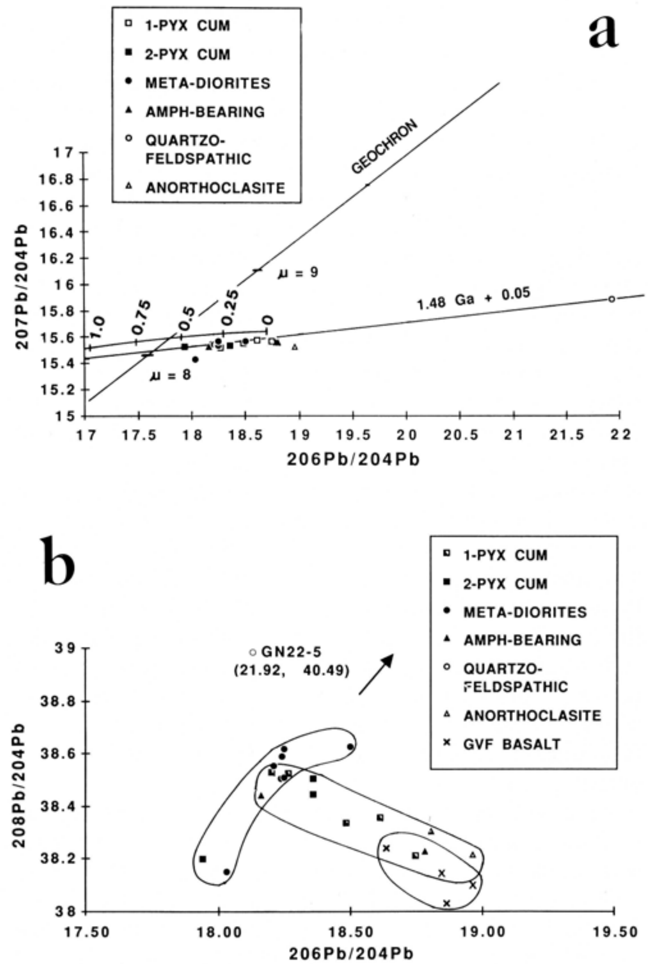

FIGURE 10—**a,** $^{207}Pb/^{204}Pb$ versus $^{206}Pb/^{204}Pb$ for GVF granulites. Regression of the data yields an age of 1.48 Ga$\pm$0.05. **b,** $^{208}Pb/^{204}Pb$ versus $^{206}Pb/^{204}Pb$. GVF basalt data are from Everson (1979) and Kempton (unpubl.).

that the Sr-isotopic relationships no longer record the age of the xenoliths. Nd and the other REE elements, on the other hand, are known to be less mobile during crustal processes. Calculated Nd model ages for metadiorites range from 1.1 to 1.4 Ga. Metacumulate granulites, however, exhibit a wide range of calculated ages and generally have low Sm/Nd ratios, inconsistent with their radiogenic $^{143}Nd/^{144}Nd$. This probably reflects relatively recent accumulation of low Sm/Nd clinopyroxene from a magma with a relatively high $^{143}Nd/^{144}Nd$, such that, again for these xenoliths, the isotopic values have no age significance.

Lead isotopes for GVF granulites exhibit the following range in values: $^{206}Pb/^{204}Pb$ = 18.198–21.921; $^{207}Pb/^{204}Pb$ = 15.522–15.887; $^{208}Pb/^{204}Pb$ = 38.152–40.488 and on a $^{207}Pb/^{204}Pb$ vs. $^{206}Pb/^{204}Pb$ diagram the GVF xenolith data exhibit a linear distribution that yields an age of approximately 1.5 Ga, i.e., similar to the range of Nd model ages for metadiorites (Fig. 10a). The GVF metacumulates, however, display a negative slope on a plot of $^{208}Pb/^{204}Pb$ vs. $^{206}Pb/^{204}Pb$ which trends away from the positive slope shown by the metadiorites (Fig. 10b). These data are interpreted as evidence that GVF metacumulate granulites are the crystallization products of Cenozoic alkalic magmas that were similar to their host basalts; isotopically, these parent magmas were contaminated by mixing with preexisting lower to middle crustal rocks such as the GVF metadiorites or early Proterozoic (1.4–1.6 Ga) granitic rocks like those exposed to the west and north. Similar mixing relationships are observed on isotopic diagrams of Pb vs. Sr and Pb vs. Nd.

In summary, chemical and isotopic analyses of granulite xenoliths from GVF indicate that the various granulite groups are not comagmtic. These data also document that the lower crust in this region is heterogeneous in composition and age. Two-pyroxene, two-feldspar granulites are intermediate-composition, mid-Proterozoic (~1.3–1.4 Ga) metadiorites that are depleted in Th, U, Rb, Nb, and Ti. K-feldspar-free granulites are younger and have more variable major- and trace-element compositions, but are distinctly more mafic and show enrichments in Sr, Ba, and Eu consistent with the accumulation of plagioclase. Similarities in mineral chemistry between metacumulus granulites and Type II ultramafic xenoliths suggest similar parent liquid compositions, although probably shallower depths of crystallization for the metacumulate granulites. The isotopic compositions of metacumulate granulites reflect mixing of Cenozoic mafic magmas with older lower crust, documenting a recent event of underplating of mafic material to the subcontinental lithosphere. As a whole, the GVF granulite suite suggests that the present lower crust is more mafic than most recent estimates of average lower crustal composition (Fig. 8).

Synthesis

The petrologic data presented in the previous sections can be summarized in a hypothetical cross section through the crust and upper mantle beneath GVF (Fig. 11). The strong enrichment in LREE relative to HREE and small range of HREE values in GVF basalts suggests that they were generated in a source where garnet was a residual phase. In addition, GVF basalts and ultramafic xenoliths show broadly OIB-like Nd- and Sr-isotopic signatures and indicate a time-integrated depletion in incompatible trace elements (Menzies et al., 1985). These data suggest that upwelling mantle material may have risen from the asthenosphere to penetrate the lithosphere. Although no petrofabric evidence for such intrusion of asthenosphere into lithosphere is observed in GVF ultramafic xenoliths, it is nonetheless consistent with the interpretation of upwelling mantle beneath the extensional regime of the Basin and Range.

Silicate melts generated in garnet lherzolite asthenosphere are not in equilibrium with overlying lithospheric mantle, and given sufficient time they must react with the mantle through which they ascend. Thus, intrusion of such silicate melts can enrich the mantle in magmaphile elements; first, and probably more importantly, by whole-scale addition of material crystallized as veins and dikes, but also by metasomatic interaction between these veins and the mantle itself. The nature and extent of this enrichment is dependent on a number of factors such as melt composition, volume of melt, magma ascent rate, etc. The variety of mafic/ultramafic layers, dikes and veins seen in the composite xenoliths attests to the complex history and multiplicity of events in the history in the sub-GVF mantle.

Unfortunately, the timing and depth relationships among the different vein assemblages cannot be established directly on the basis of GVF xenolith data alone. The lack of pressure estimates based on well-calibrated experimental data for most of the mantle xenoliths has prevented detailed evaluation of the P–T relationships among the various xenolith types, including composite relationships. However, field studies of peridotite massifs (Sinigoi et al., 1983; Wilshire and Pike, 1975) document that Type I websterite or clinopyroxenite dikes (Type I) are the earliest dikes to form and are followed by Type II mineral assemblages.

Partial melts are believed to first accumulate in horizontal layers. Then, as the critical melting threshold is exceeded, liquids are able to filter slowly toward lower-pressure zones. In so doing, these liquids fractionate, initially in-situ, via crystallization of Type I websterite or clinopyroxenite dikes. Continuous exchange with mantle wall rock over time results in decreasing SiO_2, rapid enrichments in Al_2O_3, and mild increases in FeO and CaO in the melt. Crystallization of these modified liquids produces transitional and Type II Al-augite dikes. Therefore, we suggest in Fig. 11 that Type I/Type I composite relationships occur where the melts are near their source of origin and where the volume of melt is most likely small. Here, melt compositions are probably not far from equilibrium with the surrounding peridotite and the compositions of minerals crystallized are similar to the wall-rock mineral phases. Farther from the garnet–lherzolite source in the overlying depleted, undisturbed lithosphere, however, these trace-element enriched melts are decidedly out of equilibrium and crystallization of Type II aluminous clinopyroxenite veins occurs. Metasomatic exchange may occur between the wall rock and the veins, involving modification or re-equilibration of incompatible trace elements, REE and isotopes (Type II/Type I), or more complete major-element adjustments as in Type II/Type II composites.

Composite ultramafic xenoliths record relatively small-scale intrusive events in the upper mantle, but decreasing

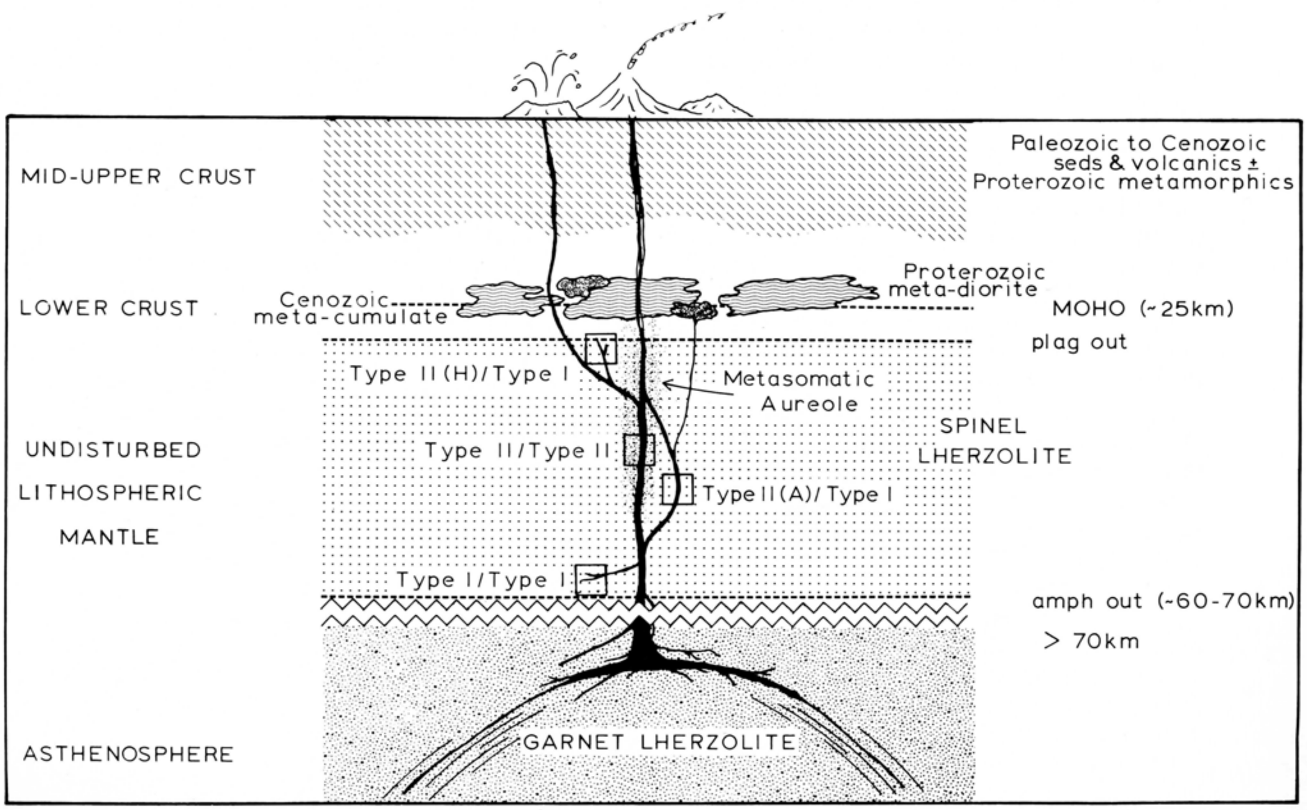

FIGURE 11—Schematic cross section of the crust and upper mantle beneath the Geronimo volcanic field. See text for discussion.

density contrasts may cause much larger volumes of basic–ultrabasic magma to stagnate in the lower crust at, or near, the crust–mantle boundary. Recent seismic-reflection studies have documented the existence of prominent, short, sub-horizontal reflectors in the lower continental crust beneath the extensional regime of the Basin and Range (Klemperer et al., 1986; Caruso, oral comm. 1987). The reflectors are well developed and the boundary appears to coincide with the MOHO. Based on these geophysical data, the MOHO beneath the Basin and Range has been interpreted as a young feature, continuous beneath both stable cratonic and allochthonous areas, and is dominated by the intrusion of mafic magmas (Allmendinger et al., 1986; Klemperer et al., 1986). Geochemical data for GVF granulites are consistent with this interpretation and indicate that recent mafic magmas have crystallized in the lower crust, probably near the crust/mantle boundary, and have intruded older Proterozoic granulitic lower crust. The isotopic compositions of GVF metacumulate granulites record this intrusion and mixing of Cenozoic mafic magmas with older (1.3–1.5 Ga) lower crust, documenting a recent event of underplating of mafic material to the subcontinental lithosphere.

Road log

Mileage

0.0 Begin trip at Shell service station in Rodeo, New Mexico. Drive south on US-80 down axis of San Simon Valley. **11.4**

11.4 Apache, New Mexico. **9.2**

20.6 **STOP 1A. Geologic overview of the Geronimo volcanic field.** At intersection of US-80 and unpaved road to Rucker Canyon, turn right (northeast) and stop immediately after crossing cattleguard. The purpose of this stop is to point out some of the general structural and petrologic aspects of the Geronimo volcanic field (GVF). The San Bernardino graben, in which the GVF is located, is oriented roughly north–south and is approximately 10 km wide in its southern extension, broadening northward to about 15 km at GVF. The San Simon graben to the north is only about 5–7 km wide at its southern end and trends northeast where it intersects GVF, but continues northward in an arcuate shape, ending in a more northwesterly orientation north of the Chiricahua Mountains where it broadens to roughly 30 km (see Fig. 1).

Looking to the northwest, the high mountains (12:00 to about 2:00) are the Oligocene–Miocene rhyolitic volcanic rocks of the Chiricahua Mountains. The lower peaks of Limestone Mountain (12:00) are mostly Paleozoic and early Mesozoic sedimentary and volcanic rocks that have been thrust to the northeast over Cretaceous rocks along northwest–southeast-oriented thrust faults of Late Cretaceous–early Tertiary age (Drewes, 1981).

Physiographic distributions of lavas of different ages at GVF are largely distinct. Lavas exposed in Mulberry Canyon in the Pedregosa Mountains (11:00) have an age range of 3.0–3.2 Ma (Kempton et al., 1987), and two basalt flows about 1 mi farther south give similar ages of 3.3 Ma (Lynch, 1978). The youngest known flows in the field are from Mangus maar (3:00, due north) dated at 0.26 Ma (Kempton, 1987) and from a flow north of Cinder Hill in the southernmost portion of the GVF (0.27 Ma; Lynch, 1978). The oldest dated valley lava is 3.6 Ma from Paramore maar; the basalts we will see at Stop 1B have been dated at 1.5 Ma. Basalts exposed in the Peloncillo Mountains on the eastern side of the valley are generally older, ranging from 4.7 to 9.2 Ma (Kempton et al., 1987). These age variations are consistent with the interpretation, based on gravity data, that the western part of the basin has been faulted downward relative to eastern part along buried faults that parallel the margins of the valley (Lynch, 1978).

The basalts erupted in the valley occur as cinder cones, maars, and associated flows. More than 125 cinder cones and eruptive vents of agglutinated spatter, bombs, and ash are observed in the San Bernardino Valley at GVF; at least 25% of these are strombolian cones 1–2 km in diameter. Most rise 70–100 m above the valley floor, but some of the youngest and least eroded reach 200 m of relief. Many of the cinder cones overlie aprons of pyroclastic-surge deposits and some vents erupted only phreatomagmatic tuffs, forming extensive tuff rings and large maar craters. Lava flows generally issue from the sides of breached cones and cover areas of only a few square kilometers; a few reach lengths of 5–7 km. In contrast, the flank lavas occur as erosional remnants or plateau-capping flows. Vents for most of these flows have largely been eroded and eruptive style is unknown, but there is no reason to suspect that eruptive style for these lavas differed from that of the strombolian activity exemplified by valley basalts.

After discussion, proceed northeast toward the southern Chiricahua Mountains along Rucker Canyon Road. Cones of valley basanites are on left after 1–2 mi. The smaller, dissected cone contains abundant lherzolite xenoliths. Pass Krentz Ranch Headquarters. The Krentz cone and flow complex lies directly north of ranch buildings. Road turns due north and then crosses Tex Creek after 1 mi. Basanite lava flow overlies gravels east of road. **6.7**

27.3 **STOP 1B. The Krentz flow valley basanite.** Pass through fence and gate at National Forest boundary. Park in campsite area on left immediately past gate. Walk back through gate and cross the road to large talus blocks of Krentz basanite.

The purpose of this stop is to view a typical valley lava flow and to discuss some of the geochemical evidence for the temporal evolution of the Geronimo volcanic field. The Krentz basanite at Stop 1B is aphyric, with a very fine-grained cryptocrystalline groundmass. Xenocrysts of anorthoclase, plagioclase, augite, spinel, and sparse olivine occur along with abundant small gabbroic xenoliths. Exposures of the flow form massive, columnar-jointed cliffs; at several locations the lower contact between the flow and the underlying rubble and fanglomerate is well exposed. Several nested cinder cones cap the flow at its northern end.

Return to highway. **6.7**

34.0 Highway 80. Turn right (southwest) onto pavement. Pass milepost 390. **6.5**

40.5 Turn left onto road with locked gate. **Do not attempt to enter fenced area unless prior arrangements have been made with ranch owners.** Proceed through gate and drive east toward cones. **0.9**

41.4 Unlocked gate north of small cone. For the next mile, the road traverses the north flank of a pyroclastic deposit (tuff ring) erupted from a partly covered vent that forms a bench to the south of a pair of coalesced strombolian cones. These younger cones occupy and cover the south rim of the tuff ring. Two areas of well-exposed resistant tuff can be seen from the road. **1.2**

42.6 **STOP 2A. Physical volcanology of the Geronimo volcanic field and an introduction to the GVF xenolith suite.** Turn right on the poorly marked track leading to water tank (0.4 mi distance from road to tank is not included in mileage log). Use caution in driving vans or cars all the way to the water tank.

This locality, pk-G-22, is of interest for the variety of pyroclastic deposits and the varied xenolith/xenocryst suite. Included in the xenolith/xenocryst suite are xenocrysts of anorthoclase, augite, and olivine, typical Type I spinel lherzolite, and Type II aluminous-augite clinopyroxenites. Crustal granulites are predominantly two-pyroxene, two-feldspar metadiorites with Nd model ages of 1.1–1.4 Ga. Fragments of kaersutite crystals and kaersutite-rich xenoliths are particularly abundant (more so than at any other Geronimo locality) and several xenoliths with veins of phlogopite ± pargasite ± plagioclase have been found here (phlogopite has not been observed at any other locality).

The pyroclastic deposits seen at this locality include three distinctive units which apparently represent a progression in eruption character from phreatomagmatic to strombolian. The lower part of the north-facing slope, up to the elevation of the water tank, is underlain by weakly bedded, well-indurated tuffs rich in small angular lithic fragments. The tuffs dip gently to steeply away from the vent. These early deposits are interpreted as transitional in character between pyroclastic surge deposits and typical strombolian deposits, and are thought to have been deposited as a tuff ring during a phreatically dominated vent-clearing phase of the eruption. These deposits contain a magmatic component as well as the same xenolith/xenocryst assemblage that is found in younger phases of the eruption.

These early deposits are overlain by an inward-dipping unit which is fundamentally similar in character. Large bombs of basanite containing high concentrations of xenoliths and xenocrysts are much more abundant than below. In the western outcrop the angular discontinuity between the two units is very marked and well exposed. Overlying the deposit that forms the topographic rim of the tuff ring are spatter, bomb, and ash deposits typical of the strombolian cones of the Geronimo field. The progression from early bedded, lithic-rich deposits suggestive of a highly explosive origin (possibly surge deposits related to early phreatic activity) to strombolian activity and lava flows is typical of these cones.

Return to main dirt road.

42.6 Turn right on road. Go less than 100 m to intersection of several roads. Turn right (south) onto road paralleling dry gully. This road climbs to a broad divide on a lava flow among several cones. A series of water tanks marks the location of the road. Approximately 2.4 mi from last turnoff the road crosses another gully (proceed with caution). **3.7**

46.3 **STOP 2B. More xenoliths and evidence for mantle-enrichment processes.** Park vehicles in depression west of Cochise maar and Little Cochise crater (see Fig. 12). This locality encompasses several xenolith-bearing cones.

Cochise crater (1.3 km in diameter) is a 50 m deep volcanic depression which has had a complex history. Units exposed on the walls include flows and spatter beds that are both older and younger than the crater. Poorly bedded, lithic-rich deposits resembling the lower unit at the previous locality are well exposed in a small cliff outcrop northeast of Little Cochise crater. This highly indurated zone grades upward into a less indurated tuff with abundant large magmatic bombs. Several xenolith-bearing cones, including the prominent Little Cochise crater (west rim of Cochise crater), postdate the main tuff ring. Bombs in the tuff ring deposit contain minor xenolithic and xenocrystic material. The prominent cone west-southwest of Little Cochise crater contains abundant xenoliths and is breached on its south side by a xenolith-rich lava.

Although amphibole peridotites seen at the previous stop are far less abundant, this locality is interesting for the variety of mafic and ultramafic rocks. Type IIa and IIb aluminous augite-rich xenoliths comprise a high proportion of the population, and composite xenoliths with veins and dikes of Type II material crosscutting Type I spinel lherzolite and Type II wehrlite are relatively common. Both Type Ia and Type Ib lherzolites have been found. Granulite xenoliths are predominantly one- and two-pyroxene metacumulates, although rare metadiorites occur as well.

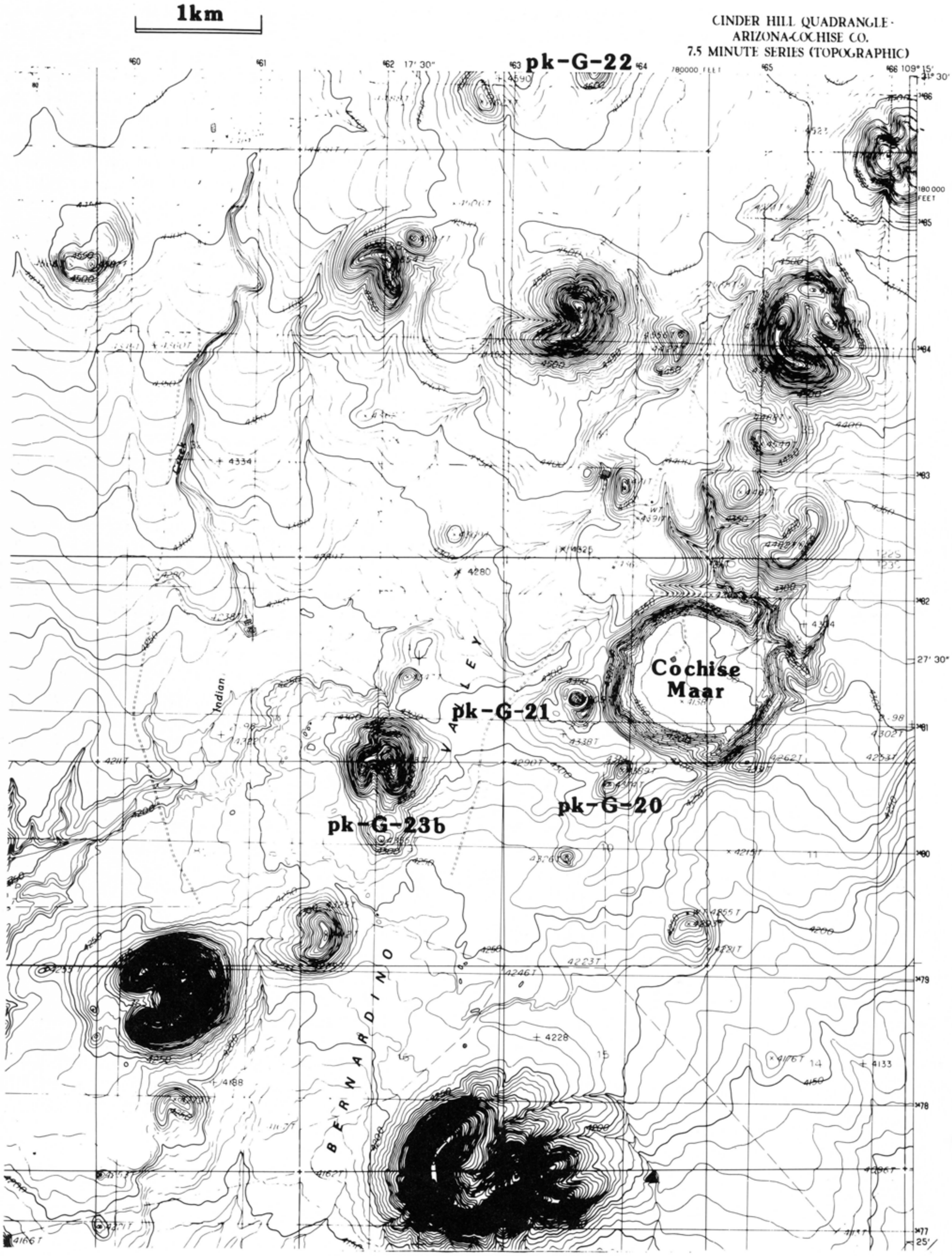

FIGURE 12—Topographic map for area surrounding Stop 2B, including sample localities pk-G-20 through pk-G-23b and Cochise maar.

Field guide to Kilbourne Hole maar, Doña Ana County, New Mexico

Elaine R. Padovani[1] and Mary R. Reid[2]

[1]*Office of Earthquakes, Volcanoes and Engineering, U.S. Geological Survey, Reston, Virginia 22090;*
[2]*Department of Earth & Space Sciences, University of California, Los Angeles, California 90024*

Introduction

Kilbourne Hole maar is one of three large, late Pleistocene maar craters formed along the trace of the Fitzgerald–Robledo fault system on the mid-Pleistocene La Mesa surface in southern New Mexico and northernmost Mexico (106°57′W, 31°59′N) (Lee, 1907; Reeves and De Hon, 1965; De Hon, 1965; Hawley and Kottlowski, 1969; Hoffer, 1976a). Kilbourne Hole is the northernmost, Hunts Hole maar is located 3 km to the south (Fig. 1), and Potrillo maar is located 8 km to the southwest, straddling the international border. The maars are found in the central part of the Potrillo volcanic field, which is composed of the Santo Tomas–Black Mountain basalts on the east, a central area containing the maars and the Afton–Aden basalts, and the West Potrillo Mountains to the west, a large expanse of spatter and cinder cones, related flows, and several small maars (Hoffer, 1971, 1975, 1976a). The Potrillo volcanic field is located on the western margin of the Rio Grande rift (Chapin, 1971, 1979; Seager and Morgan, 1979).

The maars in the central area were formed as a result of pyroclastic surges, erupted through alluvium and through a thin basalt flow originating from the Gardner cones to the north of Kilbourne Hole (Hoffer, 1976a). The basalt flow thins in the vicinity of the southern rims of Kilbourne Hole and Hunt's Hole maars, and pinches out in the southeastern and southwestern portions of the maar rims. The maar ejecta, composed of pyroclastic surge deposits (Wohletz and Sheridan, 1983), form elevated rims above the craters. The ejecta lie on the thin basalt flow in the northern portions of the maar rims, but, where the basalt flow is absent on the southern portions of the rims, the ejecta rest directly on beds of the Santa Fe Group (Hawley and Kottlowski, 1969).

The Kilbourne Hole ejecta contain abundant crustal and mantle xenoliths, in marked contrast to ejecta at Hunts Hole which contain none. The xenoliths comprise a wide variety of rock types, including: sedimentary inclusions such as limestone, sandstone, quartzite, and conglomerate; upper crustal igneous and metamorphic rocks; a varied suite of siliceous and mafic granulites; and abundant mafic and ultramafic rocks. The xenolith suite at Kilbourne Hole is exceptional because of the variety and abundance of rock types sampled from the lower crust and upper mantle. In addition, their large size (10–90 cm maximum diameter, Fig. 2a, b) has permitted a spectrum of observations and analyses to be made on individual samples. As a result, the geophysical, petrological, and geochemical characterization of these xenoliths provides a comprehensive calibration of models of rheological structure, crustal evolution, and transport phenomena in the continental lithosphere beneath the southern Rio Grande rift.

In the sections that follow, we will review briefly the tectonic setting, characterize the xenolith suites, and then summarize the results of our studies on the evolution of the lower crust beneath the southern Rio Grande rift. A brief road log follows which describes the three major stops followed by a brief description of the spectacular base-surge deposits (Bahar and McCurry, this volume). More detailed discussions of each of these topics can be found in Chapin (1979), Seager and Morgan (1979), Padovani and Carter (1977a, 1977b), James et al. (1980), Wohletz and Sheridan (1979, 1983), and Reid (1987).

Geologic overview

The Rio Grande rift dominates the regional geology and tectonic setting of southern New Mexico. It is characterized throughout its length by anomalously high heat flow, recent volcanism, deep sedimentary basins, and Quaternary faulting. Rifting began about 32 Ma ago, with the first occurrence of alkali olivine basalts 13 Ma ago. Seager and Morgan (1979) interpret these initial basaltic eruptions to be the result of "critical stretching" of the crust, which allowed extraction of partial melts from the upward bulging mantle beneath. Another surge of basaltic magmatism 5 Ma ago is interpreted to reflect an accelerated rate of crustal thinning from 8 to 3 Ma. The crustal thinning initiated the development of shallow faulting in areas of high heat flow, with horst and graben development elsewhere. The broad band of observed high heat flow, which extends from Colorado and northern and central New Mexico, narrows in south-central New Mexico, Mexico, and west Texas. From measurements of the heat flow, Decker and Smithson (1975) suggest that its origins are deep-seated and igneous and/or tectonic. Heat-flow modeling (Cook et al., 1978) indicates that the present surface heat flow represents the time-integrated thermal history of the crust during the past 30 Ma and that any deep thermal event associated with late stage basaltic magmatism cannot be expected to be reflected in present surface observations (due to time constants on the order of tens of millions of years). Further evidence for present high crustal temperatures comes from the xenolith data to be discussed later.

Seismic refraction and reflection data also indicate extensive crustal thinning in the axis of the central and southern Rio Grande rift, with a P_n velocity of 7.6–7.8 km/sec, similar to results from other active rifts such as the Rhinegraben and the East African rift (Olsen et al., 1979).

Global magnetometer observations from the Magsat mission and subsequent research on the magnetic properties of xenolith suites worldwide have provided new information about the origins and spatial distribution of magnetization contrast in the earth's crust. Magnetic and geobarometric measurements on the xenolith suites from Kilbourne Hole and Potrillo maar indicate a shallowing of the Curie isotherm beneath the rift to a depth of about 15 km, which agrees with aeromagnetic and Magsat data (Wasilewski and Padovani, 1981). Results of modeling the in-situ remanence and other properties of the magnetic minerals in the xenoliths will be discussed later.

FIGURE 1—U.S. Geological Survey high-altitude areal photograph of Kilbourne Hole and Hunts Hole maars, Doña Ana County, New Mexico. The dimensions of Kilbourne Hole (top of photo) are approximately 2.7 km north–south by 1.6 km east–west. The two maars are aligned along a north-trending fault.

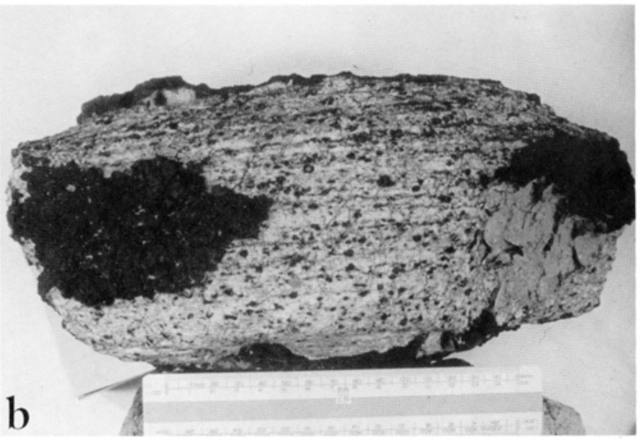

FIGURE 2—**a,** Spinel lherzolite xenolith from Kilbourne Hole. **b,** Pelitic paragneiss xenolith, sample 1977, from Kilbourne Hole. Note strongly foliated texture and partial coating of alkali olivine basalt.

In southern New Mexico, exposures of basement lithologies consist of Precambrian crystalline rocks and Paleozoic to Mesozoic sedimentary cover. The metamorphic and granitic basement of southern New Mexico formed between 1.65 and 1.9 Ga, but was subsequently intruded by granitic rocks of 1.35–1.5 Ga age (Condie and Budding, 1979). Since that time, the crust has been largely stable isostatically. Exposed metamorphic rocks are mainly greenschist to amphibolite grade and granulites are unknown from surface exposures or drill holes. Pennsylvanian rocks, where present, are separated from older Paleozoic rocks by an angular unconformity (Bachman, 1975), but the extent of missing section diminishes southward, so that the section may be largely continuous at Kilbourne Hole. Locally, the amount of Pennsylvanian subsidence may have been less than 500 ft (McKee et al., 1975) and the total Paleozoic–Mesozoic sedimentary cover may be less than 4 km thick (Ramberg et al., 1978). Thus, to a first order, the crust has been stable with respect to uplift since formation, and does not appear to have either subsided or been uplifted appreciably.

Kilbourne Hole and Hunt's Hole were first described by Willis T. Lee in 1907. He recognized the volcanic origins of the "Kilburn crater" and the "Stehling crater" (Hunt's Hole), which were then known as the "Afton craters," and provided a sketch map of the former (Lee, 1907). He recognized the phreatomagmatic nature of the ejecta and the probable Quaternary age of the crater, comparing its features with Zuni Salt Lake Crater. He also noted the presence of geothermal water within "Kilburn" crater and attributed the thermal effects to the presence of basaltic magma at shallow depths. The young age was inferred from the presence of vertebrate fossils of Pleistocene age found while drilling a well in the bottom of the maar. Other Pleistocene fossils have been found in the area including the remains of a ground sloth in a lava tube in the Aden–Afton flows (De Hon, 1965).

Sample descriptions and analytical schemes

In this section, the emphasis will be on the deep crustal materials found as xenoliths in the Kilbourne Hole maar ejecta. However, it is important to note the presence of the mafic and ultramafic rocks which occur along with the deep crustal samples and describe them briefly.

Mafic–ultramafic xenoliths

The mafic–ultramafic group consists mainly of medium- to coarse-grained Type I lherzolites; pyroxenites in this group are surprisingly rare, but have been found as thin bands in the lherzolite. Perhaps 10% of the mafic–ultramafic suite is composed of comparatively Fe-rich Type II pyroxenites and peridotites. These are dominantly pyroxenites and wehrlites with widely varying mineral proportions. Composite xenoliths with pyroxenite bands in Type II peridotite and multiple bands of Type II pyroxenite–wehrlite occur as well. Unusual xenoliths in this suite collected at Kilbourne Hole include interleaved metagabbroid and Type I lherzolite, Type I lherzolite with thin veins of phlogopite, coarse Type II wehrlite, and kaersutite-rich inclusions (Wilshire and Padovani, 1977). Xenoliths of Type II peridotite were first described by Carter (1970) in his detailed study of the chemistry and mineralogy of the mafic–ultramafic suite, which resulted in a partial fusion–partial crystallization model for the upper mantle beneath the maar (Carter, 1965, 1970). Megacrysts of olivine, augite, orthopyroxene, and anorthoclase occur, but are uncommon and have not been studied systematically. Additional discussions about this suite can be found in Wilshire and Shervais (1975), Wilshire et al. (1985), Morgan (1986), Roden et al. (1988), Sawyer and Pallister (this volume), and Kempton and Dungan (this volume).

It should also be noted that several other minor occurrences of mafic–ultramafic xenoliths exist in the region: (1) small inclusions of clinopyroxenite, kaersutite–clinopyroxenite, kaersutite-rich inclusions, wehrlite and olivine–clinopyroxenite as well as megacrysts of feldspar, augite, kaersutite, and spinel are found loose on the flanks of cinder cones, and as inclusions within lava flows and within cores of alkali olivine basaltic bombs in the West Potrillo volcanic field (Hoffer, 1976a; Ortiz, 1980); (2) spinel lherzolite xenoliths (4 cm maximum dimensions) are found in late-stage cinder cones at Potrillo maar; (3) a mafic–ultramafic suite similar to that at Kilbourne Hole can be found at Potrillo maar, but it is neither as diverse nor as abundant.

Lower crustal xenoliths

The deep crustal materials found at Kilbourne Hole consist of both siliceous and mafic granulites. The range of rock types includes garnet-bearing paragneisses, two-pyroxene-bearing orthogneisses, charnockite, and anorthosite. The paragneisses were divided into two groups by Padovani and Carter (1977a): Group 1 consists of strongly foliated rocks with almandine–pyrope garnet, sanidine, quartz, and sillimanite, with or without andesine feldspar (Fig. 2b); Group 2 contains orthopyroxene (hypersthene) instead of sillimanite. Accessory minerals in both groups consist of rutile, ilmenite, apatite, and zircon. Large concentrations of graphite are occasionally observed in Group 1 garnet granulites.

Preliminary petrographic and microprobe analyses revealed that most of these rock types are pristine, that individual minerals are of gem quality, and that, except for minor amounts of decompression melting, that the xenoliths overall have anisotropies and mineral assemblages that are representative of in-situ conditions at depth. Because samples are of sufficient size and abundance, a multifaceted study has been undertaken which builds on the initial studies by Padovani (1977c) and Padovani and Carter (1977a, 1977b). To date, representative xenoliths have been characterized with respect to mineralogy, seismic velocity, density, magnetic properties, major-, minor-, and trace-element geochemistry, and/or isotopic geochemistry (Rb/Sr, Sm/Nd, U/Th/Pb, O).

The results of our studies to date can only be summarized briefly in this guide. Further details may be found in the above citations and others that follow. The major questions being addressed focus on the growth and evolution of the continental crust beneath the Rio Grande rift, the nature and scales of geochemical (major, minor, trace, and rare-earth geochemistry) and isotopic equilibration in the lower crust during a fairly well-constrained metamorphic history, and the variability of in-situ physical properties at depth. Specifically, the interaction between crustal material, in this case paragneisses, and ascending magmas are of particular interest because these processes can lead to vertical stratification of the crust. Both Kilbourne Hole and Potrillo maar have been well sampled, although only the pelitic granulites have been comprehensively analyzed. The individuals who have contributed in various ways to our knowledge to date on these xenoliths include E. Padovani, M. Reid, S. Hart, S. Richardson, and G. Wandless, primarily at Massachusetts Institute of Technology and the U.S. Geological Survey; D. James at Department of Terrestrial Magnetism, Carnegie Institution of Washington, F. Spear at Rensallear Polytechnic Institute, and P. Wasilewski at the National Aeronautics and Space Administration, Goddard.

Physical properties

Cook et al. (1979) constructed a velocity profile for the Rio Grande rift in which seismic P-wave velocities increase from 6.2 km/sec at intermediate crustal depths to 7.4 km/sec at the base of the crust, estimated to be about 28 km thick in the southern Rio Grande rift (DeAngelo and Keller, 1988). Laboratory velocity measurements on garnet-bearing paragneisses yield intermediate average velocities for typical Group 1 granulites of 7.2 km/sec at 6 kb pressure and room temperature and densities ranging from 2.9 to 3.1 gm/cm^3 (Padovani, unpubl. data). Typical velocities for mafic granulites span this range (Griffin and O'Reilly, 1987). The similarity of these velocities and densities to those of the metasedimentary xenoliths at Kilbourne Hole implies that it may be impossible to distinguish underthrust metasedimentary crustal materials from underplated basaltic materials beneath the rift on the basis of geophysical measurements alone.

The crustal granulites from the rift all have ilmenite-dominated magnetic mineralogies, which, combined with the elevated temperatures in the lower crust, are responsible for the shallowing of the Curie isotherm to about 10–15 km depth. All the silicic and mafic rocks analyzed show textural and chemical evidence of reduction due to the anhydrous nature of the lowermost 15 km of the crust. If the rift were to cool down, as it must eventually, the lower crust would remain non-magnetic because any regional geotherm, in the absence of fluids, would ensure that the low-Curie-point metabasic rocks remain in a reduced state. Magnetotelluric soundings in the rift indicate the presence of a conductive layer in the crust at about the same depth of 10 km; such a major decrease in electrical resistivity could be due to the presence of conductive hydrous phases, such as amphibole at temperatures of about 500°C (Jiracek et al., 1979). Amphibole-rich metabasalts, which are found as xenoliths at Potrillo maar, appear to represent a shallower portion of the crust not represented in the Kilbourne Hole assemblages and perhaps corresponding to the conductive layer. These rocks have 550°C Curie points and represent intermediate crustal depths at or above the magnetic "bottom" of the crust in the rift (Wasilewski and Padovani, 1981).

Petrology

Group 1 garnet granulites are generally monolithologic, although occasional crosscutting relationships are observed with mafic veins and felsic dikes. Isoclinal folds are preserved in a few xenoliths. The opportunity for chemical exchange between the xenoliths and the transporting magma was limited; basalt crusts form a quench contact with the xenoliths and fast ascent times (less than 3 days) are required from considerations of settling velocities of xenoliths of this size in basaltic liquids (Spera, 1980) and from the observed short-term effects of decompression melting of garnet (Padovani and Carter, 1977b; Padovani, unpubl. data).

Padovani and Carter (1977a) obtained pressure and temperature estimates for the lower crust based on Ca-exchange equilibria between garnet and plagioclase (Ghent, 1976) and on K, Na, and Ca equilibria between potassium feldspar and plagioclase (Stormer, 1975). These estimates are consistent with geothermal gradients based on heat flow in the southern Rio Grande rift. Equilibrium on a mineral–mineral scale was assumed on the basis of failure of electron-microprobe analyses to detect any zoning within the minerals analyzed. As shown below, this assumption is further strengthened by measurements of isotopic equilibrium between minerals. Moreover, the isotopic results show that equilibration at the calculated pressures and temperatures was attained recently and not in the Precambrian. Therefore, relatively recent high temperatures (700–1000°C) in the lower crust of the Rio Grande rift are predicted, at least to the extent that the temperature and pressure dependence of the exchange coefficients are known.

Trace-element and isotope geochemistry

In this section, we review pertinent aspects of the trace-element geochemistry of the xenoliths and general conclusions relative to isotope geochemistry. In doing so, we focus on the paragneiss xenoliths because these provide the most convincing evidence for the geochronologic and geochemical evolution of the lower crust of southern New Mexico. Details for these and other lithologies may be found in Reid (1987). Before discussing these results, the internal compositional heterogeneity of the samples is highlighted, as it provides the rationale for our mode of sample analysis.

All the paragneiss and many of the orthogneiss xenoliths which have been analyzed are foliated. In the case of the paragneisses, the planes of foliation are defined by garnet-rich layers alternating with wider, more felsic bands. Compositional zoning transverse to the plane of foliation is also observed. For example, the paragneisses are often compositionally zoned from garnet-rich to garnet-poor across the xenoliths (e.g., Fig. 2b). In order to take advantage of this compositional heterogeneity, each xenolith was treated as a veritable outcrop. A working slab was cut from each xenolith transverse to the plane of foliation and the slab was then sawed into 1–2 cm Krogh layers (Krogh and Davis, 1968, 1971) parallel to the plane of foliation. Details of the analytical techniques can be found in Reid (1987).

The best estimate for the metamorphic age of the lower crust is ~1.6 Ga and is based on the concordance of Sr isochrons constrained by layer–layer isochrons (e.g., sample 1977, Fig. 3a) and by whole-rock (xenolith) isochrons (Fig. 3b). This age is consistent with metamorphic ages of basement rocks exposed in the region (Condie and Budding, 1979). Moreover, these isochrons have been preserved in spite of the centimeter-scale isotopic equilibration evidenced by ~zero age mineral isochrons (e.g., Fig. 3a). Together, these results suggest a two-stage thermal history for the lower crust of this region: early–middle Proterozoic pervasive metamorphism related to crustal stabilization, and subsequent reheating of the lower crust and local re-equilibration related to Rio Grande rift development.

Sm–Nd isochrons are largely equilibrated both within and between xenoliths, that is at centimeter and decimeter scales (Fig. 4a). This contrasts significantly with the Rb–Sr-isotope systematics and is contrary to the idea that Nd isochrons are unresponsive to metamorphism. The most dramatic example is sample 1977 whose layers are in virtual isotopic equilibrium with respect to Nd-isotope systematics, in spite of retaining the best layer–layer Rb–Sr isochron. The different response of the Sr- and Nd-isotope systems may reflect the interplay of several factors including the high temperature, absence of hydrous fluids, and mineralogy of the xenoliths.

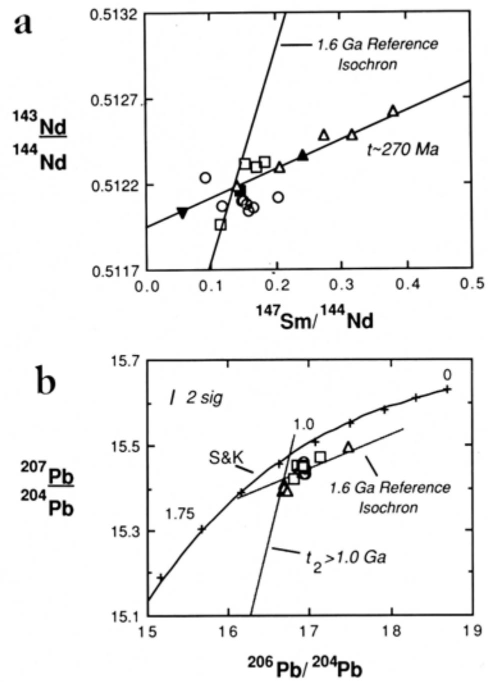

FIGURE 4—**a**, Sm–Nd isochron diagram for layers (open symbols) and whole rocks (closed symbols) of paragneisses from Kilbourne Hole. Symbols as in b. In contrast to Sr isotopes, Nd isotopes have been largely re-equilibrated at the layer scale. Layers from sample 79k6 conform to an ~270 Ma apparent isochron. **b**, $^{207}Pb/^{204}Pb$ diagram comparing layers from paragneiss xenoliths from Kilbourne Hole to crustal Pb evolution curve labeled S&K (Stacey and Kramers, 1975). Symbols as in Fig. 10. Layers are unradiogenic, i.e., fall below and to the left of average crust of zero age (point labeled 0). *Minimum* age of U-depletion is approximately given by the intersection of a single-stage Pb isochron with the crustal Pb evolution curve and is greater than 1 Ga.

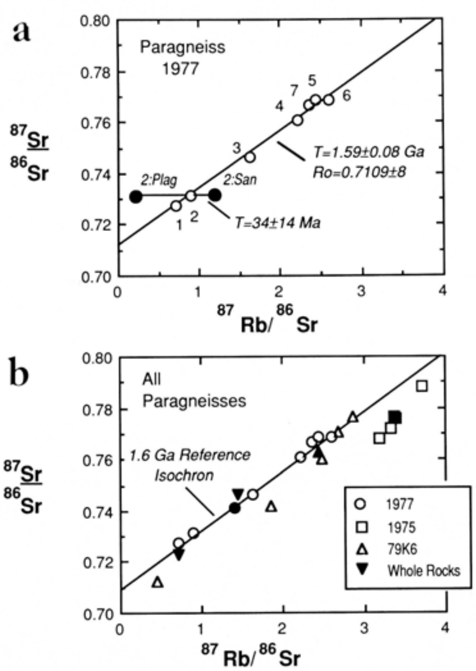

FIGURE 3—**a**, Rb–Sr isochron diagram for layers (open symbols) and minerals (closed symbols) of paragneiss xenolith, sample 1977. Layers are numbered sequentially across the xenolith and yield best internal isochron of 1.59 Ga. Minerals within layers have been largely isotopically equilibrated by recent rift-related heating. **b**, Rb–Sr isochron diagram for layers (open symbols) and whole rocks (closed symbols) of paragneisses from Kilbourne Hole, showing extent to which Rb-Sr systematics measured at various scales conform to a 1.6 Ga isochron.

Evidence for early–middle Proterozoic high-grade metamorphism is also found in the Pb-isotope systematics. The Pb-isotope data for the paragneisses fall largely within error of a 1.6 Ga isochron. The paragneisses have very unradiogenic $^{207}Pb/^{204}Pb$–$^{206}Pb/^{204}Pb$-isotope signatures which can only have developed over a period of >1 Ga (Fig. 4b). These unradiogenic Pb-isotope signatures corroborate the low abundances of U, both with respect to Pb and overall, measured in the xenoliths directly.

Wandless and Padovani (1985) studied four pelitic xenoliths using INAA to determine how the cross-foliation compositional heterogeneities expressed by the isotopic systematics are reflected in the REE patterns. The layers range from being strongly LREE-deleted to having REE patterns somewhat more LREE-enriched than an average shale. In general, however, the relative REE patterns for the whole-rock paragneisses are similar to shale composites: $(La/Sm)_n = 3.25 - 3.59$ and $(Tb/Lu)_n = 0.99 - 1.16$. The LREE abundances are nearly identical to, or slightly depleted from, values typical of shales, while HREE abundances are relatively enriched. Most samples have negative Eu anomalies with $(Eu/Eu^*) = 0.41 - 0.92$. These observations suggest that the pelitic granulites have not undergone a significant amount of partial melt extraction, which would have tended to more strongly fractionate the REE, and thus they retain the trace-element signature of their precursor.

James et al. (1980) found that the paragneisses also retained the oxygen-isotope signature of their precursors. They studied a broad range of mafic to felsic xenoliths from Kilbourne Hole. In spite of ample opportunity for oxygen exchange with the mantle, the paragneisses all had $\delta^{18}O$ values of 9–12‰, typical of metasediments, and the mafic granulites had $\delta^{18}O$ values of 6.1–6.6‰ within the range of uncontaminated basalts. Layers from within samples are in isotopic equilibrium.

The pelitic paragneisses are grossly similar to middle Proterozoic crust with respect to $^{143}Nd/^{144}Nd$. Their lack of significant trace-element depletion has, however, yielded time-integrated isotopic signatures which are radiogenic with respect to $^{87}Sr/^{86}Sr$ and $^{208}Pb/^{204}Pb$ when compared to existing estimates for average lower crust. Moreover, the pelitic paragneisses are also relatively K- and Th-rich, resulting in higher heat production than considered typical of the lower crust. Therefore, if pelitic paragneisses are present in the lower crust at geologically reasonable abundances of 10–20%, they raise the estimate for heat production of average lower crust and reduce the heat flux required at the subcontinental mantle by up to 50%.

Based on geochemical studies of Kilbourne Hole xenoliths, the following tectonothermal and geochemical evolution for the lower crust in southern New Mexico is proposed:

1. Crust formation at a convergent margin and cessation of orogenesis by at least 1.6 Ga. With a few exceptions (U and Cs), the lower crust is probably not geochemically depleted, thereby precluding such phenomenon as partial melt extraction.

2. Thermal decay and tectonothermal stability of the crust through the remainder of the Precambrian and much of the Phanerozoic, in spite of proximity to a convergent margin during late Precambrian (Grenville) time.

3. Recent reheating of the lower crust related to opening of the Rio Grande rift, resulting in phase equilibria on a local (intralayer) scale and resetting of mineral–mineral isochrons.

Road log

Mileage

0.0 Begin road log at La Mesa (Route 20) and I-10 in El Paso, Texas. Head west on La Mesa, which becomes Country Club Road. Stay on TX-260 at fork with TX-20. **2.5**

2.5 State line. Continue straight on Route 1884, entering New Mexico. **0.7**

3.2 At junction with NM-273, turn right. **1.6**

4.8 Turn left at junction for Santa Teresa Aeropuerto; Doña Ana County, NM A-17. **2.6**

7.4 Left on paved road at sign for John Nobles, Inc. (pink stripe on building). **0.3**

7.7 Dirt road begins. **0.1**

7.8 Bear right at fork just after RR tracks. **0.85**

8.65 Jct AC-3; bear right at fork; RR tracks on right. **0.55**

9.2 Cross cattleguard. **4.8**

14.0 Cross cattleguard; turn left toward JCJ Ranch. Mt. Riley and East Potrillo Mountains ahead on the horizon until next turn. **10.2**

24.2 Road passes over first flows of the Afton–Aden volcanic field. **1.1**

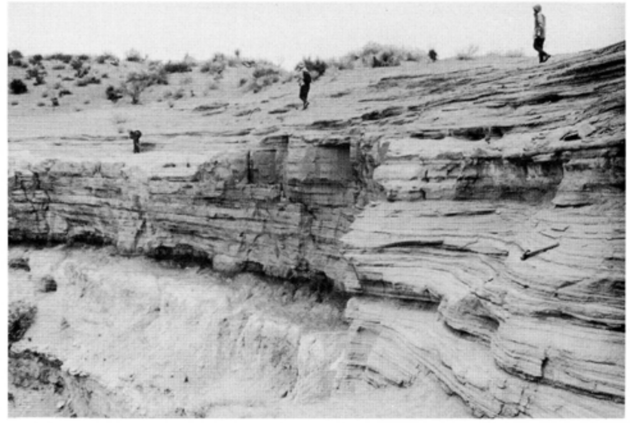

FIGURE 5—Base-surge deposits on the southeastern rim of Kilbourne Hole maar. These well-exposed rim ejecta rest directly on sediments of the Santa Fe Group. Bedforms seen at this locality include sandwave, planar, and massive beds with interbedded accretionary lapilli.

25.3 Pass road on right. **0.3**

25.6 Turn right toward Hunt's Hole on prominent dirt road; continue around left side on graded road. **1.3**

26.9 Gate (please close after you pass through). **1.0**

27.9 Push up in lava flow on the right, ahead. **1.7**

29.6 **STOP 1. South end of Kilbourne Hole.** While at this locality, be sure to keep track of members of the group. It is easy to become separated and the ground is difficult to cover. This stop provides an overview of Kilbourne Hole maar and the spectacular pyroclastic surge deposits along the southern and eastern rim (Fig. 5). We will hike along the southeastern rim to examine these deposits. Most of the stratigraphy described by Wohletz and Sheridan (1983) can be seen here, except for the basal explosion breccia which is only exposed in the northern and eastern rim. Be sure to note the beautiful bomb-sag structures (Fig. 6) in the middle unit at this stop. **1.0**

30.6 **STOP 2. Eastern margin of Kilbourne Hole.** We will return to the vehicles and drive to the prominent eastern rim to look at the distribution of xenoliths in this area. This stop involves hiking up and over the rim, which is capped with blow sand. Pelitic paragneisses can be found here, as well as a diverse suite of mafic and ultramafic rocks.

FIGURE 6—Large bomb-sag structure on eastern rim of Kilbourne Hole maar. The bomb is an angular block of pre-eruption Afton basalt.

Base-surge deposits at Kilbourne Hole maar, southern New Mexico

Dana Bahar and Michael McCurry

New Mexico State University, Las Cruces, New Mexico 88003

Kilbourne Hole is a late Pleistocene maar that is blanketed by a rim of ejecta attributed to base-surge eruptions (e.g., Wohletz and Sheridan, 1983; Hoffer, 1976b). The well-exposed rim ejecta consist of pyroclastic-surge and fallout deposits, and exhibit many classic features associated with base-surge deposits such as dune-like bed forms, low-angle crossbedding, and reverse grading within beds. Beds consist of a mixture of accidental, accessory, and essential rock fragments, in some areas including abundant lower crustal and mantle-derived xenoliths (e.g., Padovani and Carter, 1977a). They rest directly on 0.1 Ma Afton basalt and sediments of the Santa Fe Group. The basal unit is an explosion breccia consisting primarily of angular blocks of Afton basalt in a poorly consolidated sandy matrix consisting of debris derived from the Santa Fe sediments. These were emplaced during the first eruptive phase of low-energy Strombolian activity (Wohletz, 1980). The eruption subsequently evolved into more violent Surtseyan-type activity that produced the overlying thinly bedded surge deposits. These are characterized by three principal bedforms: sandwave, planar beds, and massive beds. Bomb sags are common within some beds. In addition, several fallout deposits of accretionary lapilli are interbedded with the surge deposits. An up-section increase in the ratio of essential to accidental ejecta, abundance of accretionary lapilli, and occurrence of flame structures suggest a dynamic change in water/magma interaction during the eruption. The present crater was probably formed during these last eruptions by caldera-like collapse (Seager, 1987), as suggested by inward-dipping surge deposits and slumped blocks of Afton basalt around the inside of the north and east sides of the margin. Minor eolian reworking of the unconsolidated rim deposits have subsequently thickened and steepened the northern and eastern parts of the rim (Gile, 1987).

References

Aguillera, J. G., 1888, Fenomenos seismicos del 3 de Mayo de 1887: Anales del Ministerio de Fomento de la Republica Mexicana, 10: 5–56.

Allmendinger, R. W., Sharp, J. W., Tish, D. von, Serpa, L., Brown, L., Kaufman, S., Oliver, J., and Smith, R. B., 1983, Cenozoic and Mesozoic structure of the eastern Basin and Range Province, Utah, from COCORP seismic reflection data: Geology, 11: 532–536.

Anderson, C., and Silver, L. T., 1976, Yavapai Series—A greenstone belt: Arizona Geological Society Digest, 10: 13–26.

Anderson, J. L., 1983, Proterozoic anorogenic granite plutonism of North America: Geological Society of America, Memoir 161: 133–154.

Anderson, R. E., 1971, Thin skin distension in Tertiary rocks of southeastern Nevada: Geological Society of America, Bulletin, 82: 41–58.

Anderson, S. R., 1987, Cenozoic stratigraphy and geologic history of the Tucson basin, Pima County, Arizona: U.S. Geological Survey, Water-Resources Investigations Report 87-4190: 20 pp.

Anderson, T. H., and Silver, L. T., 1978, Jurassic magmatism in Sonora, Mexico (abs.): Geological Society of America, Abstracts with Programs, 10(7): 359.

Armin, R. A., 1987, Sedimentology and tectonic significance of Wolfcampian (Lower Permian) conglomerates in the Pedregosa basin: Southeastern Arizona, southwestern New Mexico, and northern Mexico: Geological Society of America, Bulletin, 99: 42–65.

Asmerom, Y., Zartman, R. E., Damon, P. E., and Shafiqullah, M., 1988, U–Th–Pb zircon ages from Santa Rita Mountains, SE Arizona: Implications for timing of early Mesozoic magmatism (abs.): Geological Society of America, Cordilleran Section, Abstracts with Programs, 20(3): 140.

Assadi, S. M., 1964, Structure of Golden Gate Mountain, Pima County Arizona: Unpublished M.S. thesis, University of Arizona, Tucson, 62 pp.

Atwater, T., 1970, Implications of plate tectonics for the Cenozoic tectonic evolution of western North America: Geological Society of America, Bulletin, 81: 3513–3536.

Bachman, C. O., 1975, New Mexico; *in* McKee, E. D., Crosby, E. J., et al. (eds.), Paleotectonic investigations of the Pennsylvanian System in the United States: U.S. Geology Survey, Professional Paper 853 (I): 233–243.

Bacon, C. R., 1985, Implications of silicic vent patterns for the presence of large crustal magma chambers: Journal of Geophysical Research, 90(B13): 11,243–11,252.

Banks, N. G., and Dockter, R. D., 1976, Reconnaissance geologic map of the Vaca Hills quadrangle: U.S. Geological Survey, Miscellaneous Field Studies Map MF-793.

Bikerman, M., 1963, Origin of the Cat Mountain Rhyolite: Arizona Geological Society Digest, 6: 83–89.

Bikerman, M., and Damon, P. E., 1966, K–Ar chronology of the Tucson Mountains, Pima County, Arizona: Geological Society of America, Bulletin, 77: 1225–1234.

Bilodeau, W. L., 1982, Tectonic models for Early Cretaceous rifting in southeastern Arizona: Geology, 10: 466–470.

Bilodeau, W. L., Kluth, C. F., and Vedder, L., 1987, Regional stratigraphic, sedimentologic, and tectonic relationships of the Glance Conglomerate in southeastern Arizona; *in* Dickinson, W. R., and Klute, M. A. (eds.), Mesozoic rocks of southern Arizona and adjacent areas: Arizona Geological Society Digest, 18: 229–256.

Brown, W. H., 1939, Tucson Mountain, an Arizona desert range: Geological Society of America, Bulletin, 50: 697–760.

Bryan, C. R., Geology and geochemistry of mid-Tertiary volcanic rocks in the eastern Chiricahua Mountains, southeastern Arizona: Unpublished M.S. thesis, University of New Mexico, Albuquerque, 137 pp.

Cameron, K. L., Clark, L. F., and Cameron, M., 1983, A preliminary report on the nature of the lower crust and mantle beneath southeast Chihuahua; *in* Geology and mineral resources of northcentral Chihuahua: El Paso Geological Society, Field Conference Guidebook, pp. 102–107.

Carter, J. L., 1965, The origin of olivine bombs and related inclusions in basalts: Unpublished Ph.D. thesis, Rice University, Houston, Texas, 264 pp.

Carter, J. L., 1970, Mineralogy and chemistry of the earth's mantle based on the partial fusion–partial crystallization model: Geological Society of America, Bulletin, 81: 2021–2034.

Chapin, C. E., 1971, The Rio Grande rift, Part I: Modifications and additions; *in* James, H. L. (ed.), Guidebook of the San Luis basin, Colorado: New Mexico Geological Society, Guidebook 22: 191–201.

Chapin, C. E., 1979, Evolution of the Rio Grande rift—A summary; *in*

Riecker, R. E. (ed.), Rio Grande rift: Tectonics and magmatism: American Geophysical Union, Washington, D.C., pp. 1–15.

Chen, J. H., and Moore, J. G., 1982, Uranium–lead isotopic ages from the Sierra Nevada batholith, California: Journal of Geophysical Research, 87(B6): 4761–4784.

Christiansen, R. L., and Lipman, P. W., 1972, Cenozoic volcanism and plate tectonic evolution of the western United States. Pt. 2, Late Cenozoic: Philosophical Transactions of the Royal Society of London, 271: 249–284.

Condie, K. C., 1981, Precambrian rocks of southwestern United States and adjacent areas of Mexico: New Mexico Bureau of Mines & Mineral Resources, Geologic Map 13, scale 1:1,000,000.

Condie, K. C., 1982, Plate-tectonics model for Proterozoic continental accretion in the southwestern United States: Geology, 10: 37–42.

Condie, K. C., and Budding, A. J., 1979, Geology and geochemistry of Precambrian rocks, central and south-central New Mexico: New Mexico Bureau of Mines & Mineral Resources, Memoir 35: 58 pp.

Condie, K. C., Bowling, G. P., and Vance, R. K., 1985, Geochemistry and origin of early Proterozoic supracrustal rocks, Dos Cabezas Mountains, southeast Arizona: Geological Society of America, Bulletin, 96: 655–662.

Coney, P. J., 1980, Cordilleran metamorphic core complexes: An overview; *in* Crittenden, M. D., Jr., Coney, P. J., and Davis, G. H. (eds.), Cordilleran metamorphic core complexes: Geological Society of America, Memoir 153: 7–31.

Coney, P. J., and Reynolds, S. J., 1977, Cordilleran Benioff zones: Nature, 270: 403–406.

Conway, C. M., and Wrucke, C. T., 1986, Proterozoic geology of the Sierra Ancha–Tonto basin–Mazatzal Mountains area, road log and field guide: Arizona Geological Society Digest, 16: 227–247.

Cook, F. A., Decker, E. R., and Smithson, S. B., 1978, Preliminary transient heat flow model of the Rio Grande rift in southern New Mexico: Earth and Planetary Science Letters, 40: 316–326.

Coombs, D. S., and Wilkinson, J. F. G., 1969, Lineages and fractionation trends in undersaturated volcanic rocks from the East Otago volcanic province (New Zealand) and related rocks: Journal of Petrology, 10: 440–501.

Cooper, J. R., 1959, Reconnaissance geologic map of southeastern Cochise County, Arizona: U.S. Geological Survey, Mineral Investigation Field Studies Map MF-213, scale 1:62,500.

Davis, G. H., 1979, Laramide folding and faulting in southeastern Arizona: American Journal of Science, 279: 543–569.

Davis, G. H., 1980, Structural characteristics of metamorphic core complexes; *in* Crittenden, M. D., Jr., Coney, P. J., and Davis, G. H. (eds.), Cordilleran metamorphic core complexes: Geological Society of America, Memoir 153: 35–77.

Davis, G. H., 1983, Shear-zone model for the origin of metamorphic core complexes: Geology, 11: 342–347.

Davis, G. H., and Hardy, J. J., Jr., 1981, The Eagle Pass detachment, southeastern Arizona: Product of mid-Miocene listric(?) normal faulting in the southern Basin and Range: Geological Society of America, Bulletin, pt. I, v. 92: 749–762.

Davis, G. H., Showalter, S. R., Benson, G. S., McCalmont, L. S., and Cropp, F. W., III, 1981, Guide to the geology of the Salt River Canyon region, Arizona: Arizona Geological Society Digest, 13: 47–98.

DeAngelo, M. V., and Keller, G. R., 1988, Geophysical anomalies in southwestern New Mexico: New Mexico Geological Society, Guidebook 39: 71–75.

Decker, E. R., and Smithson, S. B., 1975, Heat flow and gravity interpretation across the Rio Grande rift in southern New Mexico and West Texas: Journal of Geophysical Research, 80: 2542–2552.

De Hon, R. H., 1965, Maars of La Mesa: New Mexico Geological Society, Guidebook 15: 204–209.

Derlich, S., 1970, Underground nuclear explosion effects in granite rock fracturing; *in* Symposium on Engineering with Nuclear Explosives, Conference 700101, Las Vegas, Nevada, January 14–16, 1970, sponsored by the American Nuclear Society in cooperation with the U.S. Atomic Energy Commission, Proceedings Volume 1: National Bureau of Standards, Springfield, Virginia, pp. 505–518.

Dickinson, W. R., 1981, Plate tectonic evolution of the southern Cordillera: Arizona Geological Society Digest, 14: 113–135.

Dickinson, W. R., 1984, Reinterpretation of Lime Peak thrust as a low-angle normal fault: Implications for the tectonics of southeastern Arizona: Geology, 12: 610–613.

Dickinson, W. R., and Klute, M. A. (eds.), 1987, Mesozoic rocks of southern Arizona and adjacent areas: Arizona Geological Society Digest, 18: 394.

Dickinson, W. R., Goodlin, T. C., Grover, J. A., and Mark, R. A., 1987, Low-angle normal-fault system along the range front of the southwestern Galiuro Mountains in southeastern Arizona: Geology, 15: 727–730.

Downes, H., 1987, Relationship between geochemistry and textural type in spinel lherzolites, Massif Central and Languedoc, France; *in* Nixon, P. H. (ed.), Mantle xenoliths: John Wiley & Sons, pp. 125–134.

Drewes, H., 1980, Tectonic map of southeast Arizona: U.S. Geological Survey, Miscellaneous Investigations Map I-1109, scale 1:125,000.

Drewes, H. D., 1981, Tectonics of southeastern Arizona: U.S. Geological Survey, Professional Paper 1144: 96 pp.

Drewes, H. D., 1982, Cochise Head quadrangle and adjacent areas, southeastern Arizona: U.S. Geological Survey, Miscellaneous Investigations Map I-1312, scale 1:24,000.

Drewes, H. D., and Williams, F. E., 1973, Mineral resources of the Chiricahua Wilderness Area, Cochise County, Arizona: U.S. Geological Survey, Bulletin 1385-A: 53 pp.

Drewes, H. D., Houser, B. B., Hedlund, D. C., Richter, D. H., Thorman, C. H., and Finnell, T. H., 1985, Geologic map of the Silver City 1° by 2° Quadrangle, New Mexico and Arizona: U.S. Geological Survey, Miscellaneous Investigations Series Map, scale 1:250,000.

Eberly, L. D., and Stanley, T. D., 1978, Cenozoic stratigraphy and geologic history of west-central Arizona: Geological Society of America, Bulletin, 89: 921–940.

Eggler, D. H., 1987, Solubility of major and trace elements in mantle metasomatic fluids; *in* Menzies, M. A., and Hawkesworth, C. J. (eds.), Mantle metasomatism: Academic Press, pp. 21–41.

Ehrenberg, S. N., 1982, Rare earth element geochemistry of garnet lherzolite and megacrystalline nodules from minette of the Colorado Plateau province: Earth and Planetary Science Letters, 57: 191–210.

Ehrenberg, S. N., and Griffin, W. L., 1979, Garnet granulite and associated xenoliths in minette and serpentinite diatremes of the Colorado Plateau: Geology, 7: 483–487.

Eichelberger, J. C., Carrigan, H. R., Westrich, H. R., and Price, R. H., 1986, Non-explosive silicic volcanism: Nature, 323: 598–602.

Einaudi, M. T., 1982, Description of skarns associated with porphyry copper plutons, southwestern North America; *in* Titley, S. R. (ed.), Advances in the geology of the porphyry copper deposits: University of Arizona Press, Tucson, pp. 139–184.

Engebretson, D. C., Cox, A., and Gordon, R. G., 1985, Relative motions between oceanic and continental plates in the Pacific basin: Geological Society of America, Special Paper 206: 58 pp.

Engebretson, D. C., Cox, A., and Thompson, G. A., 1984, Correlation of plate motions with continental tectonics: Laramide to basin–range: Tectonics, 3(2): 115–119.

Enlows, H. E., 1955, Welded tuffs of the Chiricahua National Monument, Arizona: Geological Society of America, Bulletin, 66: 1215–1246.

Epis, R. C., 1956, Geology of the Pedregosa Mountains, Cochise County Arizona: Unpublished Ph.D. dissertation, University of California, Berkeley, 263 pp.

Evans, K. V., and Clemons, R. E., 1988, Cambrian–Ordovician (500 Ma) alkalic plutonism in southwestern New Mexico: U–Th–Pb isotopic data from the Florida Mountains: American Journal of Science, 288: 735–755.

Everson, J. E., 1979, Regional variations in the lead isotopic characteristics of late Cenozoic basalts from the southwestern United States: Unpublished Ph.D. dissertation, California Institute of Technology, Pasadena, 454 pp.

Fernandez, L. A., Jr., and Enlows, H. E., 1966, Petrography of the Faraway Ranch Formation, Chiricahua National Monument, Arizona: Geological Society of America, Bulletin, 77: 1017–1030.

Frey, F. A., and Green, D. H., 1974, The mineralogy, geochemistry and origin of lherzolite inclusions in Victorian basanites: Geochimica et Cosmochimica Acta, 38: 1023–1059.

Frey, F. A., and Prinz, M., 1978, Ultramafic inclusions from San Carlos, Arizona: Petrologic and geochemical data bearing on their petrogenesis: Earth and Planetary Science Letters, 38: 129–176.

Fridrich, C. J., 1987, Syntectonic caldera formation, plutonism, and porphyry Cu(Mo) mineralization in the Sierrita Mountains, Arizona (abs.): Geological Society of America, Abstracts with Programs, 19(7): 668.

Friedman, I., 1988, Are extrusive rhyolites produced from permeable foam eruptions?: Bulletin of Volcanology (in press).

Gans, P. B., 1987, An open-system, two-layer crustal stretching model for the eastern Great Basin: Tectonics, 6: 1–12.

Gans, P. B., Mahood, G., and Schermer, E., 1987, Synextensional magmatism in the Basin and Range Province: A case study from the eastern Great Basin (abs.): Geological Society of America, Abstracts with Programs, 19(7): 671.

Ghent, E. D., 1976, Plagioclase–garnet–Al_2SiO_5–quartz: A potential geobarometer–geothermometer: American Mineralogist, 61: 710–714.

Gile, L. H., 1987, A pedogenic chronology for Kilbourne Hole, southern New Mexico—II. Time of the explosions and soil events before the explosions: Soil Society of America, Journal, 51: 746–760.

Gish, D. M., Keller, G. R., and Sbar, M. L., 1981, A refraction study of deep crustal structure in the Basin and Range—Colorado Plateau of eastern Arizona: Journal of Geophysical Research, 86(B7): 6029–6038.

Glazner, A., and Supplee, J. A., 1982, Migration of Tertiary volcanism in the southwestern United States and subduction of the Mendocino fracture zone: Earth and Planetary Science Letters, 60: 429–436.

Graybeal, F. T., 1982, Geology of the El Tiro area; *in* Titley, S. R. (ed.), Advances in the geology of the porphyry copper deposits: University of Arizona Press, Tucson, pp. 487–507.

Griffin, W. R., and O'Reilly, S. Y., 1987, Is the continental Moho the crust–mantle boundary?: Geology, 15: 241–244.

Gunderson, R., Cameron, K., and Cameron, M., 1986, Mid-Cenozoic high-K calc-alkalic and alkalic volcanism in eastern Chihuahua, Mexico: Geology and geochemistry of the Benavides–Pozes area: Geological Society of America, Bulletin, 87: 737–753.

Hamilton, W. B., and Myers, W. B., 1967, The nature of batholiths: U.S. Geological Survey, Professional Paper 554-C: 30 pp.

Hawkesworth, C. J., Rogers, N. W., van Calsteren, P., and Menzies, M. A., 1984, Mantle enrichment processes: Nature, 311: 331–335.

Hawley, J. W., and Kottlowski, F. E., 1969, The Santa Fe Group in the south-central New Mexico border region; *in* Kottlowski, F. E., and Lemone, D. V. (eds.), Border stratigraphy symposium: New Mexico Bureau of Mines & Mineral Resources, Circular 104: 52–67.

Haxel, G. B., Tosdal, R. M., May, D. J., and Wright, J. E., 1984, Latest Cretaceous and early Tertiary orogenesis of southcentral Arizona: Thrust faulting, regional metamorphism, and granitic plutonism: Geological Society of America, Bulletin, 95: 631–653.

Hayes, P. T., and Drewes, H., 1978, Mesozoic depositional history of southeastern Arizona; *in* Callender, J. T., Wilt, J. C., and Clemons, R. E. (eds.), Land of Cochise: New Mexico Geological Survey, Guidebook 29: 201–207.

Helmstaedt, H., and Doig, R., 1975, Eclogite nodules from kimberlite pipes of the Colorado Plateau—samples of subduction related Franciscan-type oceanic lithosphere: Physics and Chemistry of the Earth, 9: 95–111.

Herd, D., and McMasters, C., 1982, Surface faulting in the Sonora, Mexico earthquake of 1887 (abs.): Geological Society of America, Abstracts with Programs, 14: 172.

Hoffer, J. M., 1971, Mineralogy and petrology of the Santo Tomas–Black Mountains basalts, Potrillo volcanics, south-central New Mexico: Geological Society of America, Bulletin, 82: 602–612.

Hoffer, J. M., 1975, The Aden–Afton basalt, Potrillo volcanics, south-central New Mexico: Texas Journal of Science, 26(3–4): 380–390.

Hoffer, J. M., 1976, Geology of Potrillo basalt field, south-central New Mexico: New Mexico Bureau of Mines & Mineral Resources, Circular 149: 30 pp.

Hoffer, J. M., 1976, The Potrillo basalt field, south-central New Mexico: New Mexico Geological Society, Special Publication no. 3: 89–92.

Irving, A. J., 1980, Petrology and geochemistry of composite ultramafic xenoliths in alkali basalts and implications of magmatic processes within the mantle: American Journal of Science, 280A: 389–426.

Jagoutz, E., Lorenz, V., and Wanke, H., 1979, Major trace elements of Al-augites and Cr-diopsides from ultramafic nodules in European alkali basalts; *in* Boyd, F. R., and Meyer, H. O. A. (eds.), The mantle sample: Inclusions in kimberlites and other volcanics: American Geophysical Union, Washington, D.C., pp. 382–390.

James, D. E., Padovani, E. R., and Hart, S. R., 1980, Preliminary results on the oxygen isotope composition of the lower crust, Kilbourne Hole maar, New Mexico: Geophysical Research Letters, 7: 321–324.

Jiracek, G. R., Ander, M. E., and Holcombe, H. T., 1979, Magnetotelluric soundings of crustal conductive zones in major continental rift zones; *in* Riecker, R. E. (ed.), Rio Grande rift: Tectonics and magmatism: American Geophysical Union, Washington, D.C., pp. 209–222.

Karlstrom, K. E., Bowring, S. A., and Conway, C. M., 1987, Tectonic significance of an Early Proterozoic two-province boundary in central Arizona: Geological Society of America, Bulletin, 99: 529–538.

Kay, R. W., and Kay, S. M., 1981, The nature of the lower continental crust: Inferences from geophysics, surface geology and crustal xenoliths: Reviews of Geophysics and Space Physics, 19: 271–297.

Kay, S. M., and Kay, R. W., 1983, Thermal history of the deep crust inferred from granulite xenoliths, Queensland, Australia: American Journal of Science, 283A: 486–513.

Keith, S. B., and Wilt, J. C., 1986, Laramide orogeny in Arizona and adjacent regions: A strato-tectonic synthesis: Arizona Geological Society Digest, 16: 502–554.

Kempton, P. D., 1984, I. Alkalic basalts from the Geronimo volcanic field: Petrologic and geochemical data bearing on their petrogenesis, II. Petrography, petrology, and geochemistry of xenoliths and megacrysts from the Geronimo volcanic field, southeastern Arizona, III. An interpretation of contrasting nucleation and growth histories from the petrographic analysis of pillow and dike chilled margins, Hole 504B, DSDP Leg 83: Unpublished Ph.D. dissertation, Southern Methodist University, Dallas, 275 pp.

Kempton, P. D., 1987, Mineralogic and geochemical evidence for differing styles of metasomatism in spinel lherzolite xenoliths: Enriched mantle source regions of basalts; *in* Menzies, M. A., and Hawkesworth, C. J. (eds.), Mantle metasomatism: Academic Press, pp. 45–89.

Kempton, P. D., Dungan, M. A., and Blanchard, D. P., 1987, Petrology and geochemistry of xenolith-bearing alkalic basalts from the Geronimo volcanic field, SE Arizona: Evidence for polybaric fractionation and implications for mantle heterogeneity; *in* Morris, E. M., and Pasteris, J. D. (eds.), Mantle metasomatism and alkaline magmatism: Geological Society of America, Special Paper 215: 347–370.

Kempton, P. D., Dungan, M. A., and Menzies, M. A., 1982, Petrography and geochemistry of amphibole peridotites from the Geronimo volcanic field, SE Arizona (abs.): Geological Society of America, Abstracts with Programs, 14: 528.

Kempton, P. D., Menzies, M. A., and Dungan, M. A., 1984, Petrography, petrology, and geochemistry of xenoliths and megacrysts from the Geronimo volcanic field, southeastern Arizona; *in* Kornprobst, J. (ed.), The mantle and crust mantle relationships—mineralogical, petrological, and geodynamic processes: Elsevier, Amsterdam, pp. 71–85.

Kinnison, J. E., 1958, Geology and ore deposits of the southern section of the Amole mining district, Tucson Mountains, Pima County, Arizona: Unpublished M.S. thesis, University of Arizona, Tucson, 123 pp.

Klemperer, S. L., Hauge, T. A., Hauser, E. C., Oliver, J. E., and Potter, C. J., 1986, The Moho in the northern Basin and Range province, Nevada, along the COCORP 40°N seismic reflection transect: Geological Society of America, Bulletin, 97: 603–618.

Kluth, C. F., 1986, Plate tectonics of the ancestral Rocky Mountains; *in* Peterson, J. A. (ed.), Paleotectonics and sedimentation in the Rocky Mountain region, United States: American Association of Petroleum Geologists, Memoir 41: 353–369.

Kluth, C. F., Butler, R. F., Harding, L. E., Shafiqullah, M., and Damon, P. E., 1982, Paleomagnetism of Late Jurassic rocks in the northern Canelo Hills, southeastern Arizona: Journal of Geophysical Research, 87(B8): 7079–7086.

Knight, L. H., 1967, Structural geology of the Cat Mountain Rhyolite in the northern Tucson Mountains, Pima County, Arizona: Unpublished M.S. thesis, University of Arizona, Tucson, 68 pp.

Koski, R. A., and Cook, D. S., 1982, Geology of the Christmas porphyry copper deposit, Gila County, Arizona; *in* Titley, R. (ed.), Advances in geology of the porphyry copper deposits, southwestern North America: University of Arizona Press, pp. 355–360.

Krogh, T. E., and Davis, G. L., 1968, Geological history of the Grenville Province: Carnegie Institution of Washington, Yearbook, 66: 44–52.

Krogh, T. E., and Davis, G. L., 1971, Paragneiss studies in the Georgian Bay area, 90 km southeast of the Grenville Front: Carnegie Institute of Washington, Yearbook, 69: 339–341.

Kurat, G., Palme, H., Spettel, B., Baddenhousen, H., Hofmeierter, H., Palme, C., and Wänke, 1980, Geochemistry of ultramafic xenoliths from Kapfenstein, Austria: Evidence for a variety of upper mantle processes: Geochimica et Cosmochimica Acta, 44: 45–60.

Larson, E. E., Mutschler, F. E., Munoz, J. L., Drexler, J. W., and Fears, D. W., 1987, Laramide and younger magmatism in Colorado—new petrologic and tectonic variations on old themes (abs.): Geological Society of America, Abstracts with Programs, 19(5): 313.

Latta, J. S., 1983, Geochemistry and petrology of the ash flows of Chiricahua National Monument, Arizona, and their relation to the Turkey Creek caldera: Unpublished M.S. thesis, University of Arizona, Tucson, 194 pp.

Lee, W. T., 1907, Afton Craters of southern New Mexico: Geological Society of America, Bulletin, 18: 211–220.

Leyreloup, A., Dupuy, C., and Adriambololona, R., 1977, Catazonal xenoliths in French Neogene volcanic rocks: Constitution of the lower crust: Contributions to Mineralogy and Petrology, 62: 283–300.

Lines, H. L., 1940, Mining and milling methods and costs at the Ash Peak Mines of the Veta Mines, Inc., Duncan, Arizona: U.S. Bureau of Mines, Information Circular 7119: 26 pp.

Lipman, P. W., 1976, Caldera-collapse breccias in the western San Juan Mountains, Colorado: Geological Society of America, Bulletin, 87: 1397–1410.

Lipman, P. W., 1980, Cenozoic volcanism in the western United States:

implications for continental tectonics; *in* Continental tectonics: Geophysics Study Committee, National Research Council, Washington, D.C., pp. 161–174.
Lipman, P. W., and Sawyer, D. A., 1985, Mesozoic ash-flow caldera fragments in southeastern Arizona and their relation to porphyry copper deposits, Geology, 13: 652–656.
Lynch, D. J., 1978, The San Bernardino volcanic field of southeastern Arizona: New Mexico Geological Society, Guidebook 29: 261–268.
Macdonald, G. A., 1972, Volcanoes: Prentice–Hall, Inc., Englewood Cliffs, New Jersey, p. 211.
Macdonald, G. A., and Katsura, T., 1964, Chemical composition of Hawaiian lavas: Journal of Petrology, 5: 82–133.
MacGregor, I., 1979, Mineralogy of model mantle compositions; *in* Wyllie, P. J. (ed.), Ultramafic and related rocks: Robert E. Krieger Publ. Co., Huntington, N.Y., pp. 382–393.
Machette, M. N., Personius, S. F., Menges, C. M., and Pearthree, P. A., 1986, Map showing Quaternary and Pliocene faults in the Silver City 1° × 2° quadrangle and the Douglas 1° × 2° quadrangle, southeastern Arizona and southwestern New Mexico: U.S. Geological Survey, Miscellaneous Field Studies Map MF-1465-C.
Mahood, G. A., and Hildreth, W., 1983, Large partition coefficients for trace elements in high-silica rhyolites: Geochimica et Cosmochimica Acta, 47: 11–30.
Marjaniemi, D. K., 1969, Geologic history of an ash-flow sequence and its source area in the Basin and Range Province of southeastern Arizona: Unpublished Ph.D. dissertation, University of Arizona, Tucson, 176 pp.
Mauger, R. L., Damon, P. D., and Giletti, B. J., 1965, Isotopic dating of Arizona ore deposits: American Institute of Mining, Metallurgical and Petroleum Engineers, Transactions, 232: 81–87.
May, S. R., and Butler, R. F., 1987, Paleomagnetism of the Jurassic Canelo Hills Volcanics, southeastern Arizona; *in* Dickinson, W. R., and Klute, M. A. (eds.), Mesozoic rocks of southern Arizona and adjacent areas: Arizona Geological Society Digest, 18: 121–138.
Mayo, E. B., 1963, Volcanic orogeny of the Tucson Mountains (a preliminary report): Arizona Geological Society Digest, 6: 61–82.
Mayo, E. B., 1971a, Defense of "volcanic orogeny": Arizona Geological Society Digest, 9: 39–60.
Mayo, E. B., 1971b, Feeders of an ash flow sequence on Bren Mountain, Tucson Mountain Park, Arizona: Geological Society of America, 9: 137–170.
McGetchin, T. R., and Silver, L. T., 1972, A crustal–upper mantle model for the Colorado Plateau based on observations of crystalline rock fragments in the Moss Rock dike: Journal of Geophysical Research, 77: 7022–7037.
McKee, E. D., Crosby, E. J., et al. (eds.), 1975, Paleotectonic investigations of the Pennsylvanian System in the United States: U.S. Geological Survey, Professional Paper 853, pt. III.
Mehnert, K. R., 1975, The Ivrea Zone—A model of the deep crust: Neues Jahrbuch für Mineralogie, Abhandlungen, pt. 2, v. 125: 156–199.
Menzies, M. A., Kempton, P. D., and Dungan, M., 1985, Interaction of continental lithosphere and asthenospheric melts below the Geronimo volcanic field, Arizona, USA: Journal of Petrology, 26: 663–693.
Menzies, M. A., Leeman, W. P., and Hawkesworth, C. J., 1984, Isotope geochemistry of Cenozoic volcanic rocks reveals mantle heterogeneity below western USA: Nature, 303: 205–209.
Morgan, J. W., 1986, Ultramafic xenoliths: Clues to Earth's late accretionary history: Journal of Geophysical Research, 91: 12,375–12,287.
Nash, W. P., and Crecraft, H. R., 1985, Partition coefficients for trace elements in silicic magmas: Geochimica et Cosmochimica Acta, 49: 2309–2322.
Olsen, K. H., Baldridge, S. W., and Callender, J. F., 1987, Rio Grande rift: an overview: Tectonophysics, no. 143: 119–139.
Olsen, K. H., Keller, G. R., and Stewart, J. N., 1979, Crustal structure along the Rio Grande rift from seismic refraction profiles; *in* Riecker, R. E. (ed.), Rio Grande rift: Tectonics and magmatism: American Geophysical Union, Washington, D.C., pp. 127–144.
Oppenheimer, J., and Sumner, J., 1980, Depth-to-bedrock map, Basin and Range province, Arizona: Tucson, University of Arizona, Laboratory of Geophysics, scale 1:1,000,000.
Ortiz, T. S., 1980, Occurrence and mineral chemistry of high pressure phases, Potrillo basalt, south-central New Mexico: Unpublished M.S. thesis, University of Texas, El Paso, 94 pp.
Padovani, E. R., 1977, Granulite facies xenoliths from Kilbourne Hole maar and their bearing on deep crustal evolution: Unpublished Ph.D. dissertation, University of Texas, Dallas.
Padovani, E. R., and Carter, J. L., 1977a, Aspects of deep crustal evolution beneath south-central New Mexico; *in* Heacock, J. G. (ed.), The Earth's crust: Its nature and physical properties: American Geophysical Union, Washington, D.C., pp 19–55.
Padovani, E. R., and Carter, J. L., 1977b, Non-equilibrium partial fusion due to decompression and thermal effects in crustal xenoliths: Oregon Department of Geology and Mineral Industries, Bulletin, 96: 43–57.
Pasteris, J. D., 1987, Fluid inclusions in mantle xenoliths; *in* Nixon, P. H. (ed.), Mantle xenoliths: John Wiley & Sons, pp. 691–708.
Pearce, J. A., and Cann, J. R., 1973, Tectonic setting of basic volcanic rocks determined using trace element analysis: Earth and Planetary Science Letters, 19: 290–300.
Perry, F. V., Baldridge, W. S., and DePaolo, D. J., 1987, Role of asthenosphere and lithosphere in the genesis of late Cenozoic basaltic rocks from the Rio Grande rift and adjacent regions of the southwestern United States: Journal of Geophysical Research, 92(B9): 9193.
Pohl, J., Stöffler, D., Gall, H., and Ernstson, K., 1977, The Ries impact crater; *in* Roddy, D. J., Pepin, R. O., and Merrill, R. B. (eds.), Impact and explosion cratering: Pergammon Press, New York, pp. 343–404.
Poldervaart, A., 1955, Chemistry of the Earth's crust; *in* Poldervaart, A. (ed.), Crust of the Earth—a symposium: Geological Society of America, Special Paper 62: 119–144.
Press, S., Witt, G., Seck, H. A., Eonov, D., and Kovalenko, V. I., 1986, Spinel peridotite xenoliths from the Tariat Depression, Mongolia. I: Major element chemistry and mineralogy of a primitive mantle xenolith suite: Geochimica et Cosmochimica Acta, 50: 2587–2599.
Proffett, J. M., 1977, Cenozoic geology of the Yerington district, Nevada, and implications for the nature and origin of Basin and Range faulting: Geological Society of America, Bulletin, 88: 247–266.
Ramberg, I. V., Cook, F. A., and Smithson, S. B., 1978, Structure of the Rio Grande rift in southern New Mexico and West Texas based on gravity interpretation: Geological Society of America, Bulletin, 89: 107–123.
Raydon, G. T., 1952, Geology of the northeastern Chiricahua Mountains, Arizona: Unpublished M.S. thesis, University of California, Berkeley.
Reeves, C. C., Jr., and De Hon, R. A., 1965, Geology of Potrillo maar, New Mexico and northern Chihuahua, Mexico: American Journal of Science, 263: 401–409.
Reid, M. R., 1987, Chemical stratification of the crust: Isotope, trace element, and major element constraints from crustally contaminated lavas and lower crustal xenoliths: Unpublished Ph.D. dissertation, Massachusetts Institute of Technology, Cambridge, 324 pp.
Reid, M., Hart, S. R., and Padovani, E. R., 1982, Evolution of the lower crust beneath Kilbourne Hole, NM (abs.): Geological Society of America, Abstracts with Programs, 14: 597.
Reynolds, S. J., Shafiqullah, M., Damon, P. E., and DeWitt, E., 1986, Early Miocene mylonitization and detachment faulting, South Mountains, central Arizona: Geology, 14: 283–286.
Reynolds, S. J., Spencer, J. E., and DeWitt, E., 1987, Stratigraphy and U–Th–Pb geochronology of Triassic and Jurassic rocks in west-central Arizona; *in* Dickinson, W. R., and Klute, M. A. (eds.), Mesozoic rocks of southern Arizona and adjacent areas: Arizona Geological Society Digest, 18: 65–80.
Richard, K., and Courtright, J. H., 1966, Structure and mineralization at Silver Bell, Arizona; *in* Titley, S. R., and Hicks, C. (eds.), Geology of the porphyry copper deposits: University of Arizona Press, Tucson, pp. 158–163.
Richardson, S. H., Padovani, E. R., and Hart, S. R., 1980, The gneiss syndrome: Nd- and Sr-isotopic relationships in lower crustal xenoliths, Kilbourne Hole, New Mexico: American Geophysical Union, Transactions, 61: 388.
Richter, D. H., Houser, B. B., and Damon, P. E., 1983, Geologic map of the Guthrie quadrangle, Graham and Greenlee Counties, Arizona: U.S. Geological Survey, Miscellaneous Investigations Series Map I-1455, scale 1:48,000.
Richter, D. H., and Lawrence, V. A., 1983, Mineral deposit map of the Silver City 1° × 2° quadrangle, New Mexico and Arizona: U.S. Geological Survey, Miscellaneous Investigations Series Map I-1310-B, scale 1:250,000.
Richter, D. H., Shafiqullah, M., and Lawrence, V. A., 1981, Geologic map of the Whitlock Mountains and vicinity, Graham County, Arizona: U.S. Geological Survey, Miscellaneous Investigations Series Map I-1302, scale 1:48,000.
Richter, D. H., Lawrence, V. A., Drewes, H., Damon, P. E., Young, T. H., Enders, M. S., and Thorman, C. H., 1988, Reconnaissance geologic map of the San Simon quadrangle and western part of Mondel quadrangle, Cochise and Graham counties, Arizona, and Hidalgo County, New Mexico: U.S. Geological Survey, Miscellaneous Field Studies Map I-1951, scale 1:48,000 (in press).
Riggs, N., 1987, Stratigraphy, structure, and geochemistry of Mesozoic rocks in the Pajarito Mountains, Santa Cruz County, Arizona; *in* Dick-

inson, W. R., and Klute, M. A. (eds.), Mesozoic rocks of southern Arizona and adjacent areas: Arizona Geological Society Digest, 18: 165–176.

Risley, R., 1987, Sedimentation and stratigraphy of the Lower Cretaceous Amole Arkose, Tucson Mountains, Arizona; *in* Dickinson, W. R., and Klute, M. A. (eds.), Mesozoic rocks of southern Arizona and adjacent areas: Arizona Geological Society Digest, 18: 215–228.

Roden, M. F., Irving, A. J., and Murthy, V. R., 1988, Isotopic and trace element composition of the upper mantle beneath a young continental rift: Results from Kilbourne Hole, New Mexico: Geochimica et Cosmochimica Acta, 52: 461–473.

Rogers, N. W., 1977, Granulite xenoliths from Lesotho kimberlites and the lower continental crust, Nature, 270: 681–684.

Rudnick, R. L., McDonough, W. F., McCullough, M. T., and Taylor, S. R., 1986, Lower crustal xenoliths from Queensland, Australia: Evidence for deep crustal assimilation and fractionation of continental basalts: Geochimica et Cosmochimica Acta, 50: 1099–1115.

Sabens, E. F., Jr., 1957, Geology of the Cochise Head and western part of the Vanar Quadrangles, Arizona: Geological Society of America, Bulletin, 68: 1315–1342.

Sawyer, D. A., 1986, Late Cretaceous caldera volcanism and porphyry copper deposits, Silver Bell Mountains, southern Arizona (roadlog): Arizona Geological Society Digest, 16: 408–421.

Sawyer, D. A., 1987, Late Cretaceous volcanism and porphyry copper mineralization at Silver Bell, Pima County, Arizona: Geology, petrology and geochemistry: Unpublished Ph.D. dissertation, University of California, Santa Barbara, 400 pp.

Scandone, R., and Malone, S. D., 1985, Magma supply, magma discharge and readjustments of the feeding system of Mount St. Helens during 1980: Journal of Volcanology and Geothermal Research, 23: 239–262.

Scarborough, R. B., and Pierce, H. W., 1978, Late Cenozoic basins of Arizona; *in* Callender, J. T., Wilt, J. C., and Clemons, R. E. (eds.), Land of Cochise: New Mexico Geological Society, Guidebook 29: 253–259.

Schmitt, H. A., 1966, The porphyry copper deposits in their regional setting; *in* Titley, S. R., and Hicks, C. L. (eds.), Geology of the porphyry copper deposits, southwestern North America: University of Arizona Press, Tucson, pp. 17–35.

Schweickert, R. A., Bogen, N. L., Girty, G. H., Hanson, R. E., and Merguerian, C., 1984, Timing and structural expression of the Nevadan orogeny, Sierra Nevada, California: Geological Society of America, Bulletin, 95: 967–979.

Seager, W. R., 1983, Laramide wrench faults, basement-cored uplifts, and complementary basins in southern New Mexico: New Mexico Geology, 5: 69–76.

Seager, W. R., 1987, Caldera-like collapse at Kilbourne Hole maar, New Mexico: New Mexico Geology, 9: 69–73.

Seager, W. R., and Morgan, P., 1979, Rio Grande rift in southern New Mexico, West Texas, and northern Chihuahua; *in* Riecker, R. E. (ed.), Rio Grande rift: Tectonics and magmatism: American Geophysical Union, Washington, D.C., pp. 87–106.

Selverstone, J., and Stern, C. R., 1983, Petrochemistry and recrystallization history of granulite xenoliths from the Pali-Aike Volcanic Field, Chile: American Mineralogist, 68: 1102–1112.

Shafiqullah, M., Damon, P. E., Lynch, D. J., Kuck, P. H., and Rehrig, W. A., 1978, Mid-Tertiary magmatism in southeastern Arizona; *in* Callendar, J. F., Wilt, J. C., and Clemons, R. E. (eds.), Land of Cochise: New Mexico Geological Society, Guidebook 29: 231–241.

Shride, A. F., 1967, Younger Precambrian geology in Arizona: U.S. Geological Survey, Professional Paper 566: 89 pp.

Silver, L. T., 1978, Precambrian formations and Precambrian history in Cochise County, southeastern Arizona; *in* Callender, J. T., Wilt, J. C., and Clemons, R. E. (eds.), Land of Cochise: New Mexico Geological Society, Guidebook 29: 157–164.

Sinigoi, S., Comin-Chiaramonti, P., Demarchi, G., and Siena, F., 1983, Differentiation of partial metls in the mantle: evidence from the Balmuccia peridotite, Italy: Contributions to Mineralogy and Petrology, 82: 251–259.

Sinno, Y. A., Keller, G. R., and Sbar, 1981, A crustal seismic refraction study in west-central Arizona: Journal of Geophysical Research, 86: 5023–5028.

Sinno, Y. A., Daggett, P. H., Keller, G. R., Morgan, P., and Harder, S. H., 1986, Crustal structure of the southern Rio Grande rift determined from seismic refraction profiling: Journal of Geophysical Research, 91(B6): 6143–6156.

Skinner, A., and Tarney, J., 1973, The geochemistry of the Scourian gneisses of the Assynt district; *in* Park, R. G., and Tarney, J. (eds.), The Early Precambrian of Scotland and related rocks of Greenland: University of Keele, Keele, England, pp. 13–30.

Smithson, S., 1978, Modeling continental crust: Structural and chemical constraints: Geophysical Research Letters, 5: 749–753.

Spera, F. J., 1980, Aspects of magma transport; *in* Hargraves, R. B. (ed.), Physics of magmatic processes: Princeton University Press, Princeton, N.J., pp. 265–323.

Stacey, J. S., and Kramers, J. D., 1975, Approximation of terrestrial lead isotope evolution by a two-stage model: Earth and Planetary Science Letters, 26: 207–221.

Steiger, R. H., and Jager, E., 1977, Subcommission on geochronology: Convention on the use of decay constants in geo- and cosmochronology: Earth and Planetary Science Letters, 36: 359–362.

Stewart, J. H., 1988, Latest Proterozoic and Paleozoic southern margin of North America and the accretion of Mexico: Geology, 16: 186–189.

Stöffler, D., Knöll, H.-D., and Maerz, U., 1979, Terrestrial and lunar impact breccias and the classification of lunar highlands rocks: Proceedings of the 10th Lunar and Planetary Science Conference, pp. 639–675.

Stormer, J. C., 1975, A practical two-feldspar geothermometer: American Mineralogist, 60: 667–674.

Stosch, H.-G., Lugmair, G. W., and Seck, H. A., 1986, Geochemistry of granulite-facies lower crustal xenoliths: implications for the geological history of the lower continental crust below the Eifel, West Germany; *in* Dawson, J. N., Carswell, D. A., Hall, J., and Wedepohl, K. H. (eds.), Geological Society (London), Special Publication 24: 309–317.

Swift, P. N., 1987, Subduction zone setting for early Proterozoic turbidite deposition and melange deformation, southeast Arizona (abs.): Geological Society of America, Abstracts with Programs, 19(7): 862.

Tatsumoto, M., 1978, Composition of lead in oceanic basalt and its implication to mantle evolution: Earth and Planetary Science Letters, 38: 63–87.

Taylor, S. R., 1977, Island arc models and the composition of the continental crust; *in* Talwani, M., and Pitman, W. (eds.), Island arcs, deep sea trenches and back arc basins, Maurice Ewing Series, v. 1: American Geophysical Union, Washington, D.C., pp. 229–242.

Titley, S. R., 1976, Evidence for a Mesozoic linear tectonic pattern in southeastern Arizona: Arizona Geological Society Digest, 10: 71–101.

Titley, S. R. (ed.), 1982, Advances in geology of the porphyry copper deposits, southwestern North America: University of Arizona Press, Tucson, 555 pp.

Tsugii, K. S., 1984, Silver mineralization of the El Tigre mine and volcanic resurgence in the Chiricahua Mountains, Cochise County, Arizona: Unpublished M.S. thesis, University of Arizona, Tucson, 140 pp.

Vedder, L. K., 1984, Stratigraphic relationship between the Late Jurassic Canelo Hills Volcanics and the Glance Conglomerate, southeastern Arizona: Unpublished M.S. thesis, University of Arizona, Tucson, 129 pp.

Walker, R. J., 1988, Magmatism and mineralization of the Ash Peak area, Arizona: Geochemical interpretations: Unpublished Ph.D. dissertation, Oregon State University, Corvallis.

Walker, R. J., and Richter, D. H., 1987, Petrogenesis of the Ash Peak–Rhyolite Peak eruptive complex, southeastern Arizona (abs.): Geological Society of America, Abstracts with Programs, 19(7): 879.

Wandless, G. A., and Padovani, E. R., 1985, Trace element geochemistry of lower crustal xenoliths from Kilbourne Hole maar, New Mexico: American Geophysical Union (EOS), Transactions, 66: 1110.

Wasilewski, P. J., and Padovani, E. R., 1981, Crustal magnetization beneath the Rio Grande rift: Conference on the Processes of Planetary Rifting, Extended Abs., Lunar and Planetary Institute, pp. 153–155.

Weaver, B. L., and Tarney, J., 1984, Empirical approach to estimating the composition of the continental crust: Nature, 310: 575–577.

Wernicke, B. P., Christiansen, R. L., England, P. C., and Sonder, L. J., 1987, Tectonomagmatic evolution of Cenozoic extensions in the North American Cordillera; *in* Coward, M. P., Dewey, J. F., and Hancock, P. L. (eds.), Continental extensional tectonics: The Geological Society, Special Publication 28: 203–221.

Williams, S. A., 1978, Mineralization at Granite Gap, Hidalgo County, New Mexico; *in* Callender, J. T., Wilt, J. C., and Clemons, R. E. (eds.), Land of Cochise: New Mexico Geological Society, Guidebook 29: 329–330.

Wilshire, J. G., 1984, Mantle metasomatism: the REE story: Geology, 12: 395–398.

Wilshire, H. G., and Padovani, E. R., 1977, Basalt nodule guide: Second International Kimberlite Conference, pp. 1–6.

Wilshire, H. G., and Pike, J. E. N., 1975, Upper-mantle diapirism; evidence from analogous features in alpine peridotites and ultramafic inclusions in basalt: Geology, 3: 467–470.

Wilshire, J. G., and Shervais, J. W., 1975, Al-augite and Cr-diopside ultramafic xenoliths in basaltic rocks from western United States; Structural and textural relationships: Physics and Chemistry of the Earth, 9: 257–272.

Wilshire, H. G., Meyer, C. E., Nakata, J. K., Calk, L. C., Shervais, J. W., Nielson, J. E., and Schwartzmann, E. G., 1985, Mafic and ultramafic rocks of the western United States: U.S. Geological Survey, Open-File Report No. 85.

Wilson, E. D., and Butler, G. M., 1930, Manganese ore deposits in Arizona: Arizona Bureau of Mines, Bulletin 127: 107 pp.

Wohletz, K. H., 1980, Explosive hydromagmatic volcanism: Unpublished Ph.D. dissertation, Arizona State University, Tempe, 303 pp.

Wohletz, K. H., and Sheridan, M. F., 1979, A model of pyroclastic surge: Geological Society of America, Special Paper 180: 177–193.

Wohletz, K. H., and Sheridan, M. F., 1983, Hydrovolcanic explosions, II: Evolution of basaltic tuff rings and tuff cones: American Journal of Science, 283: 385–413.

Wood, D. A., Tarney, J., and Weaver, B. L., 1981, Trace element variations in Atlantic Ocean basalts and Proterozoic dykes from northwest Scotland: Their bearing upon the nature and geochemical evolution of the upper mantle: Tectonophysics, 75: 91–112.

Wright, J. E., Haxel, G., and May, D. J., 1981, Early Jurassic uranium–lead isotopic ages for Mesozoic supracrustal sequences, Papago Indian Reservation, southern Arizona (abs).: Geological Society of America, Abstracts with Programs, 13: 115.

Zartman, R. E., and Tera, F., 1973, Lead concentration and isotopic composition in five peridotite inclusions of probable mantle origin: Earth and Planetary Science Letters, 20: 54–66.

EXCURSION 8A:
Magmatism associated with lithospheric extension: Middle to late Cenozoic magmatism of the southeastern Colorado Plateau and central Rio Grande rift, New Mexico and Arizona

W. S. Baldridge[1], F. V. Perry[2], D. T. Vaniman[1], L. D. Nealey[3], B. D. Leavy[4], A. W. Laughlin[1], P. Kyle[5], Y. Bartov[6], G. Steinitz[6], and E. S. Gladney[7]

[1]Earth and Space Sciences Division, Los Alamos National Laboratory, Los Alamos, New Mexico 87545; [2]Department of Geology, University of New Mexico, Albuquerque, New Mexico 87131; [3]U.S. Geological Survey, 2255 North Gemini Drive, Flagstaff, Arizona 86001; [4]P.O. Box 1052, Los Alamos, New Mexico 87544; [5]Geoscience Department, New Mexico Institute of Mining & Technology, Socorro, New Mexico 87801; [6]Geological Survey of Israel, 30 Malkhei Yisrael, Jerusalem 95501; [7]Health, Safety, and Environment Division, Los Alamos National Laboratory, Los Alamos, New Mexico 87545

Introduction

Magmatism is an integral feature of continental extension and, in particular, of continental rifting. Some rifts, such as the East African rift, are associated with huge volumes of volcanic rocks (Williams, 1982). Others, such as the Rio Grande rift, have relatively small volumes of magmatic rocks exposed at the surface (e.g., Olsen et al., 1987), although large quantities may exist at depth (e.g., Morgan et al., 1986a). Regardless of the volume, the compositions of magmatic rocks and their distribution and secular variation are of key importance in understanding the processes involved in extension of continental lithosphere.

In this paper we present an overview of volcanic and hypabyssal rocks of the central Rio Grande rift and southeastern Colorado Plateau (Fig. 1), part of a broad region of the western United States that underwent crustal extension and lithospheric thinning in middle to late Cenozoic time. Magmatism associated with this crustal extension is very complex. Huge volumes of basaltic andesites and more evolved rocks, including widespread ash-flow tuffs, were erupted 40–20 Ma (Fig. 2). This magmatism was possibly of key importance to extension in that it weakened the lithosphere, allowing it to break apart in the subsequent extensional setting. This mid-Tertiary magmatic event, probably representing back-arc or intra-arc magmatism, resulted from subduction of the Farallon plate along the western margin of the North American plate. Magmatism overlapped with crustal extension, which began in isolated locations 36–37 Ma and became widespread after 30 Ma (Chapin and Seager, 1975; Eaton, 1982; Aldrich et al., 1986); it diminished after subduction of the Farallon plate ceased. Following a lull in magmatism, a second period of magmatism, characterized by widespread basaltic eruptions and by formation of isolated central volcanoes of intermediate composition, began about 17 Ma (Fig. 2). This latter phase of magmatism reflects the current tectonic setting, dominated by transform motion along the western margin of North America and extension throughout most of the western U.S. Thus, the complex magmatic history of this area closely parallels the unique and complex structural history of the region leading to formation of the Basin and Range province and the Rio Grande rift.

The area of the central Rio Grande rift and southeastern Colorado Plateau is uniquely suited to understanding magmatism associated with lithospheric extension in that it spans several tectonic provinces (Great Plains; Rio Grande rift; Colorado Plateau, including transition zone; and Basin and Range), each with its separate geologic history and lithospheric structure. Thus, this region facilitates comparative studies which can identify features common to, or unique to, these tectonic provinces. In the present paper, we limit ourselves to rocks emplaced after the beginning of widespread crustal extension some 31 Ma (e.g., Aldrich et al., 1986). This paper is in part a review of previously published data and ideas. However, we present much new data herein (Fig. 3), some from work still in progress, that allow us to construct a more complete picture of magmatism throughout the area of the southeastern plateau and central rift. We also correlate volcanism with tectonic setting, both spatially and temporally, in order to gain an understanding of controls on magmatism and of underlying processes of continental extension and lithospheric thinning.

Geologic setting

Cenozoic extensional deformation in New Mexico and eastern Arizona occurred in two phases: late Oligocene–early Miocene and middle Miocene–Holocene (e.g., Chapin and Seager, 1975; Seager et al., 1984). The earlier phase resulted in formation of broad, relatively shallow basins bounded, in part at least, by low-angle faults. The style of deformation and the fact that extension closely followed, and partially overlapped with, widespread mid-Tertiary magmatism suggest that the lithosphere was relatively hot and the brittle–ductile transition relatively shallow (Morgan et al., 1986b). In the southeastern plateau and central rift area, the early phase of crustal extension began about 31 Ma and lasted into early Miocene time (e.g., Aldrich et al., 1986). The latter phase of deformation, part of the classical "Basin and Range extensional event" which affected most of the western United States (e.g., Shafiqullah et al., 1980; Eaton, 1982), began about 10 Ma and resulted in formation of a north-northeast-trending series of asymmetrical grabens—the modern Rio Grande rift—and development of a broad "transition zone" along the southeastern and southern margins of the Colorado Plateau (Fig. 1). Grabens were generally narrow and bounded by steep faults, suggesting that the lithosphere was cooler and the brittle–ductile transition deeper than in the previous extensional event (Morgan et al., 1986b). The transition zone is characterized by normal faults which tend to be oriented in east-northeast or north-northeast directions and form long fault zones approximately concentric to the Plateau margin (Fig. 1). Offsets along these faults, however, are not great compared to axial rift grabens and probably do not exceed a few hundred meters. The

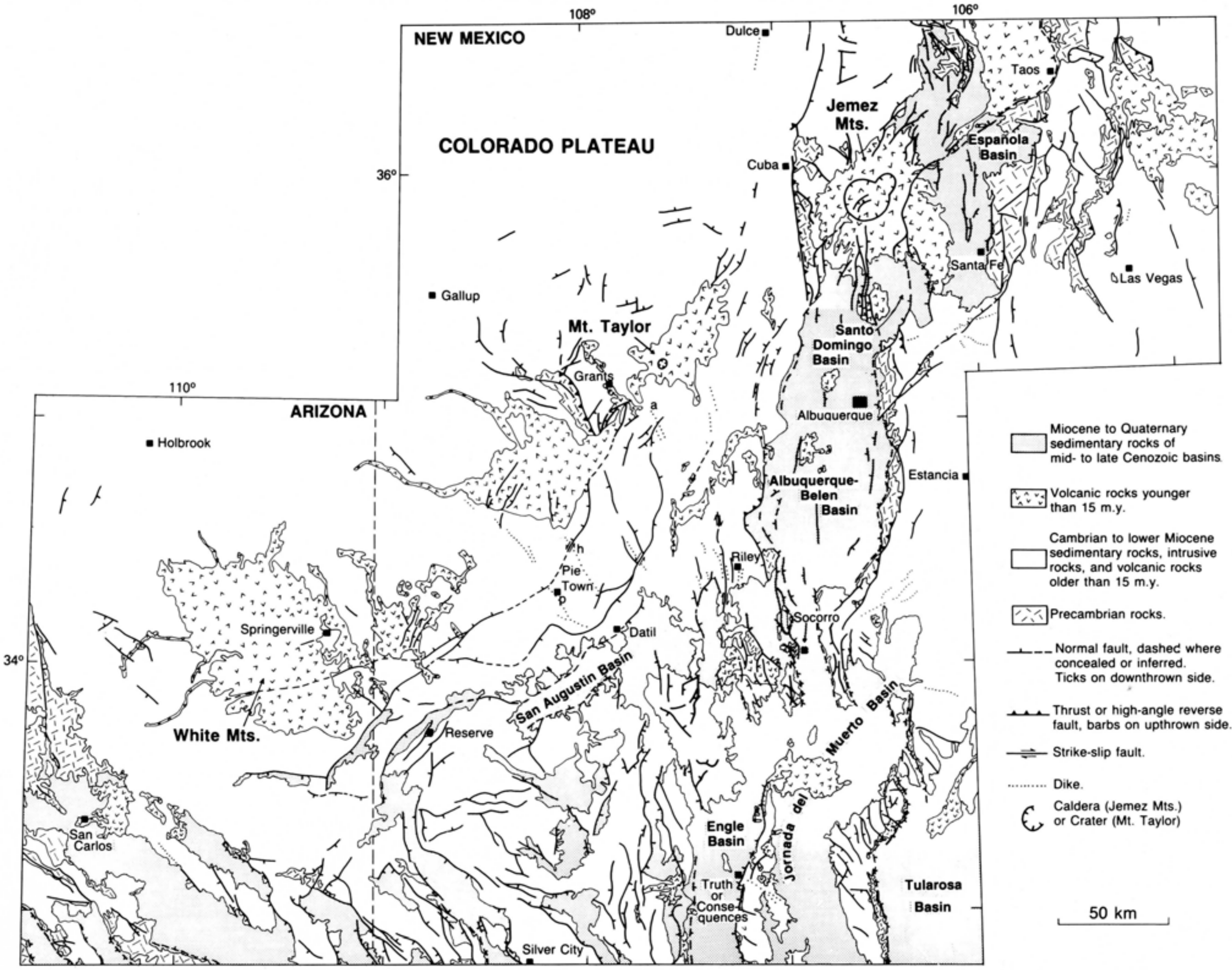

FIGURE 1—Tectonic map of central Rio Grande rift and southeastern Colorado Plateau (modified from Baldridge et al., 1983). The letters *a*, *h*, and *p* designate the Acomita, Hickman, and Pie Town dikes, respectively.

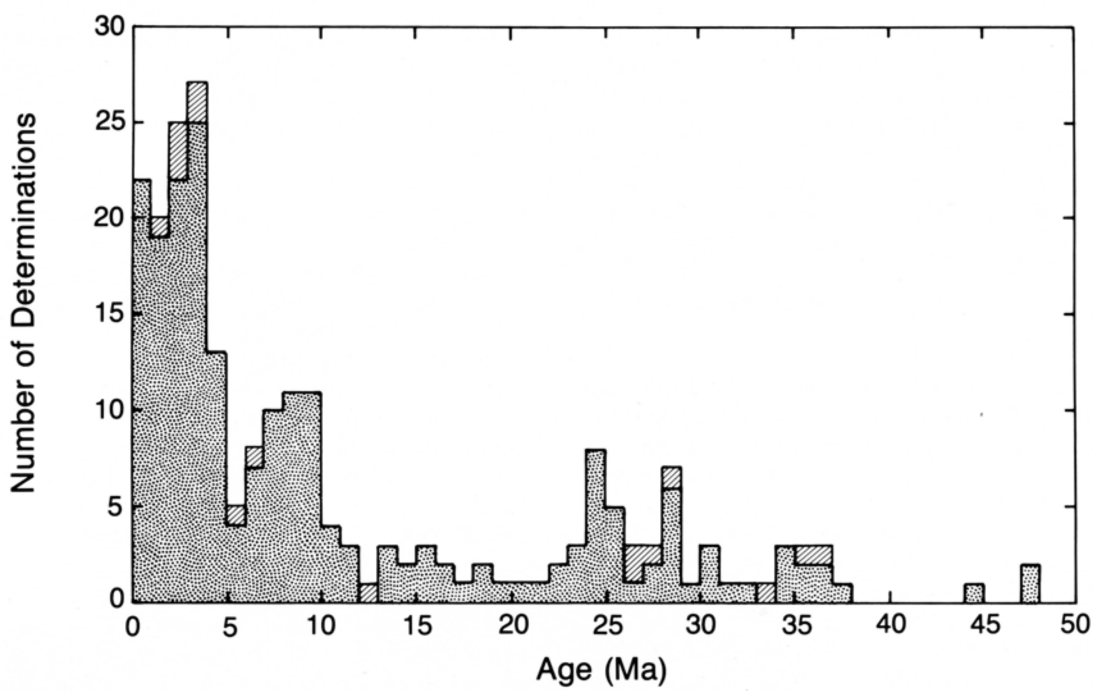

FIGURE 2—Frequency diagram of radiometric ages of igneous rocks in part of New Mexico. Modified from Aldrich et al. (1986), which included area between 104°W and 108°W longitude, by addition of dates from Table 1 of this paper.

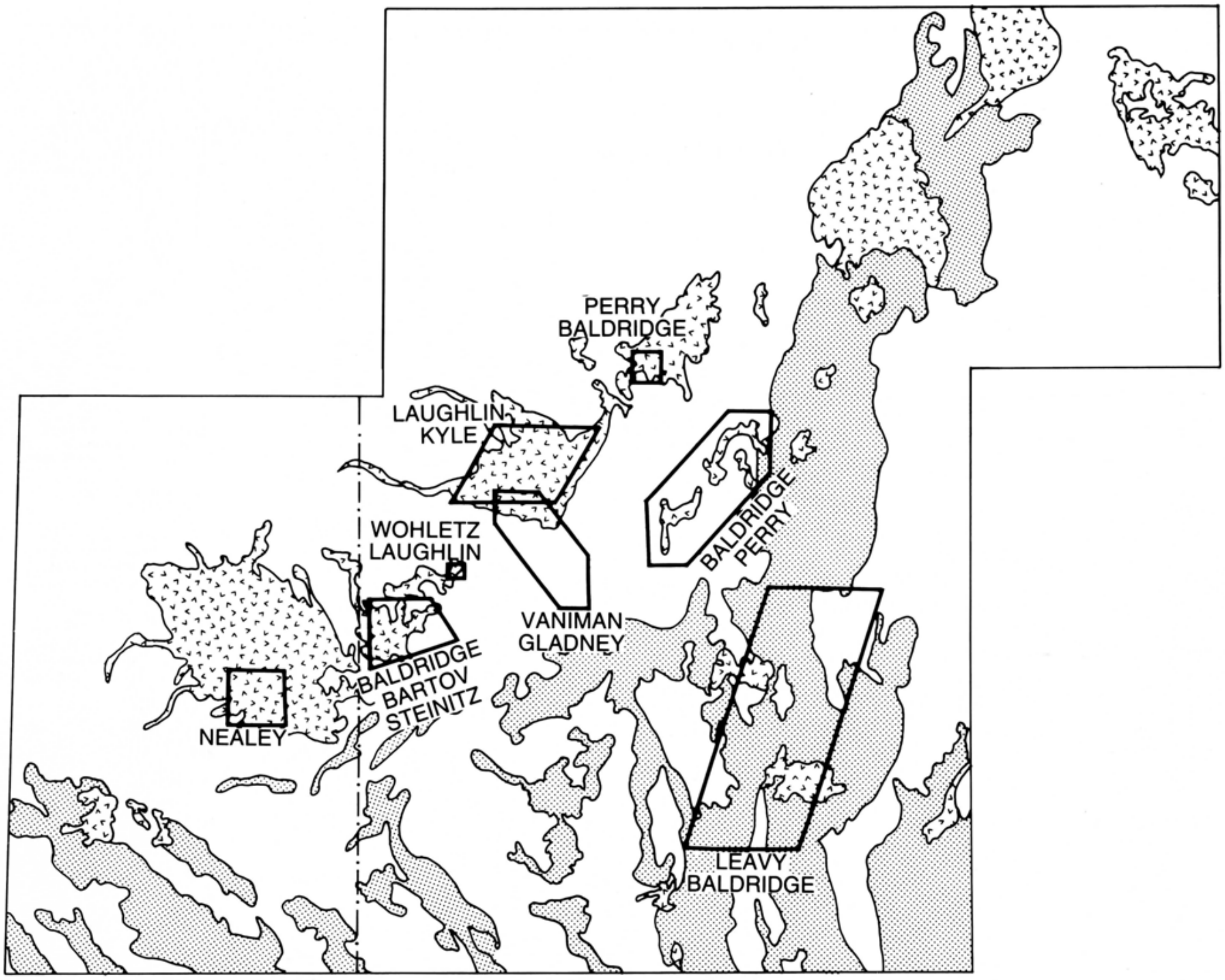

FIGURE 3—Index map identifying individual authors' contributions to new data presented in this paper. Area is same as shown in Fig. 1.

northern rift, because of its position between the Colorado Plateau and the Great Plains (part of the continental craton), is a well-defined morpho-tectonic feature. The southern rift, where the earliest and most extension has occurred, is physiographically indistinguishable from the adjacent Basin and Range province. The Colorado Plateau has acted as a semi-independent microplate since at least the Late Permian, resisting breakup except along its margins (Steiner, 1988).

Timing and composition of magmatic activity

Late Oligocene to early Miocene

In the middle Tertiary (approximately 40–20 m.y. ago), huge volumes of magmas, dominantly of intermediate to silicic composition, were emplaced throughout the southwestern U.S., including along the southern margin of the Colorado Plateau in New Mexico and Arizona and in the area now occupied by the southern rift. Examples include the Mogollon–Datil volcanic field, which consists of numerous overlapping calderas and probably overlies a large composite pluton (e.g., Elston et al., 1976), and the Trans-Pecos magmatic province of west Texas (e.g., Barker, 1979; Price et al., 1986). The early (late Oligocene to early Miocene) phase of magmatism in the Rio Grande rift and along the transition zone of the Colorado Plateau (Table 1, Fig. 4) was either part of this mid-Tertiary magmatic event, or was closely related to it, in that magmatism was triggered by rifting of heated lithosphere. Discussion of these large regions of mid-Tertiary magmatism is outside the scope of this paper.

In the central Rio Grande rift and transition zone of the southeastern Colorado Plateau, magmatism associated with late Oligocene to middle Miocene extensional deformation is manifested in part as dikes and small intrusions and as small flow remnants. Major dike swarms occur in the Dulce, Riley, and Pie Town areas west of the rift (Fig. 1). The dikes are particularly important in defining the stress field during this early phase of crustal extension (Laughlin et al., 1983; Aldrich et al., 1986). Typically, the largest and/or longest dikes are basaltic andesite in composition (Laughlin et al., 1983). However, compositions include alkali olivine basalts (Aldrich et al., 1986) and more alkalic types (see below) and, in the central rift, olivine nephelinites (Baldridge et al., 1980).

One of the largest dike swarms in New Mexico is exposed over a large area between Datil and Pie Town on the south, and Mount Taylor on the north (Fig. 1). The three largest dikes (Fig. 1), the Acomita, Hickman, and Pie Town dikes, trend N30W to N35W, defining a N60E to N65E orientation for the least principal horizontal stress at the time of dike

TABLE 1—New whole-rock K–Ar dates, sample descriptions, localities, and analytical data for middle to late Cenozoic magmatic rocks of the southeastern Colorado Plateau transition zone. GSI = Analysis performed at the Geological Survey of Israel, Jerusalem. Geo = Analysis performed by Geochron Laboratories, Division of Krueger Enterprises, Inc., Cambridge, Massachusetts. Constants: $\lambda_\beta = 4.963 \times 10^{-11} yr^{-1}$; $\lambda_e = 0.581 \times 10^{-10} yr^{-1}$; $\lambda = 5.544 \times 10^{-10} yr^{-1}$; $^{40}K/K = 1.167 \times 10^{-4}$ atom/atom.

Sample No.	Description, location, comments	K (%)	Radiogenic Ar^{40} ($\times 10^{12}$ mole/g)	Atmospheric Ar^{40} (%)	Age (Ma)
419	Basalt flow in lower Harris Canyon. GSI. 34°07.11′N, 108°36.82′W	0.782	3.140	80.0	2.3 ± 0.4
420	Basalt flow from Black Peak cinder cone. GSI. 34°03.70′N, 108°47.34′W	0.854	2.850	85.3	1.9 ± 0.4
421	Basaltic andesite from north side of Escondido Mountain. GSI. 34°12.41′N, 108°25.64′W	1.144	55.68	52.0	27.8 ± 1.7
422	Andesite from north side of Escondido Mountain. GSI. 34°13.08′N, 108°25.71′W	1.987	100.44	25.7	28.9 ± 1.2
423	Andesite from quarry south of Quemado. GSI. 34°07.57′W, 108°35.12′W	2.728	159.15	11.45	33.3 ± 1.1
424	Andesite from Harris Canyon south of Quemado. GSI. 34°05.17′N, 108°37.63′W	2.496	155.19	45.4	35.4 ± 2.0
426	Basalt, older flow, Red Hill volcanic field. GSI. 34°08.52′N, 108°49.95′W	1.290	14.270	39.1	6.4 ± 0.3
427	Andesite from S A Creek, south of Spur Lake basin. GSI. 33°54.22′N, 108°55.22′W	2.112	134.20	25.6	36.3 ± 1.5
428	Basalt flow from Red Butte cinder cone, Spur Lake basin. GSI. 33°54.22′N, 108°55.23′W	1.286	6.049	79.2	2.7 ± 0.4
429	Basalt, Red Hill volcanic field. GSI. 34°01.76′N, 108°56.22′W	1.052	4.642	84.6	2.5 ± 0.5
468	Basaltic andesite, basal volcanic unit, Agua Fria Mountain. GSI. 34°07.89′N, 108°33.58′W	1.674	77.76	33.0	26.6 ± 1.0
AWL-2-80	Basalt underlying Cerro Rendija, Zuni–Bandera volcanic field. Geo. 34°56.03′N, 108°07.50′W	0.446	3.025	93.9	3.8 ± 0.4
AWL-3-80	Basalt, North Plains, Zuni–Baldera volcanic field. Geo. 34°41.90′N, 108°02.50′W	0.540	3.525	95.4	3.7 ± 0.4
Z2.81.7	Basalt, Cerro Prieto. Geo. 34°33.29′N, 108°34.18′W	1.310	14.15	80.25	6.0 ± 0.5
Z2.81.9	Basalt, Veteado Mountain. Geo. 34°34.32′N, 108°18.57′W	1.160	26.25	87.8	12.6 ± 0.8
Z2.81.22	Alkaline dike, southwest of Adams Diggings. Geo. 34°27.54′N, 108°18.47′W	2.260	107.75	53.0	26.5 ± 1.2

emplacement 27.3–29.9 Ma (Laughlin et al., 1983). These dikes, which are compositionally similar to each other, have lower MgO and higher K_2O, TiO_2, and P_2O_5 than most other basaltic andesites of similar age from New Mexico (Laughlin et al., 1983).

Early Miocene dikes of the Pie Town–Adams Diggings area (Fig. 5) trend northwest and extend over a linear zone some 75 km in length. Most of the Pie Town–Adams Diggings dikes are basaltic andesites, which are divided into two groups depending on whether or not they contain olivine microphenocrysts (Fig. 5). The aphyric dikes (those without olivine microphenocrysts) typically contain two pyroxenes and small amounts of groundmass olivine; plagioclase crystallites range from An_{52} to An_{29}, but many dikes contain clots of other feldspars, e.g., labradorite (Fig. 6). Contamination of the aphyric basaltic andesites is evident in the many fragments of clastic sedimentary rocks found as inclusions and in their high isotopic ratios ($^{87}Sr/^{86}Sr = 0.712$–0.714 for the Pie Town, Acomita, and Hickman dikes, Laughlin and Brookins, unpubl. data; $E_{Nd} = -3.86 \pm 0.44$ for the Hickman dike, Perry, unpubl. data). The phyric basaltic andesites (those with olivine microphenocrysts, Fo_{70-76}) have more calcic plagioclase (An_{66}–An_{43}) and typically contain a single pyroxene. Dikes of this type terminate to the north in the Katy Bess lopolith, which is an asymmetric intrusion, slightly concave upward, dipping gently to the south. The lopolith contains two pyroxenes and a more Fe-rich olivine (Fig. 6). Although the phyric basaltic andesites have a much more restricted occurrence than the aphyric basaltic andesites, the volume of the phyric basaltic andesites is significantly augmented by the volume of the Katy Bess lopolith (>0.25 km^3).

The two types of basaltic andesite are distinct in their compositions. The phyric basaltic andesites are higher in MgO and Al_2O_3, and lower in TiO_2, FeO, and P_2O_5, than the aphyric basaltic andesites of comparable differentiation index (Table 2). The lower P_2O_5 of the phyric basaltic andesites corresponds with their generally lower incompatible-element contents (Fig. 7). The higher REE content and lower La/Yb of the aphyric basaltic andesites may reflect either a different source or extensive assimilation of crustal rocks with relatively flat REE patterns prior to or during frac-

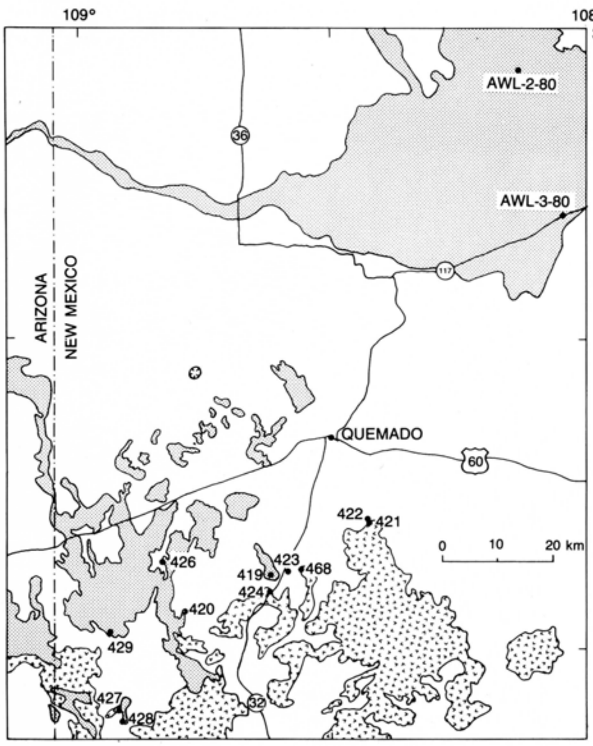

FIGURE 4—Locations of Oligocene to Pliocene magmatic rocks from the transition zone of west-central New Mexico for which K–Ar dates are tabulated in Table 1.

tionation. An isotopic study of the basaltic andesites and their clasts may resolve this uncertainty.

Alkaline basaltic dikes (Fig. 5) are less common than the basaltic andesite dikes. South of Pie Town they occur with a more westerly strike than the dike of basaltic andesite. The southernmost alkaline dike both interfingers with, and is crosscut by, the basaltic andesite. The alkaline dike near Adams Diggings has the same strike as the basaltic andesite dikes and a comparable age (26.5 Ma; Z2.81.22, Table 1). Of the alkaline dikes, only the one near Adams Diggings is nepheline-normative. The alkaline dikes contain clinopyroxene, olivine (Fo_{89-79}), and two feldspars (labradorite–andesine and sanidine). Their La/Yb is higher than that of the basaltic andesites (Fig. 7).

Minettes (25–28 Ma) of the Mujeres plugs, located just north of the dike zone (Fig. 5), are contemporaneous with the basaltic andesite and alkaline basalt intrusions. These minettes, which have much higher La/Yb (~64) than the basaltic andesites and alkaline dikes, represent the southeastern limit of the Navajo volcanic field (Vaniman et al., 1985).

Middle Miocene to Holocene

Following a minimum in eruption rates 17–22 Ma (Fig. 2; see also Chapin and Seager, 1975, fig. 9), magmatism resumed again in the central rift and throughout the transition zone. Volcanism, associated with extension of the rift Basin and Range region, during this period of time was widespread and was particularly concentrated around the margins of the Colorado Plateau (e.g., Luedke and Smith, 1978). In eastern Arizona and in New Mexico, volcanic centers form a very striking, north-northeast-trending linear array referred to as the Jemez zone (or lineament) (Mayo, 1958). The locations of individual volcanic fields are clearly structurally con-

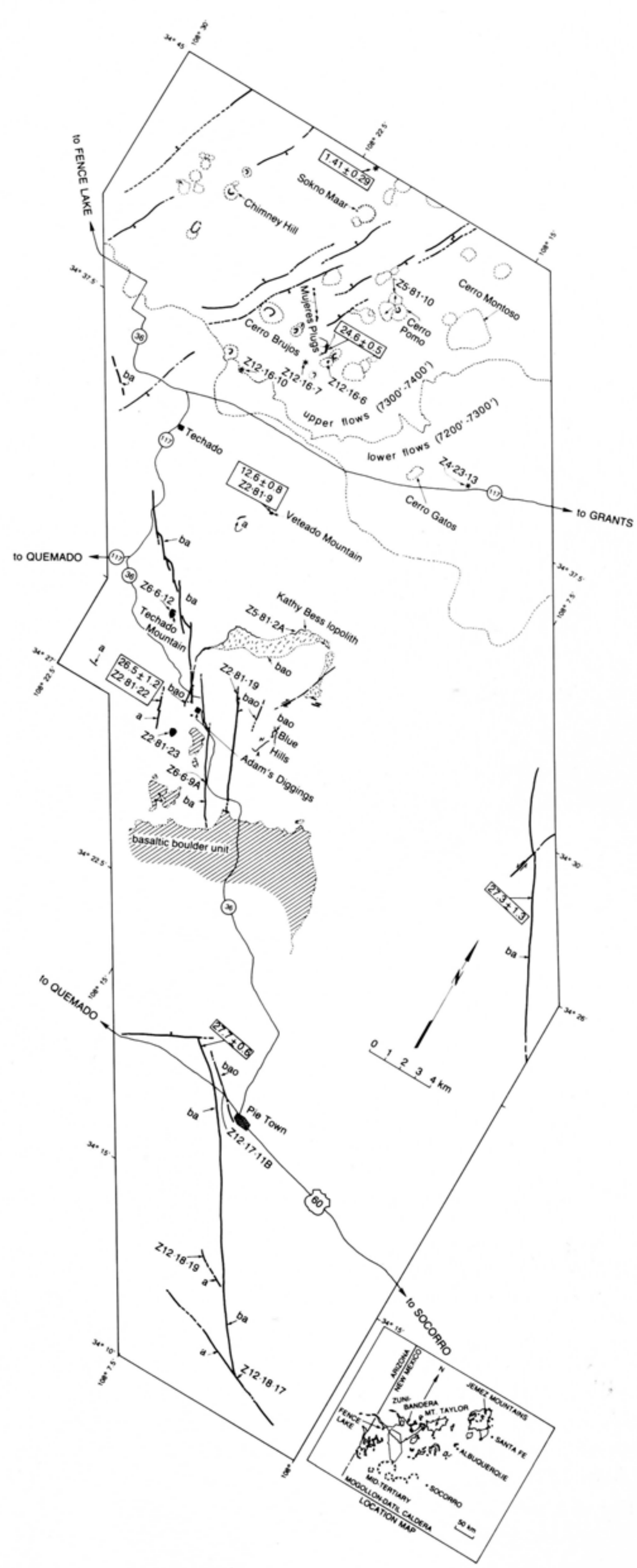

FIGURE 5—Late Oligocene and Miocene dikes and related intrusive rocks of the Pie Town–Adams Diggings area, and basalts of the southern Zuni–Bandera volcanic field. Phyric basaltic andesite dikes, i.e., those containing olivine microphenocrysts, are labeled *bao;* those without phenocrysts ("aphyric") are labeled *ba*. Alkaline dikes are labeled *a*. Dotted line shows approximate southern edge of Zuni–Bandera volcanic field. Samples designated Z correspond to chemical analyses listed in Tables 2, 4, and 5. Ages for Z2.81.9 and Z2.81.22 are presented in Table 1; other ages are from Laughlin et al. (1982, 1983) and Vaniman et al. (1985). The basaltic boulder unit, consisting of boulders of basalt and basaltic andesite with little matrix sediment, is a major mesa-capping marker unit within Santa Fe Group-equivalent sediments.

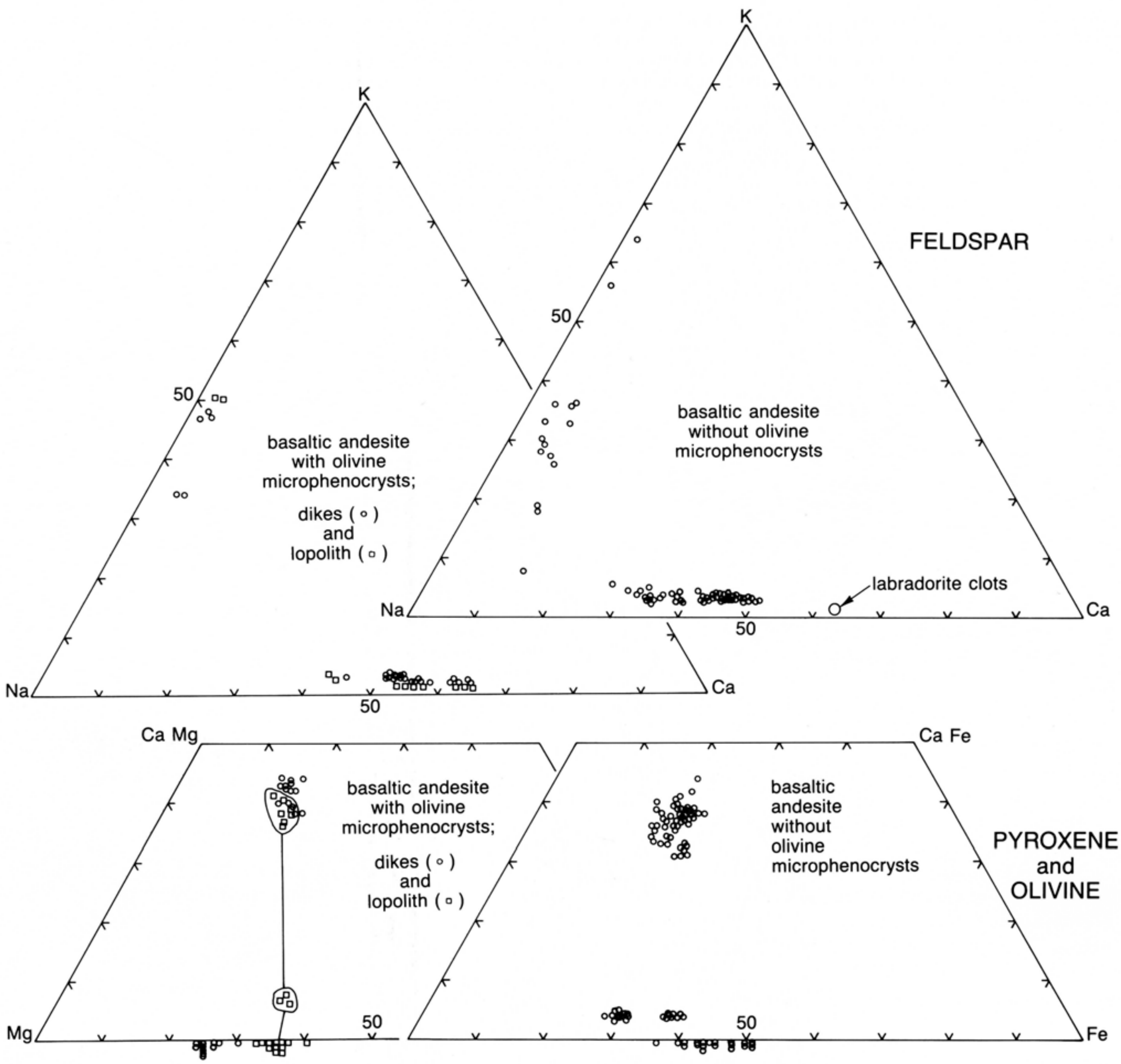

FIGURE 6—Compositions of plagioclase, pyroxene, and olivine (in cation proportions) in aphyric (Z4.24.16, Z6.4.4, Z6.6.9) and olivine-phyric (Z12.17.11, Z2.81.17) basaltic andesite dikes and a lopolith from the Pie Town–Adams Diggings area.

trolled, but the trend of the Jemez zone as a whole has a well-defined structural expression only where it crosses the Rio Grande rift (Aldrich, 1986). It does, however, correspond to a boundary between an essentially undeformed core of the Plateau to the northwest, which has resisted breakup, and a transition zone to the southeast (e.g., Baldridge et al., 1983a; Aldrich et al., 1986), which has undergone extension during formation of the rift and Basin and Range province (Fig. 1). Along the Jemez zone, basaltic rocks are most widespread, but several central volcanoes (Jemez volcanic field, Mount Taylor, Mount Baldy; Fig. 1) consisting dominantly of evolved magmas occur prominently. Inception of volcanism did not progress systematically along the Jemez zone (e.g., Laughlin et al., 1976; Lipman, 1980), as would be required if the volcanic lineament were a hotspot track (Suppe et al., 1975).

Late Miocene to Holocene magmatism includes a range of alkalic and tholeiitic basaltic rocks ("true basalts"), in contrast to more silicic basaltic andesites of the earlier magmatic event. Basaltic lavas were generally erupted from small shield cones and from cinder cones aligned along fissures; intermediate magmas were erupted from central volcanoes and volcanic complexes.

Recent detailed stratigraphic studies of basalts in the southeastern Plateau transition zone (Baldridge et al., 1983b, 1987) showed that middle Miocene to Holocene volcanism occurred in two phases, separated by a minimum between 6 and 4 Ma. This minimum is also confirmed by a more regional compilation of radiometric dates (Aldrich et al., 1986).

Middle to late Miocene—Middle to late Miocene volcanic activity in the central rift transition zone ranged from 13 to 6 Ma.

JEMEZ VOLCANIC FIELD: Resumption of magmatism following the middle Miocene minimum occurred earliest in the Jemez volcanic field. The oldest volcanic rocks in the

TABLE 2—Major-element compositions (in %) and trace-element compositions (in ppm) of Oligocene magmatic rocks from the southeastern Colorado Plateau transition zone. Sample locations are given in Figs. 4 and 5; ages in Table 1. Compositions of 421–468 determined by x-ray fluorescence (hydrous basis); compositions of z-numbered samples determined by a combination of electron-probe microanalysis of fused beads (Baldridge, 1979) and instrumental neutron-activation analysis (anhydrous basis) (Vaniman et al., 1982). Analyses performed at Los Alamos National Laboratory. $Fe_2O_3^T$ = total Fe as FeO.

	Relative error (%)	421	422	423	424	427	468	Z2.81.22	Z2.81.19	Z4.24.16	Z5.81.2A	Z6.6.9A	Z12.17.11B	Z12.18.17	Z12.18.19
SiO_2	2	51.51	53.21	57.04	60.14	59.79	53.17	51.5	51.8	56.7	53.6	55.4	51.4	51.3	54.6
TiO_2	7	1.46	2.34	1.25	0.90	0.85	2.05	1.42	1.96	2.50	1.85	2.70	1.92	1.37	1.53
Al_2O_3	2	15.54	15.65	15.20	16.03	15.89	16.82	14.8	15.9	14.4	16.3	14.0	15.9	14.2	16.5
$Fe_2O_3^T$	3	9.71	10.78	7.78	6.41	5.87	10.49	9.88	11.5	11.3	10.4	11.3	10.9	10.4	7.9
MnO	5	0.14	0.16	0.15	0.12	0.06	0.15	0.16	0.15	0.19	0.14	0.20	0.15	0.15	0.09
MgO	3	6.91	2.99	1.54	2.49	2.44	3.10	8.0	5.9	3.3	5.2	3.02	5.9	8.9	5.7
CaO	2	7.91	6.34	6.51	4.96	5.06	7.01	7.5	7.6	5.9	7.3	5.9	7.7	7.2	7.2
Na_2O	3	2.72	3.50	3.34	3.12	3.11	3.89	2.92	3.12	3.23	3.04	3.52	2.77	2.81	4.12
K_2O	4	1.58	2.69	3.42	3.25	3.19	2.36	2.80	1.50	2.53	1.85	1.81	1.97	2.63	1.77
P_2O_5	15	0.42	0.79	0.38	0.20	0.20	0.72	0.81	0.71	1.18	0.62	1.34	0.75	0.73	0.27
Total		97.90	98.45	96.61	97.62	96.46	99.76	99.79	100.14	101.23	100.30	99.19	99.36	99.69	99.68
Cs	13							2.4	1.8	0.8	1.6	1.4	1.1	0.4	0.3
Rb	15							53	41	65	36	81	36	69	24
Ba	10							1433	923	1006	912	1042	773	1231	868
Sr	10							956	803	495	719	519	738	869	1154
La	7							30	36	52	45	51	33	43	33
Sm	10							6.5	8.8	15.0	8.8	15.0	7.9	8.5	6.5
Eu	10							1.87	2.32	4.12	2.59	4.05	2.65	2.50	1.88
Tb	12							0.83	1.10	2.00	1.10	2.19	1.13	1.08	0.76
Yb	15							1.84	2.82	6.33	3.00	6.14	2.64	2.54	1.68
Lu	20							0.42	0.32	0.66	0.50	0.98	0.46	0.32	0.18
Th	6							6.0	6.4	9.7	7.4	9.5	5.9	5.9	3.3
U	6							1.5	1.9	2.3	1.6	2.4	2.0	1.1	1.2
Hf	5							5.2	6.0	9.7	7.1	9.1	7.1	7.6	4.4
Cr	5							327	125	5.0	112	4.2	168	272	107
Sc	5							23	20	24	19	23	20	19	15

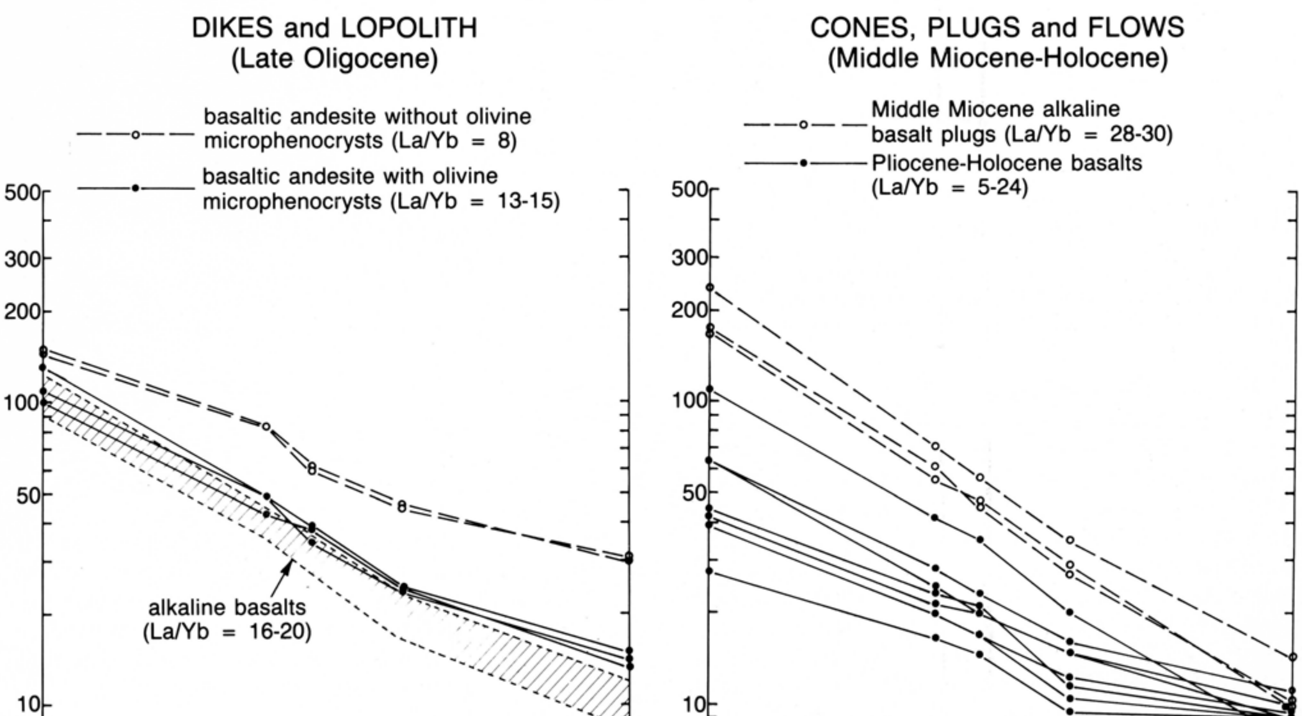

FIGURE 7—Chondrite-normalized rare-earth-element compositions of late Oligocene to Holocene magmatic rocks of the Pie Town–Adams Diggings and southern Zuni–Bandera areas. **Left:** late Oligocene dikes and related intrusive rocks. **Right:** middle Miocene to Holocene intrusions and volcanic rocks, including selected data from the adjacent Zuni–Bandera volcanic field.

Jemez are 14–13 Ma (Gardner et al., 1986; Aldrich, 1986), but probably became voluminous only after 11 Ma. The Jemez field is a large, complex central volcano. More than 2000 km^3 of lavas were erupted from numerous vents. Compositions range from basaltic to rhyolitic, but consist dominantly of dacites and andesites (e.g., Gardner et al., 1986). Detailed discussion of the Jemez volcanic field is provided in Excursion 17B (Goff et al., this volume).

WHITE MOUNTAINS VOLCANIC FIELD: The main edifice of the White Mountains volcanic field, Mount Baldy, was constructed 9–8 Ma. Mount Baldy is a polygenetic, alkalic shield volcano composed of more than 20 lithologic units that erupted from a central vent area (Fig. 8) located between Mount Baldy and Mount Ord. Chemical variations in the sequence require an open-system magmatic process involving several episodes of magma mixing and fractional crystallization, with wall-rock assimilation occurring periodically. Basaltic lavas are stratigraphically both older and younger than the shield lavas.

Most mafic rocks are alkali olivine basalt and olivine tholeiite. Intermediate to silicic lavas of the Mount Baldy shield range from trachyandesites and tristanites to trachytes and quartz trachytes (Table 3). Major-element variations are characterized by decreasing FeO, CaO, and TiO_2, and increasing K_2O and Na_2O with increasing SiO_2. Al_2O_3 and P_2O_5 increase in the mafic rocks and decrease in the intermediate to silicic rocks with increasing SiO_2. These patterns are consistent with the fractionation of feldspar and apatite from residual liquids.

Trace-element abundances are similar for the various rock types, but two groups of silicic rocks are easily distinguished. Intermediate to silicic lavas are enriched in trace elements relative to a primitive mantle source. The most incompatible trace elements (e.g., Cs and Th) are 15–500 times higher than mantle abundances. Less incompatible elements (e.g., Y) are 10–50 times higher than mantle abundances. The largest group of intermediate to silicic rocks has Sr_m (mantle-normalized Sr; Wood, 1979) = 8–25. The second group is depleted in Sr (10 ppm) relative to primitive mantle, and shows strong negative Sr anomalies (Sr_m = 0.4).

The most mafic basalts of the White Mountains field can be derived from a spinel peridotite or garnet peridotite source by 5 to 9% melting. High light-rare-earth-element abundances in the basalts (chondrite-normalized La = 50–175) require sources that were enriched in incompatible elements prior to melting. Suitable enrichments for spinel peridotite sources are similar to rare-earth-element abundances in spinel peridotite xenoliths from the San Carlos volcanic field of central Arizona (Frey and Prinz, 1978).

Variations of Rb and La, typical of many of the trace elements, are shown in Fig. 9. The concentration of these elements is variable in the older units, but tends to be more uniform (especially for La) in the younger units. The variability in the older units reflects the complexity of processes, including fractional crystallization, magma mixing, and wall-rock assimilation, involved in the origin of these magmas.

Based on Th and Hf abundances (Fig. 10), fractional crystallization was an important mechanism in the evolution of the Mount Baldy volcanic series. Abundances of these

Explanation

	Qc	Quaternary colluvium	
	Qtb	Quaternary-Tertiary basalt	1.7, 8.9 Ma
Mount Baldy Group	Tmo	trachyte of Mount Ord	8.5 Ma
	Tbo	trachyte of Boggy Creek	
	Toc	trachyte of Ord Creek	
	Tpu	trachyte of Purcell Cienega	
	Tbe	trachyte of Becker Creek	
	Trc	trachyte of Reservation Creek	
	Tsc	Sheep Crossing Formation (Merrill and Pewe, 1977)	
	Tcr	trachyte of Coulter Ranch	
	Tsp	trachyte of Sunrise Peak	
	Tbm	trachyte of Burnt Mountain	
	Tlv	trachyte of Lee Valley Reservoir	
	Tmb	trachyte of Mount Baldy Ridge	
	Tsm	trachyte of Spruce Mountain	
	Tpc	trachyte of Pacheta Cienega	8.66 Ma
	Thc	trachyte Hurricane Cienega	
	Tdc	trachyandesite of Deep Creek	
	Tpb	trachyte of Paradise Butte	
	Tmw	trachyte of Mount Warren	
	Tef	trachyte of East Fork Little Colorado River	
	Twf	trachyte of West Fork Little Colorado River	
	Tet	trachyte of East Fork Trail	
	Tlb	trachyte of Lofer Butte	
	Tbr	trachyte of Bonito Rock	

Note: Minor lithologic units are not labelled on geologic map.
Older mafic and younger basaltic rocks are listed as Qtb.

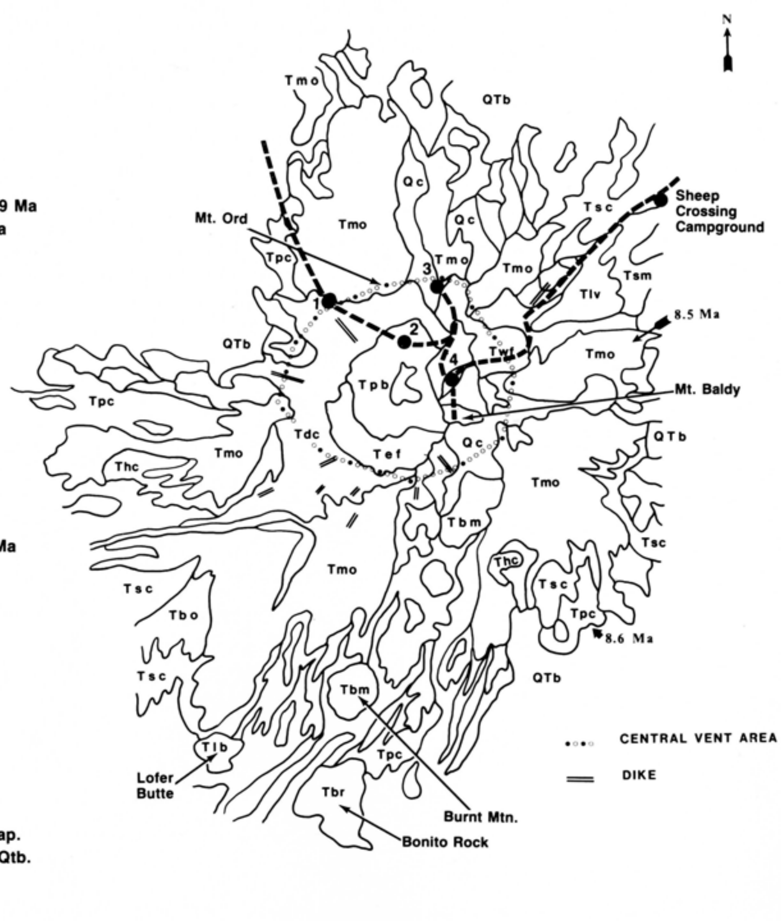

FIGURE 8—Generalized geologic map of the Mount Baldy shield volcano. Dashed line is excursion route for Day 4; numbers indicate stops.

TABLE 3—Selected chemical analyses of White Mountains volcanic rocks. Major-element values in %, trace-element values in ppm. Unit designations are given in Fig. 8. Analyses by x-ray fluorescence spectroscopy and instrumental neutron activation, performed at the U.S. Geological Survey. LOI = loss on ignition. Analysts: G. A. Wandless, L. Schwarz, R. Johnson, H. J. Rose, B. McCall, G. Sellers, J. Lindsay, A. J. Bartel, J. S. Wahlberg, and J. Baker.

Sample Unit	NMO-60 QTb	NMO-85 Tmo	NMO-47 Twf	NMO-126 Tpc	NHE-380 Tdc
SiO_2	46.3	62.5	62.3	54.0	54.5
Al_2O_3	15.9	17.3	16.7	17.6	18.0
Fe_2O_3	12.5	4.58	5.12	8.24	8.05
MgO	7.46	0.61	1.13	1.12	1.43
CaO	7.52	2.43	2.35	4.26	4.80
Na_2O	4.00	4.74	5.11	4.51	4.38
K_2O	2.31	4.24	4.18	4.60	3.56
TiO_2	2.56	0.80	0.95	1.92	1.82
P_2O_5	0.78	0.33	0.48	1.10	0.82
MnO	0.17	0.07	0.12	0.13	0.16
LOI	0.59	1.30	0.92	1.19	1.90
Total	100.09	98.90	99.36	98.67	99.42
Ni	98	12	nd	13	12
Nb	55	224	105	141	60
Sr	958	418	448	430	754
Rb	15	123	146	181	88
Ba	280	1180	1000	1100	1300
Cr	239	0.9	nd	1.7	2.5
Hf	6.59	10.7	10.7	16.1	8.36
Th	3.05	20.3	22.1	28.7	12.5
U	0.93	4.52	6.42	5.2	2.7
Sc	18.5	5.87	5.93	11.90	10.6
La	38.2	64.6	66.2	119	104
Ce	74.3	112	132	175	149
Nd	34	48.2	57.8	91	91
Sm	6.07	7.4	10.6	14.7	17.2
Eu	2.25	2.31	2.65	3.43	3.84
Gd	6.9	8.3	9.53	15.3	15.3
Tb	0.83	1.22	1.36	2.17	1.93
Tm	<0.2	<0.2	nd	<0.4	0.83
Yb	2.14	3.59	3.59	5.6	5.0
Lu	0.24	0.494	0.54	0.75	0.713

elements are greater in some Mount Baldy lavas than in Proterozoic rocks from the region, and are greater than average crustal abundances (Conway and Wrucke, USGS, pers. comm. 1985; Condie and Budding, 1979; Condie and McCrink, 1982; Taylor and McLennan, 1985). Thus, bulk contamination of mantle-derived liquids and upper crustal materials would not produce such high concentrations of Th and Hf. The high concentrations can be explained by the fractionation of phases with low distribution coefficients for these elements.

Evidence of the involvement of magma mixing in the evolution of the White Mountains volcanic field sequence is suggested by the covariation of incompatible-element ratios with Th abundance (Fig. 10). Best-fit lines through ratio-element plots are curvilinear, and are consistent with magma mixing (Vollmer, 1976; Condomines et al., 1982). The compositions of the endmembers are not well constrained, but the patterns in Fig. 10 indicate that the endmembers had different U/Th and Ta/Th.

$^{87}Sr/^{86}Sr$ and trace-element abundances are consistent with derivation of trachyte magma by combined assimilation and fractional crystallization. The youngest unit in the Mount Baldy sequence, the trachyte of Mount Ord, can be related to one of the older basalts by contamination with crustal material having $^{87}Sr/^{86}Sr = 0.716$ and 150 ppm Sr, values similar to those in Proterozoic granitic basement rocks from northern Arizona (R. Kistler and A. Robinson, USGS, pers. comm. 1986).

BASALTIC FIELDS: In addition to the large central volcanic complexes of the Jemez and White Mountains fields, basaltic lavas were erupted from several small vents in the central rift and from numerous vents throughout the transition zone. Lavas erupted during this time period, dominantly alkali olivine basalt, range from about 13 to 6 Ma (Tables 1, 4; Figs. 4, 7). Between about 13 and 6 Ma, several alkaline basaltic plugs were emplaced near Adams

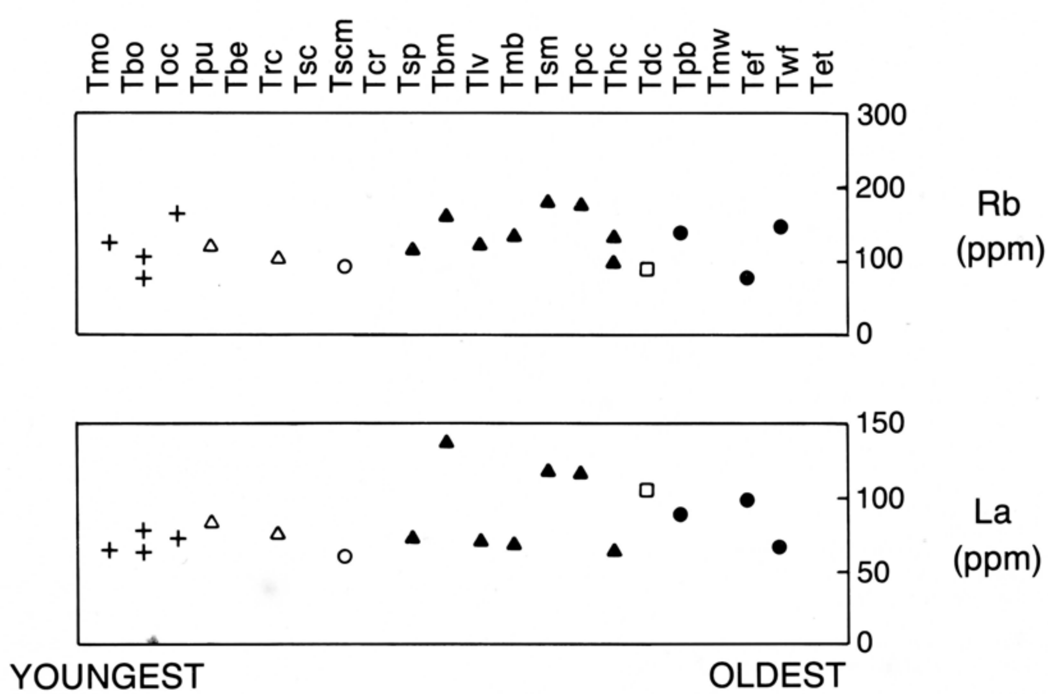

FIGURE 9—Chemostratigraphic diagrams for Mount Baldy. Solid circle = lower trachyte units; open square = trachyandesite of Deep Creek; solid triangle = middle trachyte units; open circle = Sheep Crossing Formation; open triangle = upper tristanite; and crosses = upper trachyte. Unit designations same as in Fig. 8. Tscm = Marshall Butte Member of Sheep Crossing Formation.

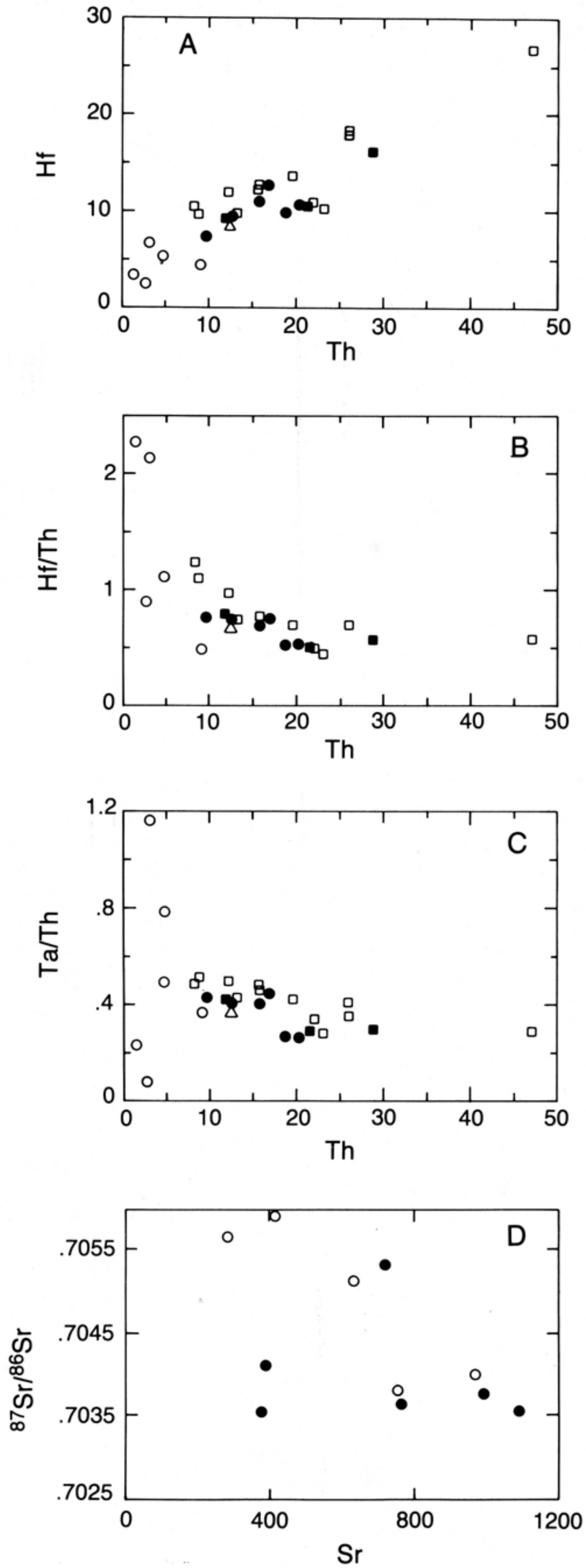

FIGURE 10—**A–C,** Trace-element variation diagrams for the White Mountains volcanic field. Open circle = basalt; open triangle = trachyandesite; solid square = tristanite; open square = trachyte; solid circle = quartz trachyte. Values in ppm. **D,** $^{87}Sr/^{86}Sr$ vs. Sr for the White Mountains suite (open circles) compared with selected data from the Springerville volcanic field (solid circles).

Diggings (Veteado Mountain, Techado Mountain, and plug Z2.81.23, Fig. 5) as well as to the west and south at Cerro Prieto and Tejana Mesa. The three plugs near Adams Diggings are basanitic; all contain magnesian clinopyroxene, olivine (Fo_{80-91}), and labradorite zoned to K-rich andesine. The Techado Mountain plug contains abundant xenoliths of spinel lherzolite (Table 4). It also contains large blocky crystals of anomalously Fe-rich clino- and orthopyroxene [Mg/(Mg + Fe) = 0.65 cpx and 0.60 opx] that may have been derived from associated coarse-grained basaltic rocks that crystallized at depth. La/Yb of the basanitic plugs (Fig. 7) is 28–30, higher than any other middle Miocene to Holocene rocks of this region (see below) and lower only than the late Oligocene minettes of the Mujeres plugs (Fig. 5).

Pliocene to Holocene—Beginning about 4 Ma, basaltic volcanism became widespread throughout the southeastern transition zone of the Colorado Plateau and in the central rift. Volcanism continues to the present day: the McCartys basalt flow southeast of Grants was the most recent eruption in this region (about 1000 yrs ago; see first-day field guide below). In addition, seismic data, historical seismicity, and uplift data strongly suggest that magma presently exists in the middle crust near Socorro (Sanford and Einarsson, 1982; Sanford, 1983; Larsen et al., 1986).

BASALTIC FIELDS OF TRANSITION ZONE: In the southeastern transition zone, the Zuni–Bandera and Springerville volcanic fields and basalts of the Lucero and Red Hill areas were mainly erupted during this time. In the Lucero area, two periods of Pliocene–Holocene volcanism exist: 4–3 Ma and approximately 1.1 Ma to the present (Baldridge et al., 1987). These intervals of eruptive activity, with the corresponding lull between, appear to hold for the Zuni–Bandera field.

Compositions of basalts erupted in the Lucero area underwent a slight but systematic shift with time (Baldridge et al., 1987). Miocene volcanism consisted exclusively of alkali olivine basalt (see above). However, the first phase of Pliocene volcanism (4–3 Ma) included significant volumes of tholeiitic basalts. The most recent volcanism (1.1–0 Ma) consisted of both tholeiitic rocks (much lower in alkalis than the previous phase), erupted from a single shield volcano, and a suite of high-alkali, ne-normative basalts (Table 5). At present, comparable data do not exist from other volcanic fields of the transition zone to determine whether such a systematic shift toward more tholeiitic compositions exists in other areas, but certainly many of the youngest (<1.5 Ma) basaltic rocks throughout the transition zone are tholeiitic (e.g., Perry et al., 1987).

The oldest basalt recognized in the Zuni–Bandera field is 3.8 Ma (Table 1; also Laughlin et al., 1982). Most of the basalts presently exposed in the Zuni–Bandera field are Quaternary in age. Older Quaternary rocks were erupted mainly from a group of 30 cones called the Chain of Craters (e.g., Maxwell, 1986). Younger Quaternary basalts were erupted mainly northeast of the chain, forming an area referred to as El Malpais (see Stop 1-4 below). On geomorphic evidence, Gawell (1975) and Gawell and Laughlin (1975) recognized a gradual decrease in age from southwest to northeast along the northern portion of the Chain of Craters. A progressive change from alkalic basalts to tholeiites with an increase in SiO_2 and decrease in K_2O, MgO, TiO_2, and Cr accompanied this decrease in age. Elsewhere in the Zuni–Bandera field, compositions range from basanites to tholeiites (Table 5). Incompatible-element concentrations in the

TABLE 4—Major-element compositions (in %) and trace-element compositions (in ppm) of Miocene magmatic rocks from the southeastern Colorado Plateau transition zone. Compositions of 183–426 determined by x-ray fluorescence; compositions of z-numbered samples determined by a combination of electron-probe microanalysis of fused beads (Baldridge, 1979) and instrumental neutron-activation analysis (Vaniman et al., 1982). Analyses performed at Los Alamos National Laboratory. $Fe_2O_3^T$ = total Fe as Fe_2O_3. [1]Location shown in Fig. 4. [2]Locations shown in Fig. 5. [3]Spinel lherzolite xenolith. [4]30% if <300 ppm. [5]Cerro Mohinas, Lucero volcanic area. [6]Hidden Mountain, Lucero volcanic area. [7]Mesa Gallina, Lucero volcanic area.

	Relative error (%)	426[1]	Z2.81.9[2]	Z2.81.23[2]	Z6.6.12(2)[2]	Z6.6.12[2,3]	183[5]	184[6]	406[7]	411[7]
SiO_2	2	54.72	42.0	45.1	44.1	44.4	48.66	48.36	53.00	45.81
TiO_2	7	1.24	3.37	3.30	3.30	0.12	1.90	1.95	2.11	2.25
Al_2O_3	2	15.03	9.9	12.3	11.1	1.64	16.25	16.35	15.59	14.36
$Fe_2O_3^T$	3	9.47	13.1	12.4	12.7	9.0	10.59	11.24	8.16	11.85
MnO	5	0.14	0.17	0.20	0.19	0.16	0.17	0.16	0.15	0.17
MgO	3	6.06	14.7	10.5	14.3	42.7	7.14	6.95	5.00	10.03
CaO	2	7.02	11.9	10.5	9.9	2.14	8.19	8.20	6.96	10.16
Na_2O	3	2.82	2.30	3.93	2.14	0.13	3.30	3.54	4.04	2.55
K_2O	4	1.83	2.37	1.38	1.77	0.0	1.61	1.50	2.86	1.52
P_2O_5	15	0.22	0.90	1.32	0.93	0.0	0.55	0.57	0.56	0.54
Total		98.53	100.71	100.93	100.43	100.29	98.36	98.82	98.43	99.24
Cs	13		1.0	1.3	1.0	0.1				
Rb	15		4.8	39	49	5				
Ba[4]	10		1175	856	700	58				
Sr	10		992	1356	1237	58				
La	7		57	79	58	2.9				
Sm	10		11.2	13.4	10.1	0.93				
Eu	10		3.15	3.88	3.35	0.25				
Tb	12		1.28	1.65	1.37	0.16				
Yb	15		2.02	2.86	1.94	0.40				
Lu	20		0.17	0.35	0.41	0.10				
Th	6		7.0	9.6	7.4	1.9				
U	6		1.8	2.6	1.7	0.1				
Hf	5		6.7	8.4	7.0	0.4				
Cr	5		521	309	640	2519				
Sc	5		24	21	25	10				

Zuni–Bandera basalts are generally lower than in the adjacent Miocene volcanic rocks of the region (Fig. 7), but within the field there is a large range in La/Yb (from 5 to 24). While there is a large difference in Sr between the alkalic and tholeiitic basalts of this field, both groups have significantly lower Sr than do comparable rocks from elsewhere in the western U.S. (Laughlin et al., 1972).

Volcanism in the Red Hill area (also referred to as the Catron County fields in Laughlin et al., 1982) includes small shield cones, cinder cones, and maar volcanoes, and widespread flows. Eruptions ranged from 6.4 Ma (Table 1, Fig. 4) to 22,900 ± 1400 yrs (Bradbury, 1966). Compositions include both alkali olivine basalts and tholeiitic basalts (Table 5; also Perry et al., 1987). Little petrologic or geochemical work has been done on volcanic rocks of this area.

Volcanism in the Springerville field began about 4 Ma (Laughlin et al., 1980). This volcanic field is described in Excursion 5A (Ulrich et al., this volume).

MOUNT TAYLOR VOLCANIC FIELD: The Mount Taylor volcanic field (Fig. 11) is dominated by Mount Taylor, a composite latitic-to-rhyolitic volcano active from >3 to 1.5 Ma (Lipman and Mehnert, 1979; Perry et al., 1989). Growth of the volcano began with eruption of rhyolite, followed by quartz latite, and finally latite. The major episode of cone building occurred early in the history of the field between 3 and 2.6 Ma. During this period, eruption of quartz latite formed about 65% of the volume of the cone. Alkali basalts were erupted mainly around the periphery of the volcano (Fig. 11) but, unlike most of the other volcanic fields within the transition zone, no low-alkali tholeiitic basalts are associated with the volcanic field.

The alkali basalts of the Mount Taylor volcanic field are divided into five distinct groups based on their geochemistry. The two major basalt groups are hy-hawaiites (0–16% normative hy) and ne-hawaiites (0–6% normative ne). Ne-hawaiites are distinguished from hy-hawaiites by lower TiO_2 at similar SiO_2 and by higher Mg numbers [$100 \times Mg/(Mg + Fe^{2+})$] (63–56 versus 57–40). The other basalt groups, which occur with less frequency within the Mount Taylor volcanic field, are plagioclase basalts (containing large plagioclase phenocrysts and high CaO, Al_2O_3, and Sr), high-Ti hawaiites (0–1% normative ne), and basanites (8–16% normative ne, SiO_2<45%, TiO_2>4%).

Latites (58–63% SiO_2), quartz latites (63–70% SiO_2), and rhyolites (70–75% SiO_2) of the Mount Taylor field generally form smooth and continuous series on variation diagrams. An exception to this general trend is a small group of rocks ("Type B" latites, quartz latites, and rhyolites) which have distinctly lower alkali content at equivalent SiO_2 and a unique phenocryst assemblage consisting of two alkali feldspars + quartz.

On all major- and trace-element variation diagrams, hy-hawaiites consistently form continuous trends with the main group of latites, quartz latites, and rhyolites (see second-day field guide below). Hy-hawaiites were also erupted contemporaneously with the main latite–rhyolite series and are the most voluminous basalt group of the Mount Taylor volcanic field. Based on these observations and petrologic modeling, Perry et al. (1989) suggested that the main latite–rhyolite series is derived from hy-hawaiite parental magmas by fractional crystallization. Nd- and Sr-isotopic compositions suggest that fractional crystallization was accompanied in all cases by a small amount (<10%) of crustal assimilation. Magma mixing involving extreme endmembers occurred in a few instances when evolved hy-hawaiite magmas mixed with "Type B" rhyolites to produce "Type B" latites and quartz latites.

Knowledge of multiple magmatic processes, petrographic

TABLE 5—Major-element compositions (in %) and trace-element compositions (in ppm) of Pliocene–Holocene basalts from the southeastern Colorado Plateau transition zone and central Rio Grande rift. Compositions of Z-numbered samples determined by a combination of electron-probe microanalysis of fused beads (Baldridge, 1979) and instrumental neutron-activation analysis (anhydrous basis) (Vaniman et al., 1982) at Los Alamos National Laboratory (LANL). Samples prefixed by QCJ, QBO, and QBW analyzed by x-ray fluorescence (XRF) and instrumental neutron-activation analysis (hydrous basis) at New Mexico Institute of Mining & Technology. All other samples analyzed by XRF (hydrous basis) at LANL. $Fe_2O_3^T$ = total Fe as Fe_2O_3.

	Red Hill				Zuni–Bandera								central Rio Grande rift				
	419[1]	420[1]	428[1]	429[1]	Z4. 23.13[2]	Z5. 81.10[2]	Z12 16.6[2]	Z12 16.7[2]	Z12 16.10[2]	QCJ 402[5]	QBO 602[6]	QBW 203[7]	SC-2[8]	SC-3[8]	MR-12[8]	MR-2[8]	MR-6A[10]
SiO_2	49.66	49.99	46.53	52.85	53.9	54.1	52.0	52.3	48.1	48.20	44.88	51.50	50.17	50.57	51.12	51.02	51.51
TiO_2	2.02	1.54	2.45	1.35	1.42	1.62	1.40	1.35	1.50	1.85	2.81	1.21	1.54	1.48	1.42	1.41	1.42
Al_2O_3	16.73	15.35	15.36	15.32	15.2	14.9	15.5	15.6	14.6	14.60	14.44	15.02	17.39	17.96	17.25	18.00	17.93
$Fe_2O_3^T$	11.71	11.23	12.69	10.86	10.4	8.99	10.4	10.88	11.88	11.85	13.78	11.28	9.39	9.00	8.13	8.51	8.35
MnO	0.16	0.16	0.18	0.16	0.17	0.15	0.09	0.16	0.17	0.18	0.18	0.15	0.13	0.14	0.12	0.13	0.13
MgO	5.43	7.28	7.89	7.61	6.4	7.8	6.9	7.6	10.1	10.29	9.36	8.44	5.72	5.29	5.09	5.52	5.63
CaO	8.69	8.78	8.18	7.88	9.6	7.6	9.5	9.3	10.4	9.20	9.00	9.44	8.05	8.00	8.14	7.93	7.55
Na_2O	2.98	2.61	2.99	3.11	2.30	3.11	2.35	2.44	2.56	3.06	3.96	3.15	3.58	4.28	3.63	4.17	4.15
K_2O	1.00	1.08	1.53	1.44	0.64	1.63	0.72	0.58	0.71	1.10	1.70	0.48	1.94	2.08	2.16	2.19	2.20
P_2O_5	0.34	0.25	0.57	0.21	0.29	0.33	0.21	0.19	0.26	0.37	0.64	0.15	0.86	0.92	0.80	0.91	0.86
Total	98.72	98.28	98.39	100.78	100.32	100.23	99.07	100.4	100.28	100.70	100.75	100.82	98.77	99.72	97.86	99.79	99.73
Cs					1.0	0.5	0.9	0.6	0.6			0.3					
Rb					17	27	10	23	13	16	23	11	24	15	43	19	12
Ba					279	456	235	160	228	167	366	126					
Sr					371	565	297	324	359	289	823	257	1423	1380	1553	1338	1247
La					15	21	13	13	14	12	36	9					
Ce										27	74	20					
Sm					4.3	4.4	3.7	3.6	3.9	3.9	7.6	3.1					
Eu					1.45	1.38	1.19	1.17	1.39	1.30	2.40	1.00					
Tb					0.55	0.70	0.48	0.57	0.70	0.60	0.94	0.44					
Yb					1.79	2.02	1.88	1.83	1.80	2.20	1.50	1.80					
Lu					0.44	0.21	0.22	0.23	0.41	0.32	0.22	0.25					
Th					2.4	2.5	2.3	2.0	2.2	4.3	3.4	4.0					
U					0.9	1.0	0.6	0.6	0.6								
Hf					3.1	4.0	2.6	2.6	2.9	3.1	6.3	2.3					
Cr					223	269	138	140	333	417	234	307					
Sc					28	20	23	23	26	29	21	25					
Ni										187	165	186					
Zn										96	113	88					
Y										26	24	20					
Zr										122	270	85					
Nb										13	50	9.9					
Ta										1.00	3.40	0.49					
Pb										7.6	0.4	4.7					

	central Rio Grande rift														Lucero	
	SO-1[11]	SO-2[12]	BM-1[12]	BM-2[11]	M4-2[12]	MA-8[8]	MP-2[11]	MP-3[12]	V 18-1[13]	V 18-2[13]	V 18-5[10]	V 29-1[8]	V 29-2[8]	29-3[8]	343[14]	347[15]
SiO_2	49.95	50.33	50.07	50.15	52.72	53.69	47.95	48.87	50.54	49.07	52.09	48.74	47.95	48.19	48.47	48.14
TiO_2	1.55	1.53	1.67	1.65	1.73	1.69	1.48	1.52	1.65	2.08	1.73	1.92	1.91	1.92	2.52	2.31
Al_2O_3	16.49	16.28	16.15	16.28	17.56	17.13	16.42	16.84	16.39	16.03	16.16	15.59	15.29	15.22	16.58	16.41
$Fe_2O_3^T$	12.81	12.38	12.32	12.04	8.61	8.23	10.49	10.81	10.54	10.87	10.63	11.41	11.42	11.54	11.99	12.51
MnO	0.17	0.17	0.17	0.17	0.15	0.14	0.16	0.16	0.16	0.16	0.14	0.16	0.17	0.17	0.15	0.09
MgO	7.17	7.06	6.81	6.90	3.68	2.83	6.20	6.00	6.52	6.69	5.53	8.36	8.41	8.46	5.27	4.98
CaO	8.97	8.93	9.21	9.05	5.36	6.70	10.54	9.78	8.47	8.25	7.87	8.32	8.38	8.55	6.69	8.70
Na_2O	2.71	2.69	3.18	3.22	4.91	4.56	4.28	4.11	3.45	3.25	3.41	3.18	2.92	3.08	5.57	5.67
K_2O	0.74	0.74	0.75	0.77	2.89	2.90	1.38	1.40	1.69	2.17	1.61	1.82	1.75	1.73	2.84	1.51
P_2O_5	0.22	0.22	0.24	0.25	0.91	0.90	0.40	0.43	0.42	0.83	0.39	0.47	0.45	0.44	0.54	0.57
Total	100.78	100.33	100.57	100.48	98.52	98.77	99.30	99.92	99.83	99.40	99.56	99.97	98.65	99.30	100.62	100.89
Cs																
Rb	3	6	8	6	72	58	32	37	17	40	27	37	28	41		
Ba																
Sr	322	322	305	315	1090	849	506	527	444	516	450	552	543	532		

1. Location shown in Fig. 4.
2. Location shown in Fig. 5.
3. Basalt underlying Cerro Rendija.
4. North Plains basalt.
5. El Caldera Crater.
6. Oso Ridge flow.
7. Hoya di Cibola flow.
8. Location shown in Fig. 12. Mesa-capping flow.
9. Location shown in Fig. 12. Dike cutting cone.
10. Location shown in Fig. 12. Flow on upper flank of cone.
11. Location shown in Fig. 12. Upper of two flows capping mesa.
12. Location shown in Fig. 12. Lower of two flows capping mesa.
13. Location shown in Fig. 12.
14. Mush Mountain.
15. Unnamed vent 1 km south-southwest of Mush Mountain.

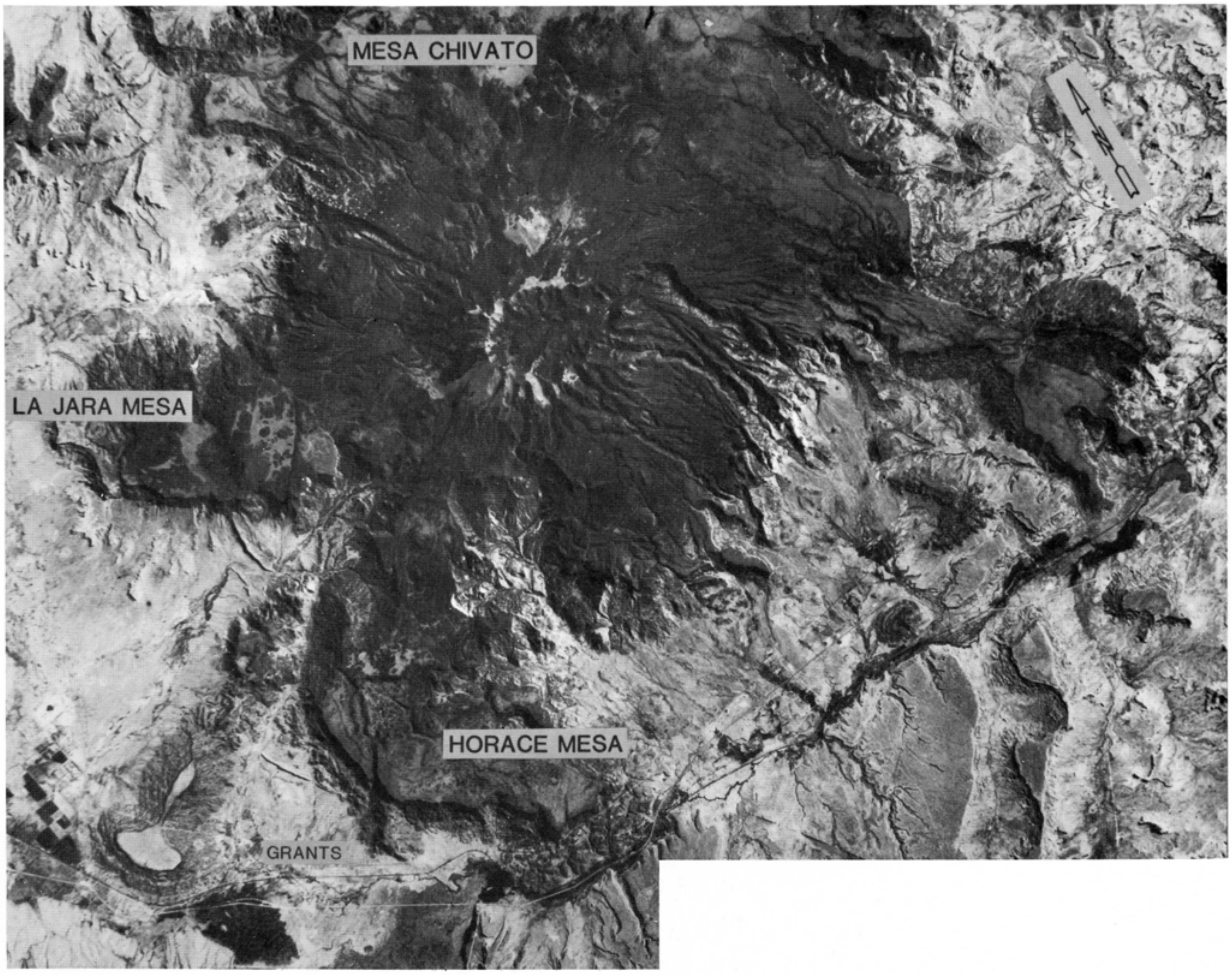

FIGURE 11—Skylab 3 view of Mount Taylor and surrounding basalt-capped mesas.

and field observations, and thermal arguments indicate that a succession of short-lived magma chambers existed beneath the Mount Taylor volcanic field, rather than a single, long-lived magma chamber (Perry et al., 1989). This multiplicity of chambers was probably a consequence of low magma-production rates in the mantle, typical of the Rio Grande rift region, which limited the possibility of magma recharge that could sustain a long-lived chamber.

Despite multiple magma chambers, the compositions of lavas erupted from Mount Taylor became systematically more mafic through time, indicating a common control on magma evolution. One possibility is that a reduced state of crustal extension in the early history of the volcanic field inhibited the ascent of magmas and favored differentiation of magmas to more evolved compositions. Increasing crustal extension later in the history of the field facilitated the ascent of magmas without protracted differentiation. A larger magma flux through the crust earlier in the history of the field may have also contributed to more differentiated lavas by locally heating the crust, lowering both its density and its ability to sustain brittle fracture, thereby inhibiting magma ascent.

BASALTIC FIELDS OF THE CENTRAL RIO GRANDE RIFT: Most of the basaltic rocks of the central rift, including the Cerros del Rio and other volcanic fields closely associated with the Jemez field, and the voluminous Taos volcanic field, were erupted during this interval. The basalts consist of a variety of ne- and hy-normative types which are generally similar to other late Cenozoic basaltic rocks of the western U.S. The most voluminous of the Pliocene–Holocene basaltic fields, the Taos Plateau field, consists dominantly of a distinctive, low-alkali tholeiitic basalt (Servilleta Basalt), with lesser volumes of more alkaline (but still hy-normative) magmas. Minor quantities of intermediate to silicic magmas represent melts formed by crystal fractionation processes and by melting of the lower crust. The Taos field reflects a major thermal source which generated large quantities of magmas at or near the top of the mantle, and began to involve the crust in a major way (Lipman and Mehnert, 1979; Basaltic Volcanism Study Project, 1981: 108–131; Moorbath et al., 1983; Dungan et al., 1984).

In the central and southern rift, only very minor volumes of Servilleta-type magmas were erupted. No single composition is dominant and major-element compositions do not correlate in any unique way with tectonic setting. In the Cerros del Rio volcanic field (see sixth-day field guide below), a variety of compositions was erupted: high-alkali tholeiite, basaltic andesite (called "shonkinites" by Duncker, 1988), alkali olivine basalt, and basanite (Baldridge, 1979a; Duncker, 1988). Basaltic andesites (shonkinites) are cogenetic with a suite of much more silicic rocks ("latite-andesites" of Baldridge, 1979a; "benmoreites" of Duncker, 1988), which probably formed by a combination of fractional crystallization and crustal contamination.

Farther south, both tholeiitic and alkalic magmas were erupted (e.g., Aoki and Kudo, 1976; Kelley and Kudo, 1978; Baldridge et al., 1982, 1987). New compositional data for Pliocene–Holocene basaltic rocks of the central rift are presented in Table 5 and Fig. 12.

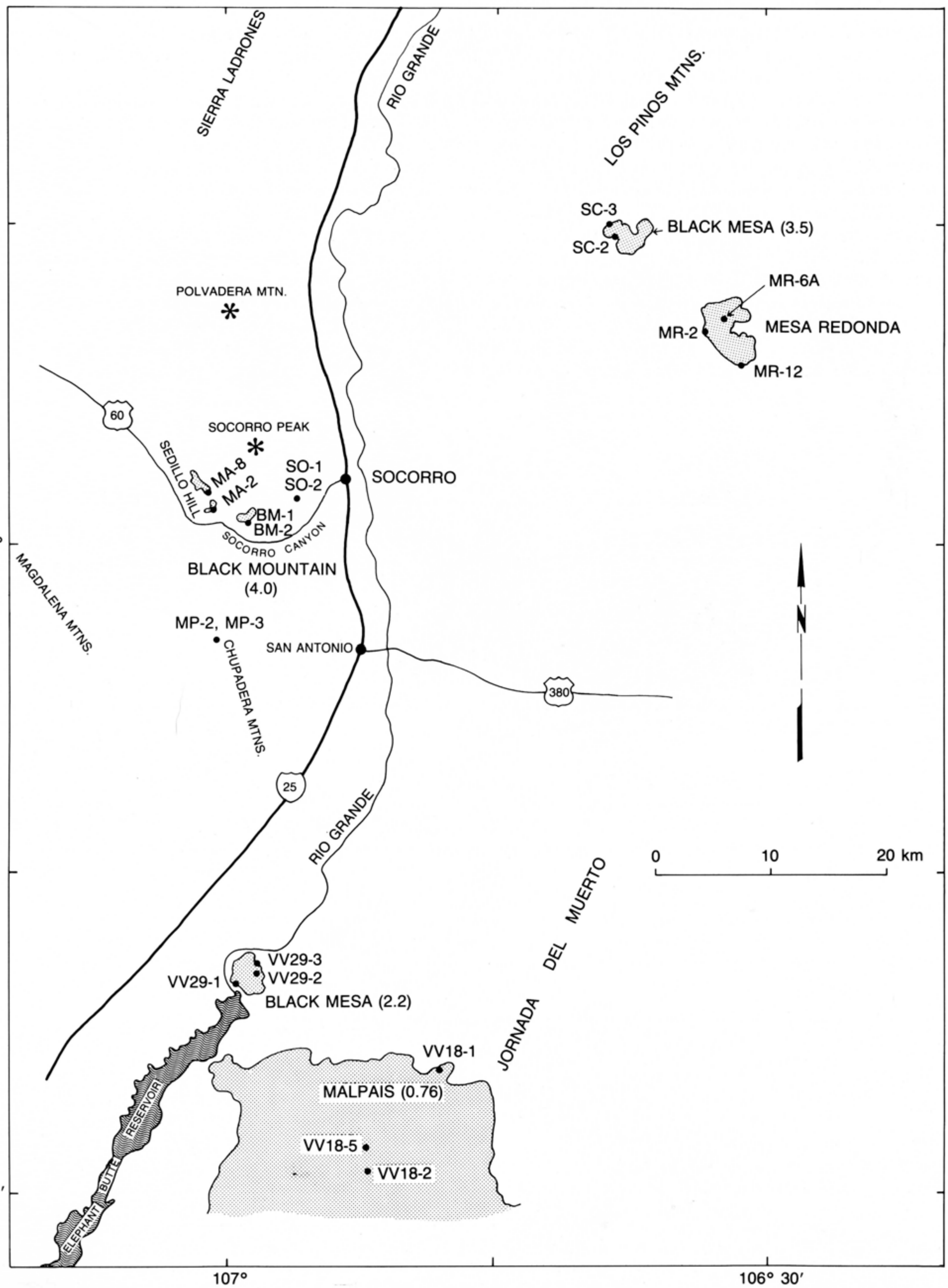

FIGURE 12—Locations of analyzed Pliocene–Holocene basaltic rocks (Table 5) from the central Rio Grande rift. Numbers in parentheses are K–Ar ages (in Ma) from Bachman and Mehnert (1978).

Discussion

Late Oligocene to early Miocene magmatism is characterized by mafic rocks of predominantly basaltic andesite composition. True basalts, while present, are relatively rare. Typically, the basaltic andesites have relatively high $^{87}Sr/^{86}Sr$ (0.712–0.714; Laughlin and Brookins, unpubl. data), suggesting that their origin involves a significant amount of crustal contamination. Little detailed geochemical/isotopic work has been done on these basaltic andesites.

Pliocene–Holocene ($\leq$4 m.y.) basaltic volcanism within the transition zone is characterized by the coexistence of alkalic and tholeiitic basalts in close spatial and temporal proximity. Throughout most of the central rift and transition zone, alkalic and tholeiitic basalts have distinctly different Nd- and Sr-isotopic compositions, with tholeiites more isotopically "enriched" (e.g., $E_{Nd} = +6.6$ to $+4.1$ for alkali basalts, $E_{Nd} = +1.4$ to -0.6 for tholeiites; Perry et al., 1987). Among alkalic basalts, E_{Nd} correlates with tectonic setting. These isotopic data indicate that basalts are derived from two isotopically distinct mantle reservoirs, one relatively more enriched than the other. Where little or no lithospheric extension has occurred, such as the Great Plains, basalts are derived from enriched lithospheric mantle (Fig. 13A). Where significant lithospheric extension has occurred, such as the southern rift and Basin and Range, basalts are derived from underlying depleted asthenospheric mantle. In the transition zone, basalts are derived from a mixture of these two sources. Tholeiites generally have more enriched signatures because they are generated at shallower depths, essentially at the base of the crust and dominantly within lithospheric mantle.

A major exception occurs in the northern rift, including the area of the Jemez Mountains and Cerros del Rio volcanic field. Basalts from these areas are isotopically enriched (indicating lithospheric mantle), even though geophysical (i.e., seismic refraction) studies show that asthenosphere lies at or near the base of the crust (e.g., Olsen et al., 1987). This apparent discrepancy suggests that basaltic magmas were derived from lithospheric mantle that was recently converted to asthenospheric mantle in place ("thermal thinning"), and not yet displaced by lithospheric extension. While probably not a major process of lithospheric thinning, this interpretation suggests that upwelled asthenosphere may be surmounted by a carapace of partially melted "lithosphere."

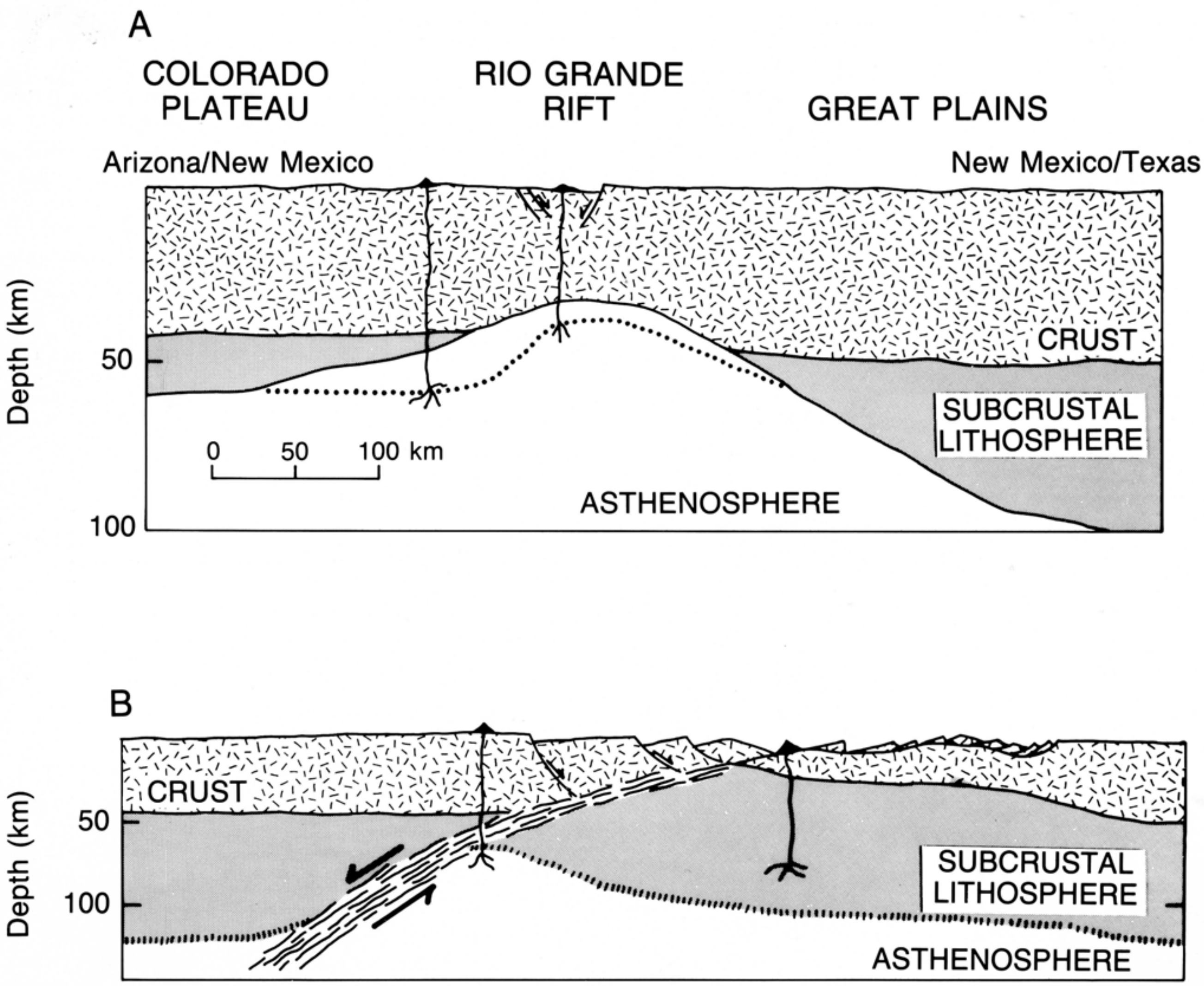

FIGURE 13—Possible models of the lithosphere beneath the Rio Grande rift and Colorado Plateau transition zone. **A,** Lithospheric model from Perry et al. (1987, 1988). A feature of this model, in agreement with geophysical data, is that the region of maximum crustal thinning occurs above the region of maximum lithospheric thinning, and that both are essentially centered beneath the axis of the rift. **B,** Model of lithospheric extension involving simple shear, modified from Wernicke (1985). This model predicts that the region of maximum crustal thinning is offset laterally from the region of maximum lithospheric thinning.

In the Lucero volcanic field, isotopic compositions of alkalic and tholeiitic basalts record the thinning of lithospheric mantle and its replacement/displacement by asthenospheric mantle (Perry et al., 1988). E_{Nd} of alkalic basalts is more enriched in 8–6 Ma Miocene basalts than in Pliocene–Holocene basalts, suggesting a greater component of lithospheric mantle. Alkali basalts $\leq$4 Ma have significantly more depleted isotopic signatures, indicating a source containing a larger asthenospheric component. These data suggest that the asthenosphere/lithosphere boundary had risen in this area between 8 and 4 Ma. Tholeiitic basalts were erupted in the Lucero field only in the period 4 Ma or less and have isotopic compositions which indicate derivation from lithospheric mantle. The beginning of tholeiitic volcanism 4 Ma (both in the Lucero field and elsewhere within the transition zone) may mark the time when shallow lithospheric mantle was sufficiently heated to allow partial melting, a consequence of the rise of the asthenosphere/lithosphere boundary beneath this area.

The model of lithospheric thinning developed above implies that older mafic rocks in the central rift transition zone region, such as those of the late Oligocene to early Miocene Mogollon–Datil region, should have "lithospheric" (i.e., "enriched") isotopic ratios. Although little isotopic work has been done on these rocks, available Nd- and Sr-isotopic ratios are compatible with this model (Bikerman and Bell, 1986). In addition, the high $^{87}Sr/^{86}Sr$ of these rocks strongly suggests that the magmas underwent major crustal contamination.

Finally, the model presented above (Fig. 13A) for the configuration of the lithosphere beneath the Rio Grande rift and southeastern Colorado Plateau (Perry et al., 1987, 1988), based both on available geophysical and chemical data, contrasts with models of lithospheric thinning involving simple shear along low-angle detachment faults (Fig. 13, B), as postulated for the western margin of the Plateau by Wernicke (1985) and for the East African rift by Bosworth (1987). The essential feature of simple-shear models is that the region of greatest crustal thinning is offset laterally from the region of greatest lithospheric thinning, leading to strong asymmetry in volcanism and other features. As applied to the Rio Grande rift, the simple-shear model implies that the greatest asthenospheric signature should occur displaced from the rift axis toward the Colorado Plateau, and that signatures beneath the rift and Basin and Range should be essentially lithospheric. While interpretation of geochemical signatures is to some extent model-dependent, this predicted spatial distribution of E_{Nd} does not match the observations. In addition, available geophysical data do not seem to support a simple-shear model for the central rift–southeastern Colorado Plateau region (e.g., Olsen et al., 1987; de Voogd et al., 1988).

Acknowledgments

This paper and the following field guide to Excursion 8A summarize results acquired by many scientists from a variety of institutions and agencies working on different projects over a period of many years. Sponsoring institutions include the U.S. Department of Energy (DOE), U.S. Geological Survey, National Aeronautics and Space Administration, Institute of Geophysics and Planetary Physics (IGPP) (Los Alamos Branch) of the University of California, and Geological Survey of Israel. We thank F. Goff for a careful review of this manuscript and the accompanying excursion guide. Preparation of these manuscripts was supported by the IGPP (Los Alamos Branch), Office of Basic Energy Sciences of the DOE, and U.S. Geological Survey.

FIELD GUIDE TO EXCURSION 8A: Oligocene to Holocene magmatism and extensional tectonics, central Rio Grande rift and southeastern Colorado Plateau, New Mexico and Arizona

W. S. Baldridge[1], F. V. Perry[2], L. D. Nealey[3], A. W. Laughlin[1], and K. H. Wohletz[1]

[1]*Earth and Space Sciences Division, Los Alamos National Laboratory, Los Alamos, New Mexico 87545;*
[2]*Department of Geology, University of New Mexico, Albuquerque, New Mexico 87131;* [3]*U.S. Geological Survey, 2255 North Gemini Drive, Flagstaff, Arizona 86001*

Introduction

The area of the central Rio Grande rift and southeastern Colorado Plateau is particularly important for the study of magmatic and tectonic processes because it spans several tectonic provinces (e.g., Great Plains, Colorado Plateau, Rio Grande rift, Basin and Range), each with its unique geologic history and lithospheric characteristics. Therefore, although this region is a relatively restricted area, it is possible to discern features that are unique to, or common to, these different tectonic provinces. Excursion 8A is designed to show essential features of the middle Oligocene to Holocene magmatism of the central rift and the transition zone of the southeastern Colorado Plateau, and the relationship of magmatism to regional tectonic setting. Oligocene and early Miocene magmatic rocks are exposed mainly as dikes and small intrusions. Younger rocks occur as widespread basaltic vents and flows and as major central volcanic complexes of intermediate composition, e.g., Mount Taylor and the White Mountains. Features emphasized on this excursion include: (1) the compositional range (major-element, trace-

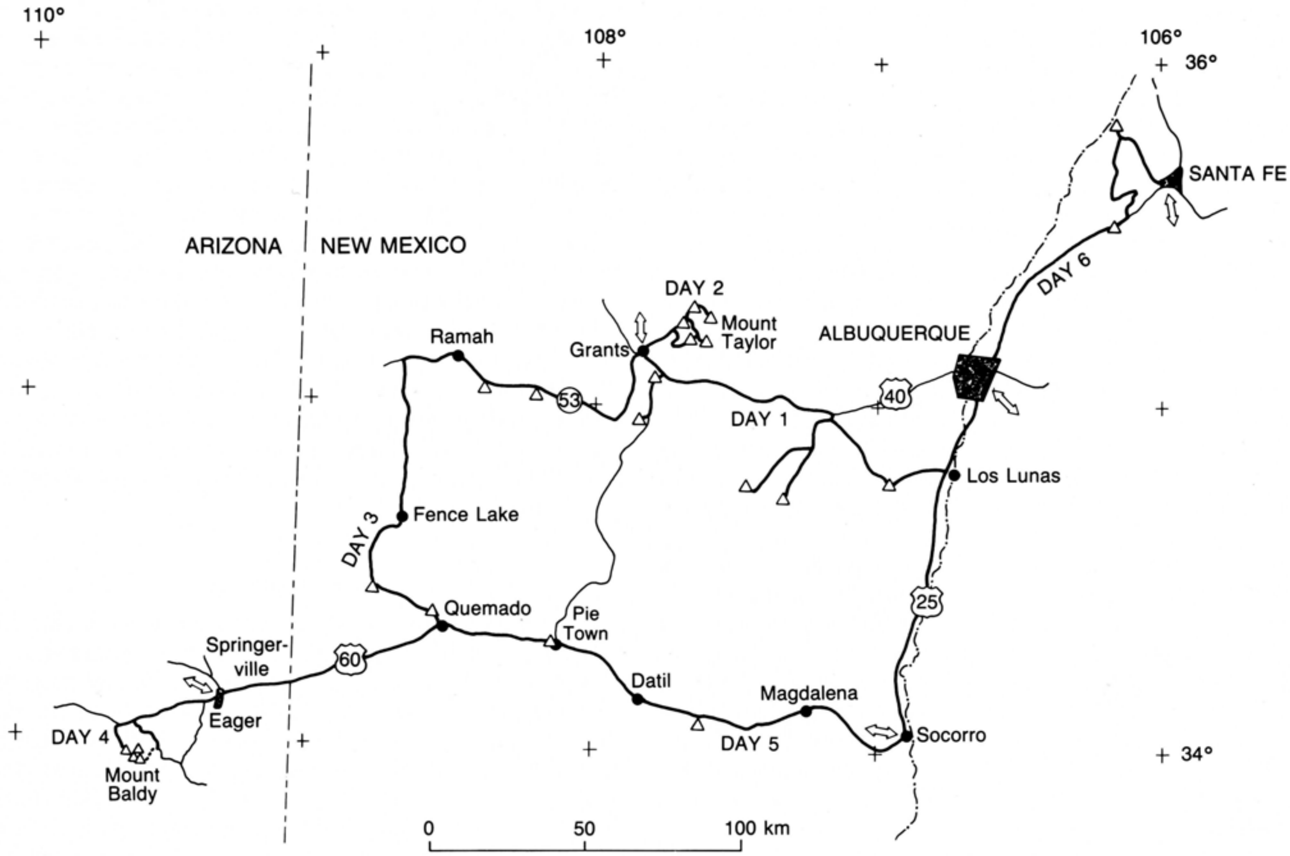

element, and isotopic characteristics) of basaltic rocks, which are important as probes of mantle-source regions, and their temporal and spatial variation; (2) the compositions, origin, and evolution of intermediate rocks of the major central volcanoes, which provide information mainly on crustal processes; (3) structural setting of magmatic rocks, which can provide unique information on the orientation and evolution of the stress field; and (4) morphology of volcanic units and eruption mechanisms, surface and near-surface phenomena.

Day 1: Albuquerque to Grants

Summary

The first day's excursion focuses primarily on late Miocene to Holocene basalts of the central Rio Grande rift and Colorado Plateau transition zone. It includes an overview of structures along the western margin of the rift. Major-element, trace-element, and isotopic compositions of basalts of this region, which range from alkalic to tholeiitic types, are a function of the depth and amount of partial melting, crustal contamination, and mantle-source composition. Compositional data allow delineation of two isotopically distinct mantle-source reservoirs ("enriched" and "depleted" reservoirs), which places constraints on the depth to the lithosphere–asthenosphere boundary in this area and provides insight into the processes of lithospheric thinning beneath a major continental rift.

Note: Part of this day's field guide coincides with the New Mexico Geological Society's Second Day Road Log (Albuquerque to Grants), 1982. See Grambling et al. (1982) for more details, particularly on sediments and sedimentary rocks.

Mileage

0.0 I-25 and Rio Grande bridge, **east** end. **Cross** Rio Grande. **1.7**

1.7 Straight ahead is Isleta Volcano, a small basaltic shield cone built within an earlier maar crater that is almost completely buried by flows of the shield cone (Kelley and Kudo, 1978). Outside the maar, pyroclastic rocks are as much as 60 m thick. These deposits are truncated toward the vent by an arcuate, inward-dipping collapse surface overlain by maar breccias. The shield cone (2.8 ± 0.1 Ma; Kudo et al., 1977), which is centered within the maar, consists of six separate basalt units. The basal flow unit rests on a maar accumulation of basaltic tuff and tuff breccia. The lowermost flows may have been part of a lava lake that erupted in the maar. Basalt compositions include both ne-normative (alkali olivine basalt to hawaiite) and hy-normative (high-alkali olivine tholeiite) types (Aoki and Kudo, 1976; Kelley and Kudo, 1978; Baldridge, 1979a).

Here the highway is cut through a flow of olivine tholeiite (Baldridge, 1979a), one of several outlying basalt flows which have no exposed connection with Isleta Volcano. Sediments of the Santa Fe Group are exposed beneath the flow. **2.0**

3.7 Low roadcuts along both sides of I-25 expose southward-dipping, finely bedded basaltic ash overlain by a unit, 2–3 m thick, of coarser-grained basaltic breccia containing clasts of the underlying Santa Fe sediments. The breccia and ash at this outcrop lie

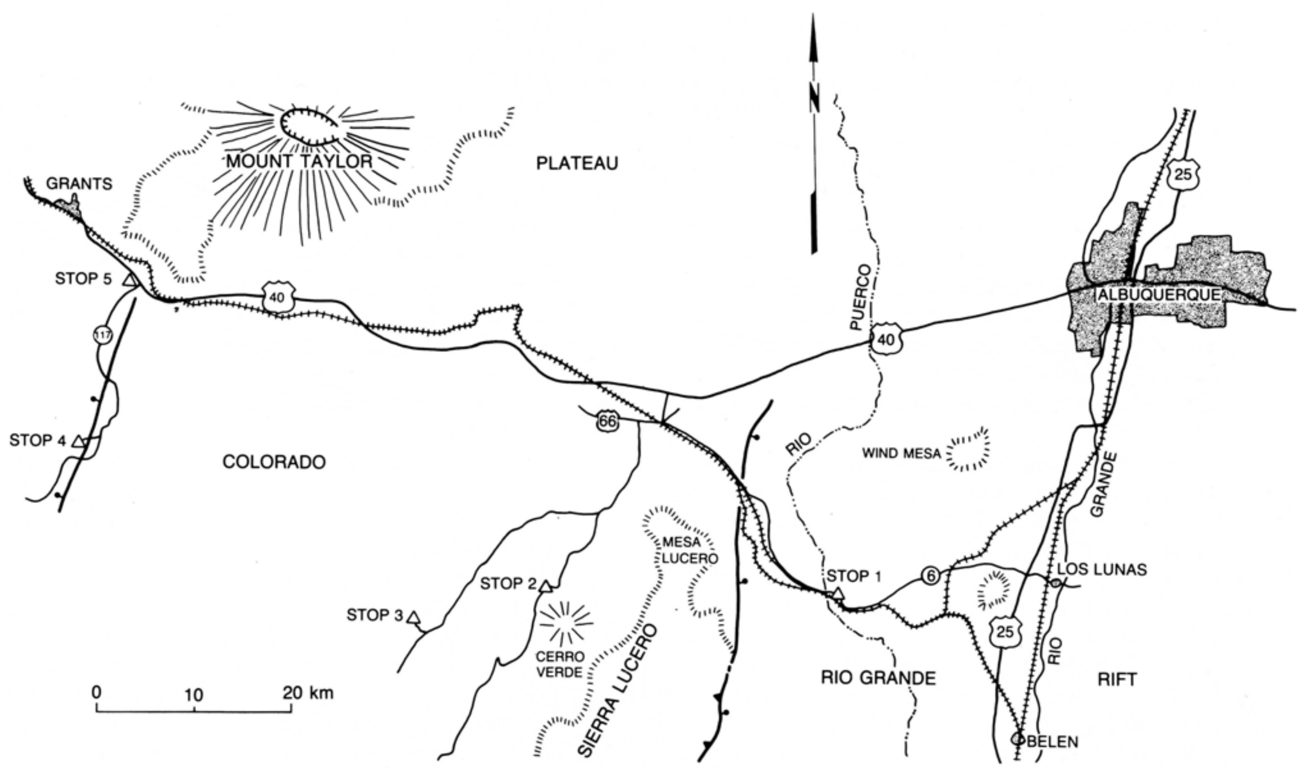

outside the arcuate subsidence surface of the maar and thus probably represent a distal part of a tuff ring. The ash displays soft-sediment deformation beneath the larger basaltic clasts. The change from fine-grained ash to coarser-grained breccia is a common feature of basaltic eruptions in this area and may represent a "drying out" of the volcanic conduit. Above these units lies flow unit 2 of Isleta volcano (Kelley and Kudo, 1978). **7.2**

10.9 **Exit right** (Exit 203) to Los Lunas and **turn right** onto NM-6. On the left is Los Lunas Volcano, an andesitic complex consisting of at least five flows erupted from several separate vents. Flows were erupted near the edge of the mesa surface to the west and cascaded down the mesa side and onto a terrace or valley floor (Kelley and Kudo, 1978). K–Ar ages range from 1.31 to 1.01 Ma (Bachman and Mehnert, 1978). Phenocrysts consist of plagioclase, augite, hypersthene, olivine, and basaltic hornblende. Zimmerman and Kudo (1979) proposed that the andesitic magmas are primary magmas derived by partial melting of hornblende-bearing mantle. Subsequent evolution was controlled by fractional crystallization of plagioclase + olivine ± magnetite ± pyroxene from low-silica andesites, followed by hornblende–plagioclase fractionation from the high-silica andesites, with concomitant crustal contamination. **5.2**

16.1 On the right is the Cat Hills volcanic field, which consists of a broad apron of basaltic flows covering an area of about 65 km^2. The flows are surmounted by 23 cinder cones aligned along a north-northeast-trending fissure zone (Kelley and Kudo, 1978). Seven flows are present, the lowermost of which has a K–Ar age of 0.14 ± 0.04 Ma (Kudo et al., 1977). SiO_2 ranges from 49 to 51.5% and $(Na_2O + K_2O)$ from 4 to 5%. Normative hy is between 1 and 8%. Mg values $[100 \times Mg/(Mg + Fe^{2+})]$ range from 61 to 53. Petrologic modeling indicates that the observed range in composition resulted from fractional crystallization of small amounts of olivine (5–6%) and of plagioclase (3–6%), the observed phenocryst phases (Baldridge et al., 1982). Although slightly to moderately hy-normative, these basalts are similar to the alkalic basalts in their trace-element and isotopic compositions, and were classified as alkalic by Perry et al. (1987). $^{87}Sr/^{86}Sr$ and $^{143}Nd/^{144}Nd$ are 0.70392 and 0.512080 ($E_{Nd} = +4.8$), respectively. These values, which are typical for basalts from the central Rio Grande rift and Colorado Plateau transition zone, were interpreted by Perry et al. (1987) to indicate that the basaltic magmas were derived from a mixture of enriched and depleted mantle sources, i.e., from across the lithosphere/asthenosphere boundary.

In the distance to the north is the Wind Mesa shield volcano. The shield cone is cut by several north–south-trending normal faults, resulting in a central graben and several tilted fault blocks (Kelley and Kudo, 1978). Flows are basalt to basaltic andesite, with SiO_2 ranging from 50.5 to 53.1% (Kelley and Kudo, 1978; Baldridge, 1979a). **7.7**

23.8 **STOP 1-1. Overview of western margin of Rio Grande rift. Pull off** highway onto right shoulder 0.1 mi past small bridge (at mile 20). The escarpment in the distance to the west is part of the Sierra Lucero, a fault-block uplift, hinged to the west, which forms the eastern rim of the Colorado Plateau. It locally forms the western topographic and structural boundary of the Rio Grande rift. The complex fault zone along which the Lucero block is uplifted possibly records a two-stage history, with rift-related extensional faulting superimposed upon early Tertiary (Laramide) compressional deformation (e.g., Callender and Zilinski, 1976). Strata exposed in the uplift range from Pennsylvanian to Cretaceous, and are typical of the units exposed over wide areas of the Colorado Plateau in New Mexico.

The two buttes in the Rio Puerco Valley, Cerro Mohinas on the left (south) and Hidden Mountain on the right, are subvolcanic intrusions (Kelley and Kudo, 1978) of late Miocene age (Hidden Mountain: 8.3 Ma; Baldridge et al., 1987). Cerro Mohinas is high-alkali tholeiite; Hidden Mountain is alkali olivine basalt (table 4 of preceding paper by Baldridge et al.).

On the skyline, to the left of Hidden Mountain, capping the Sierra Lucero is Mesa Gallina. The basalt capping Mesa Gallina (table 4 of preceding paper) and those of Hidden Mountain and Cerro Mohinas, are part of the oldest of three eruptive cycles of the Lucero area (8.3–6.2, 4.3–3.3, and 1.1–0 Ma; Baldridge et al., 1987). The basalt mesa (Mesa Carrizo) below Mesa Gallina is capped by 3.7 Ma (Bachman and Mehnert, 1978) olivine tholeiite. The skyline to the right of Hidden Mountain is the eastern edge of Mesa Lucero, which is capped by 4.1 Ma olivine tholeiite (Baldridge et al., 1987). Basalts of both Mesa Carrizo and Mesa Lucero are part of the intermediate cycle of the Lucero volcanic area. **1.5**

25.3 Cross Rio Puerco. **4.7**

30.0 Road ascends low scarp onto basalt flow and continues on the surface of this young (0.3 ± 0.2 Ma; Bachman and Mehnert, 1978; Leavy and Shafiqullah, 1987) flow. This flow of olivine tholeiite was erupted from Cerro Verde, a small shield cone located 23 km to the southwest (Stop 1-2). It followed a 42 km long path, first north and then east in the drainage of the Rio San Jose, around the northern end of the Lucero uplift. **4.2**

34.2 Road crosses trace of faults (buried beneath the basalt flow) along east side of Lucero uplift. These faults form the structural boundary between the Colorado Plateau and the Rio Grande rift. The northern part of the Lucero uplift is an asymmetrical, northward-plunging, faulted anticline. Strata exposed in the steeply eastward-dipping limb have been eroded into low hogbacks along the front of the Lucero uplift (Fig. 1-1). Rocks exposed along both sides of the road at this point are Jurassic (Entrada Sandstone, Wanakah and Morrison Formations) to Cretaceous (Dakota Sandstone). North of this point the rift border lacks physiographic expression.

To the west is Mesa Redonda, a faulted syncline in Jurassic and Cretaceous rocks. The Mesa is capped by a flow of high-Ti basanite, estimated to be 3–4 Ma (Baldridge et al., 1987). **7.5**

41.7 **Turn left** onto remnant of old US-66 and **cross over** railroad overpass. Drive through Correo (Spanish, "mail"), former site of a post office (1914–1959), general store, and gas station. Correo derived its name from the fact that it was the only place for many miles where mail could be received and dispatched (Pearce, 1965). **1.5**

43.2 **Turn left** onto Alamo School Road. **13.0**

56.2 **STOP 1.2. Cerro Verde (Suwanee) flow.** This stop is located on the 0.3 Ma (Bachman and Mehnert, 1978; Leavy and Shafiqullah, 1987) basalt flow, which was erupted from the Cerro Verde shield cone 4 km to the south-southeast. Only the uppermost part of the flow (pressure ridges) is exposed here. Much of the flow is obscured by a blanket of fine-grained, wind-blown silt and sand. The broad tholeiitic shield cone, part of the youngest cycle of basaltic volcanism recognized along the Colorado Plateau transition zone, is capped by a cinder cone of alkali olivine basalt.

The Cerro Verde basalt flow is a low-alkali olivine tholeiite containing sparse phenocrysts of olivine and plagioclase (Fig. 1-2). It is similar in composition to the voluminous Servilleta Basalt of the Taos Plateau. Vesicular segregations (consisting of vertical pipes and horizontal sheets) occur elsewhere in this flow, but are not present at this site. These segregations, which are enriched in incompatible elements relative to the surrounding flow, result from the concentration of in-situ-produced differentiation products by movement of residual melt through the partially solid framework of the crystallizing flow (Goff, 1977; Dungan et al., 1984).

Volcano Hill, 2 km to the northwest (Fig. 1-3), is a young (0.8 Ma; Baldridge et al., 1987) cinder cone of alkalic composition. Both Cerro Verde and Volcano Hill are part of the youngest volcanic cycle in the Lucero area. The close spatial and temporal proximity of alkaline and tholeiitic compositions is characteristic of volcanism throughout the area of the rift and Colorado Plateau transition zone, implying that melting is a very discontinuous process, i.e., that it occurs only locally and over a range of depths, and that it proceeds to various degrees.

Isotopic compositions of these two lavas are characteristic of the region in that tholeiites have higher $^{87}Sr/^{86}Sr$ and lower $^{143}Nd/^{144}Nd$ than alkalic basalts. This difference probably results from the fact that tholeiites, which are derived from shallower depths than alkalic basalts, are generated within subcrustal lithosphere (relatively "enriched" in isotopic composition). Alkalic basalts (of the Colorado Plateau transition zone) are generated essentially at the lithosphere/asthenosphere boundary, and thereby incorporate the more depleted isotopic signature of the asthenosphere (Perry et al., 1987).

To the northeast is Black Mesa (Fig. 1-3); to the southwest is Mesa del Oro. Both are tholeiites of the intermediate cycle. To the southwest, beyond Cerro Verde, is Mesa Gallina, capped by alkali olivine basalts of the oldest volcanic cycle.

Turn around and return (north) along Alamo School Road. **6.1**

62.3 **Turn full left. Cross** Cerro Verde flow. **3.5**

65.8 **Turn left. Cross arroyo and drive through gate. 7.2**

73.0 The two buttes exposed along the right (west) side of the road (informal name: North and South Alkali Buttes; Baldridge et al., 1987) are capped by phreatomagmatic deposits of alkali olivine basalt com-

FIGURE 1-1—Upturned strata along the east side of the Lucero uplift, which flanks the Rio Grande rift. View is to the south. In the middle ground is the Cerro Verde flow, which flowed from right to left (west to east).

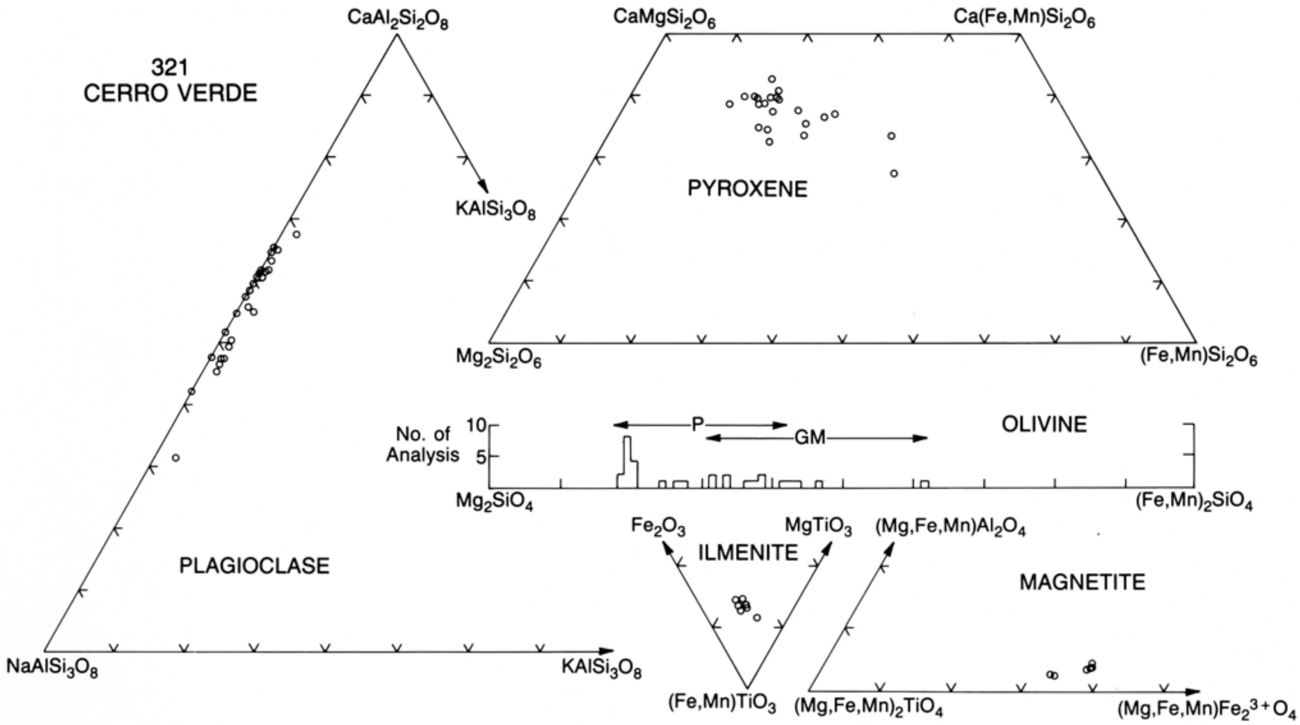

FIGURE 1-2—Compositions of plagioclase, pyroxene, olivine, and opaque phases in basalt flow from Cerro Verde. P = phenocryst, GM = groundmass.

position. Both represent remnants of tuff rings or possibly structures intermediate between tuff rings and tuff/cinder cones. They are composed in their lower part of fine-grained, well-bedded palagonitized ash. The deposits become coarser-grained upward, containing volcanic bombs. The deposits in both North and South Alkali Butte are roughly bowl-shaped, with inward dips. A surface of agglutinate forms the inner rim of the bowls. North Alkali Butte is surmounted by a ridge, suggesting that near the end of eruptive activity the vent began to dry out and evolve toward the cinder cone.

The phreatomagmatic deposits of both North and South Alkali Buttes were erupted onto a paleosurface (the Mush Mesa surface of Wright, 1946) dated at 0.7–0.8 Ma by Baldridge et al. (1987). Remnants of this surface are also preserved beneath Middle Tsidu-Weza Mesa (straight ahead) and other basalt-capped mesas in this valley. The fact that eruptive activity in these and several other young vents in this valley began with largely pyroclastic activity indicates extensive interaction with the near-surface ground water of the present Arroyo Colorado drainage.

Lavas of both North and South Alkali Butte are alkali olivine basalt. They contain xenocrysts of plagioclase and black augite; and xenoliths of spinel lherzolite, granulite, shale, and sandstone. **5.1**

78.1 **Turn right. 1.4**

79.5 **STOP 1-3. Pleistocene basaltic vents.** Stop at ruined homestead. Here in close proximity are two basaltic vents characteristic of the young eruptive episode in the Lucero area. The butte to the southwest is a crudely bowl-shaped eruptive center. The butte consists dominantly of cinders, bombs, agglutinate, and palagonitized ash. Ash is particularly exposed near the center of the bowl. Lithologic relationships are complex in detail. Crude bedding in the pyroclastic deposit is generally inward-dipping. Massive basalt, probably emplaced as sills and dikes, is intercalated within the pyroclastic pile. The lower part consists dominantly of vent agglomerate. Overlying the agglomerate is massive basalt, in places overlain by cinders and agglomerate. Typically the lower basalt contact dips inward, defining a "bowl." This vent illustrates an intermediate stage in development between a tuff ring and cinder cone. Initial eruptions were phreatomagmatic, the result of extensive interaction between the ascending magmas and the shallow ground-water table in this broad valley.

This basalt, which is characterized in massive outcrops by platy parting and prominent whitish "spots," is hawaiite (#347, table 5 of preceding paper). Xenoliths of lower crustal (granulite and pyroxenite) and upper crustal rocks (shale, quartzo-feldspathic gneiss) are abundant. Mantle inclusions (spinel lherzolite) occur rarely. Single crystals of pyrope [ex.: $(Mg_{1.68}Fe^{2+}{}_{0.82}Mn_{0.03}Ca_{0.43})$ $(Al_{1.96}$ $Fe^{3+}{}_{0.04})$ $Si_{3.04}O_{12}]$ are locally abundant in ant hills.

To the east is Mush Mountain and the southwestern corner of Middle Tsidu-Weza Mesa. Mush Mountain is a partially eroded cinder cone, which fed the basalt flow capping the mesa. The cone is extensively eroded, exposing the intrusive neck and a feeder dike. This basalt is also hawaiite (#343, table 5 of preceding paper). It is characterized by a "spotted" texture, platy parting, flow-banding, abundant xenoliths and xenocrysts, and by the fact that it rings when struck with a hammer, all of which are typical of the youngest alkalic rocks in the Lucero area.

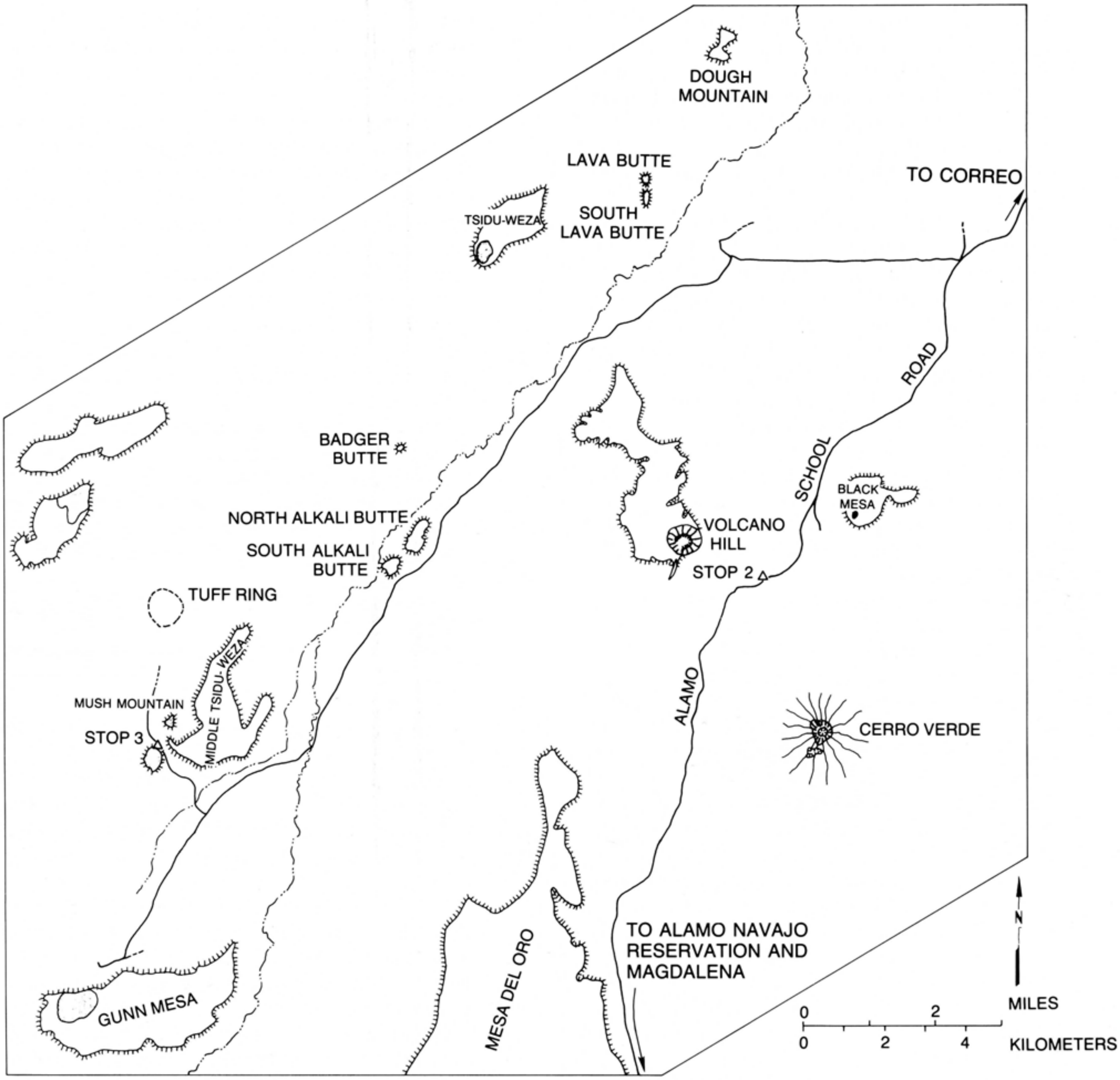

FIGURE 1-3—Physiographic map of northern part of Lucero volcanic area.

The basalt of Mush Mountain has a K–Ar date of 0.7 ± 0.1 Ma (Baldridge et al., 1987). Xenoliths include two-pyroxene granulites and pyroxenites, and possibly lherzolite (badly weathered). Megacrysts consist of plagioclase and augite.

Retrace route to NM-6. **25.6**

105.1 **Turn left (north)** onto NM-6. **1.9**

107.0 **Cross** overpass and **bear left** onto I-40. To the north, the dark-red sandstone exposed in the lowest cuesta is Petrified Forest Member of the upper Chinle Formation (Upper Triassic); it is capped by the Correo Sandstone Bed of the Petrified Forest Member. Units exposed in the slope of the higher mesa behind are, in ascending order: pale-orange to white Entrada Sandstone (upper Middle Jurassic); limestone- and gypsum-bearing Todilto Member of the Wanakah Formation; reddish-brown to pale-orange Beclabito Member of the Wanakah Formation; reddish-brown, cliff-forming Horse Mesa Member of the Wanakah Formation; and greenish-gray Morrison Formation (top of Jurassic sequence). Basal Dakota Sandstone (Cretaceous) forms the high cliffs of the mesa cap (Grambling et al., 1982). **10.9**

117.9 Laguna flow on right side of highway. Tholeiitic flow, 0.38 ± 0.25 Ma, following drainage of Rio San Jose (Lipman and Mehnert, 1979). $^{87}Sr/^{86}Sr = 0.70594$ and $^{143}Nd/^{144}Nd = 0.511892$ ($E_{Nd} = +1.1$), suggesting that this basalt was derived entirely from a reservoir that was enriched (cf. Cerro Verde flow, Stop 1-2) relative to that sampled by adjacent alkalic basalts. This reservoir is interpreted as subcrustal lithosphere (Perry et al., 1987). **2.5**

120.4 Scenic view of Laguna Pueblo. The Pueblo was established in 1699, largely by refugees fleeing the rebellion of 1680–1692 and the revolt of 1696 against Spanish rule (Jenkins and Schroeder, 1974). **6.8**

127.2 Straight ahead is Flower Mountain, capped by a basaltic cinder cone and flows. This basalt is undated and unanalyzed, but is likely to be alkali olivine basalt about 2 Ma. **2.5**

129.7 Straight ahead is Mt. Taylor. See second day of this excursion. **9.9**

139.6 Distal end of McCartys flow. This flow, an olivine tholeiite, originated from a small cone 40 km to the southwest. The lava flowed northward 40 km to the Rio San Jose and then turned eastward for 8 km. The McCartys flow is probably about 1000 years old but could possibly be as young as about 500 years (Crumpler, 1982; Maxwell, 1982). Indian potsherds of Pueblo I period, A.D. 700–900, have been found buried beneath 1.2 m of the youngest valley fill, 17 km east of this point. Nichols (1946) correlated this alluvium with material beneath the McCartys flow. A lower limit on the age of the McCartys flow is provided by the fact that Coronado's expedition crossed it in the year 1540. See Stops 1-4 and 1-5. **4.4**

144.0 **Exit right** (Exit 89) onto NM-117. **Turn left (south).** The mesa on the left for the next 10 mi is capped by Dakota Sandstone (Cretaceous). It overlies Morrison Formation and Horse Mesa Member of the Wanakah Formation (Jurassic) exposed in the cliffs. Morrison Formation wedges out 4 km south of this point, leaving Dakota directly on Wanakah Formation. **10.0**

154.0 **Turn right** to Sandstone Bluffs Overlook. Road ascends dipslope on lower Dakota Sandstone. **1.7**

155.7 **Park** in parking area. **Walk** west to edge of mesa.

STOP 1-4. Overview of El Malpais (Spanish, "The Badland"), part of the Zuni–Bandera volcanic field. The Zuni–Bandera field is one of the most extensive volcanic fields of the Jemez zone. Basalts of the Zuni–Bandera volcanic field were erupted during two time periods: 3.8–3.7 Ma and 1.7 Ma to about 1000 yrs ago. Quaternary basalts are divided into two age groups. The older Quaternary flows, which are exposed mainly in the western and southern part of the Zuni–Bandera field, are deeply weathered and mostly covered by soil and eolian deposits. Eruptions of these flows occurred mainly from a group of 30 cones called the Chain of Craters. Younger flows, exposed in the northeastern part of the field, are generally devoid of covering alluvium. The term El Malpais, referring to the rugged surface morphology, is applied to these younger Quaternary flows (Maxwell, 1982, 1986).

In the foreground is the McCartys flow, seen in detail at the next stop (Stop 1-5). The source for the McCartys flow is an 8 m high cinder cone which sits atop a low, broad lava shield about 24 km south of this overlook. From this source some of the lava flowed 9 km to the southwest. Most of the lava, however, flowed northward (Figs. 1-4, 1-5) (see Stop 1-5).

The northern part of the McCartys flow was mapped by Dutton (1885). Darton (1915) also briefly described the flow, and Nichols (1946) reported the results of an extensive geomorphic study. Among Nichols' major contributions was recognition that the flow moved by the flow-unit mechanism (see Stop 1-5).

Near the source of the McCartys flow, the basalt is a quartz-normative tholeiite containing mainly plagioclase phenocrysts. At distances greater than 4 km from the source, the flow is an olivine-normative tholeiite with dominantly olivine phenocrysts. No significant vertical chemical or mineralogic variations occur (Carden and Laughlin, 1974).

Beneath the McCartys flow lies the tholeiitic Laguna flow of Nichols (1946), Renault (1970), and Laughlin et al. (1972), which probably originated from El Calderon crater on the west side of the lava field (Maxwell, 1986). A K–Ar date on this flow is 0.54 ± 0.50 Ma (A. W. Laughlin, unpubl. data). Petrographically, this flow is very similar to the overlying McCartys flow. Like other tholeiites of the transition zone, $^{87}Sr/^{86}Sr$ is relatively high (0.70521) and $^{143}Nd/^{144}Nd$ relatively low (0.511910, $E_{Nd} = +1.4$) compared to alkalic basalts (Perry et al., 1987).

See also Stop 8, Second Day Road Log, Grambling et al. (1982).

Continue around loop and **return** to NM-117. **1.8**

157.5 **Turn left** onto NM-117. **9.6**

167.1 **Turn left** onto small dirt road; **park** at gate. **Walk** 325 m around west side of low hill and **climb** up onto the pahoehoe surface of the flow. **Walk** southward. **WARNING!!! Watch where you walk. Western Diamondback and Prairie rattlesnakes are particularly common on this lava flow and along its edges!**

STOP 1-5. Geomorphic features of McCartys flow. This is the narrowest and thickest part of the McCartys flow. The narrow width and great thickness resulted from confinement of the flow in a narrow channel (60 m wide) between the edge of the older Laguna flow to the west and the low hill of Jurassic Morrison Formation capped by Dakota Sandstone (Cretaceous). To the north the flow widened again before turning east down the San Jose Valley (Fig. 1-5).

Note the medial cracks and ropy pahoehoe structures, and the unweathered, glassy surface of the lava. Farther to the south is an abrupt transition to aa structure, representing the breakout of the younger pahoehoe-surfaced flow unit from the aa-covered front of the older flow unit. The classic paper by Nichols (1946) described many features of the McCartys flow, such as flow units, collapse depressions, pressure ridges, and kipukas (isolated protrusions of bedrock).

Return to I-40. **0.2**

167.3 **Turn left** onto I-40 (westbound) toward Grants. **4.0**

171.3 **Exit right** (Exit 85) to Grants. **0.5**

171.8 **Enter** Grants, a mining, ranching, and lumbering town with a population of 11,451. For years called Grants Station, Grants was originally a coaling station for the Santa Fe Railroad. It was named after

FIGURE 1-4—Aerial view toward the north of McCartys flow. Mount Taylor in the background.

FIGURE 1-5—Aerial view toward the south of McCartys flow. Basalt flowed through narrow channel near highway (approximately 60 m wide) before widening again and turning eastward (lower left). Stop 1-5 is approximately in center of photo.

the Grant brothers, Angus A., Lewis A., and John R., contractors in the construction of the railroad, who maintained a camp for workers called "Grants' Camp." In 1950 the area's vast uranium deposits were discovered. Post office, 1882–present (Pearce, 1965).

Day 2: Mount Taylor volcanic field

Summary

Today's route will highlight the magmatic processes that produced the great range of lava compositions at Mt. Taylor. Mt. Taylor is a Pliocene composite volcano with a fairly simple eruptive history. Construction of the cone began with eruptions of rhyolite, followed by quartz latite, and ending with eruptions of latite. Access to the entire eruptive sequence is provided by a large erosional amphitheater within the cone. The relatively simple eruptive history, small volumes, and short lifetime (i.e., compared to more complex volcanic fields such as the Jemez volcanic field to the northeast) contribute toward more certain petrogenetic interpretation. An understanding of the processes active in the Mt. Taylor system may thus serve as a model for more complex systems in regions of extensional tectonics.

Mileage

0.0 **Junction** of Santa Fe Avenue and First Street in Grants. Proceed north on First Street. **0.8**

0.8 **Turn right** onto Roosevelt Avenue. **0.4**

1.2 **Turn left** at stop light onto Lobo Canyon Road (NM-547). Ahead and to the left are basalt-capped mesas and the rhyolite dome of Grants Ridge. **4.8**

6.0 Narrow dirt road on right. To the left, on Grants Ridge, is a natural cross section of a basaltic vent (Fig. 2-1). The prominent basaltic plug, representing the magma conduit, intrudes both rhyolitic tuff, associated with a rhyolitic dome to the northeast, and the overlying cinders of the cinder cone. The basalt flow that erupted from this vent caps a portion of the rhyolite dome and also the surface behind (north of) the vent (Thaden et al., 1967). The basalt is a mildly alkaline, hy-normative hawaiite (hy-hawaiite) that is part of a basalt group parental to the intermediate and silicic rocks of Mt. Taylor; it is probably not related directly to the silicic rocks of Grants Ridge.

The northwest end of Grants Ridge is a prominently flow-banded rhyolite dome that was emplaced about 3.34 Ma (Lipman and Mehnert, 1979), prior to the major activity at Mt. Taylor. The rhyolitic lavas and tuffs of Grants Ridge are high-Fl topaz rhyolites typical of those found in extended regions of the western United States (Christiansen et al., 1983). They differ in both their mineralogy and chemistry from the rhyolites which erupted at Mt. Taylor (Table 2-1). Lithophysae found within the outer portions of the rhyolite dome are lined with millimeter-size crystals of tridymite, garnet, and topaz (Kerr and Wilcox, 1963).

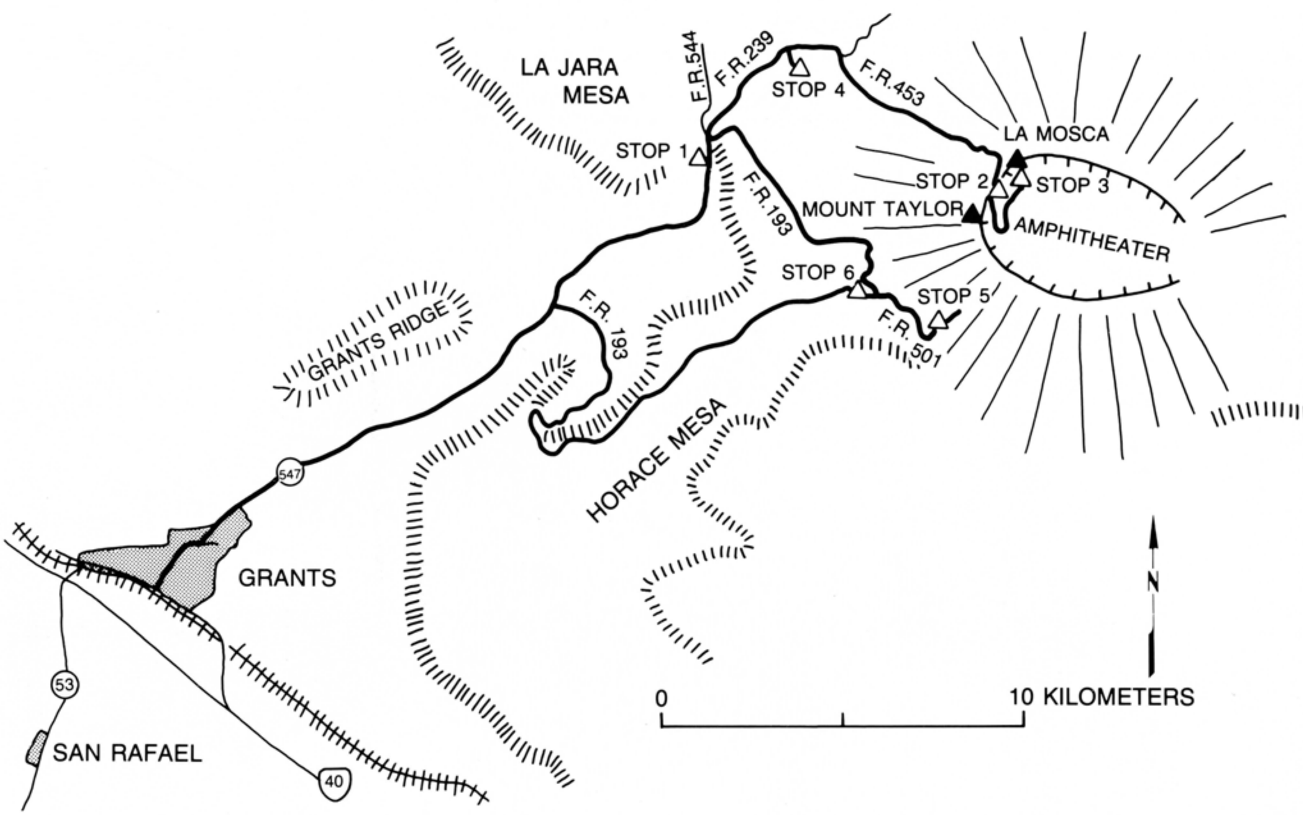

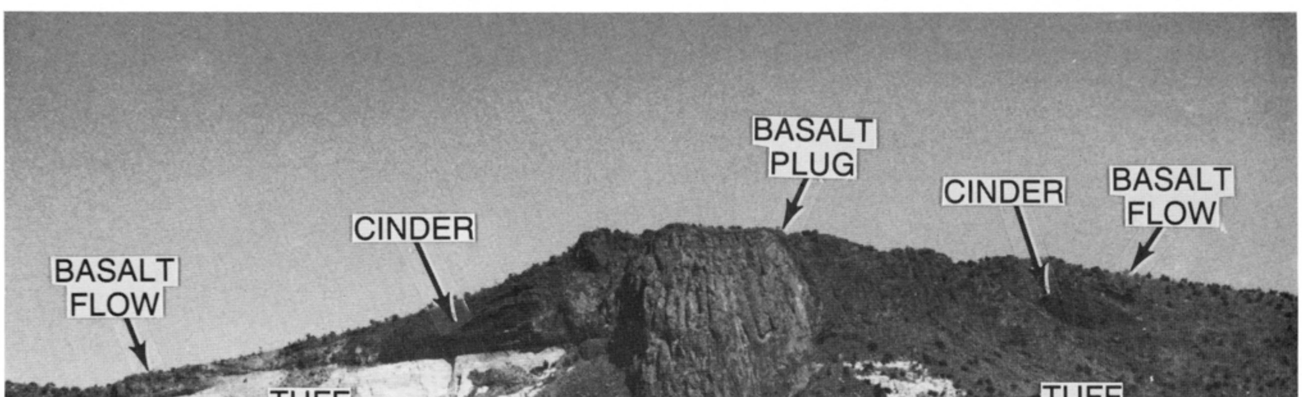

FIGURE 2-1—Subvolcanic basaltic plug on Grants Ridge. The plug is the conduit which fed the basaltic flows capping the ridge. It intrudes the tuff of the Grants Ridge rhyolite (white unit), as well as cinder beds of the basaltic vent.

TABLE 2-1—Representative analyses of rocks from the Mount Taylor volcanic field.

Sample	1 MT7	2 MT132	3 MT97	4 MT26	5 MT1	6 MT57	7 MC57	8 MT80	9 MT144	10 MT5
SiO_2	47.72	47.79	59.73	60.94	66.72	61.21	55.34	71.12	72.90	74.83
TiO_2	2.77	2.13	1.02	0.84	0.35	1.23	1.57	0.19	0.30	0.03
Al_2O_3	15.17	15.46	16.52	16.85	15.69	16.28	16.06	15.34	13.34	13.23
Fe_2O_3	1.90	1.82	1.00	0.89	0.53	1.07	1.39	0.25	0.35	0.15
FeO	9.70	9.27	5.08	4.55	2.69	5.46	7.11	1.29	1.77	0.78
MnO	0.17	0.14	0.15	0.12	0.07	0.12	0.32	0.01	0.06	0.11
MgO	7.26	6.68	1.32	1.01	0.36	1.70	2.22	0.04	0.20	0.03
CaO	8.42	7.45	3.01	3.40	1.18	4.12	4.90	0.43	1.08	0.50
Na_2O	3.22	3.99	5.51	5.09	5.21	4.41	4.29	5.19	3.61	4.50
K_2O	1.38	1.66	3.68	3.70	5.26	2.75	2.50	5.33	4.43	4.33
P_2O_5	0.59	0.60	0.42	0.37	0.06	0.47	0.79	0.01	0.08	0.00
Total	98.30	96.99	97.44	97.76	98.12	98.82	96.49	99.20	98.12	98.49
An	44.2	38.9	16.1	21.1	7.7	29.4	30.8	4.3	13.0	5.8
Q	0.0	0.0	3.5	6.6	11.1	11.1	5.0	17.3	29.9	28.5
or	8.3	10.1	22.1	22.3	31.4	16.5	15.4	31.5	27.0	26.
ab	29.5	31.2	50.4	46.5	47.3	40.3	40.2	46.6	33.4	41.1
an	23.4	19.9	9.6	12.4	3.9	16.8	17.9	2.1	5.0	2.5
ne	0.0	3.3	0.0	0.0	0.0	0.0	0.0	0.0	0.0	0.0
C	0.0	0.0	0.0	0.0	0.0	0.0	0.0	0.3	0.9	0.3
di	12.3	11.2	2.2	1.8	1.3	0.7	1.64	0.0	0.0	0.0
hy	3.1	0.0	8.7	7.5	3.8	10.7	14.3	1.7	2.8	1.3
ol	16.2	18.0	0.0	0.0	0.0	0.0	0.0	0.0	0.0	0.0
mt	2.0	2.0	1.1	0.9	0.6	1.1	1.5	0.3	0.4	0.2
il	3.9	3.1	1.5	1.2	0.5	1.7	2.3	0.3	0.4	0.0
ap	1.3	1.3	0.9	0.8	0.1	1.0	1.7	0.0	0.2	0.0
Zr	240	233	326	337	441	207	256	340	125	104
Sr	711	820	414	472	98	555	679	13	134	8
Rb	33	33	91	83	106	56	57	161	109	513

1. hy-hawaiite, lower flow on La Jara Mesa
2. ne-hawaiite, flow on rim of El Rito Canyon
3. hornblende latite flow, west flank
4. latite flow, northeast Horace Mesa
5. quartz latite dike, west end of amphitheater
6. "mixed magma" latite, southwest flank
7. mafic clot in MT57, mixed latite
8. Type-A rhyolite, amphitheater
9. Type-B rhyolite, amphitheater
10. rhyolite of Grants Ridge, dome at northeast end of Grants Ridge

Christiansen et al. (1983) proposed that topaz rhyolites represent partial melts of lower crustal granulitic rocks. The Nd isotopic composition of the Grants Ridge rhyolites ($E_{Nd} = -1$ to -2) are much higher than that expected for the Proterozoic lower crust beneath this region ($E_{Nd} = -10$ to -20), however, and suggest that the Grants Ridge rhyolites were differentiated from a mantle-derived parent and still retain a large mantle component (Perry et al., 1989). **2.0**

8.0 Perlite mine and dump to left. **0.5**

8.5 **Junction** with Forest Road (FR) 193. Straight ahead is La Jara Mesa, one of the basalt-capped mesas that surround Mt. Taylor. To the right is Mt. Taylor. Cinder cones and basalt flows capping La Jara Mesa are of hy-hawaiite composition. White to pink units exposed in the mesa edges below the basalt cap are tuffs and pumice units erupted from the area of Grants Ridge. On La Jara Mesa, Grants Ridge tuff overlies Cretaceous sandstones. Farther to the east, on Horace Mesa, Grants Ridge tuff in places overlies a high-Ti basanite flow dated at 3.7 Ma (Perry et al., 1989), equivalent in age and composition to a high-Ti basanite in the Lucero volcanic area (Day 1). Grants Ridge tuff is exposed for the next 3 mi in cliffs to left of road. **4.4**

12.9 **STOP 2-1. Contact between uppermost Grants Ridge pyroclastic sequence and base of Mount Taylor volcanic rocks. Pull off** on broad left shoulder of road. The upper Grants Ridge pyroclastic rocks here form a sequence of pumice beds and thin ash flows, separated in places by well-developed soils (Figs. 2-2, 2-3), indicating that rhyolitic volcanism continued intermittently for several thousands or tens of thousands of years about 3.3 Ma.

The Grants Ridge pyroclastic units are overlain here by two flows of hypersthene-normative hawaiite, the lowest of which is dated at 2.9 Ma (Perry et al., 1989). These basalt flows mark the base of the Mt. Taylor volcanic section at this location. Between the two basalt flows is a rhyolite or quartz latite pumice bed which is probably derived from Mt. Taylor, and a basaltic ash which probably was erupted from a local cinder cone. The lower basalt flow (MT7, Table 2-1) has a Mg number of 57, and is the most primitive hy-hawaiite known from the Mt. Taylor field. Hy-hawaiite magmas were parental to the latites, quartz latites, and rhyolites of Mt. Taylor, which were derived by fractional crystallization combined with assimilation of small amounts of both lower (predominantly) and upper crustal rocks.

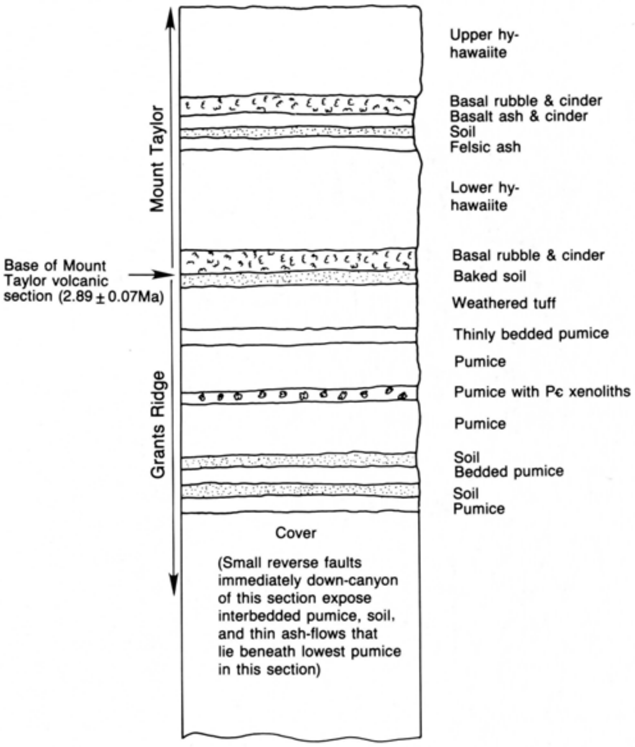

FIGURE 2-2—Schematic stratigraphic section of volcanic rocks at east end of La Jara Mesa (Stop 2-1).

A second major group of basalts at Mt. Taylor are nepheline-normative hawaiites (ne-hawaiites, Table 2-1) which are distinguished from hy-hawaiites by lower TiO_2, higher Mg numbers, and occasional presence of spinel lherzolite xenoliths (Stop 2-4). Ne-hawaiite magmas may have been parental to a group of early erupted trachytes found on Mesa Chivato (Crumpler, 1980), but are not related to the latites, quartz latites, and rhyolites of Mt. Taylor.

Both hy- and ne-hawaiites at Mt. Taylor have $^{87}Sr/^{86}Sr$ of 0.7035–0.7038 and E_{Nd} of +4 to +5, which is typical of alkali basalts from the southeastern Colorado Plateau boundary, indicating derivation from a mixture of enriched and depleted components at the asthenosphere/lithosphere boundary (Perry et al., 1987). **0.2**

13.1 **Junction** of FR-544 (left) and 193 (right). **Continue straight ahead** on FR-239 (changes here from NM-547). For the next 2 mi the road lies on volcaniclastic debris derived from the cone of Mt. Taylor. **2.1**

15.2 Road ascends onto at least two flows of ne-normative hawaiite, one of which carries spinel lherzolite xenoliths (Stop 2-4). Road is on surface of basalt flows for next 3.4 mi. **1.2**

16.4 **Junction** of FR-453. **Turn right** to La Mosca Lookout. **2.2**

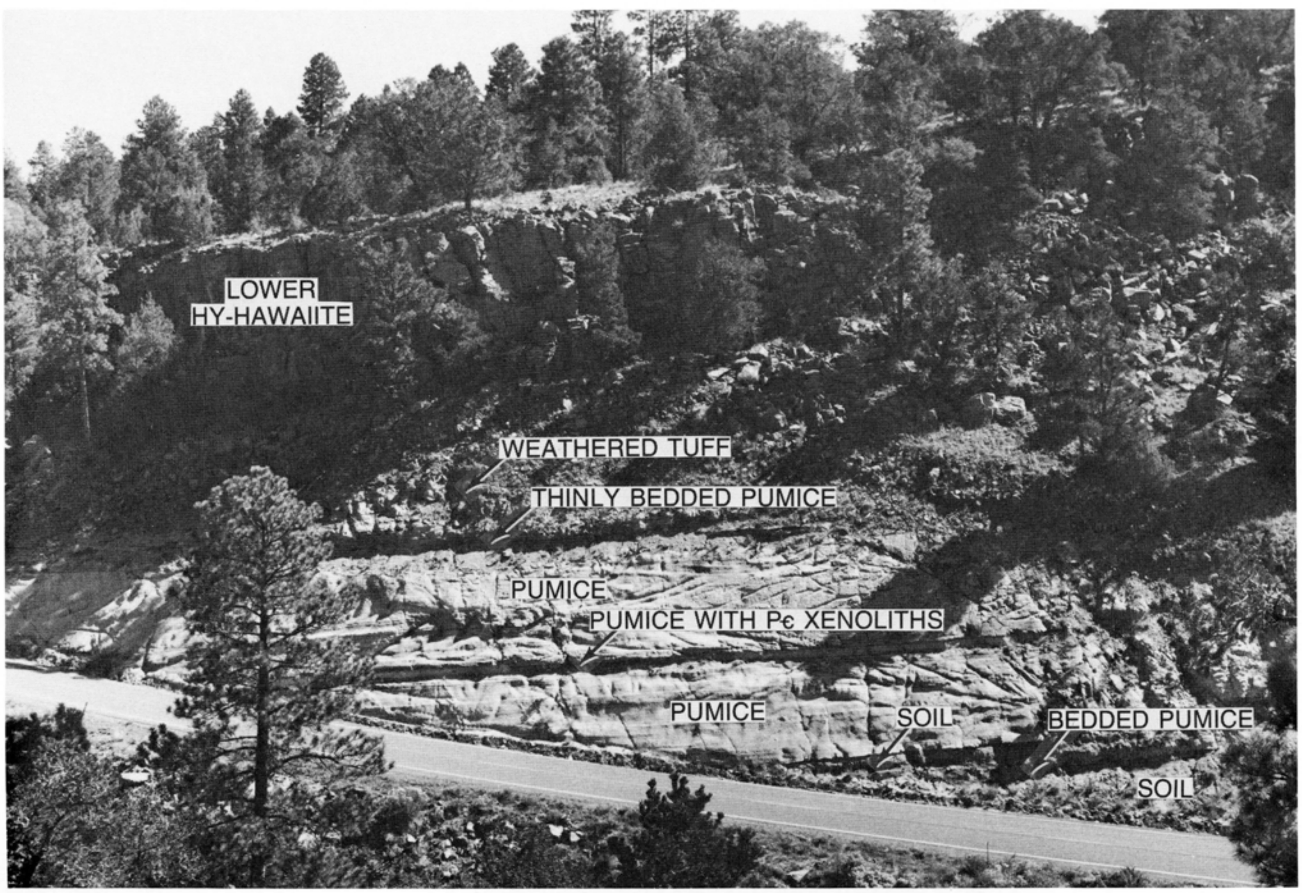

FIGURE 2-3—Photograph of volcanic rocks at the east end of La Jara Mesa (Stop 2-1). Units correspond to stratigraphic section shown in Fig. 2-2; not all units are visible in this view.

18.6 La Mosca Canyon. Outcrops from here to the summit are mostly quartz latites. **0.9**

19.5 **Junction. Turn right. 1.4**

20.9 **Junction** with Mount Taylor Trail #77. **Turn right. 0.1**

21.0 **STOP 2-2. Quartz latite dike and view of amphitheater. Park** vehicles and **walk** 100 m to southeast (just to right of trees). The amphitheater resulted from erosion and enlargement of the original summit crater, and provides access to the entire eruptive sequence of the volcano, which generally progressed from rhyolite to quartz latite to latite. Except for trachyte exposed at the east end of the amphitheater (3.3 Ma), which is related to alkalic volcanism on Mesa Chivato to the north (Crumpler, 1980), the oldest rocks exposed within the amphitheater are mostly rhyolites that erupted between 3.3 and 3.0 Ma.

Rhyolites of Mt. Taylor fall into two geochemically and mineralogically defined groups (Table 2-1). The first group ("Type-A" rhyolites), related by fractional crystallization to the hy-hawaiites, latites, and quartz latites, are characterized by phenocrysts of anorthoclase and microphenocrysts of magnetite and zircon. The second group of rhyolites ("Type-B" rhyolites) have a distinctly different phenocryst assemblage of two feldspars (sanidine + oligoclase, Fig. 2-4), embayed quartz, hornblende, biotite, and magnetite. Type-B rhyolites (Table 2-1) are characterized by relatively high concentrations of compatible elements (CaO, MgO, Sr), and lower alkali content (Fig. 2-5). The prominent hill (possibly a dome) to the southeast (along strike of the dike), within the amphitheater, consists of Type-B rhyolite.

Eruption of rhyolite was followed by eruption of porphyritic quartz latite between 3.0 and 2.6 Ma. This phase of volcanism marked the most intense period of cone construction, accounting for about 65% of the volume of the cone. Quartz latites are characterized by phenocrysts of sodic plagioclase, clinopyroxene, biotite, magnetite, apatite, and, in the more evolved rocks, zircon. Radial dikes of

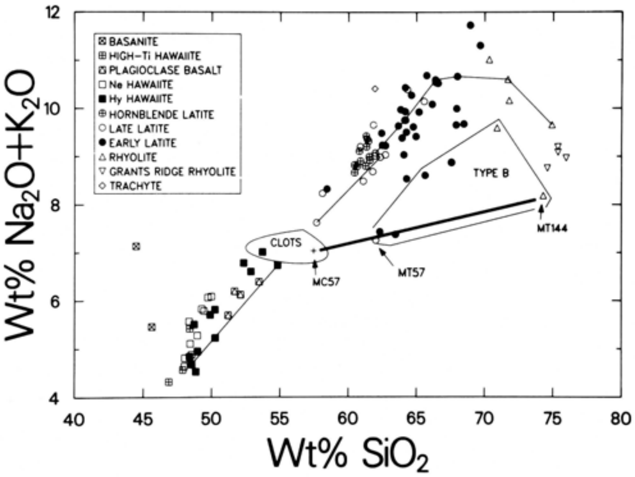

FIGURE 2-5—Alkalis versus SiO_2 for rocks of the Mount Taylor volcanic field. "Type-B" rocks are characterized by lower alkalis, Zr, and Rb, and share a phenocryst assemblage consisting of two alkali feldspars and quartz. Type-B rocks of intermediate composition (e.g., MT57) are produced by mixing of evolved hy-hawaiite magmas and Type-B rhyolite magmas. The heavy line is a representative mixing path. The field labeled "clots" includes mafic clots found in Type-B intermediate rocks. Line to the left and above the Type-B field is a model evolutionary path for closed-system fractional crystallization that produced the majority of evolved rocks in the Mount Taylor volcanic field (Perry et al., 1989).

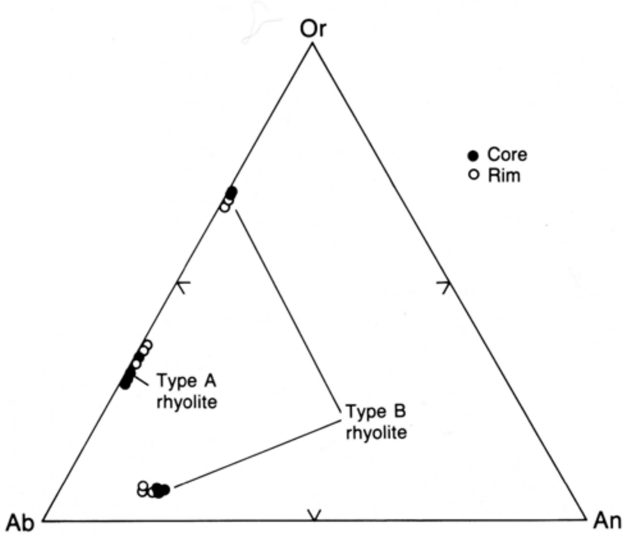

FIGURE 2-4—Feldspar compositions of Type-A and Type-B rhyolites.

quartz latite intrude flows of the quartz latite series and were probably feeder dikes. The dike at this outcrop (MT1, Table 2-1) is an evolved quartz latite with 68% SiO_2. It is dated at 2.9 Ma and intrudes about 250 m of quartz latite and rhyolite flows.

The youngest intermediate rocks at Mt. Taylor are porphyritic latites which overlie the quartz latite series. Latites are characterized by phenocrysts of plagioclase, clinopyroxene, olivine, orthopyroxene, magnetite, apatite, and occasional biotite. The summit of Mt. Taylor, to the south, consists of flows of hornblende latite (Table 2-1) characterized by large (up to 4 cm) megacrysts of hornblende. The flows erupted from a vent above the site of the present amphitheater and flowed down the west flank of Mt. Taylor at about 2.5 Ma.

The latites, quartz latites, and rhyolites have E_{Nd} values ranging from +1 to +3, and $^{87}Sr/^{86}Sr$ ranging from 0.7041 to 0.7126 (Perry et al., 1989), indicating that all of the evolved rocks underwent a small amount of crustal contamination during fractionation of the hy-hawaiite parent. $^{87}Sr/^{86}Sr$ generally increases with increasing SiO_2 and decreasing Sr (Sr decreases due to plagioclase fractionation).

Return to vehicles and **continue straight** into amphitheater. **0.2**

21.2 View to east along axis of amphitheater. The low plug in the middle distance in center of amphitheater is an early ne-normative hawaiite. Several quartz latite radial dikes can be seen on ridges near the bottom of the amphitheater. **0.8**

22.0 Saddle at west end of rhyolite dome. **Bear left. 1.0**

23.0 Hairpin turn to right.

STOP 2-3. Flow-banded rhyolite in light-colored, rubbly outcrop at the beginning of the curve to the left is among the earliest (3.0 Ma) eruptive units of Mt. Taylor. This outcrop is about 400 m below the present summit of Mt. Taylor. This rhyolite (Sample MT144, Table 2-1) is a Type-B rhyolite, characterized by a two-feldspar phenocryst assemblage of sanidine + oligoclase (Fig. 2-4), and embayed phenocrysts of quartz, indicating higher pressure crystallization relative to the Type-A rhyolites.

Type-B rhyolites are significant because they form the silicic mixing endmember for a small group of mixed latites (Stop 2-5) that are mineralogically and chemically distinct from latites produced by fractional crystallization at Mt. Taylor (Fig. 2-5).

Turn around and **retrace route** to FR-239. **6.6**

29.6 **Junction** with FR-239. **Turn left. 0.9**

30.5 Cattleguard. After crossing, **turn left** onto dirt road. **0.4**

30.9 **STOP 2-4. Quarry in basalt flow.** This basalt flow contains abundant xenoliths of spinel lherzolite (reaching 10 cm in diameter), occasional pyroxenite, and possibly granulite. The textures and modes of the xenoliths are variable. The basalt here, which has not been analyzed, is probably a ne-hawaiite, the only basalt type at Mt. Taylor observed to carry mantle xenoliths. The presence of mantle xenoliths indicates that ne-hawaiites ascended from the mantle more quickly than hy-hawaiites. The relatively lower ascent rates of hy-hawaiites may have favored prolonged residence and differentiation in crustal magma chambers.

Retrace route to FR-239. **0.4**

31.3 **Junction** with FR-239. **Turn left. 2.3**

33.6 **Junction** with FR-193. **Turn left.** The road is on volcaniclastic debris which mantles the 2.9 Ma basalt seen at Stop 2-1. **1.5**

35.1 The thick flows exposed across canyon to left are hornblende latites that were erupted about 2.5 Ma and flowed down the west flank of Mt. Taylor. Several of these flows are exposed along left side of road for next 2.5 mi. **3.7**

38.8 **Junction** with FR-501. **Bear left** through gate on FR-501. **1.6**

40.4 **STOP 2-5. Debris from a "mixed magma" latite flow** on the southwestern flank of Mt. Taylor. The toe of this flow can be seen up the slope to the left. This flow (MT57, Table 2-1) was produced by mixing of Type-B rhyolite magma (Stop 2-3) and evolved hy-hawaiite magma (Fig. 2-5). The phenocryst assemblage of this latite is identical to that of the Type-B rhyolite seen at Stop 2-3 (large, subrounded phenocrysts of sanidine and oligoclase; smaller laths of quartz, hornblende, and biotite), and was inherited from a Type-B rhyolite magma during mixing. Mafic clots in this flow are compositionally equivalent to an evolved hy-hawaiite (MC57, Table 2-1, Fig. 2-5). The petrography and chemistry of this flow thus clearly indicate an origin via mixing of Type-B rhyolite and evolved hy-hawaiite.

The latite flow here is one of several on the southwest flank that erupted late in the history of the volcano. More latite flows can be seen across the canyon to the right. All of these flows apparently vented from a central crater above the present amphitheater, but erosion has removed the upper portions of the flows and exposed the underlying flows and radial dikes of the quartz latite series on the upper flanks of the volcano. The view to the south is of Horace Mesa, capped by hawaiites, and the Zuni–Bandera field, over the top of Horace Mesa. **0.2**

40.6 Road widens at curve. **Turn vehicles around and return** to FR-193. **1.8**

42.4 **Junction** with FR-193. **Turn left. 0.5**

42.9 **STOP 2-6. Latite flow** to right across small meadow. This latite flow (MT26, Table 2-1) has about 61% SiO_2 and is typical of the late flows that capped the flanks of the volcano between 2.5 and 1.5 Ma. Flows of this composition are produced by about 65% fractional crystallization of plagioclase + clinopyroxene + olivine + magnetite + ilmenite + apatite from a hy-hawaiite parental magma. The phenocryst assemblage of this flow is primarily plagioclase (An_{42-30}) and olivine (Fo_{50-43}), with lesser amounts of clinopyroxene, orthopyroxene, and magnetite. This flow overlies a hornblende latite flow exposed a short distance to the west that erupted about 2.5 Ma.

Return to vehicles and **continue** on FR-193. From here, the road descends onto the basalts that cap Horace Mesa. **6.7**

49.6 To the right is an excellent view of Mt. Taylor and the surrounding basalt-capped mesas. At this point the road descends through one of the basalt flows (a hy-hawaiite) that caps Horace Mesa. **4.0**

53.6 **Junction** with NM-547. **Turn left** and **return** to Grants. **7.3**

60.9 **Junction** with Roosevelt Avenue. **Turn right** at traffic light. **0.1**

61.0 **Turn left** onto Second Street. **1.1**

62.1 **Junction** with Santa Fe Avenue.

Day 3: Grants to Springerville

Summary

This day's excursion, which begins and ends near two of the major central volcanoes of the Jemez zone (Mount Taylor and the White Mountains, respectively), skirts along much of the transition zone of the southeastern Colorado Plateau. Features emphasized relate mainly to eruption mechanisms: the classic lava tubes at Bandera Crater; the spectacular Zuni Salt Lake maar volcano; and possible ponded lavas at Tejana Mesa. Together, these features illustrate the variety of eruption morphologies typical of basaltic fields of the central rift–Colorado Plateau transition zone region.

Mileage

0.0 **Intersection** of Santa Fe Avenue and NM-53 at west end of Grants. **Cross over** railroad tracks and **drive south** on NM-53. **0.3**

0.3 **Cross over** I-40. To right of overpass is an aa flow from Zuni Canyon. The Zuni Canyon flow is an alkali olivine basalt that erupted at the crest of the Zuni uplift along a north-trending fault. **2.5**

2.8 Northern turnoff to San Raphael **(continue straight).** El Gallo Spring (Ojo del Gallo), 0.5 km north of San Rafael, was the site of an important military

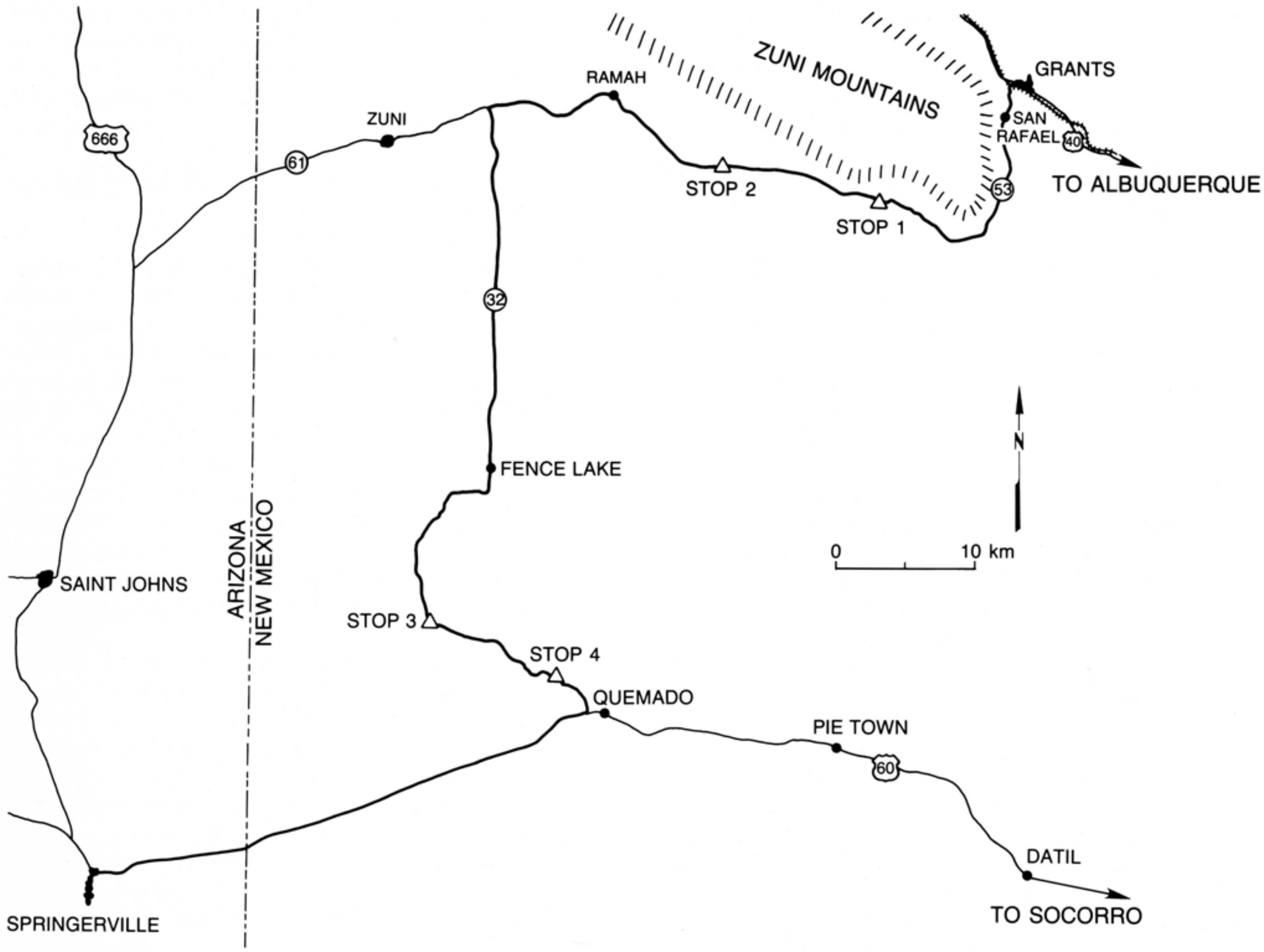

establishment, (old) Fort Wingate, of which no traces remain. Fort Wingate was established in 1862 for military action against the Navajos. From here, Militia Colonel Christopher (Kit) Carson and Lt. Col. J. Francisco Chaves conducted a two-year campaign to subjugate the Navajos. Navajo resistance was broken by the systematic destruction of Navajo crops and confiscation of livestock. Individual bands of Navajos were rounded up and sent to Bosque Redondo on the Rio Pecos, near Fort Sumner. In 1868, conditions at Fort Sumner deteriorated to the extent that the Navajos were permitted to return to their Four Corners homeland, where a permanent reservation was established for them. Fort Wingate at San Rafael was too far from the Navajo country for effective control of the resettled population. In 1868, the fort was abandoned and its garrison transferred to the site of the former Fort Fauntleroy on the Ojo del Oso near Gallup, the present location of Fort Wingate (Pearce, 1965; Jenkins and Schroeder, 1974). In December 1988, the congressionally established Committee on Base Realignment and Closure recommended to the Secretary of Defense that, in the interest of economy, Fort Wingate be closed and its functions transferred elsewhere. **1.0**

3.8 Southern turnoff to San Rafael. Ahead are the Zuni Mountains, which expose Precambrian, Paleozoic, and Mesozoic rocks. The Zuni block was first uplifted during the Ancestral Rocky Mountain orogeny (Pennsylvanian and Permian), again in the Laramide orogeny (Late Cretaceous–early Tertiary), and subsequently during middle and late Tertiary extensional deformation. To left is the Malpais area of Zuni–Bandera volcanic field (see Stop 1-4). For the next 22 mi, the road skirts around the southern end of the Zuni Mountains, occasionally crossing Precambrian and upper Paleozoic/Mesozoic rocks. The basalts, exposed mainly on the left, but in places along both sides of the road, are Quaternary flows of Zuni–Bandera volcanic field (Maxwell, 1982). **21.4**

25.2 **Turn left** to Bandera Crater and the Ice Caves. Bandera Crater cinder cone on right. **0.6**

25.8 **STOP 3-1. Bandera Crater and Ice Caves. Turn right** into parking lot of trading post. In 1987 Congress created El Malpais National Monument. Bandera Crater and the Ice Caves, currently privately owned and operated, will be added to the National Monument in the future.

Register at trading post. **Follow trail** around north side of trading post. **Walk** up southern flank of Bandera Crater and **pass through** breach into cinder cone. Distance about 0.8 km.

Bandera Crater is a breached, symmetrical cinder cone about 1 km in diameter and 150 m high. The central depression is about 180 m deep, extending

80 m below the level of the breach. A large lava tube, which extends at least 20 km to the south, is exposed in the breach. Although collapsed for the first 800 m, most of the remainder of the tube is intact. After the McCartys flow, the flows from Bandera Crater are the youngest in the Zuni–Bandera lava field. These lavas flowed south and east around the Zuni Mountains to a point about 12 km south of Grants. The Bandera flows overlie 0.199 Ma basalt (Laughlin et al., 1979) but are themselves too young to date by the K–Ar method. Flows from Bandera Crater are nepheline-normative, with silica as low as 44.5% (Laughlin et al., 1972). They are typically holocrystalline, vesicular, and microporphyritic, with phenocrysts of olivine up to 1 mm across, rare clinopyroxene, and plagioclase. One of the Bandera flows has $^{87}Sr/^{86}Sr = 0.70366$ and $E_{Nd} = +5.4$ (Perry et. al., 1987), typical of alkalic basalts from the transition zone.

Xenocrysts of orthopyroxene and anorthoclase occur in the Bandera flows and in the cores of bombs exposed in the cinder pit north of the crater. A wide spectrum of crustal and mantle rocks also occurs in the cores of these bombs (Laughlin et al., 1971).

Return to trading post and **follow trail** 300 m southwestward to Ice Caves.

The Ice Caves are located in the main lava tube from Bandera Crater. Here, because of the overhang of the collapsed lava tube and the insulating properties of basalt, ice that forms in winter is preserved throughout the year. The green color of the ice is due to presence of algae. In frontier days, ice from the caves was transported to nearby Fort Wingate. Other ice caves occur in lava tubes in this area, but are not open to the public.

The flows from Bandera Crater exhibit both pahoehoe and aa features. Tree molds are also present in these flows. Rare, small, mantle-derived xenoliths occur in some of the large basaltic blocks near the tops of the flows.

Follow trail back to parking lot. **Return** to NM-53. **0.7**

26.5 **Turn left** onto NM-53. **1.9**

28.4 Road crosses basalt flow dated at 0.199 ± 0.042 Ma (Laughlin et al., 1979), part of the "Older Basalts" of the Zuni–Bandera field (Maxwell, 1982). **13.9**

42.3 **Turn left** into El Morro National Monument. **1.0**

43.3 **Park** in parking lot of Visitor Center. **Enter** Visitor Center and **follow** trail to Inscription Rock (0.8 km round trip).

STOP 3-2. El Morro is Spanish for "headland," "bluff," or "fortress." Until it was bypassed by the railroad in the 1880's, its waterhole made El Morro an important stop for travelers in the region. The great triangular rock at this site (Inscription Rock) is made of light-colored Zuni Sandstone (Jurassic), soft enough to be cut with a knife or swordpoint. For more than a century and a half, the Spaniards carved names, dates, and short messages on this great "autograph album." The earliest dated inscription is by Juan de Oñate, colonizer and first governor of New Mexico. In translation it reads: "Passed by here the Adelantado Don Juan de Oñate from the discovery of the Sea of the South, the 16th of April of 1605." Oñate was returning from a journey to the Pacific Coast and the Gulf of California (Pearce, 1965). More than 500 separate carvings have been preserved, including those of early American emigrants, traders, Indian agents, soldiers, surveyors, and settlers (Pearce, 1965).

Follow trail back to Visitor Center and parking lot. **Return** to NM-53. **0.8**

44.1 **Turn left** onto NM-53. **11.2**

55.3 Enter Ramah. Ramah, settled in 1874 by Mormons, was named for a figure in the Book of Mormon (Pearce, 1965). It is a center for the Ramah Navajo Reservation. The Ramah band of the Navajos settled here after their return from Fort Sumner in 1868 (Jenkins and Schroeder, 1974). **2.9**

58.2 Enter Zuni Reservation. **9.1**

67.3 **Turn left** onto NM-36 to Fence Lake. **26.3**

93.6 Road ascends onto low mesa capped by the 1.5 Ma Fence Lake flow (Laughlin et al., 1979). This flow, an olivine tholeiite, originated in the Zuni–Bandera field and flowed westward along a stream drainage into eastern Arizona, a distance of more than 50 km. The flow, exposed here along the edge of the mesa and discontinuously for the next 3 mi, is vuggy and vesicular, and is characterized by diktytaxitic texture and by vesicular segregations. It is microporphyritic, with phenocrysts of olivine 1–2 mm across. **5.8**

99.4 Fence Lake, a farming and ranching community, is named for a reservoir 2.4 km to the southeast enclosed by stockmen. Most of the settlers came in 1930 and 1931 from the Dust Bowl. Post office, 1936–present (Pearce, 1965). **0.2**

99.6 **Junction** of NM-36 and NM-32. **Continue straight ahead (south)** on NM-32. **8.8**

108.4 Sharp bend to right. **Descend** steep grade. Capping unit, well exposed here, is Fence Lake Formation, which unconformably overlies Cretaceous sandstones. The Fence Lake Formation consists of fanglomerates containing clasts of Oligocene basalts, basaltic andesites, and rhyolites derived from the Mogollon–Datil volcanic field to the south. The Fence Lake is Miocene in age, equivalent to the Santa Fe Group of the Rio Grande rift (McLellan et al., 1982). **10.1**

118.5 **Junction** with NM-191. **Bear left** on NM-32 toward Quemado. **0.2**

118.7 **Bear right** onto narrow dirt track. **Proceed** 0.2 mi and **cross** dirt road. **Proceed** another 100 m to gate. **Park** at gate.

STOP 3-3. Zuni Salt Lake. The lake occupies the northern half of a maar crater, about 1.6 km in diameter (Fig. 3-1). Three small cinder cones rise from the center of the maar. This maar is the northernmost and best preserved of a group of maars and cinder cones extending in a linear array 60 km to the south-southwest. Phreatomagmatic deposits record a history of decreasing magma–water interactions, as seen also in the Lucero area (see Day 1). An early Surtseyan stage of nearly continuous phreatomagmatic surges gave way to a Strombolian stage of intermittent explosions, and finally to a stage of cinder eruptions forming the central cones. The particles of Surtseyan surge deposits were pro-

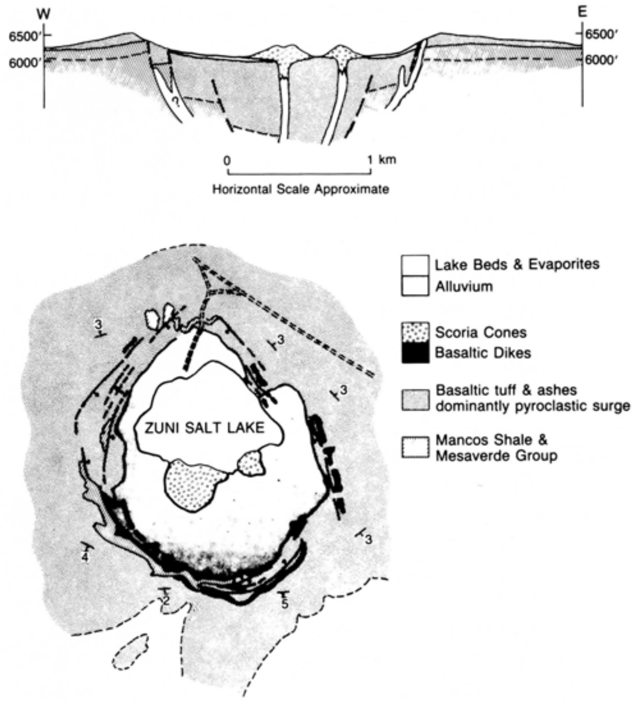

FIGURE 3-1—Simplified geologic map (after Cummings, 1968) and schematic cross section of Zuni Salt Lake maar.

pelled and rapidly transported along the ground in a cushion of turbulent steam. Consequently, they are abraded, fine-grained, and moderately to poorly sorted. During the early high-energy Surtseyan stage, sand-wave and massive surge beds built up a tuff ring. Accretionary lapilli and armored mudballs are common. Ash particles are strongly altered to palagonite. During transition to the Strombolian stage, weakening surges deposited their load in planar beds; coarser ash- and lapilli-fall deposits became abundant and mantled the earlier tuff ring. In contrast to the abraded and altered particles of surge deposits, the coarser particles of Strombolian-fall deposits are better sorted, angular, glassy (sideromelane), and vesicular. Fine ash was deposited downwind as much as 8 km from Zuni Salt Lake. Large (up to 30 cm) clasts of basalt and prevolcanic sedimentary rocks were ejected ballistically throughout the eruption (Elston and Wohletz, 1987).

Water–magma interaction may have decreased because of emplacement of a basalt ring dike during the eruption. The ring dike, which may have progressively sealed rising magma from contact with ground water, penetrated to the surface to form spatter and short flows (Elston and Wohletz, 1987). Also, crystallization at the margins of the main conduit may have sealed water out of the vent.

Subsidence of the maar occurred during the eruption, as is shown by numerous small faults. At the end of the eruption, the rim of the crater stood 30 m above the surrounding country, and its floor was about 120 m below the rim. It subsequently became filled with water and lacustrine sediments (Elston and Wohletz, 1987). Zuni Salt Lake is dated at 22,900 ± 1400 yrs by ^{14}C (Bradbury, 1966).

Indians have used the salt from Zuni Salt Lake for hundreds of years, often traveling great distances to obtain it. The people of Zuni Pueblo consider the Lake an important religious site. However, in 1877 when the U.S. Government established the boundaries for the Zuni Reservation, it excluded the Lake. Between 1910 and the late 1970's, various commercial operations extracted salt from the Lake. After years of lobbying, the Zunis persuaded Congress to deed the Lake to them. In 1978 Congress directed the Interior Department to acquire the Lake, a process taking seven years. In 1985, Zuni Salt Lake was deeded to Zuni Pueblo (Robinson, 1987).

Turn around and bear right. Return to NM-32. **0.4**

119.1 **Bear right** onto NM-32. **13.2**

132.3 **STOP 3-4. South end of Tejana Mesa.** Tejana Mesa consists of nearly flat-lying, light-pinkish, poorly lithified sandstones and mudstones of the Baca Formation unconformably overlain by Miocene gravels of the Fence Lake Formation and capped by basaltic lavas. The basalt capping Tejana Mesa is K–Ar dated at 6.7 ± 0.2 Ma (Dethier et al., 1986). The lavas of Tejana Mesa greatly thicken, from several meters to the north along the mesa to over 75 m on the south-facing exposure, 0.5 km northeast across the arroyo (Fig. 3-2A). This great thickness of basalt is elongate along strike of the Tejana Mesa fault zone, which forms a northeast-striking lineament along which several vents and feeder dikes have been mapped (Guilinger, 1982). Adjacent to the road is El Porticito, a thick accumulation of basalt resembling a plug.

Near the eastern (right-hand) edge of the exposure (Fig. 3-2A), basalts are separated from the underlying volcaniclastic sediments by about 15 m of red scoria; calcite-cemented, volcaniclastic breccias; and pyroclastic surge beds. These pyroclastic units may be part of a tuff ring, now largely buried by lavas. Where thickest, along the south-facing exposure, three distinct units are visible. Each unit has a vesicular top and massive base, suggesting that these units were ponded flows. The upper unit shows colonnade and entablature structure typical of thick flows. Near the base of the lower lava unit are numerous light-colored, sill-like structures, varying in thickness from several centimeters to over 5 m (Fig. 3-2B, C). Numerous centimeter-sized dikelets and sills occur throughout the lava unit. These are especially apparent along the southeastern faces of El Porticito (Fig. 3-2B). The origin of the sills and their relationship to the host lavas have yet to be completely determined.

The lavas are phonolites, consisting of olivine and titanaugite phenocrysts in a holocrystalline groundmass (Table 3-1). They contain no identifiable plagioclase. The groundmass contains abundant clinopyroxene microlites poikilitically enclosed by optically continuous patches of sanidine and nepheline(?) (Fig. 3-2D). These lavas (particularly of the uppermost unit) have a mottled surface texture, consisting of centimeter-sized patches of finer-grained, lighter-colored rock rising above patches of darker-colored, more vesicular rock in which numerous olivine phenocrysts are visible.

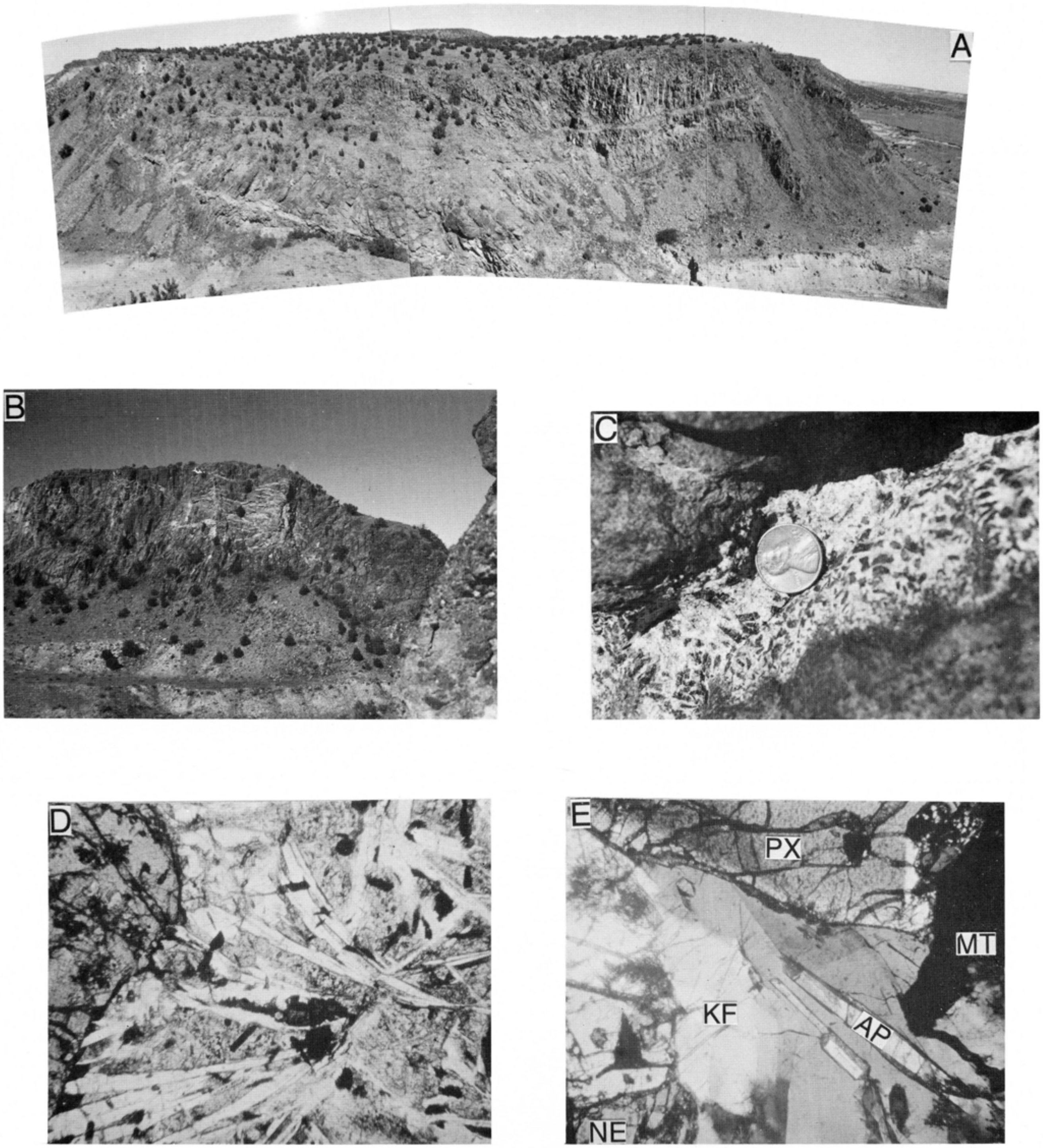

FIGURE 3-2—Relations at south end of Tejana Mesa (Stop 4). **A,** Panoramic view of thick lava units exposed at end of mesa. **B,** View of El Porticito, showing sills of nepheline syenite. **C,** Small sill of nepheline syenite, showing prominent crystals of pyroxene. **D,** Photomicrograph of nepheline phonolite, showing prominent bostonitic texture consisting of laths of potassium feldspar with interstitial pyroxene; width of field is 2 mm. **E,** Photomicrograph of nepheline syenite; width of field is 2 mm.

This texture, distinctive of many alkalic basalts, is apparently related to segregations of mafic phenocrysts from groundmass potassium feldspar/nepheline. These segregations may perhaps represent "domains" of the basalt that were preferentially quenched relative to the rock as a whole.

The distinctive intrusive rocks are nepheline syenites. They are coarse-grained, with abundant centimeter-sized clinopyroxenes surrounded by slightly smaller nepheline crystals, all poikilitically enclosed by potassium feldspar (Table 3-1). Sill rocks and host lavas are of similar mineralogical composition. The clinopyroxenes are titanaugites; in thin section (Fig. 3-2E), they show deep purplish color with a strong hourglass zonation. Also distinctive in thin section is a bostonitic texture, in which K-spar forms irregular interlocking laths (easily mistaken for plagioclase crystals showing well-

TABLE 3-1—Petrography of Tejana Mesa phonolite and nepheline syenite. [1]Analyses by electron microprobe (Los Alamos National Laboratory). FeO^T = total Fe as FeO; tr = trace.

Modal compositions

Phase	Phonolite (%)	Syenite (%)
Titanaugite	56	15–24
Augite	0	5– 7
Nepheline	?	21–26
K-spar	10	21–34
Fe–Ti oxides	10	8–14
Apatite	1	4
Zeolite	tr	4– 6
Spinel	tr	—
Clay minerals	—	2– 3
Amphibole	—	0– 1
Olivine	20	0

Compositions of minerals in syenite[1]

	Augite (10)	Ti-Augite (9)	Nepheline (6)	K-spar (13)	Apatite (3)	Fe–Ti oxides (9)
SiO_2	50.26	44.31	45.13	64.88	0.34	0.04
TiO_2	1.08	4.00	0.05	0.07		24.76
ZrO_2						0.04
Al_2O_3	1.81	7.69	33.48	19.27	0.01	1.06
Cr_2O_3	tr	0.04				0.02
FeO^T	11.42	7.22	0.38	0.17	0.14	67.09
MnO	0.33	0.12				1.20
MgO	10.95	11.32	tr	0.01	0.10	1.22
BaO			0.07	0.05		
CaO	21.45	22.52	0.25	0.30	53.72	
Na_2O	1.03	0.69	17.61	5.64		
K_2O			3.92	8.29		
P_2O_5					38.40	
F					2.83	
Cl					0.13	
CeO_2					1.25	
Total	98.33	97.91	100.89	98.68	96.92	95.43

developed albite twinning), as well as a poikilitic texture.

Guilinger (1982) suggested three interpretations for relations along southern Tejana Mesa: (1) lava flows filling a depression in underlying sediments; (2) intrusion of a volcanic plug or dike into the Spears Formation; and (3) a lava lake ponded in a tuff ring. Flow features (separate, subhorizontal units with scoriaceous, vesicular tops and massive bases) of these rocks seem to rule out the intrusion hypothesis. The volcaniclastic breccias cropping out near the eastern edge of the exposure show typical features (bedded pyroclastic surges and inward dips) of a tuff ring. A lava lake hypothesis is viable, because the thickening of the lavas seems to extend along the fault zone where a paleovalley could have existed.

The bedded volcaniclastic section might be interpreted as reworked materials deposited on the valley slopes and derived from a nearby vent that went through phases of explosive volcanism. Petrographic inspection of the volcaniclastic deposits reveals that juvenile lapilli and crystal fragments make up over 60% of the rocks and lithic constituents are generally less than 5%. Overall the gradation from volcaniclastic strata to lava shows a gradual transition from what can be interpreted as wet hydrovolcanic explosions producing pyroclastic surges and lahars to drier strombolian ejections of scoria falls. Near the contact between this unit and the overlying lavas, scoria is notably agglutinated, suggesting that lava emplacement followed shortly after deposition of the scoria. These observations support the hypothesis of a nearby vent and suggest that the volcaniclastic section is part of a tuff-ring structure, the center of which is buried beneath the mesa. The form of such a vent structure might be similar to that observed at Zuni Salt Lake crater (Stop 3-3). Thus, the apparently linear form of this thickened wedge of basalts overlying volcaniclastic sediments typical of tuff rings suggests that some combination of the first and third hypothesis might be most appropriate.

Continue south on NM-32. **4.7**

137.0 **Junction** of NM-32 and US-60. **Turn right** onto US-60. **14.5**

151.5 The topography between here and Springerville is dominated by volcanic rocks, part of what is informally referred to as the Red Hill volcanic field. Basalt flows form mesas at various levels, depending on the ages of the flows. Cinder cones form hills, and the few maars form broad, closed depressions. Ages range from 6.4 Ma (see table 1 of preceding paper) to 23,000 yrs (Zuni Salt Lake, see Stop 3-3; Bradbury, 1966). Compositions include both tholeiites and alkali olivine basalts. **18.0**

169.5 Arizona state line. **12.5**

182.0 **Enter** Springerville. A tourist and trading center, Springerville was established in 1879 at the site of Henry Springer's Trading Post. Its population (together with the adjacent town of Eager) is 6600 (Springerville Community Profile, Arizona Department of Commerce, May 1988).

Day 4: White Mountains volcanic field

Summary

This day's excursion examines a representative section through Mt. Baldy, a major central volcano of the Colorado Plateau transition zone. Mt. Baldy, part of the White Mountains volcanic field, differs from Mt. Taylor, seen on Day 2, in that it is slightly older and its compositions are more alkaline. Yet many features of its origin and evolution may be similar, and it affords an excellent opportunity for understanding the chemical and physical processes that can operate in a magmatic system in a continental setting.

Mileage

0.0 **Junction** of US-60 and AZ-260 in downtown Springerville. **Drive** south on AZ-260. **1.6**

1.6 **Turn right** toward McNary. **Stay on** AZ-260. **1.5**

3.1 **Ascend** onto Airport mesa basalt flow, an alkali olivine basalt dated at 3.06 ± 0.08 Ma (Laughlin et al., 1979). **16.0**

19.1 **Enter** Fort Apache Indian Reservation. **5.4**

24.5 **Turn left** onto Apache-78. **1.5**

26.0 **Turn left** onto Apache-79. **Note: At this point, access is restricted to authorized personnel only. Do not continue without permission of the White Mountain Apache Tribe. 9.0**

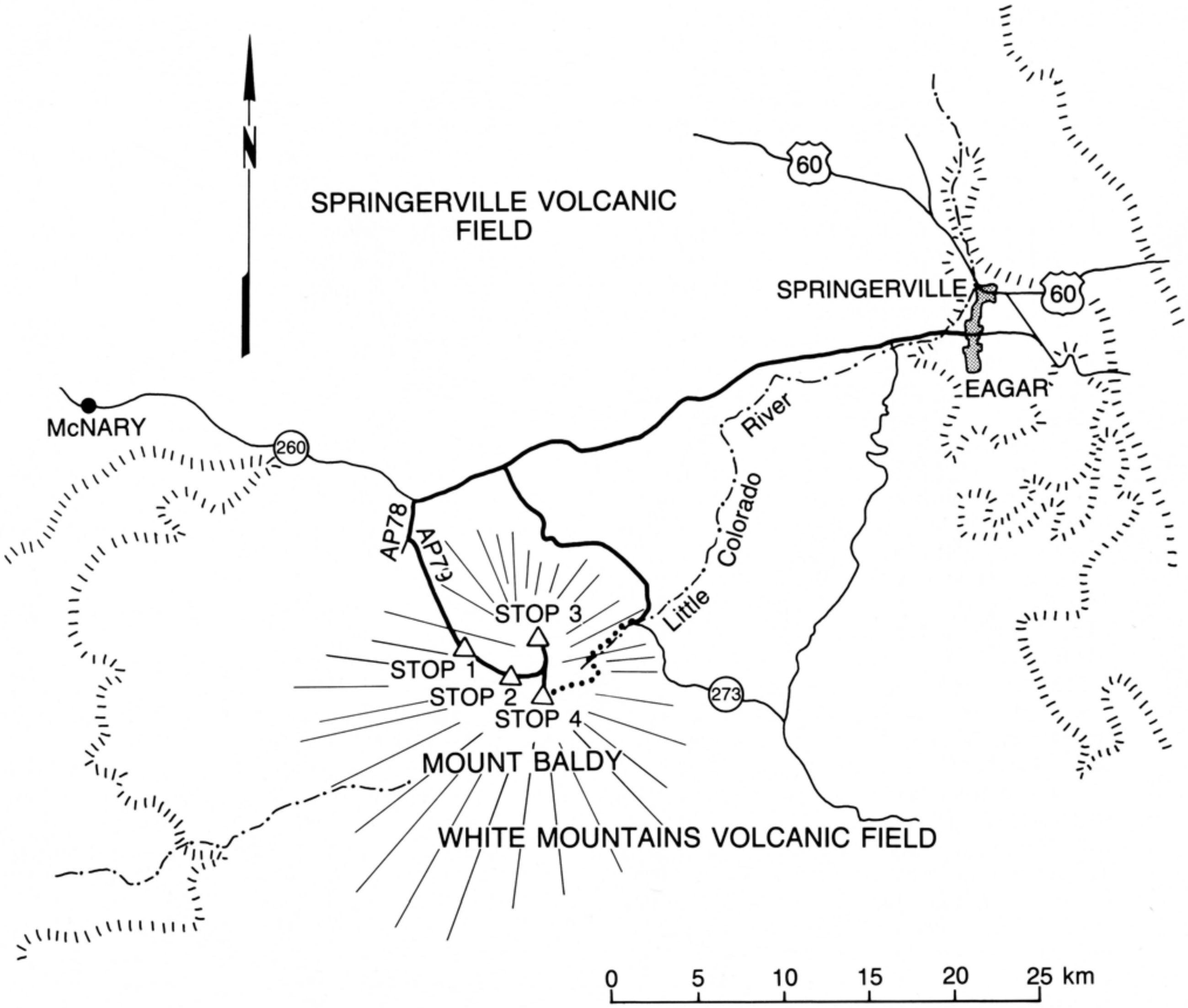

35.0 **STOP 4-1. Mount Ord;** flow breccias of the trachyandesite of Deep Creek. This unit, one of the older eruptive units in the Mt. Baldy complex (fig. 8 of preceding paper), consists of reddish-gray, pebble-sized clasts of trachyandesite with abundant sieve-textured phenocrysts of plagioclase 2–5 mm across, set in a glassy matrix. (Geologic units on Mt. Baldy are defined mainly on petrographic characteristics. Units may be single flows or may consist of several flows of similar mineralogy. Poor exposure, resulting primarily from a heavy cover of vegetation, makes it difficult to discern individual eruptive units.) The trachyandesite of Deep Creek, which crops out mainly on the west side of the shield, is the most mafic unit (54–57% SiO_2) of Mt. Baldy. It rests on older mafic rocks and volcaniclastic sediments on the flanks of the volcano, and overlies the trachyte of East Fork White River in other parts of the shield. This trachyte is high in Sr (750 ppm), Co (16 ppm), and Sc (11 ppm), and low in Nb (60 ppm) compared with other evolved units of Mt. Baldy. One sample of the trachyandesite of Deep Creek has a moderate negative Eu anomaly (Eu/Eu* = 0.75, where Eu* is extrapolated between Sm and Gd).

Continue on Apache-79. **1.0**

36.0 **STOP 4-2. Trachyte of Paradise Butte and view of Smith Cienega Creek.** The trachyte of Paradise Butte, which underlies the trachyandesite of Deep Creek (Stop 4-1), forms a domal mass in the interior of the Mt. Baldy shield volcano. The trachyte, typically medium to light green on fresh surfaces, contains phenocrysts of plagioclase and clinopyroxene 3–5 mm across, set in a glassy matrix.

The trachyte of Paradise Butte is one of the more evolved units in the sequence. It ranges in composition from tristanite to quartz trachyte (60–65% SiO_2). A sample of the unit contains 90 ppm Nb, 240 ppm Sr, 12 ppm Hf, and 140 ppm Rb. It is enriched in light-rare-earth elements relative to average chondrites [La/Yb = 18.6, La/Yb_N (chondrite-normalized) = 12] and has no Eu anomaly (Eu/Eu* = 0.97). (All units in the White Mountains are enriched in rare-earth elements relative to chondrites. For example, chondrite-normalized La/Yb ranges from 7 in basalt to 19 in trachyte.)

View of the glacial valley of Smith Cienega (Spanish, "marsh, marshy place") Creek (Merrill and Péwé, 1977) and the central part of the Springerville volcanic field in the distance. Mt. Baldy is to the southeast.

Continue on Apache-79. **3.7**

39.7 **STOP 4-3. Smith Cienega on top of Mt. Baldy shield cone; trachytes of Pacheta Cienega and Burnt Mountain.** At the bottom of Smith Cienega are remnants of the trachyandesite of Deep Creek. The unit here is overlain by the trachyte of Pacheta Cienega and also appears to be overlain by the trachyte of Burnt Mountain.

The trachyte of Pacheta Cienega is a distinctive dark-gray, coarse-grained rock, with clinopyroxene and sieve-textured plagioclase phenocrysts. Plagioclase phenocrysts exceed 2 cm in length. It is the most widespread trachytic unit in the White Mountains, and is present from the central vent area to Pinetop, some 30 km to the west (Condit, 1984). Samples from the southeast side of Mt. Baldy and from Pinetop have been dated at 8.5 ± 0.25 Ma (T. McKee, USGS, written comm. 1988) and 8.66 ± 0.19 Ma (Condit, 1984), respectively.

The trachyte of Pacheta Cienega is one of the more mafic units in the Mt. Baldy sequence, ranging from hawaiite at Pinetop to trachyte on the southeast side of the shield. The unit also shows a wide range in trace-element composition. A sample from the southeast side of the volcano contains 47 ppm Th; two other samples each contain about 28 ppm Th. The former sample is also rich in Nb (224 ppm), Cs (9 ppm), Hf (27 ppm), Ta (13 ppm), U (9 ppm), and Zr (1500 ppm) compared to other samples of the same unit and to the rest of the Mt. Baldy sequence. The trachyte of Pacheta Cienega is one of the few silicic units that show relatively strong negative Eu anomalies ($Eu/Eu^* = 0.79$).

The trachyte of Burnt Mountain is a green-to-gray unit composed of alkali feldspar and biotite phenocrysts in a glassy matrix. In the bottom of Smith Cienega, this unit overlies a small exposure of pre-Mt. Baldy mafic rocks. Stratigraphic relationships between the trachyte of Burnt Mountain and silicic units are difficult to establish because the trachyte forms thick domal masses rather than thin flows.

The trachyte of Burnt Mountain is one of the most evolved units in the White Mountains (67–68% SiO_2; 11.5% total alkalies, anhydrous). This unit is low in Sr (10 ppm); and high in Y (70 ppm), Zr (820 ppm), Nb (170 ppm), and Rb (160 ppm) compared with other silicic units. The low Sr content of the unit is similar to that of the trachytes of East Fork White River and Hurricane Cienega; all three units contain about 10 ppm Sr and less than 600 ppm Ba. The trachyte of Burnt Mountain has a large negative Eu anomaly ($Eu/Eu^* = 0.52$).

Return to vehicles and **retrace route** for about 1 mi. **Turn left** and **continue** to end of road. **3.4**

43.1 **STOP 4-4. Mt. Baldy shield volcano. Park vehicles** at end of road. This stop is a hike of about 12 km length, mainly downhill. It ends at the Sheep Crossing Campground on the east side of Mt. Baldy at an elevation of 9200 ft (2804 m). The hike requires shuttling vehicles to the Sheep Crossing Campground. **Follow trail south along west side of Mt. Baldy Ridge to south end of Ridge.**

The ridge that forms Mt. Baldy is composed of several lithologic units that decrease in age from north to south. The oldest unit is the trachyte of Mt. Baldy Ridge, one of the more evolved units in the Mt. Baldy sequence, which the trail crosses between this point and elevation 11,400 ft (3475 m). The trachyte is a light-gray to black, glassy rock containing phenocrysts of plagioclase, biotite, and quartz. Compositions range from trachyte to quartz trachyte (66–68% SiO_2; 8.5–11.5% total alkalies). The unit has average concentrations of trace elements for Mt. Baldy shield lavas (80–100 ppm Nb, 1100–1420 ppm Ba, 9–11 ppm Hf, and 12.5–16 ppm Th). It is enriched in light relative to heavy rare-earth elements [$La/Yb = 17$; $La/Yn_N = 11$], and has no Eu anomaly.

Elevation 11,400 ft (3475 m) (south end of Mt. Baldy Ridge)

On the south end of Mt. Baldy Ridge, the trachyte of Mt. Baldy Ridge is overlain by the trachytes of Pacheta Cienega, Spruce Mountain, and Mt. Ord, in that order.

The trachyte of Pacheta Cienega, which forms a thin lava flow on the summit of Mt. Baldy, is easily distinguished by the large, sieve-textured plagioclase phenocrysts. The unit is 1000 ft (305 m) higher here than it is where we examined it in Smith Cienega, just 5 km away.

The trachyte of Pacheta Cienega is one of the most heterogeneous units in the White Mountains. It is sparsely porphyritic, with phenocrysts of plagioclase, alkali feldspar, biotite, and clinopyroxene. The unit is commonly vesicular to vuggy, and locally resembles a flow breccia.

The trachyte of Spruce Mountain ranges in composition from trachyte to low-silica rhyolite (61–70% SiO_2; 10.5–11.5% total alkalies). One sample of the unit has high Sr (200 ppm), La (70 ppm), and Co (1 ppm) compared with most of the other silicic units. The unit also has a moderate negative Eu anomaly ($Eu/Eu^* = 0.79$).

At the south end of Mt. Baldy is the youngest silicic unit in the White Mountains, the trachyte of Mt. Ord. This unit caps most of the ridges on Mt. Baldy, and forms the plug and small lava flow which make up Mt. Baldy Peak. It flowed as much as 9.5 km from the central vent area. Two K–Ar dates for this unit indicate tha the trachyte of Mt. Ord erupted about 8.5 Ma.

The trachyte of Mt. Ord is a brownish-gray to purplish, flow-banded rock with phenocrysts of plagioclase, pyroxene, biotite, and hornblende. Plagioclase is the dominant phase, and ranges from microscopic to 1.5 cm. It is locally sieve-textured, and occasionally contains apatite microlites. Amphibole megacrysts as large as 2 cm are rare in lobes on the southeast side of the shield. The unit ranges in composition from tristanite to rhyolite. It is enriched in light rare-earth elements (La/Yb = 18.1; La/Yb_N = 11.9), and has the highest initial Sr-isotopic composition (0.7059) of any yet analyzed unit in the White Mountains.

The ridgelines west of Mt. Baldy (Mt. Ord) and southwest of Mt. Baldy are capped by the same series of lavas. These relationships indicate that the source of Mt. Baldy lavas was a central vent area located in the vicinity of Paradise Butte and Mt. Warren, between Mt. Baldy and Mt. Ord. The central vent area was approximately 0.3 × 5 km and elongate in a northeast direction. The elevation of the trachyte of Pacheta Cienega on Mt. Baldy and in Smith Cienega indicates that Mt. Baldy was a topographic high, even early in the development of the volcanic center.

Walk to north end of Mt. Baldy Ridge.

Elevation 11,300 ft (3444 m) (north end of Mt. Baldy Ridge)

On the north end of Mt. Baldy, the trachyte of Mt. Baldy Ridge is overlain by the trachyte of West Fork Little Colorado River. This latter unit contains phenocrysts of alkali feldspar, plagioclase, and quartz in a matrix of hornblende, plagioclase, and clinopyroxene. Feldspar phenocrysts are dominantly corroded and embayed; plagioclase phenocrysts are rimmed by alkali feldspar. The unit is distinguished from most other formations of Mt. Baldy by the presence of fractured and embayed quartz. This unit also contains numerous fine-grained hornblende–plagioclase inclusions. SiO_2 averages 63.5% in this trachyte.

Walk to the ridge top and pick up the Sheep Crossing Trail, which is maintained by the Apache–Sitgreaves National Forest. **Follow this trail down the northeast slope of Mt. Baldy.**

Elevation 11,000 ft (3353 m)

The first 2.4 km of the trail traverses the trachyte of West Fork Little Colorado River, which here forms a steep-sided flow ridge of variable width.

Elevation 10,960 ft (3341 m)

Basalt fragments that locally occur along the trail are derived from a 1.7 Ma basanite dike that intrudes the trachyte of West Fork Little Colorado River. The dike rock has the lowest Ba (281 ppm), and highest Zr (460 ppm) and Sr (958 ppm) of any basalt from Mt. Baldy. Its age indicates that volcanism took place in the White Mountains volcanic field at the same time that there was activity in the adjacent Springerville field.

Elevation 10,600 ft (3231 m)

The internal structure of the trachyte of West Fork Little Colorado River is exposed in a steep face along the trail. At the top of the exposure, flow foliation and fracturing are primarily horizontal, but vertical jointing is prominent in the face itself. Below the face, the trachyte is exposed only locally along the trail.

Elevation 10,400 ft (3170 m)

The trail crosses the coarse-grained, gray trachyte of East Fork Trail here. This unit contains abundant large plagioclase phenocrysts up to 5 cm across. It petrographically resembles the trachyte of West Fork Little Colorado River, as both contain quartz phenocrysts, but has slightly higher SiO_2 (67.1%). The two units may represent the same magma but they do not occur in contact with each other, making it difficult to confirm their consanguinity.

Elevation 9500 ft (2896 m)

After crossing the West Fork of the Little Colorado River, the trail traverses pre-Mt. Baldy mafic rocks for about 0.8 km before passing through exposures of the trachyte of Burnt Mountain. Pre-Mt. Baldy mafic rocks are exposed for another 1.6 km beneath the trachyte of Burnt Mountain before being covered by the trachytes of Lee Valley and Mt. Ord.

Locally, pre-Mt. Baldy mafic rocks form alternating layers of lavas and pyroclastic beds, indicating that this unit was the result of numerous eruptive events. These exposures are probably old cinder cones that were covered and intruded by silicic lavas.

Older mafic rocks in the White Mountains volcanic field tend to be evolved compared with the younger basalts in this field and in the Springerville volcanic field (see Day 5). Rock types in the older sequence range in composition from hawaiite to trachyandesite (50–57% SiO_2). A sample from the Sheep Crossing Trail has 52% SiO_2 and 6% total alkalies. Older mafic rocks from the southwest side of the shield have a wide range in trace-element composition (Ba = 375–1700 ppm, Sr = 210–720 ppm, Th = 1.4–4.7 ppm).

Elevation 9450 ft (2880 m)

The trachyte of Burnt Mountain forms a moderate size dome, covering about 0.3 km^2, on the north side of the trail. The dome overlies older mafic rocks and underlies the trachytes of Spruce Mountain and Mt. Ord.

Elevation 9400 ft (2865 m)

Paralleling the trail, on the north side of the stream, is one of many late-stage dikes that intrude the Mt. Baldy shield. This dike projects above ground level for 15–25 m and strikes northwest for about 1 km before turning sharply to the east for another 350 m. It intrudes older mafic rocks and the trachyte of Burnt Mountain. The dike swarm in the White Mountains forms a radial pattern around the central vent area. Lithologically, the dikes resemble the trachyte of Mt. Ord.

Elevation 9360 ft (2853 m)

The ridge on the southeast side of the trail is composed of the trachyte of Lee Valley Reservoir. This is a sugary-textured rock that contains abundant sieve-textured plagioclase phenocrysts, 3–5 mm in length. It underlies the trachyte of Mt. Ord and appears to overlie the trachyte of Burnt Mountain. Although the plagioclase phenocrysts in this unit are similar in appearance to those in the trachyte of Pacheta Cienega, differences in the groundmasses of the two units are sufficient to distinguish them.

The trachyte of Lee Valley Reservoir is a moderately evolved member of the Mt. Baldy sequence. All samples of this unit are trachytic in composition

(61% SiO_2) and contain about 10% total alkalies. A sample of the unit from an exposure adjacent to the Sheep Crossing Trail has average trace-element abundances for Mt. Baldy trachytes, but is slightly higher in Ba (1420 ppm) than most trachytes. The trachyte of Lee Valley Reservoir is petrographically similar to the trachyte of Lofer Butte, which occurs several kilometers to the southwest, but is higher in Nb, Sr, Co, Cs, and Rb.

Elevation 9250 ft (2820 m)

Overlying the trachytes of Spruce Mountain and Lee Valley Reservoir is the Sheep Crossing Formation. Merrill and Péwé (1977) described this unit as an epiclastic sedimentary formation. They recognized that it includes two distinct members: the Campground Member and the Marshall Butte Member. The lower Marshall Butte Member is relatively well stratified. Pumiceous clasts from the Marshall Butte Member are tristanitic in composition. The upper Campground Member is a poorly sorted sand and gravel deposit that shows crude stratification and local graded bedding. The Sheep Crossing Formation occurs over an area of about 600 km^2. Merrill and Péwé attributed the deposits to a combination of pyroclastic and colluvial processes.

Elevation 9200 ft (2804 m) (Sheep Crossing Campground)

Young (late Tertiary–Quaternary) basalts at the end of the Sheep Crossing Trail (parking lot) overlie lavas and epiclastic deposits of Mt. Baldy. The basalts are mostly porphyritic, containing olivine and clinopyroxene phenocrysts. They were derived from cinder cones and probably fissures distributed around the flanks of the shield volcano. The olivine basalt flow on the south side of the Sheep Crossing Campground was dated at 8.9 Ma by Merrill and Péwé (1977). This date is probably too old, but is in the range of other dates for the Mt. Baldy volcano. The flow overlies the Sheep Crossing Formation.

Meet vehicles. Turn left out of parking lot onto AZ-273. **Return** to Springerville via AZ-260.

Day 5: Springerville volcanic field. Springerville to Socorro

Summary

The fifth day's excursion traverses the entire Colorado Plateau transition zone, beginning near the boundary between the transition zone and the core of the plateau and ending in the Rio Grande rift. In the morning, the excursion focuses on basaltic rocks of the Springerville volcanic field—their compositions and petrogenesis, structural setting, and relationship to the White Mountains volcanic field. In the afternoon, en-route to Socorro, the trip examines late Oligocene dikes related to the earliest phase of extension in this region. These dikes are important for determining the orientation of the regional paleostress field. Petrogenesis of these rocks potentially conveys unique information related to the earliest stages of lithospheric thinning culminating in rifting.

Note: The road log for the first part of this day follows Stops 1, 2, 4, and 7 of Day 4, Excursion 5A (Ulrich et al., this volume). To return to Springerville from Stop 7, retrace the route east on FR-3 (Dripping Vat Road) 1.2 mi. Turn left (north) on FR-224 and proceed 7.1 mi to US-60. Turn right (east) on US-60 and continue to Springerville (about 25 mi).

Begin the road log for the second part of the fifth day. From mileage 149.8, the route coincides with a road log by Chapin et al. (1978). See that reference for additional details.

Mileage

0.0 **Junction** of US-60 and US-180 in downtown Springerville. **Drive east** on US-60. **14.1**

14.1 New Mexico state line. **10.6**

24.7 Red Hill. **23.1**

47.8 Quemado (Spanish, "burned"), a small ranching community. About 1880, Jose Antonio Padilla and his family moved from Belen to a place they called Rito Quemado. He brought sheep and started the stock industry in this part of New Mexico. A few years later the name was shortened to Quemado. A post office was established in 1886. The origin of the name Quemado is not certain. One possibility is that it derived from the Indian practice of burning off the sage and rabbitbrush. A second is that the name refers to the scorched appearance of nearby volcanic rocks (Pearce, 1965). **20.2**

68.0 **STOP 5-1. Large Pie Town dike.** This dike is aphyric basaltic andesite (see preceding paper by Baldridge et al.). Here, the dike is 5–6 m thick and steeply east-dipping. It is intruded with a very irregular contact into fluvial sandstones and overbank mudstones of the Eocene Baca Formation. This dike also cuts volcaniclastic sediments of the Spears Formation about 1 mi north and south of the highway. A bleached (reduced) zone extends outward into the sediments for a distance of about 1 m. The Pie Town dike, K–Ar dated at 27.7 ± 0.6 Ma (Laughlin et al., 1979), is discontinuously exposed in an en-echelon

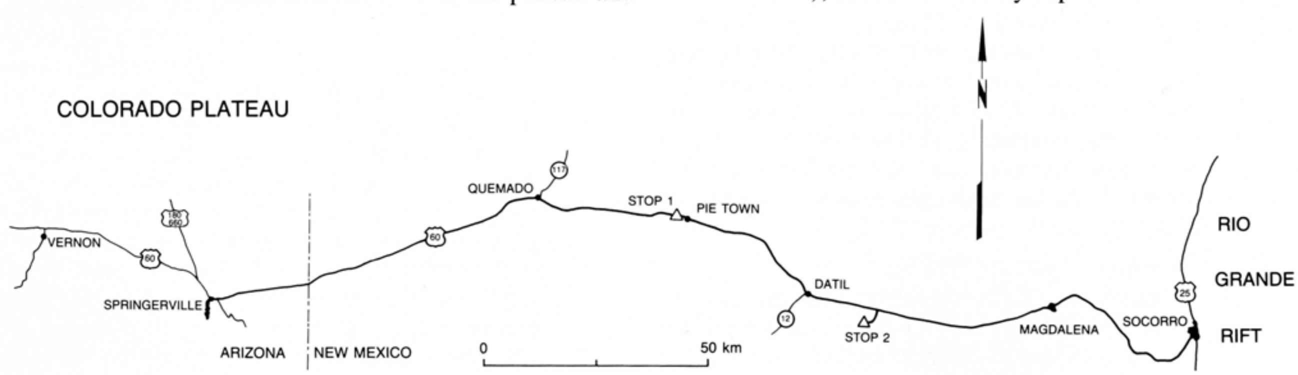

pattern for 75 km along strike (Laughlin et al., 1983). This dike is one of a group of northwest-trending dikes emplaced in the transition zone of the southeastern Colorado Plateau 25–30 m.y. ago. Many of the largest dikes, including the Pie Town dike, are basaltic andesite in composition. Several smaller dikes, oriented parallel or subparallel to the Pie Town dike, also occur in the transition zone. Compositions of these smaller dikes include basaltic andesite and alkaline basalt (Laughlin et al., 1983). The large dike at Pie Town and related large dikes are interpreted to indicate that the regional least-principal stress axis during middle Tertiary extension was oriented in an east-northeast direction (Laughlin et al., 1983). **0.6**

68.6 Small Pie Town dike (actually consisting of two separate small dikes in this roadcut). This is the southernmost occurrence of phyric basaltic andesite (see preceding paper by Baldridge et al.). **0.9**

69.5 **Enter Pie Town.** After service in World War I, one Clyde Norman homesteaded here and began serving coffee and pie to local cowboys and sheepherders. Subsequently the name Pie Town was applied to Norman's settlement. Most of Pie Town's original settlers arrived in the 1920's and 1930's from Texas, refugees of the Dust Bowl. The chief source of income was pinto-bean farming, an uncertain proposition at best due to the short growing season and sparse rainfall. In its heyday, Pie Town had about 300 families, but now its population has dwindled to about 100 residents. Pie Town earned an enduring place in art history through the work of Russell Lee, a photographer with the Farm Security Administration, whose role was to record the Great Depression (Smith, 1983). **1.9**

71.4 Continental Divide. **1.9**

73.3 Sawtooth Mountains on left. The Sawtooth Mountains are composed of volcaniclastic sediments of the Spears Formation, derived from the late Eocene to early Miocene Mogollon–Datil volcanic field to the south. See second-day road log, Excursion 6A, this volume, for photographs and discussion of spectacular debris flows and soft-sediment deformation in the Sawtooth Mountains. The geology between here and Socorro is covered in the first two days of Excursion 6A. **17.1**

90.4 **Enter** Datil (Spanish, "date"), settled in 1884. The town is named for the Datil Mountains, 15 km to the north. Two versions account for the name. The first is that the seedpods of the broad-leafed yucca sufficiently resembled dates to bestow the name. The other is that the Spanish applied the name to the fruit of the prickly pear cactus (Pearce, 1965). **3.3**

93.7 **Enter** Plains of San Agustin, a south-southwest-trending graben of the Rio Grande rift. **12.2**

105.9 **Turn right** onto NM-52. **2.4**

108.3 **Turn right** onto NM-166. **1.7**

110.0 **STOP 5-1. National Radio Astronomy Observatory** (Very Large Array, or VLA). **Turn right** into parking lot of Vistors' Center. The VLA consists of 27 dish-shaped antennas, each 25 m in diameter, which are connected together to form a single large radio telescope. The antennas are placed in a Y-shaped pattern, with each arm of the Y 21 km long. The resolution of the array is changed by moving the antennas in and out on each arm of the array on self-propelled transporters along railroad tracks. The VLA, completed in January 1981, is administered by Associated Universities, Inc., for the National Science Foundation.

Return to US-60. **4.1**

114.1 **Turn right** onto US-60. **19.2**

133.3 **Enter** Magdalena. Magdalena, named for Mary Magdalene, was settled in 1884. It was a major mining center, especially for lead and zinc, until the 1890's. Magdalena became one of the largest cattle-shipping centers in the Southwest (Pearce, 1965; Eveleth, 1983). See first-day road log, Excursion 6A, this volume, for geology of area between Magdalena and Socorro. **16.5**

149.8 Descend Sedillo Hill into Socorro Canyon and the Rio Grande Valley. **9.1**

158.9 **Enter** Socorro. Population about 9000. The name Socorro (Spanish, "help, aid") was given by Don Juan de Oñate in 1598 to a Piro Indian pueblo north of the present city. Before 1628 a mission church, named Nuestra Señora de Socorro de Pilabo, was established at a nearby Indian settlement. In 1693, following the Spanish reconquest of New Mexico, attempts were made to settle the Socorro Valley. However, these were largely unsuccessful because of attacks by neighboring Apaches. By the early 1800's, the Spanish population of northern New Mexico had increased significantly and warfare with the Indians had subsided. On July 4, 1815, the Governor of New Mexico, Alberto Maynez, issued a decree calling upon citizens of New Mexico to take up new lands in the Socorro Valley. By early 1816, seventy families had responded, and the community of Socorro was founded. Socorro remained primarily an agricultural town until the early 1880's, after which it underwent 10–15 years of expansion due to the mines in Magdalena and Socorro Peak (Pearce, 1965; Simmons, 1983; Eveleth, 1983).

Day 6: Socorro to Santa Fe

Summary

The sixth day's excursion entails a 220 km drive north along the axis of the Rio Grande rift. North of Socorro the rift consists of a linear series of asymmetrical grabens bounded by flanking uplifts. Individual grabens are offset from each other in a right-lateral sense along complex structural zones. Along most of its length the Rio Grande rift is characterized by relatively small volumes of late Cenozoic volcanic rocks. Most of those within the axial grabens of the rift occur along strike of the Jemez zone within the central to northern part of the rift. This day's trip examines the complex Cerros de Rio volcanic field of the central rift, which occurs in an area of major structural offset between grabens of the rift. The Cerros field is important in that a range of alkalic to tholeiitic basalt types and intermediate rocks were erupted in close proximity over a short (about 1.5 Ma) period of time.

Note: The route for Day 6 from Socorro to Santa Fe was

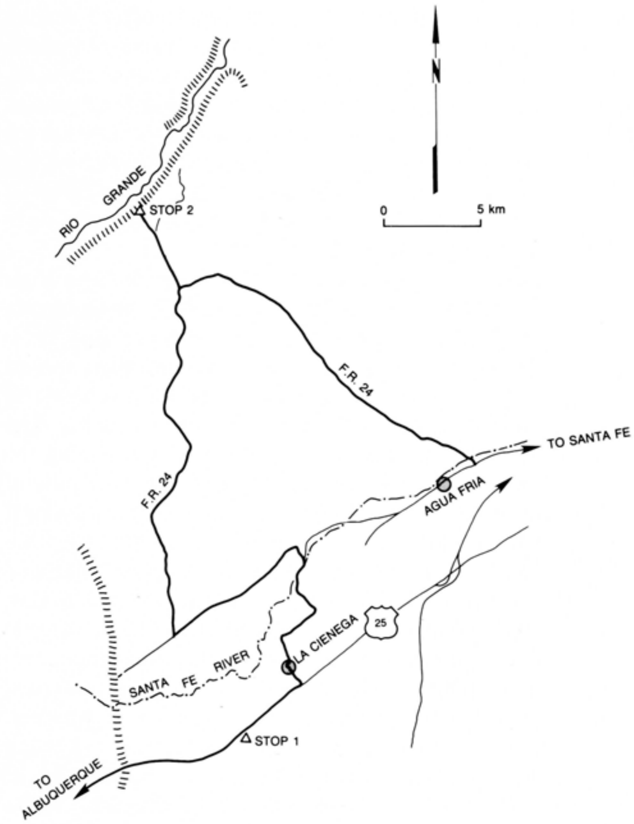

included in an excursion for the 1978 International Rift Conference in Santa Fe. See Hawley (1978) for additional details. The present road log begins at a point about 15 mi south of Santa Fe.

Mileage

0.0 Rest Area/Information Center 15 mi (24 km) south of Santa Fe on I-25.

STOP 6-1. Overview of middle and late Cenozoic magmatism of Española graben of Rio Grande rift. In the distance ahead (east) is the Sangre de Cristo Range, a Precambrian-cored uplift which bounds the Rio Grande rift on the east. The valley between this stop and the Sangre de Cristo Mountains is the southernmost part of the Española basin (graben) of the rift. Its terminus to the south is a gently northward-dipping ramp. The escarpment west of this stop marks the La Bajada fault zone, which separates the Española graben from the Santo Domingo graben to the southwest. Uplift of the Española graben, following eruption of the Cerros del Rio basalts, resulted in the modern erosional regime of the Española basin.

To the south are the Cerrillos Hills (Los Cerrillos), subvolcanic intrusions of monzonite and related rocks. These rocks, dated at 34–30 Ma (Bachman and Mahnert, 1978; Baldridge et al., 1980) are part of the widespread middle Tertiary magmatic event that preceded extension in the rift area and throughout the Basin and Range province (e.g., Baldridge et al., 1980).

In the distance to the northwest are the Jemez Mountains, part of the large Jemez volcanic field, which was active from >14 Ma to about 130,000 yrs ago (see Excursion 17B, this volume).

The low hills and mesas to the north are cinder cones and flows of the Cerros del Rio volcanic field. Several flows are prominently exposed along the canyon of the Santa Fe River, in the middle distance to the northeast. The Cerros del Rio field is the second largest volcanic field of the rift (after the Taos field). It consists of a lava platform covering an area of approximately 300 km^2 (Duncker, 1988). The volume of lava may be about 50 km^3. Approximately 60 vents—cinder cones, maars, tuff rings, and tuff cones—have been identified (Aubele, 1978a). Volcanism occurred from about 2.8 to <1.4 Ma (Doell et al., 1968; Smith et al., 1970; Bachman and Mehnert, 1978). Compositions are mainly basaltic, including basanite, alkali olivine basalt (hawaiite), high- and low-alkali tholeiites, and basaltic andesites, but range to latite–andesite (Baldridge, 1979a; Duncker, 1988). **2.6**

2.6 **Exit right** (Exit 271) onto NM-22 (toward La Cienega). **Turn left** at stop sign and **cross over** I-25 (toward La Cienega). Highway becomes NM-587 (north). **1.3**

3.9 **Village of La Cienega. Junction. Bear right, then take an immediate left** onto road to north. The rock exposed near this junction is augite monzonite porphyry (Sun and Baldwin, 1958), K–Ar dated at 30.2 ± 0.7 Ma (Baldridge et al., 1980). **0.5**

4.4 Hills immediately to the west (left) are composed of Cieneguilla Limburgite (Stearns, 1953; Sun and Baldwin, 1958). This unit consists of a group of flows and tuffs of alkali olivine basalt and olivine nephelinite. An olivine nephelinite flow, K–Ar dated at 25.1 ± 0.7 Ma (Baldridge et al., 1980), contains xenoliths of harzburgite and granulite, and megacrysts of titaniferous magnetite and augite (Baldridge, 1979b). **1.6**

6.0 **Junction. Bear left.** Basalt of the Cerros del Rio volcanic field exposed along canyon of the Santa Fe River straight ahead (to west). **1.6**

7.6 **Junction. Bear left. 0.8**

8.4 Strongly inclined beds of basaltic ash from small cinder cone exposed along both sides of road. Ascend into low basalt-capped mesa of Cerros del Rio volcanic field. **0.4**

8.8 **Junction. Continue straight. 4.5**

13.3 Santa Fe National Forest Boundary. **Junction. Turn right** onto FR-24. The road for the next 20 mi winds among lava flows and cinder cones of the Cerros del Rio field (Fig. 6-1). **12.0**

25.3 Powerline. **Turn left (west)** onto track that follows powerline. **0.4**

25.7 **Junction. Continue straight** (through gate) on powerline road. **2.4**

28.1 **Triangular junction** around pair of powerline poles. **Bear right. 0.2**

28.3 **Junction. Bear left. 0.3**

28.6 **STOP 6-1. White Rock Canyon. Park** vehicles at powerline poles on crest of hill and **walk** 180 m to rim of canyon. White Rock Canyon exposes a 300 m thick section of volcanic, volcaniclastic, and sedimentary units ranging in age from Miocene to Quaternary. Relations among volcanic and volcaniclastic units change laterally along the canyon walls. Along the east side of the canyon, 2 km northeast of this

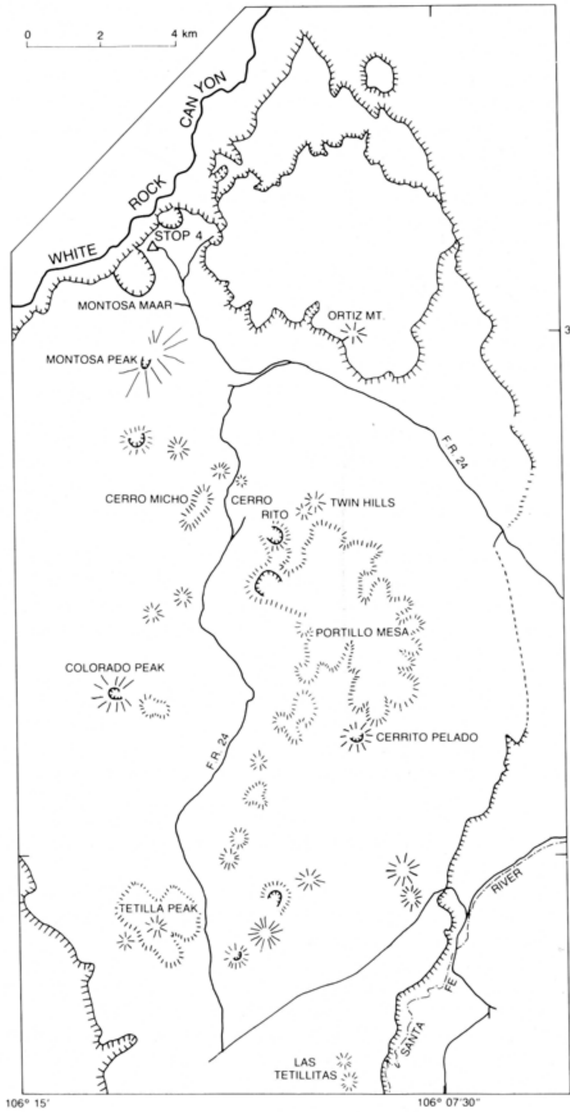

FIGURE 6-1—Physiographic map of Cerros del Rio volcanic field.

Stop, 180 m of lavas and phreatomagmatic rocks overlie sandstones and conglomerates of the Miocene Santa Fe Group (Duncker, 1988; Dethier, 1989).

The lowermost volcanic units in this section (section I of Duncker, 1988) are a series of phreatomagmatic fall and surge deposits. These pyroclastic units are intercalated with and overlain by a group of hawaiite and mugearite flows, which are exposed over much of the northern Cerros del Rio field (Aubele, 1978a, b; Duncker, 1988; Dethier, 1989). Thick flows of latite derived from the Ortiz Mountain vent form the top of the section.

Immediately south of this Stop is Montosa maar (Aubele, 1978a, b), one of at least five maar craters exposed along White Rock Canyon.

Basaltic rocks of the Cerros field are also exposed along the west side of White Rock Canyon, above sediments of the Puyé Formation (Pliocene). The hill 1.5 km northwest of this point (on which the powerline poles are located) is probably a subvolcanic plug. To the north of the hill is a group of basaltic flows. These basalts are dominantly tholeiitic in composition, but include hawaiites and basaltic andesites. The widespread presence of tholeiites along the west side of White Rock Canyon suggests that they were derived from a shield volcano located west of the Rio Grande, now buried beneath outflow sheets of Bandelier Tuff (Dethier, 1989). South of the hill is a thick section of rhyolitic ash-flow tuff, the Tschirege (upper) Member (1.12 Ma) of the Bandelier Tuff derived from the Valles caldera in the Jemez volcanic field, on the skyline to the west (see Excursion 17B, this volume). The tuff was deposited on irregular topography developed on the Cerros del Rio basalts. To the west and southwest across the river, basaltic flows lower in the section are intercalated with Miocene and Pliocene sediments (Santa Fe Group and Puyé Formation, respectively).

Turn around and **return** to gate on powerline road. **2.9**

31.5 **Gate and junction. Continue straight. 0.2**

31.7 **Junction. Bear left. 0.1**

31.8 **Junction** of FR-2555 and FR-24. **10.6**

42.4 **Junction** with County Road-70 on left. **Continue straight. 1.4**

43.8 **Junction** with Agua Fria Road. **Turn left** and **continue** to downtown area of Santa Fe.

References

Aldrich, M. J., Jr., 1986, Tectonics of the Jemez lineament in the Jemez Mountains and Rio Grande rift: Journal of Geophysical Research, 91: 1753–1762.

Aldrich, M. J., Jr., Chapin, C. E., and Laughlin, A. W., 1986, Stress history and tectonic development of the Rio Grande rift, New Mexico: Journal of Geophysical Research, 91: 6199–6211.

Aubele, J. C., 1978a, Geology of Cerros del Rio volcanic field; *in* Hawley, J. W. (ed.), Guidebook to Rio Grande rift in New Mexico and Colorado: New Mexico Bureau of Mines & Mineral Resources, Circular 163: 198–201.

Aubele, J. C., 1978b, Geology of the Cerros del Rio volcanic field, New Mexico: Unpublished M.S. thesis, University of New Mexico, Albuquerque, 136 pp.

Aoki, K., and Kudo, A. M., 1976, Major-element variation of late Cenozoic basalts of New Mexico; *in* Elston, W. E., and Northrop, S. A. (eds.), Cenozoic volcanism in southwestern New Mexico: New Mexico Geological Society, Special Publication 5: 82–88.

Bachman, G. O., and Mehnert, H. H., 1978, New K–Ar dates and the late Pliocene to Holocene geomorphic history of the central Rio Grande region, New Mexico: Geological Society of America, Bulletin, 89: 283–292.

Baldridge, W. S., 1979a, Petrology and petrogenesis of Plio-Pleistocene basaltic rocks from the central Rio Grande rift, New Mexico, and their relation to rift structure; *in* Reicker, R. E. (ed.), Rio Grande rift: Tectonics and magmatism: American Geophysical Union, Special Publication, pp. 323–353.

Baldridge, W. S., 1979b, Mafic and ultramafic inclusion suites from the Rio Grande rift (New Mexico) and their bearing on the composition and thermal state of the lithosphere: Journal of Volcanology and Geothermal Research, 6: 319–351.

Baldridge, W. S., Damon, P. E., Shafiqullah, M., and Bridwell, R. J., 1980, Evolution of the central Rio Grande rift, New Mexico: New potassium–argon ages: Earth and Planetary Science Letters, 51: 309–321.

Baldridge, W. S., Perry, F. V., and Gladney, E. S., 1982, Petrology and geochemistry of the Cat Hills volcanic field, central Rio Grande rift, New Mexico: Geological Society of America, Bulletin, 93: 635–643.

Baldridge, W. S., Bartov, Y., and Kron, A., 1983a, Geologic map of the Rio Grande rift and southeastern Colorado Plateau, New Mexico and Arizona (1:500,000); *supplement to* Reicker, R. E. (ed.), Rio Grande rift: Tectonics and magmatism: American Geophysical Union, Special Publication.

Baldridge, W. S., Perry, F. V., Gladney, E. S., and Shafiqullah, M., 1983b, Late Cenozoic basaltic volcanism of the central Rio Grande rift area, New Mexico (abs.): Geological Society of America, Abstracts with Programs, 15: 381.

Baldridge, W. S., Perry, F. V., and Shafiqullah, M., 1987, Late Cenozoic volcanism of the southeastern Colorado Plateau: I. Volcanic geology of the Lucero area, New Mexico: Geological Society of America, Bulletin, 99: 463–470.

Barker, D. S., 1979, Cenozoic magmatism in the Trans-Pecos province: Relation to the Rio Grande rift; *in* Reicker, R. E. (ed.), Rio Grande rift: Tectonics and magmatism: American Geophysical Union, Special Publication, pp. 382–392.

Basaltic Volcanism Study Project, 1981, Basaltic Volcanism on the Terrestrial Planets: Pergamon, New York, N.Y., 1286 pp.

Bikerman, M., and Bell, K., 1986, Isotopic Sr and Nd study of the Mogollon–Datil volcanic rocks, New Mexico (abs.): Geological Society of America, Abstracts with Programs, 18: 541.

Bosworth, W., 1987, Off-axis volcanism in the Gregory rift, east Africa: Implications for models of continental rifting: Geology, 15: 397–400.

Bradbury, J. P., 1966, Pleistocene–Recent geologic history of Zuni Salt Lake, New Mexico (abs.); *in* Northrop, S. A., and Read, C. B. (eds.), Taos–Raton–Spanish Peaks Country, New Mexico and Colorado: New Mexico Geological Society, Guidebook 17: 119.

Callender, J. F., and Zilinski, R. E., Jr., 1976, Kinematics of Tertiary and Quaternary deformation along the eastern edge of the Lucero uplift, central New Mexico; *in* Woodward, L. A., and Northrop, S. A. (eds.), Tectonics and mineral resources of southwestern North America: New Mexico Geological Society, Special Publication 6: 53–61.

Carden, J. R., and Laughlin, A. W., 1974, Petrochemical variations within the McCartys basalt flow, Valencia County, New Mexico: Geological Society of America, Bulletin, 85: 1479–1484.

Chapin, C. E., and Seager, W. R., 1975, Evolution of the Rio Grande rift in the Socorro and Las Cruces areas; *in* Seager, W. R., Clemons, R. E., and Callender, J. F. (eds.), Las Cruces Country: New Mexico Geological Society, Guidebook 26: 297–321.

Chapin, C. E., Chamberlin, R. M., and Hawley, J. W., 1978, Socorro to Rio Salado; *in* Hawley, J. W. (compiler), Guidebook to Rio Grande rift in New Mexico and Colorado: New Mexico Bureau of Mines & Mineral Resources, Circular 163: 121–134.

Christiansen, E. H., Burt, D. M., Sheridan, M. F., and Wilson, R. T., 1983, The petrogenesis of topaz rhyolites from the western United States: Contributions to Mineralogy and Petrology, 83: 16–30.

Condie, K. C., and Budding, A. J., 1979, Geology and geochemistry of Precambrian rocks, central and south-central New Mexico, New Mexico Bureau of Mines & Mineral Resources, Memoir 15: 58 pp.

Condie, K. C., and McCrink, T. R., 1982, Geochemistry of Proterozoic volcanic and granitic rocks from the Gold Hill–Wheeler Peak area, northern New Mexico: Precambrian Research, 19: 141–166.

Condit, C. D., 1984, The geology of the western part of the Springerville volcanic field, east-central Arizona: Unpublished Ph.D. dissertation, University of New Mexico, Albuquerque, 453 pp.

Condomines, M., Panguy, J. C., Kieffer, G., and Allegre, C. J., 1982, Magmatic evolution of a volcano studied by ^{230}Th–^{238}U disequilibrium and trace element systematics: The Aetna case: Geochimica et Cosmochimica Acta, 46: 1397–1460.

Crumpler, L. S., 1980, An alkali-basalt through trachyte suite, Mesa Chivato, Mount Taylor volcanic field, New Mexico: Geological Society of America, Bulletin, Part II, 91: 1293–1331.

Crumpler, L. S., 1982, Volcanism in the Mount Taylor region; *in* Grambling, J. A., Wells, S. G., and Callender, J. F. (eds.), Albuquerque Country: New Mexico Geological Society, Guidebook 33: 291–298.

Cummings, D., 1968, Geologic map of the Zuni Salt Lake volcanic crater, Catron County, New Mexico: U.S. Geological Survey, Miscellaneous Geologic Investigations Map I-544, scale 1:6,000.

Darton, N. H., 1915, Guidebook to the western United States. Part C. The Santa Fe Route: U.S. Geological Survey, Bulletin 613: 81–100.

Dethier, D. P., 1989, Geology of White Rock quadrangle, Santa Fe and Los Alamos Counties, New Mexico: New Mexico Bureau of Mines & Mineral Resources, Map, scale 1:24,000 (in press).

Dethier, D. P., Aldrich, M. J., Jr., and Shafiqullah, M., 1986, New K–Ar ages for Miocene volcanic rocks from the northeastern Jemez Mountains and Tejana Mesa, New Mexico: Isochron/West, no. 47: 12–14.

de Voogd, B., Serpa, L., and Brown, L., 1988, Crustal extension and magmatic processes: COCORP profiles from Death Valley and the Rio Grande rift: Geological Society of America, Bulletin, 100: 1550–1567.

Doell, R. R., Dalrymple, G. B., Smith, R. L., and Bailey, R.A., 1968, Paleomagnetism, potassium–argon ages, and geology of rhyolites and associated rocks of the Valles caldera, New Mexico; *in* Coats, R. R., Hay, R. L., and Anderson, C. A. (eds.), Studies in volcanology: Geological Society of America, Memoir 116: 211–248.

Duncker, K. E., 1988, Trace-element geochemistry and stable isotope constraints on the petrogenesis of Cerros del Rio lavas, Jemez Mountains, New Mexico: Unpublished M.S. thesis, University of Texas at Arlington, 158 pp.

Dungan, M. A., Muehlberger, W. R., Leininger, L., Peterson, C., McMillan, N. J., Gunn, G., Lindstrom, M., and Haskin, L., 1984, Volcanic and sedimentary stratigraphy of the Rio Grande Gorge and the late Cenozoic geologic evolution of the southern San Luis Valley; *in* Baldridge, W. S., Dickerson, P. W., Reicker, R. E., and Zidek, J. (eds.), Rio Grande rift: Northern New Mexico: New Mexico Geological Society, Guidebook 35: 157–170.

Dutton, C. E., 1885, Mount Taylor and Zuni Plateaus: U.S. Geological Survey, Annual Report 6: 105–198.

Eaton, G. P., 1982, The Basin and Range province: Origin and tectonic significance: Annual Review of Earth and Planetary Sciences, 10: 409–440.

Elston, W. E., and Wohletz, K. H., 1987, Quaternary basalt fields of west-central New Mexico: McCartys pahoehoe flow, Zuni Canyon aa flow, Zuni Ice Cave, Bandera Crater, and Zuni Salt Lake maar; *in* Beus, S. S. (ed.), Geological Society of America, Centennial Field Guide, v. 2, Rocky Mountain Section, pp. 431–436.

Elston, W. D., Rhodes, R. C., Coney, P. J., and Deal, E. G., 1976, Progress report on the Mogollon Plateau volcanic field, southwestern New Mexico, No. 3—Surface expression of a pluton; *in* Elston, W. E., and Northrop, S. A. (eds.), Cenozoic volcanism in southwestern New Mexico: New Mexico Geological Society, Special Publication 5: 3–28.

Eveleth, R. W., 1983, Gustav Billing, the Kelly mine, and the great smelter at Park City, Socorro County, New Mexico; *in* Chapin, C. E., and Callender, J. F. (eds.), Socorro Region II: New Mexico Geological Society, Guidebook 34: 89–95.

Frey, F. A., and Prinz, M., 1978, Ultramafic inclusions from San Carlos, Arizona: Petrologic and geochemical data bearing on their petrogenesis: Earth and Planetary Science Letters, 38: 129–176.

Gardner, J. N., Goff, F., Garcia, S., and Hagan, R. C., 1986, Stratigraphic relations and lithologic variations in the Jemez volcanic field, New Mexico: Journal of Geophysical Research, 91: 1763–1778.

Gawell, M. J., 1975, Chemical and petrographic variations in the Cerro Negro–Cerrito Arizona cinder cone chain, Valencia County, New Mexico: Unpublished M.S. thesis, Kent State University, Kent, Ohio, 57 pp.

Gawell, M. J., and Laughlin, A. W., 1975, Chemical and petrographic variations in the Cerro Negro–Cerrito Arizona cinder cone lineation, Valencia County, New Mexico (abs.): Geological Society of America, Abstracts with Programs, 7: 1084.

Goff, F. E., 1977, Vesicle cylinders in vapor-differentiated basalt flows: Unpublished Ph.D. dissertation, University of California at Santa Cruz, 181 pp.

Grambling, J. A., Wells, S. G., and Callender, J. F. (eds.), 1982, Albuquerque Country: New Mexico Geological Society, Guidebook 33: 370 pp.

Guilinger, D. R., 1982, Geology and uranium potential of the Tejana Mesa–Hubbell Draw area, Catron County, New Mexico: New Mexico Bureau of Mines & Mineral Resources, Open-file Report 176.

Hawley, J. W., 1978, Guidebook to Rio Grande rift in New Mexico and Colorado: New Mexico Bureau of Mines & Mineral Resources, Circular 163: 241 pp.

Jenkins, M. E., and Schroeder, A. H., 1974, A brief history of New Mexico: University of New Mexico Press, Albuquerque, 89 pp.

Kelley, V. C., and Kudo, A. M., 1978, Volcanoes and related basalts of Albuquerque Basin, New Mexico: New Mexico Bureau of Mines & Mineral Resources, Circular 156: 30 pp.

Kerr, P. F., and Wilcox, J. T., 1963, Structure and volcanism, Grants Ridge area: New Mexico Bureau of Mines & Mineral Resources, Memoir 15: 205–213.

Kudo, A. M., Kelley, V. C., Damon, P. E., and Shafiqullah, M., 1977, K–Ar ages of basalt flows at Canjilon Hill, Isleta volcano, and Cat Hills volcanic field, Albuquerque–Belen Basin, central New Mexico: Isochron/West, no. 18: 15–16.

Larsen, S., Reilinger, R., and Brown, L., 1986, Evidence of ongoing crustal deformation related to magmatic activity near Socorro, New Mexico: Journal of Geophysical Research, 91: 6283–6292.

Laughlin, A. W., Brookins, D. G., Kudo, A. M., and Causey, J. D., 1971, Chemical and strontium isotopic investigations of ultramafic inclusions and basalt, Bandera Crater, New Mexico: Geochimica et Cosmochimica Acta, 35: 107–113.

Laughlin, A. W., Brookins, D. G., and Causey, J. D., 1972, Late Cenozoic basalts from the Bandera lava field, Valencia County, New Mexico: Geological Society of America, Bulletin, 83: 1543–1552.

Laughlin, A. W., Brookins, D. G., and Damon, P. E., 1976, Late Cenozoic basaltic volcanism along the Jemez zone of New Mexico and Arizona (abs.): Geological Society of America, Abstracts with Programs, 8: 598.

Laughlin, A. W., Brookins, D. G., Damon, P. E., and Shafiqullah, M., 1979, Late-Cenozoic volcanism of the central Jemez zone, Arizona–New Mexico; Isochron/West, no. 25: 5–8.

Laughlin, A. W., Damon, P. E., and Shafiqullah, M., 1980, New K–Ar dates from the Springerville volcanic field, central Jemez zone, Apache County, Arizona: Isochron/West, no. 29: 3–4.

Laughlin, A. W., Aldrich, M. J., Jr., Ander, M. E., Heiken, G. H., and Vaniman, D. T., 1982, Tectonic setting and history of late-Cenozoic volcanism in west-central New Mexico; *in* Grambling, J. A., and Wells, S. G. (eds.), Albuquerque Country II: New Mexico Geological Society, Guidebook 33: 279–284.

Laughlin, A. W., Aldrich, M. J., and Vaniman, D. T., 1983, Tectonic implications of mid-Tertiary dikes in west-central New Mexico: Geology, 11: 45–48.

Leavy, B. D., and Shafiqullah, M., 1987, New K–Ar analyses of basalts from southern California and central New Mexico: Isochron/West, no. 48: 19–20.

Lipman, P. W., 1980, Cenozoic volcanism in the western United States: Implications for continental tectonics; *in* Studies in geophysics: Continental tectonics: National Academy of Sciences, Washington, D.C., pp. 161–174.

Lipman, P. W., and Mehnert, H. H., 1979, Potassium–argon ages from the Mount Taylor volcanic field, New Mexico: U.S. Geological Survey, Professional Paper 1124-B: 8 pp.

Luedke, R. G., and Smith, R. L., 1978, Map showing distribution, composition, and age of late Cenozoic volcanic centers in Arizona and New Mexico: U.S. Geological Survey, Miscellaneous Geologic Investigations Map I-1091-A, scale 1:1,000,000.

Mayo, E. G., 1958, Lineament tectonics and some ore districts of the Southwest: American Institute of Mining Engineers, Transactions, 10: 1169–1175.

Maxwell, C. H., 1982, El Malpais; *in* Grambling, J. A., and Wells, S. G. (eds.), Albuquerque Country II: New Mexico Geological Society, Guidebook 33: 299–301.

Maxwell, C. H., 1986, Geologic map of El Malpais lava field and surrounding areas, Cibola County, New Mexico: Geological Society of America, Miscellaneous Investigations Map I-1595, scale 1:62,500.

McLellan, M., Robinson, L., Haschke, L., Carter, M. D., and Medlin, A., 1982, Fence Lake Formation (Tertiary), west-central New Mexico: New Mexico Geology, 4: 53–55.

Merrill, R. K., and Péwé, T. L., 1977, Late Cenozoic geology of the White Mountains, Arizona: Arizona Bureau of Geology & Mineral Technology, Special Paper 1: 65 pp.

Moorbath, S., Dungan, M. A., Harmon, R. S., McMillan, N. J., and Hoefs, J., 1983, Pb-, O-, and Sr-isotopic evidence for mantle and lower crustal involvement in the genesis of intermediate lavas of the Taos Plateau volcanic field (TPVF) (abs.): EOS (Transactions of the American Geophysical Union), 64: 753.

Morgan, P., Keller, G. R., and Seager, W. R., 1986a, Thermal and structural evolution of the southern Rio Grande rift: Geophysical and geological evidence for major Neogene plutonism (abs.): Geological Society of America, Abstracts with Programs, 18: 700.

Morgan, P., Seager, W. R., and Golombek, M. P., 1986b, Cenozoic thermal, mechanical and tectonic evolution of the Rio Grande rift: Journal of Geophysical Research, 91: 6263–6276.

Nichols, R. L., 1946, McCartys basalt flow, Valencia County, New Mexico: Geological Society of America, Bulletin, 57: 1049–1086.

Olsen, K. H., Baldridge, W. S., and Callender, J. F., 1987, Rio Grande rift: An overview: Tectonophysics, 143: 119–139.

Pearce, T. M. (ed.), 1965, New Mexico place names; a geographical dictionary: University of New Mexico Press, Albuquerque, 187 pp.

Perry, F. V., Baldridge, W. S., and DePaolo, D. J., 1987, Role of asthenosphere and lithosphere in the genesis of late Cenozoic basaltic rocks from the Rio Grande rift and adjacent regions of the southwestern United States: Journal of Geophysical Research, 92: 9193–9213.

Perry, F. V., Baldridge, W. S., and DePaolo, D. J., 1988, Chemical and isotopic evidence for lithospheric thinning beneath the Rio Grande rift: Nature, 332: 432–434.

Perry, F. V., Baldridge, W. S., DePaolo, D. J., and Shafiqullah, M., 1989, Evolution of a magmatic system during continental extension: The Mount Taylor volcanic field, New Mexico: Journal of Geophysical Research (submitted).

Price, J. G., Henry, C. D., Parker, D. F., and Barker, D. S., 1986, Igneous geology of Trans-Pecos Texas, Field trip guide and research articles: Bureau of Economic Geology, Texas Mining & Mineral Resources Research Institute, Austin, Texas, Guidebook 23: 360 pp.

Renault, J., 1970, Major-element variations in the Potrillo, Carrizozo, and McCartys basalt fields, New Mexico: New Mexico Bureau of Mines & Mineral Resources, Circular 113: 22 pp.

Robinson, S., 1987, Salting away bits of history: Albuquerque Journal, 22 November.

Sanford, A., 1983, Magma bodies in the Rio Grande rift in central New Mexico; *in* Chapin, C. E., and Callender, J. F. (eds.), Socorro Region II: New Mexico Geological Society, Guidebook 34: 123–125.

Sanford, A., and Einarsson, P., 1982, Magma chambers in rifts; *in* Pálmason, G. (ed.), Continental and oceanic rifts: American Geophysical Union, Washington, D.C., Geodynamics Series, 8: 147–168.

Seager, W. R., Shafiqullah, M., Hawley, J. W., and Marvin, R. F., 1984, New K–Ar dates from basalts and the evolution of the southern Rio Grande rift: Geological Society of America, Bulletin, 95: 87–99.

Shafiqullah, M., Damon, P. E., Lynch, D. J., Reynolds, S. J., Rehrig, W. A., and Raymond, R. H., 1980, K–Ar geochronology and geologic history of southwestern Arizona and adjacent areas: Arizona Geological Society Digest, 12: 201–260.

Simmons, M., 1983, The refounding of Socorro, 1816; *in* Chapin, C. E., and Callender, J. F. (eds.), Socorro Region II: New Mexico Geological Society, Guidebook 34: 83–84.

Smith, R. L., Bailey, R. A., and Ross, C. S., 1970, Geologic map of the Jemez Mountains, New Mexico: U.S. Geological Survey, Miscellaneous Investigations Map I-571, scale 1:125,000.

Smith, T., 1983, Pie Town: A trip back: Impact, Albuquerque Journal Magazine, 6(14): 4–8. (18 January)

Stearns, C. E., 1953, Tertiary geology of the Galisteo–Tonque area, New Mexico: Geological Society of America, Bulletin, 64: 459–508.

Steiner, M. B., 1988, Paleomagnetism of the Late Pennsylvanian and Permian: A test of the rotation of the Colorado Plateau: Journal of Geophysical Research, 93: 2201–2215.

Sun, M., and Baldwin, B., 1958, Volcanic rocks of the Cienega area, Santa Fe County, New Mexico: New Mexico Bureau of Mines & Mineral Resources, Bulletin 54: 80 pp.

Suppe, J., Powell, C., and Berry, R., 1975, Regional topography, seismicity, Quaternary volcanism, and the present-day tectonics of the western United States: American Journal of Science, 275a: 397–436.

Taylor, S. R., and McLennan, S. M., 1985, The continental crust: Its composition and evolution: Blackwell Scientific Publications, Palo Alto, Calif., 312 pp.

Thaden, R. E., Santos, E. S., and Raup, O. B., 1967, Geologic map of the Grants quadrangle, Valencia County, New Mexico: U.S. Geological Survey, Map GQ-681, scale 1:24,000.

Vaniman, D. T., Crowe, B. M., and Gladney, E. S., 1982, Petrology and geochemistry of hawaiite lavas from Crater Flat, Nevada: Contributions to Mineralogy and Petrology, 80: 341–357.

Vaniman, D., Laughlin, A. W., and Gladney, E. S., 1985, Navajo minettes in the Cerros de las Mujeres, New Mexico: Earth and Planetary Science Letters, 74: 69–80.

Vollmer, R., 1976, Rb–Sr and U–Th–Pb systematics of alkaline rocks: The alkaline rocks from Italy: Geochimica et Cosmochimica Acta, 40: 283–295.

Wernicke, B., 1985, Uniform-sense normal simple shear of the continental lithosphere: Canadian Journal of Earth Sciences, 22: 108–125.

Williams, L. A. J., 1982, Physical aspects of magmatism in continental rifts; *in* Pálmason, G. (ed.), Continental and oceanic rifts: American Geophysical Union, Washington, D.C., Geodynamics Series, 8: 193–222.

Wood, D. A., 1979, A variably veined suboceanic upper mantle—genetic significance for mid-ocean ridge basalts from geochemical evidence: Geology, 7: 499–503.

Wright, H. E., Jr., 1946, Tertiary and Quaternary geology of the lower Rio Puerco area, New Mexico: Geological Society of America, Bulletin, 57: 383–456.

Zimmerman, C., and Kudo, A. M., 1979, Geochemistry of andesites and related rocks, Rio Grande rift, New Mexico; *in* Reicker, R. E. (ed.), Rio Grande rift: Tectonics and magmatism: American Geophysical Union, Special Publication, pp. 355–381.

EXCURSION 9A:
Mid-Tertiary silicic alkalic magmatism of Trans-Pecos Texas: Rheomorphic tuffs and extensive silicic lavas

Christopher D. Henry[1], Jonathan G. Price[2], Don F. Parker[3], and John A. Wolff[4]

[1]Bureau of Economic Geology, University of Texas at Austin, Austin, Texas 78713; [2]Nevada Bureau of Mines & Geology, University of Nevada, Reno, Nevada 89557-0088; [3]Department of Geology, Baylor University, Waco, Texas 76798; [4]Department of Geology, University of Texas at Arlington, Arlington, Texas 76019

Introduction

This trip provides an overview of the silicic, alkalic, and commonly peralkaline magmatism of Trans-Pecos Texas, particularly in the Davis Mountains and Big Bend National Park (Figs. 1, 2). Emphasis is on caldera development, a variety of pyroclastic deposits including strongly rheomorphic welded tuffs, and unusually widespread silicic lavas. Additionally, we will visit two calderas that illustrate contrasting styles of development and a wide variety of caldera-fill volcanic rocks and breccias. Much of the trip will examine a group of rocks that have outcrop features of lava flows but areal extents and aspect ratios commonly associated with ash-flow tuffs; these include both true lavas and strongly rheomorphic tuffs, as well as some units of debatable origin. Geochemistry and petrogenesis of the rocks will also be addressed, both in the field and in discussion sessions scheduled for several evenings of the trip.

Regional geologic setting of Trans-Pecos volcanic field

The alkalic magmatism of Trans-Pecos Texas occurred between 48 and 17 Ma in two distinct tectonic settings: a probable continental volcanic arc up to about 31 Ma, and Basin and Range extension thereafter. The volumetrically dominant, older igneous rocks are part of a much larger volcanic province that continues westward into Mexico to include the Sierra Madre Occidental and northward at least into the Mogollon–Datil field in New Mexico (Fig. 1). Magmatism during each of the two tectonic episodes has been further divided into two phases (Table 1; Henry and McDowell, 1986). Rocks of the first two phases, which are the focus of this trip, are probably the most inland expression of subduction-related volcanism. The paleotrench for this magmatism lay off western Mexico; volcanism generally swept eastward from near the present Pacific Coast at about 100 Ma and reached Trans-Pecos Texas about 48 Ma. Laramide-age calc-alkaline magmatism in Mexico appears to grade eastward into middle Tertiary alkaline magmatism in Texas. The eastward sweep of magmatism was probably the result of progressive shallowing of the subducting slab with time (Coney and Reynolds, 1977; Keith, 1978; Damon et al., 1981; Price et al., 1987). About 30 Ma, volcanism either swept rapidly back or flared up nearly simultaneously from Trans-Pecos Texas across much of western Mexico. Volcanism in Texas after that time occurred in an environment of regional extension.

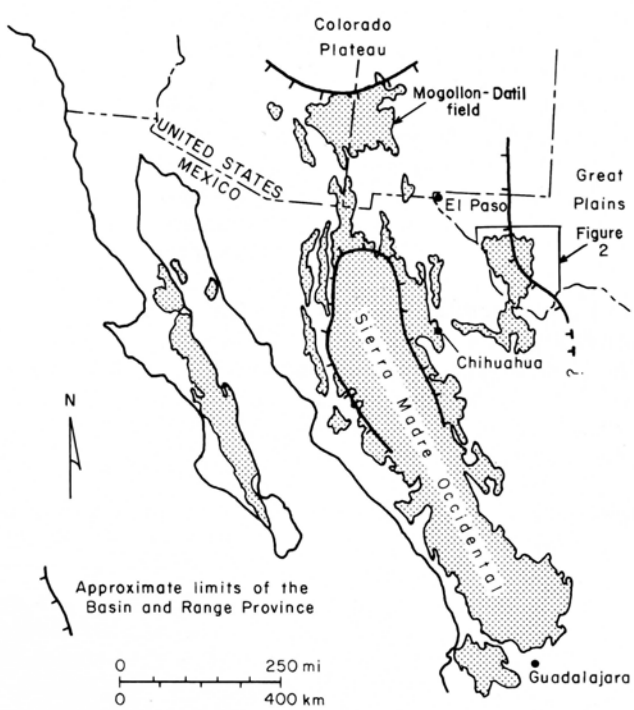

FIGURE 1—Approximate distribution of Tertiary volcanic rocks in Trans-Pecos Texas and adjacent regions of New Mexico, Arizona, and Mexico. Outline indicates area of Fig. 2.

The early phase of subduction-related magmatism in Texas occurred between 48 and 39 Ma. Small, mafic to intermediate intrusions were emplaced about 47 Ma in, and southeast of, El Paso and north of Big Bend National Park (Figs. 2, 3). At the same time an extensive basaltic lava sequence, Alamo Creek Basalt of Chisos Formation, erupted in the Big Bend region. Between 44 and 40 Ma, abundant, small, silicic to mafic intrusions were emplaced in the Christmas Mountains area northwest of Big Bend National Park. A small but impressive caldera complex, the only recognized caldera of this phase, formed in the Christmas Mountains about 42 Ma (Henry et al., 1989) and is the focus of Day 3 of this trip.

The transition to the main phase of volcanism at 38 Ma is marked by a tremendous increase in the volume of erupted magmas and by the dominance of caldera-related volcanism (Table 1, Fig. 3). This magmatism occurred throughout Trans-Pecos Texas, but shifted with time and was most abundant in the central and southern parts of the region. Volcanic rocks of the Davis Mountains, the largest contiguous remnant of the Trans-Pecos field (Fig. 4), that will be examined on Days 1, 2, and 4, and Bracks Rhyolite of Day 6, were all emplaced between 38 and 36 Ma (Parker and McDowell, 1979; Henry et al., 1988a). Identified eruptive centers of the Davis Mountains (Fig. 3) include large calderas (Parker, 1986; Henderson, 1987), small calderas (Hoy, 1986), and small calderas associated with trachyte shield volcanoes (Parker, 1983). Several more calderas probably exist in the Davis Mountains than have been identified. A

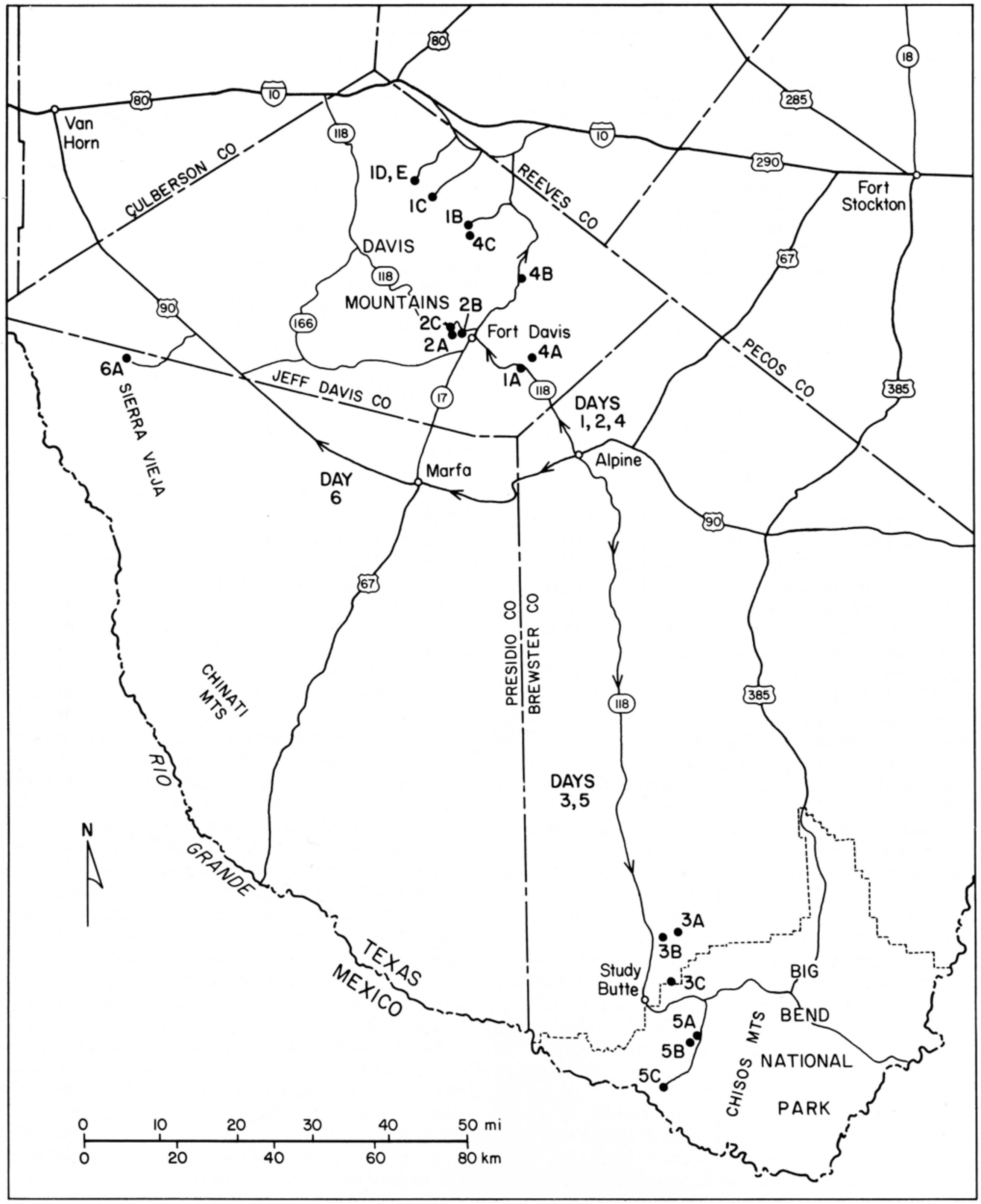

FIGURE 2—Routes and stops of this field trip.

possible complication is that some units may have erupted from downsag calderas rather than fault-bounded calderas. Resurgence of such calderas could largely disguise evidence of collapse.

Contemporaneous noncaldera magmatism consisted of numerous small intrusions and lavas scattered through the province. A northwest-trending belt of silica-undersaturated intrusions was also emplaced at this time, most notably in the Diablo Plateau of northern Trans-Pecos (Fig. 3; Barker, 1977). About 35 Ma, volcanism shifted from the northern and central parts of the region to the southern part, in the Big Bend area and Chinati Mountains.

TABLE 1—Magmatic–tectonic phases in Trans-Pecos Texas.

Phase	Style of magmatism	Distribution	Relative volume	Composition	Geographical compositional trends	Stress orientations	Faulting
Pre-main 48–39 Ma	Abundant, small intrusions; basalt lava and one small caldera complex	Mostly southern	Moderate	Mafic to silicic	?	σ_1 = ENE σ_3 = NNW	No
Main 38–32 Ma	Numerous calderas; abundant intrusions and lavas unrelated to calderas	All areas; shifts with time; calderas only central and southern	Major	Mafic to silicic	West to east increase in alkalinity	σ_1 = ENE σ_3 = NNW	No
Early extensional 31–27 Ma	Two calderas in Chihuahua; one stratovolcano; small intrusions	Southern only	Major, but less than main phase	Bimodal?; calderas exclusively silicic; ne-normative mafic and peralkaline rhyolite intrusions	?	σ_1 = vertical σ_3 = ENE	No
Main Basin and Range 24–17 Ma	Abundant dikes; some lavas	All areas	Minor	Exclusively basaltic	Locally homogeneous; silica saturation varies geographically	σ_1 = vertical σ_3 = ENE	Major Basin and Range

The change in tectonic setting is indicated by a change in stress orientations at approximately 31 Ma (Table 1; Price and Henry, 1984). During the pre-main and main phases, dike and vein orientations indicate that least principal stress (σ3) was north-northwest. This suggests that the maximum stress (σ1) was east-northeast, consistent with similarly oriented plate convergence in the middle Tertiary (Engebretson et al., 1985). A change to east-northeast σ3 and vertical σ1 at 31 Ma probably marks the beginning of regional extension (Henry and Price, 1986). Subsequent volcanism up to 17 Ma, when all volcanic activity ceased in Trans-Pecos Texas, is also divided into two phases: an early tensional phase between 31 and 27 Ma, and a main Basin and Range phase between 24 and 17 Ma.

Volcanism of the early tensional phase was restricted to southern Trans-Pecos and adjacent Chihuahua (Fig. 3). Caldera-related volcanism continued, as two large calderas (San Carlos and Santana calderas) formed at 30 and 28 Ma in Chihuahua, just across the Rio Grande. In contrast to earlier calderas, total caldera subsidence was small, erupted rocks were exclusively silicic, and eruptions after the caldera-forming tuff were negligible. In Texas, the Bofecillos stratovolcano erupted mafic to intermediate lava flows; intrusions of peralkaline rhyolite and nepheline-normative hawaiite were emplaced in Big Bend National Park. On Day 5 we will examine a series of peralkaline rhyolite domes emplaced during the early tensional phase.

After a several million year hiatus, exclusively basaltic rocks were emplaced throughout much of Trans-Pecos Texas as dikes, small stocks, and some lavas (Fig. 3). The beginning of this volcanism at 24 Ma coincided with the beginning of significant Basin and Range faulting. Although not a focus of this trip, basalts of this episode will be examined on Days 4 and 6.

Volumes of erupted rocks varied tremendously during these tectono-magmatic phases. By far the largest volumes erupted during the main phase between 38 and 32 Ma. Subordinate, but still major, volumes of magmas were emplaced during the pre-main and early tensional phases. Although widespread, magmatism during the main Basin and Range phase was volumetrically minuscule.

Geochemistry

The four magmatic–tectonic phases show distinct geochemical signatures that are in part the basis for their division. The petrology, geochemistry, and evolution of main-phase volcanism have been most thoroughly studied, but enough is known about all four phases to characterize and distinguish them. Barker (1977) first recognized that main-phase volcanism occurred in two parallel, northwest-trending belts: an eastern alkalic belt and a western metaluminous belt. Henry and Price (1984) called the latter the alkali-calcic belt, using the alkali-lime index of Peacock (1931). Both belts are relatively alkalic compared to typical calc-alkaline volcanic rocks of most continental arcs. Both silica-undersaturated rocks and peralkaline silicic rocks are more abundant in the eastern, alkalic belt than in the western, alkali-calcic belt, in which the former are nearly absent.

Rocks of the main phase exhibit two differentiation series that commonly occur together in individual igneous centers: a volumetrically dominant hypersthene-normative basalt to rhyolite series and a lesser nepheline-normative basalt or hawaiite to phonolite or nepheline trachyte series. Geochemical studies of both series indicate that crystal fractionation from a mafic parent is the dominant process that produced the chemical variations (Parker, 1983; Cameron and Cameron, 1986; Barker, 1987; Price et al., 1987; Henry et al., 1988b). However, other processes, including variable degrees of crustal assimilation and magma chamber replenishment, are locally significant (McDonough and Nelson, 1984; Price et al., 1986; Nelson and Nelson, 1986; Nelson et al., 1987). The parental mafic rocks were mantle-derived but all erupted examples were relatively evolved. For example, they are hawaiites having low Mg numbers (<66) and Ni contents (<<100 ppm) (Gunderson et al., 1986; Barker, 1987).

Rocks of the Davis Mountains, the focus of much of this trip, are alkalic with low-silica rhyolite forming the largest mode in a silica histogram (Fig. 5). A Daly gap of several weight percent silica separates basaltic rocks from trachytes; this gap has been interpreted to be the result of the efficiency of crystal fractionation (intermediate plagioclase, magnetite, olivine, clinopyroxene, apatite) in boosting silica at this

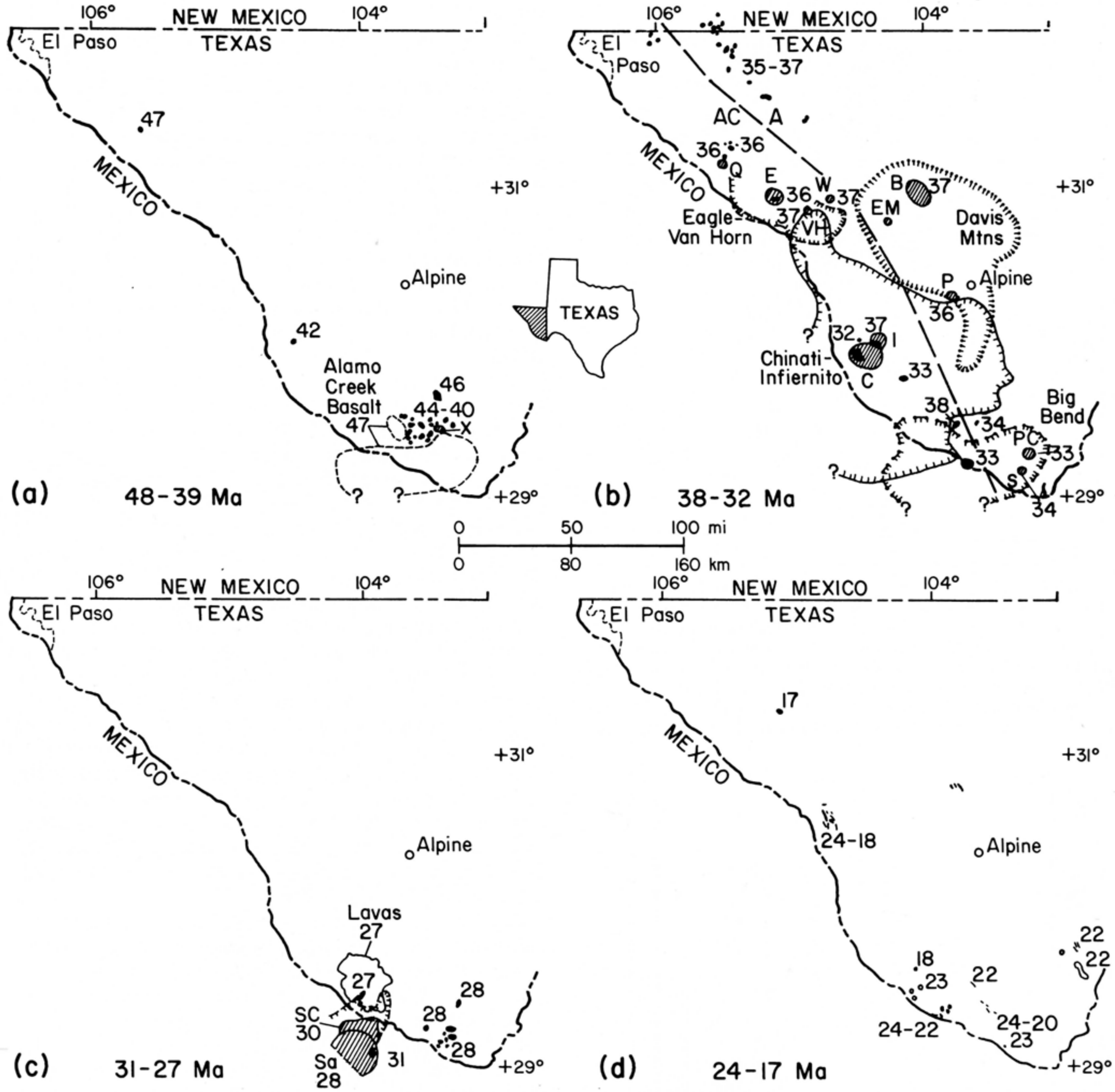

FIGURE 3—Distribution of igneous activity during four phases of magmatism in Trans-Pecos Texas. **a,** Pre-main phase; 48–39 Ma. **b,** Main phase; 38–32 Ma. Dashed line separates alkali-calcic belt (AC) and alkali belt (A) as defined by Barker (1977) and Henry and Price (1984). **c,** Early tensional phase; 31–27 Ma. **d,** Main Basin and Range phase; 24–17 Ma. Ruled areas are calderas, filled areas are major intrusions, outlined areas indicate extent of major eruptive rocks related to different centers. Numbers indicate time of major activity of calderas or intrusions. Letters next to calderas: X = Christmas Mountains caldera complex; Q = Quitman Mountains caldera; E = Eagle Mountains caldera; VH = Van Horn Mountains caldera; W = Wylie Mountains caldera; B = Buckhorn caldera; EM = El Muerto caldera (Hoy, 1986); P = Paisano volcano; I = Infiernito caldera; C = Chinati Mountains caldera; PC = Pine Canyon caldera; S = Sierra Quemada caldera; SC = San Carlos caldera; Sa = Santana caldera. Several more calderas must occur in Davis Mountains.

stage of magmatic evolution (Parker, 1983). Minor nepheline trachyte occurs as a late addition to main-phase activity and is limited to a belt of NW–SE trending intrusions, which also includes silica-oversaturated rocks (Fig. 6).

Basaltic rocks are mostly sparsely porphyritic mugearite and hawaiite with phenocrysts of olivine and magnetite, and, more rarely, plagioclase. Trachyte is usually coarsely glomeroporphyritic, with the most mafic varieties (~60% SiO_2, 0.8% MgO) having feldspar with plagioclase or calcic anorthoclase cores and alkali feldspar rims. Quartz trachyte and rhyolite are abundantly porphyritic with alkali feldspar, clinopyroxene, and magnetite the most common phenocryst assemblage. Rare vitrophyres are commonly the only samples to contain nonoxidized mafic minerals.

Rock analyses from individual centers form smooth trends on variation diagrams (Parker, 1983). In a TiO_2 Harker diagram of Davis Mountains analyses, the greatest scatter occurs in the basaltic rocks, suggesting a variety of fractionation trends. Rhyolite compositions also scatter, although related rocks form distinct trends (Fig. 6). Major- and trace-element studies suggest that fractionation of phenocryst phases was the major mechanism of differentiation

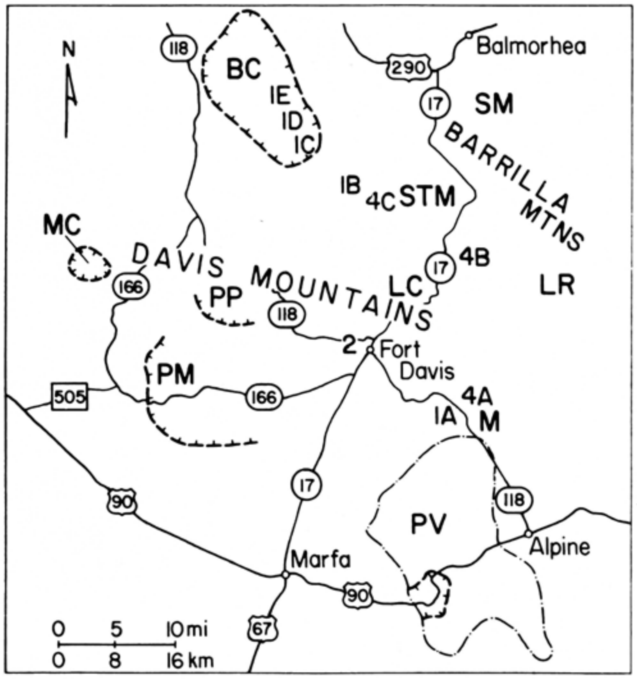

FIGURE 4—Davis Mountains location map and field-trip stops. Eruptive centers: PV = Paisano volcano (dash–dot line shows approximate limit of flows; Parker, 1976, 1983); BC = Buckhorn caldera (Parker, 1986); MC = Muerto caldera (Hoy, 1986); PP = proposed Pine Peak caldera (Larocca, 1984); PM = Paradise Mountain caldera (Henderson, 1987). Approximate caldera boundaries identified by dash lines with bars. Geographic localities: SM = Saddleback Mountain; STM = Star Mountain; LC = Limpia Canyon; M = Musquiz Canyon; LR = Leoncita Ranch.

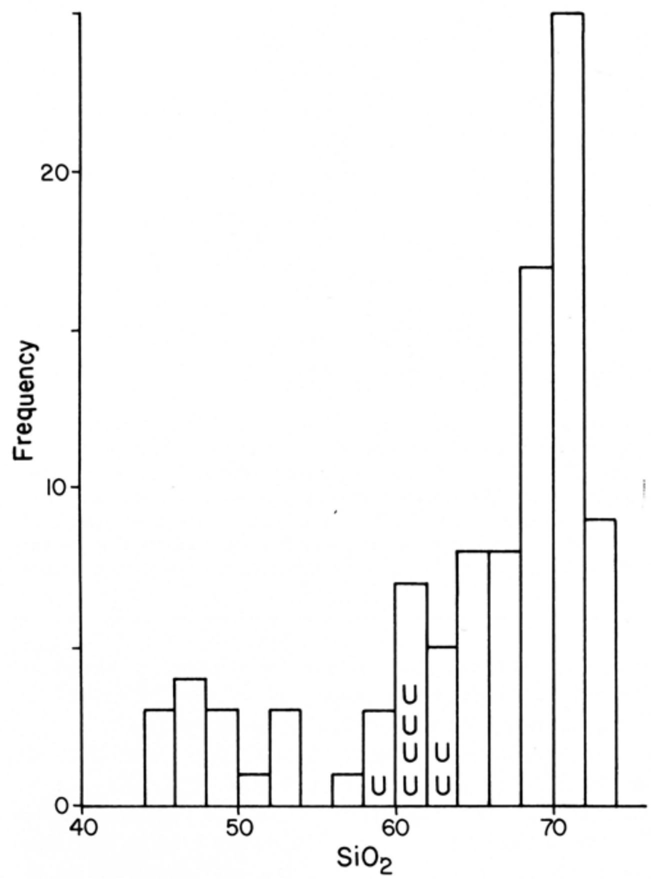

FIGURE 5—SiO_2 histogram of 97 whole-rock analyses of Davis Mountains igneous rocks from published sources, Table 2, and unpublished data. Note possible bimodality and position of silica-undersaturated trachytes (blocks with "U") clustered about 61 weight % SiO_2.

(Parker, 1983, 1986; McDonough and Nelson, 1984). Chemical analyses of many of the units of this trip are given in Table 2.

A conceptual model for main-phase Davis Mountains magmatism includes: (1) intrusion of basaltic magma into the upper crust (this magma had undergone fractionation at greater depth), (2) differentiation to form a batholith-sized body of quartz trachyte beneath the range at a depth of several kilometers, (3) eruption of widespread quartz trachytes like Star Mountain Formation, (4) differentiation of more evolved rhyolite in cupolas above this batholith, and (5) eruption of evolved rhyolites from individual centers, followed by less differentiated trachyte as deeper levels are tapped. Classic resurgent activity has been proposed for one center.

The composition of pre-main-phase magmatism has not been studied extensively, but available data suggest similarities to the main phase. Intrusions of the 40 to 44 Ma Christmas Mountains area range from nepheline-normative hawaiites to peralkaline, high-SiO_2 rhyolites (Lonsdale, 1940; Cameron et al., 1986; Henry et al., 1989). Both over- and undersaturated differentiation series are present.

In contrast to the earlier magmatism, volcanic rocks of the early tensional phase may be bimodal. The two calderas in Chihuahua produced only silicic rocks, two ash-flow tuffs and a granite (Chuchla, 1981); intermediate to mafic lavas, characteristic of the earlier calderas in Texas, are absent (Henry and Price, 1984). The tuffs are ferroaugite rhyolites showing trace-element enrichment distinct from the older rhyolites (Gunderson et al., 1986). Contemporaneous rocks in Texas are peralkaline rhyolites and nepheline-normative hawaiites. Differentiation sequences are restricted to the silica-undersaturated series, which, in places, evolved to nepheline-normative syenite (Carman et al., 1975). Otherwise, intermediate rocks are largely lacking. The source of these magmas and their relation to subduction or Basin and Range extension are uncertain.

Rocks of the main Basin and Range phase are exclusively alkali basalts and hawaiites, ranging from strongly nepheline-normative to hypersthene-normative (Henry and Price, 1986; Price et al., 1987). In contrast to the main phase, primitive compositions, characterized by high Mg numbers and Ni contents (up to 230 ppm; Gunderson et al., 1986), are common. Mantle-derived inclusions of lherzolite, peridotite, and dunite occur in these rocks in several areas (Schieffer and Nelson, 1981). The strongly tensional setting may have allowed the magmas to rise rapidly from their sources in the mantle with little differentiation.

Specific problems of rheomorphic tuffs and extensive silicic lavas

A major emphasis of this trip is the examination of several variably rheomorphic tuffs and some extensive silicic volcanic rocks whose origin is controversial (Henry et al., 1988a). Tuffs in Trans-Pecos Texas range from conventional welded ash-flow tuffs showing no rheomorphic features, to rheomorphic tuffs in which primary features are still well preserved, to strongly rheomorphic tuffs in which primary features are only locally preserved. The controversial rocks have outcrop features exclusively of lava flows but geometries of ash-flow tuffs, and have been interpreted both ways (Anderson, 1969; Gibbon, 1969; Parker and McDowell, 1979; Henry et al., 1988a). Table 3 summarizes features that traditionally have been used to distinguish ash-flow tuffs

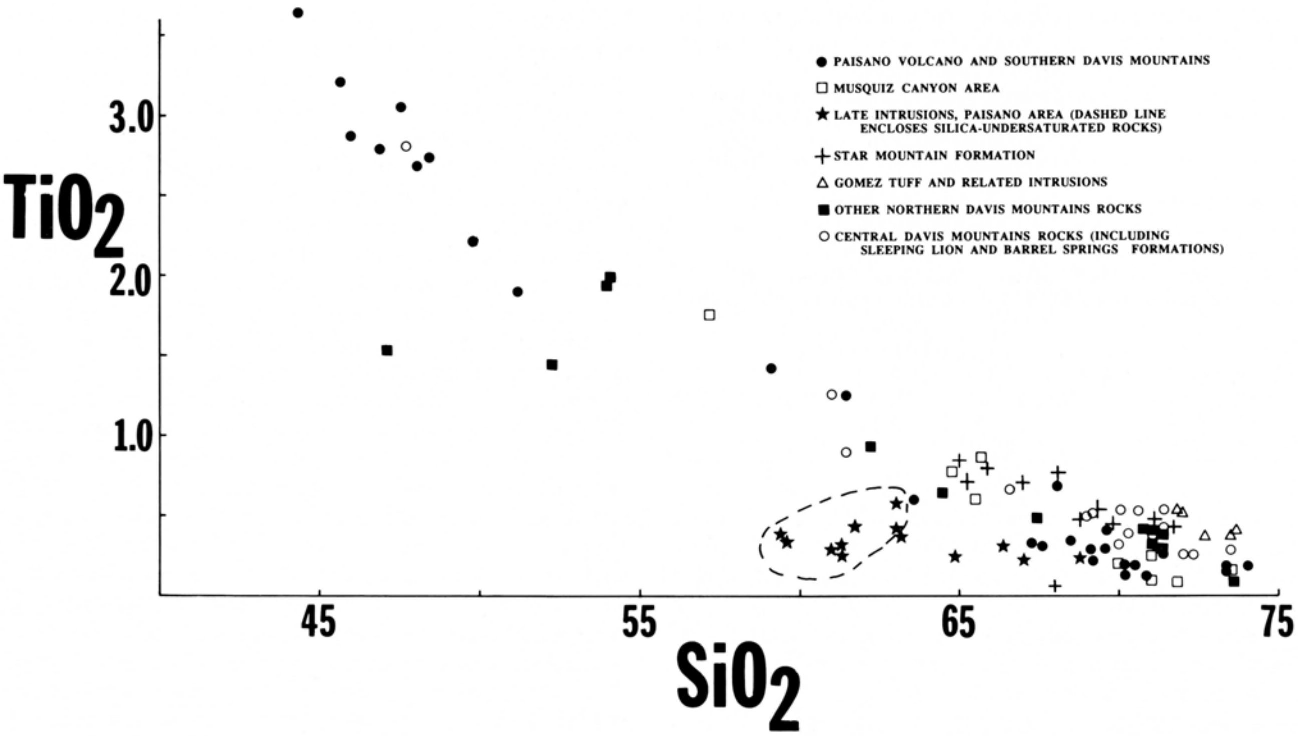

FIGURE 6—TiO_2–SiO_2 plot of Davis Mountains igneous rocks from same data base as Fig. 5.

TABLE 2—Chemical analyses.

	Day 1				Day 2					Day 4					Day 6		
	1	2	3	4	5	6	7	8	9	10	11	12	13	14	15	16	17
SiO_2	71.80	72.67	73.7	54.0	70.6	69.0	69.2	70.1	70.0	68.1	69.3	68.1	71.1	65.8	67.02	69.52	69.12
TiO_2	0.54	0.37	0.41	1.94	0.53	0.50	0.52	0.34	0.32	0.65	0.54	0.77	0.48	0.83	0.58	0.54	0.56
Al_2O_3	10.50	10.91	10.3	17.9	14.2	14.2	13.9	12.4	14.1	15.2	14.8	15.7	12.44	15.7	13.08	12.58	12.86
Fe_2O_3														1.95	1.76	4.30	4.50
FeO	5.56*	4.92*	4.63*	6.83*	3.05*	2.95*	3.33*	2.21*	3.25*	4.29*	3.06*	2.16*	4.40*	2.81	4.03	1.68	1.46
MnO	0.17	0.12	0.19	0.23	0.07	0.09	0.04	0.03	0.08	0.03	0.07	0.11	0.08	0.20	0.24	0.16	0.22
MgO	0.11	0.01	0.20	1.26	0.24	0.12	0.10	0.07	0.26	0.22	0.03	0.10	0.42	0.24	0.24	0.23	0.28
CaO	0.51	0.22	0.35	7.59	0.57	0.77	0.39	0.33	0.31	0.50	0.34	0.63	0.34	1.52	1.70	1.16	0.56
Na_2O	4.05	4.67	3.82	4.42	2.62	4.99	4.58	2.74	4.73	4.78	5.65	5.60	4.24	6.65	4.85	4.56	4.34
K_2O	4.82	4.99	5.45	2.63	7.19	6.21	5.52	6.49	5.36	5.99	6.04	6.07	5.36	4.08	4.51	5.23	5.58
P_2O_5	0.06	0.02	0.04	1.23	0.15	0.10	0.07		0.05	0.14	0.14	0.23	0.06	0.21	0.06	0.06	0.06
H_2O^+															2.50	0.48	0.56
Total	98.12	98.90	99.09	98.03	99.22	98.93	97.63	94.71	98.46	99.90	99.97	99.47	98.92	99.99	100.57	100.50	100.10

*total iron as FeO.

Analyses 1 and 2 wet chemistry at University of Texas at Austin, Department of Geological Sciences, G. K. Hoops; analyses 3–14 x-ray fluorescence, except 8 by microprobe, at Baylor University, D. F. Parker; analyses 15–17 inductively coupled argon-plasma spectrometry at University of Texas at Austin, Texas Bureau of Economic Geology, S. W. Tweedy.

1. C5, Gomez Tuff, Million Dollar Canyon (Parker, 1986).
2. 81022, Cherry Canyon intrusion (Parker, 1986).
3. 84605, Ejected block, Madera Canyon.
4. 85615, Trachybasalt, Madera volcano.
5. 87602, Basal, slightly welded tuff, Barrel Springs Formation, Davis Mountains State Park.
6. 87601, Upper flow unit (lava?), Barrel Springs Formation, Davis Mountains State Park.
7. BS4, Tbsl, Barrel Springs Formation, Seven Springs Ranch, Barrilla Mountains.
8. 87603, Glass, hydrated vitrophyre block, Barrel Springs Formation, Davis Mountains State Park.
9. 84326, Granophyre, Sleeping Lion Formation, roadcut Highway 118, Limpia Canyon.
10. 85602, Star Mountain Formation, Saddleback Mountain, Barrilla Mountains.
11. 87110, Star Mountain Formation, lower unit, Wild Rose Pass.
12. 87114, Star Mountain Formation, middle unit, Wild Rose Pass.
13. 83315, Star Mountain Formation, upper unit, Wild Rose Pass.
14. 83313, Star Mountain Formation, vitrophyre (normalized to 100% from 96%), Indian Cave Canyon.
15. J85-64A, Bracks Rhyolite, vitrophyre, central area (ZH Canyon).
16. J85-72, Bracks Rhyolite, devitrified, northern area.
17. J85-76, Bracks Rhyolite, devitrified, southern area.

TABLE 3—Characteristics commonly used to discriminate rhyolite lavas from ash-flow tuffs. *Unlike rhyolite lava flows, rheomorphic tuffs may have dimensions similar to those of other ash-flow tuffs.

Common in conventional ash-flow tuffs	Common in rhyolite lavas and in rheomorphic tuffs
Fiamme	Flow banding
Eutaxitic texture	Ramp structures
Abundant lithic fragments	Elongated vesicles
Nonwelded tops, bottoms, sides	Autobreccias
Gradual thinning at edges of units	Vitrophyres at or near tops
Wide areal extent of individual units	Lengths generally much less than 20 km*
Low aspect ratio	High aspect ratio*
Glass shards in thin section	
Broken phenocrysts ranging widely in size	
Gas elutriation pipes	

from lava flows. Two significant conclusions of this trip are that many of the controversial rocks are extensive silicic lavas and that traditional characteristics do not fully distinguish their origin.

The rheomorphic tuffs and controversial rocks occur dominantly in the eastern, alkalic belt of Trans-Pecos, particularly in the Davis Mountains, but one rheomorphic tuff (Buckshot Ignimbrite; Anderson, 1975) occurs in the western, alkali-calcic belt. Stratigraphic relations of units we will examine in the eastern Davis Mountains are shown in Fig. 7. Variably rheomorphic tuffs to be examined include Gomez Tuff (Day 1) and parts of Barrel Springs Formation (Day 2). Controversial rocks include Star Mountain (Day 4), Sleeping Lion (Day 2), Adobe Canyon (Childerss, 1984), and Mount Locke Formations of the Davis Mountains, Bracks Rhyolite (Day 6) of the Sierra Vieja to the west, and Crossen Trachyte of the southern Davis Mountains. Basic data, including distribution, areal extents, volumes, and aspect ratios, are summarized in Figs. 8, 9, and 10, and Table 4. More specific information, particularly that to be observed in the field, is presented in the individual stop descriptions.

Gomez Tuff, the focus of Day 1, is a good example of a moderately rheomorphic tuff. Gomez Tuff was erupted from the Buckhorn caldera at approximately 37 Ma and spread throughout much of the Davis Mountains (Fig. 8; Parker and McDowell, 1979; Parker, 1986). In thin outcrops distant from its source, it shows no rheomorphic features. As it thickens toward its source, flow bands, folds, and ramp structures are irregularly developed. A thick section of Gomez Tuff ponded at the margin of the Buckhorn caldera has spectacular flow folds, and pyroclastic features are obliterated except for sparse lithic fragments up to 10 cm across. The primary pyroclastic origin can be demonstrated by tracing the rheomorphic part laterally into undeformed parts.

Units within the composite Barrel Springs Formation show more extreme rheomorphism. Barrel Springs is as widespread as Gomez Tuff in the Davis Mountains, occurring over a lateral distance of about 90 km (Fig. 8). Barrel Springs is composed of several separate flows, however, and the distribution of individual flow units has not been determined. Recent mapping (Henderson, 1987) suggests a caldera source in the southwestern Davis Mountains. Through most of the central part of its outcrop, Barrel Springs Formation shows only lava-flow features. However, at several locations, particularly a well-exposed section in Davis Mountains State Park (Stop 2A), unequivocal ash-flow tuff at the base passes upward into rock that has undergone such extreme secondary flow that almost all pyroclastic features are obliterated. Additionally, distal units in the northeastern Davis Mountains, considered by one of us (DFP) to be correlative with the rheomorphic tuff, are clearly ash-flow tuff.

Bracks Rhyolite, Star Mountain Formation, and a third rock to be viewed only from a distance, Crossen Trachyte, are nearly identical representatives of the controversial rocks.

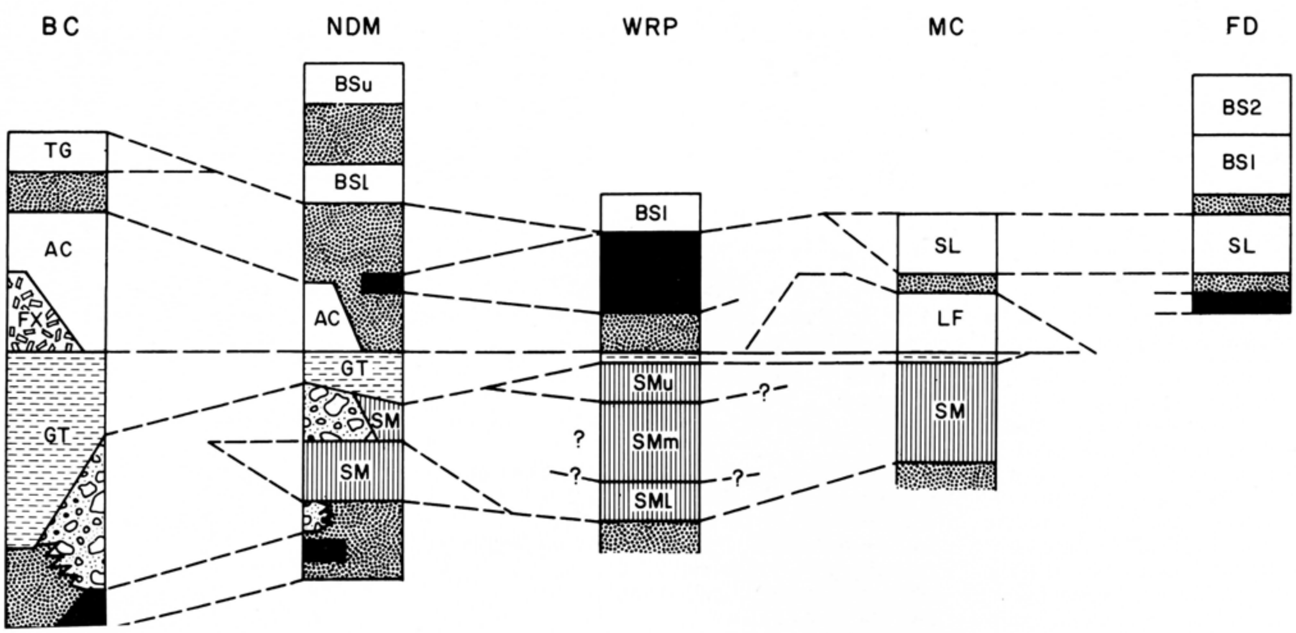

FIGURE 7—Stratigraphic relations between units exposed at five stops in the Davis Mountains. BC = Buckhorn caldera (Stop 1C); NDM = northeastern Davis Mountains (Stop 4C); WRP = Wild Rose Pass (Stop 4B); MC = Musquiz Canyon (Stops 1A and 4A); FD = Fort Davis (all stops, Day 2). Unit abbreviations: SM = Star Mountain Formation (subdivisions SMl, SMm, SMu are the lower, middle, and upper units discussed in text); GT = Gomez Tuff; FX = Fox Canyon Formation; AC = Adobe Canyon Formation; TG = rhyolite of Tricky Gap; LF = Limpia Formation; SL = Sleeping Lion Formation; BS = Barrel Springs Formation (BSu and BSl are upper and lower tuffs in northeastern Davis Mountains; BS1 and BS2 are units of Figs. 17 and 18). Other units: stippled = mostly volcaniclastic sedimentary rock; black = mafic lava; conglomerate pattern = coarse breccia.

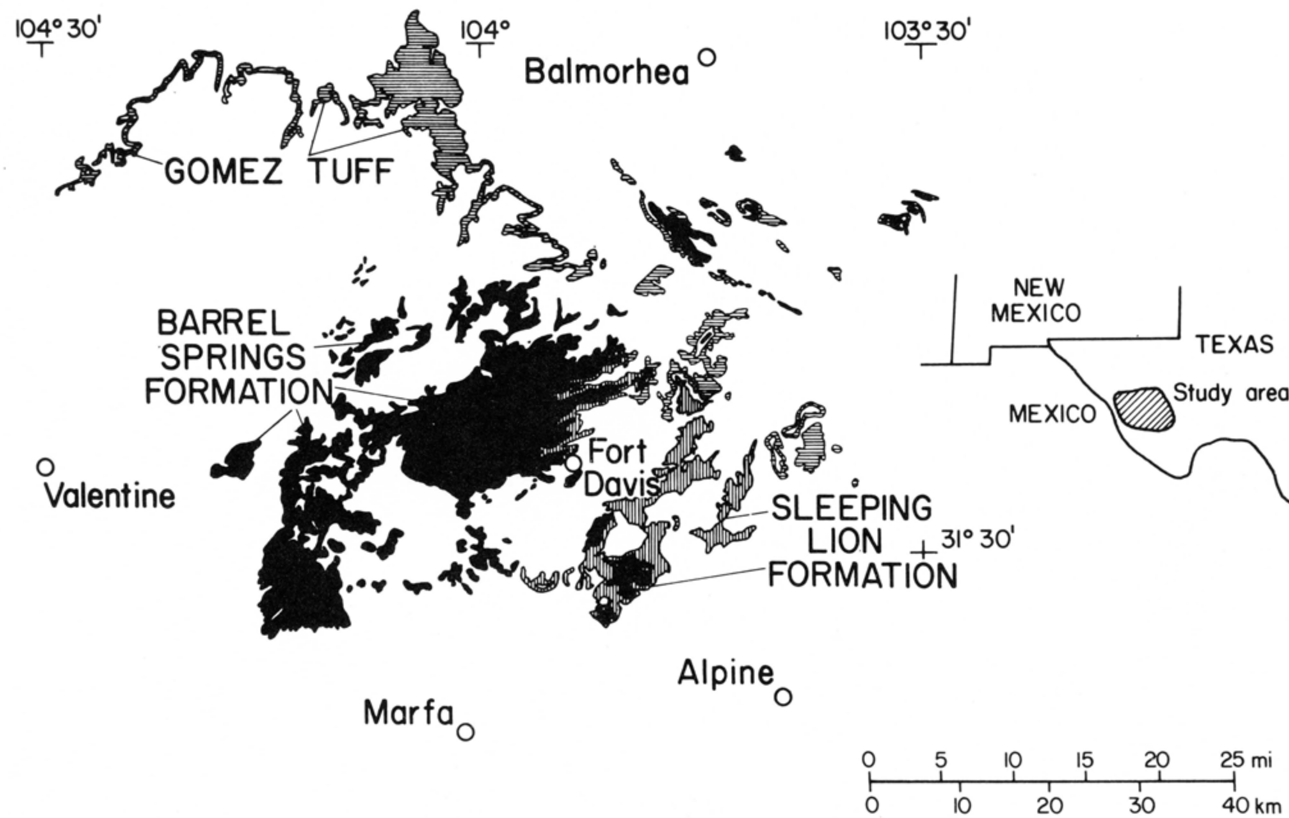

FIGURE 8—Approximate outcrop of Gomez Tuff, Sleeping Lion Formation, and Barrel Springs Formation.

Despite their various formational names, they are dominantly slightly peralkaline, silicic quartz trachytes (Table 2; SiO_2 = 68–69%, expressed H_2O free; normative acmite less than 2%). Bracks Rhyolite has lateral and areal extents of 55 km and 1000 km^2; Star Mountain Formation 70 km and 3000 km^2 (Fig. 9; Table 4). Detailed field, chemical, and mineralogic data, discussed at Stop 6A, indicate that the Bracks is a single flow over its entire outcrop. Star Mountain is composed of several flows, the individual dimensions of which are not fully established. Lava-flow features in these rocks include vitrophyres and breccias at the tops and bottoms of flows, flow-bands and flow-folds, ramp structures, and elongated vesicles. Also, they lack shards, pumice, lithic fragments, or any welding zonation. Pyroclastic-flow features include their wide areal extents, sheet-like geometries, and low aspect ratios (Fig. 10; Table 4). Additionally, viscosities calculated from chemical analyses (Fig. 11) seem too high for them to have flowed the great distances as lavas. Nevertheless, we conclude that these rocks were viscous lavas with unusually high volumes, effusion rates, or heat retention that allowed them to flow long distances. Similarity in outcrop characteristics, phenocryst mineralogy, composition, stratigraphic occurrence, and age of the Bracks, Star Mountain, and Crossen lead Henry et al. (1988a) to suggest that a unique event at 38 Ma in Trans-Pecos Texas produced nearly identical rocks.

The origin of Sleeping Lion Formation is still debated. It shows dominantly lava-flow features similar to the Bracks and Star Mountain. Additionally, it contains rare lithic fragments and debatable, fiamme-like structures. It is less widespread than the other units, occurring in an area about 30 km across (Fig. 8). Hicks (1982) suggested that it was erupted from a source west of Ft. Davis. Outcrop pattern and sparse flow-direction indicators suggest that it flowed down a paleovalley system, first northeast, then southeast and southwest. Total flow distance would have been about

TABLE 4—Areal extents and age of silicic volcanic units, Trans-Pecos Texas. [1]K–Ar age from Henry et al. (1986); [2]Composite units; [3]Thicknesses of outflow sheets only; volume includes caldera fill.

Unit	Lateral extent (km)	Thickness Average	Thickness Maximum	Area (km^2)	Volume (km^3)	Aspect ratio	Age[1] (Ma ± 1σ)
Bracks Rhyolite	55	50	120	1000	50	1:700	37.5 ± 1.2
Star Mountain Formation[2]	70	80	240	3000	240	1:600	37.9 ± 0.8
Crossen Trachyte	>50	50	90	1500	75	1:700	38.6 ± 1.6
Sleeping Lion Formation	30	50	100	600	30	1:400	37.1 ± 0.8
Barrel Springs Formation[2]	80	80?	130	>3000	300	1:600	36.4 ± 0.3
Gomez Tuff	80	25[3]	105[3]	4300	250	1:1200	37.4 ± 0.8
Adobe Canyon Formation[2]	55	100	300	1250	125	1:200	38.0 ± 0.8
Buckshot Ignimbrite	85	11[3]	19[3]	2000	30	1:3300	37.2 ± 0.8
Mitchell Mesa Rhyolite	180	30[3]	110[3]	24,000	1000	1:5800	32.3 ± 0.7

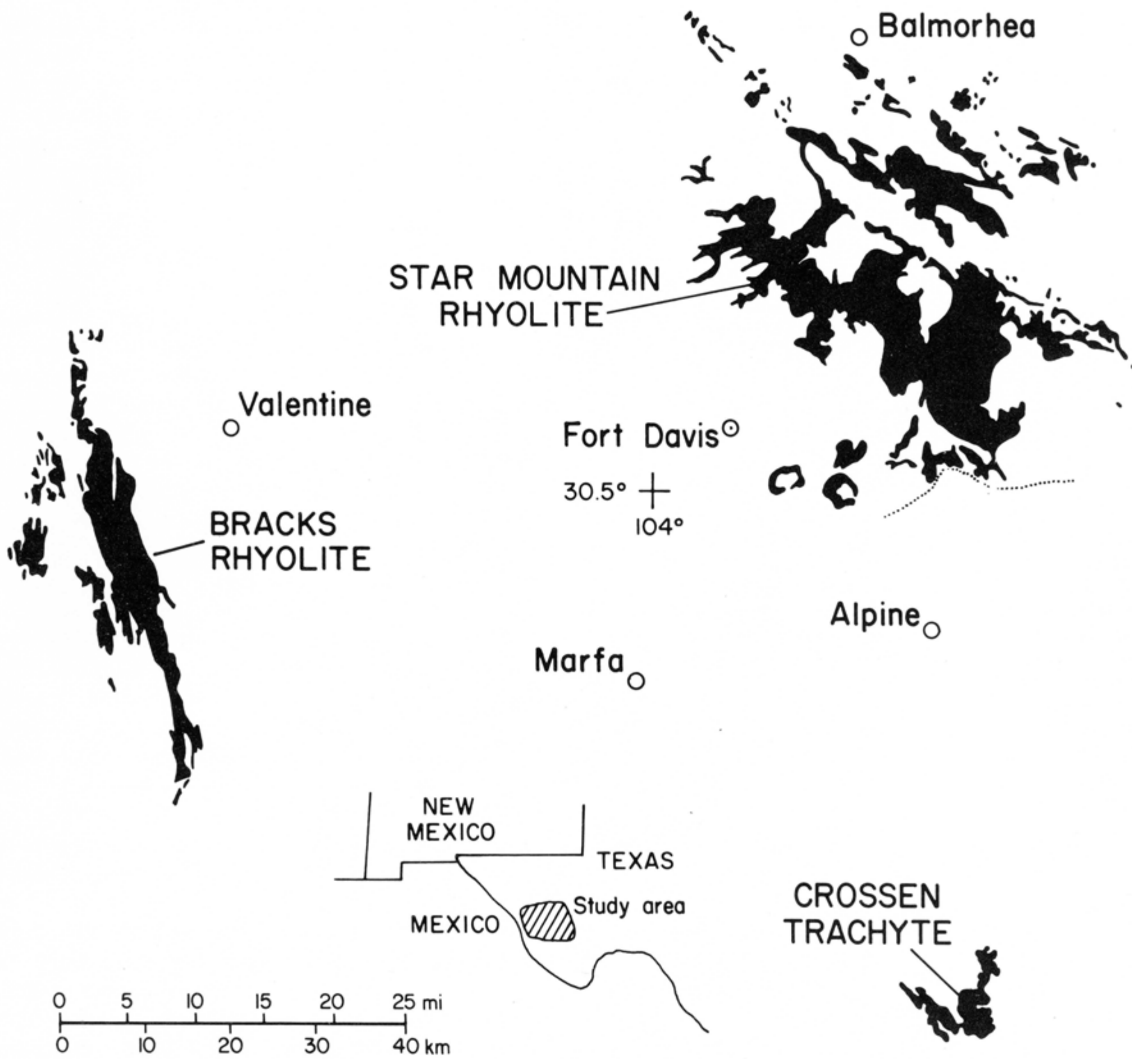

FIGURE 9—Approximate outcrop of Bracks Rhyolite, Star Mountain Formation, and Crossen Trachyte. Rock previously mapped as Crossen Trachyte in the vicinity of Alpine is mafic trachyte unrelated to true Crossen, which is petrographically similar to Bracks and Star Mountain.

40 km. No source, caldera or otherwise, has been identified for Sleeping Lion. One of us (JAW) suggests an origin as an ash-flow tuff in which primary laminar viscous flow and extreme rheomorphism obliterated primary internal features.

Road log and stop discussions

Day 0: El Paso to Alpine, Texas

Day 0 consists of a 216-mile drive from the El Paso airport, where we will meet field-trip participants, through Van Horn and Marfa to Alpine, which will be our base for the entire trip (Fig. 2). We will make no geologic stops this day, and much of the drive will be in the evening. However, we will return to El Paso along the same route on the sixth day, when features will be observable. A more detailed road log is presented in Price et al. (1986). Maps of the Geologic Atlas of Texas (1:250,000) depict the regional geology of the trip.

Day 1: Gomez Tuff

Summary—Today's trip examines Gomez Tuff, a peralkaline ash-flow tuff erupted from the Buckhorn caldera in the northeastern Davis Mountains, and the related Cherry Canyon intrusion, the most strongly peralkaline rock of Trans-Pecos Texas. Gomez Tuff is the most widespread volcanic unit in the Davis Mountains, cropping out over an area of about 4000 km^2 with a restored initial volume of about 200 km^3 (Parker, 1986). It contains about 10% phenocrysts, largely alkali feldspar (Or38), but also quartz, ferrohedenbergite, ilmenite, and rare fayalite. Fresh samples are uniformly peralkaline (6% normative acmite); unoxidized samples contain groundmass acmite, arfvedsonite, and aenigmatite. The unit contains abundant lithic fragments, mostly basalt and rhyolite from the older Huelster Formation, and associated xenocrysts.

Gomez Tuff varies from a relatively normal ash-flow tuff in thinner, more distal sections to strongly rheomorphic in thicker, more proximal sections, particularly within its source caldera. Stop 1A is a 3 m thick section of Gomez near its southern known limit. Stop 1B is a thicker section within a few kilometers of the caldera margin. Stop 1C is just within the southern margin of the caldera; Gomez there has developed spectacular secondary flow structures.

Mileage

0.0 The roundtrip of about 190 mi starts in Alpine from the intersection of US-90 and TX-118N. Proceed north on TX-118. **4.0**

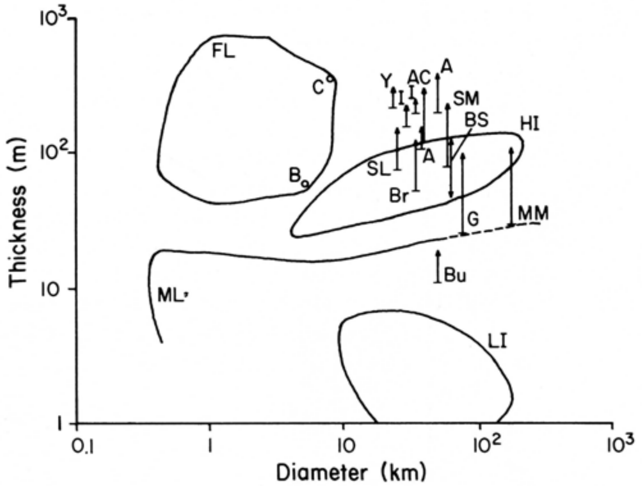

FIGURE 10—Plot of thicknesses vs. diameter of a circle with an area equal to that of unit, showing fields for mafic lavas (ML), felsic lavas (FL), and low- and high-aspect ratio ash-flow tuffs (LI and HI). Fields are from Walker (1973, 1983) and J. A. Wolff and S. Self (unpubl. data). Vertical lines indicate estimated average thickness (base) and maximum thickness (top). Trans-Pecos rocks: SL = Sleeping Lion Formation; Br = Bracks Rhyolite; AC = Adobe Canyon Formation; SM = Star Mountain Formation; BS = Barrel Springs Formation; G = Gomez Tuff; MM = Mitchell Mesa Rhyolite; Bu = Buckshot Ignimbrite. Latter three are definite ash-flow tuffs; Adobe Canyon, Star Mountain, and Barrel Springs are composite units. Other symbols are rocks interpreted to be extensive silicic lava flows: Y = Yellowstone (Pitchstone Plateau flow; data from R. L. Christiansen, pers. comm. 1987); I = Idaho (Sheep Creek and Dorsey Creek flows; Bonnichsen and Kauffman, 1987); A = Australia (Cas, 1978). Within FL, B = Banco Bonito lava and C = Chao Dacite (Guest and Sanchez, 1969).

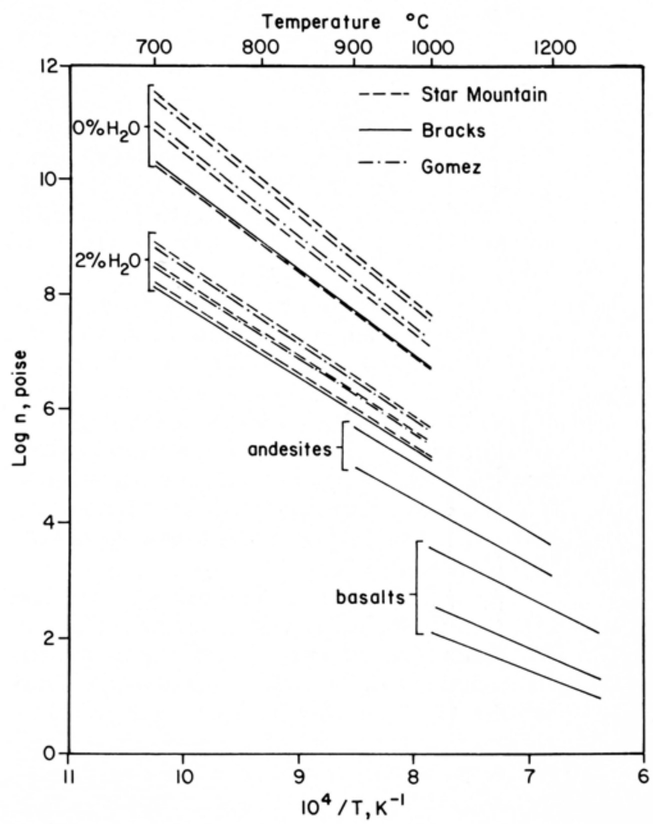

FIGURE 11—Viscosities of selected Trans-Pecos silicic magmas as functions of temperature. Viscosities are calculated by the method of Shaw (1972), using published chemical compositions: Parker (1986) and Gibbon (1969) for Star Mountain Formation, Parker (1986) for Gomez Tuff, and Henry et al. (1988a) for Bracks Rhyolite. For comparison, viscosities of typical andesites and basalts (Carmichael et al., 1974) are also shown. Water contents are values of H_2O^+.

4.0 On the west, quartz trachyte lava flows of the Decie Formation form the distal part of the lava shield of the Paisano volcano (Parker, 1976, 1983). The volcano erupted a series of lavas and subordinate ash-flow tuffs about 36 Ma. The rocks range in composition from peralkaline rhyolite to mafic trachyte. **5.8**

9.8 Barillos dome, one of several small laccoliths in the southern Davis Mountains, forms the hill on the west. The central intrusion, composed of peralkaline rhyolite and trachyte, uplifted Star Mountain Formation, the focus of Day 4. On the east side of the highway, Sleeping Lion Formation overlies mafic lava and tuffaceous sediment of Frazier Canyon Formation. **5.2**

15.0 **STOP 1-A. Distal Gomez Tuff and top of Star Mountain Formation.** This roadcut provides an introduction to Gomez Tuff in a thin (3 m thick), distal part where its pyroclastic origin is obvious. The outcrop is typical in that it is densely welded even though only a few meters thick. Basal nonwelded zones are thin; upper nonwelded zones have been found only where the unit is protected from erosion by overlying lavas. At this location, densely welded rock overlies about 30 cm of highly altered, basal ash; an upper, nonwelded part may have been stripped off. A vitrophyre about 70 cm thick overlies the basal ash. Sparse lithic fragments show normal grading from about 2 cm diameter in vitrophyre to no more than 1 cm in devitrified parts. Pumice appears to be reversely graded, ranging up to 30 cm long in upper, devitrified rock. Much of the pumice is granophyrically devitrified. Evidence of rheomorphism is absent where the Gomez is thin, although pumice elongation occurs in some outcrops. Vitrophyres show shard texture and flattened pumice.

Gomez overlies zeolitic, biotite-bearing tuffaceous sediment, which in turn overlies breccia in the top of Star Mountain. As with most pyroclastic rocks of the Davis Mountains, pyroclastic-fall deposits preceding the flows are rarely preserved. The sediment is typical of many of the soft, tuffaceous lenses that are interbedded with the more massive rocks of the Davis Mountains. The tuffs may not have erupted from local sources, because biotite is uncommon in the typically peralkaline rocks of the Davis Mountains. More likely sources are the calderas of the western, alkali-calcic belt in Texas or Chihuahua. The presence of biotite also rules out any connection between the ash and underlying Star Mountain Formation.

Star Mountain here consists of silicified upper breccia containing angular to subrounded clasts up to 20 cm of massive to vesicular rock in a matrix of finer clasts. All fragments are Star Mountain; accidental lithics are absent. The clasts commonly contain elongate vesicles. These features are typical of lava flows. **8.5**

23.5 TX-17 comes in from the left (west) at the outskirts of Fort Davis. **1.0**

24.5 Fort Davis National Historic Site. The fort was established in 1854 to protect the region from Indian raids; it was manned by "buffalo soldiers," units of black cavalry and infantry. The cliffs above the restored fort are Sleeping Lion Formation. **0.4**

24.9 Highways 118 and 17 split. Follow TX-17 northeast toward Balmorhea. **6.3**

31.2 We are entering the narrow part of Frazier Canyon, which is cut into Star Mountain Formation dipping gently to the southwest. For about the next 8 mi, Star Mountain Formation forms steep cliffs along the highway. **8.8**

40.0 The high ridge on the west is Star Mountain, source of the formation's name. **3.0**

43.0 Barrel Springs Formation is exposed next to the highway on the west and for the next several miles. In these distal outcrops, it is composed of three distinct ash-flows that form the three cuestas. Barrel Springs occupies the core of the Rounsaville syncline, a broad, open fold that probably resulted from sag into a minor Basin and Range graben. **6.0**

49.0 Turn left (west) on FM-1832. **9.4**

58.4 **STOP 1-B. Moderately rheomorphic Gomez Tuff at Million Dollar Canyon.** The Gomez Tuff is located on the downthrown side of a Basin and Range fault (Fig. 12). Displacement along this fault is estimated at 200 m, with the downdropped block tilted about 10°, partly due to drag.

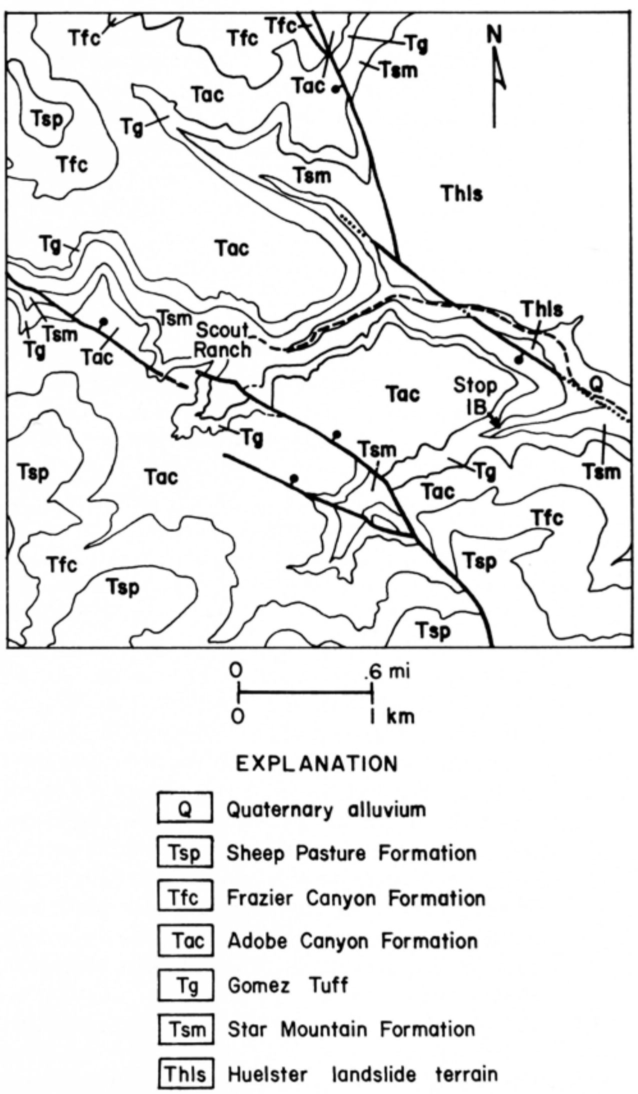

FIGURE 12—Geologic sketch map of Million Dollar Canyon area showing location of Stop 1B.

Gomez Tuff is about 100 m thick in this section, which is located approximately 7 km south of the rim of the Buckhorn caldera, source of the tuff (Parker, 1986). The tuff is densely welded throughout, although the density decreases upwards due to development of lithophysal cavities in the upper part of the unit. It overlies several meters of bedded tuff, which in turn overlies Star Mountain Formation. Gomez Tuff is overlain by basal breccia of Adobe Canyon Formation, a unit similar to Star Mountain Formation, but having higher silica and lower total iron (Table 2).

The base of Gomez Tuff is planar and, although flow bands are contorted and folded, breccia is absent (Fig. 13a). The lower several meters of the tuff has fewer total phenocrysts than typical and contains the only fayalite found in the unit. The groundmass throughout this entire section is granophyrically recrystallized; it typically is flow-banded and grades from green near the base upwards to blue in the center of the exposure due to changing relative abundances of green acmitic clinopyroxene and blue sodic amphibole in the groundmass. The upper part of the unit is oxidized. Rock fragments are present throughout the section; typically, these are smaller than 30 cm in diameter. The upper part of the unit contains stretched, vapor-phase-altered pumice, ramp structures, and large recumbent flow folds. Return to vehicles and retrace route to TX-17. **9.4**

67.8 Back at TX-17. Turn left toward Balmorhea. **6.8**

74.6 Intersection of TX-17 and US-290. Turn left on 290. **3.4**

78.0 Intersection of US-290 and Shannon Ranch Road. Turn left onto ranch road toward Madera Canyon. **WARNING: ALL PROPERTY ALONG THIS ROAD IS PRIVATE. PERMISSION TO ENTER MUST BE OBTAINED FROM LANDOWNERS. 10.7**

88.7 **STOP 1-C. Strongly rheomorphic Gomez Tuff at margin of Buckhorn caldera.** Madera Creek, one of the major drainages of the Davis Mountains, has cut a 500 m deep canyon along part of the southern margin of the Buckhorn caldera. Geologic units exposed include Cretaceous limestone, trachybasalt and lahar associated with a small volcano, tuff breccia and nonwelded pyroclastic flows at the margin of a rhyolitic dome, trachyte lava, and Gomez Tuff (Figs. 13b, 14).

Gomez Tuff ponded to thickness of more than 450 m in the Buckhorn caldera (Parker, 1986). In the Madera Canyon area, the tuff thickens across the caldera margin from 60 to 300 m over a lateral distance of 1.6 km. Extreme rheomorphism due to laminar flow during and after compaction has produced spectacular flow folds in the lower part of the tuff here (Fig. 13c). The great thickness, considerable paleorelief, and peralkaline composition probably aided secondary flow. Nearly horizontal columnar joints in the lower part of the unit suggest cooling against topographic walls. Evidence for pyroclastic origin has been largely obliterated, except for common rhyolite and basalt inclusions. Vi-

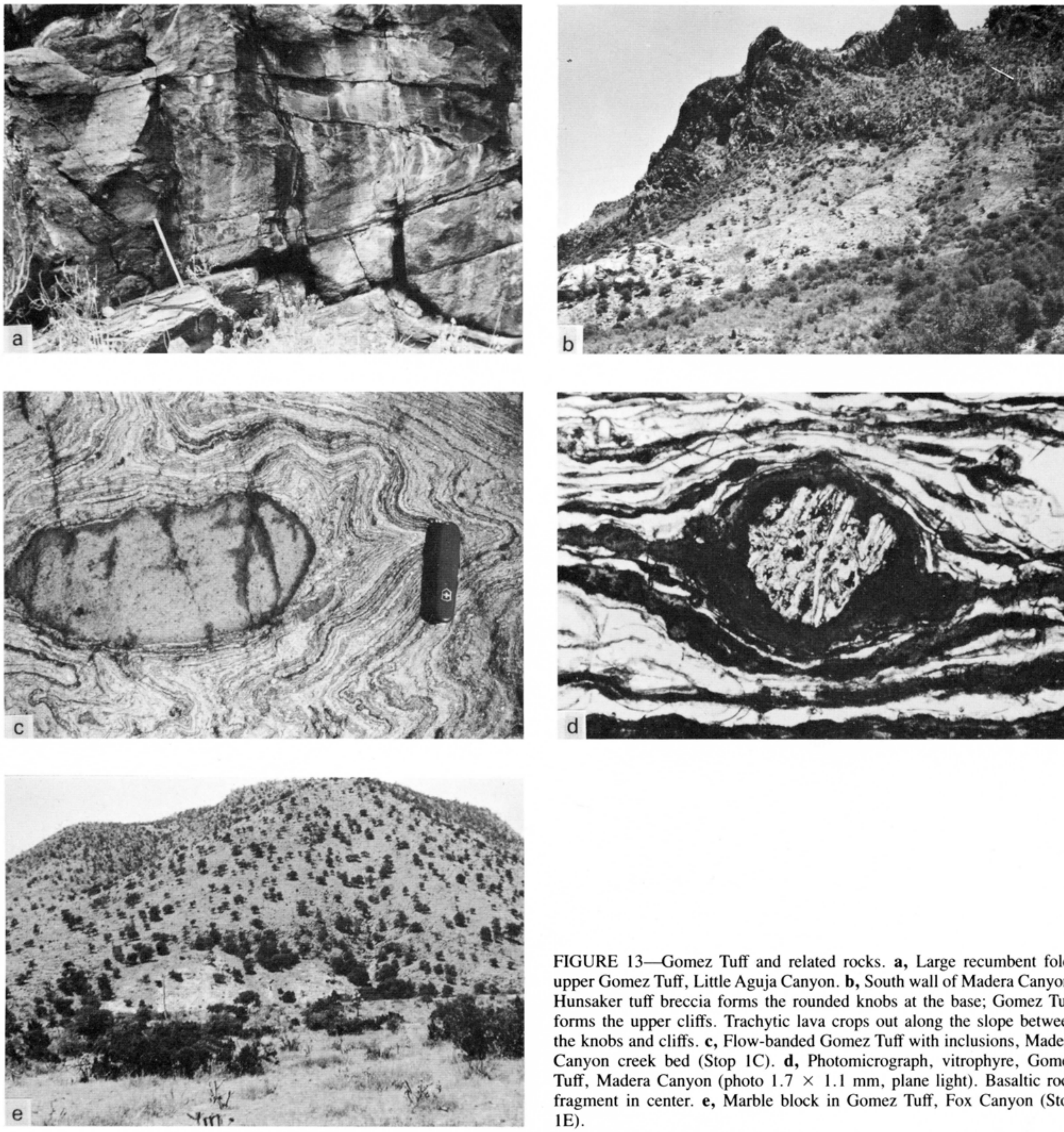

FIGURE 13—Gomez Tuff and related rocks. **a,** Large recumbent fold, upper Gomez Tuff, Little Aguja Canyon. **b,** South wall of Madera Canyon. Hunsaker tuff breccia forms the rounded knobs at the base; Gomez Tuff forms the upper cliffs. Trachytic lava crops out along the slope between the knobs and cliffs. **c,** Flow-banded Gomez Tuff with inclusions, Madera Canyon creek bed (Stop 1C). **d,** Photomicrograph, vitrophyre, Gomez Tuff, Madera Canyon (photo 1.7 × 1.1 mm, plane light). Basaltic rock fragment in center. **e,** Marble block in Gomez Tuff, Fox Canyon (Stop 1E).

troclastic texture is locally preserved in the oxidized upper part of the unit and in one exposure of vitrophyre where the tuff was chilled against a steep valley wall (Fig. 13d). Recognition of an ash-flow origin is based on the lithic fragments, local preservation of shards, and correlation with unequivocal ash-flow tuff outside the caldera.

At several localities, large boulders (as much as 3 m in diameter) of angular to rounded peralkalic microgranite and marble directly underlie Gomez Tuff. The presumably ashy matrix of this deposit has not been observed due to the thick grassy cover of the hillsides. The microgranite is chemically similar to, but more evolved than, Gomez Tuff (Table 2) and is both chemically and petrographically similar to Cherry Canyon intrusion (Stop 1D today). The boulders most likely represent selvage and metamorphosed country rock from the peralkalic magma system underlying the caldera source of Gomez Tuff.

The 39 Ma Madera volcano produced the oldest igneous rocks in the Davis Mountains; thick, localized flows of trachybasalt overlie Cretaceous strata. It may have also been the source for more widespread basaltic lava within Huelster Formation of the northeastern Davis Mountains. Lava associated with the volcano was quartz-normative, unlike the largely nepheline- or hypersthene–olivine-normative basaltic rocks common in main-phase Davis Mountains rocks, and falls off the most common trends on some major-element plots of main-phase rocks as well (Fig. 6). Parker (1986) demonstrated that it was possible to derive Gomez Tuff from sim-

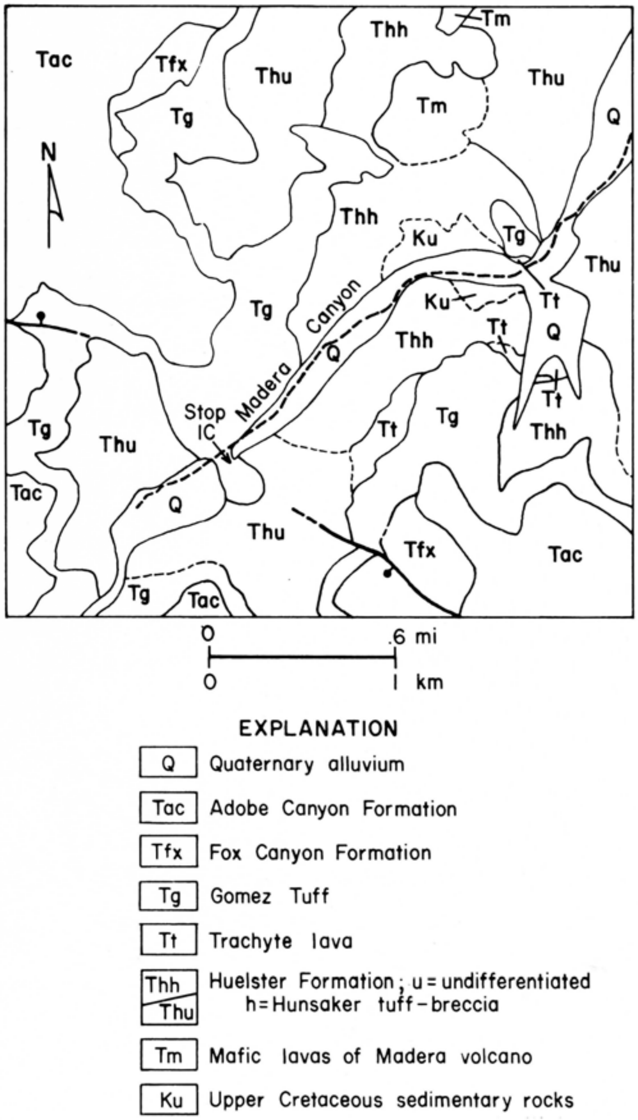

FIGURE 14—Geologic sketch map of the Madera Canyon area. Stop 1C is in the Madera Canyon creek bed, where it crosses Gomez outcrop.

ilar magma through a trachyte intermediate stage by 89 wt% crystallization of phenocrysts.

Hunsaker tuff breccia forms thick (up to 300 m) exposures along the southern margin of Madera Canyon. It consists of massive to crudely bedded, poorly sorted blocks of nearly aphyric rhyolite, and probably represents part of a silicic dome complex erupted along the southern margin of the Buckhorn caldera. The tuff breccia overlies the Madera volcano flows and is surrounded by nonwelded pyroclastic flows that contain abundant angular fragments of the same rhyolite and may have been derived from the same dome or complex of silicic domes that produced the tuff breccia. Abundant rhyolite inclusions within parts of Gomez Tuff are fragments of this and similar domes in the northern Davis Mountains. No chemical analyses have yet been made of the tuff breccia; mineralogically, it closely resembles Adobe Canyon Formation, which consists of low-silica rhyolite flows that directly overlie Gomez Tuff in part of Madera Canyon. The tuff breccia is overlain by local trachyte lava flows and, in places, by either Gomez Tuff or the boulder deposits associated with the base of Gomez Tuff. Return to vehicles and retrace route to US-290. **10.7**

99.4 Intersection with US-290. Turn left (west) toward Van Horn. **10.2**

109.6 Turn left (southwest) off US-290 onto Cherry Canyon road. **9.0**

118.6 **STOP 1-D. Strongly peralkaline granophyric intrusion containing arfvedsonite, acmite, and aenigmatite.** Although we have driven almost 30 mi (48 km) from Stop 1C, we are located only 5 km northwest of Madera Canyon and still within the Buckhorn caldera. Gomez Tuff forms the thick (~340 m) exposures flanking the entrance to Cherry Canyon. The low hill in front of the canyon mouth is underlain by Cherry Canyon intrusion, one of the most peralkalic rocks of the Trans-Pecos province (Table 2). The intrusion is composed of equigranular, fine-grained, granophyric microgranite, texturally identical to the ejected microgranite boulders. The most abundant mineral is microperthitic alkali feldspar; quartz forms "comma"-shaped, radiating blebs intergrown with the feldspar; mafic minerals include acmitic clinopyroxene, arfsvedsonite, and aenigmatite (Table 5).

The intrusion is chemically similar to, but more evolved than, Gomez Tuff (Table 2). Contacts between the intrusion and other rocks have not been observed; Gomez Tuff does not appear to have been domed by the intrusion. It is possible that the intrusion may represent a pre-Gomez dome complex, but the microperthitic feldspar suggests a shallow intrusive origin.

The Gomez magma system may have evolved from a peralkaline, relatively iron-enriched, silicic parental magma similar in composition to flows of the Star Mountain Formation (Figs. 15, 16; Parker, 1986). In this model, the Cherry Canyon intrusion and Gomez Tuff would have formed by differentiation in a cupola above a regional batholith of Star Mountain compositions. Parker (1986) suggested that another magma system related to Adobe Canyon Formation was coeval with that of Gomez Tuff; this magma system also generated silicic products, but these are less peralkaline and have lower iron contents. The tuff breccias of Madera Canyon and Indian Cave Canyon (Stop 4C) may be related to this other silicic system. **6.7**

125.3 **STOP 1-E. Limestone megabreccia in Fox Can-**

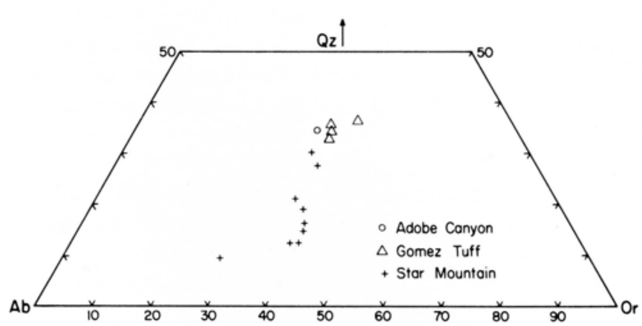

FIGURE 15—Analyses of Star Mountain Formation, Adobe Canyon Formation, and Gomez Tuff, Cherry Canyon intrusion and an ejected block (triangles) plotted in *qz–ab–or* system.

TABLE 5—Microprobe analyses of selected mafic minerals; Gomez Tuff, Cherry Canyon intrusion, and ejected block.

	1	2	3	4	5	6	7	8	9
SiO_2	47.9	51.4	52.7	52.4	41.1	42.7	49.5	50.5	49.74
TiO_2	0.40	0.52	2.02	2.34	7.84	7.96	0.27	1.21	1.46
Al_2O_3	0.12	0.25	0.27	0.37	0.38	0.00	0.21	0.00	0.18
Fe_2O_3*	3.28	27.3	24.3	29.6	3.54	0.83	4.85	4.56	5.47
FeO	27.4	5.60	5.70	0.90	38.5	40.4	30.4	29.4	29.1
MnO	1.68	0.22	1.10	0.54	1.26	1.42	1.53	1.27	1.28
MgO	0.23	0.02	0.06	0.03	0.05	0.09	0.48	0.05	0.07
CaO	18.3	2.43	0.00	0.11	0.14	0.31	1.88	0.51	0.83
Na_2O	0.97	11.4	12.4	13.6	7.04	7.02	7.45	8.68	8.48
K_2O	0.10	0.03	0.13	0.00	0.04	0.00	1.58	1.54	1.58
Total	100.4	99.2	98.7	99.9	99.9	100.7	98.2	97.7	98.2
Si	1.975	2.010	2.050	2.003	5.914	6.072	7.981	8.084	7.954
Al^{IV}	0.006				0.064	0.000	0.040	0.000	0.034
Al^{VI}		0.012	0.012	0.017					
Ti	0.012	0.015	0.059	0.067	0.849	0.852	0.033	0.146	0.176
Fe^{+3}	0.102	0.804	0.712	0.851	0.383	0.089	0.589	0.550	0.659
Fe^{+2}	0.943	0.183	0.186	0.029	4.632	4.812	4.053	3.938	3.894
Mn	0.059	0.007	0.036	0.018	0.154	0.171	0.209	0.172	0.173
Mg	0.014	0.001	0.004	0.002	0.011	0.019	0.115	0.012	0.017
Ca	0.807	0.102	0.000	0.004	0.022	0.047	0.325	0.082	0.142
Na	0.078	0.864	0.935	1.009	1.965	1.938	2.331	2.695	2.629
K	0.005	0.002	0.006	0.000	0.007	0.000	0.325	0.315	0.322
at% Na	7.1	81.9	80.6	95.5		Sum C	5.000	4.906	5.000
Fe^{+2}+Mn	91.6	18.0	19.1	4.4		Sum B	2.000	2.000	2.000
Mg	1.3	0.1	0.3	0.1		Sum A	1.000	1.010	1.000

1. Average 12 point analyses clinopyroxene phenocrysts, Gomez Tuff.
2. Groundmass clinopyroxene, Gomez Tuff.
3. Clinopyroxene, Cherry Canyon intrusion.
4. Clinopyroxene, ejected block.
5. Groundmass aenigmatite, Gomez Tuff.
6. Aenigmatite, Cherry Canyon intrusion.
7. Groundmass amphibole, Gomez Tuff.
8. Amphibole, Cherry Canyon intrusion.
9. Amphibole, ejected block.

*Fe_2O_3 calculated by charge balance.

yon. At the mouth of Fox Canyon, a 100 m block of marbleized limestone is surrounded on three sides by rheomorphic Gomez Tuff (Fig. 13e); the base of the limestone is not exposed. At other, less accessible localities, tuff entirely encloses blocks. Along the margin of the block, Gomez Tuff intruded along fractures formed when marginal splinters rotated away from the main mass of limestone. Adjacent to the block, Gomez is eutaxitic. The block probably represents part of a failed caldera wall. It is uncertain whether the block was metamorphosed in-situ or before incorporation into the tuff. The marble has not been studied in detail; a single thin section from the block shows only recrystallized calcite. The eruptive temperature of the tuff is unknown; an estimate based upon extrapolation of Fe–Ti-oxide geothermometry from less evolved units in the Davis Mountains suggests that the tuff was about 800° C (D. F. Parker, unpubl. data).

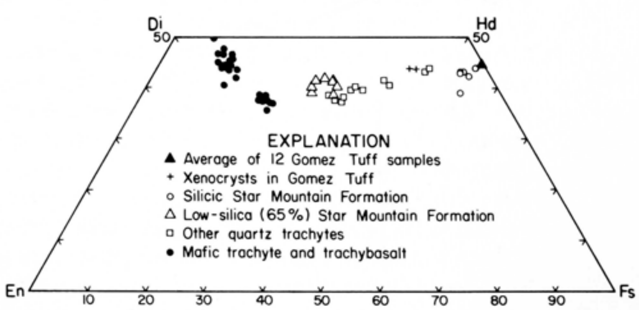

FIGURE 16—Clinopyroxene phenocrysts of northeastern Davis Mountains rocks plotted in terms of atomic percent Ca-Mg-(Fe^{+2} + Mn). Analyses by D. F. Parker.

Day 2: Rheomorphic ash-flow tuff of the Barrel Springs Formation

Summary—We will examine Barrel Springs and Sleeping Lion Formations in and around Davis Mountains State Park and Fort Davis Historic Site. Barrel Springs shows a transition upward from typical eutaxitic ash-flow tuff to strongly rheomorphic ash-flow tuff. Sleeping Lion Formation is somewhat more enigmatic. It shows dominantly lava-flow features, but some textures possibly suggestive of a pyroclastic origin are also preserved.

Mileage

0.0 Today's roundtrip is about 60 mi, starts at US-90 and TX-118N, and follows the same route as Day 1 to the intersection where TX-118 and TX-17 fork north of Fort Davis. **24.9**

24.9 Intersection of TX-118 and TX-17. Turn left (west) onto TX-118 toward Kent. Continue 2.8 mi to Davis Mountains State Park. Enter Park and take scenic drive that climbs through Barrel Springs Formation. **3.5**

28.4 **STOP 2-A. Rheomorphic Barrel Springs Formation along Scenic Drive in Davis Mountains State Park.** Barrel Springs Formation at this location is approximately 140 m thick and consists of at least two and possibly three flow units (Figs. 17, 18). The lowest (first) unit is approximately 100 m thick and shows a transition from normal ash-flow tuff in the base to strongly rheomorphic (flow-folded and brecciated) tuff within the upper part. Upper units share some similarities with the first unit and may also be rheomorphic tuffs, but show only lava-flow features. Stop 2A begins at the first

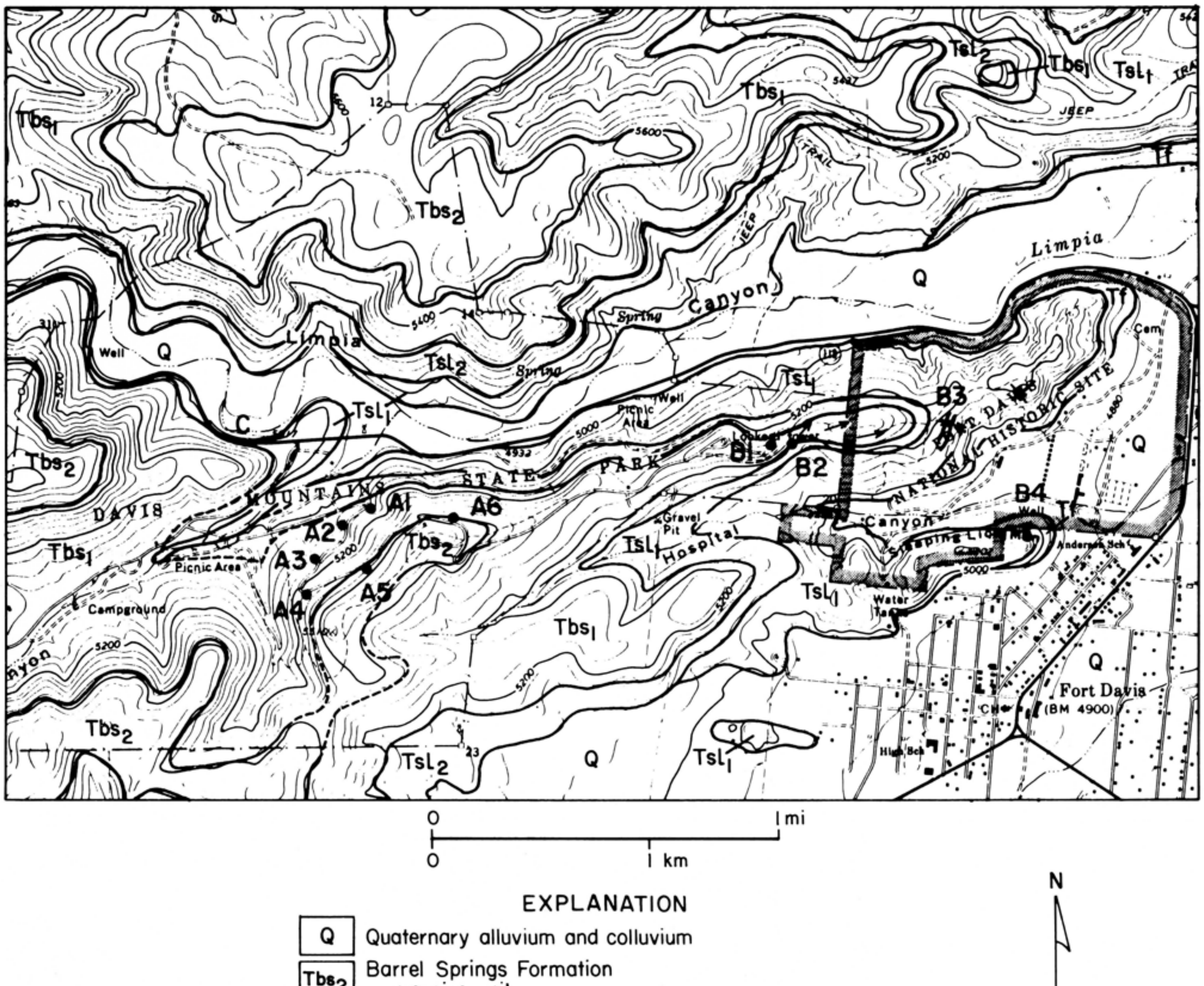

EXPLANATION

Q	Quaternary alluvium and colluvium
Tbs_2	Barrel Springs Formation massive unit
Tbs_1	glassy flow breccias overlying a lower massive unit, which overlies vitric tuff
Tsl_2	Sleeping Lion Formation tuffaceous sandstone overlying crystal tuffs, which overlie flow breccia
Tsl_1	massive unit
Tf	Frazier Canyon Formation tuffaceous sandstone overlying mafic flow

FIGURE 17—Geologic map of Davis Mountains State Park area, showing rock units and stops to be examined on Day 2.

hairpin turn on the scenic drive. From there we will hike up along the drive, examining nearly continuous roadcuts in all three units.

The first unit has a 4 m thick base of devitrified ash-flow tuff (Fig. 18; location A1). The tuff contains phenocrysts of alkali feldspar that increase in abundance from about 5% near the base to 10% near the abrupt transition to overlying foliated tuff. An oxidized mafic mineral, probably clinopyroxene, is the only other phenocryst. The feldspar phenocrysts are mostly 2–4 mm across and euhedral, but smaller broken fragments characteristic of ash-flow tuffs are also present. Nevertheless, some delicate-textured gomerocrysts as much as 6 mm in diameter apparently survived pyroclastic eruption and emplacement. Moderately flattened pumice fragments, rarely up to 20 cm long (Fig. 19a), and sparse lithics of fine-grained trachyte(?) to 2 cm comprise a few percent of the rock. Individual shards are quite large, commonly up to 2 mm (Fig. 19b), and indicate unusually coarse vesiculation during eruption. Many phenocrysts have thick, formerly glassy rims (Fig. 19b). Welding increases upward, from poorly welded near the base to moderately welded at the transition. Vertical gas-escape pipes, enriched in phenocrysts, occur in the upper 2 m of the base and are truncated at the transition to foliated tuff (Fig. 19c).

An abrupt contact with overlying foliated tuff occurs about 5 m above the base, but the transition

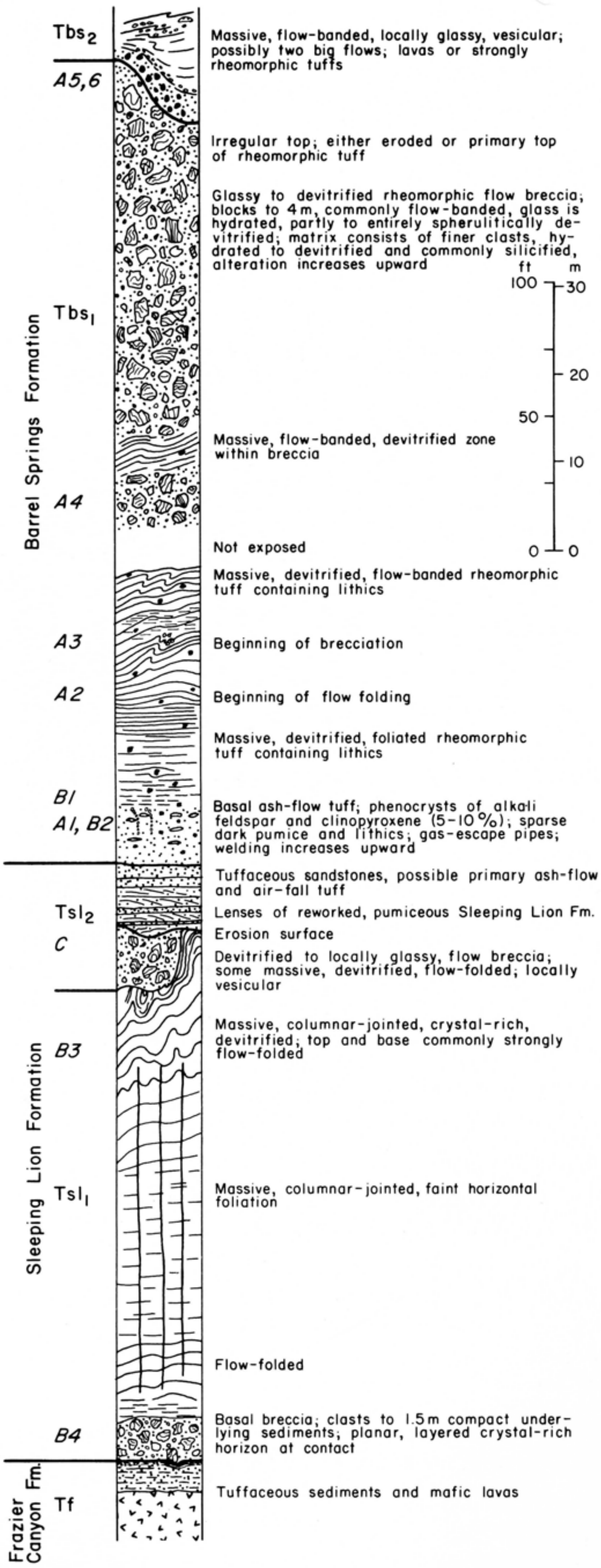

FIGURE 18—Composite stratigraphic section of Barrel Springs and Sleeping Lion Formations, Davis Mountains State Park (with contributions from S. Self, pers. comm. 1987). Stops of Day 2 on left side of section.

starts about 50 cm below the contact. At that point, the gas-escape pipes bend toward N80E (Fig. 19c), and the tuff develops short, indistinct foliations that appear to be incipient to the distinct foliation in rock above the contact. In outcrop, the rock is still clearly pyroclastic, but in thin section shard texture is largely obscured. Curvature of the gas pipes and distinct lineations in Barrel Springs at Stop 2B indicate that secondary flow of the rheomorphic tuff was slightly north of east. The amount of curvature indicates about 40–70 cm displacement just below the contact with distinctly foliated tuff. Pyroclastic features disappear over a few centimeters distance at the contact, and a distinct planar foliation consisting of 1–10 cm long partings spaced about 1 cm apart develops (Fig. 19c). These partings increase in length upward and may represent shear planes within the rheomorphic tuff. Scattered lithic fragments, identical to those in the underlying rock, are the only preserved evidence of the primary pyroclastic origin (Fig. 19d). These lithics range up to 11 cm in diameter and are found at least into the upper brecciated part of the first unit. Foliation wraps around lithics, some of which are rotated, further indicating secondary flow. Other pyroclastic features, such as pumice, shards, or gas pipes, are not preserved in the foliated tuff. Nevertheless, the lithics, sharp but still gradational contact, and similarity in size, abundance, and composition of alkali-feldspar phenocrysts tie the foliated rock to the basal tuff. Also, the lack of a breccia at the base of the foliated rock indicates that it is not a later lava flow.

Upward through the section, but before the next hairpin, the foliation becomes more pronounced and closer-spaced (about 0.5 cm). Broad, open folds begin to develop; dips on foliation gradually increase and reach 40° (Fig. 17; location A2). In places a second foliation consisting of short, nearly flat partings cross-cuts the more prominent, dipping foliation.

More pronounced folds and minor breccias first appear near the hairpin. The foliation has become more a distinct flow banding, rather than a parting, that shows contorted, almost ptygmatic folds (Fig. 17; location A3). Breccias are minor but mark the beginning of brittle failure of rheomorphic tuff.

Above a brief covered interval at the hairpin, the lowest unit is intensely flow-folded and, except for one 10 m interval, entirely brecciated (Figs. 19e and 17; location A4); breccias and flow folds within fragments persist to the top of the unit. The folds are commonly recumbent; much of the flow-banding is vertical. Blocks in the breccia range up to 2 m in diameter and are angular to moderately rounded. Breccia fragments and matrix grade irregularly from glassy and hydrated to spherulitically devitrified. Feldspar phenocrysts are similar to those in lower parts; that is, they are mostly euhedral, but some delicate glomerocrysts and some smaller, broken fragments are present. Sparse lithics occur within blocks at least in the lower parts of the breccia. The matrix consists of still finer and randomly oriented fragments, including some with highly elongate

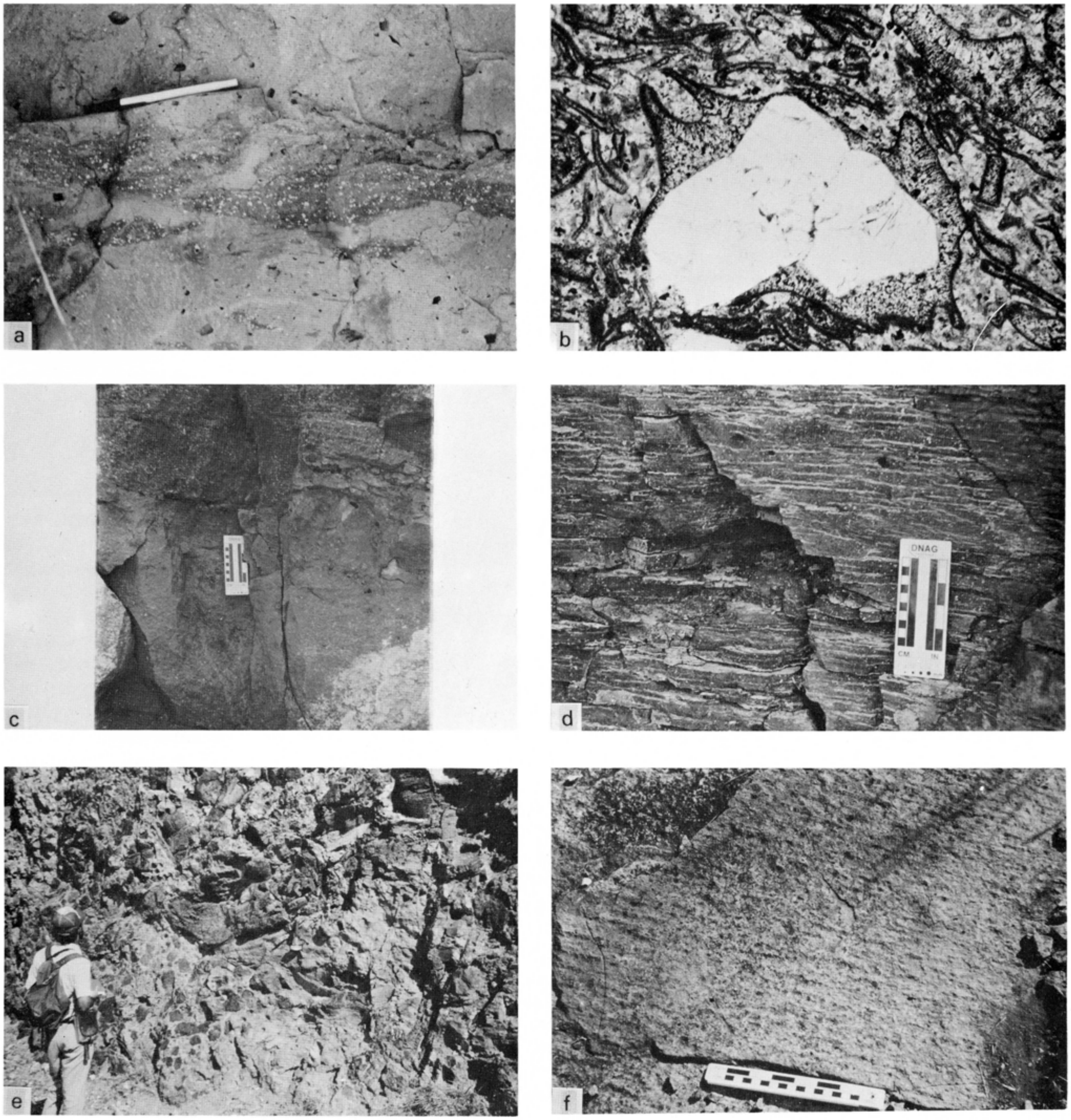

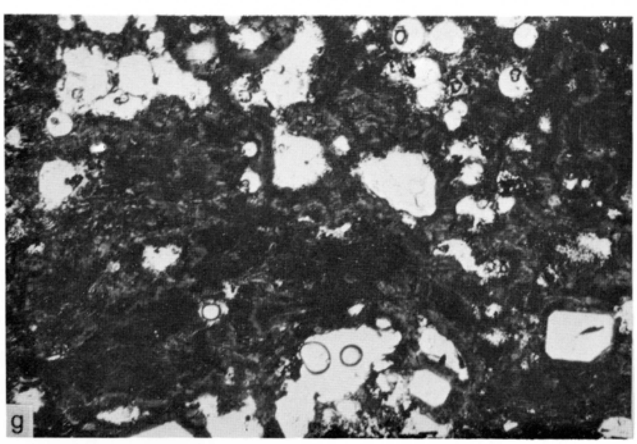

FIGURE 19—Rheomorphic tuff of Barrel Springs Formation in Davis Mountains State Park. **a,** Flattened pumice fragments and gas cavities in upper part of basal tuff (Stop 2A1). **b,** Coarse shards and feldspar phenocryst entirely enclosed within devitrified glass, basal tuff. Long dimension 3.6 mm; plane light. **c,** Transition between basal tuff and lowest, foliated, rheomorphic tuff (Stop 2A1). Note gas escape pipe (lower left) curving to left. **d,** Lithic fragments in strongly foliated, rheomorphic tuff. **e,** Upper breccia composed of vitrophyric clasts to 3 m in fragmented, silicified matrix (Stop 2A4). **f,** Flow lineations on surface of foliation shown in c and d (Stop 2B1). **g,** Secondary vesicles developing across eutaxitic texture in pumice fragment.

vesicles. It is cemented by a fine mosaic of opal or chalcedony.

An overlying flow unit first appears filling a depression in the first unit at the minor bend along the northeast-trending part of the drive (Fig. 17; location A5). Similar valley fills occur in at least four spots along the drive and can also be observed on the north side of Limpia Canyon. These relationships indicate that the first unit had an irregular top, similar to that on modern rhyolitic lava flows. Although the overlying unit is the second encountered along the drive, outcrops farther on suggest that it is actually the third flow unit. All three units are lithologically similar and must be genetically related.

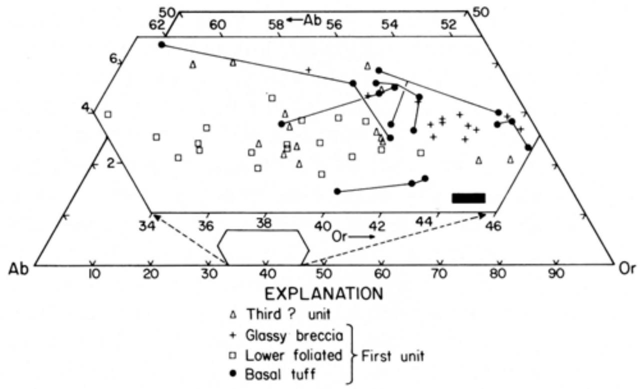

FIGURE 20—Compositions of alkali feldspar phenocrysts in Barrel Springs rocks at Davis Mountains State Park. Lines connect analyses of individual feldspars in basal tuff. Note that they have distinct compositions suggestive of mixing of different parts of the magma chamber. Solid bar shows allowable analytical error calculated at $Ab_{60}Or_{37}An_3$. Analyses by J. N. Rubin, Texas Bureau of Economic Geology.

The contact between the first and third units is marked by a clay-altered zone about 0.7–1 m thick that probably is the base of the third unit. Alternatively, it may represent reworking of fine material from the top of the first unit. A similar clay-rich zone occurs between the two units at most locations. Massive, foliated rock overlies the clay-altered material. Foliation is largely planar but parallels the contact with the underlying first unit. A clearly pyroclastic base, as in the first unit, has not been found. Feldspar phenocrysts, although compositionally similar, are petrographically different from those in the first unit. Glomerocrysts are more abundant and small, broken fragments are absent.

Evidence for a second unit, between the first and third units, is found at the fourth valley fill of the third unit (Fig. 17; location A6). On the west side of the valley, the third unit overlies typical glassy breccia of the first unit. The base of the third unit drops below the road level. The third unit is mostly not vesicular, but a thin (approximately 20 cm thick) zone at the base is vesicular in places. Where it reappears on the east side, it overlies the probable second unit which, although broadly similar to the other two units, also has some distinct differences. Most notably, the top is unbrecciated and the rock is highly vesicular. In contrast, the top of the first unit is everywhere brecciated, and we have found no vesicular zones within it. At this location, vesicles in the second unit consist of elongate tubes a few millimeters in diameter that parallel the contact. The second unit grades downward into more massive and unvesiculated rock. Still farther east, flow-banded and irregularly folded rock has alternating massive and finely vesicular zones. Sparse, extremely large vesicles, up to at least 30 cm, are younger than the smaller, more abundant vesicles. Secondary chalcedony followed by calcite entirely fill many smaller vesicles and partly fill the larger ones. An alternative interpretation is that this rock is simply a variation of the first unit not seen elsewhere.

Whole-rock and feldspar compositional data indicate that the first and third units are chemically similar (Table 2, analyses 5 and 6; Fig. 20). The differences in alkalies between the two whole-rock analyses must reflect postsolidification mobility in the basal tuff.

Microprobe analyses of feldspar phenocrysts in four samples through the sequence of units show that they are anorthoclase and sodic sanidine (Fig. 20). The compositions vary widely, but over the same range in each sample. The variation reflects both zoning of individual phenocrysts and significant differences between different phenocrysts. For example, individual feldspars in the basal tuff show variable zoning but have relatively constant anorthite contents (Fig. 20). This pattern is consistent with significant mixing between compositionally or thermally different parts of the magma chamber, which in turn is consistent with rapid, violent pyroclastic eruption. The similarity between all four samples, including the third unit, suggests they are comagmatic.

We interpret the first unit as rheomorphic tuff. Following initial pyroclastic emplacement, the base of the unit cooled rapidly and was frozen in place. Greater heat retention above the base in the moderately alkalic and low-silica rhyolite allowed secondary flow. Total displacement at the top of the clearly tuffaceous part was at most 70 cm on the basis of curvature of the gas pipes. Secondary flow in the base of foliated rock may have been only slightly more, but was sufficient to obliterate pyroclastic features. The amount of flow increased progressively upward as indicated by the development of flow folds and breccias. Breccias may mark a transition from initial, plastic secondary flow of the rheomorphic tuff to massive, brittle failure. Failure probably occurred as the total strain, represented by distance of flow, increased and as the upper part of the flow cooled and became more brittle.

The importance of primary laminar viscous flow (Schmincke and Swanson, 1967; Chapin and Lowell, 1979) in emplacement of Barrel Springs is uncertain. Preservation of a clearly pyroclastic base and development of upper breccia seem to require secondary flow. However, Barrel Springs was deposited upon a surface of negligible relief, so paleoslope, commonly considered essential for secondary flow (Wolff and Wright, 1981), probably was not a factor.

The origin of the upper units is also uncertain. The similarity in general lithology and in bulk-rock and feldspar compositions to the first unit indicates that they are comagmatic. However, unlike the first unit, no pyroclastic features are preserved; most importantly, the third unit lacks a pyroclastic base. Additionally, the lack of broken phenocrysts in the third unit suggests that it did not erupt explosively. If the source of the upper units is also to the west in the postulated caldera source of Barrel Springs Formation (Henderson, 1987), which seems most likely, then they must have flowed at least 10 km and possibly as much as 20 km. More definitive conclusions will require determining the source and distribution of individual flow units.

At the end of Stop 2A, we will drive to the overlook at the end of the scenic drive. **2.0**

30.4 **STOP 2-B. Barrel Springs and Sleeping Lion Formations in Davis Mountains State Park, and Fort Davis National Historic Site.** This stop consists of a hike from the State Park to Fort Davis National Historic Site. The hike allows us to examine additional features in the lower part of the first, rheomorphic tuff, unit of Barrel Springs Formation. We will also examine Sleeping Lion Formation, an enigmatic silicic unit that is either still more strongly rheomorphic tuff or extensive lava flow.

Barrel Springs Formation around the shelter at the beginning of the hike (Fig. 17; location B1) consists of the lower foliated part, slightly above the clearly tuffaceous base. Barrel Springs split along foliations to create a flagstone-like pavement having distinct lineations within the foliation planes (Fig. 19f). These lineations trend N30–N80E and indicate the direction of flow. Although influence of primary pyroclastic flow on these lineations is uncertain, they are consistent with a source to the west in the caldera area postulated by Henderson.

The basal ash-flow-tuff part of the first unit is exposed in an abandoned roadcut below the shelter (Fig. 17; location B2). The cut shows features similar to those in outcrop along the scenic drive, including abundant pumice, sparse lithics, and elutriation pipes. Some pumice fragments show additional features not found in those on the scenic drive, however. Pumice is up to 50 cm long, and some are relatively unflattened; length to thickness ratios are as low as 4. This suggests that some of the "pumice" consisted of relatively unvesiculated, juvenile fragments. A thin section of one relatively flattened pumice fragment shows collapsed primary vesicles. Additionally, equant vesicles from less than 0.1 up to 1 cm in diameter cut across the shards (Fig. 19g). These vesicles must have developed after primary emplacement and welding. They suggest that the glass, and therefore primary magma, was relatively enriched in volatiles, in contrast to the evidence of the anhydrous phenocrysts. Volatile enrichment may have aided secondary flow by reducing overall viscosity.

The trail drops off the high ridge within Barrel Springs Formation and into the top of Sleeping Lion Formation. Sleeping Lion is a distinctive, coarsely and abundantly porphyritic flow that is well exposed in the Historic Site and in a roadcut near the entrance to the State Park that is Stop 2C today. Breccia at the top is poorly exposed along the trail here, but is well exposed in the roadcut. Large folds within Sleeping Lion are well exposed along and southeast of the main trail (Figs. 21a and 17; location B3). The folds dominantly trend northeast to north and have amplitudes up to several meters. These folds may have developed where flow of Sleeping Lion was constricted within a paleovalley. This conclusion is consistent with a northeast flow direction indicated by ramp structures (Hicks, 1982).

Outcrops along the trail and views of Sleeping Lion Mountain to the south provide a good cross section through Sleeping Lion. Note the typical massive columnar joints and flat to low-angle sheets.

The base of Sleeping Lion is exposed on the east edge of Sleeping Lion Mountain next to the Historic Site (Fig. 17; location B4). Basal breccia overlies baked, compacted tuffaceous sediments of Frazier Canyon Formation (Fig. 21b). A zone 20–30 cm thick at the base of Sleeping Lion is distinctly layered and enriched in crystals, and may be either surge or air-fall deposit. Overlying breccia is about 2 m thick. Clasts in the breccia range widely in size up to 40 cm and include both massive and coarsely vesicular (scoriaceous) varieties. Sleeping Lion above the breccia is massive and planar-laminated to flow-folded. The lack of basal vitrophyre is typical.

If time permits, we will visit the partly restored cavalry fort. Meet vehicles at end of hike and return to roadcut on TX-118 near entrance to Davis Mountains State Park. **3.1**

33.5 **STOP 2-C. Upper Sleeping Lion Formation in Highway 118 roadcut.** This roadcut (Fig. 17; location C) provides an excellent cross section of the upper part of Sleeping Lion Formation as well as overlying soft tuffaceous rocks below Barrel Springs Formation. The ash-flow-tuff base of Barrel Springs occurs in the top of the roadcut but is difficult to reach here.

The exposed top of Sleeping Lion Formation is massive to brecciated (Fig. 21c). Most of the rock is devitrified, but a few glassy clasts occur in breccia. Pronounced flow folds are common in both massive parts and in clasts. Elongate vesicles are common in some outcrops but not here. Thin sections reveal abundant clinopyroxene, magnetite, and zircon, as well as the obvious alkali feldspar phenocrysts. A thin section of vitrophyre from a similar outcrop 3 km to the northeast contains flow bands with highly elongate and flattened vesicles or shards (Fig. 21d). These are probably highly stretched vesicles in a lava flow but could be interpreted as densely welded and partly digested shards in a strongly rheomorphic tuff.

The overlying soft tuffaceous rocks are largely sedimentary and include two thin lenses composed dominantly of small clasts of Sleeping Lion Formation. These clasts include many individual phenocrysts (many of which are broken but not disaggregated), broken parts of phenocrysts, as well as abundant coarse pumice. Vesicles in different pum-

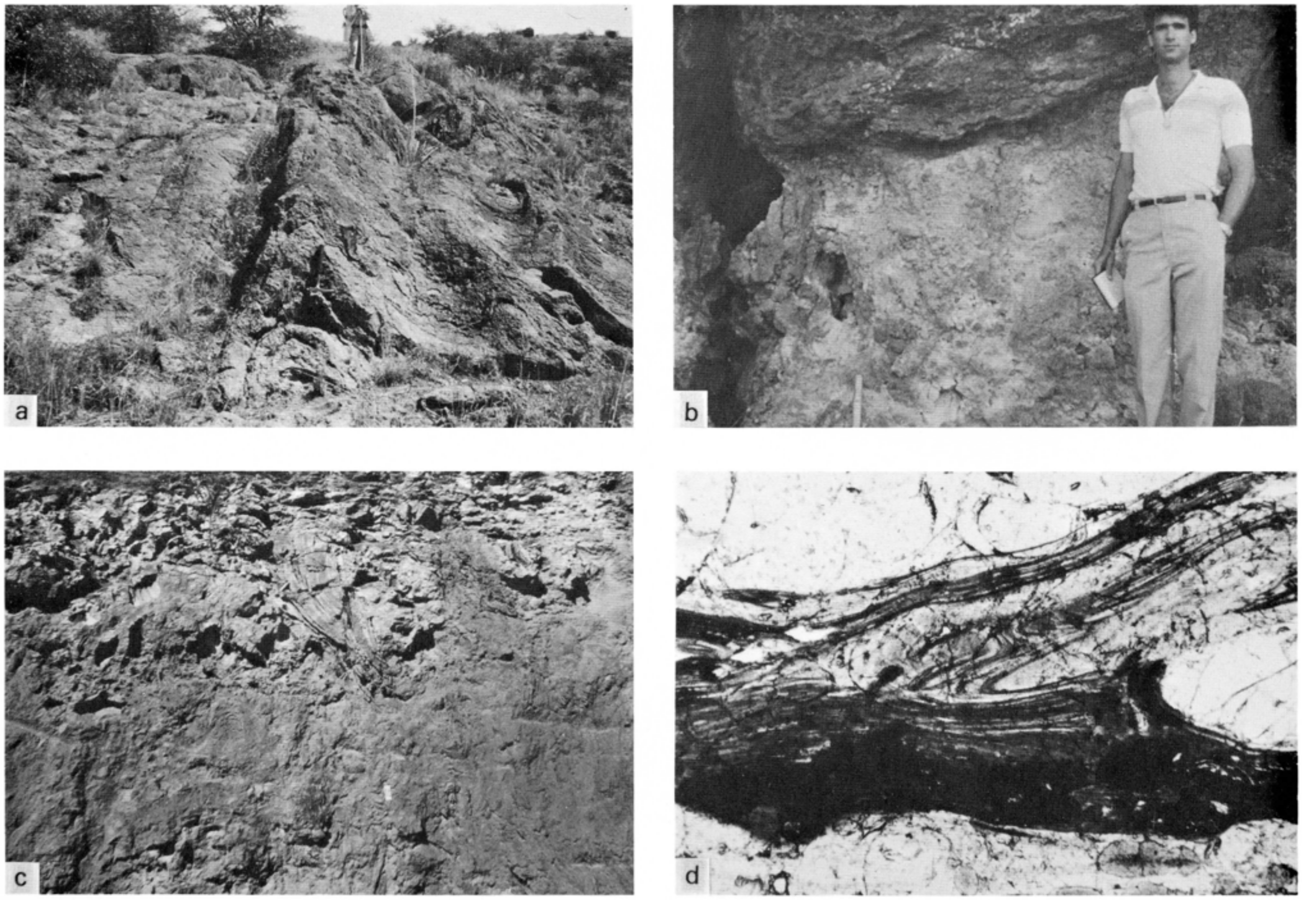

FIGURE 21—Sleeping Lion Formation. **a,** Flow folds on upper surface in Fort Davis National Historic Site (Stop 2B3). Primary flow was probably parallel to secondary fold axis. **b,** Basal breccia in outcrop east of Fort Davis (Stop 2B4). Note abrupt transition to massive rock above. **c,** Upper breccia of flow-folded clasts in fragmented matrix, roadcut on Highway 118 near entrance to Davis Mountains State Park (Stop 2C). White card is approximately 15 cm high. **d,** Photomicrograph of upper vitrophyre from outcrop immediately east of Fort Davis. Texture probably represents extended and flattened flow-banding and vesicles. Long dimension 3.6 mm; plane light.

ice are equant to highly elongate. Sparse fragments of other rock types are also present. All fragments are unoriented; there is no evidence of compaction. The matrix is largely still finer pumice. The rock is poorly cemented by clay and opal. Similar lenses are exposed in several other roadcuts at the top of Sleeping Lion but are too soft to crop out otherwise. These lenses represent sedimentary reworking of soft, upper pumiceous parts of Sleeping Lion that have been largely eroded.

Two alternative origins for the Sleeping Lion Formation, silicic lava flow or extremely rheomorphic tuff, are discussed in the conclusions for this trip.

Day 3: Christmas Mountains caldera complex

The focus of today's trip is the Christmas Mountains caldera complex, which erupted a series of ash-flow and air-fall tuff, lava, and small shallow intrusions (Fig. 22; Henry et al., 1989), about 42 Ma, contemporaneous with abundant small intrusions of the Big Bend area. Together, these rocks comprise the major part of pre-main-phase magmatism of Trans-Pecos Texas.

The Christmas Mountains calderas represent a previously unrecognized, erupting laccolith or laccocaldera type. The calderas developed on top of the Christmas Mountains dome, which consists of steeply dipping Cretaceous rocks (Fig. 22). The magma system produced both tuff and lava in several cycles leading to at least four separate major collapse structures. The two youngest and best exposed calderas lie at opposite ends of the elliptical dome. All of the calderas are no more than 1.5 km in diameter (Fig. 22). Stop 3A looks at an intracaldera sequence of interbedded ash-flow tuff and coarse caldera-collapse or debris-avalanche deposits. Stop 3B examines proximal parts of the initial eruptive sequence. Stop 3C examines distal parts of the same sequence.

Prior to doming, a silica-undersaturated gabbro intruded and marbleized Cretaceous limestone in the area that is now occupied by the western caldera (Joesten, 1974; Jungyusuk, 1977; Lewis, 1978). Gabbro is now exposed extensively around the southern and eastern rim of the caldera.

Initial emplacement of the caldera magma system created the Christmas Mountains dome. The dome is elongate northwest; dimensions are about 8×5 km (Fig. 22). Cretaceous rocks commonly dip 20–40° outward around the flanks. The dome has more than 700 m of topographic relief and at least 1 km of structural relief. The doming is much steeper than the broad, gentle upwarp typical of most calderas (Smith and Bailey, 1968). However, the Christmas Mountains dome is typical of the laccolithic uplifts of the Big Bend region.

Caldera-related rocks are divided into five distinct sequences, three of which include major ash-flow tuffs (Fig. 22).

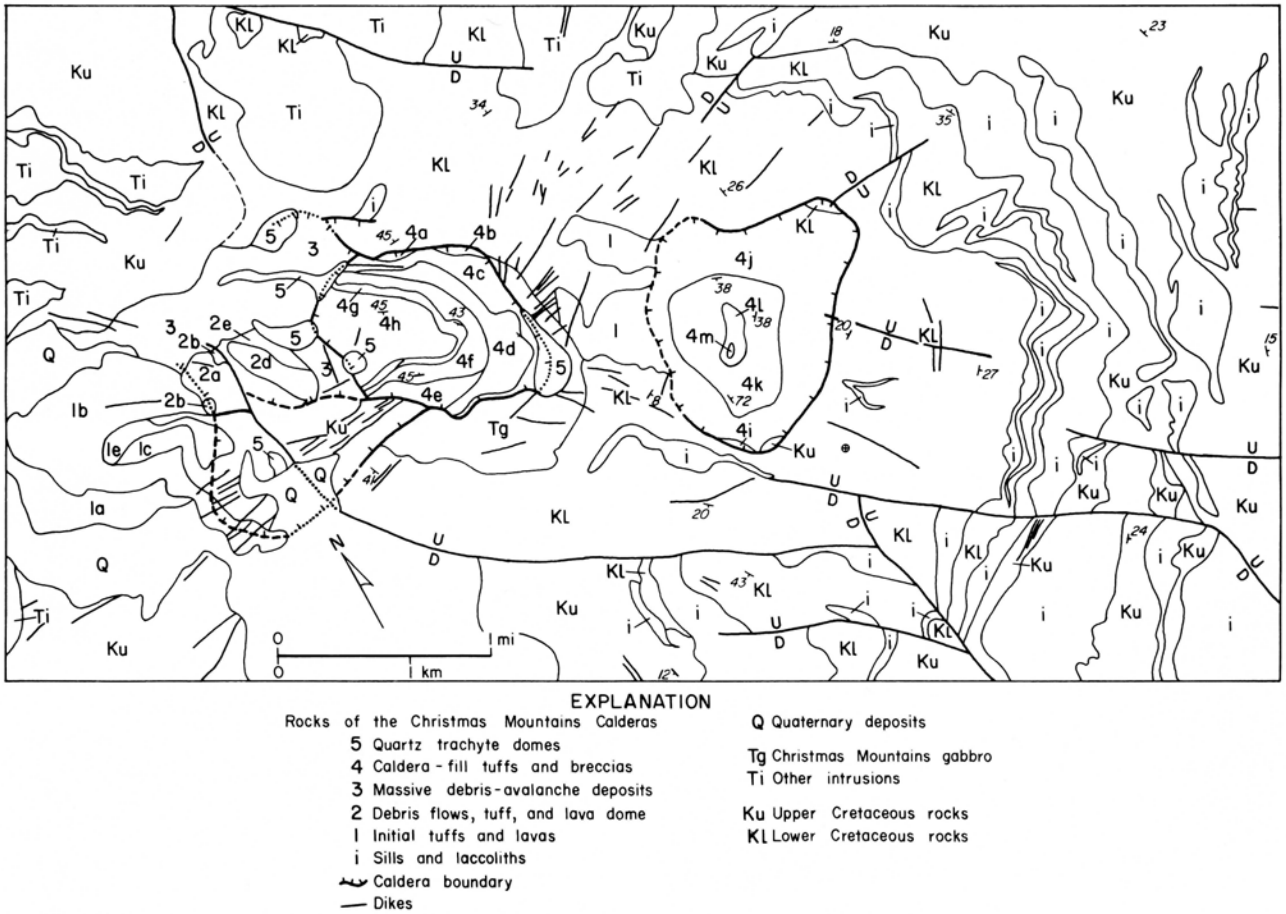

FIGURE 22—Simplified geologic map of the Christmas Mountains caldera complex. On map, Tx1 and Tx2 are subdivided into five units each (Tx1a, Tx1b, etc.); Tx4 is subdivided into 13 units. Stop 3A is a traverse through units 4a to 4h. Stop 3B examines unit 1A near the west edge of the map. Stop 3C is in unit 1A approximately 8 km south of southwestern corner of map.

(1) The earliest recognized caldera-related rocks are rhyolitic air-fall and ash-flow tuffs that probably erupted as radial fractures over the growing dome propagated to the level of the magma chamber. Initial air-fall tuff followed by ash-flow tuff is consistent with formation and collapse of a Plinian eruption column. The western flank of the dome apparently collapsed as a result of these first eruptions. The pyroclastic eruptions were followed by quartz trachyte lavas and locally by debris deposits. Unlike many calderas worldwide (Lipman, 1984) but similar to other Trans-Pecos calderas (Henry and Price, 1984), the Christmas Mountains caldera complex began with major pyroclastic eruption and did not develop on an earlier volcano.

(2) The second sequence crops out in a small area at the western edge of the dome and consists of coarse clastic sediments overlain by rheomorphic ash-flow tuff, debris-flow deposits, and a quartz trachyte lava dome. Eruption of the rheomorphic tuff apparently induced additional collapse of the early caldera.

(3) The third sequence consists of coarse debris-avalanche and debris-flow deposits and minor pyroclastic flows. They crop out in a wedge at the northwestern edge of the western caldera that may represent an alluvial fan with a source within the general area of the western caldera.

(4) The fourth sequence occurs as caldera fill within the main, western and eastern calderas and consists of peralkaline quartz trachytic ash-flow tuff interbedded with coarse caldera-collapse and debris-avalanche breccia. Caldera fill in both calderas dips radially inward, apparently as a result of late subsidence.

Both main calderas are circular to slightly elongate and 1–1.5 km in diameter. Caldera boundaries are well exposed over elevations of several hundred meters and marked by the juxtaposition of caldera fill against precaldera rocks. Cretaceous rocks in the wall commonly dip outward and are sharply truncated at the wall. The calderas are now so deeply eroded that the exposed wall is probably very close to the structural margin. The occurrence of ring-fracture intrusions along the caldera walls supports this conclusion. Collapse probably occurred by piston-like subsidence of a central block along a single fault zone as in the caldera model of Smith and Bailey (1968).

Minimum collapse in both calderas is about 300 m, the difference in elevation between Cretaceous rocks in the caldera wall and the lowest exposed caldera fill. Collapse must have been greater because the subsided block is not exposed and the original top of the caldera wall has been eroded.

(5) The fifth and final sequence consists of small, shallow intrusions of porphyritic quartz trachyte that occur dominantly along the ring-fracture zone of the western caldera.

The Christmas Mountains caldera complex represents an unusual "eruptive laccolith" style of caldera development that has not been recognized elsewhere. The extreme precaldera doming, the small size of the calderas, and the development of "twinned" calderas rather than a single, central vent, may be related to the size of the magma system and its formation in a compressional tectonic environment. The calderas are small because the magma system was small, but large enough to produce the dome, develop a radial fracture system to propagate into the magma chamber to allow eruption, and remain active during several cycles of eruption. Twinned calderas may have formed because fractures developed over an elliptical dome are concentrated near the two ends (Withjack and Scheiner, 1982).

Most calderas, at least in the western United States, formed in a tensional environment in which extension aided ascent and expansion of the underlying magma body. Trans-Pecos Texas at 42 Ma was in mild compression residual from Laramide deformation, which may have ended about 50 Ma (Price and Henry, 1984; Henry and McDowell, 1986). The Christmas Mountains calderas are the only ones recognized during the pre-main phase of Trans-Pecos volcanism. Basin and Range tension did not begin until about 31 Ma (Henry and Price, 1986). In this stress regime, a small, shallow magma body may preferentially form sills or laccoliths.

Mileage

0.0 Today's roundtrip of approximately 190 mi starts at the intersection of US-90 and TX-118S. **5.6**

5.6 Big Hill: roadcuts for next several miles are in a mafic trachyte that has been miscorrelated with Crossen Trachyte. **19.5**

25.1 Elephant Mountain on east, one of several silica-undersaturated syenites in a belt that continues to Big Bend. **1.4**

26.5 Real Crossen Trachyte caps the mesa to the west. **34.9**

61.4 Intersection of TX-118 with the Terlingua Ranch road. The numerous peaks straight ahead are small intrusions of the Christmas Mountains province; the Christmas Mountains caldera complex forms some of the highest parts within the middle of the province. Most intrusions were emplaced between 44 and 40 Ma, during the pre-main phase, and range from alkali gabbro to peralkaline rhyolite (Lonsdale, 1940; Henry et al., 1989). Also present are nepheline-normative hawaiites emplaced about 28 Ma during the early tensional phase, and mantle-xenolith-bearing hawaiites and alkali basalts emplaced as north-northwest-trending dikes about 24 to 20 Ma, contemporaneous with Basin and Range faulting. **1.8**

63.2 Rhyolite at Packsaddle Mountain has steeply domed Cretaceous wall rocks. The resistant layer is massive Santa Elena Limestone. **6.0**

69.2 Turn left (east) through Gate 9 of Terlingua Ranch. This road winds through rugged country to join the main ranch road near Terlingua Ranch. Many side roads lead off in both directions; stay on the main road. **2.5**

71.7 Road leads to south (right). Stay on main road that climbs hill toward Paisano Peak (steep peak straight ahead), a rhyolite laccolith. **5.2**

76.9 Take right turn (toward south) onto side road that leads off main road toward high part of Christmas Mountains. Follow this road approximately 4 mi to Stop A. **4.0**

80.9 **STOP 3-A. Caldera fill in western caldera of Christmas Mountains.** This stop consists of a traverse through a representative section (Figs. 23, 24a) of caldera-fill ash-flow tuff and caldera-collapse or debris-avalanche breccia. These deposits record ash-flow eruption, caldera collapse, and failure of caldera walls of the small but complex caldera. In addition, we will also be able to examine: (1) Cretaceous limestone dipping north off the dome and forming the wall of the caldera; (2) precaldera gabbro and marble in the caldera wall; (3) ring-fracture intrusions of quartz trachyte; and (4) panoramic views of the entire small (1–1.5 km in diameter) caldera.

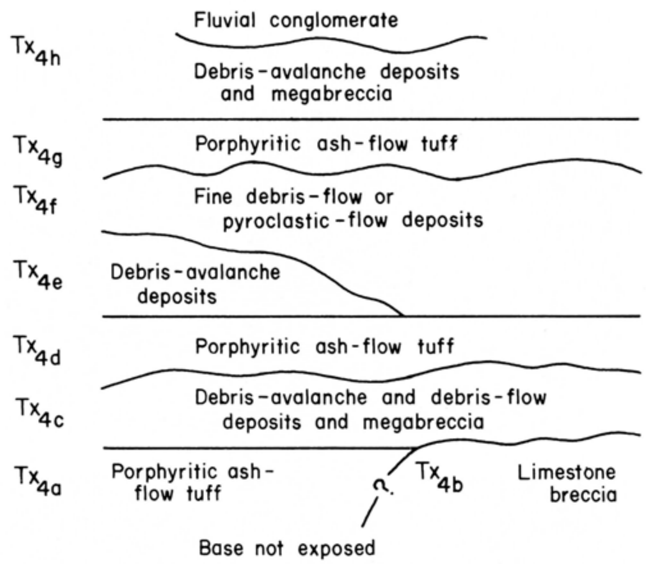

FIGURE 23—Stratigraphy of caldera fill within the western caldera of the Christmas Mountains (Stop 3A). Porphyritic ash-flow tuffs (4a, 4d, 4g) and tuffs in eastern caldera are petrographically indistinguishable.

Three separate ash-flow tuffs crop out within the caldera. All three, and those in the eastern caldera, are petrographically and probably chemically similar and densely welded throughout. The tuffs vary only in abundance of lithics and pumice. Analyses of the first tuff in the western caldera and one in the eastern caldera show that they are peralkaline quartz trachyte (Henry et al., 1989). Phenocrysts include about 15% alkali feldspar and a few percent augite. Abundant microphenocrysts of magnetite and ilmenite give the tuff a characteristic dark matrix.

The first tuff crops out only as a thin lens at the northern edge of the caldera, where it is faulted against Santa Elena Limestone. Lithic fragments are sparse. Pumice and distinct eutaxitic texture are present only near the top of the tuff, suggesting reverse grading of pumice.

Adjacent to the caldera wall is a breccia composed dominantly of limestone and marble fragments (to about 1 m) within a calcitic matrix (the limestone breccia of Fig. 23). Igneous-rock fragments are minor but large (to 6 m); fragments include several porphyritic rocks that are identical to dikes within limestone in the adjacent caldera wall. Several pods of disaggregated but undispersed dike fragments lie only a few meters away from similar rock in outcrop. These features indicate that this breccia represents collapse of the adjacent caldera wall.

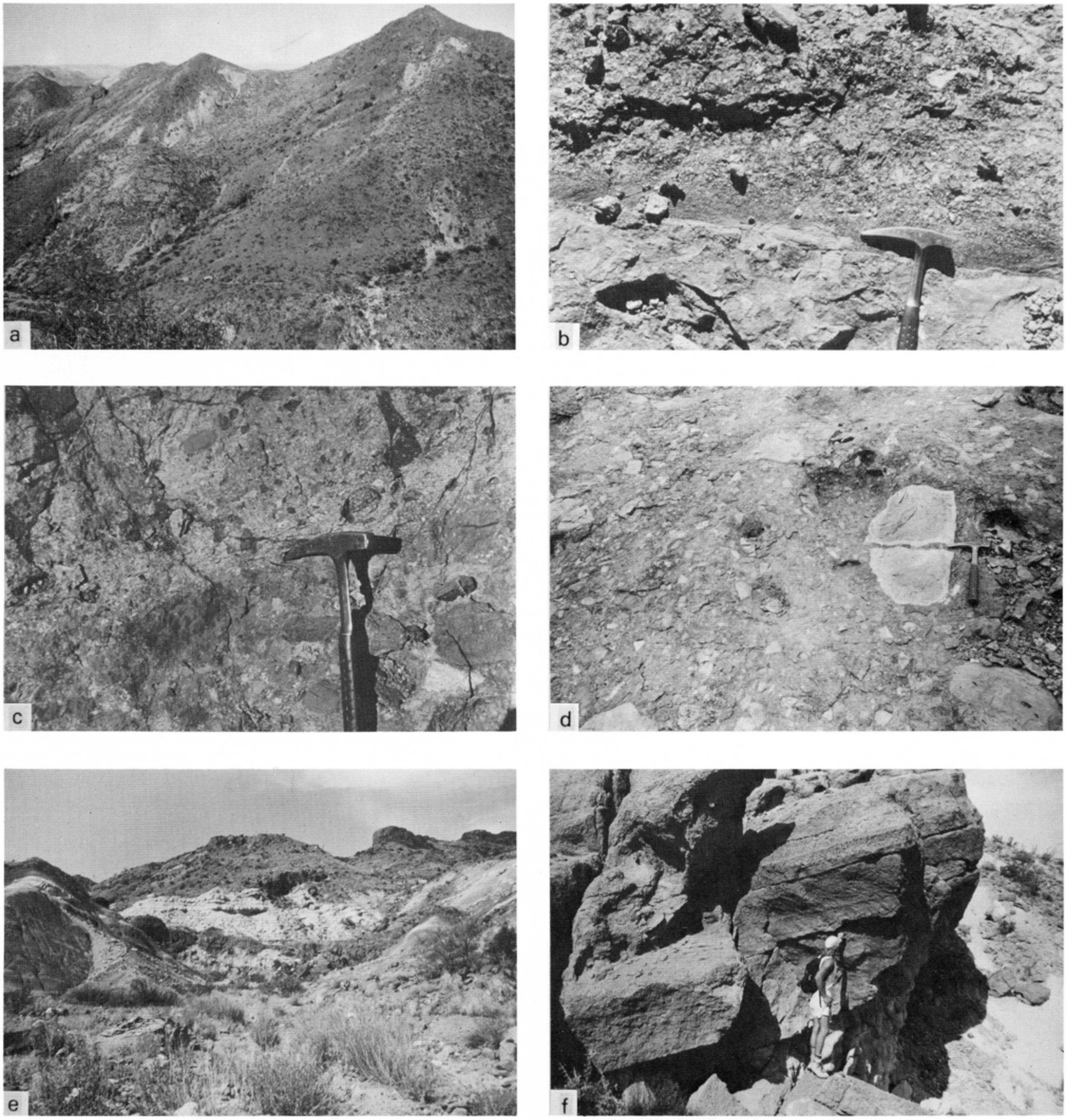

FIGURE 24—Christmas Mountains caldera complex. **a,** Interbedded ash-flow tuff and caldera-collapse or debris-avalanche breccias dipping to south (left) in northeastern part of western caldera. Field-trip route follows ridge. **b,** Base of debris flow (Tx4c) overlying limestone breccia (Tx4b). **c,** Lithic concentration zone at base of ash-flow tuff (Tx4d) in eastern part of western caldera. **d,** Debris-avalanche or caldera-collapse breccia (Tx4h) in highest preserved part of caldera fill. Note broken but nondisaggregated clast. **e,** Outcrop at Dogie Mountain (Stop 3C) showing quartz trachyte lava (skyline); ash-flow and air-fall tuff erupted from Christmas Mountains calderas; reworked tuffs derived from south (white beds in middle); Alamo Creek Basalt (dark bed below white tuff); thin, distal ash-flow tuff, possibly derived from source in Mexico (thin white bed on left); and lower Tertiary mudstones (below thin white tuff). **f,** Air-fall tuff at Dogie Mountain that contains accretionary lapilli.

Coarse debris-flow deposits, having fragments up to 1 m and thin, reversely graded bases, directly overlie limestone breccia (Fig. 24b). The first deposit has a dominantly calcitic matrix, but igneous-rock fragments are more abundant than limestone fragments.

Extremely coarse, caldera-collapse or debris-avalanche breccia forms a wedge in an arc along the northeastern and eastern caldera margin. Clasts of igneous rocks, commonly as much as 30 m in diameter, lie in a matrix of finer clasts. Extremely large clasts are generally much more abundant than matrix. Many clasts are difficult to recognize as such in single outcrops, and some may be considerably larger than 30 m. Relatively fine-grained debris-flow deposits and coarse tuffaceous sandstones fill a depression within the top of the coarse breccia, indicating considerable original relief on the surface of the breccia.

The coarse breccia and other, similar deposits in the calderas must have formed by collapse of the caldera wall. They are similar both to caldera-collapse megabreccias (Lipman, 1976) and to debris-avalanche deposits (Voight et al., 1981; Ui, 1983; Francis and Self, 1987), although Ui et al. (1986) suggested that the latter are associated with stratovolcanoes and not with calderas. Probably a major part of the caldera wall collapsed along the northeastern segment. Although 30 m clasts are small in comparison to megabreccia developed in much larger calderas, they are large for a caldera that is only 1 km in diameter.

The second tuff forms a lens that wraps around approximately 180° of the caldera, along the northern, eastern, and southern sides. It is generally about 80 m thick but thickens to as much as 200 m in the southeastern part of the caldera. The second tuff appears to dip more gently into the caldera than the first tuff, suggesting subsidence between eruptions.

The second and third tuffs show a regular vertical variation in lithic and pumice fragments that largely conforms to published models of ash-flow stratigraphy (Sparks et al., 1973; Cas and Wright, 1987). Lithic fragments are normally graded; pumice is reversely graded. A fine-grained basal layer, 10–20 cm thick, grades upward into a well-defined, coarse, lithic concentration zone commonly 1–1.5 m thick and containing 50–90% fragments up to 40 cm (Fig. 24c). The basal layer grades abruptly into the main body of the tuff as large lithics drop out, juvenile components increase in abundance, and eutaxitic texture develops. Tuff immediately above the base commonly contains 10–20% lithics, most of which are less than 10 cm in diameter. Lithics in upper parts of the tuff are less than 1 cm. This zonation indicates that the second and third tuffs were individual flows and that the interbedded caldera-fill breccias were deposited during breaks in ash-flow deposition.

Breccia above the second tuff is much finer-grained than other such deposits. Through most of its outcrop, maximum clast size is about 5 cm and generally less than 2 cm, with a slight suggestion of normal grading. It becomes much coarser at its western end, on both the north and south sides. The groundmass consists of finer rock and mineral fragments. Original shards, clearly primary juvenile fragments, or other indications of pyroclastic origin are not evident.

The third tuff is uniformly 30–50 m thick. It is distinctly enriched in pumice compared to the first and second tuffs.

The highest exposed breccia, overlying the third tuff, consists of a volumetrically dominant lower unit of coarse, massive, debris-avalanche or caldera-collapse deposits generally similar to those below, and a minor upper unit of well-stratified mudflow and conglomeratic fluvial deposits.

The lower unit is composed of as much as 90% clasts, commonly to 1 m but including one block approximately 80 m across, in a matrix of finer clasts (Fig. 24d). An exposure of the base along the traverse shows slight reverse grading. Vague internal layering is indicated by zones of different maximum clast sizes. Except for one of the megabreccia blocks, clasts are entirely of silicic igneous rocks, most commonly porphyritic quartz trachyte. Clasts are slightly rounded. Some are broken but the pieces have not been significantly displaced relative to each other (Fig. 24d).

Return to vehicles and TX-118. **11.7**

92.6 TX-118. Turn left (south). **0.9**

93.5 Turn right (east) through Gate 8 of Terlingua Ranch. Drive 1.3 mi to turnaround at end of road on west edge of Christmas Mountains 7.5 min. quadrangle. **1.3**

94.8 **STOP 3-B. Proximal tuffs and lava of Christmas Mountains caldera complex.** This stop shows rhyolitic air-fall and ash-flow tuffs that are the earliest known eruptive rocks of the Christmas Mountains calderas in a proximal location just 1 km west of the Christmas Mountains (Fig. 22). Here, approximately 5 m of moderately welded air-fall tuff are overlain by 15–20 m of moderately to poorly welded ash-flow tuff, composed of eight separate flows, and two zones of coarse breccias.

Basal, pumice-rich air-fall tuff is massive to moderately layered at scales as fine as a few centimeters. The layering is defined by variations in relative abundance and size of rock fragments and two distinct types of pumice. Rhyolitic pumice is finely vesicular and weathers brown; quartz trachytic pumice is more coarsely vesicular, almost scoriaceous, and dark gray. Two 5 cm thick zones in the middle of the tuff are almost entirely the latter type; throughout most of the rock, the two pumice types are intimately intermixed, distinctly flattened, and comprise as much as 90% of the rock. Some individual pumice fragments appear to be mixtures of both types. Rock fragments, rarely up to 20 cm, compose most of the rest of the rock.

The ash-flow tuffs are typically 1–2 m thick, moderately to poorly welded, and totally devitrified. The tuffs contain up to 30% pumice, generally 1–2 cm long but rarely up to 10 cm. The rhyolitic pumice is present in all tuffs, but the darker pumice occurs only in the lowest tuff. In most tuffs, rock fragments are up to a few centimeters in diameter and compose from a few to as much as 20%. However, two tuffs contain about 40% fragments up to 20 cm in diameter in basal lithic concentration zones.

The air-fall and ash-flow tuffs are petrographically similar. Phenocrysts include about 2% alkali feldspar and clinopyroxene. Devitrification of the rhyolitic pumice has almost entirely obscured bubble texture. The darker pumice is distinctly and coarsely vesicular, contains about 5% alkali feldspar phenocrysts in a distinctly darker matrix, and shows both axiolitic and spherulitic devitrification. The darker pumice resembles overlying quartz trachyte lava and may represent a layer of quartz trachytic magma that lay beneath rhyolitic magma which erupted to produce the tuffaceous rocks.

Two coarse breccia zones are interbedded with a lithic-rich ash-flow tuff at the top of this sequence. Both zones contain clasts, dominantly of quartz trachyte, in a variably pumiceous and welded matrix. Variations in maximum clast size (to 1 m) define a crude layering in the breccias. Most likely, these deposits are co-ignimbrite lag breccias (Walker, 1985). Alternatively, they are extremely lithic, proximal ash-flow tuffs. At the very least, the coarseness of the sequence here indicates that it is very near source.

Quartz trachyte lava up to 120 m thick overlies the tuffs. It contains 5–10% phenocrysts of anorthoclase and clinopyroxene in a trachytic groundmass of alkali feldspar laths and minor interstitial quartz.

Return to vehicles and TX-118. **1.3**

96.1 TX-118. Turn left (south). **6.0**

102.1 Turn left (east) through Gate 2 of the Terlingua Ranch. Follow graded road 5.3 mi across northeast corner of Terlingua 7.5 min. quadrangle and northwest corner of Tule Mountain 7.5 min. quadrangle to Stop C on northeast side of Dogie Mountain. **5.3**

107.4 **STOP 3-C. Distal tuffs and lava of Christmas Mountains caldera complex at Dogie Mountain.** This section exposes the same sequence as at Stop B in its most distal preserved location about 9 km from the calderas. Caldera-related rocks overlie tuff and lava unrelated to the Christmas Mountains and a sedimentary sequence which spans the Cretaceous–Tertiary boundary (Fig. 24e).

The lowest exposed volcanic rocks include (1) a 1 m thick ash-flow tuff, (2) Alamo Creek Basalt, and (3) various primary and reworked tuffs, all in Chisos Formation. The thin, distal tuff is one of the oldest volcanic rocks in Trans-Pecos but was probably erupted from a source to the south or west in Mexico. The 47 Ma Alamo Creek Basalt is the oldest volcanic rock erupted in Texas. It is composed of slightly nepheline- to hypersthene-normative alkali basalt and is widespread throughout the Big Bend region (Maxwell et al., 1967; Stewart, 1984).

The green tuffs are phreatomagmatic air-fall deposits that represent the first eruptions from the Christmas Mountains. The 5 m thick deposit is well layered in beds a few centimeters to about 1 m thick (Fig. 24f). Coarser layers contain abundant small pumice, sparse rock fragments, and a few dark, pumiceous clasts that are now totally replaced by calcite. These dark clasts may be quartz trachytic pumice similar to those seen at Stop B. Finer layers contain pumice and abundant accretionary lapilli. Variation in clast size probably reflects variable interaction with water; coarser layers were dryer, whereas finer layers were wetter.

Overlying ash-flow tuff consists of possibly three moderately to densely welded flows. Phenocrysts include a few percent alkali feldspar as well as sparse biotite. Rock fragments (to 5 mm) constitute as much as 25% and pumice (to 2 cm) less than 15% of the tuff. These tuffs are distinctly finer-grained than equivalent deposits at Stop B, reflecting their distal position here.

Quartz trachyte lava overlies the tuffs. Phenocrysts include 8% alkali feldspar (to 5 mm), 1–2% arfvedsonite (to 1 mm), and possibly minor sodic clinopyroxene. This lava can be traced discontinuously, apparently as a single flow, to outcrops on the southeast side of the Christmas Mountains, its probable source area. The apparent total flow distance of 9 km is not unusual for silicic lavas in Trans-Pecos Texas.

Return to vehicles and retrace route to TX-118 and Alpine.

Day 4: Star Mountain Formation

The Star Mountain Formation (SMF) consists of a complex of silicic (SiO_2 ~65–72%; Table 2) lava flows characterized by alkali feldspar phenocrysts set in a reddish-gray oxidized groundmass. Vitrophyres contain augite to ferroaugite, magnetite, and rare fayalite as microphenocrysts; these are rarely preserved in granophyre. SMF has long been considered a sequence of lava flows because: (1) it has a variety of features typical of lavas, including breccias at the tops and bottoms of flow units, flow bands and folds, ramp structures, vitrophyres at the tops, and elongate vesicles; and (2) it lacks outcrop-scale features of pyroclastic flows (Gibbon, 1969; Parker and McDowell, 1979). Nevertheless, this view is controversial because it has the areal dimensions and aspect ratio considered typical of pyroclastic flows (Table 4, Fig. 10; Henry et al., 1988a). The entire formation has a preserved lateral extent of 70 km and an areal extent of about 3000 km^2. However, in contrast to Bracks Rhyolite, which consists of a single flow, SMF consists of at least three and possibly many more individual flows (Figs. 25, 26a; to be observed at Stop 4B). The dimensions of individual flows are uncertain; some can be traced for at least 10 km, but discontinuous outcrop makes determining their full extent difficult.

A preliminary compilation of 12 published and unpublished whole-rock chemical analyses suggests that not only is SMF composite, but that individual flows do not extend over the entire outcrop area of the formation. The least evolved SMF flows in the northeastern Davis Mountains are not present in the Wild Rose Pass section nor, on the basis of present data, in the Barrilla Mountains. Similarly, the most silicic flow of the Wild Rose Pass section is absent from the northeast Davis Mountains and from parts of the Barilla Mountains.

Feldspar compositions also support the existence of several separate flows of distinctive major-element compositions. Microprobe analysis of feldspars from 11 samples representing much of the geographic extent of SMF shows several compositional clusters that broadly correlate with the whole-rock compositions (Fig. 27). Four samples, representing the third flow at Stop 4B and probably correlative rock that caps the formation in Limpia Canyon, contain sodic sanidines with extremely low anorthite contents. The low anorthite content is consistent with crystallization in one of the most evolved and possibly lowest-temperature SMF flows (Table 2, analysis 13). Geologic mapping suggests this flow has a minimum extent of about 10 km and possibly considerably more. In contrast, feldspars in three samples of the most mafic flow (Table 2, analysis 14; to be seen at Stop 4C) are anorthite-rich and are strongly zoned from calcic anorthoclase to sanidine. Their higher anorthite content is consistent with crystallization in a less-evolved and possibly higher-temperature liquid. Several other samples fall between these extremes, both in terms of their feldspar and bulk-rock compositions.

The most complete section, at Wild Rose Pass, is shown in Fig. 25. The basal sequence, from underlying vitric ash

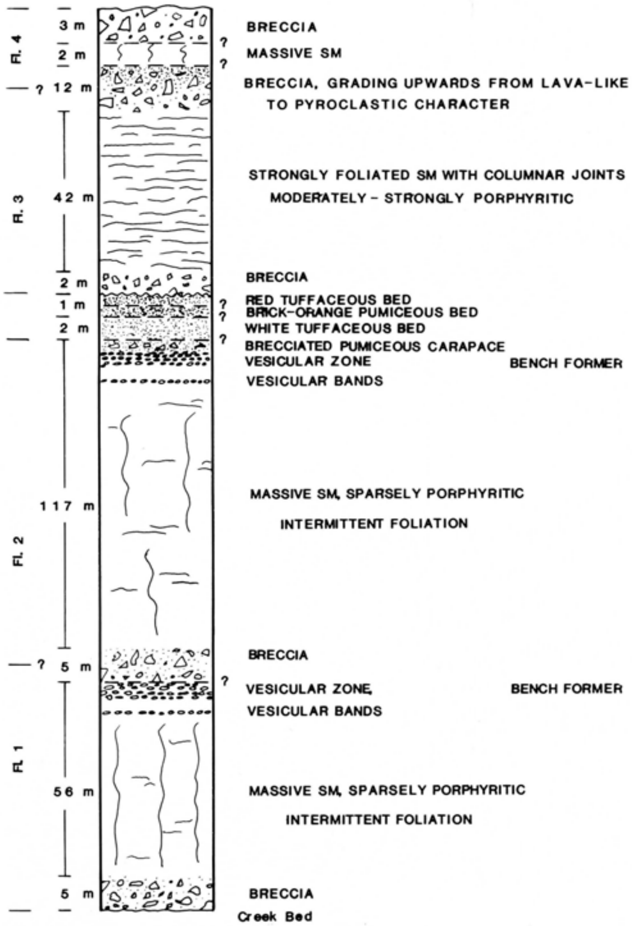

FIGURE 25—Section of Star Mountain Formation from Wild Rose Pass (Stop 4B; logged by R. R. Franklin and J. A. Wolff, 1988).

to basal breccia to massive interior, occurs at the base of the third unit in locations where the lower two units depicted in Fig. 25 are missing. In a few places, the basal breccia consists of flattened clasts with morphologies suggestive of spatter bombs (Fig. 26b). These could, however, be produced by avalanching from the front of the encroaching flow to form small, localized pyroclastic flows, followed by compaction when buried by the overriding lava. This, together with textures interpreted as eutaxitic in clasts of the upper breccia, constitutes the only textural evidence for a pyroclastic origin of SMF.

Mileage

0.0 Today's trip starts at US-90 and TX-118N and largely follows the same route as Days 1 and 2; the round-trip is approximately 140 mi. **14.2**

14.2 Turn right (east) onto ranch road to Pollard and 06 Ranches. Follow road approximately 3.4 mi, past Pollard Ranch to side road to west. **3.4**

17.6 Turn left onto side road leading to north side of Pollard Dome. **1.0**

18.6 **STOP 4-A. Base of Star Mountain Formation at Pollard Dome.** Features seen here at the base of SMF are typical of those seen over much of the areal extent of the formation. The base is marked by a baked vitric ash, here up to 50 cm thick. The origin of this ash is uncertain; it may represent air-fall material emplaced at the onset of SMF eruption or be unrelated. The ash was baked by overlying SMF. This, however, does not imply that the ash is unrelated, as it is possible for a lava or densely welded ignimbrite to bake an underlying ash deposit produced during an earlier phase of the same eruption.

The breccia overlying this consists of clasts of SMF set in a silicified matrix. At this location, the breccia clasts are vesicular and many have somewhat fluidal shapes reminiscent of spatter lumps (Fig. 26b). Recognition of spatter lumps would be critical support for an alternative pyroclastic hypothesis of the origin of SMF (see conclusions). Elsewhere, however, the basal breccia more closely resembles a lava-flow breccia, with a range of clast morphologies, including angular nonvesicular types. The breccia grades through a 30 cm transition zone with weakly developed flow bands into massive rock typical of the bulk of SMF at most locations. The upper breccia contains some clasts that faintly suggest eutaxitic texture.

Return to TX-118. **4.4**

23.0 Intersection with TX-118. Turn right (north); continue through Ft. Davis. **10.7**

33.7 Fork between TX-118 and TX-17 north of Ft. Davis. Turn right to follow TX-17 toward Balmorhea. **11.7**

45.4 **STOP 4-B. Star Mountain flows at Wild Rose Pass.** The Pass is located along the bed of Limpia Creek, not in the windgap as highway signs claim. Star Mountain (visible from the highway later today) is, of course, the type locality of SMF. The exposures here in the vicinity of Wild Rose Pass, however, are just as good and much more accessible than those of the type locality.

Many exposures of SMF show three flows (Gibbon, 1969), although the total number of flows and even the number of flows in individual sections remain controversial. The section here can be divided into four units (Figs. 25, 26a). The lowest unit is massive, pinkish-gray porphyritic quartz trachyte with anorthoclase as the most abundant phenocryst. The second unit is similar, but contains abundant vesicles, ramp structures, and flow folds. The third unit is porphyritic rhyolite. The fourth unit, with a massive zone only 2 m thick, is vesicular porphyritic rhyolite. Only the third unit can be carried laterally with any degree of certainty; the lower two units appear complex in sections exposed on nearby hillsides. Typically, no pyroclastic features are evident. An upper vitrophyre locally exposed in Limpia Canyon shows no vitroclastic texture (Fig. 26c).

The lower three units are similar mineralogically and vary only slightly in major-element chemistry (Tables 2, 5). The second unit is the least evolved, having the lowest SiO_2 and highest TiO_2, Al_2O_2, and P_2O_5. The third unit is the most evolved. All three units are peralkaline. These and other analyses of SMF plot along a trend from about Or40 toward a low-pressure minimum along the quartz–feldspar cotectic in the granite system (Fig. 15). The third unit plots closer to the cotectic with about 27% normative *qz* and is a true rhyolite; the lower two units have 13.5 and 11.7% *qz*, respectively, and are quartz trachyte in most classifications.

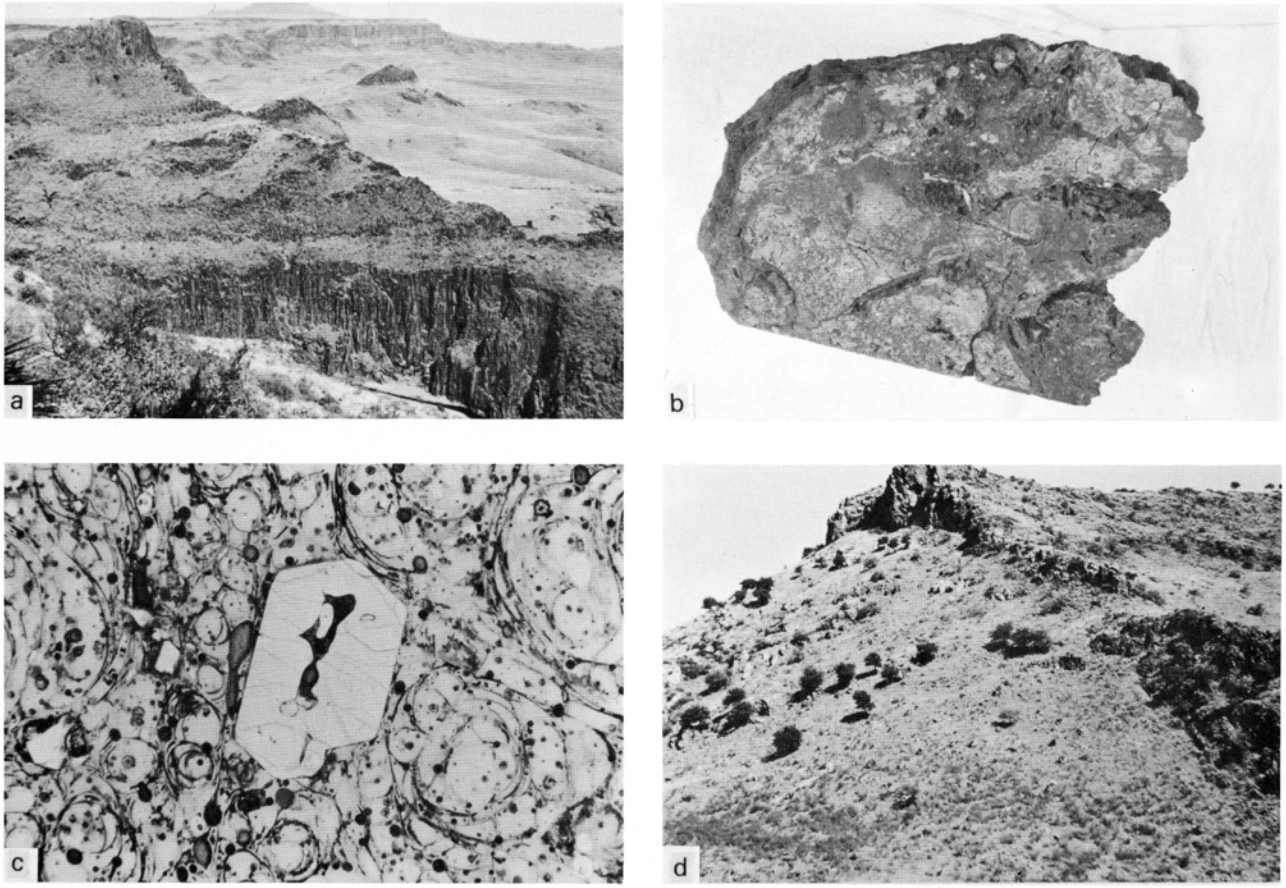

FIGURE 26—Star Mountain Formation. **a,** Section of SMF at Wild Rose Pass (Stop 4B). Massive lower unit forms prominent cliff in canyon bottom. Middle unit forms complex ledges in center of photograph; total number of flows in middle unit is uncertain. Massive upper unit caps section in upper left of photo. The type section at Star Mountain is visible in the center distance. **b,** Flattened clasts suggestive of spatter bombs from basal breccia, Pollard Dome (Stop 4A). Sample is 15 cm long. **c,** Vitrophyre, upper unit, Star Mountain Formation, Limpia Canyon (photo 4.3 × 2.9 mm, plane light). Note absence of vitroclastic texture and presence of perlitic fractures. **d,** East wall, Indian Cave Canyon (Stop 4C). Gomez Tuff (upper ledge) overlies both tuff breccia (left) and Star Mountain flow (cliff at right).

A thin lens of fine-grained tuff separates the second and third units (Fig. 25). It contains angular, 1 mm phenocrysts of alkali feldspar in a variably tuffaceous matrix and is almost certainly unrelated to the SMF. Because it is intensely baked and silicified by the overlying SMF flow, its origin, whether primary pyroclastic or detrital, is not clear. Where we will see it, the tuff is massive, but it is layered and even crossbedded in other exposures. It is significant in that it demonstrates a sufficient hiatus between flows of the SMF for its deposition.

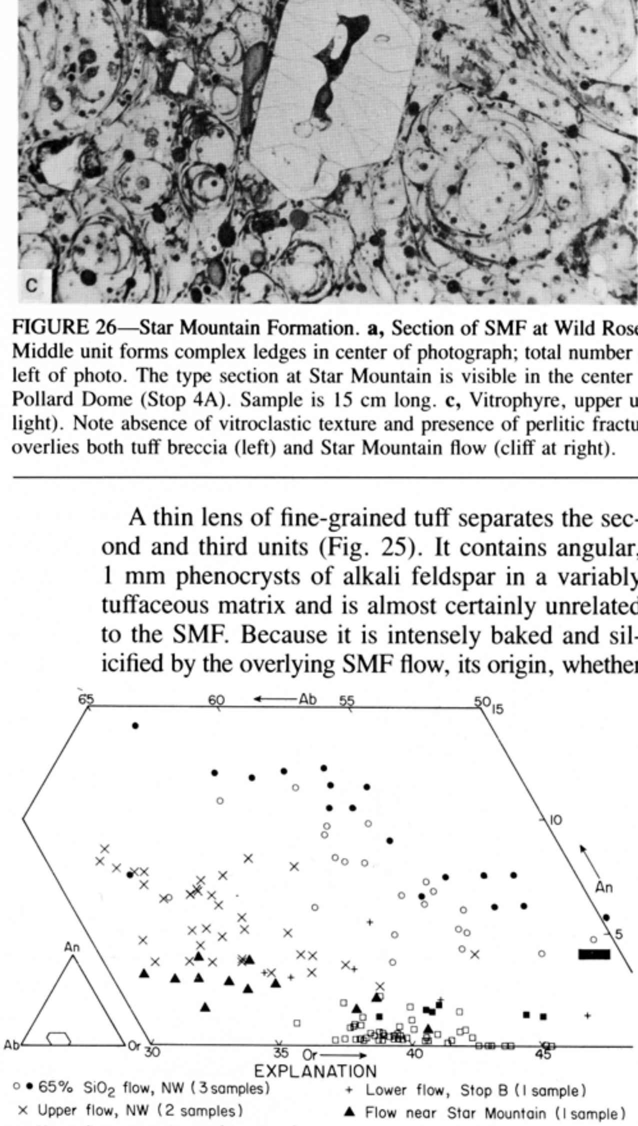

FIGURE 27—Compositions of alkali feldspar phenocrysts in 11 samples of SMF. Samples are grouped based on field correlation of individual flows. Note several distinct clusters of compositions, which correlate with whole-rock composition. Filled symbols and + are by D. F. Parker; all other analyses by J. N. Rubin, Texas Bureau of Economic Geology. Error bar as in Fig. 20.

From this vantage, the face of Star Mountain appears to consist of a lower massive unit, a complex middle unit with an irregular basal contact, and a massive upper unit. In fact, the middle unit is the basal rubble zone to the upper massive flow, and both together correlate with the third unit at Wild Rose Pass. The rubble is unusually thick (up to 70 m) here because it fills a paleovalley (note the rubble zone pinches out laterally at either end of the face) cut into the surface of the "lower" unit, itself equivalent to the second unit at Wild Rose Pass. This erosion horizon is the lateral equivalent of the reworked interval at the pass. The response of basal rubble thickness to topography demonstrates that the unit flowed through this area as a lava, not as some type of pyroclastic flow; in the latter case, the massive rheomorphic zone would fill the valley. This is critical evidence for a lava origin for at least one of the widespread silicic units of the Davis Mountains. **12.4**

57.8 Intersection of TX-17 and FM-1832. Turn left (west) onto 1832. **6.8**

64.6 Turn left (southwest) onto ranch road of H C Espy Ranch. Drive approximately 2 mi into Bob Manning and Indian Cave Canyons. **2.0**

66.6 **STOP 4-C. Star Mountain Formation at Indian Cave Canyon.** We are located approximately 15 km northwest of Wild Rose Pass, near the northwestern limit of mapped Star Mountain Formation. The walls of the canyon we have driven through consist of peralkaline quartz trachyte belonging to the Big Aguja intrusion, which domed SMF and Gomez Tuff. Just before parking the vehicles we crossed a Basin and Range normal fault (the same fault seen on Stop 1B) and crossed from the intrusion into SMF. We shall examine exposures of SMF in Indian Cave Canyon, a tributary of Bob Manning Canyon.

Indian Cave Canyon contains complicated exposures of SMF, a tuff-breccia unit, Gomez Tuff, and younger units (Figs. 26d, 28). The tuff-breccia unit is a local deposit of welded tuff and poorly sorted angular breccia probably related to a nearby silicic dome; it largely postdates SMF, but at least one flow of SMF filled a canyon cut in the tuff-breccia. Gomez Tuff, due to its momentum, was deposited over both the tuff-breccia mound and SMF.

For convenience of discussion, we refer to SMF underlying the tuff breccia as the lower part of SMF, and the post tuff-breccia flow as the upper part (note that these divisions are for this stop only and do not refer to the flows discussed in Stop 4B today).

The lower part of SMF may consist of several flows; these are typical, grayish-red porphyritic quartz trachyte. Flow features include autobreccia, vesicles, and ramp structures. A vitrophyre belonging to the uppermost flow in the lower part of SMF is exposed in the bottom of Indian Cave Canyon; it is the most mafic SMF sample yet analyzed (Table 2). The vitrophyre has flow bands and lenses that resemble fiamme, but no shard texture is visible.

The lower part of SMF is overlain by rhyolitic tuff breccia. The lower part of the breccia unit appears to be welded tuff (pinkish-gray rhyolite with sparse, small alkali feldspar phenocrysts and flattened pumice); this tuff grades upward into coarse (up to 30 cm in diameter) angular breccia composed mostly of gray rhyolite, although some basalt clasts are present. Small fragments of what may be biotite schist are also present in the rhyolite clasts.

The upper part of SMF consists of a single flow channelized into the tuff breccia (Fig. 26d). It rests directly upon the vitrophyre of the lower part of the SMF, but is flanked by the tuff breccia. Between the tuff breccia and the dense upper part of the SMF is a pink, poorly consolidated breccia with an ashy matrix and scoriaceous blocks of SMF up to 1 m in diameter.

Gomez Tuff surmounted the mound of tuff breccia and compacted over it, thereby managing to overlie both the breccia and the upper part of SMF. At this locality, the base of Gomez Tuff contains rounded to angular inclusions of white rhyolite up to about 75 cm diameter, some of which are clasts of the tuff breccia. Green lenses within the basal Gomez Tuff may represent partially molten magma "lumps" transported several kilometers from the southeastern edge of the Buckhorn caldera.

The channel geometry and poorly consolidated breccia underlying the upper flow in Indian Cave Canyon are of particular interest in regard to the mode of emplacement of SMF. The channel geometry suggests a lava-flow origin; certainly the upper flow of SMF behaved very differently than the Gomez Tuff. The ashy matrix is currently unexplained.

A poorly exposed basaltic intrusion (probably a dike) crops out along the jeep trail on the west side of Indian Cave Canyon. This intrusion is undated, but, on the basis of chemical and petrographic characteristics, most likely is related to Basin and Range extension. The intrusion contains a variety of crustal xenoliths (some glassy) and scattered mantle xenoliths. A visit to the intrusion will allow sampling of these inclusions plus an overview of the units exposed in the east wall of Indian Cave Canyon.

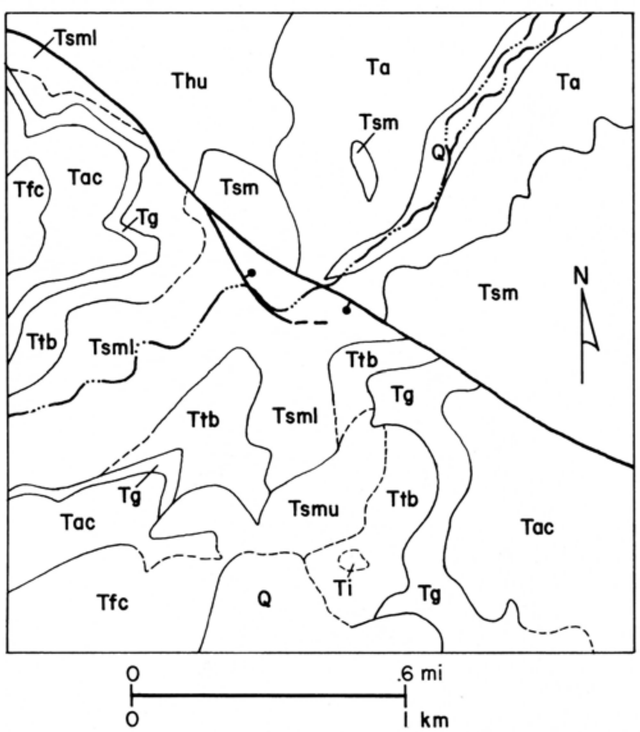

EXPLANATION

Q	Quaternary alluvium
Ti	Basin and Range basalt
Ta	Big Aguja intrusion
Tfc	Frazier Canyon Formation
Tac	Adobe Canyon Formation
Tg	Gomez Tuff
Ttb	Tuff breccia
Tsm	Star Mountain Formation; l and u designate informal lower and upper units
Thu	Huelster Formation

FIGURE 28—Geologic sketch map of area of Stop 4C in Bob Manning and Indian Cave Canyons.

Day 5: Burro Mesa Rhyolite and related rocks of Big Bend National Park

Day 5 will examine a group of strongly peralkaline rhyolitic lava domes and related pyroclastic rocks of Big Bend National Park. These rocks lie in an irregular belt that trends southwest from the Chisos Mountains (Fig. 29). Stop 5A will examine rhyolitic lavas on top of one of the domes at Burro Mesa (Fig. 30). At Stop 5B, erosion has exposed a cross section through the flank of the same dome complex. Near-vent pyroclastic-surge deposits are overlain by flow-banded lava. At Stop 5C, we will see more distal pyroclastic flows related to a different dome.

As formerly interpreted (and currently depicted on geologic maps of the area; Maxwell et al., 1967; Ogley, 1979; Barker et al., 1986), the pyroclastic rocks comprise Wasp Spring Member and the lava flows are Burro Mesa Rhyolite of South Rim Formation, a sequence of dominantly ash-flow tuffs erupted from the Pine Canyon caldera in the Chisos Mountains. Our current interpretation is that all these rocks, except possibly the occurrences at Emory Peak and Casa Grande in the Chisos Mountains (Fig. 29), are individual domes unrelated to the Pine Canyon caldera. This field trip and discussion focus only on the domes outside the Chisos Mountains. The rocks at Emory Peak and Casa Grande are petrographically similar to the rocks of the domes but are chemically distinct (Becker, 1976); also, at least part of Burro Mesa at Emory Peak is ash-flow tuff (Barker et al., 1986). Burro Mesa Rhyolite and Wasp Spring Member (and the various previous interpretations of them) offer a classic? example of the disastrous effects of miscorrelation upon interpretation of mechanisms of origin.

Burro Mesa Rhyolite outside the Chisos Mountains is composed of two petrographically distinct, peralkaline rock types: sparsely porphyritic and abundantly porphyritic (Becker, 1976; Ogley, 1979; Barker et al., 1986). On the basis of slight differences in whole-rock, major- and trace-element compositions and feldspar compositions, Becker recognized several petrologic types. Phenocrysts in both petrographic types include anorthoclase, fayalite, minor quartz, ferro-

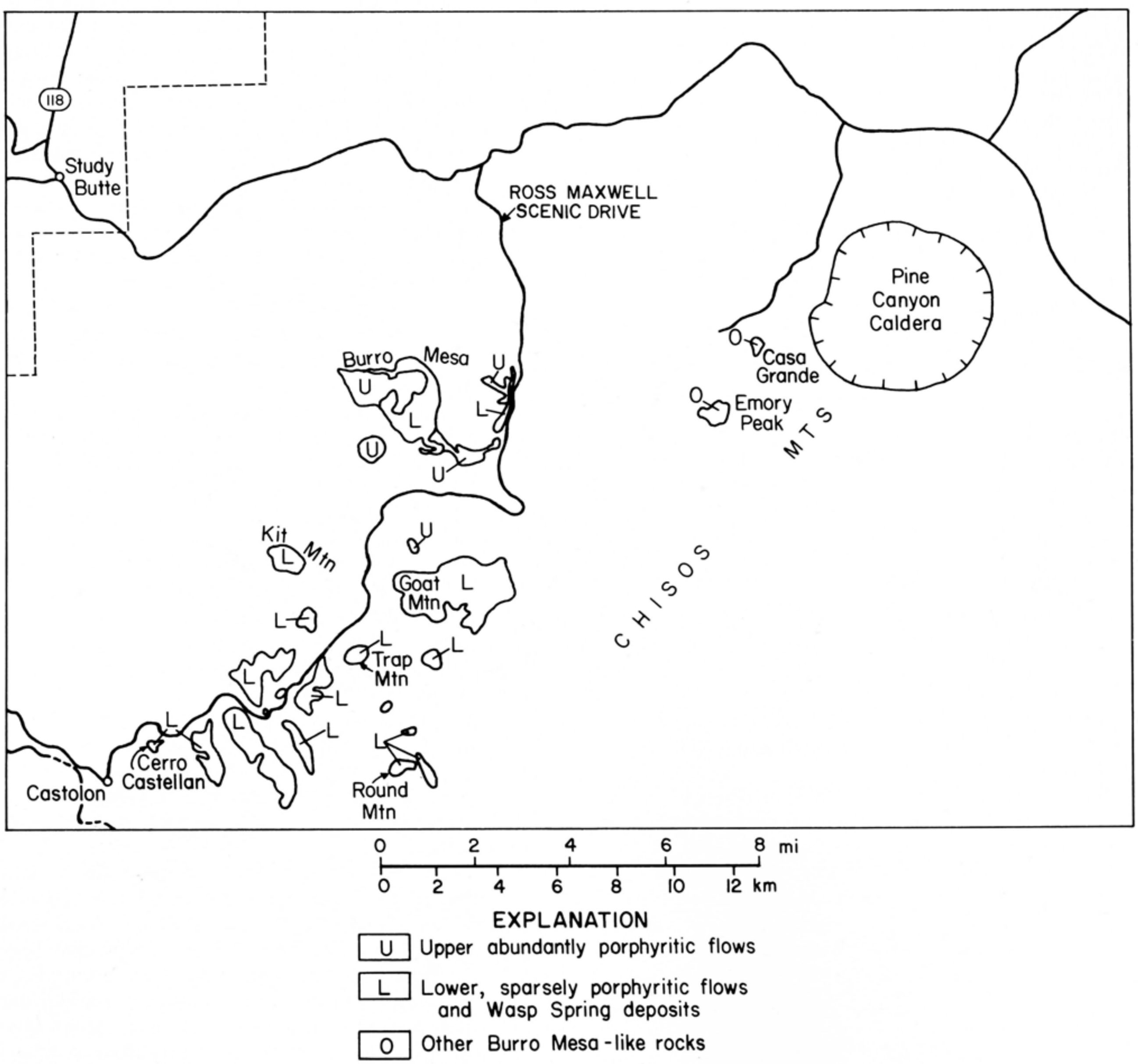

FIGURE 29—Lava domes of Burro Mesa Rhyolite and Wasp Spring Flow Breccia. Map also shows outcrops of similar rocks in the Chisos Mountains; rock on Emory Peak is a definite ash-flow tuff; rock at Casa Grande is a lava dome.

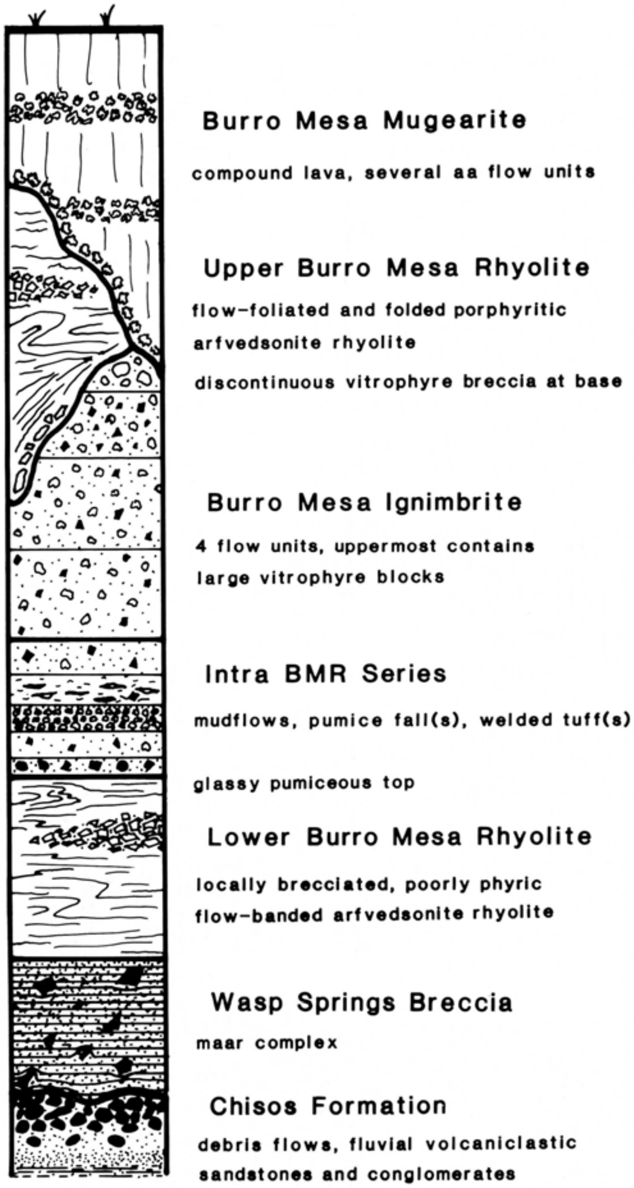

FIGURE 30—Idealized section through the Burro Mesa section. Lower three units (debris flows, Wasp Spring Flow Breccia, and lower rhyolite of the Burro Mesa) are seen at the Pouroff (Stop 5B).

hedenbergite, ilmenite, and a rare-earth silicate, which Becker identified as either chevkinite or perrierite. Groundmass or vapor-phase minerals include quartz and alkali feldspar, as well as the sodic phases, arfvedsonite, acmite, and aenigmatite. The less porphyritic type contains a few volume percent phenocrysts, whereas the more porphyritic type contains as much as 25% phenocrysts.

The less porphyritic phase is more widespread; it occurs as one or more flows in domes from Burro Mesa (Fig. 29) to Cerro Castellan, a distance of about 16 km. The dome at Casa Grande is petrographically similar but less silicic. The more porphyritic variety occurs only at Burro Mesa as an ignimbrite and lava which overlie a less porphyritic flow (Fig. 30). Rhyolite at Emory Peak is also abundantly porphyritic.

Wasp Spring Member is a heterogeneous group of pyroclastic deposits, including surges, ash-flow tuffs, and probable air-fall tuffs, as well as coarse, massive, debris-flow deposits. They preceded eruption of Burro Mesa lavas at most of the identified domes.

The overall picture that arises for Burro Mesa and Wasp Spring rocks is a series of eruptive centers trending southwest from the Chisos Mountains (Fig. 29). The largest preserved centers initially erupted a variety of pyroclastic rocks, including phreatomagmatic surge deposits (Burro Mesa and Goat Mountain); coarse, proximal, ash-flow tuffs (Cerro Castellan); and both surges and coarse debris flows (Goat Mountain). Sparsely porphyritic lavas followed the pyroclastic rocks at all centers. Abundantly porphyritic ash flows and lava subsequently erupted at Burro Mesa, which is probably the largest center. Feeder dikes or stocks are exposed at Cerro Castellan and Goat Mountain; at the latter, the feeder is several tens of meters wide. Smaller dikes and irregularly shaped intrusions of similar peralkaline rhyolite are abundant throughout the area. They may also have fed pyroclastic eruptions and lavas, which have since been eroded. Similar, contemporaneous peralkaline rhyolite domes occur approximately 50 km to the west, well outside the general Burro Mesa belt.

The sparsely porphyritic and abundantly porphyritic varieties are compositionally similar rhyolites containing 73–75% SiO_2 (Becker, 1976; Barker et al., 1986). The porphyritic upper lava flow at Burro Mesa has distinctive trace-element concentrations (Becker, 1976), probably in part reflecting its greater phenocryst content. The sparsely porphyritic flows have essentially identical major- and trace-element concentrations, although Becker suggested that the Cerro Castellan dome was slightly less silicic. Becker also thought that most Burro Mesa rocks, including those in the Chisos Mountains, were related by fractional crystallization, and suggested that they developed from an alkalic basalt, possibly similar to basalt that occurs as inclusions in most flows. The similarity of compositions over the 16 km belt is impressive; a single magma chamber underlying all the occurrences seems unlikely.

A modern analog for Burro Mesa domes is provided by Mono Craters, Long Valley, California (Bailey et al., 1976; Fink, 1983; Sampson and Cameron, 1987), where the general eruptive sequence is initial pyroclastic rocks followed by relatively dry and highly viscous lava (including progressively more porphyritic varieties) erupted from vents where a dike broke through to the surface. The complexity of magma evolution is also similar (Sampson and Cameron, 1987).

Burro Mesa Rhyolite and Wasp Springs Member were traditionally considered part of the Pine Canyon caldera assemblage. They were thought to have flowed southwest, down paleovalleys in underlying Chisos Formation, a distance of at least 20 km. Clear evidence of their eruption from a series of local sources (to be seen today) as well as a few K–Ar ages indicate that they are unrelated to, and distinctly younger than, the caldera. However, assuming this wide distribution and noting a few possible indications of a pyroclastic origin, one of us (CDH *in* Barker et al., 1986) concluded that Burro Mesa Rhyolite was strongly rheomorphic tuff and that Wasp Spring Member consisted of pyroclastic-surge deposits that were forerunners to Burro Mesa. Although the latter is true, the former is clearly wrong, and CDH now retracts that interpretation.

Nevertheless, some parts of mapped Burro Mesa Rhyolite are ash-flow tuff, and the correlation and origin of other parts have not yet been determined. Burro Mesa on Emory Peak in the Chisos Mountains is definitely ash-flow tuff, possibly an eruptive unit of the Pine Canyon caldera. At that location, a vitrophyric base shows well-preserved glass shards and pumice; lithic fragments are common (see photos in Barker et al., 1986). Within about 10 m above the base, intense devitrification and vapor-phase crystallization have destroyed the pyroclastic texture, although scattered lithic fragments are present. The resultant rock is not obviously pyroclastic, strongly resembles abundantly porphyritic Burro Mesa lava that we will examine today at Burro Mesa, but lacks flow banding. The rock at Emory Peak possibly should not be called Burro Mesa Rhyolite, as its relation to rock at the type locality at Burro Mesa is unclear. Distinction between the different types in the Chisos Mountains awaits more detailed study.

These observations also have implications for interpretation of rocks such as the Star Mountain Formation. Because Burro Mesa flows are petrographically and chemically similar and form nearly continuous outcrop, they can and have been interpreted as extremely long flows that originated in the Chisos Mountains. Recognition that Burro Mesa Rhyolite has a multitude of widely distributed sources and is composed of numerous local flows disproves this interpretation. Our understanding of Star Mountain Formation is not sufficient to disprove an origin similar to that of Burro Mesa.

Mileage

0.0 The roundtrip of approximately 240 mi starts at US-90 and TX-118S and follows the same route as Day 3 for the first 69 mi. **28.0**

28.0 **PHOTO STOP. Crossen Trachyte** crops out west of the highway (Fig. 31a). It occupies the same stratigraphic position, has the same outcrop ap-

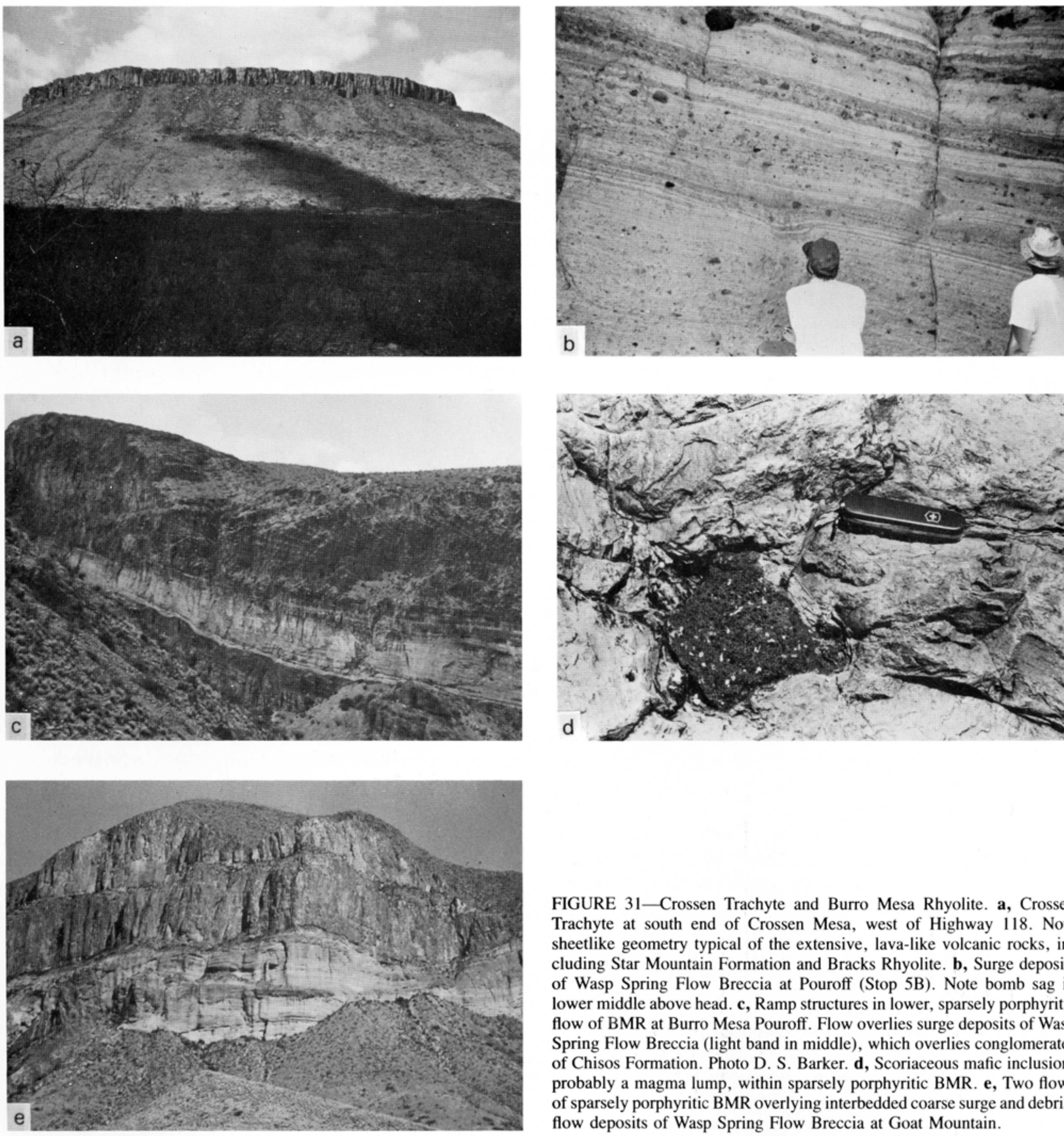

FIGURE 31—Crossen Trachyte and Burro Mesa Rhyolite. **a,** Crossen Trachyte at south end of Crossen Mesa, west of Highway 118. Note sheetlike geometry typical of the extensive, lava-like volcanic rocks, including Star Mountain Formation and Bracks Rhyolite. **b,** Surge deposits of Wasp Spring Flow Breccia at Pouroff (Stop 5B). Note bomb sag in lower middle above head. **c,** Ramp structures in lower, sparsely porphyritic flow of BMR at Burro Mesa Pouroff. Flow overlies surge deposits of Wasp Spring Flow Breccia (light band in middle), which overlies conglomerates of Chisos Formation. Photo D. S. Barker. **d,** Scoriaceous mafic inclusion, probably a magma lump, within sparsely porphyritic BMR. **e,** Two flows of sparsely porphyritic BMR overlying interbedded coarse surge and debris-flow deposits of Wasp Spring Flow Breccia at Goat Mountain.

pearance, and is petrographically and chemically similar to Star Mountain Formation and Bracks Rhyolite (which will be observed on Day 6). Henry et al. (1988a) suggest that they represent a unique eruptive event 37 Ma that occurred through much of Trans-Pecos. **49.5**

77.5 Intersection of TX-118 and TX-170, which leads to Terlingua, Lajitas, Presidio, and Chihuahua. Continue straight (south) on 118. **3.0**

80.5 Entering Big Bend National Park. **Collecting rocks or any other samples within the park is illegal. Please do not jeopardize future research and field trips in the park. LEAVE YOUR HAMMER IN THE VEHICLE!** Permission to conduct scientific research, including sampling, must be obtained by submitting a research proposal to the Superintendent, Big Bend National Park, National Park Service, Big Bend National Park, Texas 79834. **9.2**

89.7 Intersection of the main park road with Ross Maxwell Scenic Drive, the road to Castellon. Turn right (south) onto Ross Maxwell Scenic Drive. In a monumental pioneering work, Maxwell et al. (1967) mapped the geology of the park, identified most of the intrusions petrographically, and provided major-element chemical analyses of many of the igneous rocks. Maxwell was also the first superintendent of the park. **2.4**

92.1 **STOP 5-A. Burro Mesa Rhyolite on upper Burro Mesa.** A trail leads from the scenic viewpoint to the Pouroff along the top of Burro Mesa. The trail generally follows the creek bed that leads to the Pouroff and affords excellent sections through the Burro Mesa units (Fig. 30).

The uppermost unit seen at Burro Mesa is a compound mugearite lava consisting of several aa flow units. The lava is ponded in an erosional hollow cut into the underlying rhyolite and ignimbrite units; the contact can be seen at one point on the north side of the creek bed.

The uppermost rhyolite unit (the first rock encountered along the trail) is a coarsely porphyritic peralkaline rhyolite with prominent groundmass arfvedsonite. Typically the lava is flow-banded and locally exhibits spectacular flow folds, ramp structures, and platy jointing. Localized internal breccia zones occur, but it is unclear whether or not these represent flow-unit boundaries. Where it overlies paleotopographic highs, the lava is often massive to the base; basal breccias are best developed in low spots. At one place, the breccias include an apparent pyroclastic-flow deposit consisting of flow-banded vitrophyre blocks in an ashy matrix, interpreted as a local deposit generated by collapse of a gravitationally unstable lava-flow front; the pyroclastic flow moved ahead of the lava and was overridden by it.

The upper rhyolite rests on an erosional surface cut into the Burro Mesa ignimbrite; except for obvious differences arising from eruptive mechanism, the two units are virtually identical petrographically. The ignimbrite consists of at least four flow units and is nonwelded to incipiently welded. The uppermost unit is a block-and-ash flow consisting of non-banded vitrophyre blocks up to 2 m in diameter in a reddish-orange matrix. The other three units are "conventional" ignimbrites; one has weakly imbricated pumice at the base, suggesting a flow direction from east to west.

Beneath the ignimbrite is a poorly understood sequence some 50 m thick, dominated by reworked pumice layers, pumice-rich mudflows, and debris flows, with at least one thin welded ignimbrite and a probable primary pumice-fall deposit.

The deposits rest on a flow-banded, commonly pumiceous vitrophyre that is the upper carapace of lower Burro Mesa. The glass has largely decomposed to a yellow alteration product. The vitrophyre grades down into massive, stony rhyolite that forms the interior of the lower Burro Mesa flow. Flow bands are accentuated by abundant groundmass arfvedsonite. The flow contains scattered inclusions of variably vesicular basalt. These commonly exhibit crenulate margins and are believed to be magmatic inclusions. **9.1**

101.2 Turn right onto the road to Burro Mesa Pouroff. **1.8**

103.0 **STOP 5-B. Wasp Spring Member and Burro Mesa Rhyolite at Burro Mesa pouroff.** Park at turnaround at end of Pouroff road. Walk 0.5 mi (0.8 km) to pouroff to examine Wasp Spring Member and base of the lower, less porphyritic, flow of Burro Mesa Rhyolite.

The trail proceeds upsection through Chisos Formation and into fluvial conglomerates and debris-flow deposits that record erosion and redeposition of Chisos material before emplacement of the Wasp Spring (Fig. 30). Clasts of porphyritic Tule Mountain Trachyandesite, the uppermost formal member of Chisos Formation, are common.

Wasp Spring at Burro Mesa occurs as a shallow tuff ring or maar; the associated vent system is buried under Burro Mesa Rhyolite. A partial section through the crater wall is exposed in a box canyon branching off the Pouroff trail. Wasp Spring is composed of coarse, well-bedded tuff that consists dominantly of pyroclastic-surge deposits (Fig. 31b). It was emplaced on a surface of considerable relief incised into the conglomerate. Low-angle crossbeds occur in some layers, and pumice clasts are commonly imbricated, showing southwestward transport. Lithics up to 80 cm across are common. The majority of blocks were emplaced by lateral transport, as most did not form bomb sags. Blocks vary from angular to rounded and appear to have been derived dominantly from the underlying debris-flow deposits, which may have acted as an aquifer supplying water to the vent for this phreatomagmatic eruption. An intermittent water supply toward the end of the explosive phase is indicated by the presence of a thin welded/agglutinated layer in the intracrater facies, just below the contact with lower, sparsely porphyritic, Burro Mesa Rhyolite. The tuff ring thins in all directions away from the mouth of the canyon; imbricated clasts within the tuff indicate a source just east of the head of the canyon.

Rhyolite here is typical of the sparsely porphyritic variety that occurs at all domes. It has irregular basal and intraflow breccias and pronounced flow folds, as well as faint ramp structures in the cliffs above (Fig. 31c). The top is locally glassy, pumiceous, and brecciated. There is no evidence of erosion or of soil formation on the tuff ring prior to emplacement of the lava flow, which thus may have filled the crater as a later "dry" phase of the same eruption.

The rhyolite bears scattered porphyritic mafic inclusions, some of which are rounded or have crenulate margins (Fig. 31d). Similar inclusions occur in Burro Mesa Rhyolite at Goat Mountain and Cerro Castellan. The inclusions at Burro Mesa were previously considered to be lithic fragments in strongly rheomorphic tuff (Barker et al., 1986). However, their common association with the rhyolite at several domes suggests they are magmatic inclusions. The mafic magma apparently did not otherwise erupt, as no flows of it have been identified.

Return to vehicles and drive back to Ross Maxwell Scenic Drive. **1.8**

104.8 Intersection with Ross Maxwell Scenic Drive. Turn right (south). We pass Goat Mountain, another Burro Mesa eruptive center, which has two of the sparsely porphyritic flows overlying very coarse near-vent deposits, including surge and debris flows (Fig. 31e). **8.2**

113.0 **STOP 5-C. Pyroclastic rocks at Tuff Canyon overlook.** In addition to examining outcrops in the canyon, this provides a good view of Cerro Castellan, still another Burro Mesa vent. Ash-flow tuff having a phenocryst assemblage similar to the sparsely porphyritic lavas erupted initially and makes up most of the hill. A steeply dipping dike along the north side of the hill cut the ash-flow tuff and fed a sparsely porphyritic lava that caps the top of the hill. Tuff in Tuff Canyon may be related to this vent.

Tuff Canyon provides a section through the best preserved, nonwelded pyroclastic rocks in the region; primary pumice structures are well preserved. The section is cut by several minor normal faults. Intercalated between two sets of reworked pyroclastic materials is a nonwelded ignimbrite consisting of several flow units, each less than 1 m thick. The flow units have variable lithic contents, exhibit limited coarse-tail grading, and contain abundant lithic-enriched degassing pipes. Pipes crosscut flow-unit boundaries, indicating rapid successive deposition of units on a time scale of probably not more than several hours. Pipes are unusually abundant, suggesting an extraneous gas source, probably water from the underlying reworked pyroclastics.

The pyroclastic rocks overlie a basalt lava with a relatively thick, fine-grained basal breccia, probably formed when a subaerial lava flowed into shallow standing water.

Day 6: Bracks Rhyolite

On our last day of the field trip, we will examine Bracks Rhyolite (BR), the best exposed and currently most thoroughly studied of the controversial silicic rocks. It crops out over a 55 × 15 km area (Fig. 9); the width is a minimum because it is buried beneath younger rocks to the east. The cumulative field, petrographic, and chemical data strongly indicate that BR was emplaced as a single lava flow with a source in the north-central part of its outcrop, at Stop 6A.

Despite its name, BR is a quartz trachyte containing 68–69% SiO_2 (Table 2). It contains 10–15% phenocrysts of sanidine, iron-rich clinopyroxene, fayalite, and magnetite. In outcrop characteristics, composition, mineralogy, texture, K–Ar age, and stratigraphic position, it is nearly indistinguishable from Star Mountain Formation and Crossen Trachyte.

BR is well exposed along a nearly continuous cliff face of the Vieja Rim, an eroded Basin and Range fault scarp (Fig. 32a). Its thin, sheet-like geometry is apparent. It can be followed along this face as a single, massive, and crudely columnar-jointed flow; internal breccia zones that could mark boundaries between different flows are absent. It was emplaced on a surface of low relief and low gradient. The basal contact is sharp (Fig. 32b); underlying tuffaceous sedimentary rocks are commonly baked and in places ripped up or deformed in a manner similar to soft-sediment deformation. A basal breccia of vesicular or amygdaloidal blocks occurs irregularly and grades upward into massive, flow-banded rock (Fig. 32c).

Thickness variation and sparse flow-direction indicators (ramp structures and elongated vesicles) suggest that the source of BR is in the area of Stop 6A, consistent with the postulated occurrence of vents there. BR is as much as 120 m thick in the vent area and thins progressively to the north, south, and west; thicknesses in the buried eastern part are unknown. Sporadic preservation of flow-top breccias suggests that present thicknesses are only slightly less than original thicknesses. The aspect ratio is about 1:700 (Table 4, Fig. 10). The southern termination is a 3–4 m high nose that appears to be the original margin of a lava flow; for example, elongated vesicles wrap around the nose. BR thickens to about 40 m within 1 km to the north.

The BR is chemically and mineralogically homogeneous. Eight samples representing most of the areal extent contain approximately 68–69% SiO_2, expressed H_2O-free (Table 2). Minor variations in alkalies, CaO, Fe^{2+}/Fe^{3+}, and H_2O in these samples reflect hydration, devitrification, and oxidation common in many Trans-Pecos rocks. Their homogeneity is best illustrated by the narrow range of rare-earth-element concentrations (Fig. 33) and phenocryst compositions (Fig. 34). This homogeneity and the continuity of outcrop indicate that BR is a single, homogeneous flow.

Outcrop and petrographic features of BR are those of lava flows and not of pyroclastic flows. BR has breccias and vitrophyres at the top and bottom, is flow-banded and folded, and has elongated vesicles. Phenocrysts, microlites, and elongated vesicles are aligned. The feldspar phenocrysts are subhedral to euhedral and mostly 3–4 mm long, but some larger phenocrysts and glomerocrysts up to 8 mm are also present. Broken phenocrysts ranging widely in size, typical of many ash-flow tuffs, are not present. Shards, pumice, and lithic fragments are absent. Pyroclastic texture has not been found in vitrophyres, where shard texture might be better preserved than in devitrified or other crystalline samples (Fig. 32d).

Mileage

0.0 Today's trip of about 250 mi ends in El Paso. The log starts at US-90 and TX-118N. Drive west on US-90. **9.0**

9.0 Collapse terrain of Paisano volcano. Parker (1976,

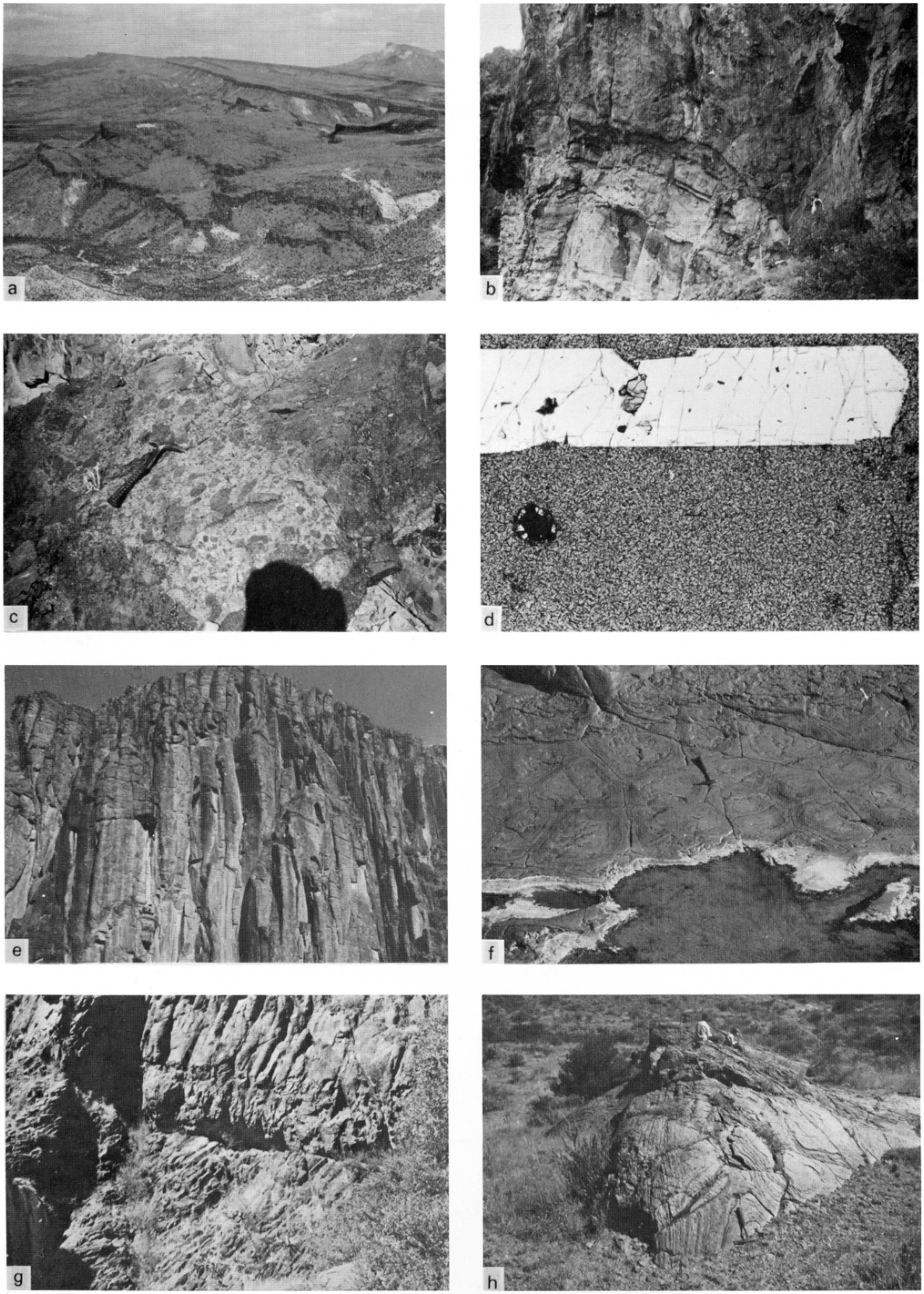
a
b
c
d
e
f
g
h

FIGURE 32—Bracks Rhyolite. **a,** Looking north at southern end of Bracks outcrop (dark, massive flow overlying poorly exposed white tuffaceous sediments) exhibiting thin, sheet-like geometry. Disruption in foreground is due to a combination of minor faults and landslides. Bracks Rhyolite continues as caprock 55 km to north (left distance). **b,** Base of flow over tuffaceous sediments. Note irregular contact due to scour or soft-sediment deformation of sediments. Base is vesicular but not brecciated. **c,** Basal breccia showing angular to rounded clasts in fragmented matrix. **d,** Photomicrograph of vitrophyre showing euhedral, unbroken alkali feldspar phenocryst with clinopyroxene inclusion and altered fayalite. Note homogeneous groundmass of glass and unoriented microlites. **e,** Typical, crude, massive columnar jointing in main part of flow in ZH canyon. **f,** Plan view of columnar joints in ZH canyon. Note columns within "megacolumns." **g,** Tilted columns within vitrophyric dome. Contact between glassy dome (bottom) and crystalline rock (top) is ledge at change from shallowly dipping to steeply dipping columns. Contact dips gently to north (away from photographer). **h,** Asymmetric fold on upper surface over vitrophyric dome. Flow bands on steep limb (left) are locally overturned.

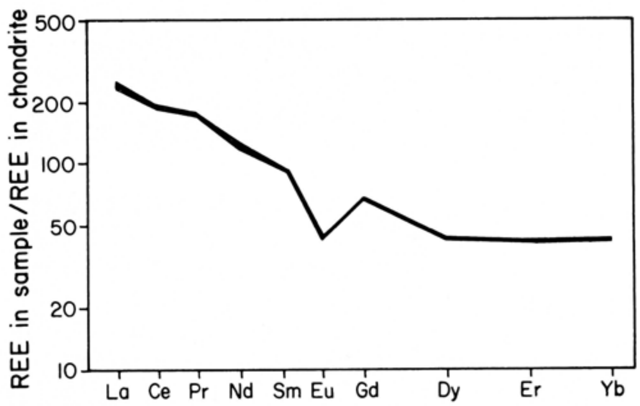

FIGURE 33—Chondrite-normalized rare-earth-element patterns for eight samples of Bracks Rhyolite representing the entire outcrop area. Note homogeneity.

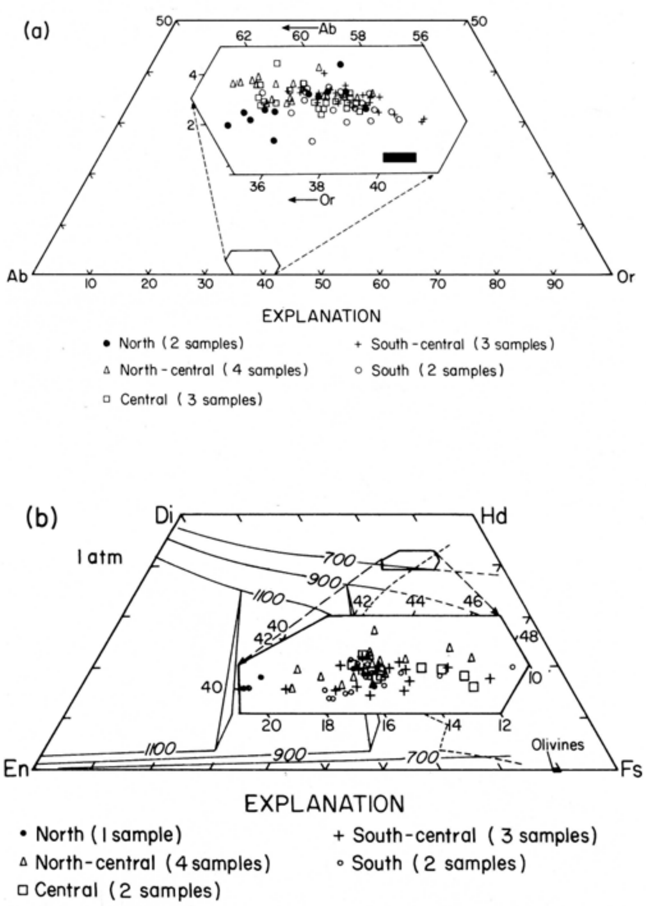

FIGURE 34—Compositions of phenocrysts in Bracks Rhyolite. Note narrow range of compositions of all phenocrysts. **a,** Alkali feldspars from 14 samples. Error bar as in Fig. 20. **b,** Clinopyroxenes and olivines from 12 samples plotted on pyroxene solvus of Lindsley (1983).

1983) mapped an area 5 km in diameter, of megabreccia, agglomeratic tuff, lahar deposits, and disoriented blocks of Decie Formation, as collapse terrain that developed during evolution of the Paisano volcano. The collapse features may have formed by landsliding from oversteepened caldera walls or, alternatively, from unstable flanks of the Paisano volcano. **17.2**

26.2 Town of Marfa. In the center of town US-67 leads south to Presidio and Ojinaga, Chihuahua. Continue straight on US-90 toward Van Horn. Northward from Marfa, the highway enters Lobo Valley, a Basin and Range graben. The southern end of the graben has no identifiable boundary faults and may be simply a broad sag. Farther north, boundary faults have up to 1 km of displacement. **36.2**

62.4 Town of Valentine. **0.7**

63.1 Turn left onto ranch road to Clay Miller Ranch. **WARNING: ALL PROPERTY ALONG THIS ROAD IS PRIVATE. PERMISSION TO ENTER MUST BE OBTAINED FROM LANDOWNERS.** Drive 9.8 mi west and south to ranch. **9.9**

73.0 **STOP 6-A. Traverse through Bracks Rhyolite flow and vent.** This traverse provides a closeup view of many of the features of Bracks discussed above, as well as a look at a probable source vent for the flow (Fig. 35). The main canyon (ZH Canyon) at the beginning of the traverse is in typical, massive, columnar-jointed BR. The base of the flow is near the bottom of the canyon but, unfortunately, is not exposed here. Nevertheless, almost a complete section of the more than 100 m thick flow is exposed. The rock is notably homogeneous, shows some lava-flow features, such as faint flow bands, and lacks any pyroclastic features. The rock is crystalline, but clasts of vitrophyre are common in the stream bed. The excellent exposures make it clear that the rock is a single flow.

Columnar joints in BR are well exposed both in cross section and plan view (Fig. 32e, f). Cross sections show distinct incremental growth bands as described by DeGraff and Aydin (1987). Plan views show that individual columns, generally about 40–60 cm wide, occur as clusters within larger columns 1–1.2 m wide (Fig. 32f). The larger columns formed first during initial cooling; the smaller columns former after and within the larger ones. Columns are vertical, as would be expected in a laterally extensive flow.

One of more than 30 vitrophyric intrusions that probably mark vents for BR is exposed approximately 400 m up a side canyon to the northwest (Figs. 32g, 35). These intrusions occur possibly as several groups aligned along slightly west-of-north

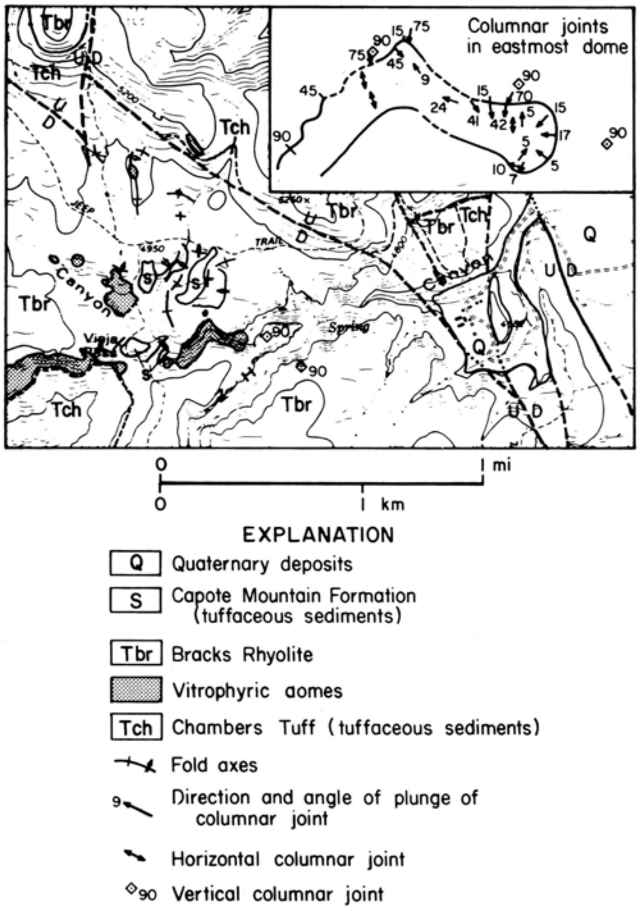

FIGURE 35—Geologic map of Bracks Rhyolite in ZH canyon area (Stop 6A).

trends in a zone extending 5 km to the south. Most are regularly dome-shaped, circular in plan view, much wider than high, and have smoothly convex upper surfaces. A few, including those observed here, are much more irregular. All these bodies consist of glassy rock that is otherwise identical to the rest of BR. Contacts are marked by abrupt transitions from glassy rock in the intrusions to totally crystalline rock outside and by abrupt changes in the orientation of columnar joints in both (Fig. 32g). Contacts, flow bands, and flow folds in both glassy and crystalline rock indicate that the vitrophyre bodies intrude the rest of BR. Columns in both vitrophyre and crystalline rock are nearly perpendicular to the contact. Thus columns in vitrophyre fan around the inside of the intrusion, whereas columns in crystalline (extrusive) rock make abrupt bends to align themselves with the contact.

The vitrophyre intrusion that we observe here crops out for about 300 m within the canyon and probably extends beneath the crystalline part to the north beneath an irregular topographic basin on top of BR (Fig. 35). The contact between vitrophyre and crystalline rock is dominantly vertical along the south side of the canyon, but dips shallowly to the north along the north side (Fig. 35). Where well exposed along the north side, both crystalline and glassy rock are intensely and finely fractured within about 50 cm of the contact. Weathering of the fractured rock has produced a distinct recess (Fig. 32g). Although fractured, neither rock is brecciated as is common at the base or top of BR.

Columns in both zones near the contact are nearly perpendicular to it (Figs. 32g, 35). Columns in the upper zone along the shallowly dipping (15°) northern contact plunge about 70–75° into the contact. Along a distinct hinge about 10 m above the contact, they change to a normal, vertical orientation. Columns within the glassy zone along the northern contact plunge 40–45° away from it. Toward the vertical, southern contact, they plunge more shallowly. Along the southern contact, they plunge no more than about 15°; many are horizontal. At the eastern end of the vent area, the contact swings through almost 180° of arc, and the columns follow the contact all along it.

A small body of vitrophyre approximately 10 m across, immediately north of the canyon, may be an apophysis from this larger body. The smaller body is more "finger-shaped," being at least 20 m high. Folds in crystalline rock around it show that the vitrophyre is clearly intrusive.

We interpret the vitrophyre bodies to represent late magma batches that intruded the still liquid flow. The orientation of columnar joints suggests that both vitrophyre and crystalline parts cooled against the contact and therefore must have cooled contemporaneously. The abrupt crystallinity boundary may reflect differences in volatile contents or in temperature between the two at the time of emplacement of the vitrophyre. The apparent alignment of groups of intrusions suggests they may ultimately overlie a dike feeder system.

A topographically irregular basin, about 800–1000 m in diameter, occurs in crystalline BR on its upper surface north of the exposed dome. Flow bands and folds are common (Fig. 32h). Numerous anticlinal folds, defined by flow bands, form topographic highs. Both symmetric and asymmetric folds are present; complex parasitic folds occur on the flanks of many larger folds. Fold axes strike in a wide range of directions and do not seem to show a regular pattern. Flow lineations indicate flow perpendicular to some folds but parallel to some others. Lows are commonly occupied by tuffaceous sediments that appear to have filled in between the highs. Several additional vitrophyre bodies occur within this area. In contrast, the upper surface of BR elsewhere is relatively featureless; flow folds are sparse.

We suggest that the folds and irregular topography reflect complex intrusion of vitrophyric domes. Additionally, some of the folds may have formed during late withdrawal of magma back into the vent. Eichelberger et al. (1985) suggested similar subsidence over a much smaller vent of one of the Inyo domes in California. In contrast to the narrow (less than a few tens of meters), dike-related fissure eruptions documented for many smaller rhyolite domes (Fink and Pollard, 1983; Fink, 1985; Eichelberger et al., 1985), this vent is much larger and more irregularly shaped, although ultimately it may also be dike-fed. The considerably larger volume of BR compared to any of these smaller rhyolite extrusions may have required a much larger vent.

Return to US-90. **9.8**

82.8 Intersection of US-90. Turn left (north) toward Van Horn. **42.3**

125.1 Town of Van Horn. Enter I-10 westbound, on which we will remain for the next 115 mi to El Paso. **4.2**

129.3 We are entering the Carrizo Mountains, an uplifted block of Precambrian rocks, including metamorphosed ash-flow tuff. Pyroclastic features are well preserved in some tuffs (Rudnik, 1983). Roadcuts for the next 5 mi are in Precambrian rocks. **29.1**

158.4 Town of Sierra Blanca. The peaks ahead and to the right are igneous rocks of the Quitman Mountains caldera and Sierra Blanca laccoliths; the highway passes between them a few miles ahead. The caldera is on the south; blocky outcrops near the highway are quartz monzonite of the 36 Ma Quitman Mountains pluton. The Sierra Blanca intrusions to the north are contemporaneous with the Quitman Mountains magmatism but appear to be geochemically unrelated (Shannon and Goodell, 1986; Mathews and Adams, 1986). The intrusions are alkalic, but not peralkaline, rhyolite highly enriched in many incompatible elements, including fluorine and beryllium (Shannon and Goodell, 1986; Rubin et al., 1987). Lower Cretaceous limestone along the contacts with the rhyolite laccoliths is locally replaced by fluorite and beryllium minerals. **9.9**

168.3 As we pass the Quitman Mountains, the highway drops down into Hueco bolson, a Basin and Range basin that the highway follows to El Paso. The basin is bounded on the west by the Sierra del Presidio, Sierra de Guadalupe, and Sierra Juarez in Chihuahua and by the Franklin Mountains near El Paso. It is bounded on the east by the Malone Mountains, Finlay Mountains, Diablo Plateau, and Hueco Mountains. The Malone Mountains consist of folded and thrust-faulted Permian and Jurassic sedimentary rocks. The ranges in Mexico are similarly deformed Cretaceous rocks. All this deformation is part of the Laramide-age Chihuahua tectonic belt. The two broad domes of the Finlay Mountains formed about 47 Ma (Mathews and Adams, 1986; Henry et al., 1986) by intrusion of mafic rocks containing abundant hornblende phenocrysts, an uncommon mineral in Trans-Pecos igneous rocks. The Franklin Mountains contain Precambrian rocks overlain by a sequence of Paleozoic sedimentary rocks. These rocks are tilted 40° to the west, probably as a result of rotation along shallow-dipping Basin and Range faults. Quaternary fault scarps are abundant in Hueco bolson in the vicinity of El Paso and to the north (Seager, 1980). **71.0**

239.3 Exit I-10 onto Airway Boulevard and drive 1.6 mi north to the El Paso Airport.

Conclusions: Origin of the extensive silicic rocks

Clearly, some of the rocks examined on this field trip are rheomorphic tuffs, including some that show dominantly lava-flow features, such as the first unit of Barrel Springs Formation in Davis Mountains State Park. Some other rocks, most notably Bracks Rhyolite and Star Mountain Formation, are equally clearly widespread silicic lavas. At least one unit, Sleeping Lion Formation, remains controversial. Here, we first discuss the sum of evidence that leads to the conclusion that many of the rocks are silicic lavas. Then we offer a model for "lava-like tuffs," i.e., pyroclastic flows that underwent an extreme combination of primary viscous flow and secondary rheomorphism to acquire many of the features of lavas.

1. Evidence for a lava-flow origin

The following discussion focuses principally on Bracks Rhyolite and Star Mountain Formation, but may also apply to Crossen Trachyte and Sleeping Lion Formation.

A. The first and most obvious evidence for a lava-flow origin is the abundance of outcrop-scale lava-flow features, including flow bands and folds, breccias and vitrophyres at the base and top of flows, elongate vesicles, and steep, relatively abrupt flow fronts. Similar features are common in unequivocal lava flows of a wide range of compositions and ages (Cas and Wright, 1987; Fink, 1987). Except for the great areal extent of the Trans-Pecos flows, a lava-flow origin probably would not be doubted. Although some of these characteristics may be acquired by rheomorphic tuffs during secondary flow, their presence proves that the units flowed as lavas at least at the end of their emplacement.

More subtle evidence for a lava origin lies in the petrography and whole-rock and mineral chemistry. Bracks Rhyolite contains unbroken and generally euhedral phenocrysts of a narrow size range; delicate-textured glomerocrysts are common. Broken phenocrysts of a wide size range, typical of many ash-flow tuffs, have not been found. The narrow whole-rock and mineral compositions indicate Bracks erupted from a compositionally homogeneous magma chamber. In contrast, feldspar phenocrysts in rheomorphic Barrel Springs tuff are commonly broken and have a much wider compositional range, consistent with the zoning that is typical of many ash-flow tuffs (Hildreth, 1981). Although the petrographic and chemical arguments are not definitive, the data are more consistent with a lava origin than a pyroclastic origin.

B. These rocks lack features of pyroclastic flows. For example, shards, pumice fragments, lithic fragments, wide size ranges of broken phenocrysts, and welding zonation typical of tuffs have not been found in Bracks or Star Mountain despite intense search. In contrast, even strongly rheomorphic Barrel Springs tuff has preserved a clearly pyroclastic base, and lithic fragments similar to those in the base occur throughout the upper foliated, flow-banded, and brecciated parts. Although several debatable features could be interpreted as evidence of a pyroclastic origin, they are equally consistent with a lava-flow origin. For example, "fiamme-like" structures (e.g., Fig. 21d) are equally well interpreted as flow bands in a lava. Coarse bubble shards are typical of textures associated with brecciation of coarsely vesicular lava flows and are ubiquitous in modern lavas (Fink and Manley, 1987; Manley and Fink, 1987; Sampson, 1987). Further, silicic lavas almost universally have some accompanying pyroclastic deposits (Heiken and Wohletz, 1987), so a complete lack of pyroclastic material associated with Bracks or Star Mountain would be surprising.

C. The large areal extents and low aspect ratios of these rocks have been the primary reasons to consider them ash-flow tuffs. However, other than tuffs ponded in calderas, unequivocal ash-flow tuffs of Trans-Pecos Texas have much greater areal extents and lower aspect ratios than any of the equivocal rocks (Fig. 10, Table 4). On a thickness/diameter plot (Fig. 10), the silicic lavas fall within the upper range or above high-aspect-ratio tuffs and possibly are transitional to more conventional, thick, areally restricted silicic lavas. Contrast Bracks Rhyolite with Buckshot Ignimbrite, a slightly older tuff that occurs in the same area and even underwent modest rheomorphism (Anderson, 1975; Henry and Price, 1984). Despite the fact that it is more silicic (74% SiO_2) than, and about half the volume ($\sim$30 km^3) of, Bracks, Buckshot is considerably more extensive and has a much lower aspect ratio. It has a maximum lateral extent of about 85 km, an area of at least 2000 km^2, maximum thickness of about 20 m, minimum thickness in distal areas of less than 2 m, and an aspect ratio of about 1:3000. A similar comparison can be made between Star Mountain Formation and Gomez Tuff, even allowing that the former is a composite unit comprised of an unknown number of flows. Mitchell Mesa Rhyolite, the most extensive ash-flow tuff of Trans-Pecos, is much thinner and more widespread than any of the equivocal rocks.

D. Development of a *basal* breccia and its relation to underlying topography may be critical in distinguishing rheomorphic tuffs from extensive silicic lavas. Basal breccias of Bracks and Star Mountain consist of a mix of massive, flow-banded, or vesicular clasts. They occur throughout the areal extent of the units, are everywhere equally coarse, but can vary markedly in thickness over short lateral distances. Breccias such as these are typical of "crumble" breccias of lavas in which clasts spalled from the front and top of a flow are overridden by it (Cas and Wright, 1987). The breccias are composed of a mix of lithologies (massive, vesicular, flow-banded, glassy, devitrified) because these are typically exposed in lava-flow fronts (Fink, 1983). Breccia thickness varied as different amounts of material spalled off the front as the flow progressed. Felsic lava breccias tend to be thicker in valleys, due to a tendency for increased breccia formation when the lava is poised on a slope; essentially the lava lays down a carpet of breccia which is later overridden by the massive interior (C. R. Manley, pers. comm. 1988). The occurrence of basal breccias throughout the entire extent of these rocks argues that the rocks flowed as lavas over the entire extent. The lack of systematic size variations argues against some unique basal accumulation layer of a pyroclastic flow.

Although we conclude from examination of the rheomorphic tuff of Barrel Springs Formation that upper breccias can develop through rheomorphism, we know of no documented basal breccias of even the most strongly rheomorphic tuffs. Additionally, although brecciation of the base of a rheomorphic tuff is conceivable, clasts in such a breccia would be composed only of material from the part of the flow that brecciated. For example, rheomorphic Barrel Springs tuff might have brecciated the contact between the basal chilled tuff and the lowest foliated zone. Such a breccia could have contained clasts of the basal tuff and the foliated rock, but clasts of other lithologies, such as glassy, vesicular, or flow-folded rocks, would not be present. Even if the entire base had brecciated, disrupting all the chilled pyroclastic base, the breccia would not look like that of a lava flow, and the pyroclastic origin would still be indicated by the presence of pyroclastic fragments.

E. Only one vent area, that of Bracks Rhyolite, has been identified for these rocks. Although the significance of the vitrophyric domes is not fully understood, they are more suggestive of fissure vents of a lava flow than any vent suggested for a pyroclastic flow. Also, Bracks clearly does not have an associated caldera. Ash-flow tuffs of Trans-Pecos Texas with volumes equal to, or even less than, Bracks have well-defined calderas. For example, eruption of the 30 km^3 Buckshot Ignimbrite produced the Infiernito caldera (Henry and Price, 1984). Also, with the exception of parts of the Davis Mountains where detailed mapping has not been done, calderas have been identified for all major tuffs and vice versa (Henry and Price, 1984). Although the eruption of any large volume of magma requires evacuation of a subjacent magma chamber, the eruption rate of a lava is probably so much less than that of a tuff that the chamber could be replenished during eruption without collapse.

F. Although a perception exists that extensive silicic lavas are anomalous (for example, Cook, 1966), numerous examples exist, including in the Bruneau–Jarbidge area of southern Idaho (Bonnichsen and Kauffman, 1987), Yellowstone National Park (Christiansen and Hildreth, 1988), Baja California (Hausback, 1987), Australia (Cas, 1978), and southern Africa (Bristow and Cleverly, 1979; Twist and French, 1983). Alternative pyroclastic origins have been proposed for some (e.g., Idaho; Ekren et al., 1984), but, as with Bracks, the Idaho flows exhibit abundant lava-flow features and lack pyroclastic features. The Yellowstone rocks are critical examples, because they are young (less than 150,000 years old) and exceptionally well exposed (Christiansen and Hildreth, 1988). Unequivocally individual flows have lateral dimensions of at least 32 km, areas of 600 km^2, maximum thicknesses of as much as 300 m, and volumes up to 50 km^3. That high-silica rhyolites, presumably considerably more viscous than the alkalic quartz trachytes to low-silica rhyolites of Trans-Pecos, could flow these distances supports the concept that the Texas lavas could flow comparable or greater distances.

In fact, the Yellowstone, Idaho, and Trans-Pecos examples show a progression in aspect ratios (Fig. 10) that correlates qualitatively with the probable magma viscosity and yield strength. Rheological properties are largely functions of composition, temperature, and volatile content (McBirney and Murase, 1984). Although little is known about the third factor, data on the other two are available. The Yellowstone flows are high-silica rhyolites erupted at 850–890°C (Christiansen and Hildreth, 1988). The Idaho rocks are low-silica rhyolites erupted at 900–950°C (Bonnichsen and Kauffman, 1987; Honjo et al., 1987). The Trans-Pecos rocks are alkalic, probably peralkaline, quartz trachytes; sparse data from magnetite–ilmenite pairs in Star Mountain Formation and Crossen Trachyte indicate temperatures of 860–940°C. These data suggest that the Trans-Pecos lavas should have had the lowest viscosities and yield strengths, the Idaho lavas were intermediate, and the Yellowstone lavas were most viscous. The Trans-Pecos rocks are thinnest and most extensive, the Idaho rocks intermediate, and the Yellowstone rocks thickest and least extensive, consistent with inferred viscosities.

In conclusion, we suggest that the question should no longer be "Were these rocks erupted as lavas?" but rather "What factors allowed the Trans-Pecos and other lavas to flow such great distances?" Criteria used to distinguish tuffs and lavas (Table 3) are still largely valid but should be modified in recognition of the large areal extent of the Trans-Pecos lavas. Nevertheless, the rocks are clearly anomalous in comparison to the more common, areally restricted silicic domes and lavas. Several features may have allowed them to flow such great distances, including high eruption rate (Walker, 1973), high temperature, and efficient heat retention (Cas, 1978; Bonnichsen and Kauffman, 1987). Although eruption rate is unknown, the large volume of the flows seems to require rapid extrusion. Also, the large size of the postulated vents of Bracks Rhyolite suggests a high eruption rate. Certainly the Bracks vent is much larger than the feeder dikes associated with typical small silicic domes (Eichelberger et al., 1985; Fink, 1985; Fink and Pollard, 1983). The ratio of surface area to volume decreases with increasing volume, so extremely large flows should retain heat more effectively than smaller flows.

A further consideration is the pre-eruptive volatile content of the magma, and the effect of eruptive degassing on the solidus temperature of felsic liquids. An almost dry rhyolitic magma must have a temperature near 1000°C to exist as a liquid. Therefore, it erupts at a temperature close to the 1 bar rhyolite solidus and is not strongly undercooled at the surface. Consequently, the magma is unusually fluid due to its high temperature, and groundmass crystallization is retarded. In contrast, a wet rhyolite initially at 750°C is thoroughly degassed upon eruption and thus is emplaced some 300°C below the rhyolite solidus (even ignoring other likely cooling effects). Groundmass crystallization may begin during degassing within the volcanic conduit (Eichelberger et al., 1986), and many "conventional" felsic lavas formed from initially wet magma may therefore emerge from the vent in a semi-solid condition, in addition to being highly viscous by virtue of low temperatures.

Eruption rates are limited by the rheological properties of magmas; maximum rise rates are constrained by viscosity and yield strength (Wilson and Head, 1981). (Very high eruption rates are permitted during explosive eruptions of felsic magma only because the effective viscosity is of the dusty gas within which pyroclasts are suspended.) Dry, hot, weakly undercooled and relatively fluid felsic magmas are capable of the high eruption rates required to produce long lava flows, whereas strongly undercooled, degassed, originally wet and highly viscous magmas are not.

Similar reasoning (see below) applies to tuffs; dense welding and rheomorphism are favored for initially hot, dry magmas (pyroclastic activity may be sustained by very low primary-magmatic-water contents). Therefore, a close association between unusually widespread silicic lavas and unusually rheomorphic ignimbrites is to be expected.

Finally, the similarity of Bracks, Star Mountain, and Crossen, both in lithologic characteristics and age, indicates that some distinctive event in the evolution of the Trans-Pecos magmatic province gave rise to nearly identical magmas over a wide area. Understanding the origin of these rocks addresses not only volcanological problems but also the tectonics and petrogenesis of the province.

2. Evidence for a pyroclastic-flow origin

The essential problem with these extensive silicic rocks is that the final stages of emplacement of an extensively rheomorphic tuff involve coherent viscous flowage after the manner of a lava. Therefore, the appearance of the final rock body is dominated by features generally considered characteristic of lava flows.

A. That the final stages of emplacement were by a "lava-flow" mechanism is not the point at issue; a rheomorphic welded tuff only differs from a true lava in that the material is erupted and emplaced over most of the final extent in a fragmental condition. Any structure or texture developed in a lava can potentially appear in a rheomorphic tuff. Flow bands, flow folds, and vitrophyres are well known from rheomorphic tuffs (Wolff and Wright, 1981). Other features such as flow breccias, although not described previously, occur in units of undoubted pyroclastic origin in Trans-Pecos (e.g., Barrel Springs Formation).

The progression in degree of development of viscous-flow structures in the spectrum Gomez–Barrel Springs–Sleeping Lion (Figs. 36–38) does not constitute proof of a pyroclastic origin for Sleeping Lion and similar units, but is nonetheless persuasive. At the very least, it does demonstrate that rheomorphism and/or related processes are capable of totally obscuring any evidence of pyroclastic origin. It follows that if the entire thickness of a unit, including the base, has undergone viscous flow, then the outcrop-scale features of a complete section through the unit will be those of a lava.

Petrography and mineral chemistry supply equivocal evidence. Broken phenocrysts are scarce in rheomorphic tuffs found elsewhere, such as the well-known Green Tuff of Pantelleria (JAW, pers. inspection). Phenocryst breakage during explosive disruption of magma is presumably controlled by magmatic viscosity and volatile content, and broken crystals would therefore be expected to be rare in relatively hot, fluid, gas-poor compositions. The logical extension of this is basaltic magma; liberated phenocrysts in mafic scoria accumulations are rarely broken.

B. To defend a pyroclastic origin for units which largely lack any diagnostic features, it is necessary to digress into an explanation of welding, rheomorphism, and related processes in tuffs. *Welding* is the process by which a pyroclastic deposit becomes compacted into a coherent rock through load-pressure deformation of hot, plastic magmatic fragments. Because it takes place after deposition of clasts, it is essentially a secondary process. *Agglutination* refers to the adhesion and deformation of clasts *upon* deposition. It differs from welding in that it is almost instantaneous, and that the energy required for deformation is imparted to the clasts at the vent or during gravitational flow in the form

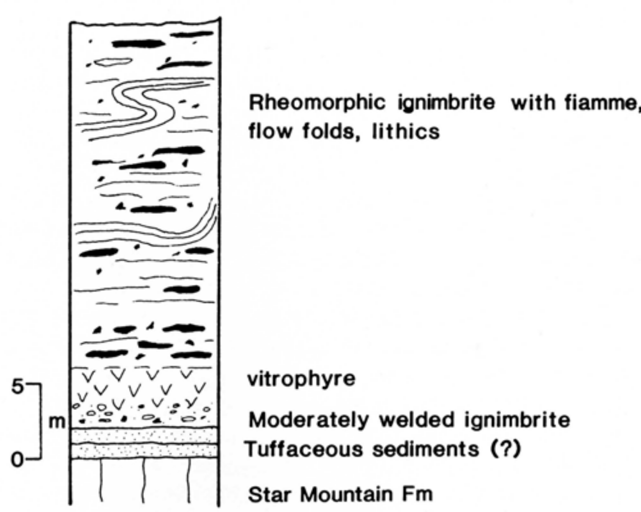

FIGURE 36—Section of Gomez Tuff, a classic rheomorphic ignimbrite with fiamme, abundant lithics, flow folds, and moderately welded base (from Franklin et al., 1987).

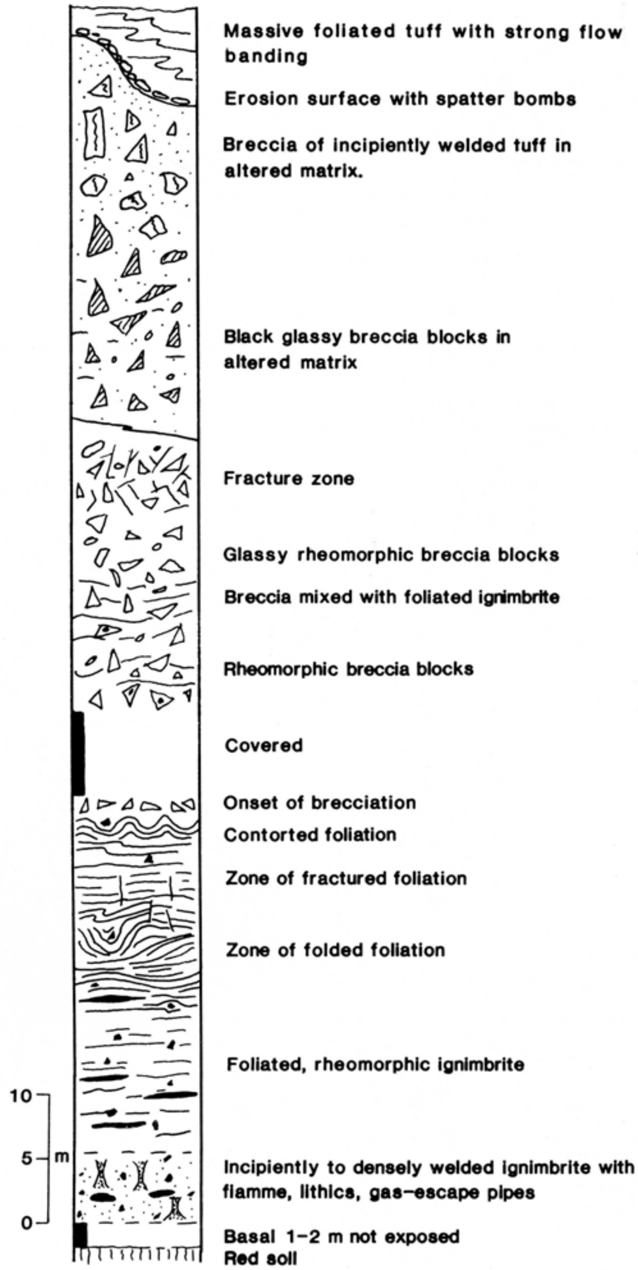

FIGURE 37—Composite section of rheomorphic ignimbrite of Barrel Springs Formation (from Franklin et al., 1987). Although unquestionably an ignimbrite because of a poorly welded base that shows gas-escape pipes, lithic fragments, and fiamme, the middle and upper zones could be mistaken for a lava because of a lack of pyroclastic features.

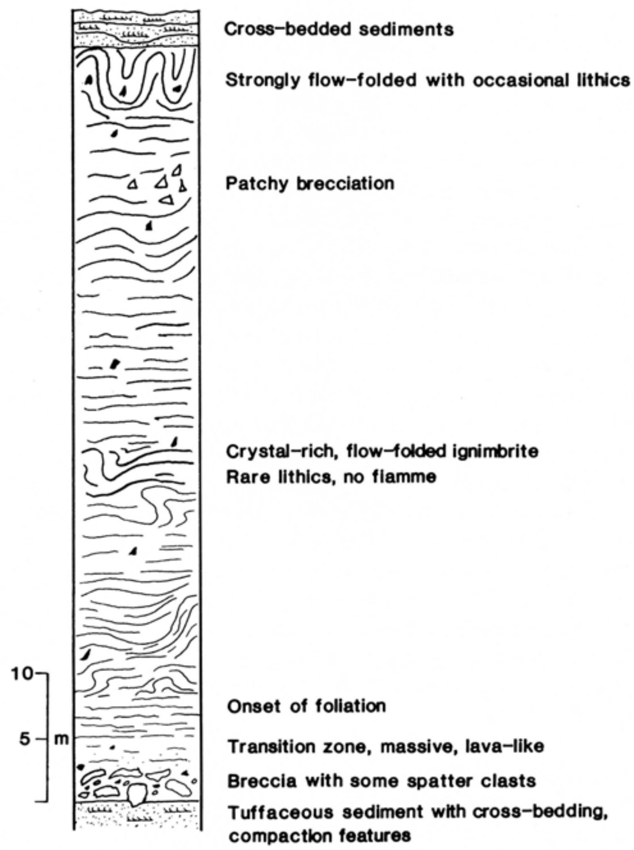

FIGURE 38—Section of Sleeping Lion Formation, which appears even more like lava (from Franklin et al., 1987). It lacks fiamme and pumice, and lithic fragments are extremely rare. It can only be interpreted as pyroclastic flow when a full section of it is seen (JAW).

of kinetic energy. Agglutination requires lower magmatic viscosities than simple welding (Wolff, 1983). *Rheomorphism* is secondary mass flowage of an already welded and/or agglutinated tuff body.

A pyroclastic-flow deposit which has undergone welding and rheomorphism, but in which clasts did not become agglutinated in the primary, fluidized particulate flow, will be *initially* deposited as loose ash and lapilli. Heat loss to the underlying surface will result in a chilled basal zone in which evidence for the pyroclastic nature of the unit will be preserved, even if the rest of the sheet undergoes extreme welding and rheomorphism. This is the case for Gomez Tuff and Barrel Springs Formation. The thickness of this basal zone will depend on the rate of heat loss and the time required for welding, itself a function of clast viscosity.

Schmincke and Swanson (1967) and Chapin and Lowell (1979) described the process of agglutination during primary laminar viscous flowage (called "primary welding") in pyroclastic flows. The mechanism is essentially one of agglutination and shearing of adjacent clasts in the primary fluidized particulate flow. The units to which Schmincke and Swanson applied this concept possess nonwelded bases and were reinterpreted as rheomorphic (s.s.) by Wolff and Wright (1981). However, Schmincke and Swanson's concept is itself valid. Primary within-flow agglutination simply requires lower clast viscosities than those necessary for welding and rheomorphism. Agglutination is syndepositional, and a pyroclastic flow would presumably halt once a certain critical proportion of its clasts became stuck together. The significant point here is that deposition occurs *when the constituent clasts have already coalesced together,* and, therefore, *little or no* particulate material is preserved at the base of the deposit; it was not there to be preserved by the time the primary flow halted. Because welding and rheomorphism are allowed at substantially higher viscosities than is agglutination, it is almost inevitable that any unit deposited in such a fashion will undergo very extensive secondary, post-depositional rheomorphism prior to final solidification (unless completely confined in some closed structure, such as a caldera).

Emplacement temperatures of ignimbrites are a function of magmatic temperature and the degree of eruptive cooling. Cooling is greatest for magmas of high gas content (Sparks et al., 1978). Gas-poor eruptions have much less explosive power and are envisaged as weak, low, collapsing eruption columns ("fountains" might be a better term) producing slow, dense, ground-hugging pyroclastic flows that are efficient retainers of heat. Lithic fragments are a very minor component, or are absent entirely from the products of weakly explosive eruptions (cf. Hawaiian and strombolian eruptions), because vent erosion is at a minimum. Phenocryst breakage is also likely to be minimal.

It should be apparent that the product of such a pyroclastic eruption would have adopted a very effective disguise as a lava by the time of final solidification. Preserved shards, lapilli, or fiamme would be entirely obscured; lithic fragments and broken phenocrysts would be few or entirely absent, and welding zonation would be absent. Agglutination will have prevented the preservation of any primary pyroclastic textures at the base, while the greater part of the unit will have been affected by extensive rheomorphism, dynamically indistinguishable from lava flowage. The term *lava-like tuff* is proposed for such rocks. We suggest that the Sleeping Lion Formation (Fig. 38) is lava-like tuff, based on sporadic preservation of clearly pyroclastic textures; rare lithic fragments, fiamme-like structures, and the apparent absence of topographic control of flow-breccia thickness as seen for SMF.

C. It is extremely difficult to propose criteria for the distinction of lava-like tuffs from true lavas. Unit aspect ratio gives no clear indication; it is limited by the proposed nature of pyroclastic flows which produce lava-like tuffs; low-energy, slow, gas-poor flows consisting of sticky particles are unlikely to travel great distances from vent. The less widespread nature of the lava-like tuffs compared to undoubted ignimbrites, such as Buckshot and Gomez, is therefore to be expected. In any case, considered the world over, ignimbrites in general may have aspect ratios as high as 1:300 (e.g., the Rio Caliente ignimbrite; Wright, 1981); this overlaps with aspect ratios for undoubted lavas in Trans-Pecos such as BR and SMF.

D. Characteristics of basal breccias may be critical for the distinction between lavas and lava-like tuffs. A breccia which consists of a range of lithologies represented within the overlying massive flow could reasonably be interpreted as a lava-flow breccia, and the ubiquitous presence of such a breccia would therefore indicate that the flow traveled from the vent to its present position entirely as a viscous fluid, i.e., a lava. This, however, is only true *if it can be demonstrated that the clast types present in the breccia could not have been juvenile components in a possible primary pyroclastic flow.* Nonvesicular magma lumps and even angular vitrophyre or obsidian fragments are common juvenile constituents of pyroclastic deposits, especially those of alkaline composition which also lack a preceding plinian phase and may be relatively gas-poor (e.g., Adeje and Arico ignimbrites, Tenerife; Wolff, 1983). Frequently, a proportion of these clasts is variably devitrified even when the bulk flow is only weakly welded.

Relationships between breccia development and pre-existing topography may provide the only sure criteria. For a lava-flow emplacement mechanism, breccias should be thicker in paleovalleys than over topographic highs. This is not to be expected in the case of a primary deposit from a pyroclastic flow; rheomorphism should more efficiently obscure primary textures in thicker accumulations.

E. The apparent paucity of calderas in the Davis Mountains applies not only to the controversial rocks, but also to several undoubted ignimbrites. Calderas may simply not be exposed today; for example, it is known that a significant portion of the total ignimbrite distribution is now buried under Neogene sediments in the Marfa Basin. Caldera recognition in old volcanic terrains abounds with problems. For example, some calderas may be downsag features without a well-defined bounding fault; resurgence would then render identification difficult even in a Quaternary center.

In addition to widespread lavas, some of the enigmatic rocks of Trans-Pecos Texas may represent an endmember type of ignimbrite. A complete gradation exists from this endmember through strongly rheomorphic welded tuffs to weakly rheomorphic tuffs to "conventional" welded ignimbrites. Factors favoring the formation of rheomorphic and lava-like tuffs are the same as those which favor extensive silicic lavas:

(1) Low magmatic-gas content, which retards eruptive cooling. Although we have no means of quantitatively estimating magmatic-gas contents, the general lack of hydrous phenocrysts and significant precursor plinian deposits associated with the ignimbrites support the notion of low gas contents for Trans-Pecos magmas.

(2) High magmatic temperature. This is consistent with low gas contents, and the lack of eruptive cooling then gives high emplacement temperatures.

(3) Alkaline composition. The alkalinity of the debated units is variable, but all are more alkaline than typical continental silicic magmas. The effect of alkalies in lowering magmatic viscosity is well known.

(4) High fluorine content. Fluorine has an affinity for silicate liquids and does not strongly partition into the vapor phase during degassing. Therefore, magmatic fluorine should be retained in the melt during eruption, and will lower the viscosity of pyroclasts. Although there is no evidence that the debated units ever had appreciable fluorine contents, the element tends to be enriched in alkaline silicic magmas.

Finally, the observation that the above factors apply to all major Davis Mountains units to some extent strongly suggests that they are the products of a single magmatic system.

Acknowledgments

We gratefully acknowledge the many landowners of the Davis Mountains who have allowed access to their property for scientific study and for this field trip. Additionally, Superintendents Ken Benad of Davis Mountains State Park, Steve Miller of the Fort Davis National Historic Site, and James Carrico of Big Bend National Park allowed study and this trip in their areas. J. N. Rubin of the Bureau of Economic Geology did many of the electron-microprobe analyses presented in this report. S. E. Laubach is participating in a study of the vitrophyric domes of Bracks Rhyolite. R. R. Franklin has been studying the Star Mountain Formation; his research has contributed significantly to this field trip. Discussions with numerous geologists, notably B. Bonnichsen, C. R. Manley, and S. Self, have influenced our views about the interesting rocks of Trans-Pecos Texas. Review by C. E. Chapin is gratefully acknowledged. The research that composes much of this report was supported by the COGEOMAP program of the U.S. Geological Survey through Agreement No. 14-08-0001-A0516 and by Grant G1144148 from the U.S. Bureau of Mines to the Texas Mining and Mineral Resources Research Institute.

References

Anderson, J. E., Jr., 1969, Development of snowflake texture in a welded tuff, Davis Mountains, Texas: Geological Society of America, Bulletin, 80: 2075–2080.

Anderson, W. B., 1975, Cooling history and uranium mineralization of the Buckshot Ignimbrite, Presidio and Jeff Davis Counties, Texas: Unpublished M.S. thesis, University of Texas at Austin, 135 pp.

Bailey, R. A., Dalrymple, G. B., and Lanphere, M. A., 1976, Volcanism, structure, and geochronology of Long Valley caldera, Mono County, California: Journal of Geophysical Research, 81: 725–744.

Barker, D. S., 1977, Northern Trans-Pecos magmatic province: introduction and comparison with the Kenya rift: Geological Society of America, Bulletin, 88: 1421–1427.

Barker, D. S., 1987, Tertiary alkaline magmatism in Trans-Pecos Texas; *in* Fitton, J. G., and Upton, B. G. J. (eds.), Alkaline igneous rocks: Geological Society of London, Special Publication no. 30: 415–431.

Barker, D. S., Henry, C. D., and McDowell, F. W., 1986, Pine Canyon caldera, Big Bend National Park: a mildly peralkaline magmatic system; *in* Price, J. G., Henry, D. C., Parker, D. F., and Barker, D. S. (eds.), Igneous geology of Trans-Pecos Texas: University of Texas at Austin, Bureau of Economic Geology, Guidebook 23: 266–287.

Becker, S. W., 1976, Field relations and petrology of the Burro Mesa "Riebeckite" Rhyolite, Big Bend National Park, Texas: Unpublished M.S. thesis, University of California at Santa Cruz, 116 pp.

Bonnichsen, B., and Kauffman, D. F., 1987, Physical features of rhyolite lava flows in the Snake River Plain volcanic province, southwestern Idaho; *in* Fink, J. H. (ed.), The emplacement of silicic domes and lava flows: Geological Society of America, Special Paper 212: 119–145.

Bristow, J. W., and Cleverly, F. W., 1979, Volcanology of the Lebombo Rhyolites: Geocongress 79, Geological Society of South Africa, pp. 60–63.

Cameron, K. L., and Cameron, M., 1986, Geochemistry of quartz-normative igneous rocks from the Chinati Mountains and Terlingua areas, West Texas: a comparison with Cenozoic volcanic rocks from Chihuahua and Baja California Sur, Mexico; *in* Price, J. G., Henry, C. D., Parker, D. F., and Barker, D. S. (eds.), Igneous geology of Trans-Pecos Texas: University of Texas at Austin, Bureau of Economic Geology, Guidebook 23: 143–163.

Cameron, M., Cameron, K. L., and Carman, M. F., Jr., 1986, Alkaline rocks in the Terlingua–Big Bend area of Trans-Pecos Texas; *in* Price, J. G., Henry, C. D., Parker, D. F., and Barker, D. S. (eds.), Igneous geology of Trans-Pecos Texas: University of Texas at Austin, Bureau of Economic Geology, Guidebook 23: 123–142.

Carman, M. F., Jr., Cameron, M., Gunn, B., Cameron, K. L., and Butler, J. C., 1975, Petrology of the Rattlesnake Mountain sill, Big Bend National Park, Texas: Geological Society of America, Bulletin, 86: 177–193.

Carmichael, I. S. E., Turner, F. J., and Verhoogen, J., 1974, Igneous petrology: McGraw–Hill, New York, 739 pp.

Cas, R. A. F., 1978, Silicic lavas in Paleozoic flyschlike deposits in New South Wales, Australia: behavior of deep subaqueous silicic flows: Geological Society of America, Bulletin, 89: 1708–1714.

Cas, R. A. F., and Wright, J. V., 1987, Volcanic successions; modern and ancient: Allen & Unwin, London, 528 pp.

Chapin, C. E., and Lowell, G. R., 1979, Primary and secondary flow structures in ash-flow tuffs of the Gribbles run paleovalley, central Colorado; *in* Chapin, C. E., and Elston, W. E. (eds.), Ash-flow tuffs: Geological Society of America, Special Paper 180: 137–154.

Childerss, K., 1984, Stratigraphy and petrography of the Adobe Canyon Formation, northern Davis Mountains, Trans-Pecos Texas: Unpublished B.S. thesis, Baylor University, Waco, Texas, 45 pp.

Christiansen, R. L., and Hildreth, Wes, 1988, Extensive rhyolitic lava flows of the Yellowstone Plateau (abs.): Geological Society of America, Abstracts with Programs, 20: 409.

Chuchla, R. J., 1981, Reconnaissance geology of the Sierra Rica area, Chihuahua, Mexico: Unpublished M.S. thesis, University of Texas at Austin, 199 pp.

Coney, P. J., and Reynolds, S. J., 1977, Cordilleran Benioff zones: Nature, 270: 403–406.

Cook, E. (ed.), 1966, Tuff lavas and ignimbrites: Elsevier, New York, 212 pp.

Damon, P. E., Shafiqullah, M., and Clark, K. F., 1981, Age trends of igneous activity in relation to metallogenesis in the southern Cordillera: Arizona Geological Society Digest, 14: 137–154.

DeGraff, J. M., and Aydin, A., 1987, Surface morphology of columnar joints and its significance to mechanics and direction of joint growth: Geological Society of America, Bulletin, 99: 605–617.

Eichelberger, J. C., Carrigan, C. R., Westrich, H. R., and Price, R. H., 1986, Non-explosive silicic volcanism: Nature, 323: 598–602.

Eichelberger, J. C., Lysne, P. C., Miller, C. D., and Younker, L. W., 1985, Research drilling at Inyo domes, California: 1984 results: EOS (American Geophysical Union Transactions), 66: 186–187.

Ekren, E. B., McIntyre, D. H., and Bennett, E. H., 1984, High-temperature, large-volume, lavalike ash-flow tuffs without calderas in southwestern Idaho: U.S. Geological Survey, Professional Paper 1272: 76 pp.

Engebretson, D. C., Cox, A., and Gordon, R. G., 1985, Relative motions between oceanic and continental plates in the Pacific Basin: Geological Society of America, Special Paper 206: 59 pp.

Fink, J. H., 1983, Structure and emplacement of a rhyolitic obsidian flow: Little Glass Mountain, Medicine Lake Highland, northern California: Geological Society of America, Bulletin, 94: 362–380.

Fink, J. H., 1985, The geometry of silicic dikes beneath the Inyo domes, California: Journal of Geophysical Research, 90: 11,127–11,134.

Fink, J. H., 1987, The emplacement of silicic domes and lava flows: Geological Society of America, Special Paper 212: 145 pp.

Fink, J. H., and Manley, C. R., 1987, Origin of pumiceous and glassy textures in rhyolite flows and domes; *in* Fink, J. H. (ed.), The emplacement of silicic domes and lava flows: Geological Society of America, Special Paper 212: 77–88.

Fink, J. H., and Pollard, D. D., 1983, Structural evidence for dikes beneath silicic domes, Medicine Lake Highland, California: Geology, 11: 458–461.

Francis, P., and Self, S., 1987, Collapsing volcanoes: Scientific American, pp. 91–97.

Franklin, R. R., Self, S., and Wolff, J. A., 1987, Lava-like tuffs of Trans-Pecos Texas: the Star Mountain Formation: EOS (American Geophysical Union Transactions), 68: 1544.

Gibbon, D. L., 1969, Origin and development of the Star Mountain Rhyolite: Bulletin Volcanologique, 33: 438–474.

Guest, J. E., and Sanchez, J., 1969, A large dacitic lava flow in northern Chile: Bulletin Volcanologique, 33: 778–790.

Gunderson, R. P., Cameron, K. L., and Cameron, M., 1986, Mid-Tertiary high-K calc-alkalic and alkalic volcanism in eastern Chihuahua, Mexico: Geological Society of America, Bulletin, 97: 737–753.

Hausback, B. P., 1987, An extensive, hot, vapor-charged rhyodacite flow, Baja California, Mexico; *in* Fink, J. H. (ed.), The emplacement of silicic domes and lava flows: Geological Society of America, Special Paper 212: 111–118.

Heiken, G., and Wohletz, K., 1987, Tephra deposits associated with silicic domes and lava flows; *in* Fink, J. H. (ed.), The emplacement of silicic domes and lava flows: Geological Society of America, Special Paper 212: 55–76.

Henderson, G. D., 1987, Intracaldera kaolinization and silicification of ash-flow tuff, Medley area, Davis Mountains, Texas (abs.): Geological Society of America, Abstracts with Programs, 19: 170.

Henry, C. D., and McDowell, F. W., 1986, Geochronology of magmatism in the Tertiary volcanic field, Trans-Pecos Texas; *in* Price, J. G., Henry, C. D., Parker, D. F., and Barker, D. S. (eds.), Igneous geology of Trans-Pecos Texas: University of Texas at Austin, Bureau of Economic Geology, Guidebook 23: 99–122.

Henry, C. D., and Price, J. G., 1984, Variations in caldera development in the Tertiary volcanic field of Trans-Pecos Texas: Journal of Geophysical Resaerch, 89: 8765–8786.

Hnery, C. D., and Price, J. G., 1986, Early Basin and Range development in Trans-Pecos Texas and adjacent Chihuahua: magmatism and orientation, timing, and style of extension: Journal of Geophysical Research, 91: 6213–6224.

Henry, C. D., Price, J. G., and Miser, D., 1989, Geology and Tertiary igneous activity of the Hen Egg Mountain and Christmas Mountains quadrangles, Trans-Pecos Texas: University of Texas at Austin, Bureau of Economic Geology, Report of Investigations no. 183: 105 pp.

Henry, C. D., Price, J. G., Rubin, J. N., Parker, D. F., Wolff, J. A., Self, S., Franklin, R. R., and Barker, D. S., 1988a, Widespread, lava-like volcanic rocks of Trans-Pecos Texas: Geology, 16: 509–512.

Henry, C. D., Price, J. G., and Smyth, R. C., 1988b, Chemical and thermal zonation in a mildly alkaline magma system, Infiernito caldera, Trans-Pecos Texas: Contributions to Mineralogy and Petrology, 98: 194–211.

Hicks, K. A., 1982, Origin and emplacement of the Sleeping Lion Formation, Davis Mountains, West Texas: Unpublished B.S. thesis, Baylor University, Waco, Texas, 73 pp.

Hildreth, W., 1981, Gradients in silicic magma chambers: implications for lithospheric magmatism: Journal of Geophysical Research, 86: 10153–10192.

Honjo, N., Bonnichsen, B., and Leeman, W. P., 1987, High-temperature rhyolites from western-central Snake River Plain: comparative geothermometers (abs.): Geological Society of America, Abstracts with Programs, 19: 706–707.

Hoy, S. M., 1986, Stratigraphy and petrography of Tertiary volcanic rocks, El Muerto Peak quadrangle, western Davis Mountains, Trans-Pecos Texas: Unpublished M.S. thesis, Baylor University, Waco, Texas, 117 pp.

Joesten, R. L., 1974, Metasomatism and magmatic assimilation at a gabbro-limestone contact, Christmas Mountains, Big Bend region, Texas: Unpublished Ph.D. dissertation, California Institute of Technology, 397 pp.

Jungyusuk, N., 1977, Petrology of the Christmas Mountains igneous rocks, Trans-Pecos Texas: Unpublished M.S. thesis, University of Texas at Austin, 117 pp.

Keith, S. B., 1978, Paleosubduction geometries inferred from Cretaceous and Tertiary magmatic patterns in southwestern North America: Geology, 6: 516–521.

Larocca, R. B., 1984, Geology of the Davis Mountains resort area, Trans-Pecos Texas: Unpublished B.S. thesis, Baylor University, Waco, Texas, 95 pp.

Lewis, P. S., 1978, Igneous petrology and strontium isotope geochemistry of the Christmas Mountains, Brewster County, Texas: Unpublished M.S. thesis, University of Texas at Austin, 120 pp.

Lindsley, D. H., 1983, Pyroxene thermometry: American Mineralogist, 68: 477–493.

Lipman, P. W., 1976, Caldera-collapse breccias in the western San Juan Mountains, Colorado: Geological Society of America, Bulletin, 87: 1397–1410.

Lipman, P. W., 1984, The roots of ash-flow calderas: windows into granitic batholiths: Journal of Geophysical Research, 89: 8801–8841.

Lonsdale, J. T., 1940, Igneous rocks of the Terlingua–Solitario region, Texas: Geological Society of America, Bulletin, 51: 1539–1626.

Manley, C. R., and Fink, J. H., 1987, Internal textures of rhyolite flows as revealed by research drilling: Geology, 15: 549–552.

Mathews, W. K., and Adams, J. A. S., 1986, Geochemistry, age, and structure of the Sierra Blanca and Finlay Mountain intrusions, Hudspeth County, Texas; *in* Price, J. G., Henry, C. D., Parker, D. F., and Barker, D. S. (eds.), Igneous geology of Trans-Pecos Texas: University of Texas at Austin, Bureau of Economic Geology, Guidebook 23: 207–224.

Maxwell, R. A., Lonsdale, J. T., Hazzard, R. T., and Wilson, J. A., 1967, Geology of Big Bend National Park, Brewster County, Texas: University of Texas at Austin, Bureau of Economic Geology, Publication 6711: 320 pp.

McBirney, A. R., and Murase, T., 1984, Rheological properties of magmas: Annual Reviews of Earth and Planetary Sciences, 12: 337–357.

McDonough, W. F., and Nelson, D. O., 1984, Geochemical constraints on magma processes in a peralkaline system: the Paisano volcano, West Texas: Geochimica et Cosmochimica Acta, 48: 2443–2455.

Nelson, D. O., Nelson, K. L., Reeves, K. D., and Mattison, G. D., 1987, Geochemistry of Tertiary alkaline rocks of the eastern Trans-Pecos magmatic province, Texas: Contributions to Mineralogy and Petrology, 97: 72–92.

Nelson, K. L., and Nelson, D. O., 1986, Magmatic evolution of the Van Horn Mountains caldera and comparison with alkaline magmatism in the eastern Trans-Pecos magmatic belt, West Texas; *in* Price, J. G., Henry, C. D., Parker, D. F., and Barker, D. S. (eds.), Igneous geology of Trans-Pecos Texas: University of Texas at Austin, Bureau of Economic Geology, Guidebook 23: 164–177.

Ogley, D. S., 1979, Eruptive history of the Pine Canyon caldera, Big Bend Park: University of Texas at Austin, Bureau of Economic Geology, Guidebook 19: 67–71.

Parker, D. F., 1976, Petrology and eruptive history of an Oligocene trachytic shield volcano, near Alpine, Texas: Unpublished Ph.D. dissertation, University of Texas at Austin, 183 pp.

Parker, D. F., 1983, Origin of the trachyte–quartz trachyte–peralkalic rhyolite suite of the Oligocene Paisano volcano, Trans-Pecos Texas: Geological Society of America, Bulletin, 94: 614–629.

Parker, D. F., 1986, Stratigraphic, structural, and petrologic development of the Buckhorn caldera, northern Davis Mountains, Trans-Pecos Texas; *in* Price, J. G., Henry, C. D., Parker, D. F., and Barker, D. S. (eds.), Igneous geology of Trans-Pecos Texas: University of Texas at Austin, Bureau of Economic Geology, Guidebook 23: 286–302.

Parker, D. F., and McDowell, F. W., 1979, K–Ar geochronology of Oligocene volcanic rocks, Davis and Barrilla Mountains, Texas: Geological Society of America, Bulletin, 90: 1100–1110.

Peacock, M. A., 1931, Classification of igneous rocks: Journal of Geology, 39: 54–67.

Price, J. G., and Henry, C. D., 1984, Stress orientations during Oligocene volcanism in Trans-Pecos Texas: timing the transition from Laramide compression to Basin and Range extension: Geology, 12: 238–241.

Price, J. G., Henry, C. D., Barker, D. S., and Parker, D. F., 1987, Alkalic rocks of contrasting tectonic settings in Trans-Pecos Texas: Geological Society of America, Special Paper 215: 335–346.

Price, J. G., Henry, C. D., Parker, D. F., and Barker, D. S., 1986, Igneous geology of Trans-Pecos Texas: University of Texas at Austin, Bureau of Economic Geology, Guidebook 23: 364 pp.

Rubin, J. N., Price, J. G., Henry, C. D., and Koppenall, D. W., 1987, Cryolite-bearing and rare metal enriched rhyolite, Sierra Blanca peaks, Trans-Pecos Texas: American Mineralogist, 72: 1122–1130.

Rudnik, R. O., 1983, Geochemistry and tectonic affinities of a Proterozoic bimodal igneous suite, West Texas: Geology, 11: 352–355.

Sampson, D. E., 1987, Textural heterogeneities and vent area structures in the 600-year-old lavas of the Inyo volcanic chain, eastern California; *in* Fink, J. H. (ed.), The emplacement of silicic domes and lava flows: Geological Society of America, Special Paper 212: 89–101.

Sampson, D. E., and Cameron, K. L., 1987, The geochemistry of the Inyo volcanic chain: multiple magma systems in the Long Valley region, eastern California: Journal of Geophysical Research, 92: 10,403–10,421.

Schieffer, J. H., and Nelson, D. O., 1981, Petrology and geochemistry of megacrysts, xenoliths, and the igneous rocks of the Terlingua district, Brewster County, Texas (abs.), Geological Society of America, Abstracts with Programs, 13: 547.

Schmincke, H.-U., and Swanson, D. A., 1967, Laminar viscous flowage structures in ash-flow tuffs from Gran Canaria, Canary Islands: Journal of Geology, 75: 641–664.

Seager, W. R., 1980, Quaternary fault system in the Tularosa and Hueco Basins, southern New Mexico and West Texas: New Mexico Geological Society, Guidebook 31: 131–135.

Shannon, W. M., and Goodell, P. C., 1986, Lithogeochemistry of intrusive rocks of the Quitman–Sierra Blanca igneous complex, Hudspeth County, Texas; *in* Price, J. G., Henry, C. D., Parker, D. F., and Barker, D. S. (eds.), Igneous geology of Trans-Pecos Texas: University of Texas at Austin, Bureau of Economic Geology, Guidebook 23: 225–236.

Shaw, H. R., 1972, Viscosities of magmatic silicate liquids: an empirical method of prediction: American Journal of Science, 272: 870–893.

Smith, R. L., and Bailey, R. A., 1968, Resurgent cauldrons: Geological Society of America, Memoir 116: 613–662.

Sparks, R. S. J., Self, S., and Walker, G. P. L., 1973, Products of ignimbrites eruptions: Geology, 1: 115–118.

Sparks, R. S. J., Wilson, L., and Hulme, G., 1978, Theoretical modeling of the generation, movement, and emplacement of pyroclastic flows by column collapse: Journal of Geophysical Research, 83: 1727–1739.

Stewart, R. M., 1984, Stratigraphy and petrology of the Alamo Creek Basalt, Big Bend National Park, Brewster County, Texas: Unpublished M.S. thesis, University of Houston, 186 pp.

Twist, D., and French, B. M., 1983, Voluminous acid volcanism in the Bushveld Complex: A review of the Rooiberg Felsite: Bulletin Volcanologique, 46-3: 225–242.

Ui, T., 1983, Volcanic dry avalanche deposits—identification and comparison with nonvolcanic debris stream deposits: Journal of Volcanology and Geothermal Research, 18: 135–150.

Ui, T., Yamamoto, H., and Suzuki-Kamata, K., 1986, Characterization of debris avalanche deposits in Japan: Journal of Volcanology and Geothermal Research, 29: 231–243.

Voight, B., Glicken, H., Janda, R. J., and Douglass, P. M., 1981, Catastrophic rockslide avalanche of May 18; *in* Lipman, P. W., and Mullineaux, D. R. (eds.), The 1980 eruptions of Mount St. Helens, Washington: U.S. Geological Survey, Professional Paper 1250: 347–377.

Walker, G. P. L., 1973, Lengths of lava flows: Royal Society of London, Philosophical Transactions (A), 274: 107–118.

Walker, G. P. L., 1983, Ignimbrite types and ignimbrite problems: Journal of Volcanology and Geothermal Research, 17: 65–88.

Walker, G. P. L., 1985, Origin of coarse lithic breccias near ignimbrite source vents: Journal of Volcanology and Geothermal Research, 25: 157–171.

Wilson, L., and Head, J. W., 1981, Ascent and emplacement of basaltic magma on the Earth and Moon: Journal of Geophysical Research, 86: 2971–3001.

Withjack, M. O., and Scheiner, C., 1982, Fault-patterns associated with domes—an experimental and analytical study: American Association of Petroleum Geologists, Bulletin, 66: 302–316.
Wolff, J. A., 1983, Petrology of Quaternary pyroclastic deposits from Tenerife, Canary Islands: Unpublished Ph.D. dissertation, University of London, 542 pp.
Wolff, J. A., and Wright, J. V., 1981, Rheomorphism of welded tuffs: Journal of Volcanology and Geothermal Research, 10: 13–34.
Wright, J. V., 1981, The Rio Caliente ignimbrite: analysis of a compound intraplinian ignimbrite from a major late Quaternary Mexican eruption: Bulletin Volcanologique, 44: 189–212.

EXCURSION 15B: Roots of ignimbrite calderas: Batholithic plutonism, volcanism, and mineralization in the Southern Rocky Mountains, Colorado and New Mexico

Clark M. Johnson[1], James R. Shannon[2], and Christopher J. Fridrich[3]

[1]Department of Geology and Geophysics, University of Wisconsin, Madison, Wisconsin 53706;
[2]Crown Resource Corporation, 820 16th Street, Suite 415, Denver, Colorado 80202; [3]U.S. Department of Energy, Nevada Operations Office, Las Vegas, Nevada 89193

Introduction

The Questa, Mount Aetna, and Grizzly Peak calderas and associated volcanic and plutonic rocks provide a view of crustal magmatism from the surface through 4 to 8 km of crust. The petrologic relations between spatially and temporally related volcanic and plutonic rocks will be studied in the 28–19 Ma Latir volcanic field and associated Questa caldera. Deeply eroded ring-zone structures and brittle and ductile deformation are the focus of the trip through the 34–35 Ma Mount Aetna caldera in southern Colorado. Intracaldera structures related to caldera collapse and resurgence, in addition to petrologic relations between high-level intrusive stocks and ash-flow magmatism, will be the topic of discussions at the 34 Ma Grizzly Peak caldera north of Mount Aetna. The Questa caldera occupies the eastern flanks of the Rio Grande rift in northern New Mexico, and the Mount Aetna and Grizzly Peak calderas occupy the western flank of the extreme northern part of the rift in central Colorado (Fig. 1).

Inasmuch as this trip focuses on the roots of calderas, we wish to comment on the usage of the terms "caldera" and "cauldron."

Clough et al. (1909) originally used the term cauldron subsidence for a roughly circular structure formed by foundering of a cylindrical block of crust into an underlying magma body. Historically, the term cauldron has been applied to eroded volcanic collapse structures (e.g. Clough et al., 1909; Kingsley, 1931; Esher, 1932; Williams, 1941; Williams and McBirney, 1968; Oftedahl, 1953, 1978; Reynolds, 1956; Hills, 1958; Turner and Bowden, 1979). Williams and McBirney (1968) stated that the phrase cauldron subsidence has been applied to all downdropped blocks enclosed by ring dikes. They recommended restriction of this phrase to ring complexes, or arcuate and circular intrusive bodies produced by erosion of a caldera.

In contrast, Smith and Bailey (1968) suggested that the term cauldron should include all volcanic subsidence structures regardless of shape or size, depth of erosion, or connection with surface volcanism. According to this usage, calderas are a type of cauldron. More recently, Lipman (1984) stated that a distinction between calderas and cauldrons, as defined by Williams and McBirney (1968), is not purposeful "because all transitions are present in the examples described." However, four other papers in the same volume (Hildebrand, 1984; Yoshida, 1984; Wunderman and Rose, 1984; Elston, 1984) used the term cauldron in their titles.

There is a growing problem with the terminology used for large silicic volcanic collapse structures. One of the focuses of this field excursion is to demonstrate that there are systematic and significant variations in the characteristics expressed by different erosional levels of these systems. Shannon (1988) suggested a new classification scheme which is most compatible with the historic application of the terms caldera and cauldron. He recommended that the phrase volcanoplutonic subsidence system (or structure) be used as the general descriptive phrase for all features produced by collapse of roof rocks into a magma chamber, regardless of shape, size, depth of erosion, structural level, or connection with surface volcanism. The term caldera (similar to Williams and McBirney, 1968) is used for a high-level, geomorphic and structural feature related to the volcanic depression produced by collapse into a subvolcanic magma chamber. The term cauldron (similar to Williams and McBirney, 1968) is used for the deeper subsurface analog which no longer retains its high-level topographic and structural expression. No distinction in the mechanism of formation is implied and most cauldrons are inferred to have had a related caldera on the surface. Possible exceptions are subterranean cauldron subsidences (Clough et al., 1909; Pitcher, 1978). Ring-dike complexes and ring complexes occur below the volcanic edifice, and differ from cauldrons in that they no longer retain syncollapse volcanic rocks within the ring structure.

Usage of the terms "caldera" and "cauldron" in describing the three volcanoplutonic complexes covered by this trip follows that used in most of existing literature that covers the three complexes: "caldera" is used for the Questa and Grizzly Peak localities, and "cauldron" is used for the Mount Aetna locality. These usages do not imply that a fundamentally different level of erosion exists at any of the three localities.

Acknowledgments

Michelyn Hass and Paul Dombrowski are thanked for assistance in manuscript preparation and drafting, respectively.

The Latir volcanic field and Questa caldera: Relations between volcanic and plutonic rocks

July 1–3, 1989

Leader: Clark M. Johnson

Summary

An exceptional cross section is exposed through precaldera and caldera-related volcanic rocks, resurgent plutons, and later intrusions of the Latir volcanic field and Questa

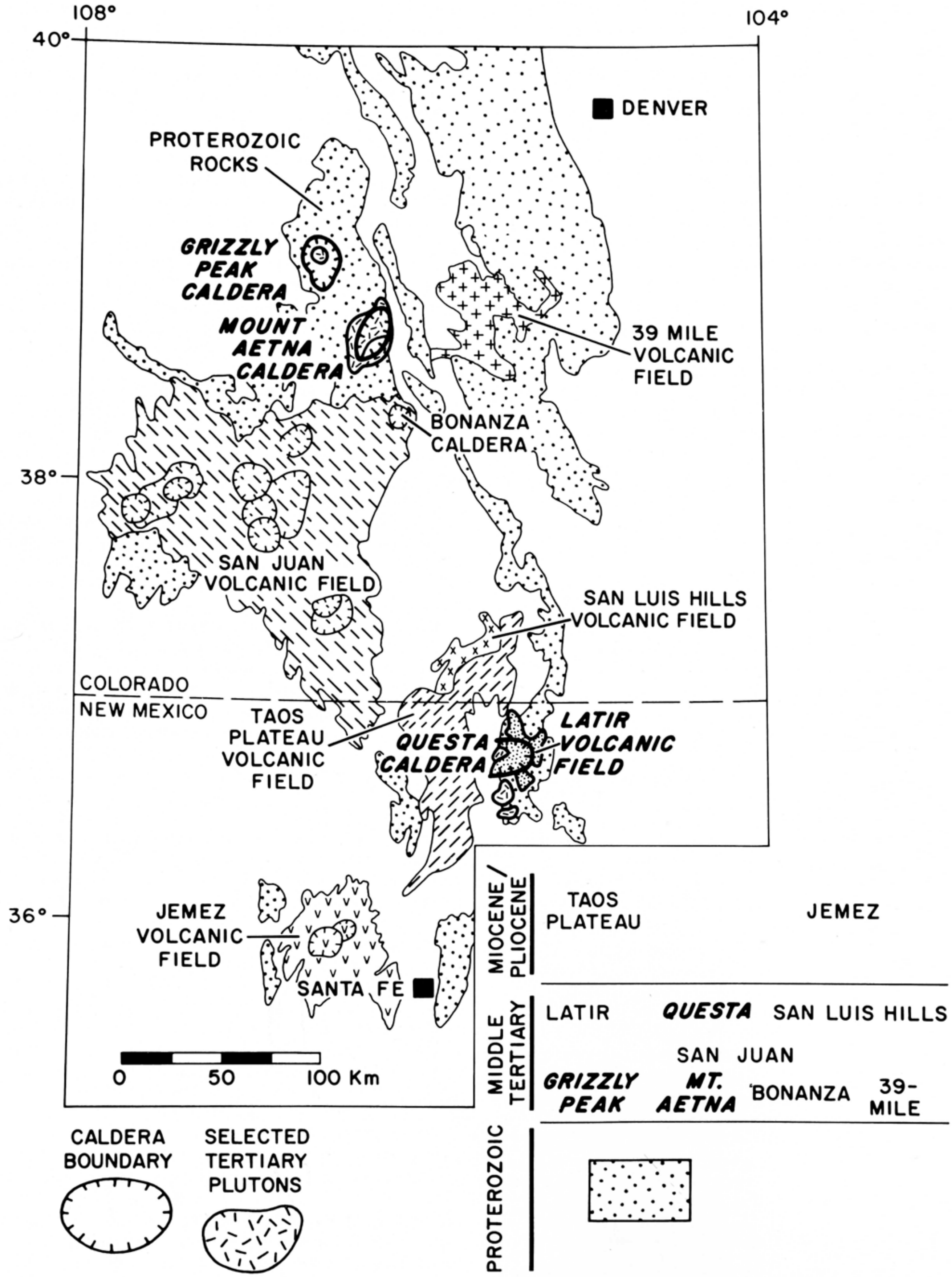

FIGURE 1—Generalized geologic map of northern New Mexico and southern Colorado in the vicinity of the Rio Grande rift. Our trip focuses on the Latir volcanic field and Questa caldera in northern New Mexico, and the Mount Aetna and Grizzly Peak cauldrons/calderas in southern Colorado.

caldera. This cross section is largely due to the combination of regional northeast tilting and dissection of the field by the Rio Grande rift (Lipman, 1983; Lipman and Reed, 1984, 1989; Figs. 2, 3). The majority of the precaldera volcanic rocks (28.5–26 Ma) have metaluminous, intermediate compositions, from olivine basaltic andesite (53 wt% SiO_2) to quartz latite (67 wt% SiO_2; Johnson and Lipman, 1988). The earliest rocks also include high-SiO_2 (75–77 wt%) rhyolites that whole-rock and mineral–chemical data indicate have fractionated from intermediate-composition magmas that did not reach the surface.

Inception of alkaline magmatism (alkalic dacite, comendite, and high-SiO_2 peralkaline rhyolite) correlates with initiation of regional extension approximately 26 Ma ago (Lipman, 1983; Hagstrum and Lipman, 1986). The Questa caldera formed 26 Ma ago upon eruption of the >500 km^3 (possibly as much as 1000 km^3) high-SiO_2 peralkaline Amalia Tuff.

Chemical and isotopic data indicate that all of the precaldera and caldera-related volcanic rocks evolved in an open system by crystal fractionation, magma mixing, and crustal assimilation (Johnson and Lipman, 1988). Probably all precaldera rocks evolved from mantle-derived basaltic magmas; few, if any, represent crustal melts.

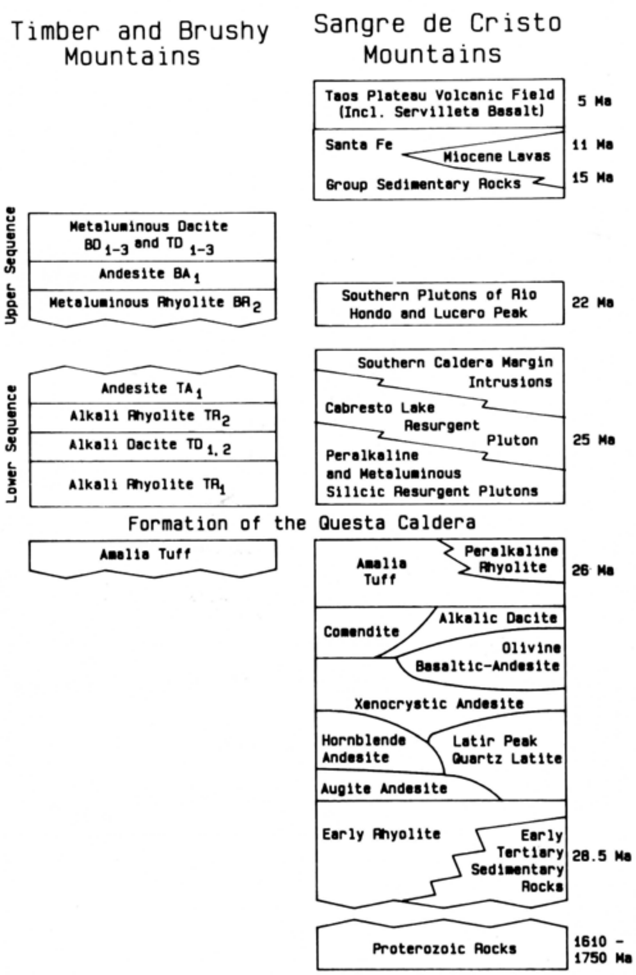

FIGURE 2—Stratigraphy of volcanic and plutonic rocks of the Latir volcanic field and younger volcanic and sedimentary units. Silicic resurgent plutons include Virgin Canyon, Cañada Pinabete, and Rito del Medio. Southern caldera-margin intrusions include the Bear Canyon and Sulphur Gulch plutons and Red River intrusive complex. From Johnson et al. (1989).

Four resurgent plutons (Virgin Canyon, Cañada Pinabete, Rito del Medio, and Cabresto Lake) were emplaced within 1 Ma of caldera formation, possibly within several hundred thousands years (Lipman et al., 1986; Hagstrum and Lipman, 1986). The oldest intrusive unit, the peralkaline granite of the Virgin Canyon and Cañada Pinabete plutons (Figs. 3, 4), has chemical and isotopic compositions that are indistinguishable from those of the early ring-fracture dikes and late-erupted parts of the Amalia Tuff. Phenocryst compositions preserved in the peralkaline granite suggest that the Amalia Tuff magma initially formed from a trace-element-enriched, high-alkali metaluminous magma (Johnson et al., 1989; Czamanske and Dillet, 1988); isotopic data indicate that the parental magmas contained a large crustal component (Johnson and Lipman, 1989). High halogen fluxes from degassing alkali basalts that were injected into the lower part of the magmatic system during regional extension are interpreted as the driving force for establishing silicic peralkaline compositions.

Trace-element-rich metaluminous granites in the Virgin Canyon, Cañada Pinabete, and Rito del Medio plutons were intruded immediately after emplacement of the peralkaline granite; the most mafic metaluminous granites (71 wt% SiO_2) may have compositions that are similar to those of the magmas which were parental to the Amalia Tuff (Johnson et al., 1989). The relatively mafic (monzogranite to granite) Cabresto Lake pluton probably does not represent the compositions that are similar to parental magmas of the more silicic resurgent plutons of Virgin Canyon, Cañada Pinabete, and Rito del Medio.

Intrusions exposed along the southern margin of the Questa caldera include 26–23 Ma granodiorite, syenogranite, and alkali feldspar granite. The two western plutons at Bear Canyon and Sulphur Gulch (Fig. 3) are composed of alkali feldspar granite which contains molybdenite mineralization (Leonardson et al., 1983). The easternmost intrusive complex near the town of Red River is composed of multiple intrusive units that may contain both precaldera and postcaldera rocks.

The youngest plutons of the Latir field are south of the Questa caldera, and include the 22–21 Ma Rio Hondo granodiorite to granite pluton, and the 20–19 Ma Lucero Peak granite pluton. The Lucero Peak pluton contains minor molybdenite mineralization on its eastern margin (Ludington, 1981). These plutons are relatively coarse-grained and were emplaced at deep structural levels, as much as 7 km below the Miocene surface.

Postcaldera volcanic rocks are not preserved in the Sangre de Cristo Mountains. The Amalia Tuff and postcaldera lavas are, however, preserved on an intrarift horst (Timber and Brushy Mountains). The Cabresto Lake pluton and southern caldera-margin intrusions are chemically and temporally similar to lower sequence lavas in Timber and Brushy Mountains, and the youngest plutons of Rio Hondo and Lucero Peak are chemically and temporally similar to upper sequence lavas (Thompson et al., 1986; Johnson et al., 1989).

Comparison of mineralogic, chemical, and isotopic data of extrusive and intrusive rocks of the Latir field indicates dramatic differences in the evolution of crystal-poor magmas which erupt as volcanic rocks and crystal-rich magmas that solidify to form plutons, particularly those which form coarse-grained rocks. In contrast to the open-system evolution of the precaldera and caldera-related volcanic rocks, high-level evolution of the plutonic rocks largely involved closed-sys-

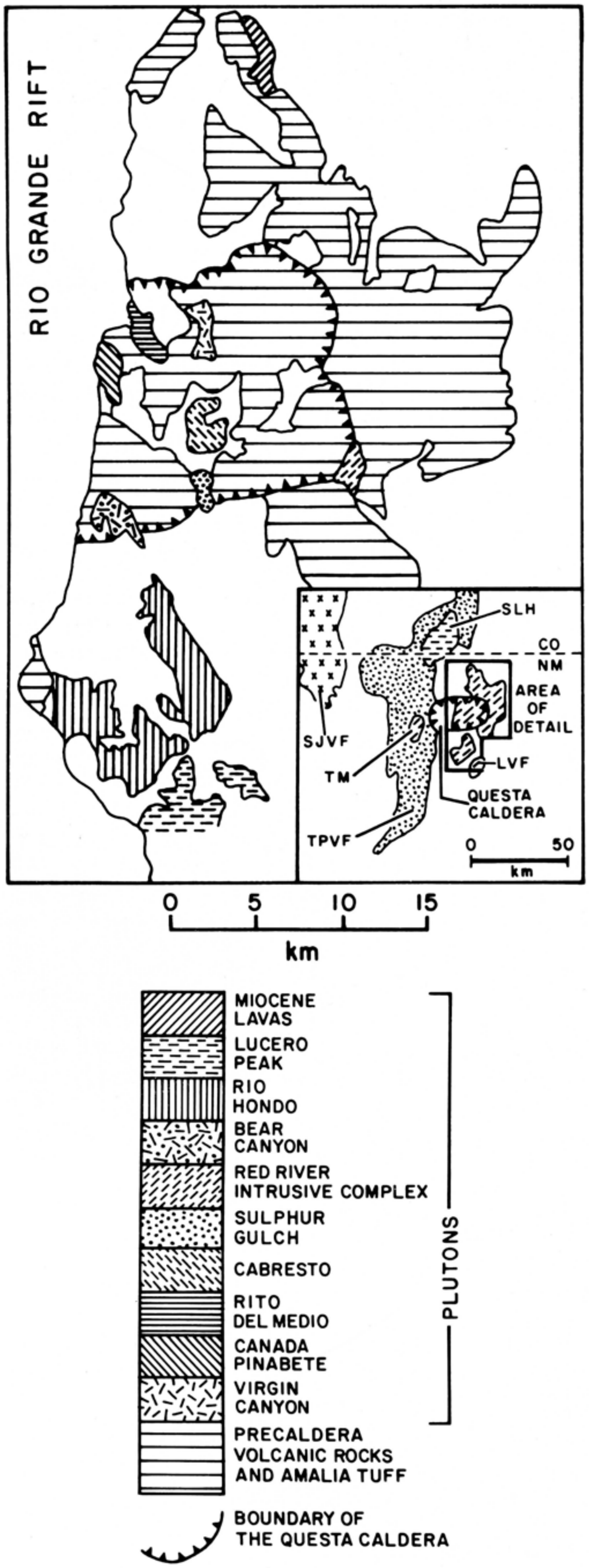

FIGURE 3—Generalized geologic map of the Latir volcanic field and the Questa caldera, emphasizing the postcaldera intrusive rocks, LVF, Latir volcanic field and associated intrusions; TM, Timber and Brushy Mountains; SJVF, San Juan volcanic field; SLH, San Luis Hills; TPVF, Taos Plateau volcanic field. From Johnson et al. (1989).

tem crystal fractionation (Johnson et al., 1989). Coarse-grained plutons do not have isotopic gradients, despite emplacement into Proterozoic crust, indicating that assimilation at high levels in the crust did not occur (Johnson and Lipman, 1989). This contrasts with data from the volcanic rocks, particularly the Amalia Tuff.

Although major-element compositions of both extrusive and intrusive rock suites in the Latir field are broadly similar, and both suites have highly evolved rocks with low Ba and Sr and high Nb, Th, and U contents, highly evolved plutons are markedly depleted in rare-earth-element (REE) contents. Differences in abundance of REE-rich accessory minerals cannot explain these differences, because evolved rocks from both suites contain abundant, early formed accessory minerals such as sphene and apatite. The lower REE contents of the evolved plutonic rocks are instead interpreted as a result of filter-pressing of an evolved magma from a crystal-rich cumulate zone with residual accessory minerals. The relatively elevated REE contents of the volcanic rocks suggest decoupling of major- and accessory-mineral fractionation, and possibly repeated replenishment of the subvolcanic magma chambers (Johnson et al., 1989). The presence of a cumulate-rich zone probably reflects evolution during the waning stages of a magmatic center, when basalt inputs were low. Such a zone probably does not characterize magmatic systems beneath active volcanoes.

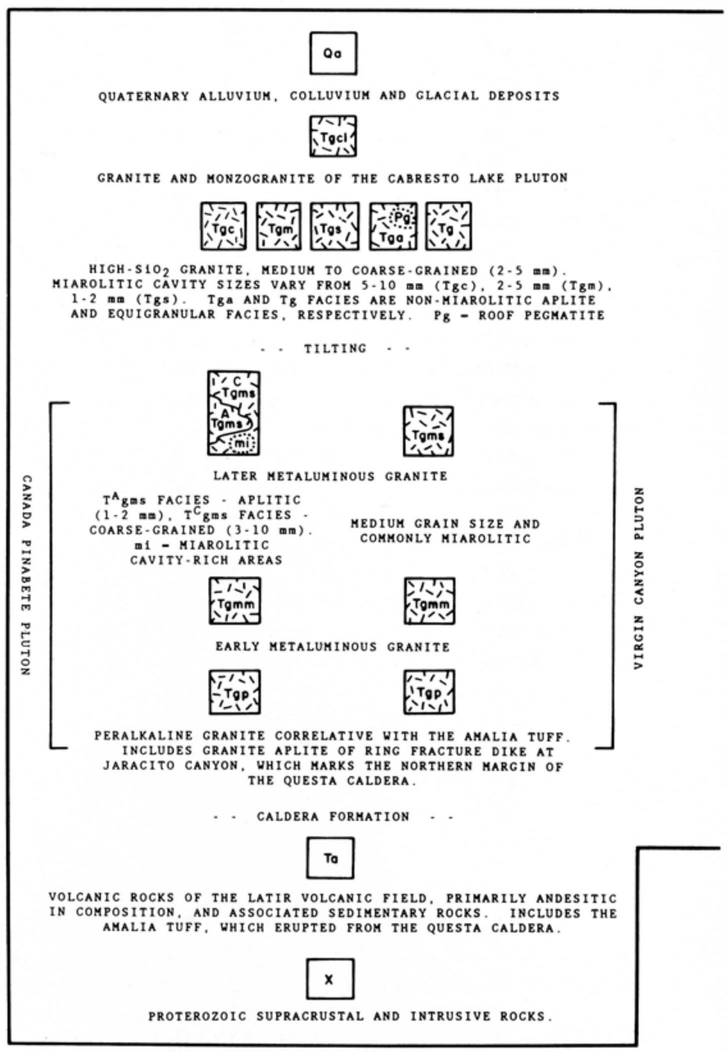

First day: Santa Fe to Questa, New Mexico

Assembly point: IAVCEI Meeting, Santa Fe, New Mexico
Departure time: 14:00
Distance: approximately 90 miles
Stops: 1

The northern Rio Grande rift is represented by a series of en-echelon basins. Our route begins in the city of Santa Fe and continues north through the Española Basin to the town of Questa in the southern San Luis Basin. The Española Basin formed 3–7 Ma ago and is flanked by the largely Pliocene to Pleistocene Jemez and Cerros del Rio volcanic fields on the west and Proterozoic rocks in the Sangre de Cristo Mountains on the east (Manley, 1979, 1984; Baldridge, 1979). The Pliocene Taos Plateau volcanic field joins the basin on its northern end, approximately 20 mi north of the town of Española.

The Taos Plateau volcanic field is dominantly composed of tholeiitic mafic- and intermediate-composition lavas and occupies the southern part of the San Luis Basin (Lipman and Mehnert, 1975; Dungan et al., 1986). We will spend a large portion of the trip in the San Luis Basin, which represents the physiographic expression of the Rio Grande rift in northern New Mexico and southern Colorado. The Taos graben, which occupies the southern part of the basin, formed less than 5 Ma ago (Manley, 1984) and has been partially filled with large volumes of younger lavas. This contrasts with the largely sedimentary fill in the Española Basin.

The Taos graben is flanked on both sides by Proterozoic rocks which underlie the Sangre de Cristo and Tusas Moun-

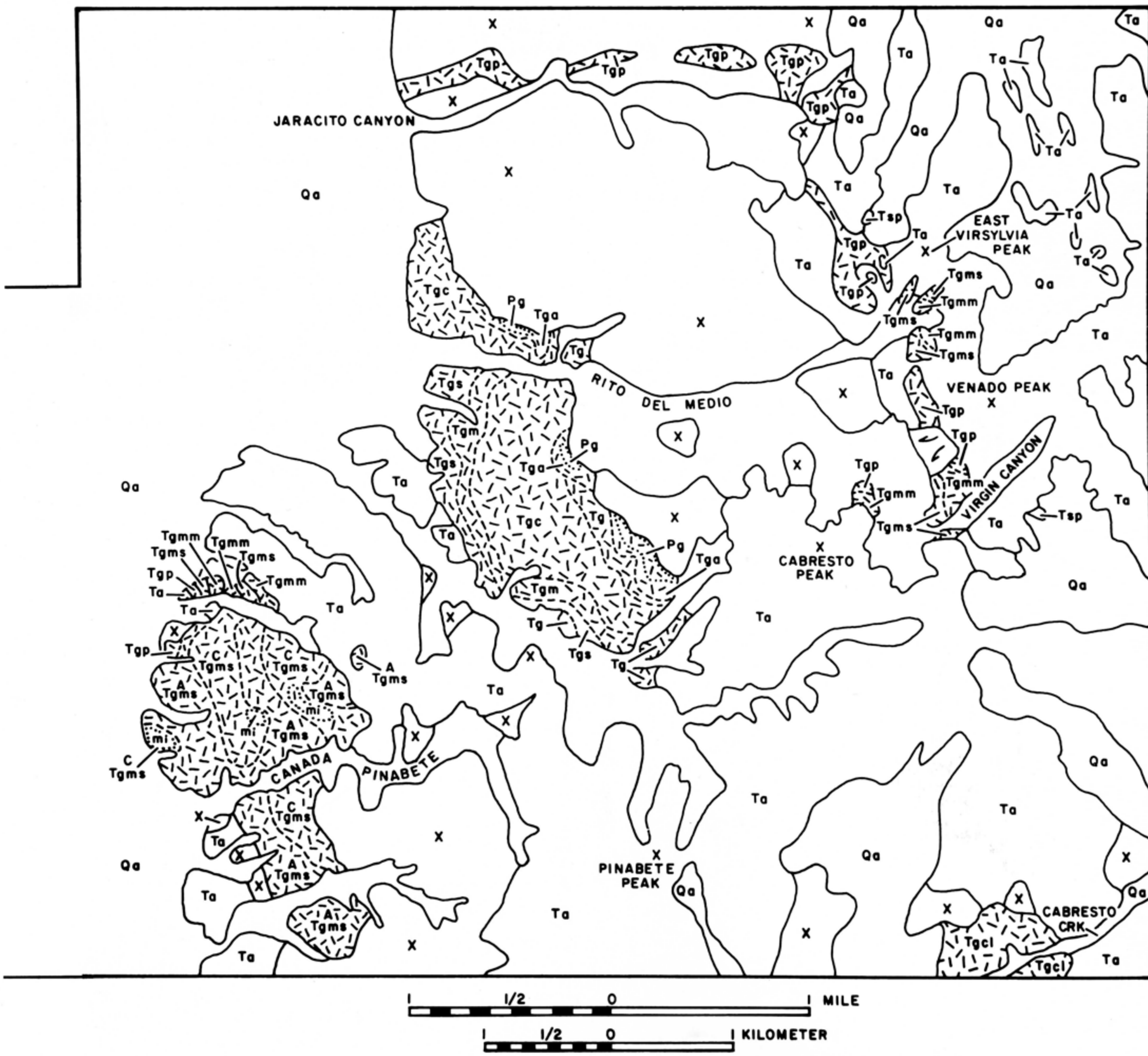

FIGURE 4—Geologic map of the resurgent dome of the Questa caldera. Important units of the silicic resurgent plutons include the peralkaline granite and early and later metaluminous granites of Virgin Canyon and Cañada Pinabete, and medium- to coarse-grained, high-SiO$_2$ granite of Rito del Medio, which is slightly younger. The Cabresto Lake pluton is also related to caldera resurgence, but is petrologically distinct from the three silicic resurgent plutons. Detailed mapping by C. M. Johnson, P. W. Lipman, and J. C. Reed, Jr. Larger-scale mapping from Lipman and Reed (1989).

tains on the east and west sides of the Rio Grande rift, respectively. The Oligocene to Miocene Latir volcanic field occupies a large portion of the Sangre de Cristo Mountains between the town of Taos and the Colorado–New Mexico state line (Fig. 1). A large gravity low is coincident with the Latir volcanic field in the Sangre de Cristo Mountains and its inferred extent in the San Luis Basin, indicating that a large volume of low-density volcanic and plutonic rocks underlie the region (Keller et al., 1984; Cordell et al., 1986).

Mileage

0 **Santa Fe.** Travel north on US-84. **27**

27 **Junction of US-84 and NM-68.** Turn north onto NM-68. **18**

45 **Junction of NM-68 and NM-75.** Continue north on NM-68. **13**

58 **STOP 1-1. Vieww of the Taos Plateau volcanic field from picnic area.** The Rio Grande Gorge (cut through the plateau-forming Servilleta Basalt) is directly north. The mountains in the far north are intermediate- and silicic-composition volcanoes of the Taos Plateau volcanic field. Proterozoic rocks and the southern plutons of the Latir volcanic field underlie the Sangre de Cristo Mountains visible on the east (right) side of the rift. **8**

66 **Junction of NM-68 and NM-522.** Turn north onto NM-522. **4**

70 **Town of Taos.** Continue north through traffic light. **20**

90 **Town of Questa.** Dinner and lodging.

Second day: Precaldera volcanic rocks to postcaldera mesozonal plutons

Assembly point:	Sangre de Cristo Motel, Junction of NM-522 and NM-38
Departure time:	8:00
Distance:	147 miles
Stops:	13

The second day's route continues north from Questa along the east side of the Rio Grande rift, west of the Sangre de Cristo Mountains. We will examine the precaldera and caldera-related volcanic rocks of the Latir volcanic field, as well as later Miocene lavas and domes and the Pliocene Servilleta Basalt. After returning to Questa in mid-day, we will follow the Red River, which generally follows the southern caldera margin. Much of the mineralization associated with the Questa caldera is localized along the southern margin in the Bear Canyon and Sulphur Gulch plutons. The Red River intrusive complex, near the town of Red River (elev. 2640 m), is farther east on NM-38 (not covered in this road log). The Red River complex contains a complicated sequence of granodiorite, syenogranite, and alkali feldspar granite (26–24 Ma). A road log through the Red River complex and into the Cabresto Creek drainage can be found in Lipman and Reed (1984).

The last section of the second day road log travels south from Questa through progressively deeper portions of the volcanic field to the southern plutons of Rio Hondo and Lucero Peak. This section completes the traverse through a cross section of the field, from surface rocks in the north, to 2–4 km below the Miocene surface near Questa, to 7–8 km below the Miocene surface near Rio Hondo.

Mileage

0.0 **Town of Questa** (elev. 2260 m). Junction of NM-522 and NM-38. Proceed north on NM-522 toward the town of Costilla. Major drainages to east are Cabresto Creek on the north (bisecting the Cabresto Lake pluton, 25 Ma) and Red River on the south (bisecting the southern caldera-margin plutons, 26–23 Ma). The ridge between Cabresto Creek and Red River is welded intracaldera Amalia Tuff. Alteration scars in general mark weathering of zones of high pyrite and/or zones of rock that are tectonically shattered by low-angle faulting (J. Meyer, pers. comm. 1988). The scar by Questa has low pyrite content, but is highly shattered by low-angle structures (Fig. 5). Guadalupe Mountain, a set of rhyodacite volcanoes (4.8 Ma) of the Taos Plateau volcanic field, may be seen on the northeast. **3.9**

3.9 **New Mexico Port of Entry. 2.9**

6.8 **Junction with road to town of El Rito** on right (east). Continue straight. The silicic resurgent plutons of Virgin Canyon, Cañada Pinabete, and Rito del Medio, precaldera volcanic rocks, and Proterozoic rocks occupy the hills directly east. **9.8**

16.6 **Junction with road to Cedro Canyon** on right (east). Continue straight. The large cliff on the north side of the canyon is welded outflow Amalia Tuff, erupted from the Questa caldera 26 Ma ago (Fig. 6). The Amalia Tuff is underlain successively by alkalic dacite, olivine basaltic andesite, and xenocrystic andesite (lower slopes on the south side). The tuff is overlain conformably by tilted volcaniclastic sedimentary rocks that were eroded from the Latir field (volcaniclastic lower part of the Santa Fe Group), which are in turn overlain unconformably by weakly consolidated gravels consisting of Proterozoic clasts (upper part of the Santa Fe Group). The section is capped by the Servilleta Basalt of the Taos Plateau volcanic field. **2.8**

19.4 **Town of Costilla** (elev. 2380 m). Junction of NM-196 and NM-522. Turn right (east) on NM-196 to town of Amalia. **2.0**

21.4 **Cross Costilla Creek.** Surrounding hills capped by Servilleta Basalt. **2.7**

24.1 **STOP 2-1. Outflow Amalia Tuff overlain by Santa Fe Group.** Included in the Santa Fe group are alkali basalt lavas (16 Ma) dipping northeast, interlayered with volcaniclastic sedimentary rocks and capped

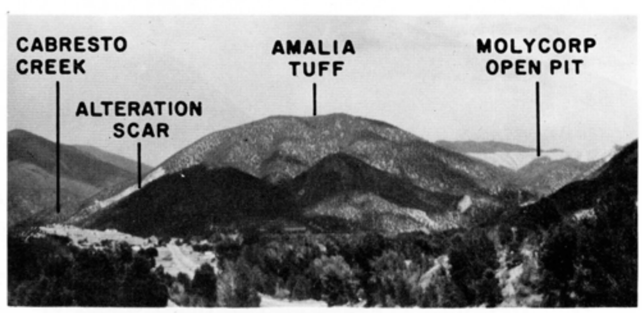

FIGURE 5—North view, just south of the town of Questa. The prominent hill with the alteration scar on the north side is >1 km of intracaldera Amalia Tuff.

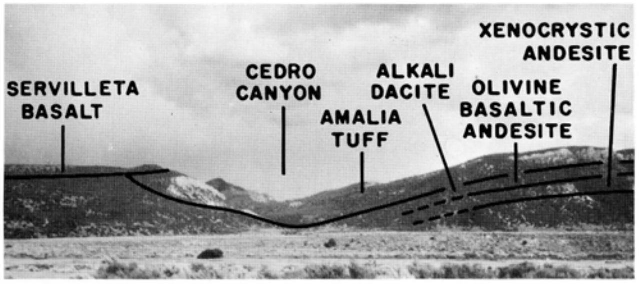

FIGURE 6—East view at Cedro Canyon of precaldera Latir volcanic rocks, Amalia Tuff and Pliocene Servilleta Basalt. Note recent fault scarp in alluvial fan.

unconformably by Servilleta Basalt. The high hills directly east on north side of Costilla Valley are mainly Proterozoic supracrustal rocks. One 8 Ma rhyolite center (elev. 2700–3000 m) intrudes the Proterozoic rocks. Rocks south of the Costilla Valley are mainly precaldera lavas of the Latir volcanic field, indicating that a major dip–slip fault is coincident with the valley. **0.9**

25.0 **Town of Amalia** (elev. 2490 m). As road bends south, we are traveling through alkalic basalts (15 Ma) on north side of road. **2.7**

27.7 **Precaldera alkalic dacite.** Exposed on south. (House addresses: 907–911 NM-196). **1.4**

29.1 **STOP 2-2. Precaldera augite andesite.** Exposed on south. This unit contains abundant reversely zoned, high-Mg and Cr clinopyroxene phenocrysts that are interpreted as indicating late-stage mixing with basaltic magmas (Johnson and Lipman, 1988). **5.0**

34.1 **Junction with road to Latir Lakes** (on south). Continue straight. An optional trip is to drive up Latir Creek (1 mi), turn right (west) up Lemos Creek for 1 mi to outcrops of Amalia Tuff and cogenetic peralkaline rhyolite lavas. **2.1**

36.2 **STOP 2-3. View of comendite, peralkaline rhyolite, and quartz latite.** Carson National Forest Boundary (elev. 2710 m). High hills on south up to Ortiz Peak (elev. 3417 m) are underlain by voluminous comendite lavas and minor ash-flow tuffs that were erupted immediately prior to eruption of the Amalia Tuff (Fig. 7). Peralkaline rhyolite lavas cogenetic with the Amalia Tuff have been faulted down to the lower hills south of the road. Intrusive quartz latite crops out on the north side of the road, surrounded by Proterozoic supracrustal rocks. The intrusions are localized along faults paralleling the Costilla Valley and are cogenetic with voluminous extrusive units exposed in the core of the caldera in the Latir Lakes region (southwest). The quartz latite unit is probably similar to the magmas which were parental to the earliest units in the Latir volcanic field, the early rhyolites (Johnson and Lipman, 1988). The early rhyolite (28 Ma) lavas and ash-flow tuffs crop out in the eastern parts of the Latir volcanic field and include the Tuff of Tetilla Peak (28 Ma). Accessible outcrops include Comanche Point (elev. 2820 m), 2 mi east of Stop 2-3. A road log for the area east of this stop can be found in Lipman and Reed (1984). **11.2**

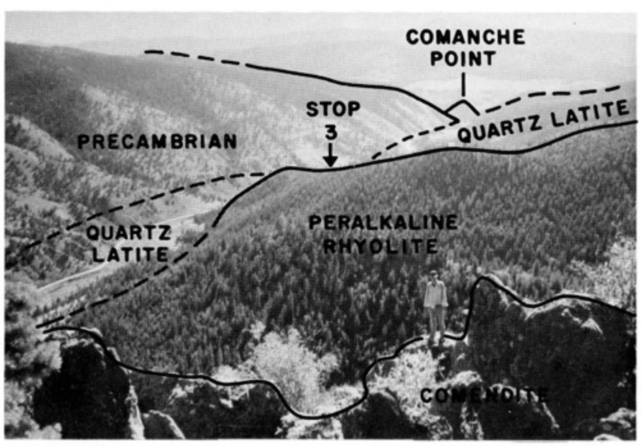

FIGURE 7—East view of Costilla Valley from ridge extending from Ortiz Peak (right off picture). A large portion of the ridge (>700 m above Costilla Valley) is underlain by peralkaline rhyolite that is cogenetic with the Amalia Tuff and minor ash-flow tuffs. Location of Stop 2-3 indicated.

Turn around and travel west on NM-196.

47.4 **Town of Amalia. 5.6**

53.0 **Town of Costilla.** Junction of NM-196 and NM-522. Turn left (south) toward Questa. Rhyodacite volcanoes of the Taos Plateau volcanic field are visible south on NM-522, including Ute Mountain (elev. 3094 m) at 2:00 and Guadalupe Mountain at 12:00 (Lipman and Mehnert, 1979). **2.7**

55.7 **Road to Cedro Canyon** on left (east). Continue straight. **0.8**

63.7 **Milepost 33.** North margin of the Questa caldera as marked by peralkaline ring-fracture dike cutting Proterozoic supracrustal rocks along north side of Jaracito Canyon (Fig. 8). The crest of the south slope of Jaracito Canyon is Virsylvia Peak (elev. 3839 m), the highest peak in view, and is part of the intracaldera resurgent uplift. **1.8**

65.5 **STOP 2-4. View of resurgent dome of the Questa caldera** at junction of road to El Rito. Directly east, the silicic resurgent granite of Rito del Medio (Fig. 8) forms the prominent cliffs (top elev. 3170 m) on the north side of Rito del Medio Canyon. Most of this pluton is coarse-grained, high-SiO_2 granite that contains abundant miarolitic cavities. Border phases include coarse-grained pegmatites and fine-grained, relatively mafic granite.

The highest peak visible directly up Rito del Medio Canyon is Venado Peak (elev. 3881 m). The top of Virsylvia Peak is just visible immediately to the north. Both peaks are capped by precaldera andesite and volcaniclastic sedimentary rocks that are intruded by the Virgin Canyon pluton. The outermost and oldest unit in the Virgin Canyon pluton is peralkaline granite porphyry, which probably grades into the Jaracito Canyon ring-fracture dike. The peralkaline granite is intruded by a relatively mafic metaluminous granite, termed the early metaluminous granite. This is in turn intruded by a more silicic metaluminous granite, termed the later metaluminous granite. The Cañada Pinabete pluton, visible at 2:00 to the south, contains the same intrusive sequence as that exposed in Virgin Canyon (Johnson et al., 1989). **2.9**

68.4 **STOP 2-5. View of plutons along south margin of the Questa caldera** from New Mexico Port of Entry. The Cañada Pinabete pluton occupies the

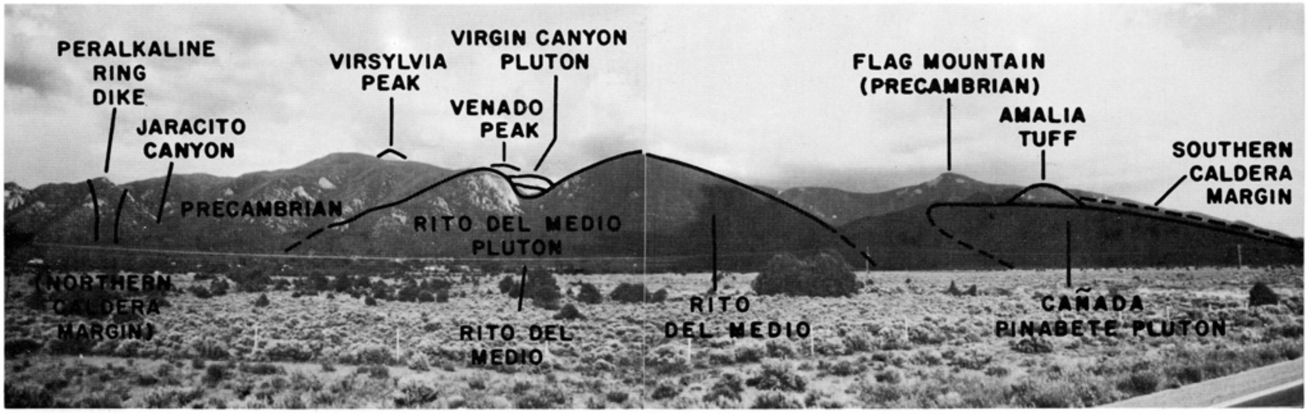

FIGURE 8—View east into the resurgent dome of the Questa caldera, from turnoff to town of El Rito.

lower slopes directly east (elev. 2500–3800 m) and is mainly composed of later metaluminous granite, with early metaluminous and peralkaline granite exposed on its north and west margins. Cabresto Peak (elev. 3794 m) is prominent at 11:00 and is primarily precaldera quartz latite intruded by the Virgin Canyon pluton. Pinabete Peak (elev. 3642 m) lies directly east and is composed of Proterozoic supracrustal rocks on its lower slopes, overlain by precaldera volcanic rocks of the caldera floor. Several kilometers of intracaldera resurgence are required to elevate these rocks relative to the thick intracaldera tuff exposed south of Cabresto Creek (alteration scars at 2:00). A portion of this apparent elevation difference may be related to tilting. Directly south is Flag Mountain (elev. 3641 m), the top of which is composed of Proterozoic plutonic rocks. The lower slopes of the mountain south of Red River comprise the dominant part of the Bear Canyon pluton and mark the southern margin of the Questa caldera. North at 10:30, the Platoro caldera (120 km distant) of the San Juan volcanic field can be seen, along with the intervening San Luis Hills (Oligocene volcanic rocks) within the rift. The Timber and Brushy Mountains horst block is southwest in the center of the rift (behind Guadalupe Mountain), where the only postcaldera Latir lavas are exposed (Thompson et al., 1986). Erosional remnants of the Latir field are found as far as 45 km west in the Tusas Mountains, on the west side of the Rio Grande rift, and merge with distal rocks of the San Juan volcanic field. **3.9**

72.3 **Town of Questa** (elev. 2260 m). Junction of NM-522 and NM-38. Proceed east on NM-38 toward the town of Red River. The conical hill (Goat Hill, elev. 2947 m) directly ahead is altered intracaldera Amalia Tuff that contains lenses of caldera-collapse megabreccia (Fig. 5). The majority of intracaldera tuff has been tilted westerly about a north-northwest axis to nearly vertical. Approximately beneath this hill is the site of the underground Molycorp molybdenum mine. The timbered slope on the south side of Red River is the Bear Canyon pluton, the westernmost of the southern caldera-margin intrusions. The caldera floor near Questa lies beneath the surface (<2200 m). **2.0**

74.3 **STOP 2-6. Bear Canyon pluton** at Eagle Rock campground (elev. 2300 m). This is the north end of the Bear Canyon pluton, which ends immediately north above the cliffs and intrudes intracaldera Amalia Tuff and precaldera andesite. The Bear Canyon pluton is a high-SiO_2, mildly porphyritic granite that was intruded along the southern caldera margin 23–25 Ma ago. Subeconomic levels of molybdenite are concentrated in K-alteration zones within precaldera andesites above the aplitic roof of the pluton. Drilling indicates that the Bear Canyon pluton connects with the Sulphur Gulch pluton (5 km east) at depth (Leonardson et al., 1983). Hydrogen- and oxygen-isotope data indicate that hot meteoric waters circulated along the southern caldera margin during cooling of the plutons that were in part related to the mineralization (Hagstrum and Johnson, 1986; Johnson and Lipman, 1989). **1.7**

76.0 Good exposures of altered, chaotic, andesite caldera-fill on south side of Red River, indicating proximity of the southern caldera wall. **1.3**

77.3 **STOP 2-7. Rhyolite dike swarm** at Columbine Canyon campground (elev. 2400 m). Vertical cliffs (top elev. 2700 m) on north side of road are part of a massive swarm of largely metaluminous, rhyolite porphyry dikes that trend east–west and cut Proterozoic intrusive rocks along the general trend of the south caldera margin (Fig. 9). The northermost dikes cut intracaldera Amalia Tuff and caldera-floor andesite, and some cut the Sulphur Gulch pluton. Low-angle structures with top-to-the-east offsets controlled the emplacement of these northernmost dikes (J. Meyer, pers. comm. 1988). Low-angle faulting occurred between the time of caldera formation and cooling of the subvolcanic plutons, and is responsible for the near-vertical tilt of the intracaldera units. Greater than 100% extension has accompanied the faulting in some areas (Meyer, 1988).

The metaluminous dikes are associated with the southern caldera-margin intrusive activity and are not related to earlier caldera collapse or resurgence. Some dikes, however, are peralkaline rhyolite porphyry similar to the Amalia Tuff, indicating minor leakage of Amalia Tuff magma along the southern caldera margin. One peralkaline rhyolite dike that crops out south of the diabase contains pumice that

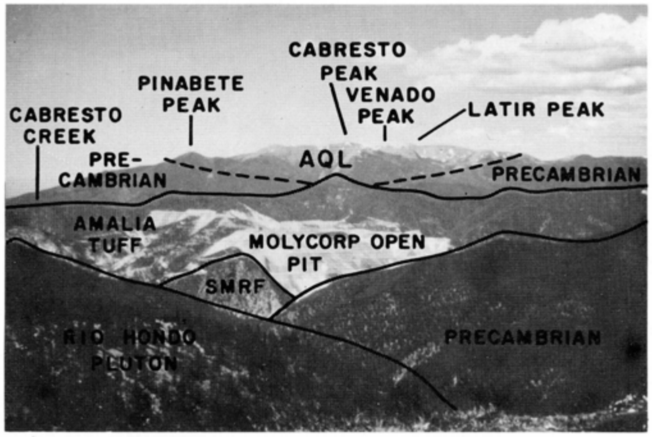

FIGURE 9—North view looking toward the southern caldera margin and resurgent dome from the center of the Rio Hondo pluton at the head of Columbine Creek. AQL, precaldera andesite and quartz latite lavas; SMRF, southern caldera-margin ring-fracture dikes (these crop out directly across the road from Columbine Creek campground on NM-38 and are discussed at Stop 2-7).

are flattened parallel to the dike margin; this dike may represent a vesiculating feeder dike to the Amalia Tuff (J. Meyer, pers. comm. 1988). Dark-colored dikes are pre-Mississippian diabase that cut Proterozoic intrusive rocks. Hydrogen- and oxygen-isotope data indicate that meteoric hydrothermal alteration occurred within the Tertiary rocks, as well as Proterozoic rocks (Hagstrum and Johnson, 1986; Johnson and Lipman, 1989). Molycorp open pit (inactive) behind cliffs to north; the talus spoils are visible east along the road, where they fill Sulphur Gulch (Fig. 9). **1.6**

78.9 **STOP 2-8. Sulphur Gulch pluton.** Ahead is Molycorp mill. Hydrothermal minerals are similar to those in the Bear Canyon pluton (pyrite, alkali feldspar, fluorite, calcite, and quartz), and are generally restricted to the aplite. Molybdenite mineralization is concentrated along the contact with precaldera andesite within the caldera (Leonardson et al., 1983). The Sulphur Gulch pluton and associated dikes are 23–25 Ma old. Turn around and travel west on NM-38. **6.6**

85.5 **Town of Questa** (elev. 2260 m). Junction of NM-522 and NM-38. Proceed south on NM-522 toward to the town of Taos. Pliocene lavas of the Taos Plateau volcanic field can be seen to the west. The extensive flat regions are underlain by the Servilleta Basalt. **3.6**

89.1 **Road to Red River Fish Hatchery on right.** Continue straight. Directly east (9:00) is Flag Mountain, which is underlain by Proterozoic intrusive rocks. The northern contact of the Rio Hondo pluton lies on the far side (east) of Flag Mountain. The southern contact of the Bear Canyon pluton occurs on the lower slopes (elev. 3000 m), marking the southern boundary of the Questa caldera. **6.2**

95.3 **STOP 2-9. View of Rio Hondo pluton and dike swarm** at junction of road to San Cristobal. High peaks along this part of the Sangre de Cristo Range are, from north to south, Flag Mountain (elev. 3641 m), Lobo Peak (elev. 3693 m), and Gallina Peak (elev. 3318 m), all of which have upper slopes composed of Proterozoic intrusive and supracrustal rocks. The lower slopes (elev. 2500–3400 m) are underlain by granodiorite to granite of the Rio Hondo pluton (21–22 Ma). A massive dike swarm is associated with the Rio Hondo pluton (Reed et al., 1983; Lipman and Reed, 1989); aspen-covered slopes of Gallina Peak are underlain by rhyolite dikes that have completely obliterated the Proterozoic roof rocks of the Rio Hondo pluton. **3.3**

98.6 **Junction with road to Arroyo Hondo** on south side of bridge. Turn left (east). **0.9**

99.5 **Town of Arroyo Hondo** (elev. 2200 m). **3.3**

102.8 **Junction with NM-230.** Turn left (north) toward town of Valdez. **0.7**

103.5 **Junction with east–west dirt road at edge of Rio Hondo Canyon.** Turn right (east) and follow along southern rim of Rio Hondo Canyon. Town of Valdez in canyon bottom to the north. Note 60–120 m of dissection of the alluvial fans. **1.3**

104.8 **Junction with NM-150** at canyon edge. Continue straight (east), down canyon side. **1.0**

105.8 **Cross bridge over Rio Hondo** (elev. 2320 m). **1.3**

107.1 **STOP 2-10. Highly sheared western margin of Rio Hondo pluton** (21–22 Ma). Structural reconstruction indicates that we are 7–8 km below the Miocene surface. The majority of the Rio Hondo pluton is composed of granodiorite (64–70 wt% SiO_2). The deepest exposed parts of the Rio Hondo pluton occur in Hondo Canyon. Only the upper and northern parts of the Rio Hondo pluton contain granite (up to 78 wt% SiO_2). Hydrogen- and oxygen-isotope data indicate that widespread circulation of hot meteoric waters occurred during late-stage solidification of the pluton; hydrothermal circulation was dominantly concentrated along fractures zones that developed during deformation of the pluton on its margins (Fig. 10; Hagstrum and Johnson, 1986; Johnson and Lipman, 1989). **1.2**

108.3 **STOP 2-11. Mafic inclusions in Rio Hondo pluton.** Pull out left and right past prominent outcrop on left (north). Mafic inclusion-rich, compositionally heterogeneous zones, as shown in this outcrop, are common in the lower parts of the Rio Hondo

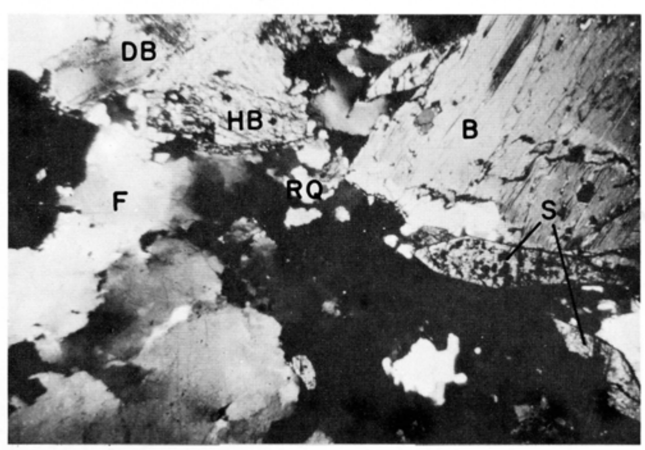

FIGURE 10—Polarized-light thin section of sheared Rio Hondo granodiorite taken from Hondo Canyon. RQ, recrystallized quartz; F, feldspar; DB, deformed biotite; HB, hornblende; B, biotite; S, sphene. Field is approximately 2 cm across.

pluton (Fig. 11). Textural relations and chemical compositions of the coarse-grained inclusions suggest that they represent fragments of cognate mafic cumulates disrupted from the bottom of the Rio Hondo magma chamber (Johnson et al., 1989). Large volumes of hydrothermal fluids circulated through the highly fractured granodiorite at this outcrop, resulting in partial recrystallization of quartz; relatively massive granodiorite 0.2 km east of this outcrop has not undergone significant hydrothermal alteration. **1.5**

109.8 Tertiary rhyolite dikes cutting Proterozoic amphibolite are exposed on north side of road as it curves left at Taos East Condominiums. **0.9**

110.7 **STOP 2-12. Rhyolite dikes of Rio Hondo pluton.** Pull off 0.1 mi past outcrop as road curves left. Outcrops of rhyolite dikes can be traced up the canyon walls. The younger Lucero Peak pluton (21–19 Ma) crops out on the southern, upper slopes of Hondo Canyon. The Lucero Peak pluton does not cut the Rio Hondo pluton and is not cut by the Rio Hondo dike swarm. Turn around and travel west on NM-230. **4.9**

115.6 **Cross Rio Hondo Bridge. 1.0**

116.6 **Follow paved road as it turns left** (south) to town of Arroyo Seco. **1.3**

117.9 **Town of Arroyo Seco** (elev. 2330 m). Follow road as it turns right (west). **1.9**

119.8 **Junction with NM-230.** Stay left (south). **2.1**

121.9 **STOP 2-13. View of Lucero Peak pluton** from Stewart's Studio. Directly east is the rounded top of Lucero Peak (elev. 3301 m). The rounded shape follows the pegmatite- and aplite-rich roof zone of the Lucero Peak pluton (Fig. 12). Proterozoic rocks underlie the highest terrain, including Wheeler Peak (elev. 4012 m, the highest point in New Mexico), which is behind Lucero Peak from this view. Pueblo Peak (elev. 3750 m) is seen south of Arroyo Seco canyon (occupying the prominent canyon south of Lucero Peak). This is a sacred mountain of the Taos Pueblo, and has not been mapped since 1920. It is presumably underlain largely by Proterozoic rocks, although the Lucero Peak pluton extends south of Arroyo Seco canyon for an unknown distance. **0.5**

FIGURE 11—Coarse-grained mafic enclave in Rio Hondo granodiorite. Plagioclase (P) and alkali feldspar (A) that are petrographically and chemically similar to those in the host pluton are common in the enclaves, and often protrude from the enclaves. The coarse-grained enclaves are interpreted as cognate crystal cumulates. Holes are for paleomagnetic cores.

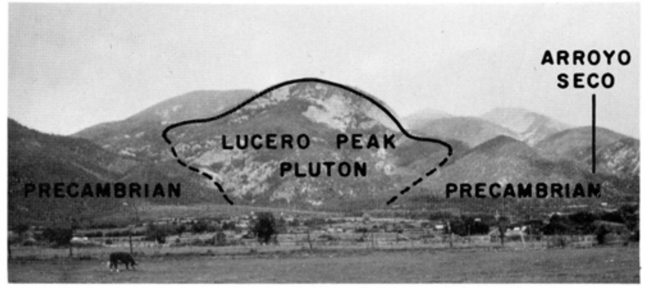

FIGURE 12—East view of the Lucero Peak pluton from near the town of Arroyo Seco. Coincidence of pegmatite and aplite with the convex-up surface of Lucero Peak (center) indicates that this surface marks the roof of the pluton.

122.4 **Junction of NM-150** with **US-64/NM-522.** Turn left (south) onto US-64/NM-522 toward the town of Taos. **2.3**

124.7 **Town of El Prado.** Continue into the town of Taos. **1.9**

126.6 **Junction of US-64 and NM-522 in the town of Taos** (traffic light). Following dinner in Taos, return to Questa by following NM-522 north. **20.0**

146.6 **Town of Questa** (elev. 2260 m).

Third day: Silicic resurgent plutons of Rito del Medio and Virgin Canyon, and regional geology to Alamosa, Colorado

Assembly point:	Sangre de Cristo Motel, Junction of NM-522 and NM-38
Departure time:	8:00
Distance:	approximately 9 miles of hiking and 95 miles by vehicle
Stops:	2

Today's route involves a hike through the eroded resurgent dome of the Questa caldera to examine the magmas that were present in the subcaldera magma chamber immediately following eruption of the Amalia Tuff. We will be hiking for most of the day, from approximately 2400 to 3600 m elevation. Bring plenty of water (stream waters contain giardia and should not be drunk) and a rain coat. Following the hike, we will travel by vehicle north past the northern margin of the Latir field (near the town of Costilla). Farther north, the Sangre de Cristo Mountains are almost exclusively underlain by Pennsylvanian, Permian, and Proterozoic rocks. Blanca Peak (elev. 4372 m), for example, dominates the skyline during our travel north to the town of Fort Garland. The town of San Luis (the oldest town in Colorado, established in 1851) lies near the northern end of the Taos Plateau volcanic field. Directly west of the town of San Luis are the alkaline and tholeiitic lavas of the San Luis Hills, which make up the northernmost exposed intrarift horst in the San Luis Basin. As is typical of the Timber and Brushy Mountains horst block farther south, the early rift San Luis lavas are not tilted, in contrast to younger lavas along the flanks of the Rio Grande rift. A gravity high is centered on the San Luis Hills horst, and extension of this high north of the town of Alamosa indicates (in addition to drilling data) that this horst system extends most of the length of the basin (Tweto, 1979a; Keller et al., 1984). Neogene mafic lavas within, and on the flanks of, the basin generally become more alkaline northward, possibly reflecting increasing crustal thickness (Lipman, 1969; Lipman and Mehnert, 1975).

Mileage

0.0 **Town of Questa** (elev. 2260 m). Junction of NM-522 and NM-38. Proceed by vehicle north on NM-522. **3.9**

3.9 **New Mexico Port of Entry. 2.9**

6.8 **Junction with road** to El Rito. Turn right (east) and drive 1.0 mi to sharp left at town of El Rito (elev. 2448 m). Turn left onto dirt road, drive approximately 0.5 mi to first right that continues up (east) alluvial fan. Turn right (east) and drive as far as possible (0.5–1.0 mi, elev. 2500 m, depending on extent of private development). Park vehicles.

Hike dirt road up alluvial fan (east) 0.2–0.5 mi to prominent north–south dirt road following cliffs (elev. 2620 m). Walk south on road for approximately 0.5 mi until directly west of prominent cliffs of Rito del Medio granite. You have gone too far if you have crossed Rito del Medio Creek, which runs year-round.

0.0 **Start hike at National Forest Service marker** indicating trail to Latir Wilderness. Trail follows north side of Rito del Medio Creek once adjacent to prominent granite cliffs. Hike 0.8 mi to prominent granite cliffs of Rito del Medio granite. **0.8**

0.8 **STOP 3-1. Rito del Medio pluton** (trail elev. 2900 m). Most of the Rito del Medio pluton consists of coarse-grained granite (76 wt% SiO_2) that is texturally similar to the coarser parts of the Cañada Pinabete pluton to the southwest. The Rito del Medio granite is considered to be a late-stage differentiate of the metaluminous granite of the Virgin Canyon and Cañada Pinabete plutons. The roof of the Rito del Medio pluton is at the top of the cliffs 270 m above, and is locally more mafic and fine-grained, commonly associated with feldspar–quartz pegmatites and unidirectional solidification textures. The pluton intrudes Proterozoic supracrustal rocks and precaldera volcanic rocks at high structural levels. Paleomagnetic data show that the Rito del Medio pluton is not tilted, in contrast to the Virgin Canyon pluton farther east, indicating that it is the youngest of the three silicic resurgent plutons (Hagstrum and Lipman, 1986).

The Rito del Medio granite is composed almost entirely of alkali feldspar and quartz, with minor biotite and plagioclase. A notable feature of the pluton is the occurrence of primary muscovite and hematite, which is interpreted as indicating loss of alkalies by late-stage volatile exsolution at relatively high oxygen fugacities (Dillet and Czamanske, 1987).

Miarolitic cavities as large as 6 cm are common throughout the pluton, although the largest cavities are restricted to the interior of the pluton (Fig. 4). This may reflect inward crystallization and volatile saturation in the core. Cavities comprise up to 4.2 vol% of the granite. The cavities are partially filled with euhedral quartz, alkali feldspar, magnetite, hematite, muscovite, and fluorite, indicating late-stage exsolution of a volatile-rich silicate fluid during crystallization.

Continue up trail on north side of Rito del Medio Creek. Trail is steep for next 0.4 mi, then flattens for 1.0 mi. **1.4**

2.2 **Junction with abandoned north–south logging road** (elev. 3230 m). Turn right (south), and cross Rito del Medio Creek. Continue up (east) Rito del Medio Creek on south side. Cabresto Peak lies immediately south (elev. 3794 m) and is underlain by precaldera quartz latite on its upper part, indicating that the caldera floor is at elevations greater than 3800 m in this part of the resurgent dome. The break in slope on the west side of Cabresto Peak (elev. 3470 m) marks the Proterozoic–Tertiary unconformity. The roof of the Rito del Medio pluton on the south side of Rito del Medio Creek lies on the timbered shoulder west of this point (elev. 3350 m). Several trails follow the Rito del Medio Creek; the easiest are just above the creek gully, although they may be difficult to find. Following the creek gully is also possible. **1.0**

3.2 **STOP 3-2. Virgin Canyon pluton.** Open meadow between Cabresto and Venado Peaks (elev. 3500 m). This cirque is at the base of Virgin Canyon (up stream to the east), and is in the southern part of the Virgin Canyon pluton. The southern cirque wall is entirely composed of precaldera quartz latite more than 300 m thick, which is intruded by peralkaline granite (25 Ma) of the Virgin Canyon pluton. The peralkaline granite is well exposed on the low ridge to the west at 3540 m (extreme northern flank of Cabresto Peak), as well as high on the western flank of Venado Peak (east of the meadow, elev. 3881 m) at 3690 m, where the granite intrudes precaldera andesite. The eroded caldera floor is probably at elevations greater than 4000 m in this part of the resurgent dome, indicating that possibly more than 2 km of the resurgence has occurred relative to the southern part of the caldera, near the range front at Goat Hill.

The peralkaline granite margin of the Virgin Canyon pluton varies from a few meters thick on the north side of Cabresto Peak, to approximately 30 m thick on the west side of Venado Peak. The peralkaline granite is at least 50 m thick on Virsylvia Peak (East Virsylvia Peak elev. 3839 m, West Virsylvia Peak elev. 3819 m), visible directly north. The peralkaline granite is intruded in both the Virgin Canyon and Cañada Pinabete plutons by a distinctive, more mafic (71–74 wt% SiO_2), metaluminous granite termed the early metaluminous granite. The early metaluminous granite is intruded in both plutons by a generally more silicic (75–78 wt% SiO_2) equigranular granite termed the later metaluminous granite (Fig. 13), which typically contains miarolitic cavities. The consistent sequence of these three units in the Cañada Pinabete and Virgin Canyon

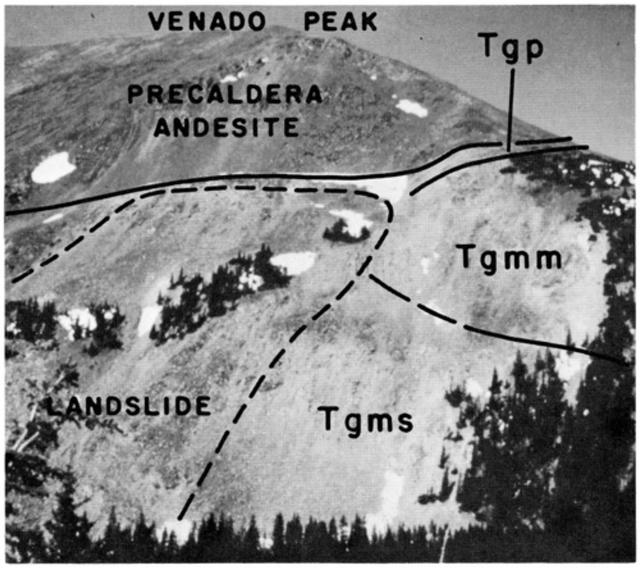

FIGURE 13—East view of Venado Peak from meadow between Venado and Cabresto Peaks. Intrusive units of the Virgin Canyon pluton are: Tgp, peralkaline granite; Tgmm, early (mafic) metaluminous granite; Tgms, later (silicic) metaluminous granite.

plutons and the correlation of the Rito del Medio granite with the Cañada Pinabete pluton indicate that the units are not volumetrically small, isolated bodies, but large volumes of magma which underlay most of the resurgent dome of the Questa caldera.

Unlike the southern caldera-margin intrusions and the southern plutons of Rio Hondo and Lucero Peak, meteoric hydrothermal alteration of the resurgent plutons is minimal (Johnson and Lipman, 1989). This is interpreted to be a result of rapid cooling of the relatively fine-grained silicic resurgent intrusions.

Parts of the Virgin Canyon pluton have been tilted during major structural disruption which occurred immediately after caldera formation 26 Ma ago (Hagstrum and Lipman, 1986). The peralkaline granite continues the chemical and mineralogical trends of the Amalia Tuff, and is interpreted as the solidified remnants of the Amalia Tuff magma. Relict biotite and calcic amphibole in the peralkaline granite suggest that the granite evolved from a metaluminous parental magma, possibly associated with high halogen fluxes and accompanying alkali enrichment (Czamanske and Dillet, 1988; Johnson et al., 1989). The early metaluminous granite may reflect fractionation during relatively low volatile fluxes. The later metaluminous granite in Virgin Canyon and Cañada Pinabete was probably derived by crystal fractionation of the early metaluminous granite, and continued fractionation likely produced the Rito del Medio granite. The Cabresto Lake pluton crops out south of Virgin Canyon and is the most mafic resurgent pluton. Chemical and isotopic data suggest, however, that the Cabresto Lake granite and monzogranite do not represent parental magmas to the more silicic resurgent plutons of Virgin Canyon, Cañada Pinabete, and Rito del Medio (Johnson et al., 1989). **3.2**

Turn around and follow the Rito del Medio Creek trail west.

6.4 **National Forest Service marker.** Turn right on north–south dirt road and return to vehicles parked to the northwest (approximately 0.7–1.0 mi). Return to town of El Rito (1.0–1.5 mi southwest). Turn right (west) at pavement and travel 1.0 mi to NM-522. **3.6**

10 **Junction of El Rito road and NM-522.** Turn right (north) toward Colorado. **13**

23 **Town of Costilla.** Continue north on NM-522. **4**

27 **Enter Colorado.** NM-522 becomes CO-159. **18**

45 Town of San Luis, Colorado. **Break for dinner. 16**

61 **Junction of CO-159 and US-160** at town of Fort Garland. Turn left (west) onto US-160 toward Alamosa. **25**

86 **Town of Alamosa.** Overnight lodging.

The Mount Aetna cauldron: Structures in deeply eroded ring zones

July 4–5, 1989

Leader: James R. Shannon

Summary

The Mount Aetna cauldron complex (Shannon, 1988), in the Sawatch Range, central Colorado (Fig. 14), consists of three main elements: (1) the 36.6 Ma Mount Princeton pluton, (2) the 34.4 Ma Mount Aetna cauldron, and (3) the 29.8 Ma, chemically evolved A-type granites (Fig. 15). These three elements represent the major Tertiary magmatic events in the south-central Sawatch Range. They occurred during a fundamental change from Laramide magmatism and compressional tectonism during the early Tertiary to Rio Grande rift-related magmatism and extensional tectonism during the middle Tertiary to Recent (Shannon et al., 1987a). The Mount Princeton pluton and Mount Aetna cauldron, together with the Bonanza and Grizzly Peak calderas (Fig. 14), represent different erosional and structural levels of volcanoplutonic subsidence systems.

The Mount Princeton pluton is an elliptical (24 × 34 km), compositionally and texturally zoned, flat-topped pluton. Compositional (granodiorite, quartz monzonite, and granite/aplite) and textural zonations in the roof-zone border unit of the pluton are interpreted as the complex record of crystallization during numerous volcanic ventings. A correlation between the low-silica rhyolite Wall Mountain Tuff (Epis and Chapin, 1974) of the Thirtynine Mile volcanic field, east of the Rio Grande rift (Fig. 14), and the Mount Princeton pluton is suggested based on spatial relations and similar ages (Shannon, 1988). The Mount Princeton pluton was breached by erosion prior to collapse of the Mount Aetna cauldron, for which it provided a relatively uniform, massive-textured, and structurally isotropic host. The Mount Princeton pluton is interpreted to represent the plutonic roots of a caldera in which all evidence of the volcanic edifice and collapse structure has been completely removed by erosion.

The Mount Aetna cauldron consists of two collapse structures: a 13 × 27 km elliptical main cauldron and a nested, northern cauldron 12 km in diameter (Fig. 15). A 0.5 km thick sequence of gently south-dipping precollapse volcanic

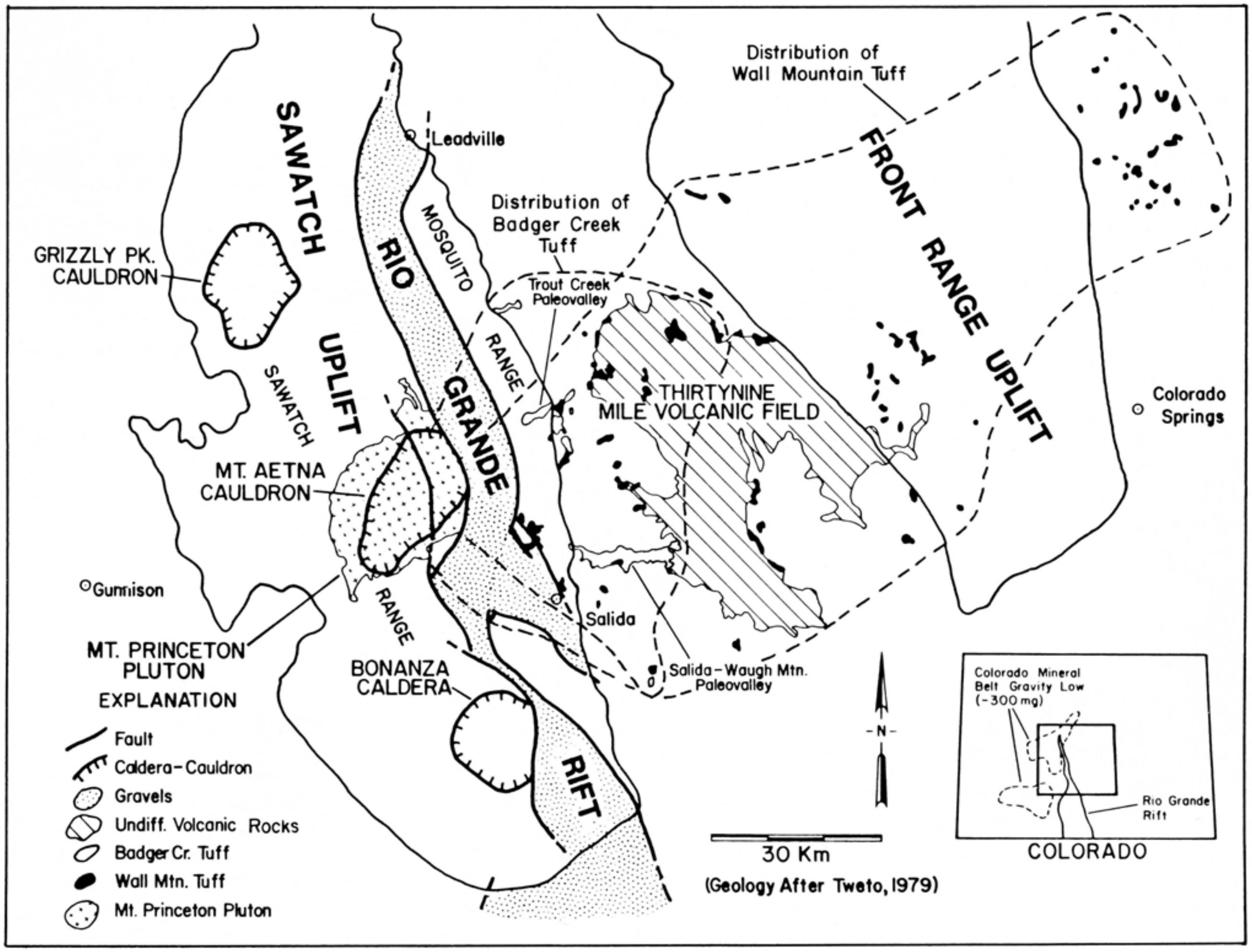

FIGURE 14—Geologic and tectonic setting of the Sawatch Range calderas–cauldrons and the Thirtynine Mile volcanic field, central Colorado. From Shannon et al. (1988).

rocks and syncollapse intracauldron tuff and megabreccia are preserved in the southern part of the main structure. The Mount Aetna intracauldron tuff is correlated with the Badger Creek Tuff (Epis and Chapin, 1974) of the Thirtynine Mile volcanic field (Fig. 14) and an intrusive tuff dike (Fig. 15) based upon spatial associations, similar ages, mineralogy, and chemistry (Shannon et al., 1988; Shannon, 1988). All are pheno-andesites (IUGS classification) and have rhyodacitic compositions. The above intracauldron features, as well as the outflow-sheet remnants clearly establish the Mount Aetna center as a classic example of the roots of an ash-flow caldera. All of the northern part of the cauldron, however, is eroded to a structural level below both caldera fill and precollapse lavas. This northern part has the features of a ring-dike complex: the cauldron structure is manifested as a system of ring shears and ring intrusions cutting across the Mount Princeton pluton country rocks. The caldera (cauldron) blocks that subsided into the Mount Aetna magma chamber collapsed as coherent units; they consisted of a minimum of 2 km thickness of Mount Princeton country rocks.

The Mount Aetna cauldron provides a rare opportunity to characterize ring-zone features at a relatively deep erosion level (Shannon and Epis, 1987; Shannon, 1988). The collapse structures are delineated by the distribution of five ring-zone features which are present in zones from 20 to 300 m wide. In general paragenetic sequence, these features are: (1) brittle–ductile ring shears, (2) microbreccias, (3) flinty crush rock, (4) intrusive breccias, and (5) ring dikes. The distribution and crosscutting relations of the various ring-zone features indicate at least two main collapse–resurgence cycles; the first related to the main cauldron and the second related to the northern cauldron. Collapse–resurgence cycles are defined as paired collapse and resurgence events (Shannon, 1988).

Collapse of the main cauldron formed dominantly outward-dipping (60–80°) ring shear zones (Figs. 16, 17). The minerals in these shear zones were deformed by both brittle (feldspars) and ductile (quartz) processes. The resultant proto- and orthomylonite textures typically display S–C fabrics (Simpson and Schmid, 1983). The initial ring shears exerted a strong structural control on subsequent ring-zone activity; most later-formed ring-zone features follow these initial shears in distribution and orientation. Thin seams of microbreccia were injected along the C-surfaces after ductile shearing. The change from ductile to brittle deformation may be related to rapid and fluctuating changes in strain rate during cauldron collapse.

Flinty crush rock, first described at the Glen Coe cauldron in Scotland (Clough et al., 1909) is present at a number of localities around the main collapse structure (Fig. 16a). It is a microfragmental intrusive rock resembling pseudota-

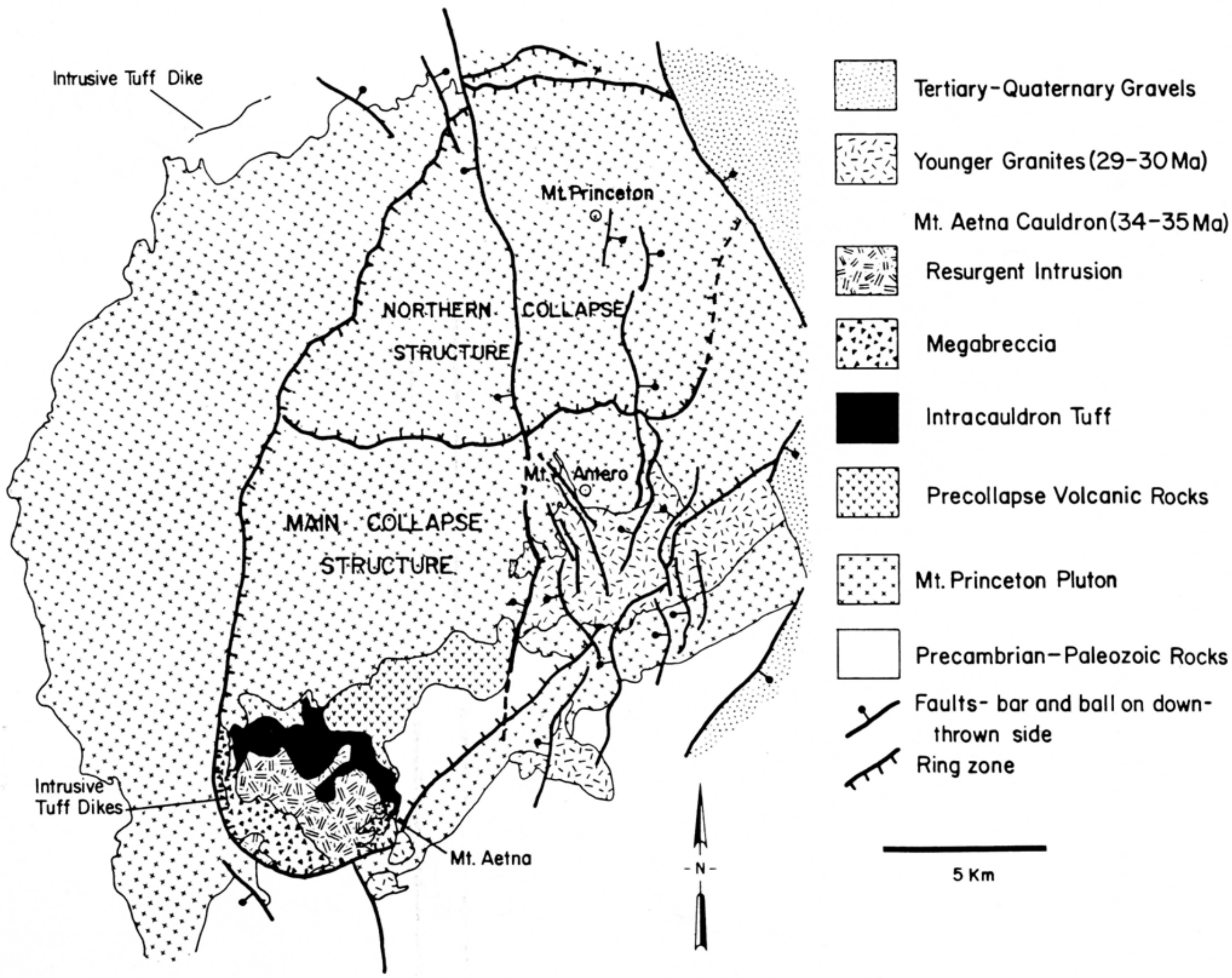

FIGURE 15—Geology of the Mount Aetna cauldron complex, Sawatch Range, central Colorado. From Shannon (1988).

chylite and is present along the margins of ring dikes and as thin, irregular, discontinuous seams in the wall rocks (Figs. 17, 18). Flinty crush rock crosscuts ductile shears and is crosscut by the ring dikes. It is interpreted as a hybrid mixture of phyric magma and microbreccia and may represent the subtle remnants of conduits of ignimbrite vents along the ring zone (Shannon, 1988).

Dike-like bodies (0.5 cm–100 m) of intrusive breccia are common along the western, northwestern, and northern portions of the main collapse structure. They are matrix-supported and contain subrounded clasts of wall rock in a clastic, hydrothermally altered matrix. Rarely, the intrusive breccias are physically mixed with early ring-dike material. They are interpreted to have formed largely by fluidized flow in a medium of venting volcanic gas (and/or by phreatomagmatic processes) along the ring zone.

There are three textural varieties of porphyritic rhyodacitic to quartz monzonitic ring dikes. Type 1 dikes are fine-phenocryst porphyritic rhyodacite which occurs as thin selvages on later ring dikes, as thin dikelets, and as mixtures with intrusive breccias. These dikes are considered to be relatively early, intruded during or after collapse of the main cauldron, but prior to resurgence of the main cauldron. Type 2 ring dikes are very coarse-phenocryst porphyritic quartz monzonite. They are preferentially developed around the southern portion of the main cauldron and are continuous with an asymmetric (i.e., off-center) resurgent intrusion which cuts intracauldron tuff and megabreccia (Fig. 15). Type 2 dikes are interpreted to represent a magmatic resurgence event following collapse of the main cauldron.

Type-3 ring dikes are medium-phenocryst rhyodacite and are preferentially developed around the northern cauldron, but were also locally intruded along the (reactivated) main cauldron boundary. Type-3 ring dikes are interpreted as related to a magmatic resurgence event following collapse of the northern cauldron. This magmatic resurgence was also expressed by preferential uplift of the northern cauldron block (restored nearly to its original level). The remaining portion of the main cauldron block (i.e., the southern part) was apparently tilted to the south during this resurgence event.

Intrusive tuff dikes are present approximately 5 km outside of the northwestern ring zone (Figs. 15, 19). They are in cone-sheet orientation and cut Precambrian country rocks (Fig. 16b). The intrusive tuff dikes are interpreted to represent the conduits to ignimbrite eruptions (of Badger Creek Tuff) on the surface (Shannon et al., 1988; Shannon, 1988). These observations suggest that some tuff may be vented from cone-sheet-oriented structures outside of the main ring zone, and that at deep erosional levels vitroclastic textures

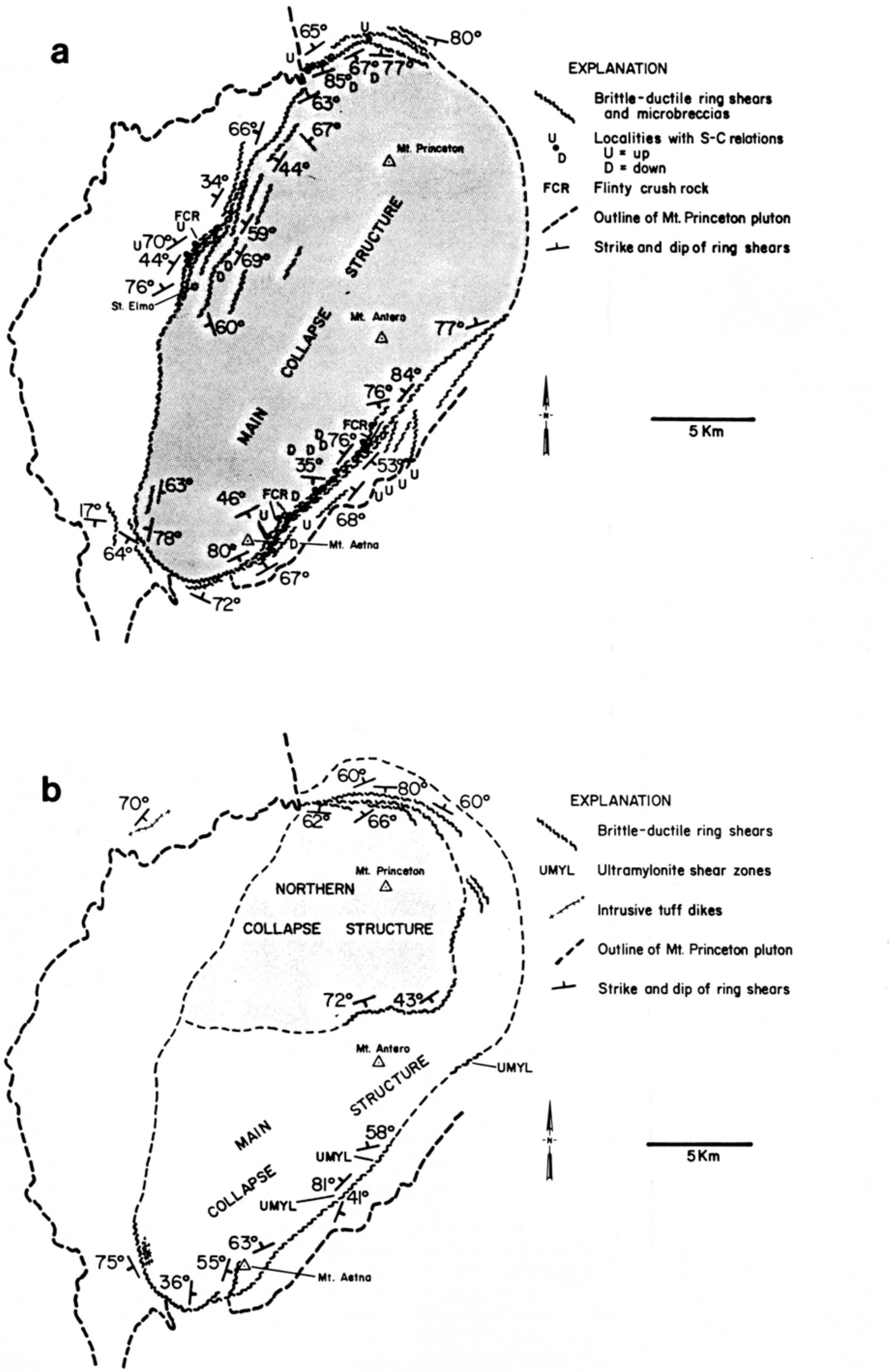

FIGURE 16—Distribution and orientation of brittle–ductile ring shears and flinty crush rock related to the main **(a)** and northern **(b)** cauldron ring zones, Mount Aetna cauldron, Colorado. From Shannon (1988).

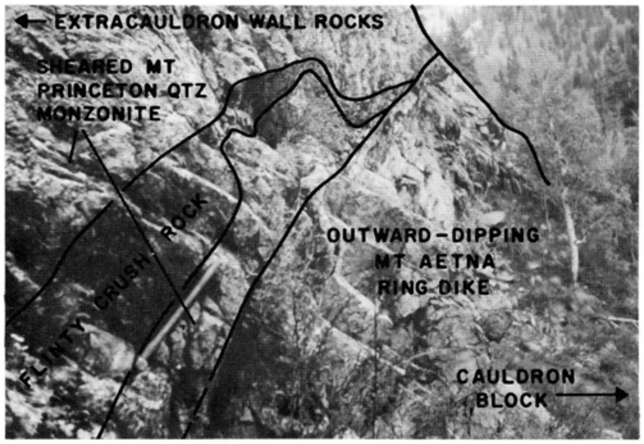

FIGURE 17—Ring-zone features (displayed at Stop 4-4) near St. Elmo. Note outward dipping ring-zone features (flinty crush rock, ring shears, ring dike) with cauldron block to right and sheared Mount Princeton wallrocks to left. Hammer handle is on the inner contact of flinty crush rock "dike."

FIGURE 19—Photomicrograph of intrusive tuff dike from Stop 5-2. Note crystal-fragment-rich matrix with well-preserved shard shapes and "collapsed" pumice clasts. Field is approximtely 2.8 mm across.

related to explosive venting of tuff are more likely to be preserved in that distal setting in contrast to the main, highly dynamic ring zone.

Microstylolites are present in two different settings associated with the Mount Aetna cauldron (Shannon and Nelson, 1987; Shannon, 1988). They are not considered to be an integral ring-zone feature, but are particularly well developed in the ring zone of the northern collapse structure. The microstylolites are interpreted to be the result of hydrothermal pressure solution of crystalline silicate rocks (Shannon, 1988). They are present in flinty crush rock, intrusive breccia, ring dikes, and sheared wall rocks, and are interpreted as formed during the resurgence of the northern cauldron block.

The occurrence of ductile shearing at the subvolcanic level (as shallow as 1–3 km) at Mount Aetna is probably related to the large thermal anomaly around the subcaldera magma chamber and to the capacity of the ring zones to act as thermal conduits once they form (Shannon and Epis, 1987; Shannon, 1988). Ductile-deformation processes may also be enhanced by hydrolytic weakening (Griggs, 1967; Yund and Tullis, 1980) related to the mechanical breakdown of hydrous minerals (biotite and hornblende) or introduction

FIGURE 18—Slab from Stop 4-4, showing contact between flinty crush rock (left) and sheared Mount Princeton quartz monzonite wallrock (right). Note flow laminations in flinty crush rock and ductile shears in Mount Princeton wallrock.

of meteoric and/or magmatic water into the ring zone (Shannon, 1988). S–C surfaces in the ring shear zones dominantly yield a sense of shear indicating the caldera (cauldron) blocks went down (Fig. 16a). In addition, ductile-deformation processes were apparently not active, or of minor importance, during the resurgence stage of each collapse–resurgence cycle.

Following caldera formation by about 4 Ma, the Mount Aetna area was the site of renewed magmatic activity associated with the shift to an active extensional tectonic setting (Shannon et al., 1987a). Topaz rhyolites (Nathrop topaz rhyolites) and chemically evolved A-type (anorogenic) granite and rhyolite intrusions (Mount Aetna granites) are present in a 36 km long, N50E-trending belt which is, in part, coincident with the southeastern margin of the Mount Aetna cauldron (Fig. 15). These rocks, together with granites associated with Climax-type porphyry Mo deposits represent a subgroup of A-type granites (distinguished by trace-element signatures) that is associated with the Rio Grande rift province in Colorado (Shannon et al., 1987b; Shannon, 1988).

Faulting related to development of the upper Arkansas axial graben segment of the Rio Grande rift began at about 28–29 Ma (Tweto, 1979b; Shannon et al., 1987a; Shannon, 1988). Formation of the graben was also associated with asymmetric uplift of the western Sawatch Range marginal-block uplift (Figs. 14, 20). This resulted in relatively deep erosion of the Mount Aetna cauldron complex in the Sawatch Range, in contrast to the Mosquito Range (eastern marginal block uplift) which retains remnants of outflow ash-flow tuff from the inferred Mount Princeton caldera (Wall Mountain Tuff) and the Mount Aetna cauldron (Badger Creek Tuff), and extrusive topaz rhyolites (Nathrop topaz rhyolites).

Fourth day: Alamosa to Buena Vista, Colorado, and the Mount Aetna cauldron

Assembly point:	Alamosa
Departure time:	7:00
Distance:	182 miles
Stops:	6

Our route traverses the eastern flanks of the San Juan volcanic field and continues north into the Sawatch Range. The Platoro caldera (30 Ma), the oldest and southernmost

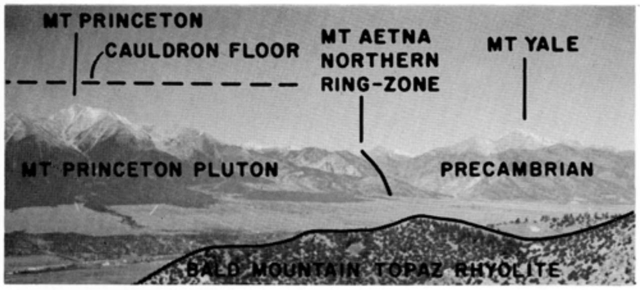

FIGURE 20—Sawatch Range and upper Arkansas axial graben photographed from the southern Mosquito Range (looking west-northwest). Sawatch Range (western marginal block uplift) containing the Mount Aetna cauldron complex (background) has experienced more uplift and erosion than the southern Mosquito Range (eastern marginal block uplift foreground). The upper Arkansas axial graben (middle ground) separates the two marginal block uplifts. Bald Mountain topaz rhyolite cone resting on Proterozoic rocks in foreground.

caldera of the San Juan volcanic field (Steven and Lipman, 1976) can be seen at 9:00 (southwest) during the drive between the towns of Alamosa and Monte Vista. Farther north, the low hills directly west of the highway are the eroded remnants of the intermediate-composition Summer Coon volcano, which is several million years older than the Platoro caldera.

The route turns east at the town of Saguache, then curves north and skirts the eastern side of the Bonanza caldera (36 Ma) and associated volcanic rocks at the northern end of the San Luis Basin (Varga and Smith, 1984). Although the Bonanza caldera has been previously grouped with the San Juan volcanic field, its close temporal and spatial relations with the older Mount Aetna and Grizzly Peak calderas suggest that it is more appropriately grouped with the Sawatch Range calderas (Fig. 14). While traveling north of the town of Villa Grove, the high peaks (Mt. Shavano, Mt. Princeton) of the Sawatch Range can be seen to the north over Poncha Pass. Along the east side of the upper Arkansas Valley, the mid-Tertiary ash-flow tuffs of the Thirtynine Mile volcanic field overlie Permian, Pennsylvanian, and Proterozoic rocks in the southern Mosquito Range. The Mount Aetna cauldron and Mount Princeton pluton are emplaced into Proterozoic rocks in the Sawatch Range, and these can be seen to the west.

The relationship of the Mount Aetna cauldron to the older Mount Princeton pluton, the Thirtynine Mile volcanic field, the Eocene–Oligocene erosion surface, and the Rio Grande rift will first be discussed, followed by examination of a variety of ring-zone features (brittle–ductile ring shears, flinty crush rock, microbreccias, ring dikes and microstylolites) near St. Elmo.

Mileage

0 **Town of Alamosa.** Travel on US-160 to west side of town where it joins US-285 at stoplight. Continue straight on US-285/160. **17**

17 **Town of Monte Vista.** U.S. 285 and US-160 split. Turn north onto US-285. **35**

52 **Town of Saguache.** Junction of CO-114 and US-285. Continue on US-285. Stay right (east). **33**

85 **Poncha Pass** (elev. 2750 m). **9**

94 **Town of Poncha Springs.** Junction of US-50 and US-285. Continue north on US-285. **22**

116 **Junction of US-285 and US-24.** Continue north, highway becomes US-24. **2**

118 **Town of Buena Vista** (elev. 2425 m). Brief rest/coffee stop. Travel south on US-24. **2**

120 **Junction of US-285 and US-24.** Johnson Village. Turn left (east) on US-285. After approximately 2.1 mi, turn left (north) to scenic overview. **2.1**

122.3 **STOP 4-1. Overview of regional geologic and tectonic setting of the Mount Aetna cauldron and vicinity** (Figs. 14, 15). The timing of magmatic and tectonic events in the Sawatch Range and extreme northern Rio Grande rift are summarized in Table 1. The Wall Mountain Tuff and Badger Creek Tuff are preserved as valley fill on the Eocene–Oligocene erosion surface (Epis and Chapin, 1975) on Triad Ridge, to the southeast. The Badger Creek Tuff has been correlated with the Mount Aetna intracauldron tuff based upon spatial associations and similarities in chemistry, mineralogy, and age determinations. Turn around and drive west on US-285. **2.2**

124.5 **Junction of US-285 and US-24.** Johnson Village. Turn left (south) on US-285. **5.8**

130.3 **Junction of US-285 and CO-162.** Town of Nathrop. Turn right (west) on CO-162 (Chalk Creek Road). Route enters the Sawatch Range and crosses the Mount Aetna cauldron (Fig. 16). **4.6**

134.9 **Mount Princeton Hot Springs. 11.2**

146.1 **Junction of CO-162 and Hancock Road.** Turn left (south) on Hancock Road. Route follows upper Chalk Creek along the western cauldron margin. **5.6**

151.7 **STOP 4-2. Overview of the Mount Aetna intracauldron volcanic rocks.** The Mount Aetna cauldron is one of the most deeply eroded collapse structures which still retains some of the classic features typically associated with higher-level caldera systems. The precollapse lavas of the Mount Aetna cauldron mark the floor of the caldera, upon which the intracauldron Badger Creek Tuff and multilithic megabreccias were deposited. Ring-zone features (e.g., ring shears, flinty crush rock, microbreccias, and ring dikes) in the south are developed in a zone separating intracaldera volcanic rocks, including megabreccias, from the Mount Princeton quartz monzonite. The remainder of the day will concentrate on the parts of the ring zone, cauldron, and Mount Princeton pluton that are below the level of the caldera floor. Turn around and drive north on Hancock Road. **5.7**

157.4 **STOP 4-3. Ring shear in cauldron block.** Saint Elmo at junction with Hancock Road. Park in pullout on south side of CO-162 just east of CO-162/

TABLE 1—Summary of events and timing in the Sawatch Range, central Colorado.

Event	Age
Sawatch uplift	Laramide to 45 Ma
Eocene–Oligocene erosion surface	>36 Ma
Mount Princeton pluton/Wall Mtn. Tuff	36.6 Ma
Bonanza caldera	36 Ma
Mount Aetna cauldron/Badger Creek Tuff	34.4 Ma
Grizzly Peak caldera	34 Ma
Evolved granites and rhyolites	29–30 Ma
Beginning Rio Grande rift faulting	28–29 Ma
Opening of upper Arkansas graben	<28 Ma
Uplift of Sawatch Range block	<20 Ma

Hancock Road intersection. Outcrops on south and north side of CO-162 (west of parking area) show that a subtle but continuous ring shear is developed in the caldera block approximately 0.75 km inside of the main ring zone. A narrow (<1.0 m), steeply outward-dipping zone of brittle–ductile shearing and intrusive breccia cuts Mount Princeton quartz monzonite. A short distance to the north, the Mount Princeton quartz monzonite is unaffected by ring shearing and is typical of the caldera block far from the ring zone. These relations indicate that the caldera block collapsed as an essentially coherent unit with little or no internal disruption. Drive west on CO-162 to town of Saint Elmo. **0.2**

157.6 **Saint Elmo. 0.4**

158.0 **STOP 4-4. Northern ring zone.** Turn right (north) and then left (west) on Tincup Pass Road. Park at Poplar Gulch trailhead. Hike approximately 0.5 km to landslide, then up scree slope to base of cliffs.

The most accessible outcrop that displays many of the ring features is at this stop (Fig. 21). The important relations to observe are the outward inclinations of all ring-zone features and their crosscutting relation (Figs. 17, 18). All ring features at this stop dip outward at angles ranging from approximately 30 to 80°.

In general, ring shears have well developed S–C fabrics. Fig 16 (a, b) shows that S–C fabrics in ring shears around the main collapse structure indicate that the caldera block has been faulted down. The occurrence of ductile deformation at depths as shallow as 1–3 km is highly unusual. This is probably related to heating of the ring zone, possibly assisted by hydrolitic weakening.

Flinty crush rock was first described from the Glen Coe caldera in Scotland (Clough et al., 1909) and is present in the ring zone around the main collapse structure of the Mount Aetna cauldron (Fig. 16a). Based on observations at Mount Aetna, a new mechanism of formation for flinty crush rock is suggested, involving injection of phyric magma with a cataclastic component during ring shearing. Flinty crush rock may represent the subtle remnants of magmatic venting from the ring zone during caldera collapse.

Two varieties of ring dike are present at this stop: evidence (non-fragmental textures) suggests that non-explosive, forceful emplacement of the majority of ring dikes occurred during magmatic resurgence stages. Chlorite microstylolites in the flinty crush rock and ring dikes are important because they indicate pressure solution of silicate minerals by the action of hydrothermal fluids. They crosscut all ring-zone features and are interpreted to have formed during resurgence of the northern cauldron block. Return to Saint Elmo. **0.4**

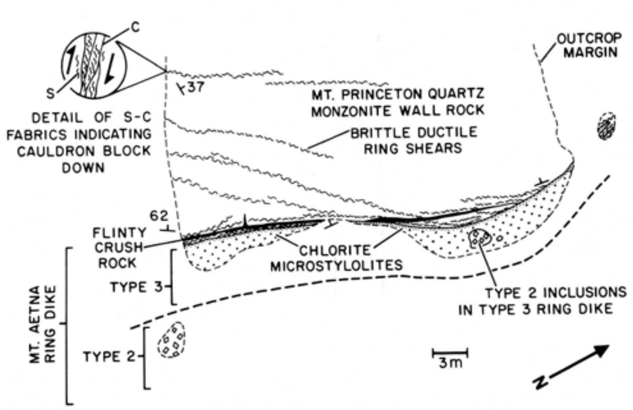

FIGURE 21—Plan sketch map showing the distribution, orientation, and relation of ring-zone features at Stop 4-4.

158.4 **Saint Elmo.** (drive east on CO-162). **8.3**

166.7 **Junction of CO-162 and Quarry Road.** Turn north (left) on Quarry Road. **0.3**

167.0 **STOP 4-5. Cauldron block of Mount Princeton quartz monzonite.** The younger structures and porphyritic rhyolite dikes related to northern Rio Grande rift tectonism and magmatism are well exposed here. The high-angle, brittle, rift-related faults with associated zeolitic alteration contrast with the brittle–ductile ring shears in terms of the style of deformation.

Porphyritic, high-SiO_2 rhyolite dikes contain microphenocrysts of garnet and have high incompatible-element (Rb, Nb) contents. They, together with lamprophyre (kersantite and spessartite) dikes, represent a rift-related, bimodal, magmatic association. Turn around and return to CO-162. **0.3**

167.3 **Junction of CO-162 and Quarry Road.** Turn east on CO-162. **3.8**

171.1 **Mount Princeton Hot Springs and junction of CO-162 and CO-321.** Turn north (left) on CO-321. **0.7**

171.8 **STOP 4-6. Overview of southern Mosquito Range and extreme northern Rio Grande rift.** Pull over at turnout at sharp 180° turn. This stop provides an overview of major tectonic elements in an opposite view from that of Stop 4-1. The Eocene–Oligocene erosion surface that preserves remnants of outflow Wall Mountain Tuff and Badger Creek Tuff and extensive topaz rhyolites represents a geologic datum that was disrupted by the younger Rio Grande rift. The relation between ignimbrite calderas/cauldrons and continental rifts will be explored using the relation of the Sawatch Range calderas/cauldrons and the northern Rio Grande rift. **9.8**

181.6 **Town of Buena Vista** (elev. 2425 m).

Fifth day: Northern ring zone of the Mount Aetna cauldron

Assembly point:	Buena Vista
Departure time:	8:00
Distance:	Approximately 35 vehicle miles and 5 hiking miles
Stops:	4

This section concentrates on ring-zone features (brittle–ductile ring shears, intrusive breccias, ring dikes) exposed in the northern ring zone on Sheep Mountain. We will also examine an intrusive tuff dike in Grassy Gulch, which provides compelling evidence for an ignimbrite vent.

Mileage

0.0 **Town of Buena Vista** (elev. 2425 m). Junction of US-24 and CO-306. Travel west on CO-306. **7.1**

7.1 **Junction of CO-306 and CO-344.** Travel south on CO-344 (South Cottonwood Creek Road). **3.3**

10.4 **STOP 5-1. Overview of the Mount Aetna cauldron and northern ring zone.** Pull out on the north side of Cottonwood Lake. View to south of the northern flank of Mount Princeton consists entirely of Mount Princeton quartz monzonite of the Mount Aetna cauldron block. Sheep Mountain to the north contains the northern ring zone of the Mount Aetna cauldron. High-angle, brittle, rift-related faults with associated zeolitic alteration and bimodal (rhyolite and lamprophyre) dikes are also present on Sheep Mountain. **0.8**

11.2 **Junction of CO-344 and CO-443.** Continue southwest on CO-344. **4.8**

16.0 **Junction of CO-344 and Grassy Gulch Road.** Park vehicles and walk north (approximately 1 mi) on Grassy Gulch Road. **1.2**

17.2 **STOP 5-2. Intrusive tuff dike at Grassy Gulch.** Brock and Barker (1965, 1972) provided preliminary descriptions of an intrusive welded-tuff dike in Grassy Gulch (Mount Harvard 15 min. topographic quadrangle) and suggested that it was a feeder to an extrusive ash-flow tuff. Further studies have shown that this dike consists of relatively nonwelded but well-indurated tuff which contains abundant crystals and pumice fragments (Fig. 19). This dike has been correlated with the Badger Creek extra- and intracaldera tuff, based upon spatial relations, mineralogy, chemistry, and age determinations, and is believed to be a cone-sheet dike that vented the Mount Aetna magma chamber outside the main ring zone (Shannon et al., 1988; Shannon, 1988). The dike is subparallel to, and approximately 5.5 km away from, the main ring zone. Ring shearing has not been observed in the adjacent Precambrian wall rocks. This dike is unusual in that it provides a rare, unequivocal example of an intrusive tuff vent. Return to vehicles and drive east on CO-344. **5.7**

22.9 **Junction of CO-344 and CO-443.** Turn north on CO-443. Park at valley edge. **0.4**

23.3 **STOP 5-3. Outer northern ring zone and intrusive breccia** exposed near Sheep Mountain. Hike approximately 1 mi up dirt road to Porphyry Gulch. At switchbacks, hike directly up hill to the east. Caution: the talus slope is steep and dangerous. We will examine the northern ring zone of the Mount Aetna cauldron. A large (up to 100 m thick) intrusive breccia body cuts early formed brittle–ductile ring shears and contains subrounded, transported clasts of the Mount Princeton pluton and Precambrian rocks. S–C fabrics in the Mount Princeton wall rock indicate downward movement of the cauldron block.

Ring-zone features dip predominantly steeply outward here. Intrusive breccias which were asymmetrically developed along the northern ring zone are interpreted to represent a major episode of venting of volcanic gases, and only rarely with a magma component. Return to vehicles and drive south on CO-443. **0.4**

23.7 **Junction of CO-344 and CO-443.** Turn east on CO-344 **2.8**

26.5 **STOP 5-4. Ring dike** exposed near Sheep Mountain. Park in bend in road, cross creek, hike up scree slope to base of cliffs. The inner portion of the northern ring zone is well exposed at this stop. Early brittle–ductile ring shears are cut by a ring dike (type 3) which is approximately 50 m thick and generally dips steeply outward. The dike has dark and narrow chilled margins. Chlorite microstylolites and devitrification textures are common in the dike margins. S–C fabrics indicate downward movement of the caldera block. Return to vehicles and drive to Buena Vista via CO-344 (north) and CO-306 (east). **8.4**

34.9 **Town of Buena Vista** (elev. 2425 m).

The Grizzly Peak caldera: Structure, stratigraphy, and resurgence in an eroded caldera

July 6–7, 1989

Leader: Christopher J. Fridrich

Summary

The 34 Ma, 17 × 23 km Grizzly Peak caldera lies on the crest of the Sawatch Range about 30 km north of the more deeply eroded Mount Aetna cauldron (Figs. 14, 22). Sufficient intracaldera tuff is preserved in portions of the Grizzly Peak caldera for resolution of intracaldera stratigraphy as well as the geometry of collapse and resurgence structures (Fridrich, 1987). In more strongly uplifted and less deeply collapsed areas, erosion has exposed resurgent intrusions and deep-seated structures of the ring-fracture zones (Figs. 23, 24).

Volcanic and shallow intrusive features of the Grizzly Peak caldera document evolution of the magmatic center from precaldera through post-resurgent stages. Precaldera intrusions, alteration zones, and lavas were emplaced along

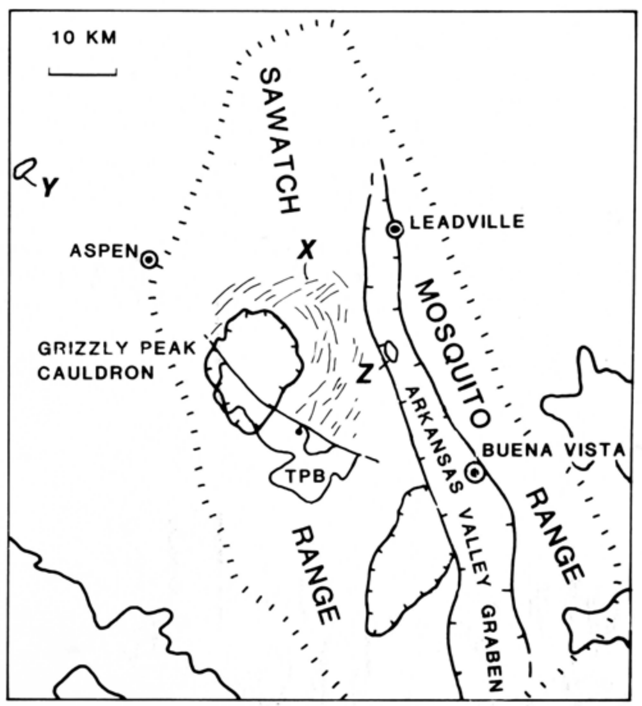

FIGURE 22—Location map of the Grizzly Peak caldera in the vicinity of the Sawatch Range. Y and Z are remnants of the outflow sheet of the Grizzly Peak Tuff. X is the precaldera dike swarm. North is to top of page.

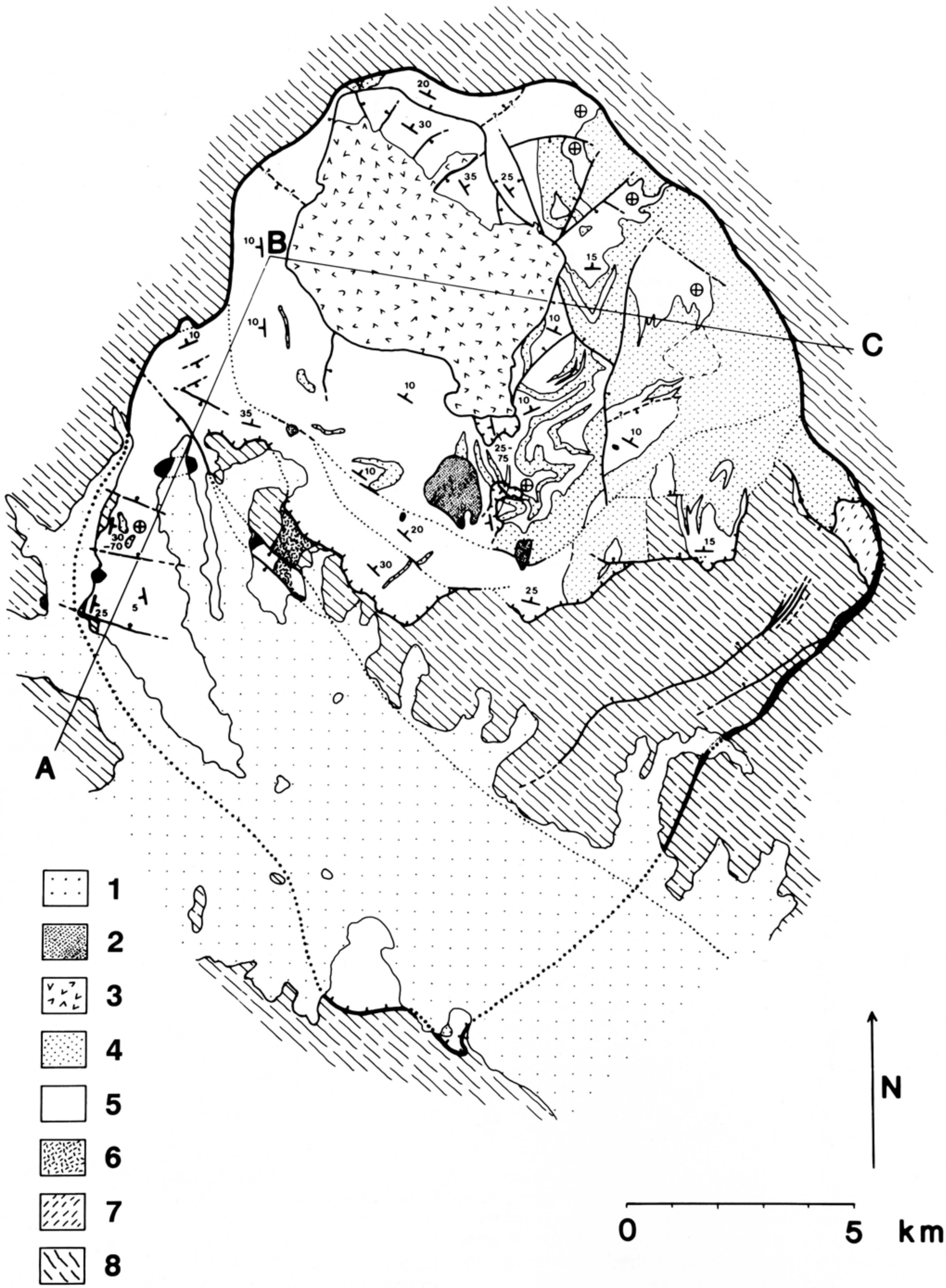

FIGURE 23—Geologic map of the Grizzly Peak caldera. Units, from oldest to youngest: 8, precaldera rocks (not divided); 7, precaldera alteration zone; 6, precaldera lavas; 5, Grizzly Peak Tuff, 4, caldera-collapse breccia; 3, resurgent intrusions; 2, late- and post-resurgent intrusions; 1, Quaternary rocks. ABC line marks cross section in Fig 24.

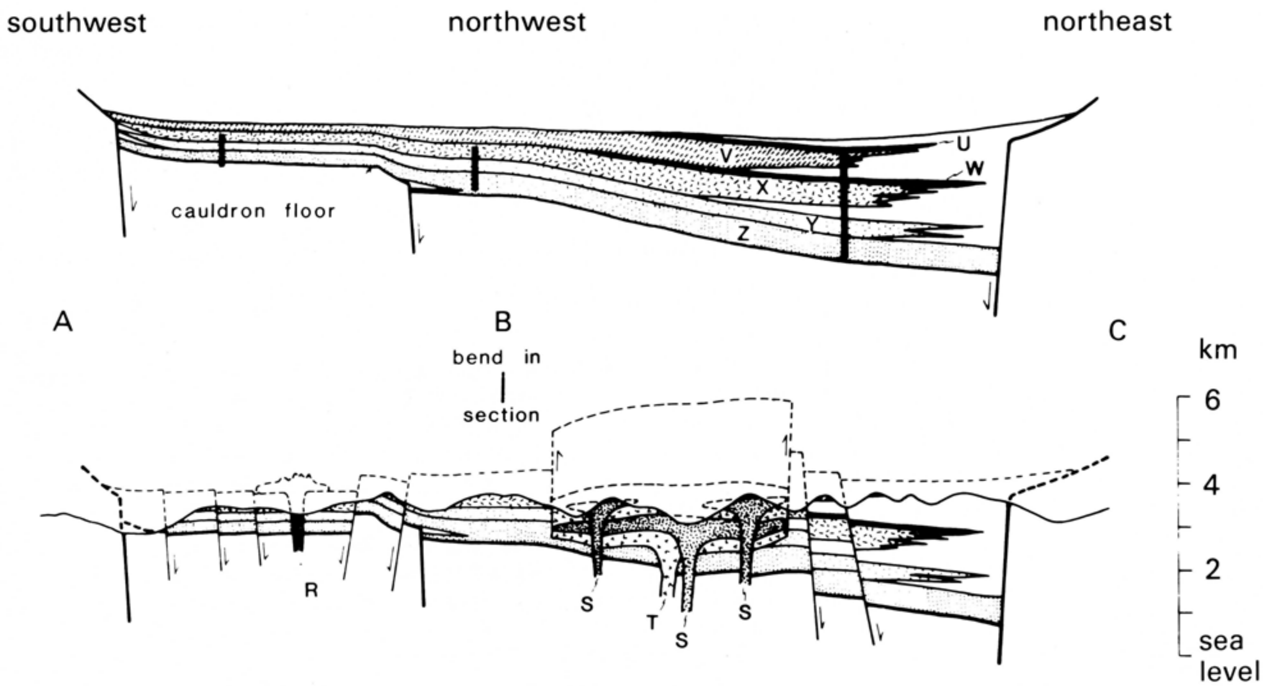

FIGURE 24—Cross section of the Grizzly Peak caldera (no vertical exaggeration). The top section is a reconstruction of the caldera immediately after collapse; the lower section below is the caldera today (after resurgence, extensional faulting, uplift, and erosion). R, late-resurgent intrusion; S and T, intrusions Two and One of early-resurgent intrusion (Fridrich, 1987); Z through U, six subunits of the Grizzly Peak Tuff (Fridrich, 1987).

a 20 km radius semicircular fracture swarm in and around the site of the future caldera (Fig. 22; Fridrich et al., 1988). Activity in this early dome field culminated in the caldera-forming eruption of the Grizzly Peak Tuff. Much of the tuff ponded in the >600 km^3 depression, filling the asymmetric caldera to a compacted thickness locally >2.7 km, including intercalated rock-avalanche breccias shed from ring-fault scarps. Following collapse, the caldera was uplifted to form a complexly faulted resurgent dome (Fig. 24). A belt of post-resurgent intrusions across the center of the caldera formed during the waning stages of the magmatic center.

Caldera subsidence at Grizzly Peak formed a fault-bounded depression having the shape of an asymmetric bowl. The bowl-like shape is due to faulting of the caldera floor downward in steps across wide ring-fracture zones and to slumping of ring-fault scarps. Asymmetry of collapse is manifested mainly by an inner ring-fracture zone dividing the caldera block into two major segments that collapsed to different depths (Figs. 23, 24).

Welding zonation of the intracaldera tuff is that of a single cooling unit. The only observed cooling breaks are envelopes of quenching around wedges of caldera-collapse breccia that were cold upon incorporation in the accumulating tuff. There are no sediments or lavas intercalated in the unit, no erosional breaks, no soil horizons, and no lithic fragments in the tuff or clasts in the breccias of any other tuff unit; there are none of the features that are indicators of multicyclic caldera activity. The Grizzly Peak Tuff is the product of a single eruption.

The intracaldera tuff is offset and shows thickening across the inner ring-fracture zone. The tuff is not brittly deformed in the collapse fault zones; it is welded across these faults and to their scarps. Field evidence that collapse faults were active while the intracaldera tuff was still hot is one of the criteria used to distinguish collapse structures from later-formed resurgence structures.

Caldera resurgence was accomplished partly by emplacement of a composite laccolith now exposed in the core of the resurgent dome in the northern caldera segment. Room for the resurgent intrusions was created largely by >1 km of uplift of their common roof along a vertical, piston-like fault that forms the walls of the composite laccolith where the fault is preserved. A portion of the roof of basal intracaldera tuff remains at the current level of erosion on the north side of the laccolith. Normal faults in surrounding intracaldera tuff are radial to the intrusion-cored piston block.

Each of the resurgent intrusions is concentrically zoned from leucocratic granodiorite margins to a mafic granodiorite/quartz monzodiorite core. This type of zoning is the reverse of the silicic-coreward zoning found in intrusions that fractionally crystallize during inward solidification. Reverse zoning in these intrusions evidently formed by rearrangement of a vertically graded magma column by the flow dynamics of magma emplacement and is therefore inferred to be analogous to the zoning found in ash-flow tuffs (Fridrich and Mahood, 1984).

Compositional zoning of the Grizzly Peak Tuff, defined by fiamme (collapsed pumice lumps), is a step function rather than a continuous gradient. Seven petrographic groups of fiamme each have distinct compositions separated by compositional gaps. As the same clusters are found in collections of fiamme from widely separated stratigraphic levels, step-function zoning must be intrinsic to the chamber rather than a consequence of the tapping process. Fridrich and Mahood (1987) interpreted the seven fiamme groups as seven separately convecting layers in a density-stratified reservoir tapped by eruption of the Grizzly Peak Tuff.

The Grizzly Peak Tuff is zoned from high-silica rhyolite at the base to low-silica rhyolite at the eroded top. Two horizons of heterogeneous tuff in the caldera fill contain fiamme of dacite to mafic latite along with the rhyolitic fiamme that make up the rest of the tuff. The total zonation, from 57 to 77% SiO_2, is one of the largest gradients documented in a single volcanic unit, excluding those that have large compositional gaps. Occurrence of the two heterogeneous tuff horizons under caldera-collapse megabreccias suggests that these horizons represent surging of magma from exceptionally deep levels of the chamber in association with two large caldera-collapse events (Fridrich and Mahood, 1987).

Major-element trends of the Grizzly Peak Tuff can be modeled by crystal fractionation using observed phenocrysts. The trends of several trace elements are strongly non-linear with differentiation, hence late-stage mixing can be eliminated as a significant factor in generation of the compositional gradient. Inflections in trace-element trends correlate with observed changes in phenocryst mineralogy and composition, indicating control by crystal–liquid equilibria. The abundance of some trace elements increases too strongly with differentiation to fit the major-element crystal-fractionation model, suggesting the zonation is the result of a combination of processes (Fridrich, 1987; Fridrich and Mahood, in prep.). Oxygen-, strontium-, neodymium-, and lead-isotopic compositions indicate that substantial crustal contamination occurred, but crustal melting is ruled out as a source for the tuff because the tuff extends to compositions that are too mafic (Johnson and Fridrich, 1987, and in prep.).

Compositional trends defined by the zoned resurgent intrusions can be modeled as mixing lines between the compositions of the fiamme groups found in the tuff. Fridrich (1987) inferred from this result that magma mixing had progressively diminished compositional zonation in the subcaldera chamber during resurgence.

"Quenched blob" inclusions of phenocryst-poor latite porphyry in the resurgent intrusions have a chemical signature that is distinct from those of latite fiamme in the Grizzly Peak Tuff. These latite inclusions probably represent a new infusion of mafic magma from the roots of the system into the high-level magma chamber during resurgence. Continued insurgence of the new latite, after solidification of the subcaldera magma chamber, formed the dominantly latitic post-resurgent intrusions, which commonly include boulder-size inclusions of a granite interpreted on chemical grounds and field evidence as the subcaldera granite.

In addition to the intrusions that are clearly resurgent in age and those that are clearly post-resurgent, there is another set of small stocks emplaced in the caldera intermediate in age between those two groups. These late-resurgent(?) intrusions are spatially associated with stockwork veining and alteration resembling that found in porphyry-type Cu–Mo ore deposits, but do not contain commercial mineralization.

Sixth day: Cross section through intracaldera fill and resurgent intrusions

Assembly point:	Buena Vista
Departure time:	8:00
Distance:	125 vehicle miles and approximately 5 hiking miles
Stops:	8

After driving north from Buena Vista through the Arkansas Valley graben, we will travel west to the northeastern margin of the Grizzly Peak caldera at Independence Pass to examine the stratigraphy of the intracaldera tuff as well as major resurgence faults. Our route continues farther west, then southeast to see internal contacts and compositional zoning in the resurgent intrusions in the north-central part of the caldera.

Mileage

0.0 **Town of Buena Vista** (elev. 2425 m). Travel north on US-24. **17.4**

17.4 **Town of Granite. 2.6**

20.0 **Junction of US-24 and CO-82.** Turn west (left) onto CO-82, the road to Aspen. **2.5**

22.5 **STOP 6-1. View of extracaldera intrusions** from Fisherman's parking for Twin Lakes Reservoir. The pyramidal peak on the massif to the northwest is Mount Elbert, the highest peak (4400 m) in Colorado. A composite rhyolite porphyry stock on the first spur south of Mount Elbert crops out as a large area of white rock. This intrusion is part of a large extracaldera swarm of dikes and stocks forming an arc extending from the northeast perimeter of the caldera clockwise to the southeast perimeter and probably beyond under glacial cover (Fig. 22). These dominantly rhyolitic intrusions predate the caldera by no more than 3 Ma, based on K–Ar dates and the presence of clasts of these porphyries in the caldera-collapse breccias. **22.9**

45.4 **Independence Pass** (elev. 3700 m). **Start hike.** From here we will hike 2.5 mi south (300 m elevation gain). Bring lunch, rock hammer, and clothes appropriate for rain and cold wind, regardless of how nice it may look now. Gloves or warm pockets and a warm hat are recommended. **0.2**

0.2 **STOP 6-2. View of core and margin of the Grizzly Peak caldera.** Looking southeast, the southeastern caldera margin can be seen starting at East Red Mountain which appears as a large red, yellow, and white scar ending abruptly at the caldera-margin fault along its eastern side.

From East Red Mountain, the caldera margin turns northeast across Star Mountain, forming the prominent V-shaped contact near its top. The caldera margin dips inward there at 75°, separating wall rocks of gray uniform Precambrian gneiss from brownish, strongly layered caldera-collapse breccias inside the "V." On the ridge west of Star Mountain is a prominent outcrop of tuff breccia that has a compositionally mixed appearance like a fruitcake. Both of these peaks are stops on tomorrow's tour.

From Star Mountain, the caldera margin proceeds northeast approximately at treeline, crossing the ridge we are on at the saddle ahead. **0.6**

0.8 **STOP 6-3. Caldera margin.** The margin here is a high-angle contact between welded ash-flow tuff and Precambrian St. Kevin granite (in place). **0.6**

1.4 Small fault separating mixed vitrophyric tuff and breccia to the north from uninterrupted caldera-collapse breccia to the south. **1.1**

2.5 **STOP 6-4. Overlook of resurgent intrusions and type section of the Grizzly Peak Tuff.** In the distance, note the Pennsylvanian red beds that dominate the Elk Mountains to the west of the Sawatch Range. Remnants of outflow Grizzly Peak Tuff have only been recognized on the northern flank of Mount Sopris, the northwesternmost gray peak in the Elk

Mountains, and east of the Sawatch Range in the Rio Grande rift, just south of the Twin Lakes Dam which we passed this morning.

The margin of the composite laccolith which comprises the resurgent intrusions of the Grizzly Peak caldera crops out as the vertical contact that bisects Grizzly Peak, straight ahead, into dark tuffs and intercalated breccias on the east side and light gray granodiorite porphyry on the west side (Fig. 25). From there the contact winds to the northeast to the base of the peak we are standing on, where it makes a right-angle turn to the northwest. The largely vertical contact that surrounds the resurgent intrusions is the piston fault (Figs. 23, 24, 26).

The valleys immediately to our left and right follow two of the resurgence faults that are radial to the intrusion-cored piston block. Other resurgence faults are visible in the valley below Grizzly Peak (Fig. 25).

The ridge to our right is largely a remnant of the roof of the resurgent intrusions. This tilted section of high-silica rhyolite tuff is the basal third of the type section of the Grizzly Peak Tuff, shown as the vertical bar on the right side of the upper section in Fig. 24. The middle third of the type section is the medium-silica rhyolite tuff forming the east side of Grizzly Peak. The upper third is the low-silica tuff exposed in the rust-colored peak immediately southeast of this overlook. This total section is 2.7 km thick. It is an incomplete section of a single cooling unit; the base is not exposed and the top is eroded. Return to vehicles. **2.5**

45.4 **Independence Pass.** Continue west on CO-82. **8.9**

54.3 **Junction of CO-82 and the Lincoln Creek Road.** Turn left onto the Lincoln Creek Road. **1.6**

55.9 **STOP 6-5. Precambrian wallrocks** at Middle Grottos of Lincoln Creek. Precambrian migmatites, unusually well exposed here, comprise a major portion of the wallrocks of the caldera. **2.8**

58.7 **STOP 6-6. Roadcut through high-silica rhyolite tuff** just inside the northwestern caldera margin. **2.0**

FIGURE 25—Overlook of Grizzly Peak from end of Independence Pass trail, showing layer-cake stratigraphy of caldera block. On the left, the cliff-forming unit is the Grizzly Peak Tuff, and the slope-forming unit is intracaldera breccia. The resurgent intrusions occupy the right side of the photo. The foreground consists of thick tuff, downfaulted relative to the background. The layering is composed of horizons of boulders (up to 3 m) that are strewn along flow-unit horizons. There are, however, no cooling breaks.

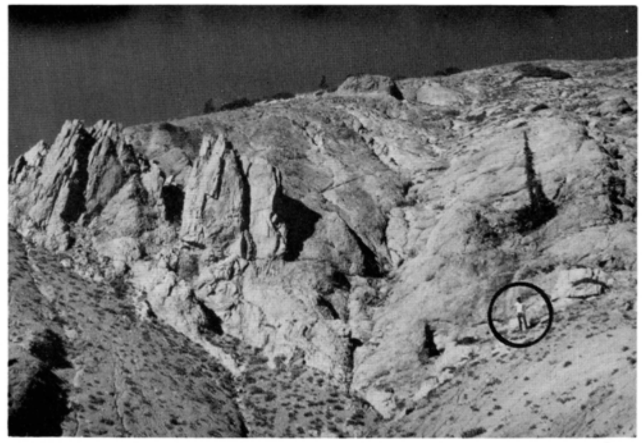

FIGURE 26—Vertical contact of the piston fault, marked by flaggy fault rocks that are running across the middle of the photo. This fault largely surrounds the composite resurgent intrusions. Intrusive rocks in foreground are quenched against this intrusive/fault contact with intracaldera welded tuff (background). The intrusions are compositionally zoned relative to the fault contact. Chris Fridrich circled for scale.

60.7 **Grizzy Reservoir dam.** Stretch your legs while the leader gets the keys to the gate. Drive across the dam and then left up the New York water-diversion canal service road. Turn around at the big bend in the road at Tabor Creek (1.8 mi) and backtrack 0.2 mi to the contact between tan-pink welded tuff and gray granodiorite porphyry. **2.0**

62.7 **STOP 6-7. Cut through the resurgent intrusions on NY Canal.** After examining the tuff-granodiorite contact, we will walk 0.4 mi each way across a lobe of one of the resurgent intrusions. Note the gradational internal changes in texture, mineralogy, and color index. The zoning is from 69 wt% SiO_2 at the margin to 58 wt% SiO_2 in the core. The core of the intrusion has a flow foliation and contains abundant inclusions; both are uncommon near the intrusion's margins. These, and other features we will see, provide important constraints on the origin of reverse concentric zoning in these intrusions.

Before leaving, collect a sample of the leucocratic granodiorite at the margin of the outermost resurgent intrusion, which is bluish or tan rather than the greenish gray of the later-emplaced interior intrusion. Return toward Lincoln Creek Road stopping on the south side of the Grizzly Reservoir dam. **1.4**

64.1 **STOP 6-8. Core rock of resurgent intrusions** at Grizzly Reservoir dam. Walk down the spillway to see the more mafic core rock of the outermost resurgent intrusion. Cross the dam. **0.2**

64.3 Return to Buena Vista by the same roads taken in. **60.7.**

125.0 **Buena Vista** (elev. 2425 m).

Seventh day: Margin of the Grizzly Peak caldera

Assembly point:	Buena Vista
Departure time:	8:00
Distance:	79 vehicle miles and 7 hiking miles (elevation gain of 550 m)
Stops:	5

Our route follows a ridge in the northeastern portion of the caldera margin to examine some of the best exposures of caldera-collapse breccia at Grizzly Peak.

Mileage

0.0 **Town of Buena Vista** (elev. 2425 m). Travel north on US-24. **20.0**

20.0 **Junction of US-24 and CO-82.** Turn west (left) onto CO-82. **14.2**

34.2 **South Fork Lake Creek Road.** Turn left. **2.0**

36.2 **Caldera'margin.** The contact is expressed here as a change from ruggedly polished, nearly continuous outcrop to scattered crumbly knobs separated by trees and grass. The caldera wall here is composed of the Twin Lakes Granodiorite, whereas the caldera fill is megabreccia with a matrix of crushed rock and tuff. **1.2**

37.4 **McNasser Gulch.** Turn right onto the road to Sherman mine in McNasser Gulch. **2.2**

39.6 **STOP 7-1. Caldera-collapse megabreccia** at the Sherman mine. This Au–Ag–Pb–Zn mine has never been a profitable venture, but has produced small volumes of ore with Au grades as high as 5 ounces per ton. The thin and highly discontinuous quartz–sulfide veins mined here are developed in fractures running through one of the major caldera-collapse megabreccias of the caldera. At depth, the fractures are filled with calcite and chlorite. It is only within the upper 50–100 ft below the capping layer of welded tuff that the vein mineralogy changes first to simple quartz–pyrite and then to quartz–multiple sulfides–native gold.

Note the shattered appearance of the megabreccia wallrocks around the veins being mined. Internal shattering in clasts in the megabreccias makes the clast size appear to be much smaller than it actually is. True clast size is shown by continuity of original structures such as dikes. Prebrecciation structures are offset and rotated to varying degrees across the seams of crushed and sheared rock formed by the shattering, resulting in a jigsaw-puzzle appearance.

Backtrack down the McNasser Gulch Road to intercept a faint hiking trail that climbs the ridge to the north. **0.4**

40.0 **Invisible trailhead for a nearly invisible trail. Start hike.** Park along the side of the road. From here, we will hike almost directly north to the saddle between Ouray Peak and the gendarme-covered ridge on the east flank of Grizzly Peak. Bring a lunch, rain gear, warm clothes, and hiking boots. **0.9**

0.9 **STOP 7-2. Resurgence fault** at saddle between McNasser and Graham Gulches. This saddle follows a major resurgence fault, the throw of which is greater than the local topographic relief. The rocks to the west are medium-silica rhyolite tuffs interlayered with extensive breccia sheets. The rocks to the east, on the other hand, are mostly wedges of breccias with masses of low-silica rhyolite tuff banked against them. Climb over to the east side of Ouray Peak, the double knob just to the east. **0.4**

1.3 **STOP 7-3. Megabreccia and quenched tuff** at Ouray Peak. The tuff that caps this peak shows well-developed welding zonation up from the breccia layer it was deposited on (Fig. 27). This cooling break is only a local one; where breccia wedges pinch out in the intracaldera tuff, the envelopes of quenched tuff around them pinch out as well.

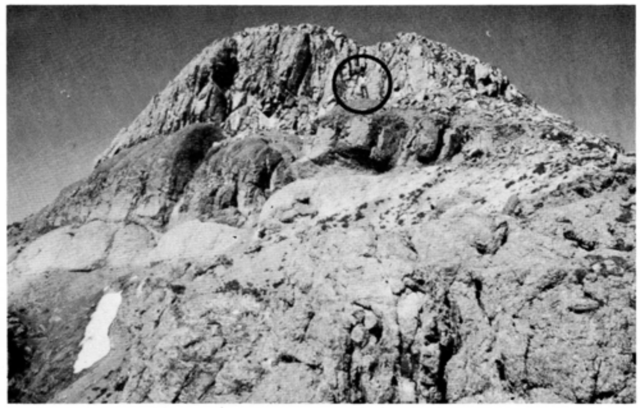

FIGURE 27—Welding zonation in the Grizzly Peak Tuff. Lower half of photo is caldera-collapse breccia that is primarily composed of three large clasts in this photo and represents the basal contact of the Grizzly Peak Tuff. Chris Fridrich (circled) is standing on vitrophyre (dark horizon). Light band below is partially welded tuff, and rock above is densely welded and devitrified tuff. Quench envelopes such as these are equally well developed where the breccias overlie the tuff; the envelopes pinch out where the breccias pinch out.

The first breccia under the tuff that caps the peak is a megabreccia with only minor tuff matrix. This matrix takes the form of seams of tuff that appear almost to be dikes because they show evidence of internal fluidized flow, namely size sorting developed inward from contacts (Bagnold effect). The tuff seams are not dikes; they are rootless. The tuff matrix in the breccias was fluidized at the time of deposition and is therefore intrusive; the tuff matrix continued moving upward after the remaining breccia came to rest.

About 12 m below, we pass into an underlying breccia. This breccia has abundant tuff matrix and the dominant clast is the pinkish-tan St. Kevin's granite from the north side of the caldera. The dark-colored breccia above is derived from the Denny Creek Granodiorite, which is from east of the caldera.

Hike east to the next major knob on this ridge. **0.7**

2.0 **STOP 7-4. Tuff breccia** at Fruitcake Hill. The tuff breccia making up this hill is the only one in the caldera that is nearly matrix-supported (Fig. 28). It also differs from other breccias in the caldera in having well-developed size sorting and rounding of the boulder-like clasts. In the rest of the caldera, rock types that are not found together in the caldera walls are not mixed together in the breccia. This breccia is the exception; rock types from all along the north and east caldera walls are intimately mixed here. Cruson (1973) interpreted this feature as a possible breccia pipe and pyroclastic vent. In support of his interpretation, this distinctive tuff breccia crops out in a nearly round area 1 km in diameter, with high-angle contacts on at least two sides. **1.5**

3.5 **STOP 7-5. Megabreccia lenses** at Star Mountain. The consistency in foliation attitudes across Star Mountain make it appear that the mountain is a mass

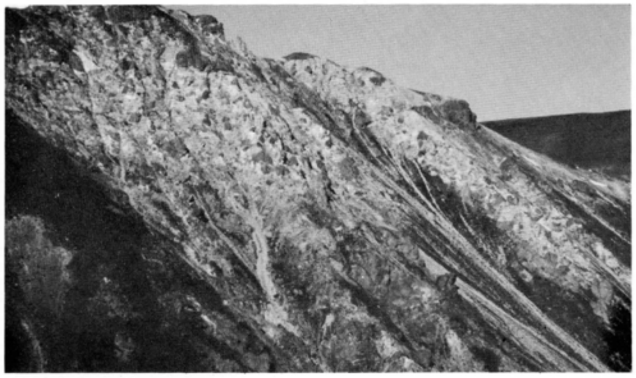

FIGURE 28—Matrix-supported tuff megabreccia exposed 1 km inward of the northeast caldera margin.

of Precambrian rock in place. As we now look at the cliff-like, northeastern face of Star Mountain, it is clear that this mountain is composed of megabreccia.

The breccia is a composite of numerous lenses laminated together along zones of concentrated shearing. Some lens-like contacts coincide with lithology changes. Each lens may have started out as a giant boulder that caved off the wall of the caldera in a collapse event. This breccia has no real matrix; it is just a mass of giant boulders that have been brittly deformed into interlocking lens shapes. The fact that this brittle deformation of the boulders did little to disrupt the attitudes of metamorphic foliations within the rock is an interesting clue to the physical nature of the breccia emplacement process.

Before we leave, inspect the caldera margin contact immediately to the northeast. Return to the vans by the path taken in. **3.5**

7.0 **Trailhead.** Return to Buena Vista by the roads taken in. **39.2**

79.2 **Buena Vista** (elev. 2425 m).

Supplemental log A: To the center of the Grizzly Peak caldera

Assembly point:	Buena Vista
Departure time:	8:00
Distance:	122 vehicle miles and 9 hiking miles with an elevation gain of 600 m
Stops:	1

Our route takes us to the center of the Grizzly Peak caldera to examine the compositional zoning of the Grizzly Peak Tuff defined by fiamme in the lower heterogeneous tuff horizon of the caldera fill, as well as post-resurgent intrusions and a feature interpreted as a possible fissure vent.

Mileage

0.0 **Town of Buena Vista** (elev. 2425 m). Travel north on US-24. **20.0**

20.0 **Junction of US-24 and CO-82.** Turn west (left) onto CO-82. **25.4**

45.4 **Independence Pass.** Continue west on CO-82. **8.9**

54.3 **Junction of CO-82 and the Lincoln Creek Road.** Turn left onto the Lincoln Creek Road. **6.8**

61.1 **Portal campground. Start hike.** Drive just beyond the campground and park. From here we will walk up the remainder of the Lincoln Creek Road, which is strictly a four-wheel-drive road from here on. Bring lunch, rock hammer, rain gear, and warm clothes. **3.9**

3.9 **Below Mount Garfield cirque.** At this point, we turn off the road and bushwack uphill into the lower part of the cirque on the south side of Mount Garfield. Four-wheel-drive vehicles park here. **0.6**

4.5 **STOP A-1. Lower heterogeneous tuff horizon** at Mount Garfield cirque. On both the north and south sides of the cirque, moderately dipping, black welded tuff is plastered on this side of the ridge against a contact which truncates the nearly flat-lying tuffs and breccias and an altered porphyry sill that make up the body of the ridge. This contact may be one side of a 3 km long fissure vent that cuts through the lower half of the caldera fill in the center of the caldera (Fridrich, 1987).

The black tuff is the lower heterogeneous tuff horizon. Compositions of individual fiamme in this subunit of the Grizzly Peak Tuff range from high-silica rhyolite to mafic latite. The entire range can be found in single large slabs of bulk tuff (Fig. 29).

FIGURE 29—Welded tuff of the lower heterogeneous tuff horizon subunit of the caldera fill. Collapsed and devitrified pumice lumps in this rock range in color from light to black, and from high-silica rhyolite to mafic latite (75–57 wt% SiO_2) in composition.

The altered sill above is one of the late-resurgent intrusions; alteration of the sill is similar to that which is characteristic of porphyry systems that do not contain commercial mineralization.

The dikes on the north side of this cirque are part of a large radial swarm of dikes around a post-resurgent stock in the valley below. The more mafic of the dikes commonly contain large engulfed granite boulders (Fig. 30). No outcrop has been found of this granite, which is chemically dissimilar to all other silicic rocks in the central Sawatch Range, except the Grizzly Peak rhyolite. Return to the vehicles. **4.5**

9.0 **Parking area.** Return to Buena Vista by the route taken in. **61.1**

122.0 **Buena Vista** (elev. 2425 m).

Supplemental log B: To the top of East Red Mountain

Assembly point:	Buena Vista
Departure time:	8:00
Distance:	80 vehicle miles (4WD vehicle required), or 74 vehicle miles and 6 hiking miles with 800 m elevation gain
Stops:	2

This trip goes to a prominent overlook on the eastern margin of the Grizzy Peak caldera to see a precaldera alteration zone, welded-tuff dikes that were vents for the caldera-forming eruption, and, looking into the caldera, four major faults along which the northeastern quadrant of the caldera collapsed a minimum of 4 km.

Mileage

0.0 **Town of Buena Vista** (elev. 2425 m). Travel north on US-24. **20.0**

20.0 **Junction of US-24 and CO-82.** Turn west (left) onto CO-82. **14.2**

34.2 **South Fork Lake Creek Road.** Turn left. **2.7**

36.9 **Signpost without a sign.** Turn left, proceed 15 m, then turn right on a road marked with a brown plastic stick labeled 382. To walk, stay left at the brown plastic stick and park immediately. Cross South Fork Lake Creek on the wooden footbridge 30 m ahead **0.2**

37.1 **Road crossing of South Fork Lake Creek.** Stop and check conditions before crossing. **0.1**

37.2 **Locked green gate.** Turn left and, after 6 m, go through green gate that is made to appear locked but is not. The drive to the top of East Red Mountain is about 2.8 mi from here, but the upper part of the road is dangerously washed out and is usually blocked by snowdrifts until later summer. **1.3**

38.5 **STOP B-1. Caldera floor.** Park and walk off the road on the right side to see the basal contact of the Grizzly Peak Tuff inside the caldera. We may have to walk from here even in the lightest snow year. **1.5**

40.0 **STOP B-2. Caldera faults and welded-tuff dikes.** Top of East Red Mountain. From here, we can see four major faults related to caldera subsidence which separate the northeastern quadrant of the caldera from rocks outside the caldera. In the field, we will discuss the constraints on their throws (Fig. 31).

On the east side of the mountain is a cornice of snow which, if sufficiently melted, will allow us to see a welded-tuff dike emplaced in the outer ring fracture of the Grizzly Peak caldera. There are four welded-tuff-dike segments emplaced along the ring-fracture zone in this area; they cover most of the compositional range of the intracaldera rhyolite tuffs. Only the most mafic of these dikes, the one with vitrophyric margins on both sides, is unsheared. The most silicic of the four dikes is most sheared.

The East Red alteration zone is developed around a swarm of northeast-trending quartz porphyry dikes. Sharp truncation of this zone by the caldera-margin ring fault clearly establishes the alteration as precaldera in age.

Return to Buena Vista by the roads taken in. **40.0**

80.0 **Buena Vista** (elev. 2425 m).

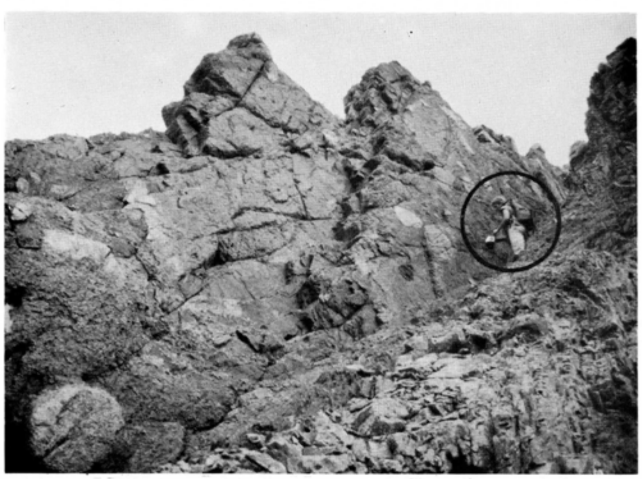

FIGURE 30—Professor Anita Grunder (circled) ponders the origin of granite boulders that are included in post-resurgent latite dikes. The granite that makes up these boulders does not crop out on the surface; the granite may represent solidified, non-erupted tuff from a postcaldera pluton.

Eighth day: Buena Vista to Denver, Colorado

Assembly point:	Buena Vista
Departure time:	8:00
Distance:	149 miles
Stops:	None

We will return to Denver in time for late afternoon and evening flights from Stapleton International Airport. After traveling north out of the northern end of the Rio Grande rift, we will intersect the northeastern end of the Tertiary Colorado Mineral Belt near the Climax molybdenum mine. After turning east on I-70, or trip will continue mainly through Precambrian rocks (1.0–1.8 Ga) of the Colorado Front Range.

Mileage

1 **Town of Buena Vista.** Travel north on US-24. **17**

17 **Town of Granite.** **3**

20 **Junction of US-24 and CO-82.** Continue north on US-24. **18**

38 **Town of Leadville.** **1**

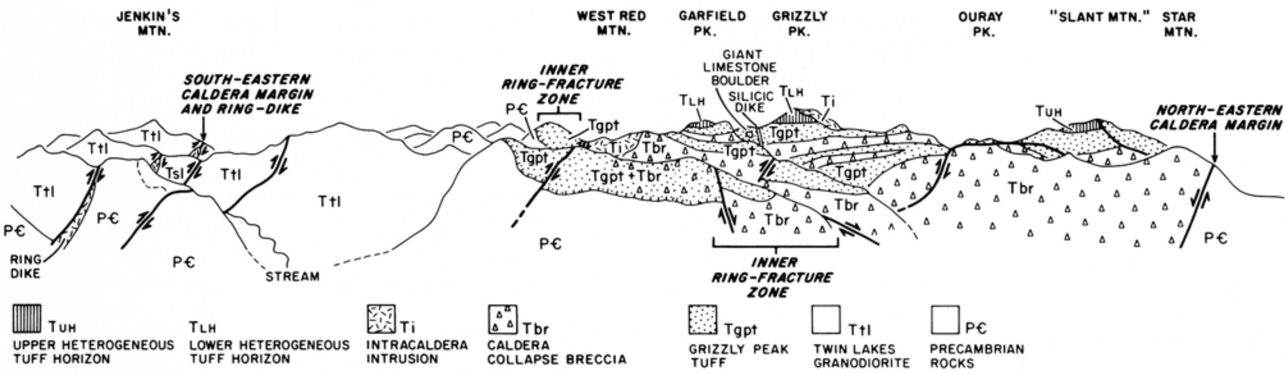

FIGURE 31—Sketch of panoramic view looking westward from East Red Mountain, illustrating geology through the Grizzly Peak caldera.

39 **Junction of US-24 and CO-91.** Turn right (east) on CO-91. **12**

51 **Climax molybdenum mine. 12**

63 **Junction of CO-91 and I-70.** Turn right (east) on I-70 toward Denver. **41**

104 **Junction of US-40 and I-70.** Continue on I-70 east. Stay on I-70 through Denver; follow signs to Stapleton International Airport. **45**

149 **Turnoff for Stapleton International Airport.** Mileage approximate. Turn south to airport.

References

Baldridge, W. S., 1979, Petrology and petrogenesis of Plio-Pleistocene basaltic rocks from the Central Rio Grande rift, New Mexico, and their relation to rift structure; *in* Riecker, R. E. (ed.), Rio Grande rift: Tectonics and magmatism: American Geophysical Union, Washington, D.C., pp. 323–353.

Brock, M. R., and Barker, F., 1965, Intrusive welded tuff in the Sawatch Range, Colorado: Geological Society of America, Special Paper 82: 320–321.

Brock, M. R., and Barker, F., 1972, Geologic map of the Mount Harvard quadrangle, Chaffee and Gunnison Counties, Colorado: U.S. Geological Survey, Map GQ-952.

Clough, C. T., Maufe, H. B., and Bailey, E. B., 1909, The cauldron-subsidence of Glen Coe, and the associated igneous phenomena: Geological Society London, Quarterly Journal, 65: 611–678.

Cordell, L., Long, C. L., and Jones, D. W., 1986, Geophysical expression of the batholith beneath Questa caldera, New Mexico: Journal of Geophysical Research, 90: 11263–11274.

Cruson, M. G., 1973, Geology and ore deposits of the Grizzly Peak cauldron complex, Sawatch Range, Colorado: Unpublished Ph.D. disseration, Colorado School of Mines, Golden, 180 pp.

Czamanske, G. K., and Dillet, B., 1988, Alkali amphibole, tetrasilicic mica, and sodic pyroxene in peralkaline siliceous rocks, Questa caldera, New Mexico: American Journal of Science, 228-A: 358–392.

Dillet, B., and Czamanske, G. K., 1987, Aspects of the petrology, mineralogy and geochemistry of the granitic rocks associated with Questa caldera, northern New Mexico: U.S. Geological Survey, Open-File Report, 87-258: 228 pp.

Dungan, M. A., Lindstrom, M. M., McMillan, N. J., Moorbath, S., Hoefs, J., and Haskin, L. A., 1986, Open system magmatic evolution of the Taos Plateau volcanic field, northern New Mexico, I, the petrology and geochemistry of the Servilleta Basalts: Journal of Geophysical Research, 91: 5999–6028.

Elston, W. E., 1984, Mid-Tertiary ash-flow tuff cauldrons, southwestern New Mexico: Journal of Geophysical Research, 89: 8733–8750.

Epis, R. C., and Chapin, C. E., 1974, Stratigraphic nomenclature of the Thirtynine Mile volcanic field, central Colorado: U.S. Geological Survey, Bulletin 1395-C: 23 pp.

Epis, R. C., and Chapin, C. E., 1975, Geomorphic and tectonic implications of the post-Laramide, late Eocene erosion surface in the southern Rocky Mountains; *in* Curtis, B. F. (ed.), Cenozoic history of the southern Rocky Mountains: Geological Society of America, Memoir 144: 45–74.

Escher, B. G., 1932, De ned.-indische caldeiras en bet caldeira-problem: Dertiende Kolonide vacantie-cursus voor Geografen, Amsterdam, pp. 8–11.

Fridrich, C. J., 1987, The Grizzly Peak caldera, Colorado: Structure and petrology of a deeply dissected resurgent ash-flow caldera: Unpublished Ph.D. dissertation, Stanford University, Stanford, California, 201 pp.

Fridrich, C. J., and Mahood, G. A., 1984, Reverse zoning in the resurgent intrusions of the Grizzly Peak cauldron, Sawatch Range, Colorado: Geological Society of America, Bulletin 95: 779–787.

Fridrich, C. J., and Mahood, G. A., 1987, Compositional layers in the zoned magma chamber of the Grizzly Peak Tuff: Geology, 15: 299–303.

Fridrich, C. J., Smith, R. P., and DeWitt, Ed, 1988, Structural evolution of the Grizzly Peak caldera, Colorado (abs): Geological Society of America, Abstracts with Programs, 20: A398.

Griggs, D. T., 1967, Hydrolytic weakening of quartz and other silicates: Royal Astronomical Society, Geophysical Journal, 14: 19–31.

Hagstrum, J. T., and Johnson, C. M., 1986, A paleomagnetic and stable isotope study of the pluton at Rio Hondo near Questa, New Mexico: Implications for C.R.M. related to hydrothermal alteration: Earth and Planetary Science Letters, 78: 296–314.

Hagstrum, J. T., and Lipman, P. W., 1986, Paleomagnetism of the structurally deformed Latir volcanic field, northern New Mexico: Relations to formations of the Questa caldera and development of the Rio Grande rift: Journal of Geophysical Research, 91: 7383–7402.

Hildebrand, R. S., 1984, Folded cauldrons of the Early Proterozoic Labine Group, northwestern Canadian Shield: Journal of Geophysical Research, 89: 8429–8441.

Hills, E. S., 1958, Cauldron subsidences, granitic rocks and crustal fracturing in S.E. Australia: Geologische Rundschau, 47: 543–561.

Johnson, C. M., and Fridrich, C. J., 1987, Sr, Nd, and Pb isotopic zonation in the mafic latite to high-silica rhyolite Grizzly Peak Tuff, Colorado (abs.): Geological Society of America, Abstracts with Programs, 19: 718.

Johnson, C. M., and Lipman, P. W., 1988, Origin of metaluminous and alkaline volcanic rocks of the Latir volcanic field, northern Rio Grande rift, New Mexico: Contributions to Mineralogy and Petrology, 100: 107–128.

Johnson, C. M., and Lipman, P. W., 1989, H, O, Sr, Nd, and Pb isotope geochemistry of the Latir volcanic field and cogenetic intrusions, New Mexico, and relations between evolution of a continental magmatic center and modifications of the crust: Contributions to Mineralogy and Petrology, in press.

Johnson, C. M., Czamanske, G. K., and Lipman, P. W., 1989, Geochemistry of intrusive rocks associated with the Latir volcanic field, New Mexico, and contrasts between evolution of plutonic and volcanic rocks: Contributions to Mineralogy and Petrology, in press.

Keller, G. R., Cordell, L., Davis, G. H., Peeples, W. J., and White, G., 1984, A geophysical study of the San Luis Basin; *in* Baldridge, W. S., Dickerson, P. W., Riecker, R. E., and Zidek, J. (eds.), Rio Grande rift: northern New Mexico: New Mexico Geological Society, Guidebook 35: 51–58.

Kingsley, L., 1931, Cauldron-subsidence of the Ossipee Mountains: American Journal of Science, 22: 139–168.

Leonardson, R. W., Dunlap, G., Starquist, V. L., Bratton, G. P., Meyer, J. W., Osborn, L. W., Atkin, S. A., Molling, P. A., Moore, R. F., and Olmore, S. D., 1983, Preliminary geology and molybdenum deposits at Questa, New Mexico; *in* The genesis of Rocky Mountain ore deposits: changes with time and tectonics: Denver Region Exploration Geologists Society, Proceedings, pp. 151–155.

Lipman, P. W., 1969, Alkalic and tholeiitic basaltic volcanism related to the Rio Grande depression, southern Colorado and northern New Mexico: Geological Society of America, Bulletin, 80: 1343–1353.

Lipman, P. W., 1983, The Miocene Questa caldera, northern New Mexico: Relation to batholith emplacement and associated molybdenum mineralization; *in* The genesis of Rocky Mountain ore deposits: Changes with time and tectonics: Denver Region Exploration Geologists Society, Proceedings, pp. 133–148.

Lipman, P. W., 1984, The roots of ash-flow calderas in western North America: Windows into the tops of granitic batholiths: Journal of Geophysical Research, 89: 8801–8841.

Lipman, P. W., and Mehnert, H. H., 1975, Late Cenozoic basaltic volcanism and development of the Rio Grande depression in the Southern Rocky Mountains; *in* Curtis, B. F. (ed.), Cenozoic history of the southern Rocky Mountains: Geological Society of America, Memoir 144: 119–154.

Lipman, P. W., and Mehnert, H. H., 1979, The Taos Plateau Volcanic field, northern Rio Grande rift, New Mexico; *in* Riecker, R. E. (ed.), Rio Grande rift: Tectonics and magmatism: American Geophysical Union, Washington, D.C., pp. 289–311.

Lipman, P. W., and Reed, J. C., Jr., 1984, Second-day road log from Taos to Hondo Canyon, Questa, Red River, Amalia, and back to Taos; *in* Baldridge, W. S., Dickerson, P. W., Riecker, R. E., and Zidek, J. (eds.), Rio Grande rift: northern New Mexico: New Mexico Geological Society, Guidebook 35: 321–347.

Lipman, P. W., and Reed, J. C., Jr., 1989, Geologic map of the Latir volcanic field and adjacent areas, northern New Mexico: U.S. Geological Survey, Miscellaneous Investigations Map I-1907.

Lipman, P. W., Mehnert, H. H., and Naeser, C. W., 1986, Evolution of the Latir volcanic field, northern New Mexico and its relation to the Rio Grande rift, as indicated by K–Ar and fission-track dating: Journal of Geophysical Research, 91: 6329–6346.

Ludington, S., 1981, Quartz–pyrite–molybdenite stockwork near South Fork Peak, Taos County, New Mexico: U.S. Geological Survey, Open-File Report, 81-180: 8 pp.

Manley, K., 1979, Stratigraphy and structure of the Española Basin, Rio Grande rift, New Mexico; *in* Riecker, R. E. (ed.), Rio Grande rift: Tectonics and magmatism: American Geophysical Union, Washington, D.C., pp. 71–86.

Manley, K., 1984, Brief summary of the Tertiary geologic history of the Rio Grande rift in northern New Mexico; *in* Baldridge, W. S., Dickerson, P. W., Riecker, R. E., and Zidek, J. (eds.), Rio Grande rift: northern New Mexico: New Mexico Geological Society, Guidebook 35: 63–66.

Meyer, J. W., 1988, Magmatic–tectonic interaction during early "Rio Grande rift" extension at Questa, New Mexico (abs.): Geological Society of America, Abstracts with Programs, 20: A232.

Oftedahl, C., 1953, The cauldrons 13, Studies on the igneous rock complex of the Oslo region: Norske Videnskaps-Akademi i Oslo, Matematisk-Naturvidenskapelig Klasse, Skrifter, 108 pp.

Oftedahl, C., 1978, Cauldrons of the Permian Oslo rift: Journal of Volcanology and Geothermal Research, 3: 343–371.

Pitcher, W. S., 1978, The anatomy of a batholith: Geological Society of London, Quarterly Journal, 135: 157–182.

Reed, J. C., Jr., Lipman, P. W., and Robertson, J. M., 1983, Geologic map of the Latir Peak and Wheeler Peak Wildernesses and Columbine–Hondo Wilderness Study Area, Taos County, New Mexico: U.S. Geological Survey, Miscellaneous Field Studies Map MF-120B.

Reynolds, D. L., 1956, Calderas and ring complexes: Nederlandsch Geologisch-Mijnbouwkundig Genootschap, Verhandelingen, Geologische Serie, 16: 355–379.

Shannon, J. R., 1988, Geology of the Mount Aetna cauldron complex, Sawatch Range, Colorado: Unpublished Ph.D. dissertation, Colorado School of Mines, Golden, Colorado, 434 pp.

Shannon, J. R., and Epis, R. C., 1987, Deeply eroded ring-zone structures of the Mount Aetna cauldron, Colorado: Hawaii Symposium on How Volcanoes Work, Hilo, Hawaii, p. 232.

Shannon, J. R., and Nelson, E. P., 1987, Stylolites in hydrothermally-altered igneous rocks (abs.): Geological Society of America, Abstracts with Programs, 19: 333.

Shannon, J. R., Naeser, C. W., DeWitt, Ed, and Wallace, A. R., 1987a, Timing of Cenozoic magmatism and tectonism in the Sawatch uplift and the northern Rio Grande rift, Colorado (abs.): Geological Society of America, Abstracts with Programs, 19: 839.

Shannon, J. R., Stein, H. J., and Smith, R. P., 1987b, Geology and geochemistry of Oligocene topaz rhyolites and A-type granites, northern Rio Grande rift, Colorado (abs.): Geological Society of America, Abstracts with Programs, 19: 840.

Shannon, J. R., Epis, R. C., Naeser, C. W., and Obradovich, J. D., 1988, Correlation of intracauldron and outflow and an intrusive tuff dike related to the Oligocene Mount Aetna cauldron, central Colorado, *in* Drexler, J. W., and Larson, E. E. (eds.), Cenozoic volcanism in the southern Rocky Mountains revisited, Colorado School of Mines Quarterly, 82(4): 65–80.

Simpson, C., and Schmid, S. M., 1983, An evaluation of criteria to deduce the sense of movement in sheared rocks: Geological Society of America, Bulletin, 94: 1281–1288.

Smith, R. L., and Bailey, R. A., 1968, Resurgent cauldrons; *in* Coats, R. R., Hay, R. L., Anderson, C. A. (eds.), Studies in volcanology: Geological Society of America, Memoir 116: 613–662.

Steven, T. A., and Lipman, P. W., 1976, Calderas of the San Juan volcanic field, southwestern Colorado: U.S. Geological Survey, Professional Paper 958: 35 pp.

Thompson, R. A., Dungan, M. A., Lipman, P. W., 1986, Multiple differentiation processes in early-rift calc-alkaline volcanics, northern Rio Grande rift, New Mexico: Journal of Geophysical Research, 91: 6046–6058.

Turner, D. C., and Bowden, P., 1979, The Ningi–Burra complex Nigeria: dissected calderas and migrating magmatic centres: Geological Society of London, Quarterly Journal, 136: 105–119.

Tweto, O., 1979a, The Rio Grande rift system in Colorado; *in* Riecker, R. E. (ed.), Rio Grande rift: Tectonics and magmatism: American Geophysical Union, Washington, D.C., pp. 33–56.

Tweto, O., 1979b, Geologic map of Colorado: U.S. Geological Survey, scale 1:500,000.

Varga, R. J., and Smith, B. M., 1984, Evolution of the early Oligocene Bonanza caldera, northeast San Juan volcanic field, Colorado: Journal of Geophysical Research, 89: 8679–8694.

Williams, H., 1941, Calderas and their origin: University of California, Publications in Geological Sciences, 25(6): 239–346.

Williams, H., and McBirney, A. R., 1968, An investigation of volcanic depressions: Part 1. Geologic and geophysical features of calderas: University of Oregon, Center for Volcanology, 87 pp.

Wunderman, R. L., and Rose, W. I., 1984, Amatitlan, an actively resurging cauldron 10 km south of Guatemala City: Journal of Geophysical Research, 89: 8525–8539.

Yoshida, T., 1984, Tertiary Ishizuchi cauldron, southwestern Japan arc: Formation by ring fracture subsidence: Journal of Geophysical Research, 89: 8502–8510.

Yund, R. A., and Tullis, J., 1980, The effect of water, pressure and strain on Al/Si order–disorder kinetics in feldspar: Contributions to Mineralogy and Petrology, 72: 297–302.

EXCURSION 16B: Oligocene–Miocene San Juan volcanic field, Colorado

Compiled by P. W. Lipman

U.S. Geological Survey, Denver, Colorado 80225

Introduction

The San Juan Mountains are the largest erosional remnant of a composite volcanic field that covered much of the southern Rocky Mountains in middle Tertiary time (Fig. I-1). The field consists mainly of intermediate-composition lavas and breccias, erupted about 35–30 Ma from scattered central volcanoes (Conejos and San Juan Formations), overlain by about 15 widespread voluminous ash-flow sheets erupted 30–26 Ma from caldera sources (Table I-1). At about 26 Ma, volcanism shifted to a bimodal assemblage dominated by trachybasalt and silicic rhyolite, concurrent with the inception of regional extension during establishment of the Rio Grande rift zone.

Volcanic rocks of the San Juan field now occupy an area

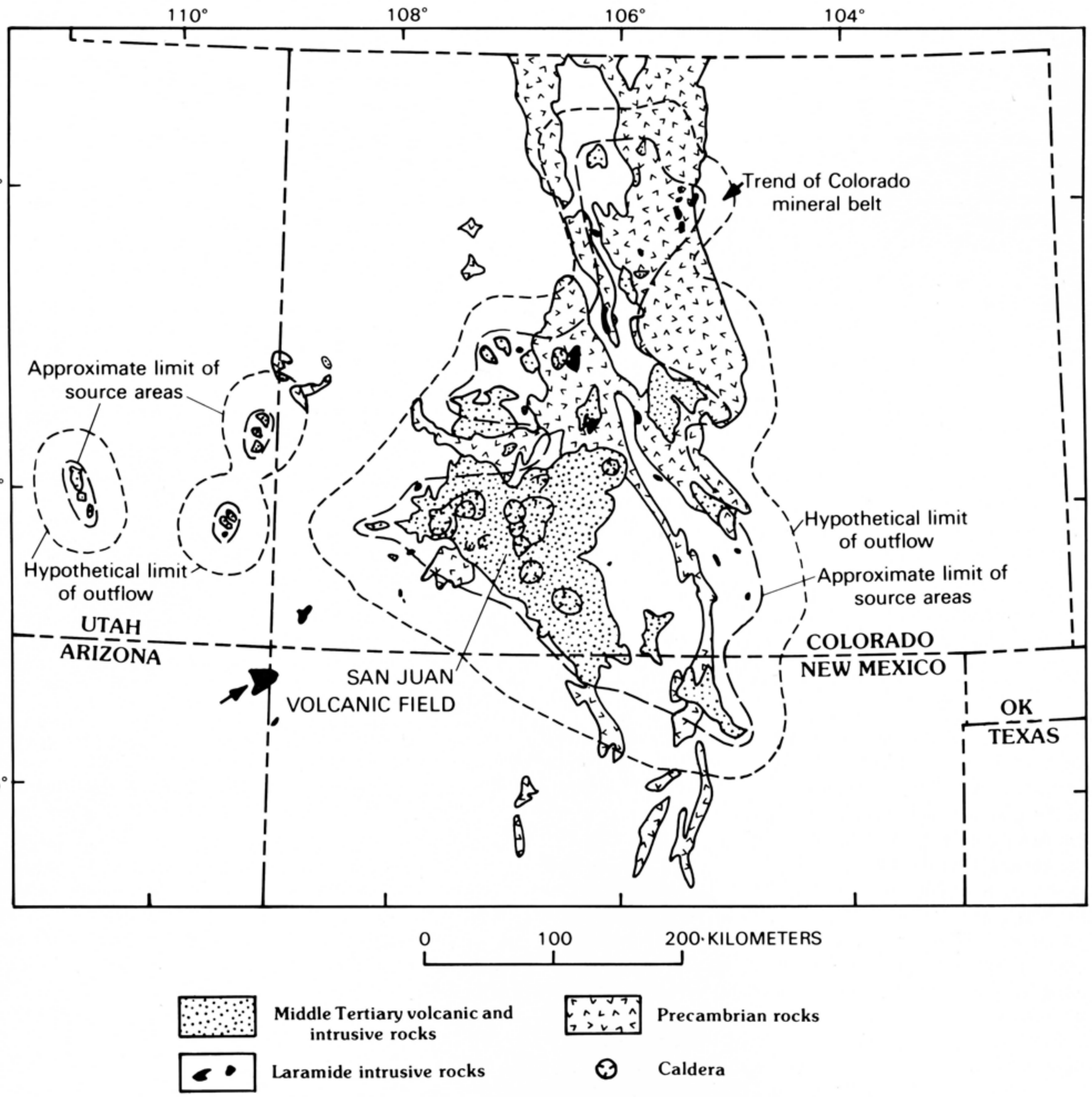

FIGURE I-1—Map of the Southern Rocky Mountains, showing location of San Juan volcanic field in relation to other Tertiary igneous centers (modified from Steven, 1975).

TABLE I-1—Ash-flow units of the San Juan volcanic field. Abbreviations: plag, plagioclase; san, sanidine; qtz, quartz; bio, biotite; aug, augite; hbl, hornblende.

Tuff unit (intracaldera)	Caldera; (age, Ma)	Dominant composition	Petrologic character	Estimated vol., km^3
		Southeastern caldera complex		
TREASURE MOUNTAIN TUFF:				
Ra Jadero Member	Summitville (28.4?)	Silicic dacite	20–25% plag>bio + aug>san	100–150
Ojito Creek Member	Summitville (29)	Silicic dacite	20–25 plag>bio + aug	40–70
Middle member				
Upper units	Summitville?	Silicic dacite	5–20% plag>bio + aug	20–50
La Manga units	Platoro? (29.2)	Silicic dacite	5–20% plag>bio + aug	20–50
La Jara Canyon Member	Platoro (29.3)	Silicic dacite	20–35% plag>bio + aug>>san	500–1000
Lower member				
Black Mtn. unit	Platoro? (29.5)	Silicic dacite	20% plag>bio + aug	>50
Rhyolite units	Platoro?	Low-Si rhyolite	5–10% plag>bio>aug	20–50
Tuff of Rock Creek	Platoro? (32)	Trachyandesite	2–5% plag>aug	10–30
		Central caldera cluster		
Tuff of Cochetopa Cr.	San Luis (26.1)	Zoned rhyolite–silicic dacite	20–35% pheno, plag>bio + aug in	50–100
Nelson Mountain Tuff	San Luis (26.1)	Zoned rhyolite–dacite	upper parts; 5–10% san + plag	100–500
Tuff of Cebolla Creek	San Luis	Zoned rhyolite–silicic dacite	>bio in lower part; Cebolla Cr	50–100
Rat Creek Tuff	San Luis (26.3)	Zoned rhyolite–silicic dacite	hbl-rich	<50
Snowshoe Mountain T	Creede (26.65)	Zoned silicic dacite–andesite	40–50% pheno: plag>bio + aug	>500
Wason Park Tuff	South River (27.15)	Zoned rhyolite–silicic dacite	20–40% plag + san>bio + aug	>500
Carpenter Ridge Tuff	Bachelor (27.35)	Zoned rhyolite–dacite		>1000
(Mammoth Mtn. m;		Upper dacite	30–50% plag>bio + aug	
Bachelor Mtn. M)		Main rhyolite	5% san + plag>bio	
Fish Canyon Tuff	La Garita (27.75)	Dacite	40–50% plag>san + bio + qtz + hbl	>3000
Masonic Park Tuff	Mount Hope (28.4)	Zoned rhyolite–dacite		500–1000
Upper dacite			30–40% pheno: plag>bio + aug	
Lower rhyolite			15–20% pheno: plag>san + bio	
		Western caldera cluster		
Sunshine Peak Tuff	Lake City (23.1)	Zoned silic rhyolite-qtz trachyte		100–500
Upper qtz trachyte			25–35% plag + san>bio + aug	
Main rhyolite			15–20% san + qtz>bio	
Crystal Lake Tuff	Silverton (27.8–28.4)	Low-Si rhyolite	10–15% san + plag>bio	50–100
Sapinero Mesa Tuff	Uncompahgre/	Low-Si rhyolite	5% san + plag>bio(+ aug)	>1000
(Eureka Member)	San Juan (27.8–28.4)	Low-Si rhyolite		
Dillon Mesa Tuff	Uncompahgre?	Low-Si rhyolite	2–5% san + plag>bio	25–100
Blue Mesa Tuff	Lost Lake	Low-Si rhyolite	2–5% san + plag>bio	100–500
Ute Ridge Tuff	Ute Creek (28.4)	Silicic dacite	30–40% plag>san + bio + aug	>500

of more than 25,000 km^2 and have a volume of about 40,000 km^3. They cover a varied basement of Precambrian to early Tertiary rocks, along the uplifted and eroded western margin of the Late Cretaceous–early Tertiary (Laramide) uplifts of the Southern Rocky Mountains and adjoining portions of the eastern Colorado Plateau (Fig. I-1). The San Juan field is one of many loci of Tertiary volcanic activity—including the Sierra Madre Occidental, Trans-Pecos, Mogollon–Datil, Absaroka, Challis, and Lowland Creek fields—that developed along the eastern Cordilleran margin of the North American plate in response to subduction along its western margin.

San Juan igneous rocks and associated ore deposits have been a focus of research throughout the past century. Early studies (1890–1925) by Whitman Cross, Esper Larsen, and associates included mapping and petrologic study of the entire volcanic field and recognition of the broad stratigraphic relations among volcanic units (Emmons and Larsen, 1923; Cross and Larsen, 1935; Larsen and Cross, 1956; Luedke and Burbank, 1963) Building on this framework, Wilbur Burbank and associates (1930–60) studied relations between volcanic structures and vein mineralization, especially in the western San Juan area, and recognized the caldera-subsidence origin of the circular volcanic structures at Silverton and Lake City—the first such features identified in North America (Burbank, 1933, 1940). Thomas Steven and James Ratté investigated relations between volcanism and vein mineralization in the Creede area (1952–65), leading to recognition of the importance of welded ash-flow tuffs in the volcanic field and identification of most of the calderas within the central cluster (Steven and Ratté, 1965; Ratté and Steven, 1967). Steven and P. W. Lipman then restudied the entire volcanic field (1965–74); they recognized additional ash-flow sheets and their caldera sources, established an isotopic geochronology and new petrologic concepts of magmatic evolution based in part on isotopic data, and proposed the relationships between the volcanism and regional plate-tectonic setting (Steven and Lipman, 1976; Lipman et al., 1970, 1978). Concurrent detailed studies of the epithermal vein deposits at Creede by Paul Barton, Philip Bethke, and associates (1960 to the present) have made this mining district perhaps the most thoroughly studied epithermal vein system in the world (Bethke et al., 1976; Barton et al., 1977). Such work has led to selection of the Creede district for a program of research scientific drilling into mineralized systems as part of the U.S. Continental Scientific Drilling Program (Bethke and Lipman, 1987). In the past decade, the volcanic rocks and associated ore deposits of the San Juan field have inspired diverse volcanologic, petrologic, and geophysical studies by government, academic, and industry scientists; many of these are noted in discussion of the field-trip stops.

The field trip will focus on many aspects of the volcanic processes, magmatic history, regional tectonics, and mineralization in the San Juan Mountains. This volcanic field has served as a crucible for the early development of concepts of caldera-related volcanism. We will emphasize the impact of new data on the evolution of these concepts. The trip will progress from east to west, and into broadly younger igneous rocks (Fig. I-1). It will focus during days 1 and 2 on the southeastern caldera complex (28–29 Ma), where the relations of ash-flow volcanism to intermediate-composition lavas are especially clear. We then move to the six large clustered calderas and more silicic ash-flow deposits (28.4–26.1 Ma) in the central San Juan area during days 4 and 5. Days 5 and 6 will be used to examine the more recent Lake City caldera (23 Ma) of the western caldera complex where stratigraphy and structure of caldera-fill deposits are exceptionally well exposed.

Volcanic-rock names are used in general accord with the IUGS classification system (Le Bas et al., 1986), except that the term quartz latite (silicic dacite) is in places retained in continuity with historic regional usage. Most of the volcanic rocks constitute a high-K assemblage that is transitional between subalkaline and alkaline suites, similar to those at other Tertiary volcanic fields in the Southern Rocky Mountains (see Fig. 1-4). For simplicity and continuity with previous usage, such modifiers as "high-K" or "trachy" are omitted from most rock names. Names, divided on the basis of percent SiO_2, are: <52, basalt; 52–57, basaltic andesite; 57–62, andesite; 62–66, dacite; 66–70, silicic dacite (quartz latite); 70–75, rhyolite; >75, silicic rhyolite (all compositions recalculated to 100%, volatile-free).

Revised values for pre-1977 radiometric ages for San Juan rocks are taken from the compilation by Hon and Mehnert (1983), which utilizes the presently accepted IUGS constants. More recent dates are mainly from Lanphere (1988 and unpublished) for the central cluster, and from D. Lux (unpubl. data) for the southeastern caldera complex.

This field guide constitutes a revision and update of earlier versions prepared and distributed informally for a GSA Penrose Conference on "Silicic Volcanism" in 1980 and a SEG workshop on the "Relationship of Mineralization to Volcanic Evolution" in 1982. In addition to work by the authors of this guide, it incorporates important data on San Juan geology provided by P. M. Bethke, D. Bove, L. Brown, T. Casadevall, T. Grauch, M. Lanphere, D. Lux, R. Reynolds, J. Rosenbaum, J. C. Ratté, T. A. Steven, R. Stoffregen, J. C. Stormer, Jr., D. Williams, J. Whitney, and others.

Southeastern (Platoro) caldera complex

M. A. Dungan[1], P. W. Lipman[2], M. Colucci[1], K. Ferguson[1], and S. Balsley[1]

[1]*Department of Geology, Southern Methodist University, Dallas, Texas 75275;* [2]*U.S. Geological Survey, Federal Center, Denver, Colorado 80225*

Summary

The southeastern caldera complex (Figs. 1-1, 1-2) is a nested collapse structure about 20 km in diameter. The caldera complex is centered within a cluster of broadly precursory basaltic andesite to dacite volcanoes (Conejos Formation). The present topographic highs along the exhumed caldera rim are precaldera edifices truncated during caldera collapse. Petrologically diverse precaldera volcanism between ca. 34 and 29.2 Ma records a complex episodic magmatic evolution. Three members of the Conejos Formation correspond to three mineralogically and petrologically distinct magmatic series (Figs. 1-3 to 1-5). Pyroclastic units erupted from southeast San Juan calderas comprise five members of the Treasure Mountain Tuff (Table I-1). These include three regional ash-flow sheets (La Jara Canyon, Ojito Creek, and Ra Jadero Members, from oldest to youngest), which are approximately coextensive over 5000 km^2, and two members (lower and middle), each containing multiple tuff sheets that are compositionally diverse and largely more local in distribution.

The Treasure Mountain Tuff and postcollapse lavas were erupted during two cycles of caldera activity, an early Platoro cycle and a later Summitville cycle (Fig. 1-3). In comparison to the prolonged history of precaldera volcanism, the caldera cycles were relatively short in duration. Activity of the Platoro cycle appears to have occurred between 29.5 Ma and 29.2 Ma. The Summitville cycle began shortly thereafter (ca 29.2 Ma) and may have extended only to 28.8–28.7 Ma, but some uncertainty in the age of late Summitville eruptions remains. The last major tuff eruption from the southeastern complex may have occurred as late as about 28.4 Ma, just prior to emplacement of the overlying Masonic Park Tuff (Lanphere, 1988). Ash-flow eruptions were succeeded by construction of postcollapse intracaldera and ex-

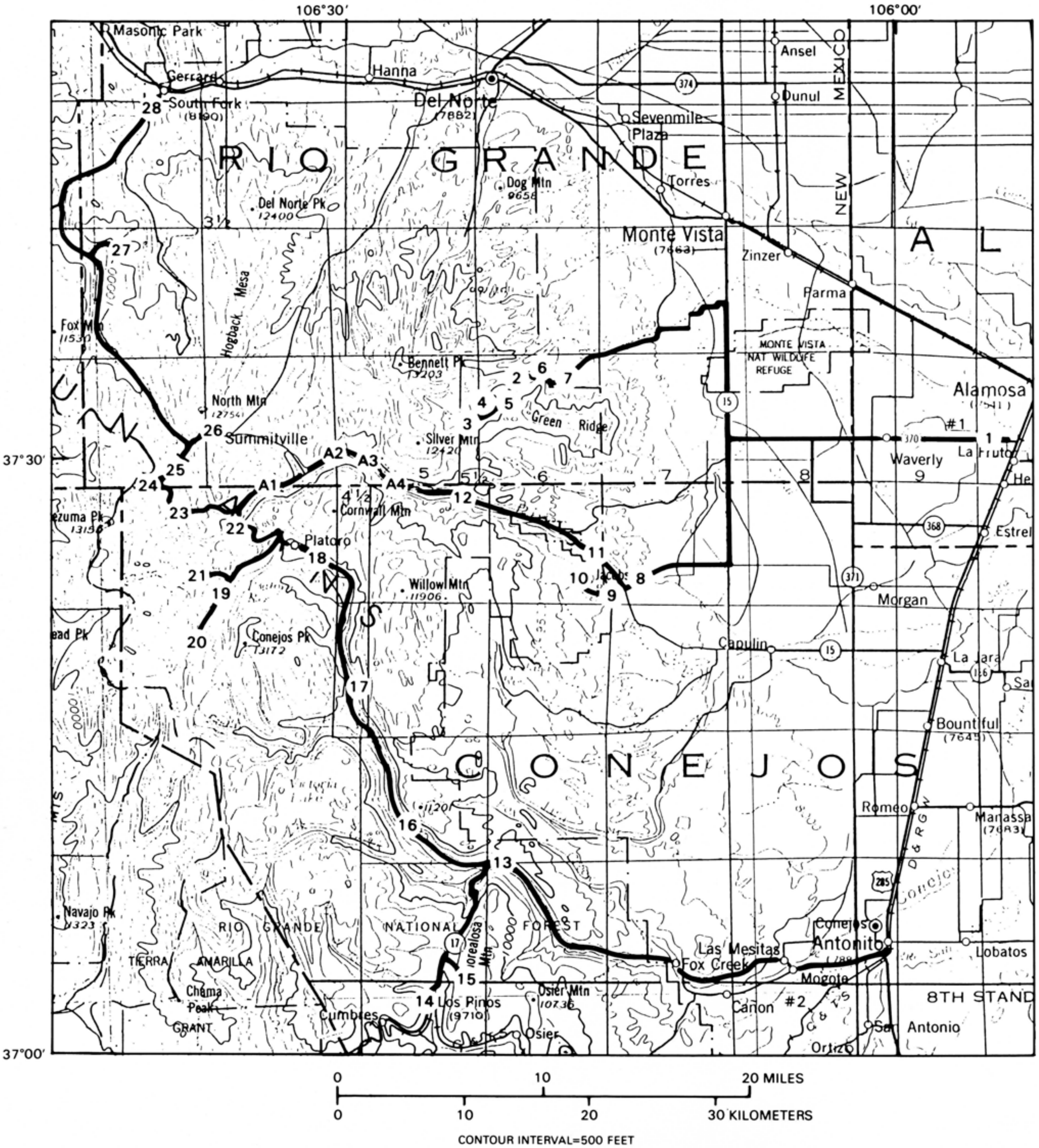

FIGURE 1-1—Route map, southeastern San Juan Mountains.

tracaldera andesite to dacite volcanoes considered to be integral to the two cycles of caldera volcanism. The youngest phases of this activity overlap with, and partly postdate, eruption of the Masonic Park and Fish Canyon (27.8 Ma) Tuffs.

The lower member of the Treasure Mountain Tuff, the La Jara Canyon Member, and early units of the middle member were erupted during the Platoro cycle. Major collapse of the Platoro caldera occurred during the eruption of the La Jara Canyon Member (500–1000 km^3). Accumulation of La Jara Canyon tuff within the subsiding Platoro caldera (>800 m thick, base not exposed) was followed by the eruption of additional tuffs (middle member), a large lava dome (dacite of Fisher Gulch) from the La Jara Canyon magma chamber, and by voluminous caldera-filling lavas of the Summitville Andesite (lower member). The intracaldera sequence was resurgently uplifted as an asymmetric trap-door block concurrent with the eruption of the lower Summitville. Prior to collapse of the Platoro caldera, two distinctive units of the lower member were erupted at about 29.5 Ma. The lower unit is rhyolitic, shows close affinities to the subsequent La Jara Canyon tuff, and may have been a precursory eruption from the La Jara Canyon magma

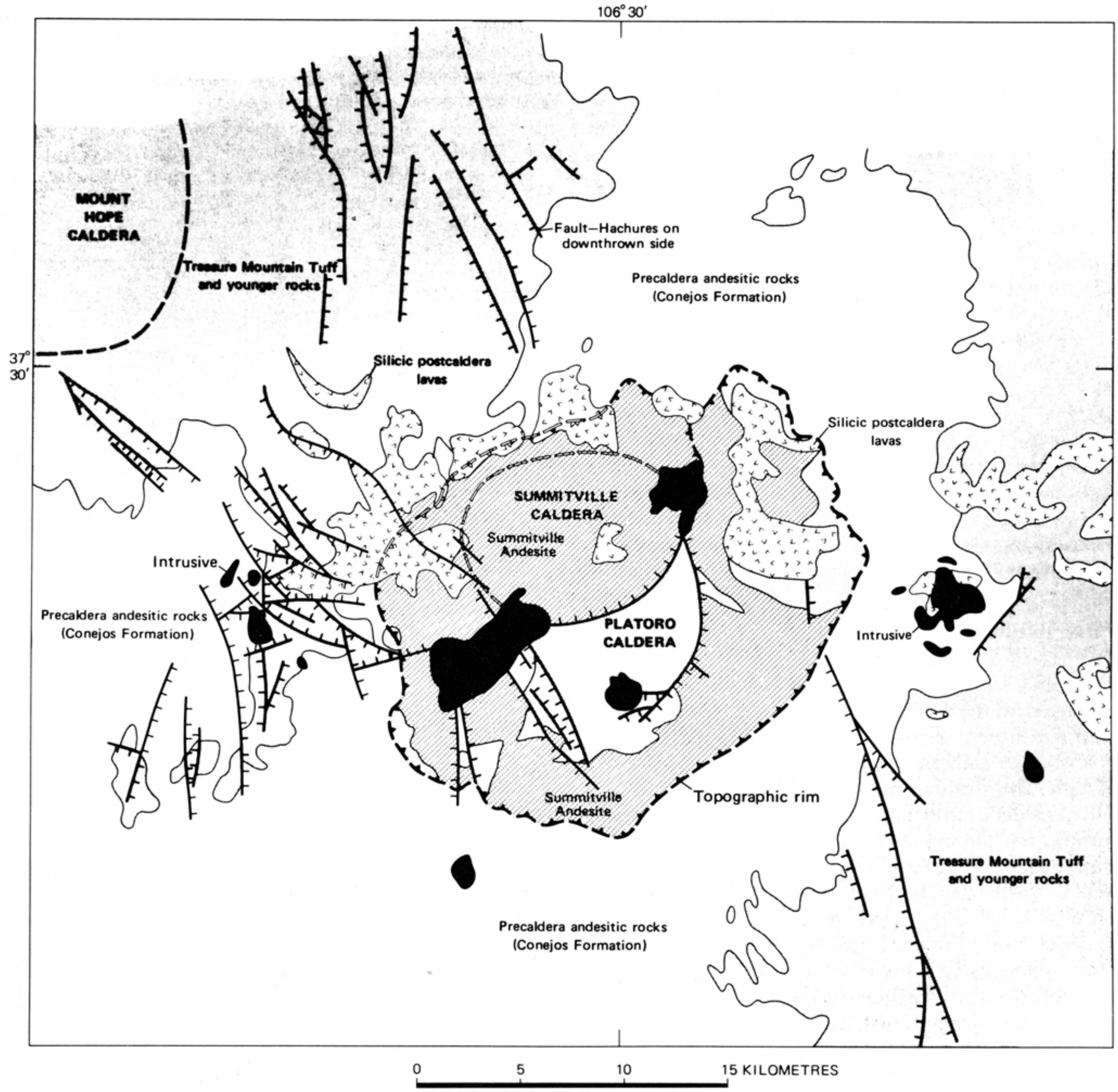

FIGURE 1-2—Generalized geology of the southeastern caldera complex (modified after Steven and Lipman, 1976).

chamber. The overlying Black Mountain unit is a regional sheet coextensive with the La Jara Canyon tuff. It probably had a volume large enough (>50 m^3) to have caused associated caldera subsidence for which the geologic record is obscure. The genesis of the Black Mountain magma is also poorly understood, but its chemical and isotopic affinities are closer to the later Summitville cycle tuffs than to La Jara Canyon magma.

The Summitville cycle began with eruption of at least 12 relatively small tuffs of the upper middle member (total volume <50 km^3) that are compositionally diverse and variably welded. These record the concurrent evolution of two discrete source magma chambers which subsequently gave rise to eruption of the Ojito Creek (40–70 km^3) and Ra Jadero Members (100–150 km^3) from the Summitville caldera. Prolonged and separate histories for these magma bodies are documented by alternations of the two contrasting magma types among the units of the upper middle member. No resurgence has been recognized in this later caldera, but it was filled to overflowing by a thick accumulation of lavas (upper member, Summitville Andesite and dacite of Park Creek). Postcollapse magmatism, thought to be broadly contemporaneous with the Park Creek lavas, produced the large Cat Creek volcano (volcanics of Green Ridge and Cat Creek stock) northeast of the Platoro caldera, and Summit Peak andesite lavas were erupted along the western margin of the caldera complex. Following the final eruptions of the Summitville cycle, increasingly silicic porphyritic dacite to rhyolite lavas, dikes, and stocks were emplaced around the margins of the Summitville caldera. Hydrothermal alteration and local ore deposition were recurrent during the interval 28–23 Ma in the Summitville and Platoro mining districts, and in other mineralized areas at Stunner, Gilmore, Jasper, Crater Creek, and Cat Creek.

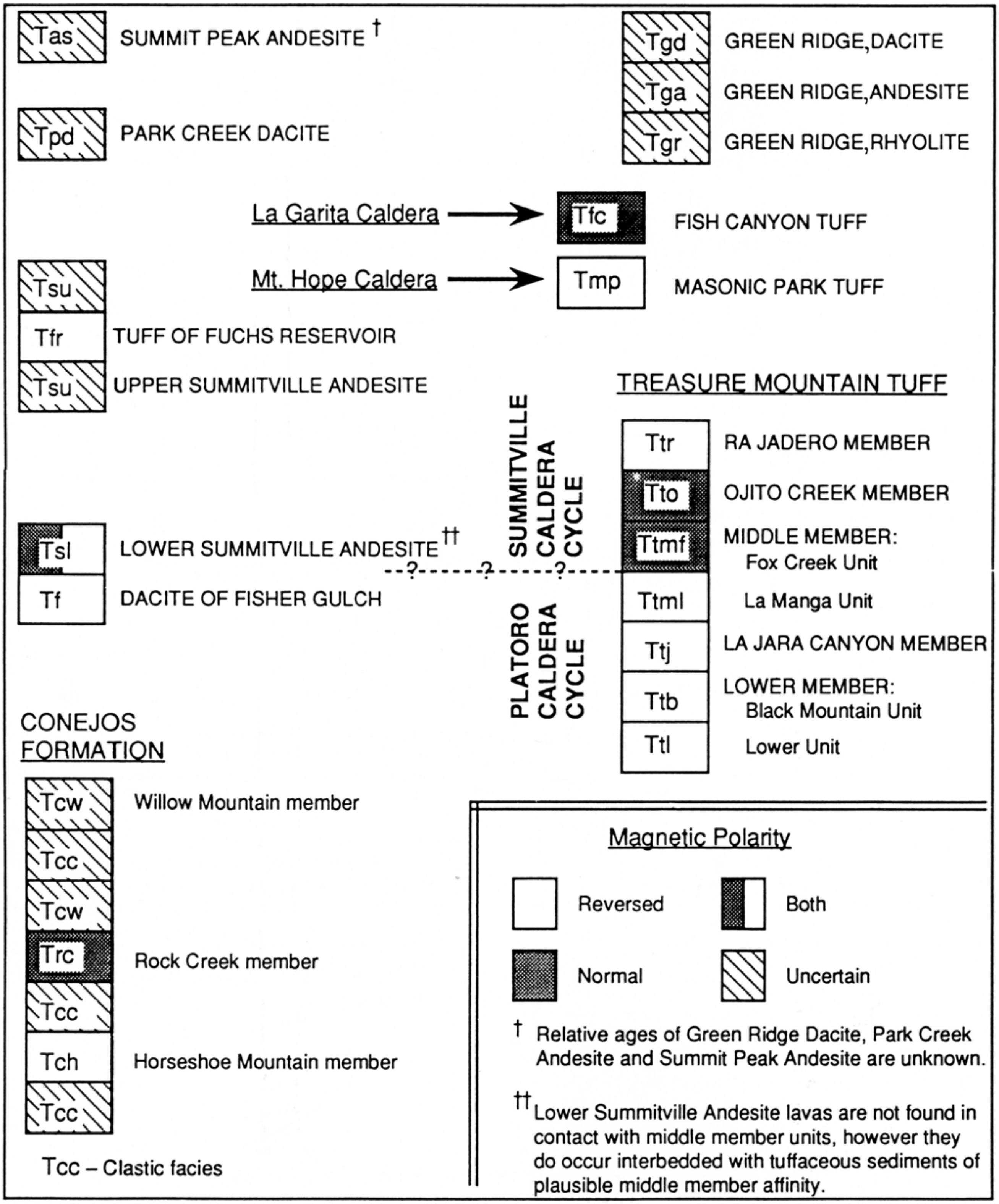

FIGURE 1-3—Stratigraphic sequence in the southeastern San Juan Mountains, modified from Lipman (1975a). Subdivision of the Conejos Formation is based on mapping by M. Colucci: the Willow Mountain member is broadly equivalent to the upper member of the Conejos Formation of Lipman (1975a). The Black Mountain unit of the lower member of the Treasure Mountain Tuff is equivalent to the upper unit of the lower member as mapped previously. The middle member of the Treasure Mountain Tuff has been subdivided into two units, each containing multiple tuff sheets, based on recent work by M. Dungan, L. Brown, and S. Balsley. The tuff of Fuch's Reservoir was included within the upper member of the Treasure Mountain Tuff by Lipman (1975a). Other tuff units within the upper member have been shown to be either part of the Ra Jadero Member or a basal rhyolitic unit of the Masonic Park Tuff. Age relations of several postcollapse lava sequences are uncertain relative to ash-flow tuffs and to other lava sequences. Most probably, the lower Summitville Andesite is broadly contemporaneous with the Fox Creek units of the middle member, and the La Manga units probably immediately predate the dacite of Fisher Gulch. Part of the upper Summitville Andesite (upper South Fork of Rock Creek) underlies Masonic Park and Fish Canyon Tuff, but Summitville–Park Creek volcanism spans the period during which these tuffs were erupted. The andesite of Summit Peak, dacite of Park Creek, and volcanics of Green Ridge all postdate the Masonic Park and Fish Canyon Tuffs; these lavas are broadly contemporaneous but have not been dated precisely.

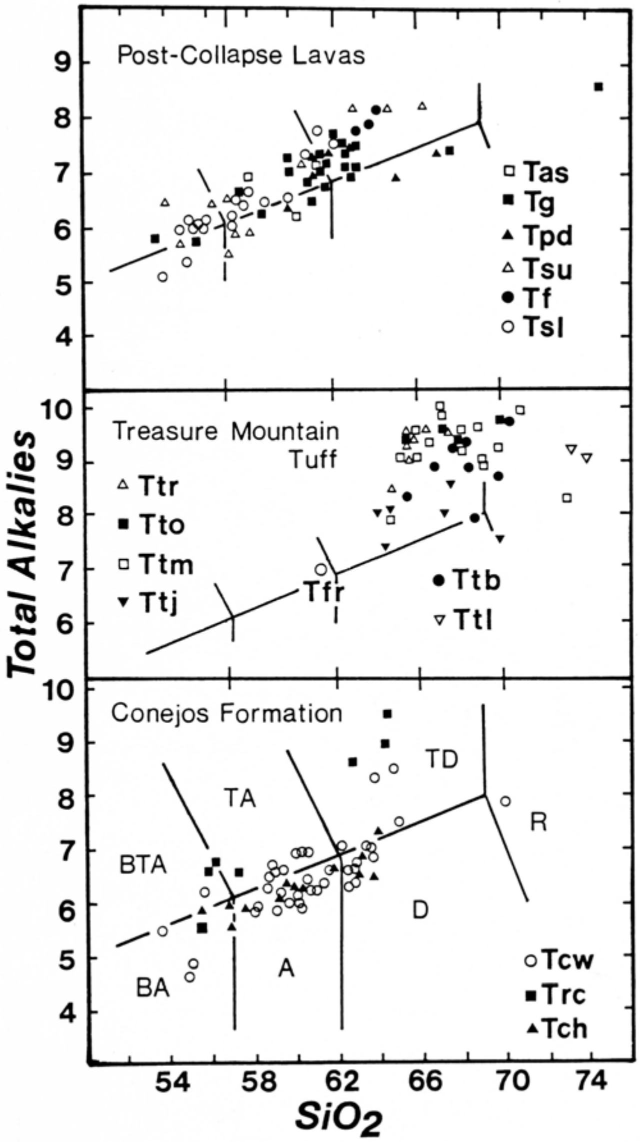

FIGURE 1-4—Silica–total alkalis plot for volcanic rocks of the southeastern caldera complex, San Juan volcanic field. Boundaries of compositional fields are from Le Bas et al. (1986): A, andesite; BA, basaltic andesite; BTA, trachybasaltic andesite; D, dacite; R, rhyolite; TA, trachyandesite; TD, trachydacite. Units and symbols are from Fig. 1-3. Except for the alkalic Rock Creek member and some members of the Treasure Mountain Tuff, compositions tend to straddle the boundary between the basaltic andesite–dacite series and the more alkalic series extending from basaltic trachyandesite to trachydacite. To conform with previous local usage, most southeastern San Juan rocks are referred to as basaltic andesite, andesite, and dacite (quartz latite).

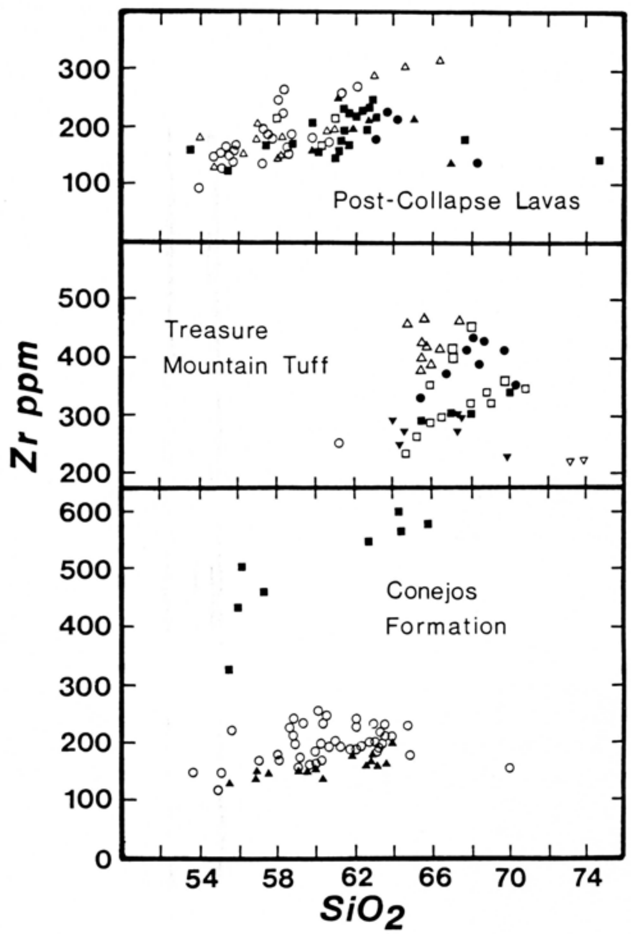

FIGURE 1-5—Silica–zirconium plot for volcanic rocks, southeastern caldera complex. Same symbols as in Fig. 1-4.

Maps

Published geologic maps of southeastern San Juan field at 1:48,000 scale, useful for the field trip, include Platoro caldera (Lipman, 1974), Lower Conejos River Canyon (Lipman, 1975b), Del Norte (Lipman, 1976a), and South Fork (Lipman and Steven, 1976). Virtually the entire field-trip route described in this section is encompassed by the 1:100,000 Antonito topographic map.

Field guide 1: Alamosa to Rock Creek and Chiquito Peak

Precaldera volcanism and outflow ash-flow stratigraphy

The San Juan volcanic field is bordered on its eastern margin by the San Luis Basin, a large asymmetric axial graben of the northern Rio Grande rift. The basin is bounded on its east side by high-angle, large-displacement faults along the west base of the Sangre de Cristo Mountains. A 50–70 milligal gravity anomaly at the base of Blanca Peak on the east side of the basin suggests a maximum of 5–7000 m of late Cenozoic basin-fill sediments within the lowland (Cordell et al., 1982).

Oligocene lavas and tuffs of the southeastern San Juan field dip gently eastward into the basin. As a result, drainages from the southeast San Juan Mountains, such as Rock Creek, Alamosa River, and Conejos River, provide exposures of tilted sections through the volcanic strata. This trip segment examines stratigraphic and age relations of extracaldera units exposed in these drainages, as well as rocks within the Platoro and Summitville calderas.

Mileage

0.0 Junction of US-160 and US-285 in Alamosa (2300 m). Proceed south on US-285. **2.9**

2.9 Junction with CO-370. **Turn right** (west).

STOP 1-1. San Juan panorama, to the west. Pull off onto right shoulder within 100 m of turn. Panoramic view of the southeastern San Juan volcanic field. To the south, mesas underlain by Treasure Mountain Tuff from the Platoro caldera complex dip gently into the San Luis Valley. Compare this simple dip-slope topography of the regional volcanic sequence to the complex terrain within the caldera area (directly to west). Greenie Mountain (straight ahead) is the northeast flank of the eroded Cat Creek stratovolcano (26.5 ± 1 Ma), located on the east side of the Platoro caldera. It consists of andesitic and dacitic lava flows (volcanics of Green Ridge), capped by volcaniclastic conglomerates of the Los Pinos Formation and basaltic lavas of the Hinsdale Formation. Cornwall Mountain, to the southwest (left) of Greenie Mountain, is a structurally uplifted resurgent dome of densely welded ash-flow tuff (La Jara Canyon Member, Treasure Mountain Tuff) within the Platoro caldera. Bennett Peak (4024 m) to the northwest (right) of Greenie Mountain consists of postcaldera andesite lavas and silicic dacitic welded tuffs (Ojito Creek and Ra Jadero Members), marking the limit of the northeastern caldera fill.

Continue west on CO-370. **6.4**

9.3 Waverly. La Garita Mountains at 1:30 are the resurgent core of the La Garita caldera, 40 km in diameter, in the central San Juan Mountains; south end of Sawatch Range is at 2:30. San Antonio Mountain at 9:00 is a late Pliocene dacitic stratocone. Los Mogotes at 10:00 is a basaltic shield volcano of the Hinsdale Formation, dated at 5 Ma. **8.1**

17.4 Junction Rio Grande County Hwy 15. **Turn right** (north); drive 8 mi. On left (west), cliffs halfway up Greenie Mountain are porphyritic flows of silicic dacite (volcanics of Green Ridge), dated at 26.5 ± 1 Ma. Talus slopes above are Hinsdale basalt and basaltic andesite. **8.2**

25.6 Intersection of Hwy 15 and Hwy 28 to Rock Creek. **Turn left** (west) onto Hwy 28. Stay on paved road past Rock Creek Cemetery (mile 31.0), then follow main gravel road. This route traverses down section, from Miocene volcanic rocks to the oldest exposed unit of the Conejos Formation (Stop 3) in upper Rock Creek. Turning west up lower Rock Creek, note the gently east-dipping flows of Hinsdale basalt that cap covered slopes underlain by the Los Pinos Formation, a volcaniclastic alluvial apron derived from the Cat Creek volcano. Entering the Platoro caldera map area (Lipman, 1974). Bulbous-weathering pale orangish-brown Masonic Park Tuff underlies the Los Pinos Formation and crops out north of the road for 2 mi, from mile 34.5 to Bishop Rock (Stop 7). Continue past Bishop Rock on main gravel road. **13.4**

39.0 **STOP 1-2. Rock Creek overlook** (2900 m); **stratigraphy of Conejos Formation.** Park in road-base repository on left, just past cattleguard, and walk

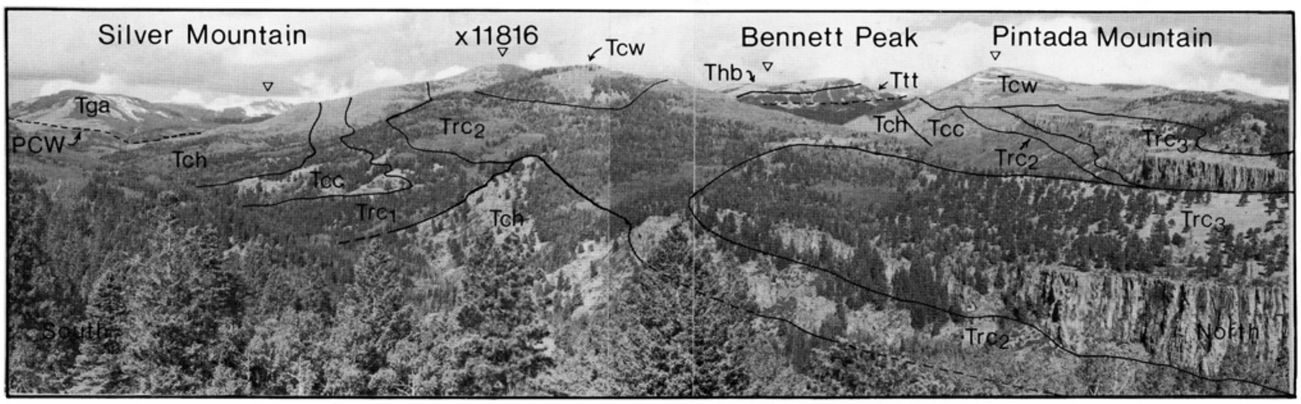

FIGURE 1-6—Panoramic view (to the west) of the upper Rock Creek drainage basin. This view illustrates geologic relations along the northeastern topographic wall of the Platoro caldera and the stratigraphy of the Conejos Formation. Pertinent contacts and units are shown, but many details have been omitted. Refer to Fig. 1-7 and Map I-828 (Lipman, 1974). Bennett Peak (4024 m) and Silver Mountain (3786 m), on the western horizon, lie just within the northeastern topographic wall of the Platoro caldera (dashed line—PCW). Pintada Mountain (3914 m) and an unnamed peak (3601 m; 11,816 ft) are outside the caldera in precollapse volcanic and volcaniclastic rocks of the Conejos Formation, the main focus of Stops 1-2 through 1-5. The South Fork of Rock Creek heads below Silver Mountain, the North Fork heads in the cirque on the east face of Bennett Peak. Lipman (1975a) noted that the presently high elevation of the caldera wall reflects the truncation of precollapse Conejos vents at the time of collapse. The Platoro caldera was filled to overflowing by intracaldera La Jara Canyon tuff, later Summitville cycle tuffs, tuffs erupted from the central San Juan volcanic field, and postcollapse andesite to dacite lavas. On Bennett Peak, the Ra Jadero Member of the Treasure Mountain Tuff, plus the lower rhyolitic unit of the Masonic Park Tuff (previously mapped as upper member of Treasure Mtn. Tuff), accumulated to anomalous thicknesses due to ponding against the topographic escarpment of the caldera wall (shown as Ttt). The tuffs are in turn overlain by Green Ridge andesite (not shown separately) and a thick sequence of Miocene Hinsdale basaltic lavas (Thb). The upper slopes of Silver Mountain, an east-trending flat-topped ridge, are andesite of Green Ridge (Tga). These postcollapse lavas overlie a sequence similar to that on Bennett Peak (Fig. 1-7). All three members of the Conejos Formation are exposed in stratigraphic succession in the Rock Creek drainage. The Horseshoe Mountain member (Tch) crops out on lower slopes, primarily in the upper part of the basin. Above a highly irregular erosion surface, the Horseshoe Mountain lavas are overlain by a widespread conglomeratic unit (Tcc) containing abundant clasts of hornblende-phyric Horseshoe Mountain lithologies. Overlying the Horseshoe Mountain member and the volcaniclastic unit are two distinctive lava units (Trc_1, Trc_2) and the tuff of Rock Creek (Trc_3) of the Rock Creek member. The trachydacitic tuff of Rock Creek forms prominent cliffs that rim both valleys. A vent region for Rock Creek lavas exposed on the unnamed peak (11,816 ft) is recognized on the basis of voluminous monolithologic scoria grading laterally into mineralogically identical lavas. Lavas of the Willow Mountain member (>300 m) cap the Rock Creek units on the upper slopes of Pintada Mountain and elsewhere.

across road (50 m) to small quarry that exposes a stratigraphically high flow of the Conejos Formation. This vantage point provides a view of the North and South Forks of Rock Creek (Fig. 1-6), in which three members of the Conejos Formation are exposed. The divide at the head of the North Fork roughly coincides with the northeast topographic wall of the Platoro caldera.

Stratigraphic relations within the Conejos Formation in Rock Creek (Fig. 1-7) are critical to understanding the precaldera volcanic history: only here and on the southeast flank of Pintada Mountain are flows of the three Conejos members exposed in stratigraphic sequence. The three members, corresponding to three magmatic suites, are delineated by field, paleomagnetic, mineralogic, compositional, and age criteria. In upward sequence, they have been designated the Horseshoe Mountain, Rock Creek, and Willow Mountain members.

Horseshoe Mountain high-K andesites are distinguished by hornblende phenocrysts in relatively mafic compositions (55–57% SiO_2), low-K plagioclase phenocrysts ($Or_{1.5}$, at An_{50}), and low concentrations of incompatible trace elements. Horseshoe Mountain lavas have been identified only within the Rock Creek drainage and on the northern flank of the Platoro caldera. Over a kilometer of lava flows and volcaniclastic rocks of apparent Horseshoe Mountain type also occur in the subsurface north of Pintada Mountain (Calvert et al., 1987). Late andesite and dacite dikes of Summer Coon volcano, located northeast of Del Norte (Zielinski and Lipman, 1976), also have Horseshoe Mountain characteristics. Within the Rock Creek drainage, the Horseshoe Mountain member (Stop 1-3) is overlain by a monolithologic volcanic conglomerate composed of rounded to subangular clasts of hornblende andesite (Stop 1-4). The conglomerate forms a stratigraphic marker between underlying Horseshoe Mountain and overlying Rock Creek lavas.

Rock Creek lavas differ from the Horseshoe Mountain member in (1) the absence of hydrous phenocrysts even in the most evolved compositions (64% SiO_2), (2) distinctive large tabular plagioclase phenocrysts (1–3 cm) charged with melt inclusions in mafic lavas, (3) high Or contents in plagioclase

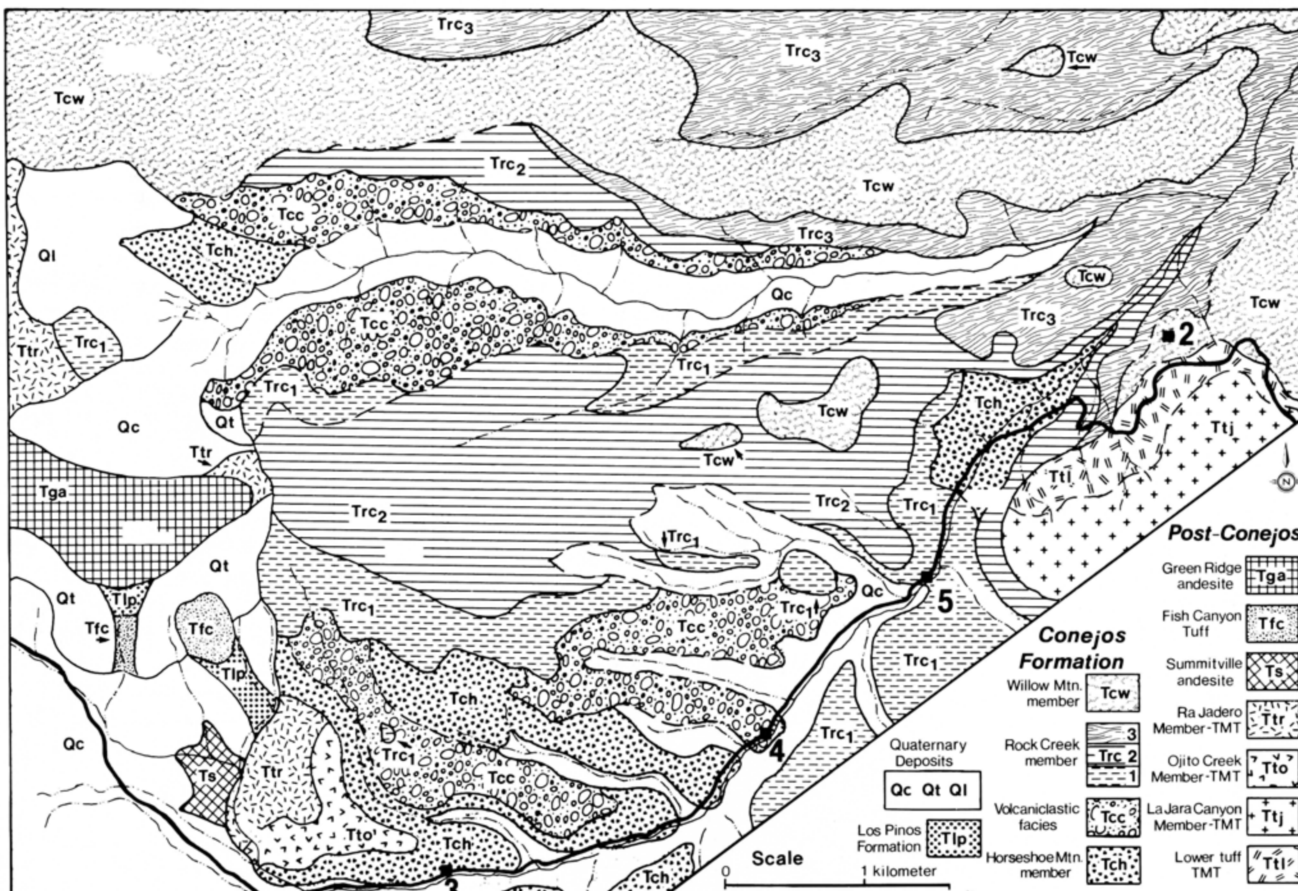

FIGURE 1-7—Geologic map of the upper Rock Creek drainage, showing subdivision of the Conejos Formation based on mapping by M. Colucci (1985–87); other contacts modified from Lipman (1974). Conejos units in stratigraphic succession are: lavas of Horseshoe Mountain member (Tch); conglomeratic breccia (Tcc), dominated by clasts of Horseshoe Mountain lithologies; Rock Creek member (Trc_1, platey-plagioclase trachybasaltic andesite lava, Trc_2; sparsely phyric trachyandesitic to trachydacitic lava; Trc_3, trachydacitic tuff of Rock Creek); lavas of the Willow Mountain member (Tcw). Also present are two outflow tuffs of the Platoro cycle (Ttl, lower member; Ttj, La Jara Canyon Member), two tuffs of the later Summitville cycle (Tto, Ojito Creek Member; Ttr, Ra Jadero Member), two postcollapse lava units (Ts, Summitville Andesite; Tga, andesite of Green Ridge), volcaniclastic conglomerates and mudflow breccias of the Los Pinos Formation (Tlp), and the Fish Canyon Tuff (Tfc). All the latter units exposed near the western limit of the map area are ponded within or overlap the northeastern topographic wall of the Platoro caldera (see Fig. 6). Quaternary deposits include colluvium (Qc), talus (Qt), and landslides (Ql). Locations of Stops 1-2 through 1-5 are shown along the Rock Creek Road.

(Or_{3-6}, at An_{50}), and (4) higher incompatible element concentrations (Figs. 1-4, 1-5). Whole-rock compositions of Rock Creek lavas and tuffs are systematically more evolved up-section. The youngest and most evolved magmatic composition is the tuff of Rock Creek, a trachydacite ash-flow sheet (Lipman, 1975a). Erosional remnants of the tuff of Rock Creek constitute a stratigraphic marker around the northern and eastern flanks of the caldera complex. The Rock Creek lavas were erupted from vents located near the head of the divide between the forks of Rock Creek. If the tuff of Rock Creek also vented from this area, distal flows near Del Norte and at The Pinnacles (Stop 2-5) traveled 15 and 25 km, respectively, down paleovalleys.

The younger Willow Mountain member is compositionally and mineralogically intermediate between, and more variable than, the Horseshoe and Rock Creek members. Willow Mountain lavas overlie the Rock Creek member north of Pintada Mountain, in the Rock Creek area, in the Alamosa River valley, and locally in the Conejos River valley (Pinnacles area). Virtually all Conejos lavas exposed near the southern rim of the caldera are Willow Mountain member. Lipman (1975a) defined an upper member of the Conejos Formation as those lavas and clastic rocks overlying the tuff of Rock Creek. The Willow Mountain member is stratigraphically equivalent to the upper member of the Conejos Formation, but is more widespread than previously mapped by Lipman. Unlike the older rocks, the Willow Mountain lavas commonly show textural evidence for mingling of contrasting magmas.

The lava exposed in the quarry at this stop is a Willow Mountain andesite (61% SiO_2) with phenocrysts of plag + aug + hbl + opx + fe-ti ox, and abundant quenced inclusions of more mafic magma. The tuff of Rock Creek forms prominent cliffs in both forks of Rock Creek and is well exposed in the slope below the quarry. The tuff of Rock Creek is relatively mafic (63% SiO_2), containing large phenocryst-poor fiamme (An_{50-60} + aug + hyp) in a lithic-rich matrix of variably welded orangish-brown devitrified ash. A good outcrop of this tuff can be reached from the north end of the quarry by descending to the northwest.

Geochemical modeling of the three Conejos magma series has shown that they were derived from distinct parent magmas and had contrasting differentiation histories. The marked differences in trace-element contents and mineralogy between the Horseshoe Mountain and Rock Creek members must be in large part due to parent magma differences. The Horseshoe Mountain parent magmas appear to have had higher H_2O, lower alkalies, and lower incompatible-trace-element contents than the more alkaline Rock Creek parents. The erupted mafic endmembers of both series assimilated substantial Proterozoic crust characterized by non-radiogenic lead (Lipman et al., 1978). Early stages of crust–magma interaction probably occurred at the base of the crust or in the lower crust. Subsequent differentiation of these contaminated basaltic andesites was accompanied by continued assimilation (Horseshoe Mountain ⟩⟩ Rock Creek) of more radiogenic crust at shallow crustal levels. The younger and more diverse Willow Mountain member is intermediate in character between the two earlier members, and may reflect hybridization of compositionally divergent magmas (or sources) similar to those parental to the Horseshoe Mountain and Rock Creek lavas.

Continue downroad, descending through the Conejos Formation into the South Fork of Rock Creek. **5.1**

44.1 **STOP 1-3. Horseshoe Mountain member, Conejos Formation.** Outcrop on the north side of the road (3050 m) of hornblende-phyric dacite of the Horseshoe Mountain member (63% SiO_2). Biotites from this outcrop, and from a Horseshoe Mountain flow north of the caldera, have been dated at 32.9 ± 0.6 Ma by $^{40/39}Ar$; hornblende from the northern locality yielded a condordant age of 33.2 ± 1.0 Ma. The eastern topographic wall of the Platoro caldera is exposed in the upper slopes of the South Fork, about 1 km west of this locality.

Turn vehicles around; **proceed east. 1.8**

45.9 **STOP 1-4. Monolithologic conglomerate, Conejos Formation.** This unit, containing clasts of Horseshoe Mountain lava, is a widespread stratigraphic marker between the underlying Horseshoe Mountain member and the younger Rock Creek lavas. Throughout the San Juan field, the Conejos Formation and equivalent units include voluminous volcaniclastic sediments that reflect erosion during and between volcanic episodes. This clastic facies has not been studied in detail.

Continue east. 1.2

47.1 **STOP 1-5. Rock Creek member, Conejos Formation.** Past Deer Gulch, at a sharp bend, is a roadcut of a plagioclase-phyric trachyandesite (Tcr_1) of the Rock Creek member (2815 m). Plagioclase phenocrysts 1–2 cm in length and charged with melt inclusions are abundant (15–20 vol. %). Lipman (1975a) and co-workers recognized similar plagioclase-phyric lavas throughout the San Juan field and termed them "platey-plagioclase andesite." Although texturally variable, this petrographic type dominates the mafic lavas (<60% SiO_2) of the Rock Creek member. More evolved Rock Creek lavas (Tcr_2) contain less abundant, smaller, and inclusion-free plagioclase phenocrysts. Despite the textural differences, plagioclase phenocrysts in trachydacites retain a high-K character (Or_{3-7}, at An_{50}). Incompatible-trace-element contents increase regularly with SiO_2 (Figs. 1-4, 1-5).

Continue east, past Stop 1-2. **2.9**

Treasure Mountain Tuff

The Treasure Mountain Tuff records a complex history of magma differentiation and caldera eruptions. Many aspects of this tuff assemblage are unusual in the San Juan volcanic field, and they provide important constraints on the overall magmatic evolution of the southeast San Juan caldera complex. Recent field, petrologic, and geochemical studies of the Treasure Mountain members have refined the stratigraphy of Lipman (1975a) and built on the petrologic model of Lipman et al. (1978).

The diversity in Conejos magma compositions (Figs. 1-4, 1-5) has been interpreted by us as a reflection of chemically distinct parental magmas during the >4 m.y. of precollapse magmatism. Like the relatively young Willow Mountain lavas of the Conejos Formation, trace-element compositions of the Treasure Mountain tuffs and postcollapse lavas are intermediate between the extremes defined by the Horseshoe Mountain and Rock Creek magma series. Tuffs such as the La Jara Canyon, Ojito Creek, Masonic Park (Mount Hope caldera), and related smaller units have low concentrations of incompatible elements similar to those in Horseshoe Mountain and Willow Mountain magmas, whereas the Ra Jadero Tuff and related units in the middle member have higher concentrations of incompatible elements akin to those of the alkalic Rock Creek member. These differences appear to record continued diversity in parental magmas during the caldera-related phase of magmatism, and persistence of similar parental types over a lengthy period.

Lipman (1975a) and Steven and Lipman (1976) noted that the ash-flow tuffs of the southeastern San Juan volcanic field were generally more mafic than silicic tuffs erupted from the western or central San Juan caldera clusters; i.e., the Treasure Mountain Tuff is largely dacitic to silicic dacitic in composition. Compositions of Treasure Mountain magmas are obscured to some degree by crystal/ash fractionation during eruption, and the rarity of pumice clasts adequate for chemical analyses from the densely welded tuffs has made it difficult to determine these compositions directly. Available data suggest that few of the Treasure Mountain magmas contained more than 70–71% SiO_2.

Despite trace-element distinctions among the tuffs and systematic differences in mineral chemistry, the mineral assemblages in Treasure Mountain units are remarkably uniform. All the tuffs contain plag + bio + aug + ap + ox. Quartz is absent from all caldera-related magmas of the Platoro–Summitville system, sanidine is minor in the most evolved portion of the La Jara Canyon tuff, and sanidine is abundant only in the relatively alkalic Ra Jadero tuff. Even the rhyolitic lower unit of the lower member lacks quartz and sanidine. Hornblende and hypersthene are also absent as phenocrysts in silicic dacitic portions of the tuffs. All the voluminous tuffs, and some small units in the middle member, contain a second magmatic component more mafic than the host silicic dacite. This component commonly occurs as andesitic fiamme in upper parts of the outflow sheets (Stop 1-6) and may also be represented by a secondary phenocryst population. The andesitic fiamme (glass, 58–60% SiO_2) contain calcic plagioclase (An_{60-85}) and hornblende; additional phases may include magnesian biotite, aluminous augite, and hypersthene. The absence of quartz and the scarcity of sanidine in the most silicic Treasure Mountain tuffs are qualitative indicators that these magmas equilibrated at relatively shallow levels in the crust in comparison to some units erupted from the central caldera complex (e.g., Fish Canyon Tuff—qtz + san + plag + bio + hbl + sph: Whitney and Stormer, 1986).

The discontinuous magmatic zonations recorded by two distinct mineral assemblages (and compositions) and the presence of more mafic fiamme in most of the Treasure Mountain units indicate eruption from layered magma chambers: a relatively evolved silicic dacitic magma derived from, and overlying, a dominant volume of andesitic magma appears to have been the typical pre-eruptive configuration in the southeast San Juan complex. This is confirmed by the voluminous outpourings of postcollapse andesite lavas that filled both calderas to overflowing. Compositions as mafic as these, either as lavas or as components in tuffs, are rare in the central San Juan caldera cluster, except for lavas erupted around the periphery of the cluster.

The southeastern-caldera magma chambers appear to have evolved as physically separate but contemporaneous reservoirs, not as cupolas above a single large magma body. This conclusion is based on chemical variations among middle member units, in relation to magmas erupted during the major caldera-collapse events. These and other observations are inconsistent with the presence of a large silicic batholith underlying the southeastern calderas. Plouff and Pakiser (1972) interpreted the sharply demarcated gravity low, within which the central and western complexes are centered, as an indication that these calderas are underlain by a large solidified granitic batholith. We cannot determine the time of emplacement of this batholith to its present level relative to the caldera-collapse events. Possibly, the southeastern calderas record an early primitive phase of magma evolution in relatively small and separate chambers, and the later central San Juan calderas a more mature phase coupled with the coalescence of distributed chambers into a larger silicic-magma body.

50.0 **STOP 1-6. Upper (Black Mountain) unit of lower member, Treasure Mountain Tuff.** Park on left side of road, adjacent to pine trees (2935 m). Walk east along road, to outcrop. The Black Mountain unit predates the La Jara Canyon Member (exposed 50 m to east) and associated major collapse of the Platoro caldera. Phenocryst mineralogy consists of the plag + bio + aug assemblage typical of most Treasure Mountain tuffs. At most exposures, the Black Mountain unit has an upper vitric hybrid zone containing two fiamme compositions (dacite, hornblende andesite), in contrast with its compositionally homogeneous basal vitrophyre (dacite). The prominent bench below road level is the upper lithic-rich vitric zone of mixed fiamme; the basal vitrophyre is well exposed in the south-facing hillside. The andesitic fiamme contain phenocrysts of large subhedral hornblende, resorbed calcic plagioclase (An_{65-85}), minor Mg-rich biotite, orthopyroxene, and aluminous augite. Analogous mixed compositions characterize the upper vitric zone of the Ra Jadero Member. The Ojito Creek Member locally contains similar andesitic fiamme, but no comparable upper vitric zone is present.

Return to vehicles; **continue ahead** to Bishop Rock. **1.9**

Masonic Park Tuff

Throughout its areal extent, the Treasure Mountain Tuff is overlain by the Masonic Park Tuff (28.4 Ma; Lanphere, 1988, and written comm.), a large-volume, primarily crystal-rich dacite. Larsen and Cross (1956) originally included the Masonic Park rocks within their Treasure Mountain Rhyolite due to close similarity in petrography and appearance to the La Jara Canyon Member, but subsequent mapping has shown that the Masonic Park was erupted from a separate source caldera (Mount Hope) located northwest of the Platoro–Summitville complex (Steven and Lipman, 1976).

The Mount Hope caldera is poorly exposed, as it is largely buried by the Fish Canyon Tuff from the central San Juan caldera cluster (27.8 Ma; Lanphere, 1988). Thus, the intermediate age of the Masonic Park Tuff is complemented by a source located between those of earlier and later regional tuff sheets. The Mount Hope caldera also lies along the gravity gradient marking the southern margin of the subvolcanic batholith that underlies the central San Juan calderas.

Recent field and petrologic studies have shown that the Masonic Park Tuff: (1) has close affinities to the La Jara Canyon tuff and therefore had a similar parent magma, and (2) contains three units (lower rhyolite, middle dacite, and upper dacite) that were probably erupted from two magma chambers. The lower rhyolite, previously mapped as the upper member of the Treasure Mountain Tuff, is present sporadically beneath the upper dacite (middle dacite absent) on the north flank of the Platoro caldera and at Wolf Creek Pass. The middle dacite forms the bulk of the type section east of South Fork and appears to dominate throughout the South Fork region. The upper dacite is the dominant unit southeast of the Mount Hope caldera. Only at the type section and at Wolf Creek Pass have all three units been found in sequence. The rhyolite unit appears to be an early-erupted differentiate of the upper dacite. The middle dacite differs from the upper dacite in having subtly different mafic phenocryst compositions, more abundant sanidine, and sparse resorbed quartz. Thus, the middle dacite shares some characteristics with the Fish Canyon Tuff and may have been erupted from a magma chamber at greater depth than the source of the lower rhyolite and upper dacite. Although no firm evidence exists for a second caldera, the anomalously thick Masonic Park Tuff at the type section (Lipman, 1975a, fig. 27) may result from ponding in a syneruptive depression.

51.9 **STOP 1-7. Bishop Rock** (2650 m); **Masonic Park Tuff.** This is the western promontory of the first (southern) of three en-echelon ridges of Masonic Park Tuff. Turn left onto rough secondary road; drive carefully for 0.7 mi, to middle ridge.

Stop 1-7A. Directly north of the middle ridge of Masonic Park Tuff are outcrops of the upper (Black Mountain) unit of the lower member. Though only 3 km east of Stop 1-6, the Black Mountain unit has thinned from about 10 m to less than 5 m. A thin distal section (10 m) of the overlying La Jara Canyon Member is exposed near road level. At this locality, a basal vitrophyre overlies nonwelded La Jara Canyon tuff, forming a small cliff below red-brown hummocky outcrops of densely welded devitrified tuff. Where thick, the La Jara Canyon is devitrified throughout, and no basal vitrophyre is present (see Fig. 2-3).

All the voluminous tuff sheets of the Treasure Mountain have undergone some syneruptive crystal–ash fractionation; this crystal enrichment is especially pronounced in the La Jara Canyon Member. The intracaldera facies shows the most extreme fractionation; crystal contents are commonly nearly twice those in the outflow sheet. Because of these sorting effects, mineral and glass chemical data, along with isotopic compositions, are used to document pre-eruptive compositional gradients in the La Jara Canyon magma chamber. The most evolved (sanidine-bearing) magmatic component is rhyolite (71–73% SiO_2), exposed only at the base of the intracaldera tuff where it wedges out against the caldera wall (Stop 2-8). The most mafic component is documented by a second population of magnesian biotite phenocrysts, along with aluminous augite and hornblende in upper parts of outflow sections, that apparently reflect a downward zonation in the La Jara Canyon magma body into hornblende dacite. Hornblende and biotite from the dacite component of the La Jara Canyon tuff have higher Fe/Mg ratios than do these phenocryst phases in andesitic fiamme of other Treasure Mountain Tuff sheets, and the plagioclase compositions are less calcic than in the andesitic fiamme. Biotite phenocrysts have variable intermediate compositions in outflow basal vitrophyres of the La Jara Canyon; sanidine and hornblende phenocrysts are absent.

Continue past Stop 1-7A, to northernmost ridge of Masonic Park Tuff. Where the road turns west, continue on foot across a small ridge of Black Mountain unit toward the cliff of Masonic Park Tuff (Fig. 1-8).

Stop 1-7B. This Masonic Park locality includes a rarely exposed lower nonwelded zone (directly overlying the Black Mountain unit), containing abundant pumice blocks up to 25 cm and scattered lithic fragments up to 1.5 m across, overlain by typical densely welded tuff showing compound cooling. Phenocryst contents (30–40% of plag + bio + aug) and compositions are the same in both zones, and typical of the Masonic Park Tuff throughout the southeast San Juan field. Thus, the abrupt change in welding characteristics is unrelated to petrologic changes. The large pumices (67% SiO_2), useful for chemical and mineralogic study, are rare elsewhere in welded Masonic Park Tuff. In this area, all the tuffs vary greatly in thickness over short distances, due to ponding and shadow effects in the lee of a paleotopographic high of Willow Mountain lavas (Stop 1-2); e.g., the La Jara Canyon tuff is absent at Stop 1-7B.

The dominant silicic dacitic Masonic Park Tuff, exposed here, is elsewhere locally underlain by related sanidine-bearing rhyolitic tuff (Stop 8), indicating a compositional gradient in the pre-eruptive magma chamber. In addition to being compositionally zoned, both the Masonic Park and La Jara Canyon tuffs are large-volume units (>500 km^3) of similar phenocryst mineralogy and chemistry. The Masonic Park Tuff at Bishop Rock must have traveled a minimum of 50–60 km from its source.

Return to Rock Creek road (Hwy 28) south of Bishop Rock; drive east to Hwy 15. **11.5**

63.4 Junction of Hwy 28 and Hwy 15. **Turn right** (south). **10.2**

73.6 Rio Grande–Conejos County line. Pavement ends; road on right is most direct way to Platoro. Continue straight ahead. **3.5**

77.1 **Turn right** on unnumbered Alamosa River road (2434 m). Volcanic units in this area dip about 10° ENE. The sparsely wooded ridge ahead is Chiquito Peak (2939 m), capped by andesite–dacite lavas and flow breccias of the Green Ridge volcanics. Ex-

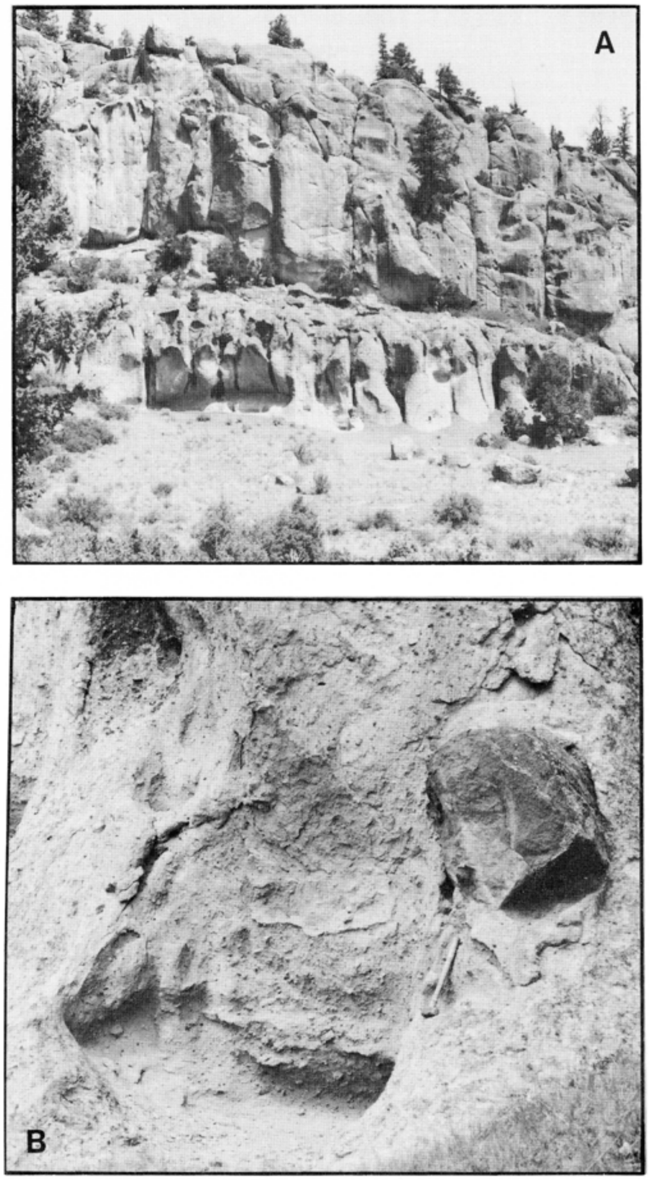

FIGURE 1-8—Cooling units in the Masonic Park Tuff, Bishop Rock (Stop 1-7B). **A,** The lower cliff of nonwelded tuff is overlain by a more typical thick, densely welded unit. Both units are compositionally similar silicic dacite, characteristic of the upper Masonic Park Tuff found throughout the southeast San Juan volcanic field. **B,** Detail of the nonwelded cooling unit at Stop 1-7B, a pumice-rich tuff containing scattered large lithic clasts. The majority of visible clasts in this view are pumice. The large block of vitric La Jara Canyon tuff (0.5 m hammer handle) was probably entrained in the ash flow as it surmounted the topographic obstruction 1 km to the west.

posed on the south flank of Chiquito Peak are Masonic Park Tuff and upper sheets of the Treasure Mountain Tuff. Entering the Platoro caldera area map (Lipman, 1974). **4.7**

81.8 **STOP 1-8. Basal rhyolitic Masonic Park Tuff.** Park in cottonwood grove on left, adjacent to cliff of Masonic Park Tuff (2510 m). Walk to small gully at the curve immediately north of the Alamosa River bridge. Proceed west along cliff for about 100 m. The key outcrop is a dark welded bench of slabby rhyolitic lower Masonic Park Tuff, below the main welded cliff, and just past a large prominent boulder of welded tuff.

The rhyolitic unit (72% SiO_2) was formerly mapped east and north of the Platoro caldera as part of the upper member of the Treasure Mountain Tuff (Lipman, 1974), but rare exposures indicate that most of this unit is a basal rhyolitic zone of the dominant silicic dacitic upper Masonic Park. The rhyolitic unit contains ~10% phenocrysts (plag + san + bio + aug), with compositional affinities to silicic dacitic Masonic Park. The rhyolitic unit is sporadically present on the east and north flanks of the southeastern caldera complex. It ponded to a thickness of 25 m against the Platoro caldera wall on Bennett Peak, and is also present south of the Mount Hope caldera, near Wold Creek Pass.

Return to vehicles. **Continue ahead** (west) to the intersection. **Turn left** (south), toward Capulin. **0.7**

82.5 **STOP 1-9. Outflow stratigraphy on south flank of Chiquito Peak.** Exposed above the Alamosa River (Fig. 1-9A) are compound cooling units of the Treasure Mountain Tuff related to the Summitville cal-

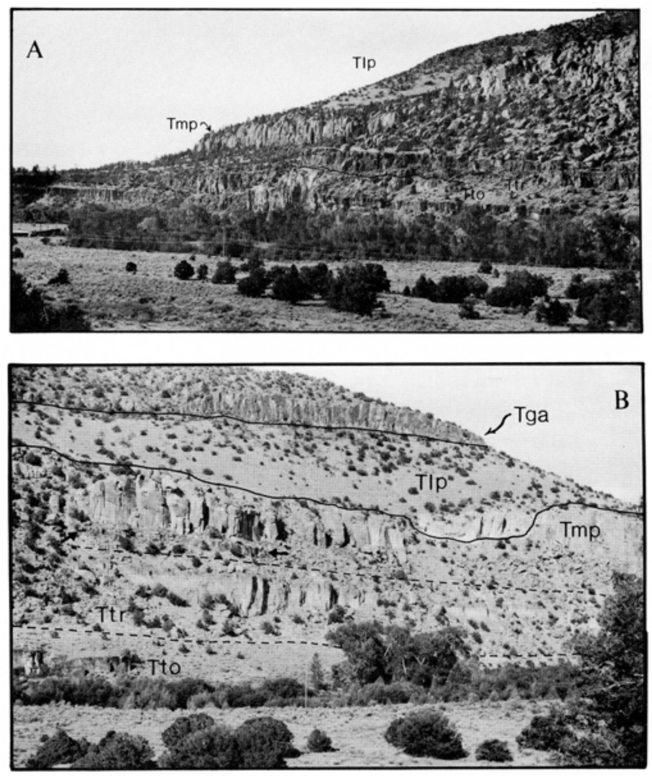

FIGURE 1-9—Volcanic stratigraphy of eastern Chiquito Peak. **A,** Exceptional exposures along the Alamosa River provide evidence for substantial erosion between eruptions of the major Summitville-cycle tuffs (Ojito Creek and Ra Jadero Members). The Ojito Creek Member typically contains two or more flow units. In this area, the upper (light-colored), weakly welded zone of the upper flow unit has been largely stripped by erosion prior to deposition of the Ra Jadero Member. **B,** The thick orangish-brown cliff of Ra Jadero tuff (Ttr) in this view is only moderately to weakly welded. To the west, this unit is poorly exposed in the bench below the cliff of Masonic Park Tuff (Tmp). The lower, densely welded Ra Jadero unit (with a dark upper vitric zone) forms a cliff exposure to the west (Fig. 1-9A; Stop 1-11). The characteristically dark-brown outcrops of lower Masonic Park rhyolite (Stop 1-8) are indicated with arrows. The prominent light-colored deposit filling a valley cut in the top of the Masonic Park Tuff is reworked material derived from distal nonwelded Fish Canyon Tuff. Most of the overlying Los Pinos Formation (covered slopes) is a volcaniclastic apron shed from the nearby Cat Creek volcano, the eruptive sources of Green Ridge andesite lava near the top of the section.

dera. Two flow units of the Ojito Creek Member are well exposed upstream from this viewpoint, and they can be observed on the drive to Stop 1-11. A lower densely welded flow unit is overlain by a moderately welded and vapor-phase-altered unit which has an undulatory eroded contact with the overlying Ra Jadero Member. The lower orangish-brown cliff directly across the river is the upper cooling unit of the Ra Jadero. The rhyolitic unit of the Masonic Park Tuff overlies the eroded top of the Ra Jadero: white, weakly welded tuff grades upward into the typical dark welded bench beneath the Masonic Park cliff (Fig. 1-9B). The top of the Masonic Park is also eroded, and a local valley-filling unit of fluvially reworked, weakly welded Fish Canyon Tuff underlies the Los Pinos Formation.

Continue along road. **0.4**

82.9 Jacobs Hill road. **Turn right.** Travel west across a plateau underlain by the Ra Jadero and Ojito Creek Members, eventually descending an escarpment into variably welded ash-flow sheets of the middle member. Continue along road, along the contact between the middle member and the top of the La Jara Canyon. **2.4**

85.3 **STOP 1-10. Jacobs Hill area; lower member, Treasure Mountain Tuff.** Jacobs Hill is capped by conglomerates of the Los Pinos Formation, derived from the postcaldera Cat Creek volcano. The underlying cliffs are Masonic Park Tuff. Stratigraphic and structural relations are complicated in this area by faulting peripheral to a small intrusion which has upwardly domed the Treasure Mountain section, exposing the lower unit of the lower member. This is the only easily accessible field-trip locality for the lower unit. At this locality and to the south (Conejos valley), the lower unit is a variably welded rhyolitic tuff that is lithic-rich and phenocryst-poor; phenocryst compositions resemble those in the La Jara Canyon Member. North of the caldera, mineralogically similar lithic-poor rhyolitic tuff is more welded.

Return to the Alamosa River road. **2.4**

87.7 **Turn left** (northeast) on Alamosa River road. Drive along the southwest flank of Chiquito Peak, toward Terrace Reservoir. Cliffs high on Chiquito Peak are lavas and breccias from the postcaldera Cat Creek volcano, underlain by reworked distal Fish Canyon Tuff, Masonic Park Tuff, and the Ra Jadero and Ojito Creek Members of the Treasure Mountain Tuff (Fig. 1-9B). **2.7**

90.4 **STOP 1-11. Members of the Treasure Mountain Tuff related to the Summitville caldera.** Drive past a prominent cliff, and park on left side of road (2550 m). The middle member contains 12–15 laterally extensive ash-flow units interbedded with air-fall tuffs. Although many of the individual flow units are limited in distribution and cannot be confidently traced laterally, several units are widely dispersed and locally exceed the Ojito Creek or Ra Jadero Members in thickness. Many units of the middle member contain pumice clasts of mafic dacite up to 50 cm in diameter. At some localities 30 km from the caldera rim, these clasts are >30 cm in diameter and occur within a lithic-rich matrix. The middle member shares petrologic and paleomagnetic affinities with the major Treasure Mountain ash-flow sheets. South of the Platoro caldera, the lowest 2–3 units have phenocryst compositions similar to the underlying La Jara Canyon Member and are similarly reversely magnetized. Overlying units of the middle member are normally magnetized and are compositionally similar to either the Ojito Creek (normal polarity) or the Ra Jadero (reverse polarity) Members.

At this stop, gently dipping pumice-fall beds of the middle member (normal magnetic polarity) drape the sides of a well-exposed paleovalley. The fall beds are 2–60 cm thick and contain varying proportions of pumice fragments, lithic clasts, and ashy matrix. Pumice is concentrated near the tops of a few units, possibly indicating deposition in standing water. Crosslaminations and local channeling within some units result from reworking by water. An ash-flow sheet 4–5 m thick overlies the fall units and fills the paleovalley. Several rubbly lithic zones mark lag deposits at the bases of discrete flow pulses; these are overlain by tuff showing a well-preserved welding profile. Flattening of pumice fragments increases steadily from the base to near the middle of the unit, then decreases upward. Large mafic pumice clasts occur throughout the unit. A multibedded fall deposit 0.5 m thick is sandwiched between this ash-flow sheet and an overlying unit (2–3 m thick), which marks the top of the middle member.

Climb to glacial-outwash terrace above middle member, where the base of the Ojito Creek Member is well exposed to the west in cuts along the old Alamosa River road. A typical thick basal vitrophyre is overlain by a poorly developed lithophysal zone. Upward in the section, dark fiamme as much as 0.5 m long appear abruptly near the top of the main cliff, defining a flow-unit contact within the densely welded devitrified zone. To the south (east of La Jara Reservoir), the zonation by welding and crystallization of the Ojito Creek is more complex, and as many as four cooling subunits are locally present, each with a basal vitrophyre.

Phenocryst and glass analyses document two discrete Ojito Creek magma compositions in addition to the rare andesitic fiamme. Locally, compositions are more mafic at the base of the unit, forming a "reverse" zonation. The distribution of these two compositions suggests that the Ojito Creek magma chamber was layered, but that these layers were tapped irregularly during eruption.

Walk eastward along the cliff to a small side canyon. Traverse up the far side of this canyon, to compare the Ojito Creek Member at the top of the bench with the basal vitrophyre of the Ra Jadero Member. Above this bench (about 2600 m), the basal vitrophyre of the Ra Jadero Member is exposed. Although superficially similar to the Ojito Creek, the Ra Jadero: (1) generally has an upper vitrophyre; (2) has reverse remanent-magnetic polarity, in contrast to the normal polarity of the Ojito Creek; (3) contains more abundant and larger phenocrysts, blocky rather than tabular plagioclase (commonly intergrown with augite and biotite), and more lithic fragments; (4) is the only member of the Treasure Mountain Tuff that contains substantial sanidine phenocrysts (about 10% of total feldspar); and (5) has biotite phenocrysts that are distinctively high in Fe, Ti, and Ba. Its high contents of incompatible trace elements closely resemble those of the Rock Creek member of the Conejos Formation.

The rim of the side canyon is formed by a broad bench that exposes two additional vitrophyres of Ra Jadero tuff, indicating compound cooling. The highest vitrophyre (a small step, just below the main cliff of Masonic Park Tuff) contains abundant fiamme of hornblende andesite.

Traverse northwest below the cliff of Masonic Park, into the first canyon; bear to the right and upward, to the top of the thick compound-cooling unit of Masonic Park Tuff. Above the Masonic Park is a thick-covered slope underlain by Los Pinos Formation, a volcaniclastic conglomerate containing clasts of Green Ridge dacite in an ashy matrix. The triangular cliff face above is a dacitic lava flow, typical of compositionally similar flows cropping out on Green Ridge, Greenie Mountain, and Chiquito Peak. These flows represent flanks of the Cat Creek volcano. The cliffs above the flow are monolithologic andesitic flow breccias.

Cat Creek volcano

The Cat Creek volcano postdates the Summitville caldera cycle; its eroded core of hypabyssal stocks and laccoliths is exposed in Cat Creek north of Terrace Reservoir. Extrusive products of the Cat Creek volcano include: (1) the volcanics of Green Ridge exposed on Chiquito Peak, Jacobs Hill, and Greenie Mountain; (2) volcaniclastic rocks of the Los Pinos Formation that form an alluvial apron adjacent to the volcanic edifice; and (3) thick western flows capping Sheep, Silver, and Windy Mountains within the Platoro caldera. Significant petrologic differences exist between the Green Ridge flows and those within the caldera.

Extracaldera lavas show a general progression from early andesite to late dacite, although andesite and dacite are intercalated on Green Ridge. Andesites have phenocrysts of plag + aug ± opx ± ol + fe-ti ox in an intergranular groundmass; coarsely porphyritic dacites have plag + aug + bio ± opx ± hbl + fe-ti ox in a hyalopilitic groundmass. Chilled magmatic inclusions of basaltic andesite to andesite are abundant within the dacites, especially in upper parts of flows. In contrast, the intracaldera lavas (mostly dacites) lack a compositional range or temporal progression comparable to the extracaldera flows. They are less coarsely porphyritic than the extracaldera flows, have hornblende instead of biotite as the common hydrous phase, have a microgranular groundmass, and generally lack evidence for mingling/mixing of compositionally diverse magmas.

The intracaldera lavas are enriched in incompatible elements relative to most extracaldera flows of similar silica content (~60% SiO_2). This enrichment corresponds most closely to mixing models or models involving combined assimilation and fractional crystallization (AFC), in which the enriched endmember has trace-element characteristics like the Rock Creek lavas of the Conejos Formation or the Ra Jadero Member of the Treasure Mountain Tuff. These characteristics, in conjunction with proximity to the vents for the Rock Creek lavas and to the Summitville caldera, suggest that those Cat Creek magmas erupted within the Platoro caldera incorporated some earlier products of the magmatic system or associated hybridized crust. Isotopic compositions of Cat Creek lavas are consistent with this model. Intracaldera flows have isotopic ratios that become more radiogenic with increasing differentiation, shifting toward values similar to those of the Treasure Mountain Tuff, whereas extracaldera lavas have isotopic compositions suggesting extensive interaction with relatively non-radiogenic material (i.e., lower crust).

Return to vehicles; continue up Alamosa River road (west), traversing down-section through the La Jara Canyon tuff and into the Conejos Formation. **1.2**

91.6 Terrace Reservoir spillway. The dam is constructed around the terminal moraine of the main Wisconsin glacier. **1.4**

93.0 Terrace Reservoir overlook. Large roadcut exposure on right is La Jara Canyon Member, here somewhat altered and propylitized. Ahead, bluish-gray outcrops are underlying lavas of the Conejos Formation. **0.5**

93.5 Lavas of the Conejos Formation, and viewpoint of Terrace Reservoir laccolith. Basal and upper flow breccias, separated by thin interbeds of fine-grained volcanic sediments, are well exposed between several Conejos flows. About 100 m west along road, relatively mafic-appearing biotitic welded tuffs that underlie the upper lavas of the Conejos Formation are assigned to the lower member of the Treasure Mountain Tuff.

The Terrace Reservoir laccolith (Lipman, 1975a: 82) is a flanking dacite intrusion (64% SiO_2) related to the Cat Creek volcano; its base is visible in midslope as the overhanging roof of a cave. **2.0**

95.5 Phillips University Camp. Unmarked road to the right (north) leads to the base of a cliff of Conejos Formation, containing a lower sequence of clastic sediments, platey-plagioclase trachybasaltic andesite lavas of the Rock Creek member, additional clastic sediments, and capping lavas of the Willow Mountain member. This locality documents the laterally extensive nature of the stratigraphic sequence present in Rock Creek (Stops 1-2 through 1-5). **2.6**

98.1 **STOP 1-12. Alamosa River Guard Station; caldera-fill units at Platoro caldera.** Park on right, at Ranger Creek. Moat-filling sediments and tuffs are exposed in roadcuts along the incline which rises to the west for 200 m. These units are broadly equivalent to the middle member of the Treasure Mountain Tuff, and are overlain by dark, sparsely porphyritic lavas of the Summitville Andesite (lower member). Up the hill to northwest, these lavas are overlain by the Ojito Creek ash-flow sheet, here more than 200 m thick. These rocks are all banked against the eastern topographic wall of the Platoro caldera, which is exposed up-slope north-northeast of the vehicles.

High along the caldera wall are well-bedded welded ash-fall tuffs that agglutinated because of high-temperature emplacement. These must have erupted nearby to permit sorting, yet were deposited before cooling. In sedimentary intervals between flows of Summitville Andesite within the caldera, angular blocks of lava as much as 1.5 m across represent both ejected bombs showing breadcrust-jointed margins and other blocks that may have slid in from the caldera wall.

Two thick lava sequences of the lower member of the Summitville Andesite are preserved within the Platoro caldera: in the Alamosa River valley between Ranger Creek and the town of Jasper, and in the Platoro Reservoir area. Both sequences consist of high-K basaltic andesite and andesite, typically with sparse phenocrysts of plag + aug + opx ± ol. Lavas in the Alamosa valley overlie densely welded intracaldera La Jara Canyon Tuff and are intercalated with moat-filling sediments. Upper member lavas fill the Summitville caldera west of this stop. Basal lavas of the upper andesite are similar to those in the lower member, but higher flows are more porphyritic and contain phenocrysts of bio ± san. Stratigraphic boundaries between the two members of the Summitville Andesite are poorly known, because the two units are nearly indistinguishable in the field, and intervening units of the Treasure Mountain Tuff are only locally present to define stratigraphic position.

[Stop 1-12 coincides with Stop A4 of Optional field guide A. An alternate route, which connects with latter parts of Field guide 2 (mile 86.7), is to continue up Alamosa River, using Optional field guide A. This east–west transect through the Platoro and Summitville calderas examines relations between the volcanic fills of the two calderas, caldera structures, and associated intrusions and mineralization.]

Field guide 2: Conejos River and Platoro caldera to South Fork

Outflow ash-flow stratigraphy, caldera structure, and related mineralization

This segment of the field trip follows the Conejos River Canyon, providing a spectacularly exposed southeast–northwest cross section through the outflow volcanic field and the complex interior of the caldera. Leaving the caldera at its northwest rim, the trip passes by the recently reopened (1985) gold mine at Summitville, then descends along tributaries of the Rio Grande to South Fork, where outcrops are mainly of younger ash-flow sheets from calderas farther northwest in the central San Juan Mountains.

Mileage

0.0 **Begin trip** at junction of US-285 and CO-17, southwest of Antonito (2430 m), in Lower Conejos River Canyon map area (Lipman, 1975b). **Drive west** on CO-17.

Lava flows of Hinsdale basalt, from the 5 Ma Los Mogotes volcano to the north, dip gently eastward. Covered slopes beneath these lavas are the Los Pinos Formation. Los Mogotes ("the mounds," in Spanish) is a composite shield volcano. Three vent areas have been identified, including the main southern crater (on the skyline: 2993 m) and two smaller centers to the north (Flat Top and Cinder Pits). As many as 12 Los Mogotes lava flows crop out in cliffs above CO-17, 3 mi west of Las Mesitas. The lower Fox Creek valley, west of Los Mogotes, is incised in Los Pinos Formation. Below these poorly consolidated volcanic sediments, which range in age from 26 to 5 Ma and interleave with older lava flows of Hinsdale basalt, are the Masonic Park and Treasure Mountain Tuffs. **13.4**

13.4 Mogote Campground. Exposed at road level is the densely welded upper (Black Mountain) unit of the lower member, here at the base of the Treasure Mountain Tuff (compare with Stop 1-6; Road Log 1). Conejos Formation lavas and volcaniclastic rocks are exposed along the lower slopes of the Conejos valley and its tributaries for the next 50 km, from this area to the Platoro caldera wall. **8.9**

22.3 **STOP 2-1. McIntyre Peak section and Cumbres fault.** Pull off CO-17 200 m prior to junction with Platoro road (2640 m). The Cumbres fault runs through a side valley on the north wall of the Conejos Canyon, 500 m northwest of this stop. The Cumbres fault is the largest of several north-trending normal faults, related to development of the Rio Grande rift, that cut the eastward-tilted dip-slope of volcanic rocks as young as Hinsdale basalt in the southeastern San Juan field. Most of these normal faults are antithetic to the Rio Grande rift; they drop strata down to the west in opposition to the eastward dip of the volcanic rocks toward the rift. The Cumbres fault has about 900 m maximum displacement; it is traceable for at least 50 km, from north of the Alamosa River southward into New Mexico.

The promontory of McIntyre Peak to the south (3219 m) is underlain on its lower wooded slopes by lavas of the Conejos Formation and by a thick section of weakly welded, lithic-rich lower unit of the lower member of the Treasure Mountain Tuff (Fig. 2-1). Higher units of the Treasure Mountain are well exposed in the landslide break-away scar higher on McIntyre Peak. The first cliff above the trees on the north slope is the Black Mountain unit of the lower member (Stops 1-6, 2-4). The second cliff is the La Jara Canyon Member, and the dark overlying unit is an andesitic flow broadly equivalent to the lower member of the Summitville Andesite. Above this lava are nine densely to weakly welded ash-flow units, previously undivided as the middle member of the Treasure Mountain Tuff (Lipman, 1975a). The lower two units, here designated

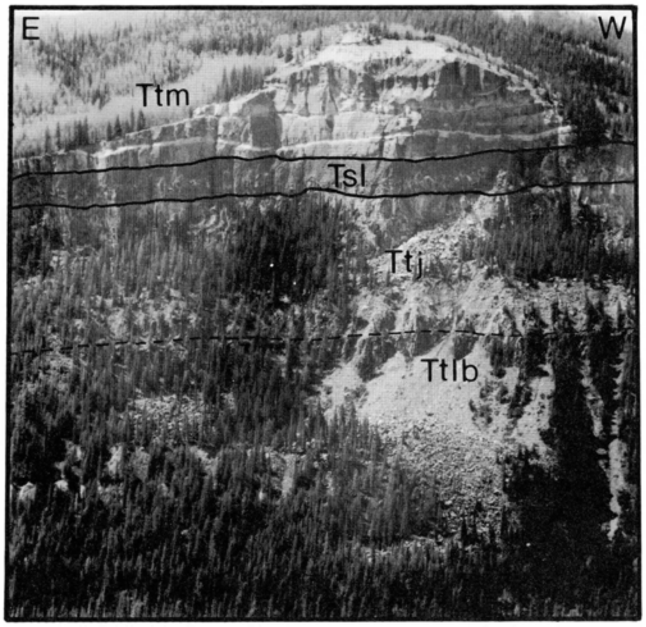

FIGURE 2-1—Treasure Mountain Tuff stratigraphy on McIntyre Peak, lower Conejos River valley. Exceptional north-facing exposures of tuff units on McIntyre Peak are present in a large Quaternary landslide scar. The two units of the lower member (Ttll, Ttlb) are overlain by the La Jara Canyon Member (Ttj) and an andesitic lava flow (Tsl; see also Fig. 2-2). Above this lava are eight units of the middle member (Ttm) separated by thin plinian-fall deposits (locally eroded by the passage of overlying pyroclastic flows). Contacts between units of the middle member are typically irregular; several of the units are compound. Only the lowest unit is densely welded (near its base).

La Manga units A and B, are moderately to densely welded ash-flow sheets of relatively small thickness and volume; they have reversed magnetic polarities and phenocryst compositions similar to the La Jara Canyon Member. The La Manga units have been recognized south of the Platoro caldera in lower La Jara Creek and in the Conejos valley (including McIntyre Peak), the Los Pinos area (Stop 2-2), Spruce Hole (Stop 2-3), and the Continental Divide east of the upper Chama basin. Over 80% of the volume of the middle member is represented by a dozen or more ash-flow sheets, mostly only slightly welded, that have petrologic affinities with both the Ojito Creek and Ra Jadero Members. These tuffs, collectively designated the Fox Creek units of the middle member, have the normal magnetic polarity of the overlying Ojito Creek, but paleomagnetic-pole positions vary substantially among successive units.

Lipman (1975a) inferred that the entire middle member of the Treasure Mountain Tuff postdated eruption of the intracaldera lower member of Summitville Andesite, based on local presence of andesite flows immediately above the La Jara Canyon tuff, as at McIntyre Peak. The close petrologic affinities of the La Manga units to the La Jara Canyon, along with paleomagnetic evidence, strongly suggest that these units represent continued eruptions from the La Jara Canyon magma chamber and predate the main body of lower Summitville Andesite. The La Manga and Fox Creek units will be examined at Stops 2-2 and 2-3.

Continue west on CO-17, past Platoro turnoff, toward La Manga Pass and Chama. **6.0**

28.3 Spruce Hole road. Continue ahead, over La Manga Pass (3125 m), and return to this turnoff for Stop 2-3. **3.2**

31.5 **STOP 2-2. Los Pinos** (abandoned townsite); **La Jara Canyon and La Manga Tuffs.** At the sharp curve, pull off paved road into a small quarry in La Jara Canyon tuff (2975 m). The La Jara Canyon here is typical densely welded and devitrified outflow tuff. Minor hornblende is present in this outcrop, which is near the top of the outflow sheet. Directly overlying the La Jara Canyon is the type locality for the two welded ash-flow sheets of the La Manga units of the middle member. The lower unit is a distinctive welded rhyolite (70% SiO_2) characterized by fiamme up to 60 cm long in an orangish-brown, lithic-rich matrix. Above this densely welded zone is a covered interval beneath the densely welded interior of the overlying unit. This second unit is markedly different; the fiamme are smaller and the lithics less abundant and smaller. These two units are also present at Stop 2-3 and on the Continental Divide (western horizon, as viewed up Rio de los Pinos—3577 m).

This locality is 30 km south of the southern topographic wall of the Platoro caldera, the nearest plausible eruptive source for these tuffs. The middle member (combined La Manga and Fox Creek units) reaches its maximum thickness, 150–200 m, at a distance of 25–30 km from the southern and southeastern caldera rim. This outward shift in the axis of deposition (i.e., circumferential thickening) led Lipman (1975a) to conclude that eruptions of the Treasure Mountain Tuff gradually built an ash-flow plateau around the southeastern side of the caldera complex. Cumulative filling of local topographic lows allowed the Ojito Creek and Ra Jadero Members to flow over nearly featureless topography.

Return to Spruce Hole road via CO-17 over La Manga pass. **3.2**

34.7 **Turn right** onto Spruce Hole road (USFS 108). Continue up hill on gravel road. **1.7**

36.4 **STOP 2-3A. La Manga Member and Conejos Valley overlook.** Park on left side of road, on curve. Walk 100 m northeast, to the edge of a bench (3200 m) overlooking the Conejos Valley. From this vantage point can be seen several high points on the Platoro caldera rim (Fig. 2-2). The bench is formed by the welded interior of La Manga ash-flow unit A. Its lithic-rich basal vitrophyre is exposed 10 m below bench level.

Return to vehicles. **Continue east. 0.3**

36.7 **STOP 2-3B. Fox Creek units.** Turn right onto side road and park. Hike south up through forest to small gully below steep exposures of nonwelded to partly welded tuffs (top of ridge 3304 m). The lowest exposed unit, La Manga unit B, has reversed magnetic polarity. The three overlying tuff sheets are Fox Creek units with normal magnetic polarities. These units correlate with only part of the sequence exposed at McIntyre Peak, illustrating the limited lateral extent of some individual flow units in the Fox Creek assemblage. The tuffs at this locality are

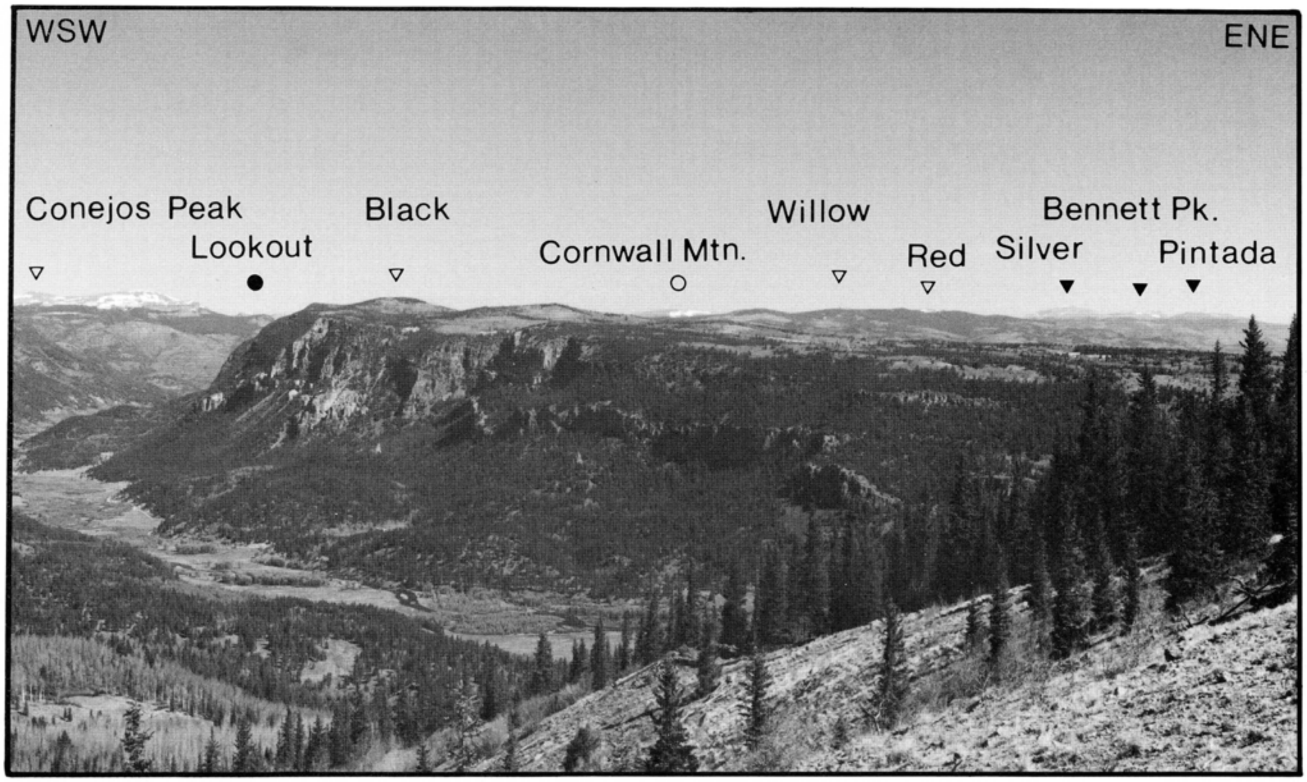

FIGURE 2-2—Panoramic view from Stop 2-3A north-northwest across the Platoro caldera. Symbols marking topographic features are coded for location relative to the caldera: open triangles, south of the caldera or along the southern margin; open circle, in the resurgent dome of the caldera; filled circle, near northwestern caldera margin; filled triangles, northeastern caldera margin. Conejos Peak (4015 m) and Willow Mountain (3629 m) are topographically high exposures of precaldera Conejos volcanoes, truncated during caldera collapse, which now mark the southwestern and southeastern margins of the Platoro caldera. Red Mountain (3663 m; small snow-capped peak behind Willow Mountain—see also Figs. 2-5, 2-8) lies just within the topographic margin of the caldera. Black Mountain (3382 m) is capped by Hinsdale basalt which overlies the Treasure Mountain Tuff (Fig. 2-3). North of Black Mountain, Treasure Mountain units wedge out against the rim of the caldera. South and east of Black Mountain, the Treasure Mountain section is typically 200–300 m thick (as far south as Cumbres Pass). The highest point on the resurgent block of the Platoro caldera is Cornwall Mountain (3744 m), a broad topographic dome capped by Hinsdale basalt (see also Fig. A-2). Structural relations of resurgence and petrologic aspects of intracaldera tuff are featured beginning at Stop 2-6. Lookout Mountain (3794 m) is capped by post-Treasure Mountain rhyolite lava erupted during the early Miocene transition from caldera-related volcanism to bimodal basalt–rhyolite rift-related Hinsdale volcanism. Bennett Peak and Pintada Mountain bracket the northeastern topographic wall of the Platoro caldera (Figs. 1-6, 1-7). Silver Mountain (Figs. 1-6, A-1) lies within the caldera and is capped by andesite of Green Ridge (post-Fish Canyon Tuff).

typical of many Fox Creek units. Thin pumice-fall deposits separate the three overlying flow units here; in other places, the fall deposits are missing and are presumed to have been eroded during the passage of energetic pyroclastic flows. The dark-gray ash-flow sheet midway up the slope contains mafic pumice clasts that are typical of many voluminous units of the middle member. Some mafic pumice clasts near the top of this unit approach 1 m in diameter. All these deposits are lithic-rich, and some units are heat-reddened at distances of more than 30 km from the Platoro caldera.

Return to CO-17. **2.0**

38.7 **Turn right** (north) on CO-17; return to Conejos valley and the Platoro road. **5.9**

44.6 Junction of CO-17 and Platoro road (USFS-250). **Turn left** (northwest) toward Platoro. **1.6**

46.2 Precambrian gneissic granite (1.45 Ga), exposed on both sides of the road (2650 m), demonstrates significant relief on the prevolcanic depositional surface, resulting from Late Cretaceous–early Tertiary (Laramide) uplift in the Southern Rocky Mountains. In contrast, west of the Continental Divide, the oldest exposed rocks beneath the volcanic field are upper Mesozoic sedimentary units of the San Juan Basin. **2.8**

49.0 **STOP 2-4. Black Mountain** (3382 m) **viewpoint** (Fig. 2-3). Cliffs in Conejos Canyon expose a thick and relatively complete sequence of Treasure Mountain Tuff (see Lipman, 1975a, fig. 21). Relations are complicated by three north-northeast-trending normal faults that parallel the Cumbres fault to the east. The largest of these occupies the sharp reentrant in the cliff southeast of this stop. The high northwest-facing cliff of La Jara Canyon Member is upthrown on the southeast side of this fault. The section of interest, to the north-northwest, lies above a lower slope of Conejos Formation volcaniclastic facies. See Fig. 2-3 and caption for stratigraphic details.

Continue up the Conejos valley, through lavas and clastics of the Conejos Formation at river level (Fig. 2-4A), and Treasure Mountain units capping the canyon rims. **8.0**

57.0 **STOP 2-5. The Pinnacles** (2850 m); **tuff of Rock Creek.** At this locality, the tuff of Rock Creek (Fig. 2-4B)—the only exposures known south of the Alamosa river—underlies virtually all the Conejos la-

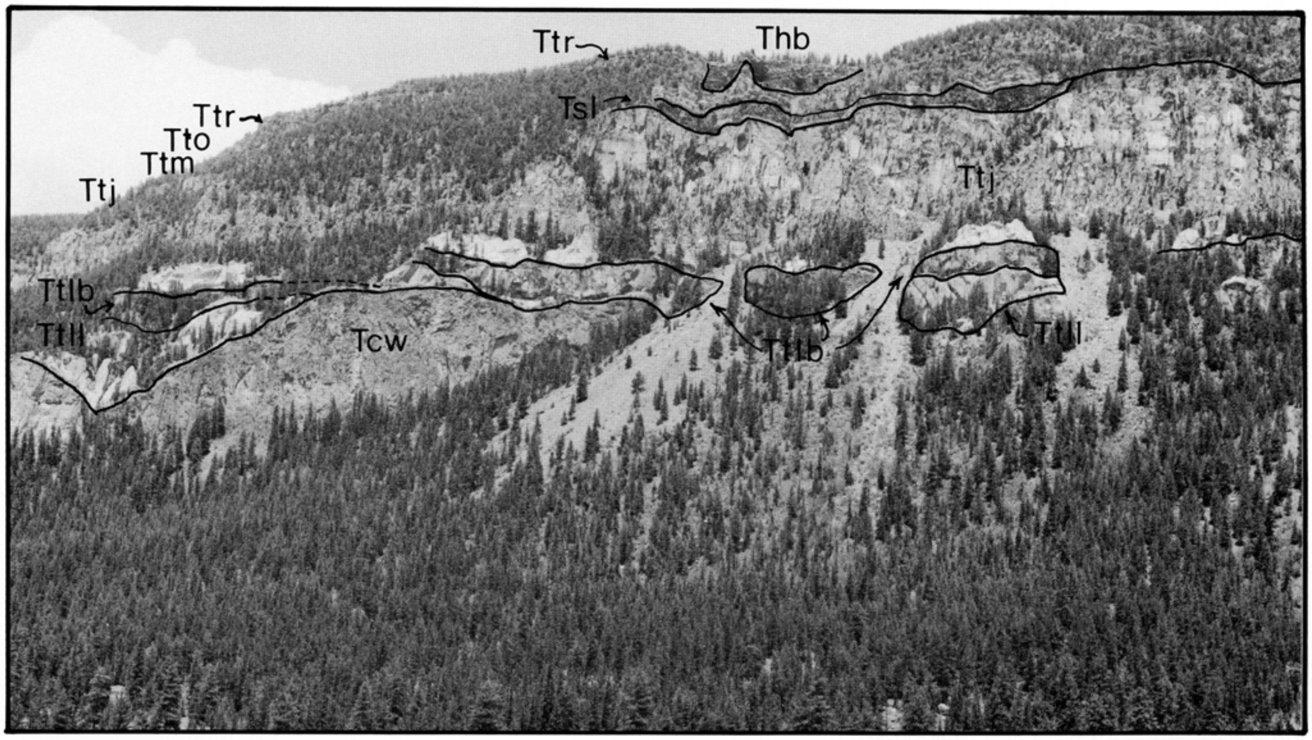

FIGURE 2-3—Treasure Mountain Tuff on cliffs southwest of Black Mountain in Conejos River canyon. A relatively complete section of ash-flow tuffs from both Platoro and Summitville caldera cycles is represented. The two units of the lower member (Ttll & Ttlb) are discontinuously exposed along the upper Conejos valley due to deposition on irregular topography. Valley-filling deposits of the lower unit (Ttll), a pale-tan nonwelded lithic-rich tuff, vary greatly in thickness. In the lower Conejos valley and in La Jara Creek, the lower unit is thicker and locally is densely welded. This is the type locality of the densely welded Black Mountain unit (Ttlb). Except for its greater thickness, it is identical in outcrop and petrographic features to the exposure at Stop 1-6. In the lower Conejos canyon, the Black Mountain unit is even thicker and more uniform in thickness. The prominent dark upper vitrophyre is easily distinguished from the gray devitrified interior of the unit. The outflow La Jara Canyon Member (Ttj) attains its greatest thickness (200 m) at this locality due to ponding in a broad depression south of the Conejos volcanoes that rim the southern Platoro caldera. To the south, the lower and middle members thicken substantially as the La Jara Canyon thins. Within the lower Conejos canyon, the La Jara Canyon Member and Black Mountain unit are comparable in thickness. Because of its great thickness here, the La Jara Canyon is devitrified to its base: a white, weakly welded zone is overlain by densely welded tuff (tan cliff) containing at least eight flow units. Above the La Jara Canyon Member is an andesite flow in the same stratigraphic position as at McIntyre Peak (Fig. 2-1); compositions are also similar. These flows are correlative with the intracaldera lower Summitville Andesite (post-La Jara Canyon and pre-middle member), but they are petrologically distinct from the intracaldera andesite. Local andesite dikes, obscurely exposed in gullies cutting the cliff wall, may be the feeders for these flows. Tuffs of the Summitville cycle exposed at the top of this section include one Fox Creek unit of the middle member, two flow units of the Ojito Creek Member, and the Ra Jadero Member (not differentiated in the figure). The single Fox Creek unit is a welded dacitic tuff of Ra Jadero affinity that pinches out 1 km to the south. This thin discontinuous section contrasts with the much thicker accumulations of multiple nonwelded to welded middle member units to the south in the lower Conejos valley and near Los Pinos.

vas high on the south rim of the Platoro caldera, demonstrating that these lavas are Willow Mountain member. The tuff is a phenocryst-poor trachydacite (K-rich plag + 2 pyx) characterized by high incompatible-element contents and large aphyric fiamme. Toward the southwest, along the South Fork of the Conejos River, are distinctively thick flows and domes (up to 300 m) of Willow Mountain lavas (Fig. 2-4C).

Continue north, toward Platoro, entering the Platoro caldera area map (Lipman, 1974). **6.1**

63.1 Beaver Creek (2950 m) marks the southern wall of the Platoro caldera (Fig. 2-5). The precaldera Conejos Formation consists mainly of poorly indurated clastic rocks, and the caldera fill includes clay-rich lake beds, which together account for the poor exposures on the caldera wall. Continue north through outcrops of caldera-filling dacite of Fisher Gulch which represents the first major postsubsidence lava eruption. The Fisher Gulch has a composition similar to the most mafic tuff of the La Jara Canyon Member and the La Manga units of the middle member. **4.7**

67.8 **STOP 2-6. Intracaldera La Jara Canyon Member** (3000 m). For the past mile, the road has passed through densely welded, propylitic, crystal-rich tuff of the intracaldera La Jara Canyon Member. In the southern part of the caldera, the tuff is strongly propylitized and therefore difficult to recognize as a pyroclastic rock. The intracaldera tuff exhibits distinctive slabby jointing that more closely resembles jointing in lavas than in outflow ash-flow sheets (Fig. 2-6). Such slabby jointing is common deep within caldera-filling ash-flow deposits in the San Juan field and elsewhere.

At this locality, porphyritic dacite (62–64% SiO_2) intrudes the intracaldera tuff; this intrusion is also exposed over an area of several square kilometers on the south ridge of Cornwall Mountain. The small road-level exposure of the intrusion contains rounded inclusions of vesicular andesite in the dacitic matrix, indicative of mingling of compositionally di-

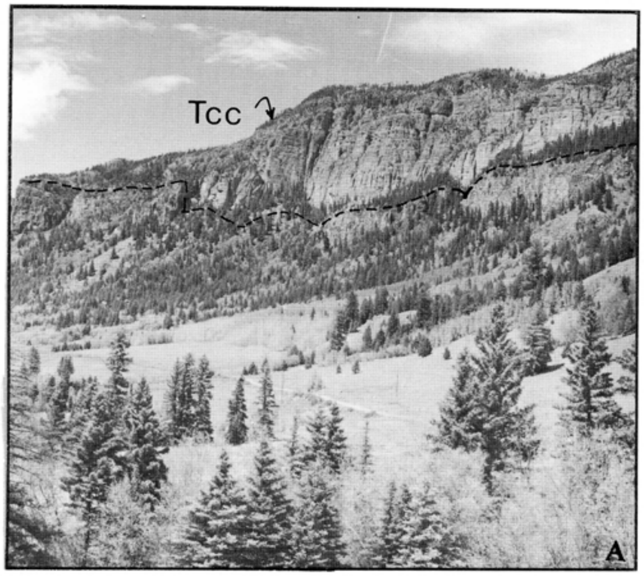

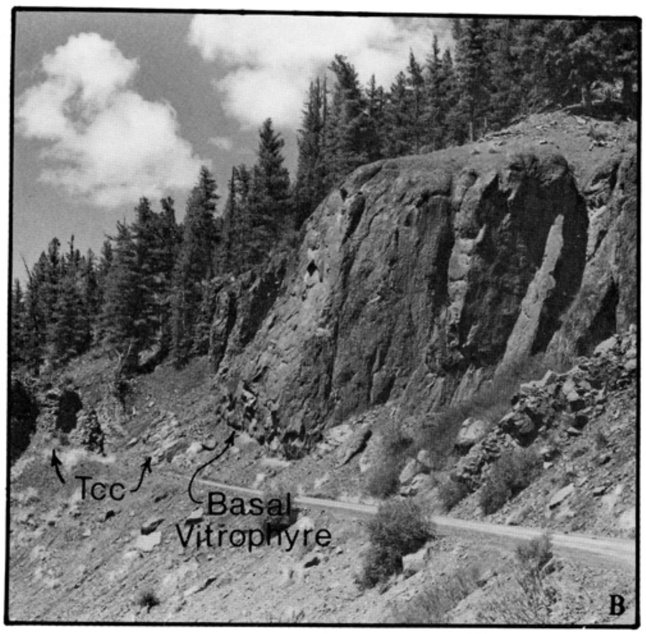

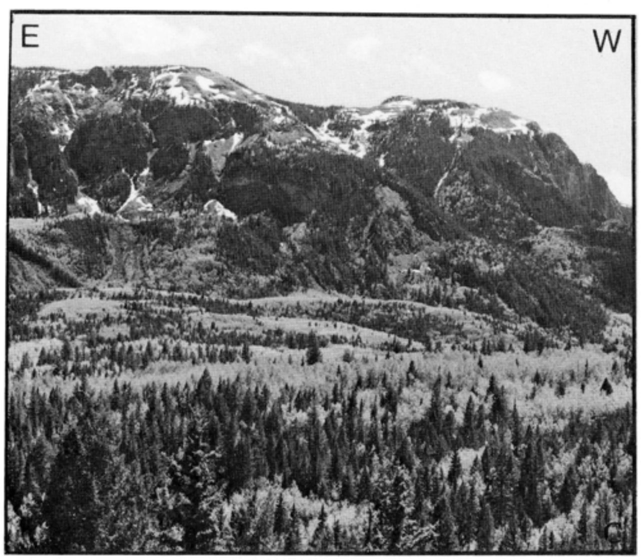

FIGURE 2-4—Precaldera stratigraphic features south of Platoro.

A, Interbedded lavas and volcaniclastic sediments of the Conejos Formation on the eastern wall of Conejos canyon between Stops 2-4 and 2-5. The lower cliffs are andesitic lavas of the Willow Mountain member. The overlying bedded clastic unit (Tcc) is a thick sequence of debris flows containing clasts that locally exceed 2 m. Coarse debris-flow deposits are characteristic of the clastic facies of the Conejos Formation south of the caldera.

B, Tuff of Rock Creek at The Pinnacles. The basal vitrophyre of a 20 m thick valley-fill deposit of this tuff is well exposed in the roadcut. Multiple-flow units have sparser lithic fragments than the proximal deposits in Rock Creek or north of the caldera. The Pinnacles are formed by resistant Conejos volcaniclastic units.

C, Conejos Formation stratigraphy, South Fork of the Conejos River. The South Fork flows eastward from the Continental Divide to join the main valley south of The Pinnacles. Lavas exposed in high cliffs along the lower South Fork are exceptionally thick andesite lava domes (to 350 m) of the Willow Mountain member. Two of these thick flows can be seen from The Pinnacles.

verse magmas. The exposed intrusion has been interpreted as the upper part of a larger body responsible for trap-door resurgent uplift of the Platoro caldera floor. East of this locality, the uplifted block of intracaldera La Jara Canyon is bounded by an arcuate fault (see Fig. A-2) that is thought by Lipman (1975a) to be a reactivted segment of the caldera ring fault (structural boundary; Optional Stop A3). The intracaldera tuff is more than 800 m thick on this uplifted block, with no base exposed, indicating ponding of the tuff within the caldera during subsidence.

Continue west past Platoro (last chance for gas for the next 50 mi). The Mammoth Revenue mine, on southwest side of the village, has been a gold producer intermittently over the past decade. This mine follows veins along northwest-trending faults and fractures that are discontinuously traceable 25 km northwest to Wolf Creek Pass. Mineralization occurs at three intersections of this regional fault zone with caldera structures, at the Platoro, Stunner, and Summitville districts. **1.4**

69.2 Intersection with Stunner Pass road. Turn left, toward Platoro Reservoir and Mix Lake. The road continues in La Jara Canyon Member for 1.5 mi. Shortly after turning southwest along the north shore of the reservoir, the road passes into basal flows of Summitville Andesite (lower member) and then into underlying moat-fill sediments containing plant fossils, which are well exposed in Rito Gato. Less than 0.5 mi past Rito Gato, the road returns to intracaldera La Jara Canyon tuff, close to its contact with underlying Conejos Formation along the caldera wall. **3.1**

72.3 **STOP 2-7. Intracaldera La Jara Canyon tuff.** Roadcuts in densely welded tuff near the basal contact reveal relatively nonpropylitized tuff with relict fiamme (Lipman, 1975a, fig. 17B). Note the low abundance and small sizes of lithic fragments. Despite features such as these, Larsen and Cross (1956) concluded that the intracaldera tuff was lava within the Conejos Formation. The history of genetic concepts concerning volcanic evolution in the southeast San Juan Mountains and implications for stratigraphic nomenclature are summarized by Lipman (1975a).

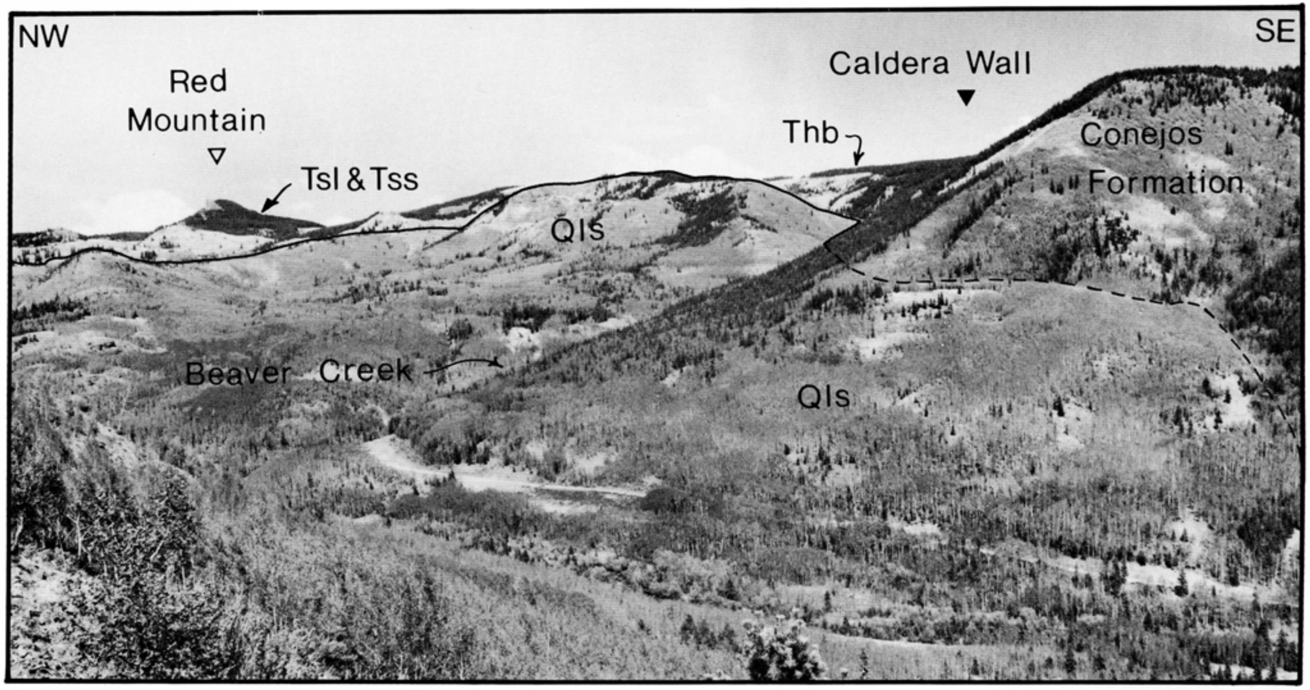

FIGURE 2-5—Structural and stratigraphic relations of the southern Platoro caldera wall near Beaver Creek (upper Conejos River, between Stops 2-5 and 2-6). Geologic relations are locally obscured on lower slopes of the Conejos valley by landslides. The unconformity between precaldera Conejos Formation rocks and caldera fill is exposed in the lower Lake Fork of the Conejos River, and can be inferred from features in this figure. This view is from a vantage point in clastic-facies Conejos Formation outside the caldera, looking northeast obliquely across the wall. This ridge, and high exposures of Conejos lavas and clastic rocks on the upper eastern slopes of the Conejos valley, lie just outside the caldera wall. Landslides comprising intracaldera sediments (Tss) and interbedded lavas of the lower Summitville Andesite (Tsl) have moved west and south into the Conejos canyon. This stratigraphy is present in place on Red Mountain. Basaltic lavas of the Hinsdale Formation (Thb: post-Treasure Mountain Tuff) have buried the contact between the precaldera lavas of Willow Mountain proper and the intracaldera units.

Continue west along the reservoir. **Bear left** at fork in road after 0.6 mi. **1.5**

73.8 **STOP 2-8. Basal vitrophyre of the La Jara Canyon Member. Turn left,** into the meadow at edge of the reservoir. The topographic wall of the Platoro caldera and the associated basal contact of the wedging intracaldera tuff run through the hill just east of the meadow. This contact relation is also well displayed across the reservoir on the lower slopes of Conejos Peak, where the La Jara Canyon tuff banks against the topographic wall (Fig. 2-7).

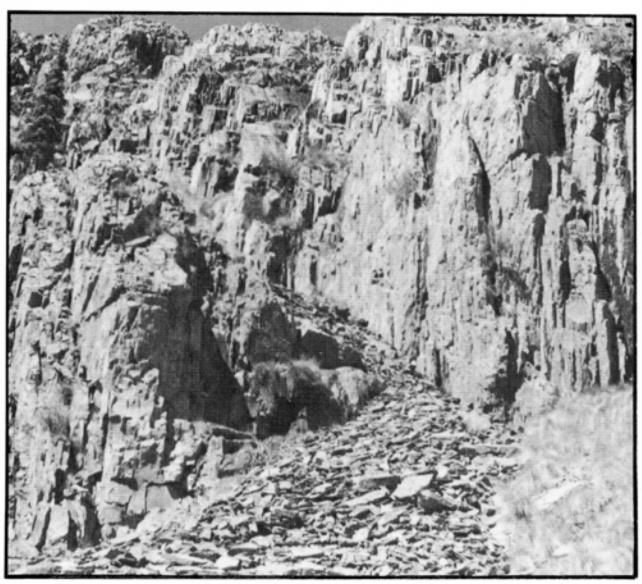

FIGURE 2-6—Jointing in intracaldera La Jara Canyon tuff. Closely spaced, slabby jointing is typical of densely welded and propylitized intracaldera tuff within the Platoro caldera (especially along the Platoro road between Fisher Gulch and Stop 2-6) and elsewhere in the San Juan volcanic field.

Walk downslope to water's edge (if reservoir is full), following a well-traveled trail. Near the bottom of the slope, exposures of a landslide-breccia deposit contain clasts of Conejos andesite. This breccia is thought to record syneruptive insliding from the oversteepened wall of the Platoro caldera, during subsidence along ring faults. Similar depos-

FIGURE 2-7—View of Conejos Peak from upper Platoro Reservoir, showing densely welded, cliff-forming ash-flow tuff of the La Jara Canyon Member (Ttj) within the caldera in depositional contact against the south caldera wall. All rocks at right side of photograph are lavas and breccias of the Conejos Formation (Tc). Top rim, above La Jara Canyon Member within the caldera, is intracaldera lava flow of the lower member of the Summitville Andesite (Tsl). Stop 2-8 (photo from Lipman, 1975a, fig. 63).

its are common within other San Juan calderas but are not exposed elsewhere within the Platoro caldera. On this basis, Lipman (1975a) concluded that the intracaldera La Jara Canyon tuff exposed here accumulated late during the eruption, and that any slide breccias resulting from early stages of caldera collapse remain buried within the caldera.

The next prominent outcrop east of the breccia is the only known vitrophyre exposure of intracaldera La Jara Canyon Member. It is more phenocryst-rich than typical outflow samples, but similar to most of the intracaldera tuff. In chemical and mineralogic characteristics, it represents more evolved magma than any other analyzed La Jara Canyon tuff, including outflow basal vitrophyres. This vitrophyre and a few other intracaldera-tuff samples contain sanidine phenocrysts, in contrast to the absence of this phase in all outflow basal vitrophyres. The biotite also has the highest Fe/Mg ratio of any La Jara Canyon sample. These compositional relations suggest early accumulation of this part of the intracaldera tuff, rather than late deposition as inferred by Lipman (1975a), assuming that a normally zoned magma chamber drained systematically from the top down. The presence of hornblende and a second population of biotite high in the La Jara Canyon outflow sheet is in accord with such a zonation. If this part of the intracaldera tuff erupted early, the slope against which it is banked must have existed prior to, or formed during, the earliest stages of caldera collapse. This dilemma has not been resolved.

Return to road; turn right. Watch for turnoff to Rito Gato road on left. **1.0**

74.8 **Sharp left turn** onto Rito Gato road. Continue uphill through lavas of the lower Summitville Andesite. **0.9**

75.7 **STOP 2-9. Lower member of the Summitville Andesite.** The roadcut exposes typical 2-pyroxene plagioclase andesite that is characteristic of both the lower and upper members of the Summitville Andesite. The lavas here correlate with flows across Platoro Reservoir, on the south slope of Conejos Peak.

Summitville Andesite and dacite of Park Creek

The two members of the Summitville Andesite represent the repeated return of the magmatic system to dominantly mafic volcanism following the climactic ash-flow eruptions which formed the Platoro and Summitville calderas. Lower member lavas, which partly fill the moat of the Platoro caldera, range from basaltic to silicic andesite (54–61% SiO_2; mostly 55–58%). The most common phenocryst assemblage in the lower member is plag + aug + opx ± fe-ti ox, but basaltic andesite commonly contains sparse olivine (now variably altered). Geochemical and petrographic variations in the lower member indicate that these lavas likely were derived from several magma chambers, rather than recording a single differentiation history. Although the basal flow overlying La Jara Canyon tuff near the Platoro reservoir dam is the most mafic Summitville lava, the lower member does not progress in any simple way toward more evolved compositions with time, suggesting episodic replenishment by mafic magma. Most Summitville lavas exposed here and in the Alamosa valley are distinct from those in the lower Conejos valley.

The upper Summitville Andesite, which fills the Summitville caldera, is more silicic than the lower member; compositions range from basaltic andesite to dacite (54–66% SiO_2). Lavas become more porphyritic and more evolved in composition up-section, and the typical mineralogy of plag + aug + opx is replaced by plag + aug ± bio ± san. Northwest of the Summitville caldera in Park Creek, and within the Summitville caldera north of the Wightman Fork of the Alamosa River, upper member lavas become coarsely porphyritic upward, and are overlain by the compositionally and mineralogically similar dacite of Park Creek. Though broadly contemporaneous with, and mineralogically similar to, extracaldera dacites of Green Ridge, the dacite of Park Creek differentiated separately as evidenced by its more radiogenic isotopic ratios and different trajectories on many chemical covariation diagrams.

Return to Mix Lake and Stunner Pass road. **5.1**

80.8 Stunner Pass road. **Bear left** and continue uphill toward Stunner Pass (3200 m). **2.7**

83.5 **STOP 2-10. Potosi overlook.** Intensely altered Summitville Andesite and Alamosa River stock form the lower southern slopes of Lookout Mountain (3794 m) and, to the east, Elephant Mountain (3605 m). Lookout Mountain is capped by the unaltered 22 Ma rhyolite lava (71–72% SiO_2) of Cropsy Ridge, and the crest of Elephant Mountain is occupied by vent breccia of an undated (Miocene) silicic rhyolite dome (76.5% SiO_2) of the Hinsdale Formation. The pyritic and alunitic alteration is overprinted on the north margin of the composite Alamosa River stock, for which several phases have yielded ages of 29.1–26.2 Ma. This episode of alteration is overlapped 3 km north-northwest of Lookout Mountain by 23 Ma alteration associated with emplacement of the South Mountain lava dome and associated Au–Cu ores at Summitville (Stop 2-6).

Continue downhill into the Alamosa River valley, cross river, and proceed to intersection of Alamosa and Summitville roads. **1.9**

85.4 Intersection with Summitville road (left fork) and Alamosa River road (right fork, down river to Chiquito Peak, etc.). The Summitville road (this log) leads north, out of the Alamosa River, past Summitville, to Park Creek and South Fork. This route provides access to another Platoro caldera wall locality, several units of postcollapse lavas, the Summitville mining district, and outflow tuff sheets from the central San Juan caldera cluster.

Optional field guide A continues down the Alamosa River, focusing on the intracaldera intrusions, stratigraphic and petrologic features of the Summitville Andesite, and structural features of the Summitville and Platoro calderas. It merges with Field guide 1 at Stop 1-12.

Turn left onto the Summitville road, pass Stunner Cabin, and continue along lower slopes of Lookout Mountain (3794 m) consisting of intensely altered Summitville Andesite. **4.3**

89.7 **STOP 2-11. Caldera wall at Prospect Mountain.**

The road circles around the north side of Lake De Nolda (3290 m). Park vehicles at pulloff near the Summitville turnoff (please respect private property).

View of the western topographic wall of the Platoro caldera (Fig. 2-8) on the southern slope of Prospect Mountain (3732 m) is one of three localities where caldera-wall relations are well exposed and observable from roads (also Stops 1-12, 2-8). Volcaniclastic rocks and lavas of the Conejos Formation and lower member tuffs of the Treasure Mountain are truncated at the caldera wall; outflow La Jara Canyon Member is draped over the wall, with compaction dips as steep as 60°, and grades into intracaldera tuff. Within 300 m of the caldera wall, the La Jara Canyon tuff is overlain by intracaldera tuffaceous sediments and upper Summitville Andesite which fill the Summitville caldera. View east, across Lake De Nolda, is toward Lookout Mountain (3974 m), where an unaltered capping rhyolite flow of Cropsy Ridge (22 Ma) overlies altered Summitville Andesite.

Bear right. Follow Summitville road, climbing up-section through Conejos Formation, lower member and La Jara Canyon Member of the Treasure Mountain Tuff, and into upper Summitville Andesite outside the caldera complex. **3.6**

93.3 **STOP 2-12. Porphyritic dike of silicic dacite.** Park at sharp bend in road at the northwest margin of Schinzel Meadows. This thick dike, dated at 26.2 Ma, is distinguished from older postcaldera porphyritic dacite and silicic dacite by the presence of phenocrystic quartz and coarse, mantled (rapakivi) sanidine (Lipman, 1975a, fig. 51). It is broadly equivalent in age and composition to the extrusive silicic dacite of South Mountain. None of the Oligocene units related to the Platoro–Summitville magma system contains quartz. This dike trends west-northwest, parallel to dikes of similar composition exposed intermittently from Prospect Mountain to the Continental Divide.

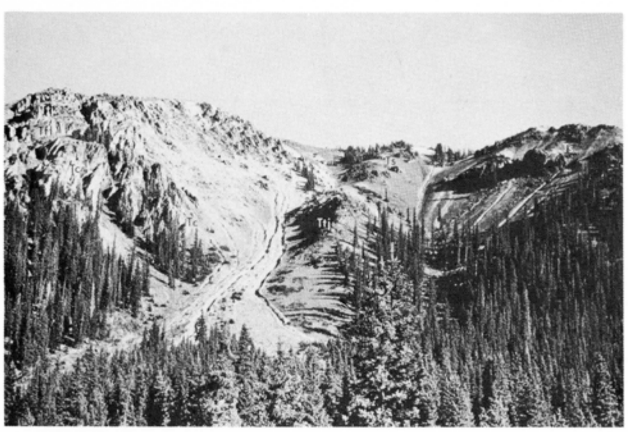

FIGURE 2-8—South slope of Prospect Mountain above Lake de Nolda, showing depositional relations at west wall of Platoro caldera. Subhorizontal units of Conejos Formation (Tc) and lower tuff member (Ttl) of Treasure Mountain Tuff are truncated by topographic wall of caldera, over which La Jara Canyon Member (Ttj) is draped. Compaction foliations in the La Jara Canyon are as high as 60° on steepest slopes. Inside the caldera, subhorizontal dark lavas of the Summitville Andesite (Ts) lap out against the dipping welded tuffs of the La Jara Canyon Member. Stop 2-11 (photo from Lipman, 1975a, fig. 64).

Continue ahead to Elwood Pass. **1.2**

94.5 **STOP 2-13. Dacite of Park Creek,** at Elwood Pass Guard Station (3520 m). Postcaldera flows of upper Summitville Andesite, exposed downslope below cabin, are overlain here by thick porphyritic flows and domes of Park Creek dacite (60–67% SiO_2), characterized by phenocrysts of plag + aug + hbl ± bio. Park Creek lavas are broadly correlative with the dacite of Green Ridge, but they show less incompatible-element enrichment than many Green Ridge lavas. In addition, Park Creek lavas lack the evidence for mixing that is common in Green Ridge lavas.

Continue ahead; roadcuts for next 3 mi are in lavas of Park Creek dacite. **1.2**

95.7 Pass at head of Park Creek, a tributary of the South Fork of the Rio Grande. **2.1**

97.8 Junction of Park Creek and Summitville roads. **Turn right.** Porphyritic silicic dacite lava flows exposed along road are part of the ring-dome complex along the northwest rim of Platoro caldera. **0.8**

98.6 Summitville Pass. To the east, the Wightman Fork drainage empties into Alamosa River west of Jasper. North Mountain (3879 m) at 12:00 and South Mountain (3827 m) at 3:30 are porphyritic silicic dacite lava domes. The road crosses the northwest-trending Summitville fault; porphyritic silicic dacite is dropped down on the west side of the fault, against intracaldera lavas of Summitville Andesite. **1.9**

100.5 **STOP 2-14. Summitville mining district** (partly based on material provided by R. Stoffregen). Discovery of gold in the Summitville area in 1870 and in the Silverton area in the same year led to the first successful mining ventures in the San Juan Mountains. The gold–silver–copper ore at Summitville occurs in a shallow volcanic environment within the South Mountain volcanic dome of coarsely porphyritic silicic dacite, located approximately on the northwest rim of the Platoro caldera. The ore occurs in intensely altered pipes and irregular tabular masses of quartz–alunite–pyrite rocks that replaced the silicic dacite along northwest-trending fracture zones. Ore minerals, chiefly pyrite and enargite, fill irregular vugs that formed by local intense leaching of the quartz–alunite rock. The quartz–alunite masses are surrounded successively by soft, argillically altered envelopes (illite–kaolinite zone) and by pervasively propylitized rocks (montmorillonite–chlorite zone). The alteration is interpreted to have resulted from shallow solfataric activity. Several exploration programs in the 1960's and 1970's resulted in intermittent reopening of the mines. Total production prior to 1975, of about $7,500,000, was mostly from gold (Steven and Ratté, 1960; Lipman, 1975a).

In 1985, a bulk-tonnage gold open-pit operation was begun by Galactic Mining Co., with recovery by heap-leaching methods. Present production (1987) involves moving about 60,000 tons of ore (0.04 oz/T Au) per day, yielding about 80,000 oz/yr of gold (Enders and Coolbaugh, 1987; Stoffregen, 1987).

The open pit is worked only in the summer months, but leaching operations continue year-round.

Most of the gold mineralization (>0.05 oz/T) occurs in vuggy silica rocks, although the current mining operation is also recovering lower-grade ore from the enclosing alunitic and illitic alteration zones. The vuggy silic rocks are best developed within 100–200 m of the surface and appear to grade downward into better defined but more restricted vein structures. Most of the ore mined at Summitville has been from the oxidized zone, which extends to depths of 50–100 m. In this zone native gold is intergrown with goethite, hematite, and local barite and jarosite. Beneath the oxidized zone, gold occurs with covellite, enargite, and luzonite. Sphalerite, galena, hinsdalite, marcasite, native sulfur, and chalcopyrite occur locally in the assemblage. A deeper tennantite–chalcopyrite assemblage does not appear to contain appreciable gold (Perkins and Nieman, 1982).

Both the geology and geochemistry of the Summitville deposit point to a close affinity with magmatic activity. Radiometric dating of alunite from the deposit indicates that it was contemporaneous with crystallization of the dacite lava dome (Mehnert et al., 1973). This temporal relation is consistent with the alteration patterns, which reflect acidic conditions probably produced by influx of magmatic SO_2. Ore deposition appears to postdate the acid-leaching event, though, and was associated with less extreme chemical conditions.

Retrace route to Park Creek Road. **0.8**

101.3 High peaks ahead to the west on the Continental Divide are Summit (4045 m) on left and Montezuma (4008 m) on right. These peaks consist of andesitic lavas overlying Masonic Park Tuff. Though stratigraphically higher, these andesites are broadly petrologically similar to the intracaldera Summitville Andesite that filled the Platoro caldera and overflowed to the west. **1.8**

103.1 Junction Park Creek Road; **continue straight ahead. 0.2**

103.3 Roadcut in late lavas of porphyritic silicic dacite on northwest rim of Platoro caldera. At 10:00, the light green cliffs are a vent–cone complex that was a source for some of the late rim lavas. At 12:00 on the horizon, Mount Hope (3911 m) and Sawtooth Mountain (3842 m) are within the Mount Hope caldera, source of the Masonic Park Tuff. Continue through porphyritic silicic dacite, moraine, and landslide for the next 5 mi. The rim on this side of the Platoro caldera is mostly covered by postcollapse lavas. **3.9**

107.2 Handkerchief Mesa ahead is capped by Hinsdale basalt flows. The flows are underlain by Fish Canyon and Carpenter Ridge ash-flow tuffs from the La Garita and Bachelor calderas, respectively. These calderas are located to the northwest, in the central San Juan caldera cluster. The capping Hinsdale flow on Handkerchief Mesa is a part of a mixed lava complex described by Thompson and Dungan (1985). **1.3**

108.5 Roadcut on right is through a pinkish altered tuff, at the contact between nonwelded to partly welded Masonic Park and overlying partly welded basal Fish Canyon Tuff. The Fish Canyon (27.75 Ma) is a phenocryst-rich silicic dacite tuff (66–68% SiO_2) superficially similar to the Masonic Park Tuff. The two are distinguished by phenocrysts, magnetic polarity, and xenoliths. Both contain plagioclase and biotite phenocrysts, but the Fish Canyon has sparse hornblende, quartz, sanidine, and sphene, while the Masonic Park has abundant clinopyroxene (where unaltered). The Fish Canyon Tuff has normal magnetic polarity; Masonic Park has reversed polarity. Xenoliths are more abundant in the Masonic Park Tuff. **1.0**

109.5 Roadcuts on right are in Carpenter Ridge Tuff, a phenocryst-poor rhyolite (73% SiO_2) erupted from the Bachelor caldera at 27.5 Ma, containing phenocrysts of sanidine, plagioclase, and biotite. **0.2**

109.7 Porphyritic platey-plagioclase andesite flows and breccias (Huerto Formation of Larsen and Cross, 1956), between Carpenter Ridge and Fish Canyon Tuffs. These andesite flows petrographically resemble mafic flows of the Rock Creek unit in the older Conejos Formation (Stop 1-5). **1.1**

110.8 Junction with Lost Mine Creek Road; **continue ahead.** Outcrops ahead are Fish Canyon Tuff and glacial outwash. **0.9**

111.7 Roadcut on left on Masonic Park Tuff underlying Fish Canyon Tuff. The wall of the Mount Hope caldera is west of these outcrops, but is buried beneath thick Fish Canyon Tuff. **2.9**

114.6 Roadcut on right in Fish Canyon Tuff. In this area, the road is near or just inside th east rim of Mount Hope caldera. This caldera was the source of the Masonic Park Tuff and later was almost entirely filled and buried by Fish Canyon Tuff from the La Garita caldera. Entering South Fork area map (Lipman and Steven, 1976). **1.0**

115.6 Cattle Mountain road (USFS-361); **turn right** on this side road. Road switchbacks through upper part of the Fish Canyon Tuff and several andesitic flows and flow breccias of the Huerto Formation, to the base of the Carpenter Ridge Tuff. **1.4**

117.0 **STOP 2-15. Basal Carpenter Ridge Tuff.** Park cars and walk up road through the section. The basal vitrophyre of the Carpenter Ridge, several meters thick here, is phenocryst-poor low-silica rhyolite (73% SiO_2, anhydrous); it grades downward, through partly welded gray tuff, to nonwelded white tuff. The vitrophyre is abruptly overlain by tan devitrified rhyolitic tuff. Gas cavities (lithophysae) several centimeters in diameter near the top of the vitrophyre were nuclei for devitrification, resulting in growth of spherulites surrounding the gas cavities. Outflow Carpenter Ridge Tuff commonly has a conspicuous lithophysal zone in the interior of the devitrified zone, but here they are developed atypically low in the section. These blotchy pale-tan exposures of devitrified Carpenter Ridge also are anomalously bleached and weakly argillically altered, in comparison to more typical light pinkish-brown rhyolitic Carpenter Ridge Tuff present nearby. The cause of alteration is unknown.

Either continue up the road on foot, or drive about 0.4 mi to upper roadcuts of Carpenter Ridge. These exposures are more lithic and phenocryst-rich; they contain conspicuous dark scoriaceous fiamme (Fig. 2-9), in addition to phenocryst-poor rhyolite pumices (Lipman, 1975a: 49–53). The scoriaceous fiamme are andesitic in composition (61–63% SiO_2), exceptionally high in Ba (up to 8000 ppm), and are interpreted as documenting magma mixing just prior to, or during, the Carpenter Ridge eruptions (Whitney and Stormer, 1988).

Return to Park Creek road. **1.4**

118.4 Park Creek road. **Turn right** (northwest); continue down valley. **0.4**

118.8 Corral Park Road (USFS-381) on left. **2.6**

121.4 Bridge over South Fork of Rio Grande and junction with US-160. **Turn right.** Continue through exposures of thick Fish Canyon Tuff. To the west along US-160, exposures to the summit of Wolf Creek Pass are mostly Fish Canyon Tuff, ponded within the Mount Hope caldera. **1.6**

123.0 Enter Rio Grande County; leave Mineral County. **1.8**

124.8 Highway Spring Campground on right. Masonic Park Tuff exposed along road on left, below higher cliffs of Fish Canyon Tuff. Numerous northwest-trending faults between here and South Fork define a complex graben system. **1.3**

126.1 South Fork Campground. Cliffs of Fish Canyon Tuff on left. **1.3**

127.4 **STOP 2-16. Base of Fish Canyon Tuff.** At curve to left, park on right (east side) of road. **Caution: high-speed traffic.**

Large-scale base-surge deposits, present at the base of the Fish Canyon Tuff, overlie gray nonwelded tuff of uncertain association (Fig. 2-10). The basal tuff may be a winnowed upper part of the Masonic Park Tuff or some local unit of unknown significance. The large-scale crossbeds are only about 5 km from the rim of the source La Garita caldera (Self and Wright, 1983). Consider whether some beds may represent draped air fall; examine overlying welded Fish Canyon Tuff for characteristic mineralogy. **0.3**

127.7 Beaver Creek Road on right. Continue straight ahead. **1.0**

FIGURE 2-9—Mafic scoria near top of Carpenter Ridge Tuff, on Ribbon Mesa (Stop 2-15).

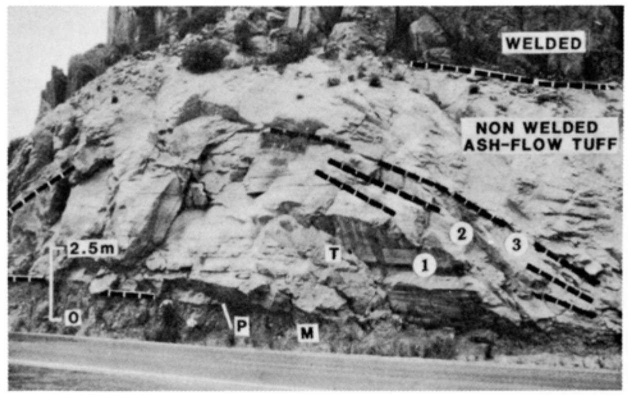

FIGURE 2-10—Surge-bedded basal Fish Canyon Tuff near South Fork (Stop 2-16). From Self and Wright (1983).

128.7 Entering South Fork, Colorado. Palisades to the west at 3:00 (up Rio Grande Valley) are Masonic Park and Fish Canyon ash-flow tuffs. In this area the Rio Grande follows the graben system previously mentioned. Fish Canyon Tuff on the south side of the river is dropped down against Masonic Park Tuff on the north. The low cliffs on the right across the South Fork are Conejos breccias overlain by Masonic Park Tuff. The Treasure Mountain Tuff that occurs between these two units to the south and east is not present this far northwest.

Optional field guide A: Down Alamosa River, from Stunner to Ranger Creek

West–east traverse through interior of Platoro caldera

Distance 12.8 mi (beginning at mile 86.7, Field guide 2)

This supplemental field guide, connecting between guides 1 and 2, examines relations between the volcanic fills of Platoro and Summitville calderas, caldera structures, and associated intrusions and mineralization.

Mileage

0.0 Junction of Summitville and Stunner Pass roads (mile 86.7, Field guide 2); head downstream (east) on Alamosa River Road. For the next 2 mi, road generally follows variably altered northern margin of the 29 Ma Alamosa River stock. **0.1**

0.1 Bridge over Alum Creek. Area of intense hydrothermal alteration to the north is in Alum Creek porphyry, a younger, more silicic phase (64% SiO_2) of the Alamosa River stock. Kaolinite and quartz–sericite alteration of the Alamosa River stock is evident along the road for the next mile. **1.1**

1.2 **STOP A1. Alamosa River stock.** Bridge over Bitter Creek. Pull off to the left, past the bridge. First outcrop to the east is a relatively unaltered dioritic phase of the Alamosa River stock (57% SiO_2). This pluton is thought to be the solidified top of the magma chamber which produced the Summitville Andesite (Lipman, 1975a). Because the present topographic highs along the ridge crest to the south, such as Klondike and Telluride Mountains, consist of this stock, a large overlying volcanic edifice of Summitville Andesite and associated lavas is inferred to have been removed by erosion.

Blocks of glassy and devitrified high-silica rhyolite of the Hinsdale Formation, from the Elephant Mountain dome upstream, can be examined in the stream gravels. The Miocene Hinsdale Formation contains minor silicic rhyolite of this type in the Platoro area, in association with volumetrically dominant lava flows of trachybasalt and trachybasaltic andesite. Hinsdale rhyolites (>76% SiO_2) characteristically contain phenocrysts of a single feldspar (sodic sanidine) and quartz.

Continue east through variably altered Alamosa River stock. At the east end of Government Park, the road enters Summitville Andesite (upper member) and remains in it for about 4 mi. **0.9**

2.1 View of Lookout Mountain (3794 m) to northwest. Caprock is unaltered 22 Ma rhyolite of Cropsy Ridge (71% SiO_2). These rocks unconformably overlie solfatarically altered rocks of the Summitville caldera. **1.1**

3.2 Canyon of Wightman Fork of Alamosa River exposes thick intracaldera flows and breccias of dark nonporphyritic Summitville Andesite (upper member).

Along road ahead and low on south side of Alamosa River are andesite lavas inside the younger Summitville caldera. Upper slopes are intracaldera tuffs of La Jara Canyon Member on upthrown side of Cornwall fault. The arcuate Cornwall fault is inferred to represent a segment of the ring fault of the Summitville caldera, occupied to the west by the Alamosa stock and to the east by the Jasper intrusive complex. This younger caldera is considered to be the source for the Ojito Creek and Ra Jadero Members. **2.5**

5.7 **STOP A2. Summitville Andesite, Jasper mining district.** Park cars at small roadside borrow pit adjacent to meadow, 1 mi west of Jasper; walk up into meadow about 50 m for a better view. Directly to the south, Cornwall's Nose (3549 m) forms promontory above steep cliffs of massive andesite flows and breccias of Summitville Andesite (upper member) within Summitville caldera. The Cornwall fault, passing through Cornwall's Nose, has dropped the Summmitville Andesite down against intracaldera La Jara Canyon tuff, indicating movement related to uplift of the resurgent block within the Platoro caldera, and perhaps also to some continued subsidence in the Summitville caldera during accumulation of the andesite sequence. The Summitville fault curves northward and intersects the similarly reactivated southeastern boundary fault of the Platoro caldera (California Gulch fault) near the townsite of Jasper.

This fault intersection localized a composite intrusion which produced the widespread intense alteration and local mineralization of the Jasper mining district. Alteration of the lower Summitville Andesite is prominent on the lower slopes of Silver Mountain (3786 m), due east of this viewpoint (Fig. A-1). Altered lavas below an unconformity are overlain by unaltered andesite flows on Silver Mountain (andesite of Green Ridge). The volcanics of Green Ridge overlie the Fish Canyon Tuff and were erupted from the Cat Creek volcano farther east. This area exemplifies the close association between zones of alteration (and mineralization) and fault intersections, particularly caldera-boundary faults, in the Platoro–Summitville area (Lipman, 1975a: 113).

Continue ahead, down canyon. **1.1**

6.8 **STOP A3. Structural boundary of Summitville caldera.** Take Forest Service trail on the right (south). Leave cars on road, pulling off to right as far as possible, and walk down to Alamosa River. The Cornwall fault, following the main gully ahead, defines the southern structural boundary of the Summitville caldera. Southeast of the fault, propylitized La Jara Canyon Member extends from valley level to the top of Cornwall Mountain (3745 m). Though the base of the La Jara Canyon is not exposed, a typically thick intracaldera accumulation of 800–1000 m is exposed. On the northwest side of the fault, Summitville Andesite is preserved to the top of Cornwall's Nose.

The small adit and dumps across the river to the east, part of the workings of the Miser mine, are

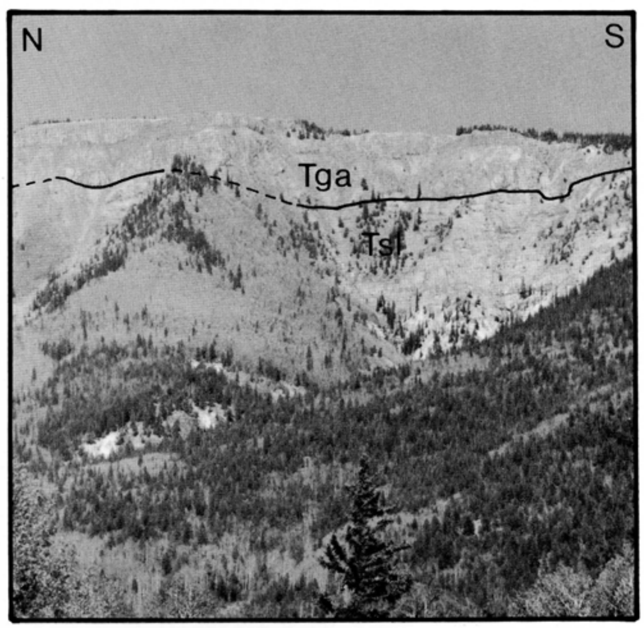

FIGURE A-1—View of the west face of Silver Mountain from Stop A2. Prominent on the cliff exposures is the unconformity between altered lavas of the lower member of the Summitville Andesite and thick overlying andesite lavas of Green Ridge (unaltered). This relation dates the alteration and mineralization of the Jasper district as pre-Green Ridge.

in a monzonite porphyry intruded along the Cornwall fault zone. The Miser mine was opened and most of the development work done in the 1880's. The main tunnel extends about 700 ft directly into the mountain side, and apparently intersected the Cornwall fault, along which the richest ore was found—vein quartz with gold stringers.

Continue east. 0.9

7.7 Jasper. Town was founded and mining began about 1874–1875. The largest workings were mainly along the south side of the Alamosa River, along the structures and alteration related to the southeast rim of the late collapse structure of the composite Platoro caldera (Fig. A-2). Small amounts of rich gold–silver ore were produced from quartz–pyrite veins, with associated sphalerite and galena (Patton, 1917). Production, mostly or entirely before the area was studied by Patton in 1913, was apparently small and complicated by acidic mine waters. **0.5**

8.2 Fern Creek. Cliffs above road, on right just before creek, are stratified tuffaceous sandstones between the La Jara Canyon Member of the Treasure Mountain Tuff and overlying intracaldera andesitic lava flows. **0.9**

9.1 **STOP A4. Top of intracaldera La Jara Canyon Member.** Small outcrops of reddish-brown, densely welded tuff along the road are overlain by intracaldera flows that dip to the east away from the resurgent core of the caldera. The reddish color here is characteristic of the upper 50–100 m of intracaldera La Jara Canyon, and changes to grayish-green propylitic hues lower in the tuff section. Small lithic fragments are present, but collapsed pumice fiamme are obscure. Intracaldera tuffs are exposed at higher elevations south of the river (nearly to the top of Cornwall Mountain), because of resurgent uplift along the fault near base of the mountain.

Continue east, through caldera-filling lavas of lower Summitville Andesite. **1.1**

10.2 Silver Creek. On north side of road, bedded tuffaceous sandstone, similar to that at Stop 1-12 (Field guide 1), is interlayered with andesitic lava flows. Across the river at 10:00, the large mountain mass (Cornwall Mountain) is mainly La Jara Canyon Tuff in the structurally uplifted central part of the caldera. **2.4**

12.6 Intracaldera flows of Summitville Andesite on right. Large landslide across Alamosa River to south. **0.2**

12.8 East margin of Platoro caldera. Same locality as Stop 1-12 (Field guide 1, mile 98.1). **Continue down valley,** to return to Monte Vista or Alamosa.

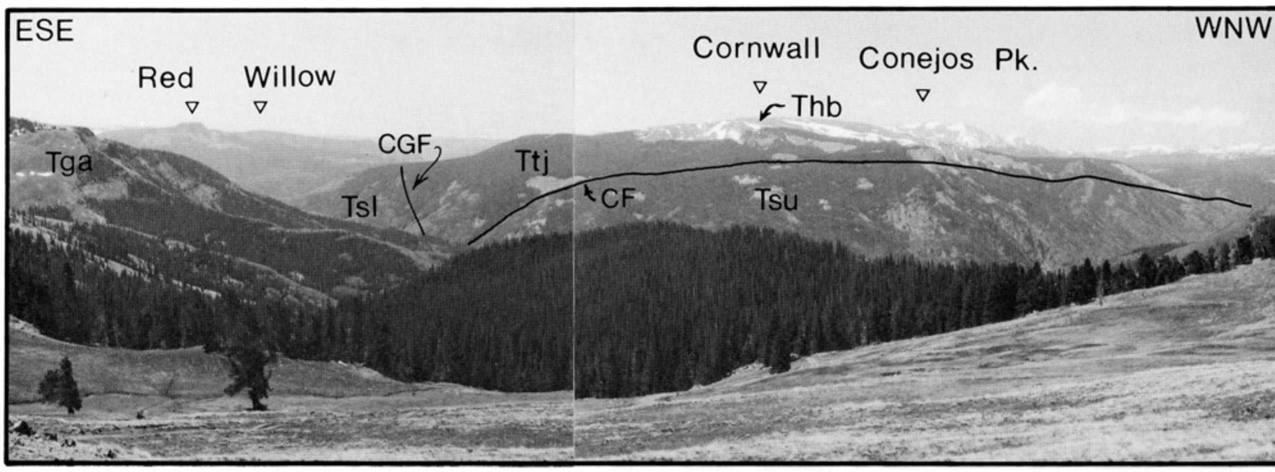

FIGURE A-2—Panoramic view of the Platoro caldera from Blowout Pass. Blowout Pass is located southeast of Bennett Peak and east of Sheep Mountain, about 3 km within the northeastern topographic wall of the Platoro caldera. The pass is reached from the village of Jasper by a locally steep (4WD) road. Conejos Peak and Willow Mountain are, respectively, on the southwestern and southeastern margins of the caldera. Red Mountain is just within the wall, and is in late caldera-fill lavas (lower Summitville Andesite) and interbedded sediments (Fig. 2-5). The north face of Red Mountain (viewed up California Gulch) is a landslide scar, and the low plateau northwest of Red Mountain is all slumped material. Cornwall Mountain is the exhumed resurgent dome of the Platoro caldera. Although capped by Hinsdale basalt lavas (Thb), the resurgent block is intracaldera La Jara Canyon tuff (Ttj) and dacitic intrusive rocks (Stop 2-6). Two large faults (shown in the figure) are reactivations of caldera ring faults. The arcuate Cornwall fault (CF, concave to the north) on the north flank of Cornwall Mountain (above the Alamosa River) drops upper Summitville Andesite lavas, filling the Summitville caldera, down against previously resurgent La Jara Canyon tuff. This structure is thought to be the southern ring fault of the younger Summitville caldera. The arcuate California Gulch fault (CGF, concave to the west) juxtaposes lower Summitville Andesite and interbedded sediments against La Jara Canyon tuff along a reactivated fault that probably originated as the southeastern structural margin of the Platoro caldera. Movement on this fault represents a late stage in the caldera resurgence. The Jasper mining district is located at the intersection of these two structures. Altered and mineralized rocks (Fig. A-1) are primarily in and around a late intrusive body localized by the fault intersection (tree-covered hills in middle foreground).

Central San Juan caldera cluster

P. W. Lipman, D. A. Sawyer, and K. Hon
U.S. Geological Survey, Denver, Colorado 80225

Field guide 3: South Fork to Lake City

Summary

This trip segment (Fig. 3-1) obliquely transects the central part of the San Juan volcanic field; major emphasis is on depositional, structural, and petrologic features within the central caldera cluster (Table 3-1), especially the caldera-filling deposits and the epithermal vein mineralization near Creede.

The six calderas of the central cluster, as in the other calderas of the volcanic field, formed within a locus of precaldera volcanoes that are discontinuously preserved as remnant topographic highs along the caldera walls (Fig. 3-2). The Masonic Park Tuff, erupted from the largely buried Mount Hope caldera at about 28.2 Ma (Steven and Lipman, 1976), is transitional in age, petrology, and caldera location between rocks of the southeastern complex and those of the younger central cluster. It is compositionally zoned from two-feldspar rhyolite (produced in relatively small volume but similar to the more voluminous silicic tuffs erupted later from the central cluster) upward into dominant silicic dacite that petrologically resembles the La Jara Canyon Member of the Treasure Mountain Tuff.

The voluminous and seemingly homogeneous 27.8 Ma Fish Canyon Tuff (3000 km^3) is associated with formation of the 30 by 40 km La Garita caldera, the largest in the field. Distinctive petrologic features of this silicic dacitic tuff (66–68% SiO_2) indicate that its phenocrysts grew at relatively high pressures, in contrast to most other tuff units of the field (Lipman et al., 1978; Whitney and Stormer, 1986). All the later ash-flow sheets of the central cluster were erupted from smaller calderas aligned north–south along the western side of the La Garita caldera, almost as if these were postcollapse moat volcanoes of the La Garita cycle.

Eruption of the Carpenter Ridge Tuff (27.6 Ma) from the Bachelor caldera produced a laterally and vertically complex ash-flow sheet that has been the cause of much interpretive confusion in the region (Lipman and Sawyer, 1988). In general, the deposit is compositionally zoned from rhyolite upward into silicic dacite (74–66% SiO_2), containing a burst of more mafic and alkalic magma (61–63% SiO_2) along the same horizon as the abrupt change in dominant eruptive composition (Lipman, 1975a: 49–53; Whitney and Stormer, 1988).

The overlying Wason Park Tuff (27.2 Ma) was erupted from the newly recognized South River caldera, which is largely covered by younger lavas (Lipman and Sawyer, 1988).

The Creede caldera, formed at 26.7 Ma as a result of eruption of the Snowshoe Mountain Tuff, was until recently interpreted as the youngest in the central caldera cluster, but new, high-precision $^{40/39}$Ar dates indicate that it may be older than the San Luis caldera (Lanphere, 1988). The Snowshoe Mountain Tuff is a relatively mafic dacite (62–66% SiO_2) that shows a weak compositional zonation in its outflow sheet (Matty et al., 1985). It shows some compositional affinities to the Fish Canyon, including a relatively high-pressure origin interpreted from its phenocrysts. The Snowshoe Mountain Tuff has an exposed thickness of more than 1.5 km on the intracaldera resurgent dome, but its outflow sheet is only locally preserved—and nowhere recognized beneath tuffs demonstrably from the San Luis caldera. Either the eruption was relatively low energy, and most erupted tuff ponded within the concurrently subsiding caldera, or some stratigraphic and age complications remain undeciphered. The near-pristine constructional morphology of the Creede caldera is largely due to erosional exhumation of its sedimentary moat by the Rio Grande during the last few million years.

The San Luis caldera complex remains the least understood of the well exposed central calderas (Steven and Lipman, 1976: 25–27), and additional detailed field and petrologic studies are presently (1988) underway by Sawyer, Lipman, and others. The San Luis caldera complex appears to be a composite feature that was the source for at least four ash-flow sheets: Rat Creek Tuff, tuff of Cebolla Creek, main Nelson Mountain Tuff, and a late unit that is currently called the tuff of Cochetopa Creek (Lipman and Sawyer, 1988). All four tuff sheets contain broadly similar phenocryst assemblages and are compositionally zoned from rhyolite to dacite (74–65% SiO_2). Major preserved features of the caldera complex are believed largely due to eruption of the Nelson Mountain Tuff; the associated subsidence is referred to simply as the San Luis caldera. Complex filling within the subsided core of the San Luis caldera is documented by several lava flows interleaved with thick welded intracaldera tuff units—a relation unlike that found in any other San Juan caldera. All the tuffs and lavas associated with the San Luis caldera complex appear to have erupted within the interval 26.4–26.1 Ma (Lanphere, 1988).

The central caldera cluster offers exceptional opportunities to study the process of resurgent doming. The La Garita, Bachelor, and Creede calderas all have fairly symmetrical and structurally simple resurgent domes. Dips on the flanks of the La Garita caldera are relatively gentle (mostly less than 15°). In contrast, the flanks of the resurgent dome within the Creede caldera dip as steeply as 45°. The crest of the resurgent dome of the Bachelor caldera appears to be eccentrically located north of the center of this caldera. In addition, steepening of dips downward in the caldera-filling Carpenter Ridge Tuff on flanks of the resurgent dome sug-

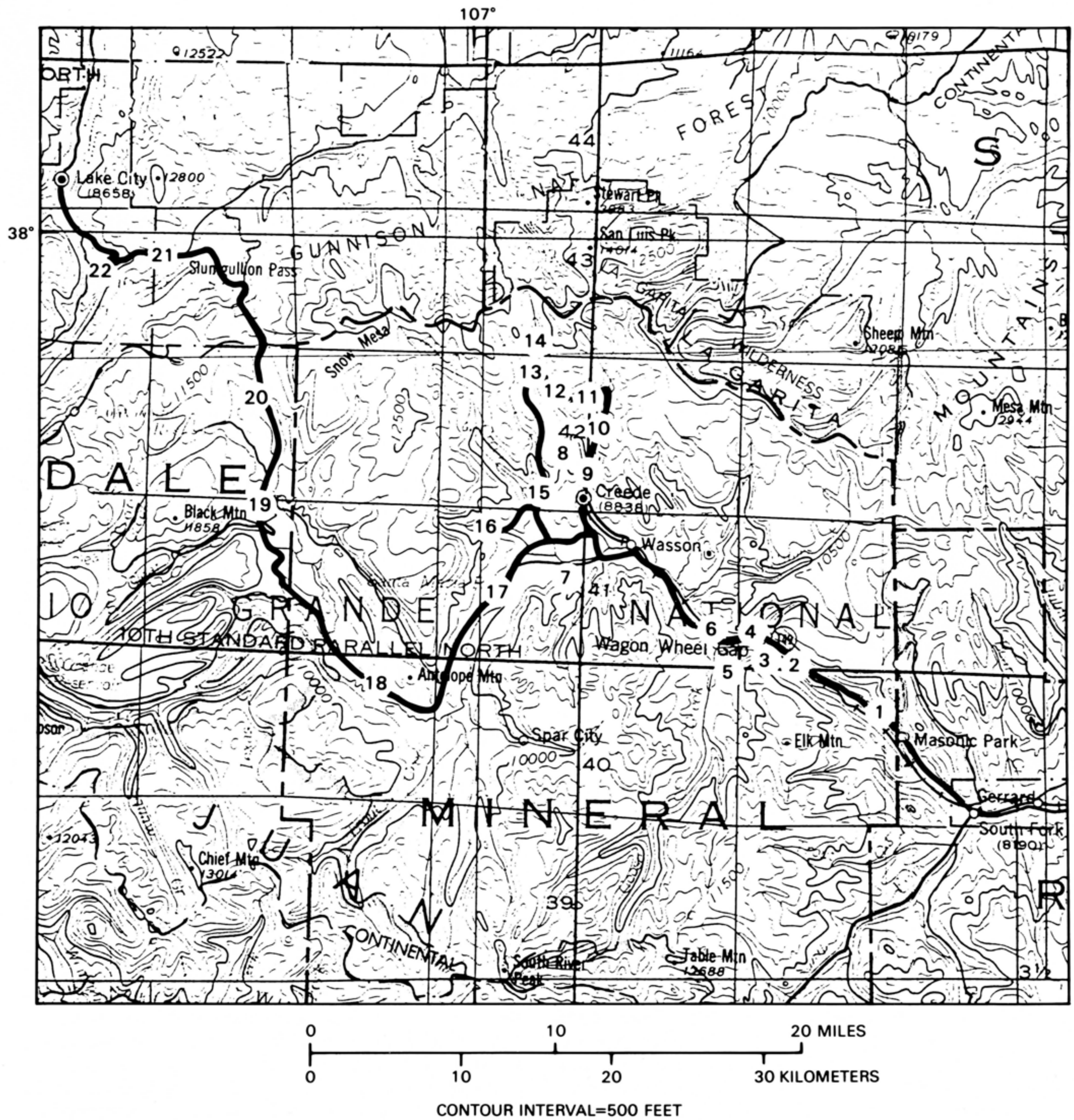

FIGURE 3-1—Route map, central San Juan Mountains.

gests that definition of the domical structure began while caldera subsidence and ash-flow eruptions were still underway.

The San Luis caldera resurged asymmetrically, as a structurally complex and still incompletely understood trap-door uplift, somewhat similar to that at Platoro. The largely buried Mount Hope caldera appears to have resurged weakly in a similar asymmetric fault-block uplift, but only after infilling by the younger Fish Canyon Tuff. Exposed levels in the newly recognized South River caldera provide no indication of any resurgent uplift at all.

Mineralization in the central cluster was mainly confined to the Creede district. Ore deposits are localized by caldera structures (keystone graben faults across the resurgent dome of the Bachelor caldera and near walls of the San Luis and Creede calderas), but are about 1 Ma younger than any associated volcanic deposits. No sizeable shallow granitic intrusions are exposed in the mining district, but such bodies are inferred to be present at shallow depth to provide heat sources for the hydrothermal systems responsible for the mineralization. Several small granitic bodies exposed low within the uplifted core of the San Luis caldera probably are high points on a larger resurgent intrusion.

Tuffs and lavas associated with the central cluster tend to be more silicic and evolved than those of the southeastern caldera complex; even more evolved compositions are pres-

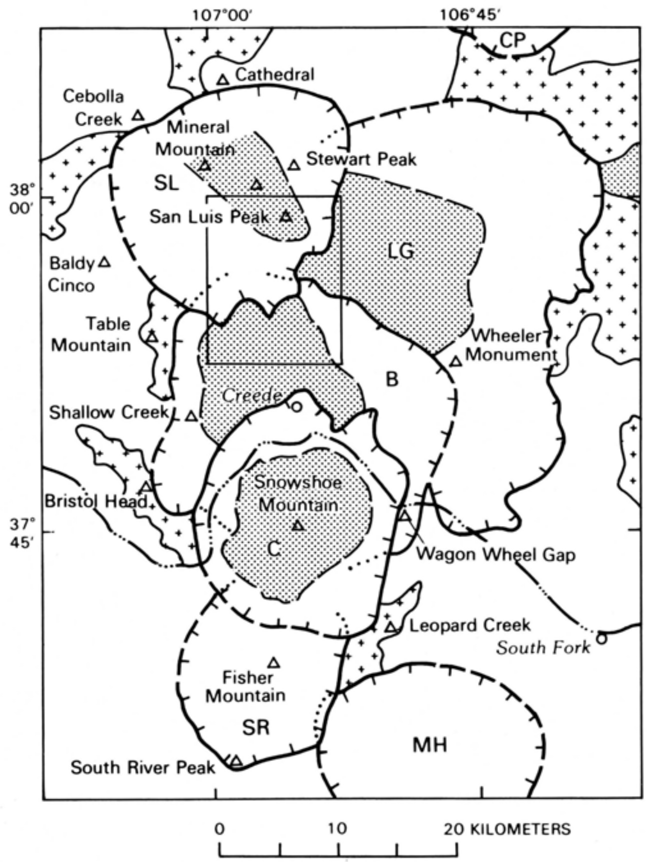

FIGURE 3-2—Generalized geology of the central San Juan caldera cluster, showing location of San Luis Peak quadrangle (Lipman and Sawyer, 1988). Caldera margins are indicated by hachured lines; stipple pattern indicates intracaldera resurgent uplifts. Key to calderas: B, Bachelor; C, Creede; CP, Cochetopa Park; LG, La Garita; MH, Mount Hope; SL, San Luis; SR, South River. Cross pattern: early intermediate-composition volcanic rocks (precaldera). Unpatterned: caldera-related ash-flow tuffs and lavas.

ent in the western San Juan region. Several of the caldera cycles, especially Mount Hope and La Garita, had limited postsubsidence lava flow activity prior to eruption of the next major ash-flow unit. Nevertheless, the same general compositions prevail, and the presence of local andesitic to dacitic lavas that interleave between all major ash-flow sheets of the central San Juan cluster documents the continued presence of mafic magmas during differentiation of the more evolved magmas associated with ash-flow eruptions (Lipman et al., 1978).

Route

Heading northwest from South Fork (Fig. 3-1), the trip follows the Rio Grande graben, an extensional feature related to regional uplift during growth of the volcanic field and inferred emplacement of an underlying composite batholith (Steven and Lipman, 1976; Gebhart, 1987). The canyon of the Rio Grande cuts a spectacular section through the east wall of the large La Garita caldera, the source of the Fish Canyon Tuff. At Wagon Wheel Gap, after examining a southeastern remnant of the Bachelor caldera (source of the Carpenter Ridge Tuff), we enter the Creede caldera, the best preserved resurgent caldera of the San Juan volcanic field and the source of the Snowshoe Mountain Tuff. The trip follows the caldera moat northwest to Creede, where we examine complex fill deposits within the Bachelor caldera, structural features of the Creede mining district, and the proposed sites for the Continental Scientific Drilling Program. The trip continues around the moat of the Creede caldera to the northwest-trending Clear Creek graben, another distensional structure related to regional magmatic adjustments below the center of the volcanic field. The road follows the graben to the Continental Divide at Spring Creek Pass, and on to Slumgullion Pass, and offers distant views of another major resurgent caldera of the central San Juan complex, the San Luis caldera—source of the Rat Creek and Nelson Mountain Tuffs. From Slumgullion Pass, we descend into the 28–29 Ma Uncompahgre caldera—source of the Sapinero Mesa Tuff—and skirt the eastern side of the nested Lake City caldera, the youngest in the San Juan field and the source of the Sunshine Peak Tuff (23 Ma). These last features are exposed by some of the most spectacular terrain in the Southern Rocky Mountains.

Maps

Published geologic maps especially pertinent to this part of the field trip include the Creede, Bristol Head, and Spar City 15-minute quadrangles (Steven, 1967; Steven and Ratté, 1973; Steven and Lipman, 1973), the South Fork area map (Lipman and Steven, 1976), Lake City caldera map (Lipman, 1976a), and the San Luis Peak 7½-minute preliminary quadrangle (Lipman and Sawyer, 1988).

TABLE 3-1—Volcanic units of the central San Juan Mountains.

Age	Source	Ash-flow tuffs	Lava flows	Sediments	Intrusions
16–23	Basaltic shields (Hinsdale Fm.)	—	Trachybasalt and trachyandesite	—	Local dikes
26.1–26.4	San Luis caldera complex	Tuff of Cochetopa Cr. Nelson Mtn. Tuff Tuff of Cebolla Cr. Rat Creek Tuff	Volc. of Baldy Cinco; Volc. of Stewart Peak; Rhyolite of Mineral Mtn.; McKenzie Mtn.—Captive Inca flows and domes	Local moat fill	Late stocks and dikes; resurgent pluton
26.6	Creede caldera	Snowshoe Mtn. Tuff	Fisher Quartz Latite	Creede Fm.	Local plugs and dikes
27.2	S. River caldera	Wason Park Tuff	Lavas of S. River Peak; Volc. of Table Mtn.		Local plugs and dikes
27.4	Bachelor caldera	Carpenter Ridge Tuff	Lavas of McClelland Mtn.	Local moat fill	—
27.8	La Garita caldera	Fish Canyon Tuff	—	Local moat fill	—
28.4	Mt. Hope caldera	Masonic Park Tuff	—	—	—
30–35	Precaldera volcanoes	—	Early intermediate-composition lavas	Laharic breccias and conglomerates	Central stocks

TABLE 3-2—Representative chemical analyses, central San Juan caldera cluster. Major-element chemical analyses are calculated to 100% volatile-free. All chemical analyses determined at U.S. Geological Survey, Denver, Colorado. Abbreviations: intrac, intracaldera; rhy, rhyolite; vitr, vitrophyre; xr, crystal-rich; xp, crystal-poor.

Field no.	Sample description	Major-element XRF									
		SiO_2	Al_2O_3	$FeTO_3$	MgO	CaO	Na_2O	K_2O	TiO_2	P_2O_5	MnO
	SAN LUIS CALDERA										
85S-121	Volcanics of Stewart Peak, andesite lava	60.8	17.0	6.87	1.81	5.00	3.56	3.48	0.91	0.36	0.07
85L-10-X	Tuff of Cathedral Creek, E. Willow Creek	66.3	15.9	4.23	1.39	3.32	3.65	4.33	0.55	0.23	0.09
85S-139	Rhyolite flow, Mineral Mountain	73.8	13.7	1.64	0.38	1.37	3.39	4.87	0.23	0.05	0.08
85L-29C	Nelson Mtn. Tuff, xr rhy vitr, Nelson Mtn.	70.2	15.3	2.40	0.68	1.89	3.63	5.44	0.37	0.10	0.09
85S-110	Nelson Mtn. Tuff, intrac dacite, San Luis Peak	62.8	16.4	5.76	1.94	4.52	3.80	3.61	0.69	0.31	0.10
SD2-1064	Nelson Mtn. Tuff, intrac rhy, SD-2 drillhole	70.7	14.8	2.25	0.57	1.84	3.72	4.77	0.33	0.08	0.08
85L-33D	Tuff of Cebolla Creek, lower xr dacite	64.2	16.2	4.70	1.54	3.91	3.67	3.71	0.62	0.30	0.08
85L-29F	Rat Creek Tuff, xr dacite vitrophyre	65.8	16.6	3.87	1.37	3.22	3.89	4.17	0.57	0.21	0.09
85L-30	Captive Inca flow, vitrophyre	69.7	15.0	3.20	1.03	2.89	3.20	4.34	0.42	0.16	0.10
SJ85-3	McKenzie Mtn. flow, near vitrophyre	63.7	15.9	5.79	1.93	4.43	3.49	3.65	0.68	0.30	0.09
	CREEDE CALDERA										
85L-39	Fisher Quartz Latite, Wagon Wheel Gap	65.4	15.4	5.01	1.66	4.07	3.46	3.85	0.66	0.27	0.07
SJ-85-20	Snowshoe Mtn. Tuff, xr dacite, Cattle Mtn.	62.3	16.6	6.38	1.33	4.53	3.73	3.43	0.73	0.31	0.11
85S-129	Snowshoe Mtn. Tuff, intrac, Point of Rocks	67.6	15.0	3.87	1.07	3.62	3.47	4.53	0.52	0.23	0.06
	SOUTH RIVER CALDERA										
TW-32	Wason Park Tuff, Antelope Park	71.2	14.6	2.19	0.53	1.40	3.65	5.57	0.38	0.08	0.09
	BACHELOR CALDERA										
87-132	Mammoth Mtn. Member, dacite, Palisades	64.3	16.5	3.86	1.90	4.47	3.51	4.13	0.71	0.29	0.07
CR-24	Carpenter Ridge Tuff, outflow rhy, Del Norte	72.1	14.7	1.76	0.39	1.51	3.75	5.17	0.27	0.00	0.07
85S-105	Bachelor Mtn. Member, intrac rhy vit, 1st Fork	73.2	13.9	1.72	0.40	1.42	3.68	4.77	0.24	0.00	0.06
	LA GARITA CALDERA										
TFC-03	Fish Canyon Tuff, Goodrich Creek	66.5	15.9	4.71	1.38	3.64	3.74	3.63	0.54	0.20	0.09

Field no.	LOI	KEVEX XRF			INAA										
		Rb	Sr	Zr	Ba	Th	La	Nd	Sm	Eu	Yb	Lu	Ta	Sc	Co
85S-121	1.08	115	644	195	1040	8.69	41.6	39.6	8.00	1.920	2.73	0.399	0.991	14.70	16.80
85L-10-X	1.90	115	524	224	998	10.60	42.6	36.3	6.54	1.580	2.54	0.377	1.040	8.10	7.53
85S-139	5.74	182	169	161	513	12.10	37.4	30.3	5.66	0.716	2.57	0.379	1.500	2.56	1.49
85L-29C	2.61	144	310	280											
85S-110	1.77	107	671	183											
SD2-1064	4.80	118	313	226	1070	11.50	41.6	35.9	6.92	1.250	2.73	0.391	1.380	4.27	2.57
85L-33D	1.46	96	571	205	1020	9.07	42.5	35.9	6.49	1.580	2.55	0.376	1.030	8.68	9.68
85L-29F	2.03	97	622	337	1910	9.24	49.1	39.1	6.78	2.080	2.75	0.415	0.973	7.49	4.81
85L-30	4.45	162	400	167	658	10.70	37.7	30.5	5.76	1.050	2.42	0.355	1.210	5.23	7.44
SJ85-3	2.29	116	628	170	870	11.00	39.5	35.5	6.75	1.530	2.14	0.320	0.911	9.53	11.60
85L-39	1.93	94	587	174	1020	7.73	38.4	30.4	5.45	1.450	1.92	0.281	0.781	10.30	13.60
SJ-85-20	1.25	107	704	155	1010	8.33	38.5	36.3	7.09	1.750	2.21	0.310	0.761	10.70	12.60
85S-129	1.64	135	472	184	823	13.50	43.6	33.2	6.30	1.360	2.48	0.376	1.130	6.34	8.05
TW-32	3.08				896	16.20	54.9	43.5	7.74	1.270	2.96	0.453	1.410	4.81	2.09
87-132	1.58	124	525	254	1187		41.0								
CR-24	3.25				1180	26.60	50.6	30.6	5.21	1.050	2.34	0.344	1.500	3.58	1.50
85S-105	3.81	166	177	175	515	17.80	49.1	37.0	6.07	0.898	2.76	0.411	1.370	4.34	1.74
TFC-03	1.67				872	11.50	42.9	33.5	6.22	1.420	2.40	0.363	1.220	7.54	9.81

Road log

Mileage

0.0 Junction of US-160 and CO-149 at South Fork (2490 m). Turn west on CO-149, and follow main Rio Grande Valley to Creede. Several major faults of the Rio Grande fault system follow the valley. As a result, the welded tuffs on the southwest side are entirely Fish Canyon Tuff, but on the northeast side the lower two-thirds of the slope is uplifted Masonic Park Tuff, capped by Fish Canyon Tuff. **3.0**

3.0 Masonic Park Tuff type locality. Compound cooling in the Masonic Park Tuff, on right, is shown by alternating ledges and benches all in the same unit. The Masonic Park is more than 250 m thick in this area, with no base exposed, yet does not resemble a typical caldera-filling tuff in degree of welding or alteration. Some sort of pre-existing depositional low seems required, perhaps a basin between older Conejos volcanic edifices. **1.2**

4.2 **STOP 1. Panorama of Rio Grande Canyon.** Pull off on right, by the Rio Grande Forest entry sign, for view of the east wall of the La Garita caldera and stratigraphic relations between related ash-flow sheets (Fig. 3-3). The eastern topographic wall of the La Garita caldera descends the broad side valley

FIGURE 3-3—Ash-flow sheets and La Garita caldera wall indicated by dashed line (Stop 1). Upper cliff on right is Fish Canyon Tuff (Tfc); multiple lower ledges are compound cooling zones within Masonic Park Tuff (Tmp). Within caldera, upper cliff is Wason Park Tuff (Twp), underlain by thick dacitic Mammoth Mountain member of the Carpenter Ridge Tuff (Tmp and Tcr). FC, shattered block of Fish Canyon Tuff that slid part way down the caldera wall.

ahead to the northwest. On the caldera rim, Fish Canyon Tuff, forming the uppermost major columnar-jointed cliff, rests on thick Masonic Park Tuff that shows compound cooling of alternating more welded ledges and less welded benches.

Along the ridge crest, thick Wason Park Tuff ponded within the caldera wedges out against the Fish Canyon at about the same elevation on the topographic wall. Underlying the Wason Park is another thick ash-flow sheet, the Mammoth Mountain member of the Carpenter Ridge Tuff (usage of Lipman and Sawyer, 1988), that is petrologically broadly similar to the Masonic Park units against which it wedges. Perched along the caldera wall is a shattered mass of outflow Fish Canyon Tuff, 1 km across, that slumped part way down the wall during collapse (see South Fork map; Lipman and Steven, 1976).

Previously, the compositionally zoned Mammoth Mountain member (66–74% SiO_2) had been considered a discrete ash-flow sheet (Ratté and Steven, 1967; Steven et al., 1974). Restudy of the Creede area by Lipman and Sawyer has shown that the previously mapped boundary between phenocryst-poor rhyolites of Mammoth Mountain and Bachelor Mountain lithologies within the source Bachelor caldera is an alteration boundary lacking evidence for a major cooling break (Stops 8, 10). Accordingly, the Mammoth is now used informally to designate the phenocryst-rich silicic dacite upper part of the compositionally zoned Carpenter Ridge ash-flow sheet. In the outflow Carpenter Ridge southwest of the Bachelor caldera, though, a partial cooling break occurs widely along the relatively abrupt rhyolite–silicic dacite transition within this tuff sheet.

In addition to the La Garita caldera, the wall of the Creede caldera is visible to the west. The large cliff-forming lava dome at Wagon Wheel Gap is within the Creede caldera, resting on diverse rocks of the caldera wall, including Carpenter Ridge and Wason Park Tuffs and associated lava flows that ponded within the La Garita caldera. In addition, a small remnant of the southeast side of the Bachelor caldera is preserved in this area (Stops 4, 5).

Continue ahead, up canyon, crossing boundary between South Fork and Creede geologic maps. **4.3**

8.5 **STOP 2. La Garita caldera wall.** Roadcut exposure, at prominent bend, is Masonic Park Tuff within reentrant on the La Garita caldera wall. A vague bench about 75 m above road level marks the basal contact of the younger Mammoth Mountain member of the Carpenter Ridge Tuff against Masonic Park Tuff on the La Garita wall. The Mammoth Mountain here is a phenocryst-rich silicic dacite, containing 25–45% phenocrysts of plagioclase, biotite, and augite—petrographically similar to the Masonic Park Tuff. The greenish-gray groundmass color of the Masonic Park, in contrast to the pinkish-brown groundmass of the Mammoth Mountain, is locally distinctive, as is a somewhat higher augite content in Masonic Park Tuff. The contact is not exposed up-slope, but blocks of Mammoth Mountain vitrophyre are present as float, documenting the presence of a cooling and depositional break, as does the absence of any intervening Fish Canyon Tuff. The La Garita wall, on which Masonic Park Tuff is obliquely buried by caldera-filling Mammoth Mountain member, can also be followed along conspicuous topographic breaks on the north-facing canyon-wall slopes of McClelland Mountain, across the Rio Grande.

Continue up canyon. Entering Spar City 15-min. quad (Steven and Lipman, 1973). **0.3**

8.8 Palisade Campground turnoff. Closer view of the Creede caldera wall and the Wagon Wheel Gap lava dome just inside the caldera. **1.4**

10.2 **STOP 3. Moat lake-bed sediments of La Garita caldera.** Park carefully on shoulder, along right side of road; **watch out for highway traffic!** These tan to gray finely laminated volcanic sediments beneath the Mammoth Mountain member of the Carpenter Ridge Tuff are interpreted as lake beds within the La Garita caldera moat. At the westernmost exposures, the lake beds are intruded by a texturally variable dacite, in which compositional boundaries and discontinuities in columnar jointing indicate several phases of emplacement. The intrusive dacite may have been a feeder for several thick lava flows that overlie Mammoth Mountain member higher on the canyon walls and were erupted prior to the ridge-capping Wason Park Tuff. These flows, and others in similar stratigraphic position, are candidates for postcaldera moat and rim lavas related to the Bachelor caldera cycle.

Continue up canyon, to Blue Creek. (Entering Creede 15-min. quad; Steven and Ratté, 1973). **0.7**

10.9 **STOP 4. Blue Creek Lodge: Bachelor caldera wall.** Pull off on right, by large roadcuts west of Blue Creek Lodge. Please don't block access to lodge! To the northeast, across Blue Creek, is the thick Blue Creek (Palisades) section of the Mammoth Mountain member, ponded in the La Garita caldera moat; this section was target of a detailed petrographic study by James Ratté (Ratté and Steven, 1967: 27–33). Ahead is Wagon Wheel Gap lava dome, on wall of the Creede caldera.

Low in Blue Creek and on poorly exposed slopes above are key features, documenting presence of parts of the Bachelor caldera wall. These features truncate fill of the La Garita caldera and older rocks, and in turn are cut off by the topographic wall of the Creede caldera (Fig. 3-4). The lowermost cliffs along the west side of lower Blue Creek are Masonic Park Tuff on the caldera wall, somewhat fractured and altered, but having coherent gently dipping pumice-compaction foliations that indicate absence of major structural disruption. On the less well-exposed slopes above, but below the rugged cliffs of the Wagon Wheel Gap lava dome, are intracaldera brecciated landslide masses of outflow Fish Canyon Tuff (some hundreds of meters across), accompanied by some Masonic Park Tuff and a few large blocks of andesitic lava, all lacking stratigraphic or structural coherence. These slid down the wall of the Bachelor caldera.

The roadcuts immediately ahead provide a limited sampling of these caldera-fill landslide breccia relations. Despite mild alteration, the resorbed quartz phenocrysts in the Fish Canyon are distinctive and diagnostic in comparison with other phenocryst-rich

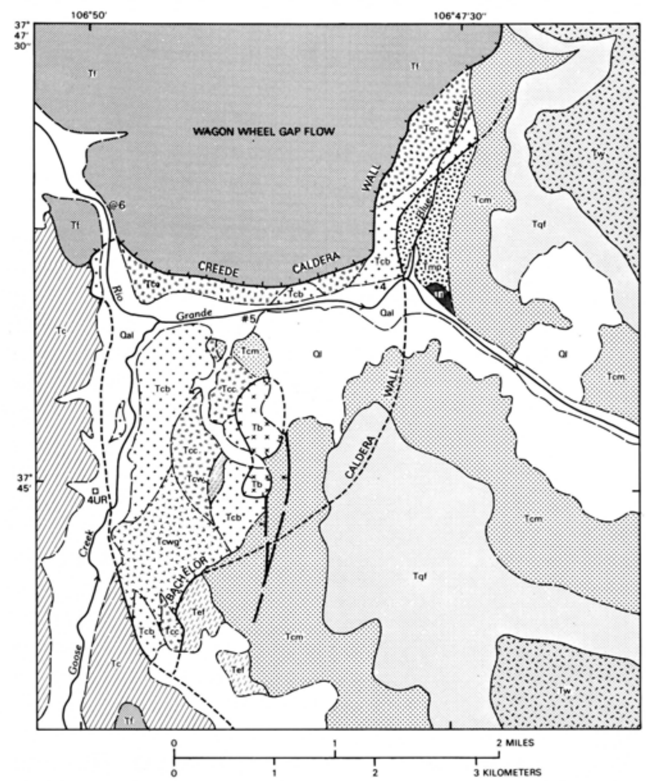

FIGURE 3-4—Generalized geologic map of Wagon Wheel Gap area (Stops 4–5); geology by P. W. Lipman (unpubl. data 1987). ★, Stop 4; #, Stop 5; @, Stop 6. Map units: Qal, Quaternary alluvium and colluvium; Ql, Quaternary landslides; Tf, Fisher Quartz Latite (postcollapse lavas of the Creede caldera); Tc, Creede Formation (sedimentary fill of the Creede caldera); Tb, landslide breccias within Creede caldera (26.7 Ma); Tw, Wason Park Tuff (27.2 Ma); Tqf, postcollapse quartz latitic lava flows of Bachelor caldera; Ti, intrusive porphyry, perhaps feeder for Tqf. Subunits of the intracaldera Carpenter Ridge Tuff (27.4 Ma): Tcm, Mammoth Mountain member (dacitic welded tuff); Tcw, Windy Gulch zone (weakly welded rhyolitic tuff); Tcc, Campbell Mountain zone (welded rhyolitic tuff); Tcb, Wagon Wheel Gap megabreccia member (breccia and lithic-rich rhyolitic tuff, containing fragments of Fish Canyon Tuff and intermediate-composition lavas up to 100 m across); Tmp, Masonic Park Tuff (28.2 Ma); Tef, precaldera intermediate-composition lavas (Conejos Formation).

silicic dacites in this part of the volcanic section, such as Masonic Park or Mammoth Mountain tuffs. The age of the deposit is bracketed as synchronous with eruption of Carpenter Ridge Tuff by the abundant blocks of Fish Canyon Tuff, and the absence of Mammoth Mountain or Wason Park blocks, despite their presence in capping of the ridges east of Blue Creek. Another important feature is the local presence of nonwelded, massive, crystal-poor rhyolitic tuff as matrix between blocks; this is interpreted as intracaldera Carpenter Ridge Tuff.

Similar features can be examined in larger scale, at the next stop, just ahead across the Rio Grande. **0.2**

11.1 Bridge across Rio Grande to River Springs Resort. **Turn left.** Immediately past bridge, turn sharply right and follow private road along river bank (only after obtaining permission at resort!) to end of road. Park at edge of meadow. **1.1**

12.2 **STOP 5. Bachelor caldera fill at mouth of Goose Creek.** Relations between several caldera-collapse megabreccia lithologies within the compositionally zoned intracaldera Carpenter Ridge are exceptionally exposed on the ridge crest ahead; it forms the divide between the Rio Grande and its Goose Creek tributary (Fig. 3-4). An off-trail walk of about 2 hrs. duration is required, involving a 500 m climb.

Walk about 250 m west across meadow, toward the rugged cliff with modern talus at its base. This mass of sparsely porphyritic andesite, several hundred meters across, is interpreted as a megablock from a precaldera volcano (Conejos Formation) within the Bachelor caldera fill. The smaller exposures along the south side of the meadow are all of welded tuff that varies from phenocryst-poor (3–5%) to as much as 30–40% phenocrysts. This section through the compositionally zoned intracaldera Carpenter Ridge Tuff becomes more mafic and crystal-rich upward and overlies a large mass of megablocks deeper in the caldera fill, including the cliff face just noted.

First, climb narrow, steep talus slope between the megablock cliff and small rib of tan rock to southeast. This rib consists of densely welded crystal-poor tuff, interpreted as intracaldera rhyolitic Carpenter Ridge, that dips as much as 70° away from the andesite mass. The steep dips are interpreted as due to welding during deposition against the andesitic megablock.

While climbing up-slope along the rib, watch the dip and phenocryst content of the rhyolitic tuff. Upon reaching the ridge crest, descend about 50 m to the east to a small saddle, where the phenocryst content increases abruptly. This is the rhyolite–silicic dacite transition in the intracaldera Carpenter Ridge Tuff. Note that the dip remains moderate (25–30°) to the east. Compare the dips here with the nearly horizontal columnar-jointed cliffs east of Blue Creek or on the northwest side of McClelland Mountain. Perhaps we are on a rotated block, due to partial slumping into the Bachelor caldera, or into the Creede caldera?

Next, climb west to the high point at the northern end of the main ridge crest, monitoring the andesite–dacite rock types, and keeping a close eye for any nonwelded tuff that could be matrix of Carpenter Ridge between megablocks. Also, note degree of fracturing and microbrecciation of the lava masses. Upon reaching the main ridge, traverse north, continuing these observations.

The high point on the ridge provides a superb view of the Creede caldera: its east wall, east moat, the Wagon Wheel Gap lava dome, and the east flank of the resurgent dome (geographic Snowshoe Mountain). To the south, up Goose Creek, the high distant hills are mostly postcaldera volcanoes of Fisher Quartz Latite. Upper Goose Creek arcs westward, following the topographic margin of the largely buried and poorly understood South River caldera, that is now thought to be the eruptive source of the Wason Park Tuff at 27.2 Ma. In the nearer hills are mine workings of the inactive Colorado Fuel and Iron Corp. Wagon Wheel Gap fluorspar mine. The light-colored subdued ridges adjacent to the mine consist mostly of nonwelded intracaldera Carpenter Ridge Tuff, enclosing scattered megablocks.

Continuing along the ridge crest, about 200 m south of the high point, are large rugged outcrops of gray rock that is much more phenocryst-rich than anything seen previously. Look closely at the abundance of biotite, and for presence of sparse glassy sanidine, resorbed quartz, and sphene. Yes, this is Fish Canyon Tuff! Now descend farther along the ridge, passing the rugged ridge-crest outcrops of Fish Canyon Tuff on the right (west side). What do you think of their contact with the underlying rock?

As you continue south, down the ridge crest, note the decreasing proportions of blocks versus nonwelded rhyolitic tuff, like that seen at the mouth of Blue Creek (Stop 4). In one place a small prospect shaft provides excellent exposures.

From the prospect area, descend diagonally to the northwest down the steep slope toward the mouth of Goose Creek, following a surprisingly good game trail. As you descend, estimate the proportion of intermediate-composition lava versus matrix. Keep in mind that the nonwelded rhyolitic tuff tends to erode preferentially. **Also, be careful about rockfalls, especially if in a large group!** At base of the slope is an old railway grade that provides a semitrail to follow to the mouth of Goose Creek; then back to vehicles. Additional excellent exposures of large blocks are present along rail grade.

All these rocks were previously assigned to the "volcanics of Wagon Wheel Gap," and were considered to represent local andesitic–dacitic volcanoes cut by many small intrusions (Steven and Ratté, 1973; Steven and Lipman, 1973). Similar brecciated slide blocks have also been confused at times with intrusions, where encountered in exploration drillcore in the Creede district. Recognition of the tuff matrix and interpreted caldera-collapse landslide origin of all these rocks eliminates the need for several local volcanic episodes in the Creede area. Instead, they can be grouped into three lithologically and geographically distinct slide assemblages, each of which correlates with the lithologies present on the adjacent caldera wall (Lipman and Sawyer, 1988). At Goose Creek, the dominant source is andesite lavas from the Conejos Formation, overlain by outflow Fish Canyon Tuff. Farther north on the east side of the Creede district, the slide breccias are dominated by Fish Canyon debris derived from the La Garita resurgent dome (Phoenix Park breccia member; Stop 10), and on the west side of the Creede district, hornblende-bearing dacitic precaldera lavas were derived from the northwestern caldera wall (Shallow Creek breccia member; Stop 16). Each of these breccia units was previously considered to represent a primary volcanic accumulation and assigned a formal stratigraphic name (Emmons and Larsen, 1923; Steven and Ratté, 1965).

Retrace route to CO-149. **1.1**

13.3 **Turn left** on CO-149; continue up valley toward Wagon Wheel Gap (2575 m). **0.7**

14.0 Small tan roadcut exposures on right (north), surrounded by talus from the overlying Wagon Wheel Gap lava dome, are unusually densely welded rhyolitic Carpenter Ridge Tuff within, or near, the megabreccia zone. Where voluminous tuff could accumulate, without large adjacent cold blocks from the caldera wall, sufficient heat was retained to permit typical welding and devitrificaiton textures. Straight ahead, through Wagon Wheel Gap, is resurgent dome of Snowshoe Mountain Tuff within Creede caldera. The Snowshoe Mountain is also a phenocryst-rich dacite, erupted at 26.7 Ma as indicated by several $^{40/39}$Ar dates (Lanphere, 1988). **1.0**

15.0 **STOP 6. Wagon Wheel Gap lava dome.** Pull over at National Forest viewpoint on left. Ahead, the present valley defines the exhumed topographic moat of the Creede caldera, where caldera-filling lacustrine sediments of the Creede Formation, deposited between the resurgent dome and the caldera wall, have been eroded by the Rio Grande (Fig. 3-4). Farther up river, the north-northwest wall of the Creede caldera forms the skyline.

The Rio Grande has cut through flank of the Wagon Wheel lava dome, a unit of the Fisher Quartz Latite, dated by $^{40/39}$Ar at 26.7 Ma (Lanphere, 1988). Similar porphyritic silicic dacite makes up most of the postcollapse Fisher lavas that blanketed the southern margin of the Creede caldera. Also note ramp structures in the Wagon Wheel Gap lava dome, where it rides up to the southwest on sediments of the Creede Formation.

Continue ahead on CO-149. **1.7**

16.7 McKinney Gulch Spring. In view to right, cliffs up Bellows Creek consist of welded tuffs erupted from the central San Juan caldera complex—mainly facies of the zoned Carpenter Ridge Tuff (shown on published maps as various units of Bachelor Mountain, Farmers Creek, and Mammoth Mountain Tuffs), the Wason Park Tuff, and interlayered lava flows. On the skyline to north are the La Garita Mountains, consisting entirely of thick Fish Canyon Tuff in the La Garita resurgent dome. **2.4**

19.1 Junction with Deep Creek road. **Turn left. 1.6**

20.7 Cross Deep Creek, and 0.1 mi later the junction with airport road to Creede. Continue straight ahead (west). **0.3**

21.0 **STOP 7. Travertine knob panorama. Turn left** on track and park at base of trees, by pioneer grave site. Continue on foot up the trail and climb to top of hill. This is one of many travertine knobs which intertongue with the lake sediments of the Creede Formation that fill the Creede caldera moat. The bounding ring fault of the Creede caldera is concealed beneath the moat fill. The resurgent dome of the Creede caldera makes up most of Snowshoe Mountain to the south. The crest of the dome is broken by keystone graben faults that follow Deep Creek, the major north–south drainage transecting the caldera. The composite section of Snowshoe Mountain Tuff exposed on the resurgent dome is 1.5–2 km thick, with no base exposed. Most outflow Snowshoe Mountain Tuff has been eroded; the only sizeable preserved areas are weakly welded tuffs along ridge crests near South Fork.

On top of the travertine knob: view northeast is toward the La Garita Mountains on the skyline. The La Garitas, on the Continental Divide (high point: 4179 m), are the resurgent core of the La Garita caldera, the earliest of the central San Juan caldera cluster, and expose more than 1.5 km of intracaldera Fish Canyon Tuff (La Garita Member), with the top eroded and the base concealed.

The view directly north, toward the town of Creede, is into the resurgent core of the Bachelor caldera, the second collapse structure of the central San Juan caldera complex, here exposed in cross section in the north wall of the younger Creede caldera (Fig. 3-5) The fill of the Bachelor caldera consists largely

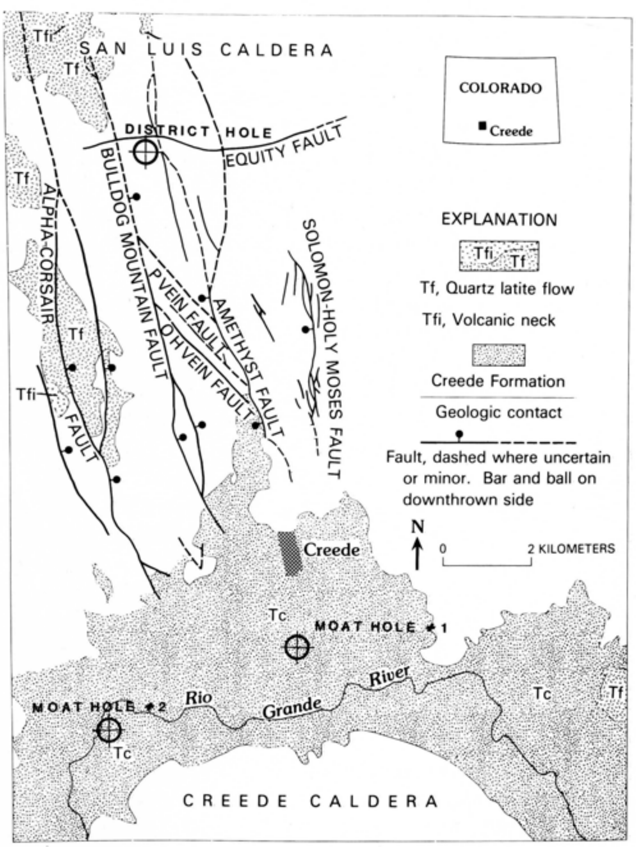

FIGURE 3-5—Major structures of the Creede district and proposed sites of drillholes for Continental Scientific Drilling Program (from Bethke and Lipman, 1987).

of variably welded rhyolitic tuff, long designated the Bachelor Mountain Rhyolite or Tuff; this unit is now recognized as the intracaldera equivalent to rhyolitic outflow Carpenter Ridge Tuff (Steven and Lipman, 1976). For nearly a century, the Bachelor Mountain has been divided into the Willow Creek, Campbell Mountain, and Windy Gulch subunits (Emmons and Larsen, 1923). These were once thought to constitute discrete eruptive deposits of stratigraphic significance, but it has become clear in recent years that they are welding zones within the thick rhyolitic caldera fill of the Bachelor caldera (Steven and Ratté, 1965; Lipman and Sawyer, 1988). Centrally within the Bachelor caldera, they define a crude stratigraphic succession, becoming less welded upward, but near the caldera margins the welding zones alternate and interfinger complexly. Welding reversals are also conspicuous near large landslide-breccia deposits from the caldera wall, which interfinger with the caldera-filling tuff. In places, the welding zones also are oblique to the compaction foliation. The Willow Creek zone is the lowermost exposed fill of the Bachelor caldera; it is an extremely densely welded, phenocryst-poor fluidal rhyolite, generally purplish gray in color and showing evidence of secondary flowage during emplacement and potassium metasomatism. The Campbell Mountain zone differs from the Willow Creek zone in less intense welding, reddish color, and generally more abundant lithic fragments. The Windy Gulch zone is porous, light-gray, nonwelded rhyolitic tuff.

The structure of the Bachelor resurgent dome is well displayed from here. The Willow Creek drainage, directly ahead to the north, roughly follows the apical graben (Creede graben) of the Bachelor caldera. Structures of the Creede graben were reopened following activity at the Creede and San Luis calderas, and these faults localized epithermal mineralization.

The cliffs to the east of Willow Creek are fluidal rhyolite (Willow Creek welding zone) of the Bachelor Mountain Member; it grades upward abruptly into thin Campbell Mountain zone, present above the cliffs as talus. The eastern vein-fault of the Creede graben, the Solomon–Holy Moses vein, runs along the east side of Campbell Mountain, the ridge between the forks of Willow Creek (Fig. 3-5). The Amethyst vein, the most productive vein in the district, runs N20°W along West Willow Creek, through Bachelor Mountain. The Amethyst fault dips west and accommodates most of the normal displacement on the east side of the graben. West of the Amethyst fault, Wason Park Tuff that ponded within the older Bachelor caldera is dropped against the Campbell Mountain and Willow Creek zones. The trace of the east-dipping Bulldog vein-fault, on the west side of the Creede graben, passes through Bulldog Mountain, the gently rounded hill just west of Windy Gulch. This structure has been mined until recently by Homestake Mining Corp. at the Bulldog Mine, at the base of Windy Gulch. Farther west (east of Miners Creek), the Alpha–Corsair vein-fault is the west boundary of the Creede graben.

The distant sawtooth peak just visible to the north is San Luis Peak (4271 m), the high point on the resurgently uplifted block within the San Luis caldera. Thus, parts of four calderas are in sight.

Two sites of the Continental Scientific Drilling Program (CSDP), for drilling 0.6–1 km through the Creede Formation in the moat of the caldera, are within view (Fig. 3-5). One is near the airport, on line with the Creede vein system; the other is several kilometers farther west. This drilling, proposed for the summer of 1989 or 1990, is intended to evaluate the connate-fluid environment at depth in the Creede sediments (Bethke and Lipman, 1987). The high salinities in fluid inclusions from the ores are a distinctive signature for the fluid component inferred to have been derived from the lake sediments, and provides a basis for fluid-flow modeling not possible in mining districts where the fluid components are less distinct compositionally. In addition, the moat drillholes will provide a record of postcaldera volcanic events; air-fall tuffs, ash-flow deposits, and even lavas may be interbedded with the moat sediments. Drill penetration into the top of the Snowshoe Mountain Tuff flooring the moat should also be possible.

Return to vehicles. **Turn right** on Deep Creek road; proceed east. In 0.2 mi **turn left** on airport road toward Creede. Cross Rio Grande bridge and continue ahead, past airport. **1.4**

22.4 Rejoin CO-149. **Bear right** to Creede. Exposures on left are lacustrine Creede Formation, showing soft-sediment deformation. Emperius Mill on left processed ore from the Amethyst-OH vein, yielding tailings ahead on right. The Homestake mill and Bulldog Mountain mine are up the hill to the left. **1.5**

23.9 Entering Creede (2694 m). CO-149 eastbound turns right. Continue straight ahead through town, to canyon of Willow Creek (Fig. 3-6). At canyon mouth, portal on left is the town firehouse! Rocks along Creek are intracaldera Willow Creek zone of Bachelor Mountain Member. **1.1**

25.0 Junction of East and West Forks of Willow Creek. **Bear left** to stay in West Fork. On left are foundations of the old Humphrey's Mill. Outcrops are the Willow Creek zone of the Bachelor Mountain Member. Note strong brecciation and sheet jointing. **0.5**

25.5 **STOP 8. Commodore 5 level. Turn left** into parking lot (with permission). The Commodore 5 level was the main haulage on the Amethyst-OH vein system (Fig. 3-7). The Commodore 4 and Commodore 3 levels are marked by buildings higher on the vein. The Amethyst vein is an epithermal Ag–Pb–Zn vein that filled the Amethyst fault at about 25 Ma (Steven and Eaton, 1975; Wetlaufer et al., 1977; Bethke and Rye, 1979). During caldera resurgence at about 27.4 Ma, rhyolitic tuffs of the Bachelor Mountain Member were faulted and brecciated while they were still hot and plastic along an ancestral Amethyst fault zone. The Creede graben was reactivated about 2.5 Ma later, along the same general trends as the ancestral Amethyst, following activity of the Creede and San Luis calderas (Steven and Ratté, 1965; Bethke et al., 1976). The Amethyst fault strikes N 15–20° W, as is typical of Creede graben structures, and dips 50–70° SW. The Willow Creek zone of the Bachelor Mountain Member comprises most of the footwall; Campbell Mountain zone makes up higher parts of the hanging wall. Some major northwest-trending splays, such as the OH vein (Fig. 3-5), were also strongly mineralized. The Amethyst vein is bounded upward by a clay cap and is little exposed at the surface, although sediments of the Creede Formation are mineralized near the Commodore 3 level.

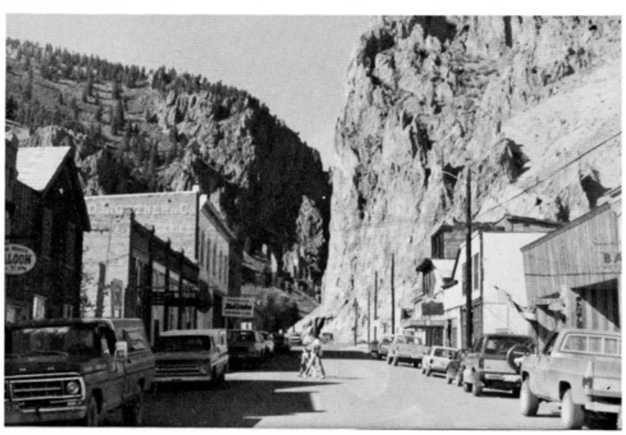

FIGURE 3-6—Town of Creede, with north wall of Creede caldera forming cliffs in background (mile 23.9).

FIGURE 3-7—Commodore 5 workings along Amethyst vein-fault, which drops Campbell Mountain zone (on left) down against Willow Creek zone of the intracaldera Carpenter Ridge Tuff (Stop 8).

Turn and retrace route south, to forks of Willow Creek. **0.5**

26.0 **STOP 9. Junction of East and West Willow Creeks; Willow Creek zone. Turn left** over bridge. Rocks immediately on left are a downdropped block of Campbell Mountain zone of the Bachelor Mountain Member, exhibiting good eutaxitic texture. East of the fault, the Willow Creek zone shows fluidal structure due to extreme compaction and flowage of pumice.

Pumice fiamme in the Willow Creek zone commonly have elongation ratios of 20–30:1; some exceed 100:1. In places, elongate pumices also define a flowage lineation in the plane of foliation. The foliation orientations are somewhat variable in attitude here, but are typically steeper than 40°. Dips decrease up-section, and are typically only 10–20° at the top of the cliffs east of East Willow Creek. Such decreases in dip up-section characterize all thick sections of the intracaldera Bachelor Mountain Member and indicate deformation during compaction, prior to completion of the intracaldera pyroclastic accumulation. The overall geometry of this deformation appears related to the inception of resurgent doming.

Locally, the pumice foliation of the Willow Creek zone is swirly and folded, and in places this fluidal rhyolite has been rheomorphically mobilized into discordant diapirs that penetrate the overlying Willow Creek and Campbell Mountain zones. These rocks were originally mapped as intrusive rhyolite of the Bachelor Mountain Member, but foliations grade from gently dipping to vertical and collapsed pumice textures are still discernible in the steeply dipping diapiric tuff. These relations are exceptionally exposed in mine workings, and interpretations have been developed jointly with Mack Roeber, formerly chief geologist of the Homestake Bulldog mine. The rheomorphic tuff is spacially associated with faults of the Creede graben, indicating initial graben faulting at the Bachelor caldera while the intracaldera tuff was still hot and plastic. Continued movement along the graben faults caused early brecciation of tuff, especially along rheomorphic zones.

From the town of Creede to approximately 1 km north of the junction of East and West Willow Creeks, the Bachelor Mountain Member is strongly brecciated. This brecciated area is bounded on the north by an area of vertically sheet-jointed Willow Creek zone. The structural significance of the complex joint patterns in this area remains poorly understood; the joints probably reflect overlapping events, including compaction and cooling of the thick Bachelor caldera fill, resurgence of the Bachelor caldera, truncation by the Creede caldera, and subsequent continued movement and mineralization along the Creede graben.

Continue up East Willow Creek. Note sheet jointing in Willow Creek zone. **0.7**

26.7 Sheeted Willow Creek zone is distorted in a series of sigmoidal folds. Entering San Luis Peak 7.5-min. quadrangle (Lipman and Sawyer, 1988). **1.0**

27.7 South end of dump at Ridge mine; Solomon mine just above. The East Willow Creek drainage follows the Solomon–Holy Moses fault system, which is the eastern margin of the Creede graben. **0.6**

28.3 **STOP 10. First Fork: Caldera slide breccias and Bachelor caldera fill.** Pull off on side track to right. High cliffs directly ahead and on right are Mammoth Mountain member of the Carpenter Ridge, showing a well-defined compositional zonation from phenocryst-poor rhyolite upward into more crystal-rich silicic dacite (Ratté and Steven, 1967; Webber, 1988). Highest exposures are Wason Park Tuff (Fig. 3-8). The general topics of this stop are the complex depositional, compositional, and welding variations in the intracaldera Carpenter Ridge Tuff between this area and Wagon Wheel Gap (Fig. 3-9).

Lower slopes of the ridge north of First Fork, leading up to a conspicuous dark-gray outcrop, are the main features to be examined. Cross the stream and climb to the top of this outcrop, noting textural and compositional changes. Observe the gray to brown devitrified tuff of the Campbell Mountain zone just across the stream. The dark-gray glassy outcrop and the reddish-brown phenocryst-rich overlying tuff were previously mapped as Phoenix Park Member of the La Garita Tuff (Emmons and Larsen, 1923; Steven and Ratté, 1965, 1973). This unit was interpreted as one of several late ash flows of Fish Canyon type from the La Garita caldera that were thought to interfinger with and overlie the Bachelor Mountain Member in this area.

We now interpret the Phoenix Park units, rather than being primary ash-flow deposits, as landslide breccias derived from the northeast wall of the Bachelor caldera (La Garita Mountains) during subsidence (Lipman and Sawyer, 1988). Do you see the evidence for such an interpretation in these outcrops? Note the phenocryst types and abundance in the vitrophyre zone. Is the vitrophyre part of the Bachelor Mountain or the Phoenix Park unit? Keep in mind that upper vitrophyres are rare in ash-flow sheets. How does the degree of welding change upward? Note evidence for matrix of crystal-poor rhyolitic tuff surrounding clasts of oxidized reddish, crystal-rich tuff. These slide breccias resemble those at Stops 4 and 5 (Wagon Wheel Gap megabreccia member), except that here the Fish Canyon blocks are derived from the thick tuff of the intracaldera resurgent dome rather than from the outflow sheet on the caldera rim. Cooling against the slide breccias caused the local reversal in welding and crystallization zones within the Bachelor Mountain Member.

Across valley to west is south end of dump at Outlet Tunnel mine. The cliffs on the left, above the mine, are Willow Creek zone; the juxtaposition with Mammoth Mountain lithologies across the valley is due mainly to the northeastward dip of these welded tuffs resulting from resurgence of the Bachelor caldera. The Outlet Tunnel mine is the type locality for another unit of Fish Canyon type, the Outlet Tunnel Member of the La Garita Tuff as mapped previously (Emmons and Larsen, 1923; Steven and Ratté, 1973). The rocks of Fish Canyon lithology are exposed there only in one small out-

FIGURE 3-8—First Fork section, showing complex welding, crystallization, and compositional zonation of Carpenter Ridge Tuff within the Bachelor caldera (Stop 10). Units of the Carpenter Ridge Tuff: Tcc, rhyolitic Campbell Mountain zone; Tcb, Phoenix Park megabreccia unit (landslide blocks of intracaldera Fish Canyon Tuff derived from the La Garita Mountains on the northeast caldera wall); Tcm, dacitic Mammoth Mountain member; Tcw, weakly welded rhyolitic Windy Gulch zone; v, vitrophyric tuff where Campbell Mountain zone quenched against overlying landslide blocks of Phoenix Park unit. Tw, Wason Park Tuff.

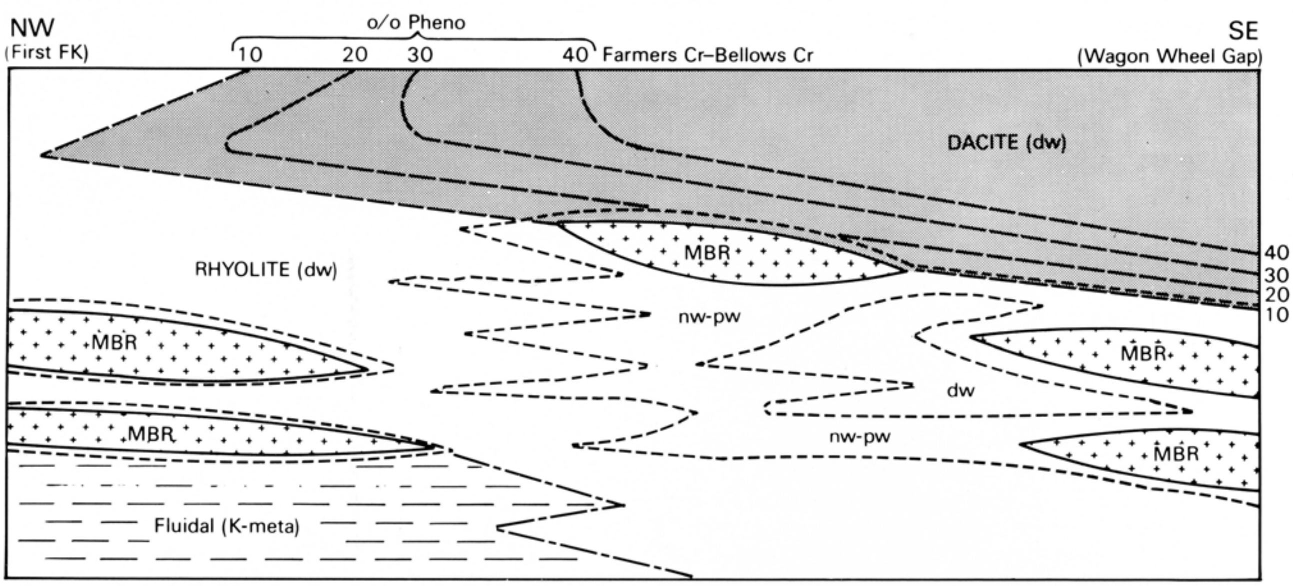

FIGURE 3-9—Diagrammatic section along east side of Bachelor caldera fill, showing complex depositional, compositional, and welding relations between caldera-filling Carpenter Ridge Tuff (Bachelor Mountain Member) and interleaved landslide-megabreccia lenses. MBR, megabreccia; nw, nonwelded; pw, partly welded; dw, densely welded; fluidal, fluidally welded Willow Creek zone; K-meta, areas affected by extreme potassium metasomatism. Also shown by dashed-line contours are percent total phenocrysts, which increase upward and southeastward as the bulk chemical composition of the tuff changes from rhyolite (Bachelor Mountain Member) to silicic dacite (Mammoth Mountain member).

crop at creek level and in the now inaccessible mine workings. These previously were correlated with the main mass of intracaldera Fish Canyon Tuff in the resurgent dome of the La Garita caldera to the northeast and were interpreted as part of the floor of the Bachelor caldera (Steven and Ratté, 1965). We now interpret all the Outlet Tunnel rocks as landslide and talus breccia of Fish Canyon Tuff, similar to the mapped Phoenix Park breccia lenses higher in the caldera-fill section, all of which were derived from the Bachelor caldera wall during subsidence. The Outlet Tunnel unit thus has no stratigraphic significance, nor does any evidence exist for Bachelor caldera floor in this area. All previously mapped Fish Canyon (La Garita) Tuff, for 4 km up East Willow Creek from the Outlet Tunnel mine, is landslide and talus debris within the Bachelor caldera, rather than in-place fill of the La Garita caldera. Steven and Ratté recognized the talus-breccia character of some of these rocks but did not recognize their relation to formation of the Bachelor caldera nor map the boundary between the slide and talus breccias versus coherent intracaldera Fish Canyon Tuff.

Higher on this ridge, the Phoenix Park breccias are overlain at the base of the rugged cliffs by vitrophyric crystal-poor rhyolite, previously mapped as rhyolitic Mammoth Mountain. Elsewhere within the Bachelor caldera, where landslide-breccia units are absent, no vitrophyre or cooling break is present along mapped contacts between Bachelor Mountain Member and rhyolitic Mammoth Mountain lithology. Such contacts are marked only by a color change and decreased intensity of potassium metasomatic alteration (Stop 12). Accordingly, the term Mammoth Mountain member is now used by us only for the phenocryst-rich silicic dacitic upper part of the section. At First Fork, the silicic dacite unit is only about 75 m thick and is overlain by additional crystal-poor rhyolitic uppermost tuffs, but the thickness of the silicic dacite increases to the south, reaching more than 250 m at Blue Creek (Stop 4). The silicic dacite wedges out northward, beyond First Fork, and the upper rhyolitic tuff wedges out southward (Fig. 3-9); these lateral changes may reflect differing vent locations for rhyolite and dacite, or changing depositional slopes within the caldera due to differential subsidence.

The overall distribution of the Mammoth Mountain member and the significance of large local variations in composition and thickness are not yet fully understood. Several aspects of this distribution, along with decreased amounts of tilt upward in section, suggest that the Mammoth Mountain may have been deposited during early phases of resurgent doming, causing ponding of the silicic dacite in the moat between the resurgent dome and topographic wall of the caldera. Other features of the compositional gradients may be due to fluctuations in discharge rate during the eruption, permitting varying drawdown and ephemeral cones of depression that crossed compositional boundaries in a layered or zoned source magma chamber.

Return to vehicles; continue up East Willow Creek. **0.6**

28.9 Crossing East Willow Creek in geographic Phoenix Park (2958 m). Follow road up onto Campbell Mountain. Workings of Phoenix Park mine just ahead on right. **1.2**

30.1 **STOP 11. View northeast, toward La Garita Mountains on skyline.** The La Garita Mountains consist entirely of intracaldera Fish Canyon Tuff in the resurgent dome of the La Garita caldera. The southwestern third of this resurgent dome caved away during collapse of the Bachelor caldera, and the wedge-out of layered units on the gentle slopes at the base of the La Garita Mountains (geographic Wason Park; 3575 m) marks the top of the fill preserved within the moat of the Bachelor caldera.

Flat-topped cliffs, at timberline to north, are geographic Nelson Mountain (3685 m), the type locality for the Nelson Mountain Tuff. The section on the southeast shoulder of Nelson Mountain contains good exposures of compositionally zoned Nelson Mountain and Rat Creek units, erupted from the San Luis caldera to the north. Continue up road. **0.2**

30.3 Road crosses flat saddle, underlain by Mammoth Mountain member. Ahead to left, jeep trail leads to Campbell Mountain, the type locality for the Campbell Mountain zone of the Bachelor Mountain Member. **0.6**

30.9 **STOP 12. Nelson Creek crossing: Features of potassium metasomatism.** The Campbell Mountain zone is intermittently exposed along roadcuts to the south for the next quarter mile, and the boundary with rocks previously mapped as rhyolitic Mammoth Mountain Tuff (Steven and Ratté, 1973) crosses the road near this point. Collect a piece of Campbell Mountain zone for reference. Walk back uphill along the road, examining color and textural changes in welded rhyolitic tuff for about 150 m, to the first sharp curve east. The changes in color from purplish gray to tan, with accompanying textural changes, have previously been used to locate contacts between Campbell Mountain and Mammoth Mountain units (Emmons and Larsen, 1923; Steven and Ratté, 1965). Despite the incomplete exposures, it should be clear that there is no significant decrease in welding or development of a vitrophyre zone, such as characterize normal cooling-unit breaks between separate welded ash-flow sheets or where the Mammoth Mountain member rests on Phoenix Park slide breccia (Stop 10). Instead, this change is interpreted as reflecting decreased potassium metasomatism in intracaldera rhyolitic Carpenter Ridge Tuff (Lipman and Sawyer, 1988). Indeed, interpretive problems with this contact were noted long ago (Emmons and Larsen, 1923: 43–44).

In places, altered intracaldera Carpenter Ridge (Bachelor Mountain Member) contains as much as 12% K_2O and less than 0.5% Na_2O, in contrast with magmatic values of about 5% and 4%, respectively, in unaltered outflow tuffs. Here the degree of K-metasomatism is much less, but it decreases gradually across the "contact" with tan (Mammoth

Mountain-type) rhyolite. The tan rhyolite also shows some alkali exchange. Such potassium metasomatism, first noted in this area (Ratté and Steven, 1967), has recently been recognized widely in Cenozoic volcanic rocks in the western U.S. (Chapin and Lindley, 1986).

Return to vehicles and continue down the road. **0.5**

31.4 Portal and dump of Midwest mine. **0.2**

31.6 Junction with West Willow Creek road. **Turn right,** back toward Midwest mine. Above switchback at the Midwest mine, for the next quarter mile, the rocks poorly exposed along road are Campbell Mountain zone. **0.4**

32.0 Amethyst mine is visible in views back through the aspen. **1.8**

33.8 Junction with Equity mine road, at West Willow Creek crossing. Small exposures surrounded by glacial till in road ahead are transitional rhyolite–silicic dacite of the Nelson Mountain Tuff, thinly plastered against an embayment in the caldera wall. Float exposures of andesitic lava just to the right of the road are inferred to be andesite of Bristol Head, part of the caldera-wall sequence. Some small mineralized structures related to the north Amethyst fault probably are present in this poorly exposed area, but displacements are small. Because of such poor exposures, data are sparse on the Amethyst fault/vein system between the Park Regent shaft and the Captive Inca mine.

Several other stratigraphic discontinuities in this area, previously inferred to result from sizeable offsets along faults of the Creede graben, have recently been reinterpreted as due to unconformities along caldera walls (Lipman and Sawyer, 1988).

Continue up-valley. **1.1**

34.9 Road crosses West Willow Creek. **0.5**

35.4 **STOP 13. San Luis caldera viewpoint; proposed CSDP Creede district drillhole.** Park along right side of built-up roadway, adjacent to modest high point (Quaternary landslide slump block) near beaver ponds. Walk to high point for best view of caldera wall structures (Fig. 3-10). We are within a large reentrant in the south wall of the San Luis caldera. Despite the heavy surficial cover, limited surface exposures and proprietary exploration drill-hole data permit confident reconstruction of the geometry of the caldera wall in this area.

On slopes to the northeast, across West Willow Creek, thick caldera-filling Nelson Mountain Tuff is compositionally zoned from upper crystal-rich dacite (informally called the Equity phase) downward into rhyolitic tuff. The Equity fault is the reddish Fe-stained structure to the northeast. Virtually all surface exposures south of the east–west-trending Equity fault are of the dacitic tuff, which wedges southward on the caldera wall against the Captive Inca lava dome and associated flow breccias (silicic dacite; 69–70% SiO_2). The Captive Inca dome, which overlies the Wason Park Tuff, is visible in the large exposure across the creek and through the trees to the southeast. This is one of several lava flows and domes emplaced around the south margin of the

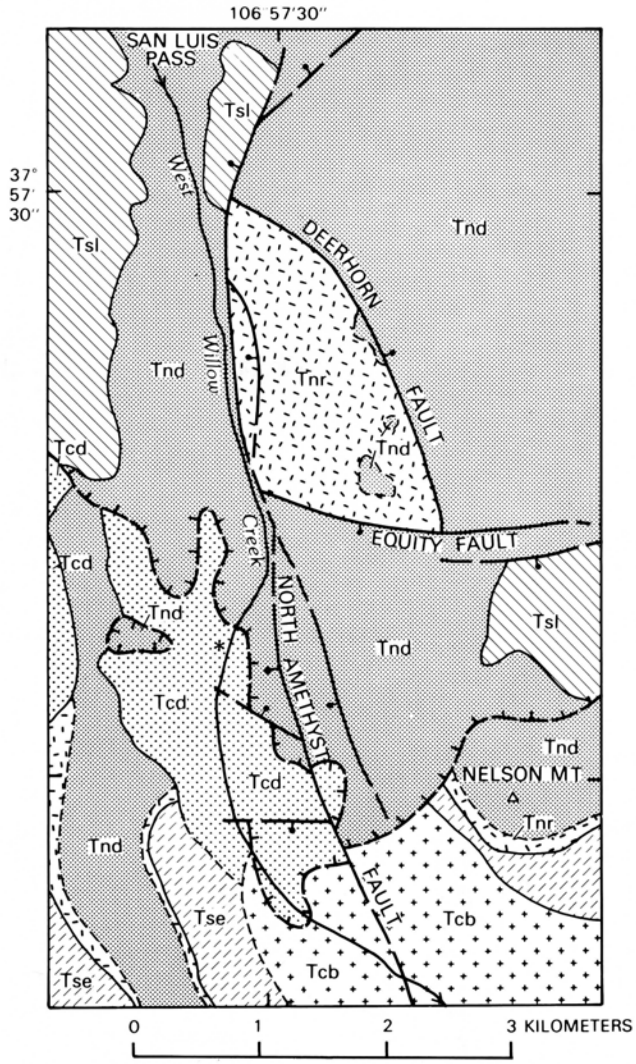

FIGURE 3-10—Geologic map of the Equity mine area; modified from Lipman and Sawyer (1988). *, location of Stop 13. Map units: Tsl, post-collapse lavas of the San Luis caldera; Tnd, Nelson Mountain Tuff (upper transitional rhyolite–dacite of outflow sheet and intracaldera dacite); Tnr, Nelson Mountain Tuff (rhyolitic); Tse, early tuffs of San Luis caldera (Rat Creek Tuff and tuff of Cebolla Creek); Tcd, precaldera lava dome (dacite of Captive Inca); Tcb, Carpenter Ridge Tuff constituting fill within Bachelor caldera.

San Luis caldera complex shortly before its initial pyroclastic eruptions (Rat Creek Tuff).

Relations to the west of the viewpoint, though complicated by Quaternary landsliding, display the transition from thick caldera-filling tuff on the north, laterally southward into relatively thin, sheet-like outflow Nelson Mountain Tuff, resting on Rat Creek Tuff and older volcanic rocks southwest across the topographic wall of the San Luis caldera (Fig. 3-10). Depositional truncation along the caldera wall is exposed in one place—a small set of cliffs to the northwest, where thick intracaldera dacitic tuff (on the east) wedges out against interior exposures of the Captive Inca dome. This contact was previously mapped as a regional fault of potential economic significance, the northern continuation of the Bulldog Mountain fault (Steven and Ratté, 1973), but it is demonstrably a depositional contact. A vitrophyre is present along the base of the dacitic tuff, demonstrating quenching along an original depositional contact; primary compaction foliation in the tuff steepens from near horizontal to about 40° adjacent to the caldera-wall contact.

The approximate site of the proposed 3–5 km CSDP Creede district drillhole is in this area (Bethke and Lipman, 1987). This hole would provide a vertical section through the fossil geothermal system responsible for the Creede epithermal veins, permitting reconstruction of physical gradients with depth, testing for possible stacked concealed mineralization of porphyry type, and hopefully penetrating the causative intrusive heat source. In addition, the hole would provide a deep section through fill of the Bachelor caldera, the upper part of which is already well constrained by natural exposures. No comparably thick caldera-fill sections are available in surface exposures.

Continue ahead, to Equity mine. **0.9**

36.3 **STOP 14. Equity mine and fault.** (3385 m). The east–west Equity fault displaces rhyolitic intracaldera Nelson Mountain Tuff several hundred meters upward against the dacitic upper part of the unit to the south (Figs. 3-10, 3-11). This fault trend is regionally anomalous, in comparison with the dominant north-northwest trend of Creede graben structures. The Equity fault bounds the southern end of a triangular uplifted block, presumably reflecting presence of an intrusion at depth, and also marks the southern limit of resurgent uplift in this part of the San Luis caldera.

The welded rhyolitic tuff of the Nelson Mountain, exposed on lower slopes of the Equity block, closely resembles units of the Bachelor Mountain Member of the Carpenter Ridge Tuff, with which they were correlated previously (Emmons and Larsen, 1923; Steven and Ratté, 1973). New surface and drillcore studies indicate that these rhyolitic tuffs grade upward into typical dacitic Nelson Mountain Tuff (Equity phase) and therefore are intracaldera equivalents of the generally weakly welded lower rhyolite of the compositionally zoned outflow Nelson Mountain Tuff (Lipman and Sawyer, 1988). These relations reduce the size and northern extent of the Bachelor caldera, as previously interpreted (Steven and Lipman, 1976).

Mineral exploration at the intersection of the Equity and north Amethyst faults has been underway intermittently since early in the century. Recent intensified exploration by the Homestake Mining Company, involving extensive core drilling and

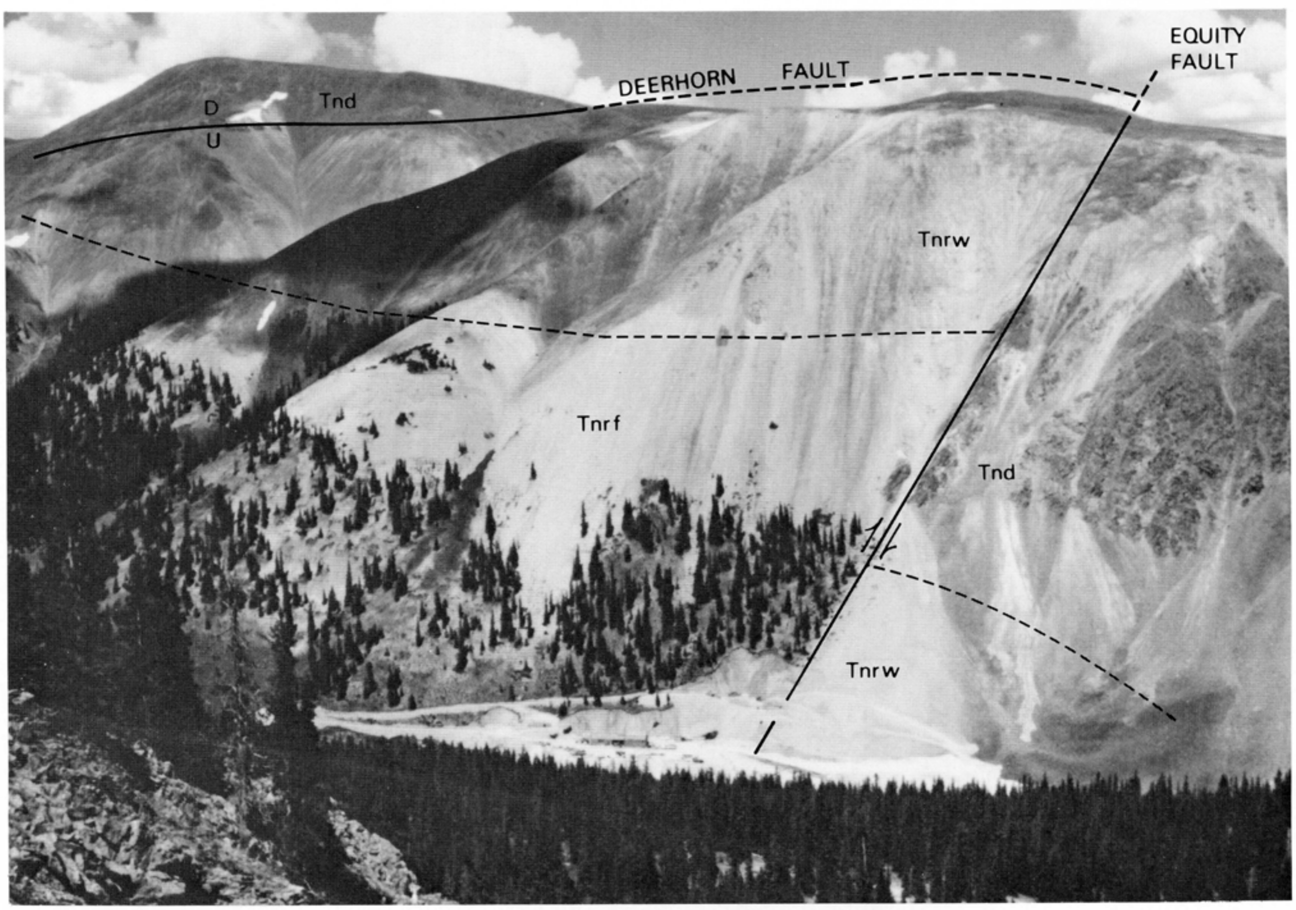

FIGURE 3-11—The Equity fault and mine workings as viewed from the west (Stop 14). The Equity fault is an east–west reverse structure that bounds the south margin of an uplifted block of intracaldera rhyolitic Nelson Mountain Tuff. The Equity block overlies a concealed dacitic intrusion (exposed in drillholes and mine workings), and is juxtaposed against surrounding dacitic Nelson Mountain Tuff; the Equity block is bounded on its east side by the Deerhorn fault. Intracaldera units of the Nelson Mountain Tuff: Tnrf, fluidally welded rhyolitic tuff; Tnrw, welded rhyolitic tuff; Tnd, welded dacitic tuff.

driving a decline near the intersection of the Equity and north Amethyst faults, has encountered significant mineralization, but few details are publicly available at the time of writing (1988). Recent work by Bethke, Barton, Plumlee, Rye, Foley, Hayba, and others (see abstracts for 1987 GSA symposium, Rocky Mtn. section) has refined the model for the mineralizing Creede geothermal system. Available evidence indicates a single hydrothermal plume that rose in the general area along the northern Amethyst vein between the Captive Inca and Equity mines and flowed laterally as far as 8 km to the south, mineralizing the Amethyst and Bulldog vein systems (Fig. 3-12). Two compositionally distinct fluid sources are required: a saline brine thought to be derived from moat sediments of the Creede Formation; and meteoric water derived from the north, near the present Continental Divide.

Turn vehicles and return to Bachelor road junction. **2.5**

38.8 Bachelor road junction. **Turn right,** cross West Willow Creek, and proceed south. **1.2**

40.0 Dump at the Park Regent shaft on left. The Park Regent is the northwesternmost shaft on the main Amethyst vein. **0.4**

40.4 Wason Park Tuff is poorly exposed for the next 0.5 mi in the aspen along sides of the road, as well as in Mineral County gravel pit on right. **0.7**

41.1 Out of the aspen into a meadow that was the site of the town of Bachelor in the late 1890's and early 1900's. Bachelor once had several thousand residents. Its location permitted easy access to the shafts along the Amethyst vein system. **0.8**

41.9 Cross Windy Gulch. The Bulldog Mountain mine of the Homestake Company is visible down-valley. **0.9**

42.8 **STOP 15. Panoramic view of resurgent Creede caldera.** Snowshoe Mountain resurgent dome (Fig. 3-13) is surrounded by a topographically low moat followed by the Rio Grande, which has excavated the Creede Formation. Flanks of Snowshoe Mountain are dip-slopes of as much as 45° in the 26.7 Ma Snowshoe Mountain Tuff. Below is the town of Creede and the Bulldog Mountain mine. In the far distance is Fisher Mountain, one of the post-caldera lava domes of Fisher Quartz Latite. The entire northern half of the Creede caldera wall is visible, extending from Bristol Head on the west through the area where we are standing around to the east at Wagon Wheel Gap. The Wagon Wheel Gap lava dome was the site of Stop 6. In the far distance is North Mountain at Summitville, the site of an earlier stop on the field trip. The drainage of Deep Creek, conspicuous on the north side of Snowshoe Mountain, follows the downdropped keystone graben on the crest of the Snowshoe Mountain dome. The large outcrops on the Bachelor caldera wall, to the east, are the Willow Creek zone of Bachelor Mountain Member, representing a small part of the thick intracaldera accumulation of the Carpenter Ridge Tuff within the Bachelor caldera.

After stop, continue downhill. **1.0**

43.8 **Sharp right turn,** onto less traveled road. (Alternative: continue ahead, and return to town of Creede.) **0.8**

44.6 Fork in road; **bear left. 0.5**

45.1 Junction with road up Miners Creek. **Turn right.** The Miners Creek drainage follows the Alpha–Corsair fault, the westernmost fault system of the Creede graben (Fig. 3-5). **0.5**

45.6 Shallow Creek road. **Turn left,** crossing Miners Creek. **0.2**

45.8 **Bear left,** through stock gate, and again at fork, to road end. **1.7**

47.5 **STOP 16. Shallow Creek breccias; Bachelor caldera fill.** Road becomes indistinct at first Shallow

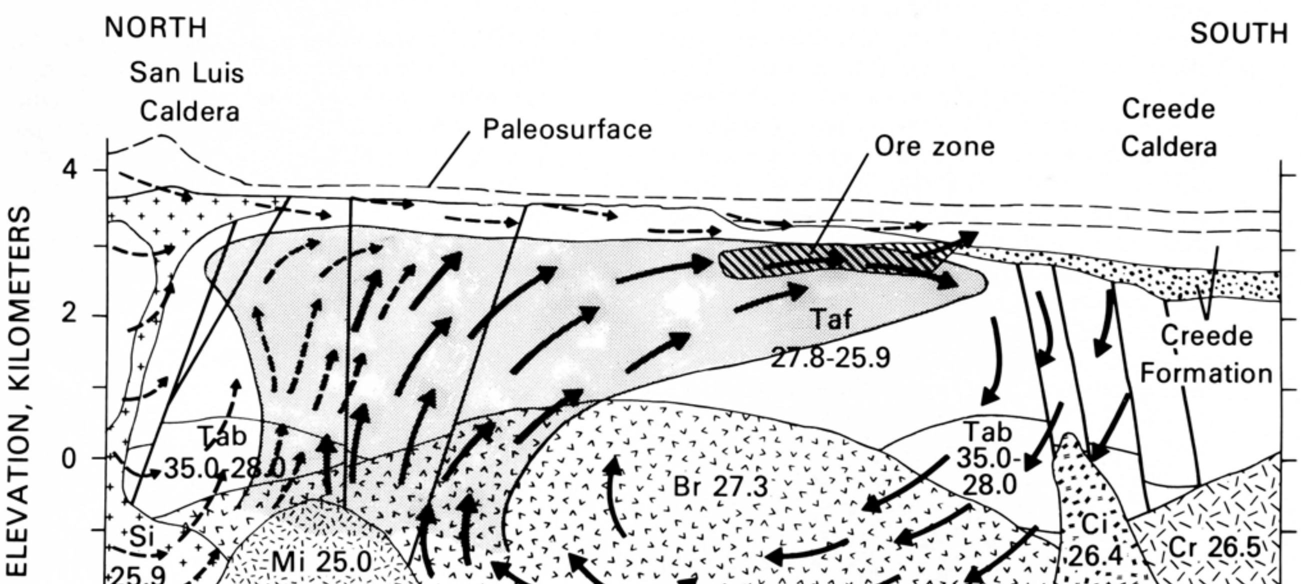

FIGURE 3-12—North–south cross section along the Creede graben, showing inferred geometry of fossil hydrothermal system (modified from Bethke and Lipman, 1987). Volcanic units: Taf, intracaldera ash-flow tuffs; Tab, precaldera andesite flows and breccias (Conejos Formation). Inferred caldera-related intrusions: Br, resurgent intrusion of Bachelor caldera; Cr, resurgent intrusion of Creede caldera; Ci, ring intrusion of Creede caldera; Si, ring intrusion of San Luis caldera; Mi, mineralization-related intrusion.

FIGURE 3-13—View of Creede caldera from the north (Stop 15), showing central resurgent dome, outer topographic wall, and structural moat. Rio Grande has excavated the soft lacustrine fill of Oligocene age that filled the moat. From Ratté and Steven (1967, color frontispiece).

Creek crossing; park vehicles in clump of trees. Walk across stream (log for crossing) to prospect in gray Willow Creek zone. This mine adit is in the fluidal Willow Creek zone of Bachelor Mountain Member. Note large mafic fiamme, containing conspicuous biotite in rocks on dump, and the strong flattening of the pumice foliation in the Willow Creek. Cross back across stream and head west along trail on north side of Shallow Creek. Small quarry in Willow Creek lithology also shows stretched pumice on the compaction foliation and the mafic pumice. Continue about a quarter mile west, to the first major drainage from north.

Head up the ridge on the east side of the drainage, watching for lithologic variations in the Bachelor Mountain Member. Note the abundant andesitic lithic debris; at the top of the first small hill, clasts (up to 2–3 m across) are andesite and dacite, enveloped by crystal-poor tuff. This mesobreccia (Shallow Creek breccia member of the Carpenter Ridge Tuff) is derived from precaldera (Conejos-age) early intermediate-composition stratovolcanoes on the west wall of the Bachelor caldera. Table Mountain, visible up Shallow Creek to the west, is one of these centers. Continue up ridge to the next minor knob.

More mesobreccia of andesite clasts crops out on the way to, and at, this knob. Farther north, in a cliff exposure in the Bachelor Mountain fill, some house-sized andesite blocks are visible. Examine the texture and color of the rhyolite tuff matrix. It passes from typical purplish-gray Willow Creek zone below, through a mesobreccia-rich interval, into reddish-brown rhyolite, originally grouped with the Mammoth Mountain, without evidence for a depositional break or intervening Campbell Mountain and Windy Gulch zones. Here the "Mammoth Mountain" rhyolite directly atop fluidal rhyolite of the Willow Creek zone provides evidence for the entire Bachelor–Mammoth sequence being part of a single caldera-fill sequence.

Return to vehicles and retrace route to Miners Creek. **1.9**

49.4 Junction with Miners Creek. **Turn right,** toward resurgent dome of the Creede caldera. **1.6**

51.0 Junction of Miners Creek road with CO-149. **Turn right** and continue toward Lake City. **1.7**

52.7 Five-Mile bridge across Rio Grande: spectacular exposure of Creede Formation. Sequence on caldera wall above is Mammoth Mountain member of Carpenter Ridge Tuff and Wason Park Tuff, capped by local andesitic–dacitic lavas of Bristol Head. **1.8**

54.5 Approaching Seven-Mile bridge and Middle Creek road intersection. Rocks on left are Point of Rocks lava dome, a white silicic rhyolite (76% SiO_2) that probably erupted after resurgent doming of the Creede caldera. This is the only silicic rhyolite erupted from the central caldera cluster. Fragments of the rhyolite are abundant in adjacent exposures of the Creede Formation.

Good outcrops of the intracaldera Snowshoe Mountain Tuff are accessible along the Middle Creek road. Lowest exposures in caldera wall ahead and on right are Masonic Park Tuff, underlain by andesitic lavas that are equivalent to the Conejos Formation on the west margin of the central San Juan caldera cluster. **1.4**

55.9 Entering Bristol Head 15-min. quad (Steven, 1967). **0.5**

56.4 **STOP 17. Caldera-margin breccia within the Snowshoe Mountain Tuff.** Roadcuts along tight curves in road; be alert for oncoming high-speed traffic (not suitable for large groups). These exposures have long been mapped as intermediate-composition volcaniclastic facies of the precaldera volcanics (Steven and Ratté, 1973). Indeed, andesite–dacite clasts up to 1 m across are the dominant component, but several features indicate that clasts slid or were washed into the Creede caldera late during its formation: (1) though most clasts are of intermediate-composition lava, a few are distinctive Wason Park Tuff; (2) crude bedding dips 25–30° inward toward core of caldera; (3) at the north end of the exposures, nonwelded phenocryst-rich dacitic tuff of Snowshoe Mountain type is present as matrix surrounding the clasts.

These deposits closely constrain the location of the Creede caldera wall in this area, for precaldera lava flows of the Conejos Formation are exposed about 200 m up-slope. Many of the clasts are well rounded, in contrast with the angular fragments typically found in landslide breccias interleaved with caldera-filling tuffs elsewhere in the San Juan field.

Thus, these deposits are tentatively interpreted as emplaced by mudflows, off the caldera walls, that scoured and incorporated nonwelded patches of Snowshoe Mountain Tuff during emplacement. Lithologically complex material such as this may be encountered deep in the CSDP moat holes, below lake beds of the Creede Formation. Continue along road. **1.8**

58.2 Approaching turn to right, in saddle between caldera wall and isolated hill of early andesite flows that underlie Masonic Park Tuff. Prominent exposures on flank of Snowshoe Mountain, at 8:00, are a ring-dome volcano of Fisher Quartz Latite, as are high hills on skyline at 10:00. High skyline Continental Divide country at 11:00 is ash-flow sequence from central San Juan caldera cluster, mainly Carpenter Ridge and Fish Canyon Tuffs. **1.5**

59.7 Climbing onto terminal moraine of the late Wisconsinan glacier that came down the upper Rio Grande. Entering the Clear Creek graben, another of the northwest-striking extensional features that trend tangentially away from the central San Juan caldera cluster. These graben are interpreted as due to broad regional deformation over the roof of the large batholith that is inferred to underlie the calderas of the central and western San Juan field (Steven and Lipman, 1976; Gebhart, 1987). **1.0**

60.7 **STOP 18. Southwest rim of Bachelor caldera.** Roadcuts of Fish Canyon Tuff, on right, are overlain by andesitic lavas and breccias of the Huerto Formation, and then by transitional rhyolitic–silicic dacitic welded units of Carpenter Ridge Tuff. These tuffs contain mafic alkalic fiamme, characteristic of upper parts of the Carpenter Ridge rhyolite unit, as well as a lag breccia of intermediate-composition lithic inclusions. Similar relations are spectacularly exposed on the relatively inaccessible southeast slopes of Bristol Head.

The absence of thick rhyolite of the Carpenter Ridge Tuff, which is as much as 200 m thick to the south and southwest, and the development of the lag breccia both indicate a wedge-out high on the Bachelor caldera wall. Despite the limited thickness of rhyolitic Carpenter Ridge Tuff, the overlying dacitic Mammoth Mountain member is as much as 200 m thick, perhaps reflecting ponding against yet higher levels of the caldera wall, continued subsidence of the Bachelor caldera, or growth of graben basins related to inception of the Clear Creek fault system.

In the distance south of the Creede caldera, hills south to the Continental Divide are dacitic lavas of Fisher Quartz Latite and earlier andesites, ponded within the largely buried South River caldera. Ridges to the west, along tributaries of Middle Creek, are underlain by Wason Park and Carpenter Ridge Tuffs that are truncated along the west wall of the South River caldera, the source of the 27.2 Ma Wason Park Tuff. **1.2**

61.9 Large outcrops of thick Mammoth Mountain member (200 m) on cliffs to right. Exposures across Rio Grande, to south, are also Mammoth Mountain member. **1.2**

63.1 Wright's Lower Ranch. Massive outcrops on right are thick Wason Park Tuff (175 m), overlying dacitic Mammoth Mountain member. **0.7**

63.8 Wetherill Ranch. One of the famous old ranches of the Creede area. Low exposures on right are Carpenter Ridge Tuff. Entering south margin of Bristol Head Quadrangle Map GQ-631 (Steven, 1967). **1.7**

65.5 Freemon Ranch. Crossing Clear Creek bridge (2740 m). Exposures on left are mostly Fish Canyon Tuff. On right, lowest exposures just above creek level are the younger Wason Park Tuff. At 3:00 is a fine view of Bristol Head, a prominent landmark that consists mostly of andesitic lavas, but of two distinct ages. The capping lavas are andesite of Bristol Head that postdates the 27.2 Ma Wason Park Tuff. The lower slopes are older andesitic lavas that underlie the Fish Canyon and Masonic Park Tuffs and are equivalent to the Conejos Formation. On the Bristol Head 15-min. quad, both lava sequences are shown as Huerto Formation, a unit now restricted to the interval between the Fish Canyon and Carpenter Ridge Tuffs. Straight ahead, prominent light-salmon-brown welded tuffs capping the ridges are rhyolitic Carpenter Ridge Tuff. **2.1**

67.6 Junction of Rio Grande Reservoir road with CO-149. **Stay right** on CO-149. On ridge between two roads, lowest light-yellowish exposures are partly welded Fish Canyon Tuff. Immediately overlying brown ledge is Crystal Lake Tuff, a phenocryst-poor low-silica rhyolite erupted from the Silverton caldera at 27.3–27.8 Ma. Upper large cliff exposures are rhyolitic Carpenter Ridge Tuff from the Bachelor caldera. In contrast with the caldera-wall environment of Stop 18, here the rhyolitic tuff is thick and the silicic dacite is absent. Dips of these units are due to jostling by structures of the Clear Creek graben. **0.5**

68.1 Entering Hinsdale County. **1.6**

69.7 Junction with South Clear Creek road. On right is fine view of Bristol Head (3873 m). The high point consists of andesite of Bristol Head, underlain by Wason Park Tuff, which forms the mesa capping ledge to the left, underlain by Fish Canyon Tuff and older andesite (Conejos Formation). Both the Fish Canyon and Wason Park Tuffs wedge out against the core of this early intermediate-composition stratovolcano. We are looking across several faults of the Clear Creek graben; at road level, poorly exposed beneath the moraine, is Nelson Mountain Tuff, which is stratigraphically above the Wason Park. **1.4**

71.1 South Clear Creek road and campground. Nelson Mountain Tuff is well exposed in South Clear Creek Falls at campground. **1.7**

72.8 **STOP 19. Scenic overlook near Black Mountain turnoff.** View is up South Clear Creek toward Brown and Hermit Lakes; the Rio Grande Pyramid (4215 m) is in the far distance. Light-tan cliffs capping each side of glaciated South Clear Creek are rhyolitic Carpenter Ridge Tuff. Obscurely exposed in the lower slopes is underlying Fish Canyon Tuff. On the Rio Grande Pyramid, exposed in spectacular sequence, are: the Fish Canyon Tuff, local andesitic lavas of the Huerto Formation, Crystal Lake Tuff from the Silverton caldera to the west, Carpenter Ridge Tuff, more local lavas, and a final capping of basalt of the Hinsdale Formation. Looking back down the road, the skyline view of the Continental Divide is toward lava domes of Fisher Quartz Latite, ponded within the largely buried South River caldera south of the Creede caldera.

Black Mountain, in the foreground, is a dome of low-silica rhyolite (72% SiO_2, plagioclase + biotite) that overlies outflow Sunshine Peak Tuff from the 23 Ma Lake City caldera. Here, the Sunshine Peak Tuff accumulated to nearly 100 m thick within a paleovalley cut into Carpenter Ridge Tuff. Cross reported large blocks of basalt from the Hinsdale Formation scattered on the surface of the rhyolite (Larsen and Cross, 1956), suggesting that the rhyolite predated eruptions of basalt at 15–16 Ma from nearby Jarosa Mesa.

Leaving the scenic viewpoint, straight ahead are skyline mesas (Table Mountain and Snow Mesa), capped by Nelson Mountain Tuff. To the left of the road, the rounded timberline mesa is Jarosa Mesa, capped by Hinsdale basalt overlying Sunshine Peak Tuff (23 Ma) from Lake City caldera. **1.3**

74.1 Continental Reservoir road. **0.6**

74.7 On left a good exposure of Nelson Mountain Tuff, faulted down within the Clear Creek graben. This unit also caps the mesas to the right. **3.7**

78.4 **STOP 20. Outflow Sunshine Peak Tuff** in roadcuts on left (Jarosa Mesa). The outflow Sunshine Peak Tuff, erupted from the Lake City caldera at 23 Ma, is a highly fractionated silicic rhyolite (76% SiO_2) containing phenocrysts of chatoyant sodic sanidine (some with anorthoclase cores), elliptically resorbed quartz, sparse biotite, Fe–Ti oxides, and traces of clinopyroxene. Minor phases include zircon, sphene, chevkinite, and apatite (Hon, 1987a). The Sunshine Peak Tuff is unique among the large ash-flow sheets of the San Juan Mountains and has closer petrologic affinities to the Miocene rift-related rhyolites than to the 26–30 Ma calc-alkaline rhyolites and dacites of the older calderas. The outflow Sunshine Peak Tuff is generally poorly to moderately welded and has a punky texture due to vapor-phase crystallization. Along this side of Spring Creek Pass, the outflow tuff is 100 m thick; more commonly, it is less than 30 m thick. These are all minimum thicknesses, because the top of the outflow unit was eroded at all known localities prior to being capped and preserved by basalts of the Hinsdale Formation.

In contrast, the intracaldera Sunshine Peak Tuff is more than 1.5 km thick and is typically densely welded. The intracaldera tuff is compositionally zoned upward from high-silica rhyolite (76.5% SiO_2) to quartz trachyte (68% SiO_2). The outflow unit is correlative with the lower member. Suggest collecting a piece of outflow for comparison with intracaldera tuff later in the trip.

On Jarosa Mesa, the outflow Sunshine Peak Tuff has been preserved beneath 15.4 Ma trachybasalt of the Hinsdale Formation (K. Hon and H. H. Mehnert, unpubl. data). This is the youngest, most mafic (50% SiO_2), and least isotopically contaminated rock from the Miocene basalt plateaus of the western San Juan Mountains (Lipman et al., 1978). Olivine, augite, and plagioclase are present both as 1–2 mm phenocrysts and as groundmass. The sparse plagioclase phenocrysts are sieve-textured and are probably xenocrysts incorporated during contamination by partial melting of lower crustal rocks.

Across the valley to the east are spectacular exposures of Nelson Mountain Tuff capping Snow Mesa; it is underlain by the Wason Park, Carpenter Ridge, and Fish Canyon Tuffs. **1.1**

79.5 Spring Creek Pass corrals. At 1:00, jagged points above timberline are andesite and dacite flows of Baldy Cinco. The highest point is Baldy Cinco (4079 m). The volcanics of Baldy Cinco are postcaldera lava domes around the margins of the San Luis caldera, the source of the Nelson Mountain and Rat Creek Tuffs. On Snow Mesa and Baldy Cinco, these lava flows overlie the Nelson Mountain and Rat Creek Tuffs. **0.7**

80.2 Spring Creek Pass (3322 m). Exposures at road level are all moraine. Ahead are Mesa Seco and Cannibal Mesa, capped by 18–19 Ma trachyandesite of the Hinsdale Formation. For next mile, partly welded Nelson Mountain is poorly exposed in roadcuts. **1.4**

81.6 On right for next 2 mi, and across Rambouillet Creek, are several exposures of somewhat altered partly welded Wason Park Tuff. These are the most northwesterly exposures known of the Wason Park Tuff. The Carpenter Ridge and Fish Canyon are obscurely exposed downstream, underlying the Wason Park. **2.5**

84.1 Exposures of lavas of Slumgullion Pass. These lavas, which underlie at least the Fish Canyon Tuff, are probably of pre-ash-flow age, generally correlative with the Conejos and San Juan Formations. The lavas here are mostly mafic dacite in composition. **1.8**

85.9 Brief but spectacular panoramic view of San Luis caldera, through gap in trees to east. From the south to north are: Snow Mesa capped by Nelson Mountain Tuff, and Baldy Cinco and associated high points that are dacite lava domes on west margin of caldera. Farther in distance, ragged high point is geographic San Luis Peak (4271 m), the high point of intracaldera resurgent Nelson Mountain Tuff within the San Luis caldera. The intracaldera accumulation of this tuff is more than 1.5 km thick. The broad northward slope is a dip-slope on the top of the Nelson Mountain Tuff (or tuff of Cochetopa Creek?), on the resurgent north side of the caldera. The resurgently uplifted area extends across the caldera wall north approximately 2 km beyond the initial collapse area. In farthest distance are high peaks at the southern end of the Sawatch Range, including Mount Ouray (4258 m). **1.7**

87.6 Slumgullion Pass (3450 m); intersection with Cathedral road. **1.1**

88.7 **STOP 21. Windy Point overlook** (Fig. 3-14): Panoramic view of Lake City caldera, Uncompahgre caldera, and Cannibal Mesa; also Uncompahgre and Wetterhorn Peaks (4361, 4272 m). The north wall of the Uncompahgre caldera, which was the source

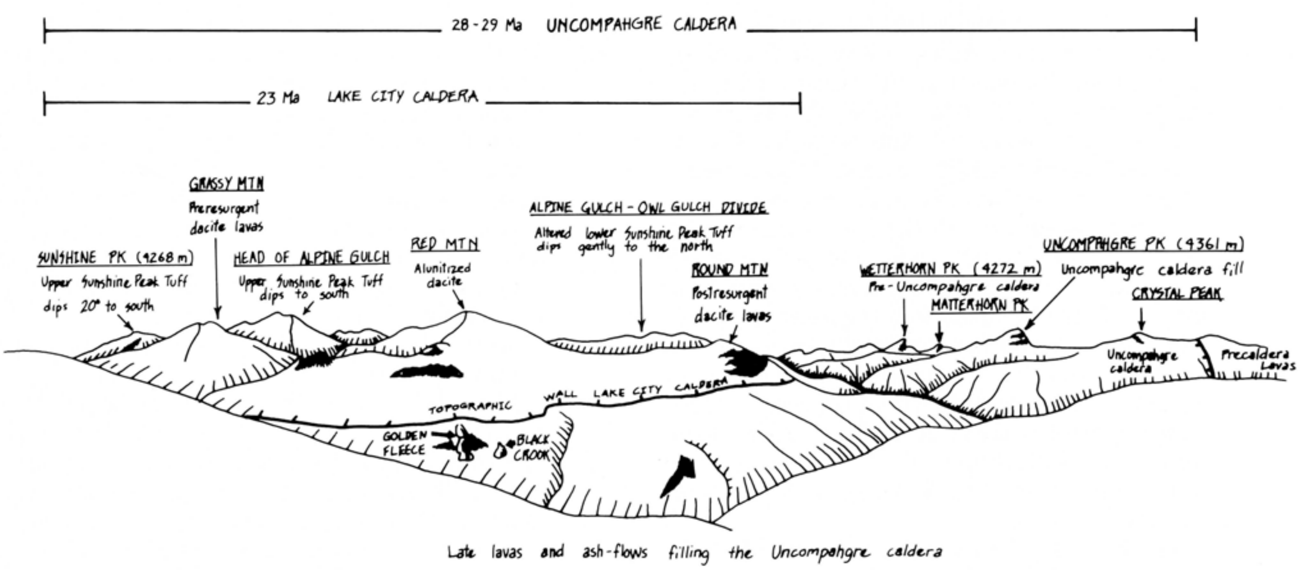

FIGURE 3-14—Lake City caldera, as viewed from Windy Point (Stop 21). See text for geologic description. Sketch by K. Hon.

of the Sapinero Mesa Tuff at 28–29 Ma (Lipman et al., 1973), passes in front of Wetterhorn Peak (capped by Ute Ridge Tuff) and just behind Uncompahgre Peak, just north of Crystal Peak, and curves around under Cannibal Plateau (Figs. 3-14, 4-1). The northeast boundary is obscurely exposed in the altered rocks near the viewpoint. In this area the boundary is defined by postcaldera intermediate-composition lavas of Uncompahgre Peak lapping out against precaldera early intermediate-composition lavas, all highly altered in the Slumgullion Pass area. This thick sequence of postcollapse lavas on the east side of the Uncompahgre caldera marks a locus of late vents. The intense alteration in the Slumgullion Pass area apparently resulted from emplacement of shallow intrusions within their own volcanic pile during the waning stages of the Uncompahgre caldera cycle. Some of these intrusions, and many narrow hydrothermal breccias, are exposed in roadcuts below this stop.

The fill of the Uncompahgre caldera, exposed but difficult to discern at this distance, includes: the intracaldera Sapinero Mesa Tuff (Eureka Member); overlain by units of the Silverton Volcanics including the Burns Member (dacite lavas), pyroxene andesite member (lavas), and Henson Member (volcaniclastic), much as originally described in the Silverton folio (Cross et al., 1905); the Fish Canyon Tuff from the central caldera cluster; outflow Crystal Lake Tuff from the Silverton caldera (about 27.5 Ma); then the Carpenter Ridge Tuff (central caldera cluster); younger, locally erupted postcollapse volcanics of Uncompahgre Peak; and finally the Nelson Mountain Tuff from the central caldera cluster (Table 4-1).

Eruption of the 23 Ma Sunshine Peak Tuff resulted in collapse of the Lake City caldera (Fig. 3-14), which is nested within the older, unrelated, Uncompahgre caldera (Hon, 1987a). The present-day drainages of the Lake Fork of the Gunnison River, coming from the south, and Henson Creek, coming from the west, formed by stream capture in the moat of the Lake City caldera. These drainages define an arcuate pattern that encloses the high area of resurgently domed intracaldera Sunshine Peak Tuff (Fig. 4-1). Most of the preserved caldera fill is within the downdropped structural block that is bounded on its north, west, and south sides by a steep inward-dipping to vertical ring fault. The original fill level of the caldera is estimated to have been 3700 m (12,000 ft), about 300 m above this stop; the present stream levels record downcutting of about 1 km.

The southward-dipping slopes on the left (southeast) side of the resurgent dome (Fig. 3-14) are dip-slopes within the upper member of the intracaldera Sunshine Peak Tuff (68% SiO_2). The high ridge to the right is lower member of the Sunshine Peak Tuff west of Alpine Gulch that was uplifted at least 1 km along the ring fault during asymmetric resurgence of the caldera. Reconstructions indicate that this area was the high point on the resurgent dome, which reached an elevation of more than 1 km above the present ridge.

The upper member of the Sunshine Peak Tuff is overlain on the eastern side of the caldera by a thick sequence of postcollapse dacite lavas which form the mountains in the foreground on the resurgent dome. Lavas that make up Grassy Mountain (south of Red Mountain), and outcrops farther to the south, were erupted prior to or during stages of resurgence and cap the intracaldera tuff sequence. Lavas to the north of Red Mountain, near Round Mountain, were emplaced after resurgence and unconformably overlie steeply dipping upper member of the Sunshine Peak Tuff.

The area surrounding Red Mountain was highly altered during the emplacement of a complex intrusion which may have fed a now-eroded lava dome late in the caldera cycle. Sulfur-rich gas released from the intrusion mixed with overlying meteoric water coming from the resurgent dome and produced a highly acidic fluid phase that pervasively alunitized and brecciated the near-surface rocks (Bove et al., 1987). As observed in core from a 1000 m drillhole, alteration grades downward through an argillic zone (kaolinite and sericite ± smectite) into the potassically altered top of the mineralized pluton, which is associated with weak Mo–Cu anomalies. Shallower drillholes reveal the presence of two centers of alunitization, one beneath Red Mountain and one beneath the summit immediately to the southwest, that extend 200–300 m below these peaks. Surface alteration grades outward from the central alunitized zones through strongly argillized rock (kaolinite), to moderately argillized rock (kaolinite, sericite, and smectite), and into weakly altered rocks on the periphery of the complex. The alunite deposit contains about 200 million metric tons of rock with grades of 30–40% alunite, making it one of the largest known domestic aluminum resources.

The boundary between the upper cliff-forming postcollapse lavas of the Lake City caldera and the lower tree-covered slopes of the Uncompahgre caldera fill marks the topographic wall of the Lake City caldera. The prominent altered area on the lower slopes is the 27.5 Ma Golden Fleece vein, which was truncated during the collapse of the Lake City caldera.

The Golden Fleece vein was the largest gold producer (35,000 ounces) in the Lake City region, and its discovery in 1874 spurred prospecting in the area (Irving and Bancroft, 1911). Most of the vein consists of early vuggy quartz and rhodochrosite with sparse base-metal sulfides. The gold is confined to later dense, fine-grained quartz veinlets that contain Au–Ag tellurides intergrown with uraninite. The uraninite was used to obtain a lead isochron age of 27.5 Ma for the mineralization (Hon et al., 1985). The Golden Fleece vein is important because it is the only significant epithermal precious-metal deposit in the San Juan volcanic field that is clearly associated with the development of a calc-alkaline caldera. This vein is also the most important gold telluride deposit of mid-Tertiary age in the San Juan Mountains. Lead-isotopic data indicate that a significant component of the metals in this deposit were probably scavenged from Precambrian rocks underlying the eastern side of the Uncompahgre caldera. **0.8**

89.5 Sharp curve with roadcuts in altered andesite of Uncompahgre Peak. Just upslope is the approximate boundary between altered precaldera and caldera-fill rocks of the Uncompahgre caldera. Downslope are altered lavas of Uncompahgre Peak, ranging in composition from andesite to rhyolite. **0.2**

89.7 Dark rock is dacite intrusion cutting altered andesitic volcanics of Uncompahgre Peak. **0.4**

90.1 Contact between andesite (above) and rhyolite (below) flows. Small dacite intrusion cuts the rhyolite immediately downslope. Entering Lake City map area (Lipman, 1976a). **0.2**

90.3 Thin (1–2 cm) hydrothermal breccias cut flow-foliated rhyolite. **0.7**

91.0 Parking area with good view of Slumgullion slide. Note chaotic orientations of trees. **0.4**

91.4 Altered rhyolite, part of the volcanics of Uncompahgre Peak, in roadcuts on left. **0.5**

91.9 **STOP 22.** Hairpin turn in Carpenter Ridge Tuff; **view of Lake San Cristobal.** Lake San Cristobal is the largest natural body of water in Colorado; it formed when the Slumgullion "slide" dammed the Lake Fork of the Gunnison River about 1100 years ago. The "slide" is a composite earthflow deposit. The boundary between the lower inactive section damming the lake and an upper active earthflow is well marked by the discontinuity between undisturbed and disturbed trees. With good reason, the Colorado Highway Department has routed the road through the inactive part of the earthflow.

Directly behind us, the headwall of the earthflow is visible. The reddish-brown rock is 18 Ma trachyandesite capping Mesa Seco that overlies highly altered 28 Ma quartz latite flows and breccias capping the Uncompahgre caldera fill. The alteration in this area is probably the same age as the Golden Fleece vein, and the instability of these decomposed rocks caused the earthflow. Due to the strong westerly winds in this area and the abundance of sand- and silt-sized particles in the earthflow, a unique alpine dune field has formed on the mesa just above the headwall.

Looking upstream along the south side of Lake Fork is the Continental Divide, including rocks both inside (foreground slopes) and outside (background) the Uncompahgre caldera. The presence of outflow Sapinero Mesa Tuff and Sunshine Peak Tuff plastered on the south side of this ridge indicates that it approximates the topographic boundary of both the Uncompahgre and Lake City calderas. The present position of the Lake Fork drainage reflects downcutting from the original topographic low in the moat of the Lake City caldera. The limits of till and glacial erratics indicate that the Lake Fork and Henson Creek valleys were occupied by valley glaciers approximately 750 m deep. In contrast, till from the large ice sheet south of the Continental Divide was deposited near the ridge crest, indicating ice thicknesses in excess of 1000 m.

This location offers an excellent view of the unconformity at the Lake City caldera wall, where the dacite of Grassy Mountain overlies and clearly truncates the Golden Fleece vein. Other veins extend across the Lake Fork drainage in a pattern that is crudely radial to the eastern end of the Lake City caldera and are presumed to be the same age as this caldera. These veins are characterized by an assemblage of barite and silver sulfosalts. Their distribution suggests they are related to interaction between hydrothermal convection on the margins of the Red Mountain system and meteoric water within the moat of the Lake City caldera (Slack, 1980). **0.6**

92.5 Crossing lower stable portion of Slumgullion mudflow. **0.5**

93.0 Roadcuts in Fish Canyon Tuff, here present as caldera fill within the Uncompahgre caldera. Below the Fish Canyon are roadcuts in tuffaceous sediments, including deltaic and lake deposits in the moat of the Uncompahgre caldera. **1.3**

94.3 Bridge over Lake Fork of the Gunnison. On right are exposures of flow-laminated silicic dacite, part of the Burns Member of the Silverton Volcanics. This is part of the lower sequence of postcollapse lavas within the Uncompahgre caldera, largely preresurgent or intra-resurgent. **0.2**

94.5 Mine dump on grassy hillside at 3:00 is from the Golden Wonder. Although this mine has had virtually no production, it is an intriguing telluride deposit with structural and textural evidence of hot-spring deposition. This deposit appears to be related to emplacement of a rhyolitic dome late in the Uncompahgre caldera cycle, but lead-isotope data indicate that it was not related to the formation of the Golden Fleece vein. The Golden Wonder mine is located in Deadman's Gulch, the site of Alferd Packer's stay in the Lake City area. Packer was convicted of using his three companions to satisfy his hunger during a forced winter encampment prior to the settling of Lake City. Cannibal Plateau, a Miocene basalt center northeast of town, was named in his "honor." Luckily, decent eating establishments are now available in the area. **0.2**

94.7 Junction with road up the Lake Fork to Lake San Cristobal. **Turn right** on Lake City road (segment from here to Lake City included at end of Field guide 4). **2.0**

96.7 Entering Lake City (2645 m).

Western San Juan caldera complex

K. Hon[1] and P. W. Lipman[2]

[1]*U.S. Geological Survey, Hawaiian Volcano Observatory, Hawaii 96718;* [2]*U.S. Geological Survey, Denver, Colorado 80225*

Introduction

The calderas of the western San Juan volcanic field, like those of the eastern and central regions, formed within a cluster of earlier stratovolcanoes. Although the source areas for many of these rocks were destroyed during later caldera development, the remnants of six volcanic centers can be recognized: the Larsen, Lake Fork, Cimarron, and Cow Creek centers north of the Uncompahgre–San Juan caldera, the Carson center to the south, and the flank of an unnamed volcano near Red Mountain Pass on the western margin of the San Juan caldera (Figs. 4-1, 4-2) (Larsen and Cross, 1956; Lipman et al., 1973; Hon et al., 1986). The vent regions are identified by thick sequences of andesitic–dacitic lavas, explosion breccias, and agglutinates intruded by stocks and radial dike swarms. Deep basins were filled by volcaniclastic sediments, tuffaceous conglomerates, and mudflow breccias shed from the surrounding stratovolcanoes (Table 4-1) (Steven and Lipman, 1976). These rocks are temporally and lithologically analogous to the Conejos Formation in the eastern San Juan Mountains (Field guides 1 and 2).

The onset of caldera-forming eruptions in the western San Juan volcanic field followed the development of the Platoro and Summitville calderas in the eastern San Juan field, but preceded the initiation of activity in the central San Juan Mountains (Steven and Lipman, 1976). Eruption of the 29 Ma Ute Ridge Tuff (62–64% SiO_2) produced the Ute Creek caldera (Fig. 4-2; Tables 4-1, 4-2), the oldest in the western San Juan caldera complex. The next caldera to form was the Lost Lake caldera, which is now largely buried by later ash-flow tuffs and lavas. This caldera was the source of the widespread 28–29 Ma Blue Mesa Tuff (73% SiO_2). Both of these early calderas are near, or in, the Rio Grande drainage, well south of the main Uncompahgre–San Juan–Silverton caldera cluster (Steven and Lipman, 1976).

The Uncompahgre and San Juan calderas are discrete structures, separated at exposed levels by an intervening ridge of Precambrian granitic rocks. Their subsidence was largely in response to eruption of the voluminous 28–29 Ma Sapinero Mesa Tuff (73% SiO_2). Initial collapse of the Uncompahgre caldera may have been triggered slightly earlier, however, by eruption of the smaller-volume Dillon Mesa Tuff (Tables 4-1, 4-2). Close interconnection of the two cupolas of magma, reflected by nearly simultaneous collapses, is also documented by their joint resurgence to form an elliptical structural dome that extends over 50 km across both calderas. The Silverton caldera, which is nested eccentrically within the San Juan caldera, collapsed at about 27.5 Ma, in response to eruption of the Crystal Lake Tuff. Fault relations suggest the Silverton caldera may have collapsed during resurgence of the two earlier calderas.

The Lake City caldera, the youngest in the volcanic field, formed at 23.1 Ma as a consequence of eruption of the petrologically distinctive Sunshine Peak Tuff. Sunshine Peak Tuff accumulated to a thickness of 1.5 km or more within the Lake City caldera, where it is compositionally zoned from high-silica rhyolite (76% SiO_2) upward into quartz trachyte (68% SiO_2). Outside the caldera, the Sunshine Peak is only a few tens of meters thick and is only preserved locally beneath capping Miocene basalts. The Lake City caldera offers exceptional exposures of many key caldera structures, including the topographic caldera wall, ring fault, local ring dikes, resurgent dome, top of the resurgent intrusion, deep levels of intracaldera fill and associated collapse breccias, and postcollapse lava domes, mineralized structures, and alteration features.

Field examination of the western San Juan caldera complex and associated outflow volcanics is divided into three segments: Field guide 4, a counterclockwise loop around the margins of Lake City caldera that largely follows the moat of the Uncompahgre caldera; Field guide 5, an all-day foot traverse through the rugged southeastern sector of the Lake City caldera; and Field guide 6, a drive from Lake City to Gunnison to examine outflow volcanic units from

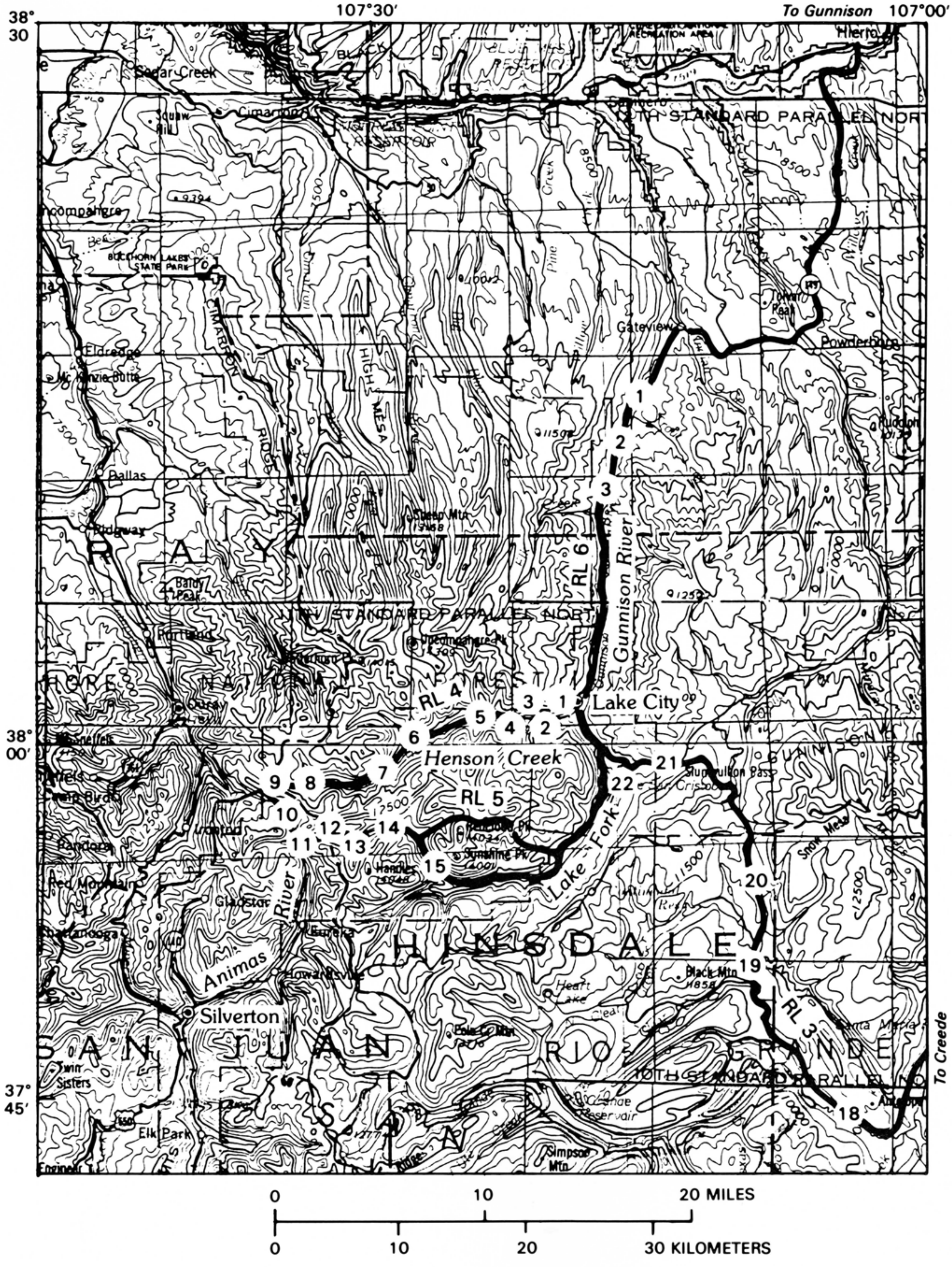

FIGURE 4-1—Route map, western San Juan Mountains, showing stops listed in Field guides 3, 4, and 6.

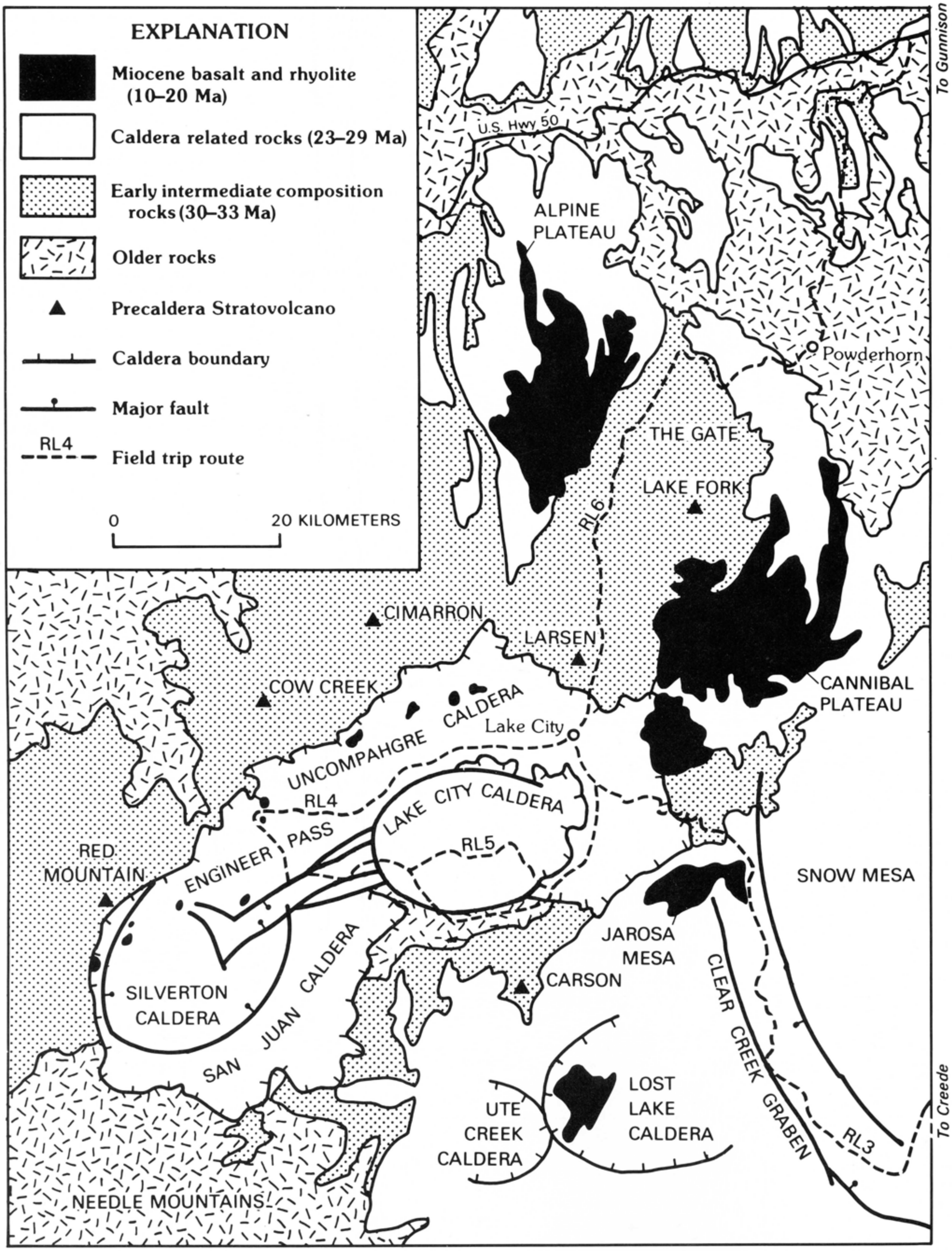

FIGURE 4-2—Generalized geologic map of the western San Juan volcanic field showing the routes described in Field guides 3 (partial), 4, 5, and 6.

TABLE 4-1—Volcanic stratigraphy of the western San Juan Mountains. Compiled from Lipman et al. (1973), Steven and Lipman (1976), Hon and Mehnert (1983), Kunk et al. (1985), Hon (1987b), Lanphere (1988), and Lipman and Sawyer (1988).

Age (Ma)	Source	Ash-flow tuffs	Lava flows	Sediments	Intrusions
	Hinsdale Formation				
4–6	Rico				Basalt and granite dikes
10–19	Silverton to Lake City				Rhyolite plugs and dikes
15–21	Western San Juans		Trachybasalt–trachyte		
23	*Lake City caldera*	*Sunshine Peak Tuff* (300–400 km^3)	Postcollapse dacite of Grassy Mountain		Late stocks and dikes Resurgent pluton
22–24	Red Mountain Pass to Engineer Pass				Sanidine-bearing dacite plugs
25.9	Central San Juans Central San Juans	Nelson Mountain Tuff Wason Park Tuff			
26–27	Uncompahgre–San Juan–Silverton calderas		Late caldera-fill and regional lavas	Local volcaniclastic sediments	Late ring-fracture and regional stocks
27.3	Central San Juans	Carpenter Ridge Tuff			
	Silverton caldera	*Crystal Lake Tuff* (25–100 km^3)			
27.8	Central San Juans	Fish Canyon Tuff			
28–29	*Uncompahgre and San Juan calderas*	*Sapinero Mesa Tuff* (Eureka Member) (>1000 km^3) *Dillon Mesa Tuff* (25–100 km^3)	Silverton Volcanics (postcollapse lavas) Pyroxene andesite member Burns Member	Silverton Volcanics (moat-filling sediments) Henson Member	
28–29	*Lost Lake caldera*	*Blue Mesa Tuff* (100–500 km^3)			
29.1	*Ute Creek caldera*	*Ute Ridge Tuff* (>500 km^3)			Ring-fracture stocks
30–33	Precaldera stratovolcanoes		Early intermediate-composition lavas	Tuffaceous conglomerate and laharic breccias	Central stocks and radial dikes

TABLE 4-2—Representative major-element analyses of volcanic rocks from the western San Juan Mountains. Analyses from Larsen and Cross (1956), Olson et al. (1968), Hon (1987b), and unpublished data of K. Hon and P. W. Lipman.

OLIGOCENE CALC-ALKALINE VOLCANIC ROCKS

	Early intermediate-composition lavas (dacite)	Early intermediate-composition lavas (andesite)	Ute Ridge Tuff (dacite)	Blue Mesa Tuff (rhyolite)	Dillon Mesa Tuff (rhyolite)	Sapinero Mesa Tuff (rhyolite)	Silverton Volcanics: Burns Member	Silverton Volcanics: Pyroxene andesite	Late ring intrusion (monzogranite)
SiO_2	64.9	58.7	62.1	73.5	73.0	73.2	66.3	58.2	65.6
Al_2O_3	16.8	16.0	16.5	14.1	14.8	15.8	16.6	15.8	15.7
Fe_2O_3	2.03	2.52	2.28	1.09	1.09	1.12	2.37	2.63	2.14
FeO	2.25	5.73	3.94	0.49	0.49	0.50	2.61	5.57	2.78
MgO	1.01	3.39	2.83	0.21	0.23	0.42	1.61	3.47	1.82
CaO	4.34	6.27	4.50	1.03	1.25	1.26	2.55	6.41	3.21
Na_2O	4.34	3.29	3.11	3.31	3.23	3.35	3.69	2.94	3.38
K_2O	3.43	2.57	3.68	5.99	5.52	3.98	3.05	3.47	4.38
TiO_2	0.52	0.98	0.73	0.24	0.27	0.27	0.84	1.05	0.62
P_2O_5	0.32	0.39	0.32	0.03	0.07		0.34	0.41	0.27
MnO	0.12	0.14	0.06	0.08	0.07	0.07	0.05	0.15	0.12

MIOCENE VOLCANIC ROCKS

	Lake City caldera					Red Mtn. Pass	Hinsdale Formation		
	Sunshine Peak Tuff			Resurgent intrusion (syneite)	Postcollapse lava (dacite)	Sanidine dacite plug	Trachybasalt	Trachyte	Rhyolite
	lower rhyolite	middle rhyolite	upper trachyte						
SiO_2	76.0	73.1	68.2	65.8	65.8	61.9	50.3	63.0	76.5
Al_2O_3	13.0	14.0	17.0	17.0	16.6	14.5	15.9	16.6	13.1
Fe_2O_3	0.78	1.34	1.61	2.21	2.55	2.33	3.40	2.44	0.66
FeO	0.36	0.60	0.72	0.96	0.96	2.80	6.59	1.71	0.29
MgO	0.16	0.50	0.35	0.63	1.24	3.07	7.18	1.61	0.17
CaO	0.28	1.62	0.83	1.72	2.78	5.93	7.88	2.92	0.69
Na_2O	3.91	4.02	4.00	4.64	3.27	3.07	3.42	4.94	4.35
K_2O	5.19	4.36	6.64	6.06	5.47	5.04	2.49	5.34	4.00
TiO_2	0.19	0.34	0.56	0.70	0.98	0.73	1.87	0.93	0.14
P_2O_5	0.05	0.11	0.11	0.22	0.33	0.55	0.87	0.45	0.05
MnO	0.08	0.09	0.01	0.09	0.06	0.10	0.14	0.10	0.09

the western caldera complex and associated rocks (Figs. 4-1, 4-2). Optional field guide B provides a clockwise loop through the Silverton caldera that emphasizes relations between caldera structure and mineralization.

Published geologic maps useful for the field trip are Lipman (1976a) for Field guide 4, Hon (1987a) for Field guide 5, and Lipman (1976a), Olson and Hedlund (1973), Hedlund and Olson (1975), and Hedlund (1974) for Field guide 6. A map of the Mineral Point area (Field guide 4) is in Burbank and Luedke (1969). Also useful are the 1:250,000 maps of the Durango and Montrose quadrangles by Steven et al. (1974) and Tweto et al. (1976). A more detailed map of the Montrose 30 × 60 minute quadrangle is in press (Steven and Hail, in press).

Field guide 4: Lake City, Uncompahgre, and San Juan calderas, via Henson Creek, Engineer Pass, and Cinnamon Pass

Summary

Distance: 48.7 miles

The route of the field trip is counterclockwise around the margins of the Lake City caldera (Figs. 4-1, 4-2). Beginning at Lake City, we follow Henson Creek through the Eureka Member of the Sapinero Mesa Tuff, which accumulated to great thickness within the Uncompahgre caldera, and examine collapse megabreccia that intertongues with lower parts of the Eureka Member. The route up Henson Creek ascends gradually through the fill of the Uncompahgre caldera, including the Eureka Member of the Sapinero Mesa Tuff, the Burns Member, pyroxene andesite member, and Henson Member of the Silverton Volcanics, the Fish Canyon and Carpenter Ridge Tuffs from the central San Juan caldera complex, and the Crystal Lake Tuff erupted from the Silverton caldera to the southeast (Table 4-1; Lipman et al., 1973). Above the forks of Henson Creek, we cross a buried ridge of Precambrian granite that separates the Uncompahgre and San Juan calderas; the stratigraphy of higher levels of the caldera fill is unchanged. Engineer Pass (3901 m) offers spectacular views of the northwestern wall of the San Juan caldera and volcanic stratigraphy of the western San Juan Mountains in the Mount Sneffels and Potosi Peak areas (4298 m and 4196 m). From Engineer Pass to Cinnamon Pass, we cross obliquely through mineralized fill of the San Juan caldera, complexly broken by faults of the Eureka graben. The Eureka graben is the downdropped keystone fault zone along the crest of the elliptical resurgent dome that jointly uplifted both Uncompahgre and San Juan calderas (Lipman et al., 1973). To the south, along the Animas River, are views of the arcuate ring fault of the Silverton caldera (Optional field guide B follows this drainage to Silverton and continues clockwise around the Silverton caldera to Ouray). At Cinnamon Pass (3840 m), blocks of Crystal Lake Tuff are preserved in the structurally deepest levels of the Eureka graben. We descend the headwaters of the Lake Fork of the Gunnison River, across the Precambrian granitic rocks between the San Juan and Uncompahgre calderas, and into the Lake City caldera, with good views of the bounding ring fault and intracaldera Sunshine Peak Tuff that is more than 1.5 km thick on Sunshine and Redcloud Peaks (4268 m and 4278 m). The road continues down the Lake Fork, recrossing the ring fault of the Lake City caldera into Precambrian rocks, which are overlain by early intermediate-composition lavas and laharic breccias outside the Uncompahgre caldera. Finally, we cross the topographic wall of the Uncompahgre caldera south of Lake San Cristobal, into postcollapse fill deposits of this caldera, as we return to the starting point.

The high-elevation Engineer and Cinnamon Passes are typically closed by snow until the end of June, and again after late September. Even in summer months the condition of these roads can deteriorate rapidly during times of heavy rains, and they should be traversed with caution. Although 4-wheel-drive vehicles are necessary for the entire loop trip, much can be seen in both directions from Lake City with 2-wheel-drive vehicles, which are generally adequate to reach Rose's Cabin up the East Fork of Henson Creek (mile 14.1) and the head of Burrows Park up the Lake Fork (mile 28.0).

Road log

Mileage

0.0 Start in Lake City at bridge over Henson Creek. **Turn west** on Engineer Pass road. **0.4**

0.4 **STOP 1.** Eureka Member of the Sapinero Mesa Tuff. The spectacular exposures in the canyon of Henson Creek are all part of a single thick cooling unit of intracaldera tuff, the Eureka Member of the Sapinero Mesa Tuff. This unit differs from outflow Sapinero Mesa Tuff in its generally intense propylitic alteration, more abundant lithic fragments, and great thickness. Like the outflow Sapinero Mesa, the Eureka Member is a low-silica rhyolite (70–72% SiO_2) containing phenocrysts of sanidine, plagioclase, and sparse biotite. Dips in these rocks define the northeast margin of the large, elliptical resurgent dome that extended across the Uncompahgre and adjacent San Juan calderas to the southwest. Only remnants of the northeastern part of the dome are preserved, the rest having been downdropped within the Lake City caldera.

Continue up the canyon. **0.3**

0.7 Prominent peak at 12:00 is at the head of T-Gulch. The ring fault of the Lake City caldera cuts through the right shoulder of this mountain. The talus-covered slopes outside of the ring fault (on right) are upper member of the Sunshine Peak Tuff, preserved within a remnant of the topographic wall of the Lake City caldera. High parts of the peak within the ring fracture are made up of lower member of the Sunshine Peak Tuff, which was uplifted more than 1 km along this section of the ring fault during emplacement of the resurgent intrusion. Small plugs of resurgent quartz syenite are present along the ring fault in T-Gulch. **0.1**

0.8 Moro mine on the right. Vertical quartz veins radial to the Lake City caldera are well exposed in the canyon walls on both sides of Henson Creek. **1.0**

1.8 Spire straight ahead on skyline is Sugarloaf Rock, a late monzonite intrusion cutting Uncompahgre caldera fill. **0.2**

2.0 **STOP 2: Megabreccia Member overlain by the Eureka Member.** Just across Henson Creek is spherulitic zone at the base of the Eureka, indicating former presence of glassy tuff, overlying chaotic megabreccia surrounded by poorly indurated matrix of Eureka Member (Fig. 4-3B). About 100 m up river, as part of the megabreccia, is a large block of densely welded tuff with contorted internal foliation, surrounded by partly welded Eureka Member (Fig. 4-3A). This block is interpreted as Sapinero Mesa Tuff that flowed rheomorphically as it slumped inward off the steep lip of the caldera wall.

Continue ahead, up Henson Creek. **0.2**

2.2 Intertonguing poorly welded Eureka and various foreign rock units (Fig. 4-3C). Especially conspicuous are lenses of mudflow-like material, containing rounded cobbles—presumably semiconsolidated material from the San Juan Formation that slid down the caldera wall. Across Henson Creek is more of the spherulitic contact between the Eureka Member and underlying megabreccia. Large spherulites (10–

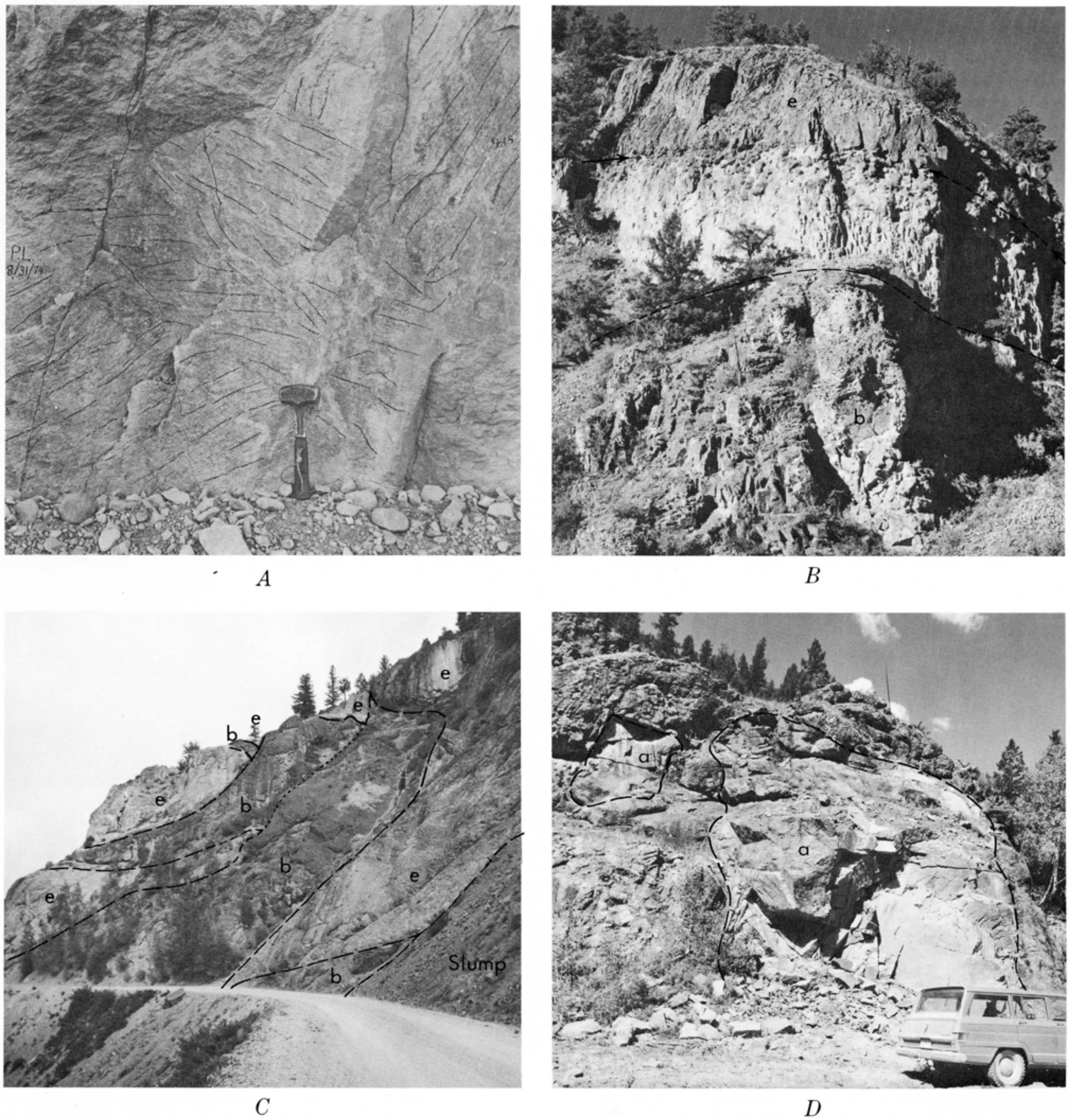

FIGURE 4-3—Caldera-collapse breccias within the Uncompahgre caldera, Henson Creek area (from Lipman, 1976). **A,** Contorted foliation in large block of Sapinero Mesa Tuff within the megabreccia. Traces of foliation are accentuated by lines marked on outcrop (Stop 2). **B,** Zonal welding and crystallization features at the base of the main Eureka Member (e), where it rests abruptly on massive large megabreccia blocks (b). Stop 2. **C,** Interlayered, weakly welded ash-flow tuff of the Eureka Member (e) and lenses of mesobreccia (b). Arrows indicate original top of glassy tuff containing spherulites in its upper part (mile 2.2). **D,** Large blocks of andesite (a) surrounded by more finely brecciated material (mile 4.5).

20 cm) can be seen in the talus pile beneath the cliff. **0.5**

2.7 **STOP 3.** Mouth of Alpine Gulch on left; **view of interior of Lake City caldera.** Rocks in the immediate foreground are Eureka Member; the ring fault of the Lake City caldera crosses Alpine Gulch about 2 km upstream. The lower part of Alpine Gulch marks a major fault within the interior of the Lake City caldera. On the eastern side of the drainage, the upper member of the Sunshine Peak Tuff dips steeply (35–40°) toward the ring fault and is overlain unconformably by the postcollapse dacite lavas of Grassy Mountain. On the western side of the drainage, the lower member dips more gently toward us (15–20°) and has been uplifted in excess of 1 km along the Alpine Gulch fault. Similar displacements are present along the ring fault immediately west of Alpine Gulch. Displacement on the Alpine Gulch fault diminishes rapidly away from the ring fault to a point 4–5 km within the caldera, where the valley is crossed by an undisturbed part of the resurgent intrusion (Hon, 1987a).

The high ridge above treeline at the head of Alpine Gulch is capped by the upper member of the Sunshine Peak Tuff, which dips away from us on the south side of the resurgent dome. Faint lines across the cliff mark welding breaks within the Sunshine Peak Tuff. This ridge is the high point of the foot traverse described in Field guide 5 (Stop 7). **0.2**

2.9 Treasure Falls dam on left was constructed to impound tailings from the Ute–Ulay mill upstream. The dam failed in 1972 and destroyed a bridge into Alpine Gulch and nearly destroyed the bridge across Henson Creek in Lake City. Remnants of the tailings can still be seen plastered to the cliffs along the top of the gorge. **0.5**

3.4 California mine. Mount of T-Gulch on left; cliffs halfway up the gulch mark the ring fault of the Lake City caldera. **0.3**

3.7 **STOP 4. Ute–Ulay mine and "town" of Henson.** Park at far western end of town; please do not leave road at this stop. Land on both sides is private property. The Ute and Ulay veins were the most productive in the Lake City area. They primarily produced silver and lead valued at $9–10 million at the time of mining (Irving and Bancroft, 1911). The Ute vein, which crosses the road east of the mine buildings, is one of the many veins radial to the Lake City caldera exposed in the drainage of Henson Creek. Slack (1980) defined zonations in mineralogy, fluid-inclusion temperatures, and salinities in veins that extend outward from the Lake City caldera. A K–Ar date of 20.8 Ma on sericite (probably slightly reset) from this deposit also suggests that it was linked temporally with formation of the Lake City caldera (Lipman et al., 1976). Lead-isotope ratios in Ute–Ulay galenas are more radiogenic than for any other veins in the area except the Golden Fleece, and suggest that hydrothermal fluids interacted with Precambrian basement flooring the Uncompahgre caldera. The host rocks of the deposit are megabreccia blocks of massive, porphyritic dacite lavas, which constitute a major rock type of the precaldera volcanoes present prior to the collapse of the Uncompahgre caldera.

The radial and concentric veins surrounding the Lake City caldera were probably filled by hydrothermal cells circulating adjacent to the resurgent intrusion and beneath the moat of the caldera. The distribution of these veins on the north side of the caldera is a result of the asymmetric emplacement of the resurgent intrusion within the northern part of the Lake City caldera. Corresponding veins on the south side of the caldera, if they exist, would remain buried beneath the resurgent dome.

Continue up valley. **0.3**

4.0 High, talus-covered peak to left is composed of upper member of the Sunshine Peak Tuff filling a topographic scallop outside of the ring fault. **0.5**

4.5 On right is a good exposure of a large block (about 20 m in diameter) within the megabreccia, surrounded by finer breccia (Fig. 4-3D). Typical megabreccia in this area contains many rounded clasts, probably from semiconsolidated mudflow conglomerates of the San Juan Formation. **0.4**

4.9 On right, exposures next to road are propylitized welded tuff, interpreted as Eureka Member dipping beneath the massive megabreccia that is exposed to the east along Henson Creek. This is the lowest exposed level of the caldera fill within this part of the Uncompahgre caldera and demonstrates that even the apparently massive lava is interlayered with the Eureka Member. All roadcut exposures from here to the forks of Henson Creek at Capitol City are within a thick, chaotic, megabreccia zone. The possibility that some of these exposures represent true caldera floor cannot be excluded, but no evidence has been found to confirm such a hypothesis. Conspicuously lacking is any continuity or stratification of the units in this area that might represent structurally coherent caldera floor.

Two talus-covered peaks to left are Sunshine Peak Tuff. The lower peak is upper member outside of the ring fault, whereas the higher peak is lower member that was displaced upward during resurgence of the caldera. **0.2**

5.1 **STOP 5. Mouth of Nellie Creek; boulders from topaz rhyolite intrusions.** Stream boulders provide an opportunity to examine pieces of 19 Ma high-silica rhyolite intrusions (76–77% SiO_2; Table 4-2) and older ash-flow tuffs filling the moat of the Uncompahgre caldera. A long jeep road up Nellie Creek provides access to plugs and sills of the rhyolite and to good sections of ash-flow tuffs capped by lavas of the volcanics of Uncompahgre Peak. A linear belt of high-silica rhyolite intrusions extends on the north side of the Uncompahgre–San Juan caldera from west of Lake City to west of Silverton. East of Engineer Pass, the high-silica rhyolites are all about 19 Ma, are highly porphyritic, and many contain vapor-phase topaz. These intrusions are enriched in Be, F, Mo, and U (Steven et al., 1977) and are similar to "topaz rhyolites" identified elsewhere in the western U.S. (Christiansen et al., 1986). Trace-element and Sr-isotopic data show minor differences between some of these intrusions, but Pb-isotopic ratios are strikingly uniform (K. Hon and

Z. C. Peng, unpubl. data). These high-level intrusions are probably the near-surface expression of a much larger magma body at depth. West of Engineer Pass, all of the high-silica rhyolites are aphyric, strongly flow-foliated, and, where dated, are only 10 Ma (Lipman et al., 1976; Gilzean, 1985). The emplacement of all these intrusions and the elongate shape of the Uncompahgre–San Juan caldera magma chamber were probably controlled by the Colorado mineral belt, a northeast-trending zone of Tertiary magmatism localized along a major Precambrian structural zone that trends through the Lake City area (Tweto and Sims, 1963).

Continue ahead, up Henson Creek. **2.5**

7.6 Copper Gulch enters on left. Ring fault of the Lake City caldera cuts across canyon at mouth of gulch. A high-silica rhyolite ring dike intruded by, and partially mixed with, quartz syenite occupies about 0.5 km of the ring fault west of Copper Gulch. The high-silica rhyolite is compositionally identical to the lower member of the Sunshine Peak Tuff. On the east side of Copper Gulch, a talus-covered ridge above the mouth of the gulch is upper member tuff just outside of the ring fault. The ring fault is defined by the vertical line separating talus from tree-covered slopes. **0.4**

8.0 Entering Capitol City area at forks of Henson Creek. The alteration on lower slopes is around margins of a large, poorly exposed, monzonite–monzogranite porphyry stock. The high point on the ridge between the forks of Henson Creek is Sunshine Mountain (elevation 3780 m), capped by lavas of the Silverton Volcanics overlying the intracaldera Eureka Member. **0.9**

8.9 **STOP 6. Capitol City townsite.** Road intersection at forks of Henson Creek. Turn left and proceed across bridge to the stop. Several small, 26–27 Ma monzonite–monzogranite porphyry stocks (64–67% SiO_2) intrude the Eureka Member in the vicinity of Capitol City. The composition of these stocks varies from monzodiorite (59% SiO_2) to monzogranite (72% SiO_2). Small patches of monzonite are exposed in prospects just north of the road. Aeromagnetic and paleomagnetic data suggest that a large body of monzonite underlies the South Fork of Henson Creek for 1–2 km west of Capitol City (Grauch, 1987). Other stocks of monzonite crop out for 5–6 km north from Capitol City to Matterhorn Peak. All these intrusions are associated with halos of pyritic alteration and Cu–Mo anomalies. The short, discontinuous base-metal veins near Capitol City may have formed during the emplacement of these intrusions (Slack, 1980).

Similar intrusions were emplaced along the southern ring-fracture zone of the Silverton caldera and in a belt that extends west to Mount Wilson (Steven et al., 1974). Another isolated, composite stock also occurs at Mount Sneffels, north of Telluride. All these intrusions show the same or even a greater diversity of compositions than those in the Capitol City area, and many of the western intrusions are also associated with weak porphyry-type mineralization. These intrusions represent a regional event in the western San Juan Mountains, and their stratigraphic position and degree of crystallization indicate that many of them must have cooled beneath their own volcanic edifices. The largest of these stocks are probably the eroded cores of stratovolcanoes. In the Capitol City area, some of these intrusions may have been the primary feeders for the volcanics of Uncompahgre Peak, which are preserved to the north and northeast within the Uncompahgre caldera (Lipman et al., 1973).

Cliffs of altered rock south of Capitol City are Eureka Member of the Sapinero Mesa Tuff (Fig. 4-4). The ring fault of the Lake City caldera runs through the trees above these cliffs. This fault then cuts southwest through the shoulder of the angular peak west of the long skyline ridge due south of Capitol City. This peak is composed of Eureka Member uplifted in the central part of the Uncompahgre–San Juan resurgent dome. The skyline ridge above treeline is composed of the middle member of the Sunshine Peak Tuff that dips 15–20° to the northwest. The two prominent bands that cut across the face of this ridge are poorly welded, lithic-rich zones that separate three distinct flow units in the middle member (Fig. 4-4). Treeline marks the contact of this member of the Sunshine Peak Tuff with underlying megabreccia, which accumulated to a

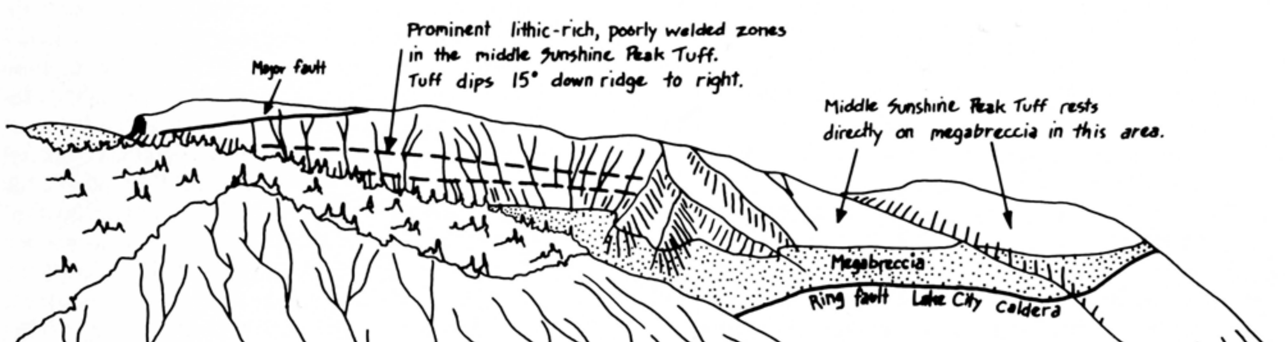

FIGURE 4-4—Sketch of welding zones in the middle member of the Sunshine Peak Tuff, as viewed south from Capitol City (see text for Stop 6).

great thickness adjacent to the ring fault in this area.

Continue left, up South Fork of Henson Creek. **1.8**

10.7 Whitmore Falls photo print. Roadcuts are in highly propylitized Eureka Member. **1.5**

12.2 **STOP 7. Megablocks of Precambrian granite.** At head of alluvial fan on right at base of steep cliffs, megabreccia in Eureka Member contains large blocks of Precambrian granite, derived from a ridge of Precambrian rock that remained high between Uncompahgre and San Juan calderas during their collapse. Local matrix is of greenish-gray, slightly welded rhyolitic tuff, interpreted as Eureka Member quenched by intermixing with the cool caldera-wall blocks.

Road sign points to Shaffer Basin. Good vista of next valley west (Horseshoe Basin), where rust-stained silicic dacite flows (Burns Member of the Silverton Volcanics) unconformably overlie more steeply tilted tuff of the Eureka Member, indicating that resurgent doming had begun before the lava flows were erupted (Luedke and Burbank, 1968, fig. 9).

Continue up the South Fork. **0.8**

13.0 Horseshoe Basin on left at head of valley; Engineer Mountain is light-colored, high point on ridge. **1.1**

14.1 Side road to Rose's Cabin. On right is Dolly Varden Mountain (3942 m). The Eureka Member disappears to the north beneath moraine and valley fill. On the slopes of Dolly Varden Mountain, this intracaldera tuff is overlain by a thick sequence of Uncompahgre caldera fill that consists of Burns Member (dacite lava), pyroxene andesite member (lava), and Henson Member (volcaniclastic sandstone) of the Silverton Volcanics (Table 4-1). These are overlain by Fish Canyon and Carpenter Ridge Tuffs from the central San Juan caldera cluster, as well as by Crystal Lake Tuff from the Silverton caldera. Dolly Varden Mountain is capped by a rhyolitic lava flow (volcanics of Uncompahgre Peak) and a 19 Ma dome complex of high-silica rhyolite. **0.4**

14.5 Sign for Hurricane Basin, which is floored by highly faulted and altered Eureka Member. Surrounding ridges are mostly Burns Member of the Silverton Volcanics on the northwest flank of the resurgent dome connecting the Uncompahgre and San Juan calderas. For the next several miles, the road follows talus from silicic dacitic lava flows of the Burns Member. **0.4**

14.9 On left, below road, are ruins of Rose's Cabin, built in 1874. This was the last stopover before crossing the old Engineer Pass road, which went through Hurricane Basin. **0.5**

15.4 Bridge across Henson Creek. Silicic dacite flow of the Burns Member is exposed just upstream. Conspicuous talus-forming cliffs on the face of Dolly Varden Mountain are the Fish Canyon Tuff, which is higher in the fill of the Uncompahgre caldera.

Above here, 4-wheel drive is recommended for Engineer Pass road during most of the year. **0.4**

15.8 Sign to Palmento Gulch. The hillcrest on right is capped by pyroxene andesite. **0.2**

16.0 **STOP 8. Approximate contact between Burns Member and overlying pyroxene andesite member of the Silverton Volcanics.** The pyroxene andesite member here is a distinctive tabular-plagioclase andesite containing large clinopyroxene phenocrysts. It is similar to that in the Huerto Formation and also in the Conejos Formation near Platoro, and similar rocks are present locally elsewhere in the early intermediate-composition sequence. On the left, virtually the entire southeast slope of Palmento Basin is a dip-slope on silicic dacite of the Burns Member.

Continue uphill. **1.0**

17.0 Cross Palmetto Gulch. Excellent views across Dolly Varden Mountain (foreground) toward Wetterhorn (4272 m), Matterhorn (4142 m), and Uncompahgre (4361 m) peaks in the background. Topographic wall of the Uncompahgre caldera passes just north of Uncompahgre Peak and just to the south of Matterhorn and Wetterhorn peaks, which are both capped by the 29 Ma Ute Ridge Tuff (Table 4-2; Lipman, 1976a).

White outcrops and talus at the top of Dolly Varden Mountain are high-silica rhyolite, similar in composition to the stream boulders examined at Nellie Creek. However, the Dolly Varden dome complex is extrusive, as indicated by pendants of identical-composition block-and-ash tuff rafted on top of the dome. Locally, small patches of high-silica rhyolite ash-flow tuff also form the eastern contact of the dome. Thus, at least some of these rhyolites had early explosive eruptive phases followed by more passive extrusion of viscous rhyolitic lava (Hon et al., 1986). Beautiful columnar joints are well exposed on the north side of this complex (not visible).

Exposed over the pyroxene andesite in Palmento Gulch are purplish-gray volcanic sediments of the Henson Member, overlain by white to reddish-brown altered Fish Canyon Tuff which floors the saddle of Engineer Pass. The light-colored ridge north of Engineer Mountain is an altered intrusion of silicic dacite dated at 14.9 Ma. The dark knob on the south side of Engineer Pass is a dacite intrusion dated at 23.1 Ma. Together with others in this area, these bodies exemplify the continued igneous activity for millions of years after formation of the Lake City caldera (Lipman et al., 1976). **0.5**

17.7 Frank Hough mine, opened in 1881, exploited high-grade Ag–Cu ore from replacement deposits in volcaniclastic sandstone of the Henson Formation on both sides of a mineralized fracture. This mine produced 350,000 ounces of silver and was the most profitable operation in the Engineer Pass–Mineral Point area (Kelley, 1946; Hon et al., 1986). **0.2**

17.9 **STOP 9. Engineer Pass** (3900 m). View west toward flat-topped Potosi Peak (4202 m) and pointed Mount Sneffels (4298 m) to the right. Potosi Peak is capped by welded tuffs, including the outflow Sapinero Mesa Tuff from the Uncompahgre–San Juan caldera complex and the older Dillon Mesa, Blue Mesa, and Ute Creek Tuffs from the western San Juan calderas (Table 4-2). Mount Sneffels consists of a composite stock that cuts the ash-flow tuff sequence and is roughly equivalent in age and chemistry to the Capitol City monzonitic intrusions. The lower slopes in the distance are all made of early intermediate-composition laharic breccias of the San Juan Formation, interlayered with a few lava flows (Steven et al., 1974).

Near Engineer Pass, the San Juan caldera wall swings through just about at treeline and encloses the same general stratigraphic sequence as observed on Dolly Varden Mountain. Here, late postcollapse lava flows that are stratigraphically equivalent to the volcanics of Uncompahgre Peak primarily overlie Crystal Lake Tuff and associated megabreccia within the Silverton caldera. The greatly thinned distal ends of tuffs from the central San Juan calderas are also locally present in the sequence. The rock flooring Engineer Pass is the distal end of the Fish Canyon Tuff, which contains atypically small and sparse phenocrysts due to winnowing during emplacement.

The small knob to the southeast is Engineer Mountain, a 23 Ma sanidine dacite porphyry intrusion (62–64% SiO_2) which contains distinctive sanidine (commonly 1–2 cm in size and partially resorbed), bipyramidal quartz, plagioclase, clinopyroxene (altered to fine-grained opaques), and biotite. Similar stocks and plugs of aphyric, high-silica rhyolite were also emplaced 22–24 Ma along the same south-southwest trend toward Red Mountain Pass. At Red Mountain Pass, stocks and plugs range from andesite to dacite (59–65% SiO_2) which contain variable proportions of quartz and sanidine phenocrysts. These intrusions are the principal host for younger breccia-pipe mineralization.

Immediately north of Engineer Pass, a mineralized breccia pipe cuts a 15 Ma dacite–rhyolite (65–74% SiO_2) dome complex (Lipman, 1976a; Maher, 1983). Preserved on the margins of this complex are pieces of cogenetic rhyolitic ash-flow tuff (72–74% SiO_2). All the ash-flow tuff outcrops dip back into the center, suggesting they were erupted into a shallow crater prior to emplacement of the dome. The ash-flow tuff is well exposed on the ridge closest to the pass, where it overlies tuffaceous conglomerate containing fragments of the 23 Ma dacite porphyry on Engineer Mountain. About halfway up the ridge, the ash-flow tuff is cut by an irregular tuff dike that apparently was a feeder for the upper part of this sequence. The dike contains large boulders of black vitrophyre, interpreted as blobs of quenched magma, in a matrix of densely welded brown ash-flow tuff. An intrusive contact with the dome rocks crosses the first saddle on the ridge. Erosion has removed most of the dacite flow dome (65% SiO_2) and exposed the underlying neck, where rocks are characterized by steep flow foliations and locally well-developed columnar joints. In the center of the complex, the silicified cap of the breccia pipe forms the prominent high knob on the ridge. The breccia pipe contains anomalous amounts of Ag, Mo, As, Pb, and Bi (Maher, 1983). Immediately below the ridge crest, limonite-stained outcrops are nearly aphyric, high-silica rhyolite (76% SiO_2) that displays mutually cross-cutting relationships with the breccia in drill core. Sericite from the pipe gave an age of 12.5 Ma (Hon and Mehnert, 1983), but it may have been reset during regional thermal events related to mineralization along the Eureka graben and at Mineral Point. Apatites from the two intrusions also give an age of 11–12 Ma (Lipman et al., 1976). The road up the west face of the ridge was constructed in 1986 to facilitate exploration drilling by Homestake Mining Company.

Several veins cutting the ridge south of Engineer Mountain contained rich pockets of silver ore. Hypogene minerals in these zones include ruby silver, acanthite, and a possible argentiferous bismuth sulfide. Little galena, sphalerite, or chalcopyrite were found in the high parts of the veins. These veins are along continuations of structures from the Mineral Point district, and are zoned downward into argentiferous base-metal deposits typical of that district (Kelley, 1946). The unique mineralogical and textural character of the veins on Engineer Pass led Burbank and Luedke (1969) to postulate that ore deposition took place in a near-surface environment. The recognition of the extrusive dome complexes north of Engineer Pass and on Dolly Varden Mountains confirms that these veins formed just below the paleoground surface (Hon et al., 1986), probably from acid-sulfate hot springs.

Continue southwest around the south side of Engineer Mountain along the ridge crest between Bear Creek and Mineral Creek. Road crosses on sediments of the Henson Member of the Silverton Volcanics, below the Fish Canyon Tuff and overlying the pyroxene andesite member. **0.6**

18.5 Cross small fault into pyroxene andesite member (platey-plagioclase type); then obliquely into top of the Burns Member. Base of slope on right is Mineral Point, with many prospects and mining roads, mostly in glaciated knobs of silicic dacite flows of the Burns Member. **0.4**

18.9 Crossing southwest extension of the Miner's Bank vein. Along the road, the Polar Star mine has exploited this vein. This mine was the only other operation, besides the Frank Hough, to produce a profit in the Engineer Pass area. Road descends for next several miles through altered Burns Member cut by mineralized northeast-trending faults that mark the northwestern boundary of the Eureka graben. At 1:00 along the ridge crest, dark-brownish rock on Wood Mountain (4160 m) is intensely altered and mineralized Burns Member near the axis of the Eureka graben. Farther south, the structures of the Eureka graben host some of the richest gold veins in the San Juan Mountains. The Sunnyside mine has been exploiting these veins for nearly a century and has produced about 700,000 ounces of gold, along with substantial silver and base-metal sulfides (Casadevall and Ohmoto, 1977). Directly below us is the Mineral Point district and ruins of the San Juan Chief mill. Most of the ore was low-grade Ag–Pb–Zn–Cu vein material. The mines and prospects are along mineralized faults just northwest of the main Eureka graben trend and tend to have curvatures that suggest they may be related to ring faulting at the northern end of the Silverton caldera.

However, these faults are short and discontinuous, as is the mineralization along them. Most of the Silverton caldera lies to the south of Mineral Point and the maximum subsidence of this caldera appears to have occurred about 10 km south of here near Silverton. Although no conspicuous subsidence has been identified along any of the Mineral Point faults, the presence of megabreccia blocks surrounded by Crystal Lake Tuff north of here indicates that some collapse occurred in this area and that the Silverton caldera may not have been a simple trap-door structure (Lipman, 1976b). **0.4**

19.3 First major switchback. **0.8**

20.1 Junction with road to Poughkeepsie Gulch and Ouray. **Turn left** (south). Still in lavas of the Burns Member. **0.2**

20.3 Sign to Horseshoe Lake. Horseshoe Basin is underlain by intracaldera Eureka Member; the cirque rims consist of overlying Burns Member. **0.2**

20.5 **STOP 10. Denver Lake** (3050 m); **rhyolite intrusion cutting the Burns Member.** Park at Denver Lake and walk downhill several hundred meters, along the rib of buff-colored, vertically flow-banded rhyolite, to where the road crosses the north fork of Animas River. This is one of two rhyolite porphyry intrusions occupying boundary faults of the Eureka graben; the second one is on California Mountain to the southwest (Burbank and Luedke, 1969). Neither has been dated because of the associated alteration. Small dikes of similar aphyric rhyolite occur along faults from Mineral Point to the Engineer Pass area. A few dikes northeast of Engineer Pass retain glassy selvages (Maher, 1983).

The wall rock of the Denver Hill intrusion begins in porphyritic dacite of the Burns Member and passes downward into ash-flow tuff of the Eureka Member. Several textural varieties of vertically flow-laminated felsite are colored brownish red due to oxidation of sulfides. Brecciated parts of the intrusions, as at the western margin of the Denver Hill body, are weakly anomalous in Pb, Zn, and Mo. Several pebble dikes are exposed along the margin of the lowest outcrop of the rhyolite.

Continue downhill, into the partly welded top of the Eureka Member of the Sapinero Mesa Tuff. **0.4**

20.9 Junction with Mineral Point road. **Turn left.** Road continues through increasingly densely welded and propylitically altered Eureka Member to Animas Forks and the junction with the Cinnamon Pass road. To the west, on Houghton Mountain (3978 m), rusty-colored, altered Burns Member overlies Eureka Member along an obvious contact. **1.3**

22.2 **STOP 11. Junction with Cinnamon Pass road. Turn left uphill** (or follow Optional field guide D from this point to Silverton). Below, at junction with California Gulch, is ghost town of Animas Forks. Along the Cinnamon Pass road for about a mile below this point, abundant megabreccia of the Picayune Member interfingers with the Eureka Member of the Sapinero Mesa Tuff. Prominent mine buildings and dumps on the north side of the creek mark the entrance to two haulage tunnels driven beneath the Mineral Point area in the 1940's. This venture met with little economic success (Kelley, 1946).

Just after leaving Animas Forks are fine views down the Animas River valley, where the arcuate drainage curving to west reflects the ring faults of the Silverton caldera. The side valley of the Animas at 1:00 is Burns Gulch, the type locality for the Burns Member. Lower Burns Gulch consists of Eureka Member. The great cliffs at middle elevations are a silicic dacite flow of the Burns Member, and capping ridges are pyroxene andesite member.

Across Cinnamon Creek, the near ridge on the west side of Cinnamon Mountain (4062 m) is Eureka Member to about treeline; the overlying layered zone of silicic dacite of the Burns Member is capped by thick, massive flows of aphanitic pyroxene andesite member of the Silverton Volcanics. Cinnamon Mountain marks the most downdropped segment of the Eureka graben, the keystone fault zone along the crest of the resurgent dome that extends between the Uncompahgre and San Juan calderas. A major bounding fault of the Eureka graben trends along the northwest side of Cinnamon Mountain, across the creek from the road. **1.4**

23.6 Cirque basin at head of Cinnamon Creek and first view of high point of Cinnamon Pass. Exposures to right on Cinnamon Mountain consist largely of two thick flows of pyroxene andesite member; thin sandstones of the Henson Member occupy a break in slope two-thirds of the way up. These are dropped down to the left against silicic dacite of the Burns Member on Wood Mountain (4160 m) along a major Eureka graben fault that cuts diagonally across Cinnamon Pass. This fault cuts the skyline on the lower southeast shoulder of Wood Mountain, where dark, craggy, pyroxene andesite member to the right is juxtaposed against brownish, iron-stained silicic dacite of the Burns Member to the left. **0.6**

24.2 Crossing sandstones of the Henson Member, between the two flows of pyroxene andesite member. **0.2**

24.4 **STOP 12. Cinnamon Pass** (elevation 12,598 ft, 3940 m). Cinnamon Mountain, on the right, owes its color and name to downfaulted blocks of Crystal Lake Tuff in the core of the Eureka graben. These are the rusty reddish-brown rocks, dropped down on the northwest-trending faults so conspicuous from the pass. Crystal Lake Tuff was erupted from the Silverton caldera at about 27.5 Ma. It is a phenocryst-poor low-silica rhyolite, which is similar in appearance to the Carpenter Ridge Tuff from the Bachelor caldera at Creede. At the pass, we are in sandstones of the Henson Member of the Silverton Volcanics; just to the southeast, the dark rocks are the pyroxene andesite member. **0.3**

24.7 Crossing Rainbow fault, a major Eureka graben structure, which drops pyroxene andesite member on the northwest down against the top of Eureka Member on the southeast side. The uppermost part of the Eureka is not particularly propylitically altered or densely welded; it is purplish brown. The quartz vein following the Rainbow fault is conspicuous just above the road at first; then it angles up-hill, toward the crest of Edith Mountain. **0.5**

25.2 On the left, a flow of silicic dacite or low-silica rhyolite in the Burns Member overlies the partly welded top of the Eureka Member. Directly down the valley, the high above-timberline country includes Redcloud and Sunshine Peaks (4278 and 4268 m) in the core of the Lake City caldera. On the right skyline, the high point is Whitecross Mountain (4128 m). The stream in this basin is the headwater of the Lake Fork of the Gunnison River. **0.5**

25.7 **STOP 13. Handies Peak viewpoint** (at the switchback). American Basin is coming into view at right; the high point on the southeast side is Handies Peak (4267 m). Most of Handies Peak is Eureka Member and megabreccia, but a small capping patch consists of Henson sediments and a flow of the Burns Member. The ridge between American Basin and the creek below the road is almost entirely Eureka and Picayune Megabreccia Members of the Sapinero Mesa Tuff. From this point, the conspicuous Anaconda fault at the head of the basin trends along the southeast side of the creek; it drops another patch of Crystal Lake Tuff down in the keystone area of the Eureka graben. **0.2**

25.9 At the switchback just above stream level, a planar surface next to an old wooden tramway tower across the stream is an exposure of one branch of the Anaconda fault, faulting Eureka Member against the Picayune Megabreccia Member. After the switchback, Whitecross Mountain is straight ahead. It is a structurally complex block, consisting largely of Precambrian granite that is bounded by faults of the Eureka graben on two sides and by the ring fault of the Lake City caldera on the third side (out of sight from this point). Ruins of Tobasco mill ahead on left. **0.3**

26.2 Crossing stream. Outcrops are Picayune Megabreccia intermixed with Eureka Member. Just ahead is direct view into American Basin. Rugged cliffs at head of American Basin are pyroxene andesite member, overlying a thin wedge of Burns Member and Henson sediments. The entire lower basin slopes are mixed Eureka Member and megabreccia, as are the steep slopes of Handies Peak that rise to the left. **0.3**

26.5 Switchback just above turnoff to American Basin road. At this point we are approximately at the southwest apex of the large triangular block of Precambrian granite of Cataract Canyon that extends to the summit of Whitecross Mountain as a structurally high block, just southwest of the Lake City caldera. **0.3**

26.8 At small creek. Crossing northeast-trending fault between Picayune Megabreccia and Precambrian ahead on uplifted Whitecross Mountain block. Ahead, this fault runs diagonally across the east nose of Edith Mountain on steep cliffs to left of road. The Precambrian in this area is all foliated granite, probably correlative with Silver Plume- or Eolus-type granites at 1.45 Ga. **1.2**

28.0 Crossing Cleveland Gulch and entering Burrows Park, still in Precambrian granite of Cataract Canyon. High country ahead is inside Lake City caldera. High point on right is Redcloud Peak (4278 m). All the slopes are intracaldera Sunshine Peak Tuff. **0.3**

28.3 **STOP 14. Burrows Park; ring fault of Lake City caldera** (Fig. 4-5). To left (northwest) is a steep gully marked by intense alteration along the western arc of the ring fault. The alteration is related to a late quartz vein that cuts a high-silica rhyolite ring dike emplaced during resurgence of the caldera. With care, it is possible to climb the ring-fault gully, where about 0.5 m of fault breccia, gouge, and quartz vein separate coherent Precambrian granite on the west from caldera fill on the east. The lower tree-covered slopes within the Lake City caldera are mostly large megabreccia blocks of volcanics that slid in from the San Juan caldera. Many of these blocks are partially surrounded or veined by thin films of Sunshine Peak Tuff. Low on the slope and adjacent to the ring fault, large masses of Precambrian granite are present on both sides of the valley. Although these may appear to be coherent at first, they are internally shattered and consist of annealed angular fragments 1–20 cm in size. Rare small fragments of lava are enclosed within the shattered granite.

The slopes above treeline north of the road are entirely composed of Sunshine Peak Tuff. Here, as above Capitol City, the middle member rests directly on thick megabreccia adjacent to the ring fault. Toward the interior of the caldera, lower

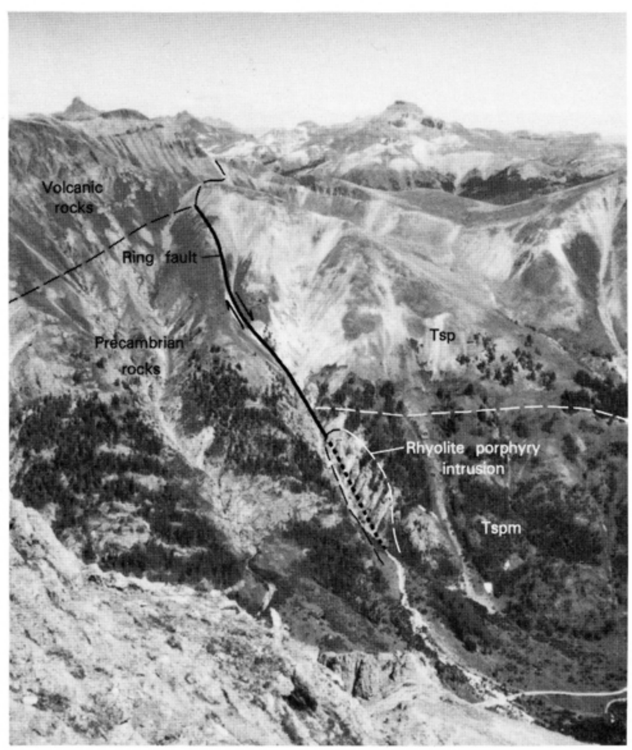

FIGURE 4-5—View of ring fault along west margin of Lake City caldera. Rocks to right of fault are thick intracaldera Sunshine Peak Tuff (Tsp), resting on collapse breccias (Tspm) that slid into caldera. Rocks to left of fault are Precambrian granitic rocks overlain by older volcanic rocks, mainly caldera-fill deposits within the San Juan caldera (from Lipman, 1984).

member tuff interfingers complexly with the megabreccia, which dwindles to a few thin (20–50 m) sheets of collapse breccia 2–3 km up Cooper Creek—the first major drainage visible on the left (Hon, 1987a).

On the south side of the valley, the ring fault begins in a gully as marked by several small prospects, but then cuts through the wooded hillslope. The fault crosses the skyline ridge on the right side of the major saddle just to the left (east) of Whitecross Peak. The lower member of the Sunshine Peak Tuff dips toward us at about 15–20°, forming a dip-slope veneer over underlying megabreccia. Within the valley of the Lake Fork, the dips are near horizontal. Near the mouths of Cooper and Silver Creeks on the eastern side of Burrows Park, lower member tuffs also dip 15°, but in the opposite direction off the resurgent dome. These dips define a syncline structure that the Lake Fork drainage and the road follow through the southwest quadrant of the Lake City caldera. Reconstructions of the resurgent dome indicate that the inward-dipping tuff south and west of the drainage is not a relict depositional surface, but rather a zone of anomalous uplift. The highest area along the southwestern part of the ring fault (between Grizzly and Campbell Gulches) was uplifted at least 1 km sometime after collapse of the Lake City caldera. It is unclear if this uplift was related to resurgence or to a later intrusion beneath the Handies Peak area (Hon, 1987a).

The western ring fault of the Lake City caldera truncates all of the major Eureka graben faults. However, the absence of any vein or mineralized material within megabreccias of the Lake City caldera indicates that the Eureka graben structures were not mineralized until after 23 Ma.

View ahead is entirely within the Lake City caldera. Lower slopes are megabreccia interleaved with lower member tuffs. The upper, altered slopes of Redcloud Peak (4278 m) are middle member, and topographic Sunshine Peak (4268 m), just in view, is capped by the upper member. This is the type locality for the Sunshine Peak Tuff, as defined by Whitman Cross near the turn of the century (Fig. 4-6). Interestingly, it is the only peak within the caldera that offers excellent exposures of all three members of the Sunshine Peak Tuff. Exposures in the bottom of the Lake Fork drainage represent some of the lowest levels of caldera fill, with no indication of the presence of caldera floor. The stratigraphic sequence exposed from the mouth of Silver Creek to the top of Sunshine Peak represents at least 1.5 km of caldera fill. **0.3**

28.6 On left in Burrows Park are several prospect pits, including some exploration work as recent as 1980. **0.5**

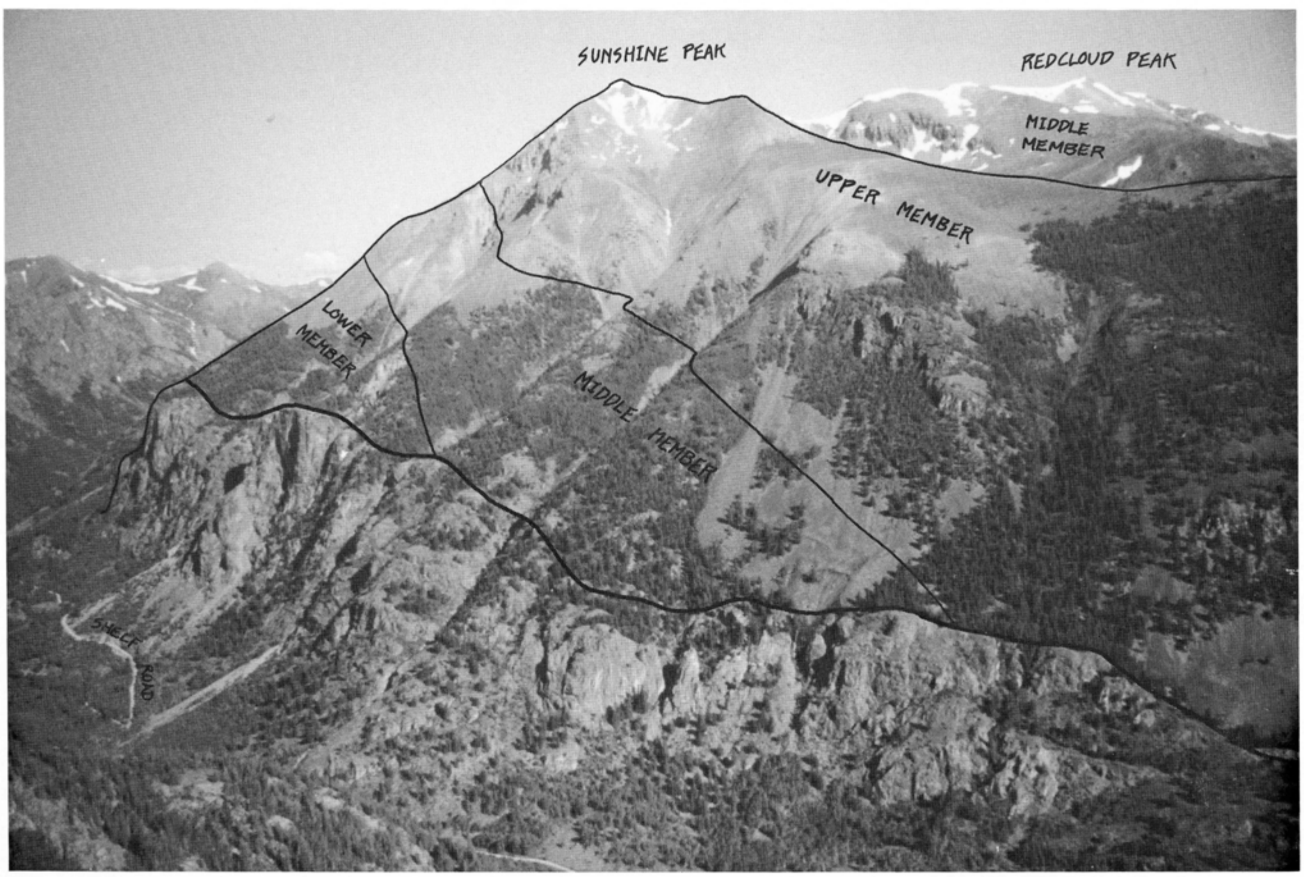

FIGURE 4-6—Photograph of the south side of Sunshine Peak (4268 m) with Redcloud Peak (4278 m) in the right background. Elevation difference from the road to the summit of Sunshine Peak is more than 1.2 km. Cliffs in the foreground are Precambrian granite that mark the ring fault of the Lake City caldera. The top of Sunshine Peak is capped by the upper member of the Sunshine Peak Tuff, which dips at about 20° to the right. Both the middle and lower members of the Sunshine Peak Tuff are also exposed. The summit of Redcloud Peak is composed entirely of middle member.

29.1 Crossing onto megabreccia interlayered with Sunshine Peak Tuff. **0.4**

29.5 Mount of Copper Creek. Exposures of interrelations between Sunshine Peak Tuff and associated megabreccia on northwest side of creek. **0.4**

29.9 Masses of andesite exposed in roadcuts are part of the megabreccia intermixed with the Sunshine Peak Tuff. **0.3**

30.2 Mouth of Silver Creek (departure point for Field guide 5). **0.7**

30.9 Good exposures of Sunshine Peak Tuff in roadcuts on left. Across the Lake Fork on right, massive glaciated cliff exposures of Sunshine Peak Tuff dip steeply toward the valley. Highest cliffs are Precambrian, and the caldera ring fault crosses approximately at treeline, roughly paralleling the slope south of the Lake Fork. **1.0**

31.9 **STOP 15. Tuff dike in slide breccia. Be careful about parking cars—do not block the road.** On left, roadcut exposures of andesite and dacite lavas are part of the voluminous collapse breccias interfingered with the lower member of the Sunshine Peak Tuff near the caldera wall. One outcrop contains a beautifully exposed dike-like mass of lower member tuff cutting andesitic megabreccia blocks. A second outcrop, farther south along the road, contains abundant fragments of mixed lithology, including lavas and sediments, embedded in a matrix of poorly welded lower member tuff.

Examine the tuff dike for internal variations. Note the well-developed internal compaction foliation in the center of the dike and the poorly welded margins. Although this and similar dikes have the appearance of intrusive feeders for the overlying ash-flows, they can be shown to follow irregular boundaries of large megabreccia blocks and commonly undergo rapid changes in both orientation and dip, sometimes switching from near vertical to almost horizontal in a few meters. These are interpreted as remobilized Sunshine Peak Tuff that was squirted either upwards or downwards into dilatent fractures in or between megabreccia blocks during the emplacement of large caldera-collapse breccias. The fluidized emplacement of these dike-like bodies is well illustrated where the tuff intruded thin fractures (<5–10 cm) and became highly winnowed and flow-foliated. The eutaxitic foliation results from quenching and compression of the tuff between large blocks of relatively cool collapse breccia.

In the other exposure, nonwelded lower member of the Sunshine Peak Tuff forms the matrix for many of the outcrop-scale collapse-breccia blocks (mesobreccia). The greenish-white color of the matrix is typical of ash-flow tuff that was rapidly quenched to nonwelded glass fragments by the surrounding cool masses of breccia. These glassy zones are porous and susceptible to later alteration by hydrothermal fluids circulating deep within the caldera. Here the original glass has been replaced by an aggregate of sericite and chlorite. Densely welded tuff at similar levels in the caldera is more resistant to such alteration, due to high-temperature devitrification to sanidine and cristobalite. However, hydrothermal alteration has also affected them, producing the "propylitic" assemblage of sericite after feldspars, and chlorite replacement of mafic minerals that is typical of lower levels of caldera fill.

Across the Lake Fork, the Lake City ring fault is about at treeline and then cuts across the Lake Fork just beyond the stop, where a big rib of Precambrian granite causes a conspicuous bend in the road. Here, the ring fault is between Precambrian rocks and various kinds of megabreccia, with Sunshine Peak Tuff plastered against it lower on the slope. The high point at the southwest end of the ridge is Precambrian rock, and the obscure gray slope behind it (at times with a snow cornice) consists of fill within the north margin of San Juan caldera (Eureka tuff and megabreccia). **0.4**

32.3 Road crosses poorly exposed Lake City ring fault, and goes into somewhat altered Precambrian granitic rocks. A second subordinate fault cuts the Precambrian rocks around the first bend, defining a small slice along the ring fault. In general, the ring fault is a sharp, clean, single or very simple structure. **0.5**

32.8 At flume crossing, excellent exposures of a Cambro-Ordovician east–west-trending diabase dike cut by quartz veins. This is one of many dikes in this area. Ahead the dike is followed by the shelf road. Directly across the valley is Cataract Canyon. Essentially all rocks in sight are the Precambrian granite; the early intermediate-composition rocks occur on high flat areas, but are foreshortened out of sight on most of these ridges. **0.2**

33.0 Back into the granite of Cataract Canyon. Below is the old townsite of Sherman, a briefly active boom area for gold placer mining. **0.8**

33.8 Another large Cambro-Ordovician diabase dike, trending west-northwest. Just ahead is junction with road up Sherman Creek on right. **Continue straight ahead. 1.1**

34.9 Down-valley, essentially straight ahead on a low ridge crest, are two knobs of brown blocky Precambrian granite, and to the left a third knob of more talus-rich grayer Sunshine Peak Tuff inside the Lake City caldera. The ring fault goes through the notch. **0.3**

35.2 Mill Creek Campground. **0.6**

35.8 **Bent Creek; optional stop to examine cobbles in Bent Creek for diversity of Sunshine Peak rock types.** The lower member of the Sunshine Peak Tuff (76% SiO_2) contains abundant, elliptically resorbed quartz (>10%) and equant sanidine (20%) phenocrysts. Small biotite flakes (<.5 mm) are rare. The middle member has similar modal percentages of quartz and sanidine, but is recognizable by the presence of conspicuous 1–2 mm biotite flakes and sparse plagioclase grains. Where this unit has been hydrothermally altered, individual fragments are indistinguishable from the lower member in hand specimen. The upper member is easily distinguished from the other members by the scarcity of quartz (0–3%) and the abundance of plagioclase (5%) and large biotite flakes (2%). Note the contrast of the densely welded, propylitically altered lower member with its outflow equivalent—the poorly welded fresh Sunshine Peak Tuff seen on Spring Creek Pass (see Field guide 3). Especially prominent are the more abundant phenocrysts (35% intracaldera, versus 20–25% outflow) and the common lithic fragments in intracaldera samples. Cobbles without visible quartz are pre-Lake City caldera lavas, sediments, and ash-flow tuff from collapse breccia lenses.

Looking back up the road to the southwest, the contact along the ring fault is obvious between the glacially scoured knobs of Precambrian rock and talus-rich hillsides of intracaldera upper member tuff dipping down valley toward us (Fig. 4-2). Several hundred meters of uplift during resurgence can be documented along this section of the ring fault. **1.1**

36.9 Road up Wager Gulch to Carson Camp. This was a brief silver camp on the mineralized intrusive core of an early intermediate-composition stratovolcano. The style of mineralization is similar in many respects to the enargite–luzonite type identified by Sillitoe in the high levels of andesitic stratovolcanoes. The intrusion has yielded K–Ar dates of 29.6–30.7 Ma. **1.2**

38.1 On right are last exposures of the Precambrian rocks. The crest of the hill on right is capped by a thick flow of the Burns Member, plastered against the wall of the Uncompahgre caldera. Across Lake Fork on the left, large rugged cliff outcrops are the Williams Creek stock, texturally zoned from equigranular monzodiorite (59% SiO_2) to monzodiorite porphyry. It was emplaced along the wall of the Uncompahgre caldera near the boundary between Precambrian granite and Tertiary volcanics. **0.5**

38.6 View up Williams Creek over the monzodiorite intrusion into the interior of Lake City caldera. The high point on right is Grassy Mountain, capped by a sequence of thick postcollapse lavas of silicic dacite within the moat of Lake City caldera. The high point on the left is the upper part of the intracaldera Sunshine Peak Tuff, dipping toward us on the southern flank of the resurgent dome. The ring fault of the Lake City caldera trends toward the Grassy Mountain dome but is covered by lava flows. There was no uplift along this section of the ring fault during resurgence of the Lake City caldera. **0.3**

38.9 Bridge across the Lake Fork. Good exposures of fine-grained marginal phase of the Williams Creek monzodiorite at the bridge. **1.7**

40.6 Good exposures on both sides of road of fill within the Uncompahgre caldera. Cliffs on left side are thick, flow-layered, light-colored silicic dacite of the Burns Member. Overlying this flow above the first set of cliffs to the right are several ash-flow sheets from the central San Juan caldera complex. A great pale orangish-brown cliff of Fish Canyon Tuff is overlain by thinner, more obscurely exposed Carpenter Ridge, Wason Park, and Nelson Mountain Tuffs. These all wedge out against early intermediate-composition lavas to the south on the wall of the Uncompahgre caldera. **1.2**

41.8 Junction with road around east side of Lake San Cristobal. Visible up Red Mountain Creek is the alunitized core of the Red Mountain intrusive complex. **1.5**

43.3 Lake San Cristobal boat facility; nearby outcrops are flow-layered silicic dacite of the Burns Member. The caldera-filling Fish Canyon and Carpenter Ridge Tuffs make the big cliffs above the Burns Member east of the lake. On the high skyline to the north, lava flows of the volcanics of Uncompahgre Peak overlie the Carpenter Ridge Tuff. These flows were probably erupted from vents centered near Slumgullion Pass. **0.8**

44.1 Remnants of buildings related to the Golden Fleece mine. **0.4**

44.5 Bridge at mouth of Lake San Cristobal (road to Golconda Lodge). Continue ahead toward Lake City. Inactive toe of Slumgullion mudflow is on right; dumps of Golden Fleece mine on left. **1.3**

45.8 Thick, flow-laminated biotite dacite lava, part of the Burns Member of the Silverton Volcanics, is exposed on left. **0.5**

46.3 Contact with underlying intracaldera Eureka Member of the Sapinero Mesa Tuff. **0.4**

46.7 Junction with Lake City–Creede road (termination point for Field guide 3). **Continue straight ahead. 0.8**

47.5 Good exposures of the Eureka Member. Exposures straight ahead on Neoga Mountain and all outcrops in between toward Lake City are of the Eureka Member within the Uncompahgre caldera. **1.2**

48.7 Entering Lake City.

Field guide 5: Interior of the Lake City caldera: Hike from mouth of Silver Creek in Burrows Park to Williams Creek campground

Summary

Distance: 46.8 road miles (including shuttle); 10.7 miles on foot.

This traverse through the Lake City caldera examines the deep interior of a resurgent dome. The trail up Silver Creek begins in thick megabreccia deposits interleaved with intracaldera tuff at the caldera margin, crosses massive tuff intruded by the resurgent pluton, and continues east through the compositionally zoned intracaldera tuff capped by postcollapse lavas (Figs. 5-1, 5-2). The stratigraphic section traversed, from the lowest intracaldera tuff to the top of the caldera fill, is more than 1.5 km thick.

The compositionally zoned Sunshine Peak Tuff consists of a silicic rhyolitic lower member (76% SiO_2; 900 m thick), a rhyolitic middle member (74% SiO_2; 300 m), and a quartz trachytic upper member (68% SiO_2; 500 m). The three tuff members (Table 4-2; Hon, 1987a, 1987b) interfinger with

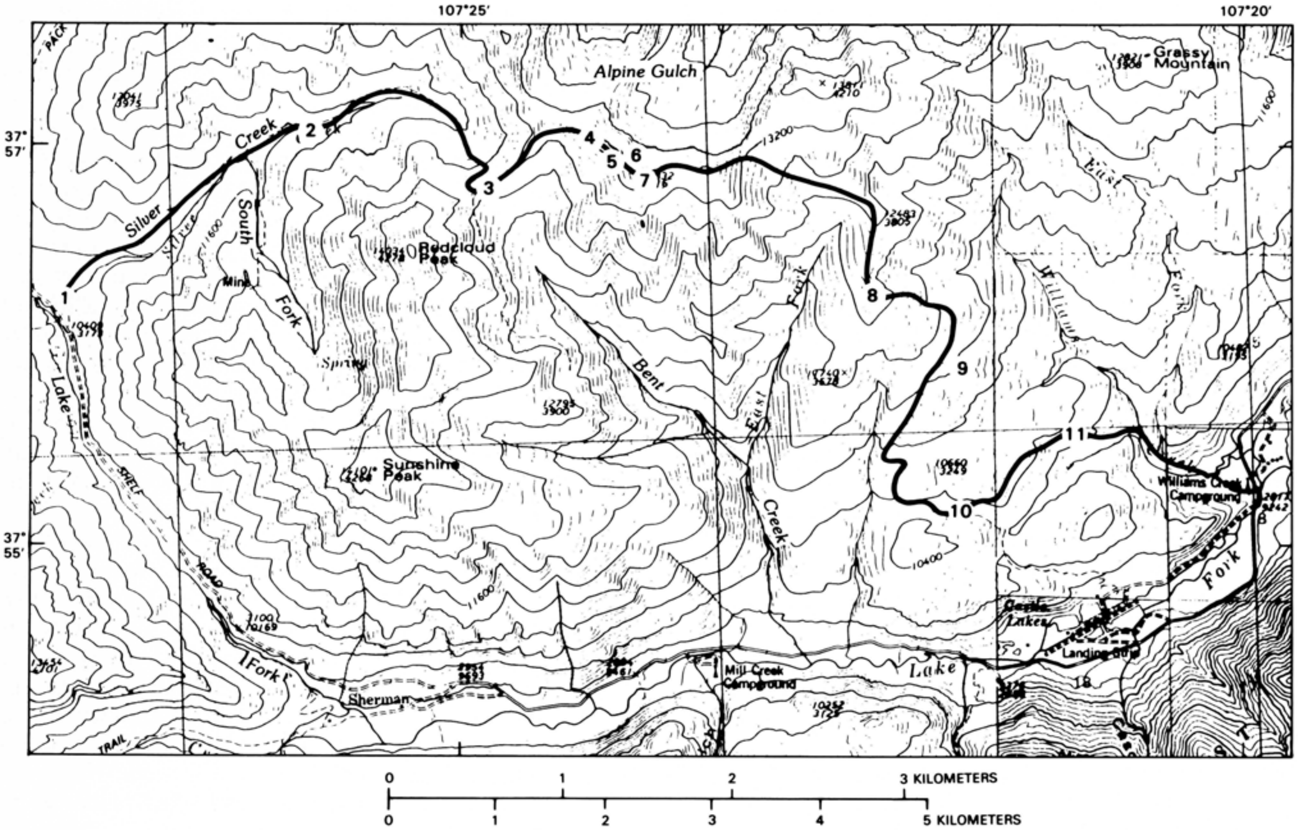

FIGURE 5-1—Route map through Lake City caldera showing stops described in Field guide 5. Interval is 400 ft between major contour lines and 80 ft between minor contour lines.

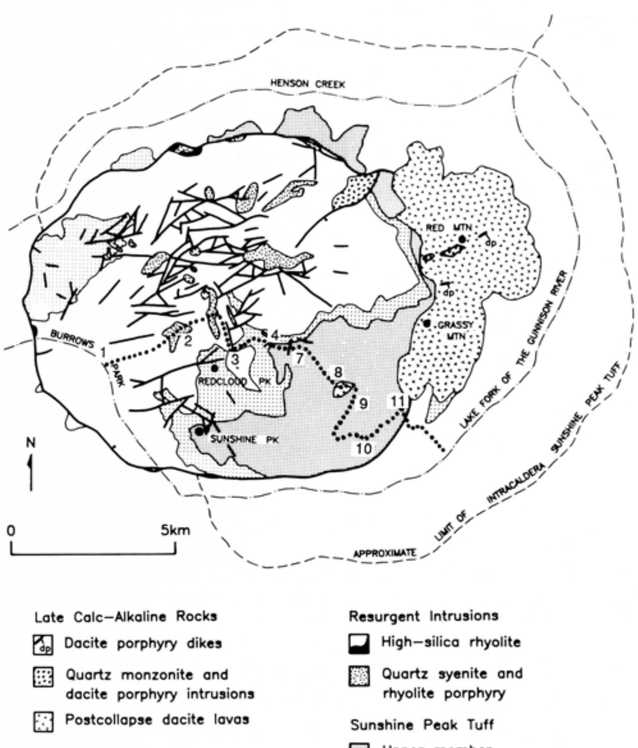

FIGURE 5-2—Geologic map of Lake City caldera showing trip route described in Field guide 5 (heavy dotted line). Numbers correspond to stops described in text.

caldera-collapse breccia produced by periodic landsliding of older rocks from the walls of the Lake City caldera (Lipman, 1976c). The contemporaneous collapse and infilling of the Lake City caldera by the Sunshine Peak Tuff was followed by eruption of the dacite lavas of Grassy Mountain (64–65% SiO_2) along the southeastern quadrant of the ring fault (Fig. 5-2). Subsequently, the emplacement of a large, comagmatic quartz syenite pluton (64–68% SiO_2) and related rhyolitic intrusions (70–74% SiO_2) into the north-central part of the caldera domed the intracaldera tuff and tilted the early lavas. Later dacite lavas erupted north of Red Mountain after resurgence. Final igneous activity in the caldera was the intrusion of the dacite of Red Mountain (63–65% SiO_2) and the quartz monzonite of Alpine Gulch (62–68% SiO_2). Although the duration of the caldera cycle is not resolvable by K–Ar dating, paleomagnetic data indicate that it was probably less than 300,000 years (Reynolds et al., 1986).

Rocks of the Lake City caldera can be divided into two petrologic groups. The Sunshine Peak Tuff and resurgent intrusions are mildly alkaline, whereas the dacite lavas and late intrusions are calc-alkaline (Fig. 5-3). The alkaline rocks from the Lake City caldera are clearly different from the older caldera-related rocks of the San Juan volcanic field and bear close affinities to the Miocene rift-related basalts found in the area (Fig. 5-3). The alkaline rocks vary from silicic rhyolite (76% SiO_2) to quartz syenite or quartz trachyte (64–68% SiO_2). Similar zonations within both the Sunshine Peak Tuff and the resurgent intrusions are thought to reflect derivation from a single, compositionally zoned magma chamber. The calc-alkaline rocks include the dacite

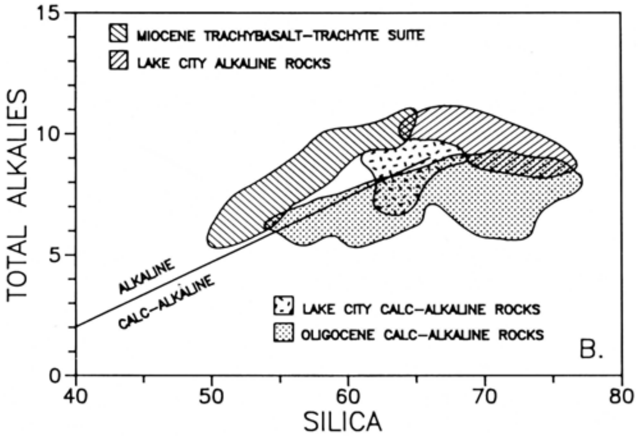

FIGURE 5-3—Total alkalies ($Na_2O + K_2O$) versus silica diagram showing fields of alkaline and calc-alkaline rocks from Lake City caldera, Oligocene calc-alkaline rocks, and Miocene rift-related alkaline rocks from western San Juan Mountains.

lavas of Grassy Mountain, the dacite intrusion of Red Mountain, and the quartz monzonite of Alpine Gulch, which are all confined to the eastern part of the caldera. These have a narrower range of silica contents (62–68%) than the alkaline rocks. Mineralogic, chemical, isotopic, and textural data indicate that both late intrusions were derived from the same magma chamber; the dacite lavas appear to represent an earlier but related phase.

Geophysical studies also support the presence of two plutons beneath the Lake City caldera. Large aeromagnetic and gravity anomalies roughly coincide with the mapped limits of the resurgent intrusion in the north-central part of the caldera. More subdued highs in the eastern third of the Lake City caldera may represent the crystallized source of the calc-alkaline magmas (Grauch, 1987; Grauch and Campbell, 1985).

This strenuous hike crosses the mountainous center of the caldera and climbs more than 3500 ft in elevation (Fig. 5-1). The trip traverses 2 mi of exposed ridge above 13,000 ft, which can be hazardous during electrical storms. Depart no later than 7 a.m. from Silver Creek to reach the ridge before mid-day storms. Generally, the higher ridges remain snow-covered until late June or early July. The one-way hike requires dropping a car at the Williams Creek campground; alternatively, you may return via Silver Creek after Stop 7. The trip guide makes extensive use of the Redcloud Peak and Lake San Cristobal topographic maps; distances and elevations are given in English units to correspond with these maps and Fig. 5-1. The geologic map of the Lake City caldera (Hon, 1987a) is also useful.

Mileage

0.0 Southern limits of Lake City. Head south on road toward Slumgullion Pass. Retrace Field guide 4 to Silver Creek (Fig. 4-1), with stop at Williams Creek campground. **2.0**

2.0 Turn right on road to Lake San Cristobal. **6.7**

8.7 Turn right into Williams Creek campground for vehicle drop near Williams Creek trail, at far end of campground. Then continue south. **6.1**

14.8 Right turn on Cinnamon Pass Road. Road climbs steeply. **3.7**

18.5 Mouth of Silver Creek at south end of Burrows Park. Park cars in grassy area at junction with old jeep road that is beginning of trail.

Trail log

Mileage (elevation in feet)

0.0 (10,400′) **STOP 1. Mouth of Silver Creek.** Attitudes in the lower member of the Sunshine Peak Tuff in this area define a synclinal structure that the Lake Fork drainage follows through the southwest quadrant of the caldera (Fig. 5-2). Across the Lake Fork, thin lenses of tuff dip northeast 25–30° toward us. Within the valley, the dips are near horizontal, but near the mouth of Silver Creek the tuffs dip southwest 10–15° into the valley and off the resurgent dome. Reconstructions of the resurgent dome indicate that the inwardly dipping tuff south and west of the drainage is a zone of anomalous post-collapse uplift, not a relict depositional surface. The greatest uplift along the southwestern part of the ring fault is nearly 1 km, across the valley and between Grizzly and Campbell Gulches. This uplift may be related to resurgence, or to a separate intrusion beneath Handies Peak (Hon, 1987a).

Some of the largest megabreccia blocks within the caldera, 500–1000 m in length, are across the valley to the west on the slopes between Campbell Gulch and Grizzly Gulch, and beneath Whitecross Mountain (Lipman, 1976a). A block of precaldera intermediate-composition sediment in Grizzly Gulch, more than 200 m thick and 1000 m long, contains large boulders of Precambrian granite derived from a paleotopographic high near Whitecross Mountain. Another huge block (>500 m), which preserves the distinctive stratigraphic sequence of San Juan caldera fill exposed on Handies Peak, slumped into the caldera adjacent to the ring fault between Campbell and Grizzly Gulches. To the south, the ring fault passes through the saddle below Whitecross Mountain, into Grizzly Gulch about 1 mi upstream from us, and behind the 13,502 ft ridge crest south of the gulch. Farther downstream, a prominent color change at the base of the Precambrian granite cliffs marks the ring fault.

The prominent ridge on the skyline to the north, above Cooper Creek, is capped by middle member of the Sunshine Peak Tuff, which forms unvegetated gray and orange cliffs. On the tundra-covered slopes below, lower member tuff interfingers complexly with caldera-collapse breccia. The collapse breccias thicken toward the ring fault, out of sight at far left, where the middle member rests directly on megabreccia. The intertonguing collapse breccias and intracaldera tuff near the ring fault record a complex history of episodic ash-flow eruptions, subsidence, and landslide events from the oversteepened caldera walls. To the right, up Cooper Creek, most of the collapse breccia wedges out, but two thin sheets can be traced into the center of the caldera. At their distal end, 5–6 km from the ring fault, the collapse-breccia sheets become discontinuous boulder zones (<5 m thick) separating flow units within the lower member. These breccias separating tuff, and similar relations elsewhere in the caldera, demonstrate that the massive Sunshine Peak Tuff in the interior of the caldera consists of multiple thin ash flows.

The Lake Fork drainage exposes some of the lowest levels of caldera fill with no indication of a caldera floor. The steep, altered slopes to the southeast are the northwest ridge of geographic Sunshine Peak, composed mostly of lower member of the Sunshine Peak Tuff, with megabreccia present only below treeline. The alteration surrounds a mineralized fault. The conspicuous break near the top of the ridge is the poorly welded base of the middle member, resting on a 15–20 m sheet of collapse breccia that overlies the lower member. This is the distal end of a major breccia sheet, which spread across most of the southern half of the caldera from the eastern wall. As we follow this important marker through the day, it will thicken greatly toward the east.

Heading east up the jeep trail, the first outcrops are megablocks of lavas derived from the San Juan caldera to the west. Close examination reveals thin (10–20 cm) fracture fills of quartz-rich lower member of the Sunshine Peak Tuff. The small scattered knobs in the valley bottom north of us are blocks of resistant megabreccia. The less resistant, poorly welded tuff matrix is covered. We cross a thin dip-slope veneer of Sunshine Peak Tuff after rounding the corner into the Silver Creek valley. **0.2** (1000 ft)

0.2 (10,600′) Trail is largely in late Pleistocene moraine and colluvium. Boulders of Precambrian granite indicate deposition as a lateral moraine from the main Lake Fork glacier. Talus of plagioclase-bearing andesite, originally from the San Juan caldera to the west, is derived from outcrops of megabreccia above the trail. **0.8** (4100 ft)

1.0 (11,120′) Trail re-enters megabreccia dominantly composed of andesitic lavas. **0.2** (1200 ft)

1.2 (11,200′) Contact between megabreccia and the lower member of the Sunshine Peak Tuff. **0.2** (1100 ft)

1.4 (11,280′) Cross small gully on north side of Silver Creek, just below junction with South Fork. On the downslope (west) side of the gully, the lower member of the Sunshine Peak Tuff was hornfelsed adajcent to the top of a resurgent quartz syenite intrusion. On the east side of the gully, quartz syenite crops out above the trail. Large boulders of quartz syenite intrusion are present in colluvium along trail. Hiking in and out of quartz syenite and colluvium for next 0.8 mi. **0.1** (500 ft)

1.5 (11,300′) Opposite mouth of the South Fork. Lower part of ridge on right is late Pleistocene lateral moraine deposited by a side valley glacier in the South Fork. The fault associated with prominent alteration on the northwest ridge of Sunshine Peak crosses about 1 km up the South Fork. A quartz vein along this fault was exploited by the Danville mine high on the western side of the South Fork. The fault and quartz vein continue up the west face of Redcloud Peak (4278 m), crossing the main ridge this side of the summit. Surficial oxidation of pyritic rock around this vein and many related quartz veins (<10 cm wide) causes the bright coloration of this peak. Good view of the summit of Sunshine Peak (4268 m), type section of Sunshine Peak Tuff. The top 70–80 m of the peak is capped by the upper member, which dips away from us on the south side of the resurgent dome. The prominent break at the top of the cirque headwall is the base of the middle member resting on a less resistant, thin sheet of collapse breccia. **0.5** (2400 ft)

2.0 (11,720′) **STOP 2. Resurgent quartz syenite intrusion.** Across creek, low outcrops of quartz syenite (64–66% SiO_2) are seriate-textured and characterized by abundant orthoclase phenocrysts and sparse glomeroporphyritic plagioclase. Biotite is conspicuous, whereas quartz is only present in the groundmass (Hon, 1987a). These rocks have been moderately to strongly propylitized. The flat roof of this and other intrusions exposed in valley bottoms within the caldera suggests that they represent the undulating upper surface of a much larger resurgent pluton. Reconstructed contours on the top of this pluton, along with gravity and aeromagnetic data, confirm the presence of a major pluton beneath the north-central part of the caldera (Hon, 1987b). Although the roof of the pluton is relatively flat, deep resistivity soundings suggest that contacts steepen on all sides and extend several kilometers below exposed levels (Pierce and Hoover, 1985). The asymmetric emplacement of this intrusion within the caldera coincides with asymmetric resurgent doming and nonuniform uplift along the ring fault. These relations tie the resurgence of the Lake City caldera to the emplacement of the quartz syenite, which was probably intruded as a stock within the caldera fill.

As we climb the side gully, watch for the transition from phaneritic quartz syenite to quartz-bearing granite porphyry and, finally, into hornfelsed lower member of the Sunshine Peak Tuff. Granite porphyry along the flat-topped margins of the phaneritic quartz syenite appears to have formed by partial assimilation of surrounding Sunshine Peak Tuff. It differs from rhyolite porphyry intrusions that have micrographic textures (discussed below) by the presence of an aplitic to microaplitic groundmass. In addition, quartz and sanidine phenocrysts in the border granite commonly have corroded margins or reaction rims, probably because many were incorporated from the surrounding tuff. Paleomagnetic data indicate that hornfelsed lower member tuff in this area was reheated above the Curie point (580°C) during contact metamorphism (Reynolds et al., 1986). This temperature approaches the solidus of the silicic rhyolite tuff (650–700°C) and supports the textural evidence for partial melting and assimilation. However, assimilation of tuff is not thought to have been important in generating either the composition or the space for intrusion.

The earliest quartz syenite intrusions were dike-like bodies, emplaced at high stratigraphic levels, that radiate outward from the center of intrusion (Fig. 5-2) in the headwaters of Cooper Creek 1–2 km to the northeast. These followed radial fractures, which were present prior to the formation of the northeast-trending apical graben faults. Most early intrusions have borders of quartz-bearing rhyolite porphyry (70–74% SiO_2) that grade inward to phaneritic quartz syenite without quartz phenocrysts. The chemical zonation suggests that these intrusions preserve upper remnants of the zoned magma chamber that gave rise to the Sunshine Peak Tuff. However, the rhyolite porphyry is not chemically equivalent to any pumice composition in the tuff and is thought to reflect mixing during post-eruptive overturn of the magma chamber (Hon, 1987b). Two intrusions with rhyolite margins are present in upper Silver Creek. Return to trail. **0.2** (1200 ft)

2.2 (11,960′) Briefly re-enter lower member of Sunshine Peak Tuff before valley floor is covered by Quaternary deposits for next 0.5 mi. **0.3** (1800 ft)

2.5 (12,120′) Dike-like body of early quartz syenite with rhyolitic margins crosses valley floor under Holocene debris fan. This intrusion extends north to the ridge crest, where it cuts a small remnant of the middle Sunshine Peak Tuff, and south about one-third of the way up the ridge of Redcloud Peak across the valley. The prominent bands cutting across the cirque headwall on the north face of Redcloud Peak are welding breaks within the middle member of the Sunshine Peak Tuff. Along the better developed lower break, poorly welded tuff at the base of the middle member rests on the sheet of caldera-collapse breccia. The breccia has roughly doubled in thickness (from 20 to 40 m), compared to the exposures on the northwest ridge of Sunshine Peak. In the less pronounced higher break, poorly welded, lithic-rich tuff separates two cooling units within the middle member. **0.2** (700 ft)

2.7 (12,000′) Trail crosses landslide deposit containing blocks of quartz syenite from dike halfway up the slope. **0.3** (1800 ft)

3.0 (12,400′) Pass back into lower member of the Sunshine Peak Tuff while climbing out of Silver Creek drainage. Look for pieces of relatively fresh rock to compare with the middle member at the next stop. **0.5** (2800 ft)

3.5 (13,000′) **STOP 3. Pass between Silver and Bent Creeks.** Tuffs in the saddle are altered lower member. A major fault trends north through the saddle and drops the collapse-breccia horizon at the base of the middle member 60 m down to the east. Blocky, reddish outcrops below and east of us are lava within the collapse-breccia member. The breccia horizon is difficult to see crossing the altererd east face of Redcloud Peak, but is exposed along the trail to the summit.

Proceed up-slope to the east, to a small remnant of middle member tuff (74% SiO_2) resting upon collapse breccia. The middle member is distinguished from the lower member by its larger biotite flakes (1–2 mm) and, to a lesser degree, by abundant plagioclase. Although the modal concentrations of biotite are not greatly different (0.5% vs. 1.0%), biotite flakes in the lower member rarely exceed 0.5 mm. Both units contain roughly equal amounts of quartz (10%) and sanidine (20–25%).

Continue along south side of the middle member outcrops. Watch for blocks of vitrophyric quartz trachyte pumice as much as 1 m long, from the base of the middle member. **Please do not needlessly damage these rare outcrops.** The bulk composition of the middle member results from mixing silicic rhyolite pumice (like that in the lower member) with about 10% quartz trachyte during eruption. The quartz-trachyte component can be identified throughout the middle member, but is vitrophyric only at the base. The conspicuous biotite flakes in the middle member are derived from the quartz trachyte, as are most of the plagioclase and clinopyroxene.

The quartz trachyte pumices from the middle member are geochemically and isotopically the most primitive rocks in the Lake City caldera system, although even they have interacted substantially with crustal rocks. They also bear close affinities to quartz trachyte lavas associated with Miocene trachybasalts north of the Lake City caldera (Hon, 1987b). This primitive or "mafic" quartz trachyte is thought to represent a batch of relatively hot magma that entered the zoned chamber and rose as a plume through more evolved quartz trachyte magma. The mafic magma probably spread out at the interface between evolved quartz trachyte and more buoyant silicic rhyolite near the top of the chamber. As the new batch of magma cooled, by transferring heat into the overlying rhyolite and surrounding quartz trachyte, it was gradually mixed into the lower part of the magma chamber, where it fractionated further. The most differentiated resultant melt may have accumulated along a boundary layer, where it could be incorporated into the base of the silicic rhyolite. Incremental growth of the magma chamber by this process probably continued until the upper volatile-rich, silicic rhyolite became unstable and eruption was triggered, possibly during the addition of a batch of "mafic" quartz trachyte.

Continue along ridge crest. Note the diverse lithologic types in the collapse-breccia unit, which includes clasts of andesitic to dacitic lavas, volcaniclastic sediments, and ash-flow tuff from within the Uncompahgre caldera. **0.5** (2300 ft)

4.0 (13,400′) At base of 13,561 ft knob dividing Silver Creek, Bent Creek, and Alpine Gulch. This knob is densely welded middle member overlying collapse breccia. More float of vitrophyric quartz trachyte is present at the base of this outcrop. We are near the center of the caldera. Along ridge to the northwest, just past the saddle, a horst of lower member tuff truncates the middle member and associated collapse breccia. Farther to the northwest, the 13,665 ft peak is another small fault block within the apical graben of the resurgent dome and is capped by partly vitrophyric middle member which forms prominent spires. Continue around the south side of the 13,561 ft knob toward next saddle. Watch for small patches of poorly welded middle member tuff at the base of densely welded zone. Thin (<5 m) zones of poorly welded tuff are present almost everywhere that ash-flow units are in contact with collapse breccias, but are rarely exposed due to weak induration and cover by talus. **0.1** (800 ft)

4.1 (13,420′) Divide between Alpine Gulch and Bent Creek. Brief stop to examine vitrophyre at the base of middle member of Sunshine Peak Tuff. Glassy pumices of both silicic rhyolite and quartz trachyte are set in a vitric matrix of welded glass shards. **Again, please do not damage or needlessly remove any of this unique outcrop.** Proceed to east up the ridge. **0.2** (900 ft)

4.3 (13,640′) **STOP 4. Lithic-rich zone in middle member of Sunshine Peak Tuff.** A poorly welded lithic-rich zone within the middle member crosses flat part of the ridge on west side of second small knob. On the north face of the ridge, this zone is expressed as a 5 m break in slope between more massive units. These lithic-rich zones at flow-unit bases are poorly welded due to their abundant (20%) xenolithic rock fragments. Such fragments could not have been incorporated from the underlying ash-flow unit, nor are they collapse breccias; they were probably introduced during flaring of the eruptive conduit. **0.2** (1000 ft)

4.5 (13,640′) **STOP 5. West side of 13,832 ft peak; contact of middle and upper members of Sunshine Peak Tuff.** Prominent parting crossing cliffs on north side of peak separates middle member, below and west of us, from upper member capping the peak. This break is caused by a <5 m sheet of caldera-collapse breccia at base of the upper member. Most of upper member is densely welded to the contact with the breccia unit, but 1–2 m of poorly welded tuff are present locally. Thin breccia sheets, such as this one, apparently lack sufficient thermal mass to inhibit welding of the overlying ash-flow unit. The more mafic upper member was also emplaced at higher temperature than either of the rhyolitic members. Spherulitic devitrification near this type of contact indicates rapid quenching; coarser granophyric textures predominate in the interior of cooling units within upper member.

The upper member (67–69% SiO_2) is readily distinguished from the lower and middle members by scarcity of quartz (<5%) and relatively abundant plagioclase (5–10%) and biotite (1–3%). The average sanidine content is 35%. Locally, 10–15 m of quartz-rich tuff at base of the upper member is similar in appearance to middle member; major- and trace-element compositions are transitional. Quartz-poor upper member resembles Fish Canyon Tuff, with which it was mistakenly correlated by earlier workers (Larsen and Cross, 1956; Luedke and Burbank, 1963). The Fish Canyon Tuff is easily recognized by presence of hornblende rather than augite, and by its hexagonal biotite flakes in contrast to ragged biotite typical of Sunshine Peak Tuff.

Chemical and mineralogical data indicate that the upper member contains a third pumice type that is similar to the quartz syenite intrusions, in addition to those identified within middle member. Mixing models suggest the upper member is composed of 70% quartz trachyte, 20% silicic rhyolite, and 10% "mafic" quartz trachyte. The abrupt compositional breaks between the three members may reflect short pauses and re-equilibration of the eruptive mixture (Hon, 1987b). **0.05** (300 ft)

4.55 (13,720′) **STOP 6.** Halfway to summit of 13,832 ft peak from Stop 5. Faint parting separates cooling units in upper member on north side of peak. Nonwelded, crystal-poor tuff (75% SiO_2, 10% phenocrysts) along this break consists mostly of bubble-wall shards and is nearly devoid of pumice and rock fragments. This winnowed tuff was probably deposited from the elutriated ash cloud associated with the underlying flow unit, rather than poorly welded base of upper cooling unit. Take a piece of this tuff (one per group, please) to compare with well-exposed, crossbedded surge deposit (Stop 11).

Cooling breaks formed within individual ash-flow members where sufficiently cool or insulating masses of rock were present. Caldera-collapse breccias, lithic-rich horizons, and other pyroclastic deposits occur along these boundaries. Where intervening material had sufficient thermal mass, welding zonations were produced in both the underlying and overlying ash-flow units. Low in the caldera, poorly welded zones are expressed as slabby tuff that is relatively dense due to intense propylitic alteration. Higher in the section, poorly welded tuff is punky and has a light greenish tint caused by replacement of glass by sericite. Definable cooling units represent at least the equivalent number of ash-flow units, but most contain multiple flow units (Hon, 1987b).

To the southwest, another internal break can be seen in the upper member on southeast side of Sunshine Peak, the pointed peak just south of Redcloud. The prominent cliffs to left of summit are upper member, overlain by a second cooling unit expressed as grassy slopes halfway down ridge. **0.05** (400 ft)

4.6 (13,832′) **STOP 7. Summit of peak and highest elevation of trip;** excellent views of the Lake City caldera and surrounding terrain.

Lake City caldera

The stratigraphic sequence along this ridge is well exposed in the cliffs to the east. Near the bottom of the cliffs on the left (north) ridge line, thick red and buff rocks are blocks of dacite lava within the collapse-breccia sheet at base of middle member of Sunshine Peak Tuff (Fig. 5-4). This is the same collapse-breccia sheet that we have traced from the mouth of Silver Creek. Here, the breccia sheet is at least 200 m thick, more than an order of magnitude greater than at its distal end to the southwest. The brownish-gray zone overlying the breccia is the lower cooling unit within middle member. Above is prominent tan lithic-rich welding break within middle member. The contact between the middle and upper members is expressed only as a faint line just below ridge crest (Fig. 5-4), because there is only a very thin (<5 m) breccia sheet and nonwelded zone at base of upper member. The ridge line contains dip-slope exposures at top of lowest cooling unit in upper member. The visible summit of the 13,811 ft peak is within upper cooling unit, roughly equivalent to our stratigraphic position.

The Lake City caldera is encircled by deep drainages of Henson Creek to north, and the Lake Fork of Gunnison River to east and south (Fig. 5-2). This pattern reflects stream incision into moat of Lake City caldera, similar to the way the moat of Creede caldera is excavated by the Rio Grande (Field guide 3). High parts of the jointly resurged dome of the Uncompahgre and San Juan calderas prevented formation of a moat on west side of Lake City caldera. The original moat surface—and final fill level of Sunshine Peak

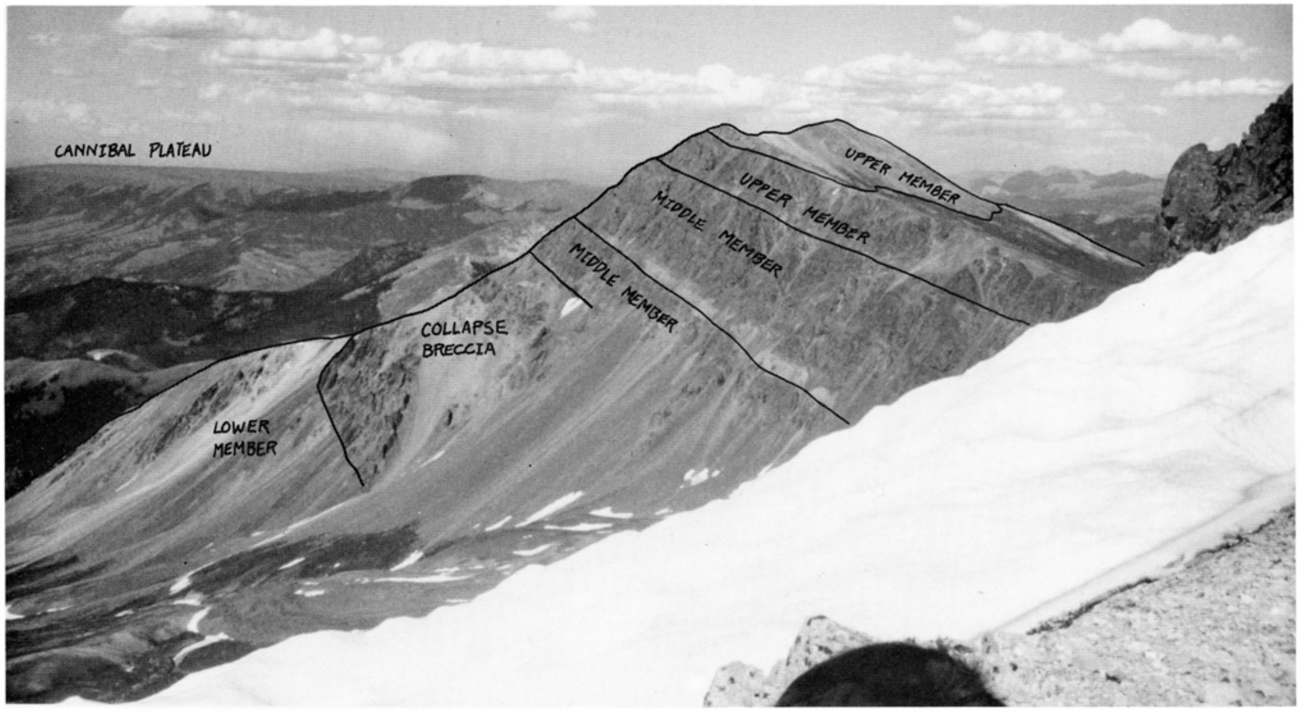

FIGURE 5-4—Photograph of cirque wall at head of middle Alpine Gulch, showing stratigraphy of intracaldera Sunshine Peak Tuff. Photo taken from vitrophyre locality just before Stop 4.

Tuff within Lake City caldera—was at about 3700 m present elevation, 500 m below our vantage point (4216 m) and 800–1000 m above present valleys.

Southeast across the Lake Fork, gentle ridges of the Continental Divide approximate location of topographic rim of Lake City caldera. Scraps of outflow Sunshine Peak Tuff (lower member) remain plastered to south side of this ridge up to 3600 m elevation and suggest that it was not much higher at 23 Ma than its present maximum elevation of 4000 m. Below us, grassy dip-slopes of upper Sunshine Peak Tuff dip 25–35° to south off resurgent dome. Where capped by a remnant of postcollapse lava near treeline (Stop 8), the upper member is 500 m thick. The upper member is of approximately the same thickness just outside of northern ring fault near T-Gulch (Field guide 4). The upper member thins to 400 m beneath Grassy Mountain, the low peak at eastern end of this ridge, where it is conformably overlain by thick postcollapse dacite lavas (63–66% SiO_2) erupted prior to resurgence. North of Red Mountain (largely blocked from view), subhorizontal postcollapse lavas unconformably overlie steeply dipping upper member tuffs and must have been erupted after resurgence. The base of the lavas (3200 m) in this area is 500 m below the caldera-fill level. These post-resurgent lavas apparently filled a deep canyon that may have formed by draining of an intracaldera lake. The only place the Lake City caldera wall could have been breached during this drainage is near town of Lake City along the Lake Fork.

Reconstruction of the top surface of upper member of Sunshine Peak Tuff places high point of resurgent dome at 5100–5200 m, 2–3 km north of us and nearly 1 km above our present elevation. Down Alpine Gulch to north, the steep rugged peaks of lower member tuffs on west side of valley differ from subdued ridges of upper member tuffs overlain by postcollapse lavas to east. The massive ridge 5 km to north (13,084 ft peak), above and west of lower Alpine Gulch, is a section of lower member tuffs 800–900 m thick, with no top or bottom exposed. East of lower Alpine Gulch, a conspicuous mine dump on a small, partially wooded hill marks base of upper Sunshine Peak Tuff. Here the upper member dips 30–40° on north side of resurgent dome. These relations record offset of at least 1 km along the Alpine Gulch fault. Similarly, the northern ring fault has more than 1 km of uplift just west of Alpine Gulch, but no detectable postcollapse movement to east. Analysis of regional tilting indicates that Lake City caldera has not been tilted.

Both the Alpine Gulch and ring faults are related to asymmetric intrusion of resurgent quartz syenite. The Alpine Gulch fault marks northeastern boundary of this intrusion. Structure contouring of quartz syenite outcrops defines a pluton more than 5 km in diameter, with a flat upper surface at about 3500 m elevation. The bright red and orange altered area 2–3 km to the northwest is complexly faulted and mineralized lower member of Sunshine Peak Tuff above a high point on resurgent intrusion. Similar strong alteration throughout western part of the caldera is related surface oxidation of quartz–sericite–pyrite altered rocks above the quartz syenite pluton. Pyritic quartz veins 0.5–3 m wide commonly occupy faults within these areas and can be argentiferous. Alteration intensity and vein density both decrease outward from the resurgent pluton. This zonation is a result of hydrothermal circulation above and along margins of the quartz syenite, as also defined by whole-rock oxygen-isotope values (Larson and Taylor, 1986). Lead-isotopic ratios of veins (Sanford and Ludwig, 1985) and volcanic rocks (Hon, 1987b; Lipman et al., 1978) suggest that the metals were derived from wallrocks, not directly from the quartz syenite. Veins cutting andesite–dacite collapse breccias have higher base-metal contents than those cutting Sunshine Peak Tuff. The latter veins also have higher concentrations of U and Mo (Sanford et al., 1987), elements that were strongly enriched (10–20 ppm) in lower member tuffs (Hon, 1987b). Silver is the principal precious metal in the veins.

In contrast, the intense acid-sulfate alteration at Red Mountain (largely obscured from view) resulted from degassing of SO_2 during emplacement of one or more late dacite porphyry intrusions (64–65% SiO_2) (Bove et al., 1987). Early phases of the late dacite porphyry intruded postresurgent dacite lavas on Red Mountain and probably fed an overlying dome complex. All rocks at the surface were alunitized and hydrothermally brecciated during emplacement of a later phase of the dacite porphyry. The potassically altered top of this stock, 1 km below the surface, is associated with weak granodiorite-type, Mo porphyry-style mineralization (Bove et al., 1987). Weak porphyry-type alteration is also associated with the late quartz monzonite stock (62–68% SiO_2) at intersection of Alpine Gulch fault and the ring fault (Hon, 1987b). This intrusion is mineralogically, geochemically, and isotopically similar to the late dacite intrusions of Red Mountain. Both are thought to have been derived from a larger magma body delineated by gravity and aeromagnetic data beneath the eastern third of Lake City caldera.

Regional geology

Southwest across the Lake Fork (just left of Sunshine Peak) is Precambrian granite (lower tree-covered slopes), overlain by precaldera intermediate-composition lavas and sediments (smooth slopes above treeline). The section is capped by the 30 Ma Ute Ridge Tuff (Ute Creek caldera), the Blue Mesa Tuff (Lost Lake caldera), and local dacitic–andesitic lavas and laharic breccias (Lipman, 1976a). In distance, the rugged Needle Mountains are usually visible (Fig. 4-2). All mid-Tertiary volcanic units in the western San Juans lap up against this highland of Precambrian metamorphic and granitic rocks, which was uplifted at 60–70 Ma. The Precambrian granite southwest of Lake City caldera is an eroded outlier of this uplift. Precaldera lavas and sediments fill deep paleovalleys within this paleotopographic high and depositionally thin against it (Steven and Lipman, 1976).

Due south across the Lake Fork valley, Wager Gulch is the wide valley with meadows that extend nearly to timberline. The intrusive core of the precaldera Carson volcano is in low saddle on Continental Divide at top of Wager Gulch (Fig. 4-2). To right of Wager Gulch, prominent cliffs on Bent Peak are early intermediate-composition lavas on west flank of Carson volcano. The triangular peak in far distance (behind Bent Peak) is Rio Grande Pyramid (4213 m), which overlooks Ute Creek caldera.

Looking to east, the high massif on skyline is core of San Luis caldera (Road Log 3). The central triangular peak, San Luis Peak (4313 m), is intracaldera Nelson Mountain Tuff on the resurgent dome. The surrounding peaks all are postcollapse dacite domes, including Baldy Cinco (4079 m). Southwest of San Luis caldera, outflow Nelson Mountain Tuff caps Snow Mesa (Fig. 4-2). On clear days, the low resurgent dome of Creede caldera is visible to right of Snow Mesa. In front of Snow Mesa, just west of Spring Creek Pass (Field guide 3), the top of Jarosa Mesa is capped by 15.4 Ma trachybasalt that overlies Sunshine Peak Tuff.

To northeast, 18–19 Ma trachyandesites and latites cap Cannibal Plateau and Mesa Seco east of Lake Fork valley. The high peak to northwest, Uncompahgre Peak (4361 m), consists of ash-flow tuffs and lava flows within upper part of Uncompahgre caldera fill. Farther west, the distinctive, sharp summit of Wetterhorn Peak (4272 m) is capped by Ute Ridge Tuff just outside of Uncompahgre caldera wall. The peaks to west, including flat-topped Handies Peak (4282 m), are all within the resurgent dome of Uncompahgre–San Juan caldera.

Continue east along ridge to complete field trip at Williams Creek (or retrace route back down Silver Creek to Burrows Peak). **0.2** (900 ft)

4.8 (13,560′) Cross-winnowed tuff forms parting that separates cooling units within upper member of Sunshine Peak Tuff. **0.2** (900 ft)

5.0 (13,520′) Begin ascending 13,632 ft peak, crossing parting between cooling units in upper member. **0.1** (400 ft)

5.0 (13,632′) Summit capped by upper cooling unit of upper member of Sunshine Peak Tuff. **0.2** (1000 ft)

5.2 (13,320′) Descending east side of summit; cross parting between cooling units in upper member. Continue to descend and traverse the headwaters of east fork of Bent Creek, heading for the 12,483 ft point on east side of this drainage (Lake San Cristobal quadrangle). Follow ridge to Stop 8, just above treeline. **1.4** (7300 ft)

6.6 (12,195′) **STOP 8. Knob of postcollapse dacite.** Upper member of Sunshine Peak Tuff (boulders in saddle north of lavas) is poorly to moderately welded, presumably near depositional top of unit. This small patch of flow-brecciated dacite is an erosional remnant of much larger flows that extended northeast to Grassy Mountain.

Descend jeep trail on east side of knob. **0.3** (1500 ft)

6.9 (11,800′) Approximate contact between float of dacite lavas (up-slope) and colluvium. **0.6** (3000 ft)

7.5 (10,360′) Jeep trail passes from colluvium into late Pleistocene lateral moraine. Glacial boulders, including Precambrian granite and lower member of Sunshine Peak Tuff, are present in roadbed for 0.5 mi. **0.1** (500 ft)

7.6 (11,280′) **STOP 9. Jeep trail crosses west end of small flat area.** Proceed about 600 ft east, to top of small knob (11,280 ft) at end of flat. Shatter textures of dacite lava within collapse breccia are typical of thin breccia sheets interbedded with middle and upper members. Angular rock fragments, 1–2 cm in diameter, are supported by a matrix of finer fragments and pulverized rock. Zones of shattered rock tend to be lithologically homogeneous, suggesting they were originally single blocks that traveled as coherent masses during emplacement.

These shatter breccias differ from most collapse breccias interlayered with lower member of Sunshine Peak Tuff; the latter are largely intact blocks of various lithologies. Most collapse breccias formed by widespread slumps and bedding-plane slides from oversteepened caldera walls adjacent to the ring fault. As the caldera evolved, the topographic wall receded from the ring fault, thereby lessening instability. Many shatter breccias are at bases of flow units in middle and upper members, suggesting deposition by rock-fall avalanches, possibly triggered during seismic activity associated with eruption. A good analogy can be made with the Sherman Glacier rock avalanche (McSaveney, 1987) during 1964 Alaskan earthquake. The avalanche traveled more than 5 km from its source over the relatively flat glacier and deposited a thin sheet (<5 m) of highly shattered rock. McSaveney (1978) proposed that individual blocks were not shattered during transport, but rather by in-situ disintegration at source prior to avalanche.

Return to jeep trail and continue downslope. **0.4** (2300 ft)

8.0 (10,900′) Cross from moraine into collapse breccia. **0.1** (600 ft)

8.1 (10,800′) Contact of collapse breccia and upper member of Sunshine Peak Tuff. Upper member is exposed in roadbed on curve about 200 ft downhill. **0.1** (700 ft)

8.2 (10,600′) Contact of upper member tuff and collapse breccia. Float of shattered dacite lava in collapse-breccia unit on hairpin turn about 100 ft downhill. **0.2** (1100 ft)

8.4 (10,400′) Trail enters flat area covered by late Pleistocene moraine and alluvium. Upslope, the upper member tuffs and related collapse breccias dip 25–30° south, off resurgent dome. Outcrops farther south near ring fault dip 10–15° into caldera and define a shallow synclinal structure in this area. The inward dips probably reflect post-depositional compaction of the tuff, which is less compressed where interleaved with thick collapse breccias near ring fault. The synclinal flexure is at base of resurgent dome, where it did not coincide with ring fault. **0.4** (2000 ft)

8.8 (10,280′) **STOP 10. Lithologically heterogeneous collapse breccia** along jeep trail, where it begins to descend into narrow valley. Most fragments are small (<5 cm) and clast-supported. The deposit is thin (<10 m), suggesting that it is remobilized material from the caldera wall or the distal end of a heterogenous breccia sheet. Alternatively, this breccia might be a near-vent coignimbrite lag in upper member of Sunshine Peak Tuff.

Head east from road, following prominent ledge on top of breccia unit. Breccia angles up talus slope to about 10,600 ft. Examine contact of breccia with overlying upper member tuff. Upon reaching flat area on top of ridge, head northeast and contour around southeast side at about 10,600 ft following breccia unit. At northeast end of ridge begin to descend onto jeep trail (not shown on map), where it turns northwest in a small gully. After reaching road level (10,400 ft), contour through gully to northeast, descending slightly. Continue obliquely down next hillside, toward small buff-colored cliffs in middle slope.

[NOTE: Route goes cross-country from Stop 10. An easier alternate route follows jeep trail heading south to valley floor and turns left on road along north side of valley to bridge over the Lake Fork. Follow the main road about 1000 ft to Williams Creek campground.] **0.9** (4900 ft)

9.7 (10,240′) **STOP 11. Cliffs of upper member of Sunshine Peak Tuff** in middle of slope. At the base of the ash-flow tuff is 1–2 m of nonwelded tuff (70% SiO_2) with conspicuous bedding (5–10 cm). The tuff contains about 30% crystals and broken-crystal fragments. This is less than the ash flows in upper member (50% crystals, uncorrected for welding), but more than the 10% crystals in winnowed nonwelded tuff at head of Alpine Gulch (Stop 6). Small rock fragments (<0.5 cm) are also abundant in the bedded tuff. The crystals and lithics are supported in a matrix of fine glass shards (0.1–0.2 mm) and "dust," which have been replaced by sericite during secondary devitrification. The relict shards are thin and wavy, and nearly devoid of bubble-wall textures characteristic of ash-flow deposits. Rare small pumice fragments (1–2 mm) are visible only in thin section. The fragmented and lithic-rich character of these bedded tuffs suggests deposition by multiple base-surge eruptions from a nearby vent along the ring fault. The surge eruptions probably immediately preceded eruption of the overlying ash-flow tuff, which contains abundant lithic fragments (up to 1 m in diameter) indicative of near-source deposition.

On way down-slope, note blocks of collapse breccia exposed in narrow gullies about 40 ft below here. **0.1** (500 ft)

9.8 (10,800′) Cross the ring fault of Lake City caldera and enter flat area. All exposures below here are postcollapse dacite lavas (Burns Member of Silverton Volcanics) within Uncompahgre caldera. Continue down hillside, angling to east. Look for faint trail into Williams Creek at about 9800 ft (about 100 ft above gulch) at top of forested area. Follow trail down this side drainage to junction of Williams Creek. **0.3** (1600 ft)

10.1 (9,520′) Cross to east side of Williams Creek just above junction with side drainage. Follow trail down east side of Williams Creek, staying 50–100 ft above stream level. **0.3** (1400 ft)

10.4 (9,360′) Cross east fork of Williams Creek. Continue downslope to fenced area around water supply for Williams Creek campground. Follow road back to campground. **0.3** (1600 ft)

10.7 (9,200′) Arrive at Williams Creek campground.

Field guide 6: Lake City to Gunnison

Distance: 45.6 miles

Summary

This trip heads north out of Lake City, along the Lake Fork of Gunnison River, and away from the western San Juan caldera complex. Beyond the unconformity that marks northern wall of Uncompahgre caldera, a thick sequence of early intermediate-composition lavas, breccias, intrusions, and related volcaniclastic sediments is exposed along the Lake Fork valley walls (Lipman, 1976a; Tweto et al., 1976). Our route goes through the eroded Larsen volcanic center and along western flank of Lake Fork volcano (Figs. 4-1, 4-2), sources for early intermediate-composition rocks.

Remnants of outflow sheets from western San Juan calderas partly cap many of the high ridges on both sides of Lake Fork drainage. North of Larsen volcano, the Lake Fork drainage is flanked by 18–19 Ma trachyandesite complexes that form Alpine Plateau to west and Cannibal Plateau to east (Lipman and Mehnert, 1975). About 20 mi north of Lake City, the road climbs out of valley through outflow sheets from western and central San Juan calderas, which fill a major Oligocene paleovalley along Cebolla Creek (Olson et al., 1968). After passing through the Cebolla Creek drainage and Powderhorn, the road ascends a paleotopographic high of Precambrian rocks that is unconformably overlain by ash-flow tuffs (Olson et al., 1968). This surface descends gently into Gunnison River drainage, where distal San Juan ash-flow sheets lap out to north against remnants of 30–35 Ma West Elk volcano (Fig. 4-2). Ash-flow sheets on both sides of Gunnison River dip gently into drainage due to late Cenozoic uplift to north and south.

Mileage

0.0 Junction of CO-149 and Henson Creek road, downtown Lake City. Cliffs west of town are intracaldera Eureka Member of Sapinero Mesa Tuff (Field guide 4). At base of hill across river to east, the Eureka Member is overlain by volcaniclastic sediments (Henson Member of Silverston Volcanics) that accumulated in low areas around resurgent dome of Uncompahgre caldera. Capping upper third of hill are Fish Canyon and Carpenter Ridge Tuffs from central San Juan Mountains, which ponded along eastern side of this caldera (Lipman, 1976a). Behind us is Round Mountain, a postcollapse dacite lava dome within Lake City caldera. Proceed north on CO-149. **0.6**

0.6 Ascend small hill, leaving Lake City. Hummocky ridge ahead is a Holocene earthflow, similar to Slumgullion slide. **0.8**

1.4 Descend north side of earthflow, beyond which is a thick section of sediments of Henson Member overlain by Fish Canyon Tuff on west side of road. **0.6**

2.0 Road runs along northeastern wall of Uncompahgre caldera (buried by alluvium) for next 0.7 mi. Caldera fill is on left, precaldera intermediate-composition breccias on hillside across river to right. **0.7**

2.7 Valley View Ranch on right. Unconformity between intracaldera sediments of Henson Member and precaldera andesitic–dacitic breccias defines topographic wall of Uncompahgre caldera on left. **0.8**

3.5 Larsen Creek; outcrops on left (west) are monolithologic explosion breccias, agglutinates, and mudflow breccias in core of the Larsen center. The upper parts of hillside to west for the next mile are within the central monzonite stock. Small dikes related to this stock cut outcrops close to road. Some dikes form resistant ridges on low hillsides to northeast. Several small masses of low-silica rhyolite alos occur in core of this volcano (Lipman, 1976a). Late Pleistocene terminal moraine of the Lake Fork glacier is across river to east. **1.7**

5.2 Road descends into gorge along the Lake Fork. Large dike from Larsen center exposed along and above road. Outcrops at road level for next 2.5 mi are precaldera intermediate-composition lavas. **2.4**

7.6 Road climbs out of canyon onto late Pleistocene river terraces. Route has left Lake City caldera area map (Lipman, 1976a). **1.0**

8.6 **STOP 1. View to northwest of 19 Ma Alpine Plateau mixed lava complex** (Hon and Bartel, 1987). The deep gulches near top of Alpine Plateau expose lavas 300–400 m thick around vent region. Initial eruptions of unmixed trachyandesite (53% SiO_2) formed a small cinder cone in bottom of paleovalley cut into Blue Mesa Tuff. Successive eruptions were mixed lavas that progress from trachyandesite (53–56% SiO_2) upward to latite and trachyte lavas (58–62% SiO_2) (Fig. 5-3). Most flows have megascopic textures produced by mixing and mingling of mafic and silicic endmembers. The highly fluid, mafic mixed lavas extend as far as 15 km north of the vent, whereas the viscous silicic lavas are restricted to the vent area. The final phase was emplacement of a trachyte dome (62–65% SiO_2), which can be traced downward into an underlying syenite intrusion that contains blobs of mingled basalt. The trachyte is thought to have formed by fractionation of trachybasalt magmas and interaction with lower crustal granulites, which occur as xenoliths in the trachyte.

The lower slopes of Alpine Plateau are 30–33 Ma breccias and sediments that interfinger complexly on west side of Lake Fork volcano. Across valley to east are hoodoos (tent rocks) in pyroclastic agglutinates related to Lake Fork volcano. These rocks are exposed intermittently along east side of valley until Gateview. The agglutinates formed by strombolian eruptions of andesite and dacite from several small centers prior to growth of Lake Fork volcano. **1.0**

9.6 Well-developed hoodoos in Lake Fork pyroclastic agglutinate to east across river. Road continues along late Pleistocene terrace. **2.0**

11.6 Junction with Alpine Plateau Road. Two late Pleistocene terraces are preserved immediately beyond. The main road is about 20 m above river level and travels along the lower of these terraces, which is probably correlative with the terminal moraine seen just north of Lake City. The upper terrace is another 20 m above road, and scraps of a third terrace level are preserved about 100 m above present river level.

These terraces record uplift during late Pleistocene. **0.9**

12.5 Hells Canyon. Across Lake Fork to east, cliffs of pyroclastic agglutinate have irregular bedding planes formed by draping over pre-existing topography. Above these are two sequences totaling 10–15 lava flows that dip off western flank of Lake Fork volcano (Fig. 6-1). These interfinger to south with volcaniclastic sediments. The agglutinates and lava flows range in composition from hornblende andesite (60% SiO_2) to biotite–hornblende dacite (66% SiO_2); a thin pyroclastic breccia unit is low-silica biotite rhyolite (70% SiO_2). All rocks examined from Lake Fork volcano are exceptionally fresh, in contrast to early intermediate-composition rocks adjacent to calderas. Good view of Alpine Plateau complex directly to west. **2.2**

14.7 **STOP 2. Lake Fork landslide.** Low outcrops west of road just before bridge are shattered andesite lavas that slid off flank of Lake Fork volcano (Fig. 6-1). This massive landslide deposit is exposed for 5–6 km along the Lake Fork; its upper surface was hummocky, with 30–40 m of relief. The brecciated lavas have a variegated red and green color due to presence of hematite and celadonite. Unconsolidated material incorporated into the landslide, such as laharic breccias or volcaniclastic sediments, generally shows similar alteration, but little evidence of deformation due to remobilization. This deposit is similar to the large landslide deposit from Mount St. Helens in 1980 and those recently identified from many other stratovolcanoes. **1.0**

15.7 Thomas Ranch on left, Trout Creek enters on right (east). Near headwaters of Trout Creek, a biotite dacite stock (65% SiO_2) is exposed within core of Lake Fork volcano. From western side of valley (not visible from road), the morphology of Lake Fork volcano is apparent (Fig. 6-1). Outward-dipping lavas define the north, west, and south flanks of a large stratovolcano whose summit may have been near 5000 m in elevation. This massive volcano blocked ash-flow deposition from central San Juans at southern end of Alpine Plateau and diverted them down Cebolla Creek paleovalley (Olson and Hedlund, 1973). **0.6**

16.3 Outcrops of shattered andesite lavas with internal shearing, above road to right. **0.4**

16.7 **STOP 3. The Gate.** Andesite flows with well-developed columnar jointing on both sides of road. These late flows from Lake Fork volcano fill a paleovalley with a trend similar to present Lake Fork drainage. Isolated remnants of these flows are present along valley to Gateview, where they were misidentified as the oldest flows in the lava sequence (Olson et al., 1968). Two distinct flows are visible across the creek. A thin flow of plagioclase andesite (58% SiO_2) with massive columnar joints is present at far left. On right, a thick flow of pyroxene andesite (60% SiO_2) was deposited in a second paleovalley cut into the older flows. Large, curved columnar joints are developed in the pyroxene andesite. Continue north. **0.2**

16.9 Dirt road into campground on left. **3.0**

19.9 Entering Gateview quadrangle (Olson and Hedlund, 1973). Good views to west across valley of north end of Alpine Plateau. The prominent white layer low on hillside is a lens of reworked ash-fall tuff in volcaniclastic sediment (Olson and Hedlund,

FIGURE 6-1—Eroded core of 30–33 Ma Lake Fork volcano taken from slopes of Alpine Plateau. High ridges on left and right sides of photo are outwardly dipping dacite lava flows. Low hills at mid-distance in center of photo are the central dacite stock. Ridge in background is capped by Miocene trachyandesite of Cannibal Plateau. The valley of Lake Fork of Gunnison in foreground is occupied by a large landslide deposit from this volcano (Stop 2). The Gate is just out of view to left.

1973). The sediments interfinger with intermediate-composition breccias and agglutinates. The prominent ledge-forming units are the Blue Mesa and Sapinero Mesa Tuffs. Capping grassy slopes of Round Mountain at end of ridge are Fish Canyon and Carpenter Ridge Tuffs topped by a thin layer of mixed lava from the Alpine Plateau complex. Locally, outflow Sunshine Peak Tuff is preserved beneath 19 Ma basaltic lavas at this end of Alpine Plateau.

Ahead is a ridge above Gateview capped by the Blue Mesa, Dillon Mesa, and Sapinero Mesa Tuffs. White outcrops at the nose of this ridge are cross-bedded surge deposits that make up Dillon Mesa Tuff at this locality. The ash-flow sequence overlies precaldera volcaniclastic conglomerates filling a paleovalley. **0.6**

20.5 Outcrops of late columnar-jointed andesites filling paleovalley on right. These are the same flows as those seen at the Gate. **0.3**

20.8 Road heads east at Gateview to go up-section through Blue Mesa, Dillon Mesa, Sapinero Mesa, and Fish Canyon Tuffs deposited in Cebolla Creek paleovalley. On right side of road are intermediate-composition agglutinate and breccia. **0.5**

21.3 Base of Blue Mesa Tuff is just above road on left. **0.8**

22.1 Ledge of Sapinero Mesa Tuff overlain by Fish Canyon Tuff on left. **1.0**

23.1 Base of Fish Canyon Tuff. **0.7**

23.8 Fish Canyon Tuff on both sides of road for next few miles. Crossing axis of Cebolla Creek paleovalley. **2.5**

26.3 Descending into Cebolla Creek toward town of Powderhorn; note large lithophysal cavities near base of Sapinero Mesa Tuff. At base of hill, we pass into Precambrian metamorphic rocks. **0.7**

27.0 Entering Powderhorn quadrangle (Hedlund and Olson, 1975). Looking to southeast up Cebolla Creek. Reddish barren hills about 2 mi up valley on left side are the Cambrian Iron Hill carbonatite. The lower hills surrounding the carbonatite are related nepheline syenites, ijolites, pyroxenites, and ultra-alkalic rocks. **0.7**

27.7 Side road to Powderhorn. Begin ascending Nine-mile Hill. Outcrops of felsic metamorphic rocks. **1.2**

28.9 Roadcuts for next 1.5 mi are in altered mid-Tertiary lavas from an unknown source. **5.9**

34.8 Miocene trachyandesite overlies Precambrian rocks on Nine-mile Hill, making low outcrops along road for next 0.5 mi. The trachybasalt caps ridges on east and west sides of road for next mile. **1.7**

36.5 Entering Big Mesa quadrangle (Hedlund, 1974). Fish Canyon Tuff rests on Precambrian basement on both sides of road. Remnants of poorly welded Carpenter Ridge Tuff from Bachelor caldera locally form upper slopes of hills. Ridge to west of road is capped by trachybasalt flow. **3.8**

40.3 Fish Canyon Tuff forms lower slopes on both sides of highway. Carpenter Ridge Tuff caps upper third of ridges. Outcrops of Precambrian rocks are exposed on east edge of valley. **1.6**

41.9 Road enters outcrops of 30–35 Ma volcaniclastic sediments, the West Elk Breccia, shed from West Elk volcano north of Gunnison River. Road continues from here around edge of Blue Mesa Reservoir in West Elk Breccia. Dillon Mesa Tuff (poorly exposed) and Blue Mesa Tuff are present at base of Fish Canyon Tuff. **3.4**

45.3 Outcrops of Precambrian metamorphic rocks. Looking west down Gunnison River are good views of mesas capped with distal ends of ash flows from San Juan Mountains sloping in toward reservoir. The Gunnison River occupies a synclinal warp between late Cenozoic uplifts to north and south of here. **0.5**

45.8 Junction with US-550. Turn right to Gunnison.

Optional field guide B: Mineral Point to Silverton

Volcanic structures and ore deposits of the Silverton caldera area.

Distance: 13.2 miles

This trip diverges from Field guide 4 at junction of Animas Forks and Cinnamon Pass roads. The route continues southward along Animas River to Silverton. At this junction, we are in mineralized fill of San Juan caldera, complexly broken by faults of Eureka graben. The Eureka graben is the down-dropped keystone fault zone along crest of elliptical dome formed by joint resurgence of Uncompahgre and San Juan calderas. To south, the arcuate drainage of Animas River follows ring faults of Silverton caldera. This caldera formed at about 27.5 Ma, during eruption of Crystal Lake Tuff. The Durango quadrangle map (Steven et al., 1974) is useful for this section of the trip.

Mileage

0.0 Junction with Cinnamon Pass Road (Stop 11, mile 22.2, of Field guide 4). **Continue ahead** downhill. Below, at junction with California Gulch, is ghost town of Animas Forks. From this point south, and along Cinnamon Pass road for about 1 mi, abundant megabreccia of Picayune Megabreccia Member interfingers with Eureka Member of Sapinero Mesa Tuff. **0.3**

0.3 Junction with switchback into Animas Forks. **Turn right** (west) and descend to townsite of Animas Forks (3402 m) (alternatively, proceed ahead on main road to mile 1.2, where Animas Forks cutoff rejoins main road). The town was established in 1873 and by 1877 was connected with Eureka to south by wagon road. The town suffered from collapse of metal prices in 1893, but experienced a revival in early 1900's, when the Silverton Northern Railroad was extended north to serve the Gold Prince mill here. The mill was dismantled in 1917, and Animas Forks became a ghost town. **0.4**

0.7 Crossing Animas River in Animas Forks. **0.5**

1.2 Road recrosses river and rejoins main road to east. **0.9**

2.1 Cross Animas River back to west; view of Niagara Peak (4208 m) at head of Burns Gulch, type section for Burns Member of Silverton Volcanics. Summit of peak is capped by a thick section of aphanitic andesite of pyroxene andesite member, which overlies a silicic dacite and a mafic dacite flow within Burns Member. The bottom part of gulch is Eureka Member interfingered with megabreccia.

On right (west) side of valley, the lower slopes of Treasure Mountain are composed of Eureka Member and megabreccia, which are truncated by ring-fault zone of Silverton caldera. Subsidence of Silverton caldera during eruption of Crystal Lake Tuff has downdropped postcollapse dacite lavas of Burns Member on west side of ring-fault zone. **0.3**

2.4 **STOP B1. Picayune Gulch** (west side of road). **Picayune Megabreccia Member of Sapinero Mesa Tuff** (Lipman, 1976c: 1403) crops out on both sides of road. Large masses of Picayune breccia accumulated along margins of San Juan caldera during collapse and have been exposed by subsequent erosion along ring-fault zone of Silverton caldera. The megabreccia in this area is intermixed with variable amounts of poorly welded ash-flow matrix of Eureka Member. The dominant breccia clast type is a coarsely porphyritic andesite containing phenocrysts of plagioclase and augite, but blocks of other lavas and volcaniclastic sediments are also present. This is the area where Whitman Cross elegantly described many key features of megabreccias at turn of the century, but was unable to correctly interpret them, as concepts of caldera formation had yet to be put forth (Lipman, 1976c). The rocks in this area are weakly propylitized and contain epidote, chlorite, and pyrite. **2.0**

4.4 View of Eureka townsite; in foreground is Waldheim, home of the Stoiber family during the 1880's; their descendants include Prof. Richard E. Stoiber (Dartmouth). Ahead on right is road to Sunnyside Basin. **0.8**

5.2 **STOP B2. Eureka townsite** (2996 m); road crosses Animas River. The ring-fault zone of Silverton caldera crosses from west to east side of Animas valley near Maggie Gulch and the townsite of Middletown, about 1.5 mi south of Eureka. The ring-fault zone is exposed on high ridges to east. Again, postcollapse lavas at mouths of gulches have been downdropped against intracaldera Eureka Member of Sapinero Mesa Tuff during subsidence of Silverton caldera. For most of the distance from Maggie Gulch to Cunningham Gulch (near Howardsville), the ring-fault zone is occupied by a monzonitic ring intrusion that is similar in texture and composition to Sultan Mountain stock south of Silverton (Stop B3).

High peaks on east side of valley are all postcollapse Silverton Volcanics within San Juan caldera, which are locally capped by small remnants of Crystal Lake Tuff from Silverton caldera (Lipman, 1976a). Downvalley, the steep, stair-stepped cliffs on west side of valley are postcollapse lavas and sediments within Silverton caldera. Stratigraphic relations within this thick volcanic pile, and correlations with Silverton Volcanics in San Juan caldera, remain poorly understood. However, dacite flow units within both sections were important hosts for epithermal Au–Ag veins in the Silverton area.

In headwaters of Rio Grande drainage, about 10–15 km southeast of here, outflow Sapinero Mesa Tuff from Uncompahgre and San Juan calderas is widely distributed and underlain by densely welded Dillon Mesa Tuff. North of Uncompahgre caldera, Dillon Mesa Tuff is composed of nonwelded ash-flow tuff, Plinian pumice beds, and base-surge deposits (Field guide 6), which are interpreted as premonitory products of Uncompahgre caldera (Lipman et al., 1973). The drastic difference in nature of Dillon Mesa Tuff to north and south of Uncompahgre caldera is suggestive of additional complexity. Perhaps the two ash-flow sheets in headwaters of Rio Grande were produced by eruptions from San Juan and Uncompahgre calderas that were separated by enough time to allow two distinct cooling units to develop. This and many other problems related to formation of the Silverton and San Juan calderas remain to be unraveled.

Eureka was established in 1873. The fortunes of Eureka were closely tied with the Sunnyside mine located in Sunnyside Basin 5 km to west (Casadevall and Ohmoto, 1977). In 1899, an aerial tramway was completed to carry ores from the mine to the new Sunnyside mill at mouth of Eureka Gulch to west. The mill was the first flotation mill in the United States and operated successfully until the 1930's, making Sunnyside one of the most important gold producers in the country. The mill closed in the late 1930's and the town was abandoned in the early 1940's when the Silverton Northern Railroad ceased operations.

The Sunnyside mine was reopened in the 1960's through the American Tunnel outside of Silverton and has since produced about 1 million ounces of gold with a Ag/Au ratio of 20/1. It is currently the only active mine in the area. Although the Sunnyside mine is the richest deposit in the Silverton area, the largest gold deposits in the San Juan Mountains were found along the structures that extend from Red Mountain Pass (north of Silverton) to Telluride. The most famous mine in the region is the Camp Bird mine. It was discovered in the late 1890's and by 1915 had produced over a million ounces of gold with a Ag/Au ratio near 1/1. **3.6**

8.8 Howardsville townsite (2932 m) and Dixilyn mill. Howardsville was established in 1873; in 1874 it was the La Plata County seat for a few months before county offices were moved to Silverton. In 1876, San Juan County was established, with Silverton as county seat. Just ahead is turnoff, on left, to Cunningham Gulch, and road across Stony Pass (3837 m) on Continental Divide.

A fascinating sidetrip for those with an extra hour heads up Cunningham Gulch. About 1 mi up the gulch, the thick monzonitic dike intruding the ring fault of Silverton caldera crosses the valley and separates downdropped lavas at mouth of gulch from intracaldera Eureka Member of Sapinero Mesa Tuff filling San Juan caldera. About 2 mi up the gulch is Buffalo Boy tram and turnoff to Stony Pass. Past here watch outcrops of Eureka Member along right (west) for whitish megablocks of Paleozoic limestone surrounded by tuff. Several small mines on left side of Cunningham Gulch, including Pride of the West and Osceola, exploited small replacement bodies that formed where veins cut these blocks.

Continue up Cunningham Gulch to end of wide part of valley and stop before road fords stream at ruins of Highland Mary mill. Spectacular views to west across creek (lighting is best in morning) of intracaldera Eureka Member thinning to left (south) against a thick wedge of megabreccia near the wall of San Juan caldera. Ruins of Highland Mary mine are visible on prominent ridge about 200 m above us and across valley to left. To right of this ridge and about 400 m above valley are Royal Tiger and Dives Basins, respectively, which are beautifully developed hanging cirque valleys. Below the lip of the valleys, most rocks are Eureka Member and megabreccia; above the lip is a thick sequence of postcollapse lava flows (Silverton Volcanics) filling moat area of San Juan caldera. Looking closely at lower section, one can see a prominent color change that angles from creek level (starting about 500 m downvalley to right) up the hillside and intersects the Highland Mary mine ridge at about the elevation of the lip of Royal Tiger Basin. Nearly all rock to right and above this color change is intracaldera tuff that thins against the thick wedge of megabreccia to left and below color change. Downvalley the tuff is greater than 200–300 m thick, with no base exposed, and displays crude subhorizontal bedding planes, whereas above the Highland Mary mine it is less than 50 m thick (Varnes, 1963). This pile of megabreccia is a heterogeneous assemblage of remobilized masses of Oligocene volcanic breccia (San Juan Formation), Paleozoic limestone blocks, and shattered blocks of Precambrian schist that, in places, approximates the original stratigraphic order of these rocks found outside of the caldera margin. Farther to south and above us (directly up Cunningham Gulch) are many small cliffs of in-place Precambrian schist that clearly define the caldera wall. All these rocks are conformably overlain by postcollapse lavas, which dip gently in toward the subsided Silverton caldera block. Return to Howardsville and continue on route. **1.9**

10.7 Above road is tramline for Shenandoah–Dives mine into Arrastre Gulch. This mine produced over 1/2 million ounces of gold (Varnes, 1963) and, next to the Sunnyside, was the second largest producer in the Silverton area. The Mayflower Mill ahead on right was originally built to process ore from the Shenandoah–Dives mine, which closed in the late 1950's, but is now used to concentrate ore from the Sunnyside mine. Downvalley is a view of Sultan Mountain (4075 m), marking south margin of both San Juan and Silverton calderas. **0.8**

11.5 Offices of Sunnyside mine on left; continue straight ahead, passing turnoff on right up Cement Creek to American Tunnel entrance of Sunnyside mine. **1.3**

12.8 Entering Silverton (2836 m). **0.4**

13.2 **STOP B3. Grand Imperial Hotel, downtown Silverton.** The Ute Indians were the residents of the western San Juans, before arrival of Spanish explorers in the 1600's. More recent exploration of the area began in the late 1860's and the town of Silverton was established in 1873.

To reach Stop B3 viewpoint from Grand Imperial Hotel, return north along Main Street to West 15th Street. Turn left (west) for several blocks, to a T-intersection. Turn right (south) at intersection and continue to a loop turnaround, where parking is available.

STOP B3 VIEWPOINT. Sultan Mountain monzonogranite and caldera viewpoint, west side of Silverton. The Sultan Mountain stock was emplaced at 26–27 Ma and is the largest granitic intrusion exposed within a caldera in the San Juan volcanic field. An aeromagnetic anomaly associated with the exposed stock continues northeast along the caldera ring fault at least as far as Howardsville, where a ring dike of similar composition is exposed, and suggests that the stock is a high point on a larger intrusion. Even on the upper slopes of Sultan Mountain, the stock is coarsely crystalline and must have cooled beneath its own volcanic edifice, most likely a large stratovolcano on the rim of Silverton caldera. Similar large intrusive bodies, which appear to be coeval with Sultan Mountain stock, are exposed in a belt that runs west of Silverton, through Ophir, to Mount Wilson (Steven et al., 1974).

The Sultan Mountain stock marks the structural boundary of both San Juan and Silverton calderas. At mouth of Animas River canyon, just south of Silverton, the stock divides volcanic rocks filling the caldera complex on north from Paleozoic and Precambrian sedimentary rocks exposed in canyon to south. To west, the Sultan Mountain stock has intruded much higher stratigraphic levels on Grand Turk and Sultan Mountains. At this level, the pluton has cut through Triassic redbeds unconformably overlain by Oligocene precaldera volcaniclastic rocks of San Juan Formation. Still looking to south, the ring-fracture zone continues past Silverton up south side of Mineral Creek drainage, the prominent valley entering from right (west), to Red Mountain Pass.

The Silverton caldera appears to have collapsed asymmetrically, with maximum subsidence in vicinity of Silverton (Burbank and Luedke, 1969; Steven and Lipman, 1976). Although the hinge zone for this trap-door subsidence is thought to be in Mineral Point area to north (Field guide 4), the recognition of caldera-collapse breccia with a matrix of Crystal Lake Tuff (erupted from the Silverton caldera) adds uncertainty to these structural relations (Lipman, 1976c). The largest measurable displacements (about 300 m) on the ring-fracture zone of Silverton caldera are found about one-third of the way up Kendall Mountain, the large mountain across Animas River from Silverton (Varnes, 1963). There, the trace of the ring-fracture zone is defined by postcollapse lavas within Silverton caldera faulted against Eureka Member of Sapinero Mesa Tuff. The top of Eureka Member is at about treeline in broad cirque that extends between the two summits of this mountain and is at roughly the same elevation as exposures of this unit in Cunningham Gulch. The total thickness of intracaldera tuff within San Juan caldera, measured on south side of Kendall Mountain, is in excess of 600 m with no base exposed (Varnes, 1963). In addition, the thick stack of lavas and intracaldera tuff exposed on face of Kendall Mountain documents an absolute minimum combined subsidence of 1.5 km for San Juan and Silverton calderas. Although Silverton caldera was the first caldera recognized in the San Juan volcanic field, much work remains to understand this structurally complex and economically important caldera complex.

Retrace route to central Silverton.

References

Barton, P. B., Jr., Bethke, P. M., and Roedder, E., 1977, Environment of ore deposition in the Creede mining district, San Juan Mountains, Colorado: III. Progress toward interpretation of the chemistry of the ore-forming fluid for the OH vein: Economic Geology, 72: 1–24.

Bethke, P. M., and Lipman, P. W., 1987, Deep environment of volcanogenic epithermal mineralization: Proposed research drilling at Creede, Colorado: EOS, 68: 177, 187–189.

Bethke, P. M., and Rye, R. O., 1979, Environment of ore deposition in the Creede mining district, San Juan Mountains, Colorado: IV. Source of fluids from oxygen, hydrogen, and carbon isotope studies: Economic Geology, 74: 1832–1851.

Bethke, P. M., Barton, P. B., Jr., Lanphere, M. A., and Steven, T. A., 1976, Environment of ore deposition in the Creede mining district, San Juan Mountains, Colorado: II. Age of mineralization: Economic Geology, 71: 1006–1011.

Bove, D. J., Hon, K., and Rye, R. O., 1987, Evolution of the Red Mountain alunite deposit, Lake City caldera, Colorado (abs.): U.S. Geological Survey, Circular 995: 607.

Burbank, W. S., 1933, Vein systems of Arrastre Basin and regional geologic structure in the Silverton and Telluride quadrangles, Colorado: Colorado Scientific Society, Proceedings, 13: 135–214.

Burbank, W. S., 1940, Structural control of ore deposition in the Red Mountain, Sneffels, and Telluride districts of the San Juan Mountains, Colorado: Colorado Scientific Society, Proceedings, 14: 141–261.

Burbank, W. S., and Luedke, R. G., 1969, Geology and ore deposits of the Eureka and adjoining districts, San Juan Mountains, Colorado: U.S. Geological Survey, Professional Paper 535: 73 pp.

Calvert, R. H., Gries, R. R., and Terbest, H., Jr., 1987, San Juan volcanics and oil exploration (abs.): Geological Society of America, Abstracts with Programs, 19: 264.

Casadevall, T., and Ohmoto, H., 1977, Sunnyside mine, Eureka mining district, San Juan County, Colorado: Geochemistry of gold and base metal ore deposition in a volcanic environment: Economic Geology, 72: 1283–1320.

Chapin, C. H., and Lindley, J. I., 1986, Potassium metasomatism of igneous and sedimentary rocks in detachment terranes and other sedimentary basins: Economic implications: Arizona Geological Society Digest, 16: 118–126.

Christiansen, E. H., Sheridan, M. F., and Burt, D. M., 1986, The geology and geochemistry of Cenozoic topaz rhyolites from the western United States: Geological Society of America, Special Paper 205: 82 pp.

Cordell, L. C., Keller, G. R., and Hildebrand, T. G., 1982, Bouguer gravity map of the Rio Grande rift: U.S. Geological Survey, Geophysical Investigations Map GP-949.

Cross, W., and Larsen, E. S., 1935, A brief review of the geology of the San Juan region of southwestern Colorado: U.S. Geological Survey, Bulletin 843: 138 pp.

Cross, W., Howe, E., and Ransome, F. L., 1905, Description of the Silverton quadrangle (Colorado): U.S. Geological Survey, Atlas, Folio 120.

Emmons, W. H., and Larsen, E. S., 1923, Geology and ore deposits of the Creede district, Colorado: U.S. Geological Survey, Bulletin 718: 198 pp.

Enders, M. S., and Coolbaugh, M. F., 1987, A geologic model of gold mineralization for exploration, development, and production at Summitville, Colorado (abs.): Geological Society of America, Abstracts with Programs, 19: 274.

Gebhart, J. W., 1987, Deformation around the Creede caldera: A consequence of isostatic adjustment following caldera formation: Journal of Geophysical Research, 92: 10601–10616.

Gilzean, M. N., 1985, The nature of the deep hydrothermal system, Red Mountain district, Silverton, Colorado: Unpublished M.S. thesis, University of California, Berkeley, 105 pp.

Grauch, V. J. S., 1987, Interpretive aeromagnetic map using the horizontal gradient: Lake City caldera area, San Juan Mountains, Colorado: U.S. Geological Survey, Geophysical Investigations Map GP-974, scale 1:48,000.

Grauch, V. J. S., and Campbell, D. L., 1985, Gravity survey data and a Bouguer gravity anomaly map of the Lake City caldera area, Hinsdale County, Colorado: U.S. Geological Survey, Open-File Report 85-208: 11 pp.

Hedlund, D. C., 1974, Geologic map of the Big Mesa quadrangle, Gunnison County, Colorado: U.S. Geological Survey, Geologic Quadrangle Map GQ-1153.

Hedlund, D. C., and Olson, J. C., 1975, Geologic map of the Powderhorn quadrangle, Gunnison County, Colorado: U.S. Geological Survey, Geologic Quadrangle Map GQ-1178.

Hon, K., 1987a, Geologic, alteration, and vein maps of the Redcloud Peak (Lake City caldera) and Handies Peak Wilderness Study Areas, Hinsdale County, Colorado: U.S. Geological Survey, Miscellaneous Field Studies Map MF-1949.

Hon, K., 1987b, Geologic and petrologic evolution of the Lake City caldera, San Juan Mountains, Colorado: Unpublished Ph.D. thesis, University of Colorado, Boulder, 244 pp.

Hon, K., and Bartel, A., 1987, Evolution of the Alpine Plateau trachyandesite–trachyte suite by repeated episodes of magma mixing, western San Juan Mountains, Colorado (abs.): Hawaii Symposium on How Volcanoes Work, Hilo, Hawaii, January 1987, p. 113.

Hon, K., and Mehnert, H. H., 1983, Compilation of revised ages of volcanic units in the San Juan Mountains, Colorado: Recalculated K–Ar age determinations using IUGS constants: U.S. Geological Survey, Open-File Report 83-668, 14 pp.

Hon, K., Bove, D. J., and Grauch, V. J. S., 1986, Geology and mineral deposits of the region surrounding the American Flats Wilderness Study Area, western San Juan Mountains, Colorado: U.S. Geological Survey, Open-File Report 86-431, 37 pp.

Hon, K., Ludwig, K. R., Simmons, K. R., Slack, J. F., and Grauch, R. I., 1985, U–Pb isochron age and Pb-isotope systematics of the Golden Fleece vein—Implications for the relationship of mineralization to the Lake City caldera, western San Juan Mountains, Colorado: Economic Geology, 80: 410–418.

Irving, J. D., and Bancroft, H., 1911, Geology and ore deposits near Lake City, Colorado: U.S. Geological Survey, Bulletin 478: 128 pp.

Kelley, V. C., 1946, Geology, ore deposits, and mines of the Mineral Point, Poughkeepsie, and Upper Uncompahgre districts, Ouray, San Juan, and Hinsdale Counties, Colorado: Colorado Scientific Society, Proceedings, 14: 289–466.

Kunk, M. J., Sutter, J. F., and Naeser, C. W., 1985, High-precision $^{40}Ar/^{39}Ar$ ages of sanidine, biotite, hornblende, and plagioclase from the Fish Canyon Tuff, San Juan volcanic field, south-central Colorado (abs.): Geological Society of America, Abstracts with Programs, 17: 636.

Lanphere, M. A., 1988, High-resolution $^{40}Ar/^{39}Ar$ chronology of Oligocene volcanic rocks, San Juan Mountains, Colorado: Geochimica et Cosmochimica Acta, in press.

Larsen, E. S., and Cross, W., 1956, Geology and petrology of the San Juan region, southwestern Colorado: U.S. Geological Survey, Professional Paper 258: 303 pp.

Larson, P. B., and Taylor, H. P., Jr., 1986, An oxygen isotope study of hydrothermal alteration in the Lake City caldera, San Juan Mountains, Colorado: Journal of Volcanology and Geothermal Research, 30: 47–82.

Le Bas, M. J., Le Maitre, R. W., Streckeisen, A., and Zanetin, B., 1986, A chemical classification of volcanic rocks based on the total alkali-silica diagram: Journal of Petrology, 27: 745–750.

Lipman, P. W., 1974, Geologic map of the Platoro caldera area, southeastern San Juan Mountains, Colorado: U.S. Geological Survey, Miscellaneous Investigations Map I-828.

Lipman, P. W., 1975a, Evolution of the Platoro caldera complex and related volcanic rocks, southeastern San Juan Mountains, Colorado: U.S. Geological Survey, Professional Paper 852: 128 pp.

Lipman, P. W., 1975b, Geologic map of the Lower Conejos River Canyon area, southeastern San Juan Mountains, Colorado: U.S. Geological Survey, Miscellaneous Investigations Map I-901.

Lipman, P. W., 1976a, Geologic map of the Lake City caldera area, western San Juan Mountains, southwestern Colorado: U.S. Geological Survey, Miscellaneous Investigations Map I-962.

Lipman, P. W., 1976b, Geologic map of the Del Norte area, eastern San Juan Mountains, Colorado: U.S. Geological Survey, Miscellaneous Investigations Map I-952.

Lipman, P. W., 1976c, Caldera-collapse breccias in the western San Juan Mountains, Colorado: Geological Society of America, Bulletin, 87: 1397–1410.

Lipman, P. W., 1984, The roots of ash-flow calderas in western North America: Windows into the tops of granitic batholiths: Journal of Geophysical Research, 89: 8801–8841.

Lipman, P. W., and Mehnert, H. H., 1975, Late Cenozoic basaltic volcanism and development of the Rio Grande depression in the southern Rocky Mountains; *in* Curtis, B. F. (ed.), Cenozoic history of the southern Rocky Mountains: Geological Society of America, Memoir 144: 119–154.

Lipman, P. W., and Sawyer, D. A., 1988, Preliminary geology of the San Luis Peak quadrangle and adjacent areas, San Juan volcanic field, southwestern Colorado: U.S. Geological Survey, Open-File Report 88-359: 35 pp.

Lipman, P. W., and Steven, T. A., 1976, Geologic map of the South Fork area, San Juan Mountains, Colorado: U.S. Geological Survey, Miscellaneous Investigations Map I-966.

Lipman, P. W., Steven, T. A., and Mehnert, H. H., 1970, Volcanic history of the San Juan Moutnains, Colorado, as indicated by potassium–argon dating: Geological Society of America, Bulletin, 81: 2329–2352.

Lipman, P. W., Doe, B. R., Hedge, C. E., and Steven, T. A., 1978, Petrologic evolution of the San Juan volcanic field, southwestern Colorado: Pb and Sr isotopic evidence: Geological Society of America, Bulletin, 89: 59–82.

Lipman, P. W., Steven, T. A., Luedke, R. G., and Burbank, W. S., 1973, Revised volcanic history of the San Juan, Uncompahgre, Silverton, and Lake City calderas in the western San Juan Mountains, Colorado: U.S. Geological Survey, Journal of Research, 1: 627–642.

Lipman, P. W., Fisher, F. S., Mehnert, H. H., Naeser, C. W., Luedke, R. G., and Steven, T. A., 1976, Multiple ages of mid-Tertiary mineralization and alteration in western San Juan Mountains, Colorado: Economic Geology, 71: 571–588.

Luedke, R. G., and Burbank, W. S., 1963, Tertiary volcanic stratigraphy in the western San Juan Mountains, Colorado: U.S. Geological Survey, Professional Paper 475-C: 39–44.

Luedke, R. G., and Burbank, W. S., 1968, Volcanism and cauldron development in the western San Juan Mountains, Colorado: Colorado School of Mines Quarterly, 63: 175–208.

Maher, B. J., 1983, Geology, geochemistry, and genesis of the Engineer Pass intrusive complex, San Juan Mountains, Colorado: Unpublished M.S. thesis, Colorado State University, Fort Collins, 226 pp.

Mayor, J. N., and Fisher, F. S., 1972, Middle Tertiary replacement ore bodies and associated veins in the northwest San Juan Mountains, Colorado: Economic Geology, 67: 214–230.

Matty, D. J., Stormer, J. S., Jr., and Whitney, J. A., 1985, Magmatic conditions of the Snowshoe Mt. Tuff, San Juan volcanic field, Colorado (abs.): EOS, 66: 396.

McSaveney, J. H., 1978, Sherman glacier rock avalanche, Alaska, USA; *in* Voight, B. (ed.), Rockslides and Avalanches—I. Natural Phenomena: Elsevier, New York, pp. 197–258.

Mehnert, H. H., Lipman, P. W., and Steven, T. A., 1973, Age of mineralization at Summitville, Colorado, as indicated by K–Ar dating of alunite: Economic Geology, 68: 399–401.

Olson, J. C., and Hedlund, D. C., 1973, Geologic map of the Gateview quadrangle, Gunnison County, Colorado: U.S. Geological Survey, Geologic Quadrangle Map GQ-1071.

Olson, J. C., Hedlund, D. C., and Hanson, W. R., 1968, Tertiary volcanic stratigraphy in the Powderhorn–Black Canyon region, Gunnison and Montrose Counties, Colorado: U.S. Geological Survey, Bulletin 1251-C: 29 pp.

Patton, H. B., 1917, Geology and ore deposits of the Platoro–Summitville mining district, Colorado: Colorado Geological Survey, Bulletin 13: 122 pp.

Perkins, R. M., and Nieman, G. W., 1982, Epithermal gold mineralization in the South Mountain volcanic dome, Summitville, Colorado; *in* The Genesis of Rocky Mountain Ore Deposits: Changes with Time and Tectonics: Society of Exploration Geologists, Denver Region, Symposium Proceedings, pp. 165–172.

Pierce, H., and Hoover, D. B., 1985, Electrical studies conducted on the Lake City caldera, Colorado: U.S. Geological Survey, Open-File Report 85-147, 43 pp.

Plouff, D., and Pakiser, L. C., 1972, Gravity study of the San Juan Mountains, Colorado: U.S. Geological Survey, Professional Paper 800-B: 183-190.

Ratté, J. C., and Steven, T. A., 1967, Ash-flows and related volcanic rocks associated with the Creede caldera, San Juan Mountains, Colorado: U.S. Geological Survey, Professional Paper 524-H: 58 pp.

Reynolds, R. L., Hudson, M. R., and Hon, K., 1986, Paleomagnetic evidence regarding the timing of collapse and resurgence of the Lake City caldera, San Juan Mountains, Colorado: Journal of Geophysical Research, 91: 9599–9613.

Sanford, R. F., and Ludwig, K. R., 1985, Lead isotopic evidence on the origin of hydrothermal veins, Lake City, Colorado (abs.): Geological Society of America, Abstracts with Programs, 17: 706.

Sanford, R. F., Korzeb, S. L., Seeley, J. L., and Zamudio, J. A., 1987, Geochemical data for mineralized rocks in the Lake City caldera area, San Juan volcanic field, southwest Colorado: U.S. Geological Survey, Open-File Report 87-54: 213 pp.

Self, S., and Wright, J. V., 1983, Large wave forms from the Fish Canyon Tuff, Colorado: Geology, 11: 443–446.

Slack, J. F., 1980, Multistage vein ores of the Lake City district, western San Juan Mountains, Colorado: Economic Geology, 75: 963–991.

Steven, T. A., 1967, Geologic map of the Bristol Head quadrangle, Mineral and Hinsdale Counties, Colorado: U.S. Geological Survey, Geologic Quadrangle Map GQ-631.

Steven, T. A., 1975, Middle Tertiary volcanic field in the southern Rocky Mountains: Geological Society of America, Memoir 144: 75–94.

Steven, T. A., and Eaton, G. P., 1975, Environment of ore deposition in the Creede mining district, San Juan Mountains, Colorado: I. Geologic, hydrologic, and geophysical setting: Economic Geology, 70: 1023–1037.

Steven, T. A., and Hail, W. J., Jr., in press, Geologic map of the Montrose 30×60 minute quadrangle, Colorado: U.S. Geological Survey, Miscellaneous Geologic Investigations Map.

Steven, T. A., and Lipman, P. W., 1973, Geologic map of the Spar City quadrangle, Mineral County, Colorado: U.S. Geological Survey, Geologic Quadrangle Map GQ-1052.

Steven, T. A., and Lipman, P. W., 1976, Calderas of the San Juan volcanic field, southwestern Colorado: U.S. Geological Survey, Professional Paper 958: 35 pp.

Steven, T. A., and Ratté, J. C., 1960, Geology aand ore deposits of the Summitville district, San Juan Mountains, Colorado: U.S. Geological Survey, Professional Paper 343: 70 pp.

Steven, T. A., and Ratté, J. C., 1965, Geology and structural control of ore deposition in the Creede district, San Juan Mountains, Colorado: U.S. Geological Survey, Professional Paper 487: 90 pp.

Steven, T. A., and Ratté, J. C., 1973, Geologic map of the Creede quadrangle, Mineral and Saguache Counties, Colorado: U.S. Geological Survey, Quadrangle Map GQ-1053.

Steven, T. A., Lipman, P. W., Fisher, F. S., Bieniewski, C. L., and Meeves, H. C., 1977, Mineral resources of study areas contiguous to the Uncompahgre Primitive Area, San Juan Mountains, Southwestern Colorado: U.S. Geological Survey, Bulletin 1391-E: 126 pp.

Steven, T. A., Lipman, P. W., Hail, W. J., Jr., Barker, F., and Luedke, R. G., 1974, Geologic map of the Durango quadrangle, southwestern Colorado: U.S. Geological Survey, Miscellaneous Geological Investigations Map I-764.

Stoffregen, R. E., 1987, Geochemistry of acid-sulfate mineralization at Summitville, Colorado: Geological Society of America, Abstracts with Programs, 19: 337.

Thompson, R. A., and Dungan, M. A., 1985, The petrology and geochemistry of the Handkerchief Mesa mixed magma complex, San Juan Mountains, Colorado: Journal of Volcanology and Geothermal Research, 26: 251–274.

Tweto, O., and Sims, P. K., 1963, Precambrian ancestry of the Colorado mineral belt: Geological Society of America, Bulletin, 74: 991–1014.

Tweto, O., Steven, T. A., Hail, W. J., Jr., and Moench, R. H., 1976, Preliminary geologic map of the Montrose $1 \times 2°$ quadrangle, southwestern Colorado: U.S. Geological Survey, Miscellaneous Field Studies Map MF-761.

Varnes, D. J., 1963, Geology and ore deposits of the South Silverton mining area, San Juan County, Colorado: U.S. Geological Survey, Professional Paper 378-A: 56 pp.

Webber, K. L., 1988, The Mammoth Mountain and Wason Park Tuffs: Magmatic evolution in the central San Juan volcanic field, southwestern Colorado: Unpublished Ph.D. thesis, Rice University, Houston, 244 pp.

Wetlaufer, P. H., Bethke, P. M., Barton, P. B., Jr., and Rye, R. O., 1977, The Creede Ag–Pb–Zn–Cu–Au district, central San Juan Mountains, Colorado: A fossil geothermal system: Nevada Bureau of Mines, Report 33: 159–164.

Whitney, J. A., and Stormer, J. C., Jr., 1986, Mineralogy, petrology, and magmatic conditions from the Fish Canyon Tuff, central San Juan volcanic field, Colorado: Journal of Petrology, 26: 726–762.

Whitney, J. A., and Stormer, J. C., Jr., 1988, The Carpenter Ridge Tuff: The development of chemical and thermal gradients through magma mixing in a periodically replenished magma chamber: American Journal of Science, 228A: 16–44.

EXCURSION 17B: Volcanic and hydrothermal evolution of Valles caldera and Jemez volcanic field

Fraser Goff[1], Jamie N. Gardner[1], W. Scott Baldridge[1], Jeffrey B. Hulen[2], Dennis L. Nielson[2], David Vaniman[1], Grant Heiken[1], Michael A. Dungan[3], and David Broxton[1]

[1]*Earth and Space Sciences Division, Los Alamos National Laboratory, Los Alamos, New Mexico 87545;*
[2]*University of Utah Research Institute, 391 Chipeta Way, Suite C, Salt Lake City, Utah 84108;*
[3]*Department of Geological Sciences, Southern Methodist University, Dallas, Texas 75275*

Introduction

Valles caldera has become world famous as an example of a resurgent caldera and as the location of a high-temperature geothermal system of volcanic origin (Smith and Bailey, 1968; Dondanville, 1978). Although the caldera and its modern hydrothermal system result from events that have happened during the last 1.12 Ma, the Jemez volcanic field has experienced continuous volcanism for more than 13 Ma and is known to have had at least three major periods of distinct hydrothermal activity (Gardner et al., 1986; WoldeGabriel and Goff, 1989). The field-trip guide presented here will emphasize the results of volcanic, tectonic, and geochemical research pertaining not only to the Valles caldera but to the entire history of the Jemez volcanic field. The last one and one-half days of the trip will also emphasize drill-hole data that have recently given researchers a wealth of information on extra- and intracaldera structure, stratigraphy, hydrothermal alteration, and fluid chemistry in the most explored Quaternary caldera complex in the United States. The accompanying paper is not intended to review exhaustively all aspects of research on the Jemez volcanic field; rather, it stresses significant discoveries and interpretations that have occurred since about 1980.

Geologic overview and summary of earlier research

The Jemez volcanic field (Figs. 1, 2) contains a diverse suite of basaltic through rhyolitic rocks that were erupted from >13 to 0.13 Ma, although the field is best known for the Valles caldera (1.12 Ma) and the Bandelier Tuff (Smith and Bailey, 1966, 1968; Gardner et al., 1986; Self et al., 1986). The volcanic field overlies the western edge of the Rio Grande rift (RGR) at the intersection of the rift and the Jemez volcanic lineament (JVL). The lineament is defined by a chain of Miocene to Quaternary volcanic centers stretching from southeast Colorado across New Mexico to central Arizona (Mayo, 1958; Laughlin et al., 1976; Aldrich, 1986). The largest volume and diversity of volcanic rocks

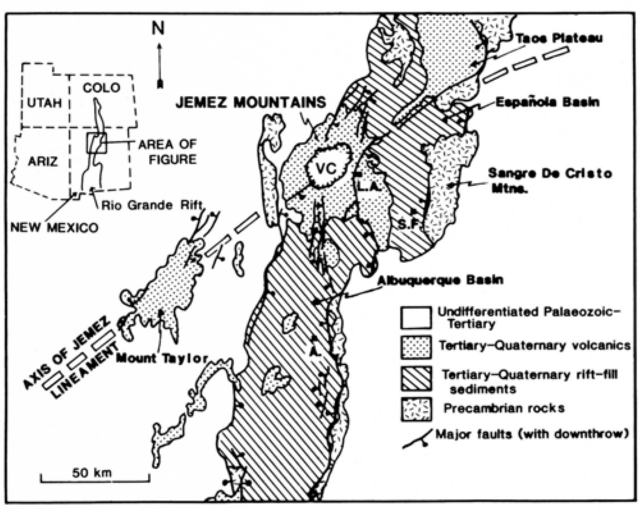

FIGURE 1—Regional map showing generalized relations of the Jemez volcanic field (Jemez Mountains) to basins of the north-central Rio Grande rift. VC is the Valles caldera; major fault zones of the region are shown. LA, SF, and A are the cities of Los Alamos, Santa Fe, and Albuquerque, respectively (from Self et al., 1987).

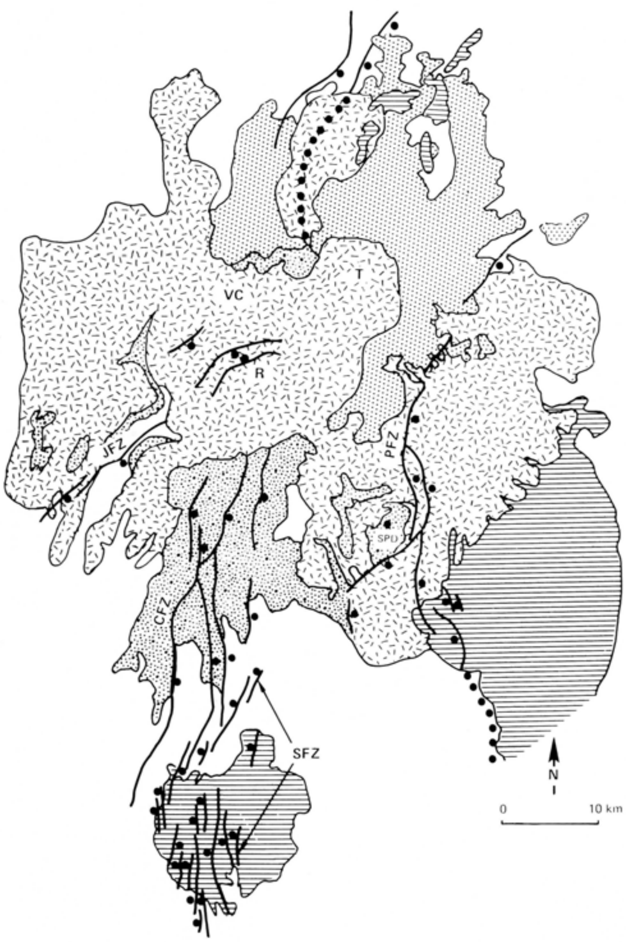

FIGURE 2—Generalized geologic map of the Jemez volcanic field showing distribution of major stratigraphic groups. Irregular stipple = Keres Group formations; coarse, regular stipple = Polvadera Group formations; random dash = Tewa Group formations; horizontally ruled pattern = young basalt fields. Major fault zones are Jemez fault zone (JFZ), Santa Ana Mesa fault zone (SFZ), Cañada de Cochiti fault zone (CFZ), and Pajarito fault zone (PFZ). VC = Valles caldera, R = resurgent dome of Valles caldera, T = Toledo embayment, SPD = St. Peter's Dome (from Gardner and Goff, 1984).

along the JVL have been erupted in the Jemez Mountains. Tertiary basin-fill rocks of the Española and Santo Domingo Basins of the RGR underlie volcanic rocks on the eastern side of the volcanic field, whereas Paleozoic to Mesozoic sedimentary rocks and Precambrian crystalline rocks of the Colorado Plateau underlie volcanic rocks on the west.

Early reconnaissance studies of the geology and petrology of the Jemez Mountains were conducted by J. P. Iddings and J. W. Powell (Iddings, 1890; Powell, 1961). Gold claims were first staked in the Cochiti Mining District in the southeast Jemez Mountains in 1893 and ore was mined from 1897 to 1903 and from 1914 to 1916 (L. C. Graton *in* Lindgren et al., 1910). Sulfur was mined from the Sulphur Springs area, inside the caldera, from 1902 to 1904 (Mansfield, 1918). There have been various topical studies of the hot springs of the Jemez Mountains (Fig. 3) during the last 100 years, beginning with O. Loew in 1875 (see Summers, 1976).

Comprehensive investigations of the geology, volcanism, and hydrology of the Jemez Mountains began in the 1920's and were intensified during the 1940's by members of the U.S. Geological Survey. These studies continued through the 1960's and, in limited fashion, to the present day (Ross and Smith, 1961; Smith et al., 1961; Griggs, 1964; Doell et al., 1968; Bailey et al., 1969; Smith et al., 1970; Smith, 1979). Valles caldera contains the type locality of the Jaramillo normal-polarity magnetic event (Doell and Dalrymple, 1966).

Although a limited number of geophysical studies were performed in the region before 1980, many were conducted by oil companies in the RGR or by UNOCAL (formerly Union Oil Company of California) in the caldera and were,

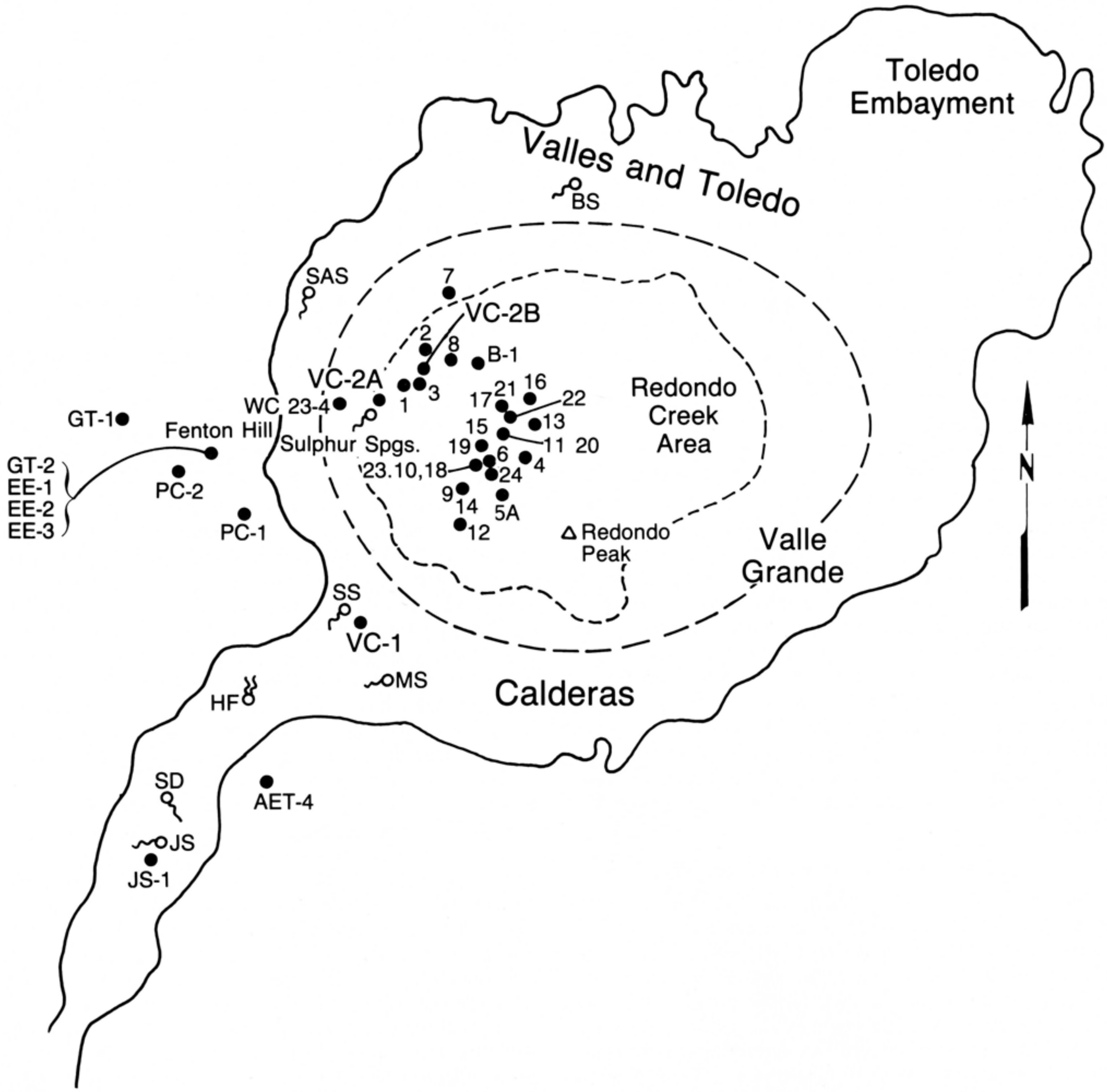

FIGURE 3—Map of Valles caldera region showing locations of hot-spring areas and geothermal wells. Hot springs: BS = Bathhouse Spring; SAS = San Antonio Hot Spring; SS = Spence Hot Spring; MS = McCauley Spring; SD = Soda Dam; JS = Jemez Spring; HF = Hummingbird Fumarole. All wells with number only have "Baca" prefix. B-1 = Westates-Bond #1.

therefore, proprietary. Nonetheless, it was known in the 1970's that large gravity anomalies were associated with the caldera and the RGR (Cordell, 1978), as were substantial heat-flow anomalies (Reiter et al., 1975, 1976).

Geothermal development and research

The first "geothermal" well was drilled in Valles caldera in 1960 as an oil test on the west flank of the resurgent dome. Instead of oil, the Westates-Bond #1 well struck superheated water (~200°C) at shallow depths (Dondanville, 1971). Three more wells were drilled during the 1960's in the same general area, achieving maximum temperatures of 220°C at a depth of 430 m (Fig. 3). UNOCAL drilled their first well in the central resurgent dome (Baca 4) in 1970 (278°C at a depth of 1435 m) and 20 more wells were drilled before the geothermal project was terminated in 1984 because of insufficient reservoir permeability (Kerr, 1982; Goldstein and Tsang, 1984).

As the prospect of geothermal development brightened during the 1970's, there were more investigations of the hot springs and caldera hydrology (Trainer, 1975, 1978). Attempts were made (with mixed success) to drill wells to extract fluids for space heating at Jemez Springs, southwest of the caldera, and on the Pajarito Plateau east of the caldera (Goff and Grigsby, 1982). Exploration efforts by GEO Operator Corporation (formerly Geothermal Resources International, Inc.) and SUNEDCO (Sun Energy Development Corporation), west and south of the caldera, respectively, resulted in two more deep wells (Shevenell et al., 1988). The body of scientific and engineering data gained from these various drilling programs is immense. Because of partial U.S. Department of Energy (DOE) funding for the UNOCAL effort (Spencer and Tsang, 1984; Mills et al., 1987), virtually all data from all wells mentioned above are in the public domain.

Fenton Hill, located on the western margin of Valles caldera, is the site of the first Hot Dry Rock (HDR) geothermal research experiment in the world (Heiken et al., 1981; Laughlin, 1981; Smith, 1983). Although intended to develop the technology for commercially extracting heat from hot, impermeable rock, the HDR project provides an extensive geologic data base from relatively unfaulted Precambrian and Paleozoic rocks just west of the caldera depression. Eleven heat-flow holes and seven intermediate to deep wells have been drilled for this project. Maximum temperatures are 325°C at a depth of 4.5 km in complex Precambrian basement lithologies. The commercial applications of HDR technology are still under investigation at Fenton Hill, but this research has spawned other HDR efforts of varying scope in Great Britain, France, Germany, and Japan.

Significant geologic research since 1980

Starting in about 1980, results from diversified research in the Valles caldera region began to appear in the geological literature. In addition to graduate-thesis projects (e.g., Stein, 1983; Gardner, 1985), much of the research was stimulated by geologic investigations of the HDR program (Kolstad and McGetchin, 1978; Laughlin et al., 1983; Heiken and Goff, 1983) or from data and samples released from the "Baca" project of UNOCAL (Faust et al., 1984; Nielson and Hulen, 1984). The largest single source of funding for new Valles research has come through the Continental Scientific Drilling Program (CSDP) (Goff and Gardner, 1988). Because the Valles caldera has been discussed for nearly 20 years as a high-priority site for the investigation of fundamental processes in magmatism, hydrothermal systems, and ore depositional mechanisms, the DOE/Office of Basic Energy Sciences has sponsored scientific investigations, task groups, and workshops to identify critical data gaps, drilling objectives, and sites (e.g., Luth and Hardee, 1980; Taschek, 1981; Heiken, 1985). The extensive subsurface data base at Valles caldera (nearly 40 deep wells) makes it the best explored Quaternary caldera complex in the USA and allows for very precise planning and realistic expectations to meet scientific goals. For example, the known composite stratigraphic section in the Valles region is nearly 7 km (wells Baca 12 and EE-2), consisting of 1950 m of Quaternary caldera fill, over 300 m of Tertiary precaldera volcanic and sedimentary rocks, over 800 m of Paleozoic sedimentary rocks, and 3700 m of Precambrian basement (Laughlin et al., 1983; Nielson and Hulen, 1984). The support of the CSDP has resulted in continuous coring of three scientific holes in the caldera (VC-1, VC-2A, and VC-2B) and the creation of a scientific constituency and long-range plan for future scientific drilling (Goff et al., 1986, 1987; Goff and Nielson, 1986).

All this new surface and subsurface work resulted in important discoveries and refinements of previous knowledge in the Valles caldera region. We categorize these discoveries and refinements in the following sections, and our field trip touches on many of the recent research topics.

Stratigraphy, petrology, and tectonic associations in Jemez volcanic field

Stratigraphy—The formalized stratigraphy for volcanic and volcaniclastic rocks in the Jemez volcanic field was developed by Griggs (1964), Bailey et al. (1969), and Smith et al. (1970). These authors divided the volcanic field into three stratigraphic groups, from oldest to youngest the Keres, Polvadera, and Tewa. The Keres Group is dominated by two-pyroxene andesite, the Polvadera Group is dominated by dacite, and the Tewa Group is dominated by high-silica rhyolite. Bailey, Smith, and coworkers believed that each group represented discrete time intervals and petrologic entities. After considerably more detailed geologic mapping, acquisition of radiometric dates, and analysis of the various rock types by several groups of researchers, it is now realized that temporal and petrologic overlap occurs among all groups and many formations (Gardner et al., 1986; Loeffler et al., 1988), although the three stratigraphic groups still retain much of their original petrologic significance.

Fig. 4 shows the generalized stratigraphic relations of major units in the Jemez volcanic field as defined by Gardner et al. (1986), compared with the age relations of the three groups as originally defined by Bailey et al. (1969). Many significant changes appear in this figure, which are summarized as follows (see Gardner et al., 1986):

1. The inception of volcanism in the Jemez Mountains region began at least 16.5 Ma ago (alkalic basalts in the Santa Fe Group), but the oldest rocks in formal units of the volcanic field were erupted between 13 and 14 Ma.

2. Hydrothermally altered volcanic and hypabyssal rocks of the Cochiti mining district (Bland group of Stein, 1983) are not Eocene or Oligocene as previously thought. They represent the altered and eroded interior of Keres Group andesitic volcanoes that were intruded by Bearhead Rhyolite and later cut by epithermal quartz veins. Ages on all units

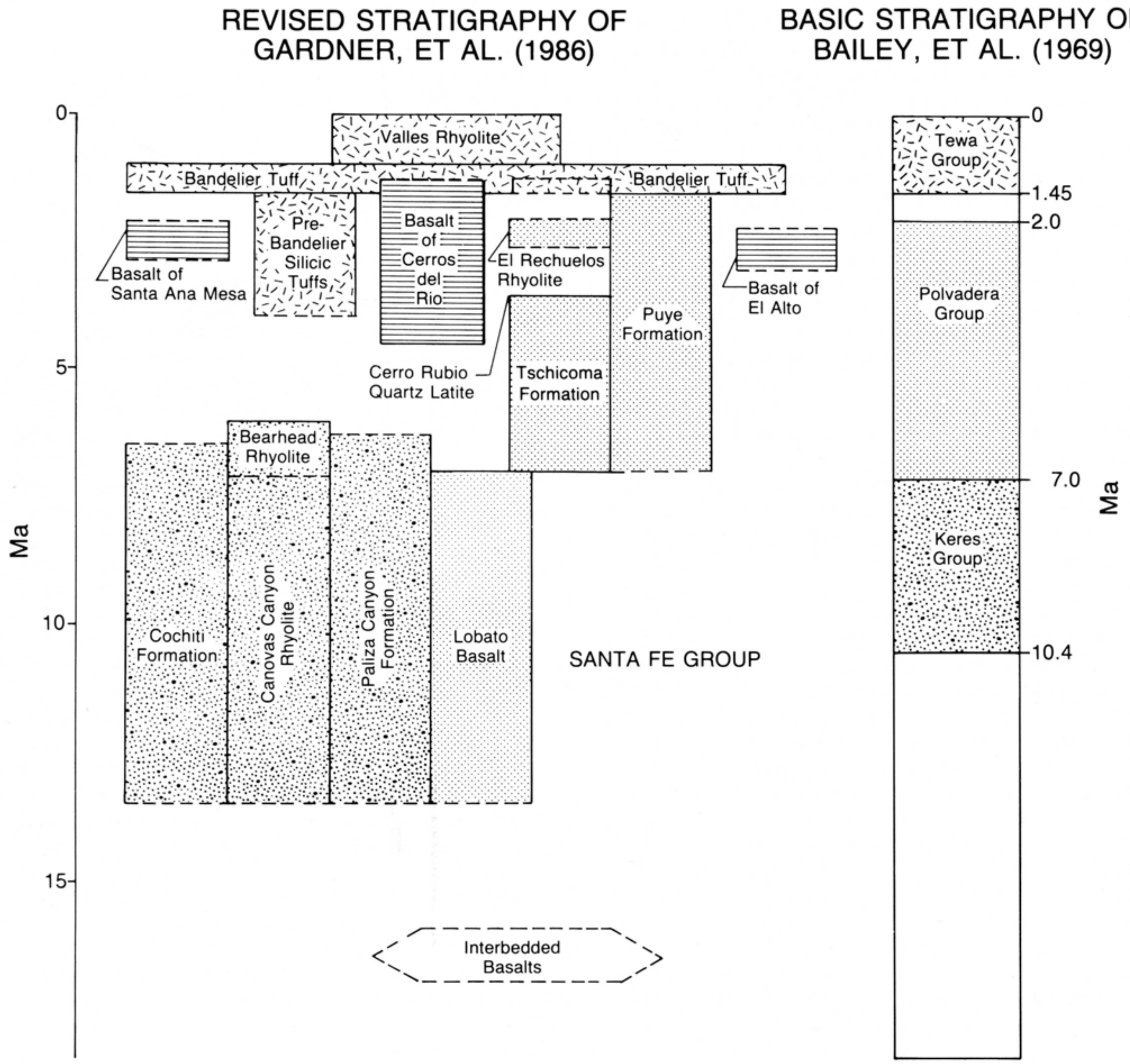

FIGURE 4—Basic stratigraphy of the Jemez volcanic field (Bailey et al., 1969) compared to revised stratigraphy of Gardner et al. (1986); patterns are the same as Fig. 2. Dashed lines indicate uncertainty and more revisions may be forthcoming (see Fig. 27, Day 2). The figure is also a schematic south-to-north (left-to-right) section through the volcanic field.

and events within this altered sequence range from 11.2 to 5.6 Ma (Stein, 1983; Wronkiewicz et al., 1984; Gardner et al., 1986; WoldeGabriel and Goff, 1989).

3. The Basalt of Chamisa Mesa (10.4 Ma) is indistinguishable from basalts of the Paliza Canyon Formation chemically, temporally, or petrographically.

4. The Cochiti Formation is included within the Keres Group because of intimate spatial, temporal, genetic, and tectonic relations to formations in the group.

5. The Lobato Basalt occupies a much wider time range (14–7 Ma) than previously thought (~8–7 Ma). Lobato basalts are petrographically and chemically similar to basalts of the Paliza Canyon Formation and the age range of the two units is practically identical, indicating that the distinction between the units is merely geographical.

6. Dacitic rocks of the Tschicoma Formation (7–3 Ma) are chemically and petrographically similar to some mapped dacites in the Paliza Canyon Formation. On the other hand, the Tschicoma Formation, originally defined by Griggs (1964) to consist only of dacite, contains large unmapped areas of two-pyroxene andesite grossly similar to andesites in the Paliza Canyon Formation. Overlap in chemistry, petrography, and age of these formations is significant and the age break between them shown in Fig. 4 acknowledges the geographical distinction built into the formal stratigraphy of Bailey et al. (1969).

7. The El Rechuelos Rhyolite, on the northern side of the volcanic field, is restricted to two domes west of Polvadera Peak dated at 2 Ma. Other rhyolites in the northern Jemez Mountains are older (5.8–7.5 Ma) (Loeffler et al., 1988). The older rhyolites resemble Bearhead Rhyolite on the southern side of the volcanic field.

8. The Tewa Group contains recently characterized ignimbrites that predate the Bandelier Tuff and temporally overlap the waning stages of Polvadera Group volcanic activity (Self et al., 1986).

9. The Cerro Rubio Quartz Latite, located in the Toledo embayment, chemically and temporally resembles Tschicoma Formation dacites and is now included in the Tschicoma Formation (Heiken et al., 1986; Gardner et al., 1986).

10. Post-Toledo caldera moat volcanism is more complicated than previously thought (e.g., Smith, 1979). Several rhyolites formerly thought to be post-Valles in age are now realized to be post-Toledo in age (Heiken et al., 1986). Chemical and petrologic variation within the Cerro Toledo Rhyolite define subgroups of rhyolite types and show restoration of compositional zonation of the Bandelier magma chamber between two caldera-forming eruptions (Stix et al., 1988).

11. Post-Valles caldera moat volcanism is far more complicated than previously thought (e.g., Smith, 1979). Several distinct magma batches gave rise to the Valles Rhyolite (Gardner et al., 1986; Spell, 1987; Self et al., 1988).

Volcanic petrology—Chemical data for selected rocks from all major stratigraphic units of the Jemez volcanic field show a wide range of compositions (Table 1; Gardner et al., 1986). Both chemical and modal classification schemes tend to obscure the diversity of rock types in the volcanic field (Gardner, 1985). With few exceptions, the rocks of the volcanic field are subalkaline (Fig. 5) and are of the calc-alkaline series. In fact, most andesites of the Jemez Mountains satisfy the criteria suggested by Gill (1981) for high-potassium orogenic andesites. A noteworthy result of recent work is that rocks previously termed dacite, latite, quartz latite, and rhyodacite are best referred to as dacite.

Fig. 6A shows a representation of dates in the volcanic field plotted with respect to magma type, while Fig. 6B shows a plot of rate of volcanism vs. time for the Jemez volcanic field (Gardner and Goff, 1984; Gardner, 1985). Several features are revealed by these figures:

1. Eruptions of mantle-derived basalt span the entire history of the volcanic field with the exception of a tectonic lull from 7 to 4 Ma (mentioned below).

2. Magmas derived by differentiation of mantle-derived material were erupted early in the history of the field with a voluminous pulse occurring from 10 to 7 Ma. These magmas are represented primarily by two-pyroxene andesites and some dacites of the Paliza Canyon Formation and constitute over half the original volume of the volcanic field (~2000 km^3). Similar rocks of similar age are now recognized in units previously mapped as Tschicoma Formation and Lobato Basalt on the north side of the volcanic field (see Table 5, Day 2 of this guide).

3. High-silica rhyolitic magmas, derived from partial melts of lower crust, were continuously erupted in the period 13–6 Ma with a pronounced volumetric pulse at 7–6 Ma (Gardner et al., 1986). These melts are represented by the Canovas Canyon and Bearhead rhyolites of the Keres Group. On the other hand, the "early rhyolite" of Loeffler et al. (1988) (formerly called El Rechuelos) is derived primarily by fractional crystallization of basalt with addition of about 5% of lower crust. El Rechuelos Rhyolite requires less than 2% of lower crust. Thus, the origin of rhyolite in the Jemez Mountains is still the subject of intense investigation.

4. Dacites formed by mixing of basalt or basaltic andesite and high-silica rhyolite were erupted beginning at about 7 Ma. Onset of eruption of these mixed magmas was contemporaneous with cessation of eruption of basalt, differentiates of basalt, and high-silica rhyolites discussed above. Most of these mixed magmas are represented by the dacites of the Tschicoma Formation, but some occur in the Paliza Canyon Formation.

5. Onset of Tewa Group volcanism, including the caldera cycles and Bandelier Tuff, was essentially contemporaneous with revival of basaltic volcanism at 4 Ma. Some overlap with eruptions of mixed magma continued to 2 Ma.

Tectonic history—Following a mid-Miocene volcanic hiatus (Chapin and Seager, 1975), revival of rifting in the vicinity of the Jemez Mountains began at roughly 16.5 Ma (Gardner and Goff, 1984). From 13 to 10 Ma, tectonic activity was intense and was accompanied by basalt and rhyolite eruptions along the Cañada de Cochiti fault zone. These eruptive rocks are interbedded with immature basin-fill gravels and laharic breccias of the Cochiti Formation

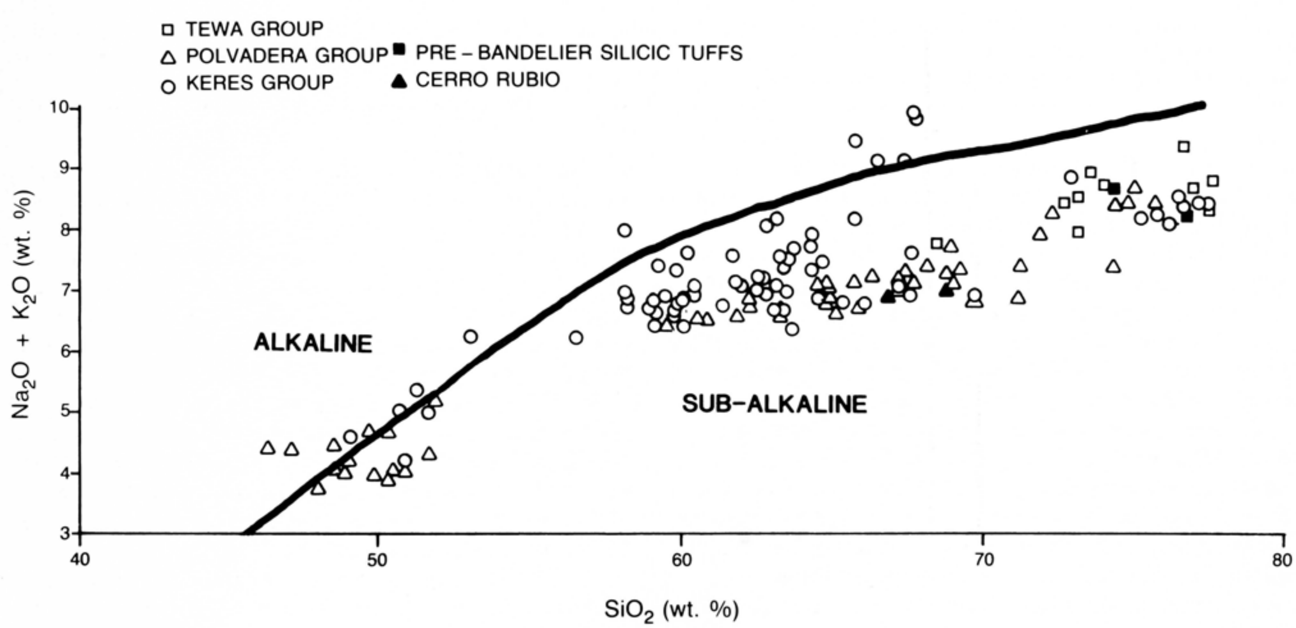

FIGURE 5—Plot of total alkalies vs. SiO_2 for rocks of the Jemez volcanic field. Curve separating alkaline and subalkaline fields is from Irvine and Baragar (1971). From Gardner et al. (1986).

that thicken dramatically from west to east into the Rio Grande rift. In the period 10–7 Ma, basalt, rhyolite, and basaltic differentiates were rapidly vented along the Cañada de Cochiti zone to form half the volume of the entire volcanic field. From 7 to 6 Ma, eruption of differentiates of basalt and rhyolite ceased and eruption of dominantly mixed magma began with a sharp reduction in the volumetric rate of volcanic activity. At 7–4 Ma, a lull in basaltic volcanism occurred and the Cañada de Cochiti fault zone became inactive.

We believe the events at about 7 through 4 Ma reflect petrogenetic response to a significant reduction in the intensity of tectonic activity in the vicinity of the Jemez Mountains. Instead of being rapidly vented along active faults as in earlier stages of the volcanic field's development, pockets of these mantle- and lower-crust-derived magmas coalesced, giving rise to the hybrid dacite volumetrically dominant in the Tschicoma Formation (Polvadera Group). Additionally, the geometry of the Puye Formation, a broad volcaniclastic alluvial fan shed off the Polvadera Group's constructive highland, strongly suggests building of most of the fan in a period of relative tectonic inactivity from 7 to 4 Ma.

Major tectonic activity shifted from the Cañada de Cochiti fault zone to the Pajarito fault zone at about 5–4 Ma. This shift was accompanied by renewed basaltic activity at 4 Ma, peripheral to and basinward of the volcanic field. By about 3.5 Ma, dacitic eruptions in the central field began to be intermixed with small-volume rhyolitic ignimbrite eruptions. Dacitic eruptions ceased by about 2 Ma and the first large-volume ignimbrite of the Tewa Group, the Otowi Member of the Bandelier Tuff, was erupted at 1.45 Ma from the Toledo caldera. The Toledo and Valles caldera (1.12 Ma) cycles, with attendant postcaldera rhyolite dome eruptions, continued to 0.13 Ma.

Tectonic activity on the Pajarito and Jemez fault zones has continued through the Quaternary (Smith et al., 1970; Golombek, 1983; Gardner and House, 1987; Goff and Shevenell, 1987). Vertical displacement on the Tshirege Member of the Bandelier Tuff is typically about 100–200 m along the Pajarito fault zone in Los Alamos County and in Bandelier National Monument. Offset of the Tshirege Member is 50 m along the Jemez fault zone in the west wall of San Diego Canyon. Numerous localities show faulting of Quaternary units younger than the Bandelier Tuff along both of these faults (Gardner and House, 1987; Goff and Shevenell, 1987).

TABLE 1—Chemical analyses of rocks from each major stratigraphic unit of the Jemez volcanic field (from Gardner et al., 1986). See Gardner (1985) for analytical methods and quality of data. [a]Chemical data from Loeffler (1984). [b]Total iron as Fe_2O_3 from analysis.

	Santa Fe Group Basanite	Paliza Canyon Basalts		Canovas Canyon Rhyolite		Paliza Canyon Andesite		Paliza Canyon Dacite		Bear-head Rhyolite	Lobato[a] Basalt	Tschicoma[a] Andesite	Tschicoma Dacite
						Type 1	Type 2	Type 1	Type 2				
	F81-50	JG80-53	F81-22	JG81-51	JG80-47C	JG80-28	JG81-4B	JG81-31	JG81-20A	JG80-49	SB224	IM153	JG80-12
Approx. age, Ma	16.5	13.2	11	11	8.7	8	8	9	8	6.18	8	6.5	5
						Major elements							
SiO_2	43.82	50.62	50.95	76.08	76.63	59.98	63.47	66.48	67.45	76.16	50.51	60.76	67.21
TiO_2	2.36	1.76	1.37	0.12	0.12	1.09	0.83	0.68	0.48	0.11	1.47	0.93	0.51
Al_2O_3	13.74	17.77	15.65	11.77	12.36	16.37	16.75	15.75	15.43	12.11	16.00	16.54	15.28
Fe_2O_3[b]	12.35	10.27	9.34	0.68	0.77	6.40	4.45	3.27	3.89	0.68	11.05	6.02	3.68
MnO	0.17	0.15	0.13	0.05	0.04	0.08	0.09	0.07	0.05	0.07	0.16	0.09	0.06
MgO	10.65	3.91	7.96	0.07	0.09	2.66	1.65	0.58	1.12	0.04	6.71	2.54	1.69
CaO	10.00	9.08	8.33	0.54	0.47	5.27	3.87	1.91	3.10	0.40	9.56	4.62	3.40
Na_2O	3.26	3.99	3.25	3.71	3.80	4.25	4.23	5.49	3.79	3.92	3.11	3.74	3.90
K_2O	1.47	1.29	1.01	4.57	4.62	2.55	3.18	3.81	3.14	4.61	0.93	2.82	3.18
P_2O_5	0.87	0.66	0.34	—	0.03	0.40	0.24	0.19	0.12	0.05	0.40	0.22	0.14
LOI	2.16	1.16	1.43	0.43	0.41	0.47	1.33	0.57	0.60	0.37	0.61	0.82	1.46
Total	100.85	100.66	99.76	98.02	99.34	99.52	100.10	98.80	99.17	98.52	100.51	99.10	100.51
						Trace elements							
Cl	—	—	—	300	480	—	620	—	200	380	n.a.	n.a.	500
Sc	24.9	23	26.3	1.9	3.2	12.9	8.1	6.1	5.5	3.1	30.5	13	5.1
V	260	254	176	—	—	144	78	31	56	—	220	104	58
Cr	350	27	280	—	—	25	11	—	31	—	250	29	22
Zn	—	72	—	—	21	71	52	52	30	—	n.a.	n.a.	—
Rb	65	30	n.a.	185	139	55	68	95	64	154	14	50	79
Sr	1058	1053	n.a.	56	60	718	769	505	470	62	716	649	510
Zr	—	151	n.a.	116	112	241	360	454	232	127	133	201	189
Nb	n.a.	20	n.a.	27	20.6	19.6	25.3	39	14.7	27.3	13	20	17.3
Cs	94	—	4.7	5.5	3.9	—	2.2	2.1	0.7	3.1	—	0.6	1.4
Ba	1400	710	590	n.a.	810	1280	1440	2400	1390	800	483	1157	1180
La	48	52	21.6	41.1	27.3	50.2	57.9	114	42.9	30.4	30	49	44.1
Ce	96	73	43	54	54	73	83	129	56	52	54	97	54
Nd	50	n.a.	—	n.a.	n.a.	n.a.	n.a.	n.a.	n.a.	n.a.	n.a.	n.a.	n.a.
Sm	9.4	7.0	4.5	2.5	3.9	5.8	6.1	13	5.3	4.4	5.8	7	4.4
Eu	2.3	2.2	1.21	0.25	0.40	1.6	1.6	2.1	0.93	0.51	1.50	1.43	1.0
Dy	5.2	5.5	4.2	1.4	3.8	4.3	5.1	12.2	3.2	5.0	5.0	5.1	3.0
Yb	2.0	2.9	1.9	1.7	3.0	2.2	3.3	5.3	1.5	2.6	2.6	2.7	1.5
Hf	4.9	4.1	3.4	3.5	3.5	5.4	6.3	9.0	3.8	3.2	3.5	5.5	3.5
Th	4.4	6.1	2.0	22.5	12.9	7.7	9.4	14.3	3.4	12.0	3.0	8.4	7.5
U	1.47	2.18	0.72	6.19	3.94	2.62	2.92	5.22	1.38	4.12	0.85	2.56	3.29

TABLE 1, continued.

	Cerro Rubio Dacite F83-245	San Diego Canyon Ignimbrite "B" F82-92	El Rechuelos[a] Rhyolite ER 3-3	Otowi Mbr. Bandelier Pumice F82-11	Cerro Toledo Rhyolite: Cerro Toledo F81-145	Cerro Toledo Rhyolite: Cerro Trasquilar F81-139	Tshirege Mbr. Bandelier, Tsankawi Pumice F82-94	Redondo Creek Rhyolite F81-109	Valles Rhyolite: San Antonio Mountain F80-74	Valles Rhyolite: Banco Bonito F82-7
Approx. age, Ma	3.6	2.85	2.02	1.45	1.38	1.27	1.12	1.0	0.54	0.13
				Major elements						
SiO_2	66.9	74.4	74.8	73.6	77.0	75.2	72.7	73.2	74.0	73.2
TiO_2	0.47	0.10	0.08	0.04	0.08	0.08	0.08	0.36	0.14	0.29
Al_2O_3	15.2	11.8	12.4	11.9	12.2	11.9	12.2	12.8	13.2	13.5
Fe_2O_3[b]	3.43	1.54	0.55	1.40	1.19	1.01	1.47	1.04	1.09	1.84
MnO	0.05	0.06	0.06	0.07	0.05	0.07	0.08	0.03	0.05	0.05
MgO	1.42	0.08	0.05	0.10	0.02	0.03	0.05	0.09	0.15	0.63
CaO	3.32	0.33	0.45	0.24	0.14	0.26	0.33	0.69	0.67	1.58
Na_2O	3.60	4.00	3.74	4.36	4.21	4.22	3.08	3.66	3.76	3.84
K_2O	3.20	4.67	4.74	4.61	4.47	4.49	5.36	4.86	5.03	4.11
P_2O_5	0.15	0.005	—	0.005	0.005	0.005	0.005	0.01	0.01	0.06
LOI	1.37	3.35	3.17	4.26	0.25	3.19	4.01	3.63	1.96	0.24
Total	99.11	100.34	100.04	100.59	99.62	100.46	99.37	100.37	100.06	99.34
				Trace elements						
Cl	390	1620	—	2800	790	1990	2200	680	680	500
Sc	6.5	2.7	3.11	0.58	1.09	1.16	1.01	2.9	2.2	4.0
V	64	—	—	16	12	14	—	—	—	19
Cr	51	5	—	5	—	4.2	—	3.6	4.0	12
Zn	73	40	—	20	60	80	33	30	40	30
Rb	52	155	139	330	205	230	330	110	160	165
Sr	500	—	—	9.9	—	10	—	—	—	—
Zr	160	180	58	190	130	150	350	210	125	160
Nb	n.a.	n.a.	40	n.a.	n.a.	n.a.	n.a.	n.a.	n.a.	n.a.
Cs	0.8	4.1	5.3	10.5	4.6	8.1	18	3.8	5.4	5.2
Ba	1170	—	17	—	—	—	—	1000	320	900
La	34	59	17.2	52	31	36	91	57	47	46
Ce	68	113	44	109	72	80	117	106	89	77
Nd	19	30	—	47	18	29	60	21	21	25
Sm	4.4	8.0	3.6	13.9	7.0	7.4	16.6	5.5	5.6	4.5
Eu	1.08	0.16	0.17	2.4	0.10	0.09	0.05	0.68	0.27	0.51
Dy	2.6	8.0	3.6	18.5	10.2	11.6	28	5.3	6.8	3.8
Yb	1.56	5.6	2.6	12.2	5.7	8.1	15.4	3.0	4.9	3.5
Hf	5.0	8.2	3.7	12.0	8.6	8.8	14.0	8.2	4.9	5.2
Th	4.6	21.1	20.4	43	24	26	40	15.6	23	23
U	1.16	6.7	8.0	15.9	8.5	8.2	11.8	4.2	6.3	5.7

Volcanic activity of Toledo–Valles caldera complex

Ignimbrite plateaus surrounding the Jemez volcanic field are mostly the product of two caldera-forming eruptions that occurred during the last 1.45 Ma. With an estimated minimum cumulative volume of 600 km^3, the two members of the Bandelier Tuff are the most evident products of silicic volcanism of the central Jemez Mountains volcanic field. Concurrent with the eruption of these two batches of rhyolitic tephra were the formation, by collapse, of the Toledo and Valles calderas. Many modern concepts of pyroclastic-flow deposits and facies, caldera formation, caldera resurgence, and zoned magma chambers were developed here (Ross and Smith, 1961; Smith and Bailey, 1966, 1968; Smith, 1979; Wright et al., 1981). What are believed to be shallow magma bodies associated with the caldera-forming and postcaldera volcanism are also responsible for the much-sought-after geothermal resources of this volcanic field.

San Diego Canyon ignimbrites—Underlying the Bandelier Tuff and extending southwest of the present-day rim of the Valles caldera are erosional remnants of at least two ignimbrites. The largest of these ignimbrites were previously designated "Pre-Bandelier ignimbrite A" and "Pre-Bandelier ignimbrite B" (Self et al., 1986) and are now called the San Diego Canyon ignimbrites (Turbeville and Self, 1988). These are best exposed along the walls of San Diego Canyon, to a distance of 18 km from the Valles caldera wall. The full extent of these deposits is unknown, but they are estimated to have a volume of >5 km^3 (Turbeville and Self, 1988).

The tuffs are lithic-rich (>30% lithic clasts) and overlie an erosion surface covered with fluvial gravels or a poorly developed soil. The ignimbrites are nonwelded, but "B" has incipient welding associated with fossil fumarole pipes. Ignimbrite "A" has very distinctive gray pumice clasts with highly elongated tube vesicles (Self et al., 1986). Co-ignimbrite lithic breccias are found within these ignimbrites and are believed to indicate proximity to source vents. These ignimbrites have been dated, with K–Ar (sanidine) ages of 2.84 ± 0.07 Ma ("B") and 3.64 ± 1.64 Ma ("A"). Chemically, they are similar to, but slightly more mafic than, the two members of the Bandelier Tuff (Table 1; Self et al., 1986; Turbeville and Self, 1988).

Field evidence indicates that these ignimbrites were once extensive, were erupted from what is now the western mar-

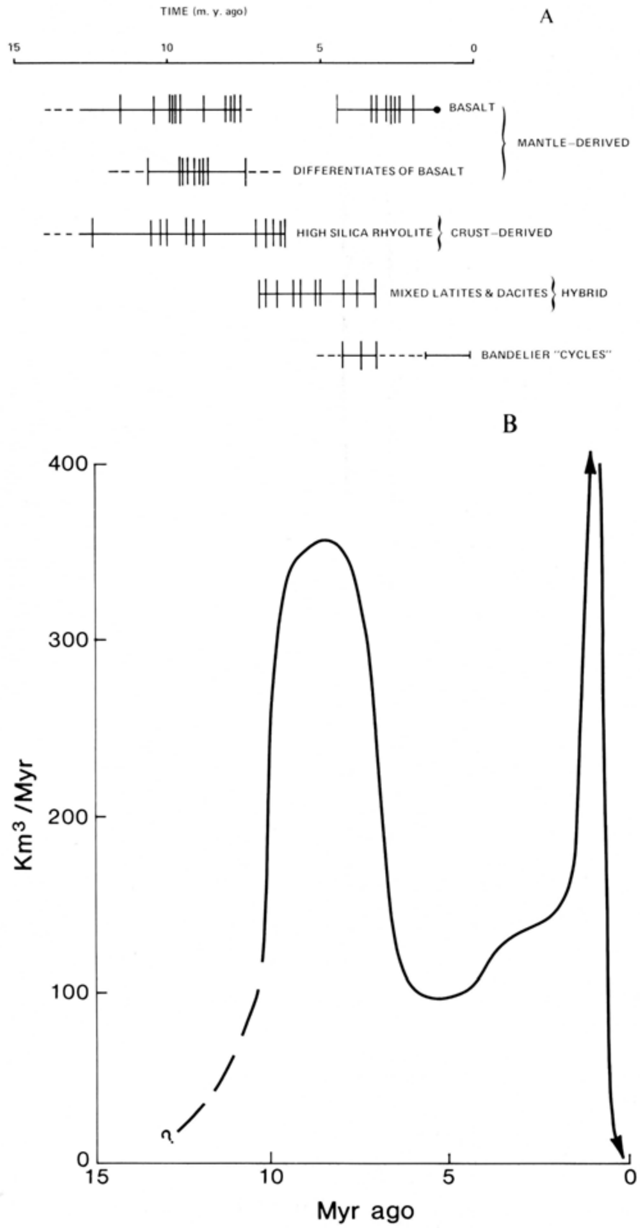

FIGURE 6—**A,** Dates of the Jemez volcanic field plotted with respect to dominant rock type (Gardner and Goff, 1984). Each vertical line represents a K–Ar date. Solid lines indicate continuous eruption of a given magma type inferred from field relations, and dashed lines indicate uncertainty. Numerous dates from Tewa Group (solid line for Bandelier "cycles") not plotted for clarity. **B,** Rate of volcanism (volume per unit time) vs. time for Jemez volcanic activity. Plot goes off-scale with major Bandelier ignimbrite eruptions (from Gardner and Goff, 1984).

gin of the Valles caldera, and may have formed a small caldera, which is now buried within the present-day caldera complex (Fig. 7A). The San Diego Canyon ignimbrites have been described from the geothermal wells drilled within the caldera (the "Lower Tuffs" of Nielson and Hulen, 1984). They appear to thicken eastward in the Redondo Creek area, reaching a thickness of nearly 400 m in geothermal well Baca-4.

Otowi Member of Bandelier Tuff and Toledo caldera—The Otowi Member of the Bandelier Tuff consists of a Plinian pumice-fall deposit (Guaje Pumice Bed), which is overlain by thin surge beds and massive pyroclastic-flow units (Fig. 8). The age of this eruption, based upon several K–Ar dates on sanidine, is 1.45 Ma (Doell et al., 1968).

The Guaje pumice-fall deposits are distributed to the east of the caldera complex. Five fall units have been defined and cumulatively have a maximum thickness of over 8 m (Fig. 7B) (Self et al., 1986). Dispersal axes obtained from isopleth maps of maximum lithic-clast diameters for these fall units may suggest that this pumice deposit was erupted from a central vent or closely spaced vents located near the center of the present Valles caldera.

Surge beds and massive ignimbrite of the Otowi Member are distributed symmetrically about the Valles caldera (Fig. 7C). Multiple flow units have cumulative thicknesses outside the caldera of as much as 180 m and within the caldera of <60 m to 800 m (possibly twice that in the eastern, undrilled half of the caldera complex). The orangish-tan, nonwelded to densely welded ignimbrite contains abundant lithic clasts and pumice clasts in a vitric-crystal or crystal-vitric ash matrix (30–35% phenocrysts of mostly sanidine and quartz). Lithic clasts, which make up from a trace to 30% of the tuffs, are mostly derived from older volcanic rocks but also contain rare fragments of Precambrian basement (Eichelberger and Koch, 1979).

Lithic ("lag") breccias are interbedded with the ignimbrite and are best exposed along the southwestern caldera margin. Lithic blocks, up to 2 m in diameter, within the breccias imply that these deposits are close to vents for the Otowi Member. Gas-escape pipes are present above some of the breccias.

The distribution and thickness of the Otowi Member ignimbrite, distribution of lag breccias, flow-direction indicators such as aligned pumices (Potter and Oberthal, 1983), and K–Ar dates on an intracaldera arc of four domes (Goff et al., 1984) support the interpretation that the Otowi Member was erupted from ring fractures more or less coincident with those of the younger Valles caldera. These features do not support the interpretation that the Otowi Member of the Bandelier Tuff was erupted from the Toledo embayment, a structure 9 km in diameter located on the northeast margin of the Valles caldera. The Toledo embayment may be of tectonic origin or may be a small crater formed at a slightly earlier time; in either case, it is mostly filled with Cerro Toledo Rhyolite. The Toledo caldera, formed during eruption of the Otowi Member of the Bandelier Tuff, is nearly coincident with the younger Valles caldera.

Within the caldera, the Otowi Member has a maximum thickness of 833 m in Baca-12 and thins to 177 m in Baca-4 (Fig. 3) (Nielson and Hulen, 1984). Thus, the unit thins toward the center of the proposed Toledo caldera. We cannot explain this contradiction with prevailing theories of caldera development. However, the data suggest that maximum subsidence was centered over the eastern ring-fracture system.

Intracaldera volcanic activity, Toledo caldera—The Cerro Toledo Rhyolite is a sequence of rhyolitic domes, flows, and associated pyroclastic deposits which postdate collapse of the Toledo caldera (Izett et al., 1981; Heiken et al., 1986). Exposed Cerro Toledo Rhyolite domes are clustered mostly within the Toledo embayment, and along the north rim and just beyond the southeast rim of the Valles caldera (Fig. 7D). K–Ar ages of these domes range from 1.5 Ma to 1.2 Ma, placing them in time between the two, large-volume members of the Bandelier Tuff. The domes consist primarily of gray, flow-banded to massive rhyolite which contains small sanidine and rare quartz phenocrysts.

Contemporaneous with the Cerro Toledo domes are tuffs and epiclastic rocks, which are best exposed in two areas:

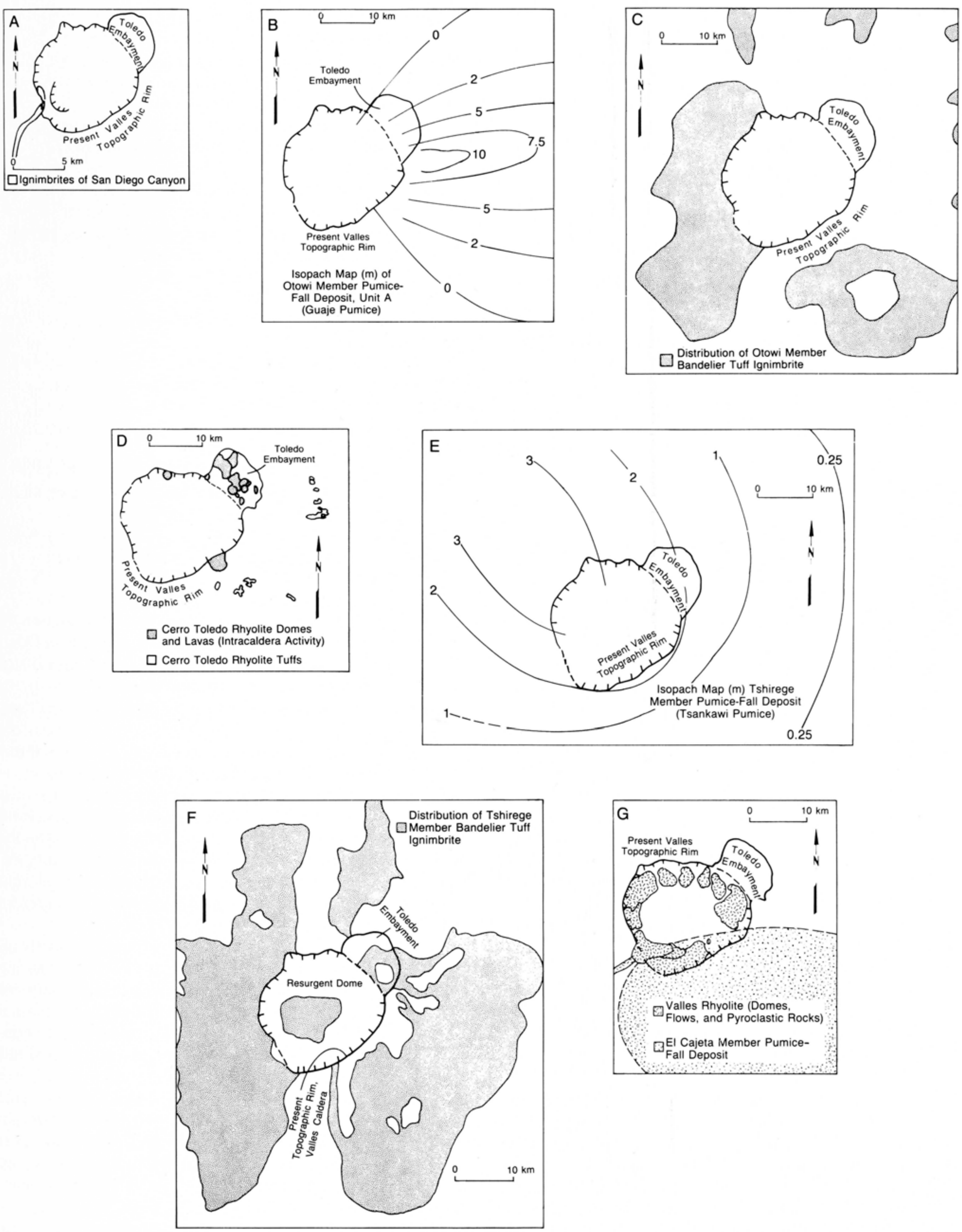

FIGURE 7—Simplified maps showing distribution of major rhyolitic tuffs and lava domes and flows erupted in the central Jemez Mountains during the last 3 Ma. For reference, the present topographic rim of the Valles caldera and the Toldeo embayment are shown on each map. **A,** Distribution of San Diego Canyon ignimbrites (from Turbeville and Self, 1988). **B,** Isopach map, in meters, of unit A of the Otowi Member, Bandelier Tuff pumice-fall deposit (Guaje Pumice) (from Self et al., 1986). **C,** Distribution of the Otowi Member, Bandelier Tuff ignimbrite (from Smith et al., 1970). **D,** Distribution of Cerro Toledo Rhyolite domes, lava flows and tuffs (from Heiken et al., 1986). **E,** Isopach map of fall unit A, Tshirege Member, Bandelier Tuff pumice-fall deposit (Tsankawi Pumice) (from Self et al., 1986). **F,** Distribution of the Tshirege Member, Bandelier Tuff ignimbrite (from Smith et al., 1970). **G,** Distribution of domes, lava flows, and pyroclastic rocks of the Valles Rhyolite (from Smith et al., 1970) and the El Cajete Member pumice-fall deposit (from Self et al., 1988).

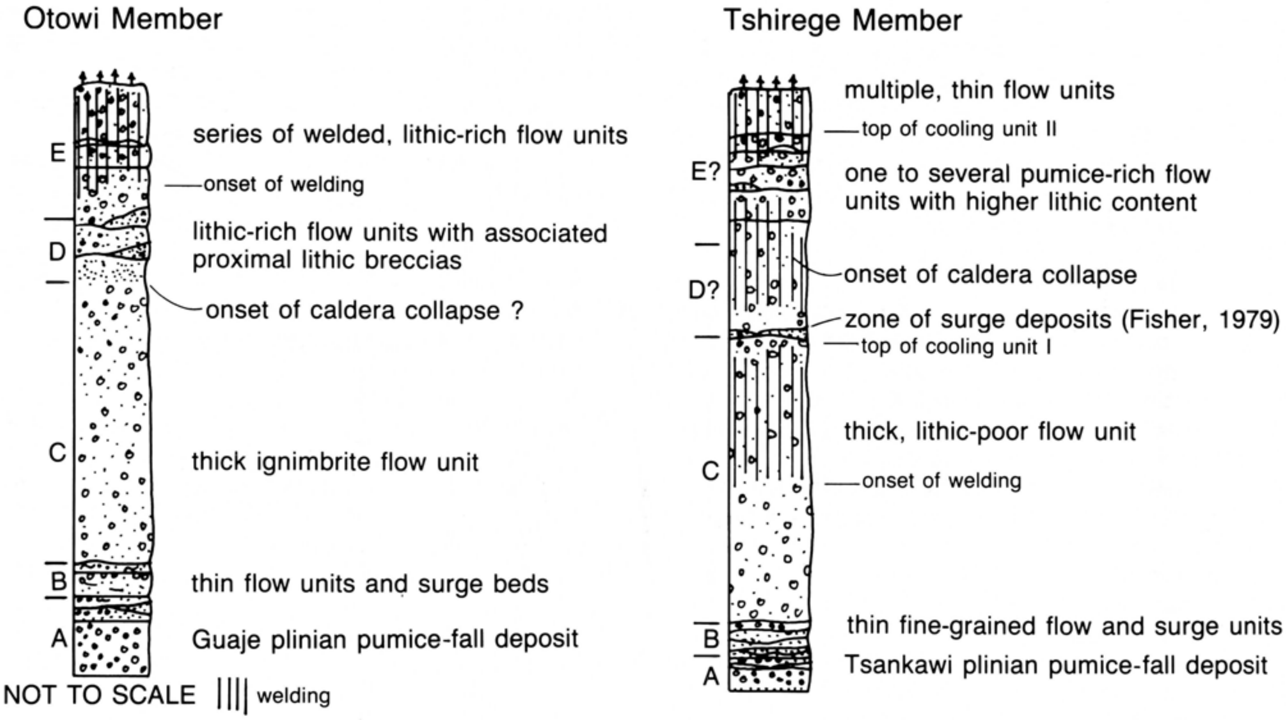

FIGURE 8—Idealized lithology of the Tshirege and Otowi Members of the Bandelier Tuff.

(1) east of the caldera on the Pajarito Plateau, and (2) southeast of the Rabbit Mountain dome (southeast caldera rim, Fig. 7D). East of the caldera, seven eruption sequences of rhyolitic tephra have been studied; most consist of very fine-grained phreatomagmatic ash, overlain by interbedded pumice-fall beds and fine-grained ash-fall beds. The tuffs are nearly aphyric, with only traces of K-feldspar and plagioclase. At isolated outcrops, the nearly aphyric nature of these tuffs can be used to separate them from the phenocryst-rich Bandelier Tuff.

Using cuttings from many deep wells, Nielson and Hulen (1984) identify a clastic deposit within the caldera fill, the S_3 Sandstone, as being correlative with the Cerro Toledo tuffs. The S_3 Sandstone reaches a maximum thickness of 70 m and separates the Otowi and Tshirege Members of the Bandelier Tuff. This unit appears to be composed of interbedded tuffs and epiclastic sandstones.

Tephra-fall patterns of the Cerro Toledo tuffs indicate sources located in the eastern Valles caldera and the Toledo embayment. The pyroclastic breccias and surge deposits along the southeast caldera margin were erupted from the same vent that erupted the Rabbit Mountain dome. Many of the tuff sequences began as phreatomagmatic eruptions, perhaps having been erupted through a caldera lake.

Stix et al. (1988) used the stratigraphy, geochemistry, and geochronology of Cerro Toledo rhyolite domes and tephra to investigate the petrogenesis of the unit and the evolution of compositional zonation within the Bandelier magma chamber. These authors found that compositional (chemical) gradients were restored over a period of 0.33 Ma after eruption of the Otowi Member of the Bandelier Tuff and that crystal fractionation of quartz, alkali feldspar, zircon, and a light-rare-earth-element-enriched phase (probably allanite) was the most likely mechanism by which these gradients were re-established.

Tshirege Member of Bandelier Tuff and Valles caldera—The Valles caldera was formed during eruption of the Tshirege Member of the Bandelier Tuff at 1.12 Ma (Doell et al., 1968). The eruption sequence consists of a basal pumice-fall deposit overlain by thin surge beds and pyroclastic-flow units that make up the ignimbrite (Fig. 8) (Self et al., 1986).

The basal Plinian pumice-fall deposit, the Tsankawi Pumice Bed, consists of four pumice-fall units and two finer-grained ash-fall units, with composite maximum thickness of 3.5 m. Each fall unit has a different dispersal axis, from south to west to north; the most common trend is to the northwest, as shown by an isopach map of fall unit "A" (Fig. 7E). Trends of dispersal axes suggest a central vent for the Plinian eruption within the center of the present Valles caldera.

The Tshirege Member ignimbrite is exposed on nearly all sides of the volcanic field and forms the plateaus flanking these mountains (Fig. 7F). It also forms thick sections of caldera fill, which have been sampled during geothermal drilling. The orangish-tan tuffs of the ignimbrite are nonwelded to densely welded crystal-vitric to vitric-crystal tuff (~32% phenocrysts of mostly sanidine and quartz, with traces of hornblende and magnetite). Thicknesses outside the caldera range from 15 to over 270 m, whereas within the caldera densely welded tuffs range from 400 to over 1100 m. Proximal breccias within the Tshirege Member are rare, with a few thin deposits exposed along the caldera rim.

Within distal parts of the Tshirege Member of the Bandelier Tuff, flow units can be separated visually by thin surge deposits and "sandy partings" and by pumice swarms (Fisher, 1979). Four to five flow units are visible in the well-exposed section along NM-501, east of Los Alamos (Day 3, Stop 1). Overprinting these textural features in the nonwelded, distal sections are vapor-phase alteration and columnar jointing of the upper half of the ignimbrite.

The Valles Rhyolite; intracaldera domes, lava flows, pyroclastic deposits, and sedimentary rocks—After the dust settled from formation of the Valles caldera, less explosive activity continued within the caldera until about 130 Ka. Rhyolitic domes and lava flows were erupted from the caldera ring-fracture system, from the massive Cerro del Medio in the eastern moat to the very small Cerro La Jara dome on the southern margin (Fig. 7G) (Spell, 1987). Some domes are up to 700 m thick. Several extensive pumice-fall deposits and small ignimbrites are associated with dome growth. Coarse breccias, gravels, and lacustrine mudstones are interbedded with tuffs and rhyolite lavas.

The youngest (130 Ka) intracaldera eruption is that of the Banco Bonito obsidian flow (Marvin and Dobson, 1979), which erupted along the southwest caldera ring fracture. The Battleship Rock ignimbrite (well-exposed in San Diego Canyon) and the widespread El Cajete pumice-fall bed are both thought to be explosive precursors to formation of the Banco Bonito lava flow (Self et al., 1988). The pyroclastic sequence is overlain by 30–70 m thick Banco Bonito obsidian lava flow (12% phenocrysts; plagioclase, hornblende, biotite, and traces of clinopyroxene, orthopyroxene, and Fe–Ti oxides). Recently obtained ages for the three eruptions are: Banco Bonito 130–180 Ka (Self et al., 1988); El Cajete 170–151 Ka (Self et al., 1988); and Battleship Rock 278 Ka (F. Goff, unpubl. data). Additional postcaldera rhyolites that have chemical similarities to the youngest moat volcanic rocks were cored in VC-1 (Gardner et al., 1986).

Within the caldera, in the resurgent dome, is a sequence of nonwelded to densely welded silicic ignimbrites with an aggregate thickness of 460 m overlying the Tshirege Member of the Bandelier Tuff ("Upper tuffs" of Nielson and Hulen, 1984). Little is known about this tuff sequence, mainly because of the intensity of hydrothermal alteration, but it is separated from the Tshirege Member by a volcaniclastic sandstone (Nielson and Hulen, 1984) and underlies tephra deposits believed to be associated with the Redondo Creek Rhyolite in CSDP core hole VC-2A; thus, its age is estimated at between 1.12 and 1.0 Ma (Hulen et al., 1987).

Subsurface structure and resurgence of Valles caldera

The structural framework of the Valles caldera is dominated by high-angle normal faulting (including ring faulting) and resurgent, domal uplift of the subsided cauldron block. Location of the caldera, and the entire Jemez volcanic field, is controlled by the intersection of northeast-trending faults of the Jemez volcanic lineament (JVL) with north-trending faults at the western edge of the RGR (Fig. 1) (Aldrich and Laughlin, 1984; Gardner and Goff, 1984). Reactivation of these earlier structures during and following caldera formation and resurgent doming is responsible for much of the complex fault pattern presently observed in caldera-fill rocks. For example, the northeast-trending apical graben of the caldera's resurgent Redondo dome clearly is directly on strike with the Jemez fault zone (the local expression of the JVL) to the southwest (Fig. 1). Ring-fracture and apical graben high-angle normal faults are believed to be the principal permeable conduits for circulation of the active, high-temperature Valles hydrothermal system.

The subsurface structure of Valles caldera has been discussed by Goff (1983), Nielson and Hulen (1984), Heiken et al. (1986), and Wilt and Vonder Haar (1986). Many of these interpretations rely on gravity data acquired by UNOCAL during geothermal exploration and on the drilling results of several organizations. The gravity data of Segar (1974), based on measurements at nearly 700 stations, show a pronounced circular gravity low of as much as 35 mgal that coincides with the location of the caldera depression (Fig. 9A). Modeling of these data by Segar (Fig. 9B) indicates that subsurface fault patterns trend northeast parallel to the trend of the JVL and the trend of nearby faults associated with the RGR. The gravity low, however, is asymmetric and is greatest in the eastern caldera, coincident with Valle Grande. In general, zones of steep gravity gradients

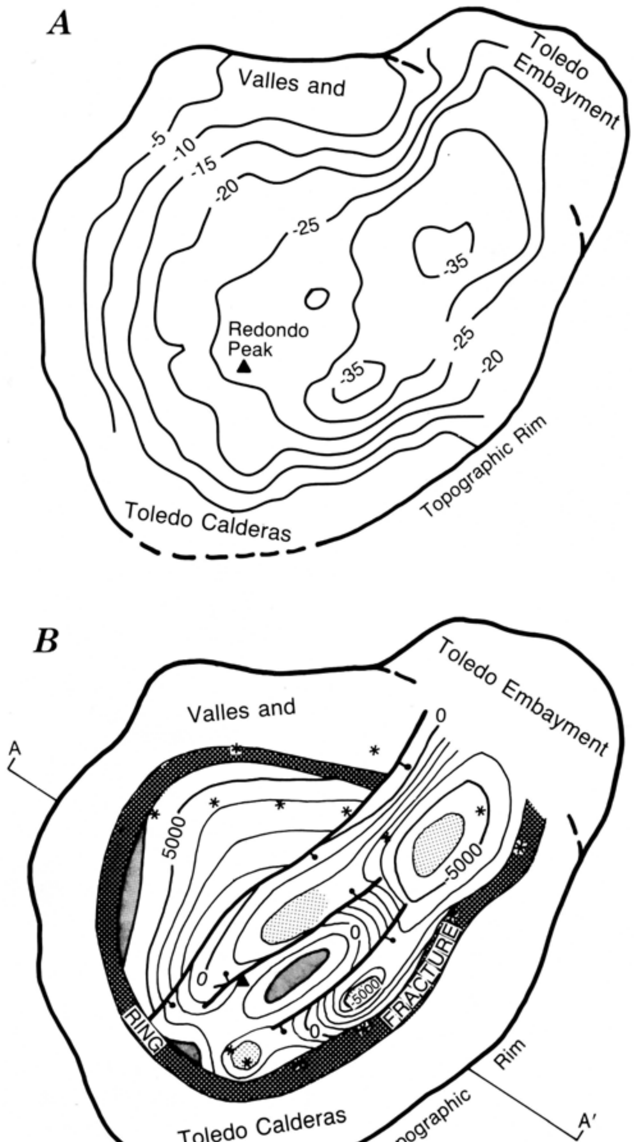

FIGURE 9—**A,** First-order residual Bouguer gravity map of Valles caldera produced from Enclosure IV of Segar (1974); values in mgal. **B,** Gravity interpretation of Segar (1974) using residual map in (A) and a density contrast of 0.35 g/cm^3. No effort was made to map features such as slump along caldera ring fracture, jagged nature of caldera rim, etc. Contour interval is 1000 ft. Checkered pattern shows approximate position of caldera ring-fracture zone in relation to moat rhyolite vents shown by stars. Dot pattern shows relative gravity lows (basins) and gray pattern shows relative gravity highs. Note apparent horst beneath Redondo Peak and northeast trend of major fault zones. Also note large gravity low extending into the Toledo embayment. The near-coaxial relationship of earlier Toledo caldera to Valles caldera was not known at the time of this interpretation. Line A–A′ approximates the location of the cross section shown in Fig. 46 (Day 3).

are interpreted to be fault zones with down-to-the-southeast displacements suggesting that rift-related faulting controls the subsurface structure of Valles caldera. An exception to this down-to-the-southeast fault pattern is the northeast-trending horst coincident with the Redondo Peak segment of the Valles resurgent dome.

The model of Fig. 9B is constrained by drilling results in the southwestern quadrant of the caldera. Contours in Fig. 9B represent the approximate elevation in feet of Precambrian basement rocks relative to sea level. For example, basement beneath the western caldera can be as shallow as 6000 ft (1830 m) above sea level or only 2500 ft (760 m) below ground surface, as verified in the WC 23-4 well (Goff et al., 1987; Hulen et al., 1987). Depth to basement increases eastward across faults, being at 5100 ft (1555 m) beneath Sulphur Springs in core hole VC-2B (J. N. Gardner and J. B. Hulen, unpubl. data 1988) and at 10,200 ft (3110 m) in well Baca-12 in the Redondo Creek graben (Nielson and Hulen, 1984). According to the gravity model, depth to basement is approximately 15,000 ft (4570 m), or about 5000 ft (1525 m) below sea level in the vicinity of Valle Grande. Such gross asymmetry prompted Nielson and Hulen (1984) and Heiken et al. (1986) to propose that the Valles caldera is a "trap-door" caldera.

Based on drilling results and gravity modeling, the negative gravity anomaly was interpreted by Segar (1974) to be caused primarily by low-density tuffs and sedimentary rocks filling an asymmetric depression. Segar used a value of 2.45 g/cm^3 for both his Bouguer and topographic corrections. Density measurements on eight samples of intracaldera tuffs and sedimentary rocks from core hole VC-2A range from 2.49 to 2.11 g/cm^3 (Musgrave et al., 1989). Segar's interpretation does not identify a deep circular intrusive or plutonic body beneath the caldera, but it is unlikely that a significant density contrast exists between Precambrian basement and recently crystallized plutonic rocks.

Formation and resurgence of the Valles caldera is well documented (Smith and Bailey, 1968). At 1.12 Ma, eruption of about 300 km^3 (minimum) of rhyolitic ash-flow tuff led to collapse of the caldera simultaneously with emplacement of the Tshirege Member of the Bandelier Tuff (Doell et al., 1968; Izett et al., 1981; Smith and Bailey, 1968; Self et al., 1986). The intracaldera Tshirege Member is therefore much thicker than corresponding outflow sheets. The intracaldera Tshirege Member, as thick as 1156 m in Baca 5 (Nielson and Hulen, 1984), was structurally uplifted during the 100,000-year interval following caldera collapse by more than 1000 m near the caldera center. During uplift, the upper portion of the resurgent dome was subjected to extension, resulting in widespread normal faulting (Fig. 10). Some of this faulting took place along and within the dome's northeast-trending apical graben and through reactivation of older basement structures. A subordinate fault set orthogonal to the apical graben apparently lacks deep-seated control (Behrman and Knapp, 1980).

Nielson and Hulen (1984) suggested a domed plate as a model for deformation of the Redondo dome. The model has two important implications. First, on the basis of the amplitude and diameter of the dome, the top of the presumed causative magma body is at depth of about 5 km. Secondly, the widespread normal faulting presently observed at the crest of the dome is predicted by the model to have formed during extension above a neutral plane situated about halfway down from the dome crest to the top of the magma body; compression prevails beneath this neutral plane. This relation, in turn, implies that fracture-controlled hydrothermal circulation is confined principally to the upper half of the domed sequence, a conclusion supported by the limited downhole data available (Hulen and Nielson, 1986a).

This general model of resurgent doming and fracture permeability would be complicated somewhat if the Valles caldera's precursor, the comparably sized and coincident Toledo caldera (1.45 Ma) (Smith and Bailey, 1968; Izett et al., 1981; Self et al., 1986; Heiken et al., 1986) had undergone a similar volcanotectonic history. However, structural evidence in core from CSDP core hole VC-2A suggests that the Toledo caldera did *not* undergo resurgence. Compaction foliation attitudes in the Tshirege and Otowi Members of the Bandelier Tuff are essentially identical in the VC-2A core (Goff et al., 1987); had the Toledo caldera experienced resurgence, attitudes measured in the Otowi Member presumably would be steeper than those in the overlying Tshirege. However, on the basis of a single intercept, this hypothesis must remain tentative until tested by further scientific drilling.

Petrogenesis of Bandelier magma chamber and associated rhyolites

A comprehensive interpretation of the petrogenesis of the Bandelier magma system (and indeed, the entire Jemez volcanic field) has not been published, but much is hidden in theses (e.g., Loeffler, 1984; Gardner, 1985; Kuentz, 1986; Spell, 1987). Smith and Bailey (1966) proposed from looking at chemical and petrologic variations in the outflow sheets of the ignimbrites (primarily the Tshirege Member) that the Bandelier magma chamber was compositionally zoned. Smith (1979) discussed chemical variations as functions of time with respect to both the Toledo and Valles cycles and suggested that the Bandelier pluton evolved from a (Tschicoma) dacitic parent magma. This concept was substantiated by Gardner (1985) using trace-element and REE data for all Jemez volcanic rocks. Chemical variations with respect to time were elegantly investigated for the Cerro Toledo Rhyolite by Stix et al. (1988), who found that these post-Toledo caldera rhyolites were generated by fractional crystallization of Bandelier magma and not by diffusive processes or wall-rock assimilation.

The first, post-Valles caldera moat rhyolites also appear to have a close genetic relationship to Bandelier magma (Spell, 1987), but the latest moat rhyolites, in the southwestern ring-fracture zone, do not (Gardner et al., 1986; Self et al., 1988). This latest package (VC-1 Tuffs, VC-1 Rhyolite, Battleship Rock Tuff, El Cajete Pumice, Banco Bonito Rhyolite) is more "mafic" in composition, has $^{87}Sr/^{86}Sr$ of about 0.705 (versus about 0.710 for Bandelier Tuff), and could be derived from a mixture of high-silica rhyolite (Bandelier) and dacite magmas (J. N. Gardner and F. Goff, unpubl. data 1989). Unfortunately, a systematic investigation of Sr and Nd isotope ratios of Jemez volcanic rocks does not exist, although the available Sr data have been compiled by Vuataz et al. (1988). Where both ratios have been determined on Jemez rhyolites (El Rechuelos Rhyolite), the results indicate derivation primarily by fractional crystallization from a basaltic parent (Loeffler et al., 1988).

Sommer (1977) analyzed the volatile contents of silicate melt inclusions in quartz phenocrysts of the Tshirege Member of the Bandelier Tuff and concluded that the depth of burial to the top of the chamber was about 5 km (~1.5

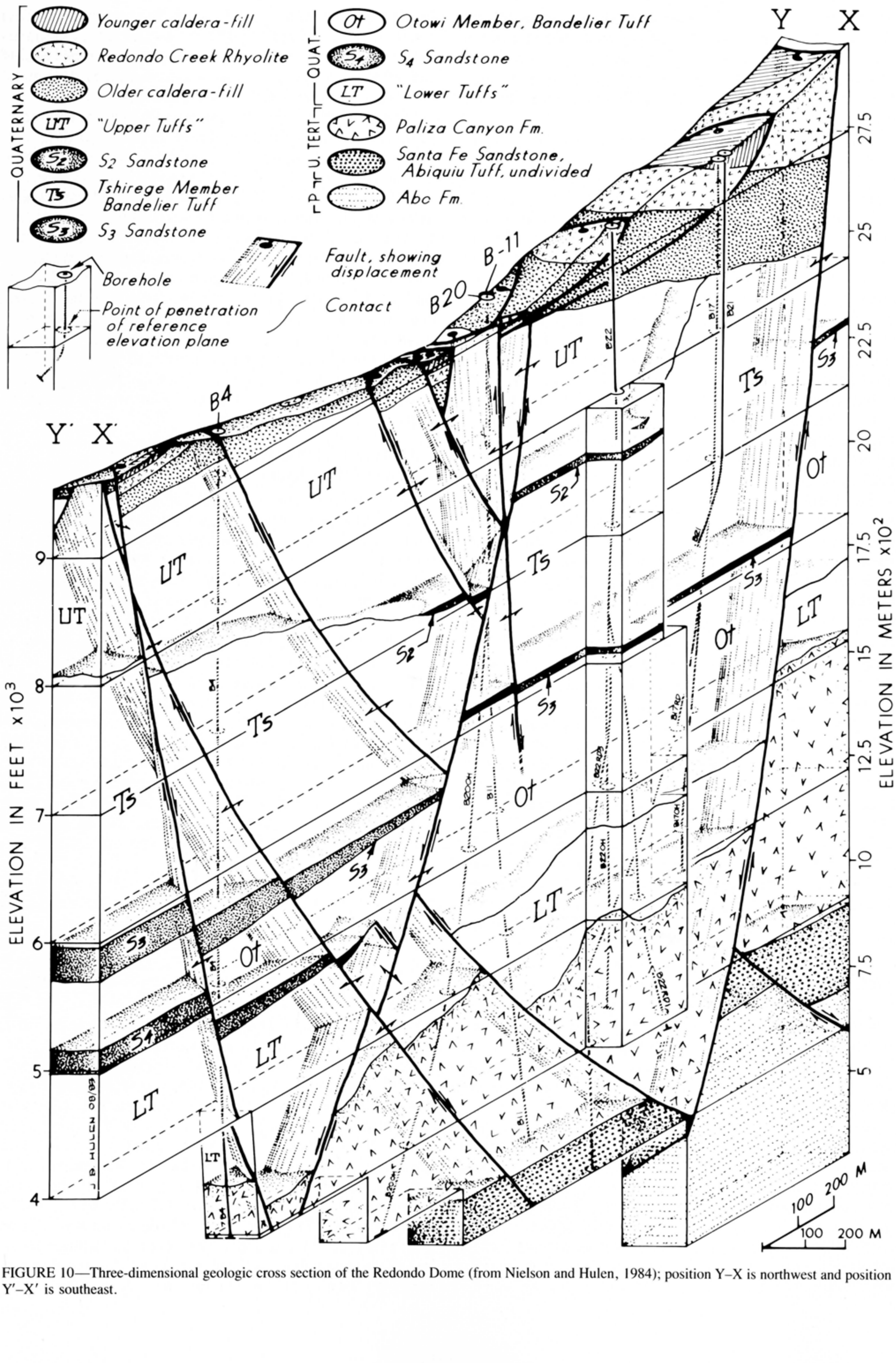

FIGURE 10—Three-dimensional geologic cross section of the Redondo Dome (from Nielson and Hulen, 1984); position Y–X is northwest and position Y′–X′ is southeast.

kbar). Warshaw and Smith (1988) investigated the compositions of pyroxenes, fayalites, and iron–titanium oxides in both members and reported that the basal ash fall of the Tshirege (Tsankawi Pumice Bed) formed at a pre-eruption temperature of about 700°C, while the uppermost Tshirege ignimbrite formed close to 850°C. Depths of formation were estimated between 5 and 7 km (1.5 to 2.0 kbar). Nielson and Hulen (1984) used a structural model (mentioned above) to estimate the depth to the present top of the (crystallized) Bandelier pluton at about 4.7 km. Because this estimate accounts for post-eruption resurgence, the depth to the magma chamber before ignimbrite effusion would be between 5 and 6 km.

Precambrian geology

Precambrian rocks occur as small, tectonically disturbed lenses of granite gneiss at Soda Dam and Guadelupe Box on the Jemez fault zone southwest of Valles caldera, as granitic and metamorphic rocks in the core of the Nacimiento uplift (Laramide age) west of the caldera, and as granitic and metamorphic rocks in the San Pedro Park area northwest of the caldera. Precambrian rocks have been encountered in geothermal wells JS-1 (Goff et al., 1981), AET-4, WC 23-4 (Shevenell et al., 1988), Baca-2 (Dondanville, 1971), Baca-7 (Lambert and Epstein, 1980), Baca-12 (Nielson and Hulen, 1984), VC-1 (Hulen and Nielson, 1988a), and VC-2B (J. B. Hulen and J. N. Gardner, unpubl. data 1988), in addition to the wells drilled for the Hot Dry Rock program (Laughlin et al., 1983) (Fig. 3). Precambrian lithologies in all non-HDR wells are variously described as "fresh" to hydrothermally altered granitic rocks, gneisses and schists (Table 2), and no detailed work has been performed on them except for samples from VC-1. If the rock descriptions in non-HDR wells are accurate, it appears that metamorphic rocks dominate the upper Precambrian section outside the caldera, while plutonic rocks dominate the upper section inside the caldera. Depth to Precambrian basement increases dramatically from outside the caldera on the west to inside on the east and from west to east across the grain of precaldera RGR faults.

The thick Precambrian section penetrated by HDR wells at Fenton Hill, located a scant 0.5 km west of the topographic rim of Valles caldera (Fig. 11), has been studied extensively (Laughlin, 1981). The section is very complex in detail and the orientations of contacts are not well known. Gneissic rocks interlayered with many schist intervals dominate the section. Various types of granitoid rocks occur as dikes and as small and large intrusive bodies. A very large body of biotite granodiorite was observed in the interval 2590–3000 m and the first HDR circulating system was engineered in this rock mass. Laughlin et al. (1983) discussed the petrography, chemistry, fracturing, and secondary minerals of the various Precambrian rocks.

Brookins and Laughlin (1983) performed a Rb–Sr geochronologic investigation on 76 Precambrian samples from the HDR wells. They concluded that major metamorphism occurred at 1.62 ± 0.04 Ga, which is in agreement with radiometric ages reported for similar rocks elsewhere in

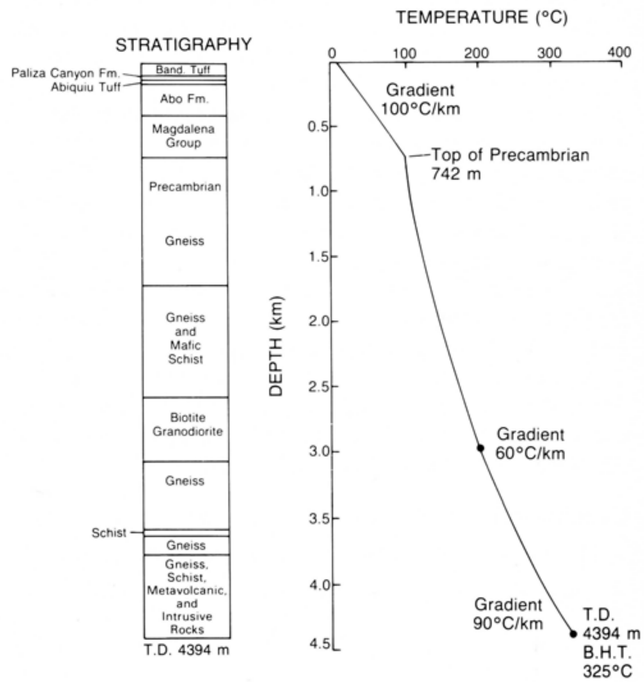

FIGURE 11—Stratigraphic column and temperature profile, Fenton Hill (modified from Laughlin et al., 1983).

TABLE 2—Wells penetrating Precambrian basement rocks in the Valles caldera region, New Mexico. [a]See Fig. 3 for well locations; all wells also penetrate Permian Abo Formation and Pennsylvanian Madera Limestone except well JS-1 (Pennsylvanian only).

Well[a] name	Total depth (m)	Top of Precambrian (m)	Rock types	Reference
Wells drilled for Hot Dry Rock program				
GT-1	785	642	Amphibolite and granite–gneiss	Perkins, 1973
GT-2	2930	730		
EE-1	3060	730	Gneiss, schist, granite, granodiorite;	Laughlin et al., 1983
EE-2	4390	730	minor amphibolite and metavolcanic rock	
EE-3	3980	730		
PC-1	664	655	Granite	Shevenell et al., 1988
Wells drilled for other projects				
JS-1	253	235	Granite–gneiss	Goff et al., 1981
AET-4	1221	997	Gneiss; minor schist and amphibolite	Shevenell et al., 1988
WC23-4	2101	737	Granite	Shevenell et al., 1988
Baca-2	1725	1524	Granite	Dondanville, 1971
Baca-7	1687	1650	Granite	Lambert and Epstein, 1980
Baca-12	3211	3101	Altered granite	Nielson and Hulen, 1984
VC-1	856	843	Gneiss; brecciated, altered granite–gneiss	Hulen and Nielson, 1988a
VC-2B	1762	1558	Altered biotite quartz monzonite	This report

north-central New Mexico. The same authors reported an age of 1.50±0.12 Ga for the large biotite granodiorite intrusive which agrees with the U–Th–Pb age of 1.50±0.02 Ga obtained by Zartman (1979). Brookins and Laughlin (1983) also indicated that minor dike emplacement continued to 1.44±0.03 Ga. Harrison et al. (1986) used $^{40}Ar/^{39}Ar$ analyses on microcline to suggest that additional Precambrian metamorphic events occurred at 1.03 and 0.87 Ga.

Thermal history—Much attention has been paid to the Quaternary thermal regime beneath Fenton Hill and the southwestern caldera margin (Heiken and Goff, 1983). Kolstad and McGetchin (1978) used heat-flow data and dates on major events in the history of the caldera to derive a model of conductive thermal cooling of the Bandelier pluton after formation of Valles caldera. Heat flow beneath Fenton Hill averages about 4 HFU but, as can be seen in Fig. 11, the thermal gradient increases from 60 to 90°C/km with depth in the Precambrian section. Although most estimates on the age of most recent thermal heating at the Fenton Hill site vary from 1 to 4 Ma, Harrison et al. (1986) use transient analyses on the thermal gradients to suggest that the heating event may be as young as 10 Ka. Sasada (1988a) also recognized a young (postcaldera) heating event from detailed examination of fluid inclusions in Fenton Hill core samples. The source of this heating is not entirely clear (the youngest volcanism in the Valles region is 130 Ka), but it must be related to magmatic/hydrothermal activity associated with the southwestern caldera (see also Sass and Morgan, 1988). Thus, two "magmatic" episodes are recognized in the Precambrian rocks of the caldera region: a series of Precambrian events at 1.62–0.87 Ga and much more recent events, or a series of closely related events, associated with the Jemez volcanic field and Valles caldera.

Geophysical surveys other than gravity

The thermal regime of Valles caldera was investigated by UNOCAL during their geothermal endeavors and later interpreted by Swanberg (1983) and Sass and Morgan (1988). A map of thermal-gradient data (Fig. 12) shows a broad area in the southwestern caldera where shallow gradients exceed 450°C/km. This area includes the Redondo Creek reservoir and the Sulphur Springs reservoir. These areas are known upflow zones for thermal fluids and hot-water production. Shallow heat flow in the caldera locally exceeds 10 HFU, caused by convective processes (Reiter et al., 1975; Sass and Morgan, 1988), whereas heat flow along the western RGR averages about 2.8 HFU (Reiter et al., 1976). Deep magnetotelluric investigations of the Valles caldera and adjacent RGR (Hermance and Pedersen, 1980) recognized a widespread electrical conductor at 15 km depth, but were not able to discriminate unique (magmatic?) sources beneath the caldera or the rift. A combination of shallower electrical and telluric techniques was integrated by Wilt and Vonder Haar (1986) to define a broad conductive anomaly beneath the southwestern caldera region at 1–3 km depth (Fig. 13). Parts of this anomaly correlate with known fluid production in the Redondo Creek and Sulphur Springs areas. Depending on interpretation, the areal extent of the geothermal reservoir(s) in the caldera varies from 10 to 30 km^2.

The most recent compilation of natural seismic activity for the Valles caldera region has been presented by Gardner and House (1987) for their investigation of seismic hazards in the Los Alamos region. Fig. 14 shows a cumulative plot of all earthquakes located by the Los Alamos Seismic Network from September 1973 to December 1984. A band of seismicity extending south of Chama, New Mexico, to a point about 70 km west of Los Alamos coincides with the Nacimiento uplift (originally a Laramide age structure), which is bounded by a zone of oblique-slip faults on its western edge. The cluster of seismic events northwest of Española lies near the intersection of the Pajarito and Embudo fault zones on the western side of the RGR. Additional seismicity

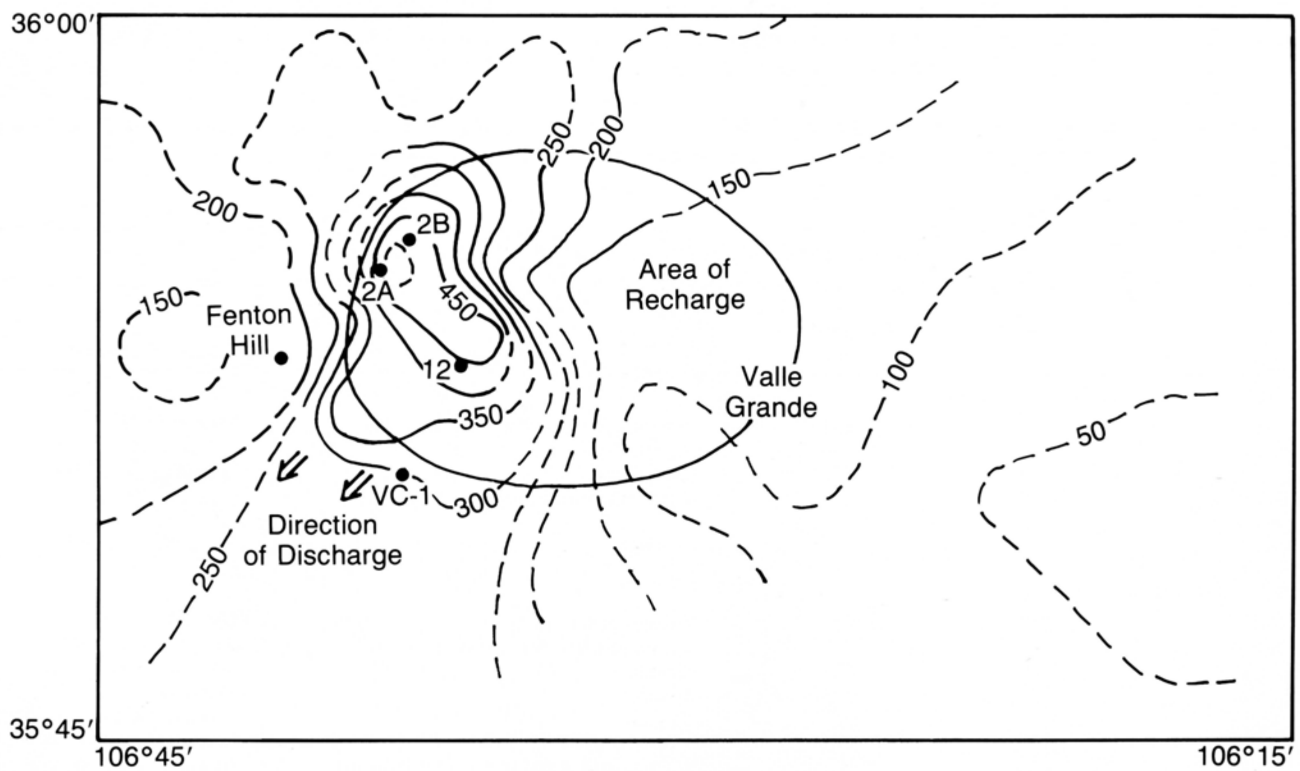

FIGURE 12—Thermal-gradient contours (°C/km) of Valles caldera area (modified from Sass and Morgan, 1988).

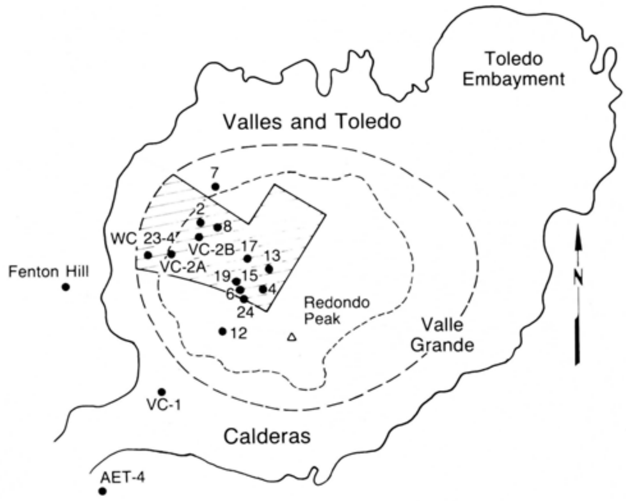

FIGURE 13—Map showing maximum area of geothermal reservoir(s) as defined from electrical surveys (modified from Wilt and Vonder Haar, 1986).

is evident associated with faults of the Pajarito fault system in the Los Alamos area and south. A belt of seismicity generally follows the trend of the northeast-trending JVL from a point west of Albuquerque to a point northeast of Taos. The seismically quiet area west of Los Alamos corresponds with the Valles caldera and is attributed to the presence of high subsurface temperatures and/or relict zones of partial melt that exist beneath the caldera.

Attenuation of seismic waves beneath the caldera complex was first recognized by Suhr (1981). Olsen et al. (1986) studied the complex, shallow crustal structure beneath the Jemez volcanic field using a time-term technique to process first-arrival-time data from a network of temporary seismic stations of the Caldera and Rift Deep Seismic Experiment (CARDEX). Station time terms are highly correlated to

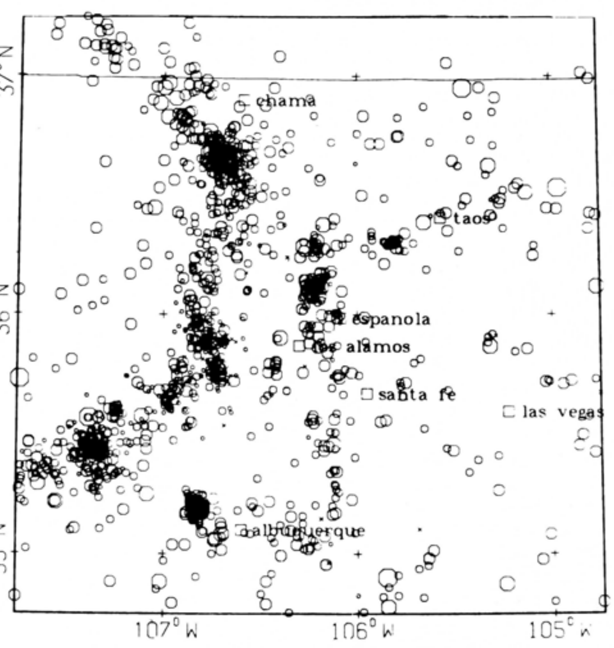

FIGURE 14—Cumulative plot of all earthquakes located by the Los Alamos Seismic Network from September 1973 to December 1984. The size of circle indicates magnitude scale (M_L) with the largest indicating >3 and the smallest indicating a range of –1 to 0. The seismically quiet area west of Los Alamos coincides with the Valles caldera. See text for discussion. From Gardner and House (1987).

gravity anomalies and generally support models for which crystalline basement drops eastward to depths of 600 m below sea level beneath the axial basins of the RGR. Although Olsen et al. (1986) implied that the large gravity low of the caldera and associated time-term delays are caused by residual melt in the silicic Bandelier pluton, other workers have suggested that the gravity low can be modeled solely as a deep asymmetric hole filled with low-density caldera fill (Segar, 1974; Nielson and Hulen, 1984; Wilt and Vonder Haar, 1986). This ambiguity may result because the density contrast between Precambrian basement and nearly crystallized silicic melt is small, as mentioned above.

Ankeny et al. (1986) applied a simultaneous inversion of earthquake and travel-time data to derive a velocity model of the upper 10 km of crust beneath the Jemez volcanic field. The model displays a prominent, low-velocity, cylindrically shaped body beneath the caldera that is 15 km in diameter and 12–15 km thick. This low-velocity body is interpreted to result from the combined effects of a silicic magma body and associated high temperatures, and is centered beneath the southwestern sector of the caldera complex. A possible model incorporating the seismic data is shown in Fig. 15.

Configuration of hydrothermal system

Valles caldera possesses a diverse suite of thermal waters that are typical of those existing at many geothermal areas around the world (Trainer, 1975; Goff and Grigsby, 1982). Table 3 gives selected chemical data for these types of fluids and Fig. 16 compares water types on a plot of δD versus $\delta^{18}O$. Acid-sulfate waters with associated mud pots and fumaroles discharge in the central and western resurgent dome areas, particularly at Sulphur Springs (Goff et al., 1985). These springs result from condensation of steam and oxidation of H_2S to form natural sulfuric acid that mixes with near-surface ground waters. Thermal meteoric waters occur at isolated spots throughout the western ring-fracture zone of the caldera. They appear to be mostly dilute ground water heated by the relatively high subsurface temperatures present at shallow depths. They are not the classic, steam-heated, $NaHCO_3$ waters of Mahon et al. (1980). Deep reservoir waters are those encountered by wells in the Redondo Creek and Sulphur Springs areas beneath the acid-sulfate/vapor zone capping the liquid-dominated part of the hydrothermal system. They are neutral-chloride in character, with anomalous concentrations of As, B, Br, Cs, Li, Rb, and other trace elements. Hot springs derived in part from deep reservoir water are encountered outside the southwest caldera margin in San Diego Canyon (along the Jemez fault zone) and in wells drilled in the flanking plateaus. They appear to be mixtures of reservoir water and various types of ground water (Goff et al., 1981, 1988). Yet another type of thermal water is encountered in Precambrian basement rocks at the Fenton Hill HDR site and at the WC23-4 well in the ring-fracture zone just west of Sulphur Springs (Grigsby et al., 1984; Meeker and Goff, 1988). These waters are more concentrated than reservoir waters and their origin is still not resolved (pore-fluid brine?; magmatic emanations?). The origin and relation of these fluids in Precambrian rocks to overlying reservoir waters is one of the objectives of core hole VC-2B in Sulphur Springs.

Vuataz and Goff (1986) presented stable-isotope and tritium data on over 100 thermal and non-thermal waters in the Valles caldera region. They concluded that recharge to

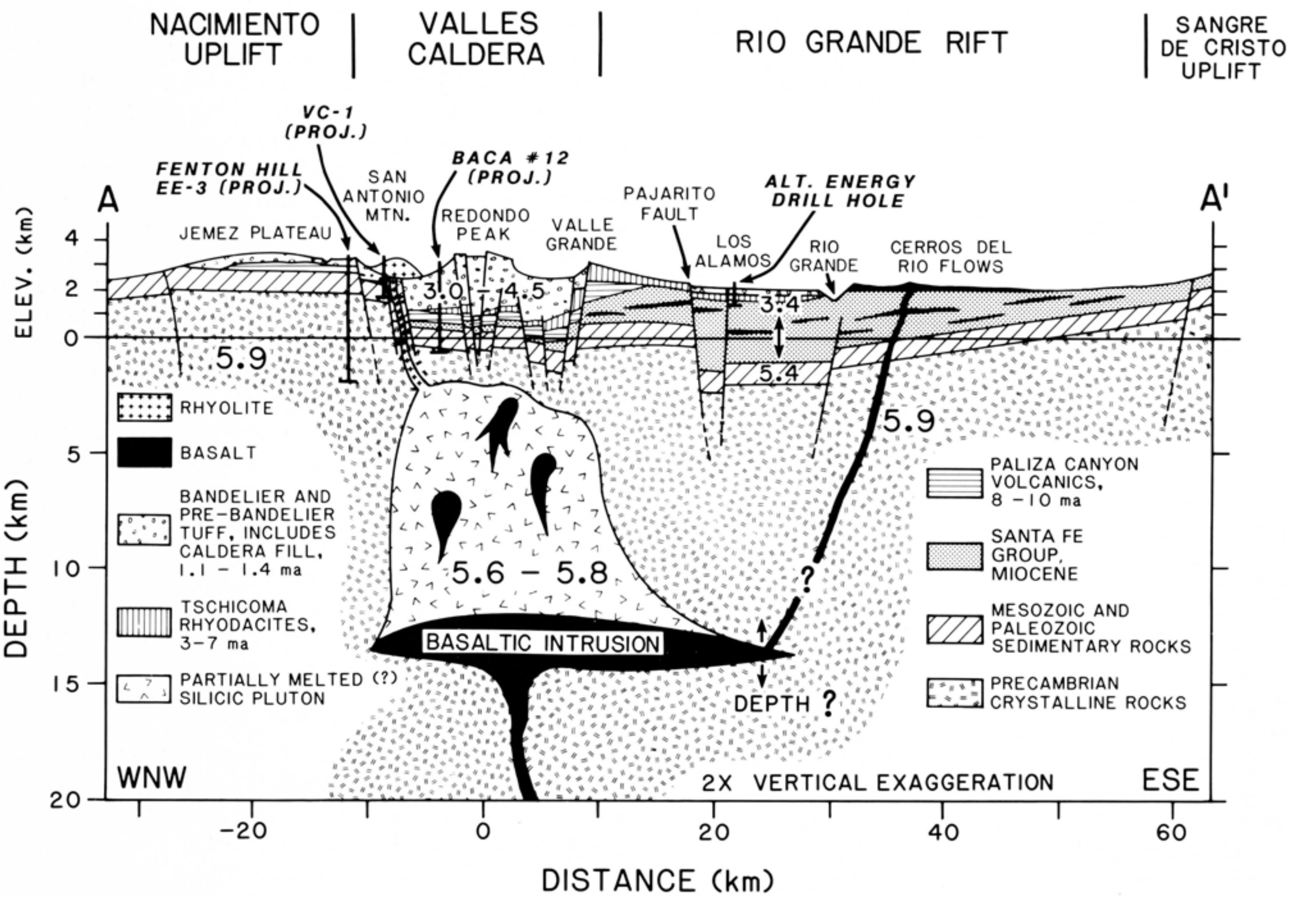

FIGURE 15—A schematic cross section through the Valles caldera and Rio Grande rift based on the three-dimensional inversion interpretation of Ankeny et al. (1986). Velocity values (large numbers) in km/sec are averages determined from the inversion technique. The presence and depth of a tabular basaltic intrusion in the crust are unknown, but, if present, the most likely location would be at the base of the upper crust. For list of references on surface and subsurface control see Ankeny et al. (1986).

TABLE 3—Selected geochemical data for hot springs and geothermal wells, Valles caldera, New Mexico (values in mg/kg except where noted. Locations shown in Fig. 3; data from Goff et al. (1985), Goff et al. (1988), Grigsby et al. (1984), Shevenell et al. (1987), Vuataz et al. (1988), and White (1986); VC-2A data previously unpublished. [a]Acid-sulfate springs occur at Sulphur Springs (Fig. 3). [b]VC-2A data are average of five analyses.

	Hot springs						Geothermal wells						
	Acid-sulfate springs[a]		Thermal meteoric springs		Derivative hot springs		Pore fluid(?) Precambrian rocks		Sulphur Springs	Redondo Creek		Outflow plume	
	Women's Bathhouse Spring	Footbath Spring	Spence Hot Spring	San Antonio Hot Spring	Soda Dam Spring	Main Jemez Spring	EE-3 Fenton Hill	WC23-4 Thompson Ridge	VC-2A[b]	Baca-13	Baca-15	VC-1	JS-1
Sample	S-6-80	S-4-80	VA-120	VA-128	VA-140	VA-216	V56	VA-116	—	BA-1	BA-8	VA-209	VA-15
Date	9/80	9/80	1/83	3/83	2/1/84	10/4/85	5/3/83	1/4/83	8/27/87	6/4/82	9/8/82	9/5/85	1/79
Depth, m							>3000	1921	490	>1000	>1000	483.2	152
Temperature, °C	90	33	42.3	41.3	46.8	73.7	>200	233	210	278	267	111	60.5
pH (field)	1.40	1.10	7.60	7.88	6.71	6.90	6.67	7.10	6.20	7.30	7.12	7.06	6.69
SiO_2	168	214	66	74	47	91	156	450	315	546	441	74	24
Ca	131	56	5.9	3	342	137	140	46.0	5.9	3.35	12.4	49	120
Mg	50.0	26.5	1.6	0.5	21.9	5.1	9.8	0.45	0.14	0.04	0.02	17.8	9.31
Sr	0.14	0.10	0.08	0.06	2.84	0.64	—	1.98	0.76	0.14	0.13	1.33	0.40
Na	18.9	10.8	50	23	960	638	4830	5890	1842	1146	1196	883	185
K	72	94	1.4	1.8	160	68	730	1020	308	244	261	85	29.9
Li	0.17	0.10	0.58	0.06	13.8	8.90	106	68.0	26.5	17.0	15.0	8.00	2.27
Rb	0.1	—	<0.1	—	1.8	0.7	—	—	4.3	2.7	3.1	0.4	—
HCO_3	0	0	140	57.3	1488	745	1100	382	273	168	48	942	479
SO_4	6400	7900	17.1	9.5	34	40.8	51	95	55	42	29	56.8	38.0
Cl	<1	<1	8.2	7.0	1480	917	10500	9960	2943	1897	2093	964	243
F	5.2	10.6	0.76	0.79	3.33	4.99	2.3	13.8	5.68	7.2	5.5	3.94	3.30
Br	<0.4	<0.4	0.10	<0.02	4.60	2.40	71	27.0	5.9	5.3	5.9	2.80	—
B	0.2	0.2	0.12	<0.01	12.1	7.34	272	96.2	25.6	17.0	17.0	8.55	2.20
As	0.04	—	0.05	—	1.5	0.7	18.3	7.8	1.92	1.6	2.3	<0.1	—
δD,‰	–60.8	–82.1	–86.5	–91.6	–84.9	–81.9	—	–71.5	–74.4	–86.0	–84.0	–88.0	–85.9
$\delta^{18}O$,‰	–8.45	–20.4	–12.25	–12.70	–10.56	–10.46	—	–5.05	–7.1	–10.0	–8.7	–11.35	–11.8
$(^{87}Sr/^{86}Sr)m$	0.710614	—	0.708453	—	0.721932	0.721742	—	—	0.718670	0.708423	0.709412	0.715220	—

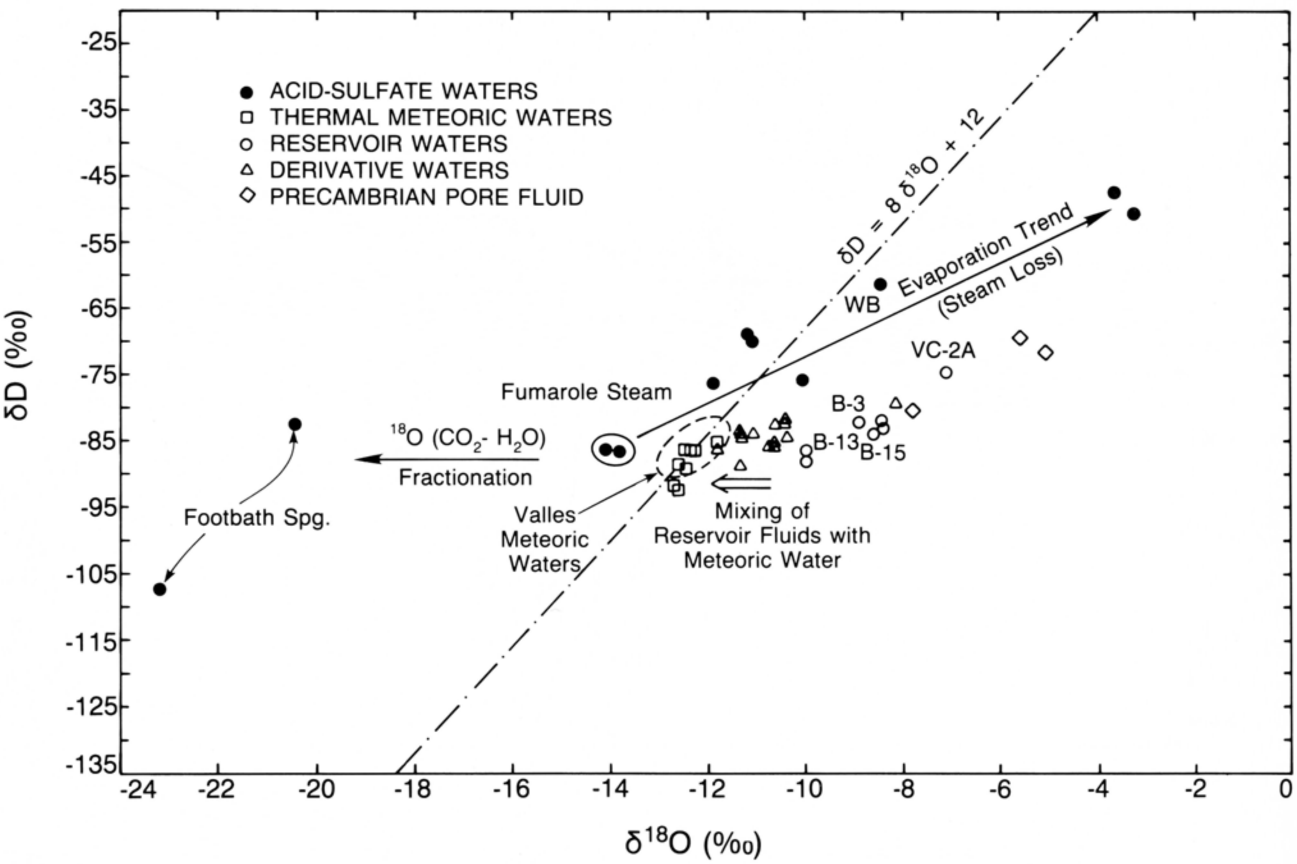

FIGURE 16—Plot of δD versus $\delta^{18}O$ for all thermal water types in the Valles caldera region (data from Vuataz and Goff, 1986; Goff et al., 1988; and unpubl.).

the geothermal reservoir comes from meteoric precipitation and slow infiltration of cool ground water to depth, particularly from the basins of the northern and eastern caldera moat. They also concluded that derivative thermal waters in San Diego Canyon and beneath the southwestern plateaus were mixtures of reservoir water and various cooler ground waters (Fig. 16). Tritium data could only bracket the mean age of reservoir water between 60 and 10,000 years, but an appropriate analytical model has not been applied to the data (e.g., Pearson and Truesdell, 1978). A ^{36}Cl investigation of a limited number of hydrothermal fluids in the caldera (Phillips et al., 1984) concluded that the chloride of the deep Valles hydrothermal fluid was in secular equilibrium with tuffaceous reservoir rocks (half-life of $^{36}Cl = 3 \times 10^5$ yrs).

From examination of thermal-water hydrogeology and hydrogeochemistry in the many geothermal wells drilled inside and outside the caldera (including CSDP corehole VC-1), a reasonably accurate model of the configuration of the present hydrothermal system in the Redondo Creek area can be depicted (Fig. 17) (Faust et al., 1984; Goff et al., 1988). Meteoric precipitation recharges the hydrothermal system, which equilibrates at depths of 2–3 km and at temperatures of about 300°C in caldera-fill tuffs and precaldera volcanic rocks. Thermal waters rise convectively to depths of roughly 500–600 m before flowing laterally to the southwest toward the caldera wall. A vapor zone that contains steam, CO_2, H_2S, and other volatile components has formed above a boiling interface at about 200°C. This interface is the upper surface of a convecting liquid-dominated system. Acid springs, mudpots, and fumaroles occur in a surface condensation zone only a few meters thick (Goff et al., 1987). The lateral flow system crosses the southwestern caldera wall above Precambrian basement through the Jemez fault zone and semipermeable Paleozoic strata. Mixing of reservoir water and other ground waters occurs along the lateral flow path to form derivative waters that issue as hot springs or flow in subsurface aquifers southwest of the caldera. An extremely good correlation is found in the $^{87}Sr/^{86}Sr$ ratio between hydrothermal fluids and coexisting rocks in the geothermal reservoir and its lateral flow system (Vuataz et al. 1988).

The model in Fig. 17 is relatively simple in concept and resembles general models of hydrothermal systems presented by Henly and Ellis (1983). However, we know the hydrothermal system is more complex when examined in detail. Smith and Kennedy (1985) and Truesdell and Janik (1986) demonstrated that the Redondo Creek area contains two somewhat discrete reservoir fluids with subtle differences in chemical and stable-isotopic composition and $^3He/^4He$. A reservoir fluid (separate from Redondo Creek) or set of superimposed reservoirs exists beneath the Sulphur Springs area that is being investigated in CSDP coreholes VC-2A and VC-2B. Inverse variations between temperature and chloride content and stable-isotope variations in the derivative waters southwest of the caldera demand that different reservoir waters and different ground waters produce the mixed waters that are observed (Goff et al., 1988).

Chronology of the hydrothermal system(s)

Hydrothermally altered rocks occur in precaldera volcanic rocks throughout the central and southeastern Valles caldera region (Fig. 18). Based on surface mapping, crosscutting

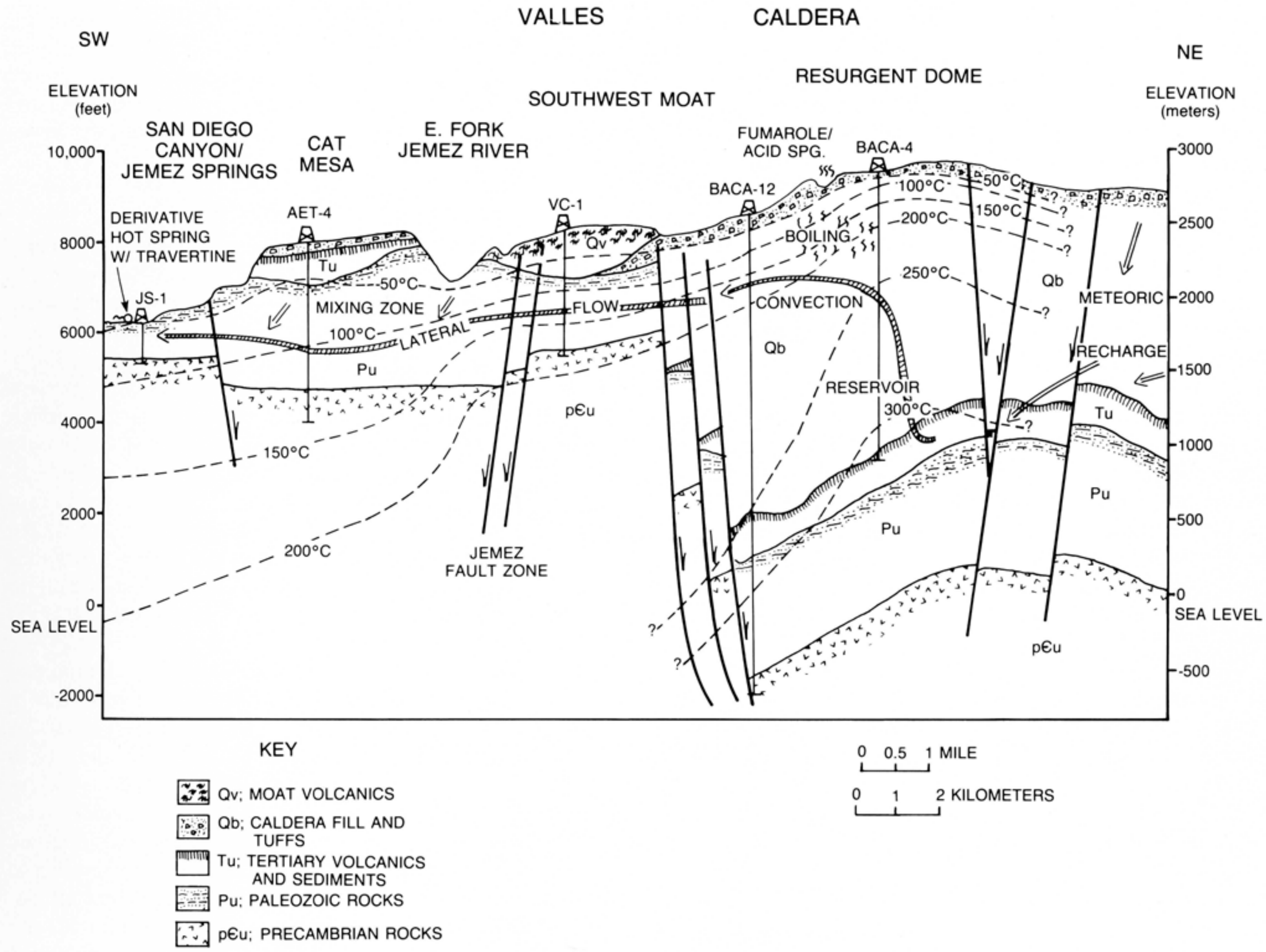

FIGURE 17—Cross section of southwest margin Valles caldera showing general configuration of the active hydrothermal system (modified from Goff et al., 1988). Well locations are shown in Fig. 3.

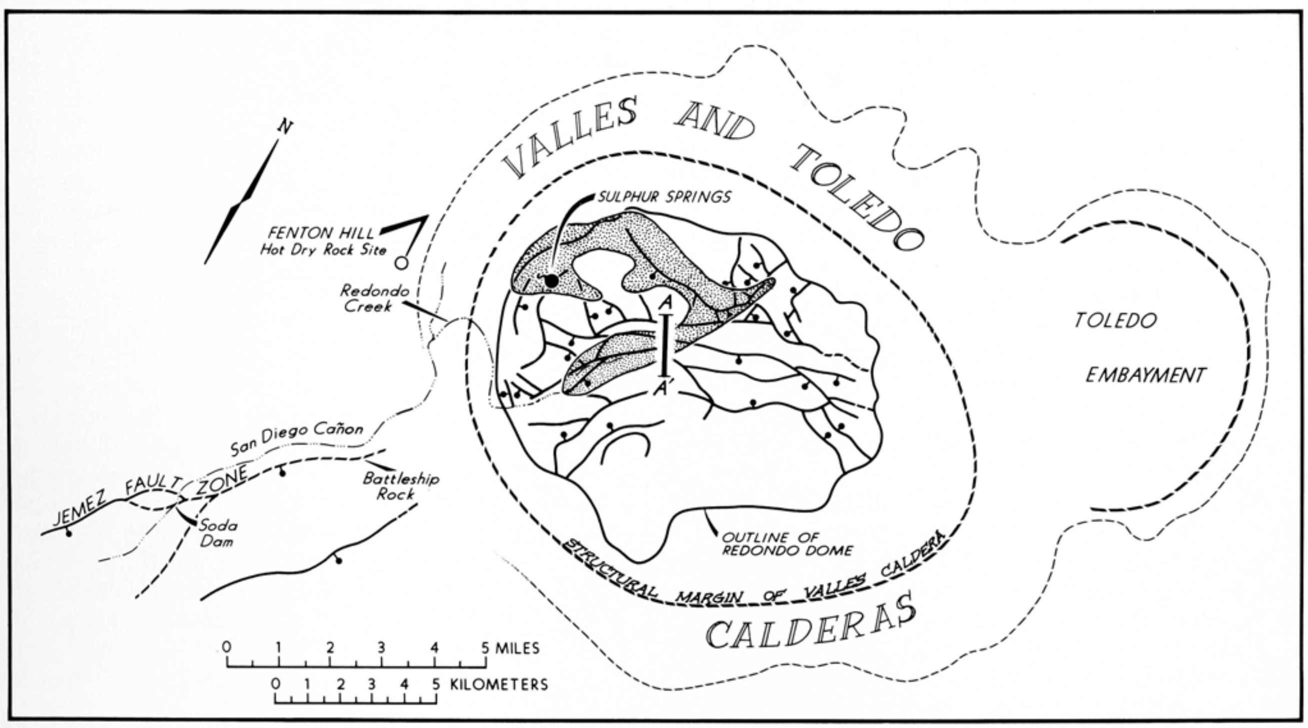

FIGURE 18—Structural map of the interior of Valles caldera showing the extent of active or recent surficial alteration (stippled pattern). Note location of alteration cross section A–A′ (Fig. 19) through the apical graben of the Valles resurgent dome. Sulphur Springs is the location of core hole VC-2A (Fig. 20).

relationships of veins and intrusive rocks, and K–Ar dates on volcanic units, Wronkiewicz et al. (1984) and Gardner et al. (1986) concluded that the gold-bearing quartz veins and hydrothermally altered rocks of the Cochiti mining district in the southeast Jemez Mountains were formed about 6 Ma, considerably more recently than postulated by previous workers. Recent K–Ar dates by WoldeGabriel and Goff (1989) on hydrothermal illites pinpoint this event at 6.5–5.6 Ma. The latter authors have used stable-isotopic evidence to argue that the epithermal deposit was formed from a hydrothermal system composed predominantly of meteoric water. Wronkiewicz et al. (1984) have demonstrated from fluid-inclusion studies that the Cochiti veins were formed at temperatures of about 195–375°C and that the fluids had salinities of about 0–4.9 wt% equivalent NaCl. Gardner et al. (1986) also suggested that other hydrothermal events occurred in the time frame 10–7 Ma in Keres Group mafic to intermediate rocks of the southern Jemez volcanic field, but these altered rocks have been barely studied.

Hydrothermally altered, precaldera volcanic rocks along the northern and western Valles caldera wall (Gardner et al., 1986) and K–Ar dates on hydrothermal illites from altered Paleozoic rocks in CSDP corehole VC-1 (Ghazi and Wampler, 1987) suggest that other hydrothermal events may have occurred between 6 and 1.12 Ma, associated with volcanism of the Polvadera Group or with formation of the Toledo caldera. The absolute ages of these events have not been verified.

Much more is known about the evolution of the hydrothermal system created after formation of Valles caldera. Goff and Shevenell (1987) applied U–Th disequilibrium and U–U dating techniques to the present and ancient travertine deposits at Soda Dam hot springs to show that the hydrothermal system was initiated at about 1 Ma. Ghazi and Wampler (1987) obtained a K–Ar date of 1.0 ± 0.1 Ma on hydrothermal illite from Paleozoic limestone at about 500 m depth in corehole VC-1. Geissman (1988) obtained a reverse magnetic polarity of unique magnetic character on hydrothermally altered Paleozoic rocks in VC-1 and concluded that high-temperature (300°C) fluids permeated the rocks ≥ 0.98 Ma. WoldeGabriel and Goff (1989) dated hydrothermal illite throughout the VC-2A core by K–Ar and obtained ages of 0.83 to 0.66 Ma. Because temperatures in VC-2A are still 200°C at only 400 m depth, these dates may have been slightly reset and could reflect the minimum age of initial hydrothermal activity.

Lateral flow has been a characteristic feature of the hydrothermal system during the last 1 Ma. Dates on the travertine deposits of Soda Dam (Goff and Shevenell, 1987) and U–Th dates on calcite veins in VC-1 core (Sturchio and Binz, 1988) indicate that hydrothermal fluids have discharged continuously from the caldera along the Jemez fault zone throughout this period.

The age of the vapor cap above the liquid-dominated reservoir is less constrained. Goff and Shevenell (1987) suggested that the vapor cap began to form about 0.5 Ma. This age corresponds to cessation of travertine deposition of the oldest, large travertine deposit at Soda Dam and coincides with the age of breaching of the southwest caldera wall and draining of intracaldera lakes (Doell et al., 1968; Nielson and Hulen, 1984). It is postulated that draining of the lakes and resulting loss of hydraulic head on the hydrothermal system caused the maximum elevation of the hydrothermal fluids in the geothermal reservoir to drop (Trainer, 1984). If so, this is a completely different hypothesis for formation of vapor zones above liquid-dominated systems than the "hydrothermal sealing and boiling-down" theory proposed by White et al. (1971). Table 4 summarizes related volcanic, hydrothermal, and geomorphic events of the Valles caldera.

Intracaldera hydrothermal alteration

Well-zoned hydrothermal alteration and metallic mineral assemblages recognized in deep geothermal wells have proven useful not only for locating permeable fluid channels in the Valles hydrothermal system, but also for understanding how that system has evolved with time. For example, we know from detailed alteration studies based on drill cuttings (Hulen and Nielson, 1986a, b) that phyllic (quartz–sericite–pyrite) alteration in the Redondo Creek area is commonly associated with widely spaced but active thermal-fluid entries, and that similar but impermeable phyllic zones represent analogous channels now hydrothermally sealed. We also know that the Redondo Creek sector of the active Valles system (the "Baca" geothermal system) and its alteration are similar in many respects to fossil systems that formed certain epithermal precious-metal ores.

Known areas of intracaldera hydrothermal alteration and mineralization are concentrated at Redondo Creek and in the Sulphur Springs area, site of CSDP coreholes VC-2A and VC-2B (Fig. 18). The two areas differ considerably in alteration mineralogy, texture, zoning, paragenesis, and intensity. At Redondo Creek, for example, only widely scattered fumaroles, gas seeps, and small patches of acid-sulfate alteration indicate the liquid-dominated reservoir boiling at depth (Dondanville, 1978). At Sulphur Springs, by contrast, these thermal phenomena are much more concentrated, and occur within a bleached wasteland devoid of vegetation (Goff and Gardner, 1980; Charles et al., 1986).

Alteration in the Redondo Creek sector of the Valles geothermal system, from the surface through the base of the Miocene Paliza Canyon Formation, is of three principal types: argillic, phyllic, and propylitic (Fig. 19; Hulen and Nielson, 1986a). Argillic alteration forms a weak to moderate intensity, high-level blanket, mostly within the system's present vapor cap, and developed within formerly permeable, non-welded tuffs and tuffaceous sediments. The argillic zone is dominated by Ca-smectite, but includes subordinate, R1-ordered, mixed-layer illite/smectite and kaolin. All but kaolin were probably deposited under water-dominated conditions, even though the present water table is now at a nominal depth of 500 m. Beneath the argillic zone, pervasive propylitic alteration is dominant. Comprising the assemblage chlorite–calcite–epidote–albite–sericite–pyrite–hematite–sphene (in various combinations), this propylitic alteration is weakly developed in the thick, intracaldera rhyolite ash-flow-tuff sequence, but is moderately to strongly developed in the intermediate-composition volcanic rocks of the Paliza Canyon Formation; the deeper, more intense propylitic alteration may be inherited in part from a precaldera (Miocene, as in the Cochiti district?) hydrothermal system. Phyllic alteration, as noted above, is tightly confined to present and past thermal-fluid channels, including fault and fracture zones as well as discrete stratigraphic aquifers.

The deepest well in the Redondo Creek area (B-12; 3424 m) may have penetrated the base of the active Valles geothermal system. Below a depth of 2440 m in B-12, the rocks

TABLE 4—Geochronology of volcanic, hydrothermal, and geomorphic events associated with Valles caldera, New Mexico.

Event	Age	Method	Reference
1. Eruption of Tshirege Member, Bandelier Tuff; formation of Valles caldera.	1.12 Ma	K/Ar	Doell et al., 1968; Izett et al., 1981
2. Uplift of resurgent dome; eruption of early rhyolites.	~1.0 Ma	Inference	Smith and Bailey, 1968
3. Eruption of northern arc of postcaldera moat rhyolites.	1.04–0.45 Ma	K/Ar	Doell et al., 1968
4. Initial formation of Valles hydrothermal system and voluminous travertine deposit at Soda Dam.	~1.0 Ma 1.0 Ma >0.97 Ma	U/U K/Ar Paleomag.	Goff and Shevenell, 1987 Ghazi and Wampler, 1987 Geissman, 1988
5. Formation of Sulphur Springs subsystem of Valles hydrothermal system.	≥0.83 Ma	K/Ar	WoldeGabriel and Goff, 1989
6. Formation of Sulphur Springs molybdenite deposit.	≥0.66 Ma	K/Ar	WoldeGabriel and Goff, 1989
7. Breaching of SW caldera wall; deep erosion of SW caldera moat zone.	~0.5 Ma ~0.5 Ma	Inference K/Ar	Doell et al., 1968; Nielson and Hulen, 1984 Hulen and Nielson, 1988a
8. Cessation of voluminous travertine deposition at Soda Dam.	0.48 Ma	U/U	Goff and Shevenell, 1987
9. Initial formation of vapor zone above liquid-dominated hydrothermal system.	≤0.5 Ma	Inference	Goff and Shevenell, 1987
10. Eruption of southern cluster of postcaldera moat rhyolites.	0.49–0.13 Ma	K/Ar; FT; U/Th	Doell et al., 1968; Marvin and Dobson, 1979; Gardner et al., 1986; Self et al., 1988
11. Partial filling of SW caldera breach.	≤0.65 Ma <0.5 Ma	Paleomag. K/Ar	Geissman, 1988 Hulen and Nielson, 1988a
12. Formation of hydrothermal calcite veins along Jemez fault zone beneath SW caldera moat.	>400–95 Ka	U/Th	Sturchio and Binz, 1988
13. Late hydrothermal fluorite vug in Sulphur Springs subsystem.	~150 Ka?	U/Th	N. Sturchio, unpubl. data
14. Second period of travertine deposition at Soda Dam.	110–60 Ka	U/Th	Goff and Shevenell, 1987
15. Last pulse of thermal activity at Fenton Hill.	40–10 Ka	Transient analysis	Harrison et al., 1986
16. Final period of travertine deposition at Soda Dam.	5 Ka–Present	U/Th	Goff and Shevenell, 1987

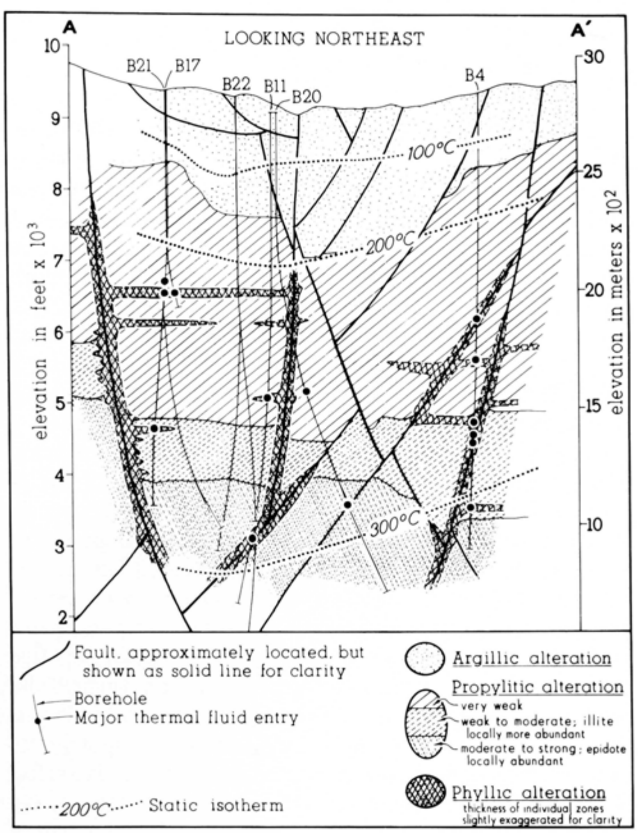

FIGURE 19—Northwest–southeast alteration cross section through the apical graben of the Valles caldera's resurgent dome (from Hulen and Nielson, 1986). Control provided by deep geothermal wells completed by UNOCAL. For location of cross section refer to Fig. 18.

are essentially devoid of veinlets and appear more metamorphic than hydrothermal; they contain high-temperature phases such as diopside and actinolite (Hulen and Nielson, 1986a), possibly formed by isochemical thermal metamorphism. The appearance of these phases and the simultaneous disappearance of veinlets coincide with a prominent change in the downhole temperature profile from an upper, near-isothermal convective signature to one characterized by a steep conductive gradient of about 75°C/km.

The Redondo Creek sector of the Valles geothermal system is similar in many respects to fossil systems which produced Creede-type (or adularia–sericite, or low-sulphur type; Barton et al., 1982; Hayba et al., 1985) epithermal silver/base-metal ores. The Valles and Creede-type systems are similar in terms of tectonic setting, host rocks, alteration mineralogy and zoning, temperature range, fluid type, and geochemical zoning (Hulen and Nielson, 1986a; White and Heropoulous, 1983). The Creede-type systems, however, are generally more saline than the relatively dilute Valles fluids (40,000–120,000 vs. 5000–8000 ppm total dissolved solids), and no Valles borehole has intersected ore-grade silver concentrations. However, argentiferous (up to 71 ppm) pyrite is locally present in well B-17 (Fig. 19) and minor amounts of pyrargyrite (Ag_3SbS_3) were discovered in the upper levels of CSDP corehole VC-2B. It is entirely possible that the relatively widely spaced Valles geothermal wells have missed intervening Creede-type deposits, or that such ores may remain concealed in another part of the Valles caldera complex.

Fluids circulating in the Valles hydrothermal system just southwest of the Valles caldera may have intermittently sealed portions of the Jemez fault zone through deposition of quartz and other hydrothermal phases. This "self-sealing" appears to have led to frequent hydraulic rupture of the Paleozoic and Precambrian rocks penetrated by CSDP corehole VC-1 (Fig. 18; Hulen and Nielson, 1988b). The rupture is recorded by fluid inclusions with homogenization temperatures exceeding those appropriate for a hydrostatic boiling-point curve at the assumed depth of brecciation (see also Sasada, 1988b). The overpressurized fluid responsible for the brecciation apparently also led to intense quartz–illite–phengite alteration and sparse molybdenite mineralization in the resulting hydrothermal breccias.

Alteration and metallic mineralization in the Sulphur Springs area of the Valles caldera complex (Fig. 18) differ considerably from their Redondo Creek counterparts. The Sulphur Springs alteration is much more pervasive and intense, and generally of higher grade than at corresponding levels in the Redondo Creek area. Surficial alteration at Sulphur Springs, mapped by Goff and Gardner (1980), has been studied in detail by Charles et al. (1986), who note that typical acid-sulfate alteration (kaolin–opal–pyrite–alunite–miscellaneous sulfates) is concentrated around active thermal phenomena. Although this acid-sulfate alteration is the surface expression of an underlying vapor cap on a deep, liquid-dominated geothermal system (Goff et al., 1985, 1987), it is superimposed on an older, higher-temperature, liquid-dominated assemblage. Subsurface alteration in Sulphur Springs area geothermal wells and scientific coreholes has been characterized by Hulen and Nielson (1986b), Hulen et al. (1987), Sasada (1987), Gonzalez and McKibben (1987), Bayhurst and Janecky (1987), and Janecky et al. (1987). In the northern part of the Sulphur Springs area, as exemplifed by borehole B-8, a high-level, mixed-layer illite/smectite zone overlies an intermediate-depth phyllic interval which in turn overlies an unusual adularia–illite–quartz–epidote zone (Hulen and Nielson, 1986b). The illite in this zone is late-stage, replaces adularia, and is believed to indicate a shift toward more acidic conditions after adularia deposition.

Hydrothermal alteration of the rocks penetrated by CSDP corehole VC-2A is the most intense and pervasive yet encountered in any Valles borehole. The alteration is separable into an intense, upper phyllic zone (0–163 m depth) and a subjacent, mostly moderate-intensity chlorite–sericite zone (163–528 m; Fig. 20; Hulen et al., 1987). The high-level phyllic zone is notable in containing a unique occurrence of poorly crystalline molybdenite, locally reaching concentrations of 0.56 wt% in scattered breccia zones. The molybdenite occurs in veinlets and vugs intergrown with quartz, sericite, fluorite, and pyrite, and locally with traces of rhodochrosite, sphalerite, and chalcopyrite. Fluid-inclusion homogenization temperatures obtained for quartz and fluorite intergrown with the molybdenite suggest that it was deposited from dilute liquid at temperatures averaging about 200°C (Hulen et la., 1987; Sasada, 1987; Gonzalez and McKibben, 1987).

Clay mineralogy and zoning in VC-2A support fluid-inclusion data in suggesting that a high-temperature, liquid-dominated reservoir once extended up to, and probably above, the level of the present ground surface in the Sulphur Springs area (Hulen and Nielson, 1988b), even though the system is now vapor-dominated to a depth of at least 240 m. Textural evidence from VC-2A core suggests that the high-temperature alteration postdated or accompanied the waning stages of resurgent doming. Baca-8, located north of VC-2A, has shown a similar cooling and drop in the water table (Hulen and Nielson, 1986b). Wells in the Redondo Creek area also show cooling of 50–100°C relative to past activity; this temperature decline has been attributed to draining of an intracaldera lake (Hulen and Nielson, 1988b).

Intense sericitization affects the uppermost in-place rocks penetrated by the VC-2A corehole. This high-level sericite is principally R3-ordered, illite-rich, mixed-layer illite/smectite (I/S), which, according to the methods of Srodon (1980) and Srodon and Eberl (1984), contains an average 5–10% interlayer smectite. Numerous clay studies (e.g., McDowell and Elders, 1980; Steiner, 1968; Muffler and White, 1969) in active geothermal systems worldwide have shown that illitic I/S of this type forms under water-dominated conditions at temperatures near 200°C. This is also the approximate average homogenization temperature for primary fluid inclusions in quartz and fluorite intergrown with the sericite at high levels in VC-2A. Thus, both fluid-inclusion and sericite geothermometer data indicate that the present vapor-zone evolved from a much higher-temperature, liquid-dominated precursor.

Conclusions

The major conclusions that we would like to stress are as follows:

1. The Jemez volcanic field has been continuously active for more than 13 Ma and volcanic rocks are predominantly calc-alkaline in composition. Although basaltic to rhyolitic rocks have been produced, the most voluminous pulses of activity consisted of two-pyroxene andesite erupted from about 10 to 7 Ma and high-silica rhyolite erupted from 1.45 to 0.13 Ma. Petrogenesis of the older volcanic sequences involved mostly fractional crystallization, although magma mixing and melting of lower crust were involved in some of the more silicic rocks. Volcanism is intimately related to tectonic activity associated with the RGR and the JVL.

2. High-silica rhyolite ignimbrites erupted from the evolving "Bandelier" magma chamber were first produced as early as 3.64 Ma from the approximate center of the volcanic field. It is now known that the Valles caldera complex contains at least two small and two large calderas, but the earlier collapse features have been nearly obliterated by Valles caldera (1.12 Ma). Several petrologic studies indicate that the Bandelier magma chamber is compositionally zoned, but the petrogenesis of the chamber (estimated volume at least 3000 km^3) is still not resolved.

3. The subsurface structure of the caldera complex is controlled by northeast-trending structures associated with the earlier RGR and JVL. Drill holes throughout the southwestern sector of the caldera and gravity modeling over the entire caldera indicate that the caldera-fill sequence is three or more times thicker than originally proposed and that the depth of the caldera floor is asymmetric, relatively shallow on the west and deep on the east. As a result, the interior structure of the resurgent dome is much more complex than previously thought. Drilling results have not verified that resurgence occurred after the comparably sized and coincident Toledo caldera (1.45 Ma). Structural models and petrologic studies indicate that the roof of the Bandelier magma chamber was at a depth of 5–6 km when the Tshirege Member was vented and that the eruption temperature varied from 700 to 850°C.

4. The highest convective heat flow and subsurface seismic attenuation in the caldera complex occur in the southwestern sector coincident with the main zones of hydrothermal upflow and the youngest moat rhyolite eruptions (<0.5 to 0.13 Ma). Two different investigations in the thick Precambrian section on the west caldera margin indicate that subsurface temperatures beneath the caldera may be increasing. If so, the "reheating" must be caused by evolution of the new batch of "mafic" rhyolite in the southwestern moat.

5. The Valles hydrothermal system is configured like most volcanic-hydrothermal systems the world over. The basic hydrologic elements consist of local meteoric recharge, equilibration at temperatures approaching 300°C, convective upflow along faults and fractures, and lateral flow along structures that cut the southwestern caldera wall (Jemez fault zone). A vapor zone and acid-sulfate condensation zone

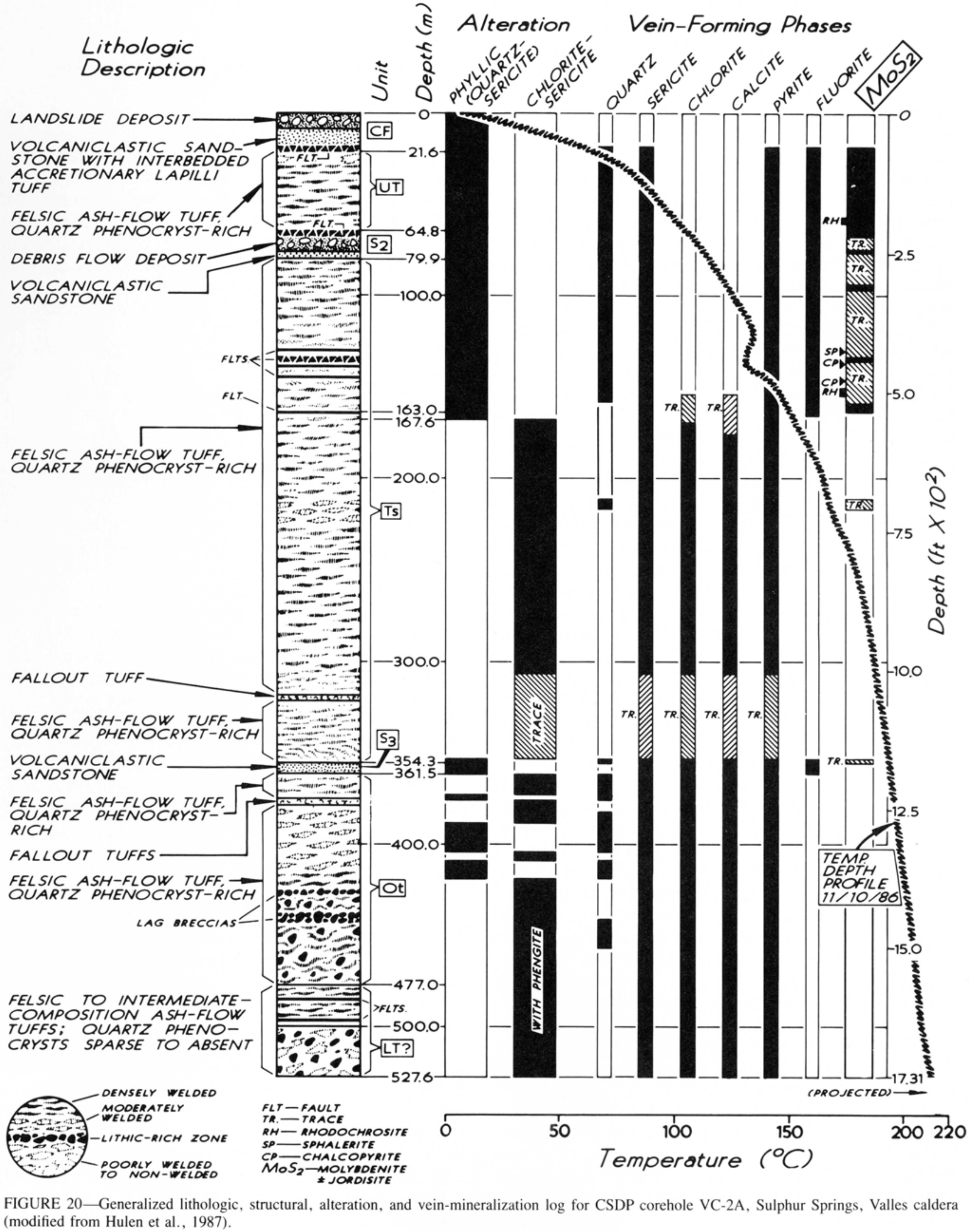

FIGURE 20—Generalized lithologic, structural, alteration, and vein-mineralization log for CSDP corehole VC-2A, Sulphur Springs, Valles caldera (modified from Hulen et al., 1987).

originate from subsurface boiling (200°C) above the liquid-dominated reservoir inside the caldera. The lateral flow system produces a subsurface tongue of mixed reservoir water and cooler ground waters in Paleozoic rocks around the southwestern caldera margin. The areal extent of the geothermal reservoir inside the caldera is 10 to 30 km^2, but permeability is extremely localized. About 20 MW(e) was proven by UNOCAL before they terminated their lease in 1984.

6. Episodic hydrothermal events have occurred in the Jemez volcanic field for about the last 8 Ma (e.g., the Cochiti gold–silver district at 6.5–5.6 Ma). The Valles hydrothermal system has been continuously active for the last 1 m.y., but the vapor zone first formed about 0.5 Ma. Creation of the vapor zone is apparently linked to breaching of the southwestern caldera wall by the ancestral Jemez River, draining of intracaldera lakes, and resulting loss of hydraulic head on the liquid-dominated hydrothermal reservoir.

7. Hydrothermal alteration and ore mineralization in Valles caldera resemble those found at many fossil calderas hosting economic ore deposits. Alteration style ranges from advanced argillic to anhydrous calc-silicate, depending on depth and location. Secondary mineral assemblages and fluid-inclusion studies indicate temperatures of formation and salinities similar to those presently occurring in the hydrothermal system, although a complex evolutionary history can be unraveled. Sub-ore-grade molybdenite (up to 0.56 wt% MoS_2) is the primary ore mineral found so far, but Cu, Pb, Zn, Mn, and Ag minerals have also been recently identified.

First-day road log: Tectonic and magmatic development of the southern Jemez volcanic field

Summary—The route of the first day takes us across the southern Jemez Mountains where we will see representatives of most precaldera magma types described by Gardner (1985) and Gardner et al. (1986). Although most of the rocks we will look at today are of the Keres Group, the group also contains rocks petrologically analogous to rocks of the Polvadera Group. We will also view the Pajarito fault zone, which is a major active fault along the Rio Grande rift, and deposits of the Cochiti Formation. Much of the early tectonic activity in the volcanic field's history can be interpreted by analysis of the Cochiti deposits.

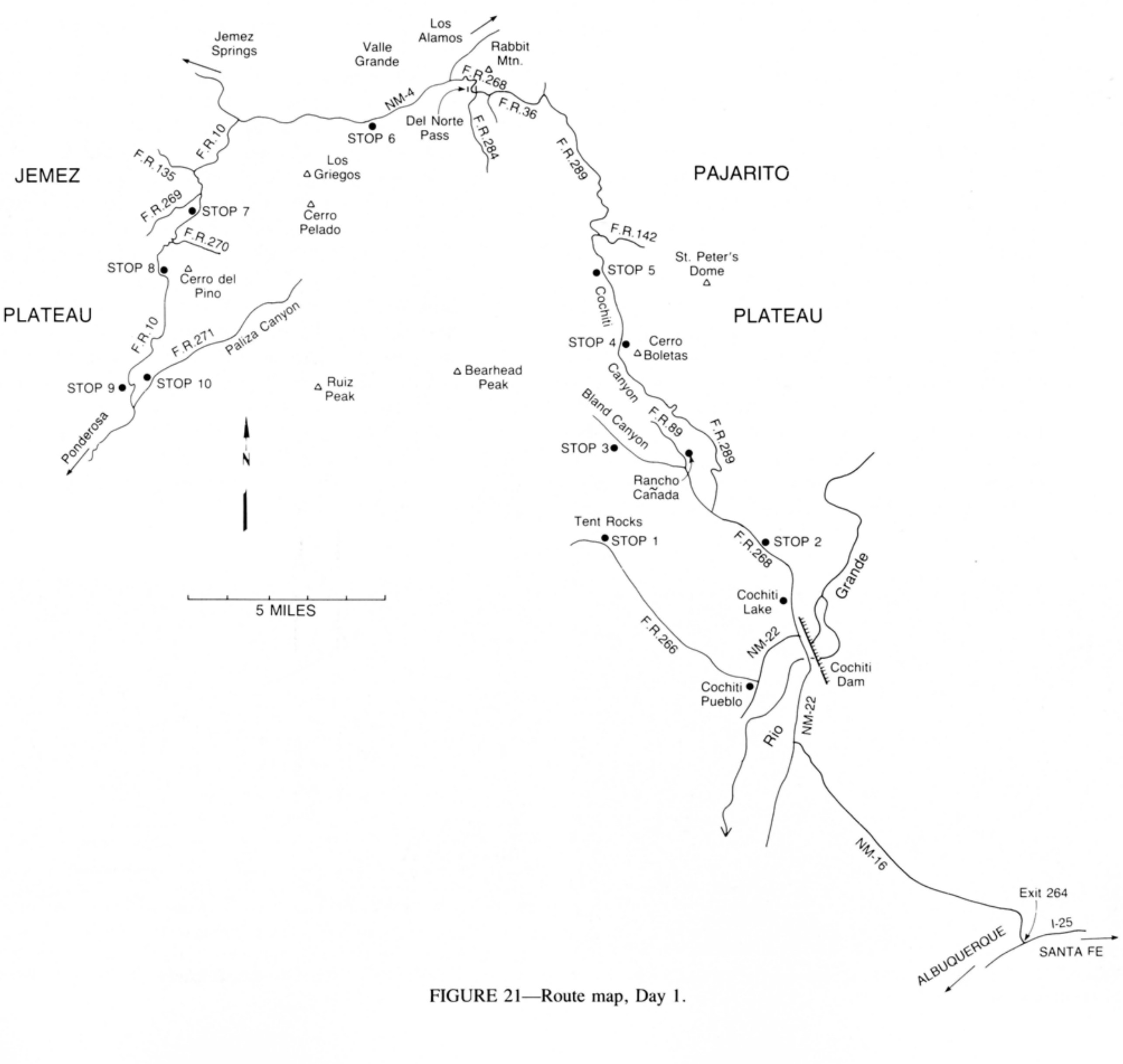

FIGURE 21—Route map, Day 1.

Mileage

0.0 Overpass at junction I-25 and US-285 on south side of Santa Fe. Head south on I-25 into the southern Española Basin of the Rio Grande rift. Between 1:00 and 3:00 in distance are the Jemez Mountains. In middle distance are the low hills of the Cerros del Rio. At 10:00 are the Ortiz Mountains; the white scar marks the Ortiz gold mine. **10.6**

10.6 On left are the Cerrillos Hills, consisting of Oligocene volcanic rocks and plutons known for their turquoise mines. On right, roadcuts of Santa Fe Group and basalts of Cerros del Rio. **3.8**

14.4 Santo Domingo Basin of the Rio Grande rift comes into view with Sandia Mountains on skyline. **1.4**

15.8 Head of La Bajada grade, a fault scarp separating the Santo Domingo and Española Basins. **1.3**

17.1 **Exit** on turnoff #264 toward Cochiti Pueblo. **0.2**

17.3 **Turn right** on NM-16. **0.9**

18.2 Zia Sandstone of Oligocene age (white outcrops) at base of La Bajada fault on right. **5.1**

23.3 Junction with road to Cochiti Lake; continue on NM-16. **2.0**

25.3 Junction with NM-22. **Turn right** toward Cochiti Pueblo. **2.6**

27.9 **Turn left** toward Cochiti Pueblo on NM-22. **1.7**

29.6 **Turn right** on Forest Road (FR) 266 (dirt road) toward Bear Springs. **1.2**

30.8 Rift-fill gravels on hills at right. **1.3**

32.1 Bandelier Tuff overlies rift sedimentary rocks on right. **2.3**

34.4 **Turn right** on dirt road toward white cliffs. **0.1**

34.5 **STOP 1. Peralta Tuff Member of the Bearhead Rhyolite.** Park anywhere on dirt road. This is the type area for the Peralta Tuff Member of the Bearhead Rhyolite (Bailey et al., 1969). Here the bedded, high-silica rhyolitic pyroclastic rocks are mainly reworked or water-lain tuffs with subordinant fallout and flow units (Fig. 22). The tuff was apparently vented from within a dome and flow complex of high-silica Bearhead Rhyolite about 10 km northwest of here. Sanidine from pumice lumps, collected about 200 m north of here, yielded a K–Ar age of 6.85 ± 0.15 Ma (Gardner et al., 1986). The Peralta Tuff forms a prominent stratigraphic marker in the southern Jemez Mountains, and as such approximates the somewhat arbitrary boundary, at about 7 Ma, between the Canovas Canyon and Bearhead rhyolites (Gardner et al., 1986). These two rhyolite formations are the products of a continuum of high-silica rhyolite volcanism from 13 to about 6 Ma. The Bearhead Rhyolite represents an apparent volumetric pulse that postdated most of the voluminous andesitic activity of the southern Jemez Mountains. Working within the rift basin to the south, Kelley et al. (1976) included the tuffs at this locality as a facies of the Santa Fe Group rift-fill sequence. These are also some of the most photographed "tent rocks" in New Mexico.

Turn vehicles around and retrace route to Cochiti Pueblo. **4.9**

39.4 **Turn left** on NM-22 toward Cochiti Dam. **1.6**

41.0 Junction, **turn left** on FR-268 toward town of Cochiti Lake. **2.1**

43.1 **STOP 2. Vista of the southeastern Jemez Mountains.** Park on right side of road just beyond summit of hill. From this vantage point we can look west-northwest and see Tertiary to Quaternary domes and ignimbrites of the southeastern Jemez volcanic field (Fig. 23). The rounded hills are primarily andesitic and rhyolitic domes of the Keres Group (>13–6 Ma). Bearhead Peak is the type locality of the Bearhead Rhyolite. Cerro Boletas is a sequence of bedded rhyolite tuffs of the Bearhead Rhyolite. Cerro Picacho is yet another Bearhead dome and St. Peter's Dome is a complicated pile of andesitic lavas and interstratified volcaniclastic rocks (both to right of photo). Low places in volcanic rocks of the Keres Group were subsequently filled by the mesa-forming Otowi and Tshirege Members of the Bandelier Tuff (1.45–1.12 Ma) erupted from the Toledo and Valles calderas. The visible scarp is the Pajarito fault, which has been periodically active in this area over the last 16 Ma. In the foreground are various sedimentary units that are mostly Quaternary in age and have been shed from the Jemez Mountains toward the Rio Grande.

Continue straight ahead (FR-268). **1.2**

44.3 Golf course on right; begin dirt road. **0.8**

45.1 Junction FR-289 on right; continue straight ahead on FR-268. **1.4**

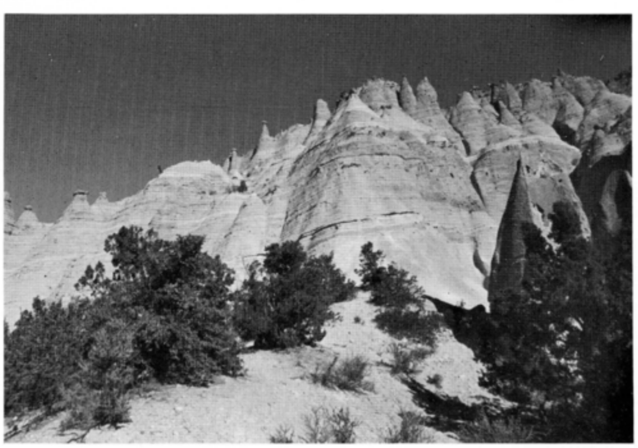

FIGURE 22—Peralta Tuff type section; lower Peralta Canyon, Jemez Mountains. View to north.

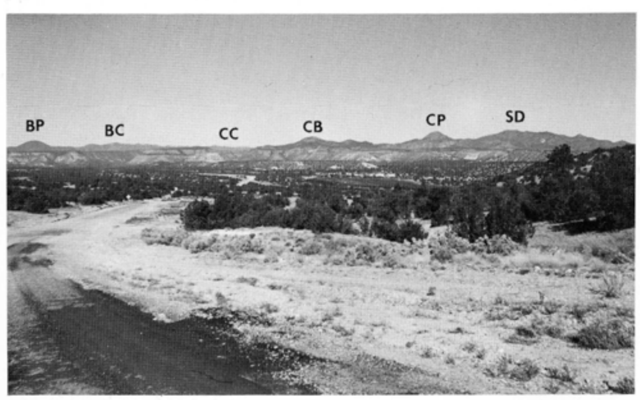

FIGURE 23—View to west-northwest of southeastern margin of the Jemez volcanic field; BP = Bearhead Peak, BC = Bland Canyon, CC = Cochiti Canyon, CB = Cerro Boletas, CP = Cerro Picacho, and SD = St. Peter's Dome.

46.5 Junction FR-89; **bear left** toward Bland Canyon. **1.3**

47.8 Mouth of Bland Canyon; mesas on both sides are capped with Bandelier Tuff and mesa on right has a large, ancient pueblo ruin. **0.3**

48.1 **STOP 3. Pajarito fault in Quaternary terrace gravel.** Park along road near culvert and walk 150 m south to small hill along Bland Creek. The outcrop adjacent to Bland Creek shows a high-angle trace of the Pajarito fault that dips southeast toward the Rio Grande rift (Fig. 24). The fault juxtaposes 6.85 Ma Peralta Tuff (west) against Quaternary terrace gravels shed from the Jemez Mountains. The fault is easily followed in either direction from here and produces spectacular benches in mesas of Bandelier Tuff. Because this exposure is one of the best along this sector of the fault and involves post-Bandelier Tuff rocks, it has been considered as a site for trenching to document possible Holocene movements (Gardner and House, 1987).

Turn around and retrace route (east) to FR-289 (past FR-89). **3.0**

51.1 **Turn left** on FR-289 toward low ridge. **0.2**

51.3 Cattleguard; as you cross over ridge note that Bandelier Tuff is capped with Quaternary gravels. **1.8**

53.1 Contact between Otowi and Tshirege Members of the Bandelier Tuff can be seen in roadcut on left and across canyon to right. **1.4**

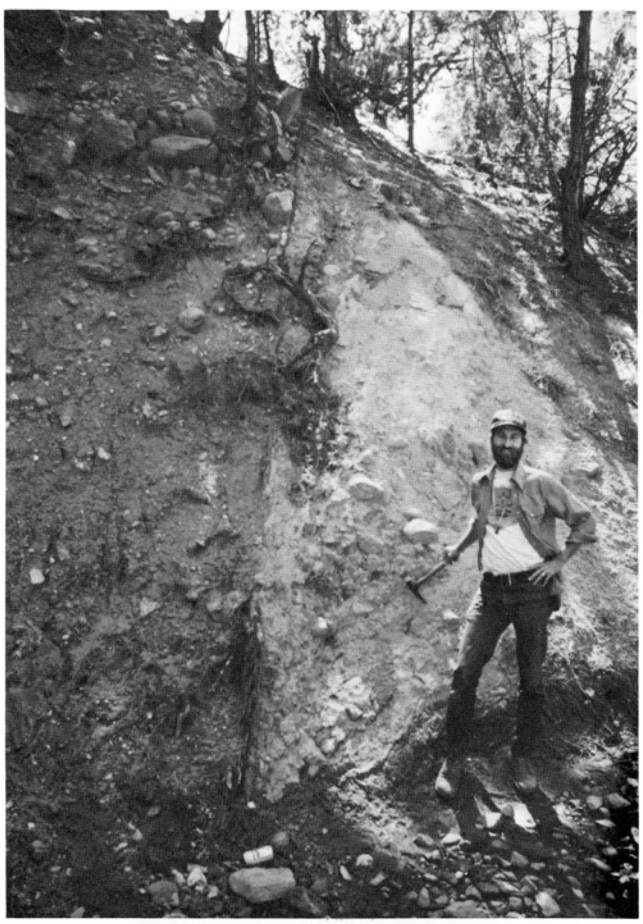

FIGURE 24—Pajarito fault on southwest side of Bland Creek; Quaternary terrace gravels (left) are juxtaposed against the Peralta Tuff (6.85 Ma) of the Bearhead Rhyolite.

54.5 Ascend Pajarito fault scarp. **0.7**

55.2 Tshirege Member of Bandelier Tuff over Keres Group gravels and andesites on right; good view of Pajarito fault zone to left. **0.7**

55.9 Ridge at right is capped with two-pyroxene andesites of the Paliza Canyon Formation (Keres Group), but flanked by younger Bandelier Tuff. **0.2**

56.1 Landslide overlook into Cochiti Canyon on left. **1.3**

57.4 **STOP 4. Intrusive Bearhead Rhyolite.** The hill on the right is Cerro Boletas, which is composed primarily of well-bedded Peralta Tuff (6.85 Ma) of the Bearhead Rhyolite. Along the road we can see a vertically sheeted intrusion of Bearhead Rhyolite that is devitrified to the southeast but is glassy to the northwest along the intrusive contact with tuff. This intrusion has a K–Ar age of 6.2 Ma and is very typical of Bearhead and Canovas Canyon rhyolitic intrusive rocks (13–6 Ma) exposed in the labyrinth of canyons in the southeastern Jemez Mountains. Using major- and trace-element chemistry and strontium-isotope data, Gardner (1985) concluded that these rhyolites were derived primarily from partial melts of lower crust (see Table 1).

Continue straight ahead on FR-289. **2.4**

59.8 **STOP 5. Cochiti Canyon overlook. Turn left** into turnout by edge of cliff. We are looking southeast into Cochiti Canyon, which exposes orange cliffs of Bandelier Tuff overlying a thick sequence of gravels of the Cochiti Formation (Fig. 25). Near the bottom of the canyon some hydrothermally altered andesite flows are interbedded with the gravels. The Cochiti Formation dips primarily to the south and east toward the Rio Grande rift and apparently fills in paleotopography that developed between the evolving Keres Group andesitic volcanoes. Ages of these andesites in this area range from 9.5 to 8.5 Ma (Gardner et al., 1986).

Continue straight ahead on FR-289. **0.6**

60.4 Junction of FR-142 to St. Peter's Dome; **bear left** on FR-289. **0.2**

60.6 Road now winds through cluster of andesitic and dacitic domes and lavas of the Paliza Canyon Formation of the Keres Group (see Table 1). **0.8**

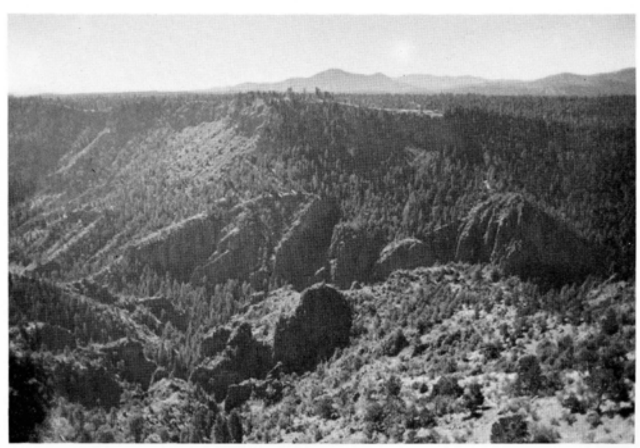

FIGURE 25—View south into Cochiti Canyon; canyon exposes thick sequence of Cochiti Formation capped by the Bandelier Tuff. Bearhead Peak rises in central distance.

61.4 Two-pyroxene andesite dome and vent at summit of hill. **1.1**

62.5 Road winds over north shoulder of coarsely porphyritic dacite dome. **1.3**

63.8 View of Rabbit Mountain (1.4 Ma), a post-Toledo caldera dome of Cerro Toledo Rhyolite (Stix et al., 1988). Chemically, this rhyolite is extremely similar in composition to the rhyolite vented at Cerro Toledo (Table 1). **0.7**

64.5 Junction FR-248; **bear left** on FR-289. **0.7**

65.2 Junction FR-36 at Graduation Flats; **turn left** on FR-36. **1.6**

66.8 Bedded rhyolitic tuffs erupted from Rabbit Mountain along road. These tuffs are described by Heiken et al. (1986). **0.2**

67.0 Hydrothermally altered Keres Group andesitic lavas. **0.5**

67.5 Junction FR-268; **turn right** on FR-268. Redondo Peak on skyline. **0.3**

67.8 Junction FR-284 on left; **continue ahead** on FR-268. **0.2**

68.0 Del Norte Pass; descend into Valles caldera along southeast caldera wall in hydrothermally altered andesitic and rhyolitic lavas. **1.0**

69.0 Junction with NM-4; **turn left** on pavement. Redondo Peak and South Mountain Rhyolite straight ahead. Keres Group andesites and dacites of Los Griegos and Los Conchas Peak to left (south). Drive into southeastern moat of Valles caldera. **1.7**

70.7 Vertically sheeted core of South Mountain flow (0.49 Ma) of Valles Rhyolite on right. **1.0**

71.7 **STOP 6. South Mountain Rhyolite and hydrothermally altered basaltic lavas.** Pull off into parking area of campground or along side of NM-4. At this location we can observe the geology of the southern moat of Valles caldera. South Mountain Rhyolite (north side of highway) is a postcaldera, crystal-rich, high-silica rhyolitic lava (0.49 Ma) that flowed over and against caldera wall rocks. At this point, caldera wall rocks consist of hydrothermally altered basalt of the Paliza Canyon Formation, Keres Group (Fig. 26). The age of the alteration is not known. The alteration may be correlative with hydrothermal events in the Cochiti mining district ($\geq$6 Ma) or it may be associated with hydrothermal systems formed after creation of Valles and Toledo calderas ($\leq$1.45 Ma). Zones of alteration such as these occur at a few places along the west, north, and southeastern wall of the caldera, but they have only been investigated recently (Gardner et al., 1986; WoldeGabriel, 1989).

Continue west on NM-4. **1.0**

FIGURE 26—Landslide block of hydrothermally altered Paliza Canyon basalt along southern wall of Valles caldera.

72.7 El Cajete Pumice overlies South Mountain Rhyolite. **2.4**

75.1 **Turn left** on FR-10 (unmarked) at the long row of mailboxes. **1.4**

76.5 Ascend south caldera wall in Bandelier Tuff and enjoy views of Redondo Peak and southern moat of Valles caldera. **1.0**

77.5 Junction with FR-135 at rim of caldera; **continue straight ahead** on FR-10 toward Ponderosa. **0.8**

78.3 Junction with FR-269; **bear left** on FR-10. **1.1**

79.4 **STOP 7. Two-pyroxene andesitic lava of the Paliza Canyon Formation.** This andesite, although a bit glassy, is fairly typical of the rocks that originally constituted half of the volume (1000 km^3) of the entire volcanic field. The Paliza Canyon andesites contain augite, bronzite–hypersthene, labradorite–andesine, magnetite–illmenite $\pm$ minor olivine as phenocrysts. All phenocryst phases occur in clots that apparently represent the form in which the minerals were removed from the magmas during fractional crystallization. Chemically, this andesite closely resembles "Type 1" Paliza Canyon Andesite in Table 1 and appears to be derived from fractional crystallization of basalt (Gardner, 1985).

Continue ahead on FR-10. **0.9**

80.3 Tshirege Member, Bandelier Tuff on left; Cerro del Piño straight ahead. **0.1**

80.4 Descend grade through tilted and faulted sequence of Santa Fe Group sedimentary rocks and Keres Group basalt flows. **0.6**

81.0 Junction with FR-270; **bear right** on FR-10. **1.1**

82.1 **STOP 8. Cerro del Piño dacite of the Paliza Canyon Formation.** We have just driven around the toe of a thick flow vented from a dome about 2 km east of here. This is the westernmost dome of a 6 km long chain of dacite domes that have a curious east–west trend. We have identified no structural control on the trend of this dome complex which is, in fact, transverse to the main structural grain of the Jemez Mountains. The Cerro del Piño dacite occurs in large boulders of float in the gully at the bend in the road. The rocks are typical of Paliza Canyon dacite (Type 1, Table 1) and are megascopically identical to dacites of the Tschicoma Formation. The dacite contains phenocrysts of plagioclase, augite, bronzite–hypersthene, hornblende $\pm$ minor biotite. Cores of plagioclase phenocrysts are identical to those in the andesites, but rims and microlites range to oligoclase. The megascopic "mafic" inclusions consist of vesiculated glass, acicular hornblende, and skeletal Ca-plagioclase. These inclusions may represent basaltic magma that was injected into the differentiating dacitic chamber (Eichelberger, 1980).

Continue ahead on FR-10. **2.8**

84.9 **STOP 9. Overlook of Paliza Canyon and Borrego Mesa.** From this perch atop the Tshirege Member of the Bandelier Tuff, we can see ridges of Paliza Canyon andesite cut by faults of the Cañada de Cochiti fault zone (east to southeast); Borrego Mesa, basalt capped with andesite (9 Ma; Luedke and Smith, 1979) (south-southeast); the transition from the Albuquerque Basin of the Rio Grande rift to the Colorado Plateau (south to southwest); a distant Mount Taylor, the next volcanic field of the Jemez lineament to the southwest; and the Nacimiento Mountains, a Laramide structure (southwestern to western skyline).

Continue ahead on FR-10. **2.1**

87.0 Poorly exposed Triassic red shales of Chinle Formation. **0.1**

87.1 **Turn left** on FR-271 toward Paliza Canyon. **0.5**

87.6 Gravels of Cochiti Formation on left. **0.4**

88.0 **STOP 10. Dacitic plug and Cochiti Formation deposits.** Pull off along side of road beyond cattleguard. This volcanic plug is one of several in the southern Jemez Mountains that show geochemical similarities to dacite of the Tschicoma Formation. Petrologically, these dacites appear to have been generated by mixing of andesite and high-silica rhyolite magmas. This plug probably intruded surrounding Cochiti Formation gravels, which are well exposed about 100 m farther up the canyon. This is close to the western limit of the Cochiti Formation. Here the maximum thickness of the immature basin-fill sequence is about 30 m, but the formation thickens to over 300 m eastward into the rift.

Turn around and retrace route toward south. **0.9**

88.9 Junction with FR-10; **turn right** and retrace route (about 12 mi) back to NM-4; **turn right** and drive about 22 mi to Los Alamos.

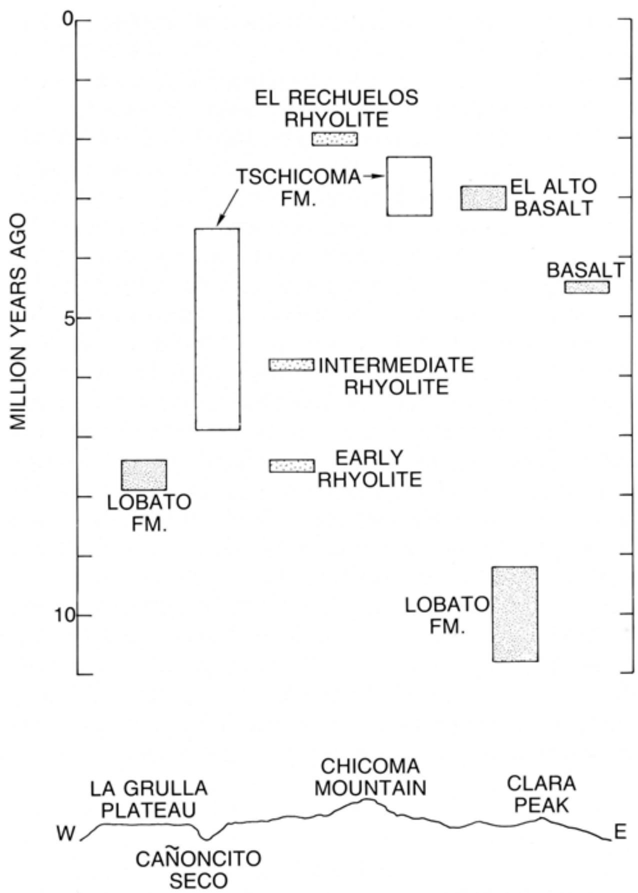

FIGURE 27—Generalized stratigraphic relations of volcanic units in the northern Jemez volcanic field. Units are arranged schematically from west (left) to east (right). Note, however, that distribution of Tschicoma Formation is portrayed simplistically; much overlap of older and younger dacites actually occurs. A schematic topographic profile is shown across the bottom of the figure.

Second-day road log: Tectonic and magmatic development of the northern Jemez volcanic field

Summary—This day's field trip focuses on rock types and stratigraphic relationships of the northern Jemez volcanic field. The basic stratigraphy for the area was established by Bailey et al. (1969) and Smith et al. (1970). Volcanic rocks range in age from 10.8 to 2.0 Ma and in composition from basalt to rhyolite. The earliest rocks are predominantly basalts (but include minor volumes of dacite) erupted in the eastern part of the area 10.8–9.2 Ma ago (Fig. 27). The sources for the basalts included several broad shield cones. These basalts were followed (7.9–7.4 Ma ago) by a suite of rocks ranging from basalt to dacite erupted in the western part of the area. Evolved rocks of this suite were probably derived from the basaltic endmember by a combination of fractional crystallization and assimilation of granitic crust (Singer and Kudo, 1986). Rocks from both of these areas were defined as Lobato Basalt by Bailey et al. (1969) and Smith et al. (1970). Because of the range of compositions (basalt to dacite), Baldridge and Vaniman propose to rename this unit Lobato Formation. In addition, a single dome of rhyolite ("Early Rhyolite" of Loeffler et al., 1988) was erupted 7.5 Ma ago.

Large volumes of andesites, dacites, and rhyodacites were erupted 6.9–2.3 Ma ago. K–Ar dates define two main periods of activity: 6.9–3.5 and 3.3–2.3 Ma ago. Rocks of the older phase of activity, which consist mainly of hornblende- and biotite-bearing dacites, many containing mafic clots, are exposed predominantly in the western part of the area. Flows on the northern flank of the Valles/Toledo calderas were erupted from highlands (named by us the "precaldera highlands"; Baldridge et al., 1987) that existed in the area presently occupied by the calderas. These highlands subsequently collapsed and were buried during caldera formation, leaving only the flows on the lower slopes exposed. Fewer dacitic lavas from the highlands are recognized after the first rhyolitic ignimbrites were erupted from the developing Bandelier magma chamber at 3.6 Ma.

Rocks of the younger phase consist both of hornblende- and biotite-bearing dacites and of relatively anhydrous dacites, many of which are clot-free. These younger dacites erupted both from the precaldera highlands and from a group of domes and flows in the eastern part of the area. Flows from the precaldera highlands were erupted as recently as 2.18 Ma (Heiken et al., 1986). This timing overlaps with early rhyolitic ignimbrites from the Bandelier system (San Diego Canyon ignimbrites of Turbeville and Self, 1988), indicating that multiple magma chambers still existed beneath the central volcanic field at that time. Small quantities of basalts were erupted 4.6–4.4 Ma ago. The areal and temporal extent of this phase of basaltic activity is poorly characterized at present. A single dome of rhyolite ("intermediate rhyolite" of Loeffler et al., 1988) was erupted at 5.8 Ma. Both the early and intermediate rhyolites are probably related to the Keres Group rhyolites (Canovas Canyon and Bearhead Rhyolites) south of the Toledo/Valles calderas.

In the northern part of the area, basaltic lavas (El Alto Basalt) were erupted between 3.2 and 2.8 Ma (Baldridge et al., 1980; Manley, 1982), contemporaneously with nearby dacite domes of the Tschicoma Formation. The close spatial and temporal association suggests a close petrological relationship. In addition, three rhyolite domes (El Rechuelos Rhyolite) were erupted 2.0 Ma ago. Although extrusion of these domes occurred while precursor rhyolitic ignimbrites were being erupted from the Bandelier magma chamber, Sr- and Nd-isotopic data suggest that the El Rechuelos was not derived from the upper-crustal Bandelier chamber, but rather from lower-crustal magma chambers. The origin of this rhyolite is compatible with fractional crystallization from a basaltic parent with concomitant assimilation of small amounts (<6%) of lower crust (Loeffler et al., 1988).

Note: The following trip is divided into three main and two optional segments. If it is desired to complete the trip in one day, only segments A, C, and E should be followed. Two days are required to complete all segments. All segments are on poorly to non-maintained dirt roads; four-wheel-drive vehicles are strongly recommended!

Segment 2A: US-84/285 to Forest Road 427

Mileage

0.0 Junction of US-84/285 and Forest Road (FR) 144 (District 7 Headquarters of New Mexico State Police), 0.1 mi (160 m) north of stop light at junction of US-84/285 and NM-584, Española. Drive west on FR-144. **0.3**

0.3 For the next 4 mi (6.6 km) the road ascends onto a series of successively older geomorphic surfaces, labeled (from lowest to highest) Q4 to Q1. These surfaces formed over the periods 130 to >80, 240 to 150, 350 to 240, and 1100 to >350 ka, respectively, in response to climatic variations and downcutting during the Pleistocene (Dethier et al., 1988). **9.0**

9.3 Sharp curve to left; begin steep ascent. You are crossing the trace of the northeast–southwest-trending Santa Clara fault zone, part of a transfer fault connecting the Española graben with the San Luis graben to the northeast (Aldrich, 1986). Eight kilometers to the southwest, this fault zone merges with the north–south-trending Pajarito fault zone. Cerro Roman, the ridge to the east, is the remnant of a Lobato shield cone. **1.7**

11.0 Basalts of Clara Peak. The basalt here, part of the

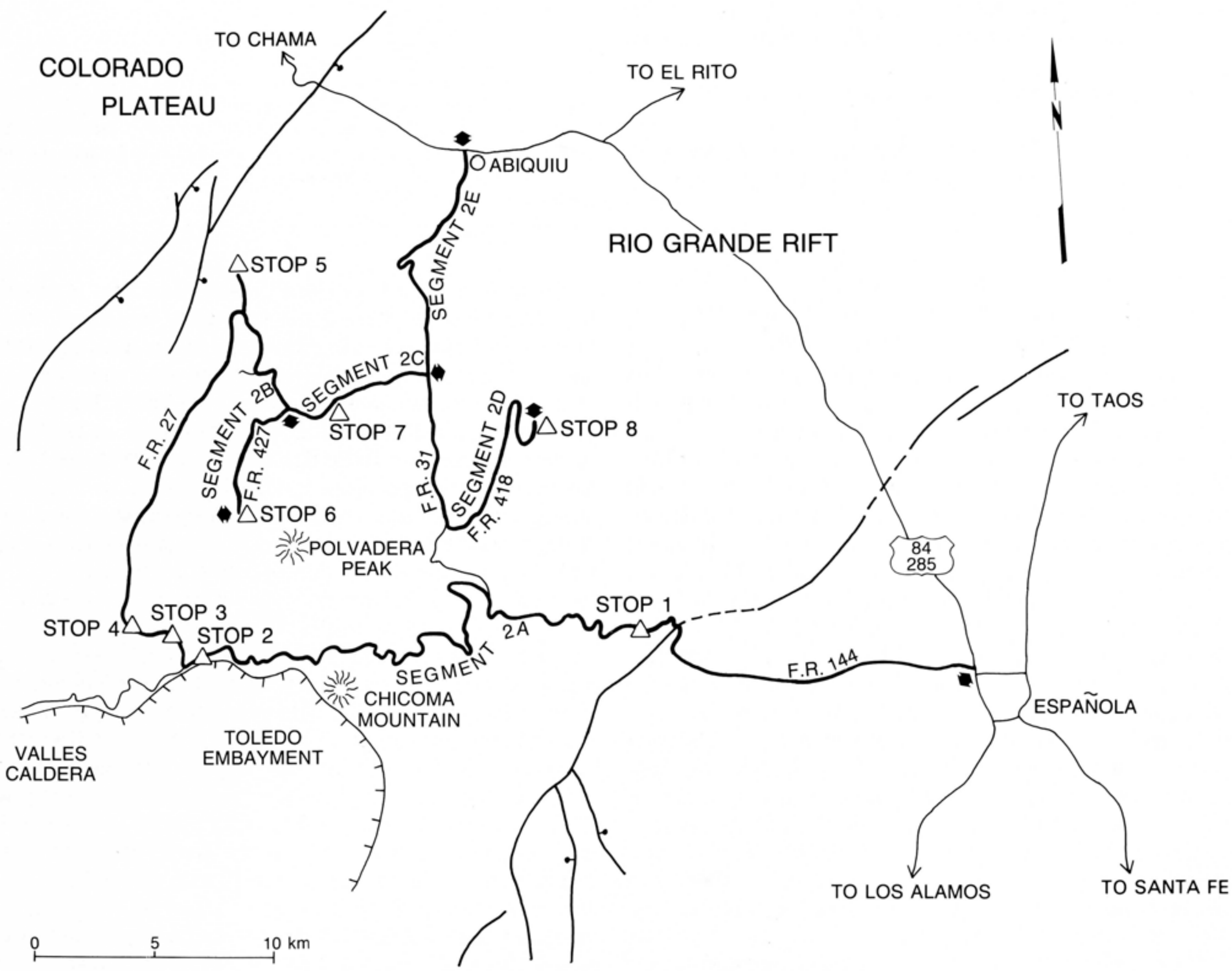

FIGURE 28—Route map, Day 2.

Lobato "Formation," is olivine-phyric and hypersthene-normative (P533 and P534, Table 5), with a K–Ar age of 9.99 ± 0.27 Ma (P533). It was erupted from a shield cone on the mesa directly above (one of several shield vents from which basalts of the Lobato "Formation" were erupted). For the next 1.4 mi (2.2 km) you will be driving through the subsurface conduit of this vent. **0.2**

11.2 Subvolcanic plug underlying the Clara Peak shield cone. This basalt (P551, Table 5) is the intrusive equivalent of the flows on the mesa above. **0.6**

11.8 Cinders, inferred to be an interior part of the Clara Peak shield cone, intruded by the basaltic plug. **0.6**

12.4 **STOP 1. Lobato Basalt.** This stack of thin flow units separated by scoriaceous rubble (Fig. 29) represents a cross section through Clara Peak shield cone. The basalt is an olivine-phyric, hypersthene-normative tholeiite (P552, Table 5), equivalent to other basalts associated with the Clara Peak center. Here the basalt contains resorbed crystals of quartz. Low hills in the foreground to the west (Los Cerritos, Fig. 30) are underlain by dacite (of the Lobato "Formation") dated at 9.6 ± 0.2 Ma (P75, Table 5). The peaks in the background (including Polvadera Peak and Tschicoma Mountain) are younger (<4 Ma) dacites of the Tschicoma Formation. Gallina Mesa is underlain by a dacite flow, dated at 3.90 ± 0.15 Ma (P68), which was vented from near the top of Tschicoma Mountain. **2.1**

14.5 Lobato dacite is exposed in low outcrops along the south side of the road (P74, Table 5). This dacite contains phenocrysts of hastingsitic hornblende (with cores of orthopyroxene) and of plagioclase (Fig. 31). **2.3**

16.8 Canyon at bottom of Gallina Mesa flow. For the next 7 mi (11.2 km) you will drive along the surface of the Gallina Mesa flow. This dacite is characterized by phenocrysts of hastingsitic hornblende, plagioclase, and in some samples biotite; and microphenocrysts of bronzite, augite, magnetite, and occasionally apatite (Fig. 31). **14.8**

31.6 **STOP 2A. Overview of the northern Jemez volcanic field and Rio Grande rift/Colorado Plateau margin.** The high peaks to the northeast (Fig. 32), including Polvadera Peak (3.13 ± 0.07 Ma) and Cerro Pelon (2.96 ± 0.27 Ma), are younger dacitic domes of the Tschicoma Formation. The low hills in the foreground are remnants of older (up to 6.6 Ma) domes(?) and flows of dacitic lava. The low terrain to the west is formed on Tschicoma andesitic lavas (approximately 5 Ma) that flowed to the north along paleovalleys.

FIGURE 29—Thin flow units of olivine-phyric, hypersthene-normative basalt, probably representing a cross section through the Clara Peak shield cone.

The paleovalleys followed a set of major faults along the western margin of the Rio Grande rift. Channels along these faults persisted after Tschicoma time and provided the major northern route for Bandelier ignimbrites (erupted at 1.45 and 1.12 Ma), which form the buff-colored columnar-jointed plateau in the middle ground to the north. In the middle distance to the northwest is a 7.5 Ma rhyolite dome, the oldest rhyolite in the northern volcanic field (Stop 4). Beyond and to the north is Cerro Pedernal, capped by 7.8 Ma basalt flows of the Lobato "Formation" (Manley, 1982), and thick strata of the Colorado Plateau above Abiquiu Reservoir. In the far distance to the north are the Tusas and San Juan Mountains.

Walk 160 m farther west to a small dirt road, then 160 m south to the rim of the Toledo embayment.

STOP 2B. Panorama of the Toledo embayment and Valles caldera. Due south is the large Cerro Toledo rhyolite dome (1.38 Ma; Heiken et al., 1986). In the distance to the southwest is the far rim of the Valles caldera, 24 km away. The Redondo resurgent

TABLE 5—Major-element compositions of selected volcanic rocks from the northern Jemez volcanic field.

	Early Rhyolite P8	North Rim P52	Tschicoma Mt. P69	Cerro Pelon P71	Lobato Dacite		North Rim P79	Cerrito Chato P99				Clara Peak Shield			
					P74	P75			F212	P430	P487	P533	P534	P551	P552
SiO_2	73.68	58.40	65.94	65.68	64.32	65.63	60.94	64.85	52.25	51.03	51.31	48.59	51.03	51.74	51.32
TiO_2	0.25	0.88	0.56	0.57	0.57	0.56	0.86	0.60	1.48	1.30	1.20	1.40	1.25	1.19	1.20
Al_2O_3	13.91	15.86	15.29	15.71	16.40	16.51	16.48	15.03	16.80	17.06	16.50	15.88	16.02	16.53	15.97
Fe_2O_3	1.79	6.21	3.93	4.04	4.09	4.01	5.47	4.52	9.26	10.37	8.47	10.86	9.98	10.14	9.68
MnO	0.07	0.12	0.07	0.07	0.07	0.07	0.09	0.08	—	0.16	0.13	0.17	0.16	0.15	0.14
MgO	0.26	3.62	1.72	1.95	1.99	2.05	2.59	2.29	5.84	7.34	5.39	7.33	7.01	7.12	6.84
CaO	1.29	6.25	3.67	3.98	4.17	4.27	4.89	4.22	8.45	9.39	8.75	10.08	8.68	8.84	9.38
Na_2O	3.98	3.63	2.78	3.11	3.32	3.33	2.97	3.66	4.46	3.29	3.92	2.49	2.53	3.17	3.17
K_2O	3.88	2.18	3.18	2.93	2.04	1.98	2.71	2.76	1.53	0.64	1.98	0.74	0.89	0.86	0.99
P_2O_5	0.05	0.48	0.22	0.25	0.26	0.26	0.43	0.25	0.64	0.24	0.61	0.29	0.24	0.25	0.24
Total	99.16	97.63	97.36	98.29	97.23	98.67	97.43	98.26	100.71	100.82	98.26	97.83	97.79	99.99	98.93

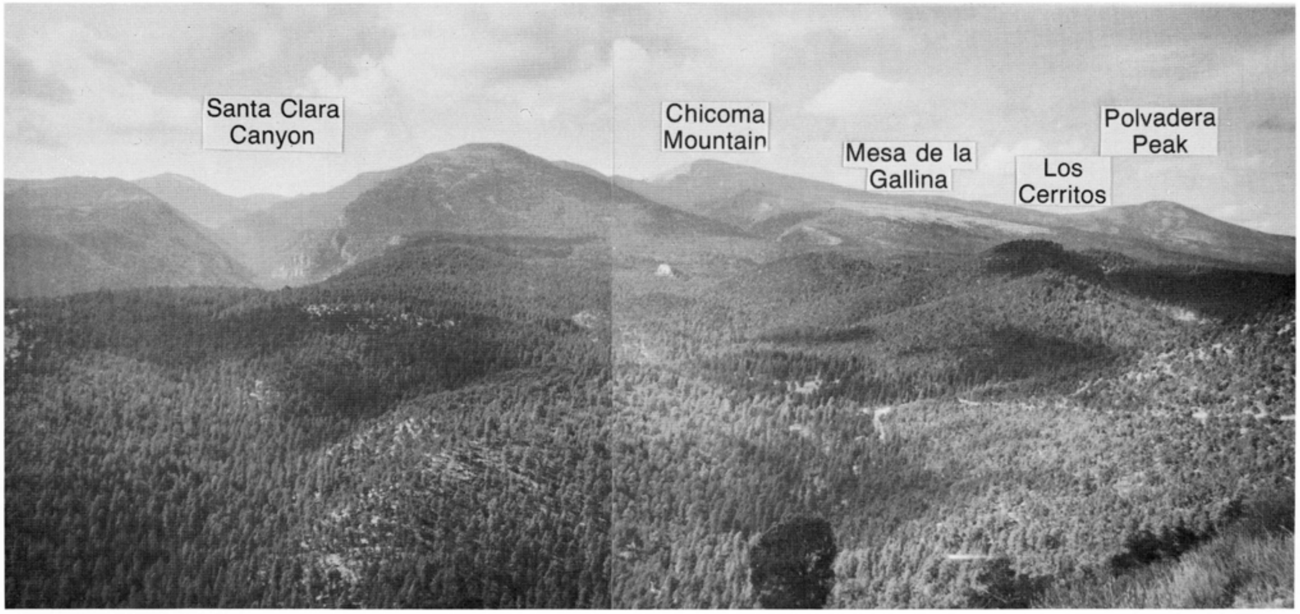

FIGURE 30—Panorama of Tschicoma terrain from Stop 1.

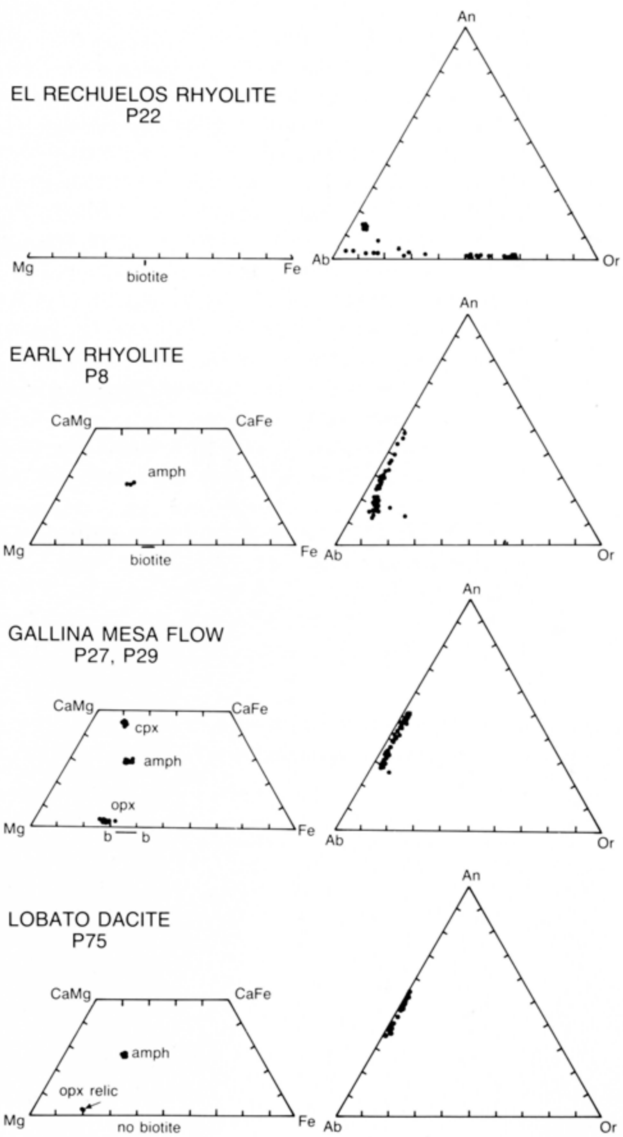

dome dominates the middle of the caldera; from this observation point you are looking along the southwest-trending axial graben which cuts the resurgent dome. The rhyolitic domes of Cerro Santa Rosa (0.88 Ma), Cerro San Luis (0.69, 0.82 Ma), and Cerro Seco (0.73 Ma; Doell et al., 1968) lie within the northern moat of the caldera. To the east, the dacites of Tschicoma Mountain (3.2 ± 0.1 to 3.7 ± 0.2 Ma; P47 and P69, respectively, Table 5) are high on the rim of the Toledo embayment.

The origin of the Toledo embayment is still uncertain. It may be partly tectonic, partly erosional, and partly the result of Tschicoma pyroclastic eruptions which deposited dacite pumices (2.5 ± 0.1 Ma) in the Puye Formation to the east. The Otowi Member of the Bandelier Tuff may lie buried within the embayment, but the major deposits within the embayment are the Cerro Toledo Rhyolite domes, onlapped by a thick sequence of the Tshirege Member of the Bandelier Tuff (1.12 Ma). The Tshirege partly filled the Santa Clara paleocanyon but has since been deeply eroded. The ridge on which this stop is located is underlain by flows from the precaldera highlands, which once occupied the region of the Toledo embayment. These flows, which form the northern rim of the Toledo embayment, range in age from 2.3 to 4.2 Ma. The flow which caps this ridge (P52, Table 5) is a distinctive dacite with remnants of olivine crystals (Fo_{82}), probably inherited from a basaltic magma which was petrographically similar to the Lobato and El Alto basalts. A small remnant of the precaldera highlands may be preserved within the embayment as Cerro Rubio dacite (2.2–3.6 Ma), a pair of dacite plugs at the far eastern end of the embayment (Table 1; Gardner

FIGURE 31—Mineral compositions for Lobato dacite, Gallina Mesa flow, and Early and El Rechuelos Rhyolites.

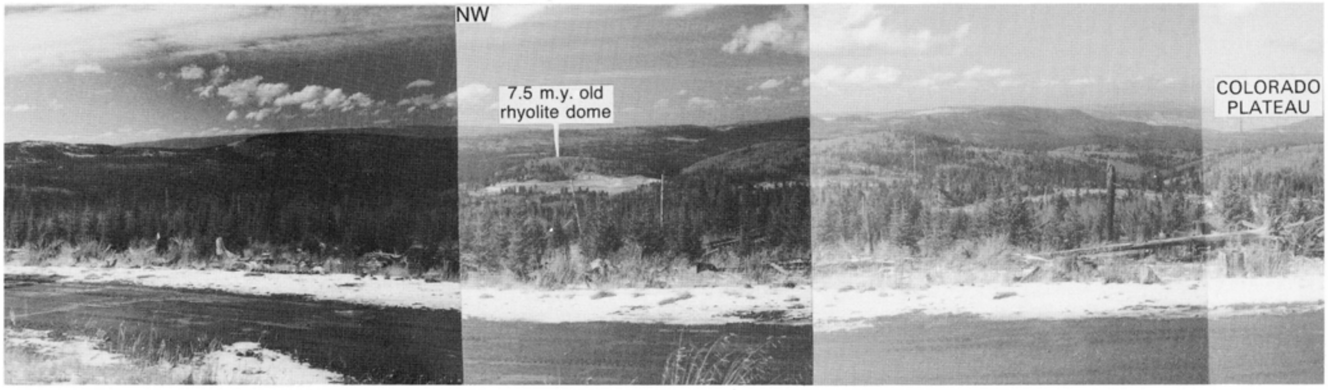

FIGURE 32—Panorama from Stop 2A of the northern Jemez

et al., 1986; Heiken et al., 1986), which are hidden behind the Cerro Toledo Rhyolite domes and the Bandelier Tuff. **0.4**

32.0 **Turn right** onto FR-27. Clot-rich Tschicoma dacite extends for the next 1.9 mi. **0.7**

32.7 **STOP 3. Clot-rich dacite.** Park at junction with minor road to right. Mafic clots are common in dacites of the Tschicoma Formation, but they are rarely as large or as abundant as they are in this unit (P79, Table 5). These clots have generally been interpreted as remnants of quenched mafic magma that was mixed into a more silicic host (Eichelberger, 1980). This clot-rich unit, dated at 4.2 Ma, is one of the major dacite flows from the precaldera highlands.

Continue to left (northwest). **1.8**

34.5 **STOP 4. Dome of early rhyolite** (7.5 Ma; Loeffler et al., 1988). This rhyolite (P8, Table 5) is unusual in that it contains phenocrysts of plagioclase, biotite, and edenitic amphibole, but not quartz or alkali feldspar. The compositions of these phenocrysts (Fig. 30) are similar to those of Tschicoma dacites. Another rhyolite plug (Intermediate Rhyolite, 5.8 Ma old) occurs 2 km to the southeast, and the El Rechuelos Rhyolite domes (2.0 Ma) lie a few kilometers to the east and northeast (Stop 6). Each of these three rhyolites is chemically and petrographically distinctive, but all three appear to have originated from mafic magmas with little crustal assimilation (Loeffler et al., 1988). **0.8**

35.3 Road crosses onto the Tshirege Member of the Bandelier Tuff, which extends for the next several miles. **8.5**

43.8 **Turn left** onto small track. **0.8**

44.6 **STOP 5. Overview of western margin of Rio Grande rift** (Fig. 33). The broad valley in the distance is underlain by continental red beds of the Chinle Formation (Triassic). Above it, the Entrada Sandstone and overlying gypsum of the Todilto Formation (Jurassic) form a very prominent white marker unit over wide areas of the Colorado Plateau. The Morrison Formation (Jurassic) forms the slopes and benches above the Todilto. Above the Morrison is the Dakota Sandstone (Cretaceous), which crops out as a cliff-forming unit capping the mesas.

The Entrada and Todilto Formations are visible in the cliffs northeast of Cañones, the small village lying in the valley (foreground). The white rocks cropping out in the canyon walls to the east (right) of Cañones at the same elevation are Abiquiu Formation of late Oligocene to early Miocene age, deposited in broad basins during an early phase of rifting. The bounding faults along which the Abiquiu was displaced downward underlie Cañones. The Bandelier Tuff, capping the mesa to your left, flowed down paleovalleys excavated along these rift-bounding faults. The nearest mesa to the right consists of Tschicoma dacite, with internal structure that indicates flow from the southeast. The farther mesa behind it is capped by El Alto Basalt dated at 2.8 Ma (Manley, 1982).

The ruin of Tsiping, a prehistoric Tewa pueblo, is visible on the mesa capped by Bandelier Tuff to the left. Occupied during the 13th and 14th centuries A.D., Tsiping had over a hundred ground-floor masonry rooms constructed of cut blocks of Bandelier Tuff. A line of "caveate" rooms hollowed out of the soft tuff is visible at the base of the escarpment immediately below the main pueblo. Fifteen or more "kivas" (subterranean ceremonial chambers) were also excavated into the tuff bedrock along the western edge of the pueblo. Tsiping was a fortified village. Protected on the north, east, and west by a vertical escarpment, a high masonry wall protects the site on the south.

Return to FR-27. **0.8**

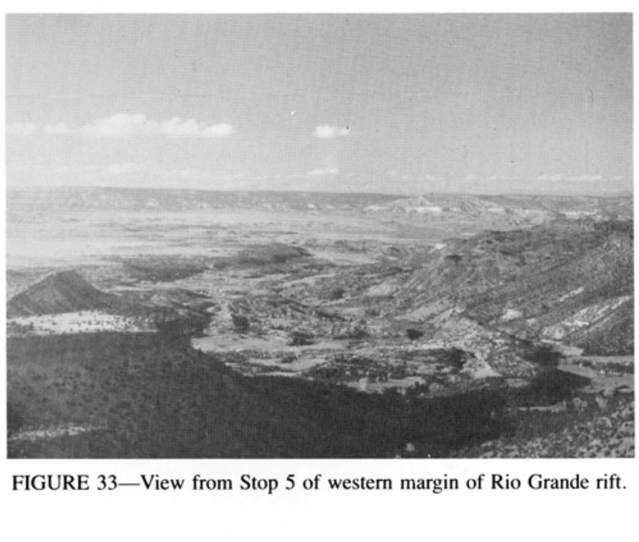

FIGURE 33—View from Stop 5 of western margin of Rio Grande rift.

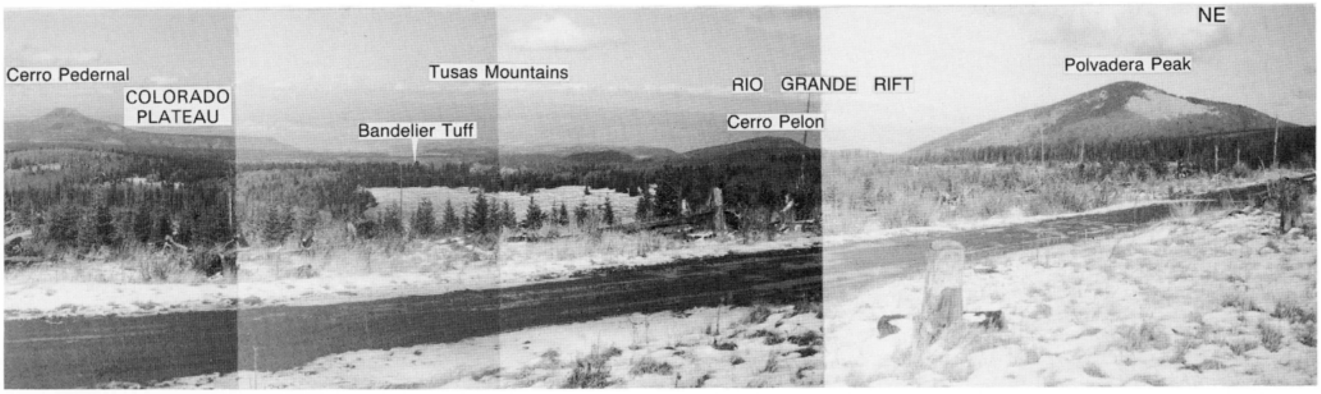

volcanic field and Rio Grande rift/Colorado Plateau margin.

45.4 **Junction** with FR-27. Turn left. **2.1**
47.5 **Junction** with FR-422. Bear left and continue on FR-27. **1.7**
49.2 **Junction** of FR-27 and 427. Bear left on FR-27 for continuation of one-day trip; refer to Segment 2C of road log. Turn right onto FR-427 for Optional Segment 2B.

Optional Segment 2B: El Rechuelos Rhyolite dome

Mileage

0.0 **Junction** of FR-27 and 427. Follow FR-427 (main track) to south (see map, Fig. 34). **4.3**
4.3 **STOP 6. Middle dome of the El Rechuelos Rhyolite (2.0 Ma).** End of road. This is a very fine-grained biotite rhyolite (Fig. 31), which is distinctive from the Early Rhyolite of Stop 4. The El Rechuelos Rhyolite is higher in SiO_2 and K_2O (P22, Table 5) and has lower overall REE contents. Nd- and Sr-isotopic data indicate that the El Rechuelos Rhyolite is derived from fractional crystallization of basalt similar to that of the Lobato "Formation," combined with assimilation of a small amount of lower crust (Loeffler et al., 1988).

Obsidian remnants within the banded perlite are visible along the flanks of the rhyolite dome. Obsidian–perlite associations in the El Rechuelos Rhyolite were used by Friedman and Smith (1958) to study deuterium–hydrogen relations. They deduced that the water in obsidian is largely magmatic, whereas the additional water in perlite is meteoric.

The dacites (3.7–6.6 Ma) across the canyon to the west form an older and lower terrain. The younger dacite flanks of Polvadera Peak (3.1 Ma) lie beneath the El Rechuelos Rhyolite to the east.

Return to FR-27.

Segment 2C: Forest Road 427 to Forest Road 31

Mileage

0.0 **Junction** of FR-27 and 427. Bear left on FR-27. **1.4**
1.4 **STOP 7. Cerrito Chato.** This is a dome, dated at 3.81 ± 0.19 Ma, of hornblende–biotite dacite with minor pyroxene (P99, Table 5). To the north is Cerro Pelon, a younger (2.96 ± 0.27 Ma) dacite vent with

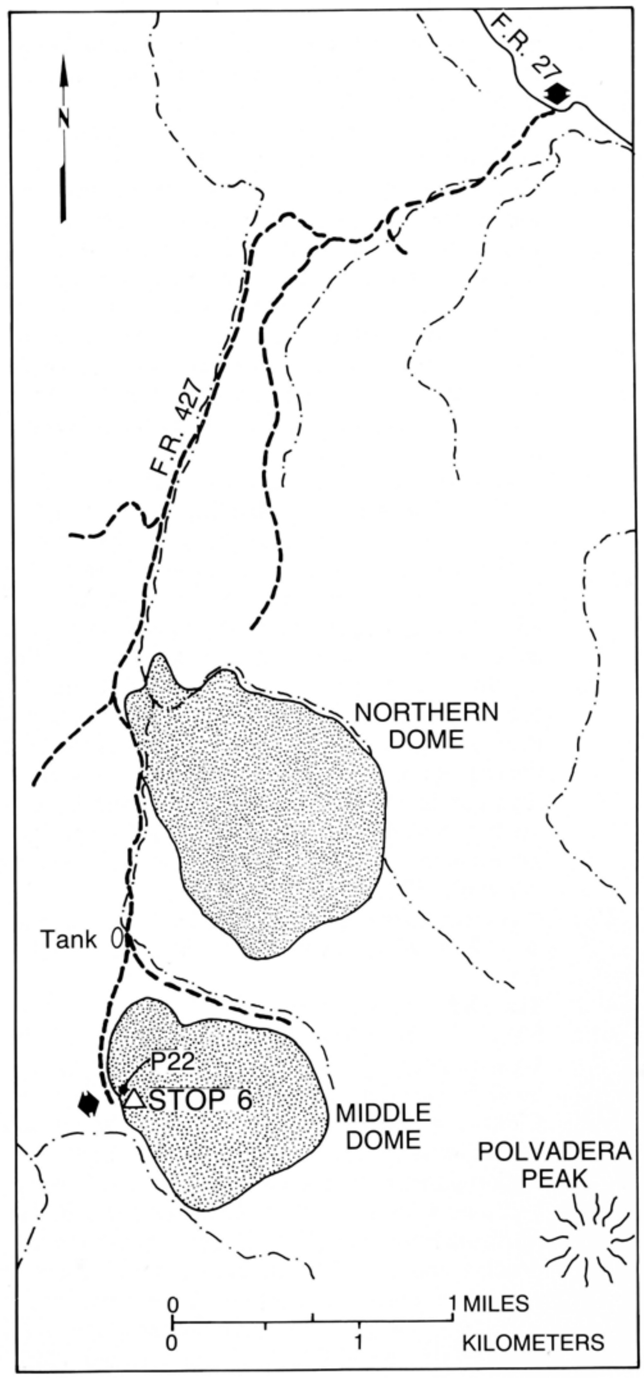

FIGURE 34—Map of Segment 2B of road log.

a well-preserved steep flow lobe emanating from the central crater, which breached to the south. The dacite from Cerro Pelon is similar in composition to that of Cerrito Chato, but contains augite and orthopyroxene with minor hydrous minerals (P71, Table 5). A similar petrographic relationship occurs throughout the younger (3.3–3.2 Ma) Tschicoma Formation: the hydrous mafic minerals which are abundant in the earlier dacites are largely absent from the later. Absence of hydrous minerals from the youngest dacites probably reflects decreasing P_{H_2O} in these magmas. If this difference in water pressure results from evolution of the youngest dacites at the shallowest depths, then the younger eruptions came from chambers at <2 kb (<7 km, assuming $P_{H_2O} = P_{total}$). **2.7**

4.1 Flow of the El Alto Basalt. The El Alto basalts, which include both hypersthene- and nepheline-normative types, were erupted approximately concurrently (3.2–2.8 Ma; Baldridge et al., 1980; Manley, 1982) with young dacite domes of the Tschicoma Formation, such as Cerro Pelon (Stop 7).

Junction of FR-27 and FR-31 (Vallecitos Road). Turn left for continuation of one-day trip; refer to Segment 2E of road log. Turn right for Optional Segment 2D.

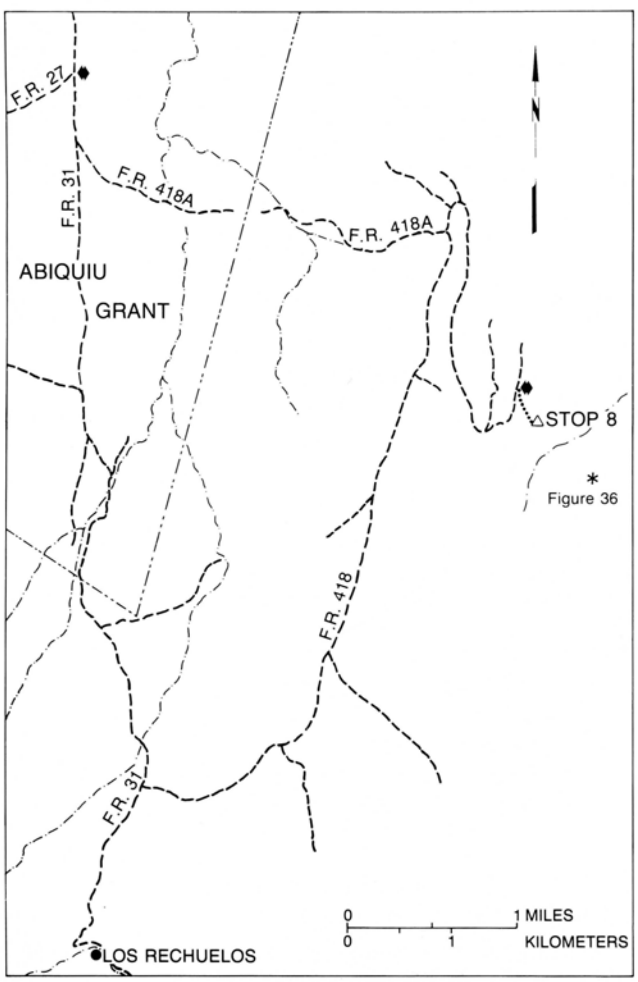

FIGURE 35—Map of Segment 2D of road log.

Optional Segment 2D: Lobato Mesa

Mileage

0.0 **Junction** of FR-27 and 31 (Vallecitos Road). Proceed south (see map, Fig. 35). **4.1**

4.1 **Junction** of FR-31 and FR-418. Turn left. **4.3**

8.4 **Junction** with FR-418A. Turn right and continue bearing to right (south). Road ascends fault scarp. **2.1**

10.5 **STOP 8. Lobato basalt and overview of the Rio Grande rift.** Park along edge of meadow. Walk 0.3 mi to the south-southeast along ridge crest and descend approximately 100 ft to view point. The flow exposed along this ridge is hawaiite, dated at 9.2±0.2 Ma (P487, Table 5). It is typical of the youngest flows on Lobato Mesa, which in general are slightly more evolved than most of the Lobato "Formation" on Lobato Mesa. The source of this flow was a broad vent 3.3 km to the north-northwest, which was subsequently downfaulted some 130 m relative to the block on which this stop is located. The platy structure which characterizes this flow and other hawaiites of the Lobato "Formation" probably resulted from alignment of plagioclase microlites during flow.

Across the canyon to the south, a section of more than 30 flows is exposed (Fig. 36). These flows consist of fine-grained, olivine-phyric tholeiitic basalt of fairly uniform composition. The lowermost flow (P430) is dated at 10.8±0.3 Ma and an upper flow (P465) at 10.1±0.3 Ma. We interpret these flows to be part of a shield cone (La Sotella shield), the central vent of which was located on the ridge crest 1 km west of the exposure. Evidence for a shield structure comes mainly from topography and from the uniformity of basalt compositions, both vertically and areally. Subsequent faulting displaced these flows 120 m upward relative to the vent. The central vent was bisected by a normal fault. The western half was displaced at least 190 m downward and is now buried beneath the alluvium in the small valley west of the fault scarp. The La Sotella shield cone is one of a small number of shield vents from which basalts of the Lobato "Formation" were erupted.

To the east is an excellent overview of the Española Basin. The Sangre de Cristo Mountains in the far distance mark the eastern side of the Rio Grande rift. The rift is filled dominantly with continental sediments of the Miocene Santa Fe Group, which in the foreground consist mainly of aeolian sands (Ojo Caliente Sandstone Member of the Tesuque Formation; Galusha and Blick, 1971; Dethier and Manley, 1985). In the middle distance is Black Mesa, capped by a 2.8±0.4 Ma (Manley, 1976) basalt flow that was erupted from the Taos volcanic field and flowed down the channel of the ancestral Rio Grande.

Return along same route to FR-31.

Segment 2E: Forest Road 27 to US-84

Mileage

0.0 **Junction** of FR-27 and FR-31 (Vallecitos Road). Proceed north. **3.1**

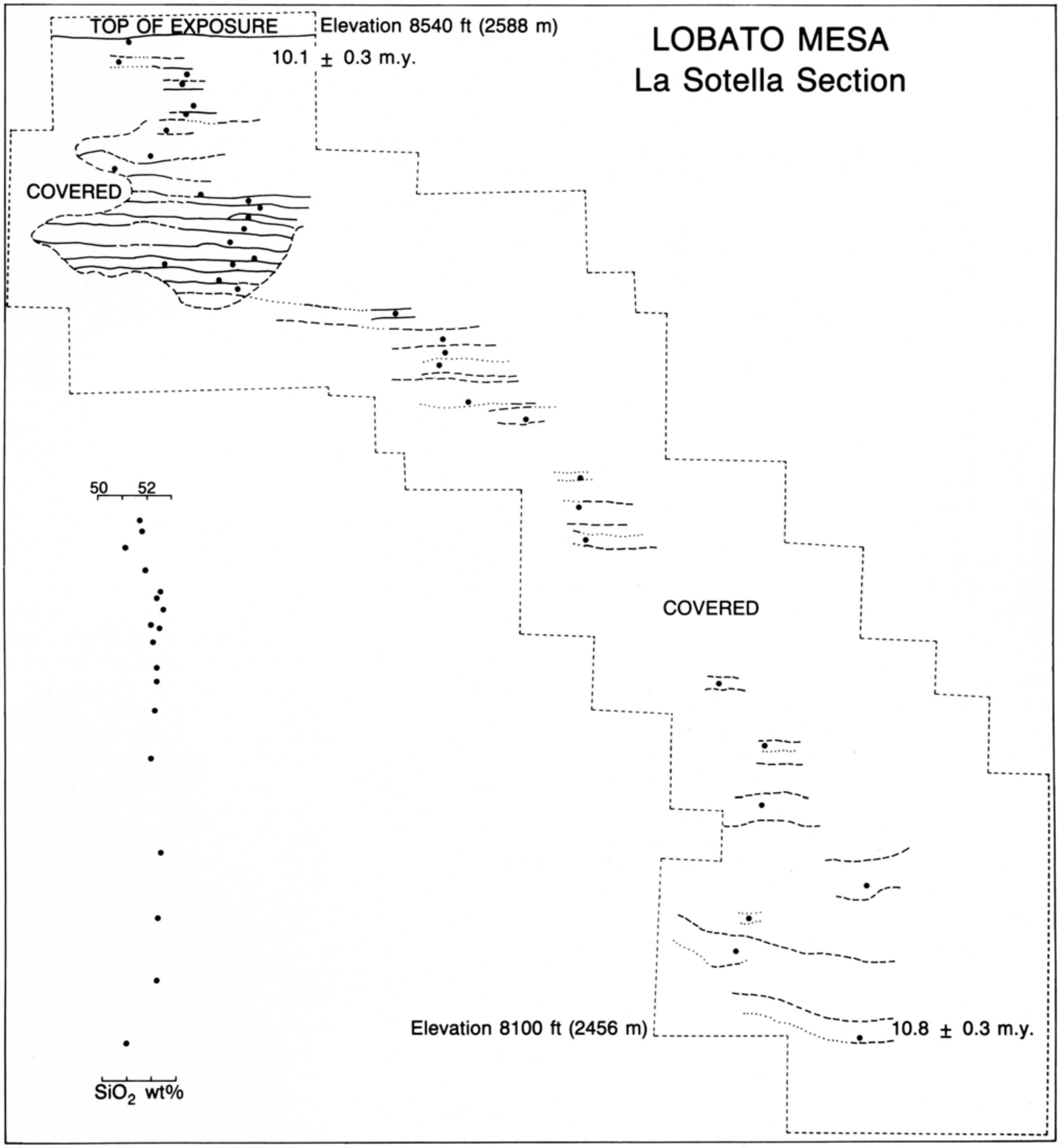

FIGURE 36—Section through La Sotella basaltic shield cone as seen from Stop 8, showing individual lava flows (where discernible). Fault somewhere near base of section duplicates lower part of section. Dots show sample location. Dashed line is limit of photomap base. Inset: SiO_2 composition of flows (only alternate flows analyzed). Location of Fig. 36 is shown in Fig. 35.

3.1 Flow of El Alto basalt. This hawaiite flow (F212, Table 5), which extends 6 km to the northeast, flowed down the ancestral channel of Abiquiu Creek. It now caps Mesa de Abiquiu, which at its northern end is 224 m above Abiquiu Creek and the Rio Chama. This flow, K–Ar dated at 3.2 Ma (Baldridge et al., 1980), contains xenoliths of pyroxenite and megacrysts of plagioclase and orthopyroxene (Baldridge, 1979). **0.6**

3.7 **Ford** Abiquiu Creek and turn right. Sediments of the Santa Fe Group are exposed along the sides of this canyon. Lobato basalts cap the mesa to the left; the Mesa de Abiquiu flow (El Alto) is on the right. **3.1**

6.8 **Bear left. 0.8**

7.6 **Junction** with US-84. Turn right and drive about 36 mi to Los Alamos.

Third-day road log: Bandelier Tuff, Valles caldera, and resurgent dome

Summary—The route of the third day will begin with a distal view of the Bandelier Tuff (Smith and Bailey, 1966) and will progress toward the rim and center of Valles cal-

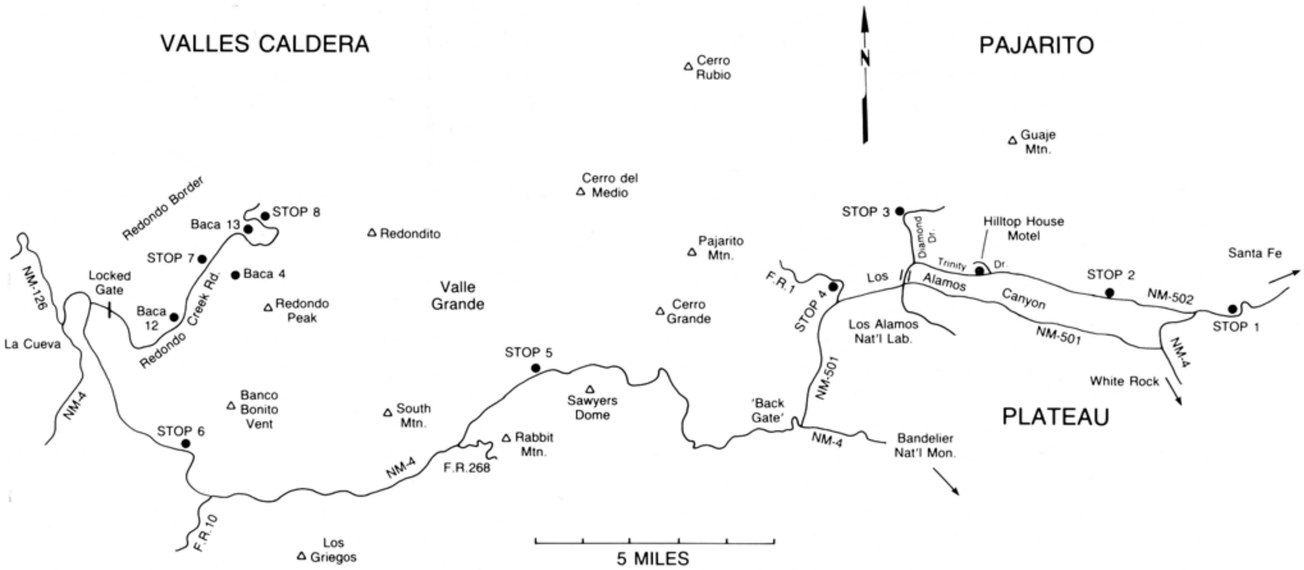

FIGURE 37—Route map, Day 3.

dera. The ignimbrites will appear more welded with each stop and we will have an opportunity to look at some base-surge deposits. Within the caldera we will discuss early and present models of caldera development and structure, look at the youngest moat rhyolites, and wander into the Redondo Peak resurgent dome. From within the Redondo Creek graben we will begin our detailed discussion of the intracaldera stratigraphy, structure, hydrothermal system, and alteration.

Mileage

0.0 Hilltop House parking lot at the junction of NM-502 (Trinity Drive) and Central Avenue, Los Alamos. Drive east on NM-502. In the distance (east) are the Sangre de Cristo Mountains forming the east flank of the Rio Grande rift. **3.3**

3.3 Clinton P. Anderson Memorial Overlook. The cliffs are composed of the Tshirege Member of the Bandelier Tuff. Cerro Toledo Rhyolite tuffs and the Otowi Member of the Bandelier Tuff are mostly buried by talus. Pink, sculptured sediments of the Rio Grande rift can be seen in the middle distance between the mesas. These sediments are part of the Santa Fe Group of Miocene age. **1.1**

4.4 Junction with NM-4; continue straight ahead (east). **0.9**

5.3 **STOP 1. Guaje Pumice and late Tertiary stratigraphy.** Park in large turn-out, right side of highway. Guaje Pumice Bed of the Otowi Member of the Bandelier Tuff overlies 2.4 Ma basalt in roadcut on left (Fig. 38). Note soil developed on top of basalt. In the slopes and cliffs above the basalt, about 100 m of Bandelier Tuff is exposed. The Guaje Pumice Bed is about 7 m thick here, but the bed is commonly as much as 10 m thick on the east side of the mountains. Underlying the slopes and exposed in gullies to the base of the cliffs are about 50 m of nonwelded Otowi ash flows. At the base of the cliffs is 1 m of fine-grained ash fallout of the Tsankawi Pumice Bed of the Tshirege Member, and above are 50 m of partly welded Tshirege ash flows. In the upper 30 m of columnar-jointed tuff, at least eight distinct flow units separated by sandy partings and pumice concentrations are discernible.

Rocks exposed in lower Los Alamos Canyon are typical of sequences along the length of White Rock Canyon. They record interfingering stratigraphic re-

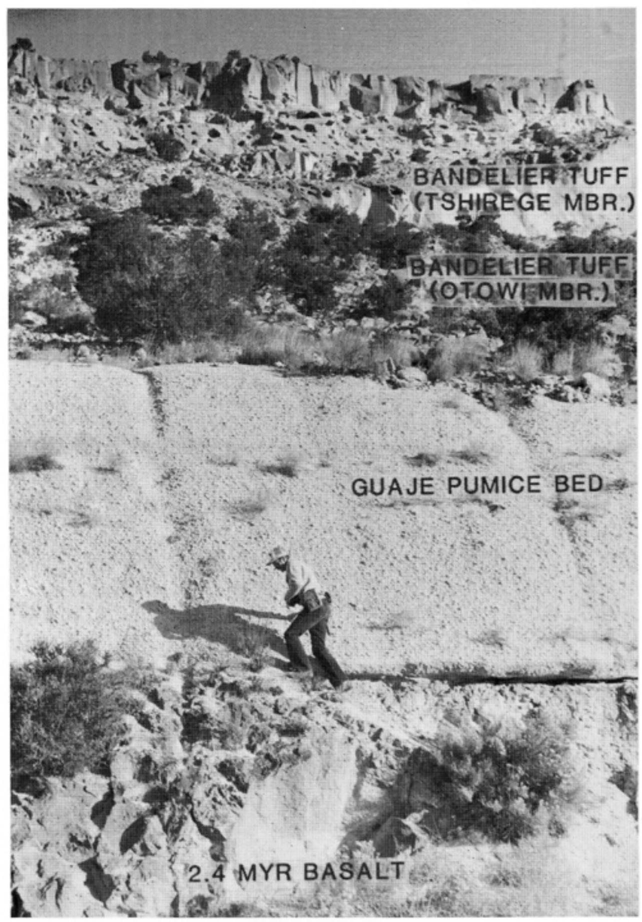

FIGURE 38—Photo of the Guaje Pumice (1.45 Ma), the ash-fall unit at the base of the Otowi Member, Bandelier Tuff. The pumice bed overlies a thin soil horizon, lake deposits and olivine basalt and pillow breccia (2.4 Ma) of the Cerros del Rio volcanic field.

lations between lavas and tuffs of the Cerros del Rio volcanic field with rift-basin sedimentary units (especially those derived from the Jemez volcanic field), regional tilting, uplift, and erosion of the Española Basin in the late Cenozoic, and the Quaternary pyroclastic deposits erupted from the Valles and Toledo calderas. Locally, there were interactions between magma and meteoric/surface waters resulting in phreatomagmatic tuff rings; lava flows erupted within the course of the ancestral Rio Grande repeatedly dammed it to produce lakes in which lacustrine-deltaic sedimentary sequences were deposited. The geology of the small area included in Fig. 39 illustrates this complex history.

Sedimentary units of the lower Puye Formation (Waresback, 1986) comprise a volcaniclastic apron shed from the northeastern margin of the Jemez volcanic field. The roadcuts along NM-502 expose coarse debris-flow and fluvial facies (plus minor tuff and lacustrine facies) containing a high proportion of Tschicoma andesite to dacite clasts. The Totavi Formation, which underlies the Puye Formation, is similar but also contains a significant fraction of Precambrian clasts, carried southward by the ancestral Rio Grande. Transport directions of fluvial-sediment systems were dominantly south-southeast. The debris-flow dominated unit (Ts1) is abruptly succeeded in this area by a lacustrine sequence (Ts2) that overlies an erosion surface and grades upward from dark, thinly laminated silts, through lighter colored sandy beds, to fluvial gravels with southerly transport directions and dominantly Precambrian clasts (derived from reworking of the Totavi). This sequence records the damming of the ancestral Rio Grande and filling of the consequent lake basin. The basalt flow that formed the drainage obstruction is exposed to the southeast on the rim of Los Alamos Canyon. The paleotopography of the lake basin is recorded by the geometry of this sediment package, which thins to the east, north, and west from a maximum local thickness of 30 m.

At 2.4 Ma (Baldridge, 1979), a basaltic eruption west of the map area produced a lava flow and associated dark-green, thinly laminated basaltic tuff

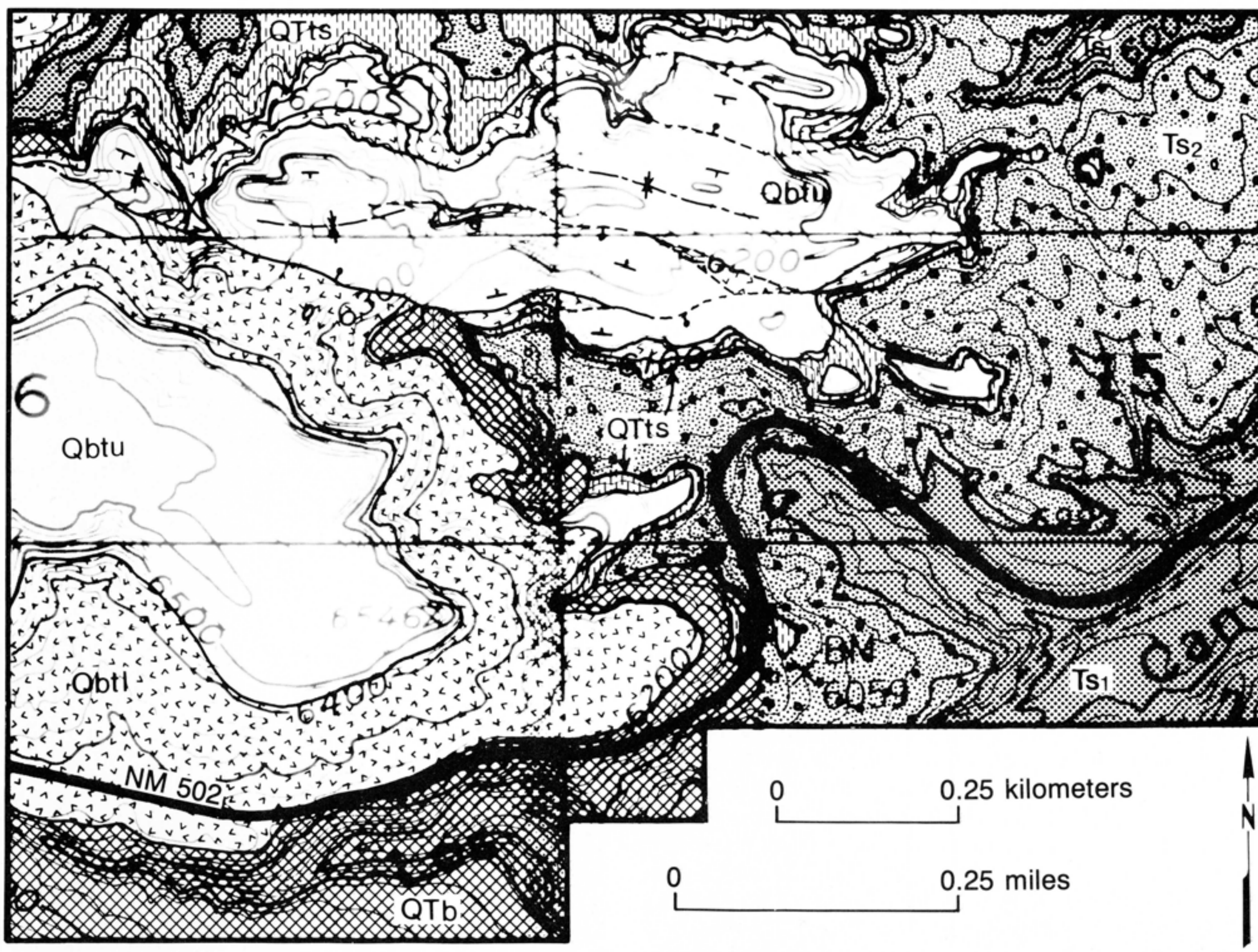

FIGURE 39—Detailed geologic map of northern rim Los Alamos Canyon. Map units: Ts1 and Ts2 = informal units of Puye Formation (volcaniclastic facies of the Tschicoma Formation, Polvadera Group). The lower unit (Ts1) consists of coarse debris flows, tuffs, and fluvial sediments dominated by material derived from contemporaneous Tschicoma andesite and dacite volcanic constructs to the west. The upper unit (Ts2) is an upward-coarsening, lacustrine silt to fluvial pebble-conglomerate sequence deposited in a lake basin. QTb = basalt lava flow and pillow breccia, locally forming well-developed east-dipping foreset beds (vent located 1 mi west). QTts = tuffaceous sedimentary units related to eruption and subaqueous emplacement of basalt QTb. A basaltic tuff (0.2–3 m), locally fluvially reworked, has been overridden by the basalt and associated pillow breccia. Lava and tuff are overlain by green lacustrine silt (gypsum-bearing) deposited in lake basin dammed by the basalt (QTb). Qbtl and Qbtu = Otowi and Tshirege Members of the Bandelier Tuff. Dips in slumped and tilted Bandelier Tuff in northern part of the map area are 15–25°.

(<1 m) that spread across a braided-stream system in the map area. Where the basaltic ash was deposited within channels, it was reworked, mixed with clastic sediment, and filled these paleochannels to thicknesses >3 m. As the basalt flow moved eastward it overrode the tuff, which exhibits both brittle and soft-sediment deformation (see roadcut exposures near water tank). The river became dammed to the south by the lava and the flow front became a pillow-palagonite delta. Eastward-dipping foreset beds of this delta are spectacularly exposed in Los Alamos Canyon south of the water tank. Ashy sediment, forming the green lacustrine shale unit, filled the lake to a level which locally topped the lava flow.

The Bandelier section is in place where it rests on the basalt flow, but northeast of the flow front it is thinned by erosion of the Otowi Member prior to eruption of the Tshirege Member and it is allochthonous, having slumped extensively. The green lacustrine shales have acted as a highly deformable decollement; the underlying basaltic tuff is virtually undeformed by post-Bandelier slumping.

Turn around and go west on NM-502. **0.8**

6.1 Junction with NM-4; return toward Los Alamos on NM-502. **2.0**

8.1 **STOP 2. Pueblo Canyon and Cerro Toledo Rhyolite tuffs.** Park vehicles in turn-out on right side of road where canyon view fades away. Walk right (north) toward canyon rim. From this vantage point we can look into Pueblo Canyon, named for the many Indian ruins that occur here (Fig. 40). The tip of the near mesa displays a beautiful exposure of Tshirege Member of the Bandelier Tuff (1.12 Ma) overlying bedded air-fall and reworked tuffs of the Cerro Toledo Rhyolite (1.45–1.20 Ma). These in turn overlie Otowi Member of the Bandelier Tuff (1.45 Ma). The "Toledo tuffs" are missing to the left of the scene where the Tshirege Member rests directly on the Otowi. The Toledo tuffs were vented from domes erupted within the Toledo caldera and Toledo embayment (Smith et al., 1970; Heiken et al., 1986; Stix et al., 1988).

Continue west on NM-502. **2.6**

10.7 **Keep left** on NM-502 (Trinity Drive). **0.8**

11.5 Ashley Pond on right; one of the old sites of the Manhattan Project. **0.9**

12.4 **Junction** with Diamond Drive, turn right. **1.2**

13.6 **Turn left** into the parking lot of the Church of Christ and park; backtrack along sidewalk south to cliff face exposed on Diamond Drive.

STOP 3. Surge deposits in the Tshirege Member, Bandelier Tuff. The proximal, welded, upper part of the Tshirege Member here contains beds of pyroclastic surge material with prominent cross-bedding (Fig. 41). Thicknesses of these surge units reach 0.5 m. These units occur in the upper cooling unit of the Tshirege Member, which has a gray color because of welding. The crystal-rich surge beds are intimately related to welded flow units. Sparse lithic clasts of rocks from the Jemez volcanic field occur in the ignimbrite. These surges may be either ground surge deposits left by the passage of flow units or surge layer deposits at the edge of the flows channeled down local drainages (Self et al., 1987). Flow direction was roughly eastward, perpendicular to the outcrop face.

Turn right (south) on Diamond Drive and return toward Los Alamos. **1.2**

14.8 **Junction** with NM-502, continue straight ahead over bridge. **0.4**

15.2 **Junction** with NM-501 (West Jemez Road), turn right. **0.2**

15.4 Main entrance to Los Alamos National Laboratory on left. **1.0**

16.4 Surge deposits in Tshirege Member, Bandelier Tuff on right. **0.2**

16.6 **Junction** with FS-1 (Camp May Road); turn right. **0.3**

16.9 **Keep left** on FS-1. **0.3**

17.2 **STOP 4. Pajarito Plateau overlook. Turn left** into parking lot at top of steep grade. The escarpment below our vantage point marks the Pajarito fault, which extends 50 km along the east side of the Jemez Mountains and is one of the main displacements on the west side of the Rio Grande rift. The Pajarito fault in this area has been intermittently active throughout Pleistocene time. It has displaced 5–4 Ma dacites of the Tschicoma Formation as much

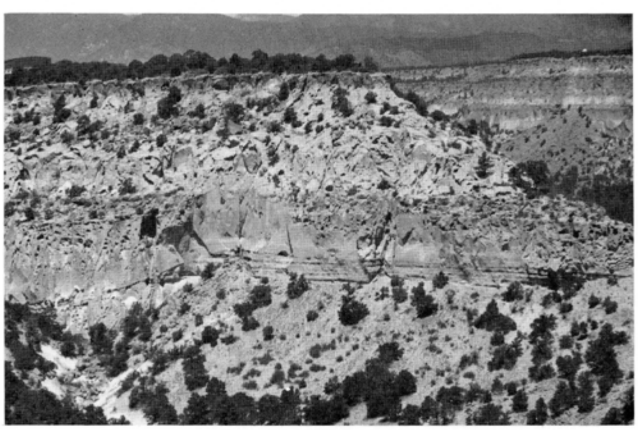

FIGURE 40—View northwest into Pueblo Canyon showing Tshirege Member, Bandelier Tuff, overlying bedded pyroclastic rocks and tuffaceous sediments of the Cerro Toledo Rhyolite. Note that Cerro Toledo Rhyolite has been cut out at left of photo and that Tshirege rests on the Otowi Member.

FIGURE 41—Surge beds between flow units of the Tshirege Member, Bandelier Tuff, along Diamond Drive, Los Alamos. Thickness of surge deposit is about 30 cm.

as 300 m and the Bandelier Tuff 100–150 m. Below the escarpment of the Pajarito fault, the Pajarito Plateau stretches eastward. The town of Los Alamos and the Los Alamos National Laboratory sit on the Tshirege Member of Bandelier Tuff on, or adjacent to, several fault strands of the Pajarito fault zone (Gardner and House, 1987). In the near distance is White Rock Canyon, gorge of the Rio Grande, and just beyond are the Cerros del Rio, composed of Pliocene and Pleistocene basaltic rocks that are covered locally by distal Bandelier Tuff. On the skyline are the Sangre de Cristo Mountains which border the east side of the Rio Grande rift.

Ignimbrites blanket the southwest segment of the Española Basin, one of the sedimentary basins of the Rio Grande rift. The Española Basin is asymmetric in configuration; being deepest on the west, next to the Pajarito fault and becoming shallower to the east. Depth to Precambrian basement just east of the escarpment is estimated to be about 3.5 km. A 3–7 ω-m resistivity low between 2 and 3 km depth adjacent to, and east of, the fault suggests that warm and/or saline fluids exist in Paleozoic–Mesozoic rocks, probably Madera Limestone above basement (Goff and Grigsby, 1982). Many seismic reflectors of continuous horizontal extent above the basement interface also suggest as much as 1.5 km of Paleozoic–Mesozoic rocks. Tertiary fill is estimated to be roughly 1400 m thick overlain by 600+ m of Puye Formation and Bandelier Tuff (Budding, 1978; LANL, unpubl. data, 1979; Williston, McNeal and Associates, 1979).

The Tshirege Member of Bandelier Tuff at this location is densely welded because of proximity to its source in Valles caldera. Pumice fragments are flattened and chatoyant blue sanidine and clear quartz phenocrysts are conspicuous.

The mountainous highlands that flank the eastern margin of the Valles caldera are made up of dacitic to rhyolitic volcanic rocks of the Tschicoma Formation. The Tschicoma Formation in this part of the volcanic field consists of coalescing lava domes with little or no pyroclastic rocks. Individual lava flows can often be recognized by their basal flow breccias and/or zones of dark cryptocrystalline devitrification. The interior of the lava flows is devitrified and in some cases has undergone vapor-phase alteration.

The oldest recognized unit is a thick accumulation of low-Si rhyolites (or rhyodacites) in the Rendija Canyon and Guaje Mountain areas. These rhyolites typically contain 72% SiO_2, 2.60% Fe_2O_{3T}, 120 ppm Rb, and 300 ppm Sr. Phenocrysts make up 11–16% of the rock and include quartz, plagioclase, anorthoclase, sanidine, biotite, sphene, and zircon. Quartz is often wormy and feldspar phenocrysts are characterized by disequilibrium textures. Clots of andesite and dacite and xenocrysts(?) of hornblende, clinopyroxene, and orthopyroxene are minor (<1%) contaminants. A K–Ar age of 4.55 ± 0.22 Ma was obtained for sanidine from the rhyolite (date courtesy of F. W. McDowell, University of Texas, Austin).

The low-Si rhyolite is overlain by two-pyroxene dacites at Pajarito Mountain. These dacites increase in SiO_2 content upsection from 66% to 69% and are relatively potassic (~3% K_2O). These dacites have 10–24% phenocrysts consisting of plagioclase, clinopyroxene, and orthopyroxene. Plagioclase crystals have sieve and skeletal textures. The rims of pyroxene phenocrysts are sometimes altered to hornblende. Xenolithic clots made up of subhedral and interlocking clinopyroxene and othopyroxene are common in these rocks. A K–Ar age of 4.81 ± 0.53 Ma was determined for plagioclase. This age overlaps that for the low-Si rhyolite; thus, the two units were probably erupted in close succession.

Hornblende-bearing dacites crop out at Cerro Grande. These hornblende dacites are chemically and petrographically distinct from the two-pyroxene dacites at Pajarito Mountain. The dacites of Cerro Grande are slightly less siliceous (63–66% SiO_2) than those at Pajarito Mountain. They are also less potassic (2.7 vs. 3.0% K_2O) and more iron-rich (4.3 vs. 3.7% Fe_2O_{3T}). The hornblende dacites contain ~20% phenocrysts, consisting of plagioclase, hornblende, and orthopyroxene. Clinopyroxene is found only in trace amounts. The stratigraphic relations between the hornblende-bearing and two-pyroxene dacites are not known, but a published age of 3.67 Ma (Dalrymple et al., 1967) for the dacites of Cerro Grande suggest they are the younger unit.

The southernmost exposures of Tschicoma Formation occur at Sawyers Dome on the southeast rim of the caldera. Sawyers Dome is made up of hornblende-bearing andesite and dacite. SiO_2 contents of lavas range from 62% near the base of the dome to 66% at the top. The rocks of Sawyers Dome are crystal-rich (32–34% phenocrysts) and have a phenocryst assemblage of plagioclase, hornblende, and minor orthopyroxene. The youthful morphology of the dome suggests an age younger than hornblende-bearing dacites of Cerro Grande. Unfortunately, critical contacts between the two units are covered by Bandelier Tuff.

Turn right on Camp May Road and return to NM-501. **0.6**

17.8 **Turn right** on NM-501. **2.9**

20.7 **Junction** of NM-501 with NM-4 ("Back Gate"); turn right toward Jemez Springs. **0.6**

21.3 Small turnout on left in hairpin turn affords another spectacular view of the Pajarito Plateau. **0.7**

22.0 Pumiceous flow top of Tshirege Member, Bandelier Tuff, on right. **1.2**

23.2 Hornblende-bearing dacite flows of Cerro Grande, Tschicoma Formation, on right. **1.0**

24.2 Frijoles Canyon on left. Thick accumulations of the Bandelier Tuff ponded in this area in a low on the pre-Bandelier topography. **2.4**

26.6 Road to St. Peter's Dome on left. Continue straight ahead on NM-4. **0.8**

27.4 East rim of Valles caldera; descend into Valle Grande. **1.3**

28.7 **STOP 5. Valle Grande overlook into Valles caldera.** Park in turnout on right side of road adjacent to yellow sign. Valles caldera formed 1.12 Ma during catastrophic eruption of approximately 300 km^3

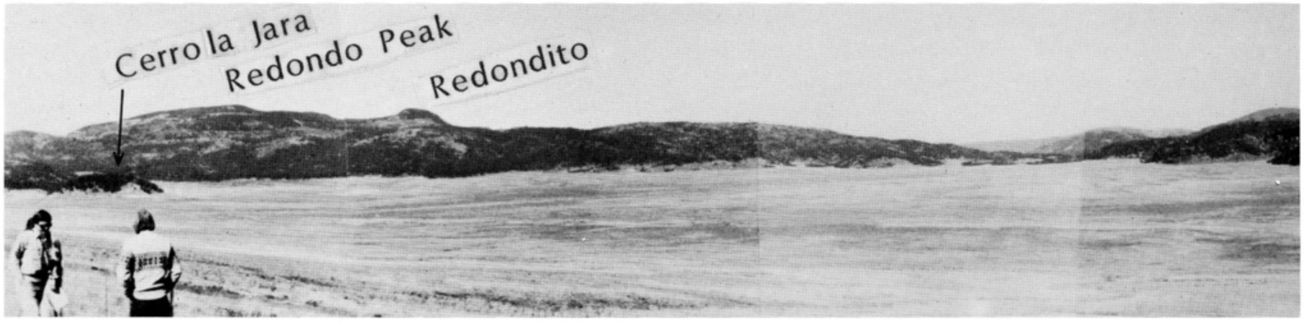

FIGURE 42—Panoramic view of Valle Grande looking northwest toward the resurgent dome of Redondo

of ignimbrite of the Tshirege Member, Bandelier Tuff. By comparison, the amount of ash released during the May 1980 eruptions of Mt. St. Helens is estimated at <2 km^3. From this vantage (Fig. 42) we can gaze across Valle Grande, the eastern section of the caldera "moat," toward the broad mountain of Redondo Peak (3460 m) forming the eastern segment of the resurgent dome. This segment is really a northeast-trending ridge that includes the knob of Redondito (see Figs. 7 and 18 for geology and geomorphology). The resurgent dome is composed primarily of densely welded Bandelier Tuff that was uplifted during postcaldera tumescence of the volatile-depleted Bandelier magma chamber (Smith and Bailey, 1968; Smith, 1979). Dips on foliations in the ignimbrite are generally south to southeast on the Redondo Peak segment of the dome. The relations between the tilted ignimbrites of the resurgent dome, overlying volcaniclastic rocks and lacustrine deposits, and postcaldera rhyolites indicate that resurgence probably occurred within 50–100 Ka after caldera formation (Doell et al., 1968; Smith et al., 1970; Hulen et al., 1987).

Visible postcaldera, ring-fracture rhyolites of the Valles Rhyolite that partly surround the resurgent dome are Cerro del Medio (1.04 Ma), Cerro del Abrigo (0.89 Ma), Cerro Santa Rosa (0.88 Ma), Cerro la Jara (0.50 Ma), and South Mountain (0.49 Ma). These rhyolites range from crystal-poor (Cerro del Medio) to coarsely porphyritic (South Mountain), but all are high-silica rhyolites (e.g., San Antonio Mtn. Rhyolite, Table 1). Geochemical data presented by Spell (1987) indicate that they were derived from Bandelier parental magma.

Geothermal development and the cooperative agreement between UNOCAL and the U.S. Department of Energy have provided drill-hole and geophysical data that give us an interesting picture of subsurface caldera structure. The gravity model of Segar (1974) indicates the floor of the caldera is very asymmetrical, being shallow on the west and deep in the east (Fig. 9); this model is verified by drill-hole data in the western and central caldera. The model also indicates a series of steep, northeast-trending gravity gradients that are probably precaldera structures inherited from the Rio Grande rift (Goff, 1983; Nielson and Hulen, 1984; Heiken et al., 1986; Aldrich, 1986). Depth to Precambrian basement west of the ring-fracture zone beneath Valle Grande is estimated at 5000 m.

If you look northwest between the extension of the resurgent dome and Cerro del Medio, you can see the northwest wall of the caldera (about 18 km distant) formed primarily of Tschicoma Formation dacites overlying hydrothermally altered Paliza Canyon Formation andesite and dacite. The caldera wall immediately to our right is formed of Tschicoma Formation, but to our left is formed mostly of Paliza Canyon Formation. The exception is Rabbit Mountain (1.43 Ma), part of the Cerro Toledo Rhyolite that was vented after formation of Toledo caldera (1.45 Ma).

Several lines of evidence indicate that the Toledo caldera, which erupted 300–400 km^3 of the Otowi Member, Bandelier Tuff, is coaxial with the Valles caldera. This evidence includes isopachs on the Guaje Pumice Bed (Self et al., 1986), radial distribution of the Otowi Member around the present Valles caldera (Smith et al., 1970), flow-direction indicators in the Otowi Member (Potter and Oberthal, 1983), an arc of post-Toledo-age rhyolite domes exposed in the northern moat of Valles caldera (Goff et al., 1984), and the thick sequence of Otowi Member beneath the Valles resurgent dome (Nielson and Hulen, 1984). The feature denoted as Toledo caldera on the northeast margin of Valles caldera by Smith et al. (1970) represents some other structural feature (see Self et al., 1986, and Heiken et al., 1986) and has been renamed the Toledo embayment (Goff et al., 1984).

Continue southwest along NM-4. **3.9**

32.6 Sheeted, devitrified core of South Mountain rhyolite flow on right. **1.9**

34.5 Several outcrops of bedded ash-fall tuff (El Cajete Pumice) are exposed for the next 2 mi. They comprise the only extensive postcaldera ash-fall eruption in the Jemez Mountains. **1.5**

36.0 View of Tshirege Member, Bandelier Tuff, along upper west wall of San Diego Canyon in far distance. **2.2**

38.2 **Cross** East Fork of the Jemez River. **0.2**

38.4 **STOP 6. Southern moat-rhyolite stratigraphy.** Park along left side of road near head of short grade. Exposed in downward succession in roadcut (Fig. 43) are three members of the Valles Rhyolite: (1) vitrophyric blocks of colluvium of the Banco Bonito Rhyolite, (2) well-bedded ash-fall tuff and ignimbrite of the El Cajete Pumice, and (3) a coarsely porphyritic flow of South Mountain Rhyolite.

The Banco Bonito Rhyolite is the youngest erup-

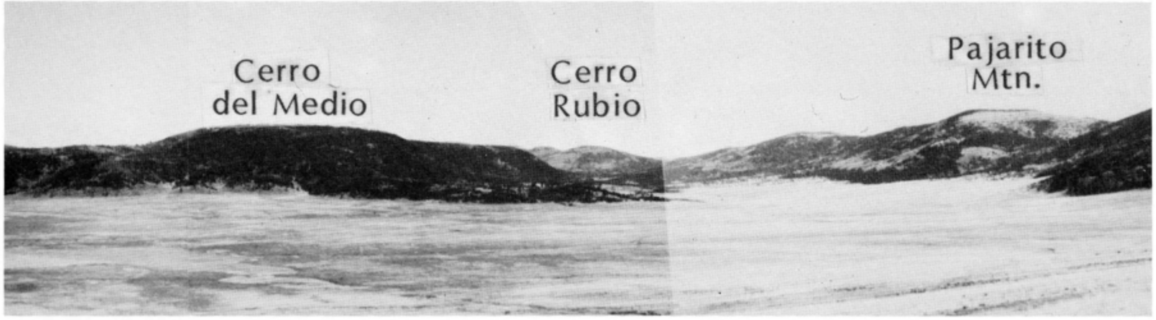

Peak and northward toward the northern moat rhyolites and Cerro Rubio, in the Toledo embayment.

tion in Valles caldera (0.13 Ma; Marvin and Dobson, 1979) and forms a 7 km long sequence of four flow units that filled a paleovalley in the southern moat of the caldera (Manley and Fink, 1987; Goff et al., 1986). The El Cajete Pumice (0.15 Ma) fills in topography on the South Mountain Rhyolite at this location but the main dispersal direction of the pumice and ash was to the southwest (Self et al., 1988). El Cajete Pumice is easily distinguished from Bandelier pumice because the latter does not have obvious, visible biotite phenocrysts but does have chatoyant-blue sanidine phenocrysts. South Mountain Rhyolite (0.49 Ma) is very frothy and perlitic at this locality. The Banco Bonito Rhyolite, El Cajete Pumice, and Battleship Rock Tuff are considered to be one co-magmatic suite of rhyolites according to Self et al. (1988), but see discussion at Stop 5, Day 4.

Two previously unrecognized moat rhyolites were discovered during drilling of CSDP corehole VC-1, located about 4 km west of here (Goff et al., 1986). One is named the VC-1 Rhyolite, a slightly porphyritic obsidian (0.365 Ma), and the other is named the VC-1 Tuffs, which consist of three flow units of lithic-rich ignimbrite (<0.49 but >0.365 Ma). South Mountain Rhyolite, VC-1 Tuffs, VC-1 Rhyolite, Battleship Rock Tuff, and Banco Bonito Rhyolite fill a paleocanyon in the southern caldera moat that was 335 m deep (Goff et al., 1986; Hulen and Nielson, 1988a).

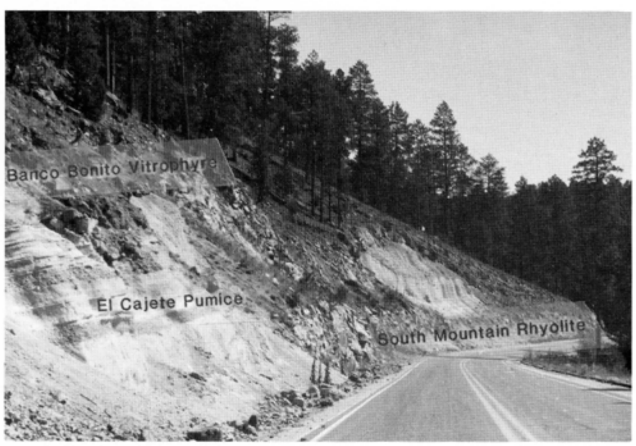

FIGURE 43—The bedded ash-fall and ash-flow deposits of the El Cajete Member of the Valles Rhyolite overlie erosional topography on South Mountain Rhyolite and underlie colluvium of porphyritic obsidian of the Banco Bonito Member.

Compositionally, the youngest moat rhyolites composed of the VC-1 Tuffs, VC-1 Rhyolite, Battleship Rock Tuff, El Cajete Pumice, and Banco Bonito Rhyolite are distinct from other members of the Valles Rhyolite because the former have less SiO_2 but more Fe_2O_3 (total), MgO, CaO, and P_2O_5 (water-free basis, see Table 1) (Gardner et al., 1986). The youngest moat rhyolites also have relatively low $^{87}Sr/^{86}Sr$ compared to other Valles rhyolites (see Vuataz et al., 1988). Thus, the youngest moat rhyolites are probably not derived solely from the Bandelier magma chamber. According to Ankeny et al. (1986), the southern moat zone appears to be the best location for a present (liquid) magma chamber and the geothermal features of the caldera are focused toward the southwest quadrant of the caldera (Sass and Morgan, 1988).

Continue west on NM-4. **1.0**

39.4 Road ascends onto top of Banco Bonito Rhyolite (0.13 Ma). **1.8**

41.2 **Junction** with FR-1850 on left; CSDP corehole VC-1 is 0.8 mi (1.3 km) south from this point on FR-1850. **1.2**

42.4 **Turn right** on Redondo Creek road. **0.7**

43.1 Locked gate to Baca Land and Cattle Co. **NOTE: Access by special permission only; do not trespass.** Continue only if on approved field trip. **0.3**

43.4 Banco Bonito Rhyolite on right. South edge of resurgent dome on left. **0.8**

44.2 Redondo Flats, a valley formed at the mouth of the Redondo Creek graben, on right. **0.7**

44.9 Enter Redondo Creek graben. Redondo Peak on right, Redondo Border on left. **0.9**

45.8 Well pad to Baca-12 on left. This was the deepest well in the old Baca geothermal lease of UNOCAL, reaching a depth of 3211 m and bottoming in hydrothermally altered Precambrian granite. **0.4**

46.2 Old UNOCAL headquarters building on right. **0.9**

47.1 **STOP 7. Redondo Creek graben and Baca-6.** Park along road and walk into clearing bounded by retaining walls on left. This beautiful site was cleared in the early 1980's for construction of a 50 MW(e) geothermal power plant (Fig. 44). UNOCAL intended to sell power to the Public Service Company of New Mexico, but after drilling 24 geothermal wells only 20 MW(e) was proven. The project was terminated in 1984 because of lack of permeability and the threat of lawsuits by various Indian pueblos over water-rights issues (Kerr, 1982; Goldstein and Tsang, 1984). The turbines intended for use at Valles

FIGURE 44—View northeast up the Redondo Creek graben from the former site of Baca-6 well (marked by pole). The gravel embankment and cement retaining wall at the back of the clearing protected the site of the proposed 50 MW(e) geothermal power plant that was never constructed due to permeability problems. Redondo Border, the west segment of the resurgent dome, is at left of photo.

caldera are now in use in the Los Azufries geothermal field, Mexico. In spite of the problems, a few wells in this area are very productive.

The principal zone of geothermal exploration was centered in the Redondo Creek graben that formed in response to stresses developed by uplift of the resurgent dome (Fig. 45). Details of the stratigraphy and structure within this area have been presented by Nielson and Hulen (1984) and are shown in Fig. 10. The steep dips observed to either side of the valley are the result of rotation along listric faults, probably representing a response to topographic instability along the boundary faults of the Redondo Creek graben. Units at depth are nearly horizontal across the crest of the dome.

Drilling results and gravity modeling indicate that the subsurface structure of Valles caldera is considerably different from that postulated by earlier workers (Goff, 1983; Nielson and Hulen, 1984; Heiken et al., 1986) (Fig. 46). The caldera floor is controlled by preexisting structures of the RGR and is much shallower on the west side than on the east side. The thickness of caldera-fill ignimbrites in the Redondo Creek area is approximately three times greater than previously thought based on surface mapping (Smith et al., 1970). Although the caldera is very symmetrical and has a near-perfect ring of moat rhyolites and a central structural uplift, the structural interior of the resurgent dome is more complicated in detail than the model presented in Fig. 45 because of preexisting structures and the presence of the earlier, coaxial Toledo caldera.

Geothermal fluids produced by wells in this area (Table 3) are very typical of volcanic-type geothermal waters the world over (Goff and Grigsby, 1982). They are neutral chloride in character, having about 5000–8000 mg/kg total dissolved solids (TDS) and anomalous concentrations of As, B, Br, Li, etc. Formation temperatures range from about 220 to 300°C depending on depth and location. Both

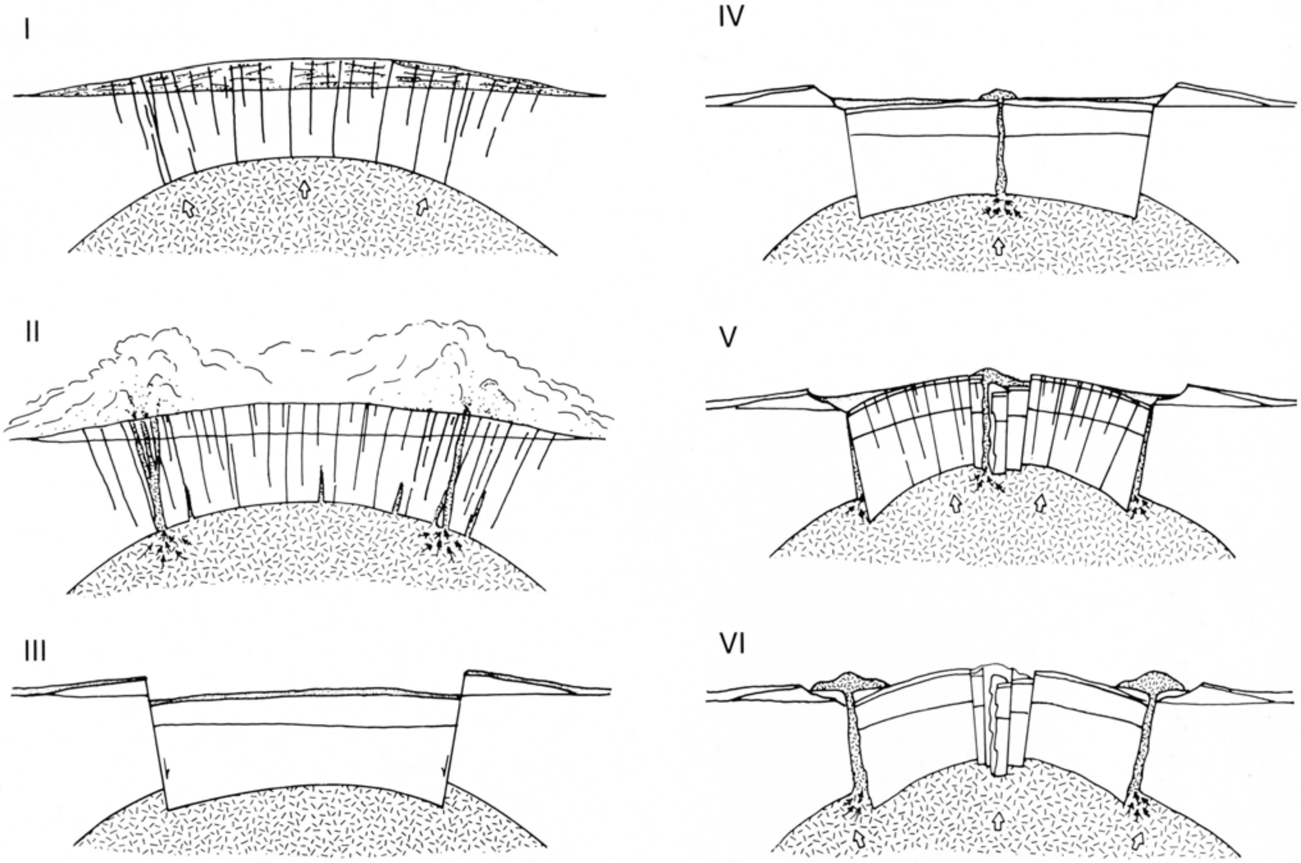

FIGURE 45—The six stages of caldera formation and resurgence according to the model of Smith and Bailey (1968). I. Regional tumescence and generation of ring fractures; II. Caldera-forming eruptions; III. Caldera collapse; IV. Preresurgence volcanism and sedimentation; V. Resurgent doming; VI. Major ring-fracture volcanism.

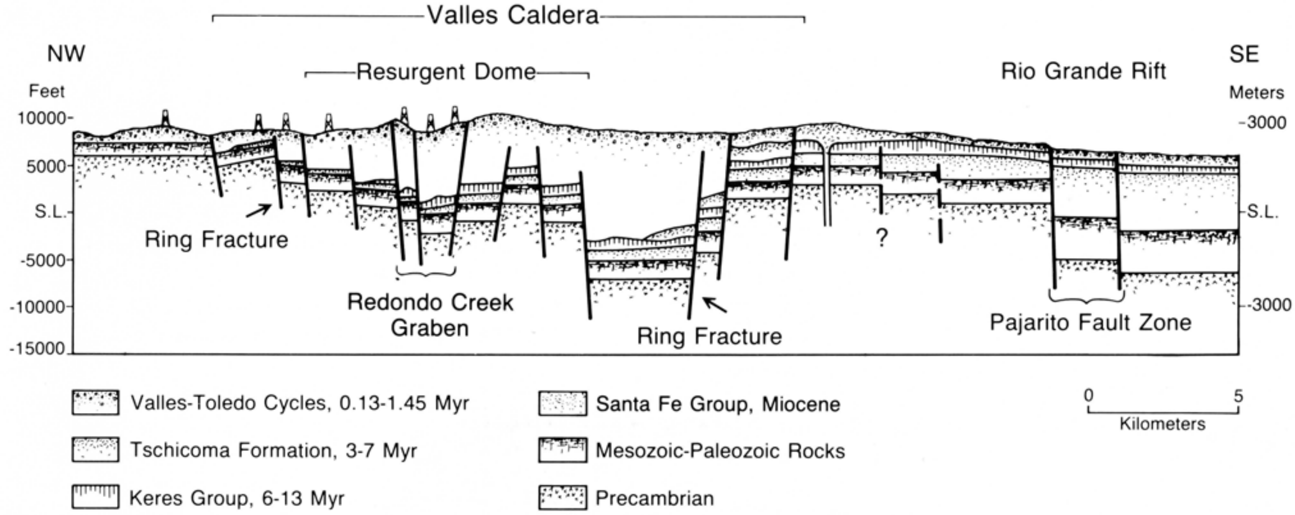

FIGURE 46—Schematic northwest–southeast cross section across Valles caldera based on the stratigraphy of many geothermal wells projected into the plane of the section and the gravity interpretation of Segar (1974); intracaldera volcanic rocks are omitted for clarity. Structure between Valles caldera and Pajarito fault zone is poorly constrained due to paucity of geophysical and drill-hole information. Structure east of Pajarito fault zone is discussed by Goff and Grigsby (1982) and Gardner and Goff (1984). Other interpretations can be seen in the section of Heiken et al. (1986, fig. 7) and in Fig. 17 of this report. See Fig. 10 for a detailed section of the interior of the resurgent dome.

Smith and Kennedy (1985) and Truesdell and Janik (1986) claim that two subtly different fluid types occur in this area. Scaling by calcite and silica was not a problem during any of the flow tests of the wells. A vapor zone about 280 m thick overlies the liquid-dominated system in Baca-6.

Hydrothermal alteration can be observed in the areas excavated for the drill pads and through the woods to either side of the road. Present alteration is acid-sulfate in character and results from small gas seeps along faults of the Redondo Creek graben. The gas seeps and alteration result from subsurface boiling and release of acid gases from the underlying liquid-dominated reservoir. There is no evidence that neutral-chloride hot springs were once present along Redondo Creek.

Rocks exposed along the walls of the graben are primarily Bandelier Tuff with caldera-fill breccias and debris. Redondo Creek Rhyolite, a postcaldera dome, flow, and intrusive complex thought to be about 1.0 Ma, also is found in this area. No intrusive rocks were ever identified in any of the wells drilled in the graben area.

Continue northeast up Redondo Creek. **0.5**

47.6 Altered caldera-fill rocks and fumarole area on left. **0.1**

47.7 **Bear** right. **0.3**

48.0 Road to Baca-13 on left. This well, drilled to a depth of 2472 m, attained a bottom-hole temperature of about 300°C and was one of the best producers in the field. **0.1**

48.1 **Bear** left up hill. **0.2**

48.3 **Bear** left; right fork leads to Baca-4 (280°C, 1915 m), the "discovery well" and also one of the best producers in the field. **0.6**

48.9 Pass at head of Redondo Creek and Jaramillo Creek. Seven dirt roads join here. **Turn left** on main road contouring around hill. **0.4**

49.3 **STOP 8. View of Redondo Peak/Redondo Creek Rhyolite.** Stop along road and be careful of cliff. From this spectacular view point, Redondo Peak and Redondito can be seen to the left (Fig. 47) and

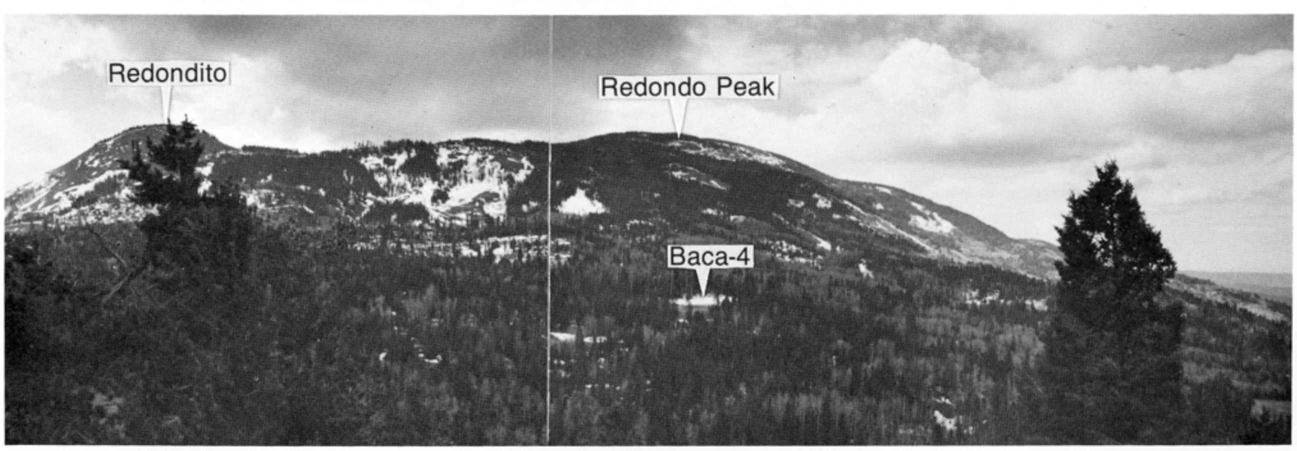

FIGURE 47—Panoramic view looking southeast to south of the east segment of the resurgent dome of Valles caldera; Redondo Peak (3430 m) on right, Redondito on left. The well pad for Baca-4, the "discovery" well of the geothermal system, is shown. The valley in foreground is part of the Redondo Creek graben. Redondo Border, the west segment of the dome, is behind photographer.

Redondo Border to the right. Looking down (southwest) the Redondo Creek graben, we can see the southern moat zone of the caldera, San Diego Canyon, the Jemez Plateau, and the Nacimiento uplift in the far distance.

Although Redondo Creek appears to be the center of resurgent uplift, Redondo Peak is the highest topographic point on the resurgent dome. Stratigraphic work (Nielson and Hulen, 1984) as well as the previously cited gravity study of Segar (1974) demonstrate that the ignimbrite section thickens to the east. It is likely that the higher topography on the eastern portion of the resurgent dome is a manifestation of isostatic uplift of this thicker, low-density tuff section.

Behind us is a small hill of Redondo Creek Rhyolite which has erupted in the graben area between the two creek drainages. Redondo Creek Rhyolite is a formal stratigraphic unit; there are several patches of it mapped in the resurgent dome area that originated from discrete eruptions. It is distinctive in the field because it lacks quartz phenocrysts (all other postcaldera rhyolites have some visible quartz) but has obvious biotite and plagioclase phenocrysts. The unit has been difficult to date by K–Ar because it is usually altered. No dikes or sills of Redondo Creek Rhyolite have been identified in cuttings in the Baca wells.

Continue straight ahead on road. **0.7**

50.0 **Turn around** in junction area of roads and return the way we have come. **1.1**

51.1 **Turn right** and drive down Redondo Creek past Stop 7. **0.6**

51.7 Bear right at junction. **5.3**

57.0 Gate. **0.8**

57.8 **Junction** NM-4; turn left and return to Los Alamos (about 28 mi).

Fourth-day road log: Hydrothermal systems/hot springs

Summary—The fourth day's route returns to Valles caldera to look at some of the hot springs and other geothermal projects besides the earlier Baca geothermal development. These projects include the Continental Scientific Drilling Program, the Hot Dry Rock program, and a small space-heating project at Jemez Springs. Besides providing abundant information on subsurface structure and stratigraphy across the boundary of the caldera, these wells and coreholes have yielded a wealth of information on hydrothermal-fluid compositions, configuration and plumbing of hydrothermal fluids, evolution of the systems with time, and secondary alterations.

Valles caldera contains a variety of hot-spring types (Table 3), although the absolute number of hot-spring sites is relatively small. Included are acid-sulfate hot springs, mud pots, and fumaroles inside the caldera; a ring of dilute, conductively heated hot springs in the caldera moat zone; and neutral-chloride hot springs derived from the deep geothermal reservoirs but located outside the caldera. Recent projects have shown that the Valles hydrothermal system has been active for the last 1 Ma and has deposited molybdenite and other ore minerals.

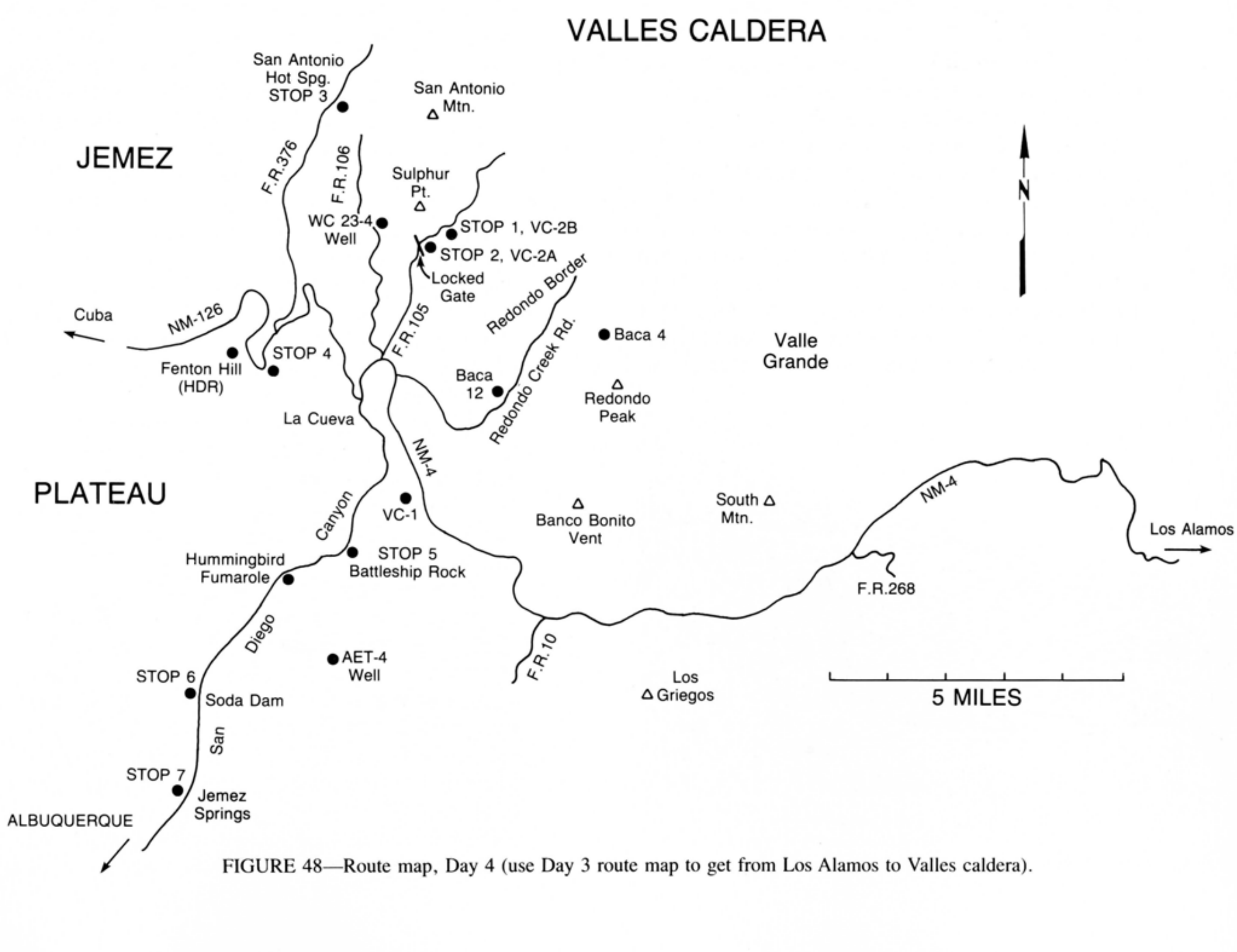

FIGURE 48—Route map, Day 4 (use Day 3 route map to get from Los Alamos to Valles caldera).

Mileage

0.0 Hilltop House parking lot. **Turn right** (west) on NM-502 (Trinity Drive). **1.7**

1.7 **Turn left** on Diamond Drive, cross bridge. **0.4**

2.1 **Turn right** on NM-501. **4.7**

6.8 **Turn right** at the "Back Gate" on NM-4 toward Jemez Springs. Drive into caldera and past the crossings over the East Fork Jemez River. **22.0**

28.8 **Junction** with FR-105. Turn right beyond row of mailboxes toward Sulphur Springs. **0.1**

28.9 Junction with Thompson Ridge Road (FR-106) on left. Continue on FR-105. **1.5**

30.4 Cross bridge over Sulphur Creek, drive past several outcrops of hydrothermally altered rhyolite flows and flow breccias of Redondo Creek Rhyolite. **0.3**

30.7 Locked gate across road to Sulphur Springs. **NOTE: Access by special permission; do not trespass.** Continue only if on approved field trip. **0.7**

31.4 The bleached-out area and the smell of hydrogen sulfide signify the location of Sulphur Springs. Continue straight ahead. **0.4**

31.8 **STOP 1. CSDP corehole VC-2B and Turkey Flats.** Park along the side of road. Walk to right (east) onto grassy meadows. Turkey Flats is a park-like spot in a large landslide complex that occurs on the west side of the resurgent dome of Valles caldera. West of the toe of the slide is the ridge capped by Sulphur Point, which consists of San Antonio Mountain Rhyolite (0.5 Ma) overlying Redondo Creek Rhyolite. The face of the northeast-trending ridge is in part the trace of the Sulphur Creek fault (Goff and Gardner, 1980) along which Sulphur Creek flows. Hydrothermally altered, tectonically brecciated, rhyolite flow breccia is well exposed along Sulphur Creek upstream of our vantage point. Typical alteration minerals are kaolinite, pyrite, silica, iron oxides, and soluble sulfates.

VC-2B is the third continuously cored hole drilled in Valles caldera for the U.S. Continental Scientific Drilling Program (Fig. 49). Objectives of the project were: (1) to penetrate through the main hydrothermal system into a conductive regime between convecting fluids and crystallizing magma, (2) to study structure/stratigraphy near the boundary of the resurgent dome and the western ring-fracture, and (3) to investigate possible ore-deposit mechanisms in a large silicic caldera. VC-2B was cored from July to October 1988 and achieved a total depth of 1762 m (5780 ft) (Fig. 50). Bottom-hole temperature was 295°C as of early November 1988, making this one of the hottest, deepest coreholes in the U.S. VC-2B penetrates a relatively thin caldera-fill sequence at 700 m and then Tertiary Santa Fe Group, Permian Abo–Yeso Formations, Pennsylvanian Magdalena Group, and Precambrian quartz monzonite. Many lost circulation zones indicate that hydrothermal fluids probably exist at all levels. Alteration minerals include quartz, calcite, fluorite, illite, chlorite, epidote, anhydrite, anorthoclase, pyrite, chalcopyrite, sphalerite, pyrargyrite, and rhodochrosite. Scientific investigations have barely begun.

FIGURE 49—Corehole VC-2B during coring operations, July 1988.

The depth to Precambrian basement in VC-2B is 1558 m (5110 ft). Just west of the Sulphur Creek fault, beyond Sulphur Point, the WC23-4 geothermal well hit Precambrian rocks at 737 m (2417 ft); thus, considerable offset occurs along this ring-fracture fault (or fault zone) going east into the caldera depression. Maximum temperature in the WC23-4 well is 233°C at 1890 m (6200 ft); temperature thus decreases noticeably going west out of the caldera depression.

Turn around in wide spots along road and retrace route. **0.4**

32.2 **STOP 2. Sulphur Springs and CSDP corehole VC-2A.** Park along road or on dike to left of road. Do not block traffic. Walk to left (east) toward pond and then walk up road to wellhead. Sulphur Springs was a small resort where people bathed in waters from the springs and mudpots. The resort burned down several years ago and most of the original facilities have fallen to ruin (Fig. 51). The hot springs occur at the intersection of the northeast-trending Sulphur Creek fault and several cross faults (Goff and Gardner, 1980). A variety of thermal features is visible here: fumaroles, hot springs, mud pots, and gaseous cold springs. Temperatures at Sulphur Springs range from background to about 94°C (the boiling point at 2530 m), pH may be less than 1, and SO_4 may be as high as 8000 mg/kg (Table 3). Gases contain 98 mol-% CO_2 and 1.25 mol-% H_2S (dry-gas basis). Empirical gas geothermometry indicates that gases originate from a reservoir at about 215°C, and stable-isotope relations between fumarole steam and meteoric water also suggest about 200°C boiling at depth (Fig. 16) (Goff et al., 1985). Wells drilled in this general area (east of the Sulphur Creek fault) have extremely low formation pressures ($\leq$0.76 MPa) to a depth of about 500 m.

CSDP corehole VC-2A (Fig. 52) was drilled at Sulphur Springs near Footbath Spring in September 1986. Scientific objectives were: (1) to study the vapor zone and its "interface" with the underlying liquid-dominated reservoir, (2) to study structure/stratigraphy, and (3) to study ore-deposit mechanisms (Goff et al., 1987). Technical objectives were to obtain a temperature of at least 200°C and a depth of at least 500 m while obtaining continuous core. VC-2A is 528 m deep and has a BHT of 212°C.

The configuration of the Sulphur Springs hydro-

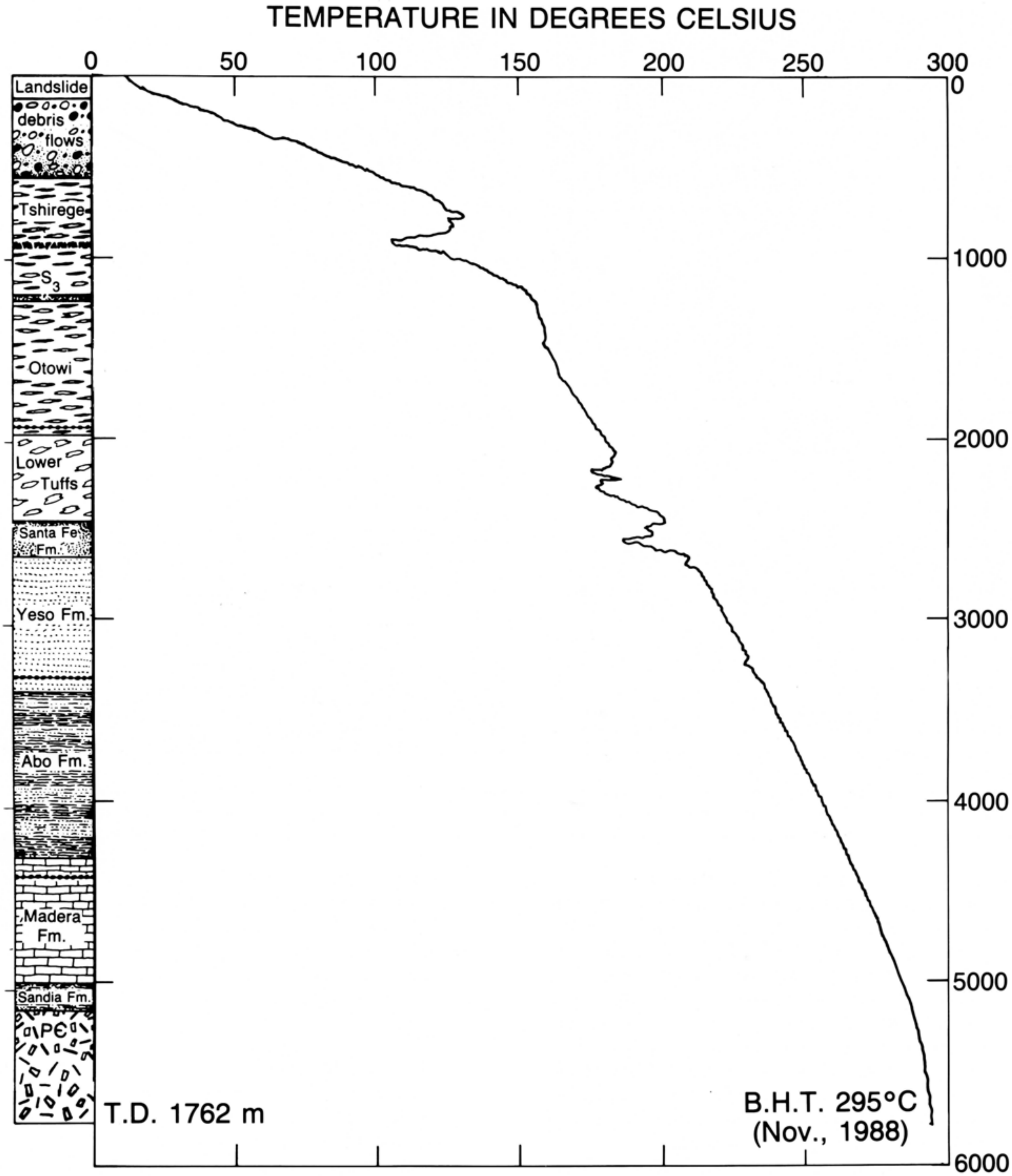

FIGURE 50—Stratigraphy and temperature log of VC-2B.

thermal system consists of an acid-sulfate condensation layer (pH <1.5) no more than 5 m thick, a vapor zone extending to roughly 240 m depth, a "transitional" layer or "cap rock" of fractured but tightly sealed rock that extends from 240 to about 490 m, and a liquid-dominated zone at the bottom. A zone at 490 m and at 210°C was perforated in 1987 and stimulated. After several months of short tests this horizon was purged of drilling fluids. Chemically, the aquifer at 490 m is similar but more concentrated than other "reservoir" fluids in Valles caldera (Table 3). Sr-isotope data indicate more interaction of the fluid with precaldera basement rocks compared with fluids to the east (Meeker and Goff, 1988).

The stratigraphy, alterations, and mineralization in VC-2A appear in Fig. 20 (Hulen et al., 1987, 1988). Shallow, sub-ore-grade molybdenite mineralization was penetrated by VC-2A from 25 to 125 m. The MoS_2 is an unusual, poorly crystalline variety that occurs in vuggy veinlets and breccia cements. Other associated minerals are quartz, fluorite, illite, pyrite, chalcopyrite, sphalerite, and rhodochrosite. Analyses of selected zones grade as high

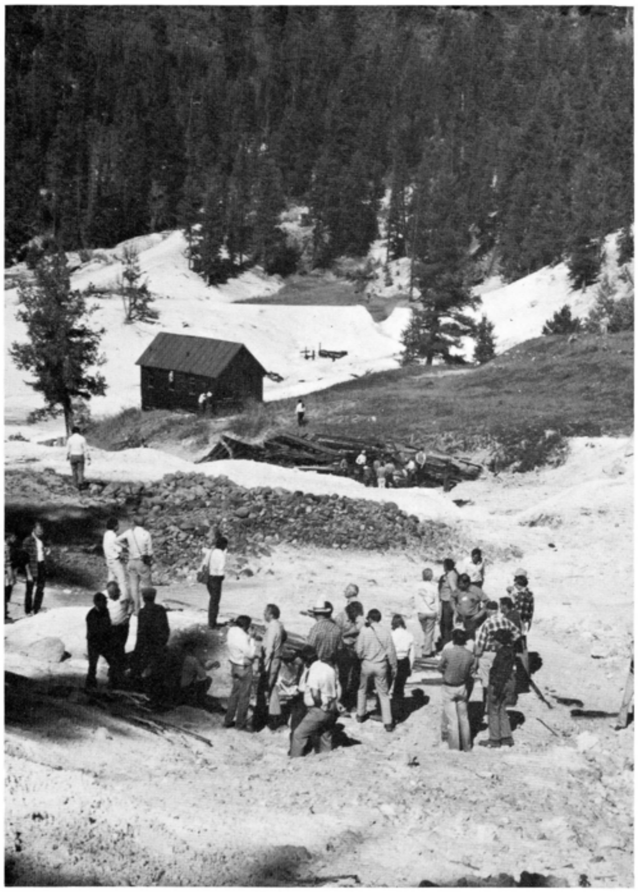

FIGURE 51—View looking north from Women's Bathhouse Spring (~90°C) toward the main area of Sulphur Springs. Men's Bathhouse Spring (75°C) lies under pile of fallen lumber of old bathhouse. Note bleached appearance of rocks that have been altered by acid-sulfate waters.

FIGURE 52—Corehole VC-2A erupting after perforation and stimulation operations, May 1987. Flashed water and steam flow from 210°C aquifer at 490 m in hydrothermally altered, pre-Toledo caldera ignimbrite.

as 0.56 wt% equivalent MoS_2. Fluid-inclusion data from quartz and fluorite suggest that this assemblage was deposited from dilute fluids (0.2–0.5 equivalent wt% NaCl) at temperatures of 195–215°C. Because the molybdenum mineralization was deposited from liquid water but now occurs in a zone where low-pressure vapor fills fractures, the surface of the liquid-dominated reservoir has descended since the deposit was formed. An illite separate from the molybdenite zone has a K–Ar age of 0.66 Ma (WoldeGabriel and Goff, 1989); thus, the present vapor zone is younger than this age.

Continue straight ahead toward NM-4. **0.5**

32.7 Gate. **2.1**

34.8 **Turn right** on NM-4. **0.8**

35.6 La Cueva and **junction** with NM-126. **Bear right** on NM-126. **2.1**

37.7 Outcrops of Permian Abo Formation on left and then on right. **1.3**

39.0 Outcrops of Miocene Santa Fe Group on right. **0.4**

39.4 **Turn right** on FR-376 toward San Antonio CC Camp. **1.2**

40.6 Outcrops of Tschicoma Dacite and Paliza Canyon Basalt underlie Bandelier Tuff along left side of road for next 2 mi (3.2 km). **2.3**

42.9 Permian Abo Formation on left. **0.9**

43.8 **Turn right** and descend into San Antonio Creek. **0.1**

43.9 **Park** in turnout before crossing bridge. **NOTE: San Antonio Hot Spring cannot be used for bathing; $50 fine.** Walk across bridge to rail fence. Walk uphill on left side of fence to big trees. Cross fence and walk south through forest to cascade from hot spring. Walk uphill to spring.

STOP 3. San Antonio Hot Spring. This spring (Table 3) is one of several dilute hot springs that issue from the western ring-fracture zone of Valles caldera (Fig. 53). Isotopically, the waters are meteoric (Fig. 16) and contain extremely low concentrations of As, B, Br, Cl, and Li that are often enriched in high-temperature geothermal fluids. Water issues at the base of fractured San Antonio Mountain Rhyolite (0.5 Ma), a moat rhyolite of the western caldera (Table 1). The rhyolite resembles South Mountain Rhyolite in appearance (seen at our earlier stops).

If you gaze west across San Antonio Canyon toward the caldera wall, you can see the Otowi Member of Bandelier Tuff overlying red stratified sandstones and shales of the Permian Abo Formation. This unit is the uppermost Paleozoic formation in the immediate vicinity of the caldera. As much as 400 m of Permian rocks have been penetrated by some geothermal wells to the southeast, and 500 m of Permian is present in corehole VC-2B. Because it is well cemented and lithified by eons of

FIGURE 53—View to north of San Antonio Hot Spring (~41°C), which issues from the contact of San Antonio Mountain Rhyolite and Redondo Creek Rhyolite. This spring is a favorite destination of cross-country skiers in winter. Cliff in background is composed of Otowi Member, Bandelier Tuff, overlying Permian red beds of the Abo Formation.

diagenesis, the Abo is fairly impermeable; thus, shallow ground waters are perched above the Abo all over the region.

Return to vehicles, turn around, and retrace route to NM-126. **4.5**

48.4 **Turn right** on NM-126. **0.5**

48.9 **STOP 4. West caldera overlook; corehole VC-1 and Hot Dry Rock project. Turn left** onto paved drive to picnic area. Park at end of drive and walk east toward overlook. From this vantage point (elev. 2615 m) on the southwest topographic rim of Valles caldera, we can gaze across the caldera moat toward Redondo Peak (elev. 3460 m), the resurgent dome occupying the approximate center of the caldera (Fig. 54). The nearer and lower ridge to the left of Redondo Peak is Redondo Border, which forms the western half of the resurgent dome. The valley between the two is the northeast-trending Redondo Peak graben.

To the northeast, in the middle distance, are San Antonio Mountain and Cerro Seco, two post-resurgent moat-rhyolite domes (Valles Rhyolite) dated at 0.54 and 0.73 Ma, respectively. A thick rhyolite flow from San Antonio Mountain overlies Redondo Creek Rhyolite on Thompson Ridge in the caldera moat immediately before us. Another flow of rhyolitic obsidian (Banco Bonito Member, Valles Rhyolite) fills the caldera moat to our right (age 0.13 Ma).

On the distant skyline to the northeast, on the northern rim of the caldera, is Cerro de la Garita formed of dacite of the Tschicoma Formation. On the skyline to the southeast is the crest of Los Griegos (on the south rim of the caldera), formed mainly of andesites of the Paliza Canyon Formation.

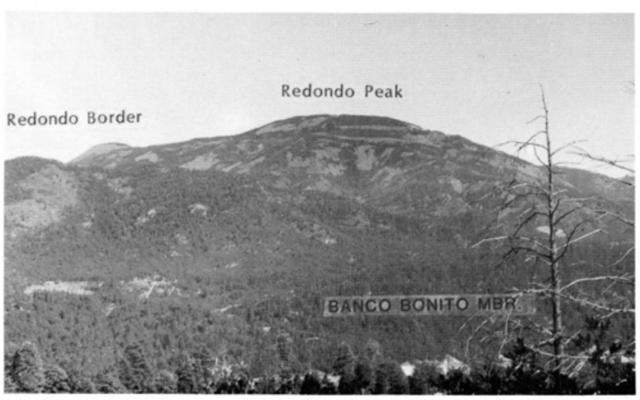

FIGURE 54—View looking east toward Redondo Peak, Redondo Border on left. The linear valley separating these two ridges is the Redondo Creek graben, the medial graben of the resurgent dome. In foreground is the southern moat of the caldera which is filled by postcaldera rhyolites, the Banco Bonito Member on the right and the Redondo Creek Member on the left. Corehole VC-1 was drilled on the south edge of the Banco Bonito rhyolite flow approximately on strike with the southwest extension of the medial graben (just right of photo). Stratigraphy of VC-1 is shown schematically in the cross section of Fig. 17.

CSDP corehole VC-1 was drilled in August 1984 on the southern side of the Banco Bonito flow on strike with the southwest projection of the Redondo Creek graben. Objectives were: (1) to intersect a hydrothermal outflow plume from the geothermal reservoir near its source, (2) to study the structure and stratigraphy near the intersection of the ring-fracture zone and the precaldera Jemez fault zone, and (3) to study the petrology of the youngest moat volcanics in the caldera. Total depth is 856 m and the BHT is about 185°C. Fluid chemistry of aquifers at 400–600 m depth in VC-1 resembles, but is more dilute than, reservoir waters in the caldera (Table 3, Fig. 16). A more detailed discussion of the outflow plume will be given at Stop 6.

VC-1 core was found to be altered and structurally disrupted below 335 m, particularly the lowermost interval of brecciated Precambrian rocks and Sandia Formation (Hulen and Nielson, 1988a; Keith, 1988). Molybdenite was also found in this breccia zone along with chalcopyrite, sphalerite, galena, pyrite, and barite. Fluid-inclusion work suggests that the molybdenite was deposited from dilute water at tempertures as high as 280°C (Hulen and Nielson, 1988a; Sasada, 1988). Ghazi and Wampler (1987) obtained a K–Ar age of 1.0 Ma on hydrothermal illite in Madera Limestone, while Sturchio and Binz (1988) obtained ages of 95 to >400 Ka on calcite veins using the U–Th disequilibrium technique. Geissman (1988) found that the paleomagnetic character of Paleozoic rocks in the corehole was overprinted by a reversed magnetic signature and concluded that major hydrothermal activity at about 300°C occurred between 1.4 and 0.97 Ma.

The location of the first Hot Dry Rock (HDR) demonstration project is a scant 0.5 km to the west of this site. In the HDR concept, two wells are drilled into hot, impermeable-rock units and connected by man-made fractures. Cold surface water is pumped down one well, where it is heated by the rock adjacent to the fracture, and removed up the second well. A heat exchanger or turbine is used to extract the heat or energy from this circulation system, after which the water is pumped down the first well for another cycle. The first (research) system (Fig. 11) was constructed at a depth of 3 km where the ambient temperature is 195°C. This system demonstrated technical feasibility (Heiken et al., 1981; Laughlin, 1981; Smith, 1983). The second system, constructed at depths of 3.7 km and a temperature of about 250°C, is designed to demonstrate commercial feasibility. For a tour of the HDR facilities call (505) 667-7900.

Small volumes of relatively concentrated fluids ($\geq$20,000 mg/kg TDS) have been encountered in Precambrian rocks in both the HDR wells (Grigsby et al., 1984) and in the WC23-4 well on Thompson Ridge in the western caldera moat (Shevenell et al., 1987, 1988). The origin of these fluids and their relation to more dilute but voluminous "reservoir" fluids is not yet resolved, but an association can be seen in the isotope plot of Fig. 16 (see also Table 3).

Turn around and return to NM-126. **0.1**

49.0 **Turn right** on NM-126. **4.3**

53.3 **Turn right** on NM-4 at La Cueva. **0.7**

54.0 Exposures of Banco Bonito Rhyolite over Battleship Rock Tuff on left side of upper San Diego Canyon. **1.3**

55.3 Contact of Permian Abo Formation (red beds) over Pennsylvanian Madera Limestone (buff rock). **1.0**

56.3 Mineral seeps in shale of Madera Limestone on right. **0.2**

56.5 **Turn left** into Battleship Rock picnic area (do not turn into Camp Shaver). Follow arrows to bridge and cross it. **0.2**

56.7 **STOP 5. Battleship Rock.** Park anywhere and walk past old restrooms to path that ascends the lower "prow" of Battleship Rock. Battleship Rock (Fig. 55) is a spectacular outcrop of columnar-jointed ignimbrite formed by a series of small eruptions that flowed down an ancestral drainage of the Jemez River. Subsequent erosion by new streams has formed canyons on either side of this beautiful example of reversed topography. San Antonio Creek drains the western caldera while East Fork Jemez River drains the eastern caldera, and the streams combine at Battleship Rock.

The ignimbrite is about 80 m thick and contains two main flow units that make up a single cooling unit (Bailey and Smith, 1978). Although the base is poorly consolidated, the center is densely welded and very striking in appearance. Abundant lithic and crystal fragments are found in the matrix of the ignimbrite along with glass shards and pumice. Chemical analyses of pumice lumps show that this ignimbrite is a rhyolite similar in composition to the youngest, more mafic group of moat rhyolites (Gardner et al., 1986). Self et al. (1988) consider the Battleship Rock Tuff to be part of the co-magmatic El Cajete Series and indicate an age of about 0.15 Ma. An age of 0.278 ± 0.052 Ma was obtained by K–Ar methods on sanidine separated from pumice lumps (F. Goff, unpubl. data 1986). In corehole VC-1, Banco Bonito Rhyolite directly overlies Battleship Rock Tuff; no El Cajete Pumice is found (Goff et al., 1986). Thus, the timing of the Battleship Rock Tuff with respect to other units is still in question.

If you examine the contact between ignimbrite and underlying rocks on the east side of Battleship Rock, note that the tuff overlies a small cliff of Pennsylvanian Madera Limestone. The limestone is extremely fossiliferous and includes crinoids, brachiopods, and bryozoans.

Return to NM-4. **0.3**

57.0 **Turn left** on NM-4. **0.5**

57.5 Smell of hydrogen sulfide and sight of bleached rock signify Hummingbird Fumarole on left of road but above level of Jemez River. **3.2**

60.7 **STOP 6. Soda Dam and Jemez fault zone.** Park in turnout on right side of road before crossing cattleguard. Walk up path to ledge overlooking the right (west) side of highway. The travertine dam (Fig. 56) across the gorge in Precambrian granite–gneiss was built by carbonated thermal waters that discharge from a strand of the Jemez fault zone. There are roughly 15 springs and seeps discharging in this area. About 20 years ago water discharged along the central fissure parallel to the trend of the dam, but the New Mexico State Highway Department eliminated the hump in the paved road by dynamiting a notch in the west end of the dam. This forever changed the plumbing of hot-spring water and today Soda Dam is slowly disintegrating.

The travertine deposits of Soda Dam proper have been dated by the U–Th technique and have a max-

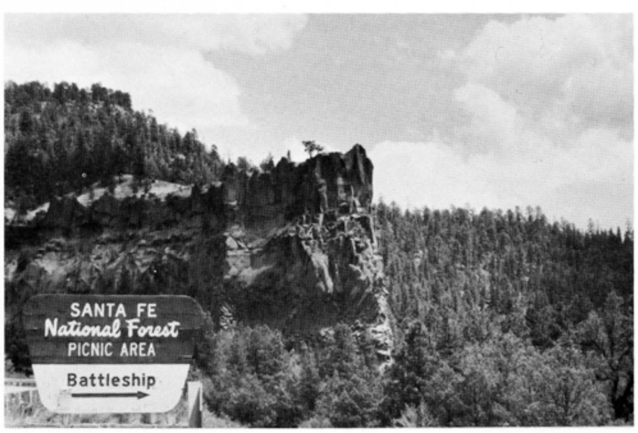

FIGURE 55—Battleship Rock, a small-volume, postcaldera ignimbrite of the Valles Rhyolite that occupies the ancestral canyon of the Jemez River. Note radial cooling joints near the "prow."

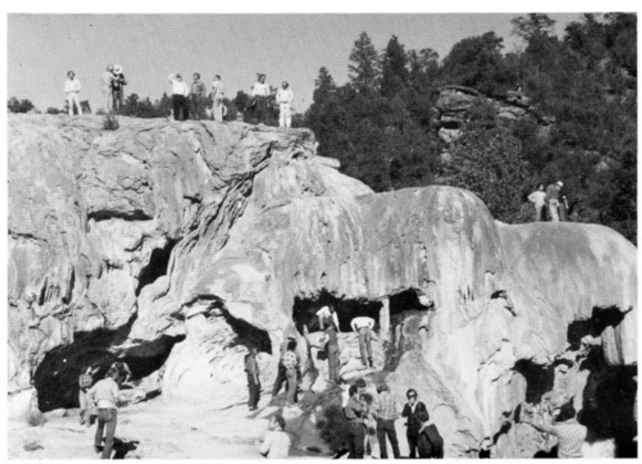

FIGURE 56—Soda Dam, a hot-spring deposit of travertine now undercut by the Jemez River (lower right). Narrow cavern in center of photo leads to Groto Spring. Main hot spring (48°C) issues along highway to left of photo.

imum age of about 5 Ka (Goff and Shevenell, 1987). Two older deposits at slightly higher elevation occur across the Jemez River (age = 60–110 Ka). On the west side of the gorge, roughly 30 m above the road, occurs an extremely large deposit of travertine that has an age range of about 0.48–1.0 Ma by evaluation with the U–U dating method. These older deposits do not overlie Bandelier Tuff; instead they lie directly on Paleozoic/Precambrian rocks. A discontinuous deposit of ancestral Jemez River gravels can be seen beneath the travertine and a large cave is located along the contact.

Hot-spring waters at Soda Dam have a maximum temperature of 48°C and contain about 1500 mg/kg Cl and substantial As, B, Br, Li, etc. (Table 3). They chemically resemble, but are more dilute than, reservoir water inside Valles caldera, and isotopically they appear to be mixtures of meteoric and reservoir water (Fig. 16). Several people have claimed that the hot waters follow the trace of the Jemez fault zone out of the caldera and mix with dilute ground waters (Dondanville, 1971; Trainer, 1974; Goff et al., 1981). By combining geochemistry of hot springs and aquifers throughout the southwestern perimeter of the caldera with other geologic data, Goff et al. (1988) showed that a major subsurface tongue of reservoir water flows out of the caldera on either side of the Jemez fault zone. During lateral flow, the waters dissolve Paleozoic limestone and become relatively rich in Ca and HCO_3. When these data are combined with the information on the travertine deposits, the age of the Valles hydrothermal system is estimated to be about 1.0 Ma.

The Jemez fault zone is very complex in this area. The main trace trends northeast across the highway and creates a 15 m scarp along the north side of the older travertine. Generally, displacement along the fault in Paleozoic rocks is about 200–250 m down-to-the-east. At Soda Dam, a local horst of sheared Precambrian granite–gneiss is uplifted and overlain by distorted Paleozoic rocks. The granite–gneiss is hydrothermally altered and contains secondary barite, galena, and sphalerite in veins and fracture fillings. The Jemez fault zone continues to the southwest and displaces the Tshirege Member of the Bandelier Tuff by about 50 m in the canyon wall.

If you gaze carefully at the upper east wall of San Diego Canyon, you can see a white band of Abiquiu Formation (late Oligocene) overlying orange Permian Yeso Formation sandstone and shale. The Abiquiu is overlain by volcanic units of the Paliza Canyon Formation (8–10 Ma?) and the mesa is capped by a thin layer of Tshirege Member, Bandelier Tuff. Looking northwest, the canyon wall is composed of Pennsylvanian Madera Limestone, Abo Formation, Abiquiu Formation, Paliza Canyon Formation, and both members of the Bandelier Tuff. The canyon is partly controlled by erosion along the Jemez fault zone and the stratigraphy is different on either canyon wall.

Return to vehicles and continue southwest (downstream) on NM-4. **0.2**

60.9 Outcrops of Precambrian granite–gneiss to left and right. **0.8**

61.7 Ruins of 17th century Spanish mission on left. **0.5**

62.2 **STOP 7. Jemez Springs and space-heating project. Turn right** just beyond Jemez Springs Police Station/Courthouse and drive to parking area by bathhouse. Jemez Springs is a small village with several religious institutions and several interesting hot springs. The bathhouse on the west side of the road is open to the public. Water is supplied mainly from an old, hand-dug well covered by the quaint gazebo. Temperature is about 55°C. Another curious spring (72°C) issues from a mound of travertine in the reeds near the Jemez River (Fig. 57). Others occur in the marshy area and discharge along the river. These springs are also derived from Valles reservoir fluids and are part of the hydrothermal plume (Table 3, Fig. 16).

In January 1979, the community of Jemez Springs drilled a well 255 m deep that penetrated the Madera Limestone and bottomed in Precambrian granite. They were seeking hot water for space heating. The hottest water (74°C) was at 25 m at the contact of alluvium and limestone. Another aquifer at 152 m has a cooler temperature of 62°C, indicating a typical temperature reversal beneath the hydrothermal plume (Goff et al., 1981). The town hall uses the aquifer at 25 m for space heating, but has problems with calcite scaling of the heat exchanger.

Return to NM-4. **0.1**

62.3 **Turn left** on NM-4 to return to Los Alamos (about 39 mi), or **turn right** on NM-4 to return to Albuquerque (about 50 mi); at San Ysidro **turn left** on NM-44; at Bernalillo **turn right** on I-25.

FIGURE 57—Travertine Mound Spring (72°C), the hottest spring outside the Valles caldera depression, is reported to contain an extremely rare species of alga. It is located in the reeds between the Jemez River and bathhouse at Jemez Springs.

Acknowledgments

This field-trip guide has evolved from the earlier guides published by Bailey and Smith (1978), Goff and Bolivar (1983), and Self et al. (1987), and from countless field trips led by the authors during the last 10 years. Many thanks to all the explorers, developers, researchers, and graduate students, past and present, who have contributed to the general knowledge of the Jemez Mountains region. Much of the information incorporated in this paper was obtained from the geothermal efforts of UNOCAL (Santa Rosa, California), GEO Operator Corp. (San Mateo, California), and SUNEDCO (Dallas, Texas), and from the research and development efforts of the Hot Dry Rock project funded by the U.S. Department of Energy. The cooperation of the U.S. Forest Service, the Baca Land and Cattle Company, John Corbin of Sulphur Springs, and other landowners in the Jemez Mountains is gratefully appreciated. Marcia Jones and Anthony Garcia typed the manuscript and prepared many of the figures, respectively. This field-trip guide was funded by the U.S. Department of Energy, Office of Basic Energy Sciences, through the helpful efforts of George Kolstad, and by an Institutional Supporting Research grant from Los Alamos National Laboratory.

References

Aldrich, M. J., 1968, Tectonics of the Jemez lineament in the Jemez Mountains and the Rio Grande rift: Journal of Geophysical Research 91: 1753–1762.

Aldrich, M. J., Jr., and Laughlin, A. W., 1984, A model for the tectonic development of the southeastern Colorado Plateau boundary: Journal of Geophysical Research, 89: 10,207–10,218.

Ankeny, L. A., Braile, L. W., and Olsen, K. H., 1986, Upper crustal structure beneath the Jemez Mountains volcanic field, New Mexico, determined by three-dimensional simultaneous inversion of seismic refraction and earthquake data: Journal of Geophysical Research, 91: 6188–6198.

Bailey, R. A., and Smith, R. L., 1978, Volcanic geology of the Jemez Mountains, New Mexico; *in* Hawley, J. W. (ed.), Guidebook to the Rio Grande rift in New Mexico and Colorado: New Mexico Bureau of Mines & Mineral Resources, Circular 163: 184–196.

Bailey, R. A., Smith, R. L., and Ross, C. S., 1969, Stratigraphic nomenclature of volcanic rocks in the Jemez Mountains, New Mexico: U.S. Geological Survey, Bulletin 1274-P: 19 pp.

Baldridge, W. S., 1979, Petrology and petrogenesis of Plio-Pleistocene basaltic rocks from the central Rio Grande rift, New Mexico, and their relation to rift structure; *in* Riecker, R. E. (ed.), Rio Grande rift: Tectonics and magmatism: American Geophysical Union, Special Publication, pp. 323–353.

Baldridge, W. S., Perry, F. V., and Shafiqullah, M., 1987, Late Cenozoic volcanism in the southeastern Colorado Plateau: I. Volcanic geology of the Lucero area, New Mexico: Geological Society of America, Bulletin, 99: 463–470.

Baldridge, W. S., Damon, P. E., Shafiqullah, M., and Bridwell, R. J., 1980, Evolution of the central Rio Grande rift, New Mexico: New Potassium–Argon ages: Earth and Planetary Science Letters, 51: 309–321.

Barton, P., Bethke, P., Wetlaufer, P., Foley, N., Hayba, D., and Goss, J., 1982, Silver/base metal epithermal deposits; *in* Erickson, R. L. (ed.), Characteristics of mineral deposit occurrences: U.S. Geological Survey, Open-File Report 82-795: 127–130.

Bayhurst, G. K., and Janecky, D. R., 1987, Investigations of alteration mineralogy and geochemistry in CSDP hole VC-2A, Valles caldera, New Mexico: American Geophysical Union, Transactions, 68: 469.

Behrman, P. G., and Knapp, R. B., 1980, Structure of the Redondo Creek area, Baca prospect—Implications concerning the nature of permeability and control on production: Union Oil Company of California, Internal Report; also University of Utah Research Institute, Earth Science Laboratory, Open-File Report NM-Baca-101: 43 pp.

Brookins, D., and Laughlin, A. W., 1983, Rb–Sr geochronologic investigation of Precambrian samples from deep geothermal drill holes, Fenton Hill, New Mexico: Journal of Volcanology and Geothermal Research, 15: 43–58.

Budding, A. J., 1978, Gravity survey of the Pajarito Plateau, Los Alamos and Santa Fe counties, New Mexico: Los Alamos Scientific Laboratory, Report LA-7419-MS: 15 pp.

Chapin, C. E., 1979, Evolution of the Rio Grande rift: A summary; *in* Riecker, R. E. (ed.), Rio Grande rift: Tectonics and magmatism: American Geophysical Union, Special Publication, pp. 1–6.

Chapin, C. E., and Seager, W. R., 1975, Evolution of the Rio Grande rift in the Socorro and Las Cruces areas; *in* Seager, W. R., Clemons, R. E., and Callender, J. F. (eds.), Las Cruces country: New Mexico Geological Society, Guidebook 26: 297–321.

Charles, R. W., Vidale-Buden, R., and Goff, F., 1986, An interpretation of the alteration assemblages at Sulphur Springs, Valles caldera, New Mexico: Journal of Geophysical Research, 91: 1887–1898.

Cordell, L., 1978, Regional geophysical setting of the Rio Grande rift: Geological Society of America, Bulletin, 89: 1073–1090.

Dalrymple, G. B., Cox, A., Doell, R. R., and Grommé, C. S., 1967, Pliocene geomagnetic polarity epochs: Earth and Planetary Science Letters, 2: 163–173.

Dethier, D. P., and Manley, K., 1985, Geologic map of the Chili quadrangle, Rio Arriba County, New Mexico: U.S. Geological Survey, Map MF-1814, scale 1:24,000.

Dethier, D. P., Harrington, C. D., and Aldrich, M. J., 1988, Late Cenozoic rates of erosion in the Western Española basin, New Mexico: Evidence from geologic dating of erosion surfaces: Geological Society of America, Bulletin, 100: 928–937.

Doell, R. R., and Dalrymple, G. B., 1966, Geomagnetic polarity epochs, A new polarity event and the age of the Brunhes–Matuyama boundary: Science, 152: 1060–1072.

Doell, R. R., Dalrymple, G. B., Smith, R. L., and Bailey, R. A., 1968, Paleomagnetism, potassium–argon ages, and geology of rhyolites and associated rocks of the Valles caldera, New Mexico; *in* Coats, R. R., Hay, R. L., and Anderson, C. A. (eds.), Studies in volcanology: Geological Society of America, Memoir 116: 211–248.

Dondanville, R. F., 1971, The hydrothermal geology of the Valles caldera, Jemez Mountains, New Mexico: Union Oil Company, Santa Rosa, California, Open-File consultant report, 36 pp.

Dondanville, R. F., 1978, Geologic characteristics of the Valles caldera geothermal system: Geothermal Resources Council, Transactions, 2: 157–160.

Eichelberger, J. C., 1980, Vesiculation of magma during replenishment of silicic magma reservoirs: Nature, 288: 446–450.

Eichelberger, J. C., and Koch, F. G., 1979, Lithic fragments in the Bandelier Tuff, Jemez Mountains, New Mexico: Journal of Volcanology and Geothermal Research, 5: 115–134.

Faust, C. R., Mercer, J. W., and Thomas, S. D., 1984, Quantitative analysis of existing conditions and production strategies for the Baca geothermal system, New Mexico: Water Resources Research, 20: 601–618.

Fisher, R. V., 1979, Models for pyroclastic surges and pyroclastic flows: Journal of Volcanology and Geothermal Research, 6: 305–318.

Friedman, I., and Smith, R. L., 1958, The deuterium content of water in some volcanic glasses: Geochimica et Cosmochimica Acta, 15: 218–228.

Galusha, T., and Blick, J. C., 1971, Stratigraphy of the Santa Fe Group, New Mexico: American Museum of Natural History, Bulletin, 144: 1–128.

Gardner, J. N., 1985, Tectonic and petrologic evolution of the Keres Group: Implications for the development of the Jemez volcanic field, New Mexico: Unpublished Ph.D. dissertation, University of California, Davis, 295 pp.

Gardner, J. N., and Goff, F., 1984, Potassium–argon dates from the Jemez volcanic field: Implications for tectonic activity in the north-central Rio Grande rift; *in* Baldridge, W. S., Dickerson, P. W., Riecker, R. E., and Zidek, J. (eds.), Rio Grande rift: Northern New Mexico: New Mexico Geological Society, Guidebook 35: 75–81.

Gardner, J. N., and House, L., 1987, Seismic hazards investigations at Los Alamos National Laboratory, 1984 to 1985: Los Alamos National Laboratory, Report LA-11072-MS: 76 pp.

Gardner, J. N., Goff, F., Garcia, S., and Hagan, R. C., 1986, Stratigraphic

relations and lithologic variations in the Jemez volcanic field, New Mexico: Journal of Geophysical Research, 91: 1763–1778.
Geissman, J. W., 1988, Paleomagnetism and rock magnetism of Quaternary volcanic rocks and Late Paleozoic strata, VC-1 core hole, Valles caldera, New Mexico, with emphasis on remagnetization of Late Paleozoic strata: Journal of Geophysical Research, 93(B6): 6001–6026.
Ghazi, A., and Wampler, J., 1987, Potassium–argon dates of clays from brecciated and hydrothermally altered rocks from VC-1, Valles caldera, New Mexico: American Geophysical Union, Transactions, 68: 1515.
Gill, J. B., 1981, Orogenic andesites and plate tectonics: Springer-Verlag, New York, 390 pp.
Goff, F., 1983, Subsurface structure of Valles caldera: A resurgent cauldron in northern New Mexico (abs.): Geological Society of America, Abstracts with Programs, 15: 381.
Goff, F., and Bolivar, S. L., 1983, Field trip guide to the Valles caldera and its geothermal systems: Los Alamos National Laboratory, Report LA-9963-OBES: 53 pp.
Goff, F., and Gardner, J. N., 1980, Geologic map of the Sulphur Springs area, Valles caldera geothermal system, New Mexico: Los Alamos Scientific Laboratory, Map LA-8634-MAP (two sheets, scale 1:5000).
Goff, F., and Gardner, J. N., 1988, Valles caldera region, New Mexico, and the emerging Continental Scientific Drilling Program: Journal of Geophysical Research, 93(B6): 5997–6000.
Goff, F., and Grigsby, C. O., 1982, Valles caldera geothermal systems, New Mexico, USA: Journal of Hydrology, 56: 119–136.
Goff, F., and Nielson, D. L. (eds.), 1986, Caldera processes and magma-hydrothermal systems, Continental Scientific Drilling Program—Thermal Regimes, Valles caldera research, scientific and management plan: Los Alamos National Laboratory, Report LA-10737-OBES: 163 pp.
Goff, F., and Shevenell, L., 1987, Travertine deposits of Soda Dam, New Mexico, and their implications for the age and evolution of the Valles caldera hydrothermal system: Geological Society of America, Bulletin, 99: 292–302.
Goff, F., Gardner, J. N., Vidale, R., and Charles, R., 1985, Geochemistry and isotopes of fluids from Sulphur Springs, Valles caldera, New Mexico: Journal of Volcanology and Geothermal Research, 23: 2734–2797.
Goff, F., Grigsby, C., Trujillo, P., Counce, D., and Kron, A., 1981, Geology, water geochemistry, and geothermal potential of the Jemez Springs area, Cañon de San Diego, New Mexico: Journal of Volcanology and Geothermal Research, 10: 227–244.
Goff, F., Shevenell, L., Gardner, J. N., Vuataz, F. D., and Grigsby, C. O., 1988, The hydrothermal outflow plume of Valles caldera, New Mexico, and a comparison with other outflow plumes: Journal of Geophysical Research, 93(B6): 6041–6058.
Goff, F., Heiken, G., Tamanyu, S., Gardner, J., Self, S., Drake, R., and Shafiqullah, M., 1984, Location of Toledo caldera and formation of the Toledo embayment, Jemez Mountains, New Mexico: American Geophysical Union, Transactions, 65: 1145.
Goff, F., Nielson, D. L., Gardner, J. N., Hulen, J. B., Lysne, P., Shevenell, L., and Rowley, J. C., 1987, Scientific drilling at Sulphur Springs, Valles caldera, New Mexico: Corehole VC-2A: American Geophysical Union, Transactions, 68: 649, 661–662.
Goff, F., Rowley, J., Gardner, J. N., Hawkins, W., Goff, S., Charles, R., Wachs, D., Maassen, L., and Heiken, G., 1986, Initial results from VC-1: First Continental Scientific Drilling Program core hole in Valles caldera, New Mexico: Journal of Geophysical Research, 91: 1742–1752.
Goldstein, N. E., and Tsang, C. F., 1984, A review of lessons learned from the DOE/Union Baca geothermal project: Geothermal Resources Council, Bulletin 8: 7–12.
Golombek, M. P., 1983, Geology, structure, and tectonics of the Pajarito fault zone in the Española Basin of the Rio Grande rift, New Mexico: Geological Society of America, Bulletin, 94: 192–205.
Gonzalez, C. M., and McKibben, M. A., 1987, Thermal history of vein mineralization in CSDP corehole VC-2A, Valles caldera, New Mexico (abs.): Geological Society of America, Abstracts with Programs, 19: 679.
Griggs, R. L., 1964, Geology and groundwater resources of the Los Alamos area, New Mexico: U.S. Geological Survey, Water Supply Paper 1753: 107 pp.
Gribsby, C., Goff, F., Trujillo, P., and Counce, D., 1984, Geochemical behavior of a hot dry rock geothermal reservoir; *in* Baldridge, W. S., Dickerson, P. W., Riecker, R. E., and Zidek, J. (eds.), Rio Grande rift: Northern New Mexico: New Mexico Geological Society, Guidebook 35: 265–270.
Harrison, T. M., Morgan, P. M., and Blackwell, D. D., 1986, Constraints on the age of heating at the Fenton Hill site, Valles caldera, New Mexico: Journal of Geophysical Research, 91: 1899–1908.
Hayba, D. O., Bethke, P. M., Heald, P., and Foley, N. K., 1985, Geologic characteristics of volcanic-hosted epithermal precious-metal deposits: Reviews in Economic Geology, 2: 129–168.
Heiken, G. (ed.), 1985, Workshop on recent research in the Valles caldera: Los Alamos National Laboratory, Report LA-10339-C: 68 pp.
Heiken, G., and Goff, F., 1983, Hot dry rock geothermal energy in the Jemez volcanic field, New Mexico: Journal of Volcanology and Geothermal Research, 15: 223–246.
Heiken, G., Murphy, H., Nunz, G., Potter, R., and Grigsby, C., 1981, Hot dry rock geothermal energy: American Scientist, 69: 400–407.
Heiken, G., Goff, F., Stix, J., Tamanyu, S., Shafiqullah, M., Garcia, S., and Hagan, R., 1986, Intracaldera volcanic activity, Toledo caldera and embayment, Jemez Mountains, New Mexico: Journal of Geophysical Reserch, 91: 1799–1815.
Henley, R. W., and Ellis, A. J., 1983, Geothermal systems ancient and modern: A geochemical review: Earth-Science Reviews, 19: 1–50.
Hermance, J. F., and Pedersen, J., 1980, Deep structure of the Rio Grande rift: A magnetotelluric interpretation: Journal of Geophysical Research, 85: 3899–3912.
Hulen, J. B., and Nielson, D. L., 1986a, Hydrothermal alteration in the Baca geothermal system, Redondo dome, Valles caldera, New Mexico: Journal of Geophysical Research, 91: 1867–1886.
Hulen, J. B., and Nielson, D. L., 1986b, Stratigraphy and hydrothermal alteration in borehole Baca-8, Sulphur Springs area, Valles caldera, New Mexico: Geothermal Resources Council, Transactions, 10: 187–192.
Hulen, J. B., and Nielson, D. L., 1988a, Hydrothermal brecciation in the Jemez fault zone, Valles caldera, New Mexico: Results from Continental Scientific Drilling Program core hole VC-1: Journal of Geophysical Research, 93(B6): 6077–6090.
Hulen, J. B., and Nielson, D. L., 1988b, Clay mineralogy and zoning in CSDP core hole VC-2A—Further evidence for collapse of isotherms in the Valles caldera: Geothermal Resources Council, Transactions, 12: 291–298.
Hulen, J., Gardner, J. N., Nielson, D., and Goff, F., 1988, Stratigraphy, structure, hydrothermal alteration and ore mineralization encountered in CSPD core hole VC-2A, Sulphur Springs, Valles caldera, New Mexico: A detailed overview: University of Utah Research Institute, Report ESL-88001-TR: 44 pp.
Hulen, J., Nielson, D. L., Goff, F., Gardner, J. N., and Charles, R., 1987, Molybdenum mineralization in an active geothermal system, Valles caldera, New Mexico: Geology, 15: 748–752.
Iddings, J. P., 1890, On a group of rocks from the Tewan Mountains, New Mexico, and on the occurrence of primary quartz in certain basalts: U.S. Geological Survey, Bulletin 66: 34 pp.
Irvine, T. N., and Barager, W. R. A., 1971, A guide to the chemical classification of the common volcanic rocks: Canadian Journal of Earth Sciences, 8: 523–548.
Izett, G. A., Obradovich, C. W., Naeser, C. W., and Cebula, C. T., 1981, Potassium–argon and fission-track zircon ages of Cerro Toledo rhyolite tephra in the Jemez Mountains, New Mexico: U.S. Geological Survey, Professional Paper 1199-D: 37–43.
Janecky, D. R., Charles, R., and Goff, F., 1987, Geochemistry of molybdenum-bearing assemblages in CSDP well VC-2A, Valles caldera, New Mexico: American Geophysical Union, Transactions, 68: 469.
Keith, T. E. C., 1988, Alteration in the Madera Limestone and Sandia Formation from core hole VC-1, Valles caldera, New Mexico: Journal of Geophysical Research, 93: 6068–6076.
Kelley, V. C., Woodward, L. A., Kudo, A. M., and Callender, J. F., 1976, Guidebook to the Albuquerque Basin of the Rio Grande rift, New Mexico: New Mexico Bureau of Mines & Mineral Resources, Circular 153: 31 pp.
Kerr, R. A., 1982, Extracting geothermal energy can be hard: Science, 218: 668–669.
Kolstad, C. D., and McGetchin, T. R., 1978, Thermal evolution models for the Valles caldera with reference to a hot-dry-rock geothermal experiment: Journal of Volcanology and Geothermal Research, 3: 197–218.
Kuentz, D. C., 1986, The Otowi Member of the Bandelier Tuff: A study of the petrology, petrography, and geochemistry of an explosive silicic eruption, Jemez Mountains, New Mexico: Unpublished M.S. thesis, University of Texas at Arlington, 165 pp.
Lambert, S. J., and Epstein, S., 1980, Stable isotope investigations of an active geothermal system in Valles caldera, Jemez Mountains, New Mexico: Journal of Volcanology and Geothermal Research, 8: 111–129.
Laughlin, A. W., 1981, The geothermal system of the Jemez Mountains, New Mexico, and its exploration; *in* Rybach, L., and Muffler, L. J. P. (eds.), Geothermal systems: Principles and case histories: Wiley, New York, pp. 295–320.
Laughlin, A. W., Brookins, D. G., and Damon, P. E., 1976, Late-Cenozoic

basaltic volcanism along the Jemez zone of New Mexico and Arizona (abs.): Geological Society of America, Abstracts with Programs, 8: 598.

Laughlin, A. W., Eddy, A. C., Laney, R., and Aldrich, M. J., 1983, Geology of the Fenton Hill, New Mexico, hot dry rock site: Journal of Volcanology and Geothermal Research, 15: 21–41.

Lindgren, W., Graton, L. C., and Gorden, C. H., 1910, The ore deposits of New Mexico: U.S. Geological Survey, Professional Paper 68: 361 pp.

Loeffler, B. M., 1981, Major- and trace-element and strontium- and oxygen-isotope geochemistry of the Polvadera Group, Jemez volcanic field, New Mexico: Implications for the petrogenesis of the Polvadera Group: Unpublished Ph.D. dissertation, University of Colorado, Boulder, 259 pp.

Loeffler, B. M., Vaniman, D. T., Baldridge, W. S., and Shafiqullah, M., 1988, Neogene rhyolites of the northern Jemez volcanic field, New Mexico: Journal of Geophysical Research, 93(B6): 6157–6168.

Luedeke, R. G., and Smith, R. L., 1978, Map showing distribution, composition, and age of late Cenozoic volcanic centers in Arizona and New Mexico: U.S. Geological Survey, Miscellaneous Investigations Map I-1091-A, scale 1:1,000,000.

Luth, W., and Hardee, R., 1980, Comparative assessment of five potential sites for hydrothermal-magma systems: A summary: U.S. Department of Energy, Report DOE-TIC-11303: 51 pp.

Mahon, W. A. J., Klyen, L. E., and Rhode, M., 1980, Neutral sodium/bicarbonate/sulfate hot waters in geothermal systems: Japanese Geothermal Energy Association, Journal, 17: 11–24.

Manley, C. R., and Fink, J. H., 1987, Internal textures of rhyolite flows as revealed by research drilling: Geology, 15: 549–552.

Manley, K., 1976, K–Ar age determination on Pliocene basalts from the Española basin, New Mexico: Isochron/West, no. 16: 29–30.

Manley, K., 1982, Geologic map of the Cañones quadrangle, Rio Arriba County, New Mexico: U.S. Geological Survey, Map MF-1440, scale 1:24,000.

Mansfield, G. R., 1918, Sulphur in Jemez Canyon, Sandoval County: U.S. Geological Survey, Mineral Resources, 1918, pt. 2: 367.

Marvin, R. F., and Dobson, S. W., 1979, Radiometric ages: Compilation B: U.S. Geological Survey, Isochron West, no. 26: 3–32.

Mayo, E. G., 1958, Lineament tectonics and some ore districts of the southwest: Mining Engineering, 10: 1169–1175.

McDowell, D. S., and Elders, W. A., 1980, Authigenic layer silicate minerals in borehole Elmore 1, Salton Sea geothermal field, California, U.S.A.: Contributions to Mineralogy and Petrology, 74: 293–310.

Meeker, K., and Goff, F., 1988, Geochemistry of the 490-m 210°C aquifer in core hole VC-2A, Sulphur Springs and comparison with other hydrothermal fluids in Valles caldera, New Mexico: American Geophysical Union, Transactions, 69: 1049.

Mills, C., Winterkamp, J., and Marusak, N., 1987, Geosciences bibliography of the Valles Caldera: A CSDP information base: Los Alamos National Laboratory, Report LA-UR-84-3148 (Rev. 3): 235 pp.

Muffler, L. J. P., and White, D. E., 1969, Active metamorphism of upper Cenozoic sediments in the Salton Sea geothermal field and the Salton Trough, southeastern California: Geological Society of America, Bulletin, 80: 157–182.

Musgrave, J., Goff, F., Shevenell, L., Trujillo, P., Counce, D., Luedemann, G., Garcia, S., Dennis, B., Hulen, J., Janik, C., and Tomei, F., 1989, Selected data from Continental Scientific Drilling core holes VC-1 and VC-2A, Valles caldera, New Mexico: Los Alamos National Laboratory, Report, in press.

Nielsen, D. L., and Hulen, J. B., 1984, Internal geology and evolution of the Redondo dome, Valles caldera, New Mexico: Journal of Geophysical Research, 89: 8695–8711.

Olsen, K. H., Braile, L. W., Stewart, J. N., Daudt, C. R., Keller, G. R., Ankeny, L. A., and Wolff, J. J., 1986, Jemez Mountains volcanic field, New Mexico: Time term interpretation of the CARDEX seismic experiment and comparison with Bouguer gravity: Journal of Geophysical Research, 91: 6175–6187.

Pearson, F. J., and Truesdell, A. H., 1978, Tritium in the waters of Yellowstone National Park: U.S. Geological Survey, Open-File Report 78-701: 3 pp.

Perkins, P. C., 1973, Petrology of some rock types of the Precambrian basement near the Los Alamos Scientific Laboratory geothermal test site, Jemez Mountains, New Mexico: Los Alamos Scientific Laboratory, Report LA-5129-MS: 12 pp.

Phillips, F., Goff, F., Vuataz, F.-D., Bentley, H. W., Elmore, D., and Gove, H., 1984, ^{36}Cl as a tracer in geothermal systems: Example from Valles caldera, New Mexico: Geophysical Research Letters, 11: 1227–1230.

Potter, D. B., and Oberthal, C. M., 1983, Vent sites and flow directions of the Otowi ash flows (lower Bandlier Tuff), New Mexico: Geological Society of America, Bulletin, 98: 66–76.

Powell, J. W., 1961, The Exploration of the Colorado River and its canyons: Dover Publications, New York, 400 pp. (Republication of Canyons of the Colorado, Flood and Vincent, 1885.)

Reiter, M., Edwards, C. L., Hartman, H., and Weidman, C., 1975, Terrestrial heat flow along the Rio Grande rift, New Mexico and southern Colorado: Geological Society of America, Bulletin, 86: 811–818.

Reiter, M., Weidman, C., Edwards, C. L., and Hartman, H., 1976, Subsurface temperature data in Jemez Mountains, New Mexico: New Mexico Bureau of Mines & Mineral Resources, Circular 151: 16 pp.

Ross, C. S., and Smith, R. L., 1961, Ash-flow tuffs: Their origin, geologic relations and identification: U.S. Geological Survey, Professional Paper 366: 81 pp.

Sasada, M., 1987, Fluid inclusions from VC-2A core hole in Valles caldera, New Mexico, U.S.A.—Evidence for a transition from hot water-dominated to vapor-dominated system (abs.): Geothermal Research Society of Japan, Annual Meeting, Abstracts with Program.

Sasada, M., 1988a, Fluid inclusion evidence for recent temperature rising at Fenton Hill hot dry rock test site west of the Valles caldera, New Mexico, USA; *in* Exploration and Development of Geothermal Resources, International Symposium on Geothermal Energy, 1988: Geothermal Research Society of Japan, pp. 526–529.

Sasada, M., 1988b, Microthermometry of fluid inclusions from the VC-1 core hole in Valles caldera, New Mexico: Journal of Geophysical Research, 93(B6): 6091–6096.

Sass, J. H., and Morgan, P., 1988, Conductive heat flux in VC-1 and the thermal regime of Valles caldera, Jemez Mountains, New Mexico: Journal of Geophysical Research, 93(B6): 6027–6040.

Segar, R. L., 1974, Quantitative gravity interpretation, Valles caldera area, Sandoval and Rio Arriba counties, New Mexico: University of Utah Research Institute, Earch Science Laboratory, Open-File Report NM/BACA-27: 12 pp.

Self, S., Gardner, J. N., and Goff, F., 1987, A field guide to the Jemez Mountains volcanic field, New Mexico; *in* Davis, G. H., and Vonder Dolder, E. M. (eds.), Geologic diversity of Arizona and its margins: Excursions to choice areas: Arizona Bureau of Geology & Mining Technology, Special Paper 5: 95–112.

Self, S., Kircher, D. E., and Wolff, J. A., 1988, The El Cajete Series, Valles Caldera, New Mexico: Journal of Geophysical Research, 93(B6): 6113–6128.

Self, S., Goff, F., Gardner, J. N., Wright, J. V., and Kite, W. M., 1986, Explosive rhyolitic volcanism in the Jemez Mountains: Vent locations, caldera development and relation to regional structure: Journal of Geophysical Research, 91: 1779–1798.

Shevenell, L., Goff, F., Miles, D., Waibel, A., and Swanberg, C., 1988, Lithologic descriptions and temperature profiles of five wells in the southwestern Valles caldera region, New Mexico: Los Alamos National Laboratory, Report LA-11165-OBES: 43 pp.

Shevenell, L., Goff, F., Vuataz, F., Trujillo, P. Counce, D., Janik, C., and Evans, B., 1987, Hydrogeochemical data for thermal and nonthermal waters and gases of the Valles caldera, southern Jemez Mountains region, New Mexico: Los Alamos National Laboratory, Report LA-10923-OBES: 100 pp.

Singer, B. S., and Kudo, A. M., 1986, Assimilation–fractional crystallization of Polvadera Group rocks in the northwestern Jemez volcanic field, New Mexico: Contributions to Mineralogy and Petrology, 94: 374–386.

Smith, M. C., 1983, A history of hot dry rock geothermal energy systems: Journal of Volcanology and Geothermal Research, 15: 1–20.

Smith, R. L., 1979, Ash-flow magmatism; *in* Chapin, C. E., and Elston, W. E. (eds.), Ash-flow tuffs: Geological Society of America, Special Paper 180: 5–28.

Smith, R. L., and Bailey, R. A., 1966, The Bandelier Tuff—A study of ash-flow eruption cycles from zoned magma chambers: Bulletin of Volcanology, 29: 83–104.

Smith, R. L., and Bailey, R. A., 1968, Resurgent cauldrons; *in* Coats, R. R., Hay, R. L., and Anderson, C. A. (eds.), Studies in volcanology: Geological Society of America, Memoir 116: 613–662.

Smith, R. L., Bailey, R. A., and Ross, C. S., 1961, Structural evolution of the Valles caldera, New Mexico and its bearing on the emplacement of ring dikes: U.S. Geological Survey, Professional Paper 424-D: 145–149.

Smith, R. L., Bailey, R. A., and Ross, C. S., 1970, Geologic map of the Jemez Mountains, New Mexico: U.S. Geological Survey, Miscellaneous Geological Investigations Map I-571, scale 1:250,000.

Smith, S. P., and Kennedy, B. M., 1985, Noble gas evidence for two fluids in the Baca (Valles caldera) geothermal reservoir: Geochimica et

Cosmochimica Acta, 49: 893–902.
Sommer, M. A., 1977, Volatiles H_2O, CO_2, and CO in silicate melt inclusions in quartz phenocrysts from the rhyolitic Bandelier air-fall and ash-flow tuff, New Mexico: Journal of Geology, 85: 423–432.
Spell, T. L., 1987, Geochemistry of Valle Grande Member ring fracture rhyolites, Valles caldera, New Mexico: Unpublished M.S. thesis, New Mexico Institute of Mining & Technology, Socorro, New Mexico, 212 pp.
Spencer, R. K., and Tsang, C. F., 1984, Listing of scientific data on the Baca geothermal field: Lawrence Berkeley National Laboratory, Report LBL-17675: 138 pp.
Srodon, J., 1980, Precise identification of illite/smectite interstratifications by X-ray powder diffraction: Clays and Clay Minerals, 28: 401–411.
Srodon, J., and Eberl, D. D., 1984, Illite; *in* Bailey, S. W. (ed.), Micas: Mineralogical Society of America, Reviews in Mineralogy, 13: 498–544.
Stein, H. L., 1983, Geology of the Cochiti mining district, Jemez Mountains, New Mexico: Unpublished M.S. thesis, University of New Mexico, Albuquerque, 122 pp.
Steiner, A., 1968, Clay minerals in hydrothermally altered rocks at Wairakei, New Zealand: Clays and Clay Minerals, 16: 193–213.
Stix, J., Goff, F., Gorton, M. P., Heiken, G., and Garcia, S. R., 1988, Restoration of compositional zonation in the Bandelier silicic magma chamber between two caldera-forming eruptions: Geochemistry and origin of the Cerro Toledo Rhyolite, Jemez Mountains, New Mexico: Journal of Geophysical Research, 93(B6): 6129–6147.
Sturchio, N. C., and Binz, C. M., 1988, Uranium-series age determination of calcite veins, VC-1 drill core, Valles caldera, New Mexico: Journal of Geophysical Research, 93(B6): 6097–6102.
Suhr, G., 1981, Seismic crust anomaly under the Valles caldera in New Mexico, USA: Unpublished consultant report, PRAKLA-SEISMOS GMBH, Hannover, Federal Republic of Germany, 56 pp.
Summers, W. K., 1976, Catalog of thermal waters in New Mexico: New Mexico Bureau of Mines & Mineral Resources, Hydrologic Report 4: 80 pp.
Swanberg, C. A., 1983, Geothermal resources of rifts: A comparison of the Rio Grande rift and the Salton Trough: Tectonophysics, 94: 659–678.
Taschek, R. F., 1981, Scientific and operational plan for drilling in the Valles caldera, New Mexico: Continental Scientific Drilling Committee, National Science Foundation, Washington, D.C., Document 0491A: 45 pp.
Trainer, F. W., 1975, Mixing of thermal and nonthermal waters in the margin of the Rio Grande rift, Jemez Mountains, New Mexico; *in* Siemers, C. T., Woodward, L. A., and Callender, J. F. (eds.), Ghost Ranch: New Mexico Geological Society, Guidebook 25: 213–218.
Trainer, F. W., 1978, Geohydrologic data from the Jemez Mountains and vicinity, north-central New Mexico: U.S. Geological Survey, Water Resources Investigation 77-131: 146 pp.
Trainer, F. W., 1984, Thermal springs in Cañon de San Diego as a window into Valles caldera, New Mexico; *in* Baldridge, W. S., Dickerson, P. W., Riecker, R. E., and Zidek, J. (eds.), Rio Grande rift: Northern New Mexico: New Mexico Geological Society, Guidebook 35: 249–255.
Truesdell, A. H., and Janik, C. J., 1986, Reservoir processes and fluid origins in the Baca geothermal system, Valles caldera, New Mexico: Journal of Geophysical Research, 91: 1817–1833.
Turbeville, B. N., and Self, S., 1988, San Diego canyon ignimbrites: Pre-Bandelier tuff explosive rhyolitic volcanism in the Jemez Mountains, New Mexico: Journal of Geophysical Research, 93(B6): 6148–6156.
Vuataz, F.-D., and Goff, F., 1986, Isotope geochemistry of thermal and nonthermal waters in the Valles caldera, Jemez Mountains, northern New Mexico: Journal of Geophysical Research, 91: 1835–1853.
Vuataz, F. D., Goff, F., Fouillac, C., and Calvez, J. Y., 1988, A strontium isotope study of the VC-1 core hole and associated hydrothermal fluids and rocks from Valles Caldera, Jemez Mountains, New Mexico: Journal of Geophysical Research, 93(B6): 6059–6067.
Waresback, D. B., 1986, The Puye Formation, New Mexico: Analysis of a continental rift-filling volcaniclastic alluvial fan sequence: Unpublished M.S. thesis, University of Texas at Arlington, 269 pp.
Warshaw, C. M., and Smith, R. L., 1988, Pyroxenes and fayalites in the Bandelier Tuff, New Mexico: Temperatures and comparison with other rhyolites: American Mineralogist, 73: 1025–1037.
White, A. F., 1986, Chemical and isotopic characteristics of fluids within the Baca geothermal reservoir, Valles caldera, New Mexico: Journal of Geophysical Research, 91: 1855–1866.
White, D. E., and Heropoulous, C., 1983, Active and fossil hydrothermal convection systems of the Great Basin; *in* The role of heat in the development of energy and mineral resources in the northern Basin and Range province: Geothermal Resources Council, Special Report 13: 41–54.
White, D. E., Muffler, L. P. J., and Truesdell, A. H., 1971, Vapor-dominated hydrothermal systems compared with hot-water systems: Economic Geology, 66: 75–97.
Williston, McNeal and Associates, 1979, A time domain survey of the Los Alamos region, New Mexico: Los Alamos Scientific Laboratory, Report LA-7657-MS: 32 pp.
Wilt, M., and Vonder Haar, S., 1986, A geologic and geophysical appraisal of the Baca geothermal field, Valles caldera, New Mexico: Journal of Volcanology and Geothermal Research, 27: 349–370.
WoldeGabriel, G., 1989, Hydrothermal systems in two areas of the Jemez volcanic field: Sulphur Springs and the Cochiti minign district: Los Alamos National Laboratory, Report LA-11509-OBES: 66 pp.
WoldeGabriel, G., and Goff, F., 1989, Temporal relationships of volcanism and hydrothermal systems in two areas of the Jemez volcanic field, New Mexico: Geology (in press).
Wright, J. V., Smith, A. L., and Self, S., 1981, A terminology for pyroclastic deposits; *in* Self, S., and Sparks, R. S. J. (eds.), Tephra studies: D. Reidel Publishing Company, Boston, pp. 457–463.
Wronkiewicz, D., Norman, D., Parkinson, G., and Emanuel, K., 1984, Geology of the Cochiti mining district, Sandoval County, New Mexico; *in* Baldridge, W. S., Dickerson, P. W., Riecker, R. E., and Zidek, J. (eds.), Rio Grande rift: Northern New Mexico: New Mexico Geological Society, Guidebook 35: 219–22.
Zartman, R. E., 1979, Uranium, thorium, and lead concentrations and lead isotopic composition of biotite granodiorite (sample 9527-2b) from LASL drill hole GT-2: Los Alamos Scientific Laboratory, Report LA-7923-MS: 18 pp.

EXCURSION 18B:
Rio Grande rift volcanism: Northeastern Jemez zone, New Mexico

M. A. Dungan[1], R. A. Thompson[2], and J. S. Stormer[3], with a short contribution by J. M. O'Neill[2]

[1]Department of Geological Sciences, Southern Methodist University, Dallas, Texas 75275; [2]U.S. Geological Survey, Denver, Colorado 80225;
[3]Department of Geology and Geophysics, Rice University, Houston, Texas 77251

Introduction

Magmatism, a predictable consequence of asthenospheric upwelling associated with lithospheric attenuation, is integral to continental rifting. The injection of mantle-derived magma into extending crust may have a profound effect on the rheology of the crust and therefore the style of deformation associated with extension (De Voogd et al., 1988). Rift-related magmatism encompasses much of the diversity of terrestrial-magma types. Compositions of mafic magmas range from tholeiite to some of the most silica-undersaturated magmas found on the continents, and their differentiates range over the entire spectrum of intermediate to salic compositions to include high-SiO_2 rhyolite, trachyte, and phonolite. Large effusive eruptions from fissures are typical of some rifts, whereas others may be dominated by central vent cones or even silicic caldera complexes. Most of these aspects of rift volcanism and a wide range of mafic to salic magma compositions are represented in the Rio Grande rift; many will be seen on this trip.

Geological setting of the Rio Grande rift

The Rio Grande rift is a late Cenozoic rift in continental crust of Proterozoic age (1.7–1.4 Ga) which, prior to rifting, experienced deformation during the Ancestral Rocky Mountain (late Paleozoic) and Laramide (Late Cretaceous–early Tertiary) orogenies. Rift basins have the same overall north–south trend as Laramide compressional structures in the Southern Rocky Mountains, and they are located near the eastern margin of the region affected by Laramide deformation. An extended episode of mid-Tertiary magmatism immediately preceded rifting. In the Southern Rocky Mountains, the eastern edge of the broad region of subduction-related calc-alkaline magmatism, which intermittently characterized the North American cordillera during early to mid-Tertiary time (Snyder et al., 1976; Coney and Reynolds, 1977; Cross and Pilger, 1978), coincides with the eastern limit of the uniquely broad and complex extensional regime that dominated late Cenozoic tectonics and volcanism of the western U.S.A. and northern Mexico. The Rio Grande rift lies close to the eastern edge of this mid-Tertiary magmatic arc, which is represented in Colorado and New Mexico by the San Juan and Mogollon–Datil volcanic fields (mainly 36–26 Ma). In fact, silicic to intermediate magmatism was still active in these fields at the time rift-related, dominantly basaltic volcanism was established in New Mexico at approximately 29–26 Ma. As with many continental rifts, the role of antecedent structures in controlling superimposed rift structures and the effects of prior magmatic events on subsequent rift-related magmatism are topics of considerable debate.

Physiography

The Rio Grande rift is a major physiographic and structural feature of the Southern Rocky Mountains, distinct from the Basin and Range provinces of southern Arizona and northern Mexico, Nevada, western Utah, southern Idaho, and eastern Oregon. However, as a well-defined volcano-tectonic province, it has been the object of concerted study for less than 20 years (Chapin, 1971, 1979; Lipman, 1969; Lipman and Mehnert, 1975, and other papers *in* Curtis, 1975; Chapin and Seager, 1975; Cordell, 1978; Seager and Morgan, 1979, and other papers *in* Riecker, 1979). The Rio Grande rift extends northward from a poorly defined terminus in northern Chihuahua, Mexico, through New Mexico into at least central Colorado (Tweto, 1979). Normal faulting, regional uplift, high heat flow (Decker et al., 1984), and scattered occurrences of volcanic rocks of late Cenozoic age are present as far north as southern Wyoming (e.g., Leucite Hills). The rift comprises two segments, the northern segment extending northward from Socorro, New Mexico, into Colorado and the southern segment extending south from Socorro into Mexico (Cordell, 1978). In the broader southern segment the tectonic style and physiography resemble the Basin and Range province: extension is distributed over several wide basins, lithospheric thinning and regional extension have reached an advanced stage, and regional elevations are lower than in the north. In the northern segment, rift basins are confined to a narrow axial zone superimposed on a region of high elevation. In effect, the rift basins of the northern Rio Grande rift separate the Colorado Plateau on the west from the High Plains to the east.

Proterozoic structures and crustal evolution

The Proterozoic history of western North America was apparently dominated by accretion of multiple exotic terranes (<2 Ga) onto a continental nucleus of Archean age. From northern Colorado to southern New Mexico and Arizona the ages of these accreted terranes decrease from about 1.8 Ga to 1.6 Ga (e.g., Reed et al., 1987; Karlstrom et al., 1987). Grambling et al. (1988) have identified six tectonostratigraphic terranes in northern and central New Mexico on the basis of differences in age (1.76–1.6 Ga), lithology, and metamorphic grade. All the rocks in these terranes are strongly deformed and display an early east–west fabric which has locally been overprinted by a northeast-trending crenulation cleavage (Montgomery, 1953; Nielsen, 1972; Nielsen and Scott, 1979; Holcombe and Callender, 1982; Holcombe et al., 1986; Grambling et al., 1988) that may be related to the Jemez lineament (see below). These terranes are locally intruded by 1.45 Ga granites.

Initiation of rifting and associated magmatism

There are four areas in the Rio Grande rift where the transition from Oligocene caldera-related magmatism to rift-related magmatism is well represented in the geologic record. They are the Trans-Pecos region of Texas, areas around Las Cruces and Socorro, New Mexico, and the San Luis Basin area of southern Colorado and northern New Mexico.

These regions have proven critical to the establishment of a chronological framework for this transition. In the northern rift, the southern San Luis Basin is exceptional for the abundance and diversity of well-exposed volcanic sequences which define the petrologic change in magmatic activity that coincided with the onset of regional extension. Major components of this record that will be touched upon to varying degrees in this report are: (1) pre-rift intermediate to silicic volcanic and plutonic rocks of the southeast San Juan volcanic field, Colorado; (2) mafic to silicic volcanic rocks of the Latir volcanic field, New Mexico, and San Luis Hills area of southern Colorado, which bracket the inception of rifting; and (3) late Miocene to Pleistocene, dominantly basaltic, rift-related lavas associated with a second phase of rifting activity. Both axial and flank exposures of rift-related volcanic rocks associated with the second phase of volcanism will be examined.

Initial age estimates of the inception of rifting were based on age dates of volcanic rocks interbedded with coarse clastic rocks of the basal Santa Fe Group sedimentary basin-fill sequences (Lipman and Mehnert, 1975; Chapin and Seager, 1975). More recent estimates, which have generally shown that rifting began earlier than originally thought, have focused on ages of dikes that also demonstrate the orientation of least principal stress at the time of intrusion (Aldrich et al., 1986; Henry and Price, 1986). Evidence for magmatism associated with the transition to crustal extension occurs in 31 Ma rocks of the Trans-Pecos area of southwest Texas and northeastern Chihuahua (Price and Henry, 1984; Price et al., 1986), and in rocks as old as 32 Ma in southern New Mexico (Aldrich et al., 1986). The earliest dates on clearly rift-related basalts are generally younger to the north, but by 26–24 Ma dominantly basaltic volcanism was firmly established throughout west Texas, New Mexico, and Colorado. Magmatism and faulting, associated with northward propagation of the rift, extended into northern New Mexico and southern Colorado between 26 and 25 Ma, immediately following the waning stages of caldera-related magmatism in the San Juan volcanic field (36–26 Ma). There are, however, no examples of basaltic rocks intercalated with San Juan calc-alkaline tuffs or clearly caldera-related intermediate lavas (Lipman and Mehnert, 1975). In the Questa caldera, extensional structures tilted calc-alkaline to peralkaline extrusives and intrusives at about 26 Ma (Lipman, 1981; Hagstrum and Lipman, 1986; Lipman et al., 1986).

Rift-basin structures

During the early stage of rifting, extension-related faults tended to have northwest trends (Aldrich et al., 1986; Henry and Price, 1986). Pliocene to Quaternary extension in the Rio Grande rift has produced normal faulting within the axis of the rift with dominantly north–south orientations (sigma 3 is east–west), in accord with estimates of regional stress orientations (Zoback et al., 1981). The younger phase of rifting, which followed a period of relative tectonic and magmatic quiescence in the middle Miocene (20–12 Ma), is marked by a narrowing of rift basins, so that early basin-fill sediments of the Santa Fe Group are commonly found on the uplifted blocks adjacent to present rift basins (e.g., Golombek, 1983; Golombek et al., 1983; Morgan and Golombek, 1984). This temporal change, from broad basins to narrow grabens bounded by high-standing uplifts, is predicted by models of necking of the lithosphere (Zuber and Parmentier, 1986) combined with small-scale convection in the underlying asthenosphere (Buck, 1986). The post-Miocene rejuvenation of rift tectonism was accompanied by widespread, dominantly basaltic volcanism, active regional uplift, and large differential movements on basin-bounding faults that resulted in deep, asymmetric basins. In the area of the northern rift from Albuquerque, New Mexico, to Leadville, Colorado, the rift basins are arrayed in en-echelon patterns and are offset along commonly northeast-trending oblique structures (accommodation zones of Rosendahl, 1987; Chapin, 1988).

The northeast-trending Jemez lineament (Mayo, 1958) is defined most clearly by an alignment of late Cenozoic volcanic fields (Laughlin et al., 1979; Luedke and Smith, 1978) extending from southeastern Colorado on the High Plains (Raton–Clayton volcanic field), through the axis of the rift (Jemez volcanic field), and along the southeastern margin of the Colorado Plateau (Perry et al., 1987). Thus defined, the Jemez lineament crosses several physiographic provinces. The occurrence of these volcanic fields along the Jemez trend has been interpreted as an indication that a major Precambrian crustal shear or suture zone, recently reactivated by extensional stresses, has acted as a conduit for the mantle-derived magmas that regionally dominate post-Miocene volcanism (Baldridge, 1979; Baldridge et al., 1984). However, the striking alignment of the volcanic fields is not matched by evidence that shallow structures with the northeast Jemez trend are important in controlling vent alignments or locations within these volcanic fields. Young faults on the Taos Plateau are almost entirely either north-trending (parallel to the general trend of the San Luis Basin and typical of the dominant regional trend of intrabasin structures) or northwest-trending (possibly reactivated faults formed during the early phase of rifting). The Ocate volcanic field lies along the eastern margin of the Sangre de Cristo Mountains (O'Neill and Mehnert, in press), in an area with dominantly northwest- and north-trending faults (north-trending faults are reactivated Laramide reverse faults). Little late Cenozoic faulting is associated with the Raton–Clayton volcanic field, although there are suggestions of west-northwest-trending fissures in the Capulin volcano–Purvine Mesa area.

Cenozoic structures that appear to be direct expressions of the Jemez trend (i.e., a strong regional northeast structural grain in Proterozoic basement rocks) are the graben faults of the resurgent dome of the Valles caldera and the Embudo fault zone (accommodation zone), which is the southern structural boundary of the San Luis Basin and Taos Plateau volcanic field. In addition to the Embudo fault zone, there are several other northeast-trending faults that serve as boundaries, or accommodation zones, separating differentially tilted, rhomb-shaped structural blocks that are generally coincident with the axis of the northern rift. Many indications point to these blocks as independently tilted and rotated structural units, bounded by reactivated zones of weakness, that have led to the pattern of en-echelon offsets and opposing tilts of the basins and uplifts of the northern rift segment. A complete synopsis of the structural geometry of the northern rift is well outside the scope of this report, but some observations about the southern San Luis Basin serve to illustrate the point.

The San Luis Basin appears to be broken into two east-tilted sub-basins by a northeast-trending fault zone (southeast side up—no Quaternary surface expression) that presumably forms the northern boundary of the structurally high

San Luis Hills and indents the front of the Sangre de Cristo Mountains in southern Colorado (northwest margin of Blanca Peak). The boundary between these sub-basins can be seen in the patterns of gravity anomalies of the central San Luis Basin (Keller et al., 1984). These structural sub-basins, therefore, apparently also have a component of southerly tilt in combination with a dominant tilt to the east. This southeasterly tilt within the San Luis Basin is opposed by a pronounced northerly tilt of the Sangre de Cristo block adjacent to the southern sub-basin (Lipman, 1981; Menges, 1987), emphasizing the independence of motion that characterizes these blocks. To the south of the Embudo fault zone, the Española Basin block has apparently undergone counterclockwise rotation (Brown and Golombek, 1985), resulting in compressional structures at the northeastern end (near Taos) of the Embudo zone and extension at the southwestern end (at Velarde).

Itinerary and goals of the excursion

Part One (Days 1 through 4): This trip begins in an axial graben (southern San Luis Basin) of the Rio Grande rift, focusing on the magmatism and rift structures of the Taos Plateau and San Luis Hills areas. A major theme of the field excursion is the interplay of volcanism, extensional tectonics, and sedimentation within an actively subsiding rift basin. Plio-Pleistocene volcanism contrasts in part with early Miocene magmatism associated with the inception of rifting, and with pre-rift Oligocene volcanism of the southeast San Juan volcanic field. Two of the goals of this guide are to examine the transition from Oligocene, caldera-forming, subduction-related volcanism to rift-related activity, and to evaluate the temporal evolution of rift magmatism from inception to the present, focusing on the critical area of the San Luis Basin and the adjacent rift flanks.

Part Two (Days 5 and 6): The remainder of the excursion is a departure from the axis of the rift to its uplifted eastern flank. This second phase of the guide will emphasize a comparison of magmatism of the Taos Plateau with: (1) the Ocate volcanic field, located on the structural and physiographic transition between the eastern Sangre de Cristo Mountains and the High Plains (also the eastern limit of Laramide east-directed overthrusting); and (2) the Raton–Clayton volcanic field, located still farther east on the High Plains. As the Taos Plateau field is actually offset to the north from the northeast-trending Jemez lineament (Fig. 1), these three fields constitute an east–west volcanic transect oriented normal to the north–south trend of axial basins in the northern Rio Grande rift (Figs. 1, 2). This comparison is based on a compilation of available major-element and trace-element data. These are briefly summarized in this report, and will be presented in more detail in subsequent publications with the addition of new isotopic data that are currently being collected.

Previous work and acknowledgments

We have cited only a small fraction of the previous studies dealing with geological problems in the area covered by this excursion. The ideas presented in this guide are generally those of the authors and co-workers, and they tend to be the results of relatively recent studies. Much more comprehensive sets of references may be found in papers cited in the guide. Our work in some cases constitutes second or third generation investigations, and we are indebted to those who provided the foundation for our studies. We have worked closely with, and are especially grateful to, Peter Lipman and Bill Muehlberger in this regard. Stephen Moorbath, Roger Nielsen, Nancy McMillan, Susan Williams, Dave Phelps, Clark Johnson, Larry Haskin, Marilyn Lindstrom, Laurie Brown, Dan Lux, Russ Harmon, Jochen Hoefs, Dave Wenner, and a host of students from several universities made many important contributions to the studies that constitute this report. We thank these colleagues for their cooperation and participation.

Supplemental field guides and special volumes

The northern Rio Grande rift is the subject of several other field-conference guidebooks. Among these are Circular 163 of the New Mexico Bureau of Mines & Mineral Resources (ed. Hawley, 1978), which was published in conjunction with an international conference on rifting held in Santa Fe, New Mexico. Circular 163 provides a road log from El Paso, Texas, to Denver, Colorado. A volume of collected papers reporting the results of geophysical and geologic studies of the Rio Grande rift was published by the American Geophysical Union in conjunction with the 1978 rift conference (ed. Riecker, 1979). A special section of *Journal of Geophysical Research,* with an introduction by G. R. Keller (1986), contains papers reporting on a wide variety of geophysical investigations along the Rio Grande rift. The 35th New Mexico Geological Society excursion and accompanying papers (ed. Baldridge et al., 1984) focus on the Taos Plateau and its immediately adjacent rift flanks. A recent guidebook by Friends of the Pleistocene (ed. Menges et al., 1987) is concerned with geomorphology, surficial geology, hydrology, and neotectonics of the northern Rio Grande rift, with special emphasis on the Española and southern San Luis Basins and the Sangre de Cristo Mountains.

Maps

Most of this excursion is located within the eastern half of the USGS Aztec 1:250,000 topographic map sheet and the adjacent Raton sheet (same scale). Part of the excursion on Day 4 is on the Trinidad 1:250,000 sheet. Another series of USGS topographic map sheets at 1:100,000 is relevant to this trip. Several sheets from this series (Santa Fe, Taos, Wheeler Peak, Alamosa, Antonito, Springer, Clayton, Raton, and Capulin Mountain) provide an extremely useful base for following the field-guide route. However, after publication of the 1:100,000 maps and during preparation of this field guide, the New Mexico Highway Department renumbered some state highways. The new numbers are used in the text, but some illustrations show the old numbers. Insets from some of these have been reproduced in this guide as location maps. With the exception of Fig. 2, aerial photographs are reproduced from U.S. Geological Survey, National High Altitude Photography (scale 1:80,000).

First day: Santa Fe to Taos

Mileage

0.0 Junction of US-285/84 and NM-68. Drive north through Española, New Mexico, toward Taos on NM-68. **12.9**

12.9 **STOP 1. Velarde graben, Black Mesa, La Mesita, Embudo fault zone, and Picuris Mountains** (1770 m). Pull off to right on shoulder of divided highway (Fig. 3a). The three axial basins of the

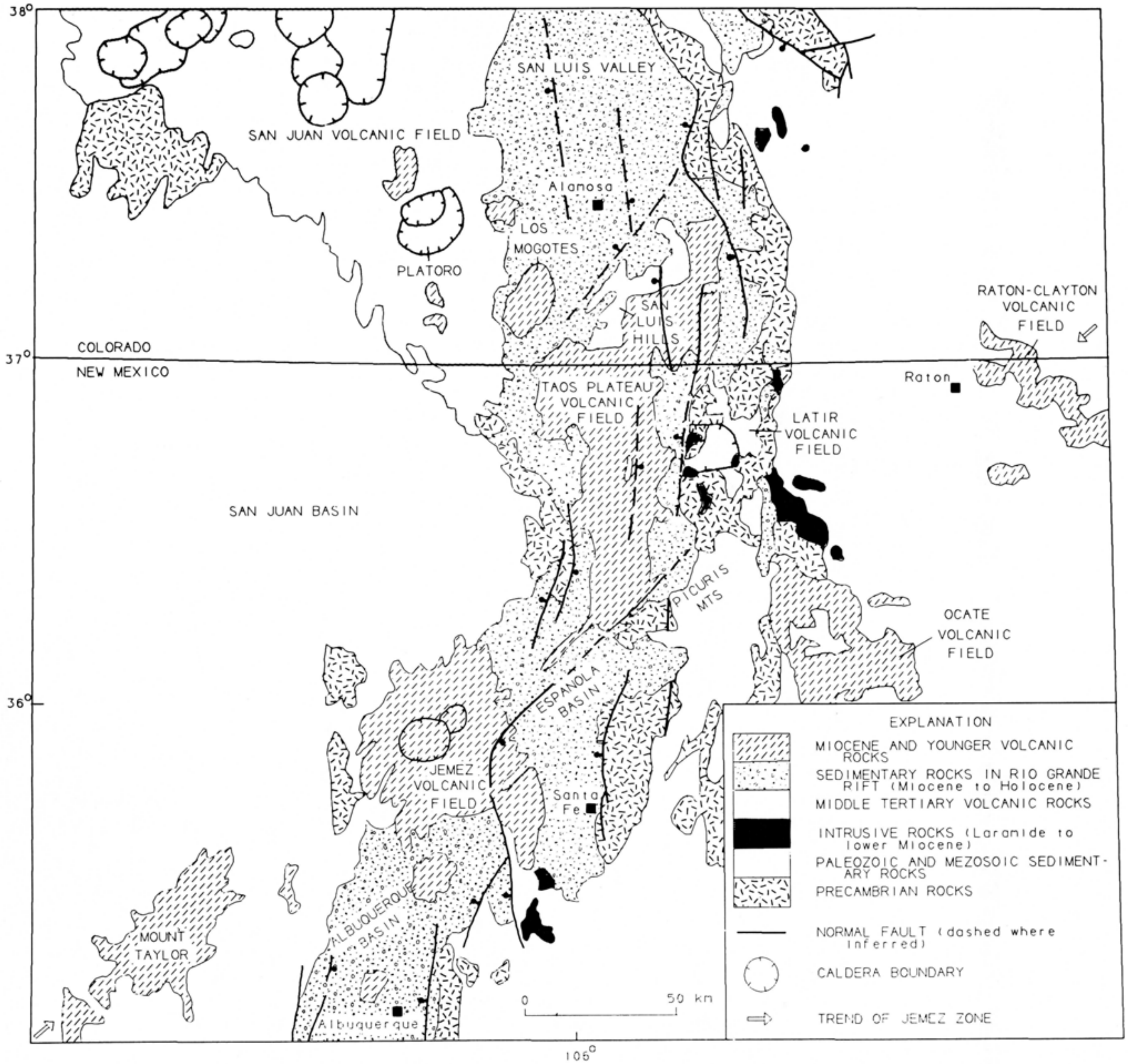

FIGURE 1—Generalized geologic map of the Southern Rocky Mountains, showing location of the middle to late Tertiary volcanic fields of the northern Rio Grande rift region and their proximity to major Precambrian uplifts and the Jemez zone.

northern Rio Grande rift are (south to north) the Albuquerque–Belen, Española, and San Luis Basins. All three are half grabens bounded by major faults on one side and monoclinal flexures on the other. From south to north, the basins exhibit progressive en-echelon offsets to the east and reversals in the polarity of tilt; i.e., the Albuquerque–Belen and San Luis Basins are tilted to the east and bounded on their eastern margins by high-standing uplifts, whereas the intervening Española Basin is tilted to the west. Similar structural geometries have been recognized in other continental rifts (e.g., east African system; Rosendahl, 1987). A complex transcurrent zone of offset, the Embudo fault zone, forms the structural boundary "accommodation zone" between the Española and San Luis Basins. The Embudo fault zone trends northeast, parallel to the Jemez lineament or Jemez zone. A component of left-lateral strike–slip motion is inferred for the Embudo zone because it forms, in a sense, an oblique continental transform linking the active zones of extension focused on the western and eastern margins of the Española and San Luis Basins, respectively. At it southwest end, the Embudo zone merges with the northern Pajarito fault system and is associated with late Cenozoic extension across the Velarde graben. At its northeast end the Embudo fault zone is in part compressive (Stop 3), indicating counterclockwise rotation of a rhomb-shaped crustal block which is bounded on the northwest by the Embudo zone (Kelly, 1979; Manley, 1979; Brown and Golombek, 1985; Dungan et al., 1984). Diktytaxitic olivine tholeiites of the Servilleta Basalt (Lipman and Mehnert, 1975, 1979; Dungan et al., 1986; Dungan, 1987) are the most voluminous lithology (1500 km^2, 200 km^3) of the Taos Plateau volcanic field. Basalt-capped Black Mesa to the north, and La Mesita to the northeast (both ~2100

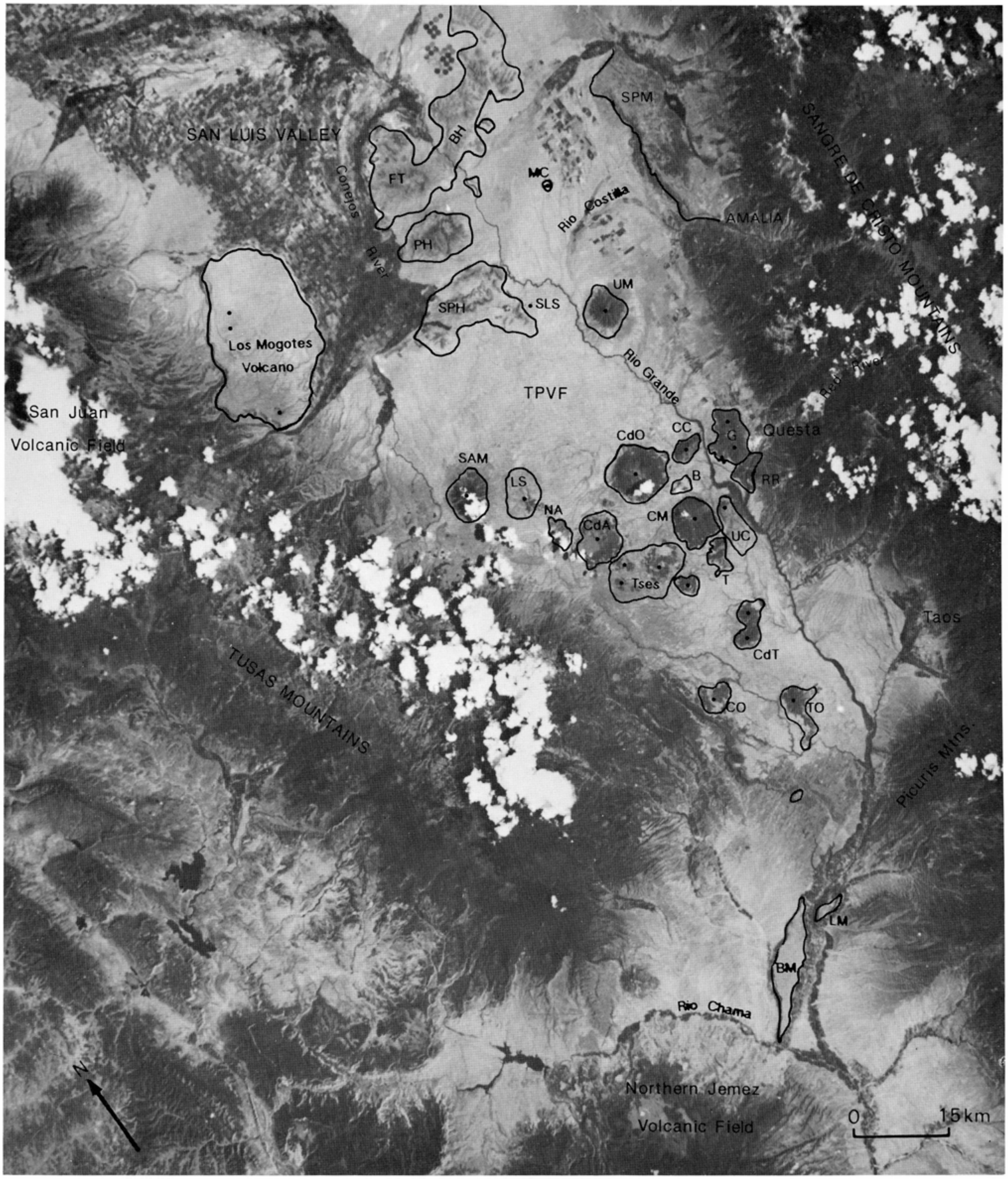

FIGURE 2—High-altitude aerial photograph of the northern Rio Grande rift region. From north to south abbreviations are: SPM, San Pedro Mesa; BH, Brownie Hills; FT, Flat Top; MC, Mesita cone; PH, Piñon Hills; SPH, South Piñon Hills; SLS, State Line shield; UM, Ute Mountain; TPVF, Taos Plateau volcanic field; G, Guadalupe Mountain; CC, Cerro Chiflo; CdO, Cerro de la Olla; RR, Red River volcano; B, Brushy Mountain; SAM, San Antonio Mountain; LS, La Segita Peaks (Wissmath Craters); NA, No Agua; CdA, Cerro del Aire; CM, Cerro Montoso; UC, UCEM; T, Timber Mountain; Tses, Servilleta shields; CdT, Cerros de los Taoses; CO, Cerro Oscura; TO, Tres Orejas; LM, La Mesita; BM, Black Mesa.

m elevation), represent the southeasternmost extent of the Servilleta Basalt lavas. The distinctive aphyric flows capping these two mesas ponded to thicknesses greater than those which characterize the southern Taos Plateau, due to accumulation in the actively extending Velarde graben. Servilleta Basalt capping the southwest part of La Mesita is offset by more than 25 m of normal displacement (down to the northwest) on the Embudo fault (Fig. 3b).

Continue to the northeast on NM-58 into Rio Grande Gorge. **7.8**

20.7 Cross Rio Embudo. **0.6**

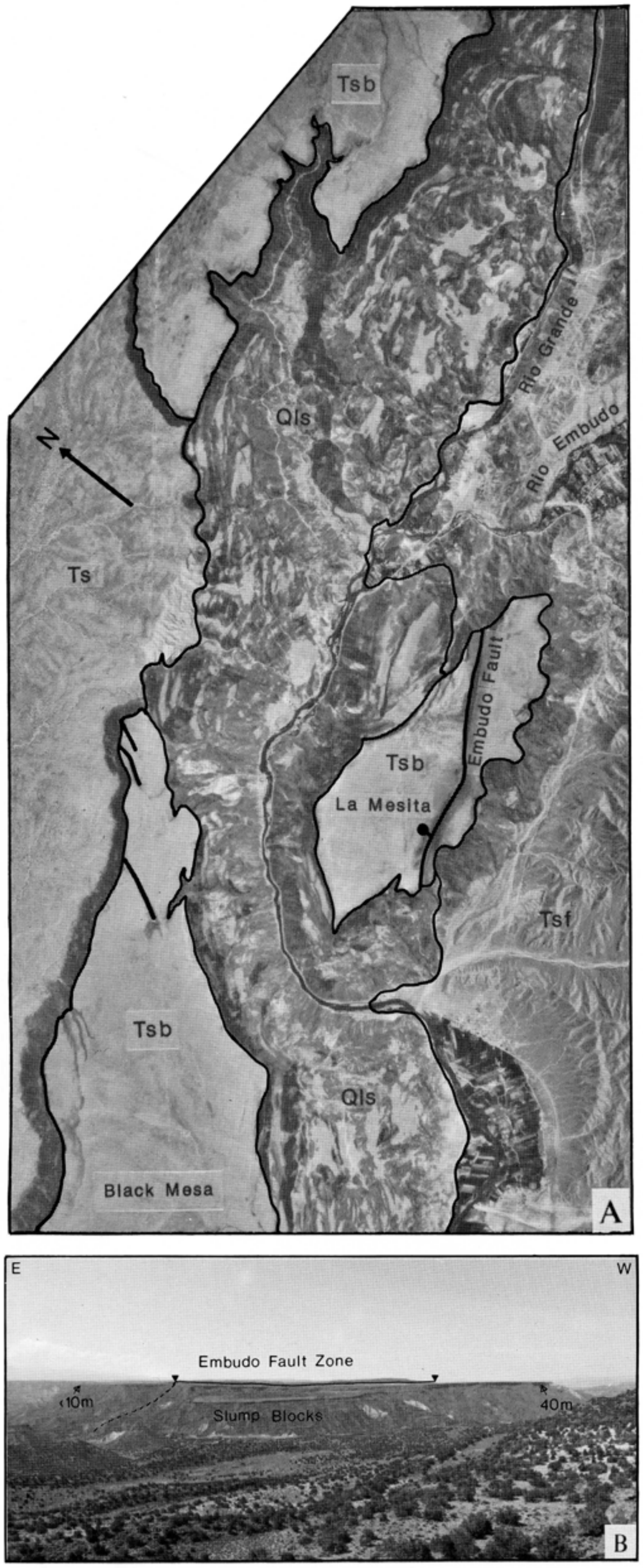

FIGURE 3—**A,** Aerial photograph of the northern end of Black Mesa and La Mesita. The main strand of the Embudo Fault is outlined as are approximate locations of contacts between Servilleta Basalt (Tsb), Santa Fe Group (Ts), and Quaternary landslide deposit (Qls). **B,** View of La Mesita from the southern end of the Taos Plateau. The volcanic section capping La Mesita is a distinctive aphyric package of Servilleta lavas that thickens from less than 10 m on the southeast edge of the mesa to more than 40 m on the northwest. These thickness variations are mirrored on Black Mesa and reflect ponding in a paleodepression thought to be related to the Velarde graben. The most recent movement on the main strand of Embudo fault is normal (northwest side down) at the southwest end of the mesa where Servilleta basalt is offset more than 50 m. Elsewhere on La Mesita, the basalt is deformed in a series of anticlines (axes parallel to fault), suggesting a compressional component at some stage.

21.3 Highly faulted sedimentary rocks of the Santa Fe Group are visible within the Embudo fault zone southeast of the highway. The southern end of the Taos Plateau (~2100 m) can be seen to the northeast. **3.4**

24.7 Proterozoic schists and metaquartzites of the Rinconada Group are exposed in the cliffs southeast of the highway. Basin-fill sediments of the Santa Fe Group are exposed across the river. For the next 5 mi the Rio Grande essentially follows the Embudo fault zone. **4.5**

29.2 **STOP 2. Embudo fault zone at Pilar, New Mexico** (Figs. 4, 5). **Cautiously** reduce speed, signal a left turn, and turn left into gravel parking area just over the crest of a small hill (1840 m). The trace of one strand of the Embudo fault zone is marked by the excavation scar of an El Paso Natural Gas Co. pipeline. Southeast of this fault, a late Pliocene Servilleta Basalt section (two flows) unconformably caps a northwest dipping Santa Fe sequence consisting of interbedded alluvial-fan and playa sediments. The five Servilleta flows northwest of the fault conformably overlie Santa Fe sediments. The stratigraphic and structural mismatch between Servilleta and Santa Fe sections across the fault may indicate significant strike–slip motion (presumably left lateral, but unconstrained) along this segment (Muehlberger, 1979; Dungan et al., 1984). Southwest of Pilar the major component of dip–slip movement is normal (Velarde graben), whereas to the northeast compression is in evidence.

Continue northeast on NM-68. Roadcuts on the left expose interbedded sediments of playa, dune, and alluvial-fan facies indicating a closed basin at the southern end of the San Luis Valley adjacent to the Embudo fault zone. Throughout this area basal basalt flows are pillowed and palagonitized, indicating emplacement into standing water (see Stop 4). Several splays of the Embudo fault zone are crossed in roadcuts on large switchbacks for 2 mi prior to Stop 3. **5.1**

34.3 **STOP 3. Taos Plateau overlook (2150 m) and roadcuts displaying reverse faulting in Santa Fe Group sedimentary units.** Park on right in parking lot at top of grade (Fig. 4). From this vantage point an excellent view of the southern Taos Plateau is obtained (Fig. 6). The Plateau surface, formed by extensive flows of the Upper Member of the Servilleta Basalt (USB), is gently tilted to the east-southeast. This tilt and other features demonstrate contemporary deformation of the Taos Plateau volcanic sequence (numerous subsequent stops). The Rio Grande Gorge is located approximately at the western margin of the Taos graben, a narrow but deep sediment-filled sub-basin bounded by the Sangre de Cristo Mountains on the east and an intrarift horst on the west. The surface expression of the horst is marked by exposures of early Miocene volcanic rocks (Timber Mountain and Brushy Mountain on the Taos Plateau—Stops 10, 13, 14), and

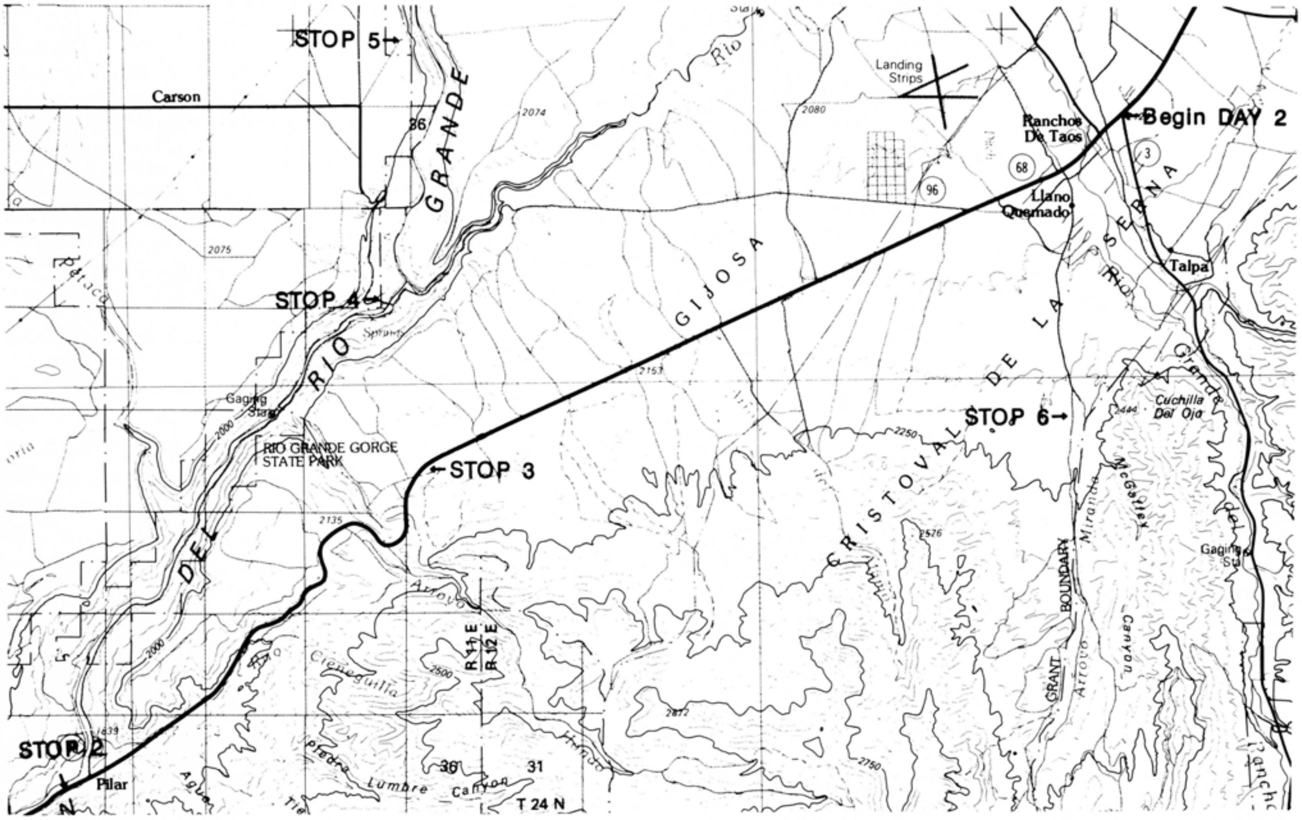

FIGURE 4—Location map for Stops 2 through 6. Note: The New Mexico Highway Department changed NM-96 to NM-570 and NM-3 to NM-518.

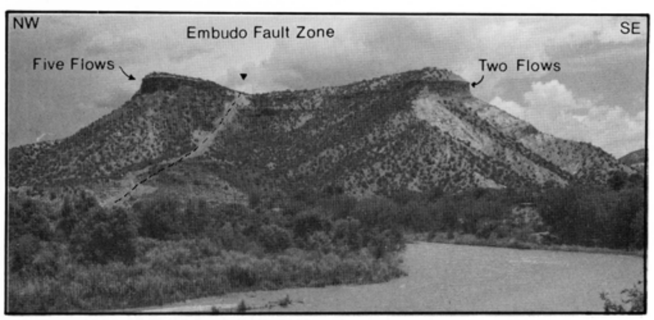

FIGURE 5—View northward from Stop 2 of the Embudo fault at Pilar, New Mexico.

by the San Luis Hills in southern Colorado (Oligocene and Miocene volcanic and plutonic rocks—Stops 30–33). Volcanic rocks on the Taos Plateau west of the horst are thought to form a relatively thin veneer over gently east-tilted early Miocene to Pliocene Santa Fe Group sediments. Also exposed within the Rio Grande Gorge and its major tributaries (Rio Petaca, Rio Pueblo de Taos, Arroyo Hondo, and Red River) are the Lower and Middle Members of the Servilleta Basalt (LSB and MSB), flows of broadly contemporaneous dacite and andesite, and interbedded sediments. The volcanic stratigraphy of the Rio Grande Gorge and its trib-

FIGURE 6—Taos Plateau and Rio Grande Gorge from Stop 3; view is to the north from Hondo Canyon rest area (photo from Muehlberger and Hawley, 1978).

utaries is discussed in Dungan et al. (1984) and at subsequent stops.

Known vents for Servilleta Basalt are located within the west-central and northern parts of the Taos Plateau, indicating that Servilleta lavas flowed as far as 50–75 km from their vents. Olivine andesite and pyroxene dacite lavas were erupted from approximately 20 shield-like vents. Lipman and Mehnert (1979) noted that the andesite and dacite cones are crudely arrayed in a concentric pattern around the main focus of Servilleta vents, with an inner ring of andesite shields surrounded by an outer ring of dacite cones. Three dacite shields (Ute Mountain, San Antonio Mountain, and Guadalupe Mountain) are underlain by andesite shields. Dungan et al. (1986) inferred that the basalt to dacite spectrum on the Taos Plateau evolved coevally in a complex magmatic system.

Roadcuts exposing several splays of the Embudo fault zone may be viewed by walking back down the highway to the south. The geology of the Embudo zone from Pilar to Taos has been mapped by Muehlberger (1978, 1979); we have reproduced a portion of his data in this report as Fig. 7. Only roadcuts 1 (first exposure at top of grade immediately south of the parking area) and 2 (last roadcut before road curves to the west to cross Arroyo Hondo) may be seen at this stop (the others are located along the highway between here and Pilar), but these serve to illustrate the points we wish to make. In both roadcuts sedimentary units of the Santa Fe Group are offset along reverse faults, demonstrating compression at this end of the Embudo zone. The lower Santa Fe strata exposed at roadcut 2 are dominated by volcanic detritus derived from the mid-Tertiary volcanic field that covered much of northern New Mexico and southern Colorado at the time rifting began (see also Stop 6). The uppermost unit in roadcut 1 comprises debris-flow deposits dominated by coarse angular clasts of the distinctive Proterozoic metasedimentary lithologies of the Picuris Mountains. These lithologies do not appear in the Santa Fe Group, even directly adjacent to the mountain front, until about the time of Servilleta volcanism, indicating that the Picuris uplift is a very young topographic feature (late Pliocene) relative to the inception of rifting in late Oligocene–early Miocene. Offset on the young reverse fault at roadcut 1 displaces a well-developed caliche horizon indicating late Pleistocene movement, and it has produced a 10 m scarp in the pediment surface along the Picuris Mountain front from this locality to the turnoff to Stop 4. Continue driving northeast on NM-68. Note strongly asymmetric drainages indicating ongoing east tilt of the plateau; note also the scarp of the Embudo fault south of the road (next 4 mi). **6.3**

40.6 Begin optional detour on NM-570 to Rio Grande Gorge (Stops 4, 5). Mileage for this loop is logged separately.

Optional loop: southern Rio Grande Gorge

Mileage

0.0 Turn left off NM-68 onto NM-570 and drive west toward to the Rio Grande Gorge. **4.6**

4.6 South rim of Rio Pueblo de Taos canyon (2000 m). Proceed downward on unpaved road through a relatively complete section of Servilleta Basalt plus interbedded Santa Fe sediments. **1.5**

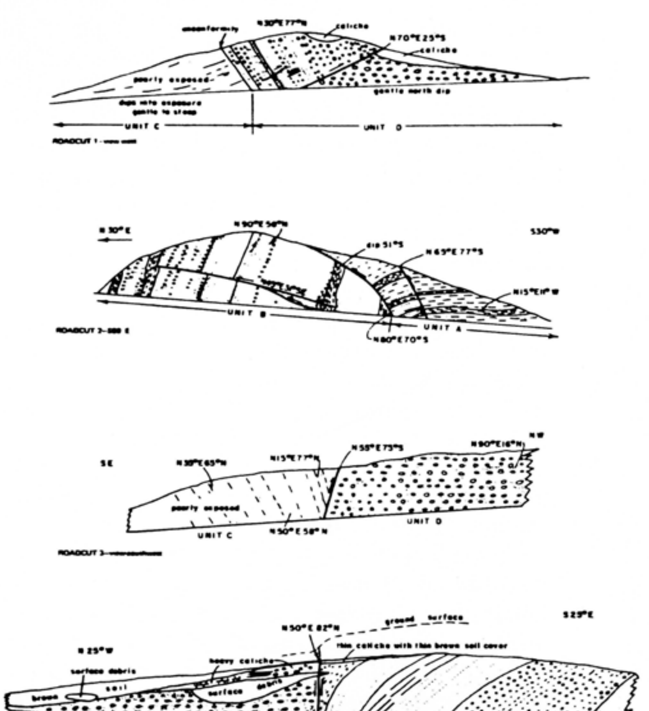

FIGURE 7—Field sketches of Stop 3 roadcuts. The following is quoted from Muehlberger (1978): **Unit D**—Upper Servilleta Formation. Cobble–boulder gravel is composed of large subangular clasts of quartzite, smaller platy clasts of black phyllite, and an unsorted matrix of schist, phyllite, and quartzite fragments, with abundant biotite and garnet grains. These materials are derived from the Picuris Mountains to the south and are mainly debris-flow deposits on an alluvial fan. Hanging wall block (Roadcut 1) shows a general coarsening-upward sequence above a basal zone of mainly reworked Santa Fe Group materials across an angular unconformity in which the beds make an angle of nearly 90°. These beds are younger than the basalts of the Servilleta Formation exposed to the north at the rim of the Rio Grande Gorge. **Unit C**—Upper Santa Fe Group, younger than or possibly equivalent to Ojo Caliente Sandstone (Tesuque Formation) of Galusha and Blick (1971). Well exposed in bluffs southwest of Roadcut 4, where it consists of alternating bands (lenses?), each 40–50 ft thick, of buff sand (mainly sand-dune facies), gray, pebbly gravel (alluvial fan debris from Picuris Mountains), and brownish silt and sandstone (lacustrine facies). Probably highly faulted in Roadcuts 1 and 3, poor exposures prevent detailed study. **Unit B**—Lower(?) Santa Fe Group, Chama–El Rito Member(?) of Galusha and Block (1971). Consists of fining-upward sequences of conglomerate, volcanic arenite, and mudstone. The subrounded clasts are mainly intermediate and silicic volcanic types, with lesser amounts of amphibolite, quartzite, olive-drab sandstone, rare basalt, and dark-gray limestone. The volcanic arenite is subangular to subrounded, poorly sorted and submature. The red-brown mudstone may be overbank or playa deposits. The coarser units show a general north-to-south transport direction of a braided stream deposit. Roadcut 2 becomes coarser upward on a larger scale than do the smaller fining-upward sequences. **Unit A**—(Santa Fe Group?; Chama–El Rito Member? of Galusha and Blick, 1971). Much finer grained; stratigraphically, probably a lower part of Unit B. Clast types are the same as Unit B and are composed of alternating units of gray pebbly sandstone and yellowish-weathering siltstone; probably meandering to braided stream deposits.

6.1 Confluence of Rio Grande and Rio Pueblo de Taos (1850 m). Note large landslide blocks and substantial width of gorge (2 km). **0.3**

6.4 Turn right across bridge over the Rio Grande and drive uphill to the first basalt outcrop on the right. Park on left side of road. **0.2**

6.6 **STOP 4. Pillowed Servilleta Basalt overlying deformed lacustrine sediments.** This outcrop is within a slump block, but it is representative of basal basalt contact relations throughout the southern Taos Plateau. Flowage of lava into standing water is indicated by a lower zone of pillows 2–3 m thick (partly palagonitized glassy rinds), pervasive alteration along columnar joints, and cylindrical injection pipes (steam spiracles) filled with sediment from the underlying lacustrine unit.

Continue on unpaved road to the top of the plateau. The road traverses sediment–basalt landslide blocks for the first mile. **1.5**

8.1 Top of plateau. Paved road traverses Plio-Pleistocene Santa Fe Group sediments. The Tres Orejas dacite cone (2431 m) is visible in the foreground to the northwest. **0.9**

9.0 Paved road turns west to Carson, New Mexico, and US-285. Continue straight ahead onto unpaved road then bear right immediately onto the less traveled road that parallels the telephone lines. **0.9**

9.9 **STOP 5. View of the Rio Grande Gorge and two exceptionally intact toreva blocks** (Fig. 8). Wherever a thin (<50 m) stratigraphic section of Servilleta Basalt overlies a thick section of Santa Fe sedimentary strata, the gorge has widened appreciably due to undercutting of the easily eroded sediments and landsliding. Dowstream from the confluence of the Rio Grande and Rio Pueblo de Taos the combined volcanic–sedimentary sequence is extensively slumped. In areas where the gorge has been widened as much as 2 km by this mechanism, multiple slump-blocks have undergone significant degradation during transport and rotation. The minimally deformed, coherent toreva blocks at this locality illustrate the initial step in this process.

Return to NM-68 via the route just traveled. **9.9**

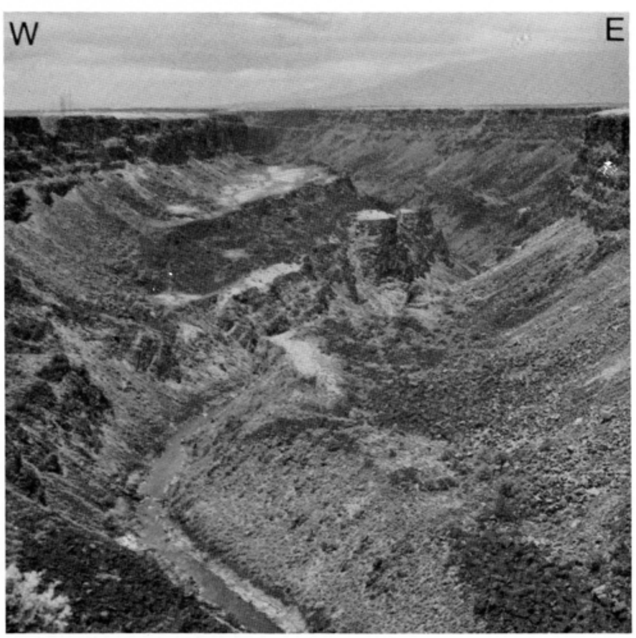

FIGURE 8—View northward from Stop 5 of the Rio Grande Gorge and toreva blocks. The lower toreva block on the west side of the gorge (just above river level) has been partly fragmented, but the upper block is largely intact.

19.8 End of gorge detour (60.4 cumulative mileage). Turn left to resume regular tour.
End of optional loop.

40.6 Resume main trip at junction of NM-68 and NM-570. Turn left onto NM-68. **1.1**

41.7 Village of Llano Quemado. Turn right onto the narrow paved road leading uphill to the south toward the Picuris Mountains. **0.9**

42.6 Pavement ends. Continue straight ahead. **1.4**

44.0 Y-junction, bear left. Do not take the road to the right nor the second. Continue **slowly** ahead. **0.1**

44.1 Take the third right fork and then stay on the **left** fork at the next confluence of roads. The hill immediately to the right is aligned with, and just north of, the second hill that is the next stop. **0.3**

44.4 Stay to the right at the next Y-junction. **0.1**

44.5 Turn right at the southern end of the second hill (2352 m, 7325 ft on Ranchos de Taos quadrangle). Park on the left after 0.1 mi. **0.1**

44.6 **STOP 6. Miranda graben,** where a resistant unit within the lower Picuris Formation is exposed. The Picuris Formation, the lowest formation of the Santa Fe Group in the Picuris Mountains and adjacent Sangre de Cristo Mountains, consists of a volcaniclastic sequence. The exposed unit is a nearly monolithologic epiclastic rhyolitic breccia. Most beds are massive debris-flow deposits dominated by coarse angular clasts of phenocryst-poor rhyolite in a reddish-brown matrix. Some finer-grained beds exhibit lacustrine and fluvial structures. These rhyolite clasts are identical in lithology to lava domes that filled the Questa caldera after eruption of the Amalia Tuff (P. W. Lipman, pers. comm. 1988), and therefore are most probably derived from a northerly source at about 25–26 Ma. The overwhelming preponderance of a single clast type, and the angularity of these clasts may argue for a source more proximal than the caldera. Clast imbrication in this deposit is poorly developed, but is suggestive of southerly transport directions. This is confirmed by paleocurrent data from elsewhere in the Picuris Formation that consistently indicate south-southwest transport directions (Rehder, 1986). In his study of the Picuris Formation, Rehder (1986) recognized that overlying clastic units (top of Picuris Tuff is to the west) contain abundant clasts of the Amalia Tuff, the distinct densely welded rhyolitic tuff of the Questa caldera (26–26.5 Ma).

Throughout its areal extent, the Picuris Formation is folded and faulted. Although the structural evolution of the Miranda graben has not been studied in detail, the vertical attitude of the Picuris Formation within the Miranda graben indicates significant Tertiary deformation associated with rifting. The Miranda graben is bounded on its west margin by a major fault system, the Pecos–Picuris fault, which is also the east boundary of the Picuris Mountain block. The Pecos–Picuris fault system was active during the late Paleozoic Ancestral Rocky Mountain orogeny, the Late Cretaceous–early Tertiary Laramide orogeny, and possibly during the Proterozoic. It is one of several examples of reactivation of major preexisting structures during rifting. Evidence presented at Stop 3 for late and rapid uplift of the Picuris block relative to the San Luis Basin is further corroborated by the scarcity of Precambrian lithologies in the Picuris Formation and the structural relief across the Pecos–Picuris fault on the west side of Miranda graben.

Return to NM-68 via the route just traveled.

Second day: Taos Plateau loop

Mileage

0.0 Begin at intersection of NM-518 and NM-68 in village of Ranchos de Taos, New Mexico (Fig. 4). Drive north through Taos. NM-518 continues north past the junction of NM-68 and US-64 (Fig. 9). **5.4**

5.4 Enter village of El Prado. **0.7**

6.1 **STOP 7. Rift tectonics and volcanism overview** (Fig. 9). Park on right shoulder at telephone pole bearing memorial to Tony Gonzales (2135 m). Taos Pueblo to the east. A Quaternary fault scarp cuts a large alluvial fan at the foot of Taos Mountain (Machette and Personius, 1984; Personius and Machette, 1984; Dungan et al., 1984). To the north of Taos Mountain, the Sangre de Cristo Mountains consist largely of Proterozoic schists and gneisses that are cut by mid-Tertiary plutons and overlain by volcanic rocks of the Latir–Questa caldera magmatic system (Lipman et al., 1986). Paleozoic and Mesozoic strata are confined almost entirely to the eastern structural boundary. This segment of the Sangre de Cristo Mountains is tilted to the north (see also Menges, 1987) so that Tertiary igneous rocks exposed above treeline (3500 m) at its south end are largely plutonic; plutons and volcanic rocks essentially contemporaneous with the plutons are exposed in and around the caldera in the central region. To the north (Rio Costilla—Stop 25) the Amalia Tuff, an outflow sheet from the caldera, is exposed at 2480 m. South of Taos Mountain, a thick sequence of late Paleozoic clastic sedimentary rocks is downdropped against Precambrian crystalline rocks along a west-northwest-trending fault.

The fault to the east is one of many Quaternary faults that cut Pliocene or younger volcanic rocks or Quaternary surficial deposits in the southern San Luis Valley (Machette and Personius, 1984). Some unusual reverse faults and the related compressive deformation of the Taos Plateau were discussed at Stop 3. Virtually all drainages that were cut into unconsolidated alluvium are deflected away from regional gradients and exhibit asymmetry of the type seen east of Stop 3. This asymmetry, a consequence of the gorge arch, is the most obvious of the features that demonstrate contemporary deformation of the Taos graben. The upper Rio Pueblo de Taos flows south-southwest (nearly parallel to the Rio Grande), rather than westward, because it is deflected to the east by the gorge arch. The lower Rio Pueblo at Taos flows nearly due west and occupies the axis of the syncline located on the southeast flank of the gorge arch. After turning west on US-64 (1.7 mi north), note the marked asymmetry of the drainages. The size and asymmetry of successive drainages diminishes near the axis of the arch (2160 m), and then the sense of asymmetry is reversed on the west flank. **1.7**

7.8 Turn left onto US-64 at the "blinking light." **8.1**

15.9 **STOP 8. Rio Grande Gorge high bridge** (2100 m). Pull off into parking area on right after crossing the bridge, and then walk back onto bridge to view Servilleta Basalt section (Fig. 10A). The three members of the Servilleta Basalt (Dungan et al., 1984), corresponding to three separate eruptive periods, are well exposed here (section 5 of Dungan et al., 1984, is located 1 km north of the bridge; see Table 1). At this locality (Fig. 10B), and for several miles south of the bridge, all three members are quite thick and sedimentary interbeds (Santa Fe Group) are much thinner. Nonetheless, the relatively thin interbeds may represent greater time intervals than the individual volcanic eruptive episodes. Thinner sediment intercalations within volcanic members separate units that are typically chemically homogeneous and probably represent the products of single eruptions (Dungan et al., 1986). Three studies have reported late Pliocene K–Ar ages on Servilleta lavas (Ozima et al., 1967; Lipman and Mehnert, 1979; Baldridge et al., 1980). These data are summarized in Machette and Personius (1984). Servilleta volcanism spans a period of approximately 1–2 million years.

Elsewhere the Servilleta section is incomplete or individual members are much thinner, due either to the shadowing effect of other topographic features, or as the result of impingement against prograding alluvial fans (Dungan et al., 1984). Because Servilleta vents are located primarily on the western

FIGURE 9—Location map for Stop 7.

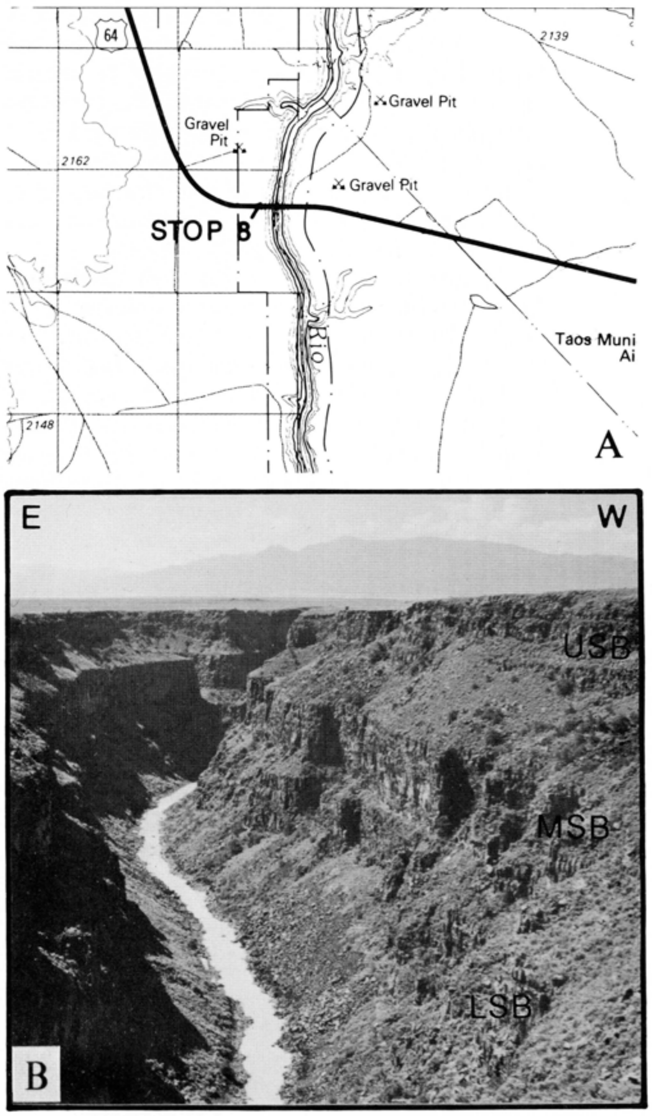

FIGURE 10—**A,** Location map for Stop 8. **B,** View southward from Stop 8 of the exceptionally thick section of Servilleta Basalt at the Rio Grande Gorge high bridge.

TABLE 1—Servilleta basalts, Taos Plateau volcanic field.

No.	1.	2.	3	4.	5.	6.	7.	8.
	LSB	LSB	MSB	USB	USB	USB	USB	USB
Sample	335	440	340	25	1	3	91	329
SiO_2	50.13	53.20	49.07	50.83	51.10	49.56	51.70	49.77
TiO_2	1.31	1.13	1.31	1.21	1.19	1.17	1.21	1.20
Al_2O_3	16.20	16.49	16.53	16.41	16.27	16.78	15.77	16.52
FeO*	10.60	8.86	11.04	10.66	10.72	10.72	10.15	10.41
MnO	0.16	0.14	0.17	0.17	0.17	0.15	0.16	0.18
MgO	8.21	6.12	8.30	7.20	7.36	7.40	6.94	8.21
CaO	9.24	8.23	9.45	9.16	8.95	9.22	8.26	8.92
Na_2O	3.13	3.21	3.04	3.03	3.22	3.39	3.13	3.12
K_2O	0.44	1.29	0.37	0.36	0.52	0.60	1.04	0.81
P_2O_5	0.18	0.23	0.18	0.16	0.20	0.25	0.21	0.19
H_2O	0.40	—	0.66	—	—	—	0.21	0.51
Total	100.00	98.90	100.12	99.19	99.70	99.24	98.78	99.84
Trace elements (ppm)								
Rb	12.6	18.1	2.7	3.6	8.9	7.6	17.2	9.7
Sr	428	534	354	280	355	445	343	360
Y	20.6	20.1	20.6	20.5	21.1	20.7	20.6	21.6
Zr	112	132	84	78	88	106	105	106
Nb	8.5	13.5	6.8	5.4	6.5	8.9	8.8	9.4
Ba	367	568	270	195	300	335	—	268
Cr	172	183	195	—	179	159	—	263
Ni	113	110	146	—	156	66	175	162
Co	41.6	38.9	49.4	—	—	—	—	48.7
Th	1.15	1.6	0.46	0.66	0.86	0.63	2.95	1.01
Hf	2.74	3.4	2.16	2.14	2.54	2.88	1.84	2.67
La	12.2	18.18	7.71	7.63	10.90	13.40	14.00	10.65
Ce	28.0	39.0	18.5	17.4	26.7	31.2	33.0	25.0
Sm	3.45	4.02	3.06	3.00	3.45	3.92	3.71	3.44
Eu	1.18	1.29	1.13	1.03	1.16	1.28	1.18	1.18
Tb	0.57	0.66	0.54	0.62	0.71	0.67	0.67	0.58
Yb	2.03	1.95	1.95	1.90	1.99	1.88	1.96	2.17
Lu	0.32	0.31	0.29	0.31	0.30	0.31	0.31	0.34
Sc	23.2	22.4	24.0	24.0	—	25.0	22.5	26.9
Ta	0.51	0.70	0.40	—	—	0.40	—	0.57
V	132	137	139	—	—	139	—	156

*Total FE reported as FeO.
1. LSKI, Section 5 (Stop 8).
2. San Cristobal lava, north of Dunn Bridge.
3. LSKI, Section 5 (Stop 8).
4. LSKI, Old State Line Bridge abutment, west embankment (between Stops 29 and 30).
5. Typical LSB, west abutment Rio Grande Gorge high bridge (Stop 8).
6. Coarse diktytaxitic texture, Rio Petaca east of Tres Piedras (Stop 17).
7. Xenocrystic Servilleta, Las Segita Peaks (north of Stop 15).
8. Relatively MgO-rich Servilleta, Commanche Rim—roadcuts on US-285, ~1 mi south of junction with Carson Hwy.

margin of the volcanic field, ongoing east-southeast-tilting of the plateau surface concurrent with volcanism caused lavas to flow mainly to the east and southeast. The chain of topographic obstructions extending northward from Cerros de los Taoses (includes Timber Mountain, Cerro Montoso, Brushy Mountain, and Cerro de la Olla) has contributed to a marked thinning of Servilleta basalts north of the high bridge. We have noted previously that rapid uplift of the Picuris and Sangre de Cristo Mountains occurred contemporaneously with Servilleta volcanism. Major ancestral alluvial fans prograded northward from the Picuris Mountain front, northwestward from the Taos embayment (Rio Fernando de Taos drainage), and westward from the Sangre de Cristo Mountains, especially in the vicinities of Arroyo Hondo (Stop 11) and Red River (Stops 18–23). Despite the potential for ponding of basalt lavas within the actively subsiding Taos graben, these fan deposits produced local topographic highs against which Servilleta flows thinned or terminated. The local lower Servilleta Basalt (LSB), and to some extent the middle Servilleta Basalt (MSB), were restricted in areal extent by the thick fan deposits shed from the Picuris front and the southern Taos embayment, whereas upper Servilleta Basalt (USB) flows spread widely over these fans. A similar relationship is observed for the ancestral Red River fan. See Stop 19 for a discussion of the role of the Red River andesite volcano in diverting alluvial deposition during the post-MSB time period.

The major-element, trace-element, and isotopic compositions of Servilleta basalts are discussed in detail in Dungan et al. (1986). The three members overlap compositionally to some degree (Table 1), and as a whole define coherent compositional trends, but each member is dominated by a restricted part of the total compositional spectrum. Dungan et al. (1986) interpreted the variations as a product of mixing moderately evolved Servilleta parent magma of a nearly fixed composition with a range of andesite and dacite magmas similar to those erupted contemporaneously with the Servilleta Basalt. The LSB comprises for the most part rocks with a high proportion of admixed andesite and/or dacite, whereas MSB lavas typically approach the parental composition. The USB spans the entire compositional range, but is dominated by rocks intermediate between the extremes. Thus, the three members do not define a progressive temporal evolution trend. Exposed at the southwest bridge abutment is the youngest USB flow in this area (sample RG-1, Table 1). Servilleta lavas form pahoehoe flows characterized by diktytaxitic or (less commonly) intergranular groundmass textures, sparse to moderately abundant (5–15%) olivine phenocrysts or (rarely) microphenocrysts, rare plagioclase phenocrysts, and vesicular segregations (vertical pipes and horizontal sheets; see Stop 17). Groundmass textures vary substantially in grain size and there is a general positive correlation between groundmass coarseness and the development of the segregations. Multiple analyses of several flows have shown that some Servilleta lavas are chemically heterogeneous on the scale of an outcrop (Stop 15).

Continue on US-64. The highway turns north and passes east of Cerros de los Taoses (olivine andesite); the highway then turns west around the north end of Cerros de los Taoses (2400 m). Timber Mountain (Stop 10) can be seen to the north (2450 m). **15.1**

31.0 **STOP 9. Taos Plateau overview** (Figs. 11, 12). Pull off on right side of the road on the second small rise past milepost 176 (2375 m). From this vantage point, the eastward dip of the plateau and the concentric distribution of andesite and dacite vents (Table 2) can be observed. McMillan and Dungan (1986) chose 60% SiO_2 as the distinction between Taos andesite and dacite because of the change in phenocryst mineralogy from olivine to orthopyroxene plus augite. Both contain microphenocrysts or sparse phenocrysts of plagioclase, but not in the abundance characteristic of typical subduction-related, calc-alkaline intermediate-composition rocks. Although both andesite and dacite are high-K compositions (IUGS—basaltic trachyandesite through trachydacite and dacite), hydrous phases are minor or absent in many dacites.

Two low, tree-covered Servilleta shield volcanoes are also visible north of the highway. All the Taos Plateau tholeiite, andesite, and dacite volca-

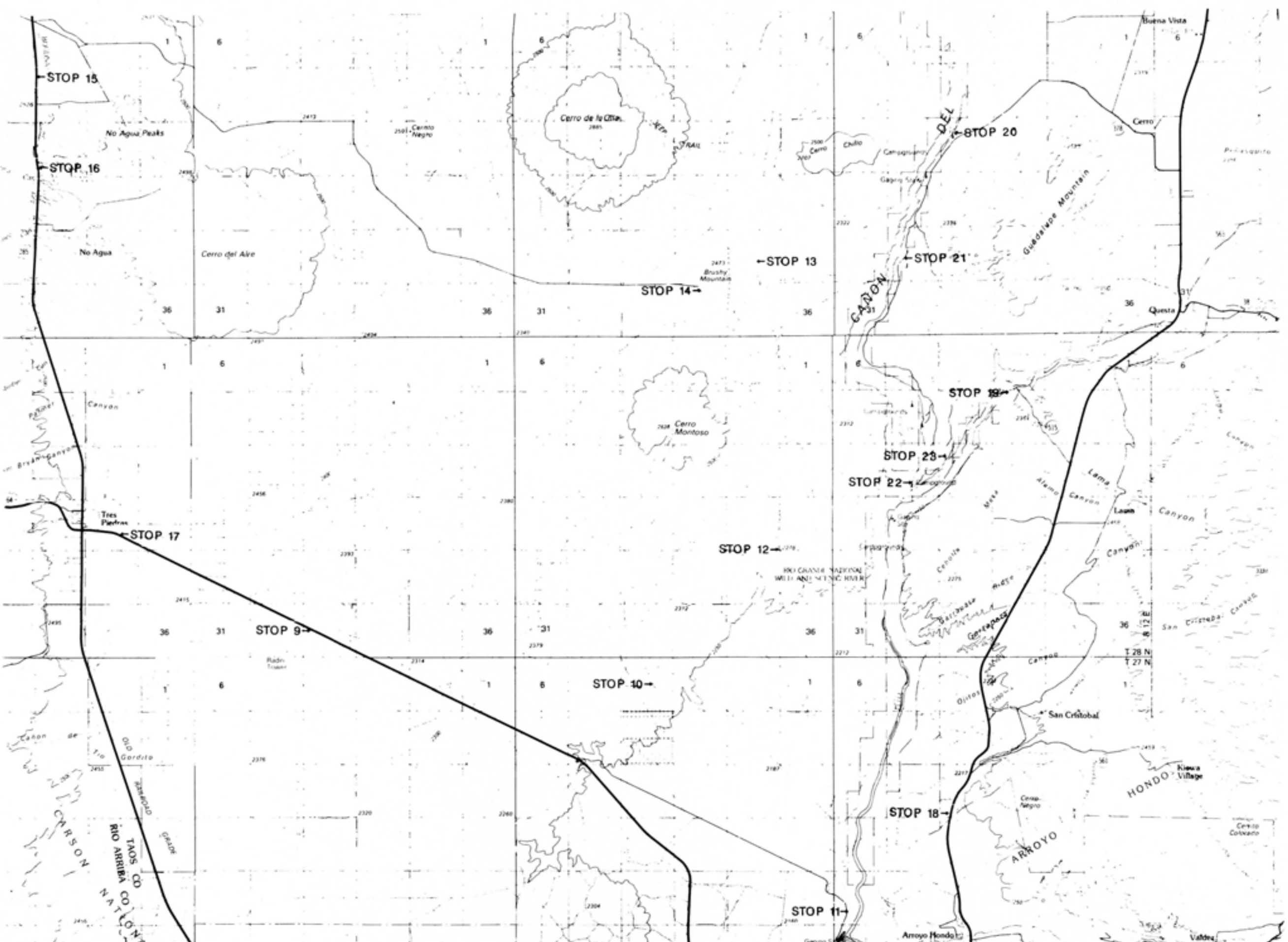

FIGURE 11—Location map for Stops 10 through 23. Note: NM-3 is now NM-522.

noes are essentially central-vent monolithologic shields virtually lacking in pyroclastic deposits (several shields are capped by late spatter cones) or fissures. Lipman and Mehnert (1979) noted that volcano slopes become increasingly steep as a function of the SiO_2 contents of their lavas (i.e., because of the increase in viscosity). Dacite cones of the outer ring, such as Ute Mountain (3076 m), Tres Orejas (2431 m), and Guadalupe Mountain (2675 m), are morphologically distinct from andesite shield volcanoes such as Cerros de los Taoses (2400 m), Cerro Montoso (2638 m), Cerro de la Olla (2885 m), and Cerro del Aire (2755 m). The prominent San Antonio Mountain (3326 m) is intermediate in morphological character and is just slightly higher in SiO_2 than the andesite volcanoes. The small da-

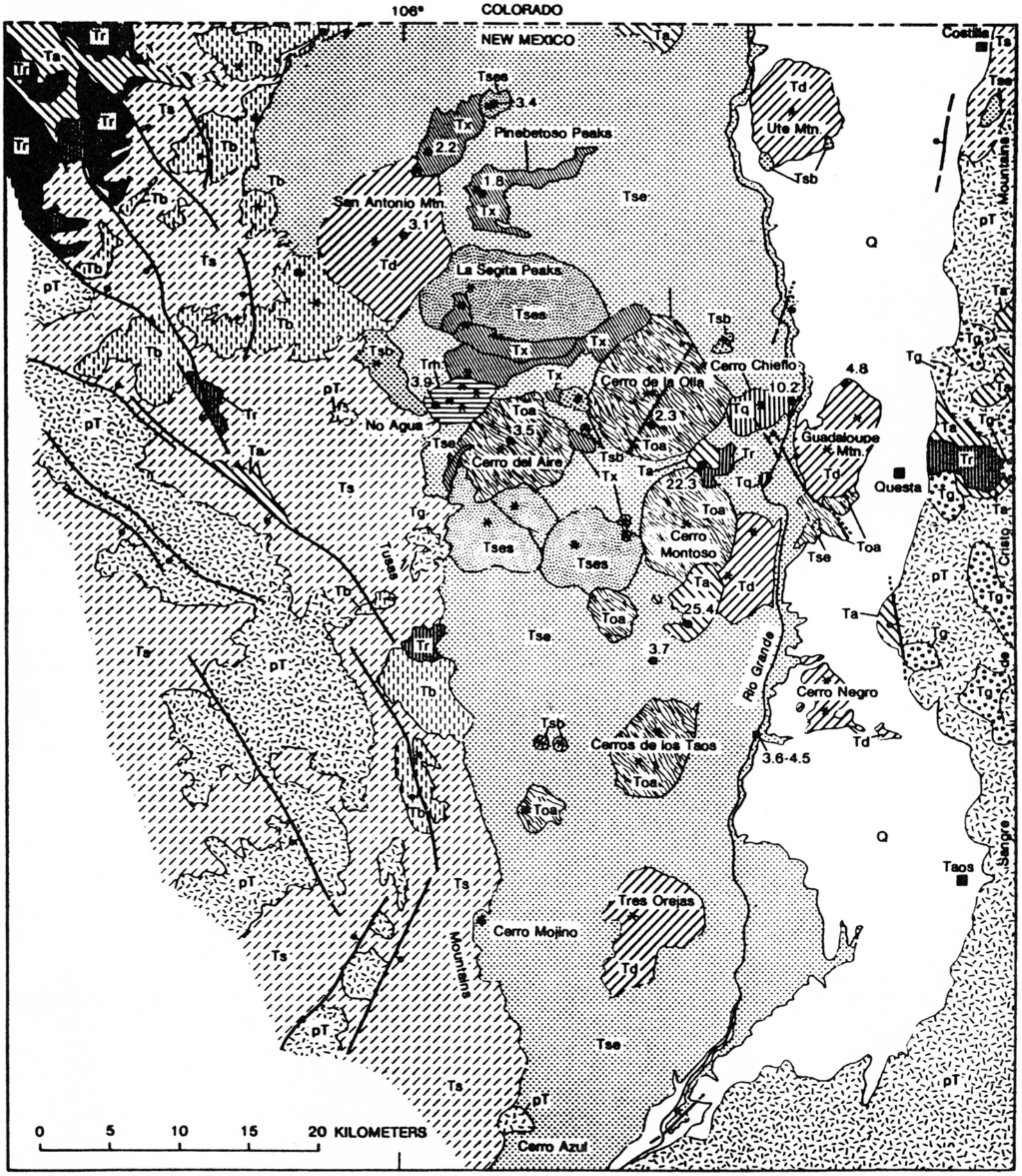

FIGURE 12—Generalized geologic map of the Taos Plateau volcanic field (from Lipman and Mehnert, 1979). Q, Quaternary and surficial deposits; Trh, rhyolite (Pliocene); Tq, dacite; Td, trachydacite; Toa, olivine andesite; Tx, xenocrystic basaltic andesite; Tsb, trachybasalt; Tse, Servilleta Basalt; Tses, Servilleta shield volcano; Ts, Tertiary rift sediments (includes Santa Fe Group and Los Pinos Formation). Pre-rift and early-rift volcanic rocks: Tb, basalt flows; Tg, granitic intrusions; Tr, rhyolitic ash-flow tuffs; Ta, andesite to dacite flows and breccias; pT, pre-Tertiary rocks, mainly Precambrian. Numbered localities denoted by small filled circles are K–Ar ages in million years (Lipman and Mehnert, 1979). Asterisks indicate vent locations.

TABLE 2—Olivine andesites and pyroxene dacites, Taos Plateau volcanic field.

No.	1.	2.	3	4.	5.	6.	7.	8.
	CN	CT	TO	UTE	UCEM	RR	SA	G
Sample	RG-17	NJ-7	RG-149	RG-58	RG-220	RG-206	NJ-180	NJ-123
SiO_2	62.56	57.33	55.96	57.09	64.33	60.49	62.51	67.32
TiO_2	0.77	0.99	1.23	1.27	0.85	0.99	0.77	0.54
Al_2O_3	15.81	15.97	15.76	15.77	14.22	16.04	15.54	15.59
FeO*	4.98	6.93	7.43	6.97	5.32	5.66	5.15	3.67
MnO	0.10	0.11	0.14	0.12	0.10	0.10	0.09	0.06
MgO	2.54	5.00	3.59	3.60	3.41	3.28	2.52	1.37
CaO	4.85	6.49	6.93	6.40	4.68	5.26	4.81	3.56
Na_2O	4.03	4.00	4.40	3.95	3.66	4.40	3.86	3.86
K_2O	2.68	2.05	2.56	2.65	2.69	2.85	3.08	3.39
P_2O_5	0.43	0.35	0.87	0.54	0.09	0.38	0.38	0.21
Total	98.75	99.22	98.87	98.36	99.35	99.45	98.71	99.57
Trace elements (ppm)								
Rb	44.5	32.5	36.9	37.8	62.2	49.2	52.5	61.6
Sr	807	727	1303	1040	224	1018	736	520
Y	21.0	19.1	24.4	30.2	17.5	18.6	24.0	16.3
Zr	231	177	247	283	92	210	271	207
Nb	23.5	18.7	43.5	24.3	16.8	29.3	20.1	14.1
Ba	1230	1139	1330	1380	332	1191	1351	1274
Cr	34	124	55	65	102	65	45	30
Ni	—	101	29	100	66	43	27	18
Th	5.10	3.47	7.34	2.73	4.54	1.6	4.36	4.85
Hf	5.83	4.36	6.11	6.56	3.00	5.30	6.61	5.59
La	47.7	31.8	68.9	50.4	10.5	40.9	47.4	38.6
Ce	103.8	62.0	138.0	104.0	22.3	82.0	97.6	79.4
Sm	6.83	5.57	10.30	8.46	2.88	6.50	7.30	5.39
Eu	1.76	1.48	2.59	2.10	0.82	1.63	1.72	1.33
Tb	0.71	0.69	0.96	0.98	0.52	0.69	0.84	0.66
Yb	1.82	1.82	2.17	2.65	1.85	1.59	2.22	1.54
Lu	0.280	0.317	0.340	0.400	0.314	0.254	0.345	0.246
Sc	10.0	15.3	15.9	14.7	12.4	11.2	11.0	8.0
V	—	131	160	—	77	—	86	56

*Total Fe reported as FeO.
1. Cerro Negro pyroxene dacite (Stop 18).
2. Cerro de los Taoses andesite.
3. Tres Orejas andesite.
4. Ute Mountain andesite.
5. UCEM glassy dacite (Stop 12).
6. Red River volcano—dacite at top of hybrid section (Stop 19).
7. San Antonio Mountain dacite.
8. Guadalupe Mountain dacite.

TABLE 3—Trachybasalts and trachybasaltic andesites, Taos Plateau volcanic field.

No.	1.	2.	3	4.	5.	6.	7.	8.
Sample	RG-15	RG-4	RG-45	RG-154	RG-57	RG-23	BB-1	BB-12
SiO_2	52.01	52.41	55.35	51.49	50.51	54.55	51.41	51.30
TiO_2	1.55	1.81	1.30	1.42	1.52	1.59	1.69	1.35
Al_2O_3	16.94	16.39	16.50	15.99	16.21	16.47	17.16	16.39
FeO*	8.81	9.32	8.02	8.17	9.43	8.33	8.97	9.76
MnO	0.15	0.14	0.14	0.13	0.16	0.14	0.15	0.16
MgO	5.64	4.15	4.75	6.03	6.40	3.41	6.28	7.48
CaO	7.76	7.33	6.60	8.46	8.44	6.34	7.92	8.36
Na_2O	4.08	3.78	3.77	4.09	3.55	3.79	4.13	3.73
K_2O	1.71	1.95	2.24	1.91	1.93	2.91	1.75	1.31
P_2O_5	0.35	0.82	0.46	0.66	0.72	0.77	0.45	0.36
Total	99.00	98.10	99.13	98.35	98.87	98.30	**	**
Trace elements (ppm)								
Rb	26.0	23.6	38.3	28.4	23.3	39.7	20.5	—
Sr	599	1025	661	1025	1067	1055	1133	759
Y	24.0	32.6	25.3	22.7	27.5	33.1	21.8	155
Zr	172	219	176	215	150	214	189	166
Nb	20.3	26.8	21.7	31.1	23.3	27.3	27.6	22.3
Ba	625	1275	1025	850	1270	1870	666	542
Cr	142	31	—	140	—	18	134	180
Ni	—	50	10	93	115	—	94	122
Co	—	—	—	—	—	—	36	42
Th	2.2	1.6	3.8	4.7	1.8	2.3	1.9	—
Hf	4.41	5.72	4.58	4.60	4.18	5.47	4.45	—
La	22.8	43.1	32.1	40.0	34.5	45.4	24.0	—
Ce	50.4	103.0	70.4	68.9	79.4	97.6	53.5	—
Sm	5.3	10.0	6.3	6.5	7.3	9.2	5.7	—
Eu	1.58	2.72	1.74	1.87	2.09	2.55	1.79	—
Tb	0.79	1.17	0.86	0.76	0.98	1.15	0.76	—
Yb	2.33	2.90	2.3	2.15	2.55	2.93	2.18	—
Lu	0.40	0.44	0.38	0.31	0.38	0.44	0.30	—
Sc	23	19	17	19	23	15	20	—
V	—	165	—	155	—	—	147	—

*Total Fe reported as FeO.
**Major element normalized to 100% before combining FeO and Fe_2O_3.
1. Xenolith-bearing lava at river level—Dunn Bridge crossing (Stop 11).
2. Red Hill cone lava at No Agua (Stop 16).
3. Xenocristic lava from Los Cerritos de la Cruz (west of Stop 15).
4. Cerro Dormilon (south of Stop 9).
5. Flank vent on SE Ute Mountain.
6. Mesita cone.
7. Base of Los Mogotes section along CO-17.
8. Top of Los Mogotes section along CO-17.

cite flow complex east of this stop is also a transitional dacite composition. Cerro Dormilon, a small alkalic cinder cone is located between this stop and Cerros de los Taoses. The majority of late alkalic vents are clustered around the No Agua–La Segita Peaks area to the north (Table 3).

Turn vehicles around and return eastward on US-64. **7.0**

38.0 Turn left (sharply) onto obscure unpaved road, drive north through gate at reduced speed. Drive cautiously with vans. This segment of the trip probably should be avoided with low-clearance passenger vehicles. **0.3**

38.3 Turn left at T-junction. **0.2**

38.5 Bear right at Y-junction and stay on main dirt track. **0.7**

39.2 Junction of several roads at sign indicating "New Road North." Bear right onto the old road and continue north. **0.8**

40.0 Y-junction. Continue on road marked "closed to north." Proceed very cautiously in vans. This road gradually climbs up onto the low east–west ridge south of Timber Mountain. In 0.5 mi park south of gate (2300 m). **0.5**

40.5 **STOP 10. Timber Mountain** (Fig. 13). The two prominent hills directly to the north, jointly referred to as Timber Mountain, are the southernmost exposures of a major intrarift horst within the San Luis Valley segment of the Rio Grande rift. Collectively, Timber Mountain and the smaller Brushy Mountain locality about 10 km to the north cover approximately 15 km^2. These erosional remnants record two periods of calc-alkaline volcanism dominated by eruption of dacite (IUGS—trachydacite) lavas, but including flows of andesite (IUGS—basaltic trachyandesite to trachyandesite), a rhyolite dome, and rhyolite ash-flow tuffs (Table 4). Stratigraphic relations and K–Ar dating (Lipman and Mehnert, 1979) indicate that these two periods of volcanism are both younger than the 26 Ma Amalia Tuff from the Questa caldera (Lipman et al., 1986),

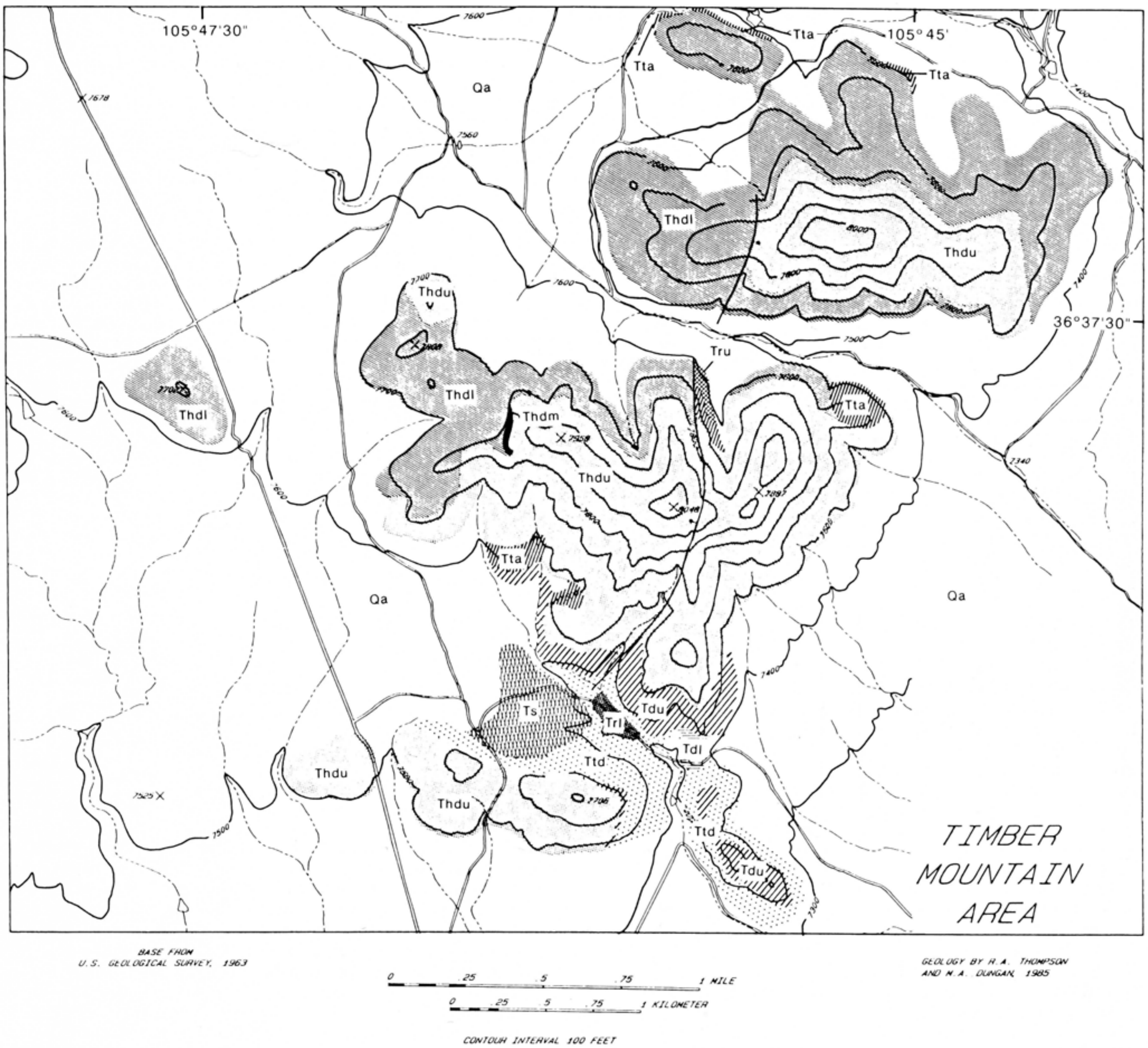

FIGURE 13—Generalized geologic map of the Timber Mountain area (Thompson and Schilling, 1988): Qa, Quaternary alluvium; Ts, Servilleta Basalt; Thdu, upper hornblende dacite; Thdm, middle hornblende dacite; Thdl, lower hornblende dacite; Tta, andesite; Tru, upper rhyolite; Tdu, upper pyroxene dacite; Tdl, lower pyroxene dacite; Ttd, undivided pyroxene dacite; Trl, lower rhyolite tuff.

but may have been separated in time by as much as three million years.

The lower volcanic sequence (25 Ma), exposed only at Timber Mountain, contains a basal ash-flow tuff of low-silica rhyolite (Trl—samples 74L-214, RG-68, Table 4) overlain by thin pyroxene dacite lava flows (Ttd—sample RG-69, Table 4). These are locally covered by a cogenetic cone of agglutinated dacite spatter (Tdl—sample RG-61, Table 4), grading vertically from a vitrophyric base to a devitrified top (Tdu). Remnants of a stratigraphically younger lava flow of glassy, low-silica rhyolite (Tru) and two olivine andesite flows (Tta) are preserved locally. Exposed thickness of the lower sequence is approximately 60 m. This is a minimum as the base is not exposed, and the top has been eroded. The lower sequence is unconformably overlain by an upper sequence (22 Ma) which at Timber Mountain consists of multiple dacite lava flows, divided into three units (Thdl, Thdm, Thdu—sample RG-71, Table 4) on the basis of mineralogy. Total exposed thickness is approximately 150 m.

Low-silica rhyolites are dominated by phenocrysts of plagioclase, sanidine, quartz, and biotite; subordinate amounts of Fe–Ti oxides, clinopyroxene $\pm$ orthopyroxene, and amphibole are present in a glassy to partially devitrified matrix. Flattened pumice fragments are ubiquitous. Lower sequence dacites contain a complex disequilibrium assemblage of phenocrysts, glomerocrysts, xenocrysts, and high-silica glass. Phenocrysts include plagioclase, clinopyroxene, orthopyroxene, Fe–Ti oxides, and minor hornblende. Two texturally and compositionally distinct plagioclase populations are present. Euhedral phenocrysts exhibiting oscillatory and normal zoning have core to rim compositions

TABLE 4—Analyses of representative samples, Timber Mountain and Brushy Mountain.

	Timber Mountain					Brushy Mountain				
No.	1.	2.	3.	4.	5.	6.	7.	8.	9.	10.
Sample	74L-214	RG-68	RG-69	RG-61	RG-71	HB-110	67L-61	RG-32	RG-33	RG-34
Map Seq.	Trl	Trl	Ttd	Tdl	Thdu	Tat	Tr2	Tr2	Tba	Thdl
SiO_2	69.20	—	63.46	65.02	63.36	77.49	78.29	—	57.40	61.49
TiO_2	0.43	—	1.48	0.94	0.80	0.22	0.10	—	1.24	0.92
Al_2O_3	14.32	—	15.66	15.46	15.24	11.09	11.72	—	16.53	16.49
Fe_2O_3	2.35	—	1.73	2.14	1.78	1.46	0.58	—	2.35	2.68
FeO	0.09	—	3.75	2.39	3.60	n.a.	0.17	—	4.37	2.73
MnO	0.09	—	0.12	0.11	0.09	0.07	0.06	—	0.07	0.05
MgO	0.60	—	1.77	1.88	3.13	0.01	0.06	—	3.99	2.76
CaO	3.44	—	4.22	3.41	4.76	0.26	0.35	—	6.05	4.92
Na_2O	4.19	—	4.07	3.34	3.89	3.60	3.81	—	4.08	4.55
K_2O	5.05	—	3.63	4.27	3.03	4.48	4.44	—	2.54	2.47
P_2O_5	0.10	—	0.43	0.28	0.19	0.04	0.01	—	0.48	0.38
Total*	99.77	—	100.32	99.24	99.87	98.72	99.59	—	99.10	99.44
H_2O	0.44	—	2.05	2.72	2.17	n.a.	0.39	—	1.51	2.27
CO_2	1.57	—	n.a.	n.a.	n.a.	n.a.	0.10	—	n.a.	n.a.
Trace elements (ppm)										
Rb	—	58.1	76.4	83.6	52.2	82.6	—	157	36.5	50
Sr	—	172	617	558	755	17.2	—	8.9	1097	916
Y	—	32.8	36.1	41	17.5	63.3	—	20.6	16.6	17.5
Zr	—	309	290	315	177	355	—	119	184	205
Nb	—	15	22.7	24.4	14.9	28.5	—	40	21.5	18
Ba	—	1650	1400	1302	1155	n.a.	—	47	1360	1400
Cr	—	10	8.8	8.4	58	n.a.	—	n.a.	113	57
Th	—	8.3	10.7	10.2	6.47	n.a.	—	22.4	4.87	5.81
La	—	72.1	53.6	55.3	41.6	n.a.	—	34.1	45.7	47.6
Ce	—	145	112	118	82	n.a.	—	62	94.5	93.5
Nd	—	n.a.	n.a.	n.a.	n.a.	n.a.	—	n.a.	n.a.	n.a.
Sm	—	10.9	9.53	9.94	5.8	n.a.	—	2.13	6.66	6.54
Eu	—	1.62	2.2	2.24	1.38	n.a.	—	0.1	1.84	1.6
Tb	—	1.15	1.15	1.06	0.59	n.a.	—	0.28	0.67	0.65
Yb	—	2.95	3.35	3.61	1.42	n.a.	—	2.7	1.29	1.35
Lu	—	0.46	0.55	0.57	0.24	n.a.	—	0.27	0.2	0.24
Sc	—	4.4	11.6	10.9	10.8	n.a.	—	1.8	13.6	10.9

*Major-element analyses on ignited samples. H_2O and CO_2 determined independently.
1. From Lipman and Mehnert (1979).
2. Sample from the same locality as analysis no. 1.
7. From Lipman and Mehnert (1979).
8. Sample from the same locality as analysis no. 7.

ranging from An_{58-53} in the lava flows and An_{52-47} in the more silicic vitrophyric agglutinate. Less abundant sieve-textured plagioclase phenocrysts are poorly zoned (An_{45-48}). Oligoclase ($An_{21}Ab_{73}Or_6$) and sanidine ($Ab_{55}An_3Or_{42}$) xenocrysts occur in complex reaction relationships with the dacite host and are often enclosed in and riddled with inclusions of high-silica rhyolite glass. Andesite micropillows, up to several millimeters in diameter are preserved in the glassy matrix of dacite spatter agglutinate and contain microphenocrysts of plagioclase, clinopyroxene, Fe–Ti oxides and skeletal olivine; the same mineral assemblage found in the andesite lava flows. The micropillows are in various stages of disaggregation, and fragmented debris trails are elongated parallel to the foliation in the glass matrix.

Thompson et al. (1986) modeled the fractionation paths of andesitic parental magmas and concluded that major- and trace-element concentrations in lower sequence dacites can be approximated by fractionation of phenocryst phases, plus mixing in proportions approaching one to one, with high-silica rhyolite similar in composition to the Amalia Tuff. Low-silica rhyolites may have been derived through fractionation of dacites plus mixing with the high-silica rhyolite. These differentiation models support a petrogenetic link between the mildly peralkaline Amalia Tuff of the caldera-forming phase of the Questa magmatic system and early postcaldera lavas. Subsequent eruption of upper sequence volcanic rocks marks the regeneration of more typical metaluminous magmas characteristic of both precaldera and postcaldera magmatism.

Continue ahead on road and return to the south. **0.6**

41.1 Turn right at four-way intersection. **0.2**

41.3 Turn left at four-way intersection. **1.5**

42.8 Turn left (east) on main unpaved road (parallel to telephone poles). Continue on this road (quality gradually improves to the east). **4.9**

47.7 Continue past the road on the left at T-junction (2150 m) and drive down toward the gorge rim. Prepare to turn left past cattleguard. **0.9**

48.6 **STOP 11. Rio Grande Gorge–Arroyo Hondo**

overlook at Dunn Bridge river crossing. Dunn fault and basalt stratigraphy. Turn left onto grass-covered parking area with central fire-ring. Park and walk to the gorge rim (2100 m). This locality (Fig. 14) is only 5 km (3 mi) north of the high bridge (Stop 7), yet the stratigraphic section has changed considerably. Sedimentary interbeds, particularly the unit between the MSB and the USB, form a much greater proportion of the section. The thick cliff-forming flow beneath the one thin MSB lava (east side of gorge) is a silicic alkalic basalt (Lipman and Mehnert, 1979; sample RG-15, Table 3) containing sparse, small (3.5 cm) crustal xenoliths (Kinsel, 1986). From this viewpoint it is also obvious that the stratigraphic section south of the switchbacks does not match the section on the east side of the river. This mismatch is due to the Dunn fault, a down-to-the-east, north-trending fault that probably marks the west margin of the Taos graben in this area. Mismatch between the stratigraphic sections across the fault is due to more than simple offset, as this is a growth fault which was active during and after Servilleta volcanism; i.e., sedimentary interbeds on the downthrown side of the fault are thicker than on the upthrown side. The fault trace runs along the road to the west, through the lowest switchback curve, and then is followed by the river to the south until it emerges on the east wall of the gorge at about the visual limit of the gorge. Hot springs occur at both ends of the fault where it intersects the river banks. This is one of many structures on the Taos Plateau which demonstrate that volcanism and rift tectonism were contemporaneous.

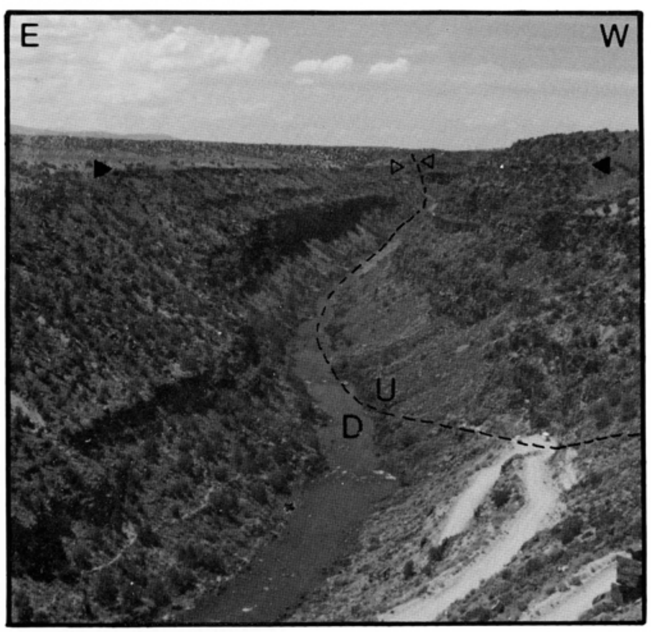

FIGURE 14—View southward from Stop 11 of the Rio Grande Gorge at the Dunn Bridge crossing. The trace of the Dunn fault is shown, and the USB is marked with solid (foreground) and open (distant) triangles to illustrate offset along the fault. Note the greater thickness of the sedimentary interbed between the middle Servilleta Basalt (MSB) and upper Servilleta Basalt (USB) on the downthrown side (east) of the fault. The USB and MSB are greatly thinned here, in comparison to the section at Stop 8, due to the shadowing effect of Timber Mountain, etc. to the west.

Despite evidence that faulting was active during volcanism, there is little indication that the locations of vents were controlled by shallow structures. Cerro de la Olla, the Red River andesite shield, and the Mesita cone in Colorado (Stop 28) are cut by faults that may have localized these vents, but there is no obvious pattern in the overall distribution of vents that suggests a relationship to the gross horst and graben configuration of the southern San Luis Valley. Moreover, there are no fissure vents or even vent alignments that could be attributed to fault control. Thus, the semiconcentric distribution of andesite and dacite cones around the main focus of Servilleta vents appears to be a function of a deep-seated control having to do more with magmatic processes than shallow crustal structure (Dungan et al., 1986).

Turn vehicles around and return to the north and west on the route just traveled. **1.0**

49.6 At the crest of the terrace surface turn right onto main dirt road to the north. Take care to remain on the primary road as many other tracks turn off from it. **4.4**

54.0 Timber Mountain is directly west (Fig. 15) Cerro Montoso is to the northwest. The road climbs up onto the rubbly surface of the dacite flow of "unnamed cerrito east of Montoso" (UCEM). This widespread dacite lava flow is approximately 10 km long, 5 km wide, and is unique in texture, mineralogy, composition, and morphology among Taos Plateau lavas. Its unusual characteristics provide some interesting insights into assimilation processes. **4.9**

58.9 **STOP 12. UCEM flow** (2300 m). Although many of the Taos dacites are glassy and phenocryst-poor, the UCEM flow is the only aphyric intermediate-composition lava (rare quartz xenocrysts and fine-grained xenoliths have been observed). The cryptocrystalline groundmass texture so closely approaches the macroscopic attributes of obsidian glass that this unit was the major source of material used by local Indians for stone points and tools. Plagioclase is lacking, but skeletal and feathery olivine and orthopyroxene are present in the groundmass. Although major-element and isotopic compositions of UCEM are broadly similar to those of other Taos Plateau dacites of comparable SiO_2 content, its trace-element signature is radically different (sample RG-220, Table 2). Unlike the characteristically incompatible-element-enriched intermediate-composition Taos lavas, most measured trace-element concentrations in the UCEM flow (except for Rb and Th) are identical to those in Servilleta Basalt. McMillan and Dungan (1988) interpreted this anomalous composition as an indication that the UCEM magma was produced by surprisingly efficient mixing of Servilleta magma and melted impure metaquartzite, despite concern about the physical limitations magma rheologies and solidi place on such a model. The UCEM flow is compositionally variable (61–64% SiO_2). This heterogeneity may reflect incomplete mixing of the endmembers. The source of the quartzite melt originally must have contained argillaceous impurities in order to contribute the el-

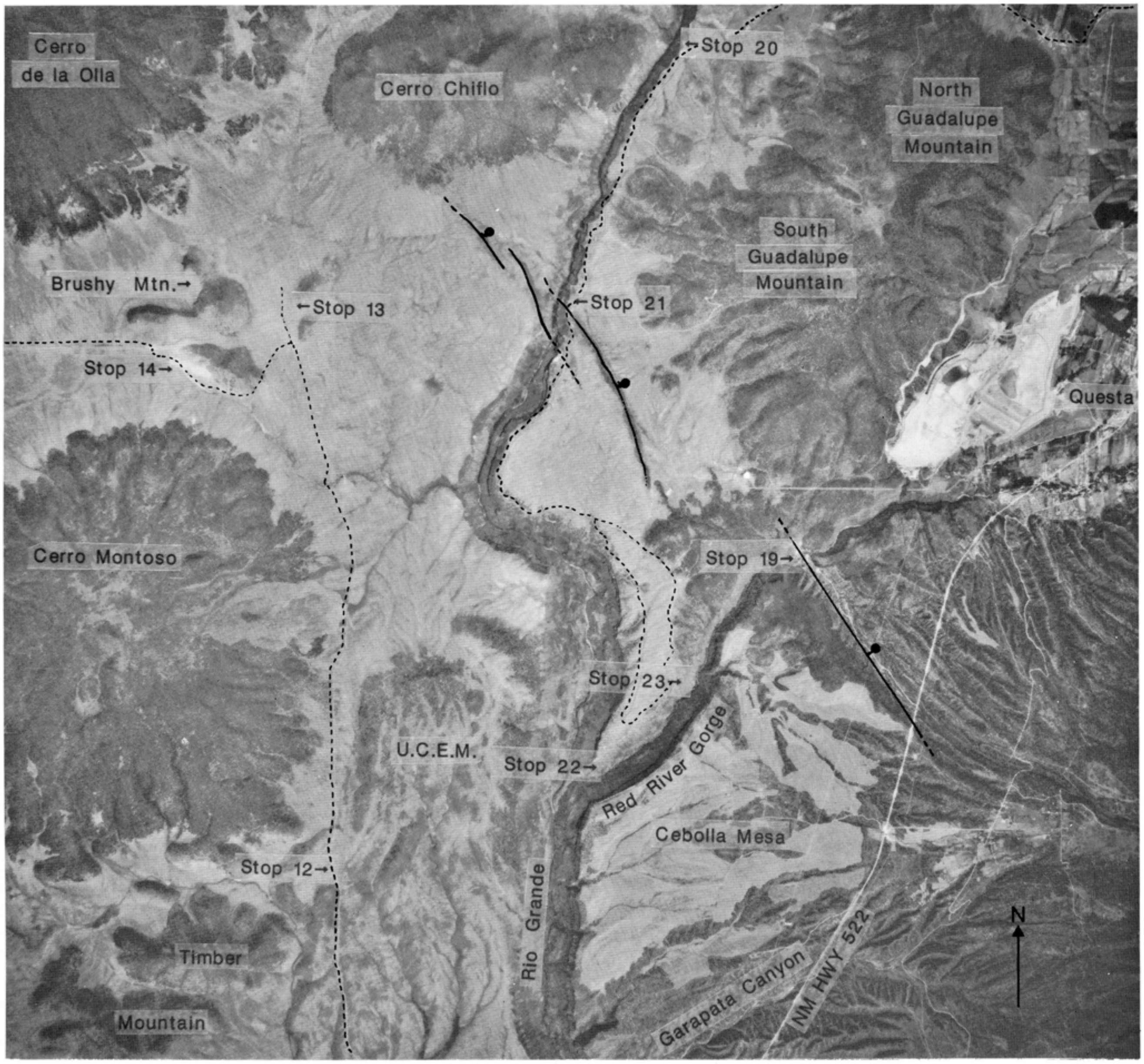

FIGURE 15—Aerial photograph of the confluence of the Rio Grande and Red River. Northwest-trending faults seen at Stops 19 and 21 are highlighted, as are the field-trip routes for Day 2 and Day 3 (shorted dashed lines).

evated K and Rb seen in the UCEM hybrid, but other elements (especially REE) do not show the strong enrichments, relative to Servilleta Basalt, that are found in every other Taos andesite and dacite. The absence of phenocrysts and obsidian-like groundmass texture of the UCEM flow may be the result of the superheated nature of the mixture.

Continue driving north. Cerro Chiflo quartz latite (IUGS—dacite, 10.2 Ma) ahead (2707 m). **1.1**

60.09 Continue left at Y-junction. **0.9**

60.9 Take the right fork toward a small, isolated hill of Amalia Tuff (2350 m). **1.3**

62.2 **STOP 13. Amalia Tuff** (Fig. 16). Park on road west of the small hill of Amalia Tuff with a quarry on its lower slope. The Amalia Tuff exposed here (0.5 km^2) is one of three known localities west of the Rio Grande where outflow tuff from the Questa caldera occurs. Additional occurrences are 1.3 km due west on the north side of the low saddle separating the two hills comprising Brushy Mountain, and 25 km to the southwest on the western edge of the Taos Plateau. The occurrence of Amalia Tuff at these localities attests to the lack of significant relief during early stages of rifting as ash-flow tuff traversed the early rift unimpeded for as much as 40 km from its source.

The welded Amalia Tuff here (sample HB-110, Table 4) is phenocryst-rich (quartz and sanidine; minor Fe–Ti oxides, sphene, and alkali amphibole), devitrified, and contains slightly to moderately flattened pumice fragments. Unlike the exposures at Stop 25, the tuff here shows only minor post-emplacement alteration.

Turn vehicles around and return south for a short distance. **0.4**

62.6 Bear right across cattleguard toward the south side

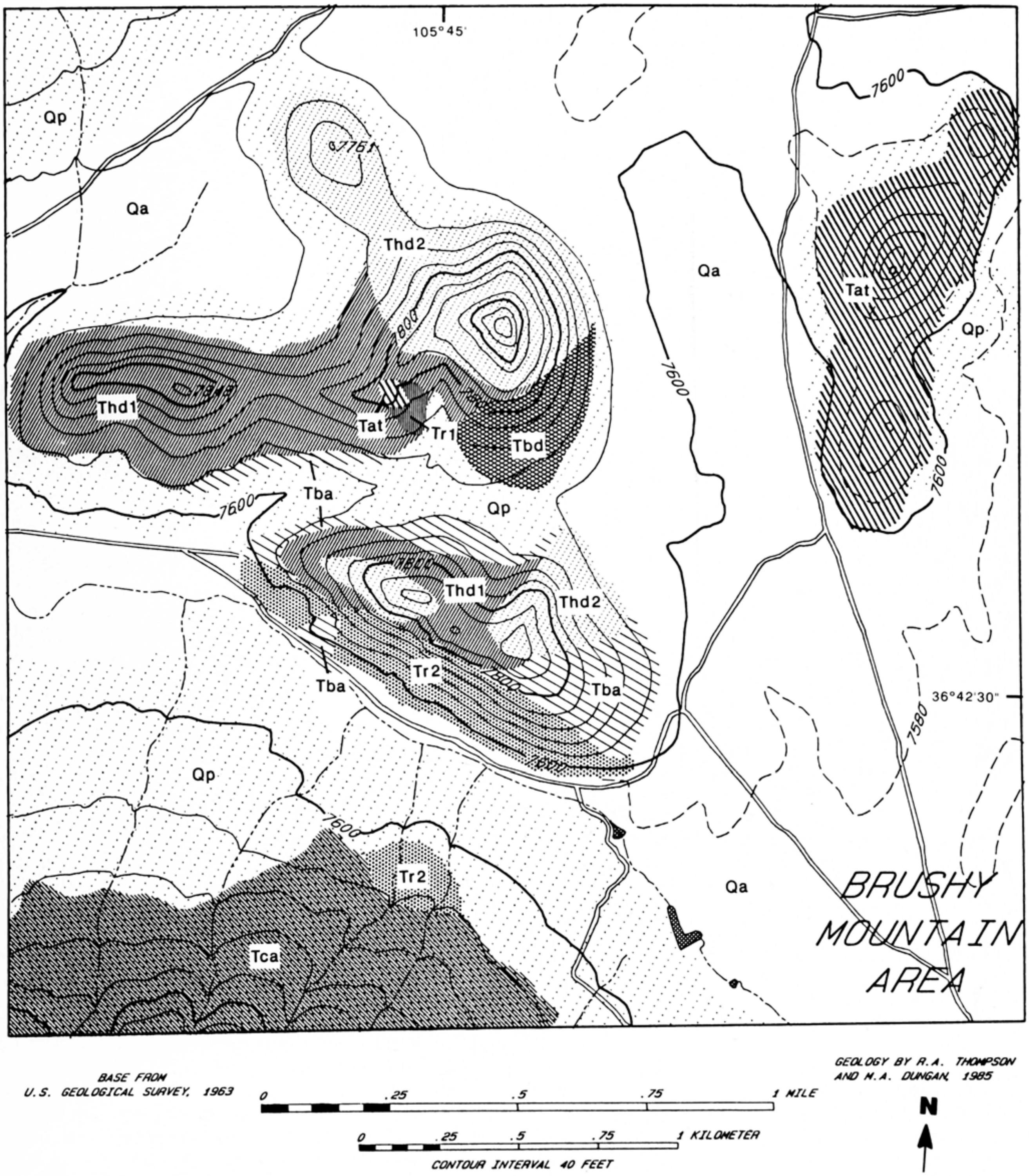

FIGURE 16—Generalized geologic map of the Brushy Mountain area (Thompson and Schilling, 1988): Qa, Quaternary alluvium; Qp, undivided piedmont-slope alluvium; Tca, olivine andesite of Cerro Montoso; Thd2, upper hornblende dacite; Thd1, lower hornblende dacite; Thd, sparsely porphyritic dacite; Tba, andesite; Tr2, rhyolite of Brushy Mountain; Tat, Amalia Tuff; Tr1, weakly welded rhyolite tuff.

of the southern hill (one of two hills collectively referred to as Brushy Mountain). **0.4**

63.0 Stay on the right fork and continue around the south side of the perlite quarry. **0.9**

63.9 Turn right on road to the mine office adjacent to the perlite mill west of the mine. If the pit road is closed, continue on to the main haul road and then double back to the buildings to request permission to enter private property. Note that subsequent cumulative road-log mileage may not reflect mileage actually traveled if gates are closed.

STOP 14. Brushy Mountain (2470 m). Outcrops of early Miocene volcanic rocks related to the Latir–Questa caldera magmatic system (Thompson et al., 1986; Lipman and Mehnert, 1979). The perlite quarry on the lower flanks of Brushy Mountain (Figs. 15, 16) is excavated into a 22 Ma high-silica rhyolite dome (Tr2—sample 67L-61, RG-

32, Table 4) which forms the base of the upper sequence in the Timber Mountain–Brushy Mountain volcanic pile. The Brushy Mountain rhyolite contains phenocrysts of sanidine, quartz, and minor biotite in a devitrified or glassy matrix (perlitized). The dome is overlain by an olivine andesite (Tba—sample RG-33, Table 4), a thin discontinuous flow of sparsely phyric dacite (Tbd), and several hornblende-bearing dacite flows and associated flow breccias (Thd1—sample RG-34, Table 4; Thd2). The olivine andesite is compositionally and mineralogically similar to the andesites of Timber Mountain. The hornblende dacites have up to 8% hornblende phenocrysts in addition to plagioclase, clinopyroxene, Fe–Ti oxides, minor orthopyroxene, sanidine, sphene, and trace zircon. These flows are believed to be correlative with the dacite flows forming the ridge crests at Timber Mountain and are more representative of the regional middle Cenozoic, calc-alkaline rock association than the anhydrous lower-sequence rocks at Timber Mountain. **0.7**

64.6 Drive west on the main haul road. Andesite shield volcanoes of Cerro de la Olla (north), Cerro Montoso (south), and Cerro del Aire (west). **2.0**

66.6 The small escarpment south of the road is a Servilleta flow front. Servilleta vents south and southeast of Cerro del Aire (2755 m) can be seen beyond this flow front. **10.5**

77.1 View of Red Hills cone (2686 m) to the west and San Antonio Mountain to the northwest. Red Hill is the source of a young silicic alkalic lava flow which is intersected by US-285 at No Agua (Stop 16). The two cones farther to the northwest are twin vents (2830 m) for a xenocrystic andesite lava (sample RG-45, Table 3). Together these three constitute Los Cerritos de la Cruz. On the western horizon are east-dipping sediments of the Los Pinos Formation (correlative with Santa Fe Group) and interbedded basaltic lavas of the Tusas Mountains. La Segita Peaks–Wissmath Craters (2650 m), in the middle distance in front of San Antonio Mountain, are parts of an erosionally breached Servilleta shield. La Segita lavas are distinctive in containing abundant xenocrysts of quartz and sodic plagioclase. Several other small cones (post-USB) scattered throughout this area erupted mildly alkalic lavas containing the same xenocryst assemblage. The multiple domes of the rhyolite of No Agua (2750 m) are to the south of this road. **0.4**

77.5 Turn right at the T-junction and proceed to US-285. **1.0**

78.5 Junction with US-285 (Fig. 11). Turn left (south). **0.8**

79.3 Road begins to descend between roadcuts. **Immediately reduce speed and signal left turn** to alert overtaking traffic which typically travels at high speeds. Proceed **cautiously** before turning left. **0.2**

79.5 Turn left into unpaved turnout immediately past roadcut (2500 m).

STOP 15. Several lavas interbedded with clastic sediments containing fragments of No Agua rhyolite are exposed in these roadcuts. These stratigraphic relations demonstrate that the youngest Servilleta lavas postdate the eruption of the domes. Intraflow compositional variations have been studied in some detail at this locality by Crossey (1979). Dungan et al. (1986) and Dungan (1987) discussed these variations and concluded that they represent cryptic heterogeneities recording incomplete mixing of Servilleta basalt and dacite magmas. Rare orthopyroxene xenocrysts in lavas at this locality are the only mineralogical indicators of mixing; no macroscopic sign of magma mingling has been recognized. The variability among samples from this outcrop is nearly as great as the entire range of Servilleta compositions. Several other flows less comprehensively sampled by Crossey exhibit lesser variations, but a thick MSB flow of parental composition (LSKI; low in silica, potassium, and incompatible-trace-elements; Dungan et al., 1986) is homogeneous. Intraflow heterogeneities in some Servilleta flows, the nature of these variations, and their absence in parent-composition lavas strongly support the magma mixing model of Dungan et al. (1986) and Dungan (1987). **1.6**

81.1 No Agua perlite mine and mill (2500 m). **0.4**

81.5 Reduce speed, signal left turn, and carefully pull across northbound lane onto left shoulder to park.

STOP 16. Red Hill silicic alkalic basalt (IUGS—basaltic trachyandesite) flow front (sample RG-4, Table 3). This young lava, of probable early Pleistocene age, is typical of the non-xenocrystic, post-Servilleta mildly alkalic lavas that were erupted from monogenetic vents scattered about the Taos Plateau. This flow differs from typical Servilleta tholeiite in its higher SiO_2, alkalies, and enrichments in incompatible trace elements. The SAB suite cannot be derived by fractional crystallization from Servilleta magma. Kinsel (1986) concluded that each eruption of post-Servilleta alkalic magma (xenocrystic and non-xenocrystic) was a unique composition not relatable to any other of the broadly kindred compositions. This appears to have arisen from variable parent magmas which were variably fractionated and variably contaminated. Quartz and sodic-plagioclase xenocrysts are interpreted as undigested fragments of crust.

The No Agua rhyolite is a composite-dome complex comprising four obsidian flows of high-SiO_2 rhyolite. Extensively perlitized zones are currently being exploited commercially. The No Agua rhyolite is a highly fractionated composition showing extreme depletions of even moderately compatible elements such as Sr and Eu (Zielinski and Lipman, 1976) and a high $^{87}Sr/^{86}Sr$ (0.73597). The phenocryst assemblage consists almost entirely of sodic plagioclase ($An_{11}Ab_{83}Or_6$). Quartz is absent, suggesting a shallow level of equilibration. This rhyolite is not an appropriate endmember, mineralogically or in bulk composition, for Taos Plateau hybrid magmas. Dungan et al. (1986) suggested that it is thermally related to the focus of mafic magma injection along the western margin of the volcanic field, but that it was not part of the magmatic system in which the basalt–andesite–dacite spectrum evolved.

Pull cautiously onto US-285. Continue south to Tres Piedras. **6.2**

87.7 Tres Piedras (2475 m). Outcrops of Proterozoic granite on both sides of road. **0.7**

88.4 Turn left (east) onto US-64 at four-way junction. **0.7**

89.1 Park on right side of road at top of hill (2445 m) above the roadcuts west of bridge across upper Rio Petaca (Fig. 11).

STOP 17. Post-emplacement vesicular segregations. Outcrops of exceptionally coarse diktytaxitic Servilleta lavas typical of those which cap the cluster of three vents south and southeast of Cerro del Aire (sample RG-3, Table 1). Because of the unusually coarse groundmass grain size of these lavas, post-emplacement segregations are especially well developed. These segregations, and the complementary polygonal voids (generally <1 mm) throughout the diktytaxitic groundmass, form by migration of volatiles plus interstitial liquid through a rigid ophitic framework after partial solidification of the lava. The gas–liquid mixture rose diapirically to form pipes in the lower one-third to one-half of the flows. Some of these pipes terminate at their tops in the lowest and largest horizontal sheet. The horizontal sheets become thinner, more closely spaced, and less laterally extensive as the top of the flow is approached. This pattern is thought to be the result of inward migration of the solidification front. Servilleta lavas generally do not display well-developed columnar joints. The largest and lowest of the horizontal segregations is typically located where the entablature–collonade interface would normally occur. The presence of segregations may interfere with formation of well-formed joints.

Continue back to Taos on US-64. **26.9**

116.0 Junction of NM-522 and US-64.

Third day: Eastern Taos Plateau

Mileage

0.0 Begin at "blinking light" at junction of US-64, NM-522, NM-150 north of El Prado (Fig. 9). Travel northward on NM-522. Over the next 5 mi the road traverses the gorge arch. Note the flip in drainage asymmetry across the axis of the anticline. **5.5**

5.5 The road descends to the Arroyo Hondo Valley (Fig. 11). The Cerro Negro dacite shield (2360 m) can be seen to the northeast (partially buried by alluvial-fan deposits). **1.6**

7.1 Cross the Arroyo Hondo Bridge (2055 m). The road to the left immediately past the bridge eventually crosses the Rio Grande at Dunn Bridge (Stop 11). **2.7**

9.8 Begin reducing speed and signaling a left turn at 9.5 mi. Pull very cautiously across the highway onto the left shoulder at the crest of the hill and park.

STOP 18. Cerro Negro dacite (2225 m). The outcrop on the east side of the road exposes typical Taos Plateau two-pyroxene dacite (sample RG-17, Table 2). The dark, glassy groundmass and lack or low abundance of plagioclase phenocrysts are characteristic of these dacites. Coarse orthopyroxene phenocrysts contain resorbed olivine. **1.3**

11.1 San Cristobal Creek. North of San Cristobal, New Mexico, the road traverses (next 4 mi) a deeply dissected alluvial-fan complex. This fan overlies the MSB at the gorge, but for a distance of 4–5 mi is not capped by USB lavas on the east side of the Rio Grande. The USB is only one or two flows thick on the west side of the gorge, due in part to the shadowing effect of Timber Mountain and Cerro Montoso. Deep erosion of this fan was probably facilitated by an absence of capping Servilleta lavas. The anomalous thickness of this fan will be discussed at the next stop. **2.9**

14.0 Garapata Canyon (2250 m). **1.0**

15.0 Cebolla Mesa (2300 m). **1.6**

16.6 Cross the Red River fault. **0.3**

16.9 Turn left onto NM-515 (New Mexico State Fish Hatchery 2 mi). Descend to Red River with northwest-trending scarp of Red River fault paralleling road. After 1.5 mi note outcrops of southwest-dipping Red River andesite on the northeast side of the gully. The Red River andesite (east side of Red River fault zone) dips below the river level east of the Fish Hatchery Visitor Center. Dacite lavas of the Guadalupe center overlie Red River andesite to the north, but locally on the east side of the Red River fault the andesite section is capped by gravels containing clasts of Precambrian lithologies derived from the Sangre de Cristo Mountains. **1.9**

18.8 Entrance to Visitor Center (2160 m). Continue ahead to the left into the southern parking area adjacent to the footbridge across Red River. **0.15**

18.95 **STOP 19. Red River volcano** (Fig. 17). The purpose of this stop is twofold. The first is to discuss the stratigraphic and structural implications of the Red River edifice, the second is to review the gen-

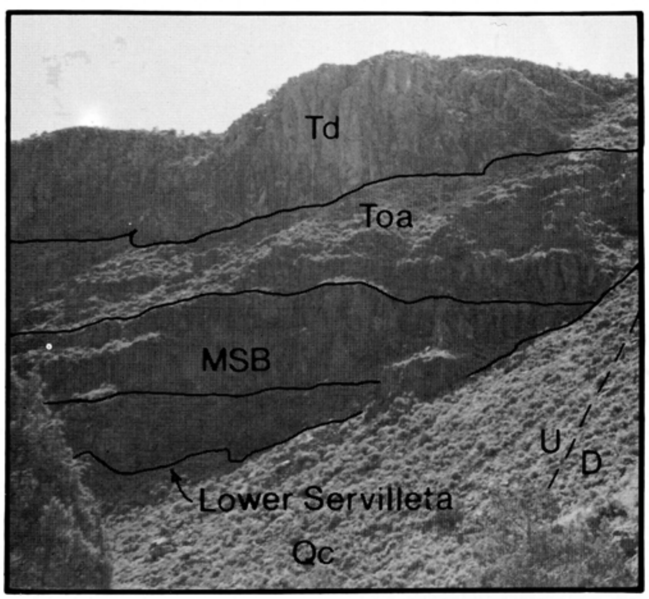

FIGURE 17—View from picnic area of part of the Red River volcano section (Stop 19). Thin flows of olivine andesite (Toa) overlie two thick middle Servilleta Basalt lavas, and underlie the thick dacite lava (Td).

esis of the Red River hybrid andesites described by McMillan and Dungan (1986).

The Red River andesite shield is a stratigraphically complex volcano comprising locally erupted intermediate-composition lavas interbedded with Servilleta lavas that flowed into the area from the west and northwest. The bulk of the section in the area of the New Mexico State Fish Hatchery interfingers extensively with MSB flows to the west and has at its base, just west of the Red River fault, two Servilleta flows. Directly west of the Red River volcano the LSB, MSB, and USB are thin and overlie a thick fluvial section which formed as the ancestral fan complex of the Red River drainage. This contrasts markedly with the stratigraphy exposed in the Rio Grande Gorge, about 8 km (5 mi) south of the present-day Red River, where the LSB and MSB are at or near river level (see fig. 5 of Dungan et al., 1984). At Garapata Canyon (southern edge of Cebolla Mesa) and LSB and MSB are overlain by the thick alluvial section noted previously. This post-MSB alluvial fan was deflected southward from the previous axis of deposition by the topographic obstruction of the Red River shield. Drill holes to the northeast of the Red River shield have penetrated a significant thickness of lacustrine sediments (Winograd, 1959, 1985; Menges, 1987). The presence of this paleolake basin supports the model of stream damming and subsequent fan deflection. Following emplacement of the USB, alluvial deposition buried the Red River volcanic pile and the current Red River Gorge was cut. These stratigraphic relations will be further clarified at Stops 22 and 23.

Cross the bridge and walk downstream on the trail to a cattleguard. Numerous large blocks of typical Red River olivine andesite lie next to the trail. Characteristic of the Red River lavas are coarse (2–3 mm) olivine phenocrysts (Fo_{82-79}). An excellent view of the hybrid-lava section is obtained from a picnic area 100 m downstream (Fig. 17). The hybrid-lava sequence lies above the thin reddish sedimentary interbed exposed on the west side of the fault-controlled gully (down-to-the-east normal fault). These sediments overlie dacite and Servilleta lavas correlative with the Lower Member. At the base of the hybrid section are two MSB flows. Similar to the LSB flows in the lower part of the section, these are presumed to have flowed into this area from the west, and are probably not directly related to the overlying hybrid andesites. Above these two basalt flows is a sequence of andesite flows which becomes increasingly silicic upsection (52–57% SiO_2, tables 1 and 2 of McMillan and Dungan, 1986). At the top of the andesite pile is one thick dacite flow that erupted from a vent located to the northwest of the Fish Hatchery. The andesite lavas most probably erupted from a vent east of the hatchery.

McMillan and Dungan (1986) demonstrated that the origin of Red River andesites may be closely approximated by two-component mixing, accompanied by minor olivine fractionation. The two endmembers were Servilleta basalt and the dacite which caps the hybrid-andesite section (sample RG-206, Table 2). No other Taos andesite or dacite is satisfactory as the silicic endmember for both major and trace elements. This occurrence establishes the efficacy of basalt–dacite mixing in the Taos magmatic system. McMillan and Dungan (1988) concluded that mixing of basaltic and more silicic magmas was an important process in the evolution of the typical andesites and dacites composing the other shields. However, these appear to be well-homogenized magmas in contrast to the highly variable Red River andesites. The explanation for the eruptive sequence of the Red River lavas (increasing SiO_2 with time) appears to be that mixing took place in a conduit immediately prior to eruption via the mechanism proposed by Koyaguchi (1985), Kouichi and Sunagawa (1982), and Blake and Campbell (1986): i.e., due to the lower viscosity of the mafic endmember, it initially rises more rapidly up the conduit, despite its greater density, leading to turbulent mixing at the interface between the two contrasting magmas. Thus, the early erupted Red River andesites are the most mafic, and successive lavas contain an increasingly large proportion of dacite (up to 60%). Isotopic compositions of the hybrids (Sr, Pb, and Nd) are not consistent with the involvement of only two homogeneous endmembers. This discrepancy may be resolved if one or both endmembers was/were isotopically heterogeneous, or if contamination occurred in the vent during ascent.

Return to NM-522. **20.5**

21.0 Junction of NM-515 and NM-522. Turn left (north) toward Questa. **1.5**

22.5 View back to the west-southwest: exhumed outcrops of the Red River volcano at the eastern end of the Red River Gorge, which previously were buried by post-MSB alluvium. **2.2**

24.7 Junction of NM-522 and NM-38 (to Red River, New Mexico). Continue straight. **2.7**

27.4 Junction of NM-522 and NM-378. Turn left onto NM-378 toward Cerro, New Mexico, and the Rio Grande Wild River Recreation Area. **3.6**

31.0 Bend in road and view of northern Taos Plateau, southeast San Juan Mountains, and San Luis Hills. Clockwise from 11:00 Cerro Chiflo (2707 m); 12:00 Cerro de la Olla (2885 m); 1:00 San Antonio (3326 m); high country in far distance is the Platoro–Summitville caldera complex, southeast San Juan volcanic field (up to 4025 m); 2:00 San Luis Hills (up to 2890 m); 3:00 Ute Mountain (3076 m); 4:00 Blanca Peak (4378 m). **2.0**

33.0 Turn right to picnic area. **0.1**

33.1 Turn right on first unpaved road. Drive through gate to overlook (2250 m). **0.1**

33.2 **STOP 20. Cerro Chiflo and gorge overlook.** The 10.4 Ma Cerro Chiflo quartz latite dome (IUGS—dacite) forms a nickpoint in the river gradient so that the northern Rio Grande Gorge is incised to a markedly lesser degree than it is to the south of Cerro Chiflo. Flows of Servilleta Basalt and dacite from the Guadalupe center have lapped against the flanks of the dome. The Cerro Chiflo quartz latite is unlike the younger silicic rocks of the Taos Plateau in that it contains abundant plagioclase phenocrysts plus biotite and hornblende phenocrysts.

In this regard, Cerro Chiflo closely resembles some early Miocene lavas of Timber and Brushy Mountain, and the Red Mountain dacites of the Raton–Clayton volcanic field.

Return to paved road. **0.2**

33.4 Turn right on paved road. **0.6**

34.0 Note the cliff of flow-banded quartz latite above the Rio Grande Gorge. **2.0**

36.0 Turnoff to right leading down to a parking area near the gorge rim. Park and walk to the edge of the gorge.

STOP 21. Red River fault zone and gorge stratigraphy. This overlook (2255 m) lies just north of the northwestern extension of the Red River fault zone. In this vicinity the fault zone is defined by several en-echelon splays which offset the youngest Servilleta lavas. Dacite lavas from the Guadalupe shield volcano occur interbedded with fluvial gravels between the MSB and USB (Fig. 18). These dacites postdate the Red River andesite lavas and further demonstrate the broad contemporaneity of Taos Plateau basaltic and intermediate-composition volcanism.

Return to paved road. **0.1**

36.1 Turn right. Road travels south and immediately crosses the fault scarp. **3.0**

39.1 Bear right to La Junta Point. **2.3**

41.4 Turnoff to La Junta Point Campground parking area. **0.3**

41.7 **STOP 22. La Junta Point overview** (2250 m). Park vehicles and walk through campground to La Junta Point overlook. Directly across the Rio Grande from La Junta Point are cliffs of the unnamed cerrito east of Montoso (UCEM) dacite lava overlying LSB and MSB lavas. USB flows in turn overlie the UCEM flow. The volcanic section at the mouth of the Red River is relatively thin and overlies a very thick section of gravels interpreted as the ancestral Red River alluvial fan. A few kilometers south of La Junta Point, the LSB and MSB lie at a much lower elevation (the LSB is near river level at San Cristobal Creek) separated from the USB by a thick section of post-MSB fluvial gravels. Note that the sedimentary unit between the MSB and USB at La Junta Point is less than 15 m thick. The higher elevation of the two lower basalt units may be due in part to flexure related to the Red River fault zone, but a major factor is pre-eruptive topography. As noted at Stop 19, the southern locus of deposition of post-MSB alluvial sedimentation is due to deflection by the Red River shield.

Return to vehicles and drive to main loop road. **0.3**

42.0 Turn right on loop road. **0.6**

42.6 **STOP 23. El Aguaje Campground and Red River Gorge overlook.** Turn right and drive to end of the loop, parking at campsite 25. Walk to the nearby viewpoint overlooking the Red River Canyon. From this vantage point a northwest-trending subsidiary fault with the same sense of movement as the Red River fault can be seen in the canyon to the southwest. At this locality the volcanic and sedimentary sections are both thicker on the downthrown side of the fault. In particular, the sedimentary unit between the MSB and USB is substantially thicker east of the fault. Lying directly beneath the USB on the downthrown side of the fault is a 2 m reworked silicic ash unit. These ash beds may have originated as pyroclastic deposits erupted from the No Agua rhyolite center. Alternatively, they may be distal ash correlative with pre-Bandelier tuffs erupted from the Valles caldera system. This ash is not present on the upthrown side of the fault, nor has it been recognized at any other locality on the Taos Plateau.

Return to the main loop road. **0.6**

43.2 Turn right on paved road. **0.8**

44.0 View to the east of panorama shown in Fig. 19. **1.4**

45.4 Turnoff to La Junta Point. Stay to the right and return to NM-552. **11.4**

56.8 Junction of NM-522 and NM-378. Turn left on NM-522 toward Costilla. **3.2**

60.0 Straight ahead in the distance are the Sangre de

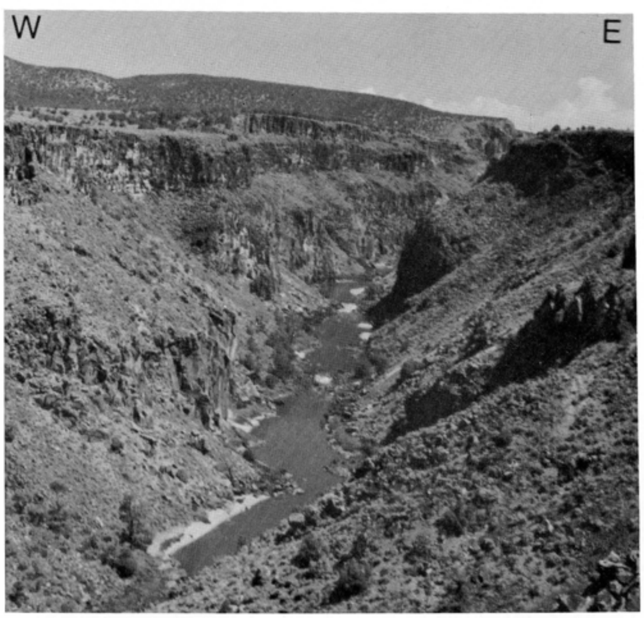

FIGURE 18—View from Stop 21 northward along Rio Grande Gorge toward Cerro Chiflo. The lower cliffs are in dacite lavas that flowed westward from Guadalupe Mountain. Cerro Chiflo quartz latite forms the ridge west of the gorge on the skyline.

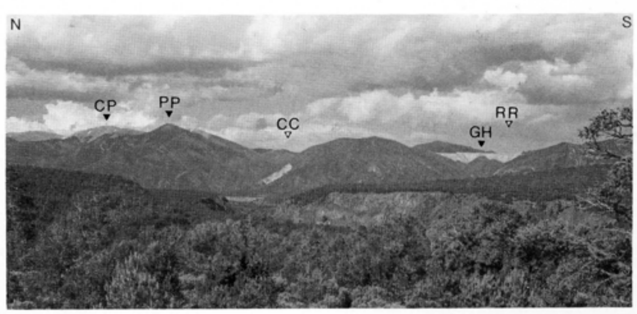

FIGURE 19—View eastward from road north of Stop 23 across Red River volcano to the Sangre de Cristo Mountains and Questa caldera. Major geographic features from north to south are: Cabresto Peak (CP), Pinabete Peak (PP), Cabresto Creek drainage (CC), Goat Hill (GH, low hill in front of mine tailings from Sulpher Gulch open-pit mine), Red River drainage south of Goat Hill (RR).

Cristo Mountains in Colorado with the 4378 m peak of Sierra Blanca at 12:30. At 11:30, the San Luis Hills can be seen as irregular mesas and low hills rising above the floor of the San Luis Valley. They are comprised of late Oligocene and Miocene volcanic and intrusive rocks exposed along a major intrarift horst (Day 4). **9.7**

69.7 **STOP 24.** Milepost 40 (Figs. 20, 21). Pull off to right on highway shoulder. Low scarp about 220 yards east is the Cedro Canyon fault (2350 m). The Cedro Canyon fault (Fig. 20) extends from a point 5 km south of Costilla, New Mexico, south and southwest about 7 km. The fault is named for Cedro Canyon, the source area for alluvial-fan deposits that are cut by the fault. The fault has undergone multiple episodes of movement with the most recent in the latest Pleistocene (10–25 Ka) (Machette and Personius, 1984).

View to the east (Fig. 20) is of the Tertiary volcanic sequence exposed along the west-facing front of the Sangre de Cristo Mountains just south of Cedro Canyon. Precambrian granite to the south is overlain by east-dipping volcanic and sedimentary rocks of the Latir volcanic field. In Cedro Canyon (1 mi to the north), the Amalia Tuff, which forms the crest of the range above the Cedro Canyon fault, is conformably overlain by tilted volcaniclastic sediments (lower Santa Fe Group) that were eroded from the Latir field. These sediments are unconformably overlain by weakly consolidated gravels containing Precambrian clasts (upper Santa Fe Group), which are in turn capped by Servilleta Basalt. **2.8**

72.5 Low mesa straight ahead is San Pedro Mesa (2600 m) capped by Servilleta Basalt (Stop 26). **1.3**

73.8 Enter Costilla (Fig. 21). Junction of NM-522 and NM-196 (2380 m). Turn right onto NM-196 and proceed toward Amalia. **1.5**

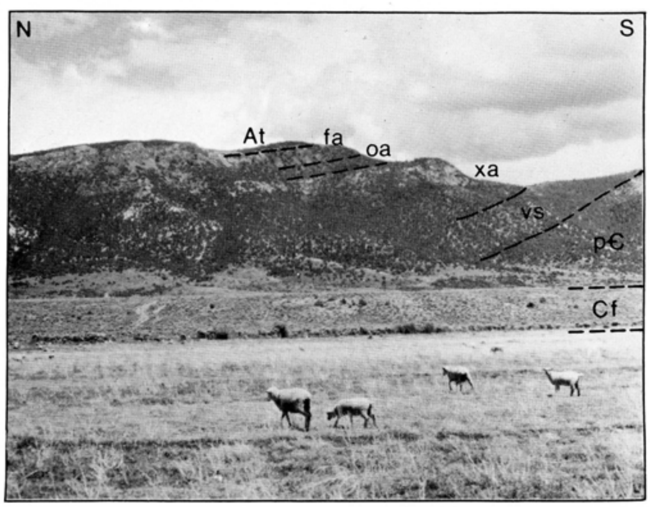

FIGURE 20—Tertiary volcanic sequence exposed on west-facing front of Sangre de Cristo Mountains, just south of Cedro Canyon. East-dipping volcanic rocks rest depositionally on Precambrian granite (p€); in ascending order, they are: tuffaceous and volcanic sedimentary rocks (vs), xenocrystic andesite flow (xa), olivine-bearing basaltic andesite (oa), alkalic andesite characterized by fissile jointing (fa), and Amalia Tuff (At). Alluvial fan in foreground has been beheaded at Pleistocene scarp of the Costilla fault (Cf).

75.3 The slopes of Costilla Valley are composed of landslide blocks of Santa Fe sediments and Servilleta Basalt. **2.7**

78.0 End of landslide area. Mesas capped by Servilleta Basalt are underlain by poorly exposed andesitic lavas and interlayered volcaniclastic sediments below the Amalia Tuff which is exposed at road level on the bend ahead. **0.4**

78.4 **STOP 25. Amalia Tuff** (2480 m). Pull as far to right on shoulder as possible and watch for traffic coming around bend in road. The Amalia Tuff at this locality is underlain by precaldera andesitic mudflows and overlain at the bend in the road by rhyolitic volcaniclastic sediments (Santa Fe Group). Much of the Amalia Tuff in this area has undergone severe potassium metasomatism resulting from low-temperature hydrothermal alteration. Despite its fresh appearance, some samples have doubled in K_2O content and are nearly devoid of Na_2O. The alteration is similar to that described by Chapin and Lindley (1986) in the Socorro, New Mexico, area and interpreted by them as being caused by alkaline-saline brines in an early rift basin.

Approximately 0.5 mi back down the road on the left is a dark outcrop of basanitic basalt dated at about 16 Ma (Lipman et al., 1986) within Santa Fe Group sediments. This is one of several mildly alkalic to alkalic basalt flows within post-Latir sediments. These flows serve as datable horizons which have been used to document Miocene rift development in this region.

Return to vehicles, turn around and proceed back to NM-522 via Costilla. **4.6**

83.0 Intersection of NM-522 and NM-196. Turn right on NM-522. **1.4**

84.4 **STOP 26. Servilleta Basalt on San Pedro Mesa and State Line shield.** Colorado–New Mexico border. Pull cars onto right shoulder of highway and be aware of high-speed traffic after exiting vehicles. The low mesa in the northeast foreground is San Pedro Mesa. Olivine basalts capping the mesa have yielded a whole-rock K–Ar age of 4.3 ± 0.8 Ma (Lipman et al., 1986). This is part of the same lava sequence that covers much of the Taos Plateau, although the vent locations for these flows are unknown. The numerous slump-blocks in the foreground repeat sequences of Santa Fe Group sediments and basalt along a major fault of the Sangre de Cristo fault zone (Machette and Personius, 1984).

The northernmost Servilleta shield volcano, informally referred to as State Line volcano, is located approximately 14.5 mi due east. This low shield is associated with a drastically thinned veneer of Servilleta Basalt in contrast to the section observed at Stop 8 (Rio Grande Gorge Bridge). The difference in elevation between Servilleta flows exposed near State Line shield and flows atop San Pedro Mesa is approximately 300–350 m. This corresponds to a minimum average uplift rate of 75–85 m/m.y. during the past 4 Ma for the southern end of San Pedro Mesa.

Return to Taos via NM-522.

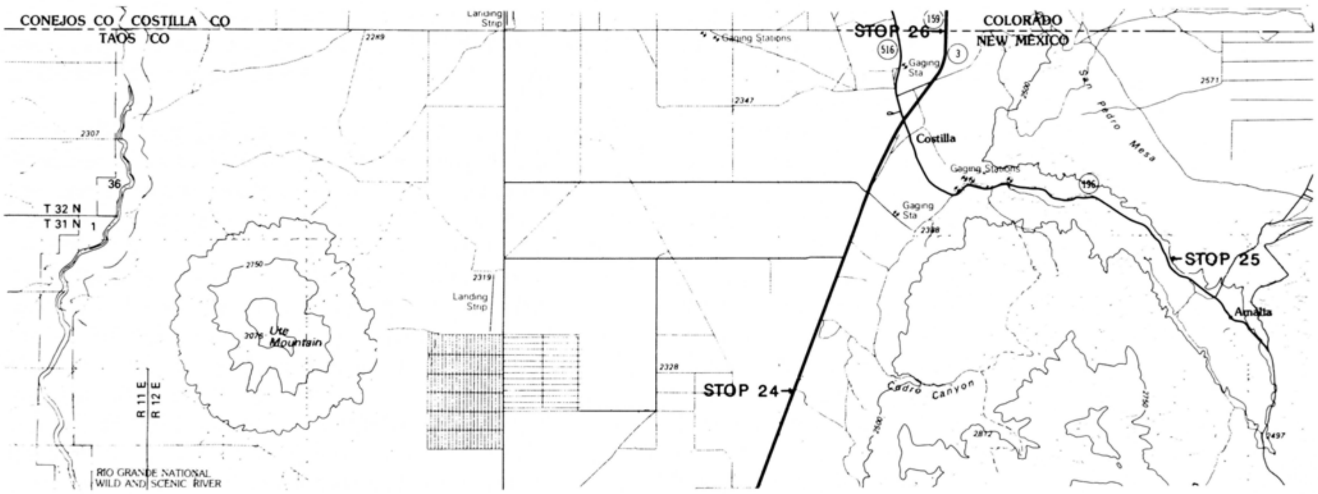

FIGURE 21—Location map for Stops 24 through 26. Note: NM-3 is now NM-522.

Fourth day: Questa, San Luis Hills, Los Mogotes volcano

Mileage

0.0 Begin at intersection of NM-38 and NM-522 in center of Questa—proceed north on NM-522. **0.3**

0.3 **STOP 27. Overview of Latir volcanic field and Questa caldera.** Turn right into Wildcat's Den parking lot (2300 m). The Latir volcanic field and associated Questa caldera have been studied extensively in recent years and it is well beyond the scope of this guidebook to provide a detailed overview of the work to this point. Much of our understanding of the area is a result of the diligent effort of P. W. Lipman and his colleagues at the U.S. Geological Survey. A brief summary of relevant studies includes: mapping of the entire volcanic field (Lipman, 1983; Lipman and Reed, in press); petrographic, petrologic, and isotopic studies (Johnson and Lipman, 1986, 1988; Johnson et al., 1986); paleomagnetism and geochronology (Hagstrum et al., 1982; Hagstrum and Lipman, 1986; Hagstrum and Johnson, 1986; Lipman et al., 1986); and geophysical studies (Cordell et al., 1986; Long, 1986). Additional field-trip material can be found in Lipman and Reed (1984).

The Latir volcanic field in the Sangre de Cristo Mountains is part of a once nearly continuous mid-Tertiary volcanic field of the Southern Rocky Mountains (Steven, 1975; Lipman, 1988). Erosional remnants of the Latir field (1200 km^2) have been truncated to the west by formation of the Rio Grande rift and extensive volcanic rocks are presumed to lie buried beneath and interlayered with post-Oligocene, basin-fill sediments. Fragmentary exposures of contemporaneous volcanic rocks occur at Timber Mountain (Stop 10) and Brushy Mountain (Stop 14) along an intrarift horst; and volcaniclastic sediments in the Tusas Mountains to the west are probably composed of debris shed from three sources; the San Juan Mountains, San Luis Hills, and the Latir volcanic field.

As a result of differential post-Miocene uplift in the region, rocks of the Latir volcanic sequence are exposed at valley floor levels near the town of Amalia to the north, whereas the pre-Tertiary surface projects into the sky south of the town of Questa. This northward tilt of the sequence and subsequent erosion to deeper levels in the south provides a unique cross section through the 26 Ma Questa caldera (Lipman et al., 1986) and cogenetic plutonic rocks. Erosional remnants of the Amalia Tuff, a weakly peralkaline rhyolite are preserved as far as 40 km beyond its source, the Questa caldera. Comagmatic 26 Ma batholithic granitic rocks, exposed over an area of 20 by 35 km, range from mesozonal granodiorite to epizonal porphyritic granite and aplite. Compositionally and texturally distinct granites define resurgent intrusions within the caldera and discontinuous ring dikes along its margins; a batholithic mass of granodiorite extends 20 km south of the caldera and locally grades vertically to granite below its flat-lying roof.

This stop offers a commanding view (Fig. 19) of the truncated south margin of the Questa caldera, dissected by two major east–west canyons—Red River to the south and Cabresto Creek farther north.

From south to north, the high mountain at 2:00 is Flag Mountain (3640 m), consisting of Precambrian quartz monzonite with inclusions of Precambrian felsic volcanic rocks 1 m to 800 m across. The north shoulder of Flag Mountain at 1:00 is occupied by a Tertiary granitic to aplitic intrusion, part of an east–west-trending alignment of ring intrusions along the south margin of the Questa caldera, which extends approximately 80 km up the Red River. The conspicuous roads zigzagging up the west face of this intrusion provide access to drill pads that were used in blocking out a large, low-grade molybdenum deposit near the crest of the north ridge of Flag Mountain. This deposit was not developed because better ore is found upstream to the east. The mine and mill have been closed since 1985.

Looking up Red River Canyon, the prominent hill with an encircling road near its top is Goat Hill.

Goat Hill consists mostly of volcanic rocks that are part of the caldera fill of the Questa caldera—mostly welded tuff and interlayered large megabreccia blocks of precaldera lava flows that slid in from the wall. At the crest of Goat Hill is an east-northeast-trending dike of altered, coarsely porphyritic rhyolite, which also represents part of the ring-intrusion complex along the south margin of the Questa caldera. In the distance up Red River Canyon, south of the caldera, is a shoulder of Gold Hill (3555 m) above treeline, consisting of Precambrian volcanic rocks, quartz monzonite, and gabbro.

At 11:00, the high timbered ridge, between Cabresto Creek to the north and Red River to the south, consists entirely of densely welded Amalia Tuff, rotated to nearly vertical with an aggregate thickness measured normal to its foliation of at least 1.9 km. This represents part of the caldera-filling welded tuff. Rotation of this block occurred late during caldera collapse, or during resurgent uplift of the caldera interior, as indicated by unrotated magnetic-pole positions of intracaldera granitic rocks that intrude the tilted welded tuff.

North of Cabresto Creek at 10:00, the high point is Pinabete Peak (3641 m) consisting of volcanic rocks of the caldera floor that have been uplifted in the resurgent core. The lower slopes are Precambrian rocks of the floor, and (difficult to see) on the north skyline are granitic rocks of the resurgent pluton within the core of the caldera.

Thus, from south to north we see a cross section through a caldera, including the caldera wall of Precambrian rock, thick welded tuff filling the moat, and the caldera floor rising up on the resurgent dome.

Turn right on NM-522 and drive north to Colorado. **27.9**

28.2 Intersection of CO-159 (NM-522) and CO-248. Turn left and proceed toward Mesita. For the next 9 km the road passes over middle Pleistocene alluvium (200–600 Ka) which progressively decreases in elevation westward until reaching the Rio Grande some 60 m below the level at the highway intersection. **4.5**

32.7 Village of Mesita (2330 m). Established in 1910 as part of an unsuccessful land development scheme by the San Luis Southern Railway, Mesita's principal product is cinder and aggregate from a quarry at Mesita cinder cone (Fig. 22). The quarry has been in operation since the early 1950's and continues to operate nearly full time. **1.4**

34.1 **STOP 28 (optional). Mesita cinder cone** (2375 m). Turn right on haul road and proceed to quarry office near top of cinder cone. Ask permission (preferably in Spanish) before entering quarry grounds. Be extremely careful! Heavy machinery and unstable footing can be hazardous.

The Mesita cinder cone (Fig. 22) is an example of the late Pliocene–early Pleistocene xenocrystic basaltic andesites that erupted during the waning stages of volcanism on the Taos Plateau (sample 24, Table 3). Unlike most of the xenocrystic basaltic andesite vents on the Taos Plateau, which occur as satellite cones on the flanks of larger volcanoes, the Mesita cone occurs as an isolated center. Its location may have been controlled in large part by the Mesita fault (Stop 29), a major north-trending, high-angle normal fault whose most recent movements postdate cone formation. According to Burroughs (1978), drilling in the area shows offset of the Servilleta Basalt by 15–30 m near the Mesita fault, implying movement prior to eruption of the Mesita lavas. Flank lavas surrounding the cone contain olivine phenocrysts and sparse xenocrysts of Oligocene and quartz, whereas flows exposed in quarry walls have abundant xenocrysts.

Return down haul road to the main road. Turn right. Note that cumulative mileages will need to be adjusted. **0.8**

34.9 **STOP 29. Mesita fault** (Fig. 23). Pull to right side of road as far as possible. At this locality the road crosses the 8 m Mesita fault scarp. This fault is a major down-to-the-west fault that records demonstrable movement in Pliocene(?) to upper Quaternary deposits and is the only exposed major fault in the vicinity of the San Luis Hills that has moved during the latest Quaternary (<25,000 yrs). The fault is marked by scarps ranging in height from less than 1.5 m on latest Pleistocene alluvium to scarps as high as 8 m as seen here. The fault cuts the western flank of Mesita cone and displaces local basalt flows 8–10 m. The decreasing offset recorded by progressively younger deposits along the fault demands a history of repeated movement on the fault. The morphology of scarps on the youngest faulted alluvium suggests that the fault was most recently active in the latest Pleistocene. The broad, undisturbed flood-plain deposits along Costilla Creek 8 km to the south, however, indicate no movement during the Holocene. **0.4**

35.3 Main road veers to left (keep left). Flank flows of Mesita cone on the right. **1.2**

36.5 Turn right, drive west toward Rio Grande. San Luis Hills rise in the distance on the west side of the river. **6.1**

42.6 Old State Line Bridge on the Rio Grande (2290 m). Servilleta Basalt (sample locality RG-25, Table 1) forms the west rim of the gorge, directly beneath bridge. At river level are the northernmost exposures of Sevilleta Basalt along the Rio Grande. These flows are representative of the attenuated northern limits of the upper Servilleta section (Servilleta Basalt is found at shallow levels in the subsurface for another 40 km northward). The source for this lava is a small shield volcano located 8.5 km to the south (difficult to see) near the Colorado–New Mexico state line.

The multicolored cliffs on the west side of South Piñon Hills, 3 km to the southwest, expose hydrothermally altered, upper Oligocene volcanic rocks of the Conejos Formation (see discussion of hydrothermal alteration, Stop 31). **2.6**

45.2 Intersection of county road with Rio Grande Breaks Road. Turn right and pull onto flat area on east flank of Kiowa Hill (2440 m).

STOP 30. Kiowa Hill, San Luis Hills overview. The San Luis Hills (Burroughs, 1972; Thompson and Machette, 1989) consist of a series of flat-topped mesas and irregular hills that trend north to

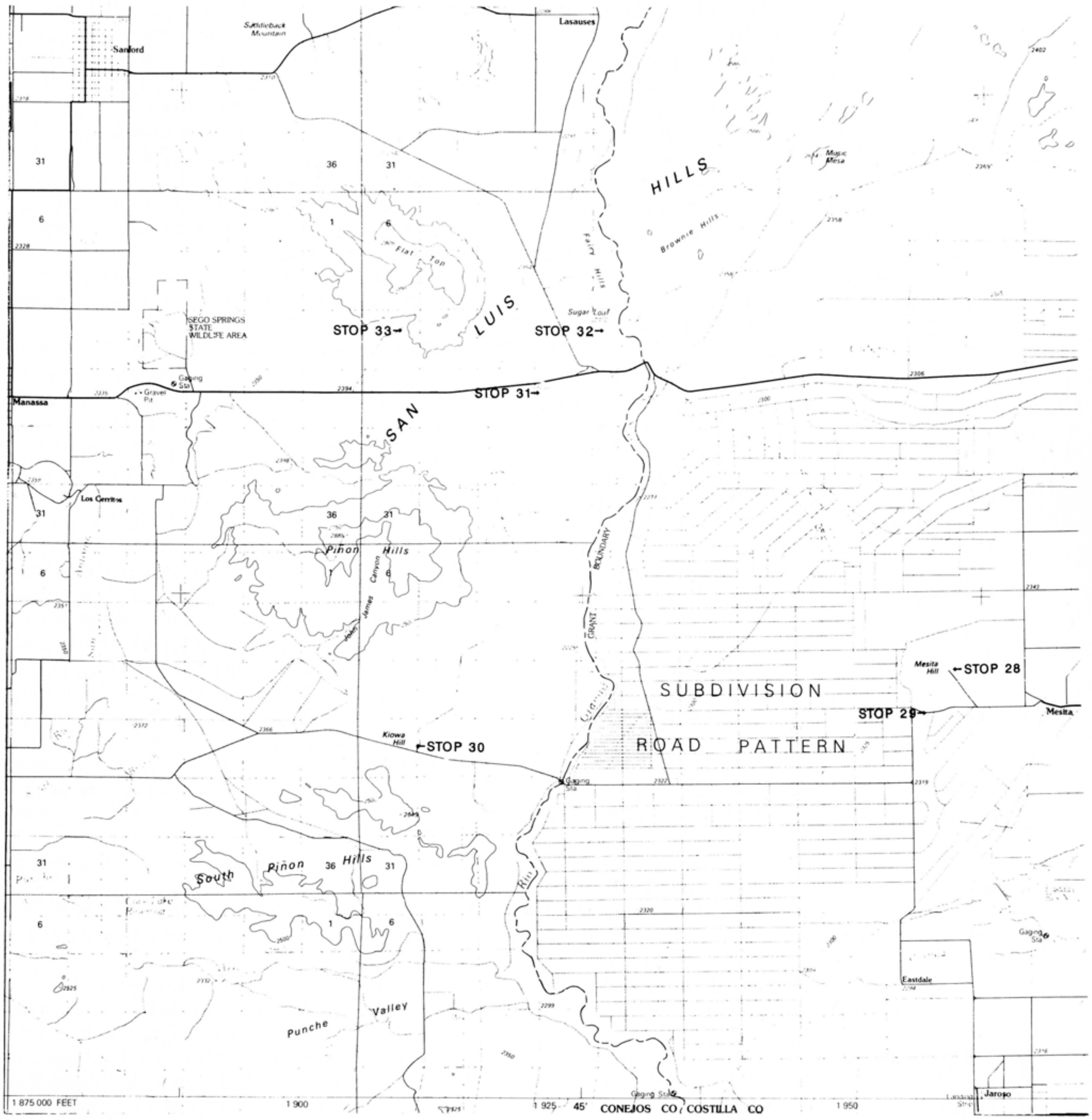

FIGURE 22—Location map for Stops 28 through 33.

northeasterly for approximately 45 km from the Colorado–New Mexico state line. They are the northernmost surface expression of a major intrarift horst within the San Luis Basin of the northern Rio Grande rift. For most of its length, the horst is confined to the subsurface (Kleinkopf et al., 1970); two additional surface exposures are at Brushy Mountain (Stop 14) and Timber Mountain (Stop 10). At all three localities exposures are formed entirely of middle Tertiary volcanic and intrusive rocks.

The oldest volcanic rocks exposed in the San Luis Hills are presumed to be correlative with the intermediate-composition Oligocene lavas and breccias of the Conejos Formation in the San Juan Mountains and Tusas Mountains to the west and southwest, respectively, despite an age 1 m.y. younger than reported for the 30 Ma uppermost Conejos Formation (Lipman et al., 1970). In addition, coeval intermediate-composition volcanic and volcaniclastic rocks in the Sangre de Cristo Mountains to the east and southeast (Lipman et al., 1986), although not specifically designated as Conejos Formation, are an extension of pre-rift volcanism believed to be part of a once nearly continuous volcanic field extending over much of the Southern Rocky Mountains in Oligocene time (Steven, 1975). These volcanic rocks were deposited on the post-Laramide erosional surface of the Uncompahgre arch. Basement rock is not exposed in the San Luis Hills, but

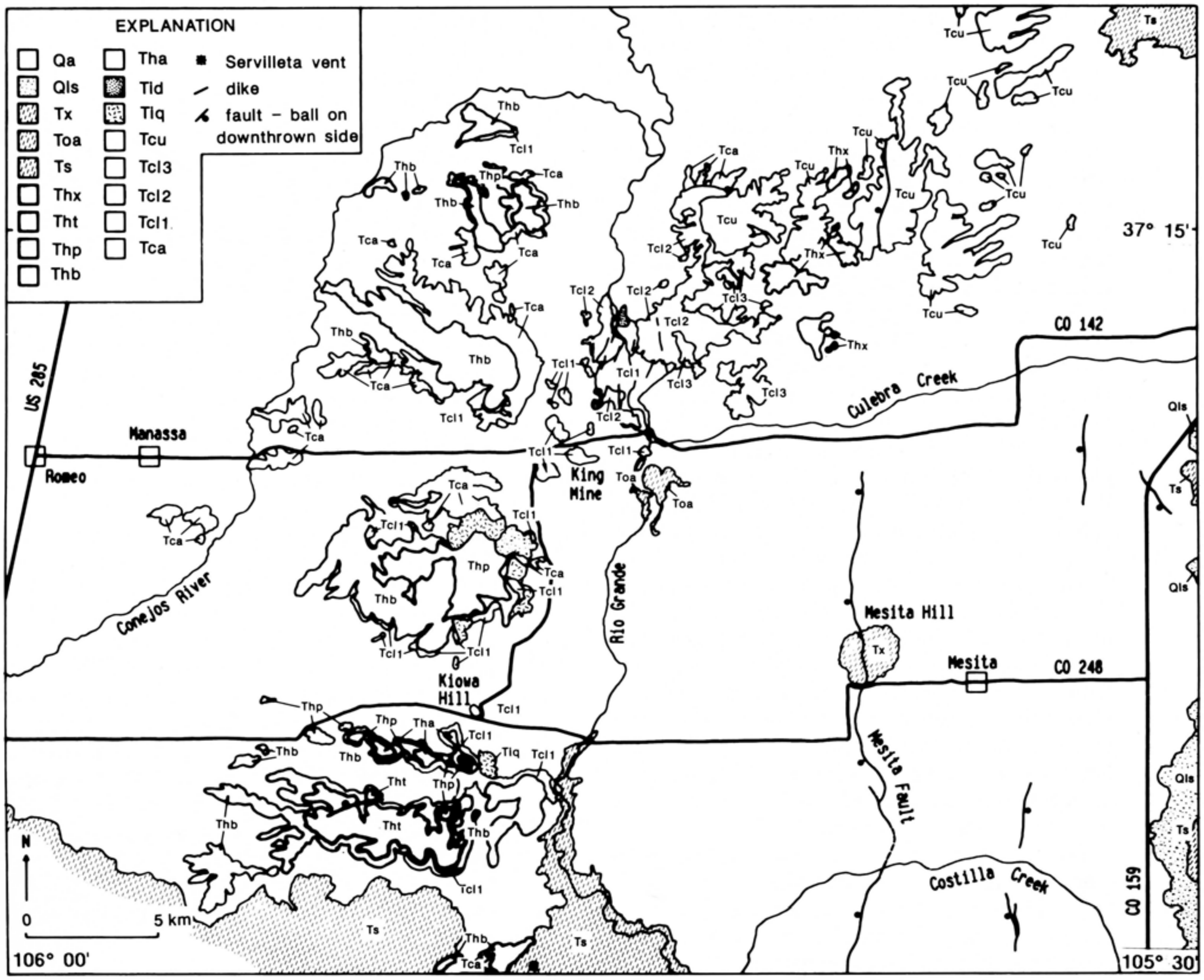

FIGURE 23—Generalized geologic map of the San Luis Hills region: Qa, Quaternary alluvium; Qls, Quaternary landslide deposits; Tx, xenocrystic basaltic andesite; Toa, olivine andesite; Ts, Servilleta Basalt. Hinsdale Formation: Thx, xenocrystic basaltic andesite; Tht, tholeiitic basalt; Thp, pyroxene trachybasalt; Thb, olivine trachybasalt to basaltic trachyandesite; Tha, trachyandesite. Intrusive rocks: Tid, porphyritic dacite stocks and dikes; Tiq, quartz monzonite stocks. Conejos Formation: Tcu, upper andesite; Tcl1, Tcl2, Tcl3, porphyritic dacite; Tca, pyroxene andesite.

Precambrian crystalline rocks have been found at a depth of 1675 m (Tweto, 1979) in a subsurface section of the horst 50 km north of the San Luis Hills. Precambrian crystalline basement is exposed in the southeastern San Juan Mountains (Lipman, 1975) and extensively in the Tusas Mountains to the southwest. To the east in the Sangre de Cristo Mountains, mid-Tertiary volcanic rocks are underlain by Precambrian crystalline rocks which have been elevated as much as 2 km above the San Luis Valley floor (Lipman et al., 1986).

Whereas intermediate-composition volcanism in the San Juan Mountains and the Sangre de Cristo Mountains was followed by major silicic ash-flow eruptions, no such history is recorded in the San Luis Hills. Andesitic to dacitic eruptions appear to have been followed closely in time by intrusions of subvolcanic, cogenetic plutons. Emplacement of quartz monzonite plutons and diorite stocks was accompanied by dike-swarm intrusions offset from the main quartz monzonitic intrusions 8 km to the northeast in the Fairy Hills. These shallow intrusions were accompanied by extensive hydrothermal hot-spring alteration, but little mineralization of economic value (Bartlett, 1984).

Subsequent uplift and erosion of the volcanic carapace unroofed the intrusive bodies and provided the irregular topography onto which basalts of the Hinsdale Formation were erupted. The 26 Ma age reported for three basaltic units (Thb, Thp, and Tht) corresponds to the oldest ages for basalts of the Hinsdale Formation in the San Juan Mountains (Lipman and Mehnert, 1975). Although basalts of the Hinsdale Formation in the San Juan Mountains are intimately associated with alkali rhyolites as a bimodal assemblage, no Hinsdale-age rhyolites are found in the San Luis Hills. Otherwise, the San Luis Hills assemblage of basaltic volcanics represents the largest and compositionally most diverse assemblage of basalts in the Hinsdale Formation. The general lack of Los Pinos-age (Oligocene) basin-fill sediments beneath or interbedded with basalts of the Hinsdale Formation suggests that the horst may have been a topographic feature as well as a structural high within the early Rio Grande rift during the late Oligocene.

After emplacement of the Hinsdale Formation and related aeolian units, the area was differentially uplifted to form the intrarift horst. Subsequent erosion and deposition in the surrounding southern San Luis Basin largely buried the older rocks. Deposition continued to fill the slowly aggrading basin, as evidenced by at least 150 m of intercalated basalts of the Servilleta Formation and sediments that are now exposed in the Taos gorge of the Rio Grande, 50–75 km south of the San Luis Hills. Faunal and floral evidence from the Alamosa Formation of Siebenthal (1910), exposed in Hansen Bluff (Rogers et al., 1985) along the east side of the Rio Grande just north of the San Luis Hills, suggests that the Rio Grande was still largely aggrading 700,000 yrs ago. The Alamosa Formation is considered by Chapin (1988) to be part of the Santa Fe Group.

The exposure of coarsely porphyritic dacite at Kiowa Hill is typical of Conejos-age dacitic rocks in the San Luis Hills. Phenocrysts of plagioclase, variably altered biotite, clinopyroxene, minor orthopyroxene, in places hornblende, and iron–titanium oxides are characteristic. Similar dacites form the lower slopes of the South Piñon Hills (due south) and are the host for extensive hydrothermal alteration at the east end of South Piñon Hills and farther north in the Fairy Hills area.

The prominent spire at 5:30 exposes the southernmost quartz monzonite intrusion in the San Luis Hills. These intrusions are stocks that consist of fine- to medium-grained, equigranular to slightly porphyritic, gray to light-tan quartz monzonite and contain K-feldspar, plagioclase, quartz, variably altered biotite, iron–titanium oxides, and minor clinopyroxene. The stocks tend to be steep-sided and occur along a north-trending belt in the south-central part of the San Luis Hills. Similarity in mineralogy and composition suggests that the stocks may merge at depth. Unconformably overlying the stocks and dacite flows of the Conejos Formation is a thick andesite flow of the Hinsdale Formation which forms the upper half of the mesa. This unit is unique in the San Luis Hills as it contains the only hydrous mineralogy observed in Hinsdale lavas. Hornblende phenocrysts are found near the base of the flow, whereas clinopyroxene is the dominant mafic phenocryst elsewhere in the flow.

The view to the north (11:00) provides an excellent opportunity to observe the unconformity between Conejos-age plutons and overlying basalts of the Hinsdale Formation. To the left of the stock is a large slump block composed of basalts, interlayered sediments (largely aeolian) and underlying dacitic mudflows. The drive north will circumvent the east side of Piñon Hills.

Proceed north on Rio Grande Breaks Rd. **7.3**

52.5 Intersection of Rio Grande Breaks Rd. and CO-142. Turn right and watch for dirt road exiting to the right. **0.6**

53.1 Turn right onto King Turquois mine access road. Proceed to gate at mine entrance. Do not enter this property without prior permission from Bill King of Manassa, Colorado. **0.15**

53.25 **STOP 31. King Turquois mine; hydrothermal alteration of Conejos Formation.** This area, which is encompassed by an elongate belt (4 km long by 2 km wide) centered approximately 1 km due north of the King mine, has been the site of extensive hydrothermal activity related to intrusion of quartz monzonite stocks and dacitic porphyry dike swarms to the north (Stop 32). This region is characterized by propylitic, argillic, and advanced argillic alteration, and silicification of varying degrees. The advanced argillic hydrothermal alteration has been of exploration interest for many years because of its similarity to major epithermal gold deposits at Summitville, Colorado.

Conejos andesites and dacites are host to the alteration and vary greatly in degree of modification. Intense hydrothermal activity centered near the low hills northwest and northeast of the King mine produced coarse-grained alunite, high-temperature kaolinite-group clays, hydrothermal breccia and pebble dikes, and is considered to be the thermal center for hot-spring activity. In contrast, the King mine area has experienced primarily supergene alteration responsible for turquoise formation. Hypogene alteration exposed below the supergene zone indicates that well-developed advanced argillization was never present. One- to two-meter wide replacement veins of quartz alunite enveloped by an argillic zone are characteristic near the small stock northeast of the King mine. Propylitic alteration surrounds the veins and extends a short distance into surrounding, poorly exposed country rock.

Return to CO-142. **0.15**

53.4 Turn right onto CO-142. **0.8**

54.2 Turn left onto gravel road. **0.2**

54.4 Veer to the left. **0.8**

55.2 Turn right onto rough dirt road. **0.1**

55.3 Road splits, keep to left. Drive to the end of the road. **0.5**

55.8 **STOP 32. Sugarloaf overlook** (2402 m). The overlook at this locality provides an opportunity to examine at a distance most of the volcanic sequence exposed in the San Luis Hills. The view to the north and east is of the Oligocene Conejos Formation comprising mafic to intermediate-composition vent facies rocks, consisting of lava flows, flow breccias, explosion breccias, and mudflow breccias. The formation is divided into upper and lower sequences based on variation in petrologic type, stratigraphic position and morphologic variation. In the proximal areas surrounding the overlook are andesitic breccias and lava flows at river level which grade upward into hornblende- and biotite-bearing lava flows similar to those at Timber Mountain and Brushy Mountain. These are overlain by moderately to coarsely porphyritic dacite lava flows and domes that contain plagioclase, variably altered biotite, clinopyroxene, minor orthopyroxene, in places hornblende, and iron–titanium-oxide phenocrysts. The massive dacite flow that forms the prominent spire (Sugar Loaf) in the foreground is correlative with the thick dacite flows seen to the northeast on the west side of the Rio Grande. Mesas to the far northeast, on the horizon, are capped by Conejos andesite flows similar in composition to those flows that form the base of Flat Top due west of this locality.

Return to CO-142. **1.6**

57.4 Intersection of gravel road and CO-142. Turn right on CO-142. **3.8**

61.2 Turn right onto dirt road. Drive toward Flat Top. **1.4**

62.6 **STOP 33. Flat Top Mesa** (2800 m); **Conejos and Hinsdale Formations.** Park vehicle (2500 m) in saddle and prepare for a long hike. The lower valley slopes to the northwest consist of calc-alkaline andesite (55% SiO_2, 3% MgO) breccias and lava flows similar to those observed at Brushy Mountain (Stop 14). Directly to the west andesites are overlain by local, thick dacite lava flows but elsewhere form the lower slopes of the entire Flat Top mesa. The andesites typically are moderately to sparsely porphyritic, containing plagioclase, olivine, and clinopyroxene phenocrysts. The thick northeast-trending dacite dike in the foreground (ca 3 m) has yielded a $^{40}Ar/^{39}Ar$ age of 27 Ma on a biotite separate from a well-developed glassy chill zone on its margin.

The above date calls into question the correlation of the San Luis Hills intermediate-composition volcanic rocks with the Conejos Formation rocks of the southeastern San Juan Mountains, which by definition, precede eruptions of multiple ash-flow sheets of the Treasure Mountain Tuff and collapse of the Platoro caldera (Lipman, 1975). Recent $^{40}Ar/^{39}Ar$ dating of the Treasure Mountain Tuff (Balsley, written comm. 1988) suggests an age of 29.5–28.4 Ma. If these preliminary findings are substantiated by additional data, they would provide an explanation for the absence of Treasure Mountain Tuff exposures in the San Luis Hills and suggest that it may be present in the subsurface beneath postcaldera lavas currently correlated with the precaldera Conejos Formation.

The older suite of volcanic rocks in the Flat Top Mesa was deeply incised prior to eruption of the Hinsdale basalts as evidenced by the lowest Hinsdale flow near the base of the west side of the valley. Midway up the slope to the east are remnants of locally derived Los Pinos Formation, volcaniclastic detritus below the Hinsdale Formation. Hinsdale flows to the northwest dip more steeply near the base of the valley but become nearly horizontal near the top of the mesa as the paleovalley was infilled by basaltic lava. The foot traverse will follow a northeasterly path cutting obliquely to the contact between the Hinsdale Formation and the underlying andesites, thence to a deeply eroded basalt vent superimposed on an older Conejos andesite vent.

Mafic volcanic rocks of the Hinsdale Formation in the San Luis Hills area are compositionally more diverse, and volumetrically more extensive than their temporal equivalents found in the southeastern San Juan Mountains to the northwest or the Tusas Mountains to the southwest. Compositions range from 49% to 60% SiO_2 (Fig. 24), and include tholeiitic basalts (sample T84089, Table 5) as well as a more alkalic series consisting of trachybasalt (sample T84098, Table 5), basaltic trachyandesite (T84163, Table 5), and trachyandesite (sample T84119, Table 5).

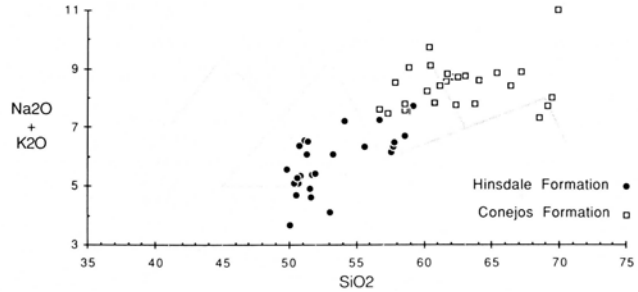

FIGURE 24—Total alkalies vs. silica plot for Hinsdale Formation and Conejos Formation volcanic rocks of the San Luis Hills region. Analyses were recalculated on a volatile-free basis. Irregular grid lines correspond to the classification scheme of Le Bas et al. (1986).

Recent whole-rock K–Ar age determinations yield ages of 26 Ma on four samples representing the compositional and stratigraphic extent of Hinsdale volcanic rocks in the area, suggesting nearly contemporaneous eruption of all members within the suite. Trachybasalts to basaltic trachyandesites are the dominant early-rift compositions in the San Luis Hills and in the centers mentioned on the western rift flanks. Diktytaxitic olivine tholeiites are restricted to the South Piñon Hills (Fig. 23) where they form the top of the section. Xenocrystic trachyandesites containing abundant quartz and plagioclase xenocrysts are found in local monogenetic centers east of the Rio Grande (Fig. 23). These erosional remnants of isolated volcanic centers are probably the youngest of the mafic extrusives although their stratigraphic relationship to the other mafic extrusives is unconstrained. The compositional spectrum for early-rift volcanism is analogous to that during major Plio-Pleistocene eruptions in the Taos Plateau volcanic field with the notable exception of the absence of two-pyroxene trachydacites. Diktytaxitic tholeiites are volumetrically subordinate relative to the more alkalic series, in sharp contrast to Plio-Pleistocene activity.

Early-rift tholeiites are compositionally within the range observed for Servilleta tholeiites (see sample T84089, Table 5 and Servilleta basalts, Table 1) for both major and trace elements (Fig. 24), although the more primitive compositions observed in the Servilleta basalts are not represented in the Hinsdale Formation. Trace-element patterns on extended chondrite-normalized diagrams (spidergrams) (Fig. 25) tend to show higher LREE enrichment trends than observed for most of the Servilleta tholeiites. Relative to the tholeiites, the more alkaline series exhibits stronger LREE enrichment with La/Sm ratios that increase in the trachybasalt–basaltic trachyandesite suite; xenocrystic trachyandesites exhibit the highest enrichments. Spidergram patterns are similar in shape within the series, exhibiting characteristic Nb depletions. Prominent troughs at Sr and Ti, especially for the xenocrystic trachyandes-

TABLE 5—San Luis Hills volcanic rocks.

	Conejos Formation				Hinsdale Formation			
No.	1.	2.	3.	4.	5.	6.	7.	8.
Sample	T84113	T84004	T84001	T84030	T84089	T84098	T84163	T84119
Map Seq.	Tca	Tcd	Tdbh	Tiq	Tht	Thb	Thp	Thx
SiO_2	56.90	62.70	65.40	64.40	50.00	49.30	50.80	58.70
TiO_2	1.06	0.66	0.61	0.63	1.59	1.55	1.52	1.19
Al_2O_3	16.10	15.10	15.30	15.60	14.90	13.70	17.60	16.50
FeO*	6.94	4.43	3.61	3.86	11.69	9.44	8.73	6.36
MnO	0.11	0.07	0.03	0.06	0.17	0.14	0.16	0.12
MgO	3.73	2.40	1.61	1.59	6.87	8.11	4.09	2.60
CaO	5.79	4.55	2.87	2.88	9.38	8.56	8.27	4.91
Na_2O	3.60	3.89	3.98	3.90	2.99	2.99	3.96	4.44
K_2O	3.82	3.77	4.33	4.84	0.69	1.97	2.56	3.23
P_2O_5	0.46	0.29	0.35	0.27	0.25	0.51	0.73	0.45
LOI	0.78	1.67	0.62	0.63	0.31	2.01	0.51	0.51
Total	99.29	99.53	98.71	98.66	98.84	98.28	98.93	99.01
Trace elements (ppm)								
Rb	76	83	98	178	23.5	48	46	46.5
Sr	862	754	734	608	367.5	685.5	1086	687
Y	15	13	13	25	18	20.5	20	24
Zr	262	176	160	359	127	166	206	320
Nb	11	7	10	18	11	20.5	25	29.5
Th	12.3	11.8	14.6	32.3	1.4	3.5	9.2	8.6
Hf	7.05	5.62	5.3	10.9	2.93	4.08	4.7	6.8
La	51.9	45.3	46.8	66.5	13.5	32.7	58	72.6
Ce	108	84.7	91	137	30.9	71.3	113	125
Sm	8.7	6.42	5.9	8.3	4.35	6.98	8.92	8.22
Eu	1.94	1.46	1.46	1.55	1.41	1.93	2.46	2.15
Tb	1.3	1	0.52	0.6	0.58	0.8	1.17	1.12
Yb	2.99	2.01	1.38	2.26	1.87	1.79	2.46	2.56
Lu	0.37	0.31	0.19	0.36	0.27	0.28	0.37	0.39
Ta	0.78	0.7	0.85	1.4	0.51	1.46	1.5	1.68

*Total Fe reported as FeO.
1. Andesite.
2. Dacite.
3. Dacite dike.
4. Quartz monzonite stock.
5. Diktytaxitic tholeiite.
6. Trachybasalt.
7. Basaltic trachyandesite.
8. Xenocrystic trachyandesite.

ites can be attributed to plagioclase and Fe–Ti-oxide fractionation. Fractionation alone or fractionation plus assimilation models are inconsistent with the major- and trace-element variations in the Hinsdale suite. Petrogenetic models are necessarily complex and probably involve polybaric fractionation coupled with selective crust/magma interaction at different levels.

Return to CO-142. **1.5**

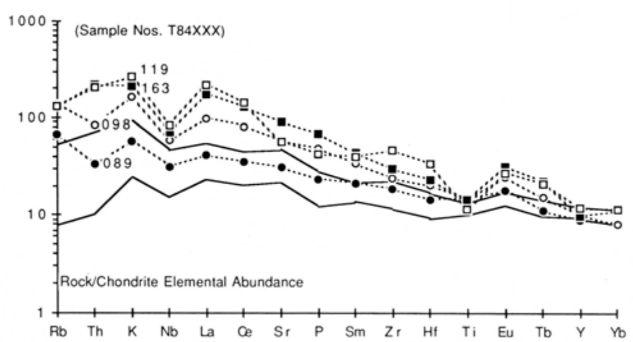

FIGURE 25—Chondrite-normalized, trace-element abundance diagrams (after Thompson, 1982) for representative samples of Hinsdale volcanic rocks of the San Luis Hills area. Key to samples: T84089, diktytaxitic tholeiite of South Piñon Hills; T84098, trachybasalt of Flat Top Mesa; T84163, basaltic trachyandesite of Piñon Hills; T84119, xenocrystic trachyandesite of Music Mesa. Solid black lines are maximum and minimum values for Servilleta Basalt.

64.1 Intersection with CO-142. Turn right and proceed west toward San Juan Mountains. **9.2**

73.3 Intersection of CO-142 and US-285. Turn left and proceed through town of Antonito. **7.6**

80.9 Intersection of US-285 and CO-17. Keep to the right. **10.8**

91.7 **STOP 34. Overview of southeast San Juan volcanic field stratigraphy.** Pull over as far as possible on the right shoulder of the highway an watch for high-speed traffic. Lava flows of the 5 Ma Los Mogotes volcano (2993 m) form a broad composite shield (250 km^2) overlying Los Pinos Formation. These lavas were erupted from the main, southern vent complex which lies north of this stop, and two subsidiary vents farther north (Flat Top and Cinder Pits). These flows have dips which are essentially identical to those of the underlying Oligocene ash-flow tuffs visible to the west. The flows on the west flank of Los Mogotes are offset by high-angle faults, several of which can be seen from this stop. Los Mogotes volcano is the youngest source of basalts in the Hinsdale Formation: an assemblage of extension-related mafic lavas and minor, associated high-SiO_2 rhyolites (26–5 Ma) which overlie the Oligocene ash-flow tuffs and lavas of the southeast San Juan volcanic field (Lipman, 1975; Lipman and Mehnert, 1975).

Lipman and Mehnert (1975) and Lipman et al. (1978) analyzed a suite of trachybasalts and basaltic trachyandesite from a thick section of Los Mogotes lavas 1 km east of this stop. Bowers et al. (written comm. 1986) have restudied these flows and others from the two northern vents. These additional data have shown that: tholeiitic basalts very closely resembling Servilleta Basalt are also present in minor amounts (erupted from the northern vents); the Los Mogotes lavas have highly variable isotopic compositions (Pb, Sr, and Nd); and these variations do not follow the same patterns as the Taos Plateau lavas (Dungan et al., 1986) or the volcanic rocks of the Oligocene southeast San Juan volcanic field. Unlike these other occurrences, which exhibit a strong imprint of crustal assimilation, the source of isotopic variations at Los Mogotes is far less clear and could be a complex combination of mantle heterogeneity and crustal contamination that must involve at least three endmembers. **1.5**

93.2 Intersection of CO-17 and Fox Creek Rd. (2585 m). Turn right. **0.3**

93.5 Intersection of Fox Creek Rd. and Big Meadows Rd. Stay left on main road. **2.4**

95.9 Masonic Park Tuff crops out in roadcut. **2.9**

98.8 **STOP 35. Northern Rio Grande rift overlook** (2750 m). This vantage point provides a vista across the structurally complex San Luis Valley. The Los Mogotes shield in the foreground dips 10° east into the basin. The San Luis Hills horst rises from a Pleistocene alluvial plain in mid-valley, and the steep mountain front of the northern Sangre de Cristo Range bounds the eastern margin. To the west a broad, east-dipping plateau surface (Almenditas Mesa) is capped by an ash-flow-tuff sequence comprising the composite Treasure Mountain Tuff (29.5–28.4 Ma: Platoro and Summitville calderas), the 28.4 Ma Masonic Park Tuff (Mount Hope caldera), overlying Hinsdale basaltic lavas and interbedded sediments of the Los Pinos Formation. The tuffs are underlain by a thick stack of intermediate lavas and breccias (plus fluvially reworked clastic interbeds) of the Conejos Formation, and are locally interbedded with andesite lavas erupted between caldera-collapse events.

Following eruption of the Treasure Mountain and Masonic Park Tuffs, and the broadly contemporaneous eruption of six voluminous tuffs from the western San Juan calderas, silicic volcanism in the San Juan volcanic field became focused on the central complex calderas near Creede, Colorado, at 27.8 Ma (Fish Canyon Tuff; Lanphere, 1988). Ash-flow tuffs and related lavas were erupted from these centers until about 26 Ma, overlapping in time with the Questa caldera and the initiation of extensional tectonics. The two most voluminous of the central San Juan ash-flow sheets, the Fish Canyon and Carpenter Ridge tuffs, are locally interbedded with Los Pinos Formation clastic sediments in the southeast San Juan area. In the southeast San Juan volcanic field, silicic magmatism shifted gradually from an association of dacite and low-SiO_2 rhyolite (quartz-free) to the bimodal association of basalt plus minor high-SiO_2 rhyolite of the Hinsdale Formation during 26–23 Ma. Extensive mineralization (Cu–Au–Ag), localized at the intersections of northwest-trending regional faults and caldera ring structures, occurred during the transition to crustal extension (Lipman, 1975); molybdenum mineralization at Questa also occurred during this interval (Lipman et al., 1988).

Return to Taos.

Introduction to Part II

Lipman and Mehnert (1975) recognized that post-Miocene volcanic rocks erupted on the flanks of the northern Rio Grande rift were in general more alkalic than those confined to the rift axis. It was noted that flank basalts are more diverse and include moderately to highly undersaturated compositions which are rare or absent in Plio-Pleistocene volcanic fields within the axis of the rift. This observation has served as a catalyst and a framework for subsequent investigation in the northern rift. Lipman and Mehnert (1975) interpreted the rift axis-to-flank compositional progression in terms of a model of asthenospheric upwelling in which the dominantly tholeiitic basalts of the rift axis (e.g., Servilleta Basalt) were generated at shallower depths than undersaturated magmas on the flanks.

As the result of our separate and joint investigations of various manifestations of volcanism in the rift, we have collected a substantial amount of new data and have come to recognize that there are also important similarities among the Taos Plateau, Ocate, and Raton–Clayton volcanic fields that are not initially apparent from comparisons based on previously published papers (Dungan et al., 1981). These affinities have been obscured by the establishment of local rock names based on diverse criteria, which as a whole do not reflect these similarities. When analogous rocks across this axis-to-flank petrologic traverse are compared, the trends noted by Lipman and Mehnert (1975) become even more impressive because there are systematic shifts in major- and trace-element chemistry among these fundamentally similar rocks that parallel the overall progression toward a more alkalic association on the rift flank.

There is a complex temporal progression in the eruptive histories of these magma types that is generally similar in all three volcanic fields (Table 6). Although there is temporal overlap among contrasting lithologies, basaltic rocks were more alkalic between 6–4.5 Ma and after 2 Ma than they were during the middle interval (4.5–2 Ma) when the Servilleta Basalt and its eastern analogues were erupted. Another observation arising from a comparison of the age data is that volcanism terminated at progressively later times with distance from the rift axis (Taos Plateau 1.8 Ma; Ocate 0.8 Ma; Raton–Clayton <10 Ka). Scattered monogenetic cones in the Tusas Mountains (eastern flank of the San Luis Basin) erupted Capulin-type lavas at about 0.25 Ma, and there are similarly young occurrences along the southwestern Jemez lineament.

Rock nomenclature, compositional comparisons, and temporal evolution

In the sections that follow, we present a nomenclature scheme for the three volcanic fields that standardizes rock names under the IUGS classification system (Le Bas et al., 1986). We have used (or modified) existing local terminology to define six magma types (Table 6). This hybrid approach establishes a link to the existing literature, emphasizes the fact that all six types have readily recognizable field

TABLE 6—Correlation of volcanic-rock type, style, and classification for the Taos Plateau, Ocate, and Raton–Clayton volcanic fields.

	Type / Style	TAOS PLATEAU	OCATE V.F.	RATON-CLAYTON V.F.
		IUGS Chemical Classification / *Normative* and Modal Characteristics		
LATE	**Capulin**	Trachybasalt to Basaltic Trachyandesite	Trachybasalt to Basaltic Trachyandesite	Trachybasalt to Basaltic Trachyandesite
	Monogenetic Cones	Xenocrystic and non-xenocrystic	Xenocrystic and non-xenocrystic	Xenocrystic and non-xenocrystic
	Mafic Feldspathoidal			Basanite to Nephelinite
	Monogenetic Cones			*ne = 5-20%* nepheline & hauyne
MIDDLE	**Diktytaxitic Basalt**	Subalkaline Basalt	Basalt	Basalt
	Flood Lavas	Low-K Olivine Tholeiite *ne = 0, hy <20%*	Transitional basalt *ne <2% to hy <1%*	Transitional basalt *ne <2% to hy <5%*
	Olivine Andesite & Pyroxene Dacite	Basaltic Trachyandesite to Trachydacite	Basaltic Trachyandesite to Trachyandesite	Trachyandesite
	Shield Volcanoes	Olivine (<60% SiO2) or 2-Pyroxenes (>61% SiO2)	Olivine; 2-px microphen. (all <57%SiO2)	2-Pyroxenes; trace ol. (all ~ 60%SiO2)
EARLY	**Alkali Olivine Basalt**		Alkaline Basalt	Alkaline Basalt
	Monogenetic Cones		*ne= <5%*	*ne= 1-7%*
	Porphyritic Dacite	Dacite		Dacite
	Lava Domes	Plag+Hbl+Bi+Px (Cerro Chiflo)		Plag+Hbl (±Bi) (Red Mt. Dacite)

characteristics, and calls attention to similarities among rocks of the same type that were erupted in the different fields. We have summarized salient points from the existing literature and added brief discussions of major- and incompatible-trace-element data which are displayed in Figs. 26 and 27. This data set is included largely for comparative purposes. In each of the normalized plots we have included the maximum and minimum values for samples of the Servilleta Basalt as a reference. In general, the data plotted on these diagrams were selected to represent the range for a given magma type. We comment on only a few of the issues raised by these data and make no attempt to resolve all relevant petrologic problems in this publication.

Porphyritic dacite—Porphyritic dacites in the Taos Plateau (10.7 Ma: Lipman and Mehnert, 1979) and Raton–Clayton (8.2–6.4 Ma: Stormer, 1972a; Staatz, 1986; Scott et al., in press; Scott and Pillmore, in press) volcanic fields are the earliest dated manifestations of Mio-Pleistocene volcanism in the northeast Jemez zone. Hybrid porphyritic dacites of the type seen at Cerro Pelon in the Ocate volcanism field (Stop 36, abundant mafic magmatic inclusions plus quartz xenocrysts and rhyolitic melt inherited from the silicic endmember) are distinct in age (younger) and petrology from the Cerro Chiflo silicic dacitic dome (67% SiO_2; quartz latite of Lipman and Mehnert, 1979) of the Taos Plateau and the numerous dacitic domes of Raton–Clayton (64–69% SiO_2) that have been grouped as the Red Mountain dacites (Collins, 1949; Baldwin and Muehlberger, 1959; Stormer, 1972a, b). The distinctive features of these lavas are their eruptive style (domes) and ubiquitous hydrous phenocrysts (hornblende in Red Mountain Dacite, hornblende and biotite in Cerro Chiflo), neither of which is characteristic of the younger olivine andesite–pyroxene dacite magma type. In general character these resemble the dacitic high-K lavas of the San Juan volcanic field and the early-rift volcanic rocks that have hydrous mineralogy, such as those on Timber and Brushy Mountains. Abundant plagioclase phenocrysts, typical of the Red Mountain dacites and of Cerro Chiflo, are not typical of the younger dacites, even those of comparably high silica contents.

The stratigraphic relationships of the early porphyritic dacites and other early eruptive products of these volcanic fields are obscured by burial under voluminous younger basalts. This is particularly true for the Taos Plateau field because there are no exposed rocks with ages between Cerro Chiflo and the oldest exposed Servilleta Basalt (ca 4 Ma).

These early dacites are the least studied and least understood components of Taos and Raton–Clayton magmatism. The scarcity of contemporaneous basalts suggests that they are not the products of fractional crystallization. On the basis of limited data, the most likely source of these magmas is melting of the lower crust triggered by injection of basalt at the crust–mantle interface during the inception of late Miocene to Pliocene magmatism. The elemental pattern shown in Fig. 27A indicates enrichments in Ba, Rb, Th, K, and the LREE over HFSE (high-field-strength elements), P, Y, and the middle to light REE. This pattern is consistent with melting of a crustal source with garnet in the residuum, but

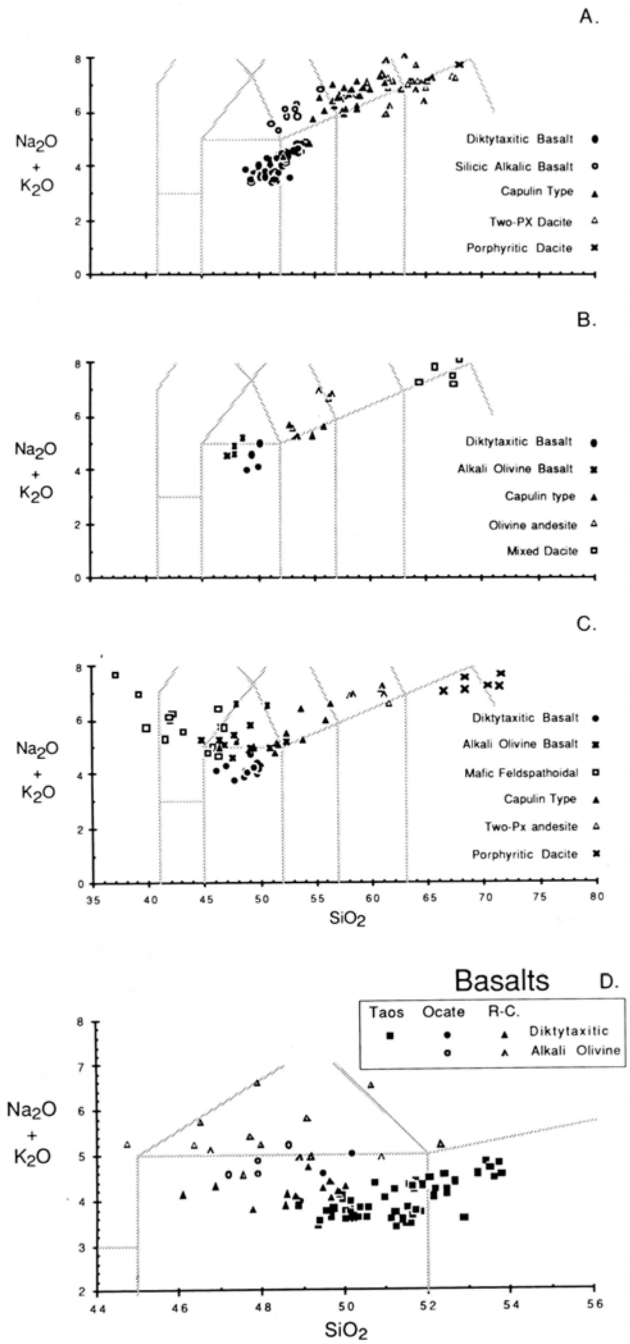

FIGURE 26—Total alkalies vs. silica plots for representative samples from **A,** Taos Plateau volcanic field; **B,** Ocate volcanic field; and **C,** Raton–Clayton volcanic field. Representative samples of the more mafic compositions from each field are shown in **D.** Irregular grid lines correspond to the classification scheme of Le Bas et al. (1986).

could not be produced from any mafic lava we have analyzed due to the much lower concentrations of Y and the HREE in the dacite. In addition to the overall steep slope and high La/Nb, the pattern has high ratios of K/Nb, Sr/P, and Hf/Ti.

Alkali olivine basalt—Undersaturated basaltic rocks (IUGS—alkaline basalt) are absent in the Taos field, but are major compoennts of early magmatism in the two flank volcanic fields. They also continued to be erupted during and after the later period in which diktytaxitic lavas dominated. The most voluminous Raton and early Ocate alkali-basalt eruptions have areal extents that approach those of some diktytaxitic flows. These basalts are distinct in composition (Ne <7–10) and mineralogy (dominantly olivine phenocrysts, no feldspathoids) from late mafic felspathoidal lavas of the Raton–Clayton volcanic field. The alkali olivine basalts of both the Ocate (Fig. 27B) and Raton–Clayton (Fig. 27C) fields have higher incompatible-element abundances than associated diktytaxitic lavas. The alkali olivine basalt patterns (gently convex upward with small HFSE depletions relative to REE and alkalies; Th displays scatter) are broadly similar in both the Octate and Raton–Clayton fields. They also resemble the patterns of the diktytaxitic basalts.

Diktytaxitic basalt—Basalts of this type are the most voluminous lithology in each volcanic field, and are largely Pliocene in age. Elsewhere along the Jemez lineament, rocks with this composition age, and texture are also present (Baldridge, 1979; Baldridge et al., 1987). Unlike any other lithology in these volcanic fields, these lavas occur as thin, widespread pahoehoe flows that are characterized by distinctive ophitic–diktytaxitic groundmass textures and related vesicular segregations such as those seen previously in Servilleta Basalt (Stops 8, 17). The Servilleta Basalt consists of olivine tholeiites (IUGS—subalkaline basalt), whereas the Clayton Basalt (Stop 40) and diktytaxitic lavas in the Ocate field (transitional olivine basalt: Stop 37) are transitional in their normative character (IUGS–basalt). In all three volcanic fields, the diktytaxitic basalts are the least alkaline mafic compositions in terms of $K_2O + Na_2O$ and normative criteria, and they have the lowest concentrations of incompatible elements. The Servilleta Basalt parental composition (LSKI; low in silica, potassium, and incompatible trace elements; Dungan et al., 1986) has significantly lower incompatible-trace-element abundances (Figs. 27B, C, D) than do analogous Ocate/Raton–Clayton lavas, which partly overlap in composition for both trace and major elements, but the general patterns for all three groups are similar.

The Servilleta olivine tholeiites define a much different major-element compositional range than the transitional basalts of the flank fields due to mixing of Servilleta parent magmas with broadly contemporaneous high-K andesite and dacite magma (Dungan et al., 1986; McMillan and Dungan, 1986, 1988): mixing has generated positive correlations among SiO_2 (48.7–52.5%; Hy = 3–20), alkalies (e.g., K_2O = 0.35–1.2%), and most incompatible elements (e.g., La = 7.7–18.5 ppm), at virtually constant Mg#. Although the most incompatible-element-enriched Servilleta samples have trace-element concentrations similar to those of the least enriched Ocate and Raton–Clayton diktytaxitic basalts, there is a critical distinction among them. For the diktytaxitic (transitional) to alkali olivine basalt spectrum in the Ocate and Raton–Clayton fields, increasing alkalies and incom-

FIGURE 27—Chondrite-normalized, trace-element abundance diagrams (after Thompson, 1982) for representative samples from the Taos Plateau, Ocate, and Raton–Clayton volcanic fields. References to specific samples in figures correspond to tables as follows: **A,** Table 8; **B,** Table 7; **C,** Table 8; **D,** Table 1; **E,** Table 2; **F,** Table 8; **G,** Table 8; **H,** Table 3; **I,** Table 7; **J,**Table 8. Solid black lines are maximum and minimum values for Servilleta Basalt.

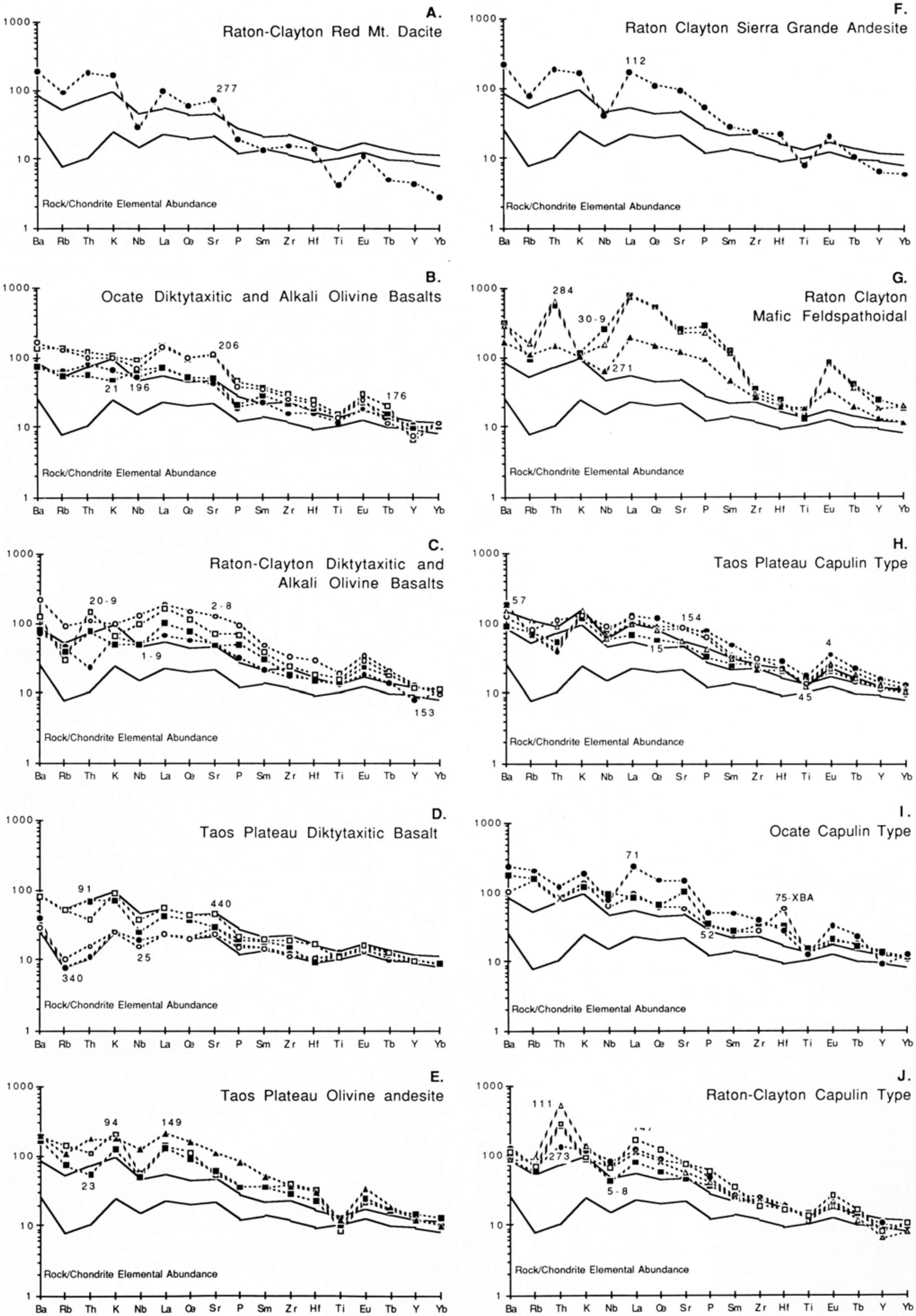
A.
Raton-Clayton Red Mt. Dacite
277
F.
Raton Clayton Sierra Grande Andesite
112
B.
Ocate Diktytaxitic and Alkali Olivine Basalts
206
21 196
176
G.
Raton Clayton
Mafic Feldspathoidal
284
30-9
271
C.
Raton-Clayton Diktytaxitic and
Alkali Olivine Basalts
20-9
2-8
1-9
153
H.
Taos Plateau Capulin Type
57
154
15
4
45
D.
Taos Plateau Diktytaxitic Basalt
91
440
25
340
I.
Ocate Capulin Type
71
75-XBA
52
E.
Taos Plateau Olivine andesite
94
149
23
J.
Raton-Clayton Capulin Type
111
273
5-8
Rock/Chondrite Elemental Abundance
1000
100
10
1
Ba Rb Th K Nb La Ce Sr P Sm Zr Hf Ti Eu Tb Y Yb

patible elements correlate positively with normative nepheline (i.e., decreasing silica). This pattern of variability is consistent with an origin by different degrees of partial melting (Frey et al., 1978; Nielsen and Dungan, 1983).

Olivine andesite and pyroxene dacite—The large Sierra Grande volcano in the central Raton–Clayton volcanic field (Stormer, 1972a, b) is morphologically, petrologically, and volcanologically equivalent to the numerous olivine andesite and pyroxene dacite (rhyodacite of Lipman and Mehnert, 1979) shields of the Taos Plateau field (McMillan and Dungan, 1988). The olivine andesite constructs of the Ocate field (e.g., early andesites of Cerro Pelon, Stop 36) are generally similar, although the cones are smaller and the silica range of these lavas is restricted to relatively mafic compositions. Although the total range of the Taos andesite–dacite suite is 55–67% SiO_2, the sampled variability within most individual shields is very small compared to the total spectrum: the limited SiO_2 range of the Sierra Grande andesite lavas is exceptional (60–61% SiO_2), but it is typical for Taos Plateau shields to be completely mantled by essentially a single lithology.

In the IUGS classification scheme, these rocks form a series from basaltic trachyandesite to trachydacite and dacite, emphasizing their high-alkali character. Previously, we focused on the high-K calc-alkaline affinities (figs. 5 and 6 of McMillan and Dungan, 1988; normative Qz) and the mafic phenocrysts (olivine or two pyroxenes) of these intermediate-composition rocks in assigning locally useful names to them. The regionally consistent change (reaction relation) from a mafic phenocryst assemblage of dominantly olivine to two pyroxenes at 59–61% SiO_2 has been used to mark the distinction between andesite and dacite. The Sierra Grande andesite, which falls on this compositional boundary, contains augite and orthopyroxene plus a trace of olivine. This association does differ markedly from typical convergent-margin calc-alkaline suites in the scarcity of rocks with hydrous minerals and low abundances of plagioclase phenocrysts. Biotite has not been observed in any of these rocks, and hornblende is rare even among the more silicic dacites, except in rocks with markedly disequilibrium mineral assemblages (i.e., probably hybrids).

Nielsen and Dungan (1983) concluded that the Ocate olivine andesites originated as the products of combined assimilation and fractionation (AFC) on the basis of major- and trace-element modeling. Two groups of andesites derived from alkali olivine basalt and diktytaxitic basalt parent magmas, respectively, were recognized. The incompatible-trace-element abundance pattern of the Ocate olivine andesite OC-71 (Fig. 27I) bears a strong resemblance to the Red Mountain dacite pattern (Fig. 27A; a very steep REE slope, low HFSE, high Sr/P and Hf/Ti), suggesting that a similar component may serve as the silicic endmember in an AFC differentiation history.

Dungan et al. (1986) and McMillan and Dungan (1988) argued on the basis of wide isotopic variations, and the impossibility of generating the basalt–andesite–dacite spectrum via fractional crystallization, that AFC in a complex open system (including repeated mafic-magma replenishment) must also have been the dominant process in deriving the intermediate-composition magmas from tholeiitic parent magmas similar to the Servilleta Basalt. McMillan and Dungan (1988) have discussed the role of crustal assimilation on the incompatible-element patterns of the Taos Plateau andesites and dacites. These lavas exhibit significant differences in the concentrations of highly incompatible elements at a given SiO_2 (up to a factor of two), and widely different ratios of certain elements. In comparison to the associated Servilleta basalts, they have greatly enriched values and increased negative Ti and Nb spikes (Fig. 27E). The lack of enrichment in Nb is ascribed to addition of crustal assimilant. The lowering of Ti and the absence of a positive Sr/P anomaly is probably due largely to the buffering effect of fractionation on these moderately compatible elements. The Sierra Grande andesite has a pattern very similar to the Taos andesites, except for much lower Y and HREE (Fig. 27F). This steep pattern suggests that a crustal component similar in composition to Red Mountain dacite mixed with mantle-derived magma to generate the Sierra Grande lavas.

Mafic feldspathoidal lavas—Highly undersaturated lavas, ranging in composition from basanite to olivine-melilite nephelinite (44–35% SiO_2: IUGS—basanite to foidite) are present only in the Raton–Clayton volcanic field (Stormer, 1972a, b,; Phelps et al., 1983). The most undersaturated compositions in this suite are the most alkalic mafic lavas erupted in association with the Rio Grande rift. Olivine and titaniferous Al-augite are phenocryst phases in all the Pleistocene feldspathoidal rocks: haüyne is present in the most undersaturated compositions. Groundmass phases (in addition to apatite + Fe–Ti oxides + glass) include nepheline + melilite in the nephelinites, and plagioclase + nepheline in basanites. Small ultramafic xenoliths are found at two localities (neither will be visited on this trip), and the feldspathoidal rocks are characterized by high Mg#'s. These observations led Phelps et al. (1983) to infer that the mafic feldspathoidal suite consists of nearly primary mantle-derived melts. We concur that this inference must be fundamentally correct and note that these are the only mafic lavas in the transect which are candidates for primitive compositions.

Phelps et al. (1983) also concluded that the spectrum of magma compositions in the feldspathoidal suite was not generated by fractional crystallization, but by differential melting of a recently enriched mantle source. An enriched source region and relatively small degrees of partial melting are necessitated by the extremely high concentrations of many incompatible elements (particularly Ba, Th, La) and the normative character of the magmas which are consistent with near-solidus melts of peridotite. The Nd-isotopic compositions of three samples (Epsilon Nd = 1.4) require that the pronounced LREE enrichment needed to produce the elemental patterns in the magmas (Fig. 27G) is a relatively recent attribute of the source (<0.2 Ga). The extreme enrichments in the LREE, Th, and Ba relative to the HFSE, K, and Rb, low Sr/P, and low K/Nb are distinct from either the relatively smooth patterns of the less enriched basaltic rocks and the HFSE-poor rocks such as the Red Mountain dacite. Irregularities in the pattern become more pronounced with increasing abundances. The most incompatible-element-enriched samples of the mafic feldspathoidal suite also have the lowest SiO_2. The most likely explanation for these extreme patterns is that the magmas represent partial melts of segregations added to the lithospheric mantle by relatively recent metasomatism. The extremely agpaitic phonolite sills to be visited at Points of Rock Mesa (Stop 38) are older (pre-rift), and appear unrelated to the Pleistocene feldspathoidal rocks which are among the youngest eruptive products of the Raton–Clayton field.

Capulin basalts and basaltic andesites—The Capulin-type lavas are present in all three volcanic fields where they are also typically the youngest eruptive products. In eruptive style and volume they are identical to the small monogenetic cones and flows of the mafic feldspathoidal suite, and in the case of the Raton–Clayton field probably overlap in age with these more undersaturated compositions. Lipman and Mehnert (1975) applied the rock names silicic alkalic basalt, for the more mafic (non-xenocrystic) members of the suite, and xenocrystic basaltic andesite for the more silicic compositions. These lavas are trachybasalts to basaltic trachyandesites (IUGS) with dominantly basaltic mineralogy and textures. They are quite distinct from the more mafic olivine andesite lavas in texture and eruptive mode despite significant similarities in major- and trace-element compositions. The more mafic members of the suite have olivine and plagioclase phenocrysts, and augite is present in some of the more silicic compositions which also commonly contain resorbed xenocrysts of a second, more sodic plagioclase population and quartz.

These magmas generally have a more alkalic, higher K_2O parentage than the diktytaxitic basalts and are distinctly younger. The most probable source of the sodic-plagioclase + quartz-xenocryst population is undigested crustal assimilant, but there are so few isotopic analyses of rocks from this suite that the role of contamination cannot be rigorously tested. The major- and trace-element petrologic models by Nielsen and Dungan (1983) are consistent with a large component of added crust for the more silicic composition in the Ocate field (Fig. 27I).

The incompatible-element patterns of the Taos Plateau trachybasalts are higher in abundance than Servilleta basalts with the same SiO_2, and comparable to those of typical olivine andesites and to alkaline basalts to the east (Fig. 27H). Capulin-type lavas in the Raton–Clayton field exhibit a wide range of incompatible-element abundances. The more enriched samples, such as 63-9 and 111, have patterns similar to the mafic feldspathoidal suite (Fig. 27J).

Discussion

Perry et al. (1987) addressed the patterns of compositional and isotopic variability expressed in basalts of the northern Rio Grande rift axis and those along the southwestern Jemez trend (or Colorado Plateau transition zone). They followed Lipman and Mehnert (1975) in emphasizing depth of origin as a major factor in determining the major-element compositions of the basalts (deeper source regions correlate with progressively undersaturated magmas), and utilized differences in Nd-isotopic composition to identify two distinct mantle components: depleted asthenospheric mantle with high Nd-isotope ratios, and enriched lithospheric mantle with lower $^{143}Nd/^{144}Nd$. We see no evidence for the depleted asthenospheric component in the present data and expect additional isotopic data to confirm that the sources of late Miocene to Pleistocene mafic magmas in the northeast Jemez zone were in mantle with the characteristics that Perry et al. (1987) ascribed to enriched lithosphere.

Wendlandt and Morgan (1982) postulated that mantle upwelling beneath continental rifts proceeds by thermal conversion of lithospheric mantle to asthenospheric mantle and that magmatism should reflect the time–space evolution of the lithosphere–asthenosphere boundary. Assuming that more alkaline magmas equilibrate at greater depths, and that melting occurs at the migrating boundary, rift magmatism in a given area should become less undersaturated with time. In the Taos–Ocate–Raton transect we are comparing basaltic rocks that were erupted at broadly the same time (<8 m.y.), but which have widely varying compositions. The entire episode represents a rejuvenation of rift-related magmatism and tectonism following a period of middle Miocene quiescence. Moreover, each of the volcanic fields is characterized by a maximum in output during roughly the interval 4–2 Ma, before and after which the basalts are generally more alkaline than the dominantly diktytaxitic (i.e., broadly tholeiitic) magmas that were erupted during the period of highest eruptive rate. This pattern does not closely match the predictions of the Wendlandt–Morgan model, primarily because their approach assumes a single-stage rifting event acting upon previously unmodified lithosphere. As we note above in the discussion of the early rift-age Hinsdale lavas present in the San Luis Hills, the mafic volcanic association erupted during the initiation of rifting does not differ significantly from the tholeiitic to mildly alkalic lavas of the Taos Plateau volcanic field or Los Mogotes: the proportion of trachybasalts to tholeiites is in fact high in both Los Mogotes and the early Hinsdale sequences.

The temporal evolution patterns seen in the northeast Jemez volcanic fields result from episodic rifting and are more consistent with magmatism generated by a discrete, shortlived thermal pulse in which the degree of undersaturation varied inversely as a function of volume erupted: i.e., as though smaller degrees of partial melting produced relatively undersaturated basalts in the waxing and waning phases of the event, and the diktytaxitic basalts with tholeiitic affinities were the products of the thermal peak of melting. Major- (i.e., normative) and trace-element compositions of the basalts correlate in such a way as to support variable degrees of partial melting, in conjunction with greater depth of melting on the rift flank, as a major factor in the origin of the regional trends. High-pressure experimental studies of peridotite–basalt systems have shown that near-solidus melts tend to be undersaturated (at a given pressure) relative to magmas generated by a large degree of partial melting at temperatures well above the solidus. Frey et al. (1978) showed that a range of basaltic compositions may be modeled on the basis of variable degrees of partial melting from the same source.

Another complicating factor that bears on the interpretation of the compositional variations among Plio-Pleistocene basaltic rocks of the northeast Jemez zone is the impact of mid-Cenozoic pre-rift and early-rift magmatism on the thermal and chemical state of the lithosphere. Of concern to the present comparison is the limited extent of Oligocene to early Miocene magmatism relative to the eastward extent of the transect. The Ocate and Raton–Clayton volcanic fields are east of the limit of Oligocene magmatic activity (and of the early rift basins) except for highly alkalic, low-volume occurrences such as the Chico Phonolite at Point of Rocks Mesa, whereas the Taos Plateau field is superimposed on the eroded remnants of the Latir–Quest magmatic system. The volcanic succession of the San Luis Hills (and to a lesser degree the Tusas Mountains) also records ongoing basaltic volcanism during the early phase of rifting. There is, however, no volcanic record related to pre-Pliocene rifting east of the Latir–Questa system. It is highly probable that the lithosphere in the vicinity of the rift axis underwent substantially greater modification and attenuation during this earlier phase of rifting than did the mantle to the east of the present rift axis, but it is extremely difficult to assess the lateral extent of very recently modified mantle and what role differential modification has played in controlling the variations discussed above.

Fifth day: Ocate volcanic field to Clayton, New Mexico

Mileage

0.0 Trip begins in La Cueva, New Mexico, at the junction of NM-442 and NM-518. Drive north on NM-442 toward Ocate, New Mexico. For the first 4 mi the road parallels sandstone ridges of Lower Permian Glorieta Formation to the west, the Upper Cretaceous Dakota Formation to the east. This deformation is a product of the Laramide orogeny; the Laramide uplift-bounding reverse fault is located east of the Dakota strike ridge. **7.4**

Late Cenozoic volcanism, uplift, and erosion, Ocate volcanic field, north-central New Mexico: Summary

J. Michael O'Neill

The Ocate volcanic field lies at the transition between the Southern Rocky Mountains and the Great Plains physiographic provinces in north-central New Mexico. The field consists of numerous basaltic to dacitic flows ranging in age from late Miocene to Pleistocene (O'Neill and Mehnert, in press). Volcanic flows 8.3 to 5.7 m.y. old preserve beneath their cover the physiographically highest gravel-covered surfaces in the volcanic field. The flows appear to rest on a surface, or a series of nearly equivalent surfaces, that slope gently southeast from a drainage divide, which in this part of the Sangre de Cristo Mountains was located east of the present divide, probably near the Rincon Range (Fig. I1). This paleosurface cuts across diverse rock types and sharp structural breaks, which suggests that late Miocene time was marked by erosion and pediplanation without tectonic activity.

About 5.5 m.y. ago, the crustal stability of the Southern Rocky Mountains during the late Miocene ended. Uplift caused moderate dissection of the late Miocene surface and the development of a younger surface which was several tens of meters lower. This intermediate-level surface wraps around the mesas capped by the older basalts and around the Cimarron Range and is continuous with the vast, broad surface of the Park Plateau in the Raton Basin. This surface also truncates diverse rock types and structures. In the vicinity of the Ocate volcanic field, it is represented by a southeast-sloping erosion surface, largely carved by the ancestral Rayado and Coyote Creeks. Much of the upper reaches of this surface was covered by volcanic rocks erupted between 4 and 5 Ma.

Profiles drawn on the Urraca surface and the older surface nearly parallel to it are locally warped, showing concave upward and downward deflections. The concave-downward aspect of the surfaces is roughly coincident with the Cretaceous hogback that marks the eastern margin of the Cimarron block. Warping was due to uplift of the Cimarron block with respect to the adjacent Great Plains. This surface is also cut by significant down-to-the-west normal faults on the west side of the field. These faults extend from the Moreno Valley south at least to the Mora Valley; displacement is as great as 275 m (900 ft).

After this period of broad uplift and volcanism, major erosion was confined to the southeast part of the field and resulted in the formation of the Ocate Valley. The ancestral Ocate Creek cut this valley to about its present size and elevation; the present floor of the valley is graded to the surface beneath the lowest-level basalts, 3.3–3.1 Ma, that cap Charette Mesa. These flows, or contemporaneous faulting, apparently dammed Ocate Creek and raised the base level, causing deposition of the alluvial-fluvial Las Feveras Formation in Ocate Valley.

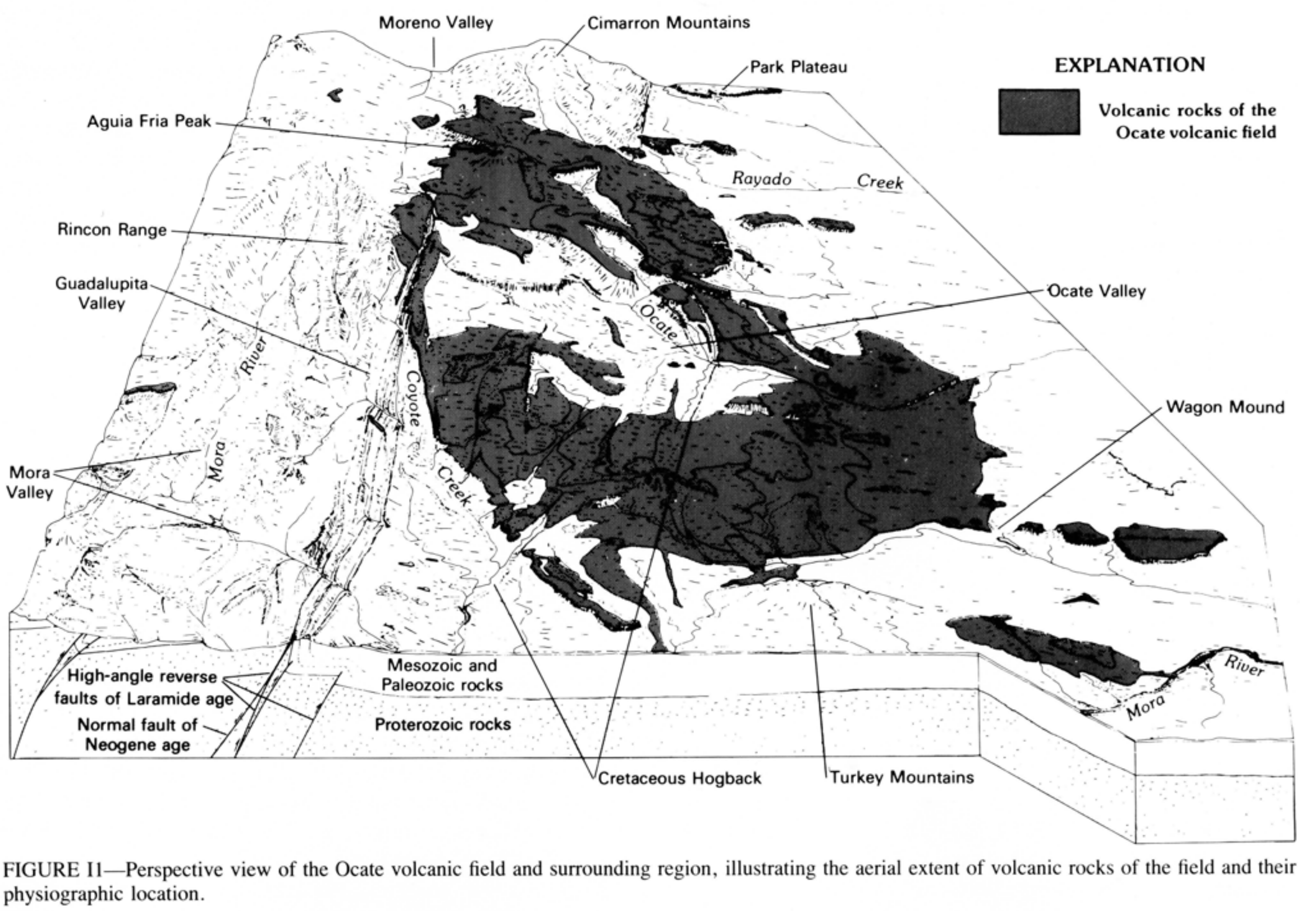

FIGURE I1—Perspective view of the Ocate volcanic field and surrounding region, illustrating the aerial extent of volcanic rocks of the field and their physiographic location.

This volcanism was followed by continued uplift; associated denudation is marked by the formation of the lowest paleoerosion surfaces and overlying gravels in the area, now preserved as isolated gravel-capped mesas standing slightly below the Charette Mesa surface. Basalts on one of these surfaces present near Wagon Mound were dated at 2.2 Ma.

By the time of the Maxon Crater eruption directly east of the Turkey Mountains, 1.4 m.y. ago, the present major drainages in this region were well established.

The youngest flows in the field were erupted from several small vents on Charette Mesa, northwest of Wagon Mound. This youngest volcanic episode is characterized by hummocky flows of limited extent that are surmounted by cinder cones.

7.4 View of Cerro Montoso (previously called Cerro Montuoso, e.g., Nielsen and Dungan, 1985), one of the Ocate volcanic field centers. **5.3**

12.7 Ojo Feliz, New Mexico (2360 m). Cerro del Amole (2530 m), the prominent conical hill north of town, is Mesozoic sandstone. **1.9**

14.6 Ojo Feliz Ranch road to left. Permission to visit Cerro Pelon (2709 m) must be obtained from the ranch manager. **2.0**

16.6 After passing through gate, drive 1 mi to windmill–water tank at the base of Cerro Pelon (2375 m).

STOP 36. Cerro Pelon andesite–dacite complex. Cerro Pelon is one of four intermediate-composition centers in the Ocate volcanic field (Fig. 28). Although Cerro Pelon was not studied in the same detail as Cerro Negro, Cerro Montoso, and Agua Fria Peak, it is broadly representative of the other centers and very different from Taos Plateau andesite and dacite cones. The primary distinction is that Ocate dacite lavas are porphyritic hybrid rocks that contain abundant quenched inclusions of andesite. Neilsen and Dungan (1983) proposed that these dacites are the products of shallow andesite–rhyolite mixing. Phenocryst assemblages in Ocate dacites frequently include two plagioclase populations, olivine, and quartz. Melt inclusions in embayed quartz phenocrysts have rhyolitic compositions.

At Cerro Pelon, late hybrid lavas have issued from several flank vents. One of these flows terminates near the parking area. This flow contains remarkably abundant mafic inclusions ranging in size from small angular fragments (<5 cm) to large oblate blobs (up to 2 m). Concentrations of these inclusions vary, locally reaching 30%. Several aspects of these inclusions are unusual in comparison to many other examples of mixed magmas. The andesitic inclusions do not exhibit quenched margins or concentric vesicular zones. Most of the small inclusions are angular or subangular, suggesting post-mixing fragmentation. The andesitic inclusions vary in their phenocryst and xenocryst (including quartz) assemblages, indicating some mixing of the rhyolite magma into the more mafic component prior to major mingling. These observations are best interpreted in terms of premixing thermal continuity between the two compositionally distinct magmas and some mixing across the boundary between them (e.g., Thompson and Dungan, 1985). Large-scale mingling of the two components during eruption from a shallow magma chamber, precluding homogenization of the components, was probably the cause of the spectacularly heterogeneous eruptive product.

Return to highway. **1.9**

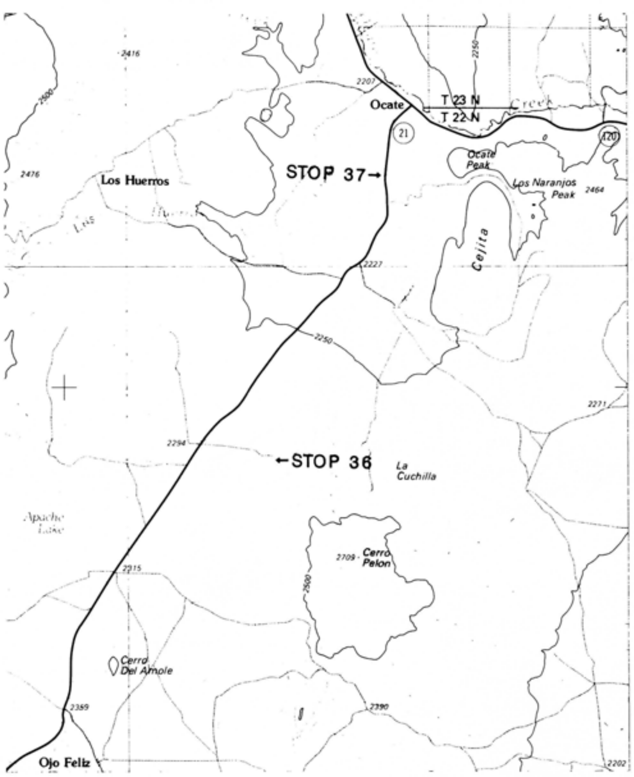

FIGURE 28—Location map for Stops 36 and 37. Note: NM-21 is now NM-442.

18.5 Turn right on NM-442 toward Ocate. **4.2**

22.7 **STOP 37. Outcrop of transitional olivine basalt** (Table 7) (2200 m). Pull off onto the right side of the road past the outcrops. Note the similarity in textural characteristics between this unit and typical Servilleta Basalt. Identical features will be seen in the Clayton Basalt (Stop 38). Diktytaxitic-textured lavas with tholeiitic or transitional normative compositions are present in all three fields (Table 6). In concert with these changes in the basaltic association from the rift axis to the rift flank, the character of the diktytaxitic-textured basalts changes systematically. The parental Servilleta magmas are olivine tholeiites (2–5% Hy), the Ocate and Clayton lavas are truly transitional (minor Ne or Hy), or marginally Ne-normative. Furthermore, the incompatible-element content increases substantially from axis to flank.

Continue on NM-442 to Ocate. **1.0**

23.7 Ocate, New Mexico, and junction of NM-442 and NM-120. Turn right (east) on NM-120 toward Wagon Mound, New Mexico. **8.2**

31.9 Basalt-capped mesas of several ages north (Rivera Mesa 2300 m; Apache Mesa 2200 m) and south (Encinosa Mesa 2400 m) of NM-120. **2.6**

34.5 Turkey Mountain anticline south of NM-120. Turkey Mountain is a laccolithic dome, possibly related to Ocate magmatism. The Wagon Mound (5.5 Ma) is at 12:00. **2.5**

37.0 Young lavas and strombolian cones (<800 Ka) on

TABLE 7—Representative analyses of rocks from the Ocate volcanic field (Nielson and Dungan, 1985).

No.	1.	2.	3.	4.	5.	6.	7.	8.
Sample	21	196	206	70	75	52	71	55
SiO_2	48.79	49.38	46.00	46.84	55.17	53.02	53.92	68.14
TiO_2	1.54	1.21	1.43	1.60	1.35	1.55	1.30	0.37
Al_2O_3	16.90	16.95	14.66	15.13	15.81	16.68	16.73	16.05
FeO*	11.62	10.23	9.12	9.89	8.87	9.73	7.46	3.50
MnO	0.17	0.20	0.19	0.18	0.14	0.15	0.13	0.08
MgO	6.81	6.92	10.89	8.05	6.07	4.45	3.54	1.26
CaO	9.73	9.71	10.35	9.06	7.62	8.00	7.03	2.47
Na_2O	3.30	3.15	3.00	3.53	3.38	3.51	4.05	3.47
K_2O	0.67	0.94	1.45	1.50	1.97	1.73	2.72	4.66
P_2O_5	0.22	0.20	0.40	0.48	0.34	0.36	0.53	0.15
H_2O	1.27	1.07	1.35	1.30	—	—	1.37	—
Total	101.02	99.96	98.84	97.56	100.72	99.18	98.78	100.15
Trace elements (ppm)								
Rb	19	22	45	47	52	56	72	93
Sr	593	492	1317	1267	681	1211	1716	460
Y	19	21	15	13	26	27	18	14
Zr	146	107	173	200	190	233	270	177
Nb	23	18	24	32	22	34	27	14.1
Ba	520	475	1119	933	705	1235	1628	1385
Cr	146	163	165	169	191	83	27	21
Ni	97	92	207	121	126	41	17	15
Co	49	51	56	51	44	38	38	17
Th	2.3	3.4	4.2	5.1	—	—	5.1	5.2
Hf	3.67	3.1	4.2	4.8	11.5	6.4	5.5	4.9
La	23.6	22.6	46.1	49.5	31.2	28	76	—
Ce	45	43.7	85	83.9	53	56	128	—
Sm	5.8	4.6	7	7.5	5.3	5.6	10.1	—
Eu	1.75	1.4	1.9	2.25	1.45	1.6	2.5	—
Tb	0.8	0.67	0.59	1.04	0.91	0.87	1.2	—
Yb	2.26	2.25	2.51	2.47	2.35	2.5	2.7	—
Lu	0.35	0.32	0.37	0.38	0.36	0.39	0.39	—
Sc	25	27.3	25.2	23.9	22.1	23	19	6.3
Ta	1.47	1.5	2.1	2.8	—	—	1.9	1.5

*Total Fe reported as FeO.
1. Transitional olivine basalt, diktytaxitic.
2. Transitional olivine basalt, diktytaxitic.
3. Alkali olivine basalt.
4. Alkali olivine basalt.
5. Xenocristic basaltic andesite.
6. Olivine andesite.
7. Olivine andesite.
8. Mixed dacite.

both sides of the highway for the next 8 mi. **10.0**

47.0 Wagon Mound city limits (1900 m). The basalt-capped terrace remnants (The Wagon Mound and Las Mesas del Conjelon 2150 m) north of the present town of Wagon Mound served as a major landmark on the Santa Fe Trail. From a distance to the northeast, The Wagon Mound does indeed resemble the profile of a covered wagon being drawn by a team of horses. From about 1820 until 1880, the Santa Fe Trail was the main trading and emigration route to the southwest. From Independence, Missouri, the trail extended about 800 mi (1300 km) southwest to Santa Fe, New Mexico (Scott, 1986). It was a dangerous trip; for instance, during one five-month period 160 travelers were killed by Plains Indians. The ruts made by the wagons on the trail can still be seen in a number of places in northeastern New Mexico. Our route today will roughly parallel one of the major branches of the trail, the Cimarron Cutoff. Many of the volcanic features we will see were distinctive and important landmarks on the trail. Our next stop (38) at Point of Rocks was also a landmark on the trail. **0.3**

47.3 Junction of NM-120 and I-25. Turn left onto freeway access after going under overpass. Drive north to Springer, New Mexico, to commence Raton–Clayton segment of the trip. Charette Mesa (2000 m, capped by transitional olivine basalt) lies to the west of I-25 for the next 10 mi (16 km). **15.0**

62.3 Enter Colfax County. **8.7**

71.0 View to the northeast of the western part of the Raton–Clayton volcanic field (Fig. 29). The axis of the Raton–Clayton volcanic field extends from near Trinidad, Colorado, 140 km (90 mi) southeastward to Clayton, New Mexico (Fig. 24). The volcanic rocks of Mesa de Maya in southeastern Colorado and western Oklahoma, and of an unnamed cluster of volcanic flows extending south into Harding County, New Mexico, are essentially identical to, and can be considered outlying parts of, the Raton–Clayton field. Including these outlying parts, the field covers nearly 20,000 km^2 (8000 mi^2). The oldest rocks of this field have ages of about 8 Ma and the youngest are less than 8000 years (Stormer, 1972b), approximately the same span of time as the Ocate field. The maximum rate of eruption appears to have taken place during a period from about 4 to 1.8 Ma, which coincides with the maxima in the Ocate field and the Taos Plateau. As we will see at Stop 40, the transitional olivine basalt produced

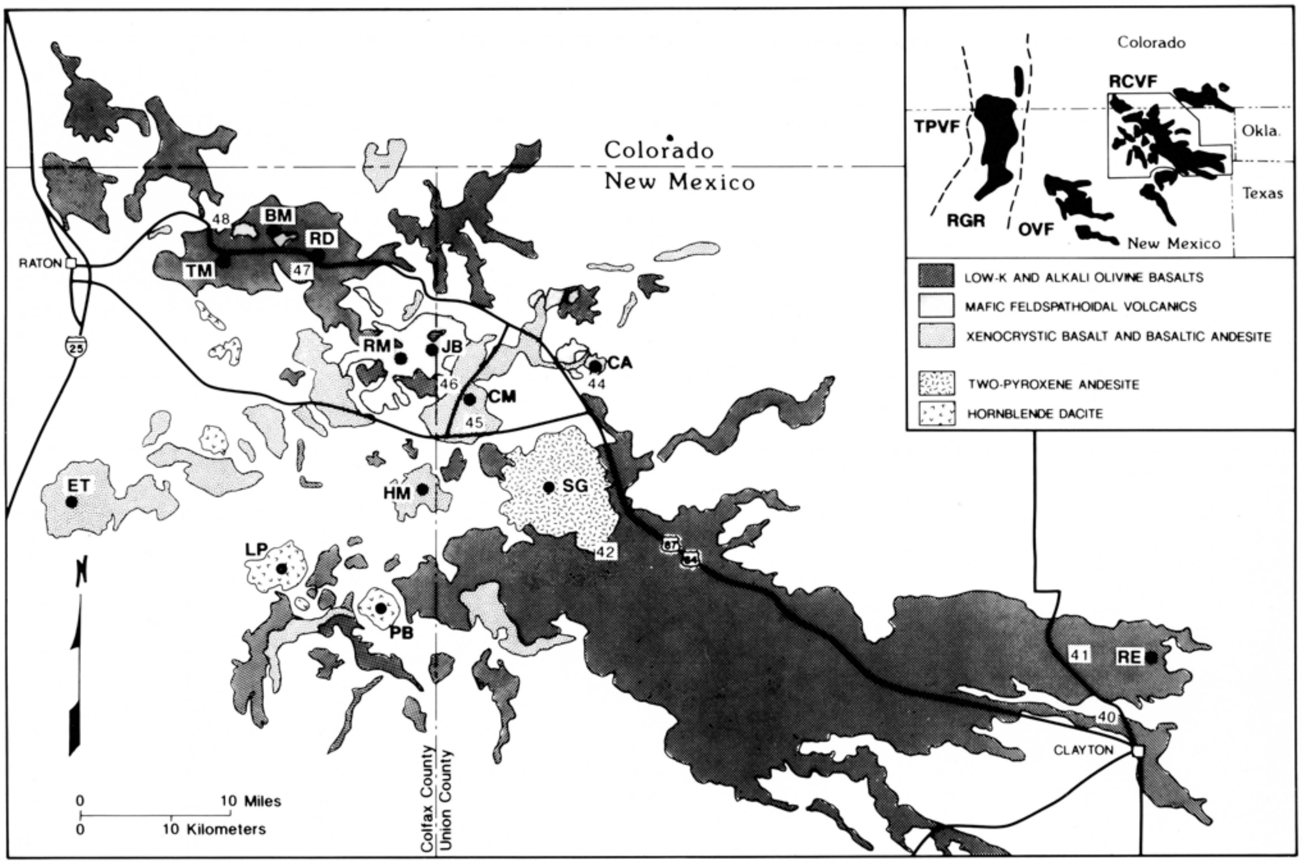

FIGURE 29—**A,** Location of the Raton–Clayton volcanic field (RCVF) with respect to the Ocate volcanic field, Taos Plateau volcanic field, and the Rio Grande rift. The outlined area is shown in B. **B,** Distribution of volcanic rock types in the RCVF (modified from Stormer, 1972a). The numbered locations refer to guidebook stops. The following volcanic features are identified: BM, Bellisle Mt.; CA, Carr Mt.; CM, Capulin Mt.; ET, Eagle Tail Mt.; HM, Horseshoe Mt.; JB, Jose Butte; LP, Laughlin Peak; PB, Palo Blanco; RE, Rabbit Ears; RD, Red Mt.; RM, Robinson Mt.; SG, Sierra Grande; TM, Towndrow Mt.

during this maximum is clearly analogous to the tholeiitic Servilleta Basalt of the Taos Plateau in mineralogy, texture, and composition, though it is slightly alkalic. Most of the other rock types in this field also correspond to types found in the Taos Plateau and Ocate fields. The distinctive feature of the Raton–Clayton field is the presence of highly alkalic mafic lavas, such as haüyne- and melilite-bearing nephelinites with SiO_2 contents as low as 35%.

The earliest lavas of the Raton–Clayton field flowed onto the surface of an alluvial apron of sediment shed from the Sangre de Cristo Mountains to the west. Continuing uplift during volcanism resulted in the erosion of this surface where it was not capped by volcanic rock. During subsequent eruptions, lava flowed down valleys cut in this surface. The oldest lavas, therefore, are now found at the highest elevations above present erosional levels, with younger lavas at progressively lower levels in a kind of inverted stratigraphy. The rate of downcutting has, however, been significantly greater in the western part of the field along the Canadian River valley. The high, lava-capped mesas in the distance to the north are over 700 m (2000 ft) above the valley floor. To the east, the elevation of the older basalt-capped mesas decreases, and at Clayton they are only a few tens of meters above the present valley floors. **1.0**

72.0 Take exit 412 to Springer, New Mexico (1780 m), and turn right toward town after 0.2 mi. **1.2**

73.2 Junction of US-56 and NM-58 in Springer. Turn right on US-56 (east). **5.0**

78.2 Valley of the Canadian River west of Taylor Springs. Mesozoic strata include the Upper Cretaceous Greenhorn Limestone, Carlisle Shale, and the Fort Hayes Limestone Member of the Niobrara Formation. **3.0**

81.2 Fort Hays Limestone caps the mesa north of the road. **11.5**

92.7 Abbott, New Mexico (1875 m), and the junction of US-56 and NM-39. Mesa surfaces here are formed on the Miocene Ogalalla Formation. To the northwest (western Raton–Clayton volcanic field), this same surface is preserved beneath the ca. 7 Ma Raton basalts. **4.1**

96.8 Turn left onto Colfax Co. Road C52 and drive toward the Chico Hills. The Chico Hills are the eroded remnants of Oligocene trachyte and agpaitic phonolite sills intruded into late Mesozoic and early Tertiary sediments. At the next stop (38) we will examine one of the phonolites. Dikes of more mafic compositions, lamprophyres, and one small occurrence of carbonatite are associated with this complex. Dates obtained on a few of these intrusions (25–37 Ma; Staatz, 1986) indicate that they are roughly contemporaneous with the calc-alkaline volcanism of the San Juan and Mogollon–Datil volcanic fields to the west and southwest and the peralkaline rhyolites and phonolites of Trans-Pecos Texas to the south. This intrusive complex is probably unrelated to the Miocene to Recent Raton–Clayton volcanic field.

The most significant structure underlying this volcanic field is the Sierra Grande arch, the crest of which runs generally north-northeast under this location and beneath Sierra Grande Volcano. This is primarily a late Paleozoic structure but also forms the eastern rim of the Laramide Raton Basin. (The Sangre de Cristo Mountains are the western rim.) Smaller scale doming in the vicinity of the Chico Hills is probably a result of the mid-Tertiary intrusions. There are no significant structures associated with the late Miocene to Recent volcanic field. However, many sets of volcanic vents are aligned along roughly west-northwest trends, suggesting that the location of the vents may be controlled by fractures in the subsurface (Baldwin and Muehlberger, 1959). Their trend is similar to that of other extensional features in the Southern Great Plains stress province during the past 28 Ma (Aldrich et al., 1986). **7.0**

103.8 Just before a cattleguard, turn right (east) on Road C53. **2.0**

105.8 Turn left (north) toward ranch and drive 1 mi. **1.0**

106.8 Ask permission and directions to visit quarry in Chico Phonolite. **1.4**

108.2 Drive west and park vehicles before proceeding up to the rim of the mesa.

STOP 38. Chico Phonolite, Point of Rocks Mesa (2155 m). The phonolite sill which forms this mesa has an extremely peralkaline composition and uniquely diverse mineralogy (Stormer and Carmichael, 1970; Stormer, 1981; DeMark, 1984). The rock is primarily composed of nepheline, sodalite, alkali feldspar, and an unusual, manganese-rich acmite (pyroxene). Villiaumite [NaF], mangan-neptunite [$KNa_2Li(Mn, Fe)Ti_2Si_8O_{24}$], serandite [$Na(Mn, Ca)_2Si_3O_8(OH)$], eudyalite [$Na_4(Fe, Ca, Ce)_2ZrSi_6O_{17}(OH, Cl)_2$], Ti-rich polylithionite [$KLi_2AlSi_4O_{10}(F, OH)_2$], and sphalerite appear to be

TABLE 8—Representative analyses of rocks from the Raton–Clayton volcanic field.

No.	1.	2.	3.	4.	5.	6.	7.	8.
Sample	855-153	1-9	855-117	20-9	855-271	855-284	30-9	218
SiO_2	48.35	49.14	46.03	45.75	44.75	37.04	35.90	56.48
TiO_2	1.39	1.51	1.90	1.65	1.87	1.64	1.32	0.14
Al_2O_3	15.00	15.81	14.78	15.13	14.72	12.76	11.84	20.50
FeO*	12.24	10.47	9.98	10.61	10.00	11.29	10.59	1.60
MnO	0.19	0.18	0.18	0.20	0.20	0.32	0.30	0.26
MgO	8.94	7.17	7.91	8.50	9.85	8.73	9.78	0.08
CaO	8.93	9.66	9.47	10.29	10.50	15.37	16.39	0.82
Na_2O	3.20	3.33	3.86	4.05	3.42	4.83	5.76	10.27
K_2O	0.92	0.72	1.37	0.95	1.47	1.53	1.65	5.25
P_2O_5	0.34	0.54	0.99	0.74	0.97	2.37	3.03	0.06
H_2O	0.64	1.36	2.92	1.28	1.54	1.19	1.92	—
Total	100.14	99.89	99.39	99.15	99.29	97.07	98.48	95.63
Trace elements (ppm)								
Rb	16	13.7	45	10.2	38	55	33.4	—
Sr	549	570	1398	856	1401	2719	3006	117
Y	16	25.6	21	23.9	26	21	48.8	48
Zr	119	129	223	168	183	235	241	1092
Nb	18	17.6	46	34.9	22	71	91	—
Ba	502	570	958	856	1142	2026	2433	137
Cr	240	243	—	267	—	236	140	4
Ni	200	146	141	172	215	173	186	—
Th	1	3.2	0	6.1	3	34	23.7	—
Hf	3.1	3	—	3.8	3.9	4.4	5	—
La	19	33.4	59	54.1	67	248	259	—
Ce	43.3	67.1	—	100.1	127	457	489	—
Nd	—	—	—	—	55	162	176	—
Sm	4.54	6.35	—	7.95	9.2	23.7	25.1	—
Eu	1.45	1.87	—	2.29	2.59	6.14	6.52	—
Tb	0.74	0.94	—	0.96	1	1.9	2.1	—
Yb	2.23	2.28	—	2.6	2.49	4.36	4.04	—
Lu	0.39	0.36	—	0.37	0.39	0.65	0.55	—
Sc	26.1	26	—	26.1	25.6	20	16.8	—
Ta	—	1.3	—	3.7	2.7	5.3	5.7	—
V	—	164	—	181	—	196	185	11

*Total Fe reported as FeO.

1. Transitional olivine basalt, diktytaxitic, Gaps flow (Stormer, 1972). Stop 40 equivalent.
2. Transitional olivine basalt, diktytaxitic, Clayton flow. Stop 40 (Phelps unpubl.).
3. Alkali olivine basalt, west end Johnson Mesa (7.2 Ma, Stormer, 1972). Stop 48, Stop 39 equivalent.
4. Alkali olivine basalt, Van Cleve flow (Phelps unpubl.).
5. Basanite, Purvine Mesa (Stormer, 1972). Stop 43.
6. Haüyne–melilite nephelinite, Carr Mt. (Stormer, 1972). Stop 44.
7. Melilite nephelinite, east side Carr Mt. (Phelps et al., 1983). Stop 44 equivalent.
8. Phonolite sill top of hill north of Dorsey Mansion (Stormer, unpubl.) Stop 38 equivalent.

TABLE 8, continued.

No. Sample	9. 111	10. 63-9	11. 5-8	12. 273	13. 112	14. 118B	15. 277	16. 77-2A
SiO_2	55.04	52.72	52.50	50.94	60.10	64.17	67.04	69.13
TiO_2	1.19	1.46	1.26	1.49	0.83	0.47	0.43	0.21
Al_2O_3	15.62	16.40	16.16	16.28	15.78	15.72	15.60	14.70
FeO*	7.34	8.40	8.84	9.96	4.92	3.33	2.54	1.59
MnO	0.13	0.15	0.15	0.18	0.10	0.08	0.04	0.07
MgO	5.62	4.65	6.53	6.32	3.30	1.71	1.29	0.50
CaO	7.23	7.42	8.77	8.12	5.90	4.00	3.96	3.51
Na_2O	3.91	4.23	3.85	3.74	4.42	4.39	4.61	4.36
K_2O	1.96	2.09	1.69	1.27	2.41	2.45	2.36	2.67
P_2O_5	0.43	0.69	0.50	0.38	0.56	0.29	0.21	0.07
H_2O	0.91	0.81		0.60	0.97	2.50	1.72	2.80
Total	99.38	99.02	100.25	99.28	99.29	99.11	99.80	99.61
Trace elements (ppm)								
Rb	32	—	23.5	20	27	—	32	—
Sr	667	—	888	539	1130	—	864	—
Y	13	—	21	15	13	—	9	—
Zr	158	—	173	132	164	—	108	—
Nb	23	—	28.5	15	14	—	10	—
Ba	595	—	888	584	1529	—	1309	—
Cr	152	55.4	155	125	62	23.2	2.4	2.9
Ni	98	50	92	92	55	25	26	—
Th	22	7.8	5.6	11	7	9.7	5	5.4
Hf	3.9	4.4	3.8	3.5	4.5	3.2	2.84	2.7
La	35	43.5	39.3	26	56	42.6	32	15.8
Ce	68.2	83.9	74.9	50.4	98	67.9	52.9	27.1
Sm	5.03	6.43	5.5	4.89	5.8	3.8	2.84	1.59
Eu	1.44	1.86	1.62	1.5	1.57	1.06	0.86	0.49
Tb	0.61	0.83	0.71	0.75	0.55	0.35	0.26	0.16
Yb	1.75	2.17	2.03	2.17	1.3	0.79	0.63	0.46
Lu	0.3	0.34	0.33	0.33	0.2	0.13	0.11	0.08
Sc	18.7	18.5	21.2	22.5	9.8	5.4	4.3	1.9
Ta	—	4.3	2.8	1.55	1.5	1.3	—	2.8
V	—	—	—	—	—	—	—	—

9. Capulin flow outcrop on US-87/67, 1.9 mi east of Capulin, NM (Stormer 1972a). Stop 45.
10. Capulin type (Phelps, unpubl.).
11. Capulin type (Phelps, unpubl.).
12. Capulin type, from railroad cut N flank Twin Mt. (Stormer, 1972a). 5 mi ENE of Stop 46.
13. Two-pyroxene andesite, N flank Sierra Grande (Stormer, 1972a). Stop 42 equivalent.
14. Porphyritic dacite (plag, hbl), E side of Towndrow Pk. (Stormer, unpubl.). 6 mi west of Stop 47 (see mile 124.2 of Day 6).
15. Porphyritic dacite (plag, hbl), E side of Towndrow Pk. (Stormer, unpubl.).6 mi west of Stop 47 (see mile 124.2 of Day 6).

primary magmatic accessory minerals. Searlesite [$NaBSi_2O_5(OH)_2$], natrolite, cancrinite, and other rare minerals are found in vugs. The unusual composition and mineralogy of these rocks are comparable to only a few other known localities, such as the Lovozero alkaline plutonic complex (Kola Peninsula, USSR). Acmite, nepheline, sodalite, and alkali feldspar along with neptunite and the polylithionite are also found in other sills in this complex, but this is the only location where villiaumite and the other rare minerals have been found. Analysis no. 8 in Table 8 is from an equivalent sill about 6 km (4 mi) north-northeast of here.

Return to ranch. **1.4**

109.6 Ranch. Turn right and retrace route to US-56 (1 mi south, 2 mi west, 7 mi south). **10.0**

119.6 Junction with US-56. Turn left (east) toward Clayton, New Mexico. The large andesite shield of Sierra Grande can be seen in the distance to the north-northeast. Don Carlos Mesa ahead to the east-northeast is capped by Pliocene basalt, as are the unnamed hills to the east-southeast. The latter are the southernmost outlier of the Raton–Clayton volcanic field. **12.3**

131.9 Village of Gladstone. **6.5**

138.4 Road climbs out of small stream valley on the southwest side of the Don Carlos Mesa. Stop and park off to the right near the roadcut.

STOP 39. Roadcut in alkali olivine basalt, southern Don Carlos Hills (1775 m). This is part of the Raton Basalt (Tb) as mapped by Baldwin and Muehlberger (1959). This rock contains abundant phenocrysts of olivine with rims altered to reddish-brown iddingsite and occasional sector-zoned augite. It has a dense aphanitic groundmass of plagioclase laths with titanomagnetite, iddingsitized olivine, and intersertal pyroxene. No analysis is available from this locality, but it is petrographically similar to sample 117 of Stormer (1972a; analysis no. 3, Table 8), which would be classified as a trachybasalt in the IUGS chemical classification of volcanic rocks (Le Bas et al., 1986). This rock is typical of the widespread alkalic basalts of the early phase of volcanism in the field. Raton alkalic basalts are slightly nepheline-normative but lack modal felspathoid. Compositionally identical rocks are abundant in the early phase of volcanism in the Ocate volcanic field, but none of the Servilleta basalts of the Taos Plateau are as silica-poor and alkali-rich. **10.0**

148.4 Rabbit Ear cone in the distance to the east-northeast. Sierra Grande andesite shield to the northwest. **8.0**

156.4 Cretaceous Dakota Sandstone caps mesa. Here, east of the Sierra Grande Arch the beds have a very gentle southeast dip. Throughout most of the eastern part of the volcanic field the lavas flowed out onto a thin veneer of Quaternary gravel resting on the Pliocene erosion surface cut into this sandstone. **2.5**

158.9 View of the Carrizo flow forming the cap of the long low mesa in the distance to the east and northeast. Several long, thin, and irregularly lobate flows of transitional olivine basalt are found here in the southeastern part of the volcanic field (see Fig. 24). Subsequent erosion has cut only a few meters into the Pliocene surface onto which they were erupted; the present outlines of the flows correspond very closely to the original extent of the flow fronts. The very high aspect ratios of these flows suggest very fluid magma. At Stop 40 we will examine one of these flows closely. **4.5**

163.4 Drive up onto the surface of the Carrizo flow. Rabbit Ear Mountain (1846 m), an eroded volcanic cone can be seen ahead. This is the easternmost volcanic vent in the field; there are no other Cenozoic volcanic vents at this latitude between this locality and the mid-Atlantic ridge. **2.1**

165.5 Continue off flowtop surface (here covered by Quaternary gravels). **11.8**

177.3 One mile to Clayton. Drive up onto top of Clayton flow (1525 m). The Clayton flow does not crop out well at the road because of the low relief and overlying gravel. Keep in mind that this and the Carrizo flow that was crossed earlier are equivalent in age to flows 90 mi to the northwest that cap mesas 700 m above present erosion levels near Raton, New Mexico. **2.1**

179.4 Junction of US-56 and NM-402 in Clayton. **0.2**

179.6 Junction of US-56/64 and US-87.

Sixth day: Clayton to Albuquerque: Raton–Clayton volcanic field

Mileage

0.0 Begin at junction of US-87/64 and US-56 in center of town of Clayton (Fig. 23). Proceed west on US-87/64 in direction of Raton. **0.4**

0.4 Turn right onto NM-370. Follow sign to Clayton Lake State Park. Rabbit Ear Mountain (1846 m) trachybasalt cone is directly ahead. **1.4**

1.8 **STOP 40. Clayton Basalt** (Fig. 24). Pull into parking area on right just before sharp curve to left (1545 m). Leave cars and walk 50–100 m down the road to basalt outcrops. Road is cut in the edge of the Clayton flow (Clayton Basalt, QTb of Baldwin and Muehlberger, 1959; equivalent to sample 153 of Stormer, 1972a; K–Ar date 2.2 Ma Stormer, 1972b; analysis no. 2 in Table 8 is from this outcrop). This is a very good example of a transitional olivine basalt. Olivine microphenocrysts are set in a relatively coarse diktytaxitic groundmass of plagioclase laths with intersertal clinopyroxene, titanomagnetite, and olivine. It has neither hypersthene nor nepheline in the norm and would be classified as subalkaline basalt in the IUGS chemical classification. The mineralogy and texture of the flow is similar to the Servilleta olivine tholeiites of the Taos Plateau. Note the late-stage segregations. Compare this rock with those seen at Stop 16 on the Taos Plateau and Stop 35 in the Ocate volcanic field. This rock type was probably the dominant product of volcanism in this field during the same time period that the Servilleta olivine tholeiites were erupted in the axis of the Rio Grande rift. In comparison with typical Servilleta olivine tholeiites, these rocks are very slightly lower in silica and higher in potassium, titanium, and incompatible trace elements.

Return to cars and then proceed downhill to the west into Apache Valley. (If optional Stop 41 is not to be visited, return to the junction of US-87/64 and recommence the road log at mile 15.0 below.) **2.6**

4.4 Good exposure of gravel of the Ogalalla Formation (1500 m) containing clasts of Precambrian lithologies derived from the Sangre de Cristo Mountains as well as phonolite from the Chico Hills. **0.4**

4.8 View of Bible Top Butte at 11:00 (1724 m). This remnant of an eroded vent was named by travelers on the Cimarron Cutoff branch of the Santa Fe Trail in the mid-19th century because it looks like an open book. The route of the old trail passes just to the north of Rabbit Ear Mountain and continues southwestward to the Point of Rocks Mesa (Stop 36) and then on to Santa Fe via Wagon Mound. Each of these volcanic features was an important landmark which could be seen and identified at a great distance. **2.9**

7.7 Park on right side of road adjacent to gate leading to windmill.

STOP 41 (optional). Rabbit Ear Mountain trachybasalt locality. In low cuts along road are exposures of the lava erupted from Rabbit Ear Mountain. Cinder cones such as these commonly overlie the extensive transitional olivine basalt sheets. The vents for the voluminous transitional olivine basalt sheets have not been identified, but the distribution of these later alkalic cones suggests that they may be superimposed on fissures that fed the transitional olivine basalt sheets. The rock is nearly aphyric with iddingsitized olivine microphenocrysts in an extremely fine-grained groundmass. Most of these do not contain modal feldspathoids but do have nepheline in the norm. These cones often appear to be aligned along possible fissures with a dominant west-northwest trend.

Aficionados of the Western novel may be interested to note that in Louis L'Amour's *Mustang Man* the gold was buried in the box canyon in the edge of the mesa just to the north of here.

Return to US-87/64. **7.3**

15.0 Turn right on US-87/64. **2.2**

17.2 The route from Clayton will travel 60 mi northwest on the surface of the Clayton Basalt flows. Petrographically they are all very similar to the unit at Stop 40. Cones of more alkalic lava were built on top of these widespread lava sheets. Rabbit Ear volcano (the two peaks to the north of this point) is the easternmost of these centers. Several others can be seen in the distance from north to west of this point. Most of these are eroded steep-sided cones of tephra and short, thick flows. The lavas are nepheline-normative but most are relatively silicic and do not have modal feldspathoids. A few, as we will see later, are strongly alkalic and contain abundant nepheline or haüyne. The prominent shield directly ahead is Mount Dora (1917 m). The morphology of this shield is unusual, and some of the flows from the lower slopes of this shield are very much like the diktytaxitic transitional olivine basalts. This suggests the possibility that Mount Dora (also called Cieneguilla del Burro Mountain) may have been one of the centers from which the voluminous transitional basalt flows were erupted. **15.9**

33.1 Town of Mount Dora (1720 m). View of Sierra Grande (2658 m) ahead. As its name implies, Sierra Grande is the largest single volcanic edifice in the Raton–Clayton field. The summit is at an elevation of 2658 m (8720 ft), 600 m (~2000 ft) above the surrounding plains, and the base is almost 12 km (5 mi) in diameter. A date of 1.9 Ma has been obtained for a flow from the north flank (Stormer, 1972b). Its position near the western (upper) end of the principal transitional basalt sheet and its shield-like morphology suggest that it may have been the site of a major vent for the diktytaxitic transitional basalt sheets. However, all rocks exposed at the surface of this large shield are two-pyroxene andesite of remarkably uniform mineralogy and composition. **8.7**

41.8 Town of Grenville (1780 m). Junction of US-87/64 and NM-453 (to Gladstone). Continue ahead on US-87/64. **11.2**

53.0 Turn left at white gate to Tom Giffin Ranch. Drive southwest on unpaved county road. Stay on this road as it circumvents the southeast flank of Sierra Grande. **3.5**

56.5 **STOP 42. Flow front of Sierra Grande Andesite** to the right (north) side of road (2000 m). This is private land; do not drive off the road or hike beyond the first outcrop without permission. This rock is a dark-gray porphyritic andesite with phenocrysts of both orthopyroxene and clinopyroxene set in a groundmass containing the two pyroxenes, plagioclase, and up to 30% brown glass. Traces of olivine and rare xenocrysts of quartz are also found. The large orthopyroxene phenocrysts characteristically have cores of iron-rich hypersthene (En_{55}) with magnesium-rich rims (En_{85}). The silica content averages exactly 60% and these rocks are classified as trachyandesite in the IUGS chemical classification. (The Na_2O:K_2O ratio puts this rock on the boundary between benmoreite and latite in this classification. See analysis no. 13, Table 8.) Rocks with both clino- and orthopyroxene are found only on Sierra Grande and nowhere else in this volcanic field. Despite the large size of the volcanic center, it appears to be extremely homogeneous in composition. All analyses cluster within 59–61% silica for example, and all have the same mineralogy. The only textural differences are in the crystallinity of the groundmass. This rock type appears to share many of the characteristics of the andesites and dacites of the Taos Plateau; i.e., presence of both orthopyroxene and clinopyroxene, glassy groundmass, no phenocrystal plagioclase, and no hydrous minerals. Sierra Grande is also morphologically similar to the monolithologic, shield-like andesite and dacite centers of the Taos Plateau (e.g., San Antonio Mountain). **3.6**

60.1 Turn left on US-87/64 and circle the north side of Sierra Grande for the next 6–8 mi. **6.5**

66.6 Village of Des Moines, New Mexico (Fig. 30). The broad cone north of town is Dunchee Hill (2050 m), a basanite vent that contains minor ultramafic xenoliths. The vent north of Dunchee Hill is Carr (Gaylord) Mountain, the site of the next stop (Stop 43). The Recent cone of Capulin Volcano (xenocrystic basaltic andesite, Stops 45 and 46) and other basanite–nephelinite cones are visible beyond Dunchee Hill. **1.1**

67.7 Leaving Des Moines. Junction of US-87/64 and NM-325. Turn right on NM-325, toward Folsom. **1.2**

68.9 Turn right at telephone lines, pass over cattleguard, and bear left to follow road north, parallel to telephone lines. Dunchee Hill is to the immediate right. The surface here is Dakota Sandstone on which the volcanoes of this area are built. The volcanic rocks often contain xenoliths of this sandstone. **1.5**

70.4 Ranch House on left; start up steep slope. The top of this slope and the surface beyond is the basanite of Purvine Mesa (Baldwin and Muehlberger, 1959). **0.5**

70.9 Ruins of small stone house on right. Park near the house.

STOP 43 (optional). Basanite flow. Low, rubbly outcrop along the road is a basanite (42% SiO_2, IUGS classification). This flow is characterized by abundant large augite phenocrysts and somewhat smaller olivine phenocrysts in a fine-grained groundmass. These augites are Ti-rich and display very well-developed sector zoning. This rock is one example of the mafic feldspathoidal lavas that occur as relatively small-volume centers overlying the voluminous, widespread, transitional basalt sheets. This rock type is not found at all in the Taos Plateau or the Ocate volcanic fields, but only here near the eastern limit of rift-related volcanism.

The ridge about 0.5 mi to the north is a fissure eruption vent of Capulin Basalt (Purvine vents, Baldwin and Muehlberger, 1959), one of the very young xenocrystic-basalt to basaltic-andesite types that will be seen more closely at Stops 45 and 46.

Just beyond (north) stone house, turn right (east) from county road onto ranch road and proceed ahead through cattleguard. **1.0**

71.9 Gate. Proceed straight ahead. **1.3**

73.2 **STOP 44. Carr Mountain** (2104 m; also known as Gaylord Mountain). **Quarry in cinder cone of**

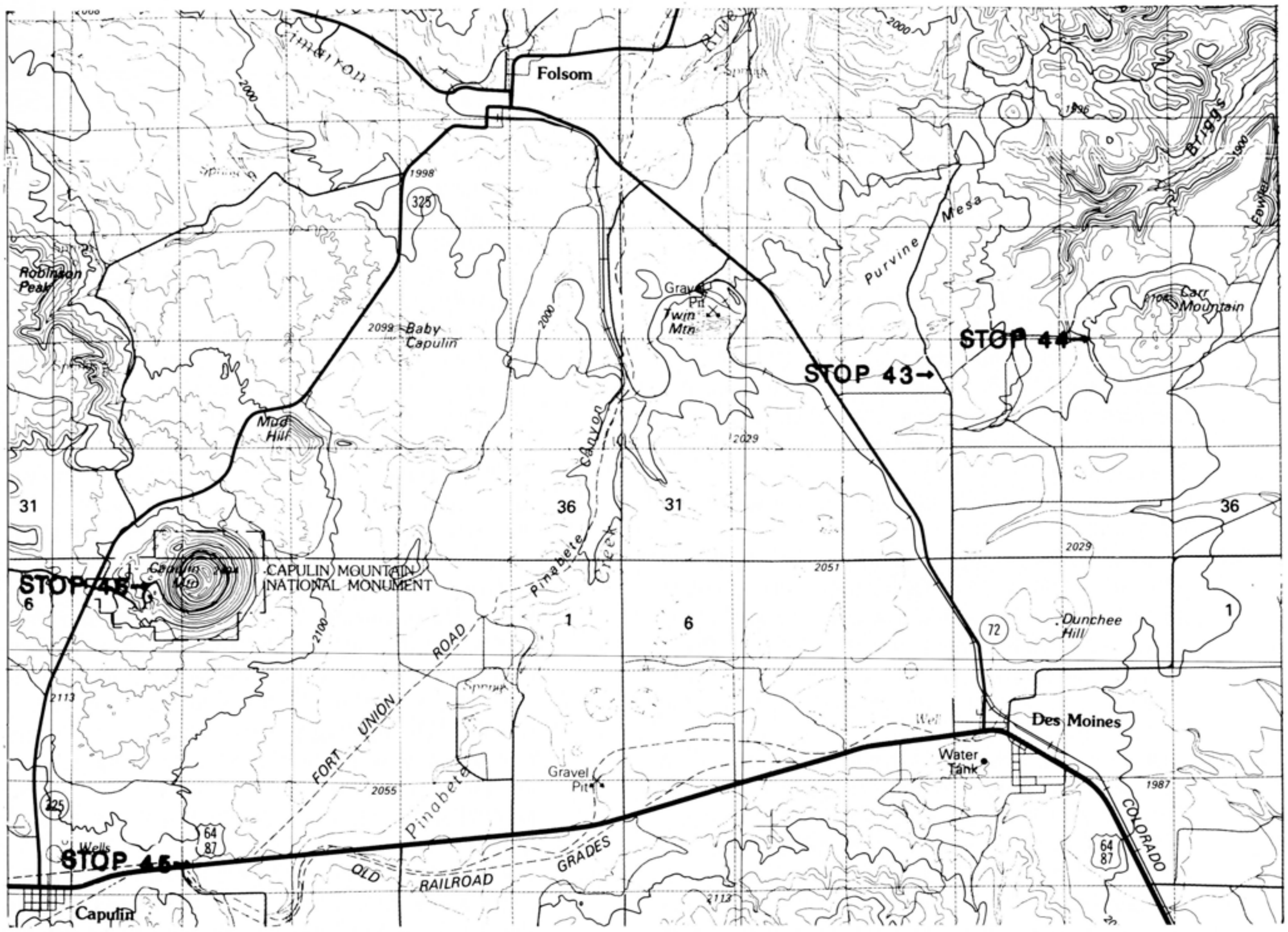

FIGURE 30—Location map for Stops 43 through 46.

haüyne–melilite nephelinite. Park near cinder pit at base of volcanic cone. The most highly mafic and alkalic lavas of the Raton–Clayton field came from this vent (SiO_2 ~36%, NA_2O ~5% CaO ~16%; see analyses nos. 6 and 7, Table 8). The cinders in this pit (sample 290 of Stormer, 1972a) are of a rock type which has prominent blue phenocrysts of haüyne with olivine and sector-zoned Ti-rich clinopyroxene. The groundmass is very fine-grained and contains sparse melilite with nepheline, magnetite, olivine, pyroxene, and glass. The flow which mantles the cone above this pit is very similar in mineralogy (sample 284 of Stormer, 1972a; sample 28-9 of Phelps et al., 1983). A sample from the flow on the east side of this cone has the lowest silica content of any rock in this field (35.9%; sample 30-9 of Phelps et al., 1983). As noted at the previous stop, rocks with abundant feldspathoids are unknown from the Taos Plateau and Ocate volcanic fields, but are quite common in younger rocks of the later stages of the Raton–Clayton field. These highly undersaturated magmas were apparently erupted during approximately the same period of time as the Sierra Grande andesites and some of the early basaltic trachyandesites. A basanite from Emery Peak (2232 m), the cone 5 km (3 mi) north-northwest of here, has been dated at 1.8 Ma (Stormer, 1972b).

Return to junction of NM-325 with US-87/67 west of Des Moines. **4.6**

77.8 Junction of NM-325 with US-87/67. Turn right (west) toward Capulin. Good views of the 300 m high Capulin Volcano strombolian cinder cone (2494 m) to the right. The Capulin National Monument was established in 1916 to preserve this cone; the road to the crater rim was built in 1963. **7.0**

84.8 **STOP 45. Capulin flow.** Toe of Capulin flow exposed in roadcut adjacent to US-87/64. Flow of xenocrystic basaltic andesite from Capulin Volcano. This rock is typical of the basalt to basaltic andesite magma that was erupted in the latest phase of volcanism in the Raton–Clayton field (trachybasalt to trachybasaltic andesite in the IUGS chemical classification). All have conspicuous olivine phenocrysts set in a fine-grained groundmass of plagioclase microlites. In the more siliceous varieties such as this flow, the groundmass consists of microlites in a glass matrix. Quartz xenocrysts with well-developed reaction rims, and large sodic plagioclase with extensively resorbed or "fritted" cores and more calcic rims are also characteristic, though they do vary in abundance and the degree of resorption. This rock type appears to be analogous to the silicic alkalic basalt to xenocrystic basaltic andesite of the Taos Plateau and Ocate volcanic field, and some particularly silica-rich samples resemble the olivine andesite of these fields.

Specimen 111 of Stormer (1972a) is from this outcrop (see analysis no. 9, Table 8). The silica content is about 55% and the olivine, xenocrystic quartz, and plagioclase are readily observable. In general, flows of this rock type overlie all other rock types, and the cones and flow tops are not significantly eroded. This flow was probably erupted between 10,000 and 4400 years ago (Baldwin and Muehlberger, 1959). **(Note: If you wish to collect samples of this rock type, take them here—no collecting of samples is allowed in the National Monument.)**

Continue on to Capulin National Monument. **1.9**

86.7 Town of Capulin and junction of US-87/64 and NM-325. Turn right to Capulin National Monument (3 mi). The road approaching the entrance to Capulin Volcano National Monument runs on top of flows from the Capulin vent. Squeeze-ups and tumuli can be seen standing above the general surface of the blocky flow. **2.9**

89.6 Capulin Volcano National Monument entrance. Turn right and proceed to Monument Headquarters. **0.5**

90.1 Continue past Visitor Center to parking area at rim of Capulin cone. The road makes a sharp left turn (north) and passes a small valley (picnic area) that was formed by the natural levees of the flow that went south of the mountain. The road then makes a sharp right (south) turn and begins spiraling up the mountain to a parking lot on the west rim. **2.1**

92.2 Rim Trail parking area, west rim of Capulin Volcano. **Note: No collecting or disturbing rocks, plants, or animals is allowed within the National Monument. This law is very strictly enforced here. Take only photographs.**

STOP 46. Capulin Volcano. The area from which the Capulin flows issued is at the west base of the cone, directly below this parking lot. Flows went both north and south from this point. Looking west and northwest from the parking lot, one can see the basalt-capped surface of the high mesas rising from the low cliffs about 3.2 km away toward the northwest where they are over 760 m above the Canadian River at Raton. The basalts that cap these mesas flowed down broad valleys. They then protected the former valley floor while erosion proceeded elsewhere. In the next episode of volcanism, the flows occupied slightly lower valleys. Repetition of this cycle has produced an inverted stratigraphy in which the basalts capping the highest mesas are the oldest. The most recent (Capulin) flows are essentially at the present erosional level.

On top of these mesas are two of the mafic feldspathoidal vents, Jose Butte (2460 m, azimuth N40°W, 6.4 km) and Robinson Peak (2450 m, N70°W, 8 km). Between these, farther in the distance, can be seen the conical, hornblende dacite domes of Red Mountain (2567 m, N50°W, 20.9 km) [Stop 47] and Towndrow Peak (2620 m, N62°W, 29 km). To the southwest is a number of basalt-capped mesas and two more large hornblende dacite volcanoes, Laughlin Peak (2688 m, S50°W, 25.7 km) and Palo Blanco (2555 m, S25°W, 24 km). Horseshoe Crater (2370 m, S25°W, 1.3 km), a treeless cone in front of Palo Blanco, is another xenocrystic basaltic andesite cinder cone of Capulin Basalt.

Walking the crater rim trail from the south end of the parking area provides the best views of the Capulin flows to the south. To the south and southeast the flows spread out over relatively flat terrain in a lobate pattern. The concentric pattern of pressure ridges on the surface of the flow can easily be seen. Sierra Grande (summit S45°E, 12.9 km) can be seen on the other side of US-64/87. This shield of two-pyroxene andesite flows is about 11.3 km across and almost 610 m above the surrounding land surface.

To the east of Capulin Mountain are spectacular views out across the high plains. On a clear day, Rabbit Ear Mountain (S68°E, 70.8 km) north of Clayton can be seen across the northeastern shoulder of Sierra Grande. To the northeast, Carr Mountain (N75°E, 14.5 km), a low, eroded cone, is the most extreme in composition of the mafic feldspathoidal centers (see Stop 44). Emery Peak (2232 m, N45°E, 14.5 km) is another mafic feldspathoidal vent.

In the foreground to the north and northeast are a number of vents younger than Capulin Mountain. The stratigraphy of these lavas was established by Baldwin and Muehlberger (1959), and they give a detailed description of the features in this area. The most distinctive feature is the small cinder cone named Baby Capulin (N40°E, 4.8 km). Baby Capulin (2099 m) erupted lavas similar to those of Capulin Mountain but with few of the distinctive quartz and feldspar xenocrysts. The lava from Baby Capulin flowed almost 32 km down the Dry Cimarron River to the northeast beyond Emery Peak. Twin Mountain (2090 m) is an elongated cinder cone 3 km east of Baby Capulin. It has been extensively mined for cinders and not much of its original form remains. Beyond it to the east is a line of four low vents, the Purvine Mesa vents. Twin Buttes (2185 m) and the Purvine Mesa vents were probably produced by essentially contemporaneous fissure eruptions and are the latest volcanic activity in the area. The eroded pyroclastic cone of Mud Hill lies between Capulin and Baby Capulin. This is an older vent of mafic feldspathoidal magma that is partially covered by the Capulin-age lavas.

Return to the monument entrance on NM-325. **2.6**

94.8 Turn right on NM-325. Drive north toward Folsom, New Mexico, across a northern lobe of the Capulin flow. **6.1**

100.9 Town of Folsom (1950 m). Stay on NM-325 as it turns left, crosses the railroad tracks, then turns right.

It may be hard to believe now, but around the year 1900 Folsom was a thriving railroad and mercantile center with the largest cattle shipping pens west of Fort Worth (Texas). There were three large stores, two hotels, restaurants and a number of saloons, a school, and two churches. In August of 1899, the famous outlaw Thomas "Black Jack" Ketchum was shot and captured between here and Des Moines after an aborted attempt to rob a train. He was tried and convicted in Santa Fe and hanged in Clayton in April 1901. **0.5**

101.4 Junction of NM-325 and NM-72. Turn left (north) on NM-72. **0.2**

101.6 Cross bridge. Junction of NM-72 and NM-456. Turn left (west) on NM-72 toward Yankee. **2.9**

104.5 The lava flow south of the road is a haüyne-bearing nephelinite erupted from Bellisle cone (western Johnson Mesa). **3.3**

107.8 Colfax County line. **0.9**

108.7 The road here cuts a small vent of Capulin-type xenocrystic basaltic andesite as the road mounts the terrace above Hereford Park. These flows underlie alluvial deposits in the valley to the left (south), in which the first Folsom Man points (distinctive fluted spear points made by early North American Indians) together with *Bison antiquus* bones were found. This was the first known evidence for the presence of ancient man in North America (ca 10,000 y. BP). These artifacts were initially discovered in 1908 by Geroge McJunkin, a black cowboy and foreman of a local ranch. Radiocarbon dating of the Folsom Man sites provide age constraints for the flows from Capulin volcano which overlie the alluvial beds containing the Folsom Man points (Baldwin and Muehlberger, 1959). **2.2**

110.9 Robinson Mountain (SSW) and Jose Butte (SSE) are two basanite cinder cones. Flows from Robinson Mountain contain haüyne. The highly alkalic nephelinite and basanite vents are concentrated in the north-central part of the volcanic field between Carr Mountain (Stop 44) and Bellisle Mountain on the mesa 10 km west of this point (Fig. 24). **0.6**

111.5 Historical Marker for the Folson Archaeological Site. **1.4**

112.9 The road climbs through Clayton and Raton basalts toward the rim of Johnson Mesa (2275 m). **0.4**

113.3 Rim of Johnson Mesa. The dacite cone of Red Mountain (2567 m) is visible ahead. **4.5**

117.8 **STOP 47. Red Mountain dacite.** Stone ranch house to right (north) side of road (2400 m). Park and ask permission to walk to the outcrops behind the house. This is the type locality for a distinctive hornblende dacite which occurs as series of domes and eroded plugs in the west-central part of the volcanic field. Towndrow Peak (2620 m) to the east, Palo Blanco (2555 m) to the south, and Laughlin Peak (2688 m) to the south-southwest are prominent examples of this rock type. Most localities are fairly silicic (67–70% SiO_2; see analyses nos. 15 and 16 in Table 8) and contain phenocrysts of hornblende and plagioclase in a groundmass that is largely glass with feldspar microlites. Biotite and quartz are rare but were found in a few samples from the southeast Pine Buttes domes. The rock here at Red Mountain is very similar to sample 277 of Stormer (1972a). Sample RMD in table 4 of Baldwin and Muehlberger (1959) is an older analysis apparently from this dome. In the IUGS chemical classification these rocks straddle the boundary between the alkali-rich dacite and low-silica rhyolite fields.

A date on a plug near Raton by Stormer (1972b) and several dates referenced by Staatz (1986) on similar domes range between 8.2 and 7.7 Ma. It thus appears that these domes may have been erupted during the initial volcanic event of the field, or at least concurrently with the earliest basaltic rocks. Their compositions and mineralogy are almost identical to the dacite of Cerro Chiflo in the Taos Plateau volcanic field (Stop 19). Although this rock type is much more abundant in the Raton–Clayton field, it is interesting to note that this hydrous and relatively silicic type of magma occurred early in the development of both fields. Unpublished isotope data suggest an origin dominated by lower-crust melting. **2.2**

120.0 Bellisle Mountain to the north. This low cinder cone was the source of a haüyne-bearing nephelinite flow that extended from this area over the edge of the mesa and down the Dry Cimarron valley more than 30 km eastward to a point north of Capulin Mountain. **1.4**

121.4 St. Johns Methodist Episcopal Church on left side of road was established in 1897, when there was a significant permanent population on the mesa and travel to towns was difficult. **2.8**

124.2 Towndrow Mountain (dacite dome) immediately to the south. **1.7**

125.9 Road bends to the right (north) sharply. View of Barela Mesa (previously Barrilla Mesa, 2620 m) and Horseshoe Mesa (2675 m) ahead to the northwest. The lavas capping Barela Mesa are part of the oldest basalt sequence (~7 Ma) of alkali olivine basalt (IUGS—trachybasalt), as are those of Johnson Mesa on which we are traveling. Horseshoe Mesa at a slightly lower level was capped by later flows of transitional olivine basalt (3.5 Ma, Stormer, 1972b; IUGS—subalkali basalt). **0.5**

126.4 From this point is a view to the northeast over the edge of the mesa. On the horizon Mesa de Maya (2100 m) in southeastern Colorado can be seen. Mesa de Maya is capped by basalts of transitional olivine basalt (3.2–3.5 Ma) which are considered the northeasternmost outlier of the Raton–Clayton field. They extend southeastward into the western Oklahoma Panhandle, where they form Black Mesa (1500 m, the highest point in Oklahoma). **1.0**

127.4 **STOP 48. Raton Basalt** (2400 m). Park to right above left curve and outcrop of basalt flow capping mesa. This flow was dated at 7.2 Ma (Stormer, 1972b). Here it overlies sandstones of the Raton Formation of Late Cretaceous and Paleocene age. This flow is an alkali olivine basalt (Sample 117 of Stormer 1972a; IUGS—trachybasalt; see analysis no. 3 in Table 8). It is very similar to the early basalt seen at Stop 37. It contains phenocrysts of olivine and augite in a fine-grained groundmass of plagioclase laths and intersertal augite and titanomagnetite. The alkali olivine basalt type seen here seems to be dominant on the higher mesas formed during the earliest pulse of basaltic magmatism. These lavas are most voluminous here in the northwestern part of the field and are not found in the eastern half. The transitional olivine basalt type, seen from here on Bartlett Mesa to the west, is roughly contemporaneous with the Servilleta Basalt of the Taos Plateau and similar basalts in the Ocate field. It is also dominant type in the eastern part of the Raton–Clayton field and in its northeastward extension to Mesa de Maya.

Continue west on NM-72 as the road drops off the top of Johnson Mesa and down the canyon toward Raton. At this point we are west of the Sierra Grande arch and well into the early Tertiary Raton Basin. Late Cretaceous and Paleocene sedimentary units that were deposited in the basin contain many coal beds. Large-scale coal mining operations exploiting these strata are located mostly to the west of Raton and near Trinidad, Colorado (~20 mi to the northwest), but there are portals and dumps of many small coal mines on the slopes of this canyon. **2.8**

130.2 The low hill directly ahead, Yankee Volcano (2375 m), is the westernmost of the mafic feldspathoidal cones. The cone and flow which can be seen at a number of points to the left of the road for several miles ahead are topographically much lower than the surface of the high mesas surrounding us. This indicates that this nephelinite postdates the period of transitional basalt volcanism and is contemporaneous with the other mafic feldspathoidal vents we have seen to the east. Petrographically it is a fine-grained nephelinite (sample 116 of Stormer, 172a; NB1 in table 4 of Baldwin and Muehlberger, 1959). **2.3**

132.5 The former town of Yankee was located here. **1.8**

134.3 Bear left to Raton. The road to Sugarite State Park and Lake Maloya joins from the right (NM-526). The Cretaceous–Tertiary boundary sequence is locally exposed in Sugarite Canyon (Pillmore and Flores, 1987). **0.5**

134.8 View ahead of Eagle Tail Mesa (2366 m, 25 km south). This center produced xenocrystic basalts and basaltic andesites similar to those of Capulin Mountain (samples 147 and 279 of Stormer, 1972a, were from this center). Its apron of flows stands higher above the present erosional level which may indicate that it is somewhat older than the Capulin lavas. However, a higher rate of erosion in the Canadian River valley must also be taken into account. **3.2**

138.0 Junction of NM-72 and I-25. Take I-25 south toward Santa Fe and Albuquerque. **17.3**

155.3 Tinaja exit. This prominent dike (Eagle Rock) is a lamprophyre (camptonite) probably related to the mid-Tertiary sill complex we visited on the previous day (Stop 36 is about 30 km southwest). It may be contemporaneous with similar dikes in the Spanish Peaks region (70–100 km northwest) and on the plains of eastern Colorado which have a similar east–west trend.

References

Aldrich, M. J., Jr., Chapin, C. E., and Laughlin, A. W., 1986, Stress history and tectonic development of the Rio Grande rift, New Mexico: Journal of Geophysical Research, 91: 6199–6211.

Baldridge, W. S., 1979, Petrology and petrogenesis of Plio-Pleistocene basaltic rocks from the central Rio Grande rift, New Mexico, and their relation to rift structure; *in* Riecker, R. E. (ed.), Rio Grande rift—Tectonics and magmatism: American Geophysical Union, Washington, D.C., pp. 323–353.

Baldridge, W. S., Olsen, K. H., and Callender, J. F., 1984, Rio Grande rift, problems and perspectives; *in* Baldridge, W. A., Dickerson, P. W., Riecker, R. E., and Zidek, J. (eds.), Rio Grande rift—northern New Mexico: New Mexico Geological Society, Guidebook 35: 1–12.

Baldridge, W. S., Perry, F. V., and Shafiqullah, M., 1987, Late Cenozoic volcanism of the southeastern Colorado Plateau—Volcanic geology of the Lucero area, New Mexico: Geological Society of America, Bulletin 99(4): 463–470.

Baldridge, W. S., Damon, P. E., Shafiqullah, M., and Bridwell, R. J., 1980, Evolution of the central Rio Grande rift, New Mexico: New potassium–argon ages: Earth and Planetary Science Letters, 51: 309–321.

Baldwin, B., and Muehlberger, W. R., 1959, Geologic studies of Union County, New Mexico: New Mexico Bureau of Mines & Mineral Resources, Bulletin 63: 171 pp.

Bartlett, R. D., 1984, Geology of an Oligocene-age acid hot spring, San Luis Hills, Conejos and Costilla Counties, Colorado: Unpublished M.A. thesis, Colorado State University, Fort Collins, 111 pp.

Blake, S., and Campbell, I. H., 1986, The dynamics of magma-mixing during flow in volcanic conduits: Contributions to Mineralogy and Petrology, 94: 72–81.

Brown, L. L., and Golombek, M. P., 1985, Tectonic rotations within the Rio Grande rift—Evidence from paleomagnetic studies: Journal of Geophysical Research, 90: 790–802.

Buck, W. R., 1986, Small-scale convection induced by passive rifting: the cause for uplift of rift shoulders: Earth and Planetary Science Letters, 77: 362–372.

Burroughs, R. L., 1972, Geology of the San Luis Hills, south-central Colorado: Unpublished Ph.D. dissertation, University of New Mexico, Albuquerque, 139 pp.

Burroughs, R. L., 1978, Alamosa to Antonito, Colorado; *in* Hawley, J. W. (compiler), Guidebook to the Rio Grande rift in New Mexico and Colorado: New Mexico Bureau of Mines & Mineral Resources, Circular 163: 33–36.

Chapin, C. E., 1971, The Rio Grande rift; Part 1. Modifications and additions: New Mexico Geological Society, Guidebook 22: 191–202.

Chapin, C. E., 1979, Evolution of the Rio Grande rift—a summary; *in* Riecker, R. E. (ed.), Rio Grande rift—Tectonics and magmatism: American Geophysical Union, Washington, D.C., pp. 1–5.

Chapin, C. E., 1988, Axial basins of the northern and central Rio Grande rifts; *in* Sloss, L. L. (ed.), Sedimentary cover—North American craton: U.S., The Geology of North America: Geological Society of America, v. D-2: 165–170.

Chapin, C. E., and Lindley, J. I., 1986, Potassium metasomatism of igneous rocks in detachment terranes and other sedimentary basins: Economic Implications; *in* Beatty, B., and Wilkinson, P. A. K. (eds.), Frontiers in geology and ore deposits of Arizona and the Southwest: Arizona Geological Society Digest, 16: 118–126.

Chapin, C. E., and Seager, W. R., 1975, Evolution of the Rio Grande rift in Socorro and Las Cruces areas: New Mexico Geological Society, Guidebook 26: 297–321.

Collins, R. F., 1949, Volcanic rocks of northeastern New Mexico: Geological Society of America, Bulletin 60(6): 1017–1040.

Coney, P. J., and Reynolds, S. J., 1977, Cordilleran Benioff zones: Nature, 270: 403–406.

Cordell, L., 1978, Regional geophysical setting of the Rio Grande rift:

Geological Society of America, Bulletin, 89: 1073–1090.

Cordell, L., Long, C. L., and Jones, D. W., 1986, Geophysical expression of the batholith beneath Questa caldera, New Mexico: Journal of Geophysical Research, 90: 11263–11274.

Cross, T. A., and Pilger, R. H., 1978, Constraints on absolute motion and plate interaction inferred from Cenozoic igneous activity in the western United States: American Journal of Science, 278: 865–902.

Crossey, L. J., 1979, Intraflow chemical variations in Servilleta basalts, Taos Plateau, New Mexico: Unpublished M.S. thesis, Washington University, St. Louis, Missouri, 105 pp.

Curtis, B. F. (ed.), 1975, Cenozoic history of the southern Rocky Mountains: Geological Society of America, Memoir 144: 279 pp.

De Voogd, B., Serpa, L., and Brown, L., 1988, Crustal extension and magmatic processes—COCORP profiles from Death Valley and the Rio Grande rift: Geological Society of America, Bulletin, 100: 1550–1567.

Decker, E. R., Bucher, G. L., Buelow, K. L., and Heasler, H. P., 1984, Preliminary interpretation of heat flow and radioactivity in the Rio Grande rift zone in central and northern Colorado; *in* Baldridge, W. A., Dickerson, P. W., Riecker, R. E., and Zidek, J. (eds.), Rio Grande rift—northern New Mexico: New Mexico Geological Society, Guidebook 35: 45–50.

DeMark, R. S., 1984, Minerals of Point of Rocks, New Mexico: The Mineralogical Record, pp. 149–156.

Dungan, M. A., 1987, Open system magmatic evolution of the Taos Plateau volcanic field, northern New Mexico—The genesis of cryptic hybrids: Journal of Petrology, 28: 955–977.

Dungan, M. A., Lindstrom, M. M., McMillan, N. J., Moorbath, S., Hoefs, J., and Haskin, L. A., 1986, Open system magmatic evolution of the Taos Plateau volcanic field, northern New Mexico—The petrology and geochemistry of the Servilleta Basalt: Journal of Geophysical Research, 91: 5999–6028.

Dungan, M. A., Phelps, D., Stormer, J. C., Blanchard, D. P., Nielsen, R., McMillan, N., and Thompson, R., 1981, Late Cenozoic volcanism of the northern New Mexico–southern Colorado portion of the Rio Grande rift (abs.); *in* Processes of planetary rifting: Lunar and Planetary Institute, Houston, Texas, pp. 137–140.

Dungan, M. A., Muehlberger, W. R., Leininger, L., Peterson, C., McMillan, N. J., Gunn, G., Lindstrom, M., and Haskin, L., 1984, Volcanic and sedimentary stratigraphy of the Rio Grande gorge and the late Cenozoic geologic evolution of the southern San Luis Valley; *in* Baldridge, W. A., Dickerson, P. W., Riecker, R. E., and Zidek, J. (eds.), Rio Grande rift—northern New Mexico: New Mexico Geological Society, Guidebook 35: 157–170.

Frey, F. A., Green, D. H., and Roy, S. D., 1978, Integrated models of basalt petrogenesis—a study of quartz tholeiites to olivine melilites from southeastern Australia utilizing geochemical and experimental petrologic data: Journal of Petrology, 19: 463–513.

Galusha, T., and Blick, J. C., 1971, Stratigraphy of the Santa Fe Group, New Mexico: American Museum of Natural History, Bulletin 144: 127 pp.

Golombek, M. P., 1983, Geology, structure, and tectonics of the Pajarito fault zone in the Española basin of the Rio Grande rift, New Mexico: Geological Society of America, Bulletin, 94: 192–205.

Golombek, M. P., McGill, G. E., and Brown, L. L., 1983, Tectonic and geologic evolution of the Española basin, Rio Grande rift—structure, rate of extension, and relation to the state of stress in the western United States: Tectonophysics, 94: 483–507.

Grambling, J. A., Williams, M. L., and Mawer, C. K., 1988, Proterozoic tectonic assembly of New Mexico: Geology, 16: 724–727.

Hagstrum, J. T., and Johnson, C. M., 1986, A paleomagnetic and isotopic study of chemical remanent magnetization associated with hydrothermal alteration in the pluton of Rio Hondo, near Questa, New Mexico: Earth and Planetary Science Letters, 78: 296–314.

Hagstrum, J. T., and Lipman, P. W., 1986, Paleomagnetism of the structurally deformed Latir volcanic field, northern New Mexico—relations to formation of the Questa caldera and development of the Rio Grande rift: Journal of Geophysical Research, 91: 7383–7402.

Hagstrum, J. T., Lipman, P. W., and Elston, D. P., 1982, Paleomagnetic evidence bearing on the structural development of the Latir volcanic field near Questa, New Mexico: Journal of Geophysical Research, 87: 7833–7842.

Hawley, J. W. (ed.), 1978, Guidebook to the Rio Grande rift in New Mexico and Colorado: New Mexico Bureau of Mines & Mineral Resources, Circular 163: 241 pp.

Henry, C. D., and Price, J. G., 1986, Early basin and range development in Trans-Pecos Texas and adjacent Chihuahua: magmatism and orientation, timing, and style of extension: Journal of Geophysical Research, 91: 6213–6224.

Holcombe, R. J., and Callender, J. F., 1982, Structural analysis and stratigraphic problems of Precambrian rocks of the Picuris Range, New Mexico: Geological Society of America, Bulletin, 93: 138–149.

Holcombe, R. J., Bauer, P. W., and Callender, J. F., 1986, A kinematic model for polyphase deformation of Proterozoic rocks, Picuris Range, northern New Mexico, U.S.A.; *in* Aldrich, M. J., Jr., and Laughlin, A. W. (eds.), Proceedings of the Sixth International Conference on Basement Tectonics: U.S. International Basement Tectonics Association, Salt Lake City, Utah, p. 199.

Johnson, C. M., and Lipman, P. W., 1986, The Questa magmatic system—Sr, Nd and Pb isotope geochemistry of the Latir volcanic field and associated intrusive rocks and relations to development of a crustal magmatic center: Unpublished Ph.D. dissertation, Stanford University, Stanford, California, chapter 3: 202–275.

Johnson, C. M., and Lipman, P. W., 1988, Origin of metaluminous and alkaline volcanic rocks of the Latir volcanic field, northern Rio Grande rift, New Mexico: Contribution to Mineralogy and Petrology, 100: 107–128.

Johnson, C. M., Czamanske, G. K., and Lipman, P. W., 1986, The Questa magmatic system: Geochemistry of plutonic rocks associated with the Latir volcanic field and relations to extensional tectonism: Unpublished Ph.D. dissertation, Stanford University, Stanford, California, chapter 2: 101–202.

Karlstrom, K. E., Bowring, S. A., and Conway, C. M., 1987, Tectonic significance of an Early Proterozoic two-province boundary in central Arizona: Geological Society of America, Bulletin, 99: 529–538.

Keller, G. R., 1986, Introduction to special section on the Rio Grande rift: Journal of Geophysical Research, 91: 6142.

Keller, G. R., Cordell, L., Davis, G. H., Peeples, W. J., and White, G., 1984, A geophysical study of the San Luis Basin; *in* Baldridge, W. A., Dickerson, P. W., Riecker, R. E., and Zidek, J. (eds.), Rio Grande rift—northern New Mexico: New Mexico Geological Society, Guidebook 35: 51–57.

Kelly, V. C., 1979, Tectonics, middle Rio Grande rift, New Mexico; *in* Riecker, R. C. (ed.), Rio Grande rift—Tectonics and magmatism: American Geophysical Union, Washington, D.C., pp. 57–70.

Kinsel, E. P., 1986, Petrology of silicic alkalic basalts, xenocrystic basaltic andesites, and crustal xenoliths from the Taos Plateau volcanic field, north-central New Mexico: Unpublished M.S. thesis, Southern Methodist University, Dallas, Texas, 138 pp.

Kleinkopf, D. M., Peterson, D. L., and Johnson, R. B., 1970, Reconnaissance geophysical studies of the Trinidad quadrangle, south-central Colorado: U.S. Geological Survey, Professional Paper 700-B: 78–85.

Kouichi, A., and Sunagawa, I., 1985, A model for mixing basaltic and dacite magmas as deduced from experimental data: Contributions to Mineralogy and Petrology, 89: 17–23.

Koyaguchi, T., 1985, Magma mixing in a conduit: Journal of Volcanology and Geothermal Research, 25: 365–369.

Lanphere, M. A., 1988, High-resolution $^{40}Ar/^{39}Ar$ chronology of Oligocene volcanic rocks, San Juan Mountains, CO: Geochimica et Cosmochimica Acta, 52: 1425–1434.

Laughlin, A. W., Brookins, D. G., Damon, P. E., and Shafiqullah, M., 1979, Late Cenozoic volcanism of the central Jemez zone, Arizona–New Mexico: Isochron West, no. 25: 5–8.

Le Bas, M. J., Le Maitre, R. W., Streckeisen, A., and Zanettin, B., 1986, A chemical classification of volcanic rocks based on the total alkali–silica diagram (Recommendations of the IUGS Subcommission on the Systematics of Igneous Rocks): Journal of Petrology, 27(3): 745–750.

Lipman, P. W., 1969, Alkalic and tholeiitic basaltic volcanism related to the Rio Grande depression, southern Colorado and northern New Mexico: Geological Society of America, Bulletin, 80: 1343–1354.

Lipman, P. W., 1975, Evolution of the Platoro caldera complex and related volcanic rocks, southeastern San Juan Mountains, Colorado: U.S. Geological Survey, Professional Paper 852: 128 pp.

Lipman, P. W., 1981, Volcano-tectonic setting of Tertiary ore deposits, Southern Rocky Mountains; *in* Dickinson, W. R., and Payne, W. D. (eds.), Relations of tectonics to ore deposits in the southern Cordillera: Arizona Geological Society Digest, 14: 199–213.

Lipman, P. W., 1983, The Miocene Questa caldera, northern New Mexico—relation to batholith emplacement and associated molybdenum mineralization: Denver Region Exploration Geological Society Symposium, Proceedings, pp. 133–147.

Lipman, P. W., 1988, Evolution of silicic magma in the upper crust—the mid-Tertiary Latir volcanic field and its cogenetic granitic batholith, northern New Mexico, USA: Royal Society of Edinburgh: Earth Science, Transactions, 79: 265–288.

Lipman, P. W., and Mehnert, H. H., 1975, Late Cenozoic basaltic volcanism and development of the Rio Grande depression in the southern

Rocky Mountains; *in* Curtis, B. F. (ed.), Cenozoic history of the southern Rocky Mountains: Geological Society of America, Memoir 144: 119–154.

Lipman, P. W., and Mehnert, H. H., 1979, The Taos Plateau volcanic field, northern Rio Grande rift, New Mexico; *in* Riecker, R. C. (ed.), Rio Grande rift—Tectonics and magmatism: American Geophysical Union, Washington, D.C., pp. 289–311.

Lipman, P. W., and Reed, J. C., Jr., 1984, Second-day road log from Taos to Hondo Canyon, Questa, Red River, Amalia, and back to Taos; *in* Baldridge, W. A., Dickerson, P. W., Riecker, R. E., and Zidek, J. (eds.), Rio Grande rift—northern New Mexico: New Mexico Geological Society, Guidebook 35: 321–347.

Lipman, P. W., and Reed, J. C., Jr. (in press), Geologic map of the Latir volcanic field and adjacent areas, northern New Mexico: U.S. Geological Survey, Miscellaneous Investigations Series Map I-1907.

Lipman, P. W., Mehnert, H. H., and Naeser, C. W., 1986, Evolution of the Latir volcanic field, northern New Mexico, and its relation to the Rio Grande rift, as indicated by potassium–argon and fission track dating: Journal of Geophysical Research, 91: 6329–6345.

Lipman, P. W., Steven, T. A., and Mehnert, H. H., 1970, Volcanic history of the San Juan Mountains, Colorado, as indicated by potassium–argon dating: Geological Society of America, Bulletin, 81: 2329–2352.

Lipman, P. W., Doe, B. R., Hedge, C. E., and Steven, T. A., 1978, Petrologic evolution of the San Juan volcanic field, southwestern Colorado: Pb and Sr isotope evidence: Geological Society of America, Bulletin, 89: 59–82.

Long, C. L., 1986, Regional audiomagnetotelluric study of the Questa caldera, New Mexico: Journal of Geophysical Research, 90: 11270–11274.

Luedke, R. G., and Smith, R. L., 1978, Map showing the distribution, composition, and age of the late Cenozoic volcanic centers in Arizona and New Mexico: U.S. Geological Survey, Miscellaneous Investigations Series Map I-1091A, scale 1:1,000,000.

Machette, M. N., and Personius, S. F., 1984, Map of Quaternary and Pliocene faults in the eastern part of the Aztec 1° × 2° quadrangle and the western part of the Raton 1° × 2° quadrangle, northern New Mexico: U.S. Geological Survey, Miscellaneous Field Studies Map MF-1465-B, scale 1:250,000.

Manley, K., 1979, Structure and stratigraphy of the Española basin, Rio Grande rift, New Mexico; *in* Riecker, R. E. (ed.), Rio Grande rift—Tectonics and magmatism: American Geophysical Union, Washington, D.C., pp. 71–86.

Mayo, E. B., 1958, Lineament tectonics and some ore districts of the southwest: Mining Engineering, 10: 1169–1175.

McMillan, N. J., and Dungan, M. A., 1986, Magma mixing as a petrogenetic process in the development of the Taos Plateau volcanic field, New Mexico: Journal of Geophysical Research, 91: 6029–6045.

McMillan, N. J., and Dungan, M. A., 1988, Open system magmatic evolution of the Taos Plateau volcanic field, northern New Mexico, 3—Andesites and dacites: Journal of Petrology, 29: 527–557.

Menges, C., 1987, Temporal and spatial segmentation of Plio-Quaternary fault rupture along the base of the western Sangre de Cristo mountain front, northern New Mexico; *in* Menges, C., Enzel, Y., and Harrison, B. (eds.), Quaternary tectonics, landform evolution, soil chronologies and glacial deposits—north Rio Grande rift of New Mexico: Friends of the Pleistocene, Rocky Mountain Cell Guidebook, October 8–11, pp. 71–93.

Menges, C., Enzel, Y., and Harrison, B. (eds.), 1987, Quaternary tectonics, landform evolution, soil chronologies and glacial deposits—northern Rio Grande rift of New Mexico: Friends of the Pleistocene, Rocky Mountain Cell, Guidebook, 213 pp.

Montgomery, A., 1953, Pre-Cambrian geology of the Picuris Range, north-central New Mexico: New Mexico Bureau of Mines & Mineral Resources, Bulletin 30: 89 pp.

Morgan, P., and Golombek, M., 1984, Factors controlling the phases and styles of extension in the northern Rio Grande rift; *in* Baldridge, W. A., Dickerson, P. W., Riecker, R. E., and Zidek, J. (eds.), Rio Grande rift—northern New Mexico: New Mexico Geological Society, Guidebook 35: 13–20.

Muehlberger, W. R., 1978, Frontal fault zone of northern Picuris Range; *in* Hawley, J. W. (ed.), Guidebook to the Rio Grande rift in New Mexico and Colorado: New Mexico Bureau of Mines & Mineral Resources, Circular 163: 44–46.

Muehlberger, W. R., 1979, The Embudo fault between Pilar and Arroyo Hondo, New Mexico; an active intracontinental transform fault; *in* Ingersoll, R. V., Woodward, L. A., and James, H. L. (eds.), Santa Fe Country: New Mexico Geological Society, Guidebook 30: 77–82.

Muehlberger, W. R., and Hawley, J. W., 1978, Rio Grande Gorge to Rio Embudo, New Mexico; *in* Hawley, J. W. (ed.), Guidebook to the Rio Grande rift in New Mexico and Colorado: New Mexico Bureau of Mines & Mineral Resources, Circular 163: 42–44.

Nielsen, K. C., 1972, Structural evolution of the Picuris Mountains, New Mexico: Unpublished M.S. thesis, University of North Carolina, Chapel Hill, 47 pp.

Nielsen, K. C., and Scott, T. E., 1979, Precambrian deformational history of the Picuris Mountains, New Mexico; *in* Ingersoll, R. V., Woodward, L. A., and James, H. L. (eds.), Santa Fe Country: New Mexico Geological Society, Guidebook 30: 113–120.

Nielsen, R. L., and Dungan, M. A., 1983, Low pressure mineral-melt equilibria in natural anhydrous mafic systems: Contributions to Mineralogy and Petrology, 84: 310–326.

Nielsen, R. L., and Dungan, M. A., 1985, The petrology and geochemistry of the Ocate volcanic field, north-central New Mexico: Geological Society of America, Bulletin, 96: 296–312.

O'Neill, J. M., and Mehnert, H. H. (in press), Petrology and physiographic evolution of the Ocate volcanic field, north-central New Mexico: U.S. Geological Survey, Professional Paper 1478.

Ozima, M., Kono, M., Kaneoka, I., Kinoshita, H., Kobayashi, K., Nagata, T., Larson, E. E., and Strangway, D. W., 1967, Paleomagnetism and potassium–argon ages of some volcanic rocks from the Rio Grande Gorge, New Mexico: Journal of Geophysical Research, 72: 2615–2621.

Perry, F. V., Baldrige, W. S., and DePaolo, D. J., 1987, Role of asthenosphere and lithosphere in the genesis of late Cenozoic basaltic rocks from the Rio Grande rift and adjacent regions of the southwestern United States: Journal of Geophysical Research, 92: 9193–9213.

Personius, S. F., and Machette, M. N., 1984, Quaternary and Pliocene faulting in the Taos Plateau region, northern New Mexico; *in* Baldridge, W. S., Dickerson, P. W., Riecker, R. E., and Zidek, J. (eds.), Rio Grande rift—northern New Mexico: New Mexico Geological Society, Guidebook 35: 83–90.

Phelps, D. W., Gust, D. A., and Wooden, J. L., 1983, Petrogenesis of mafic feldspathoidal lavas of the Raton–Clayton volcanic field, New Mexico: Contributions to Mineralogy and Petrology, 84: 182–190.

Pillmore, C. L., and Flores, R. M., 1987, Stratigraphy and depositional environments of the Cretaceous–Tertiary boundary clay and associated rocks, Raton basin, New Mexico and Colorado; *in* Fassett, J. E., and Rigby, J. K., Jr. (eds.), The Cretaceous–Tertiary boundary in the San Juan and Raton basins, New Mexico and Colorado: Geological Society of America, Special Paper 209: 111–130.

Price, J. G., and Henry, C. D., 1984, Stress orientations during Oligocene volcanism in Trans-Pecos Texas—timing the transition from Laramide compression to Basin and Range tension: Geology, 12: 238–241.

Price, J. G., Henry, C. D., Parker, D. F., and Barker, D. S., 1986, Igneous geology of Trans-Pecos Texas: Texas Bureau of Economic Geology, Guidebook 23: 360 pp.

Reed, J. C., Jr., Bickford, M. E., Premo, W. R., Aleinikoff, J. N., and Pallister, J. S., 1987, Evolution of the Early Proterozoic Colorado province—constraints from U–Pb geochronology: Geology, 15: 861–865.

Rehder, T. R., 1986, Stratigraphy, sedimentology, and petrography of the Picuris Formation in Ranchos de Taos and Tres Ritos quadrangles, north-central New Mexico: Unpublished M.S. thesis, Southern Methodist University, Dallas, Texas, 110 pp.

Riecker, R. E. (ed.), 1979, Rio Grande rift—Tectonics and magmatism: American Geophysical Union, Washington, D.C., 438 pp.

Rogers, K. L., Reppening, C. A., Forester, R. M., Larson, E. E., Hall, S. A., Smith, G. R., Anderson, E., and Brown, T. J., 1985, Middle Pleistocene (late Irvingtonian–Nebraskan) climatic changes in south-central Colorado: National Geographic Research, 1(4): 535–563.

Rosendahl, B. R., 1987, Architecture of continental rifts with special reference to east Africa: Annual Review of Earth and Planetary Sciences, 15: 445–503.

Scott, G. R., 1986, Historic trail maps of the Raton and Springer 30′ by 60′ quadrangles, New Mexico and Colorado: U.S. Geological Survey, Miscellaneous Investigations Series Map I-1641, scale 1:100,000.

Scott, G. R., and Pillmore, C. L. (in press), Geologic map of the Raton Quadrangle, New Mexico: U.S. Geological Survey, Miscellaneous Investigations Series Map, scale 1:100,000.

Scott, G. R., Wilcox, R. E., and Mehnert, H. H. (in press), Geology of the volcanic and subvolcanic rocks of the Raton–Springer area, Colfax County, New Mexico: U.S. Geological Survey, Professional Paper.

Seager, W. R., and Morgan, P., 1979, Rio Grande rift in southern New Mexico, west Texas, and northern Chihuahua; *in* Riecker, R. E. (ed.), Rio Grande rift—Tectonics and magmatism: American Geophysical Union, Washington, D.C., pp. 87–106.

Siebenthal, C. E., 1910, Geology and water resources of the San Luis

Valley, Colorado: U.S. Geological Survey, Water-Supply Paper 240: 128 pp.

Snyder, W. S., Dickinson, W. R., and Silberman, M. L., 1976, Tectonic implications of space-time patterns of Cenozoic magmatism in the western United States: Earth and Planetary Science Letters, 32: 91–106.

Staatz, M. H., 1986, Geologic map of the Pine Buttes quadrangle, Colfax County, New Mexico: U.S. Geological Survey, Geologic Quadrangle Map GQ-1591, scale 1:24,000.

Steven, T. A., 1975, Middle Tertiary volcanic field in the southern Rocky Mountains; *in* Curtis, B. F. (ed.), Cenozoic history of the southern Rocky Mountains: Geological Society of America, Memoir 144: 75–94.

Stormer, J. C., Jr., 1972a, Mineralogy and petrology of the Raton–Clayton volcanic field, northeastern New Mexico: Geological Society of America, Bulletin, 83: 3299–3322.

Stormer, J. C., Jr., 1972b, Ages and nature of volcanic activity on the southern High Plains, New Mexico and Colorado: Geological Society of America, Bulletin, 83: 2443–2448.

Stormer, J. C., Jr., 1981, The mineralogy and petrology of villiaumite bearing phonolite sills from northeastern New Mexico (abs.); Geological Society of America, Abstracts with Programs, 13: 561.

Stormer, J. C., Jr., and Carmichael, I. S. E., 1970, Villiaumite and the occurrence of fluoride minerals in igneous rocks: The American Mineralogist, 55: 126–134.

Thompson, R. A., and Dungan, M. A., 1985, The petrology and geochemistry of the Handkerchief Mesa mixed magma complex, San Juan Mountains, Colorado: Journal of Volcanology and Geothermal Research, 26: 251–274.

Thompson, R. A., and Machette, M. N., 1989, Geologic map of the San Luis Hills area, Conejos and Costilla Counties, Colorado: U.S. Geological Survey, Miscellaneous Investigations Map I-1906, scale 1:50,000.

Thompson, R. A., and Schilling, S. P., 1988, Generalized geologic maps of Brushy Mountain and Timber Mountain areas, Taos County, New Mexico: U.S. Geological Survey, Open-File Report 88-561, scales 1:11,900 and 1:15,625.

Thompson, R. A., Dungan, M. A., and Lipman, P. W., 1986, Multiple differentiation processes in early-rift calc-alkaline volcanics, northern Rio Grande rift, New Mexico: Journal of Geophysical Research, 91: 6046–6058.

Thompson, R. N., 1982, Magmatism of the British Tertiary volcanic province: Scottish Journal of Geology, 18: 49–107.

Tweto, O., 1979, The Rio Grande rift system in Colorado; *in* Riecker, R. C. (ed.), Rio Grande rift— Tectonics and magmatism: American Geophysical Union, Washington, D.C., pp. 33–56.

Wendlandt, R. F., and Morgan, P., 1982, Lithospheric thinning associated with rifting in East Africa: Nature, 298: 734–736.

Winograd, I. J., 1959, Ground-water conditions and geology of Sunshine Valley, western Taos County, New Mexico: New Mexico State Engineer Office, Technical Report 12: 70 pp.

Winograd, I. J., 1985, Commentary on hydrogeologic cross-section through Sunshine Valley, Taos County, New Mexico, by W. K. Summers and L. L. Hargis: New Mexico Geology, 7: 54–55.

Zielinski, R. A., and Lipman, P. W., 1976, Trace-element variations at Summer Coon volcano, San Juan Mountains, Colorado, and the origin of continental-interior andesite: Geological Society of America, Bulletin, 87: 1477–1485.

Zoback, M. L., Anderson, R. W., and Thompson, G. A., 1981, Cenozoic evolution of stress and style of tectonism of the Basin and Range province of the western United States: Royal Society of London, Philosophical Transactions (A), 300: 407–434.

Zuber, M. T., and Parmentier, E. M., 1986, Lithospheric necking—a dynamic model for rift morphology: Earth and Planetary Science Letters, 77: 373–383.

Selected conversion factors*

TO CONVERT	MULTIPLY BY	TO OBTAIN
Length		
inches, in	2.540	centimeters, cm
feet, ft	3.048×10^{-1}	meters, m
yards, yds	9.144×10^{-1}	m
statute miles, mi	1.609	kilometers, km
fathoms	1.829	m
angstroms, Å	1.0×10^{-8}	cm
Å	1.0×10^{-4}	micrometers, μm
Area		
in^2	6.452	cm^2
ft^2	9.29×10^{-2}	m^2
yds^2	8.361×10^{-1}	m^2
mi^2	2.590	km^2
acres	4.047×10^{3}	m^2
acres	4.047×10^{-1}	hectares, ha
Volume (wet and dry)		
in^3	1.639×10^{1}	cm^3
ft^3	2.832×10^{-2}	m^3
yds^3	7.646×10^{-1}	m^3
fluid ounces	2.957×10^{-2}	liters, l *or* L
quarts	9.463×10^{-1}	l
U.S. gallons, gal	3.785	l
U.S. gal	3.785×10^{-3}	m^3
acre-ft	1.234×10^{3}	m^3
barrels (oil), bbl	1.589×10^{-1}	m^3
Weight, mass		
ounces avoirdupois, avdp	2.8349×10^{1}	grams, gr
troy ounces, oz	3.1103×10^{1}	gr
pounds, lb	4.536×10^{-1}	kilograms, kg
long tons	1.016	metric tons, mt
short tons	9.078×10^{-1}	mt
oz mt^{-1}	3.43×10^{1}	parts per million, ppm
Velocity		
ft sec^{-1} (= ft/sec)	3.048×10^{-1}	m sec^{-1} (= m/sec)
mi hr^{-1}	1.6093	km hr^{-1}
mi hr^{-1}	4.470×10^{-1}	m sec^{-1}

TO CONVERT	MULTIPLY BY	TO OBTAIN
Pressure, stress		
lb in^{-2} (= lb/in^2), psi	7.03×10^{-2}	kg cm^{-2} (= kg/cm^2)
lb in^{-2}	6.804×10^{-2}	atmospheres, atm
lb in^{-2}	6.895×10^{3}	newtons (N)/m^2, N m^{-2}
atm	1.0333	kg cm^{-2}
atm	7.6×10^{2}	mm of Hg (at 0° C)
inches of Hg (at 0° C)	3.453×10^{-2}	kg cm^{-2}
bars, b	1.020	kg cm^{-2}
b	1.0×10^{6}	dynes cm^{-2}
b	9.869×10^{-1}	atm
b	1.0×10^{-1}	megapascals, MPa
Density		
lb in^{-3} (= lb/in^3)	2.768×10^{1}	gr cm^{-3} (= gr/cm^3)
Viscosity		
poises	1.0	gr cm^{-1} sec^{-1} *or* dynes cm^{-2}
Discharge		
U.S. gal min^{-1}, gpm	6.308×10^{-2}	l sec^{-1}
gpm	6.308×10^{-5}	m^3 sec^{-1}
ft^3 sec^{-1}	2.832×10^{-2}	m^3 sec^{-1}
Hydraulic conductivity		
U.S. gal day^{-1} ft^{-2}	4.720×10^{-7}	m sec^{-1}
Permeability		
darcies	9.870×10^{-13}	m^2
Transmissivity		
U.S. gal day^{-1} ft^{-1}	1.438×10^{-7}	m^2 sec^{-1}
U.S. gal min^{-1} ft^{-1}	2.072×10^{-1}	l sec^{-1} m^{-1}
Magnetic field intensity		
gausses	1.0×10^{5}	gammas
Energy, heat		
British thermal units, BTU	2.52×10^{-1}	calories, cal
BTU	1.0758×10^{2}	kilogram-meters, kgm
BTU lb^{-1}	5.56×10^{-1}	cal kg^{-1}
Temperature		
°C + 273	1.0	°K (Kelvin)
°C + 17.78	1.8	°F (Fahrenheit)
°F − 32	5/9	°C (Celsius)

**Divide by* the factor number to reverse conversions.
Exponents: for example 4.047×10^{3} (see acres) = 4,047; 9.29×10^{-2} (see ft^2) = 0.0929.

Editors: Charles E. Chapin, Jiri Zidek

Graphics: Monte M. Brown

Typeface: Display heads: Spartan
Text: Times

Presswork: Miehle Single Color Offset
Harris Single Color Offset

Binding: Smyth sewn with softbound cover

Paper: Cover on 17-pt. Kivar
Text on 70 lb white matte

Ink: Cover—PMS 320
Text—Black

Quantity: 2000

& Jiri Zidek, eds.

...SIONS TO VOLCANIC TERRANES IN THE WESTERN UNITED STATES, VOLUME I: SOUTHERN ROCKY MOUNTAIN REGION

New Mexico Bureau of Mines & Mineral Resources

Memoir 46